AGARD-CP-515

AGARD-CP-515

AGARD

ADVISORY GROUP FOR AEROSPACE RESEARCH & DEVELOPMENT
7 RUE ANCELLE 92200 NEUILLY SUR SEINE FRANCE

AGARD CONFERENCE PROCEEDINGS 515

High-Lift System Aerodynamics

(L'Aérodynamique des
Systèmes Hypersustentateurs)

Papers presented and discussions recorded at the 71st Fluid Dynamics Panel Meeting and at the Symposium held in Banff, Alberta, Canada, from 5th—8th October 1992.

NORTH ATLANTIC TREATY ORGANIZATION

Published September 1993

Availability on Back Cover

AGARD-CP-515

AGARD

ADVISORY GROUP FOR AEROSPACE RESEARCH & DEVELOPMENT
7 RUE ANCELLE 92200 NEUILLY SUR SEINE FRANCE

AGARD CONFERENCE PROCEEDINGS 515

High-Lift System Aerodynamics

(L'Aérodynamique des
Systèmes Hypersustentateurs)

Papers presented and discussions recorded at the 71st Fluid Dynamics Panel Meeting and at the Symposium held in Banff, Alberta, Canada, from 5th—8th October 1992.

North Atlantic Treaty Organization
Organisation du Traité de l'Atlantique Nord

The Mission of AGARD

According to its Charter, the mission of AGARD is to bring together the leading personalities of the NATO nations in the fields of science and technology relating to aerospace for the following purposes:

— Recommending effective ways for the member nations to use their research and development capabilities for the common benefit of the NATO community;

— Providing scientific and technical advice and assistance to the Military Committee in the field of aerospace research and development (with particular regard to its military application);

— Continuously stimulating advances in the aerospace sciences relevant to strengthening the common defence posture;

— Improving the co-operation among member nations in aerospace research and development;

— Exchange of scientific and technical information;

— Providing assistance to member nations for the purpose of increasing their scientific and technical potential;

— Rendering scientific and technical assistance, as requested, to other NATO bodies and to member nations in connection with research and development problems in the aerospace field.

The highest authority within AGARD is the National Delegates Board consisting of officially appointed senior representatives from each member nation. The mission of AGARD is carried out through the Panels which are composed of experts appointed by the National Delegates, the Consultant and Exchange Programme and the Aerospace Applications Studies Programme. The results of AGARD work are reported to the member nations and the NATO Authorities through the AGARD series of publications of which this is one.

Participation in AGARD activities is by invitation only and is normally limited to citizens of the NATO nations.

The content of this publication has been reproduced
directly from material supplied by AGARD or the authors.

Published September 1993

ISBN 92-835-0715-0

Printed by Specialised Printing Services Limited
40 Chigwell Lane, Loughton, Essex IG10 3TZ

Recent Publications of the Fluid Dynamics Panel

AGARDOGRAPHS (AG)

Design and Testing of High-Performance Parachutes
AGARD AG-319, November 1991

Experimental Techniques in the Field of Low Density Aerodynamics
AGARD AG-318 (E), April 1991

Techniques Expérimentales Liées à l'Aérodynamique à Basse Densité
AGARD AG-318 (FR), April 1990

A Survey of Measurements and Measuring Techniques in Rapidly Distorted Compressible Turbulent Boundary Layers
AGARD AG-315, May 1989

Reynolds Number Effects in Transonic Flows
AGARD AG-303, December 1988

REPORTS (R)

Shock-Wave/Boundary-Layer Interactions in Supersonic and Hypersonic Flows
AGARD R-792, Special Course Notes, August 1993

Unstructured Grid Methods for Advection Dominated Flows
AGARD R-787, Special Course Notes, May 1992

Skin Friction Drag Reduction
AGARD R-786, Special Course Notes, March 1992

Engineering Methods in Aerodynamic Analysis and Design of Aircraft
AGARD R-783, Special Course Notes, January 1992

Aircraft Dynamics at High Angles of Attack: Experiments and Modelling
AGARD R-776, Special Course Notes, March 1991

ADVISORY REPORTS (AR)

Air Intakes for High Speed Vehicles
AGARD AR-270, Report of WG 13, September 1991

Appraisal of the Suitability of Turbulence Models in Flow Calculations
AGARD AR-291, Technical Status Review, July 1991

Rotary-Balance Testing for Aircraft Dynamics
AGARD AR-265, Report of WG 11, December 1990

Calculation of 3D Separated Turbulent Flows in Boundary Layer Limit
AGARD AR-255, Report of WG10, May 1990

Adaptive Wind Tunnel Walls: Technology and Applications
AGARD AR-269, Report of WG12, April 1990

CONFERENCE PROCEEDINGS (CP)

Theoretical and Experimental Methods in Hypersonic Flows
AGARD CP-514, April 1993

Aerodynamic Engine/Airframe Integration for High Performance Aircraft and Missiles
AGARD CP-498, September 1992

Effects of Adverse Weather on Aerodynamics
AGARD CP-496, December 1991

Manoeuvring Aerodynamics
AGARD CP-497, November 1991

Vortex Flow Aerodynamics
AGARD CP-494, July 1991

Missile Aerodynamics
AGARD CP-493, October 1990

Aerodynamics of Combat Aircraft Controls and of Ground Effects
AGARD CP-465, April 1990

Computational Methods for Aerodynamic Design (Inverse) and Optimization
AGARD-CP-463, March 1990

Applications of Mesh Generation to Complex 3-D Configurations
AGARD CP-464, March 1990

Fluid Dynamics of Three-Dimensional Turbulent Shear Flows and Transition
AGARD CP-438, April 1989

Validation of Computational Fluid Dynamics
AGARD CP-437, December 1988

Aerodynamic Data Accuracy and Quality: Requirements and Capabilities in Wind Tunnel Testing
AGARD CP-429, July 1988

Aerodynamics of Hypersonic Lifting Vehicles
AGARD CP-428, November 1987

Aerodynamic and Related Hydrodynamic Studies Using Water Facilities
AGARD CP-413, June 1987

Applications of Computational Fluid Dynamics in Aeronautics
AGARD CP-412, November 1986

Store Airframe Aerodynamics
AGARD CP-389, August 1986

Unsteady Aerodynamics — Fundamentals and Applications to Aircraft Dynamics
AGARD CP-386, November 1985

Aerodynamics and Acoustics of Propellers
AGARD CP-366, February 1985

Improvement of Aerodynamic Performance through Boundary Layer Control and High Lift Systems
AGARD CP-365, August 1984

Wind Tunnels and Testing Techniques
AGARD CP-348, February 1984

Aerodynamics of Vortical Type Flows in Three Dimensions
AGARD CP-342, July 1983

Missile Aerodynamics
AGARD CP-336, February 1983

Prediction of Aerodynamic Loads on Rotorcraft
AGARD CP-334, September 1982

Wall Interference in Wind Tunnels
AGARD CP-335, September 1982

Fluid Dynamics of Jets with Applications to V/STOL
AGARD CP-308, January 1982

Aerodynamics of Power Plant Installation
AGARD CP-301, September 1981

Computation of Viscous-Inviscid Interactions
AGARD CP-291, February 1981

Subsonic/Transonic Configuration Aerodynamics
AGARD CP-285, September 1980

Foreword

The ability to design efficient high-lift systems for aircraft has become increasingly important for a number of reasons.

Firstly, during the last 10-15 years, the worldwide ability to design wings for efficient transonic flight has been transformed by:

a) increased understanding of how to design for mixed subsonic and supersonic flow over the wing;

b) the increased capability and reliability of CFD codes in predicting these flows.

As a result, wing loadings have been able to increase without incurring any penalty in cruise or turn performance. The corollary of this is that increased demands have been put on the design of the high-lift system in order to retain the same take-off and landing performance.

Secondly, the current world military situation, with the cessation of the Cold War, demands that NATO forces are able to react quickly to a developing situation anywhere in the world, and thus that military transport aircraft are able to operate from unprepared and short landing strips — again making increased demands on the design of the high-lift system.

Finally, the demands made by stealth requirements on the shape of the aircraft — generating configurations such as the F117 and the B2 — lead to geometries which are far from optimum aerodynamically, and hence which are likely also to make increased demands on the design of the high-lift system in order to preserve the landing and take-off performance.

Consequently, it is somewhat surprising that the last AGARD Symposium concerned with high-lift systems was as long ago as 1984 — and even then the Symposium subject was split between "High-Lift" and "Drag Reduction" (AGARD CP 365).

However, recent advances in CFD techniques, and in the understanding of the complex flows that occur over high-lift systems, suggest that more efficient systems can now be designed with a lower risk than before, and that it is therefore very appropriate that AGARD FDP should hold a Symposium, at this time, solely dedicated to the subject of "High-Lift System Aerodynamics".

The Symposium was aimed to address:

a) how, given the role and configuration of the aircraft, the most appropriate high-lift system can be selected;

b) how, having selected the type of high-lift system, an efficient detailed design can be produced;

c) the experimental and analysis techniques which are necessary to explore and enhance the performance of the high-lift system.

Thus, although the *aerodynamics* of high-lift systems was the dominant theme, the very pertinent aspects of weight, simplicity, reliability, and structural and mechanical integrity, were an integral part of the Symposium, and were treated in the papers presented. In this sense, this Symposium has attempted to take a broader view of the high-lift system than has been taken by similar conferences in the past.

Avant-Propos

La conception de systèmes hypersustentateurs performants pour aéronefs prend de plus en plus d'importance aujourd'hui, et ceci pour differentes raisons.

En premier lieu, au cours des derniers 10 à 15 ans, les capacités de la communauté aéronautique internationale dans le domaine de la conception des voilures pour le vol transsonique performant ont été transformées par:

a) une meilleure compréhension de la prise en compte des écoulements mixtes subsoniques et supersoniques autour de la voilure dès la phase d'études;

b) un accroissement de la capacité et la fiabilité des codes CFD dans la prédiction de ces écoulements.

Ceci a permis d'augmenter les charges alaires sans pénaliser les performances de croisière ou de virage. Ce développement a eu pour corollaire l'imposition de contraintes plus rigoureuses sur la conception des systèmes hypersustentateurs afin de conserver les mêmes performances au décollage et à l'atterrissage.

En deuxième lieu, la situation militaire mondiale actuelle, avec la cessation de la guerre froide, nécessite une réaction rapide de la part des forces de l'OTAN face à une éventuelle situation de crise n'importe où dans le monde. Ceci implique la mise en oeuvre opérationnelle d'avions de transport à partir de pistes d'atterrissage courtes et non-préparées et entraine de nouvelles demandes au niveau de la conception des systèmes hypersustentateurs.

Enfin, les conséquences des exigences de furtivité sur la forme des aéronefs — c'est à dire la création de configurations telles que celles des F117 et B2 — mènent à des géométries qui sont loin d'être optimales du point de vue aérodynamique. Par voie de conséquence, elles risquent d'imposer des contraintes supplémentaires sur la conception des systèmes hypersustentateurs dans le cas où les performances au decollage et à l'atterrissage devraient être conservées.

Il est donc surprenant de constater que le dernier symposium organisé par l'AGARD sur ce sujet remonte à 1984 — et que le thème de la réunion était partagé entre "l'hypersustentation" et "la réduction de la trainée" (AGARD CP 365).

Cependant, les progrès réalisés récemment en aérodynamique numérique, et dans l'analyse des écoulements complexes autour des systèmes hypersustentateurs laissent supposer que des systèmes plus performants peuvent désormais être réalisés à moindre risque que par le passé. Il était, par conséquent, tout à fait opportun pour le Panel FDP de l'AGARD d'organiser un symposium consacré au seul sujet de "l'aérodynamique des systèmes hypersustentateurs".

Le symposium a examiné les thèmes suivants:

a) le choix optimal de systèmes hypersustentateurs en fonction du rôle et de la configuration de l'aéronef;

b) la réalisation d'une étude détaillée optimale en fonction du système hypersustentateur choisi;

c) les techniques expérimentales et d'analyse nécessaires à l'examen détaillée et l'amélioration des performances des systèmes hypersustentatuers.

Ainsi, bien que *l'aérodynamique* des systèmes hypersustentateurs fût bien le thème dominant de symposium, certains aspects très pertinents tels la masse, la simplicité, la fiabilité et l'intégrité structurale et mécanique faisaient partie intégrante de la réunion et figuraient dans les communications présentées. De cette façon, le symposium a voulu donner une vue beaucoup plus large des systèmes hypersustentateurs, ce qui que n'a pas été le cas pour d'autres conférences organisées sur ce sujet dans le passé.

Fluid Dynamics Panel

Chairman: Prof. Ir J.W. Slooff
National Aerospace Laboratory NLR
Anthony Fokkerweg 2
1059 CM Amsterdam
The Netherlands

Deputy Chairman: M.C. Dujarric
ASE-Programme HERMES
Bâtiment Copernic
18 Avenue Edouard Belin
31055 Toulouse Cedex — France

PROGRAMME COMMITTEE

Mr D. Woodward (Co-Chairman)
Superintendent AP3
Low Speed Aerodynamics Division
X80 Bldg
Defence Research Agency
Farnborough, Hants GU14 6TD
United Kingdom

Mr L.J. Willaims (Co-Chairman)
Director, High-Speed Research Division
Office of Aeronautics & Space Technology
NASA (Code RJ)
Washington, DC 20546
United States

Prof. R. Decuypere
Ecole Royale Militaire
Chaire de Mécanique Appliquée (MAPP)
Avenue de la Renaissance 30
B-1040 Brussels, Belgium

Dr L. Chan
High Speed Aerodyn. Lab. — U66
Institute for Aerospace Research
National Research Council
Montreal Road
Ottawa, Ontario K1A 0R6, Canada

M.J. Bousquet
Division Avions-A/DET/AP MO 151/7
Aérospatiale
316 Route de Bayonne
31060 Toulouse Cedex 03, France

Dr B. Wagner
Dornier Luftfahrt GmbH
Abteilung Aerodynamik
Postfach 1303
D-7990 Friedrichshafen, Germany

Lt Col. D. Petridis
Hellenic Air Force General Staff
Branch C' — Directorate C1
Section 4
Holargos, TGA 1010
Athens, Greece

Prof. M. Onorato
Dipartimento di Ingegneria
Aeronautica e Spaziale
Politecnico di Torino
C. so Duca degli Abruzzi 24
10129 Torino, Italy

Prof. Dr Ir J.L. van Ingen
Department of Aerospace Engineering
Delft University of Technology
Kluyverweg 1
2629 HS Delft, The Netherlands

Dr L.P. Ruiz-Calavera
INTA
Division de Aerodinamica
Carretera de Ajalvir Km. 4.5
28850 Torrejon de Ardoz
Madrid, Spain

Dr W.J. McCroskey
Senior Staff Scientist
US Army Aeroflightdynamics
Directorate — M/S N258-1
NASA Ames Research Center
Moffett Field, CA 94035-1099
United States

PANEL EXECUTIVE

Dr W. Goodrich

Mail from Europe:
AGARD—OTAN
Attn: FDP Executive
7, rue Ancelle
F-92200 Neuilly-sur-Seine
France

Mail from US and Canada:
AGARD—NATO
Attn: FDP Executive
Unit 21551
APO AE 09777

Tel: 33(1)47 38 57 75
Telex: 610176 (France)
Telefax: 33 (1) 47 38 57 99

Contents

SESSION IV – HIGH-LIFT EXPERIMENTS IN 3D

Chairman: R. Decuypere

SESSION V – HIGH-LIFT CFD IN 3D

Chairman: L. Williams

SESSION VI – DESIGN OF HIGH-LIFT SYSTEMS FOR COMPLETE AIRCRAFT

Chairman: J. Bousquet

Technical Evaluation Report

by

D.C. Whittley
17 Book's Landing
375 Book Road
Grimsby, Ontario L3M 2M8
Canada

1. INTRODUCTION

The AGARD Fluid Dynamics Panel organized a symposium on "High-Lift System Aerodynamics" which was held in Banff, Alberta, Canada, from 5 October through 8 October, 1992. This meeting represented a natural successor to a previous FDP symposium held in Brussels, Belgium in 1984, which was entitled "Improvements of Aerodynamic Performance through Boundary Layer Control and High-Lift Systems". Considerable progress has been made in the area of high-lift systems since the Brussels conference, especially in the areas of experimental testing and theoretical prediction (otherwise referred to as computational fluid dynamics or CFD).

In view of the current aerospace climate and corresponding industrial interest, for the Banff symposium, it was decided to focus attention on aerodynamic research and technology applicable to advanced (passive) high-lift systems for subsonic transport application. Notwithstanding this emphasis, three papers were presented dealing with experimental testing of low aspect ratio wing planforms, suitable for combat type aircraft and one dealing with powered-lift for transport application.

The first paper contained a review of some past research programmes in the United Kingdom and was presented by Dr D.S. Woodward, co-chairman of the programme committee. Paper 3 was withdrawn so that, of the 13 papers which followed, 11 dealt with CFD 2D methods as applied to high-lift airfoil configurations such as single or double-slotted flap with some form of leading edge device. The next seven papers concerned experimental testing of high-lift configurations in 3D. The following session of four papers was devoted to CFD methods as applied to 3D high-lift wings and, finally, seven papers were presented in which industrial representatives described design and development of high-lift systems for complete aircraft.

References (1) through (33) list the symposium papers in the order in which they were presented.

Delegates attending the symposium numbered 105.

2. BACKGROUND

Typically, the aerodynamic high-lift design process in industry involves the use of an empirical data base, theoretical prediction methods, wind tunnel testing and flight development.

2.1 High-Lift Aerodynamic Technology

The very beginning of high-lift can be traced back to the years 1917-1920 (1), but even after 30 years, most of the design data were compiled in just four publications (27), but there was little understanding of the underlying aerodynamic principles at work. It was not until 1972 that the theoretical treatise of A.M.O. Smith provided a clear and comprehensive insight into the fundamentals of a multi-element foil (34). He showed that it was by splitting the pressure rise over several elements that the tendency for flow separation could be suppressed and, thereby, lift potential could be increased. Along with this understanding, came a deeper awareness of the role and importance of viscous effects.

Three important developments took place during the following ten years or so:

- construction of some new pressurized wind tunnels in member states, to permit a more thorough exploration of scale effects and encourage testing at higher levels of Reynolds number;
- fairly rapid development of inviscid-viscous theoretical methods as applied to multi-element foils and wings;
- an upsurge in experimental research to strengthen the empirical aerodynamic data base.

These developments were reported at the FDP symposium, Brussels, 1984.

In the past decade, continuing work has been associated with the following:

- consolidation and development of inviscid/viscous coupled methods based on integral boundary layer calculations;
- a growing effort associated with computational field methods which require a grid of the domain and permit, for example, solutions to the Reynolds averaged Navier-Stokes equations;
- a build-up of reliable experimental data relating to high-lift configurations showing separately the effect of Reynolds number and Mach number; also correlations between wind tunnel and flight measurements;
- boundary layer and wake measurements to provide a deeper understanding of the flow physics associated with multi-element foils.

It was consideration of these aspects of the subject which dominated the symposium in Banff.

2.2 The Design Process

Two important factors overshadow the design process:

- There are serious penalties for failing to meet the flight design goals of the high-lift system for a projected aircraft and, therefore, the subject must be afforded an appropriate emphasis and effort. For example, the design procedure includes extensive parametric studies at the project design stage – time is especially important here; optimization and refinement are required at the early development stage – costs can soar if undertaken solely in the wind tunnel; verification of the final configuration is usually undertaken in a wind tunnel at reasonably high Reynolds number – generally regarded as essential at whatever cost.

- The flow field of a high-lift aircraft configuration is extremely complex, including such phenomena as boundary layer growth and separation, wake development, confluence of boundary layers, viscous wake interactions, laminar separations, etc.

Therefore, as a result of these factors, theoretical and experimental aerodynamic technology is aimed toward improvement of the accuracy of prediction to reduce risk, and toward reduction in time and cost of the design process.

3. DISCUSSION

3.1 The Opening Review Paper

The introductory paper (1) by Woodward and Lean, DRA, United Kingdom, described a "National High-Lift Programme" conducted in the United Kingdom in the 1970s, and contained much data heretofore not generally available. The work was aimed toward strengthening the overall aerodynamic data base used by industry so as to make empirical methods of design more reliable. The use of such a data base was described by Butter at the 1984 Brussels symposium (35).

Systematic tests were undertaken on four models: one wall-to-wall and one endplate model for 2D studies, and, one constant chord and one tapered planform model (both having a variable sweep capability) for 3D studies.

In particular, the research programme provided a basis for optimization of slat and flap positions relative to the main foil. Rake measurements gave some insight into the growth of boundary layers and wakes on the various foil elements and thereby suggested reasons for optimum locations; of special interest were cases in which the slat wake merged with the wing boundary layer.

The research programme went beyond the purely aerodynamic aspects of high-lift systems to include consideration of variation in structure weight as geometry was adjusted for best aerodynamic performance. It was shown that, by use of weight fractions, an optimum design could be found (in terms of best fuel plus payload) taking into account both aerodynamic and structural factors.

The authors point out that this research effort, conducted jointly by industry and government groups, played a major role in overcoming a perceived shortfall in UK high-lift technology at the time.

3.2 Theoretical Methods: High-Lift in 2D

Inviscid/viscous coupled methods have been available in a form suitable for industrial use since the early 1980s (36) and (4), by de Ponte, Cella and Marcazzan, Milan Polytechnic, Italy, is a good example. These methods serve to complement and/or displace previous design procedures which were based solely on an empirical data base – they rely on an integral boundary layer/wake model. These codes are attractive on account of computational efficiency and flexibility (that is, providing a choice in the level of sophistication to suit various stages of design).

Although effective as an engineering tool, the 'coupled' method is somewhat limited in being unable to compute much beyond maximum lift and it may have other shortcomings associated with slat/flap wells, thick trailing edges, etc. Hence, potentially more accurate field methods have been sought which define the domain by means of a computational grid and permit, for example, solutions to the Reynolds-averaged Navier-Stokes equations. Such methods tend to place great demand on computer capability and capacity which result in a longer solution time and/or an increase in cost; these methods have not yet reached a level of maturity to permit routine industrial use. In order to overcome these difficulties, some investigators have considered various degrees of simplification while still seeking to retain an adequate degree of accuracy; for example, effects of compressibility can be omitted or one can opt for a fairly simple turbulence model. Likewise, attempts are constantly being made to find more efficient ways to generate and refine the computational grid.

3.2.1 *Structured Versus Unstructured Grids*

Early work was based on the generation and use of structured grids. More recently, unstructured grid solvers have been studied which, although requiring a greater memory capacity, do allow ease of automatic grid generation about multi-element configurations: also, local increase in grid density for critical areas can be easily achieved. During the symposium, some opinions were expressed regarding the relative merits of structured versus unstructured grids but it would seem unwise to make a final judgement at the present stage of development.

3.2.2 *Navier-Stokes Solutions*

In all, there were eight presentations, which described numerical solutions to the Navier-Stokes equations, six of which, as described below, used structured grid solvers. Each investigator discussed the foundation of his particular method and made comparison with experimental or test cases – generally, reasons were suggested for discrepancies in correlation.

Fritz, Dornier, Germany (5). A proper treatment of the wake of the main foil becomes important at high angles of attack: this requires fine grid resolution and the correct prediction of viscous effects within the wake. Simple turbulence models failed in prediction of the eddy viscosity for such a complex flow field and therefore a two equation model is needed.

Bartsch, Nitsche and Britsch, TU Berlin, Germany (6). As in (5), the authors indicated the need for investigating turbulence modelling more thoroughly but also pointed to a requirement for more detailed and well established experimental cases against which to test theoretical predictions. Also, there is a need to assess numerical solution errors when making comparisons between theory and experiment.

Rogers, Wiltberger and Kwak, NASA Ames, United States (7). Two different approaches for grid generation were described and two different turbulence models were studied. Test cases included single, two, three and four element airfoils. Predictions are generally good but correlation deteriorates when significant areas of separated flow arise. Again, further work in turbulence modelling is recommended.

Jasper, Agrawal and Robinson, McDonnell Douglas, United States (8). Good accuracy of prediction was achieved for a two element airfoil without confluent boundary layer flow. Similarly, good agreement was achieved on four elements without separation on the slat. The authors conclude that treatment of separation, stall and post-stall conditions requires better modelling of turbulence. Also, it was pointed out that accurate calculation of gap effects may require modelling of transitional and re-laminarizing boundary layers.

Nelson, Zingg and Johnston, Toronto University, Canada (9). Test cases were shown for a two element and three element airfoil. Grids were generated by an automated procedure which divides the domain into blocks. Good agreement with experiment is obtained when flow is attached or regions of separated flow are small. The Baldwin-Barth turbulence model works well in most instances but under-predicts eddy viscosity in wake regions and over-predicts in the outer portions of the boundary layer.

Chow, Chu and Carpenter, Grumman Research Center, United States (15). In this paper, the authors apply their method to prediction of flow around a three element airfoil with blown flap; however, in the context of the AGARD symposium, the computational method is of more interest than the test case: the paper should be read in conjunction with a previous publication by the same authors (37). The method is shown to be capable of predicting both onset and growth of separated regions and wakes with good degree of correlation – even with respect to drag. The authors seem to attribute this success to a novel "stacked-C" mesh system which was used to map the multi-element geometry into a *single* computational domain and to the fact that the flow separation zone is treated with a semi-adaptive mesh generating procedure that utilizes slat, foil and flap trailing streamline. The code uses an algebraic turbulence model loosely based on the Thomas formulation of the Baldwin-Lomax model.

Johnson and Stolcis, UMIST, Manchester, United Kingdom (13). In this case, the work was based on an unstructured grid solver but the significance lies in the fact that the authors made few simplifying assumptions at the outset.

The approach consists of solving the compressible Reynolds averaged Navier-Stokes equations, using a two-equation turbulence model. The authors conclude that a two-equation turbulence model is the lowest order model consistent with complexity of the flow physics. A baseline computational method has been developed with encouraging initial results at both low speed and transonic high-lift conditions when tested against a two element airfoil.

Bailey et al., DLR Braunschweig, Germany (14). Some interesting comparisons were made between use of structured and unstructured grids: in general, it was found that good agreement was obtained with both strategies. Like (13), the authors based their method on solution of the full Reynolds averaged Navier-Stokes equations and used a turbulence model developed by Johnson and King in which both convection and diffusion of turbulence is taken into account so as to allow a more accurate determination of turbulent stresses in separated boundary layer flow. For a single foil, this turbulence model gave superior correlation and may lead to similar success for more complex high-lift configurations.

De Cock, NLR, The Netherlands (12). The author chose to base his work on the Euler equations as a fast means of investigating grid generation techniques for multi-element airfoils. The method was adapted to simulate separated regions in slat and wing coves and was moderately successful in predicting lift, drag and pitching moment of the three element airfoil. Improvements will be sought by an extension of the mathematical model to Reynolds averaged Navier-Stokes equations.

3.2.3 *Viscous-Inviscid Interaction Methods*

Methods based on viscous-inviscid interaction have been developed primarily in Europe (38) as a means to obtain relatively fast solutions and avoid reliance upon a "super computer" even though the approach might not capture all the features of the flow.

Le Balleur and Néron, ONERA, France (11). At ONERA, Le Balleur and his colleagues have persevered with the method of viscous-inviscid interaction and made improvements so that it is now possible to make predictions for deeply separated flows over multi-element airfoils at incompressible speeds. This achievement is attributed to progress made in both coupling algorithms and generalized thin-layer modellings along with manipulation of grid resolution, especially when close to separated flow regions. Test cases are chosen in which separation occurs in the cove of both slat and flap at mid-chord of the flap. Good correlation with experiment for surface pressure distribution is shown over a broad range of flow conditions.

3.3 Theoretical Methods: High-Lift CFD in 3D

The complex flow fields associated with high-lift are difficult to predict in 2D and become even more so in 3D, so that comprehensive solutions in 3D are at a relatively early stage of development.

Four papers were presented (23), (24), (25) and (26), the first of which by Jacob, DLR, Göttingen, Germany (23) described details of a method linking 2D viscous calculations with a 3D lifting surface theory. Such methods are both fast and economical and have proved valuable for use in industry (36).

The paper (24) by Cebeci, Douglas Aircraft, United States, dealt with multi-element airfoils and wings with theory based on interaction between inviscid and boundary layer equations – such an approach serves to avoid excessive demands on the computer. In spite of some success in development of a turbulence model, the author stressed the need for further improvements in order to achieve better correlation with experiment in the presence of separated regions.

In paper (26), Le Balleur, ONERA, France, continued his earlier discourse in the conference (11) with regard to viscous-inviscid interaction methods, extending the work to include compressibility at high-lift and deeply separated flow conditions for airfoils and wings. The author pointed to the modelling success achieved using a two-equation turbulence model for a NACA 4412 2D airfoil up to 28 degrees of incidence and showed good correlation for lift and drag within the experimental range. Two examples of 3D calculations were presented, a rectangular plan wing of aspect ratio 6, and an unswept tapered wing of aspect ratio 9.5. The method is capable of predicting the spanwise spread of the separation line and the corresponding pressure distribution and boundary layer displacements on the wing and in the wake. For the tapered wing, comparisons are made with experiment for a range of incidence. So far, treatment has been limited to plain unflapped foils, but the method holds promise for multi-element foils based on the ability to cope with separated regions of flow.

The paper (25) by Baron and Boffadossi, Milan Polytechnic, Italy, dealt with a different aspect of high-lift, namely, the hazards associated with persistence of vorticity generated in the proximity of an airfield during take-off and landing procedures. By means of a complex mathematical treatment, the authors were able to predict vortex distribution and strength. The time history is shown during a typical take-off manoeuvre for a chosen high-lift wing/tailplane configuration. Effects of ground proximity are discussed.

3.4 High-Lift Experiments in 2D and 3D

Nine papers were presented in this category, an invited paper described a broad range of experiments culminating in flight test (16), four papers dealt primarily with flow physics of high-lift airfoils (2), (18), (19) and (21), and the remaining papers related to high Reynolds number testing in the wind tunnel and with specific combat aircraft configurations.

Thibert, ONERA, France (16) – Invited. A collaborative European test programme in high-lift (known as the GARTEUR action group AD-AG08) was performed in the years 1985-1989: this work was described at the symposium by J.J. Thibert, chairman of the action group. The lack of high quality 2D and 3D experimental data was evident and, therefore, a comprehensive series of tests was undertaken to help close this gap, with special emphasis on correlation between 2D and 3D wind tunnel tests, and between 3D tunnel and flight measurements. Further objectives included determination of the separate effects of Mach number and Reynolds number (with model Re overlapping flight values), a study of the effect of wing sweep on transition location as a function of Reynolds number, and the identification of technology gaps and facility needs. By way of description, suffice it to say that the research was focussed on a section of the A310 wing, represented by two 2D models and one half model, with some tests being duplicated in more than one wind tunnel. These results were supported further by a series of flight measurements. The author concluded that the programme had generated a most comprehensive, well integrated and accurate body of data dealing with high-lift airfoils and wings which will form the basis for substantial improvement in design.

The importance of a deeper understanding of flow physics was raised by several speakers; four papers dealt with this aspect of high-lift in particular.

A paper (2) by Alemdaroglu, METU, Turkey, described detailed flow measurements in and around the slat and flap cavities of a three element foil. Effects of Reynolds number on the mean flow and on the turbulence parameters were investigated using pressure probes, hot-wire anemometers and a laser Doppler velocimeter.

Hardy, DRA, United Kingdom (18), gave an account of attachment-line transition and possible re-laminarization on the leading edge slat of a combat type model. Similar occurrences have been observed on transport type wings, so the subject is of broad interest. It was determined that the boundary layer can go through more than one change in state within an incidence range of a degree or so which makes for difficulty in the prediction of Reynolds number variation. Wing root effects and spanwise variations serve to complicate the matter still further and so, not surprisingly, the author spoke of the need and outlined the scope of possible future work.

Meredith, Boeing, United States (19) continued on this theme by citing six viscous features which affect the flow field of a typical multi-element lifting system of which three might be the cause of degradation in lift with increasing Reynolds number, that is to say: viscous wake interactions, re-laminarization and attachment line transition. These three phenomena were described in some detail and then illustrated by means of test results. It was concluded that these matters are of more than academic interest and that neither the current CFD tools nor the existing experimental data base are sufficiently well established to meet the need of more thorough understanding.

Yip, NASA Langley, Vijgen, High Technology Corporation, Hardin, Lockheed and van Dam, University of California (21). The authors described an ambitious flight research programme to analyse the high-lift flap of a Boeing 737 aircraft. An outboard wing section, containing slat and triple slotted Fowler flap elements, was heavily instrumented – including surface pressures, Preston tube devices and flow – visualization by means of tufts. Variation in skin friction coefficient on the slat upper surface showed a marked variation with angle-of-attack which could be interpreted in terms of re-laminarization. Similar correlations between Preston tube readings, surface pressures and tufts, were observed to determine the state of the boundary layer on the main wing and flap elements. Two well established multi-element computer codes were used to predict pressure distribution – both codes incorporated an integral boundary layer formulation. Comparisons were made between CFD and flight, thus adding a further dimension to the usefulness of the research programme overall.

Valarezo and Dominik, Douglas Aircraft and McGhee and Goodman, NASA Langley, United States (10). The paper describes tests on two high-lift configurations in the NASA Langley low turbulence pressure tunnel at Reynolds numbers in the range 5 to 16 × 10^{6}. Favourable lift increments at approach angles of attack were experienced by optimization of leading edge slat and introduction of a trailing edge wedge. Equally important was the fact that a set of high quality tests provided further evidence of Reynolds number and Mach number effects on high-lift optimization.

Earnshaw and Green, DRA, United Kingdom (20). This paper dealt with the use of half models in high-lift wind tunnel testing. The use of half models can offer several advantages, not the least of which is to permit an increase in Reynolds number as compared to a full model in the same wind tunnel. The author conducted tests on one half of an existing full span model which had previously undergone several tests. Various half model mounting configurations were investigated and results compared to the full model results. The paper generated a great deal of interest on account of the very practical nature and potential usefulness of the findings.

Finally, in the category of high-lift experiments, two papers dealt with low aspect ratio planforms suitable for combat type aircraft. One by Walchli, USAF WPAFB (22), in fact, dealt with the X-29 forward swept wing demonstrator aircraft. Mention was made of high-lift capability required for manoeuvrability and under post stall conditions. Apart from the intrinsic interest of the paper itself, it served as a reminder that the Banff symposium focussed on only one segment of the subject of high-lift as a whole.

The other paper associated with combat aircraft (17) was presented by Moir, DRA, United Kingdom and described tests on a generic wing/fuselage model of aspect ratio 3.4 tested in the DRA Farnborough 5 metre pressurized tunnel with a Reynolds number range of 6 to 11 × 10^{-6}, approximately. The tests were designed to study leading edge slat optimization in conjunction with both a plain wing trailing edge and a single-slotted flap. The important findings from the test relate to the performance of the model under conditions of separately varying Mach number and Reynolds number, that is, the kind and quality of measurements needed to help establish an advanced data base.

3.5 Design of High-Lift Systems for Complete Aircraft

The final session of the symposium was devoted to consideration of the aerodynamic design procedures and practices found in industry, as related to transport aircraft. Development of a complete system involves a mix of design philosophy, empiricism, theory and experiment and, over the years, the methodology evolved to become an established and proven procedure which is peculiar to the design team and the company. Over the past decade, the design process has undergone some change whereby less reliance is now placed upon the empirical data base and more upon theoretical prediction – the rate of this change is, in part, a function of resources available and it is the larger companies which tend to move more rapidly toward acceptance of a new technology.

The paper by Obert and Fokker Aircraft, The Netherlands, (27), was entitled "Forty Years of High-Lift R and D – An Aircraft Manufacturer's Experience". A review such as this, not only shows the progression of aerodynamic high-lift technology at large, but also illustrates the evolution of the design procedure as guided by the design team: in this case, within the framework of a medium sized manufacturer. As such, the paper represents a valuable addition to the literature for students and professionals alike. Regarding theoretical prediction, the author concluded that the role of CFD in the design process has greatly increased but that, at present, a fair degree of empirical data has to be fed into the computational methods and therefore access to a large empirical data base remains a pre-requisite.

Next there were three papers which illustrated, in particular, the application of CFD methods to the design of a specific high-lift system: Capbern, Aérospatiale, France (28); Averado and Russo, Alenia, Italy (33), and Mathews, Short Bros., United Kingdom (29).

Capbern described the development of flap systems for the ATR 72 aircraft and explained how numerical methods (introduced in 1985) have served to complement existing empirical and experimental methods which were used exclusively until then. He outlined the computational tools and the overall methodology and showed how this has led to a more simple design for the ATR 72 flap system with additional benefits in terms of improved performance and lower production costs.

Similarly, Averado presented a flow chart of the design procedure used at Alenia showing the complementary roles of theoretical prediction and wind tunnel testing. The design methods proved successful in the determination of near-optimum selection of flap profile, slat shape and pivot position.

Mathews described theoretical methods in use at Short Brothers to define flap geometry at the project stage of design with special consideration of flap overhang and gap. Also, some structural aspects of flap design were discussed and a simple four-bar flap linkage mechanism was shown.

Eggleston and Poole, de Havilland Inc., Canada (32) described R and D high lift work at de Havilland geared toward the development of future propeller driven regional transport aircraft which employs more advanced airfoil sections suited to cruise speeds up to Mach 0.7. 2D models were tested at high Reynolds number (6 to 10 × 10^{-6}) in the 0.38m × 1.5m test section of the IAR/NRC pressurized wind tunnel. Extensive use was made of half-model testing at lower Reynolds number.

The paper by Flaig and Hilbig, Deutsche Airbus, Germany (31) was representative of a manufacturer of large transport aircraft. It was comprehensive in scope dealing, at some length, with the objectives and constraints of high-lift design and then with the design methods in terms of theoretical prediction and wind tunnel strategy. These general considerations were concluded with an outline of the high-lift design process as made up of three phases, namely, pre-development, development and pre-flight. The role of theoretical prediction was clearly identified in the pre-development phase. Finally, the Deutsche Airbus design process was illustrated in terms of the development of the high-lift system for the Airbus 321. In particular, it was shown that the significantly increased lift requirements for this stretched version of the A320 could be satisfied by a conversion from a single-slotted Fowler flap to a part span double-slotted flap, even with the geometric constraints imposed by a "minimum change" philosophy.

Finally, dealing with the category of high-lift systems for complete aircraft, a paper was presented by Nark, Boeing, United States (30) relating to powered-lift for transport category aircraft. The author gave a well illustrated presentation describing the design, development and flight evaluation of the Boeing YC-14, this being the "upper surface blowing" entry in the USAF "Advanced Medium STOL Transport" development programme. In particular, it was evident that methods and procedures for development of a powered-lift system differ widely from those well established for a passive lift system. The paper was of special interest to many of the European delegates who were not aware of the technical background to the YC-14 and YC-15 programmes.

4. CONCLUSIONS

Inviscid-viscous coupled CFD prediction methods are well established and play an important role in the design of high-lift systems for transport aircraft (39). Under active development, are more advanced field methods which have the potential to deal adequately with regions of separation and wakes but, in their present form, do not accurately predict some of the high-lift parameters of interest. These methods have not yet reached a level of maturity to allow widespread industrial use and therefore further development to this end is recommended (19).

High quality, high Reynolds number experimental data continue in short supply – as needed for test cases (comparing CFD prediction with experiment) or to upgrade the existing empirical data base for moderate to high aspect ratio configurations.

There remains an inadequate understanding of the flow physics relating to high-lift systems and, therefore, further specialized wind tunnel and flight programmes are needed to explore some of the fundamental issues associated with turbulence, boundary layers and wakes which are, as yet, not fully amenable to computational analysis (19), (40). There was clear consensus that improvement is needed in turbulence modelling and that a better understanding of flow physics would lead to improvement in CFD methods.

A gap remains between the Reynolds number achieved in the wind tunnel as compared to flight. It is unlikely that new high Reynolds number wind tunnel facilities will become available in the near future, but this shortfall can be offset, in part, by more intensive use of CFD prediction methods. Such a capability helps in the formation of wind tunnel programmes and interpretation of wind tunnel and flight measurements: in this latter role, CFD becomes a kind of phantom flow visualization in providing basic insight to the flow processes at work.

Little indication was given concerning performance improvement expected as a result of advancement in high-lift technology (say, in terms of C_L max of L/D for second segment climb). Similarly, the conference did not bring to light any new or unorthodox ways to improve performance but inferred that improvement would come as a result of careful refinement. Even quite modest improvement in high-lift can lead to significant gain in performance of transport type aircraft (19).

In short, the design and development of a modern high-lift system requires vigorous use of the wind tunnel as described, for example, by Obert (27) and Flaig (31). CFD methods play an important support with respect to design – at the pre-development stage (31), and with respect to interactive analysis – at the development and pre-flight stages (36).

The conference served to bring together mathematicians, aerodynamicists and test engineers to help foster a better mutual understanding of strengths and weaknesses in each of the disciplines. The present status of high-lift technology for transport aircraft was clearly set forth and areas in need of further attention became evident.

5. PROGRAMME COMMITTEE MEMBERS

Dr D.S. Woodward (Co-Chairman), DRA, United Kingdom.
Mr L.J. Williams (Co-Chairman), NASA, United States.
Prof. R. DeCuypere, Ecole Royale Militaire, Belgium.
Dr L. Chan, IAR, Canada.
M.J. Bousquet, Aérospatiale, France.
Dr B. Wagner, Dornier Luftfahrt GmbH, Germany.
Lt Col. D. Petridis, Hellenic Air Force, Greece.
Prof. M. Onorato, Politecnico di Torino, Italy.
Prof. Dr Ir J.L. van Ingen, Delft University of Technology, The Netherlands.
Dr L.P. Ruiz-Calavera, INTA, Spain.
Dr W.J. McCroskey, US Army Aeroflightdynamics, United States.

6. REFERENCES

(Note that references (1) through (33) list the symposium papers in the order in which they were presented.)

1. Woodward DS and Lean DE
   Where is High-Lift Today? – A Review of Past UK Research Programmes
2. Alemdaroglu N
   Experimental Investigation of the Flow about a Multi-Element Airfoil
3. Graham JMR and Giannakidis G
   Numerical Simulation of the Separated Flow in Wing Coves
4. De Ponte S, Cella A and Marcazzan M
   A Design Procedure for Slotted Flaps
5. Fritz W
   Maximum, and High-Lift Characteristics of Multi-Element Aerofoils
6. Bartsch P, Nitsche W and Britsch M
   Navier-Stokes Computations of Turbulent Flow around High-Lift Configurations
7. Rogers SE, Wiltberger NL and Kwak D
   Efficient Simulation of Incompressible Viscous Flow over Multi-Element Airfoils
8. Jasper DW, Agrawal S and Robinson BA
   Navier-Stokes Calculations on Multi-Element Airfoils using a CHIMERA-Based Solver
9. Nelson TE, Zingg DW and Johnston GW
   Numerical Solution of the Navier-Stokes Equations for High-Lift Configurations on Structured Composite Grids
10. Valarezo WO, Dominik CJ, McGhee RJ and Goodman WL
    High Reynolds Number Configuration Development of a High-Lift Airfoil
11. Le Balleur JC and Néron M
    Une Méthode d'Interaction Visqueux non-Visqueux pour Ecoulements Incompressibles Hypersustentés sur Profils Multi-corps en Régime de Décollement Profond
12. De Cock KMJ
    High-Lift System Analysis Method using Unstructured Meshes
13. Johnson LJ and Stolcis L
    Prediction of the High-Lift Performance on Multi-Element Aerofoils using an Unstructured Navier-Stokes Solver
14. Bailey R, Radespiel R, Demier A, Rossow C-C, Longo JMA, Ronzheimer A and Kroll N
    Numerical Calculations of High Lift Flows using Structured and Unstructured Methods
15. Chow R, Chu K and Carpenter G
    Navier-Stokes Simulation of Flow Field around a Blow-Flap High Lift System
16. Thibert JJ
    The GARTEUR High Lift Research Programme
17. Moir IRM
    An Experimental Investigation of the Optimum Slat Setting on a Combat Aircraft Model
18. Hardy BC
    An Experimental Investigation of Attachment-Line Transition on the Slat of a Combat Aircraft Model

19. Meredith PT
Viscous Phenomena Affecting High-Lift Systems and Suggestions for Future CFD Development

20. Earnshaw PB, Green AR, Hardy BC and Jelly AH
A Study of the Use of Half-Models in High-Lift Wind Tunnel Testing

21. Yip LP, Vijgen PMHW, Hardin JD and van Dam CP
In-Flight Pressure Distributions and Skin-Friction Measurements on a Subsonic Transport High-Lift Wing Section

22. Walchli LA
High-Lift and the Forward Swept Wing

23. Jacob K
A Fast Computing Method for the Flow over High-Lift Wings

24. Cebeci T
Calculation of Multi-Element Airfoils and Wings at High-Lift

25. Baron A and Boffadossi M
Wake Structure and Aerodynamic Behavior of High-Lift Aircraft Configurations during Unsteady Maneuvers in Ground Effect

26. Le Balleur JC
Calcul par Interaction Visqueux non-Visqueux des Ecoulements Compressibles Fortement Décollés aux Grandes Portances sur Profils d'Ailes et Voilures

27. Obert E
Forty Years of High-Lift R&D – An Aircraft Manufacturer's Experience

28. Capbern P
High-Lift Research: Application to the Design of the ATR72 Flap

29. Mathews JR
The Aero-Mechanical Design of a Novel Fowler Flap Mechanism

30. Nark TC
Design, Development, and Flight Evaluation of the Boeing YC-14 USB Powered Lift Aircraft

31. Flaig A and Hilbig R
High-Lift Design for Large Civil Aircraft

32. Eggleston BE and Poole RJD
High-Lift Systems for Transport Aircraft with Advanced Airfoils

33. Averardo MA, de Leo M and Russo V
Choice and Optimization of a High-Lift System for an Advanced Amphibious Aircraft

34. Smith AMO
Aerodynamics of High-Lift Airfoil Systems. AGARD-CP-102, April 1972

35. Butter DJ
Recent Progress on Development and Understanding of High-Lift Systems. AGARD-CP-365

36. Dillner B, May FW and McMasters JH
Aerodynamic Issues in the Design of High-Lift Systems for Transport Aircraft. AGARD-CP-365

37. Chow R and Chu K
Navier-Stokes Solution for High-Lift Multi-Element Airfoil Systems with Flap Separation. AIAA-91-1623

38. King DA and Williams BR
Developments in Computational Methods for High-Lift Aerodynamics, R.Ae.S. Aeronautical Journal, Aug/Sept 1988

39. Kusunose K, Wigton L and Meredith P
A Rapidly Converging Viscous/Coupling Code for Multi-Element Airfoil Configurations, AIAA-91-0177

40. Gatner PL, Meredith PT and Stoner RC
Areas for Future CFD Development as Illustrated by Transport Aircraft Applications, AIAA-91-1527-CP

WHERE IS HIGH-LIFT TODAY? - A Review of past UK Research Programmes

D. S. WOODWARD (DRA Farnborough UK)
D. E. LEAN (DRA Farnborough UK)

SUMMARY

Some of the history of the development of slotted high-lift systems is reviewed in this paper. In particular, the National High Lift Programme run in the UK during the 1970s is reviewed in some detail. In addition, the research programme in high lift since the completion of the National High Lift Programme is described qualitatively and references given. The contents cover techniques of high lift testing, results of positional optimisation of slats and flaps, the derivation of a simple prediction method suitable for use with a project optimisation method, and the description, with results, of a method for interpreting aerodynamic and weight data on high lift systems in the context of a complete aircraft.

1 INTRODUCTION

Barnes[1] records the amusing story of how the slotted wing came to be invented:

> "In April 1911 Frederick Handley-Page read to the Aeronautical Society of Great Britain, a paper entitled 'The Pressures on Plane and Curved Surfaces moving through the Air', ... He noted that, with a wing of moderate Aspect Ratio (6.25), lift increased approximately linearly up to 10 deg incidence, but then levelled off, while the lift of a square wing (Aspect Ratio = 1.0) continued to increase with incidence up to nearly 40 deg.... Using the wind tunnel at Kingsbury in 1917, Handley-Page and his aerodynamicist R.O. Boswall tried to combine the low-drag advantage of high aspect ratio with the delayed stall of low aspect ratio, by separating a normal narrow wing into discrete square areas by means of chordwise slots, *but found the result disappointing and incapable of being improved by varying the proportions of the slots and their distribution spanwise.* At some point in these entirely empirical experiments, someone - whether Handley-Page himself, or Boswall, or one of the carpenters, is not clear - had the idea of cutting a *spanwise* slot parallel to the leading-edge, sloping upwards and rearwards, at about the 1/4-chord line. The first experiment, using a RAF15 aerofoil section, gave a spectacular lift increase of 25%; with an improved shape of slot in a RAF6 section, this was raised to over 50%, with only a slight increase in drag..... Numerous experiments continued during 1918 and 1919, using various shapes of single slot, whose chordwise location was found to be critical on thin aerofoils....
>
> Handley-Page realised early on that the slotted wing was an extremely valuable invention, so he kept the principle strictly secret until patent applications had been accepted by both British and United States Patent Offices. To avoid premature disclosure, he did not seek protection for the original fixed slot until he was ready also to cover a moveable slot, which could be opened and closed by the pilot.....
>
> During the whole period of early development of the Handley-Page slotted wing, a parallel investigation had been made, quite

> independently, by the German engineer-pilot, G.V. Lachmann. He had transferred from the cavalry to the flying corps in 1917, and had stalled and spun-in during an early training flight, breaking his jaw. In hospital he had time to ponder on the cause of his accident and on means of preventing stall, concluding that a cascade of small aerofoils within a normal wing profile might have better properties than the equivalent single aerofoil. To study this idea, he made a simple wing model and rigged up an electric fan to entrain cigarette smoke over it, so as to obtain a crude form of flow visualisation. Satisfied with the result, he drafted a patent specification as early as February 1918, some weeks before Handley-Page's first application, but... was unable to convince the German Patent Office that the invention would work.... It was quite by chance that he saw an account of a demonstration by Handley-Page on 21 October 1920, and immediately challenged his priority in the invention. Still the German Patent Office refused to consider his claim....unless he could prove his invention experimentally. He then approached Professor Ludwig Prandtl at Gottingen, who agreed to do the necessary wind tunnel tests for 1000 marks (£50); Lachmann had nothing like this sum to spare, but his mother lent it to him, and the result... convinced the patent examiners, who then granted the application backdated to February 1918."

With an origin like that, it is perhaps not surprising that the aeronautical community should, for 54 years, have a totally incorrect view of the physical principles underlying its operation. Until the publication of A.M.O. Smith's classic paper[2] in 1972, it was accepted widely that the slot performs as a boundary layer control device[3-6] - and this is not true.

Smith showed clearly that the device works because it manipulates the inviscid pressure distribution - and that is why it is such a powerful effect. The data of Foster, Ashill and Williams[7] illustrated in Fig 1 shows the flow over a typical high-lift aerofoil with a leading-edge slat and a single-slotted flap. It will be seen that the trailing-edge of the slat sits in the high-velocity region of the flow around the leading-edge of the main wing; because of this, the pressure co-efficient at the trailing-edge is significantly negative and thus the pressure rise on the slat is reduced. The same happens at the trailing-edge of the main wing due to the high velocities around the leading-edge of the highly-deflected flap. In addition, the circulation around the slat induces a downwash on the main wing; this downwash clearly reduces with distance from the slat, so that it modifies the local velocities most strongly near the leading-edge of the wing, reducing its peak suction markedly. The same mechanism operates near the leading-edge of the flap. As a result of this, the pressure rise to the trailing-edge of the overall wing is split up into a number of smaller pressure rises; when each of these is sufficient to just cause separation of the boundary layer, the overall pressure rise can clearly be very large.

Fig 1 also shows the boundary layers flowing through the slots. Clearly if the two elements (*eg* slat/wing or wing/flap) are too close together, the boundary layer on the aft element will merge with the wake from the upstream element to form a thick boundary layer, and separation, far from being delayed, will be provoked. Thus, in contrast to earlier ideas, the flow through the slots acts to *increase* the adverse viscous effects rather than to alleviate them.

2 THE UK NATIONAL HIGH-LIFT PROGRAMME

2.1 Introduction

In 1968, K.J. Turner completed a secondment to the Defence Staff in the British Embassy in Washington; during his three years in the US, he had become increasingly aware of the advances being made by the US Industry in the exploitation of high-lift devices. The comparisons between the "slat + 3-slot flap" of the B727-100, and the "droop-nose + 2-slot flap" of the HS Trident 1, or between the "plain leading-edge + 1-slot flap" of the BAC 1-11/500 and the "slat + 2-slot flap" of the DC9-30, are indicative of the contemporary differences which worried Turner. At the same time, he was aware of the progress being made in the US in the understanding of the basic physics of how slotted wings worked. On his return to the UK, he put forward the concept of a "National High-Lift Programme" to be run as a collaborative exercise between the RAE (now DRA) and Industry. Government would provide most of the funding through RAE, whose role would be to participate strongly, but also to manage the programme and attempt to distil the general conclusions from the mass of data.

The programme had two major objectives:

(1) to provide sufficient data to enable the most appropriate high-lift system to be selected for any given project;

(2) having made this selection, to provide adequate procedures and information to permit the detailed design of systems that were efficient in aerodynamic, mechanical, structural, and weight terms.

These objectives lead to a programme that had a number of distinctive features:

(a) a research programme into the structural and mechanical design of high-lift systems would be run in parallel with the aerodynamic programme in order to:

- (i) provide a "research" environment in which new, innovative, lighter, and more reliable mechanisms could be invented;
- (ii) provide data on the weights of high-lift systems of varying complexity.

This research programme would cover high-lift system installations on a typical civil transport wing, and also on the wing of a typical "swing-wing" combat aircraft

(b) the aerodynamic programme would aim to produce data at two levels:

- (i) data of a fundamental nature which would cast light on the dominant physical processes involved and might lead to improved theoretical prediction methods;
- (ii) data of direct use in project design.

(c) all the high-lift devices were to have the shapes of their "cut-lines" *eg* regions "m" and "n" in Fig 1, designed, using the A.M.O. Smith multi-aerofoil program, to have "sensible" pressure distributions without large, and very sharp, suction peaks; the locations of the various elements to be achieved in the structural and mechanical design studies, were also to be decided on the basis of "sensible" pressure distributions calculated from the A.M.O. Smith program.

2.2 The Structural/Mechanical Design Programme

The complete set of leading- and trailing-edge devices embodied in the programme are defined in Tables 1 and 2 (located at the end of the text) and shown schematically in Fig 2. The tables indicate which of these devices were considered in the context of:

(a) a civil transport aircraft,
(b) a military combat aircraft.

Within the structural design studies issues of reliability, fail-safe design, and weight- and cost-saving were all addressed in addition to the normal stiffness and strength considerations. In some cases stiffness was particularly important in order to ensure that the designed aerodynamic lap and gap settings were maintained within tolerance under load.

At the end of the structural design programme, each of the designs was re-visited again in the light of the experience gained in the rest of the programme, and the designs and the weights were revised. This lead to a weight prediction method[8] that formed an important part of some of the final assessment work.

2.3 The Aerodynamic Research Programme

The aerodynamic research programme was conducted on four different wind tunnel models:

(i) **a Two-dimensional model** - shown in Fig 3; it had suction on the side walls to remove the side-wall boundary layer and ensure very good two-dimensional flow; it had 2 rows of chordwise pressure tappings - one at mid-span, and one near the wall, so that the two-dimensionality of the flow could be checked; results were obtained by integration of the pressure distribution[9] for lift and pitching moment, and by wake traverse for drag; the geometric Aspect Ratio of the undeployed planform was 3.2;

(ii) **an Endplate Model** - shown in Fig 4; the model was hung from an overhead mechanical balance, the results from which formed the main output, but there was also a chordwise row of pressure tappings at mid-span, and it was intended that profile drag could be obtained by wake traverse; the geometric Aspect Ratio of the undeployed planform was 3.0;

(iii) a variable sweep **Swept Panel Model** - shown in Fig 5; this 1/2-model was mounted on struts from an underfloor mechanical balance using a false wall as a reflection plane, one strut being enclosed in the false wall; the wing could be set at a number of sweeps in the range 15 deg to 36 deg and had one row of pressure tappings which was streamwise at 31 deg sweep; the wing and high-lift devices had the same profiles normal-to-the-leading-edge as Models (i) and (ii); the geometric Aspect Ratio of the undeployed planform at 31 deg sweep was 5.0;

(iv) a variable sweep 1/2 model with a tapered planform **Model 477** - shown in Fig 6; the wing could be set at 1/4-chord sweeps of 20 deg, 30 deg, and 45 deg: this model was mounted on an underfloor 4-component mechanical balance, which was in turn hung from the floor turntable, and used the tunnel floor as a reflection plane without any form of boundary layer control; it had pressure pipes run spanwise so that holes could be drilled in them at a number of spanwise locations to enable the spanwise development of the pressure distribution to be explored; the wing and high-lift devices had the same streamwise profiles at 30 deg sweep, as Model (iii) at 31 deg sweep; the geometric Aspect Ratio of the undeployed planform at 30 deg sweep was 7.0.

All four models featured slat, and flap, supports that permitted extensive variation of the fore-and-aft and height positions of the flap and slat elements. Within the programme these movements were conventionally known as "lap" and "gap" even though that is not a precise description; for simplicity this nomenclature will be retained in this paper. Within the Programme, it was soon found that the definition of angles, origins, and Cartesian axes describing the locations of the elements of the high-lift system was a major problem, because initially each member had his own way of doing it. The systems chosen are defined in Figs 7, 8, and 9.

Boundary layer profiles were measured on all four models at some time during the programme using traverse mechanisms mounted external to the models; these caused some interference with the flow, but in no case was this excessive.

The fourth model formed the contribution from RAE, and the other three models formed the contribution from industry. About a quarter of the way through the Programme, two other models were added to the aerodynamic programme - a "wall-to-wall" two-dimensional model and a complete model with a planform typical of a strike fighter - and these were aimed at the evaluation and development of high-lift systems based on Boundary-Layer-Control (BLC) by blowing with low-pressure air derived from the fan stages of a turbofan engine. The results of this additional part do not form part of this paper.

3 RESULTS FROM THE AERODYNAMIC RESEARCH PROGRAMME

3.1 Technique Development - Comparison of the Results from the Different Models

3.1.1 Two-dimensional vs Endplate Models

It was known from previous tests[10,11] that the two-dimensional technique used gave very good two-dimensional conditions - but the test technique, and the subsequent data reduction, were extremely time-consuming - and therefore expensive. The Endplate model, on the other hand, provided the data required quickly, easily and accurately from the balance. The question nevertheless remained - was the flow on the Endplate model two-dimensional?

On both models, flow visualisation indicates two-dimensional flow, and comparison of the forces obtained from the integrated pressure distributions at the centre, and near the wall, or the Endplate, shows less than 10% reduction in lift as the end of the wing is approached. However, comparison of the centre-line pressure distributions in Fig 10 shows that these are radically different. It is clear, despite the effects of the Endplates in maintaining the loading across the span of the wing, that the downwash from the trailing vorticity increases quite strongly across the chord, leading to higher loadings near the leading-edge, and lower loadings towards the trailing-edge.

At first sight, it seems probable that this flow development rules out the use of the Endplate model for serious high-lift research. However, if we form the ratios of the lift at optimum locations of the slat and flap to those achieved at off-optimum locations[12,13,16] - as shown in Table 3 - it can be seen that the Endplate Model seems to produce the same optimum locations as the two-dimensional model. This is an important result because of the financial and time implications on high-lift research - and it underpins much of the National High-Lift Programme.

Table 3
Comparison of the Effect of Flap and Slat Movements on the Endplate and "Wall-to-Wall" Models

X_s %	Z_s %	X_f %	Z_f %	$C_{L\ 2\text{-}D}$	$C_{L\ E/P}$	$\dfrac{C_{L\ 2\text{-}D}}{C_{L\ 2\text{-}D}\text{ top row}}$	$\dfrac{C_{L\ E/P}}{C_{L\ E/P}\text{ top row}}$
SLAT	**L1**	**AT**	**25**	**DEGREES**			
-1.5	2.5			4.15	3.85	1.000	1.000
-1.0	2.0			4.16	3.84	1.002	0.997
-0.5	1.5			4.02	3.67	0.969	0.953
0.0	1.0			3.52	3.20	0.848	0.833
FLAP	**T2**	**AT**	**20**	**DEGREES**			
		0.0	2.3	4.13	3.95	1.000	1.000
		2.0	2.3	4.09	3.89	0.990	0.985
		4.0	2.3	3.97	3.80	0.961	0.962
		0.0	0.5	4.05	3.86	0.981	0.977
		0.0	5.0	4.11	3.92	0.995	0.992
FLAP	**T7**	**AT**	**45**	**DEGREES**			
		-1.0	2.0	4.86	4.62	1.000	1.000
		-0.5	2.0	4.81	4.58	0.990	0.991
		+0.5	2.0	4.70	4.48	0.967	0.970
		-1.0	1.0	4.81	4.58	0.990	0.991

The strong trailing vorticity behind the Endplate model has another - and more unfortunate - consequence. The vorticity distorts and stretches the wake as it passes downstream, with the result that the drag calculated from a wake traverse varies considerably with the downstream position of the traverse, as shown in Fig 11. Because of this, the results from Wake Traverse measurements are of little use, and their collection was quickly discontinued within the Programme.

As a consequence, information on the profile drag characteristics of high-lift devices had to be derived from measurements of overall drag obtained from the balance on which the Endplate Model was mounted. By correlation between these drag values and true profile drag measurements on the "Wall-to-Wall" model for the same configuration, values of the vortex drag on the Endplate Model could be derived. Unfortunately, the values of vortex drag so-derived exhibited some dependence on device and deployment angle; this meant that drag comparisons between similar configurations (eg between single-slotted flaps with 84%, 90%, & 96% shroud position, {L1/T1, L1/T2,L1/T3}) could be made with some confidence, but that the establishment of the profile drag increment between, say, a single-slotted flap at 20 deg and a triple-slotted flap at 45 deg,{L1/T8(45) - L1/T2(20)}, involves some uncertainty.

3.1.2 Two-dimensional vs Swept Panel Model

The Swept Panel Model was included in the Programme to give information on the effect of sweep on the performance of high-lift devices and, more importantly, on the optimum location of slats and flaps. In order to interpret the data it was important to know the relationship between the pressure distribution on this wing and the two-dimensional wing; clearly with such a simple wing the two pressure distributions ought to coincide when both are referred to the velocity normal to the leading-edge (simple-sweep theory). Fig 12 shows the same type of discrepancy as shown by the Endplate model - and for the same reason. The low Aspect Ratio - chosen to maximise the Reynolds number in a small tunnel - has resulted in a significant variation, across the chord, of the downwash from the trailing vorticity. Fig 13 supports this by showing that, for each of slat/wing/flap, the pressure distributions at the various sweeps collapse reasonably well when referred to the velocity normal to the leading-edge; it is reasonable to assume that the residual differences are due to the changing Aspect Ratio with sweep.

3.1.3 Two-dimensional vs Model 477

The planform of Model 477 was chosen to:

(a) have a high enough Aspect Ratio to provide some part of the span which would give a close approximation to "Infinite Swept-Wing" conditions;

(b) resemble closely the part of a typical transport aircraft wing outboard of the crank.

Once again, it was important to establish how well these aims had been met. Referring the pressure distribution at mid-semi-span to the velocity normal to the 1/4-chord sweep, produced a fairly poor agreement with two-dimensional. However, *when the local pressure was referred to the velocity normal to the local sweep*, very good agreement was obtained - as shown in Fig 14. This concept is further supported by Fig 15 which shows the agreement between the "local-sweep normalised" pressure distributions at sweeps of 20 deg, 30 deg, and 45 deg.

3.2 Optimisation of Leading-edge Slats

Section 1 described, in qualitative terms, the effects on the pressure distributions on the slat and wing arising from their mutual interaction. Considering one of the "standard" NHLP configurations [L1(25)/T2(20)] consisting of:

(a) the 12.5% chord leading-edge slat (L1) set at 25 deg,
(b) the 33% chord trailing edge flap with the flap shroud at 90% chord (T2) set at 20 deg,

then Figs 16a and 16b show the response of:

(a) the trailing-edge pressure,
(b) the peak suction,

on the slat as the trailing-edge is moved over a grid of points (Xs,Zs), such that -5% < Xs < 0% and 0% < Zs < 4% - see Fig 7. The calculations have been done at a constant fixed incidence close to that for the maximum lift observed experimentally.

Fig 16a demonstrates the strong variation of the trailing-edge pressure to the movement of the slat through the flow-field around the leading-edge of the wing; for example, with the slat 1% chord ahead of the wing leading-edge (Xs = -1%) the slat trailing-edge pressure changes from Cp =-6 at a height Zs = 4% above the leading-edge, to Cp = -1.3 at a height 1% below the leading-edge (Zs = -1%). In contrast, the peak suction on the slat (Fig 16b) varies relatively slowly with change of height, but changes rapidly with variation of the lap (Xs) - for instance, at a height of Zs=1%, moving the slat forward from Xs = 0% to Xs = -5% reduces the peak suction from Cp = -29 to Cp = -19.

The variation of the slat peak suction on its own is important because the levels are very high, and hence compressibility effects on maximum lift can be experienced down to Mach numbers as low as 0.15 . The difference between the peak suction and the trailing-edge pressure represents the pressure rise experienced by the boundary layer over the upper surface of the slat, and hence determines the thickness of the slat wake, or even separation of the flow on the slat. The variation of this pressure rise determined from Figs 16a and 16b is shown in Fig 17, and Fig 18 shows the corresponding pressure rise over the wing. Together these show that, as the slat is moved:

(i) vertically (*ie* varying Zs, constant Xs):

(a) the pressure rise over the wing exhibits a *minimum* value; clearly this is the best position for the slat in order to delay separation of the boundary layer on the wing,
(b) the pressure rise over the slat exhibits a *maximum* value at about Zs = -1%, and decreases as Zs increases - primarily due to the negative change in the trailing-edge pressure

(ii) horizontally forwards (*ie* decreasing Xs, constant Zs):

(a) the level of the wing pressure rise *increases* markedly,
(b) the level of the slat pressure rise *decreases* markedly.

From these results, we can extract contours of constant slat and wing pressure rise, and constant slat peak suction, and plot these in the Xs,Zs plane. Suppose we assume that, to avoid boundary layer separation,

(a) the slat pressure rise $|\Delta Cp_s|$ must be <22
(b) the wing pressure rise $|\Delta Cp_w|$ must be <11
(c) the slat peak suction $|Cp_s|$ must be <26

then, with these assumptions, it can be seen that the optimum location of the slat must lie within the boundaries indicated on Fig 19a. Similar boundaries, for a slat angle of 20 deg, are drawn in Fig 19b. The experimentally determined maximum lift contours are shown in Fig 20[14]. One of these contours is also shown on both parts of Fig 19, and it can be seen that, despite the simplicity of the model, it correctly indicates,

(a) the size and direction of the migration of the optimum point, as the slat angle is changed,
(b) the reduction in the area of the contour, as the angle is reduced from 25 deg to 20 deg, suggesting that the C_{Lmax} at the optimum location is less at 20 deg than at 25 deg.

This confirms that the primary effect of the slot is to manipulate the inviscid pressure distribution.

However, it will also be apparent that the simple model used above, does not give a very good representation of the shape of the experimental maximum lift contours - in particular it gives no indication of the closure of the contours at the top. This, of course, is not surprising in view of the simplistic separation criteria used which clearly ignore the shape of the pressure distribution, but these criteria also fail to take in to account that the viscous layers on the wing and flap cannot be considered in isolation, but that each is affected by the overlying wake from the upstream element. Figs 21 and 22 show the development of the viscous layers over the wing+slat when fitted with a single-slotted flap (Fig 21) and with a double-slotted flap (Fig 22). In both cases, it can be seen that the slat wake merges with the wing boundary layer causing significant increases in the momentum deficit.

It is relatively easy, using modern CFD methods and coupling techniques[15], to couple a boundary-layer code to an inviscid code for calculating the viscous flow around multiple aerofoils, but this will not yield good estimates of the variation of maximum lift with slat (or flap) position unless the boundary-layer method is capable of dealing with the merging of the boundary layer and wake.

3.3 Optimisation of Trailing-edge Flaps

The physical processes involved in the determination of the optimum location of trailing-edge flaps are exactly the same as those for leading-edge slats - but they appear different because the balance between the viscous and inviscid effects is very different. For trailing-edge flaps, the viscous effects are much larger, and the inviscid effects are much smaller than for slats.

If we replace the lifting effect of each element by a single vortex, then these will be situated in the vicinity of the 1/4-chord of the respective elements, and it will be clear that the vortices of the slat and wing are relatively close together and there will be a significant interaction between them leading to a considerable variation of downwash from the slat across the chord of the wing; on the other hand those of the wing and flap are relatively far apart, and the downwash from the wing will vary little across the chord of the flap. Therefore to get any worthwhile reduction in pressure rise over the flap, requires the leading-edge of the flap to be very close to the trailing-edge of the wing. Clearly the limit to their proximity comes from the merging of the flap boundary layer with the wing wake.

Fig 23 shows the maximum lift contours from the optimisation of the T2 flap at 20 deg[12]; the optimum position is clearly around zero lap and the lift falls away as the flap is moved forwards or rearwards from this position. Fig 24 shows that the optimum location depends on the leading-edge device fitted, because, of course, the slat wake adds to the thickness of the wing wake over the flap. At higher flap angles, *eg* Fig 25 for T2 at 40 deg[16], the loss in lift as the flap is moved rearwards is more pronounced, and large scale separation of the flap flow sets in for quite small rearward movements. However, this flow also exhibits an even more interesting phenomena; it appears that the wing wake, flowing over the flap, also has the effect of reducing the peak suction of the flap - presumably through its displacement effect. Thus, for some flap positions (identified on Fig 25) the flow over the flap is separated at low incidence when the wing wake is thin, but, at higher incidence as the wing wake thickens, the flap flow suddenly re-attaches producing a characteristic non-linear increase in lift and negative pitching moment, and a reduction in drag. The incidence at which the re-attachment occurs gets higher as the flap moves away from the wing, until ultimately the flow fails to re-attach at all, and a large decrement in maximum lift results. This type of behaviour has also been observed during the optimisation of double-slotted flaps[17] and triple-slotted flaps[18].

It will be obvious that increases in Reynolds number will thin the wing wake and exacerbate this behaviour; indeed this has been found to be one of the prime sources of adverse Scale effect on high-lift systems[19,20]. Fig 25 shows that the potential losses in maximum lift are very large and demonstrates why it is so important to conduct high-lift development at the highest-possible Reynolds number.

3.4 Comparison of Various Leading- and Trailing-edge Devices

Fig 26 shows a set of leading-edge slats and Krugers, whose maximum lift performance as the deployment angle is varied, is shown in Fig 27. This demonstrates that the maximum lift performance is not very sensitive to the angle of the leading-edge device - so long as it is at its optimum setting for that angle. The increments in maximum lift and profile drag arising from these devices, are shown in Fig 28

Figs 29 and 30 show the lift curves for a double- and a triple-slotted flap each set at three angles. It is noteworthy that the maximum lift for both flaps varies very little with angle, but the incidence at which a given proportion of the maximum is achieved, varies quite considerably. This feature can be of great value on military aircraft where pilot vision, undercarriage length and position, and weapon carriage, can all combine to impose significant restrictions on the maximum incidence usable in the approach.

3.5 Project Level Analysis of Results

The wealth of two-dimensional and swept wing data available from this Programme raised the possibility of a major enhancement to the prediction of maximum lift within the RAE Multivariate Optimisation Programme[21]. A major strength of the dataset was that it was possible to carry out internal consistency checks, since maximum lift increments could be derived in several different ways; for instance the increment in maximum lift due to fitting a leading-edge slat (L1) could be derived from

(a) L1/T0 - L0/T0
or (b) L1/T2 - L0/T2

similarly, the increment due to the deployment of a trailing-edge flap (T2) could be derived from

(a) L0/T2 - L0/T0
or (b) L1/T2 - L1/T0.

It was soon clear that the increments so derived differed considerably one from the other, and this was because:

(a) a straightforward subtraction fails to take into account properly the differing area extensions;
(b) there is, in some cases, an interaction between the leading- and trailing-edge devices, which leads to considerable uncertainty in the evaluation of the increments.

To examine the first of these factors, let us consider the idealised situation sketched in Fig 31, where:

(a) the C_L is based, in the usual way, on the reference area of the wing (*ie* with the high-lift devices undeployed); the deployment of the high-lift devices then leads to an increase in lift-curve slope,
(b) it is assumed that deployment of the flap leads to a constant change in zero lift angle,
(c) it is assumed that the deployment of the slat leads to a constant increment in stalling angle - whether the flap is deployed or not.

From the relations set out on the lower part of Fig 31, it is clear that each of the values K_1, K_2, K_3, has to be based on the *actual* area involved, and then the addition of all the increments is brought back to the reference area at the end. This approach is confirmed in Fig 32a where, after the change in zero-lift angle has been taken out by subtracting the value of C_L at 5 deg incidence, the lift curves for the various combinations of high-lift devices collapse very well.

To look at the second factor, it can be seen from Fig 32a that, in common with most other sets of data, there is a significant decrement in stalling angle when the flap is deployed alone - and this violates the assumptions of Fig 31. This situation is examined more closely in Fig 32b. Here the two curves involving the slat represent the optimum angle in each case - and these demonstrate very similar stalling angles; if the curve for the flap deployed alone is extrapolated to the same stalling angle as the "wing alone", it can then be seen that there is complete consistency in the maximum lift increments, no matter which way they are evaluated. In this way, it can be seen that the $\Delta C_L = 0.25$ "slat/flap interaction" correctly belongs in the flap increment.

To produce a full project-level maximum lift prediction method, clearly requires a way of moving from the prediction of increments in two-dimensional, to the prediction of increments on a swept wing of finite Aspect Ratio. This was accomplished by assuming that

(a) the two-dimensional increments varied as $\cos^n$(sweep) - where 'n' was allowed to have different values for

(i) leading-edge devices
(ii) the main wing
(iii) trailing-edge devices

and "sweep" was taken as the 1/4-chord sweep of the element when deployed *ie* taking note of the dependence of the pressure distribution on "local sweep" identified in section 3.1;

(b) the ratio between the "two-dimensional value modified by sweep" defined above and the "overall max.lift" was purely a planform effect *ie* initial stall occurred at the highest local C_L point across the span

The values of 'n' which resulted from this analysis showed a fair degree of scatter, but nevertheless consistently[22,23] showed the type of wide variation across the chord indicated by the values given below in Table 4. It is difficult to devise an acceptable explanation for this behaviour, but the pressure distributions genuinely indicate that near maximum lift with increasing sweep, that the proportion of the total load carried by the slat increases, and that carried by the flap decreases.

Table 4
Values of Sweep Factor 'n' for Various Parts of the High-lift System

DEVICE	'n'
(a) Leading-edge devices	1.10 +/- 0.50
(b) Main Wing	2.10 with flap deployed 1.20 with flap retracted
(c) Trailing-edge devices	3.60 for flap angles up to 20 deg

Finally, the effect of part-span flaps was derived empirically by analysis of the changes in zero-lift angle and maximum lift found on Model 477 as the part-span extent was varied.

The final expression for maximum lift on a finite swept wing was written

$$C_{Lmax} = \frac{1}{\hat{C}_L/\bar{C}_L}\left[[A] \left(1 + \left(\frac{c_{ext}}{c}\right)_{SLAT} + \left(\frac{c_{ext}}{c}\right)_{FLAP} \left(\frac{S_n}{S_{n=1}}\right)\right)\right],$$

where

$$[A] = (C_{Lmax})_{WING} \cos^{nw}\phi \; f(t/c) + \Delta(C_{Lmax})_{SLAT} \cos^{ns}\phi + \Delta(C_{Lmax})_{FLAP} \cos^{nf}\phi \sqrt{\frac{S_n}{S_{n=1}}}$$

S_n = total area of wing + part-span flap

$S_{n=1}$ = total area of wing + (notional) full-span flap

$c_{ext_{SLAT}}$ = chord extension of the slat

$c_{ext_{FLAP}}$ = chord extension of the flap

$\hat{C}_L/\bar{C}_L$ = highest value of local C_L across the span

$f(t/c)$ = empirical function of thickness:chord ratio.

The results from this expression are compared with the achieved maximum lift values on Model 477 over a full range of sweeps and various leading-edge devices in Fig 33.

4 RESULTS FROM THE STRUCTURAL/MECHANICAL DESIGN PROGRAMME

The structural/mechanical designs were done in great detail and produced a wealth of detailed weight and cost data for each device. For a Variable Geometry fighter, the weight of each leading-edge device[24] is compared with that of the 12.5% chord leading-edge slat (L1) in Fig 34, and corresponding comparisons are made for trailing-edge devices[25] based on the 33% chord single-slotted flap (T2), in Fig 35. Similar comparisons[26-29] for a civil aircraft are given in Figs 36 and 37. All the weights of the high-lift devices lie between ±20% of the weight of the datum devices - with the exception of the Flexible Kruger which is almost 80% heavier than L1. The costs vary much more, and complicated triple-slotted flaps may cost nearly 2.5 times the cost of a simple single-slotted flap.

Despite this wealth of data, it is difficult to use it to draw guidelines for the selection and design of high-lift systems for complete aircraft because the weights have to be interpreted in relation to the aerodynamic capability, and both have to be related to exchange rates for the design of the whole aircraft. The next section describes one possible approach to this problem for civil aircraft, and reviews the results from several applications of the method.

5 ANALYSIS OF RESEARCH RESULTS IN THE CONTEXT OF A COMPLETE AIRCRAFT

5.1 Aerodynamic Model

For a civil aircraft, the take-off is usually the most demanding design case for the selection of the high-lift system - especially for a twin-engined aircraft - because the high-lift system has to supply not only high-lift (to allow a short take-off run) but also low drag so as to allow the aircraft to comply with the statutory minimum climb gradient after take-off.

Perry[30] has shown that the take-off wing loading can be expressed in a form which, after some manipulation, can be written as:

$$\frac{(W)^2}{(\sigma Sd)} = \frac{C_L}{K_d}\,\frac{(T)}{(\sigma Sd)}\,, \qquad (1)$$

where W = Aircraft Take-off weight
T = Take-off Thrust
S = Aircraft wing area
W/σSd = Parametric Take-off wing loading
T/σSd = Parametric Take-off thrust loading
d = take-off distance
σ = density ratio
Kd = Empirical relation incorporating the effects of variation of thrust during the take-off run, and the airborne transition distance, etc.

The climb gradient (γ) after take-off may be written

$$(\gamma) = \frac{(n-1)}{n}\,\frac{T}{W}\,\frac{1}{(C_L/C_d)} > (\gamma)_{req} \quad , \qquad (2)$$

where (γ) = Climb Gradient
$(\gamma)_{req}$ = minimum statutory climb gradient after take-off = f(n)
n = number of engines
C_L/C_d = Aircraft lift:drag ratio during climb-out at V_2 .

In physical terms, the lift-dependent drag, C_L/C_d *normally decreases* with increasing C_L in the range of interest for take-off, and hence for any given value of T/W there is an upper limit to the C_L at which aircraft can maintain an adequate climb gradient after take-off.

However, if we confine ourselves to conditions where the climb gradient requirement is just met, then (γ) becomes a constant in equation (2) and equations (1) and (2) may be treated simultaneously to yield solutions

$$\frac{W}{\sigma Sd} = \frac{(\gamma_{req} + C_D/C_L)}{(n-1)/n}\,\frac{C_L}{Kd} \; , \qquad (3)$$

$$\frac{T}{\sigma Sd} = \frac{(\gamma_{req} + C_D/C_L)^2}{(n-1)/n}\,\frac{C_L}{Kd} \; . \qquad (4)$$

These two equations define the required aerodynamic conditions for a given aircraft such that the *limitations set by the available take-off* distance and by the minimum climb gradient are both satisfied.

Alternatively, equation (3) may be re-written in terms of $T/\sigma Sd$ from equation (4), to yield,

$$\frac{W}{\sigma Sd} = \left[\frac{T}{\sigma Sd}\,\frac{C_L}{Kd}\right]^{0.5} \qquad (5)$$

For safety reasons, the take-off speed is required to be at least 20% greater than the stall speed - thus the take-off C_L is $0.7C_{L_{max}}$. Thus from wind tunnel data the values of

(a) $0.7C_{Lmax}$ and (b) C_L/C_d @ $0.7C_{Lmax}$

can be inserted into equations (3) and (4)[or (5)] to yield values of

"$W/\sigma Sd$" as a function of "$T/\sigma Sd$' .

If the wind tunnel data is converted to *trimmed conditions*, this, in principle, enables the aerodynamic data to be incorporated with the weight data from the Structural/Mechanical Design programme, to yield conclusions on the relative merits of different high-lift devices in a complete **aircraft context.**

Two methods have been used to convert the simple lift and drag values from wind tunnel tests to trimmed conditions. The first of these simply calculates a lift reduction corresponding to the down load on the tail to trim the aircraft with the CG assumed to lie at the 1/4-chord point of the Mean Aerodynamic chord. Thus, if we make the simple assumption that the effective tail arm is 3.5 mean aerodynamic chords in length, then

$$\text{(i)}\quad C_{Ltrim} = 0.7C_{Lmax} + \frac{C_m \ @\ 0.7C_{Lmax}}{3.5} \qquad \text{(ii)}\quad C_{Dtrim} = C_D \ @\ 0.7C_{Lmax} \ .$$

This method gives trim corrections that are, in general, too large; this is because of the neglect of the downwash at the tail arising from the trailing vorticity of the wing and flap system. However this method was used for the investigations described in sections 5.2 and 5.3; for the exercise reported in section 5.4 a more rigorous method was used which properly took into account the downwash at the tail.

5.2 Aerodynamic Optimisation of Part-span Flap Extent

Five sets of aerodynamic data were obtained from Model 477, as set out in Table 4 below. To examine the optimum part-span extent, the analysis method above was used to compare sets 1 and 2 (to demonstrate the effect of change of sweep) and sets 2 and 3 (to demonstrate the effect of changing the leading-edge device). Because the Parametric Wing Loading ($W/\sigma Sd$) varies very rapidly with the Parametric Thrust Loading ($T/\sigma Sd$), the data resulting from feeding wind tunnel values of C_{Ltrim} and C_{Ltrim}/C_{Dtrim} into equations (3) and (4), has been ratioed with corresponding data calculated for a hypothetical aircraft having an analytical variation of C_L/C_D with C_L:

$$\text{Hypothetical aircraft}\quad C_{Ltrim}/C_{Dtrim} = 14 - 3C_{Ltrim} \ .$$

The resulting "Wing Loading Ratio" $(W/\sigma Sd)_{477}/(W/\sigma SD)_{datum}$ is designated by the variable 'χ'.

Table 5
Sets of Part-span Data from Model 477

Set	Sweep and aspect ratio	Leading-edge	Flap Gaps	Shroud position
1[13]	20 deg/8.1	PLAIN	3 at each angle	90%
2[31]	30 deg/7.0	PLAIN	3 at each angle	90%
3[32]	30 deg/7.0	SLATTED	3 at each angle	90%
4	30 deg/7.0	PLAIN	3 at 20, 14, 8 deg	84%
5	30 deg/7.0	PLAIN	3 at 20, 14, 8 deg	96%

Flap Spans = 56%, 75%, 100%
Flap angles = 20, 17, 14, 11, 8, 5 degrees

Carpet plots of the variation of C_{Ltrim} and C_{Ltrim}/C_{Dtrim} for data set 2 are given in Figs 38 and 39. When these values are inserted into equations (3) and (4), the typical variation of 'χ' with variation of the Parametric Thrust loading ($T/\sigma Sd$) shown in Fig 40 is obtained. From Fig 40, it can be seen that the highest value of 'χ' at a constant value of $T/\sigma Sd$, will occur for a flap span that is less than 100%. By a process of further interpolation, the results shown in Fig 41 are obtained which show an optimum flap span of about 80%, but performance is within 0.1% for all flap spans between 70% and 90%.

The figures for data sets 1 and 3, corresponding to Fig 41, are shown in Figs 42 and 43. Comparing these three figures, it can be seen that:

(i) With a Plain Leading-edge at 20 deg sweep, and Aspect Ratio 8, the optimum flap span is 100% for all thrust levels above that necessary to achieve "matched" take-off conditions at 7-8 deg flap. For all thrust levels below this, it is better to reduce the span of the flap than to reduce the angle of the flap still further. Data from the Endplate Model at low flap angles, shows that the profile drag is a minimum at around 8 deg of flap - consequently this result might be expected.

(ii) Increasing the sweep of this high-lift configuration to 30 deg (and consequently reducing the Aspect Ratio to 7) produces an optimum span of flap which is about 80%, and the take-off C_L can be matched to the thrust in an optimum way by changing flap angle between 20 deg and 5 deg. It seems probable that this change in behaviour is a result of the differing relative rates of change of drag as either the flap span or flap angle is reduced. At 20 deg sweep, with its higher Aspect Ratio, the increase in induced drag as the flap span is reduced is *less than the increase in profile drag* as the flap angle is reduced below 7-8 deg. At 30 deg sweep, with its lower Aspect Ratio, the opposite happens - the increase in induced drag as the flap span is reduced is now *greater* than the increase in the profile drag associated with reducing flap angle.

(iii) Putting a leading-edge slat on to the wing at 30 deg sweep, increases somewhat the variation of optimum flap angle with flap span, and reduces the span by about 6%. This behaviour is to be expected because, in the slatted case, the proportion of the total span loading arising from incidence (and hence spread across the whole span irrespective of the flap span) is much greater. It is worth pointing out that the maximum lift for the slatted case is over $\Delta C_L = 1$ higher than for the plain leading-edge.

5.3 Aerodynamic/Structural Investigation of Leading-edge Devices

The above method was used on wind tunnel data from Model 477 to compare the performance of several leading-edge devices[33], using weight data obtained from the relevant structural design studies. The most interesting of the results obtained is the comparison between

(a) the 12.5% chord leading-edge slat L1 and
(b) the 17% chord flexible Kruger L7

The Kruger had a slightly higher maximum lift and lower drag, giving an advantage of about 1.5% in take-off wing loading; however the greater weight of the Kruger reduces this to about 0.75% in terms of greater fuel/payload. Further optimisation of the slat setting across the span, succeeded in reducing the drag to the point where there was no difference in the payload performance of the two devices[34].

5.4 Aerodynamic/Structural Investigation of Optimum Shroud Length

From the previous parts of the National High-Lift Programme (and from standard aerodynamic theory) it was known that moving the position of the flap shroud rearwards

(i) increased the maximum lift and the sectional value of C_L/C_D;

(ii) increased the weight of the high-lift system, mainly because of the increase in length of the cantilever tracks that carry the flap at full extension;

(iii) increased the tail load to trim because of the further aft centre of lift;

(iv) increased the induced drag of part-span configurations because of the larger discontinuity in chord distribution.

With one advantage and three disadvantages, it was unclear where the optimum shroud length would lie; in addition the evidence from different aircraft manufacturers was conflicting.

The aerodynamic data for this exercise came from sets 2, 4, and 5 - but, in this case, in addition to the analysis performed above, it was necessary to:

(a) deduce a landing flap design to go with each combination of flap angle and shroud length - so that the weight of the trailing-edge high-lift system could be estimated.

(b) conduct a tail-sizing exercise - so that a proper estimate could be made of the trim drag taking into account the downwash at the tail from the wing trailing vorticity

To do the first of these, landing and take-off speeds and weights for a large range of transport aircraft were reviewed and revealed that the ratio

$$\frac{C_L \text{ (on approach)}}{C_L \text{ (at take-off)}} \approx 1.12 \ .$$

It was further assumed that

$$C_L \text{ (at take-off)} \approx 0.7C_{Lmax} \text{ (for take-off)}$$

$$C_L \text{ (on approach)} \approx 0.6C_{Lmax} \text{ (for landing)}$$

so that

$$\frac{C_L \text{ (for landing)}}{C_L \text{ (for take-off)}} \approx 1.31 \ . \qquad (6)$$

From Endplate Model data, the following values of the ratio of maximum lifts with different flaps were obtained.

Table 6
Values of the Ratio of Maximum Lift with Various Landing Flaps to that of a Flap at Take-off Setting

	FLAP TYPE		
	SINGLE SLOTTED	DOUBLE SLOTTED	TRIPLE SLOTTED
$\frac{C_{L\max} \text{ at landing flap (40 deg)}}{C_{L\max} \text{ at landing flap}}$	1.19	1.30	1.46

Thus from the results at 20 deg flap in each of sets [illegible], 4, and 5, the max lift for each type of landing flap could be estimated, and compared with the demanded max lift from equation (6) in order to select the landing flap required. With the landing flap decided, the resulting Pitching Moment could be derived from Endplate Model data.

To work out the size of the tail, it was assumed that it was necessary to provide a usable CG range of 35% Standard Mean Chord, and the tail volume coefficient was plotted against CG position for the two conditions

(a) to trim the landing flap
(b) to provide an adequate stick-fixed static margin for the cruise configuration

leading to a typical graph shown in Fig 44. The resulting tail size, expressed as a ratio with the wing area, for a tail arm of 3.5 chords, is shown in Fig 45. Having decided the tail size, the Trim Drag can be evaluated, and this is shown in Fig 46; it will be noted that, as explained above, these trim drag increments are negative due to the downwash at the tail. The aerodynamic take-off performance can now be calculated, as before, by inserting

(i) $C_L = 0.7C_{L\max} + \frac{C_m}{3.5}$,

(ii) $C_D = C_D \text{ @ } 0.7C_{L\max} + C_{D\text{trim}}$,

into equations (3) and (4), and evaluating $(W/\sigma Sd)$ and $(T/\sigma Sd)$.

The weight of the high-lift system can then be estimated using the method due to Brookes[8]. Unfortunately for the generality of this research exercise, Brookes' method produces weights/unit area that depend on aircraft size. For relevance at the time the work was done, an aircraft approximating to a BAC 1-11, with a range of 3500 km, and a Maximum Take-off Weight (TOW) of 45350 kg, was chosen to continue the exercise. A typical weight breakdown of the high-lift system for 90% shroud position and 75% span flaps, is shown in Fig 47.

To complete the exercise, the Maximum Take-off Weight (TOW) of the aircraft was written:

$$\text{TOW} = W_{\text{structure}} + W_{\text{fuel}} + W_{\text{payload}} + W_{\text{high-lift system}} \, .$$

Kuchemann[33] shows that for this range

$$W_{\text{structure}} = W_{\text{engines}} + W_{\text{u/c+services}} + W_{\text{wing+controls}} + W_{\text{fuselage}} = 0.525.\text{TOW}$$

and therefore

$$W_{\text{fuel}} + W_{\text{payload}} = 0.475\text{TOW} - W_{\text{high-lift systems}} \, .$$

The resulting values of "fuel + payload" as the take-off flap angle and shroud length are varied, are given for 75% and 100% span flaps in Figs 48 and 49. For each shroud length, the "Fuel + Payload" weight rises as the thrust is increased and the take-off flap angle is increased to maintain matched take-off conditions; the variation is smooth until the single-slotted flap is no longer capable of supplying an adequate landing C_{Lmax} - at this point the landing flap has to become double-slotted. Because this is heavier, the "Fuel + Payload" drops discontinuously - and the same happens at higher thrusts and take-off flap angles where the landing flap becomes triple-slotted. The interesting part is that the graphs show a clear advantage to increasing the shroud length in comparison to retaining the same shroud length and increasing the complexity of the flap. However, the differences are quite small (of the order of 3% of "Fuel + Payload") and this presumably explains why different manufacturers have selected different designs of flap and all have been convinced that they have selected the optimum design - because other factors (such as cruise drag) could have effects which are larger than the differences shown here.

6 HIGH LIFT WORK IN THE UK SINCE NATIONAL HIGH LIFT PROGRAMME

Since the end of the National High Lift Programme, high lift research within RAE (now DRA) has centred around the exploration of Scale and Mach number effects on maximum lift using the capability of the DRA 5 metre wind tunnel. This has resulted in a number of papers describing the nature, and occurrence, of various identified types of Scale Effect[13,19,36,37].

7 CONCLUSIONS

A major research programme mounted in the UK in the 1970s, and known as the National High-Lift Programme has been described. In particular,

(a) the philosophy
(b) the experimental techniques
(c) the results obtained
(d) the implications for aircraft design,

have all been addressed. The programme was mounted in response to a perceived shortfall in capability in comparison with other countries - the USA in particular - and has played a major part in restoring the balance. It was one of four major research programmes mounted by the RAE in collaboration with BAe which contributed to the design of the A320 aircraft, and for which RAE and BAe were jointly awarded a Queen's Award for Technology in 1988.

Table 1
Designations for Trailing-edge Devices

T0	Plain trailing-edge
T1*†	33% chord single-slotted flap, 84%c shroud TE
T2*†	33% chord single-slotted flap, 90%c shroud TE
T2S*†	As T2, but slot sealed and flap faired into wing
T3	33% chord single-slotted flap, 96%c shroud TE
T4	33% chord double-slotted flap, 84%c shroud TE
T5*†	33% chord double-slotted flap, 90%c shroud TE
T6†	33% chord double-slotted flap, 96%c shroud TE
T7*†	33% chord double-slotted flap, 90%c shroud TE, 8.5%c extending vane
T8*†	33% chord triple-slotted flap, 90%c shroud TE, 8.5%c extending vane, 11.5%c extending tab
T8T	As T8, but vane retracted into fairing
T9*	33% chord double-slotted flap, 90%c shroud TE, 11.5%c extending tab
T10*	As T5, but deployed on an external hinge
T11*	As T7, but deployed on an external hinge

* Denotes devices on which structural and mechanical studies have been made in the context of civil transport applications. These configurations differed in some respects from their representations tested aerodynamically.

† Denotes devices on which structural and mechanical studies have been made in the context of military applications.

Table 2
Designations for Leading-edge Devices

L0*†	Plain leading-edge
L1*†	12.5% chord slat
L2*†	18% chord slat
L3†	Plain droop, from 15%c station
L4*†	Extending droop, from 12.5%c station, circular arc extension
L5*	Extending droop, from 18%c station, circular arc extension
L6*†	18% chord RAEVAM, flexible upper skin 5%c to 18%c
L7	Kruger devices, having an upper-surface profile giving an optimum pressure distribution when functioning as a flap with sealed flap/wing gap Flexible flaps: L7A Operating in slat mode, optimised configuration L7B* Operating in flap mode, optimised configuration L7C Unsealed gap, non-optimum configuration, similar to Boeing 747
L8*	Flexible Kruger slat, optimised for angle, lap and gap. Upper-surface profile designed to give optimum pressure distribution when functioning as a slat with optimised slot

* Denotes devices on which structural and mechanical studies have been made in the context of civil transport applications. These configurations differed in some respects from their representations tested aerodynamically.

† Denotes devices on which structural and mechanical studies have been made in the context of military applications.

REFERENCES

1	Barnes, C.H.	Handley-Page Aircraft since 1907, pp 210-216, Putnam (1988)
2	Smith, A.M.O.	Aerodynamics of High-Lift Airfoil Systems. AGARD CP 102, April 1972
3	Kuethe, A.M. Schetzer, J.D.	Foundations of Aerodynamics. John Wiley & Sons Inc (1959)
4	Thwaites, B.	Incompressible Aerodynamics. Oxford Clarendon Press (1960)
5	Houghton, E.L. Boswell, R.P.	Further Aerodynamics for Engineering Students. Edward Arnold, London (1969)
6	Duncan, W.J.	The Principles of the Control and Stability of Aircraft. Cambridge University Press (1959)
7	Foster, D.N. Ashill, P.R. Williams, B.R.	The Nature, Development and Effect of the Viscous flow around an aerofoil with High-Lift devices. RAE Technical Report 72227 (1972)
8	Brookes, W.	National High-Lift Programme Phase 5 - Parametric Weight Study. Report No.BAe-MFP-R-NHL-0079 (1981)
9	Woodward, D.S.	Further work on the integration of closed loops specified only as discrete data points. RAE Technical Report 73177 (1973)
10	Moir, I.R.M. Foster, D.N. Holt, D.R.	The Measurement and Analysis of the Profile Drag of a Wing with a Slotted Flap. RAE Technical Report 71158 (1971)
11	Foster, D.N. Irwin, H.P.A.H. Williams, B.R.	The two-dimensional flow around a Slotted Flap. ARC R&M 3681 (1971)
12	Cairns, I.C.D. Wedderspoon, J.R.	Analysis of Slat (L1), 20 deg single-slotted flap (T2), and 45 deg double-slotted flap (T7), tested on a two-dimensional model. BAC (Weybridge) Aero/FM/Report 041 (1973)
13	Fiddes, S.P. Kirby, D.A. Woodward, D.S. Peckham, D.H.	Investigations into the effects of Scale and Compressibility on lift and drag in the RAE 5m Pressurised Low-Speed Wind Tunnel. Journal of the Royal Aero Soc, pp 93-108, March 1985
14	Cairns, I.C.D. Wedderspoon, J.R.	Analysis of slat (L1) and 20 deg flap (T2) optimisation on a quasi-two-dimensional Endplate Model. BAC (Weybridge) Aero/FM/Report 039 (1971)

15	King, D.A. Williams, B.R.	Development in Computational methods for High-Lift Aerodynamics. Journal of the Royal Aero Soc, pp 265-288, August 1988
16	Finch, B.S.P. Wedderspoon, J.R.	Investigation into the performance of a 40 deg single-slotted flap on a quasi-two-dimensional Endplate Model. BAC (Weybridge) Aero/FM/Report 046 (19)
17	Finch, B.S.P.	Evaluation of a double-slotted landing flap (T7) on a quasi-two-dimensional Endplate Model. BAC (Weybridge) Aero/FM/Report 052 (1978)
18	Finch, B.S.P.	Evaluation of a triple-slotted landing flap (T8) on a quasi-two-dimensional Endplate Model. BAC (Weybridge) Aero/FM/Report 061 (1978)
19	Woodward, D.S. Ashill, P.R. Hardy, B.C.	Some Types of Scale Effect on high-lift Wings. ICAS Paper 43, ICAS (1984)
20	Garner, P.L. Meredith, P.T. Stoner, R.C.	Areas for future CFD development as illustrated by Transport Aircraft Applications. AIAA-91-1527-CP, Honolulu, Hawaii (1991)
21	Collingbourne, J.	Multivariate Optimisation applied to the initial design of transport aircraft. RAE Technical Report 84044 (1984)
22	Harris, K.D.	A Review of the Investigations into the effect of sweep on the Sectional High-Lift characteristics using the Panel Model Technique. BAe (Hatfield) Report HRS-R-RES-FM2362 (1978)
23	Woodward, D.S.	Steps towards an improved project level prediction of maximum lift. Unpublished RAE NHLP Review Paper 5/1978
24	Lee, N.	National High-Lift Programme Phase 1 - Comparative Report on Wing Leading-edge Devices. BAC SOR(P) 54, S&T Memo 8-72, DRIC-BR-32245 (1972)
25	Lee, N.	National High-Lift Programme Phase 1 - Comparative Report on Wing Trailing-edge Devices. BAC SOR(P) 55, S&T Memo 4-73, DRIC-BR-32940 (1972)
26	Scott, D. Taylor, J.	National High-Lift Programme - Comparative Study of Leading-edge Devices. HSA (Woodford) Proj/NHLP/M42 (1975)
27	Scott, D. Taylor, J.	Comparative Study of single-slot Flap with 84%, 90%, 96% Chord Shroud (T1, T2 and T3). HSA (Woodford) Proj/NHLP/M37 Part II (1974)

28	Scott, D. Taylor, J.	National High Lift Programme - Design Study of Externally-Hinged Double-slotted Flaps with 78% Chord Shroud (T10 and T11). HSA (Woodford) Proj/NHLP/M70 (1975)
29	Scott, D. Teagle, P.J.	National High Lift Programme Phase 5 - Weight Update of single-slotted flap with 90% Chord Shroud (T2), and triple-slotted flap with 90% Chord Shroud (T8). BAe-MFP-R-NHL-0102 (1979)
30	Perry, D.	Exchange rates between some design variables for an aircraft just satisfying take-off distance and climb requirements. RAE Technical Report 69167 (1969)
31	Woodward, D.S. Lean, D.E.	An Investigation of the optimum take-off configuration of a single-slotted flap on a swept wing. RAE Technical Report 82074 (1982)
32	Appleyard, G.M .	An investigation of the effects of part-span extent on the optimum settings for take-off of a 33%-chord single-slotted flap with a 90% shroud. BAe (Brough) Technical Note YAD 3313 (1978)
33	Woodward, D.S.	National High Lift Programme - A Preliminary Assessment of the high-lift performance of three flexible leading-edge devices. RAE Technical Memorandum Aero 1617 (1975)
34	Woodward, D.S. Cherrington, K.D.	A preliminary investigation of the performance gains obtainable by variation of the slat setting across the span of a swept wing. RAE Technical Memorandum Aero 1699 (1976)
35	Kuchemann, D. Weber, J.	Performance aspects of various types of Aircraft Progress in Aeronautical Sciences, Vol.9, pp 329-456, Fig 3.5 (1968)
36	Hardy, B.C.	Experimental Investigation of Attachment-line Transition in Low-Speed High-Lift Wind Tunnel testing. Paper 2 AGARD CP438 (1988)
37	Moir, I.R.M.	An experimental investigation of the Optimum Slat setting on a Strike Fighter Model. RAE Technical Report 84023 (1984)

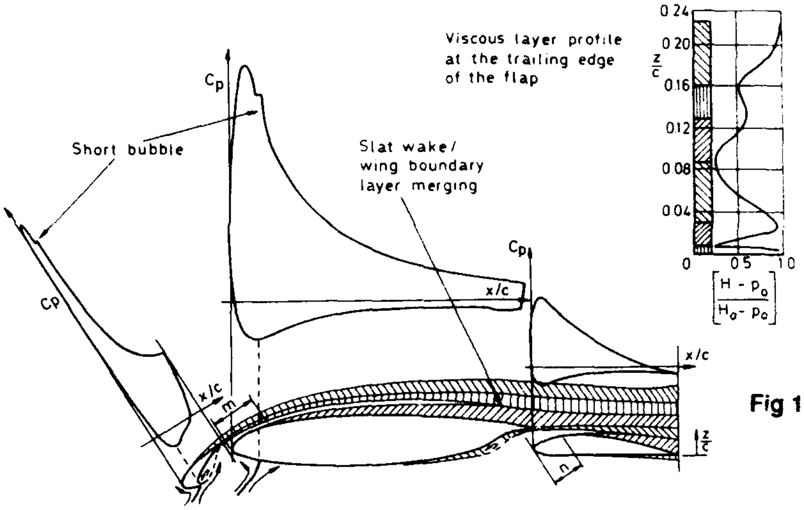

Fig 1 Flow over two-dimensional wing with slat and slotted flap

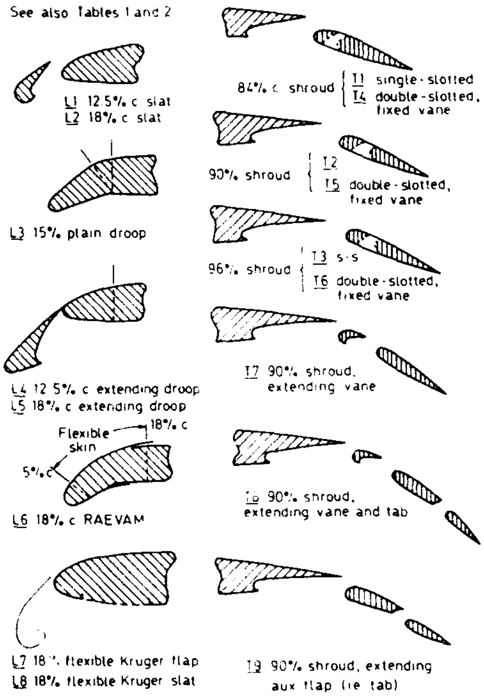

Fig 2 Basic NHLP high-lift devices (schematic)

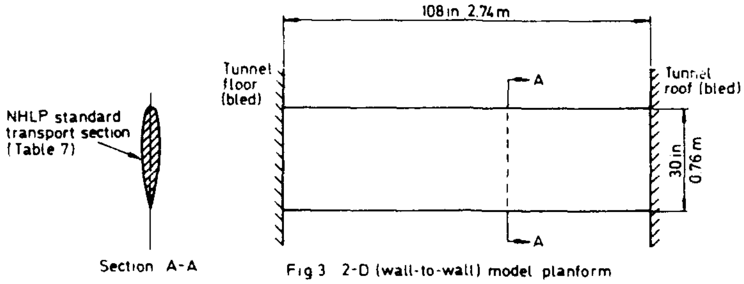

Fig 3 2-D (wall-to-wall) model planform

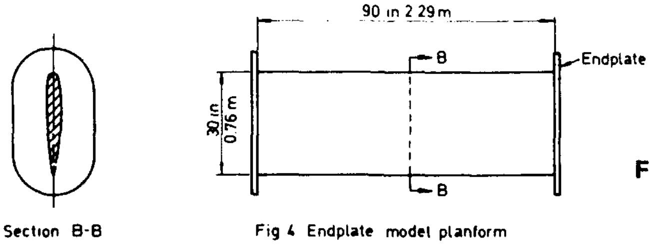

Fig 4 Endplate model planform

Fig 3&4 BAe (Weybridge) 2-D and E/P ("quasi 2-D") models

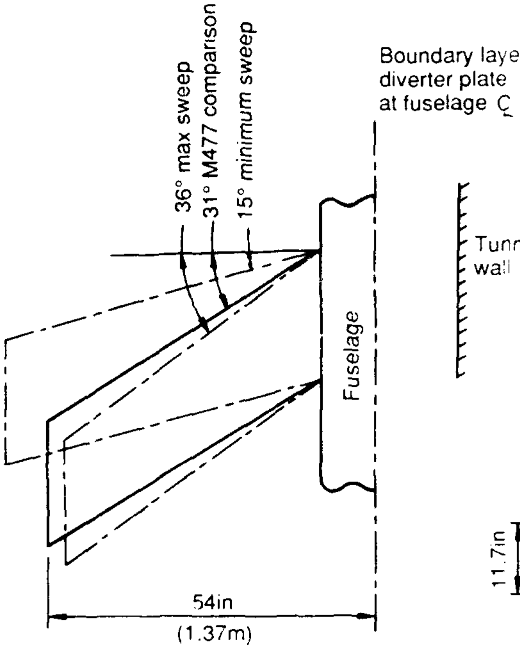

Fig 5 Constant chord swept panel model (BAe)

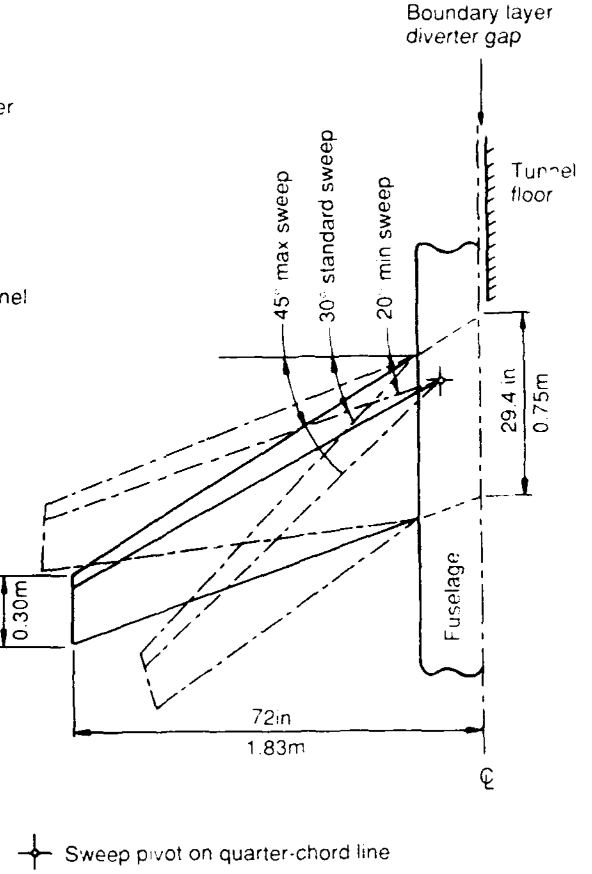

Fig 6a Tapered swept-wing model (RAE M477)

Fig 6b Model 477 in the DRA Bedford 13ft x 9ft] wind tunnel

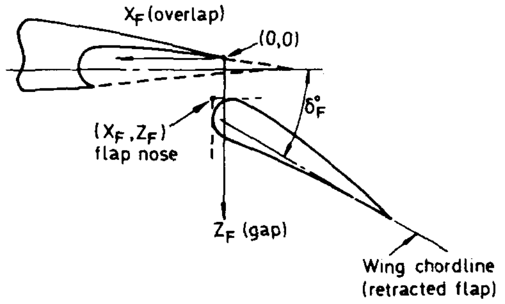

a) Single-slotted trailing-edge flap

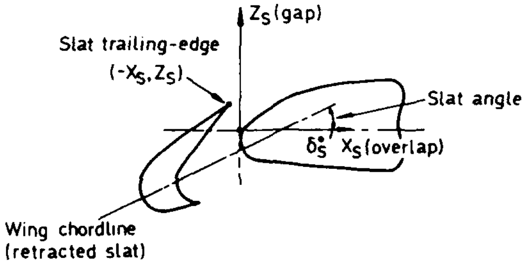

b) Simple slotted leading-edge (slat)

Fig 7 Positional coordinate systems – basic devices

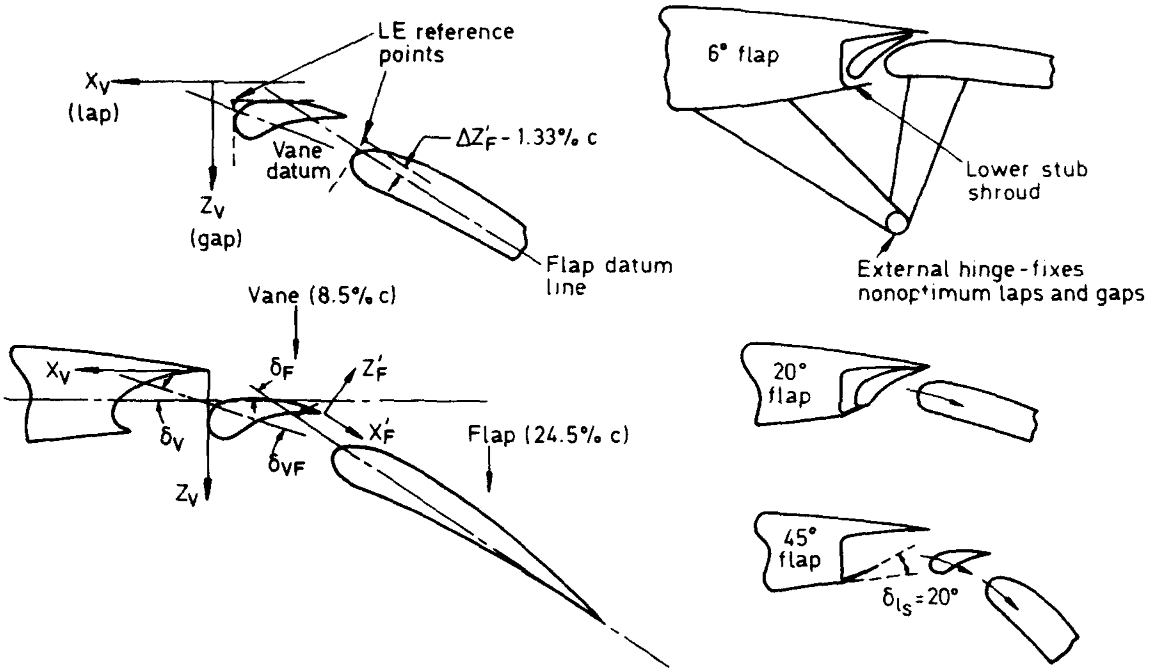

a) Standard configuration (T7) - lap and gap conventions

b) External - hinge type configuration (T10)

Fig 8 Double-slotted trailing-edge flaps (T7 & T10) – nomencalture

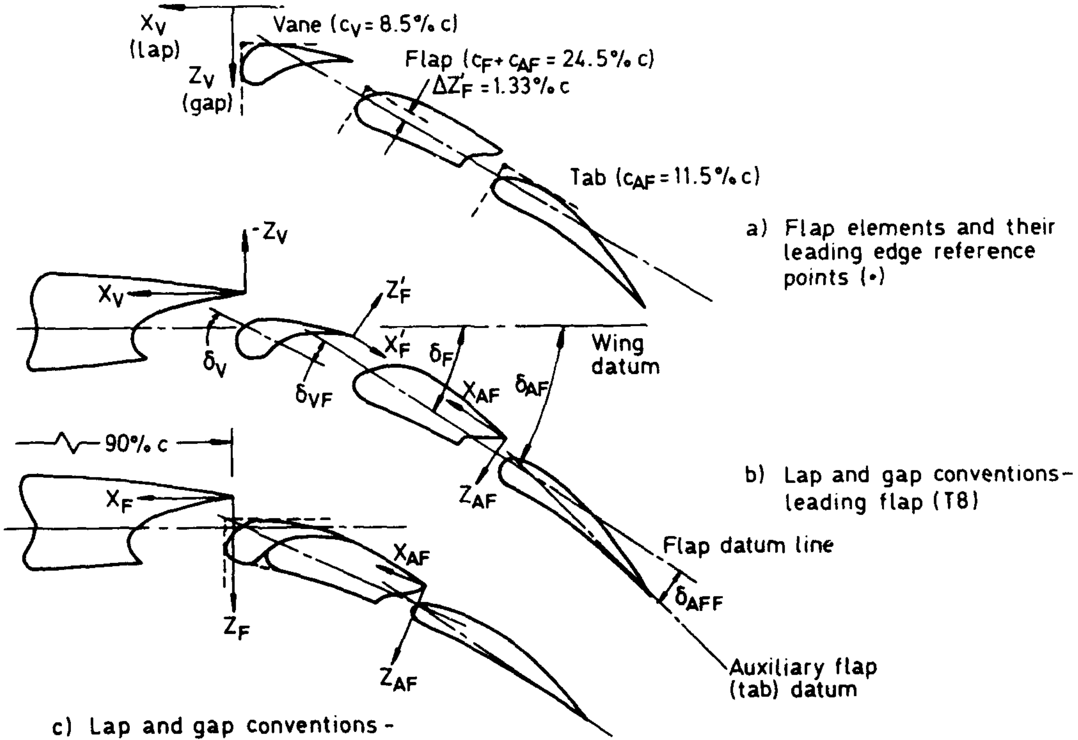

a) Flap elements and their leading edge reference points (•)

b) Lap and gap conventions - leading flap (T8)

c) Lap and gap conventions - take-off flap (T8T)

Fig 9 Triple-slotted trailing-edge flap (T8 & T8T) – nomenclature

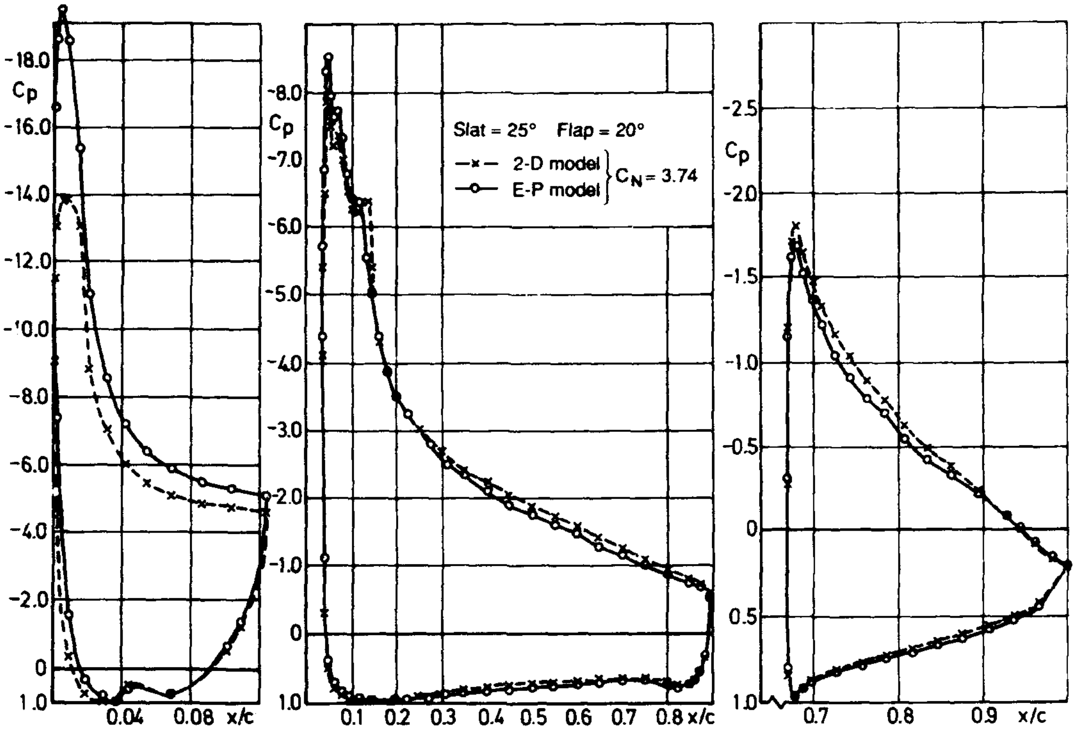

Fig 10 Comparison of wall-to-wall and end plate model pressure distributions

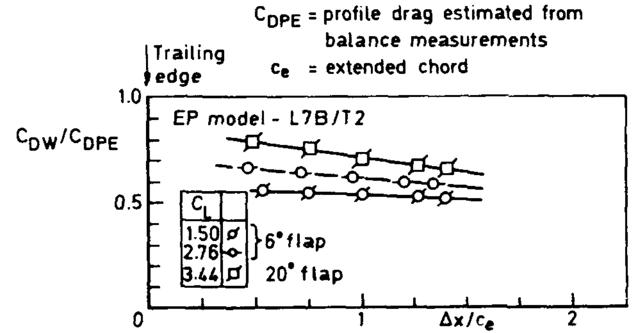

a) Streamwise variation of measured C_{DW}

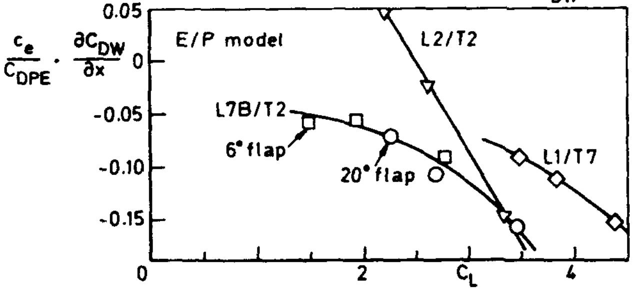

b) C_L dependence of streamwise gradient of C_{DW}

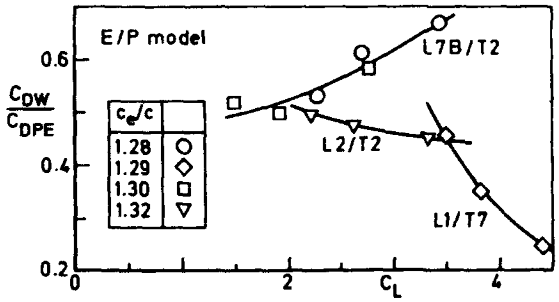

c) C_L dependence of C_{DW} measured at $\Delta x/c_e = 1.3$

Fig 11 Typical wake momentum defect coefficient (CDW) measurements

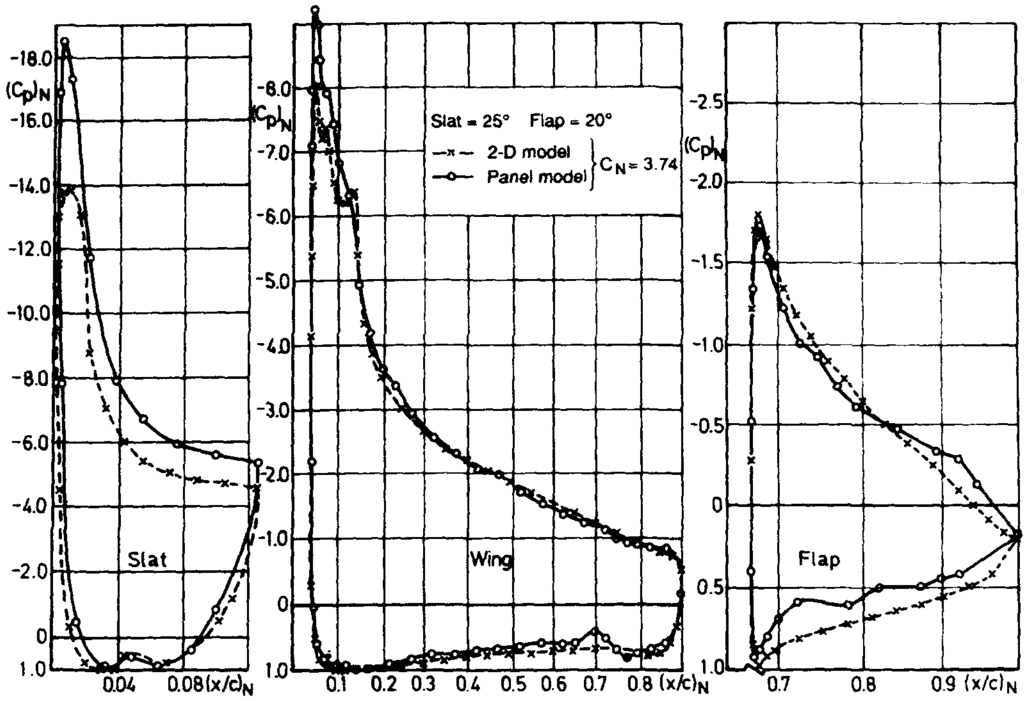

Fig 12 Comparison of wall-to-wall and normalised panel model pressure distributions

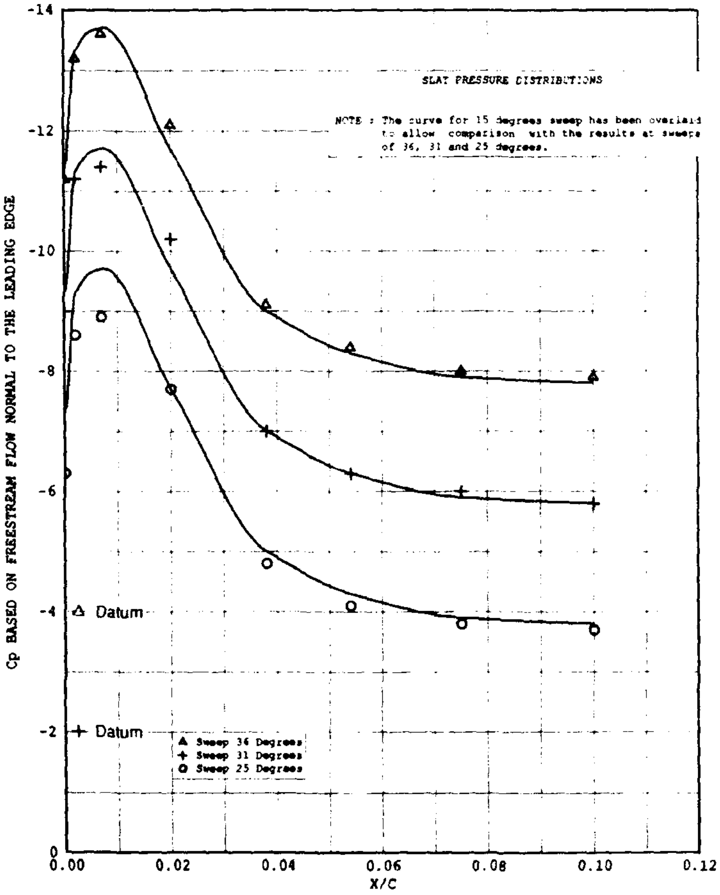

Fig 13a Comparison of swept panel model results at various sweeps for slat L1 at 25° and flap T2 at 20°

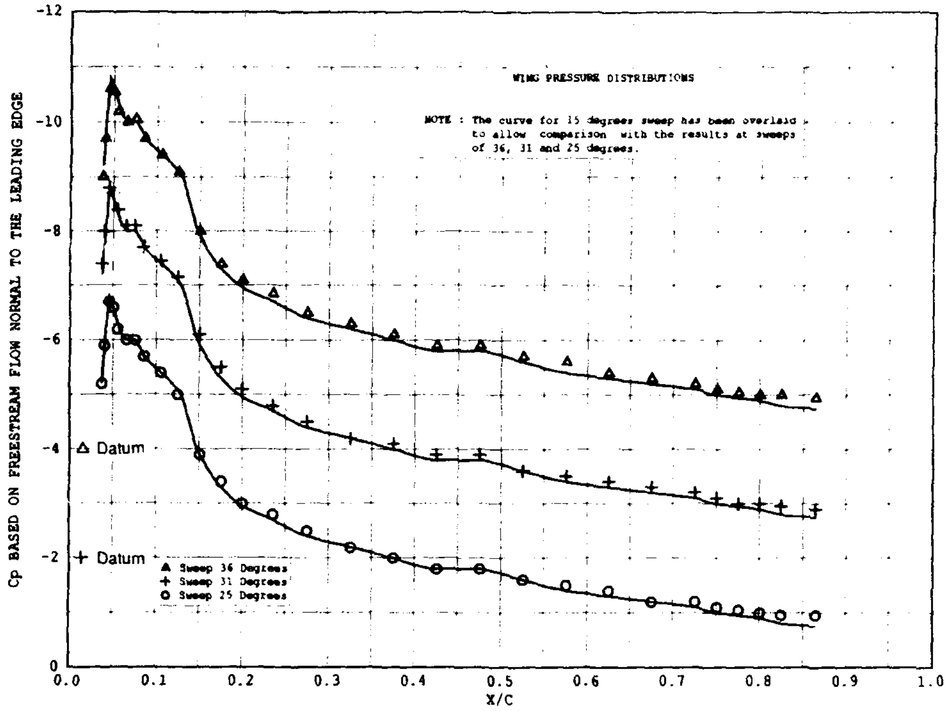

Fig 13b Comparison of swept panel model results at various sweeps for slat L1 at 25° and flap T2 at 20°

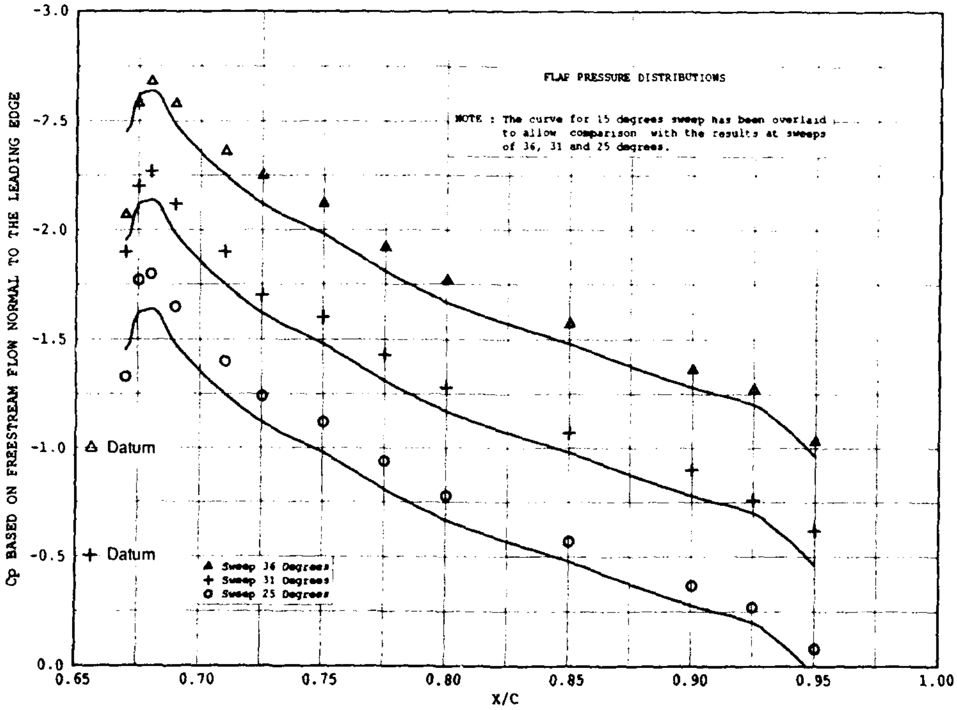

Fig 13c Comparison of swept panel model results at various sweeps for slat L1 at 25° and flap T2 at 20°

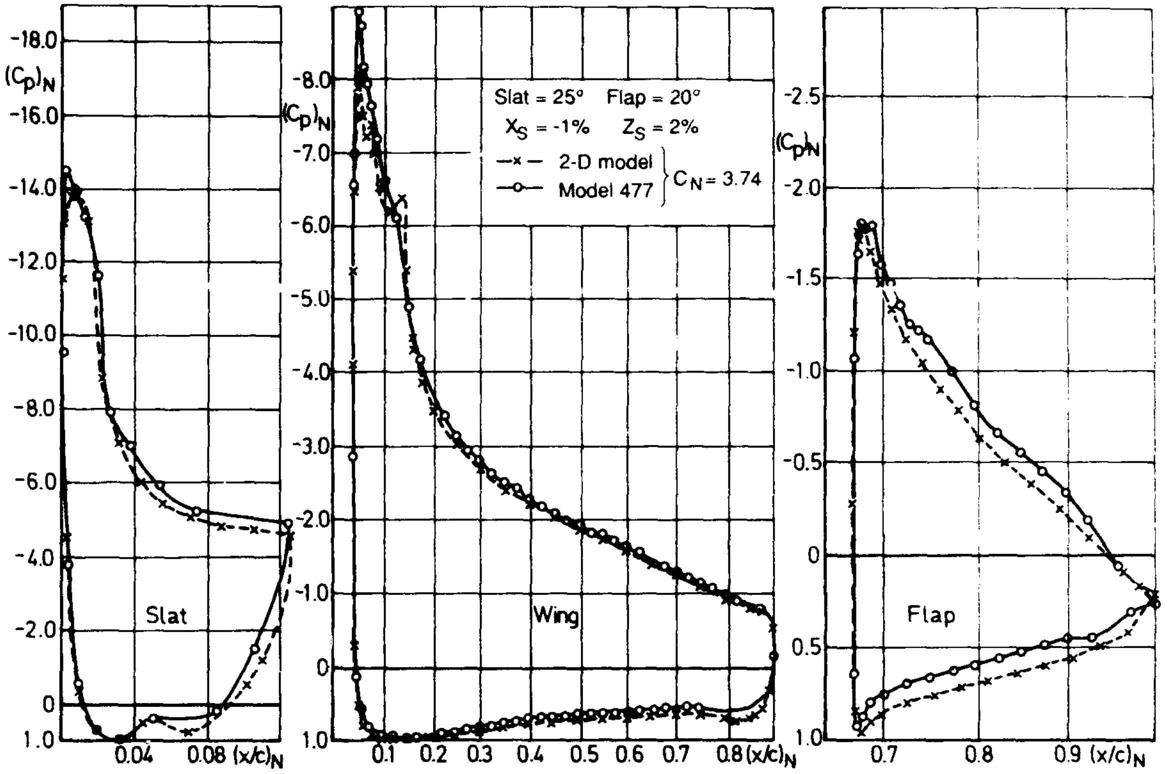

Fig 14a Pressure distributions on two-dimensional and model 477

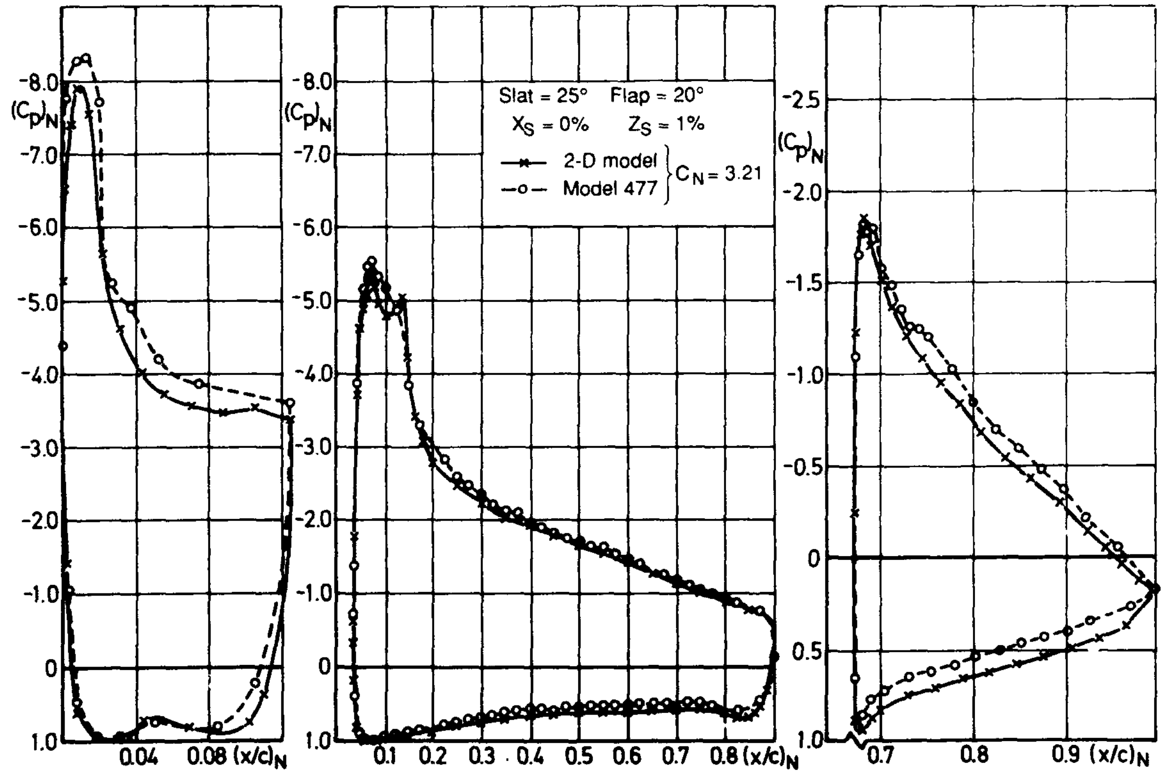

Fig 14b Pressure distributions on two-dimensional and model 477

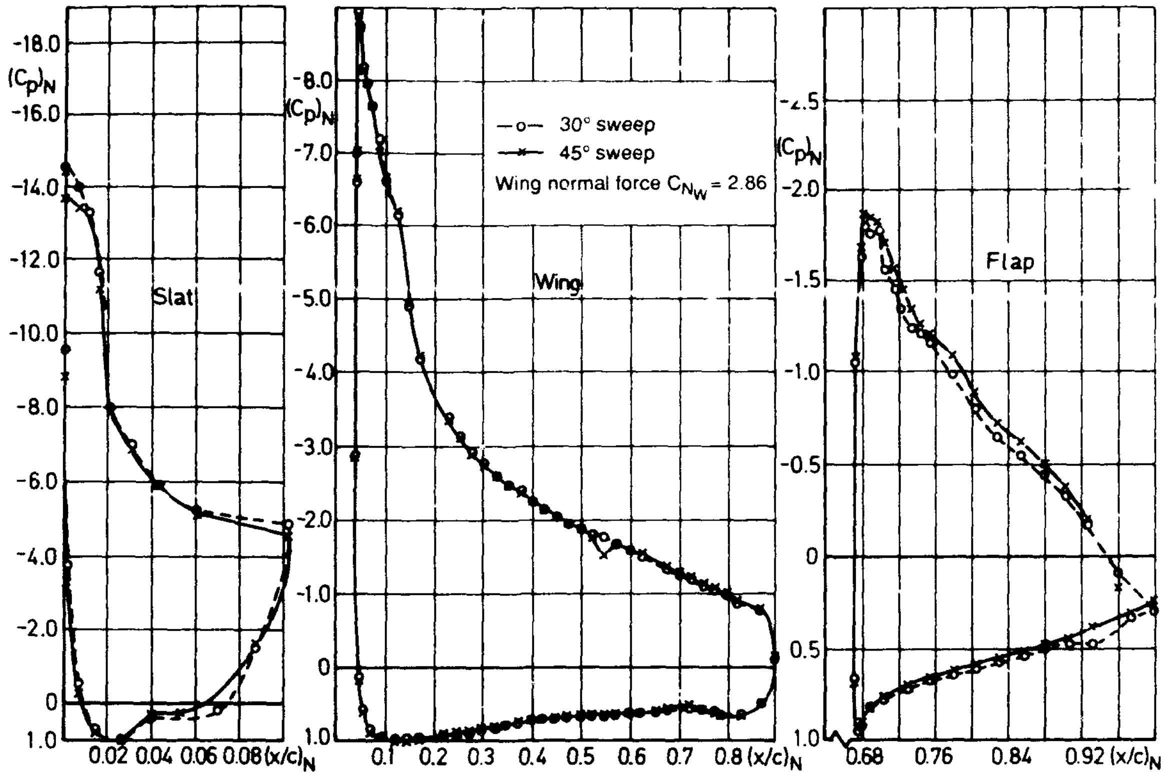

Fig 15a Comparison of normalised sheared wing pressure distributions based on local sweep angles

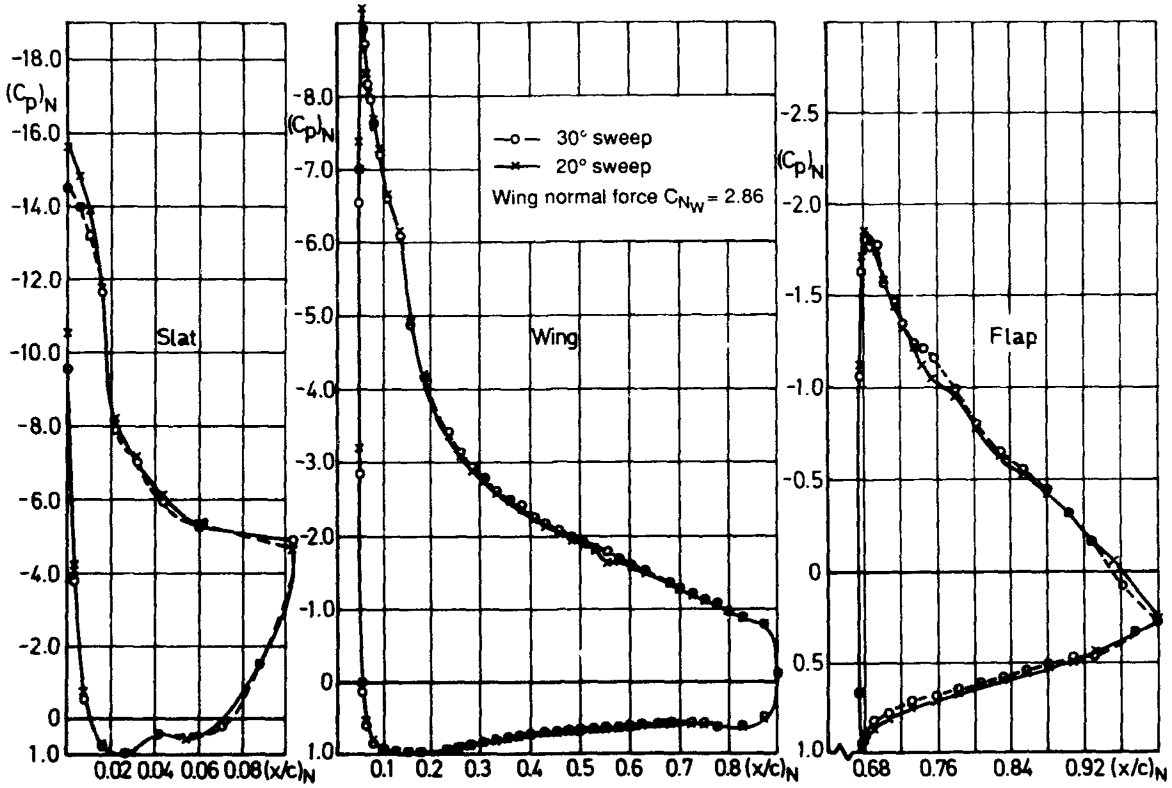

Fig 15b Comparison of normalised sheared wing pressure distributions based on local sweep angles

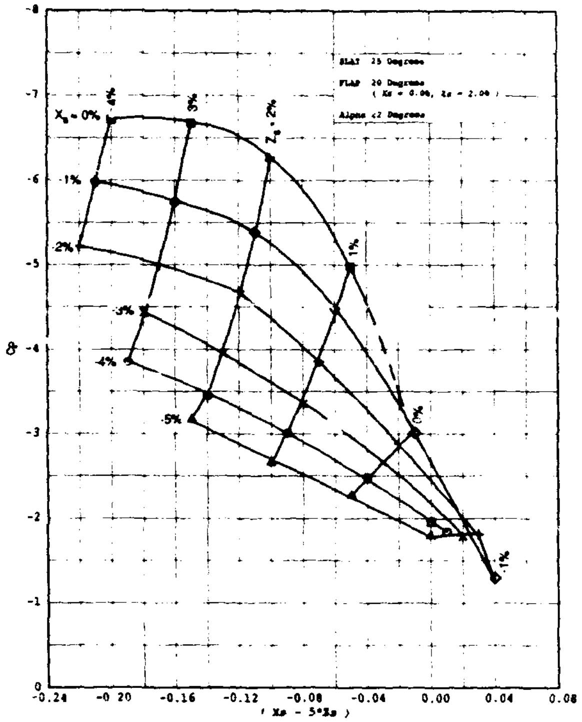

Fig 16a (slat TE) v (Xs - 5*Zs)

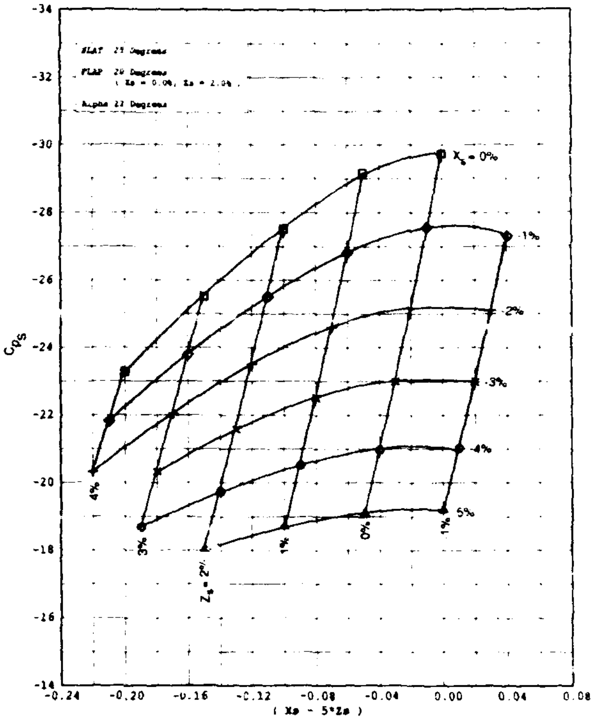

Fig 16b Slat peak v (Xs - 5*Zs)

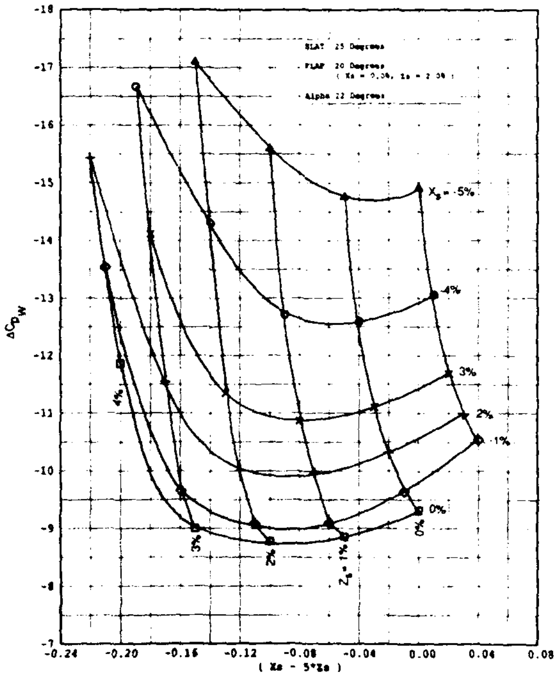

Fig 17 (slat peak - slat TE) v (Xs - 5*Zs)

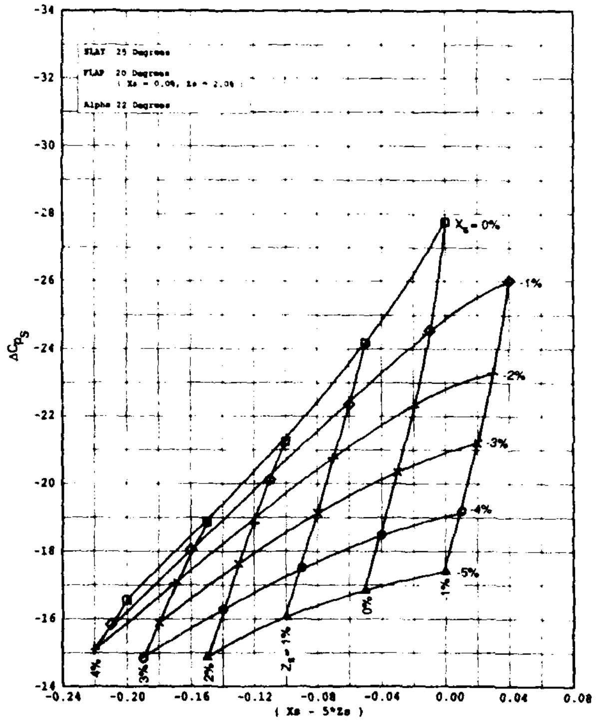

Fig 18 (wing peak - wing TE) v (Xs - 5*Zs)

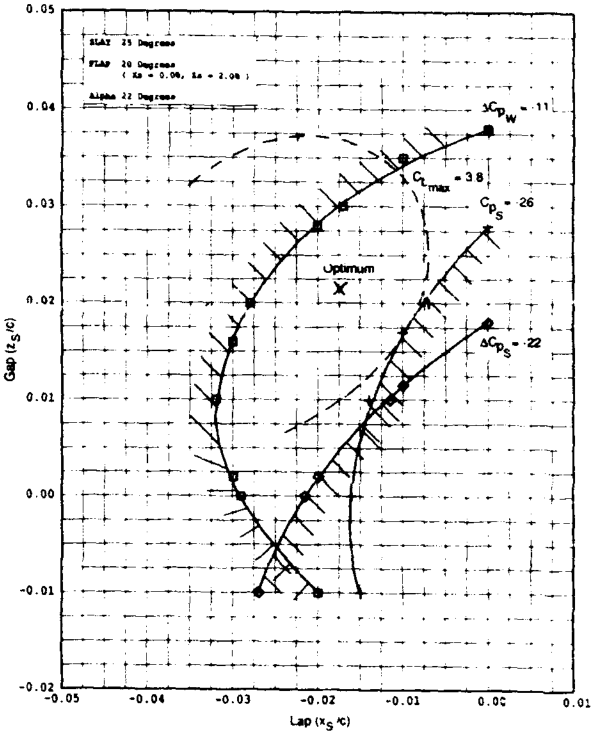

Fig 19a Prediction of optimum slat location
Slat angle = 25°

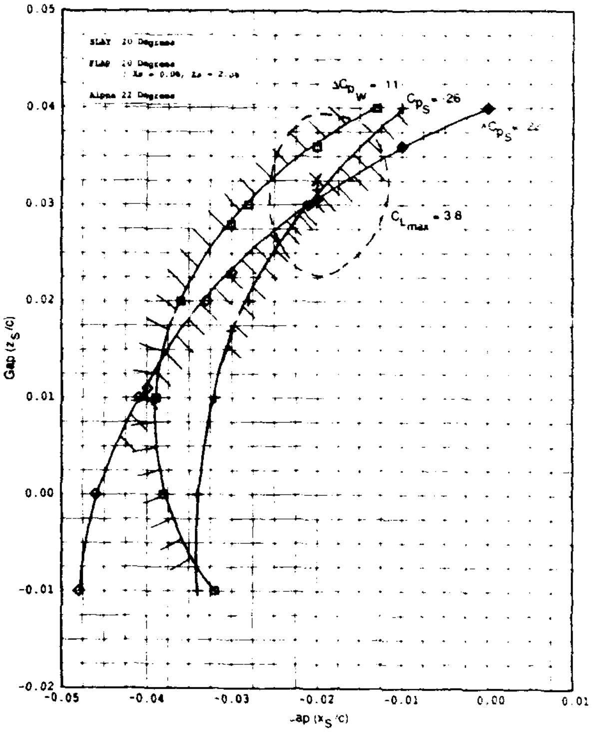

Fig 19b Prediction of optimum slat location
Slat angle = 20°

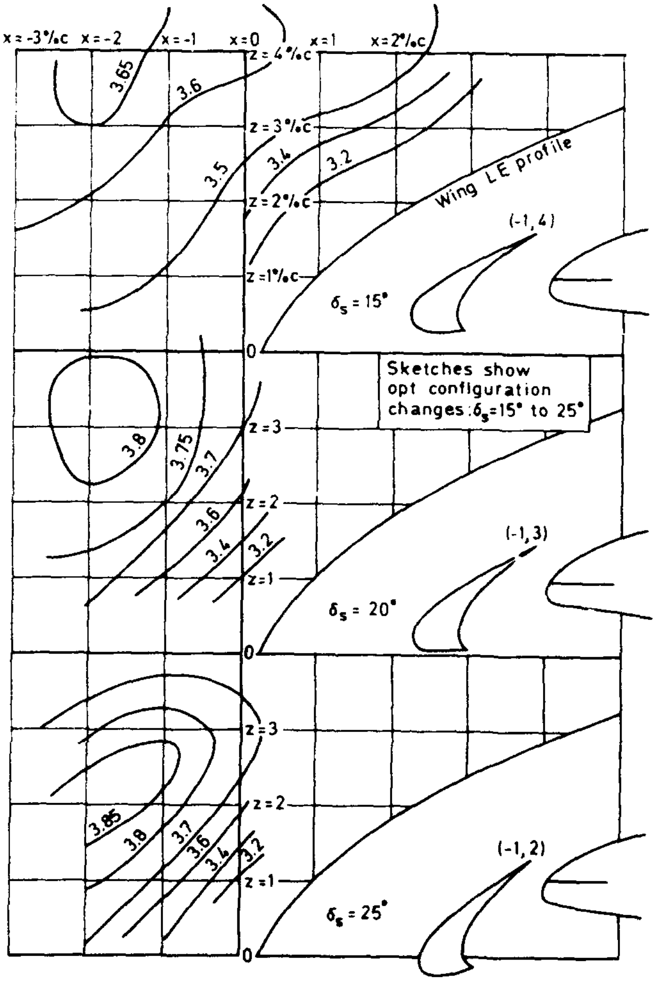

Fig 20 Optimisation of 12½% chord slat
L1 for maximum lift

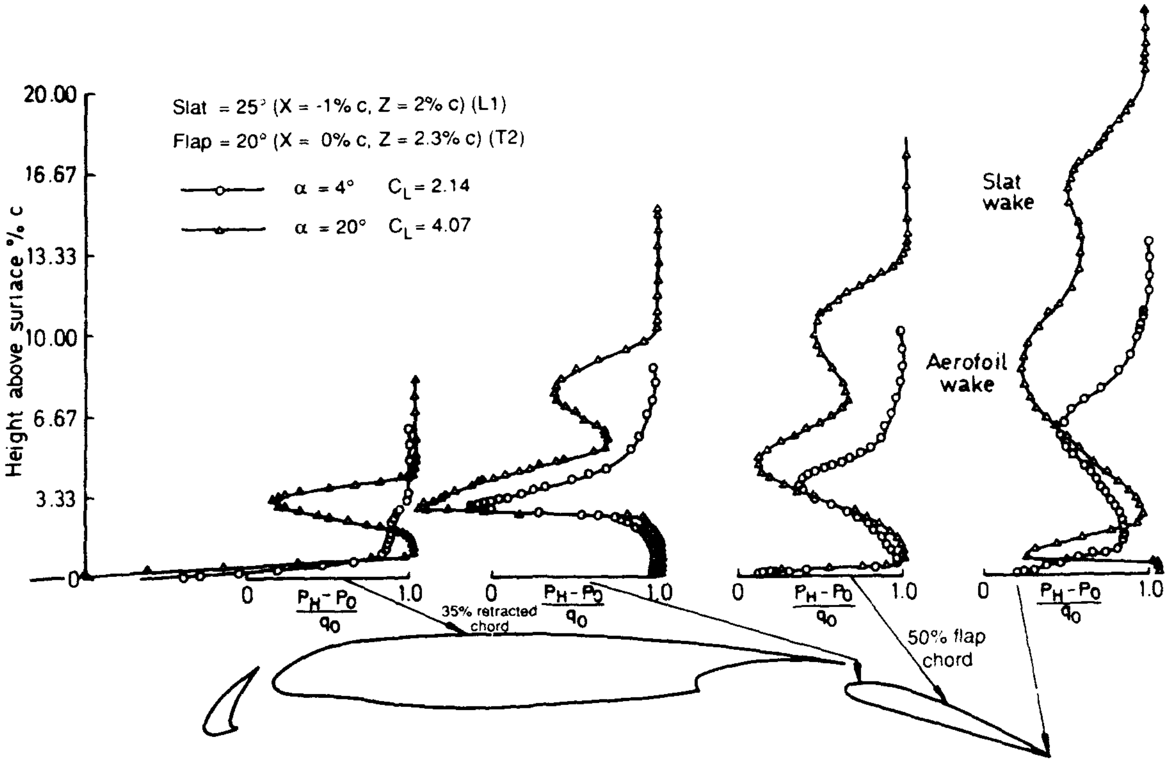

Fig 21 **Boundary layer shapes on single slotted flap (T2) at various chordwise positions on a 2-D model**

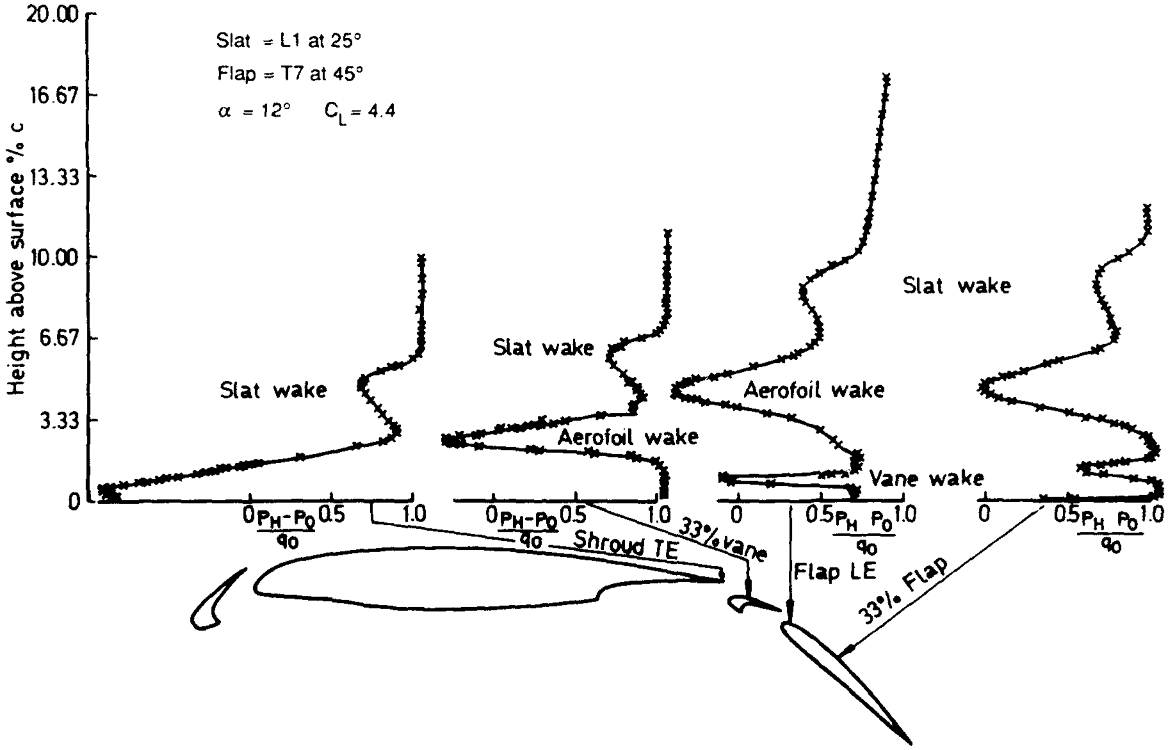

Fig 22a **Boundary layer shapes on double slotted flap (T7) at various chordwise positions on a 2-D model**

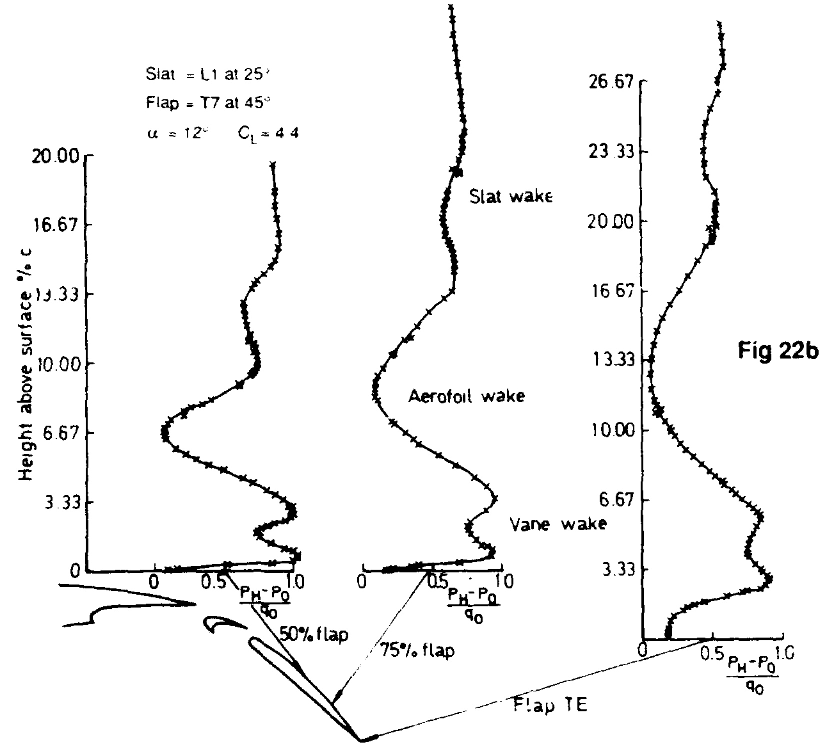

Fig 22b Boundary layer shapes on double slotted flap (T7) at various chordwise positions on a 2-D model

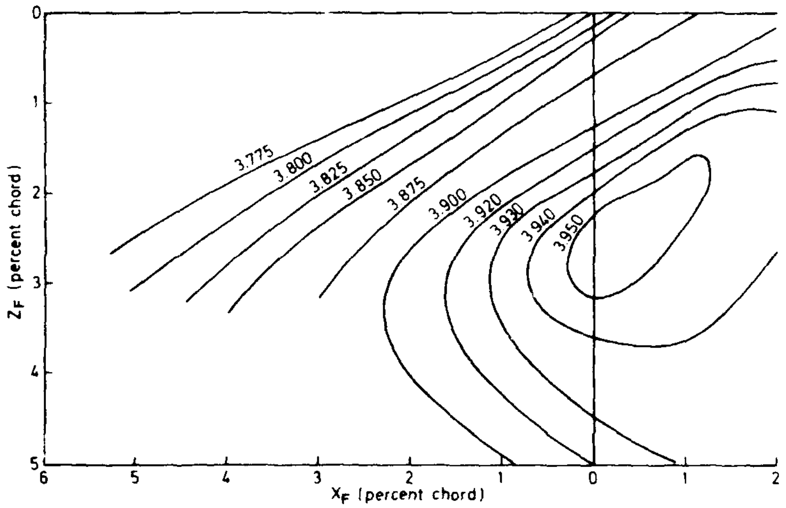

Fig 23 Contours of $C_{L_{max}}$ for 20° slat, 25° slat

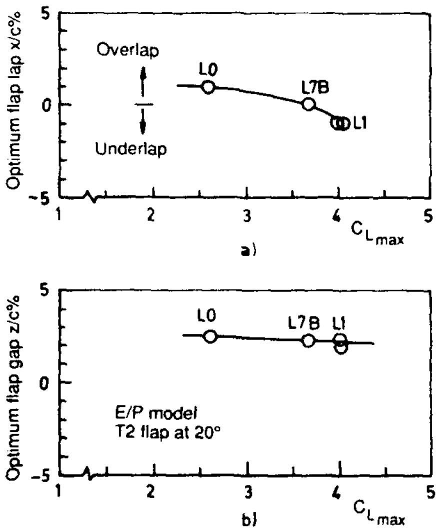

Fig 24 Effect of leading-edge device on the flap slot setting required for optimum $C_{L_{max}}$ performance

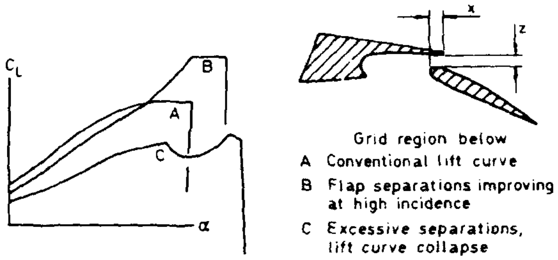

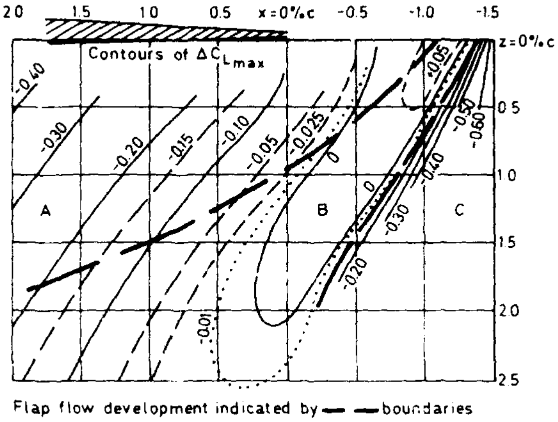

Fig 25a **NHLP 90 in x 30 in E/P model with single slotted flap (T2) Flap angle $\delta_F = 40°$ $C_{L_{max}}$ contours derived from carpet plots**

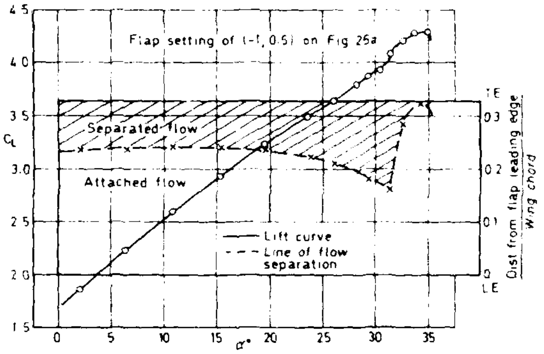

Fig 25b **NHLP 90 in x 30 in E/P model with single slotted flap (T2) Flap angle dF = 40° Variation of flap flow separation with incidence**

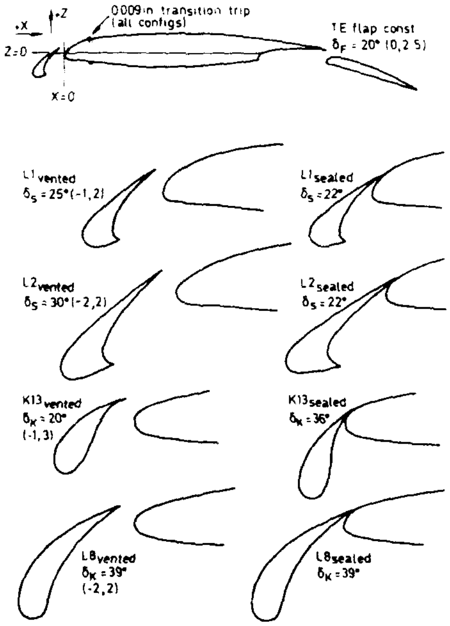

Fig 26 **Configurations of LE slats L1, L2, L8 and K13, tested on the end plate model**

7.1 Effects of Overhang

A close observation of the pressure distribution curve,

overhangs. This behavior can also be observed in the C_p distributions on the slat and on the main element while the C_p distribution on the flap remains unef-

All results obtained in conjunction with single slotted flap (T2) at δ_F = 20° (0.2 3) and V=220 FPS except where noted

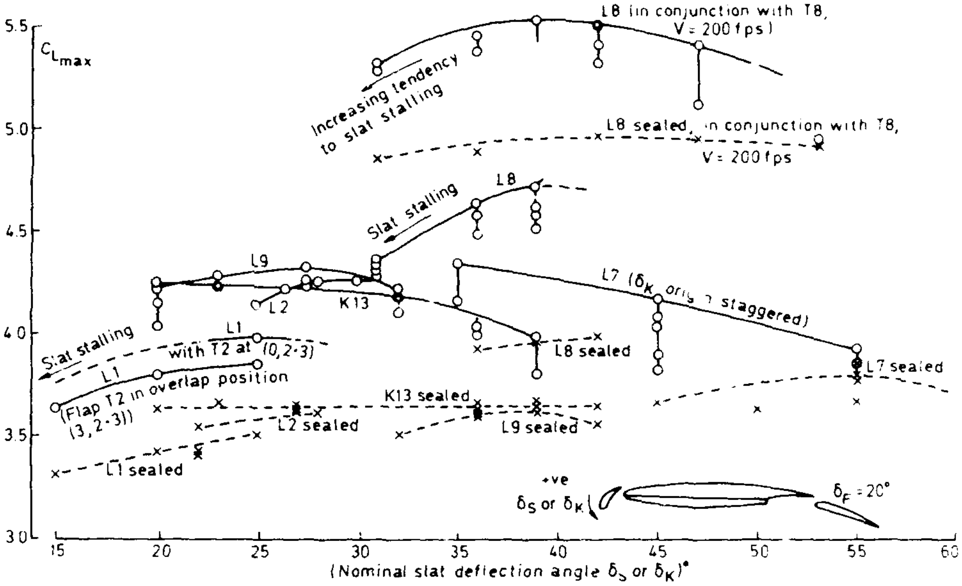

Fig 27 Summary of measured $C_{L_{max}}$ performance of 6 LE slats/Krugers on the 90 in x 30 in end-plate model

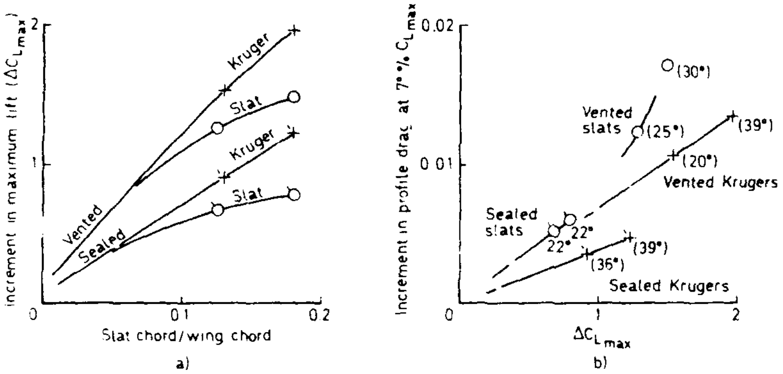

a)

b)

Fig 28 Summary of slat performance comparisons on the end-plate model

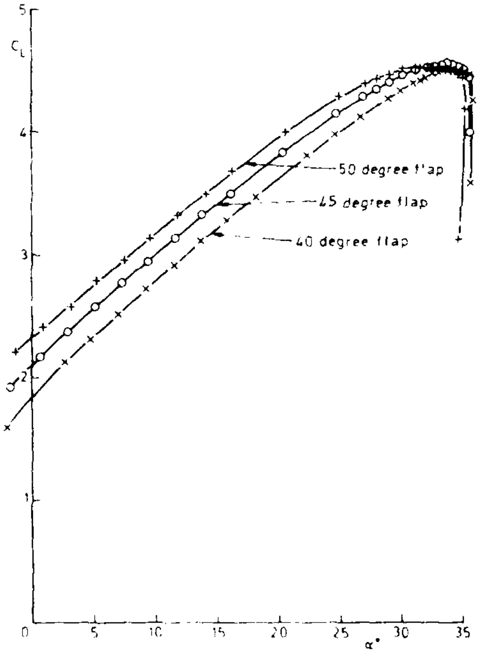

Fig 29 Lift-incidence curves for a double slotted flap at 3 angles

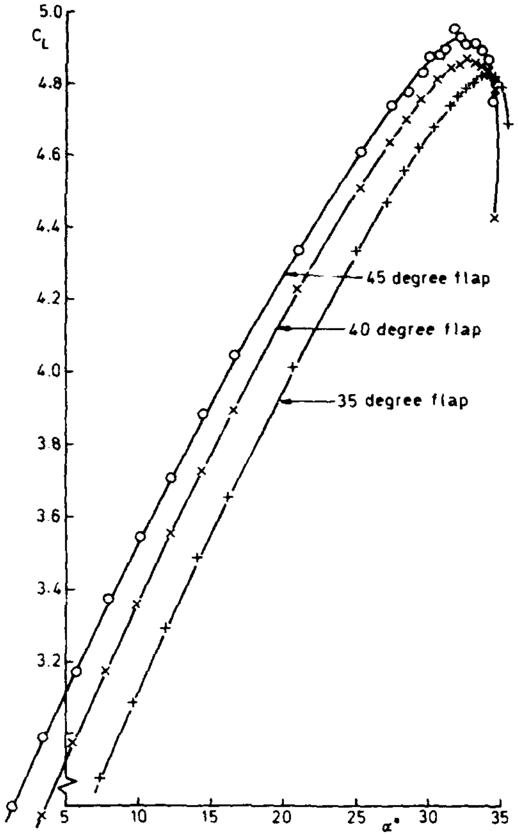

Fig 30 **Lift-incidence curves for a triple slotted flap at 3 angles**

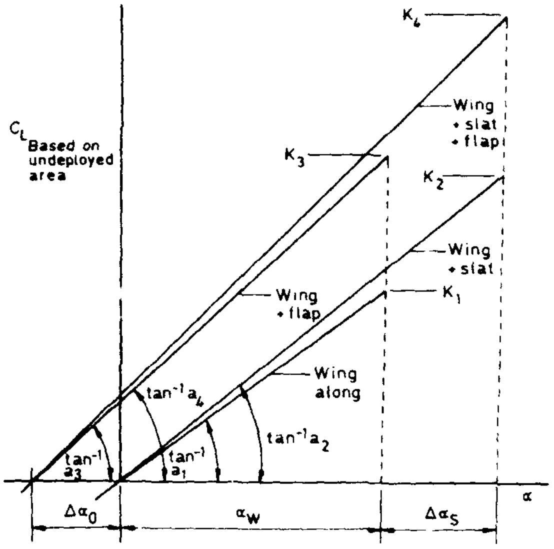

$$(C_{L_{max}})_{wing} = K_1 = a_1\ \alpha_W$$

$$(C_{L_{max}})_{wing+slat} = K_2 = a_2\ (\alpha_W + \Delta\alpha_S)$$

$$(C_{L_{max}})_{wing+flap} = K_3 = a_3\ (\alpha_W + \Delta\alpha_0)$$

$$(C_{L_{max}})_{wing+flap+slat} = K_4 = a_4\ (\alpha_W + \Delta\alpha_S + \Delta\alpha_0)$$

$$= \frac{a_4}{a_1}\left[K_1 + \left\{\frac{K_2.a_1}{a_2} - K_1\right\} + \left\{\frac{K_3.a_1}{a_3} - K_1\right\}\right]$$

Fig 31 **Method of determination of $C_{L_{max}}$ increments**

$C_R = \sqrt{C_L^2 + C_D^2}$ from the endplate model is a close approximation to the C_L on a 2D - wing

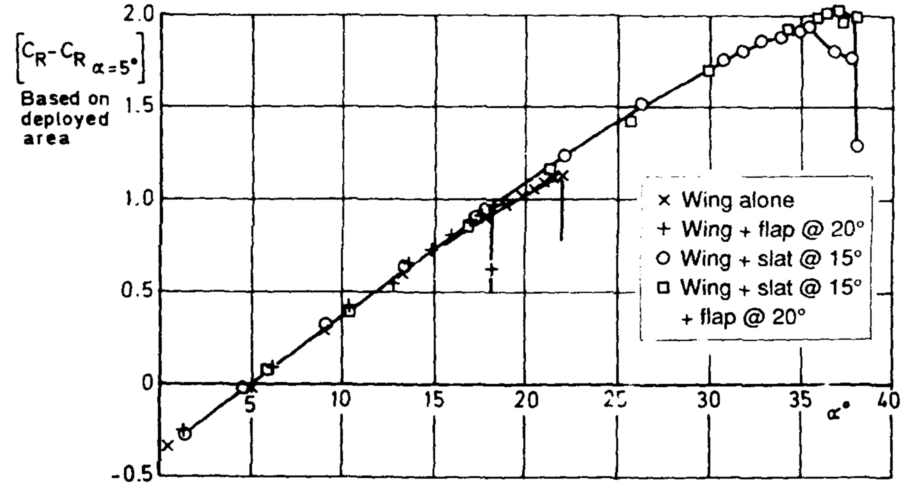

Fig 32 a **Demonstration that lift curve slope is closely proportional to deployed chord**

$C_R = \sqrt{C_L^2 + C_D^2}$ from the endplate model is a close approximation to the C_L on a 2D - wing

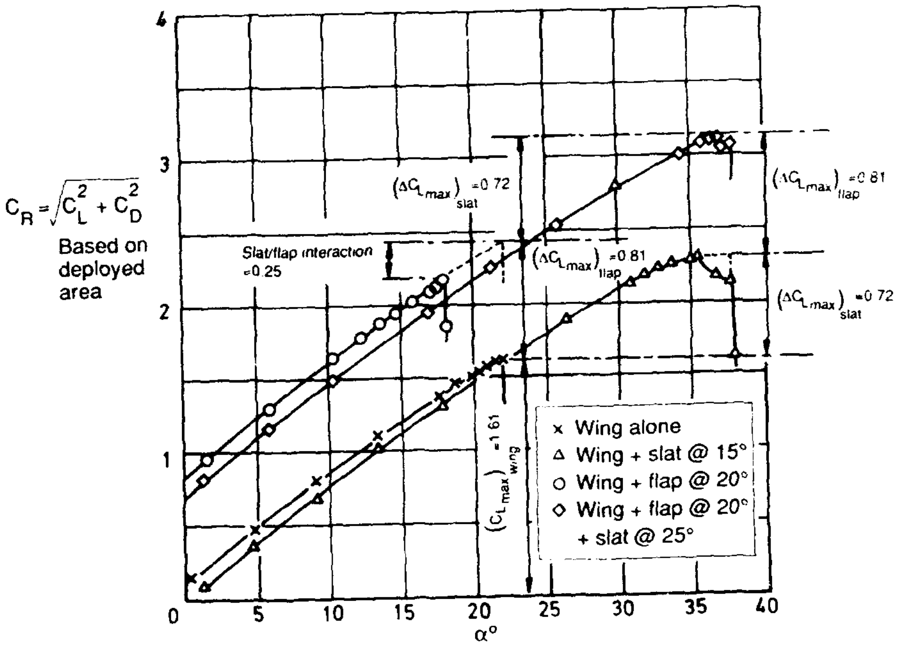

Fig 32b Derivation of flap and slat increments from typical end-plate model data

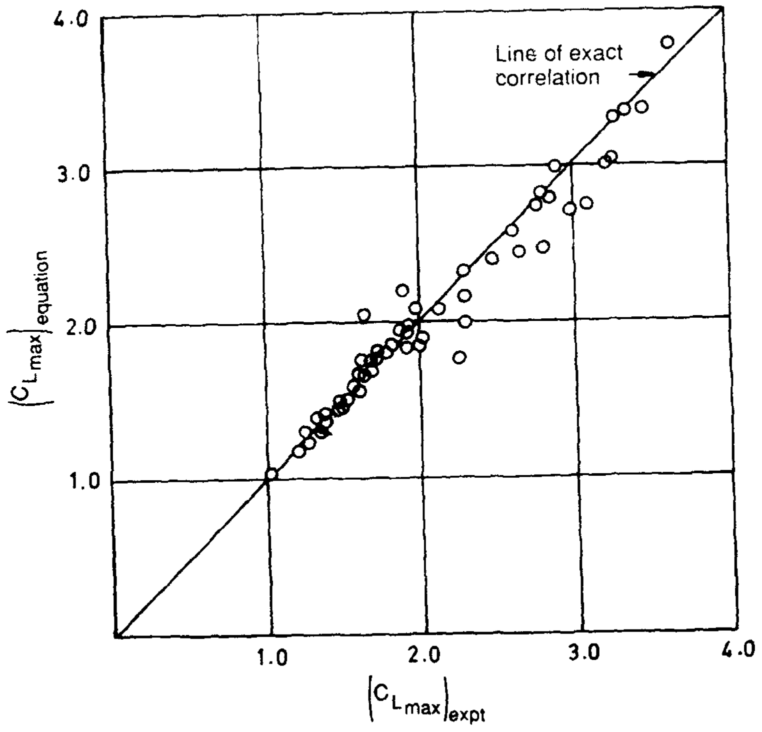

Fig 33 Correlation of $C_{L_{max}}$

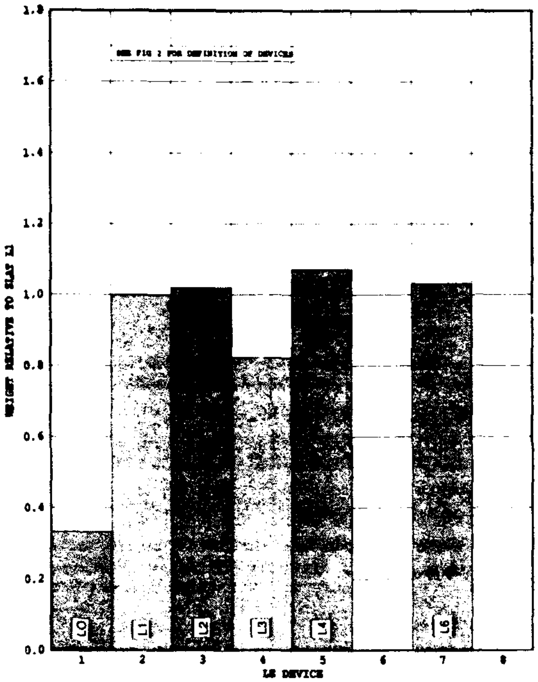

Fig 34a Weights of a range of leading-edge devices on a variable-geometry fighter

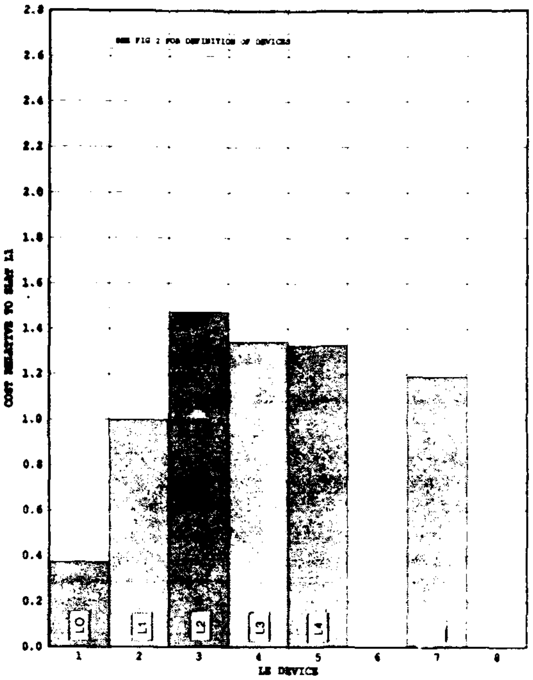

Fig 34b Costs of a range of leading-edge devices on a variable-geometry fighter

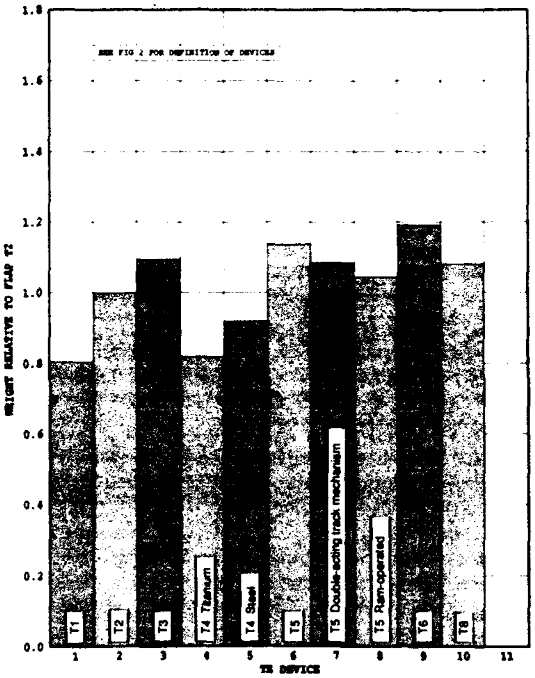

Fig 35a Weights of a range of trailing-edge devices on a variable-geometry fighter

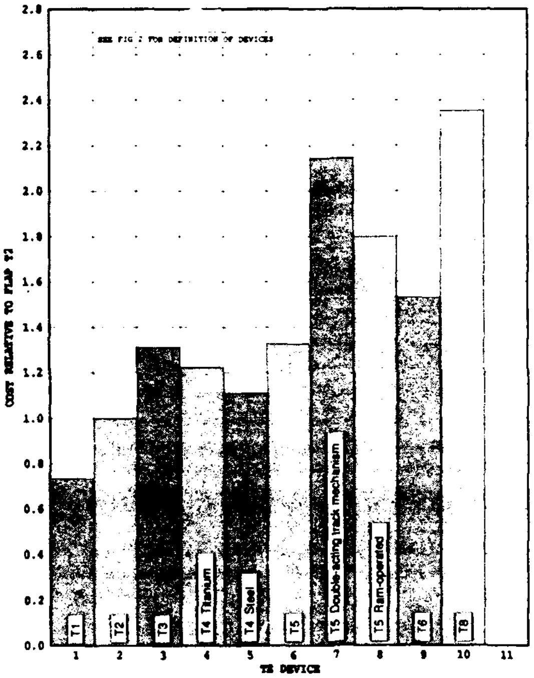

Fig 35b Costs of a range of trailing-edge devices on a variable-geometry fighter

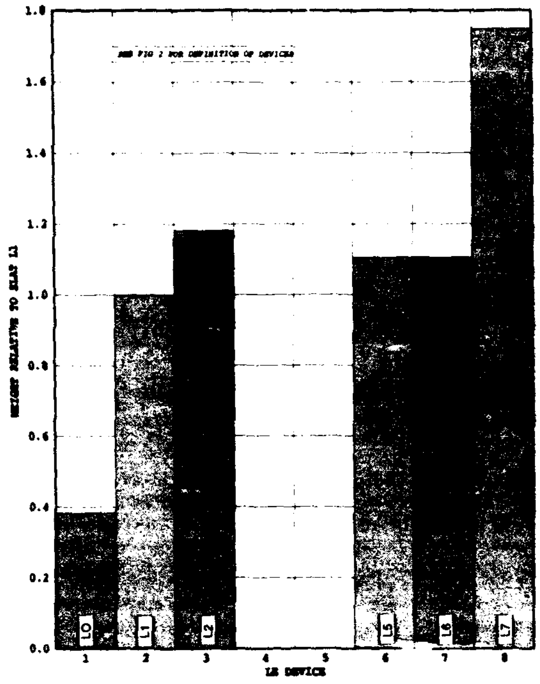

Fig 36a Weights of a range of leading-edge devices on a civil transport aircraft

Fig 36b Costs of a range of leading-edge devices on a civil transport aircraft

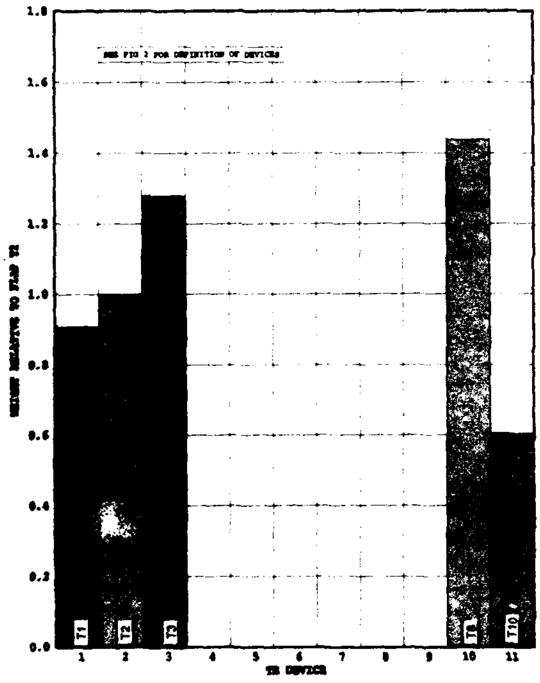

Fig 37a Weights of a range of trailing-edge devices on a civil transport aircraft

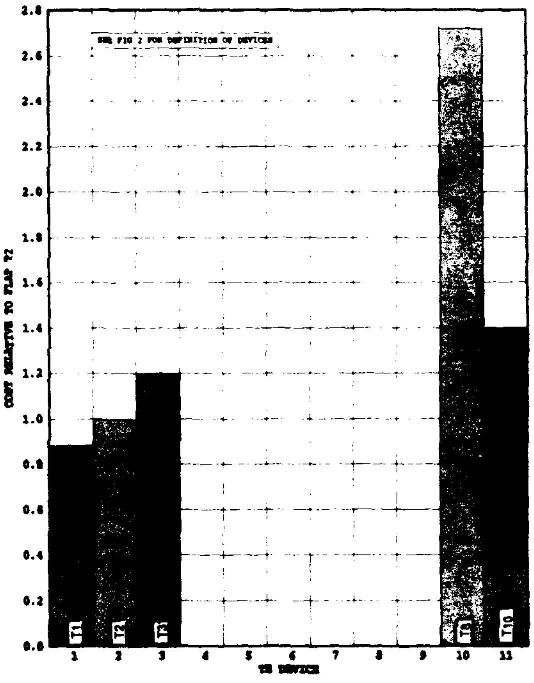

Fig 37b Costs of a range of trailing-edge devices on a civil transport aircraft

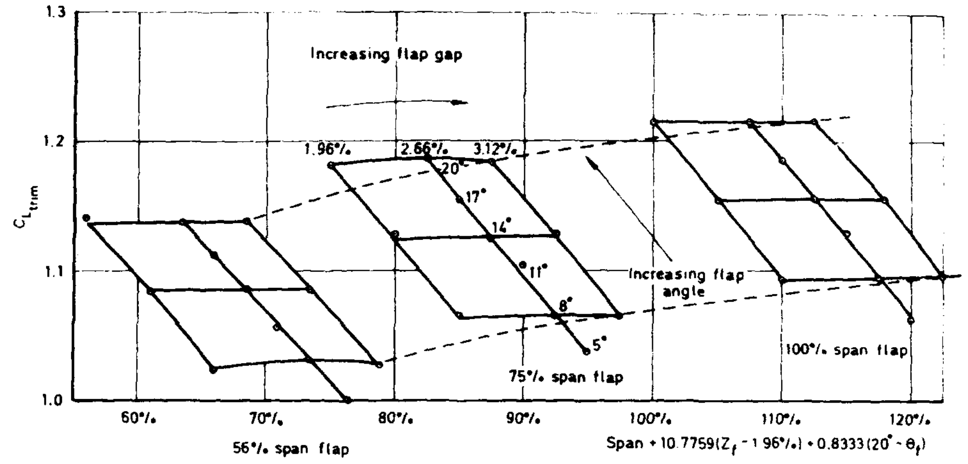

Fig 38 Variation of trimmed lift coefficient, at 0.7 C max, with flap gap, deflection and span; plain leading edge; sweep = 30°

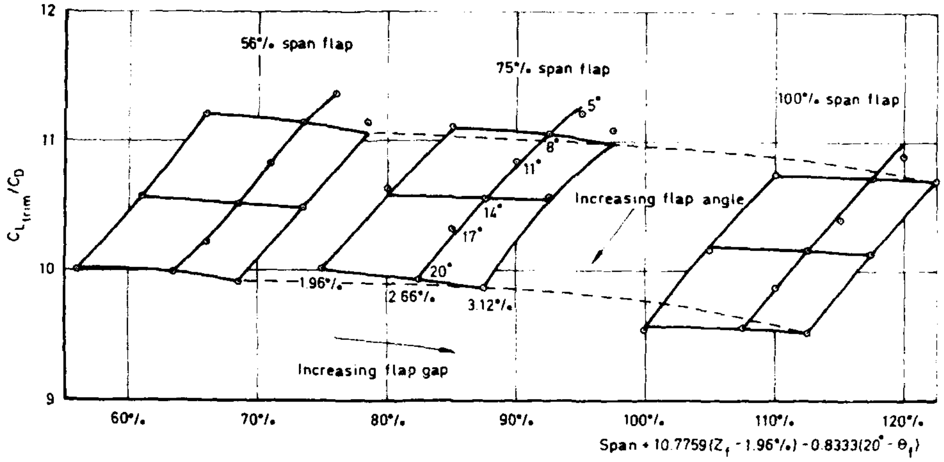

Fig 39 Variation of trimmed lift-to-drag ratio, at 0.7 C max, with flap gap, deflection and span; plain leading-edge; sweep = 30°

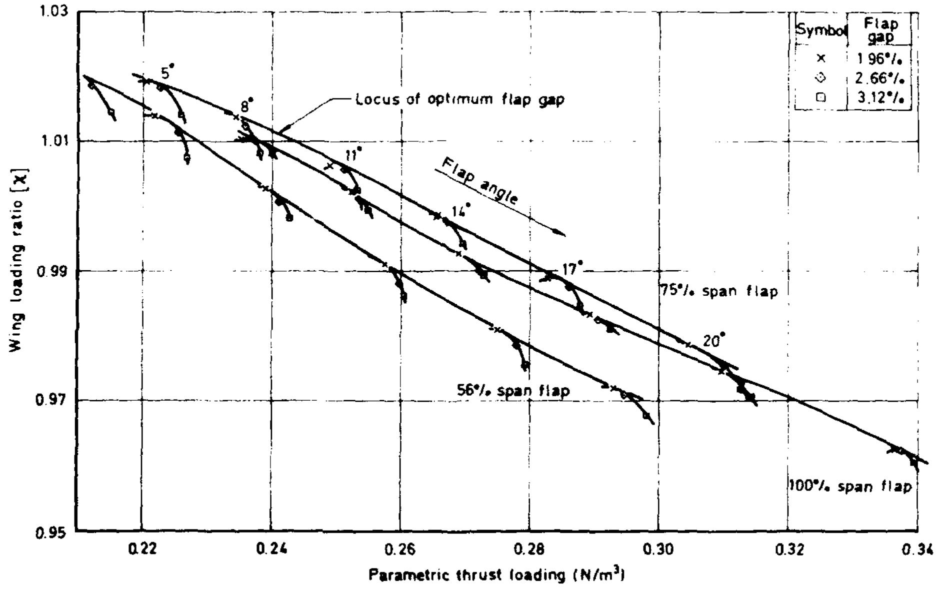

Fig 40 Derivation of optimum take-off performance at optimum flap gap; plain leading-edge; sweep = 30°

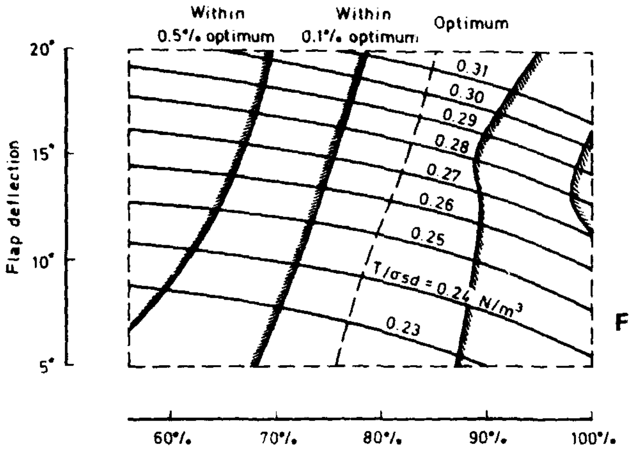

Fig 41 Variation of optimum flap deflection for take-off with flap span; plain leading edge; sweep = 30°

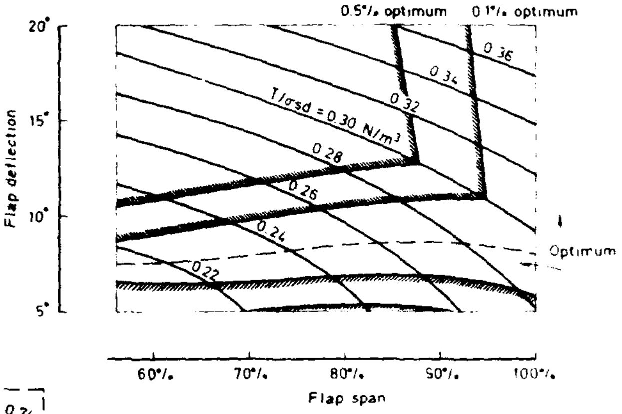

Fig 42 Variation of optimum flap deflection for take-off with flap-span; plain leading-edge; sweep = 20°

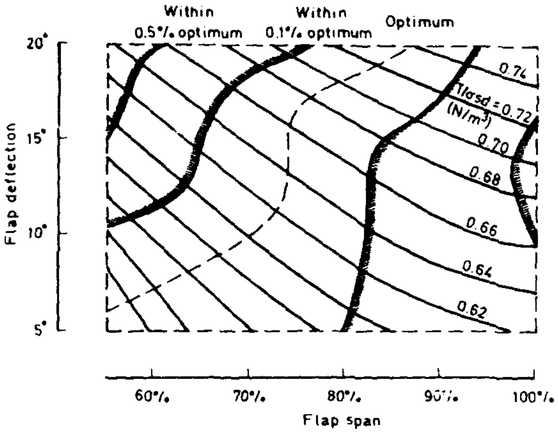

Fig 43 Variation of optimum flap deflection for take-off with flap span; sweep = 30°

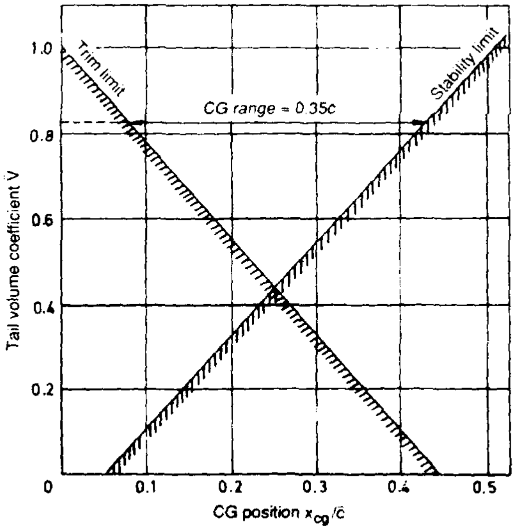

Fig 44 Graphical determination of tail volume coefficient

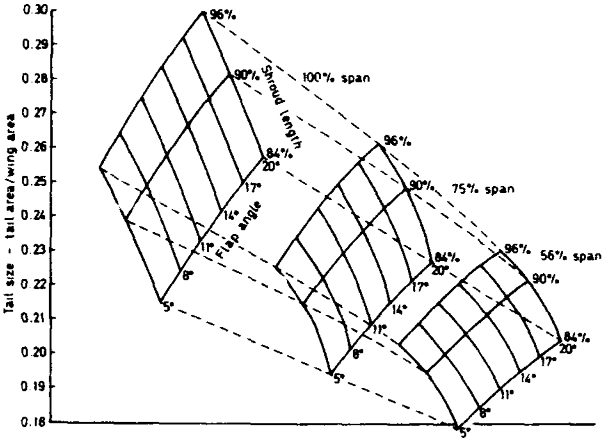

Fig 45 Tail size as a function of flap angle, span and shroud length

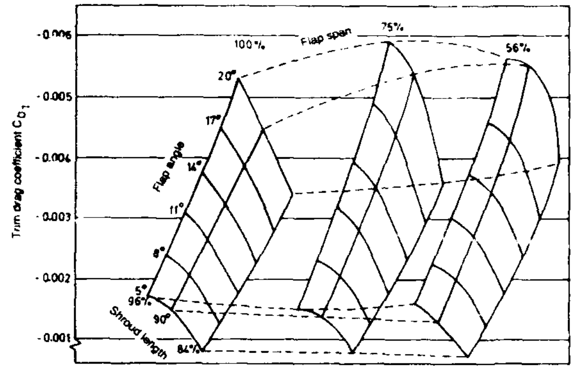

Fig 46 Trim drag coefficient as a function of a flap angle, span and shroud length

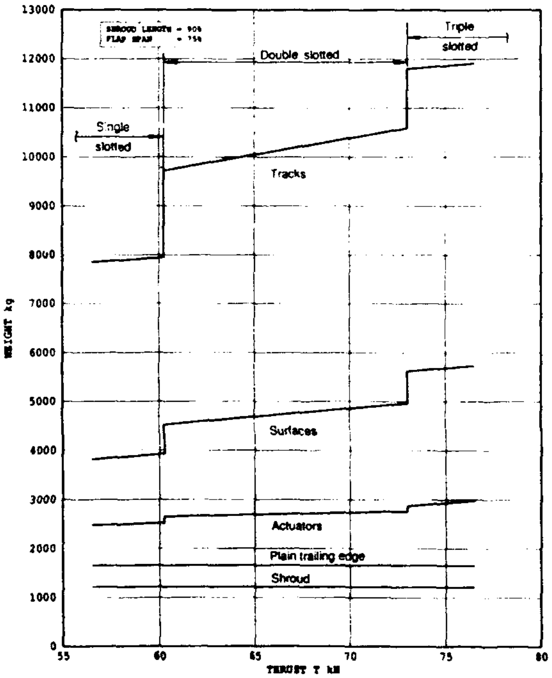

Fig 47 Typical weight breakdown of high lift system

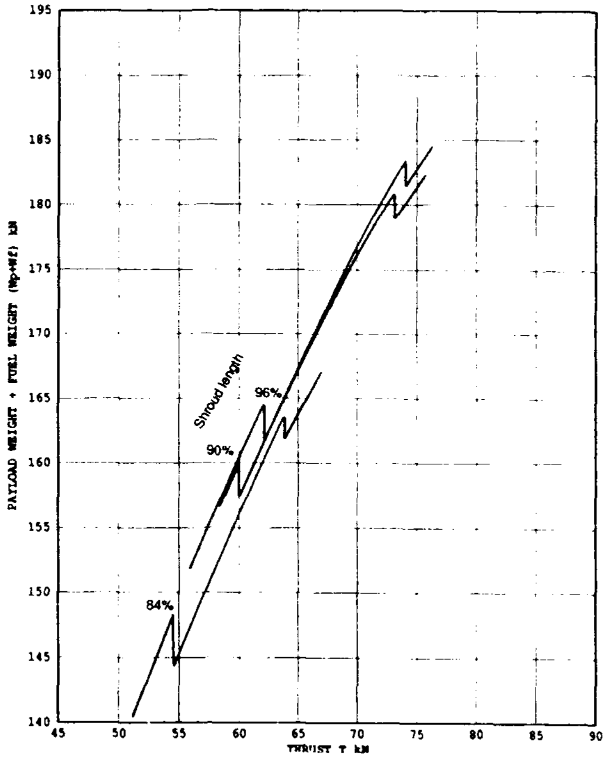

Fig 48 Variation of take-off performance with thrust for 75% flap span

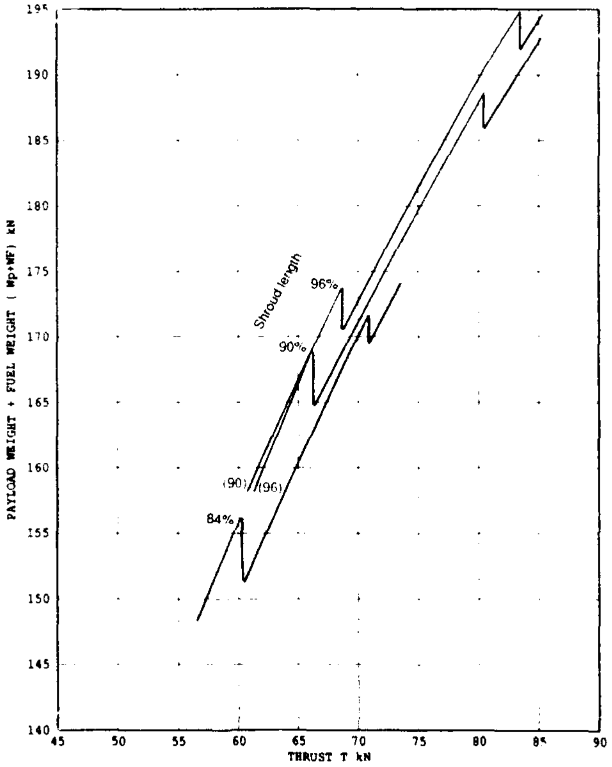

Fig 49 Variation of take-off performance with thrust for 100% flap span

EXPERIMENTAL INVESTIGATION OF FLOW AROUND A MULTIELEMENT AIRFOIL

by

Nafiz Alemdaroglu
Aeronautical Engineering Department
Middle East Technical University
Inonu, Bulvari
Ankara 06531
Turkey

1 Summary

This paper presents the results of experimental investigations performed around a multielement airfoil and gives detailed information about the flow in and around the flap-well and slat cavity regions. Measurements are made using pitot probes, hot-wire anemometer and laser Doppler velocimeter at a Reynolds number of 0.5 and 0.8×10^6. The results obtained show the complex nature of the shear flows investigated and put into evidence the necessity of accurate modelling of these flows by numerical methods.

2 Introduction

The present set of experiments is an extension of the experiments carried out by Nakayama et al. [1], [2] at the Langley Research Center low turbulence pressurized wind tunnel (LTPT). The model used in the present experiments is a scaled down version of the model used in the LTPT tests. Although the measurements of Nakayama were performed at realistic Reynolds and Mach numbers and were complete in terms of the overall external flowfield description, they lacked detailed information about the flowfield inside the flap and slat cavity regions. Hence, a series of experimental investigations were undertaken at California State University, Long Beach to complete the definition of the total flowfield around this multielement airfoil [3], [4].

The measurements inside the flap and slat cavity regions are of crucial importance for the computational aerodynamicist since the calculation of the separated flow in these regions are still not accurate enough and needs to be validated against reliable experimental data. While powerfull computational tools are available to calculate flows around single element airfoils with separation and at high angles of attack [5], accurate and reliable methods that compute the flow around high-lift systems of multielement airfoils do not exist and are still in development. The complex nature of the multielement geometry and the flow field makes the problem more difficult if the real physics of the shear flow is to be modelled. The effort undertaken by Cebeci et al. [6], tries to compute the flowfield around multielement airfoils and uses the present data and those of Nakayama [2], for code validation.

Among the available data on multielement airfoils few were involved with the flap well and slat cavity flows. In particular, references [7] and [8] were concerned with wing-flap configurations. The work of Adair and Horne [9], deals with a wing-flap configuration and contains turbulence measurements in addition to mean flow quantities. The work reported in references [10] and [11] involves three element airfoil with a leading edge slat, but is limited only to pressure and mean velocity measurements inside the boundary layers.

The recent work of Savory et al. [12], is of particular importance since it deals with slat and flap cavity measurements and in particular gives emphasis to turbulence as well as to mean quantity measurements. In these respects it is very much similar to the present experiments.

3 Experimental Set-Up

3.1 Wind Tunnel

The experiments are conducted at the low speed wind tunnel of the Aerospace Engineering Department of California State University at Long Beach. The tunnel has a test section of 22 in. × 28 in. and a streamwise length of 44 in. with a free stream turbulence level of less than 0.5%. The tunnel has no facilities for side wall boundary layer control nor any provisions for high-lift tests. However it can be considered to be sufficient for measurements at relatively low angles of attack where flow separation is small and is limited to the flap-well and slat cavity regions.

3.2 Model

The multielement airfoil model used in the present work is the two dimensional LB-572 high lift model as shown in figure 1. It is a three element airfoil with a leading edge slat and a single-segmented flap. The size of the model is such that the chord of the configuration with the elements stowed is 12 in.

The slat and the flap are attached to the main wing by means of a set of brackets at two spanwise locations. The brackets are designed in such a way as to allow optical access to the flap-well and slat cavity regions by laser velocimeter. The brackets are placed sufficiently away from the centerline so that the two-dimensionality of the flow is not altered at the measurement location. These brackets can be moved both along the chord in order to adjust the overhang, OH, and normal to the chord to adjust the gap, G.

The model is equipped with a total of 125 surface pressure tabs on all three elements. For two-dimensionality checks, there are two spanwise arrays of pressure tabs, one along the spoiler trailing edge (main element) and the other along the trailing edge of the flap. Seven pressure orifices are placed along the flap well ceiling surface and three orifices on the rearward facing step.

The model is installed inside the tunnel horizontally between circular end plates on the side walls. These end plates can be rotated to change the angle of attack. An optical quality glass is inserted in part of the end plate so that the optical paths of the laser beams and the scattered light are left clean.

3.3 Instrumentation

3.3.1 Pressure Measurements

All pressure data including the tunnel static and total pressures are measured by electronic manometers connected to two Scanivalve pneumatic scanners. The analog output is digitized with a computer controlled 12 bit A/D converter. Sufficient care was given to check and validate the response time of the pressure measurement system.

3.3.2 Flow Visualization

Flow is visualized by means of smoke wire technique. The technique uses a thin (0.1 mm diameter) nichrome wire stretched across the flow and connected to a voltage regulated AC power supply with a timing and delay control circuit. Smoke is generated by coating toy train smoke oil on the wire and then burning it by resistive heating.

3.3.3 Hot wire Anemometer

Two channels of TSI 1050 Constant Temperature Anemometers (CTA) are used with standard TSI-1243 ×-wire boundary layer type probes to measure the mean velocity and the turbulence quantities. The microcomputer based data acquisition and reduction system is fully verified and well documented in report [13].

3.3.4 Laser Doppler Anemometer

The laser velocimeter system used in the present experiments is described fully in a previous report [14]. It consists of a 3W Argon ion laser source and a two color, dual beam back scatter optics using the 488 nm and 1514.5 nm lines and a two component counter processor. In later experiments, the counters are replaced by a Burst Spectrum Analyser (BSA), which provided significant improvements in LDA signal analysis. The optical components are all mounted on a large optical bench which in turn is mounted on a milling machine bed and is traversed along three axis. The data acquisition and reduction were accomplished by means of a PDP-11/44 minicomputer which was replaced with a personal computer when BSA was introduced.

4 Flap and Slat Cavity Flows

The geometry and the definitions of the coordinates used in a typical flap-well flow are indicated in figure 2. In general a flap-well flow has the characteristic features of both internal and external flows and is composed of partly irrotational, partly turbulent and reversed flows. The two important streamlines shown in figure 2 are 1) The dividing streamline which leaves the main airfoil lower surface at the step of the flap-well and divides the flow circulation in the separation bubble from the flow that passes through the gap between the main airfoil trailing edge and the flap upper surface. 2) The flap stagnation streamline that terminates at the forward stagnation point of the flap. If this stagnation streamline is known, then the flow above this streamline can be thought of as an internal channel flow with sudden expansion on one side and a curved wall on the other. However, if one considers the pressure *distribution*, it is governed basically by the external flow and is mainly influenced by the entire geometry.

As far as the variables are concerned, the reattachment point, x_R, of the dividing streamline is the most important aerodynamic parameter since it determines a number of important quantities. This point strongly depends to the shape of the separation bubble and to the pressure distribution on the ceiling surface of the flap-well, and in particular to the location, X_{pp}, where the pressure peaks. In general we use geometric parameters such as the gap, G, and the overhang, OH, both expressed as percentages of the mean chord, the flap deflection angle, δ_F, and the overall angle of attack, α, as the parameters influencing these flow quantities. Detailed measurements of the flap-well flow were made during these experiments and the effects of the flap location on the quantities indicated in figure 2 were determined at various flow conditions. The mechanism of the separation and the reattachment of the shear layer was investigated. The coordinates x and y designate the distances along the chord (which is parallel to the flap-well ceiling surface) and normal to the chord (ceiling) and downwards respectively. One can now define the displacement thickness, δ^*, using its conventional definition.

$$\delta^* = \int_0^\delta \left(1 - \frac{u}{U_e}\right) dy \qquad (1)$$

where U_e is the external velocity measured at the edge of the boundary layer, $y = \delta$, at separation. The displacement thickness, $y = \delta^*$, will be a smooth curve extending from the step edge down through the gap. Due to a large normal to surface pressure gradient, the shear layer edge, δ, and the edge velocity, U_e, can not be defined in the usual way and hence the edge is taken as the position where the turbulence intensity is twice the free stream value.

As far as the slat cavity flow is concerned, figure 3 shows the geometry and the probe traverse positions. Similar to flap-well flow some very interesting features of the flowfield such as the large curvature of the dividing streamline, the stagnation streamline and the position of the stagnation point on the lower surface of the main airfoil, the extend of the circulation region in the slat cavity and the total mass flow rate through the gap between the slat and the main element are investigated. In addition, the effects of slat angle, δ_s, slat overhang, S_{OH}, and slat gap, S_G, on the above mentioned flow features are studied.

5 Test Conditions

The experiments are conducted to obtain detailed information of the flow in the flap-well and slat cavity regions with emphasis on the effects of parameters such as; slat gap, slat overhang, slat deflection angle, flap gap, flap overhang, flap deflection angles as well as the overall angle of attack on the separated and reattaching flows in the slat and flap cavity regions. Since flight Mach number and Reynolds number simulation was not possible, Reynolds numbers of 0.8×10^6 and 0.5×10^6 with corresponding Mach numbers of 0.13 and 0.08 are used during these experiments. Reynolds number is based on the clean wing chord length of 12 in. One of the major inconveniences of the small test section is definitely the blockage effect. However, it does not invalidate the trends of the flow characteristics with respect to the parameters changed.

The test conditions are summarized in tables (1) and (2) for flap-well and slat cavity flow measurements respectively. Due to space limitations, for hot wire measurements only 3, in some cases up to 4, streamwise stations can be traversed, whereas for LDV measurements more stations could be probed giving a better resolution of the separation bubble and the recirculating regions.

The two dimensionality of the flow is demonstrated in figures 4a and 4b which shows the spanwise variation of the pressure along the flap trailing edge at two different flap deflection angles. It is observed on these figures that the flow uniformity is maintained over a spanwise extent of about a chord length near the centerline for angles of attack up to 12°. At higher angles of attack, this distribution becomes worse near the tunnel side walls due to the thickened and probably separated side wall boundary layers.

To give qualitative pictures of the flowfield, figures 5,6 and 7 show the results of smoke wire flow visualizations. Figure 5a to d show the flow visualization in and around the slat cavity region at various slat settings and Reynolds numbers. Figure 7.a is the flow visualization at an angle of attack of 4° and at a flap deflection angle of 10°. It is observed that the boundary layers are thin and attached up to the flap trailing edge. Figure 7.b shows the same picture with a flap deflection angle of 25°. Figure 7.c shows the result when the angle of attack is increased to 10° with a flap deflection angle of 25°.

6 Results

6.1 Surface Pressure Distribution

Since it is impossible to show here all the surface pressure data, only those representative cases will be presented. Data presented in figures 8.a to 8.c are all taken at $Re = 0.5 \times 10^6$, and can be reproduced at a higher Reynolds number of $Re = 0.8 \times 10^6$. Figures 8.a and 8.b show the effects of flap overhang and gap ratios on the pressure distribution at a fixed flap angle of 10°. The effect of angle of attack on the pressure distribution for a fixed geometry setting of 2 % gap and 4 % overhang with a flap deflection angle of 10° is shown in figure 8.c. It is observed in all of the cases that the pressure distribution near the step edge and in the forward portion of the well is fairly constant, which is followed by a small pressure peak and a sharp negative pressure gradient to join the much lower upper surface pressure at the trailing edge of the main element. Similar figures can be presented for a flap deflection angle of 25°.

6.2 Hotwire Data

The mean velocity vectors obtained by the x-wire probe are shown in figures 9.a through 9.f for a flap deflection angle of 10° and in figures 10.a through 10.f for a flap deflection angle of 25°. Also shown on the same figures are the mean velocity vector distribution in the gap region between the main element trailing edge and the flap upper surface. These measurements are realized by means of a pitot tube and is used to determine the total flow rate through this gap. If this flow rate is known, it can be used in the determination of the flap stagnation streamline. The dividing streamline, the flap stagnation streamline, the edge of the separated shear layer and the displacement thickness distributions are also shown in these figures. The symbols and definitions used are the same as in figure 2. In order to obtain the dividing streamline smooth curves are drawn that are tangent to the step lower surface edge and to the local velocity vectors. The position of the flap stagnation streamline, y_s, is obtained by using the continuity equation and equating it to the total flow rate Q calculated through the gap between the main airfoil and the flap.

$$\int_{y_d}^{y_s} U\,dy = Q \qquad (2)$$

Since the directional ambiguity of the flow can not be resolved by hot wire measurements, the near wall measurements where the flow is known to reverse are inaccurate. However, an estimate of this backflow velocity can be given by using the continuity equation and the position of the dividing streamline; y_d

$$\int_{0}^{y_d} U\,dy = 0 \qquad (3)$$

where U is the velocity component parallel to the surface. These crude estimates of the back flow velocities are also shown in these figures. Calculation of δ^* is performed using equation (1) which can also be written as;

$$\delta^* = \int_0^{y_d}\left(1-\frac{u}{U_e}\right)dy + \int_{y_d}^{\delta}\left(1-\frac{u}{U_e}\right)dy \qquad (4)$$

$$\delta^* = y_d + \int_{y_d}^{\delta}\left(1-\frac{u}{U_e}\right)dy \qquad (5)$$

where the first integral reduces to y_d with the use of equation (3). The quantities y_d, δ and δ^* are very important since they can be used in the process of fairing (smoothing) the original geometry of the bodies and to include the effects of displacement thickness in interactive viscous/inviscid calculation procedures.

The mean velocity vectors in and around the slat cavity region are presented in figures 11.a through 11.h. These plots show clearly the orientation of the velocity vectors and indicate clearly the strong curvature of the streamlines. By using the same procedure as for flap-well flows, one can easily determine the locations of the dividing and the stagnation streamlines as well as the stagnation point on the main airfoil.

The results of LDV runs for flap-well flow measurements are presented in figures 12.a, b and c for the three different test conditions specified in table 1. Figures 12.a and b show the effect of different overhang ratios with other parameters kept constant. Figures 12.b and c compare the effect of two different flap angle settings. In all of these cases it is observed that the measurements are in good agreement with the hot wire data with the exception of the back flow velocity which can not be determined with hot wire.

6.2.1 Turbulence Data

The turbulent shear stress $-\overline{u'v'}$, and the total normal stress $\overline{u'^2} + \overline{v'^2}$, where u' and v' are the fluctuating velocity components along and normal to the flap well ceiling surface respectively, are shown plotted in figures 13 and 14. These quantities give ideas about the level of turbulence intensities and the degree of their correlation. Both of these turbulent stresses are significant in the momentum equations for separated and reattaching flows. The positions of the dividing streamline, y_d, and the shear layer edge, δ, as obtained from the mean velocity data are also shown in these plots. It is observed that the position of the separated shear layer, as indicated by the region of nonzero shear stress, $-\overline{u'v'}$, is not perfectly aligned with the location of the dividing streamline. This inaccordance which may seem contradictory to our intuitive guesses may be explained in terms of the influence of the stability condition of the curving flow and the position appears to shift lateraly much more than is implied by the mean streamline.

7 Discussion

The discussion of the results for flap-well and slat cavity measurements will be concentrated on the effects of two major parameters, namely the overhang ratio, OH, and the gap ratio, G, on the separated flow.

7.1 Effects of Overhang

A close observation of the pressure distribution curve, figure 8.a indicates that with increasing overhang ratio from 4% to 5% there is an abrupt change in the pressure distribution on the upper surface of the main element. A possible explanation of this sudden change can be attributed to a shift of the transition location on the upper surface of the main element.

More detailed flow analysis is presented in figure 15 for flap deflection angles of $\delta_F = 10^\circ$. This figure shows, the position of the dividing streamline, the pressure distribution along the flap-well ceiling surface, the position of the flap-stagnation streamline calculated from gap flow rates, the static pressure along the edge of the separated shear layer calculated from external velocity and the trailing edge pressures of the main element airfoil, for different overhang ratios at fixed flap deflection angle and gap ratios. Figure 15 indicates that X_{pp} and the dividing streamline move in the same direction, resulting in shorter separation bubbles for larger overhangs and vice versa. The LDV data of figures 12.a, b and c for three test cases also confirm that the position X_{pp} of the peak pressure on the flap-well ceiling surface is very closely related to the reattachment point X_R.

Figure 16 indicates more clearly the influence of overhang on the X_{pp} and C_{pp}, the peak pressure coefficient, for three different gaps. X_{pp} is inversely proportional and varies linearly with OH, indicating that X_{pp} moves almost the same distance as the displacement of the flap leading edge. The peak pressure coefficient, C_{pp}, however, remains uneffected and is practically constant with changing OH.

It is also important that the main airfoil's trailing edge pressure decreases considerably as the overhang is increased but in such a way that the streamwise pressure gradient between the peak pressure point and the gap exit is maintained nearly constant.

The surface pressure within the separated region is fairly constant whereas the pressure at the edge of the shear layer, $y = \delta$, is seen to be consistently higher than the surface value. The difference between these pressures is related to the streamline curvature of the separated flow. The difference between the surface and the shear layer pressures is larger for larger overhangs for which the separation bubble is shorter and hence the streamline curves up more sharply.

The effect of slat overhang is observed when cases C_1, C_2 and A are compared in figure 11. It is found that the slat overhang effect is more important than the slat gap effect. One can conclude that more fluid is injected through the slat gap for smaller overhangs due to smaller recirculation bubbles formed at small overhangs. This behavior can also be observed in the C_p distributions on the slat and on the main element while the C_p distribution on the flap remains uneffected by the slat overhangs. The suction peak on the main element which has a value of -3.8 at 4% slat overhang reaches a value of -5.5 when the slat overhang is reduced to 3%. With further reduction in slat overhang to 2%, the suction peak on the main element attains a value of -6.0. The behavior of the slat pressure distribution is also as expected. With decreasing slat overhang the difference in pressure between the lower (inner) and upper (outer) surfaces of the slat gets smaller and in fact with 1% slat overhang the lower surface C_p becomes equal to that of the upper surface, figure 17. As a consequence, the lift of the slat shows a continuous increase with increasing slat overhang.

7.2 Gap Effects

Figure 18 summarizes the effects of gap on the separated flap-well flow. The most noticeable effect is the opposite changes in the directions in which the dividing streamline and the flap move. As the flap is lowered, (increasing gap), the dividing streamline moves up. This is due to the fact that as the gap is increased more fluid from below the main airfoil moves into the flap-well and passes through the gap, thereby the dividing streamline is pushed farther away from the flap leading edge to allow for this increased mass flow rate. It is observed on these figures that the dividing streamline and the flap stagnation streamlines remain nearly parallel with changing G. If the flap closes in, (approaching the main airfoil), the dividing streamline will be lowered more and will even be lower than the flap and instead of going through the gap will hit the flap surface. Moving the flap further apart from the main element, causes the gap to widen, moves the dividing streamline upwards and shortens the separation bubble even more. These conditions are verified with further experiments where the flap is moved farther away from the main airfoil with new brackets. If the flap is removed altogether, however, the separation bubble becomes longer than any other case with the flap.

The flap stagnation streamline moves with the flap. With decreasing gap, (flap moving up), the shear layer edge will move against the flap which will reduce the potential core going through the gap.

From the foregoing discussions of the isolated effects of gap and overhang, their combined effect for a translational motion of the flap such that the gap is increased and the overhang is reduced at the same time, may lead to a separation bubble and a reattachment length X_R practically unaltered.

For the smallest gap, the dividing streamline is the lowest and the flap stagnation point is the highest. This leads to a very little potential flow through the gap. For $\delta_F = 25°$ case, there is no potential core left and the totaly turbulent shear flow impinges on the flap.

The effect of slat gap is observed when cases D_1, D_2 and A are compared in figure 11. With increasing gap distance more fluid is pushed into the slat cavity and through the slat/main element gap. This results in a reduced size circulation bubble in the slat cavity which in turn causes the the main element stagnation point to move closer to its leading edge. With increasing slat gap, the pressure on the inner surface of the slat decreases further due to increased and accelerated flow passing through the gap, figure 19.

7.3 Flap Deflection Angle Effect

Although only two flap deflection angles, 10° and 25°, are tested and there is not sufficient amount of data available to give quantitative information about the effect of flap deflection angle on the flow, the results presented here give some information about the general trend of the effects. With increasing flap deflection angle, the angle of attack of the flap with respect to the local flow is increased which will lead to lower suction pressures near the flap leading edge and hence an increase in the flow rate through the gap. An increase in flow rate, on the other hand, means shorter separation bubbles in the flap well.

The effect of flap angle on the slat cavity flow is observed when cases A and G are compared. Larger flap angles cause the flow to change direction much earlier. Increasing flap angle modifies the C_p distributions on the slat and on the main element. The C_p values on the upper surface of the main element are moved towards more negative values resulting in an increased lift coefficient for the main element. Same observations are also true for the slat.

The effect of slat angle is observed when cases E and A of figure 11 with respective slat angles of 20° and 30° are compared. The velocity vectors become more horizontal with smaller slat angles. While the C_p distribution for the main element does not change with increasing slat angle, that on the slat shows a drastic change. The suction peak on the slat is reduced with increasing slat angle see figure 20.

7.4 Characteristics of the Separated Shear Flow

The separated and reattaching flap-well flow is extremely complex with large pressure gradients and large turbulence intensities. Nevertheless it exhibits similar characteristics to backward facing step flow or to sudden expansion channel flow. In all of these flows the reattachment length X_P seems to be the major parameter. For an internal flow the basic parameter that determines the reattachment length is the expansion ratio. In the case of a flap-well flow the equivalence of the expansion ratio is simply the ratio of the widths of the flow that goes through the gap at the trailing edge and at the upstream edge of the flap-well. The incompressible continuity equation implies that this ratio of widths is inversely proportional to the ratio of the velocities. For cases in which there is a potential core, the velocity ratio is related to the pressure ratio. Hence the ratio of the pressures upstream the flap-well and at the trailing edge seems to be the key parameter. This pressure ratio can further be related to the pressure drop from the lower surface to the trailing edge of the main airfoil.

Therefore, the characteristics of the flow is tried to be explained in terms of the gap exit velocity. It is observed already that the most important parameter that effects the gap velocity is the gap ratio, G, and the overhang, OH, has practically very little or no significant effect. With increasing gap increasingly higher velocity flow is added near the flap upper surface. This increase in total flow rate is larger than the proportional increase of the gap itself. This is an *amplified change in the total flow rate* due to a small change in the gap width. Increasing the flap deflection angle, δ_F, has a similar effect as increasing the gap width.

In order to analyse the relationship between the gap flow rate Q and the separation bubble, the parameter $\Delta X_{pp} = X_{FLE} - X_{pp}$, (where X_{FLE} is the chordwise distance of the flap leading edge from the leading edge of the clean airfoil), or the C_{pp} is plotted against the gap flow rate. The plot of the nondimensional $\Delta X_{pp}/c$ against Q normalized with respect to the edge velocity at the flap-well step, $\frac{Q}{U_e c}$, is shown in figure 21. In this way the correlation between the location of the pressure peak distance relative to the flap leading edge and the gap flow rate is put forward.

Another important feature of the flap-well flow is concerned with the turbulent stress and its modelling. Gooray et al. [15] and Autret et al. [16] have tried to model the turbulence structure in a backward facing step using the $\kappa - \epsilon$ turbulence model and found that the model required some modifications due to the large local streamline curvature effects. The mean velocity was over and underpredicted before and after the reattachment point respectively, across which the sense of streamline curvature reverses. This local streamline curvatures are much more pronounced in flap-well flows as compared to the unobstructed backward facing step flows. As a result the lengths of the separation bubbles are much smaller than the corresponding back step flows due to the blockage effects of the flap. As far as the turbulence structure is concerned, it is observed that upstream of reattachment the sense of the streamline curvature tends to supress the turbulence and consequently the turbulent shear stress and the intensities are much lower when the separation bubble is shorter or when the curvature of the dividing streamline is larger.

In order to show this more explicitly, in figure 22, turbulent shear stress distributions are superimposed for various flow conditions. This figure not only shows the trend of the shear stress levels, but also reveals that the position of the separated shear layer shifts significantly. It is seen that as the dividing streamline's curvature increases, the position of the shear layer moves up more as indicated by the region of significant shear stress. A close examination of these profiles will yield the fact that this shift of the shear layer location is due to the increased damping of the shear layer at the lower edge of the shear layer as the streamline curvature is increased. This implies that an intuitively plausible assumption that the separated shear layer follows the dividing streamline is a poor one.

8 Conclusion

Detailed measurements of the flowfield in and around the slat cavity and the flap-well regions of a three component multielement airfoil are performed using pressure probes, hot-wire anemometer and laser Doppler velocimeter. The effects of flap angle, flap overhang and gap, slat angle, slat overhang and gap as well as the angle of attack and the Reynolds number on the mean flow and on the turbulence quantities are investigated. The data serves as test cases for computational methods. An immediate use of the experimental results in computational work will be the fairing of the separation bubbles in the slat and flap cavity regions by smooth curves corresponding to the dividing streamlines. Furthermore, detailed mean-flow and turbulence measurements provide information for better understanding of the flap-well and slat cavity flows. The rate of fluid flow through the slat and flap gaps is the key parameter in the determination of the slat cavity and flap-well flows and is very closely related to the lift coefficient of the main airfoil.

References

[1] Nakayama A., Kreplin H.P., Morgan H.L., "Experimental Investigation of Flow Field About a Multielement Airfoil", AIAA J. Vol 28, Jan 1990, pp 14-21.

[2] Nakayama A.,"Flow Field Survey Around High-Lift Airfoil Model LB546", McDonnell Douglas Report, MDCJ4827, Feb. 1987.

[3] Alemdaroglu H.N., "Experimental Investigation of the Flow About Multielement Airfoil Model", California State University, Long Beach, Aerospace Engineering Department, Report No. AS-23996-C 1988.

[4] Alemdaroglu H.N., "Experimental Investigation of the Flow About the Slat of a Multi-Element Airfoil", California State University, Long Beach, Aerospace Engineering Deparment, Contract Report No. AS-24477-C, June, 1989

[5] Cebeci, T., Jau, J., Domenico, V. and Chang, K.C., "Prediction of Post-Stall Flows on Airfoils", in "Numerical and Physical Aspects of Aerodynamic Flows", ed. Cebeci, T., Springer-Verlag, 1990. (ISBN 0-387-52259-X) pp. 97-109.

[6] Jau, J., Vitiello, D. and Cebeci, T., "A Cooperative Program With Douglas Aircraft Company and Aeritalia on the Development of Multielement Aerodynamics Code, Final Report", Report MDC K4377, August 1989, Long Beach.

[7] Seetharam, H.C. and Wentz, W.H.J., "A Low-Speed Two-Dimensional Study of Flow Separation on the GA(W)-1 Airfoil with 30-Percent Chord Fowler Flap", NASA CR-2844, May 1977.

[8] Van den Berg, B., "Boundary Layer Measurements on a Two-Dimensional Wing with Flap", Rept. NLR TR79009U, National Aerospace Laboratory, Amsterdam, Jan. 1979.

[9] Adair, D. and Horne, W. C., "Turbulent Separated Flow in the Vicinity of a Single-Slotted Airfoil Flap", AIAA paper 88-0613, Jan 1988.

[10] Ljungstrom B., "Boundary Layer Studies on a Two Dimensional High Lift Wing", Report AU-862, FFA, The Aeronautical Research Institute of Sweeden, Stockholm 1972.

[11] Bertelrud, A. and Ljungstrom, B., "The Viscous Flow Around a Two Dimensional High Lift Wing, Analysis of Boundary Layer Measurements", Technical Note AU-115, FFA, The Aeronautical Research Institute of Sweeden, Stockholm 1974.

[12] Savory E., Toy N., Tahouri B. and Dalley S., "The Flow Regimes in the Cove Regions Between

a Slat and Wing and Wing and Flap of a Multi-Element Aerofoil", Proceedings of the International Symposium on Engineering and Turbulence Modelling and Experiments" editors; Rodi, W.and Ganic, E.N., Elsevier, 1990.

[13] Akdag, V., Nakayama, A., Liu, B., Kilik, E. and Unt, H., "Automated Hot wire Measurements Using a Microcomputer", California State University, Long Beach, Mechanical Engineering Department, Report No. ME-84-5, 1984.

[14] Alemdaroglu, H. N., Nakayama, A. and Egan, D. "Two Component Laser Doppler Velocimeter for Measurements of Separated Turbulent Flows", California State University, Long Beach, Center For Aerodynamics Research, Report No. CAR-88-1.

[15] Gooray, A.M., Watkins, C.B. and Aung, W., "Improvements to the k-ε Model for Calculations for Turbulent Recirculating Flow." Proc. 4th Symposium on Turbulent Shear Flows, Univ. of Karlsruhe, Karlsruhe, FRG, 1983, pp. 18-26.

[16] Autret, A., Grandotto, M. and Dekeyser, I., "Finite Element Computation of a Turbulent Flow Over a Two Dimensional Backward Facing Step" Int. J. for Num. Meth. in Fluids, Vol. 7, 1987, pp. 89-102.

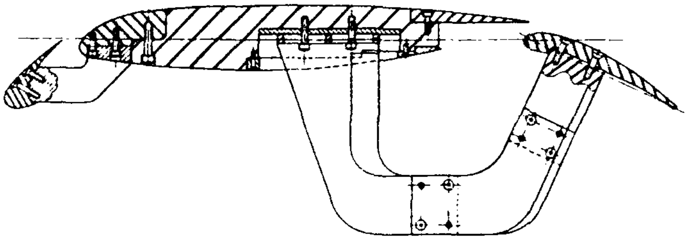

Figure 1: LB-572 3-Element high-lift model

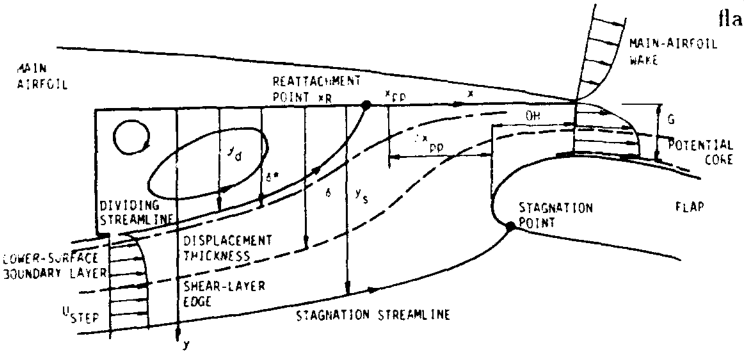

Figure 2: Flap-well flow geometry

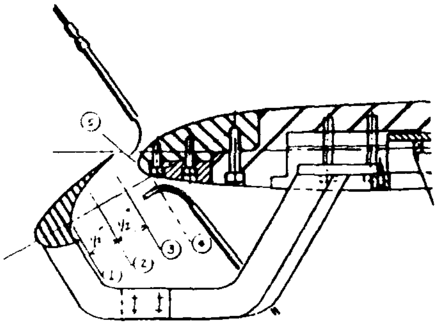

Figure 3: Slat cavity flow

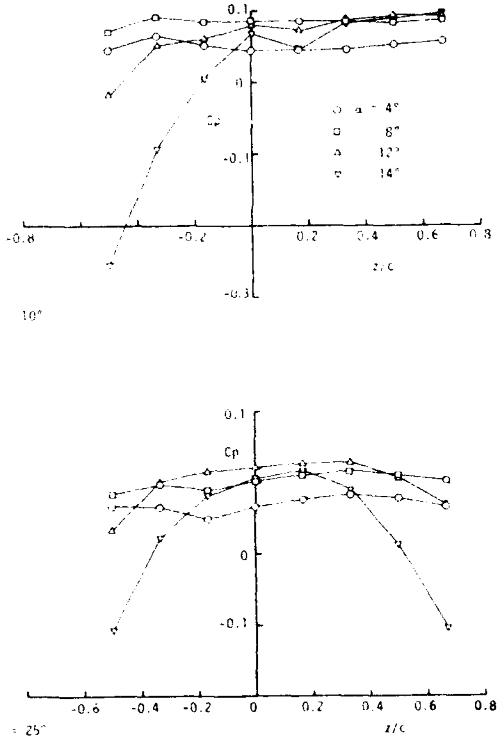

Figure 4: Spanwise pressure distribution along the flap trailing edge

Figure 5.a: $S_{OH} = 4\%$, $S_G = 2\%$, $Re = 0.2 \times 10^6$, $\alpha = 10^\circ$

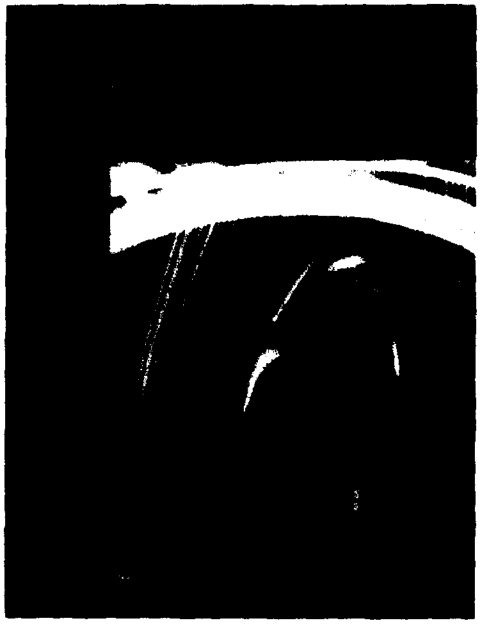

Figure 5.b: $S_{OH} = 4\%$, $S_G = 2\%$, $Re = 0.2 \times 10^6$, $\alpha = 6^\circ$

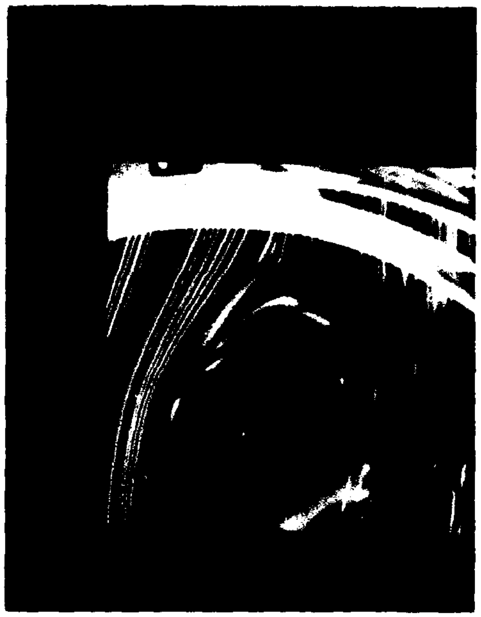

Figure 5.c: $S_{OH} = 1\%$, $S_G = 2\%$, $Re = 0.2 \times 10^6$, $\alpha = 10^\circ$

Figure 5.d: $S_{OH} = 1\%$, $S_G = 2\%$, $Re = 0.25 \times 10^6$, $\alpha = 6^\circ$

Figure 5: Smoke-wire flow visualization within the slat cavity.

Table 1: Test conditions for flap well flow measurements

Method of Measurement	$Re \times 10^6$	α	δ_F	GAP %	OH %
Surface Pressure	0.5,0.8	$0-14°$	10°	1,2,3	3,4,5,6
			25°	1,2,3	1,2,3,4
Hot-wire Measurements	0.5	10°	10°	1,2,3	3,4,5,6
			25°	1,2,3	1,2,3,4
	0.5	$0,4,6,8,12°$	25°	2	3
LDV Measurements	0.5	10°	10°	1	3
	0.5	10°	10°	1	5
	0.5	10°	25°	1	3
Flap Gap Flow, Pitot Measurements	0.5	10°	10°	1,2,3	1,2,3,4
			25°	1,2,3	1,2,3,4

Table 2: Test conditions for slat cavity flow measurements

Case	$R_e x10^6$	$\alpha(°)$	$\delta_F(°)$	F_{oh} (%)	F_g (%)	$\delta_s(°)$	S_{oh} (%)	S_g (%)	station 1	station 2	station 3	station 4
A_1	0.5	10	10	4	2	30	3	3	$x=0.0in$	$x=0.5in$	$x=1.0in$	$x=1.25in$
B_1	0.5	6	10	4	2	30	3	3	$x=0.0in$	$x=0.5in$	$x=0.9in$	$x=1.5in$
B_2	0.5	14	10	4	2	30	3	3	$x=0.0in$	$x=0.5in$	$x=1.0in$	$x=1.5in$
C_1	0.5	10	10	4	2	30	2	3	$x=0.0in$	$x=0.5in$	$x=1.0in$	$x=1.5in$
C_2	0.5	10	10	4	2	30	4	3	$x=0.0in$	$x=0.5in$	$x=1.0in$	$x=1.5in$
D_1	0.5	10	10	4	2	30	3	5	$x=0.0in$	$x=0.5in$	$x=1.0in$	$x=1.5in$
D_2	0.5	10	10	4	2	30	3	2	$x=0.0in$	$x=0.5in$	$x=1.0in$	$x=1.5in$
E	0.5	10	10	4	2	20	3	3	$x=0.0in$	$x=0.5in$	$x=1.0in$	$x=1.5in$
F_1	0.25	10	10	4	2	30	3	3	$x=0.0in$	$x=0.5in$	$x=1.0in$	$x=1.5in$
F_2	0.40	10	10	4	2	30	3	3	$x=0.0in$	$x=0.5in$	$x=1.0in$	$x=1.5in$
G_1	0.5	10	25	4	2	30	3	3	$x=0.0in$	$x=0.5in$	$x=1.0in$	$x=1.5in$
G_2	0.5	10	25	2	2	30	3	3	$x=0.0in$	$x=0.5in$	$x=1.0in$	$x=1.5in$

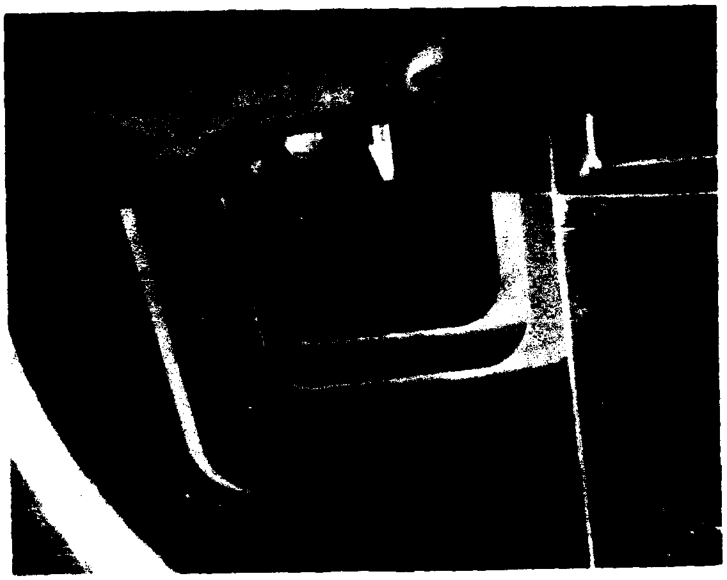

Figure 6: Smoke wire flow visualisation within the flap-well

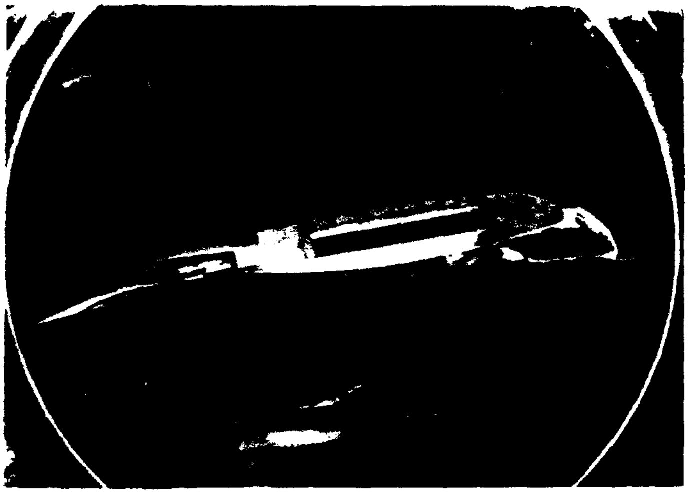

Figure 7 a: Smoke wire flow visualisation, overall flow field, $\delta_F = 10°$, $\alpha = 4°$.

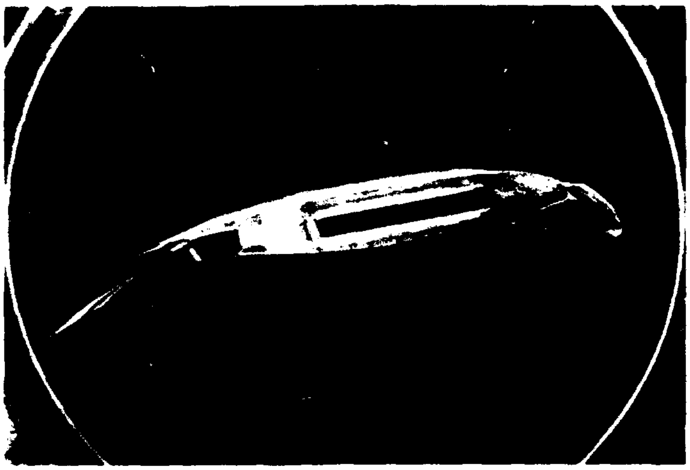

Figure 7 b: Smoke wire flow visualisation, overall flow field, $\delta_F = 25°$, $\alpha = 4°$.

Figure 7 c: Smoke wire flow visualisation, overall flow field, $\delta_F = 25°$, $\alpha = 10°$.

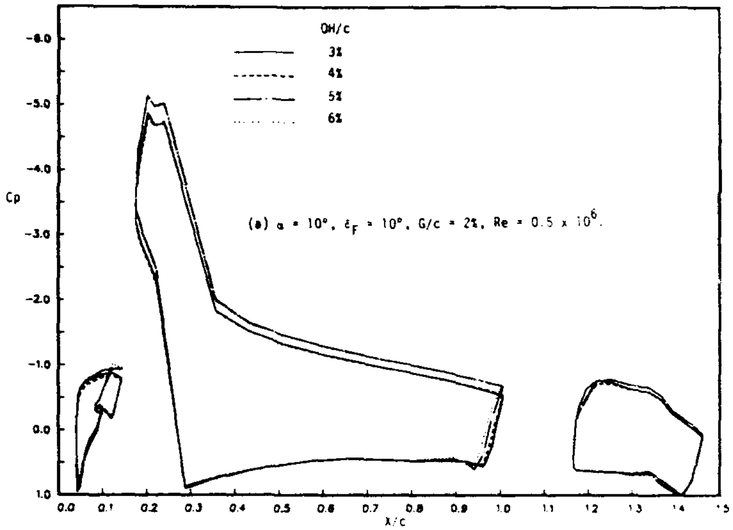

Figure 8.a: Surface pressure distribution, effect of flap overhang

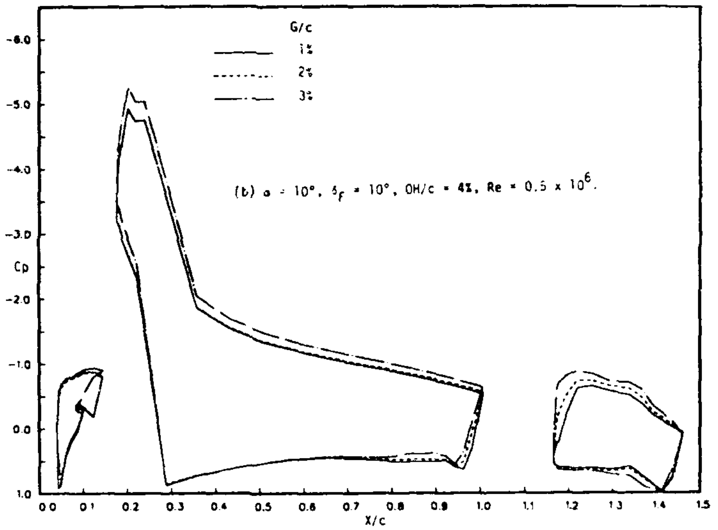

Figure 8.b: Surface pressure distribution, effect of flap gap

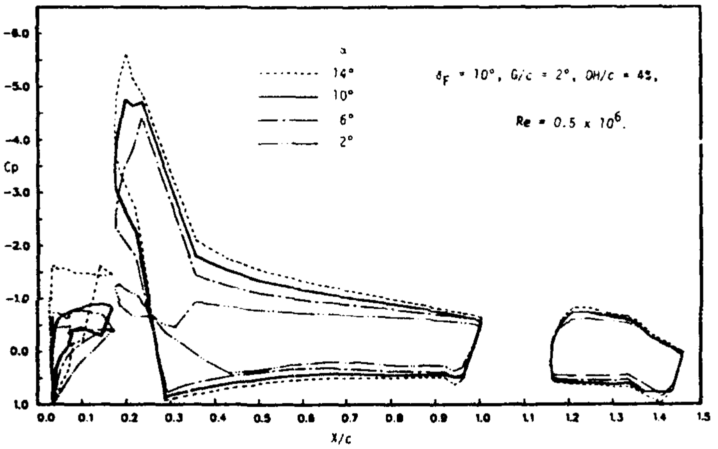

Figure 8.c: Surface pressure distribution, effect of angle of attack

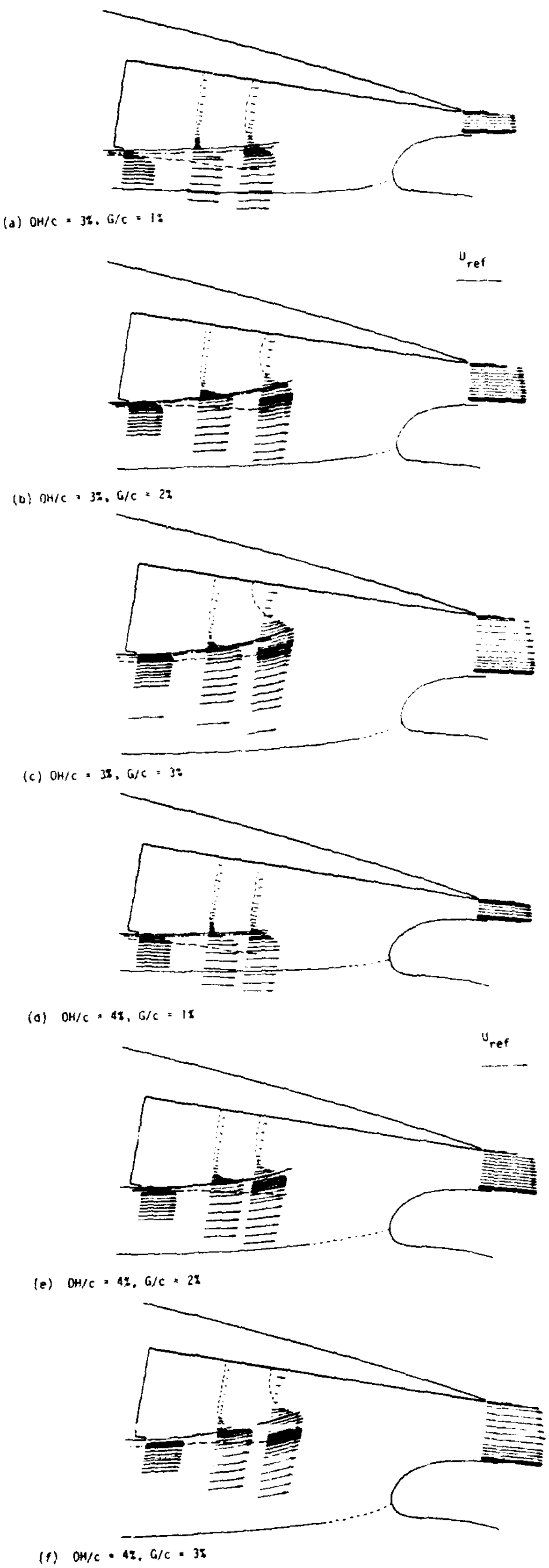

(a) OH/c = 3%, G/c = 1%

(b) OH/c = 3%, G/c = 2%

(c) OH/c = 3%, G/c = 3%

(d) OH/c = 4%, G/c = 1%

(e) OH/c = 4%, G/c = 2%

(f) OH/c = 4%, G/c = 3%

Figure 9: Mean velocity vectors in flap-well obtained by hot-wire and pitot measurements, $\delta_F = 10°$, $\alpha = 10°$.

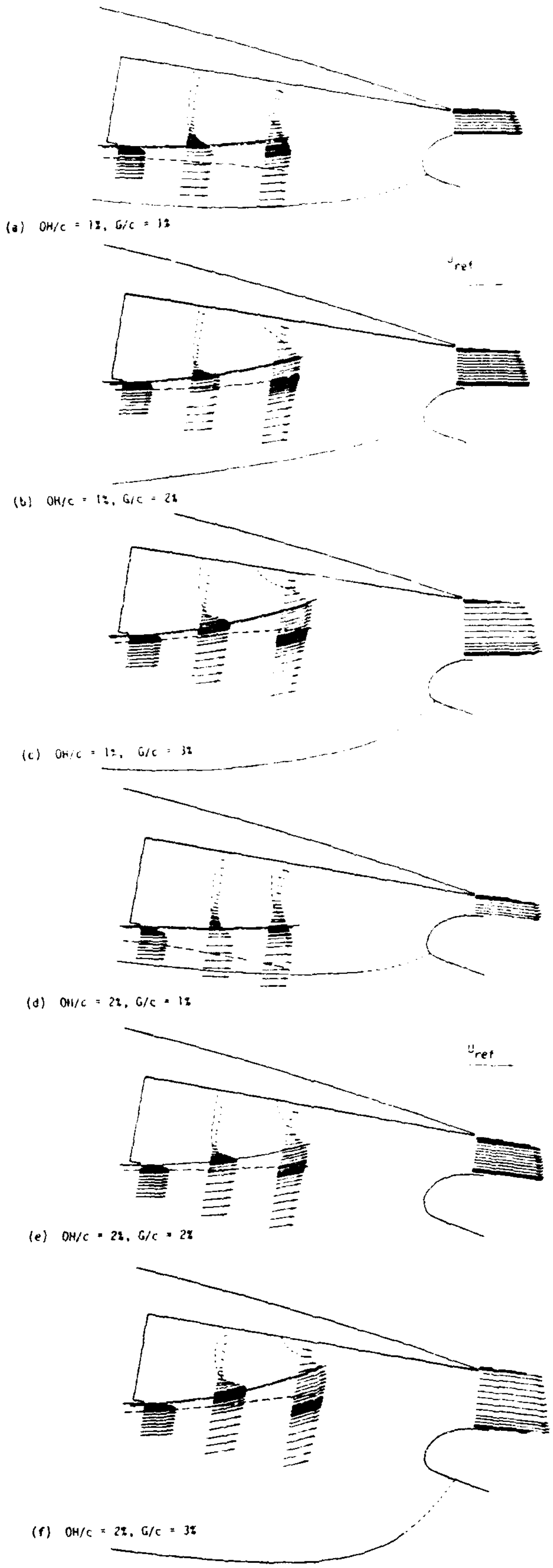

(a) OH/c = 1%, G/c = 1%

(b) OH/c = 1%, G/c = 2%

(c) OH/c = 1%, G/c = 3%

(d) OH/c = 2%, G/c = 1%

(e) OH/c = 2%, G/c = 2%

(f) OH/c = 2%, G/c = 3%

Figure 10: Mean velocity vectors in flap-well obtained by hot-wire and pitot measurements, $\delta_F = 25°$, $\alpha = 10°$.

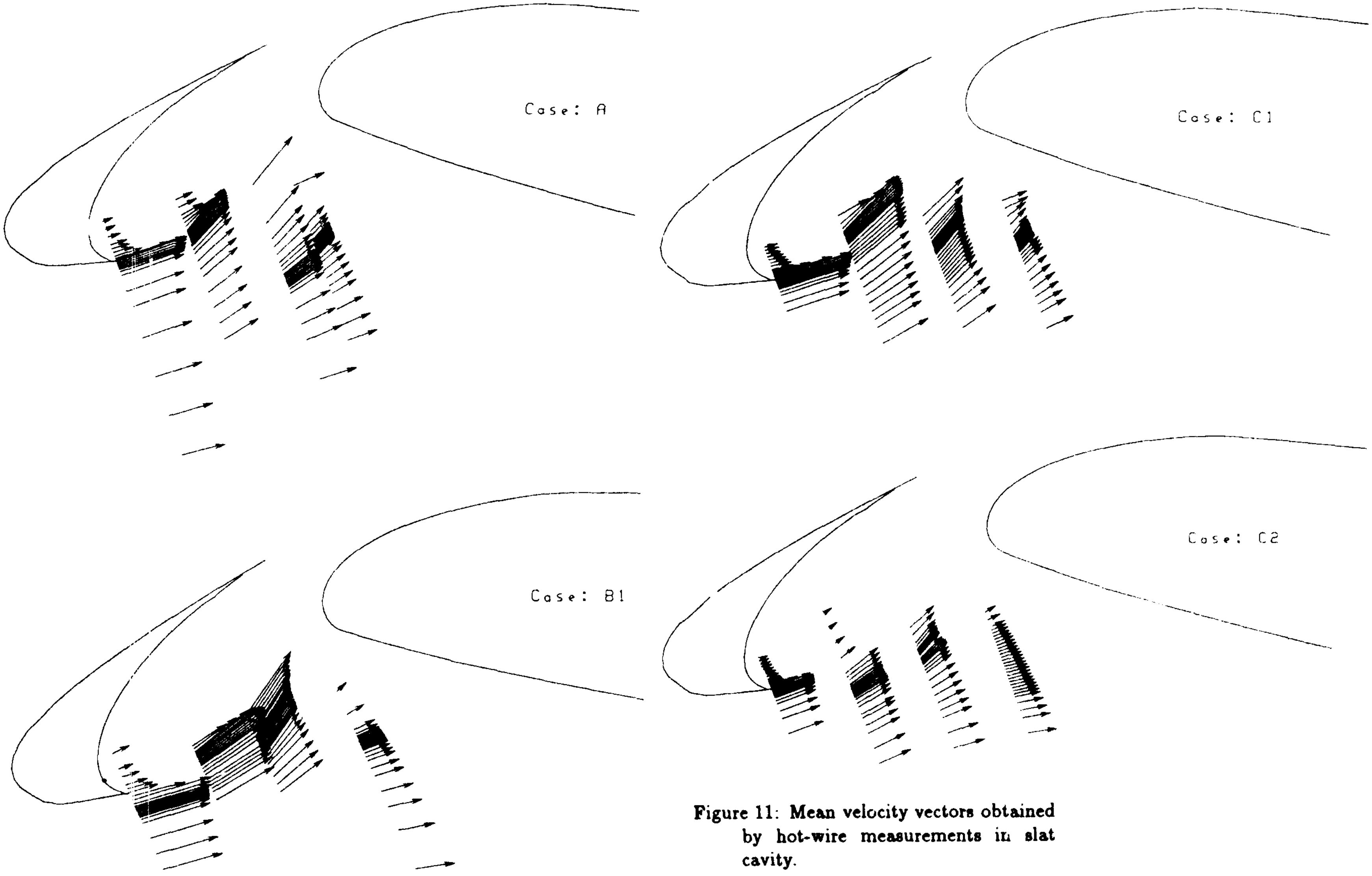

Figure 11: Mean velocity vectors obtained by hot-wire measurements in slat cavity.

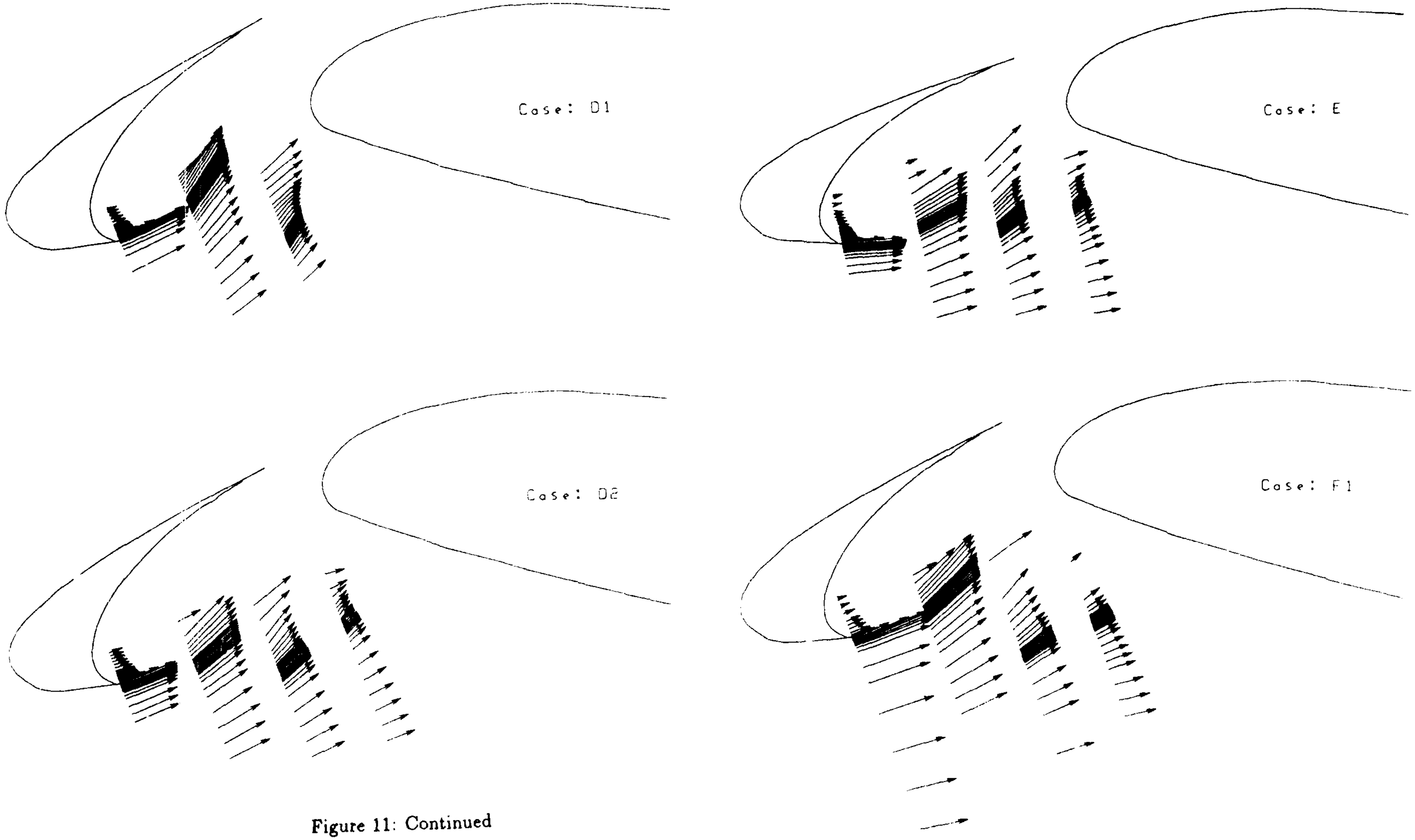

Figure 11: Continued

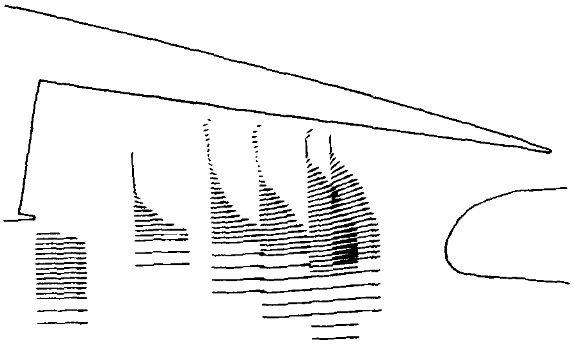

(a) δ_F = 10 deg, G/c = 1%, OH/c = 3%.

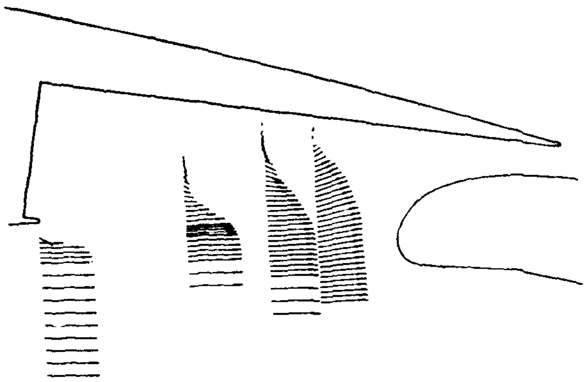

(b) δ_F = 10 deg, G/c = 1%, OH/c = 5%.

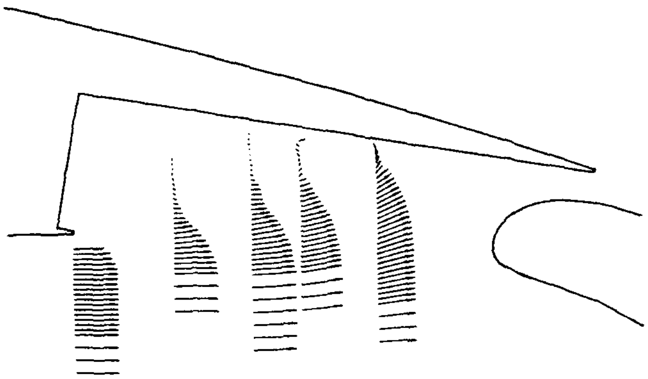

(c) δ_F = 25 deg, G/c = 1%, OH/c = 3%.

Figure 12: Mean velocity vectors obtained by LDV measurements

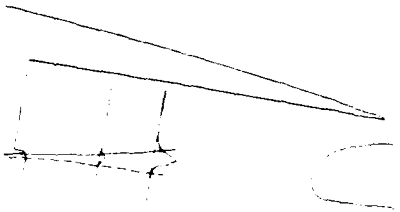

(a) OH/c = 3%, G/c = 1%

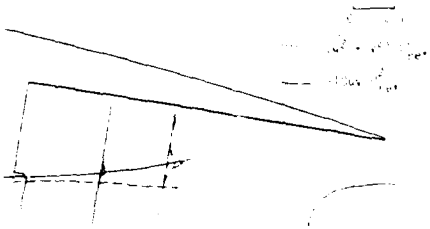

(b) OH/c = 3%, G/c = 2%

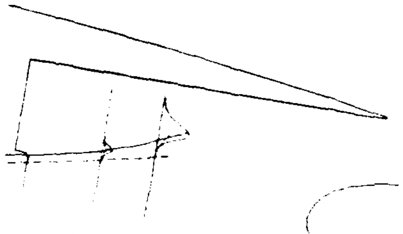

(c) OH/c = 3%, G/c = 3%

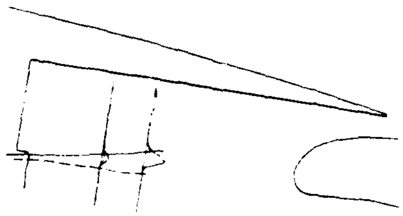

(d) OH/c = 4%, G/c = 1%

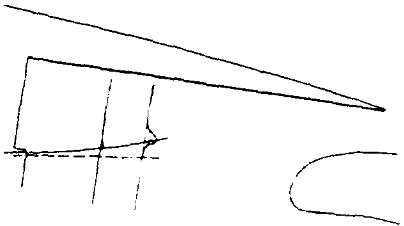

(e) OH/c = 4%, G/c = 2%

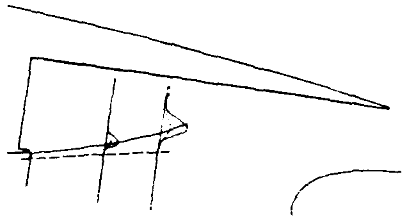

(f) OH/c = 4%, G/c = 3%

Figure 13: Turbulent shear stress and total normal stress distributions, $\delta_F = 10°$.

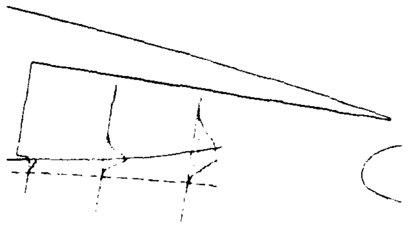

(a) OH/c = 1%, G/c = 1%

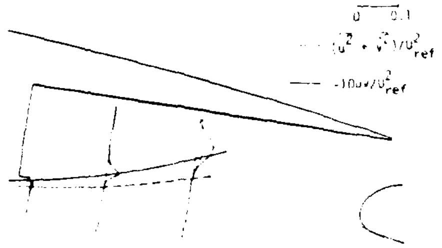

(b) OH/c = 1%, G/c = 2%

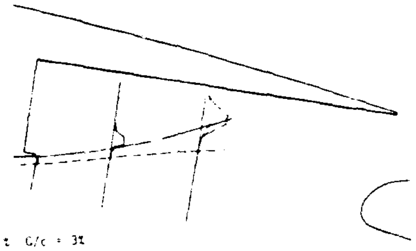

(c) OH/c = 1% G/c = 3%

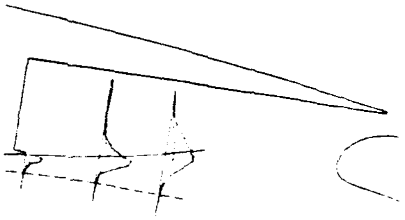

(d) OH/c = 2%, G/c = 1%

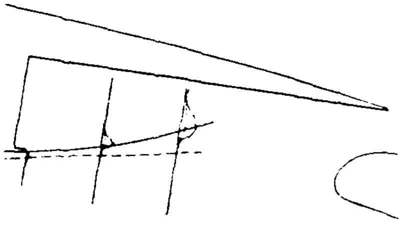

(e) OH/c = 2%, G/c = 2%

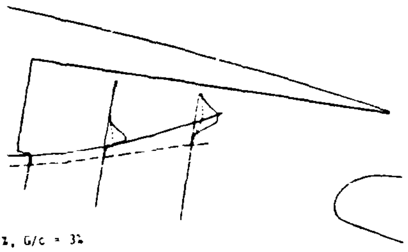

(f) OH/c = 2%, G/c = 3%

Figure 14: Turbulent shear stress and total normal stress distributions, δ_F = 25°.

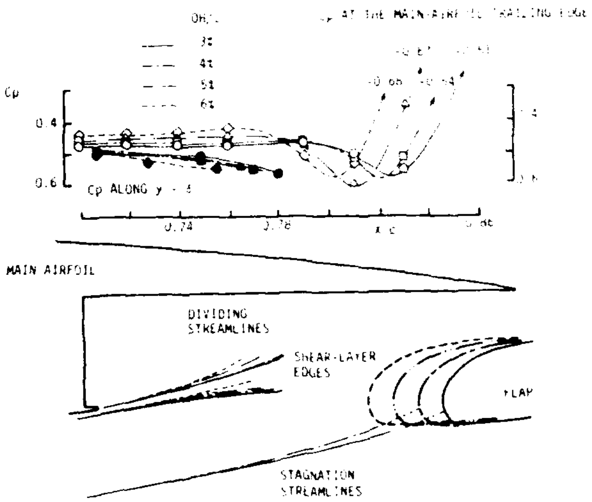

Figure 15: Effects of overhang on the dividing streamline and pressure inside the flap-well, δ_F = 10°, G/c = 2%.

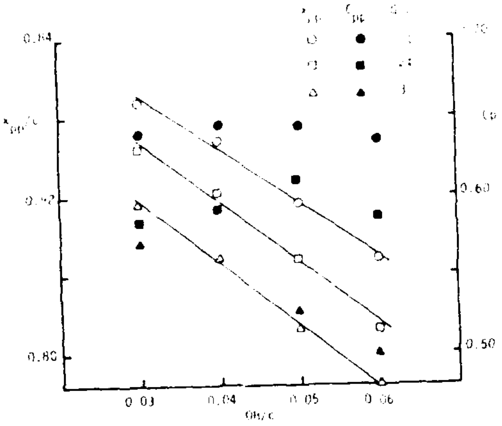

Figure 16: The positions and the values of the peak pressure on the flap-well ceiling surface as functions of OH, δ_F = 10°.

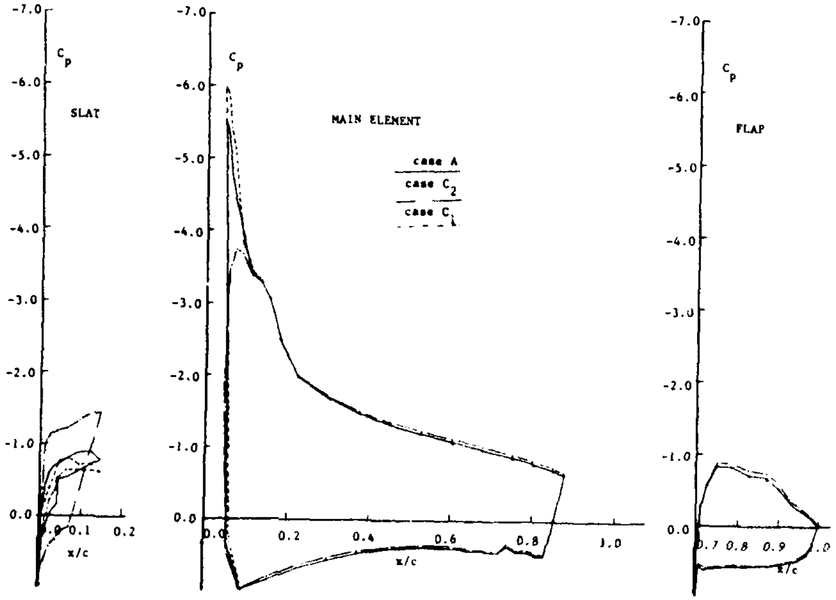

Figure 17: Surface pressure distribution, effect of slat overhang.

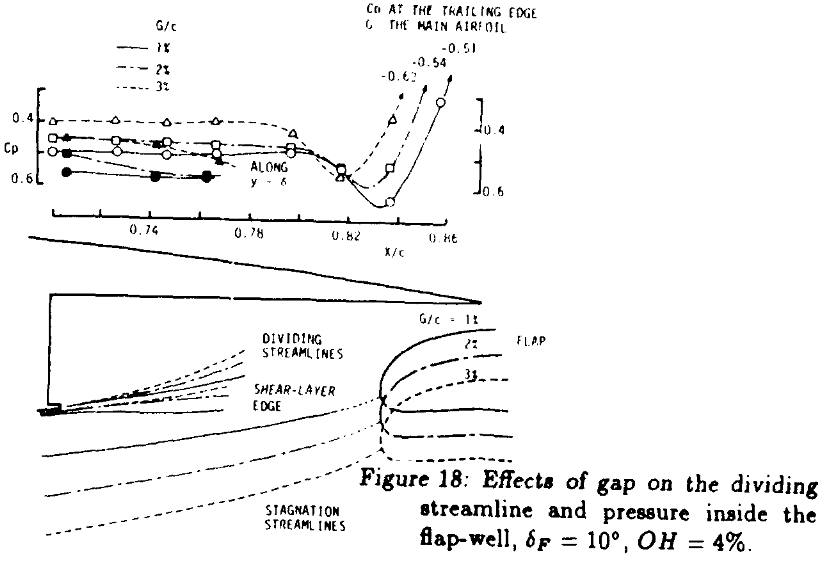

Figure 18: Effects of gap on the dividing streamline and pressure inside the flap-well, $\delta_F = 10°$, $OH = 4\%$.

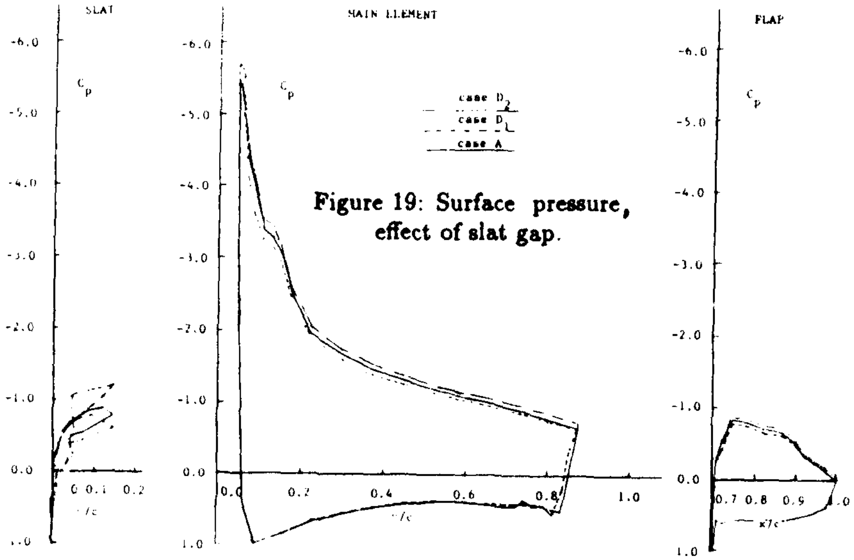

Figure 19: Surface pressure, effect of slat gap.

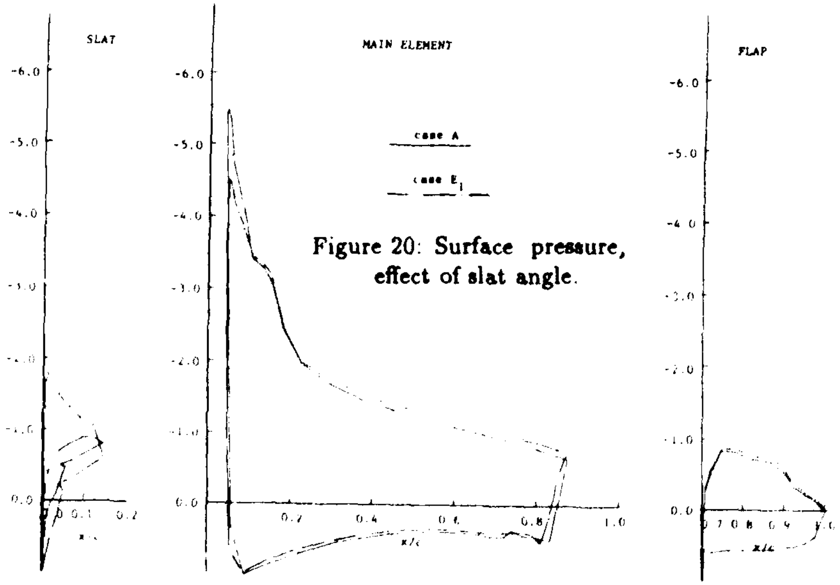

Figure 20: Surface pressure, effect of slat angle.

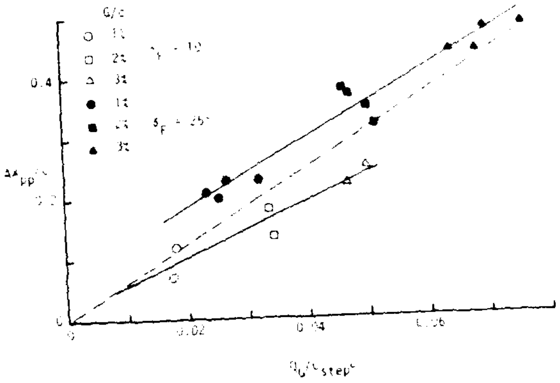

Figure 21: ΔX_{pp} and C_{pp} as function of flap gap flow rate Q.

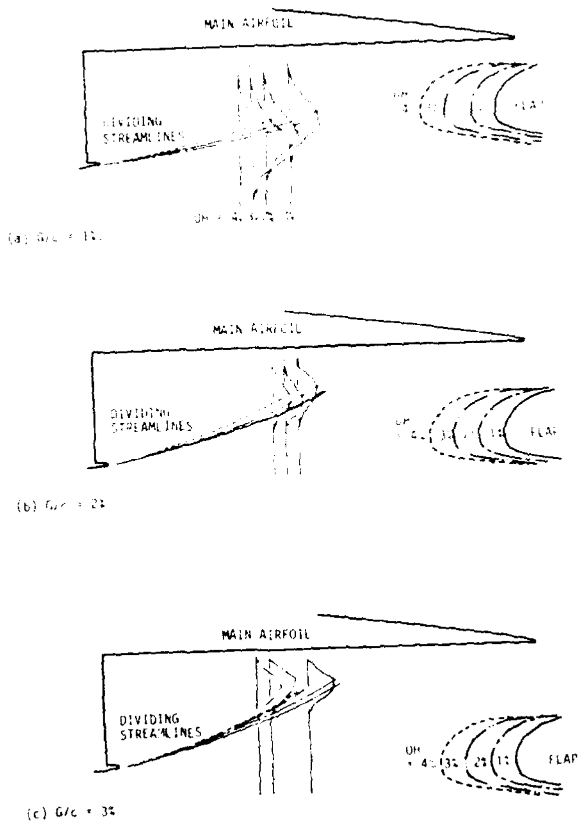

Figure 22: Effect of streamline curvature on turbulent stress in the flap-well.

A DESIGN PROCEDURE FOR SLOTTED FLAPS

by
Sergio De Ponte* - Alessandro Cella - Mario Marcazzan
* Politecnico di Milano - Dipartimento di Ingegneria Aerospaziale
Via Golgi 40 I-20133 Milano - Italy

ABSTRACT

In the design of slotted flaps it is attempted to avoid a reacceleration between the trailing edge of an upstream element of the system and the peak velocity of the downstraem element, to reach the maximum lift.

It is proved that it is possible by means of a nemerical procedure based on a vortex distribution.

The resulting shapes are then discussed with reference to the application to real design.

INTRODUCTION

The design of slotted flaps might either be done in an optimizarion way or it is in any case an attempt to have a good compromise between cruise and take-off/landing performances.

The most naif way to try this compromise is to choose the airfoil shape for cruise conditions and the wing loading for take-off, as done in many aircraft designs in a far past.

In any attempt to have a compromise between two conflicting conditions, it is useful to know which are the opposite extremes: in this case they are the plain airfoil and the unconstrained best lift flap. The former is well known since a long time, while the latter is the subject of the present research. Aim of the present work is to answer to some fundamental questions which arise on the design of maximum lift slotted airfoils. *It is not therefore a method of designing usful airfoils but a method for knowing the other extreme in a design process, to establish correctly the penalties imposed by the compromise.*

The overall scheme is similar to the procedure of Liebeck and Omsbee (1), with the main considerations of A.M.O. Smith (2) about flaps, and is conducted on a single slotted flap as an example. this will not prohibit to extend the procedure to more element airfoils.

In this way *maximum deceleration* is sought on the suction side of the airfoil and the highest *dumping velocity* at the trailing edge of the main airfoil is attempted. Observing usual flaps, it could be noted that, after the trailing edge of the main airfoil, the flow is more or less reaccelerating on the flap. Then the following question naturally arises:

Is it possible to reach at the trailing edge of the main element the same velocity as the maximum on the flap, in order to get the maximum dumping velocity?

If it could be done, large lift increment could be reached, as shown in the figure.

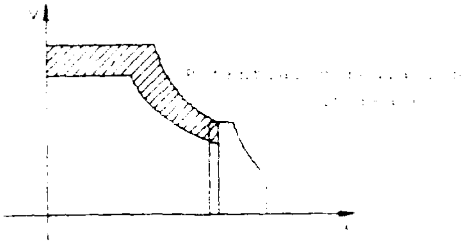

Fig. 1 Lift increment

The first approach to the problem was to see the amount of lift increment for a given flap chord that could be reached increasing the dumping velocity. In the same way it was explored the possibility of reducing the flap chord for a given lift coefficient. All this was done without any consideration about the feasibility of the airfoil.

Some very rough study has shown that the use of a flap as mean of increasing the dumping velocity could lead to very short flap chord for a given lift increment. For a double Liebeck pressure distribution some possible result is shown in the following figure, from ref. (3)

Fig. 2 preliminary lift evaluation

But if the answer to this main question could be affirmative, a second arises immediately and it is about *the shape* of such an airfoil system, mainly with respect to possibility of obtaining some cruise condition by rejoining the elements in a reasonable contour.

Of course, although the first question has larger theoretical importance, the latter is quite practical in engineering sciences. In order to answer to both questions it was thaught that the numerical choice coud be the only feasible one, due to the complexity of the problem for a pure analytical approach.

THE NUMERICAL PROCEDURE

The numerical procedure is based on a panel method, being the conformal mapping unsuitable for multiple airfoil shapes. In fact, Timman method (4) allows to treat double aiorfoils, but it seems too difficult to extend it to a larger number of contours.

On the basis of many experiences, it seems that a method which does not allow any contour modification in the *chordwise direction* is rather difficult to use, therefore a method that has no restriction on the airfoil modification was chosen.

The basis is then an iterative vortex panel technique, starting from a first approximation shape.

THE FIRST APPROACH AIRFOIL.

A first approximation is obtained by linearized small perturbation theory, superimposing mean line and thickness distribution.
The mean line is obtained by a simple standard design, while for multi component airfoils it is simply broken and shifted in the normal direction by a prescribed slot width. This shift is a still open problem.
Thickness distribution is first obtained by a discrete point source distribution prescribing tangential velocity along the chord.

At this point it is possible to iterate the computation of the thickness, placing the condition of given tangential velocity distribution along the airfoil contour instead of the chord line; this might be a good improvement in case of rather thick airfoils.

In this procedure particular care is taken to *modify the velocity distribution* in order to obtain a *closed* and *non crossing* airfoil.
These are properties of the thickness distribution and not of the camber line. The relevant *conditions ought* to be investigated before going to the detailed design, in order to avoid convergence problems during further calculations.
The problem of closure is very well posed for conformal mapping and also the *non* crossing of the contour requires only an univocal mapping of the airfoil into the cercle.

Also in the singularity method the question is rather well defined for the small perturbation problem.
In principle, the *representation* of a thickness distribution by means of a discrete number N of point sources is a 2 N unknown problem, i.e. the *strength* and *location* of each source.

But while the source strength leads to a linear system of algebric equations, their locations lead to a non linear problem: it is therefore common practice to prescribe the source locations in some reasonable way. It means that we have some degree of freedom in locating the singularities.

Putting N sources on the chord line, each of intensity q_i, the closure is related to the total outcoming flow, which should be zero. This leads to the relation:

$$\sum_{i=1,N} q_i = 0$$

To satisfy this condition, only N-1 velocities are assigned, i.e. the velocities between the points where sources are placed, being the last (zero outflow) the N_{th} condition.

The non crossing condition is similar, and says that, at any station along the chord, the total flow produced upstream by the sources should not be negative, resulting in the N-2 conditions:

$$\sum_{i=1,I} q_i > 0 \qquad I=2,N-1$$

being the first source always positive in our procedure and the total intensity equal to zero as said.

It is possible to see that the conditions are redundant if one does allow to prescribe velocities in the points where a naif idea could suggest.

Furthermore there is a set of inequalities to be satisfied for the non crossing conditions.
In our procedure the inequalities are simply verified at each iteration and the computation is stopped whenever the inequalities are not satisfied. In practice, it has been noted that, beyond a certain number of sources, the scheme does not converge.

In order to spend the freedom of choosing the chordwise location of the singularities, the first source is placed at the point along the chord, where it produces a Rankine ogee with the same velocity derivative at the stagnation point as the desired airfoil velocity distribution,thus avoiding an extra stagnation point condition, but adding a constraint.

In this way the places where sources could be located is limited and it this avoids problems near the nose . In fact, any attempt to place a source upstream to this first one, produces a sink and meaningless contours.

THE INVERSE PANEL METHOD.

The inverse panel mathod is the inversion of a classical Martensen procedure ,in an iteration process. The Maretesen method (5) represents the airfoil by a vortex distributiion according to the Chaucy formula:

$$w(z) = \frac{1}{2\pi i}\int_{\lambda}\frac{w(\zeta)}{\zeta - z}d\zeta$$

which is transformed in a *second kind*

Fredholm integral equation by putting the boundary condition *of no internal tangential velocity.*

The airfoil contour from the former iteration (the first approximation airfoil for the starting step) is divided into panels and at the midpoint of them the velocity is prescribed.This velocity gives the vortex strength, which is kept constant on each panel and, if the shape would be correct, the *inside tangential velocity* should be *zero*, according to the Martensen condition and is therefore computed. Being, in general, non zero, a modification procedure is then started.

The first attempt was to compute the derivative *of the tangential velocity* in the *direction normal* to the panel and try to use this as guide to correct the airfoil. But it resulted almost impossible to state a feasible modification criterion *on this basis*.

Therefore a more complex procedure was attempted. It consists in the computation *of the efffect of perturbing the airfoil* shape displacing each panel in the normal direction by a certain small amount, (a given fraction of its length) and *computing the perturbed inside velocity.* Only the two neighbour panels at each side are displaced in order to save aorfoil closure, as shown in the following figure.

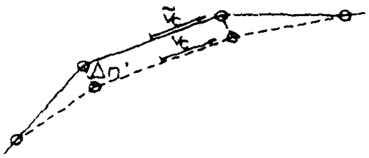

Fig 3 Panel displacement

The procedure is then repeated for each panel.
At this stage, a complete matrix [A] of influence of contour modification is obtained, in the sense that we have the effect of displacing each panel on the overall velocity distribution.

In this way it is possible to shift the contour in the *normal direction* according to the influence matrix and the difference between the computed and the target velocites by a simple relaxation scheme.
Being j the known vortex strength,and Δn the shift in normal direction used in the matrix calculation, the new velocity is *v* and the old v.

The new velocity *v* is computed as:

$$v = [A]\, j + V_\infty$$

The shift Δ required is therefore:

$$\Delta = \frac{v - \mathrm{v}}{\Delta n}$$

for relaxing the scheme the real value is then computed as:

$$\Delta n_i = \frac{\Delta n_{i-1} + 2\Delta n_i + \Delta n_{i+1}}{4}$$

GEOMETRICAL PROBLEMS

Having displaced the panels, a new set of segments represents the airfoil. Of course it is not closed and has not exactly the prescribed chordlength, which is unity in dimensionless form. This is due to the fact that the panels near the leading edge might move in the chordwise direction, as formerly stated.

It is therefore necessary to reshape again the geometry to obtain a closed airfoil and then scale all the lengths by a constant related to the increment in airfoil length. The reshaping is done reconnecting panels joining them at midpoint of the discontinuity each side point, as shown in the figure:

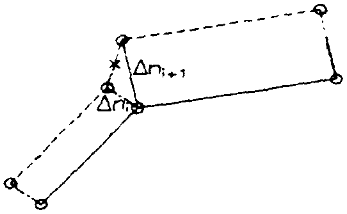

Fig. 4 Panel reconnection

We have therefore a *two step* contour modification: the first is the shifting and the second a rotation and a change in length and,of course. this last changes the slope of each panel and thus the normal and tangential velocity components. For this reason it is rather difficult to asses theoretically the *convergence* of the scheme.

But , more important, this *closes anytime* the contour, *without modifying* the velocity distribution. The question will be discussed later on.
For rescaling the lengths the most upstream point is then *found giving the new chord* length and all the geometry is normalized with respect to this latter.
The new center of panels are found and, by *interpolation*, at each center point a new velocity is given, changing accordingly the vortex strength.This is a *third step in the airfoil correction*

Incidentally, testing the program on cylinders approximated by regular polygons in the first stages of the research, it was observed that, without rescaling, all the geometrical quantities are reduced at each iteratioin, tending to a zero chord shape.
All this procedure is programmed on a personal computer

FIRST TESTS.

The first tests were made on known shapes and on analytical velocity distributions, first of all the circular cylinder and ellypses of changing aspect ratio.

Having in mind that the contour was enforced to be closed, only velocity distributions for closed contours were attempted at this stage.

Test of giving the pressure distribution of one airfoil and the first approximation shape of another gave significant results even in exteme case as shown in the following figure.

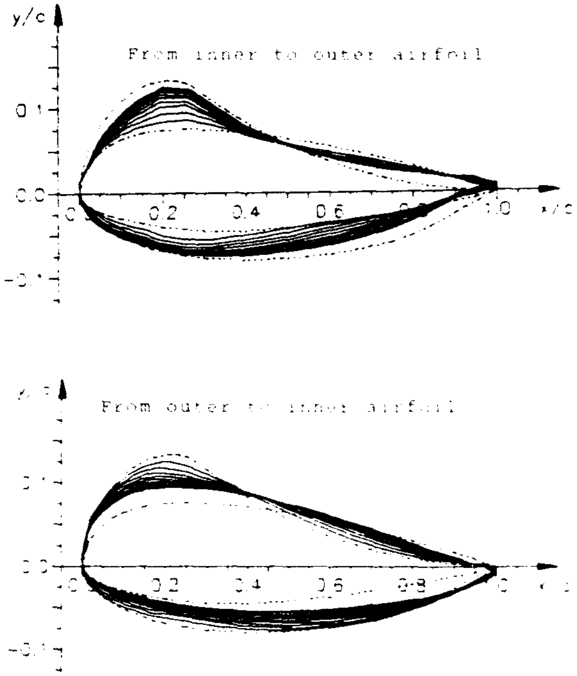

Fig. 5 Examples of iterative procedure

It has been observed that the obtained contour is different from the target one, as might be seen from the figures.
In general, the angle of attack is larger and the mean line camber is smaller.
Suspecting that this could be significant, direct computation of pressure distribution for both target and obtained airfoil were performed.

To avoid to use computational schemes with similar kind of approximations in direct and inverse calculations, a *Hess-Smith* direct method was used instead of using a *Martensen* code.

The pressure distributions were *surprisingly similar* for target and obtained airfoils suggesting that the design problem could have, at least from the pratical point, *a nearly non unique* solution, in the approximate sense that small changes in the pressure distribution, mainly near the stagnation point, may produce large geometrical changes. Similar effects were observed by Volpe in trensonic design (6)
Further tests were made on twice connected contours of known flapped airfoils.

AIRFOIL DESIGN.

Having acquired a certain confiance in the use of the method, the design of flapped airfoil was attempted, with the aim of the least reacceleretina flow beyond the velocity of the trailing edge of the main airfoil.

The pressure distribution was prescribed on the basis of "equilibrium" turbulent boundary layers and similar solutions for laminar ones.
The velocity distributions along the *chord* are therefore:
$v = A\,x^n$ for the laminar part and
$v = B\,(x-x_i)^m$
for the turbulent part and the exponent m has the minimum value of 0.25 assumed as limit for attached flows.

No closure condition was formally imposed on the velocity distribution. This is different from Liebeck approach and gives slightly different shapes but is thaught to be more conservative and easier to use. The velocity distribution is given in the following figure:

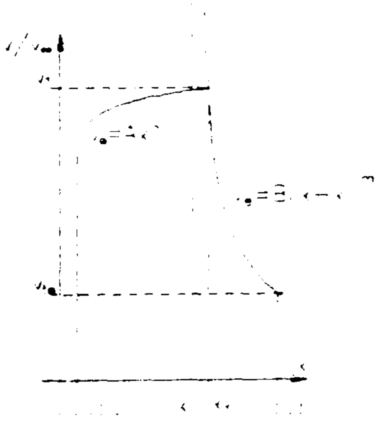

Fig. 6 Velocity distribution

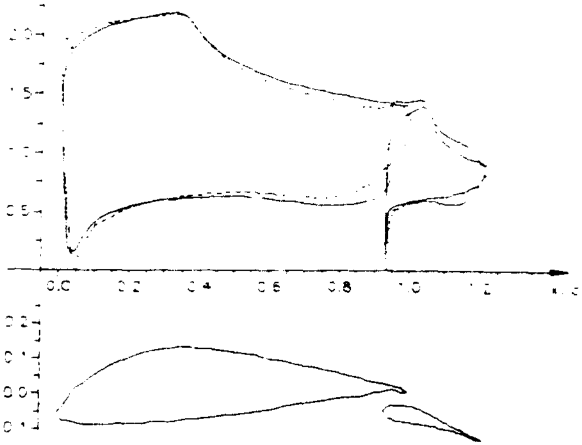

*Fig. 7 Target —— and obtained.....
pressure distributions and airfoil shape*

Again, as in the first test stages, the velocity distribution on the final shape was computed by a different code to be compared to the target one.
The results are interesting although some problem is still open.
First of all *it is possible to prevent reacceleration* without any unfeasible conditionong of the shape, as shown in the former figure.
A comparison to an airfoil of Ormsbee and Chen (7) gives an idea of the strong reacceleration on other kind of designs.
The first attempts gave almost independant airfoil shapes, without any indication about the possible slot shape. The results are similar to the one of Omsbee and Chen of the previous figure. Further designs, reducing the spacing between components, gave first ideas about a possible slot. This was obtained also *reducing the acceleration* on the pressure side upstream the slot, as shown in the figure:
But it is interesting to notice that the slot should be a *non converging channel* in contrast to the usual practice.
Furthermore, the flap curvature immediately downstream the slot is *rather small*, incidentally explaining the success of some Fowler flap.

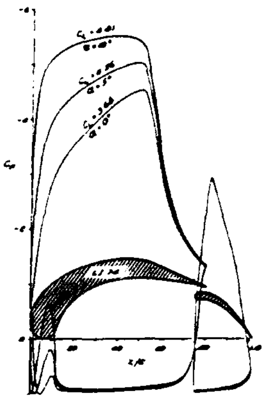

Fig. 8 Ormsbee and Chen airfoil

In this last case the pressure on the lower side was kept as high as possible, giving a very high camber and a design lift coefficient of 4.43.
Out of the design condition the velocity distribution is rather regular and possibly at 13° angle of attack there is no nose deceleration, suggesting an increase in lift *coefficent* up to 4.75 as a limit for a rooftop pressure distribution, but no boundary layer calculation was attempted up to now, because of some wiggle in the pressure distribution.

CLOSURE PROBLEMS

As said no formal closure condition was posed in the design, but is well known that a small modification of the stagnation point location could change very much the airfoil thickness.

In fact, the computed velocities show a typical peak near the leading edge and it is suspected that it is due to the lack of closure condition.
In an attempt to improve the method, it was decided to allow simply a shift in the prescribed stagnation point location. When

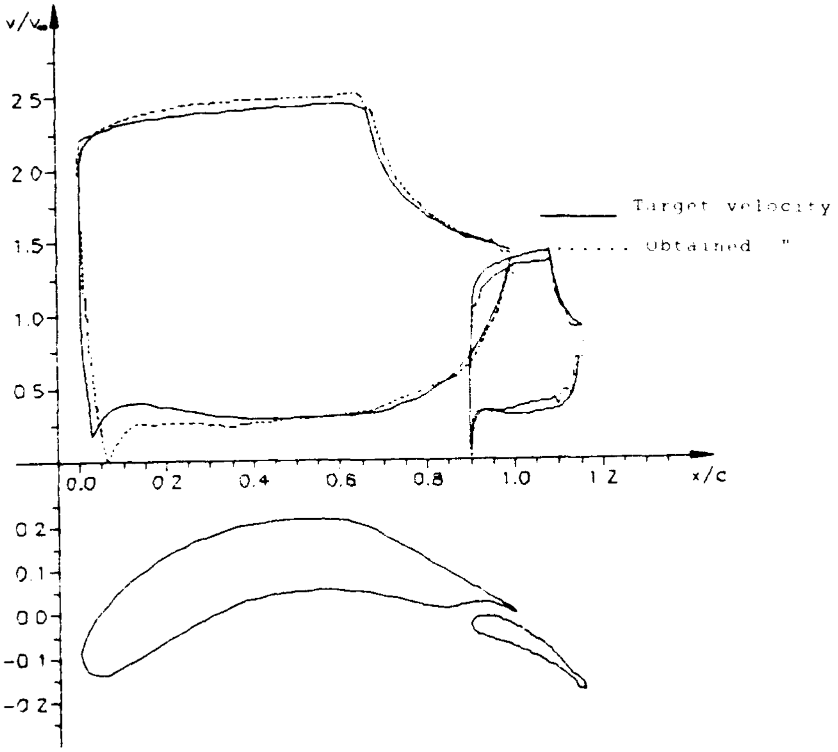

Fig. 9 A better airfoil

the airfoil is modified, the leading edge changes chordwise location with respect to the prescribed stagnation point. This new distance is then taken as new stagnation point location in the *rescaling* of the airfoil, giving a velocity that is prescribed in all points in the same way as in the previous iteration, *except near the leading edge*, where the stagnation point location is revised according to the new iteration of the airfoil shape.
This procedure allows a better agreement of the computed velocity distribution to the target one, everywhere except near the stagnation point.
This is a *third step* in the modification.

OPEN PROBLEMS

The first open problem is related to the wiggles in the contour near the leading and trailing edges. Probably something is related too the small number of panel used, but there is the suspect of the need of some *smoothing* of the contour at each *iteration*. *Lacking of any convergence* criterion, it is difficult to state that there is no dendence of some *local divergence* even in an *overall convergence* and critical points are always leading and trailing edges in panel methods.

A second problem is related to the width of the slot, which is now almost prescribed because the method does not modify it significantly. It was stated that the slot width could be related to the airfoil drag (8).
Probably the approximation of the velocity distribution used in these first examples is too crude for a reasonable insight into the slot problems and should be modified accordingly.

CONCLUSIONS

The first conclusion is that the aim of designing slotted flaps with a dumping velocity very close to the maximum velocity on the flap is almost obtained, showing, in principle, the feasibility of such a design.

Second is the result that the shapes are not so unusual for a complete design procedure.

Then it might be observed that a flap could be designed having in mind that it might be mainly *a system of increasing the dumping velocity*, instead of a system of producing *direct lift*. In this sense a rough approach suggests that a good design could reduce the flap chord for the same lift increment, saving simplicity and room for structure, fuel and equipements.
All this should, of course, verified in the overall deesign procedure.

A lot of problems are still open, both from the theoretical and from the practical point of view. Among them, the *smoothing* of the shape and a better insight in the closure condition, but in any case the way seems to be promising for further investigation.
Also the problem of a correct slot design requires first an investigation about e good velocity distribution around the slot from the basic point of view of boundary layer and interference, before going on in airfoil design.

References

1) Liebeck - Ormsbee *Optimization of Airfoils for maximum lift* Journal of Aircraft Vol 7 N 5- 1970

2) Smith A.M.O. -*Aerodynamics of High-Lift Airfoil Systems* AGARD CP 102- 1972

3) Martellini - *Verso l'ottimizzazione di ipersostentatori* Thesis, Milano, 1988

4) Timman - *The Direct and Inverse Problem of Airfoil Theory. A Method to Obtain Numerical Solutions* NLR Report F 16 - 1951

5) Martensen *Berechnung der Druckverteilung an Gitterprofilen in ebener Potentialstroemung mit einer Fredholmschen Integralgleichung* Arch. Rat. Mech and Analysis Vol 3 -1959

6) Volpe - *Inverse Design of Airfoil Contours: Constraints, Numerical Methods and Applications.* AGARD CP 463 - 1989

7) Ormsbee - Chen *Multiple Element Airfoils Optimized for Maximum Lift Coefficients* AIAA Journal Vol.10 n. 12 , 1972

8) Blom - *Comment on Paper N 13 during the discussion of* AGARD Symposium V/STOL Aerodynamics, Agard CP 143 pag A-9

* *This research was partially supported by CNR (Italian Research Council)*

Calculation of Maximum and High Lift Characteristics of Multi Element Airfoils

Willy Fritz, Dornier Luftfahrt GmbH, Deutsche Aerospace
Postfach 1303, D-7990 Friedrichshafen, West-Germany

Introduction

The flow field around multi-element aerofoil sections possesses a high degree of complexity. Due to the strong interactions between wakes from the upstream elements and and the upper surface boundary layers developing on the downstream elements, there are thick viscous layers present over the upper surface of the trailing edge flap. Large regions of separated flow can be present, even for conditions well below maximum lift. Finally the flow around the leading edge slat can become locally supersonic, even for low freestream Mach numbers, due to the large suction levels induced in this region.

The viscous-inviscid interaction methods, which are most widely in use for the prediction of multi-element aerofoil flows, are computationally very efficient, but unable to describe many of the complex flow features present.

A more complete description of the physical phenomena can be achieved only by methods based on a solution of the Reynolds-averaged Navier-Stokes equations, in conjunction with a suitable turbulence model. The generation of a suitable computational grid then becomes a major problem. Within the present work, a method to generate suitable block structured grids around multi-element aerofoils has been developed. The Dornier 2-D block structured Navier-Stokes solver has been extended for grids with arbitrary block structure. After very encouraging results for a two-element high lift system at low angles of attack [3], in this work the method was applied for realistic two- and three-element high lift systems at high angles of attack.

Grid Generation

As the configuration can become very complex, a generation of structured grids without any singular points is completely impossible. On the other side, discontinuities in the computational grid can produce large numerical errors in the solution. In order to minimize those effects, a grid generation technique, which avoids singular points and/or discontinuities in the grid spacing at least along the surfaces, has been developed. Suitable C-mesh type grids around each component are patched up to an inner grid. This inner grid is embedded into an outer C-type mesh (Figure 1). To guarantee a smooth point distribution, the elementary grids are normally generated numerically using elliptical partial differential equations for the point distribution:

$$AX_{\xi\xi} + BX_{\eta\eta} + CX_{\xi\eta} + QIX_{\xi} + QJX_{\eta} = 0 \qquad (1)$$

where $X = (x,y)$ being the physical and (ξ, η) the computational coordinates. The coefficients A, B and C are fixed by the transformation relations between the physical and the computational space, only the control functions QI and QJ can be used for grid control and/or adaptation of the grid lines [3]. The discretization of the limiting boundaries is performed according to the condition

$$W_{(i)}\Delta s_i = const. \qquad (2)$$

with s being the arc length of the boundary line. W is any weighting function such as geometric or arithmetic stretching. This elliptical grid generation technique has normally the best smoothing qualities, but it fails for large concave slopes and sharp corners which are usually present at multi-element aerofoils. Therfore a hyperbolic grid generation technique is used in such regions:

$$\begin{aligned} x_{\xi}x_{\eta} + y_{\xi}y_{\eta} &= 0 \\ -x_{\xi}y_{\eta} + x_{\xi}y_{\eta} &= V \end{aligned} \qquad (3)$$

The equations (3) specifiy the orthogonality condition for the grid lines, and the "volume" of each cell. As Steger and Chausse have shown in [1], equation (2) can be integrated by a time like marching procedure in either space direction. They chose an Euler implicit marching algorithm normal to the surface, central space differences in the other space direction an added explicit fourth order dissipation to provide some grid smoothing mechanism in that direction. This algorithm proved satisfactory for some simple shapes but showed difficulty in generating grids about surfaces with concave curvature or slope discontinuities. Therefore a more general marching algorithm suggested by Pulliam in [2] has been applied in the present work. The original algorithm of Steger and Chaussee is reformulated such that numerical dissipation can be added and controled in all space directions, thereby enhancing grid smoothencss. By adding second and fourth order dissipation, the constraint equations (2) are only approximately satisfied, it is only a matter of how much dissipation can be added without overly compromising the equations. Details of the solution algorithm can be found in [2].

Governing Equations

Navier-Stokes Equations

The Reynolds averaged Navier-Stokes equations describing two-dimensional, unsteady and compressible flows in conservation form are given by

$$\frac{\partial U}{\partial t} + \frac{\partial F}{\partial x} + \frac{\partial G}{\partial y} = 0 \tag{4}$$

where:

$$U = \begin{bmatrix} \rho \\ \rho u \\ \rho v \\ E \end{bmatrix}, F = \begin{bmatrix} \rho u \\ \rho u^2 + p + \sigma_{xx} \\ \rho uv + \sigma_{xy} \\ [E + p + \sigma_{xx}]u + \sigma_{xy}v + Q_x \end{bmatrix},$$
$$G = \begin{bmatrix} \rho v \\ \rho uv + \sigma_{xy} \\ \rho v^2 + p + \sigma_{yy} \\ [E + p + \sigma_{yy}]v + \sigma_{xy}u + Q_y \end{bmatrix} \tag{5}$$

and

$$\begin{aligned} \sigma_{xx} &= -\lambda[\frac{\partial u}{\partial x} + \frac{\partial v}{\partial y}] - 2[\mu + \mu_t]\frac{\partial u}{\partial x}, \\ \sigma_{yy} &= -\lambda[\frac{\partial u}{\partial x} + \frac{\partial v}{\partial y}] - 2[\mu + \mu_t]\frac{\partial v}{\partial y}, \\ \sigma_{xy} &= -[\mu + \mu_t][\frac{\partial u}{\partial y}\ \frac{\partial v}{\partial x}], \\ Q_x &= -k\frac{\partial T}{\partial x}, \qquad Q_y = -k\frac{\partial T}{\partial y} \end{aligned} \tag{6}$$

with density ρ and mean total energy per unit volume E:

$$E = \rho e + 0.5\rho(u^2 + v^2) \tag{7}$$

The coefficient μ is the laminar viscosity and μ_t is the eddy viscosity which takes into account the effects of turbulence. This eddy viscosity has to be estimated by the turbulence modell.The thermal conductivity k is given by

$$\frac{k}{c_p} = \frac{\mu}{Pr} + \frac{\mu_t}{Pr_t}$$

The perfect gas equation of state is used to define the mean static pressure p via the internal energy e:

$$p = [\gamma - 1]\rho e \tag{8}$$

The bulk viscosity λ is defined as $\lambda = -2/3\ \mu$, the turbulent Prandtl number is fixed at 0.90 and the ratio of specific heat, γ , is maintained constant at 1.4.

Turbulence Model.

The Reynolds-averaging of the Navier Stokes eqautions introduces a further set of unknowns, the so called Reynolds stresses. Those Reynolds stress components are normally related to the mean flow quantities through a set of additional equations that represent the turbulence model. In the present method either an algebraic turbulence model, based on the well known Baldwin-Lomax turbulence model with some extensions for free turbulence, or the Lam-Bremhorst two equation Low Reynolds Number k-ε turbulence model can be used.

The algebraic turbulence model computes the eddy viscosity by algebraic relations from the mean velocity field taking no account of the transport of turbulence. This model is only used during the calculations in the coarse meshes within the multi-level grid technique. In the Lam-Bremhorst k-ε model, the eddy viscosity is computed using two transport variables, which are the turbulent kinetic energy k and the turbulent dissipation rate ε:

$$\frac{\partial(\rho k)}{\partial t} + \frac{\partial}{\partial x_i}(\rho u_i k - \mu_k \frac{\partial k}{\partial x_i}) = P_k - \rho \varepsilon \tag{9}$$

$$\frac{\partial(\rho \varepsilon)}{\partial t} + \frac{\partial}{\partial x_i}(\rho u_i \varepsilon - \mu_\varepsilon \frac{\partial \varepsilon}{\partial x_i}) = \frac{c'_1 f_1 \varepsilon}{k} P_k - \frac{c'_2 f_2 \varepsilon^2 \rho}{k}$$

with the production term

$$P_k = \frac{\mu_t}{\mu}[\tau_{xx}\frac{\partial u}{\partial x} + \tau_{xy}(\frac{\partial u}{\partial y} + \frac{\partial v}{\partial x}) + \tau_{yy}\frac{\partial v}{\partial y}] - \frac{2}{3}\rho k(\frac{\partial u}{\partial x} + \frac{\partial v}{\partial y}) \tag{10}$$

and

$$\mu_t = \mu_l c_\mu f_\mu R_t$$

$$R_y = \frac{\rho k^{0.5} y}{\mu_l} \qquad R_t = \frac{\rho k^2}{\mu_l \varepsilon} \qquad u_\tau = \sqrt{\frac{\tau_w}{\rho_w}}$$

$$c'_1 = 1.44 \qquad \mu = \mu_l + \mu_t$$

$$c'_2 = 1.92 \qquad \mu_k = \mu_l + \lambda_k \mu_t$$

$$\mu_\varepsilon = \mu_l + \lambda_\varepsilon \mu_t$$

$$\lambda_k = 1.0$$

$$c_\mu = 0.09 \qquad \lambda_\varepsilon = 0.77$$

$$f_\mu = = [1 - \exp(-0.0165 R_y)]^{(1 + \frac{20.5}{R_T})}$$

$$f_1 = 1 + (\frac{0.05}{f_\mu})^3$$

$$f_2 = 1 - \exp(-R_T^2)$$

By introducing the additional damping functions f_1 , f_2 and f_μ, the Lam-Bremhorst k-ε model maintains the High Reynolds-Number formulation and takes into account for the influence of molecular viscosity that is not negligible in wall regions, the normal velocity fluctuation damping exhered by a solid boundary and the presence of a nonisotropic contribution to the dissipation rate of turbulence that becomes dominant in the viscous layer. As both turbulence models don't use any wall functions, both require a very fine grid resolution of all viscous layers.

Finite Volume Method.

The finite volume approach in combination with a Runge-Kutta type multi-stage time-stepping scheme developed by Jameson et al. [4] is used for the numerical solution of the above equations. Applying the integral form of equation (4)

$$\frac{\partial}{\partial t}\int_S\int U dS + \int_{\partial S}(F dy - G dx) = 0 \tag{11}$$

to each cell of the computational domain separately where all physical properties are defined to be constant, the resulting system of ordinary differential equations in time are solved by the following multi-stage Runge-Kutta type time-stepping method:

$$\begin{aligned}
u^{(0)} &= u^{(n)} \\
u^{(1)} &= u^{(0)} - \alpha_1 P u^{(0)} \\
u^{(2)} &= u^{(0)} - \alpha_2 P u^{(1)} \\
u^{(3)} &= u^{(0)} - \alpha_3 P u^{(2)} \\
u^{(n)} &= u^{(0)} - \alpha_n P u^{(n-1)} \\
u^{(n+1)} &= u^{(n)}
\end{aligned} \tag{12}$$

with the coefficients

$$\alpha_1 = \alpha_2 = 0.6, \quad \alpha_3 = 1.0$$

for the three stage scheme and

$$\alpha_1 = \frac{1}{4}, \quad \alpha_2 = \frac{1}{6,} \quad \alpha_3 = \frac{3}{8}, \quad \alpha_4 = \frac{1}{3,} \quad \alpha_5 = 1.0$$

for the five stage scheme. n denotes the previous time-level and P represents a spatial (central and therefore second order) difference operator. The viscous terms are treated using central differences throughout the domain and one-sided formulas in the wall normal direction at solid surfaces.

Filtering Technique.

To prevent an odd-even decoupling, blended second and fourth order artificial dissipation [6] is used. If the filtering technique is applied only once, stability analysis indicates the best damping property as well as the largest extension of the stability region to the left of the real axis giving latitude in the introduction of dissipative terms. In practice, the fourth order filter is active throughout the computational domain except in areas with larger pressure gradients where the second order filter takes over. Filter fluxes through walls and/or symmetry lines are avoided. In order to minimize the numerical dissipation especially near walls, the dissipative fluxes in those regions are normalized by the ratio of the local Mach number to local isentropic Mach number.

Convergence Acceleration

Introducing the residual averaging approach [6] i.e. collecting the information from residuals implicitly, permits stable calculations beyond the ordinary Courant number limit of the explicit scheme. Furthermore, as long as the steady state is of interest, a variable timestep approach has been used accelerating convergence.

The most effective way of accelerating the convergence rate is furnished by the multigrid technique ([5] and [6]). The general idea behind any multigrid time stepping scheme is to transfere part of the task of tracking the evolution of the original system onto coarser grids by introducing a sequence of grid levels. During a multigrid cycle first the flow properties of the finer grids (index h) are collected onto the coarser grids (index 2h):

$$u_{2h}^{(0)} = \sum_{1}^{4} \frac{V_h \, u_h}{V_{2h}}$$

Then a forcing function

$$P_{2h} = \sum_{1}^{4} R_h(u_h) - R_{2h}(u_{2h}^{(0)})$$

is defined for each coarser grid level and this forcing function is included into the time stepping scheme for the coarser grids.

$$u_{2h}^{(1)} = u_{2h}^{(0)} - \alpha_1 \Delta t(R_{2h}^{(0)} + Ps$$

$$\ldots$$

$$u_{2h}^{(k+1)} = u_{2h}^{(0)} - \alpha_k \Delta t(R_{2h}^{(k)} + P_{2h})$$

The corrections of the coarser subgrids are then interpolated back to the finer grids by bilinear interpolation. Besides of the faster convergence rate of the coarser subgrids the computational effort per time step is dramatically reduced on the coarser grids. During the multigrid cycle, the coarser meshes are generated by elimination of alternate points in each direction. Therefore each cell on a given grid corresponds to a group of four cells on the next finer grid.

Additional reduction of computing time can be achhieved by a multilevel grid technique. The solution process begins in a coarse mesh. This solution then is interpolated to the next finer mesh up to the finest grid. In each of the different grids the multigrid strategy can be applied. At each switch to the next finer grid this grid can be adapted by the results of the previous coarser grid.

Block Structure

The computational space is devided into multiple blocks. During the solution process the flow field is stored on an external storage device and will be updated block wise. For each block a complete time step including the complete multigrid cycle is performed, then the updated data are stored back. At the block interfaces the blocks are overlapping by two cell rows so that the physical fluxes and the fourth order dissipative terms can be constructed correctly across the block boundaries. Across the block boundaries switches between coarse and fine grid resolutions and between the Euler and the Navier Stokes equations are possible. Each block always gets the actual boundary values of the neighbouring blocks.

Boundary Conditions.

The following boundary conditions are valid for all calculations:

At the *solid wall boundary* no-slip conditions are inplemented and the flow is assumed to be adiabatic

At the boundaries of the computational domain fixed and extrapolated Riemann invariants are introduced as *farfield conditions*. At an outflow situation the tangential velocity component and the entropy are extrapolated from the interior, while at an inflow boundary they are chosen to free stream values.

Results

The first test case was a laminar airfoil with a 30° deflected thick trailing edge flap. Figure 1 shows the computational grid. More details of the grid generation technique can be seen in Figure 2. It can be seen, that the singular point is placed in a region, where the flow can be expected inviscid, so that total pressure losses, which might be produced by the discontinuities in the curvature of the grid lines across this point, will not influence the viscous region along the flap. Figure 3 shows the predicted flow field for $Ma = 0.15$, $Re = 1.7 \times 10^6$ at an angle of attack of 12 °. This angle of attack has been found in the experiment to be shortly before the lift break down. As the airfoil is a laminar type airfoil, it tends to a leading edge separation. In the veloctiy field there seems to be a small separation bubble at the airfoil leading edge. The gradients of the pressure contours in Figure 4 also indicate a small separation bubble at the leading edge of the main airfoil. The development of the boundary layer is demonstrated by the total pressure loss contours in Figure 5. As it follows from this picture, the flow along the main airfoil seems to be shortly before separation, whereas the flow along the upper side of the flap is fully attached. Above a thin core flow along the upper side of the flap, there is a very large viscous region produced by the wake of the main airfoil. Figure 6 shows a comparison of flow field and pressure distribution for two different angles of attack. The angle of attack $\alpha = 14°$ was observed in the experiment to be completely separated. The same can be seen in the calculation: the flow along the upper side of the airfoil separates at the leading edge and by this there is a complete lift breakdown. At $\alpha = 12°$ the agreement between calculation and experiment is very good. Altough the pressure distribution for $\alpha = 14°$ looks very smooth, it is not a stable solution. The convergence behaviour, which is illustrated in Figure 7 for those two cases, shows that for the separated flow field the lift and the drag are oscillating, whereas for attached flows, they converge towards a constant value. The breakdown of the lift also can be seen in in the convergence history plot.

As the experimental results of the above test case are not very reliable, it is not a very suitable test case for a validation of the separation prediction of the method. Therefore the NLR 7301 generic airfoil with flap, of which the experimental results are documented in [7], was used as next test case. Figure 8 shows the computational grid. Compared with the first test case, the geometry is very smooth. The rather thin flap is deflected 20 °. Figure 9 gives a comparison of calculated and measured surface pressure distribution for two different angles of attack. In both cases the agreement is very good. In Figure 10 the mean velocity profiles at 4 different positions are depicted. The first one is exactly at the trailing edge position of the mean airfoil and shows the velocity profile of a strongly retarded flow. The other three plots show the mean velocity profiles along the flap surface at about 33%, 66% and 100% of the local flap chord. Due to the increase of pressure in that region, the wake of the main airfoil is further retarded and spreads up. Figure 11 finally shows the comparison of a computed and a measured c_l versus α curve for this configuration. The position of the lift breakdown as well as the maximum lift are predicted quite good. Of coarse there is a large disagreement between computed and measured lift in the separated region, as the computed lift coefficients are mean values of fluctuating values.

Figure 12 shows the computational grid around a realistic 3-element high lift system. Very fine C-type meshes are imbedded into coarser outer grids. Due to the hyperbolic grid generation technique in the inner regions, the grid lines are orthogonal along the surfaces, even in the concave regions of the slat and the main airfoil. The results of the flow computation for the Reynolds number Re = 1.90×10^6 and 12.2° angle of attack are presented in the Figures 13, 14 and 15. The pressure contours in Figure 13 indicate constant pressure at the trailing edge cove of the main airfoil, but considerable pressure variations in the slat cove. The total pressure loss contours in Figure 11 give an impression of the viscously dominated flow regions. Separation occurs in the coves of the slat and the main airfoil. Along the upper surface of the main airfoil there is a confluence of the wake of the slat and the boundary layer developing along the upper side of the airfoil. Above the flap, the flow field consists of the very thin boundary layer of the flap, followed by a region of an inviscid core flow, which is limited by the viscous region produced by the common wakes of the two preceeding components. At this configuration, it was found out, that an accurate discretization of the slat region is of great importance in order to obtain a proper solution. Total pressure losses which are produced by numerical effects (such as improper grid spacing) in that region, influence the further development of the slat wake and by this also the flow field along the upper side of the main airfoil and that of the flap. Finally Figure 15 presents the surface pressure distributions compared with the experimental data of ref. [8]. The agreement is very good, only at the slat and the main airfoil, the suction levels are not matched exactly by the calculation.

Conclusions

The presented grid generation technique renders the generation of block structured grids around multi-element aerofoils. The technique of embedded C-type meshes can be applied to high lift systems consisting of any number of elements. For a certain configuration, the method can be highly automated and the regeneration of a grid for modified flap or slat settings can be done very quickly. The results of the presented work are quite encouraging. They show, that even for realistic high lift configurations without any simplifications on the geometry, the prediction of the lift up to the maximum lift is possible. The correct prediction of the drag is much more difficult than that of the lift. As the drag is estimated by an integration of the surface skin friction and the surface pressure distribution, it is very sensitive to pressure fluctuations in regions with large "drag areas". Such regions are the slat and the main airfoil coves.

References

1. *J. L. Steger, D. Chaussee*
Generation of Body-Fitted Coordinates Using Hyperblic Partial Differential Equations
SIAM J. Sci. Stat. Comput. 1 (1980), 431-437

2. *T. J. Barth, T. H. Pulliam, P. G. Buning*
Navier-Stokes Computations for Exotic Airfoils
AIAA Paper AIAA-85-0109 1985

3. *W. Fritz*
Numerical Simulation of 2-D Turbulent Flow Fields with Strong Separation
ICAS Paper ICAS-88-4.6.4 1988 1988 Miami Beach, Florida, USA

4. *A. Jameson, W. Schmidt, E. Turkel*
Numerical Solution of the Euler Equations by Finite Volume Methods Using Runge-Kutta Time Stepping Schemes.
AIAA Paper 81-1259 1981

5. *A. Jameson*
Solution of the Euler Equations by a Multigrid Method.
Appl. Math. Comput., 13 1983, pp327 - 356 1983

6. *L. Martinelli, A. Jameson*
Validation of a Multigrid Method for the Reynolds Averaged Equations.
AIAA Paper 88-0414 1988

7. *B. van den Berg*
Boundary Layer Measurements on a Two-Dimensional Wing with Flap
NLR Bericht NLR TR 79009 U

8. *M. van Lent, L. R. Buning, P. B. Rohne*
High Lift Experiments on the GARTEUR AD (AG08) Two-Dimensional Model M3 in the NLR LST and HST Wind Tunnels
NLR Report NLR TR 89124 C 1989

Figures

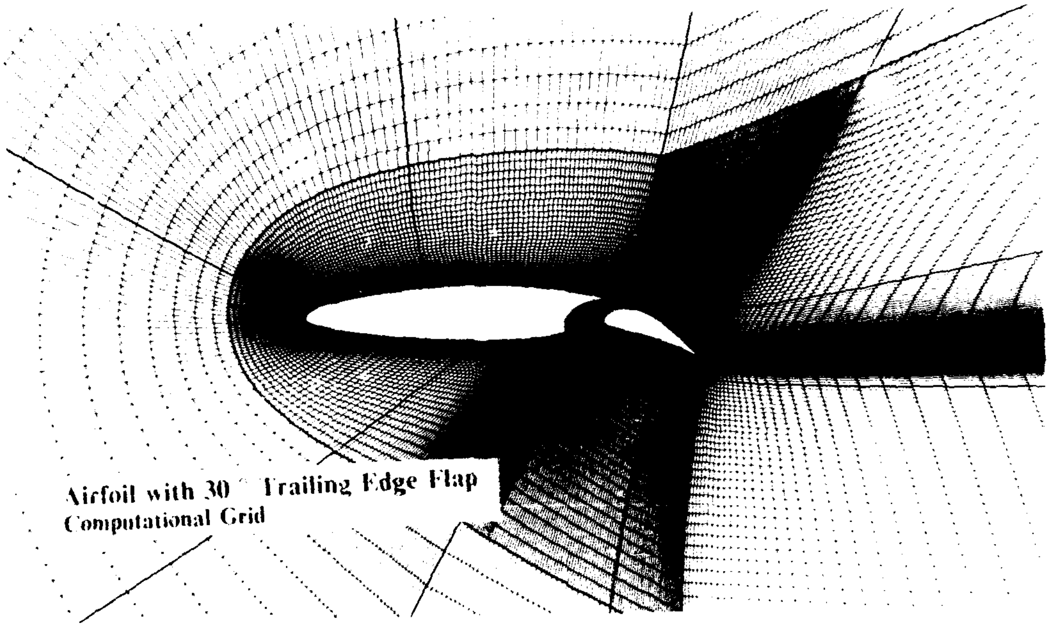

Fig. 1

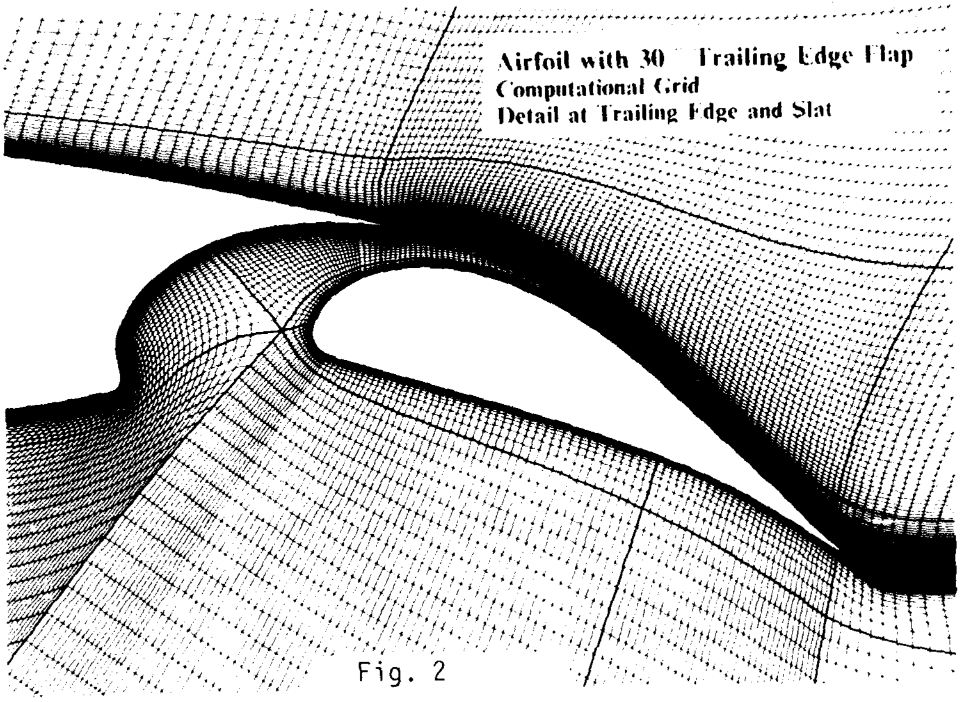

Fig. 2

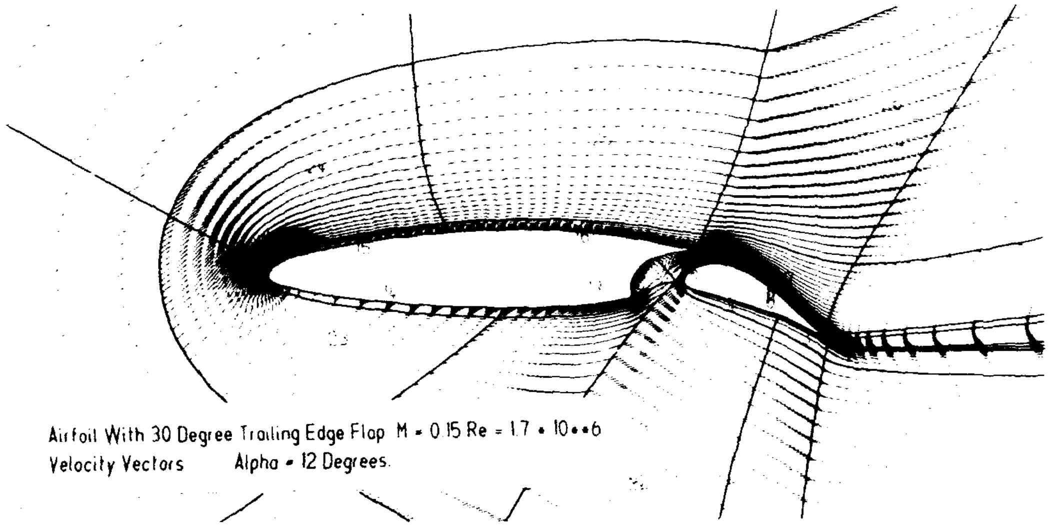

Airfoil With 30 Degree Trailing Edge Flap M = 0.15 Re = 1.7 * 10**6
Velocity Vectors Alpha = 12 Degrees.

Fig. 3

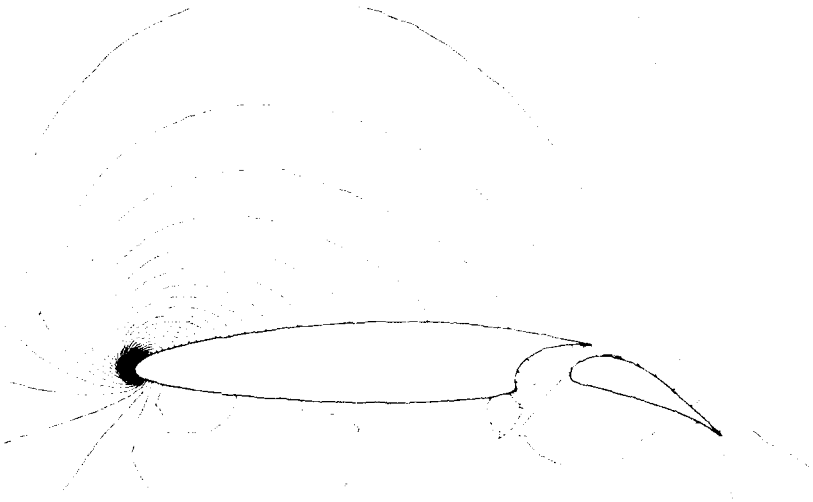

DO AL 3 FLAP = 30 DEG. GRID C RE = 2.51*10**6 M=0.200 AL. =12
PRESSURE CONTOURS (CP)

Fig. 4

Airfoil With 30 Degree Trailing Edge Flap M = 0.15 Re = 1.7*10**6
Total Pressure Loss Contours (1 - Pt/Pt0)

Fig. 5

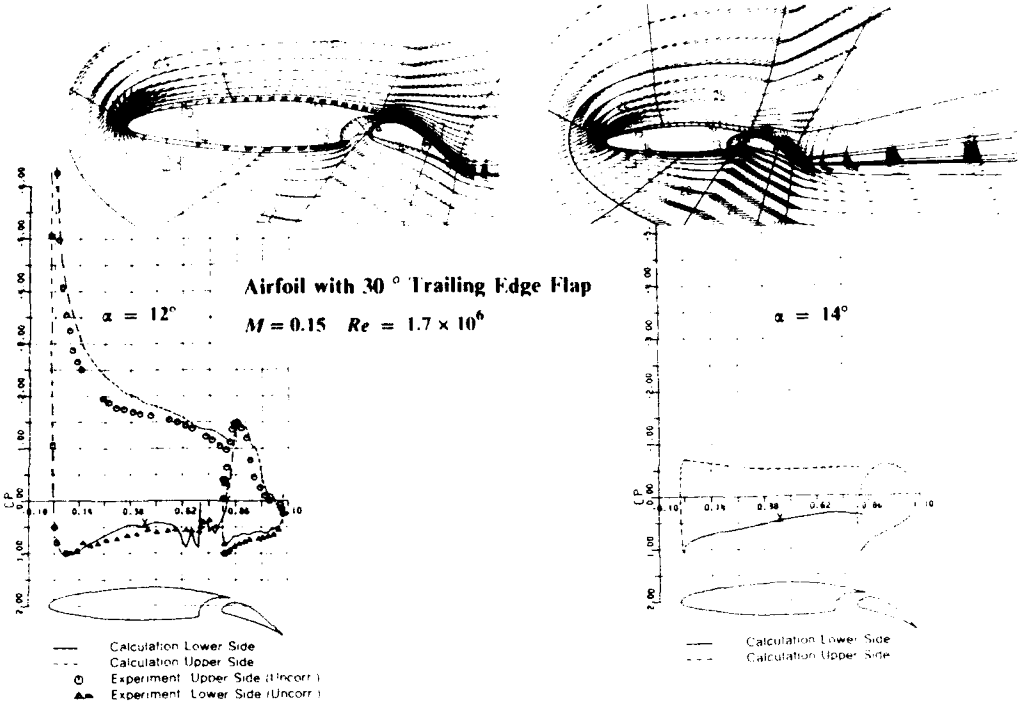

Airfoil with 30° Trailing Edge Flap

$M = 0.15 \quad Re = 1.7 \times 10^6$

Fig. 6

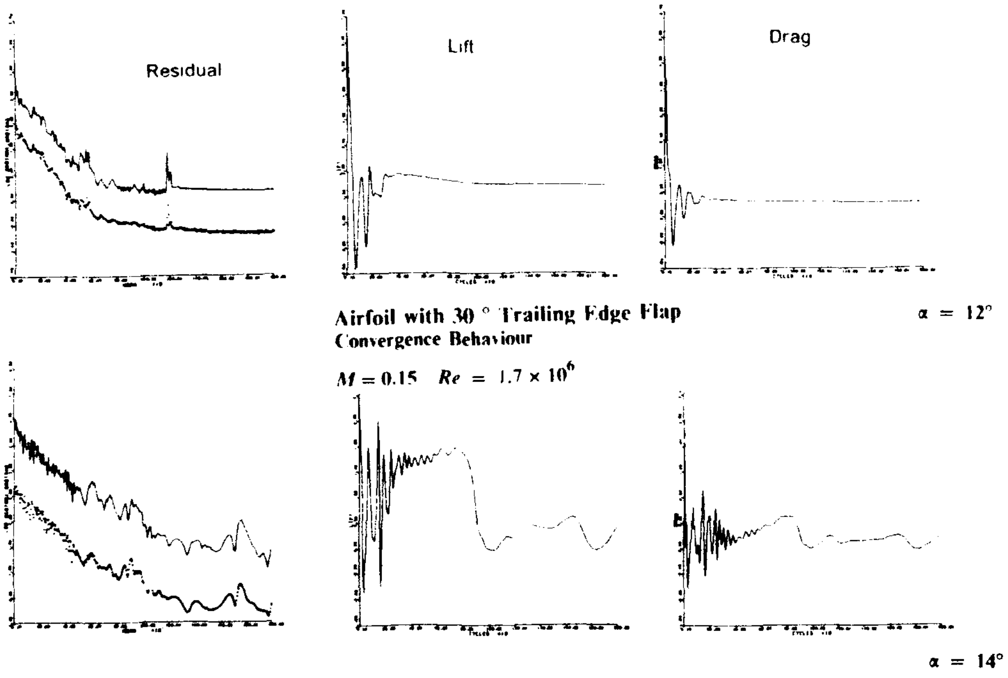

Airfoil with 30° Trailing Edge Flap
Convergence Behaviour

$M = 0.15 \quad Re = 1.7 \times 10^6$

Fig. 7

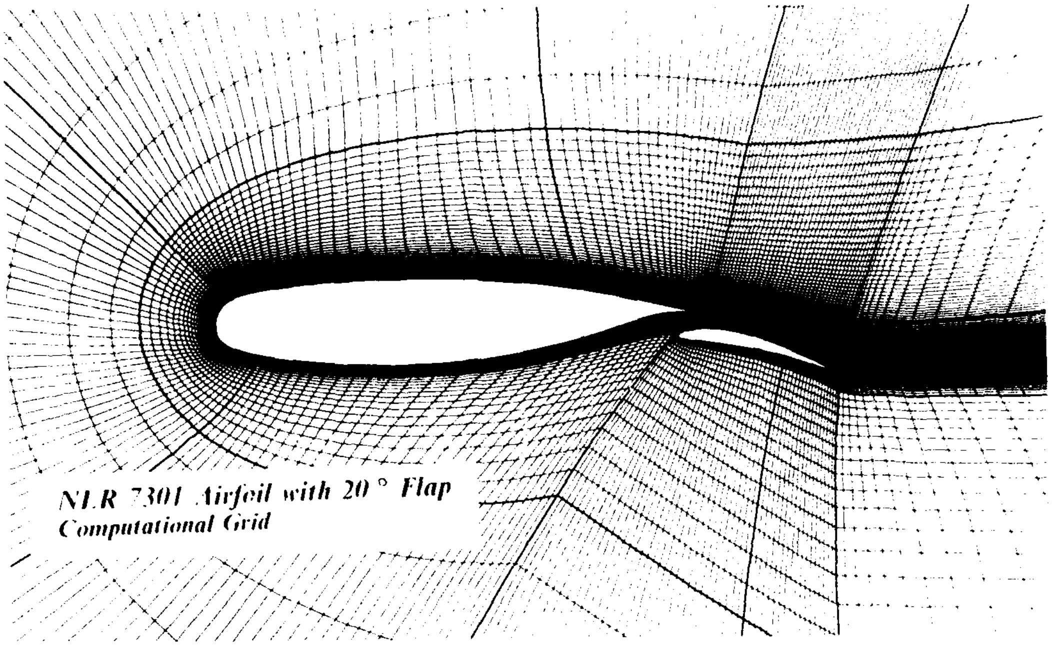
NLR 7301 Airfoil with 20 ° Flap
Computational Grid

Fig. 8

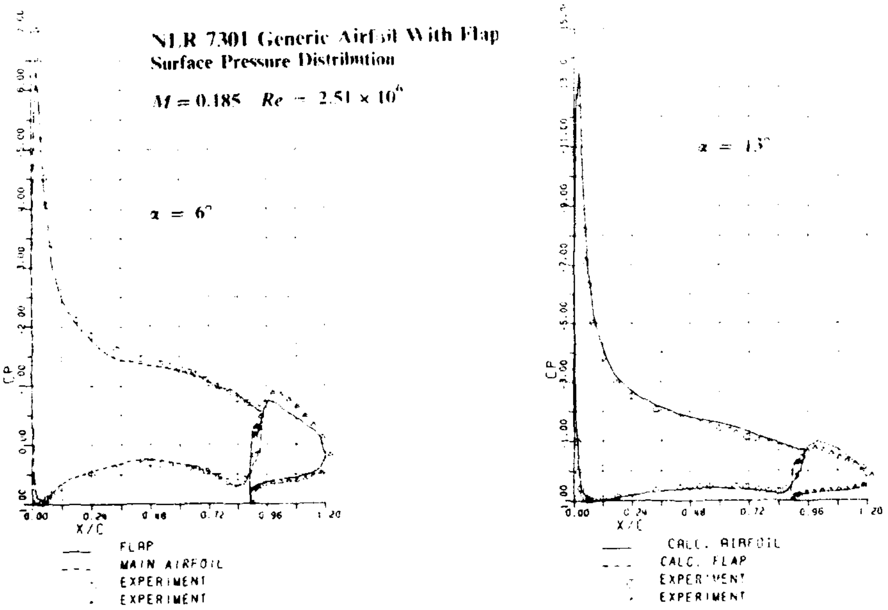
NLR 7301 Generic Airfoil With Flap
Surface Pressure Distribution
M = 0.185 Re = 2.51 × 10^6
α = 6°
α = 13°
CP
-6.00
-5.00
-4.00
-3.00
-2.00
-1.00
0.00
1.00
-11.00
-9.00
-7.00
-5.00
-3.00
-1.00
1.00
0.00
0.24
0.48
0.72
0.96
1.20
X/C
FLAP
MAIN AIRFOIL
EXPERIMENT
EXPERIMENT
CALC. AIRFOIL
CALC. FLAP
EXPERIMENT
EXPERIMENT

Fig. 9

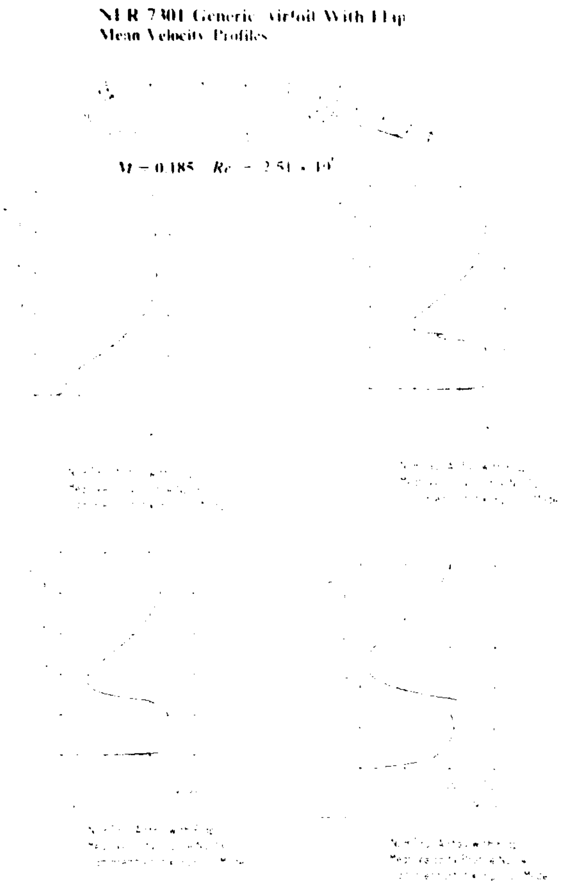

Fig. 10

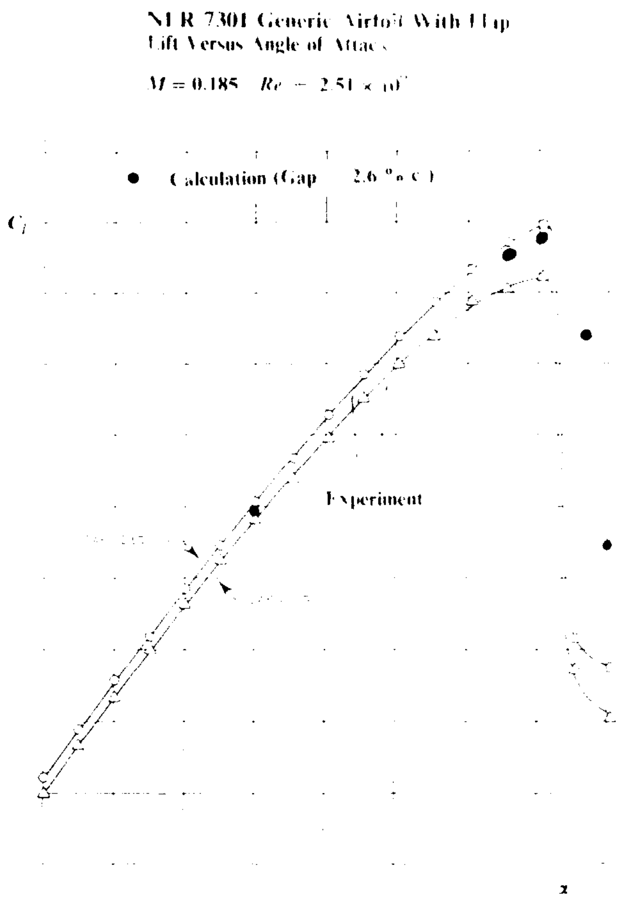

Fig. 11

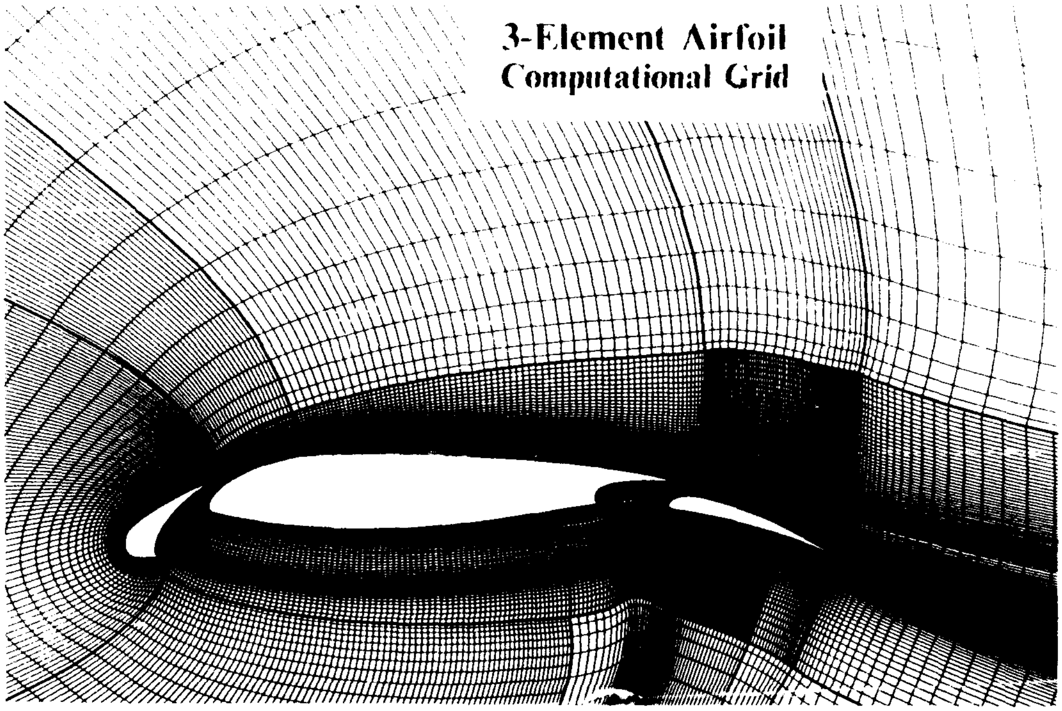

Fig. 12

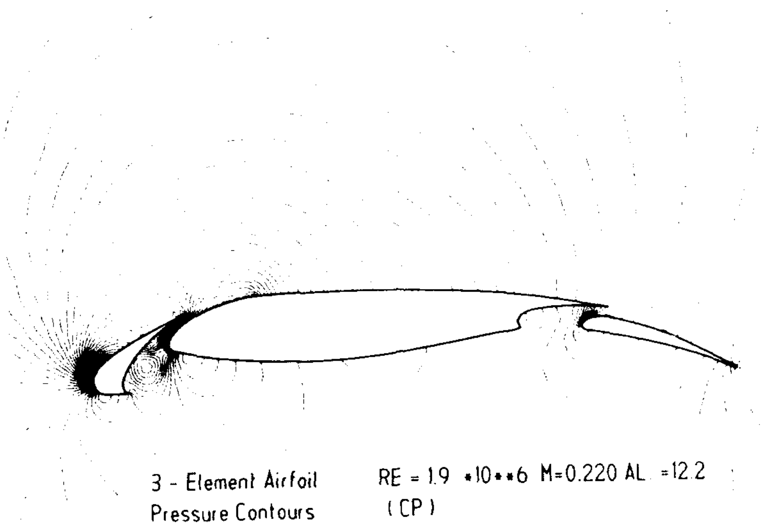

Fig. 13

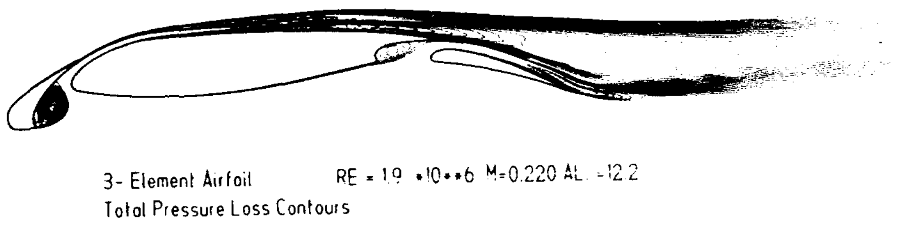

Fig. 14

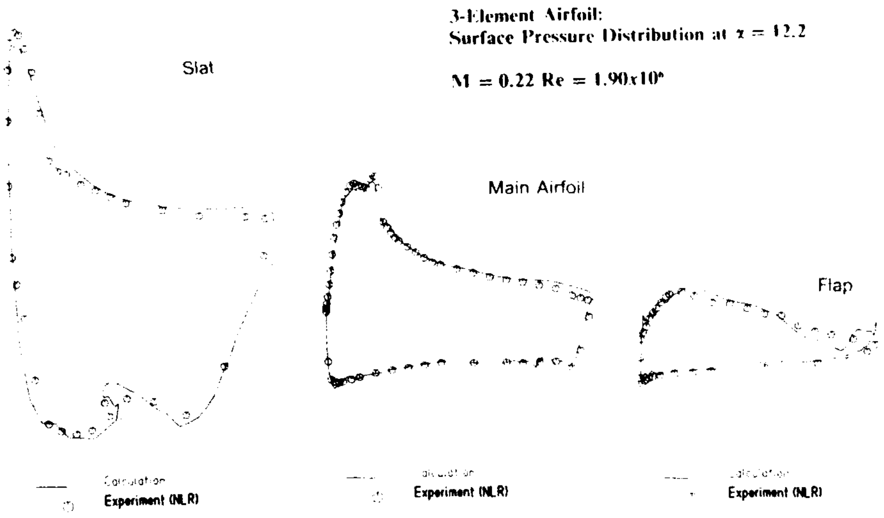

Fig. 15

Navier-Stokes Computations of Turbulent Flow Around High-Lift Configurations

P. Bartsch, W. Nitsche, M. Britsch

Institut für Luft- und Raumfahrt
Technische Universität Berlin
Marchstr. 12–14
D–1000 Berlin 10
Germany

1 SUMMARY

This paper presents Navier-Stokes calculations of the turbulent flow around two different high-lift configurations, for which experimental data exist. In the calculations, the flow field is considered as of steady-state and two-dimensional. Because of the low Mach numbers, the fluid is treated as incompressible. The solution procedure uses a finite volume method in order to solve the Reynolds-averaged Navier-Stokes equations. The effects of turbulence on the mean flow field are described by the k-ε turbulence model. The computational mesh is systematically refined in order to assess numerical solution errors.

The results presented in this paper include surface pressure distributions as well as mean velocities and turbulence quantities. If possible, the calculations are compared to experimental data.

2 INTRODUCTION

At present, the development of efficient high-lift configurations is mainly based on wind tunnel testing. However, as more and more powerful computers have become available, the 'numerical experiment' evolves as an increasingly helpful design tool.

The flow field around high-lift configurations has a very complex nature, e.g. flow separation may occur and viscous effects have to be taken into account. Hence, to resolve the steep variations of the dependent variables in a numerical calculation, many grid nodes are necessary, making the flow simulation rather expensive. In addition, due to the often complex geometry, numerical grid generation may also pose a problem. Because of these requirements, calculations of the complete three-dimensional flow field are beyond the scope of the present work. Hence, the two-dimensional Reynolds-averaged Navier-Stokes equations are solved in order to calculate the turbulent flow around multi-element airfoils. The standard k-ε turbulence model [1] is used to describe turbulence effects on the mean flow field. The aim of this work is to investigate the capabilities and restrictions of this approach when predicting the flow field around high-lift configurations.

The following sections outline the mathematical model as well as the numerical solution procedure used in the present calculations. The investigated high-lift configurations are introduced then, while results are presented in the next section. The paper is concluded with an outlook on to future work.

3 MATHEMATICAL MODEL

3.1 Mean Flow Equations

The mean flow field is considered as of steady-state, two-dimensional and incompressible. The time-averaged continuity and momentum equation read then

$$\frac{\partial(\rho U_j)}{\partial x_j} = 0 \tag{1}$$

$$\frac{\partial(\rho U_i U_j)}{\partial x_j} = -\frac{\partial P}{\partial x_i} + \frac{\partial}{\partial x_j}\left(\mu\frac{\partial U_i}{\partial x_j} - \rho\overline{u_i u_j}\right) \tag{2}$$

where U_j denotes the mean velocities and u_j the corresponding fluctuating velocities in the x_j-directions. P stands for mean static pressure and μ and ρ for viscosity and density of the fluid, respectively. An overbar indicates time averaging.

3.2 Turbulence Model

The standard k-ε model [1] is used in order to relate the Reynolds stresses $-\rho\overline{u_i u_j}$ in Eq. (2) to mean flow quantities:

$$-\rho\overline{u_i u_j} = \mu_t\left(\frac{\partial U_i}{\partial x_j} + \frac{\partial U_j}{\partial x_i}\right) + \frac{2}{3}\rho\delta_{ij}k \tag{3}$$

The eddy viscosity μ_t is given by:

$$\mu_t = \rho c_\mu \frac{k^2}{\varepsilon} \tag{4}$$

The local distributions of the turbulent kinetic energy k and the dissipation rate ε are derived from semi-empirical transport equations:

$$\frac{\partial(\rho U_j k)}{\partial x_j} = \frac{\partial}{\partial x_j}\left(\frac{\mu_t}{\sigma_k}\frac{\partial k}{\partial x_j}\right) + P_k - \rho\varepsilon \tag{5}$$

$$\frac{\partial(\rho U_j \varepsilon)}{\partial x_j} = \frac{\partial}{\partial x_j}\left(\frac{\mu_t}{\sigma_\varepsilon}\frac{\partial \varepsilon}{\partial x_j}\right) + \frac{\varepsilon}{k}\left(c_{\varepsilon_1} P_k - \rho c_{\varepsilon_2}\varepsilon\right) \tag{6}$$

with P_k being the production rate of k:

$$P_k = -\rho\overline{u_i u_j}\frac{\partial U_i}{\partial x_j} \tag{7}$$

The model constants appearing in Eq. (4–6) have their standard values as proposed by Launder and Spalding [1]:

$$\{c_\mu, c_{\varepsilon_1}, c_{\varepsilon_2}, \sigma_k, \sigma_\varepsilon\} = \{0.09, 1.44, 1.92, 1.0, 1.3\}$$

3.3 Boundary Conditions

Because of the elliptic character of the transport equations, boundary conditions are necessary along all boundaries of the flow domain.

Inlet At the inlet plane, the values for the mean streamwise velocity U and the turbulent kinetic energy k are prescribed using experimental data. In cases where k is not available from experiments, the following relation is used:

$$k = \frac{2}{3}Tu^2U^2 \tag{8}$$

with Tu being the turbulence level. The mean cross-stream velocity V is set to zero. The dissipation rate ε along the inlet plane is derived from:

$$\varepsilon = \frac{k^{3/2}}{L} \tag{9}$$

where L represents a typical turbulence length scale of the energy-containing eddies.

Outlet The streamwise gradients of all dependent variables are set to zero along the exit plane.

Walls Instead of resolving the steep gradients in the vicinity of a wall, a wall function approach [1] is used to describe the fluxes through the wall-adjacent control volumes. In the present calculations, the logarithmic law is employed.

4 NUMERICAL SOLUTION PROCEDURE

The numerical solution procedure is based on a conservative finite volume method. In this approach, it is not the transport equation itself which is approximated but a flux balance derived from a formal integration of the transport equations over a control volume. The present procedure employs a general non-orthogonal grid and Cartesian velocity components. All dependent variables are stored in the centre of the control volumes ('colocated arrangement'). Central differences are used to discretize the diffusive fluxes, whereas the convective fluxes are approximated by a combination of upwind and central differences. The coefficients are arranged in the 'deferred correction' scheme as proposed by Khosla and Rubin [2]. The resulting system of linear equations is solved by means of the strongly implicit method of Stone [3], based on an incomplete LU factorisation. When calculating incompressible fluids, there is no explicit equation for pressure. Instead, pressure and velocities are linked via the SIMPLE algorithm of Patankar and Spalding [4]. Due to the colocated variable arrangement, unphysical oscillatory pressure fields have to be suppressed by using a special interpolation practice for the cell face velocities, see [5].

		TC1	TC2
chord length [m]	slat c_S	0.12	—
	wing c	0.60	0.90
	flap c_F	0.21	0.36
angle of attack α		0°–16°	8.2°
flap deflection	δ_S	21°	—
	δ_F	15°	21.8°
Reynolds number Re		1.6×10^6	1.8×10^6

Table 1: Characteristics of the configurations

Underrelaxation has to be employed for achieving convergence of the iterative solution procedure. Typically, the relaxation factors are set to 0.7 for velocities and 0.1 . . . 0.3 for pressure depending on the grid size. Relaxation factors for k and ε are set to 0.1 and 0.7, respectively. Convergence is declared when the maximum normalized residual drops below a given limit, which is set to 0.001 in the present calculations.

5 TEST CONFIGURATIONS

The high-lift configurations investigated in this work are shown in Fig. 1. Throughout this paper, they will be referred to as TC1 and TC2, respectively. TC1 comprises a leading edge flap ('slat'), the main airfoil and a trailing edge flap ('fowler'). TC2 consists of a NACA 4412 main airfoil and a NACA 4415 flap airfoil. Some characteristics of the configurations (such as chord length, flap angles etc.) are summarized in Table 1. For both configurations, experimental data are available [6, 7]. However, TC1, as used in the present calculations, differs slightly from the wind tunnel model. In the available geometry data, slat and main airfoil are 'smoothed out' in order to allow a parabolic flow solver to be applied to this configuration. The Reynolds number based on chord length and inlet velocity is $Re = 1.6 \times 10^6$ in the case of TC1. The angle of attack is varied from $\alpha = 0°$ to $16°$ in increments of 2°. Both, free stream and wind tunnel conditions are simulated numerically. In case of TC2, the Reynolds number is $Re = 1.8 \times 10^6$. The flap deflection angle is set to $\delta_F = 21.8°$, as in the experiments.

6 Grid Generation

In order to obtain satisfactory numerical grids, the flow field is divided into several subdomains, as shown in Fig. 2 for TC1. For each subdomain, an H-type grid is created and then all subgrids are connected. Because of this approach, it is not possible to assure smooth transition from one subgrid to an other with respect to mesh size and aspect ratio in all cases. Fig. 3 shows the resulting numerical grids for both configurations.

7 RESULTS

7.1 Results for TC1

Fig. 4 shows streamlines of the turbulent flow around the configuration at different angles of attack ($\alpha = 4°, 8°, 12°$ and $16°$). The separation bubble behind the slat becomes smaller with increasing angle and finally vanishes completely. No separation is found on the upper side of the fowler flap. The flow field on the rear of the slat and through the gap between slat and main airfoil is shown in Fig. 5. It depicts velocity vectors (Fig. 5a) as well as profiles of the streamwise velocity U (Fig. 5b). The angle of attack is $\alpha = 16°$ for this case. The reverse flow near the leading edge of the main airfoil indicates the location of the stagnation point on the lower side of the wing.

Both, free stream and wind tunnel conditions were investigated when calculating the flow around this configuration. The influence of the walls can be seen in Fig. 6, which shows pressure coefficient distributions $c_p = (P - P_\infty)/(0.5\rho U_\infty^2)$ in comparison with experiments for both test cases. In Fig. 6a, free stream conditions are used as boundary condition, while Fig. 6b shows the distribution derived from simulating wind tunnel conditions. In general, a better agreement between calculation and experiment is found in the latter case. The c_p-distributions around the main airfoil as well as the fowler flap compare quite favourably with experimental data. The deviations at the upper side of the slat and near the leading edge of the main airfoil are mainly due to an insufficient grid resolution in these regions. Nevertheless, measurements and computations compare quite well. However, it must be noted that the shape of the lower side of the slat, as used in the calculations, differs from the original geometry as already mentioned in Section 5.

7.2 Results for TC2

Despite the apparently simpler geometry, the second configuration turned out to be a computationally more difficult test case. According to experiments [7], the flow remains attached on the main airfoil, whereas a small separated region exists near the trailing edge of the flap. The flow over the flap is characterized by strong wake/boundary-layer interactions.

Fig. 7 shows pressure coefficient distributions for this configuration. Results obtained with an upwind (UDS, dashed line) and a central differencing scheme (CDS, solid line) are compared to experimental data. The very strong suction peak at the leading edge of the wing is not captured by the calculations. As a consequence, the pressure remains too high throughout the suction side up to the trailing edge of the main airfoil. The numerical result compares quite favourably to experiments on the pressure side. More severe deviations are found on the flap airfoil. Again, the suction peak is computed too small. No separation is predicted at the trailing edge, which is in contradiction to experimental data. As for the main airfoil, better agreement between calculation and experimental data is found on the lower side of the flap. Furtheron, the influence of the approximation scheme on the numerical results is evident from this figure. Only a small improvement of the computed c_p-distribution is found on the main airfoil. However, on the flap the CDS results agree much better with experiments than the UDS results, except near the flap trailing edge. An overall view of the flow domain is presented in Fig. 8. It shows calculated profiles of the U velocity. The influence of the configuration on the upstream flow field can be deduced from this figure. In addition, the jet emanating from the gap between main airfoil and flap as well as the development of the wake can bee seen. A more detailed view of the flow field shortly behind the flap is given in Fig. 9. It shows distributions of U at two locations ($x/c = 1.322$ and 1.558) downstream of the flap in comparison with experiments. Again, results obtained with UDS and CDS are plotted. As is to be expected, the gradients become steeper when using the central differencing scheme because it does not introduce 'numerical diffusion' as is the case with the upwind differencing scheme. As a consequence, the computed spreading rate of the wake becomes smaller, which leads to a much better agreement of the distributions with measurements, see Fig. 9a. Nevertheless, the 'gap-jet' is still predicted too weak and the upper mixing layer profile which stems from the main airfoil boundary layer is not captured correctly, see Fig. 9a. Calculated as well as measured distributions of the Reynolds shear stress $-\overline{uv}$ are given in Fig. 10. In general the computed profiles agree reasonably well with the experimental data. The minima and maxima locations of the calculated distributions correspond with the positions of the points of inflection in the mean velocity profiles, see Fig. 9, as to be expected because of the production rate term of the turbulent kinetic energy in the k-ϵ turbulence model.

7.3 Error estimation

In order to assess the numerical solution error, all calculations are performed on different grids, which are refined in a consistent manner. Each coarse grid control volume is divided into four fine grid control volumes, thus doubling the number of elements in each direction. The applied error estimation method is based on Richardson extrapolation, see Caruso et al. [8]. Assuming that the numerical error can be expressed as a Taylor series, the error ϵ_h on a mesh with size h becomes for a discretisation scheme with first order truncation error:

$$\epsilon_h = \Phi_h - \Phi = \Delta h \frac{\partial \Phi}{\partial h} + \mathcal{O}(h^2) \qquad (10)$$

where Φ denotes the exact solution and Φ_h the numerical solution. On the coarser grid (with mesh size $2h$), the error reads:

$$\epsilon_{2h} = \Phi_{2h} - \Phi = 2\Delta h \frac{\partial \Phi}{\partial h} + \mathcal{O}(h^2) \qquad (11)$$

Subtraction of Eq. (11) from Eq. (10) gives an approximation of the numerical error on the fine grid:

$$\Phi_{2h} - \Phi_h = \Delta h \frac{\partial \Phi}{\partial h} \approx \epsilon_h + \mathcal{O}(h^2) \qquad (12)$$

Fig. 11 shows as an example the solution error derived from Eq. (12) for the streamwise velocity U and static pressure P. In the case of the streamwise velocity (Fig. 11a), the error is well below 5% except for a small region near the slat. In the case of the static pressure (Fig. 11b) the error amounts to about 10% near the slat with a maximum of up to 25% in a very small region. Therefore, with an even finer grid, better resolution of the strong suction peaks in these regions can be expected.

8 CONCLUSION AND OUTLOOK

The results presented in this paper clearly show the capabilities as well as some restrictions of Navier-Stokes computations using k-ε turbulence modelling to predict flow around high-lift configurations. In general, good agreement with experimental data is found for the two different 2D-configurations investigated in this work. However, when considering the details of the flow field, some deviations between calculations and measurements are found. When discussing results such as these, numerical solution errors have to be separated carefully from deficiencies of the applied turbulence model.

In order to improve the reliability of Navier-Stokes codes for calculating the flow around high-lift configurations, first of all, more detailed experimental data must be available. This includes mean flow as well as turbulence quantities, such as fluctuating velocities and pressure and distributions of turbulent kinetic energy and Reynolds stresses. Based on these data, further numerical investigations have to be performed in order to facilitate the selection of an appropriate turbulence model for numerical simulations of high-lift flows.

References

[1] Launder, B.E., Spalding, D.B., 'The Numerical Computation of Turbulent Flow', *Comp. Meth. Appl. Mech. and Eng.*, Vol. 3, pp. 269–289, 1974

[2] Khosla, P.K., Rubin, S.G., 'A Diagonally Dominant Second-Order Accurate Implicit Scheme', *Computers and Fluids*, Vol. 2, pp. 207–209, 1972

[3] Stone, H.L., 'Iterative Solution of Implicit Approximations of Multi-Dimensional Partial Differential Equations', *SIAM J. Num. Anal.*, Vol. 5, pp. 530–558, 1968

[4] Patankar, S.V., Spalding, D.B., 'A Calculation Procedure for Heat, Mass and Momentum Transfer in Three-Dimensional Parabolic Flows', *Int. J. Heat Mass Transfer*, Vol. 15, pp. 1787–1806, 1972

[5] M. Perić, R. Kessler and G. Scheuerer, 'Comparison of Finite-Volume Numerical Methods with Staggered and Colocated Grids', *Computers & Fluids*, Vol. 16, No. 4, pp. 389–403, 1988

[6] Szodruch, J., Kotschote, J., 'Grenzschichtmessungen an einem Transsonikprofil im MBB-LSWT', Ergebnisbericht Nr. 36, MBB GmbH., 1983

[7] Adair, D., Horne, C., 'Turbulent separated flow over and downstream of a two-element airfoil', *Experiments in Fluids*, Vol. 7, pp. 531–541, 1989

[8] Caruso, S.C., Ferziger, J.H., Oliger, J., 'Adaptive Grid Techniques for Elliptic Flow Problems', Rept. No. TF-23, Thermosc. Div., Stanford University, 1985

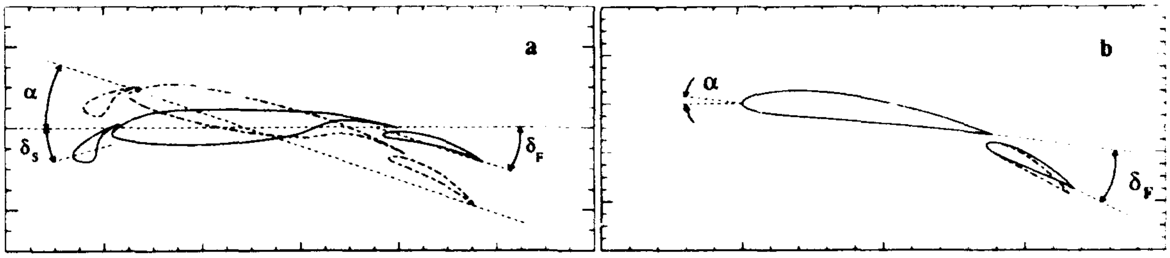

Figure 1: Test Configurations: a) TC1 b) TC2

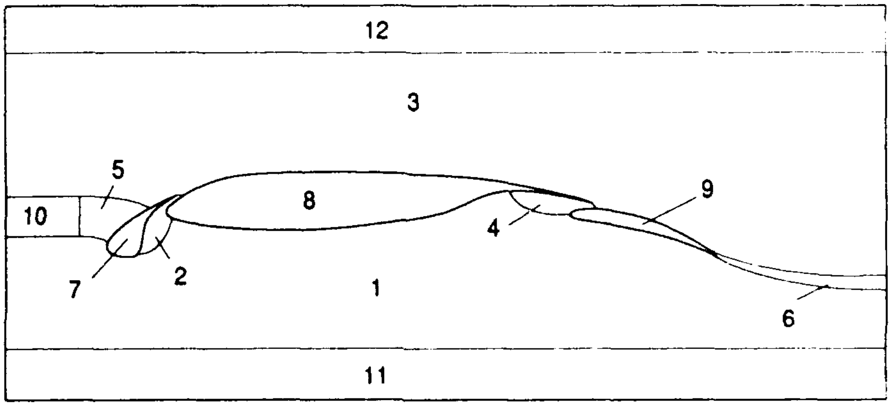

Figure 2: Subdomains for grid generation (TC1)

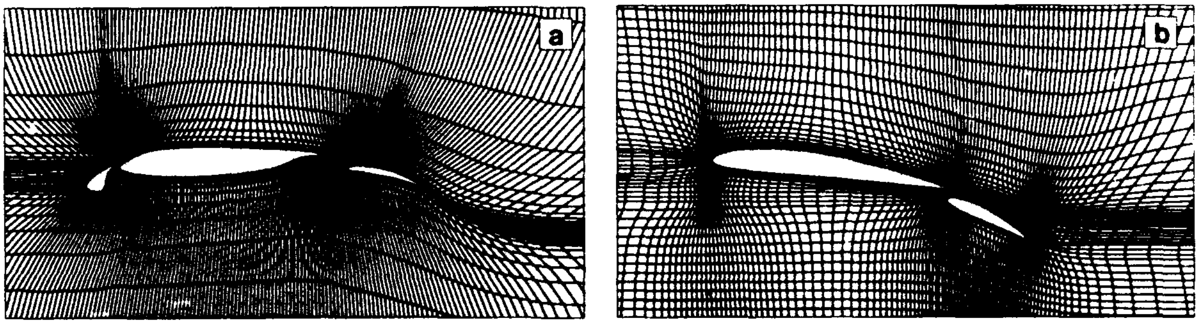

Figure 3: Numerical grids (grid lines omitted for clarity) a) TC1 b) TC2

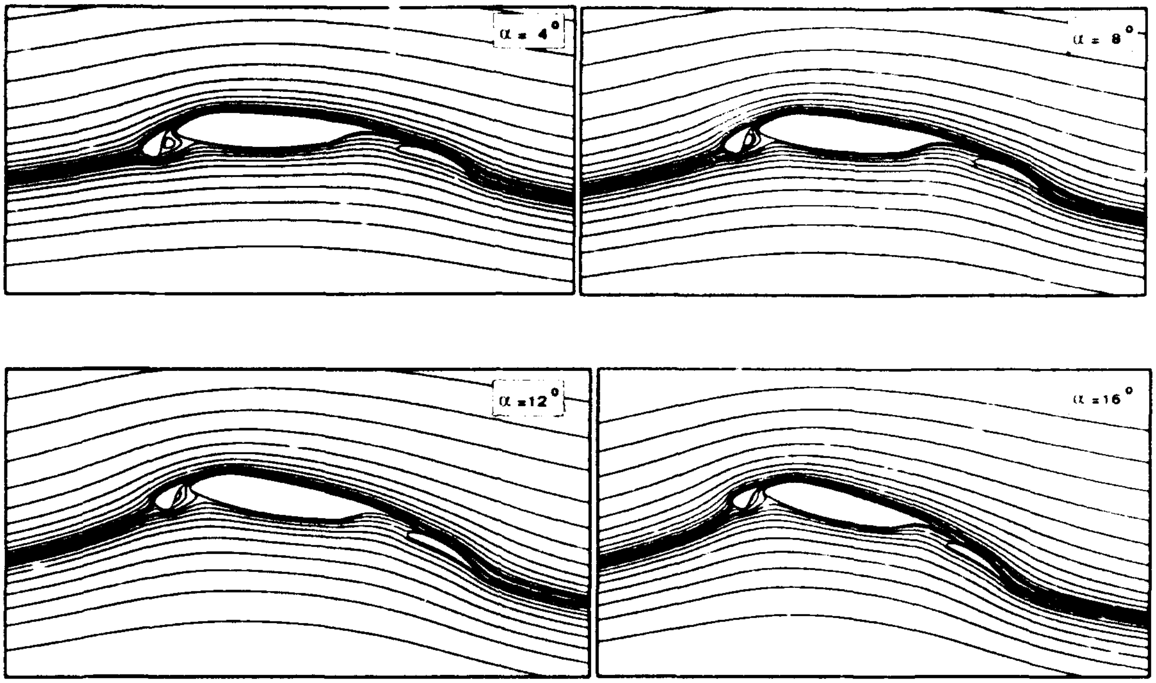

Figure 4 Computed streamlines (TC1)

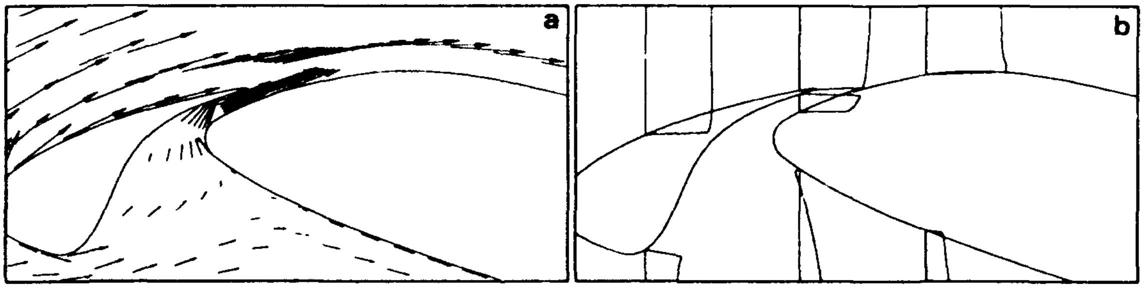

Figure 5: Computed flow field between slat and main airfoil (TC1)

a) Velocity vectors
b) Profiles of the streamwise velocity U

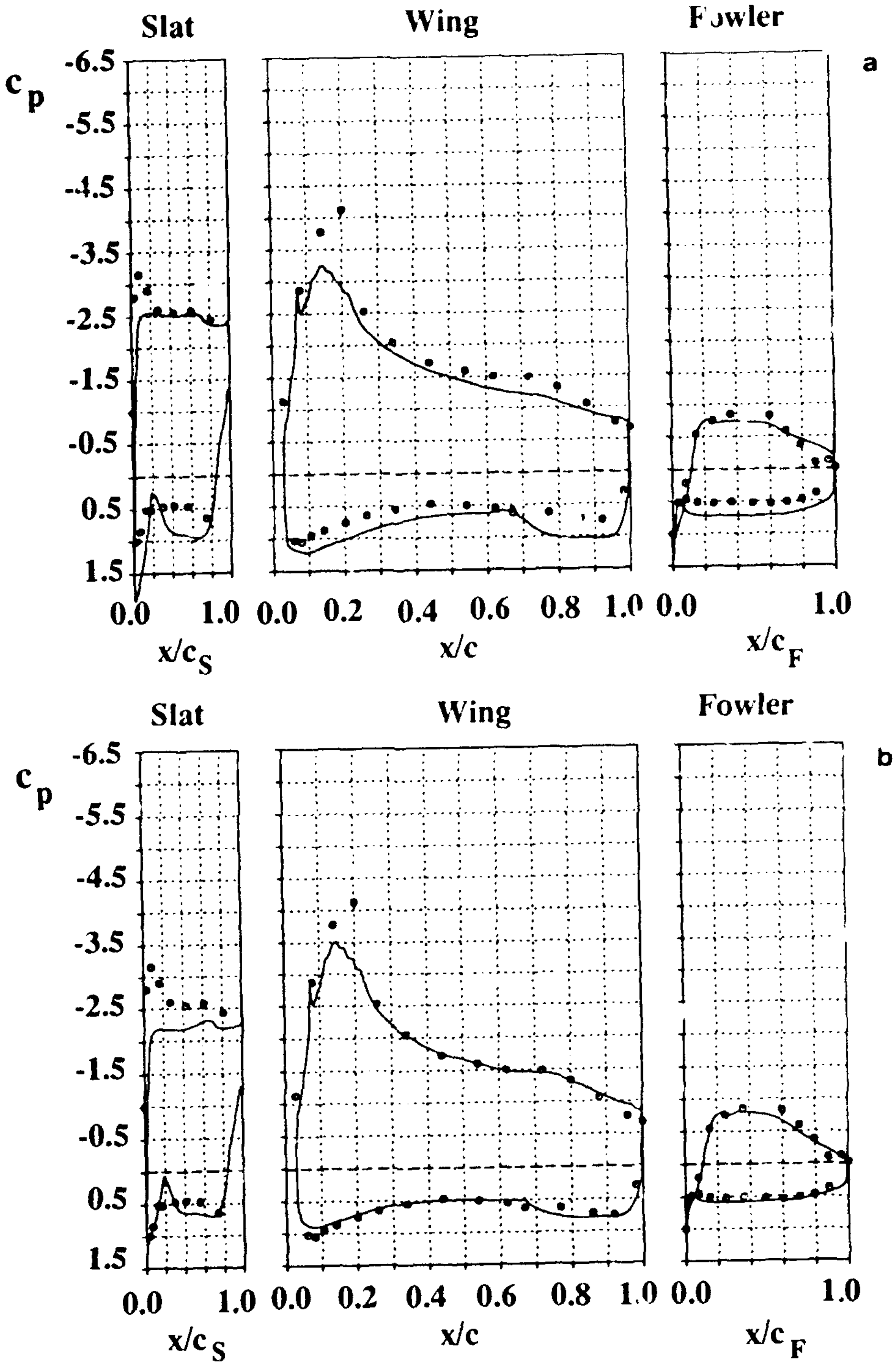

Figure 6: Surface pressure distributions (TC1) ◇ Experiments [6], —— present calculations

a) free stream conditions
b) wind tunnel conditions

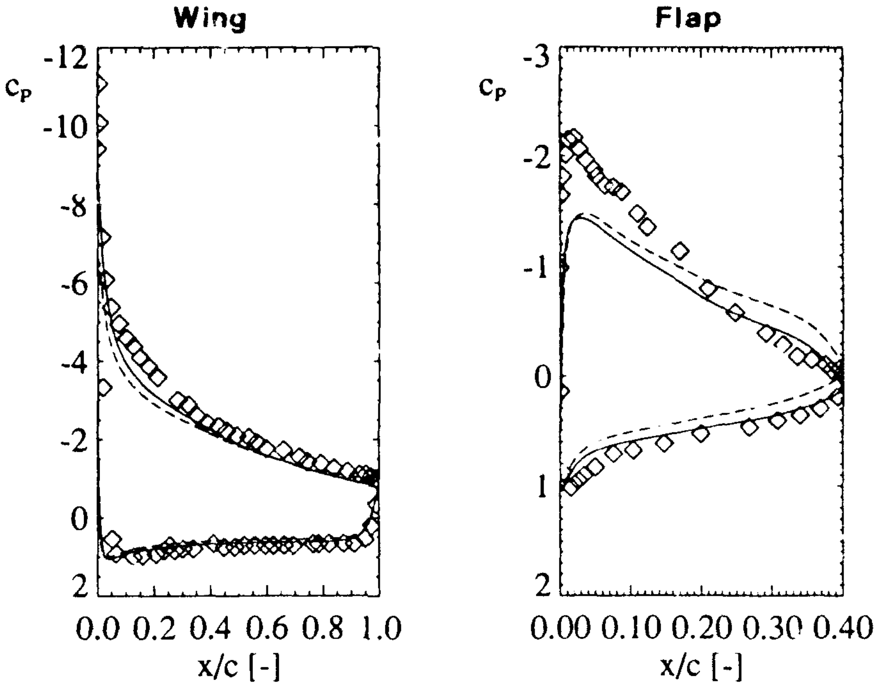

Figure 7: Pressure coefficient distribution (TC2)
◇ Experiments [7], - - - - - (UDS) —— (CDS) present calculations

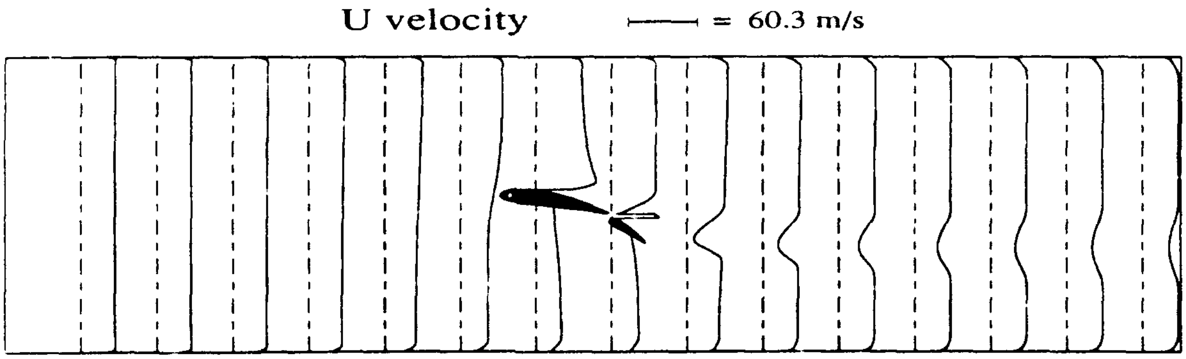

Figure 8: Computed profiles of mean streamwise velocity U (TC2)

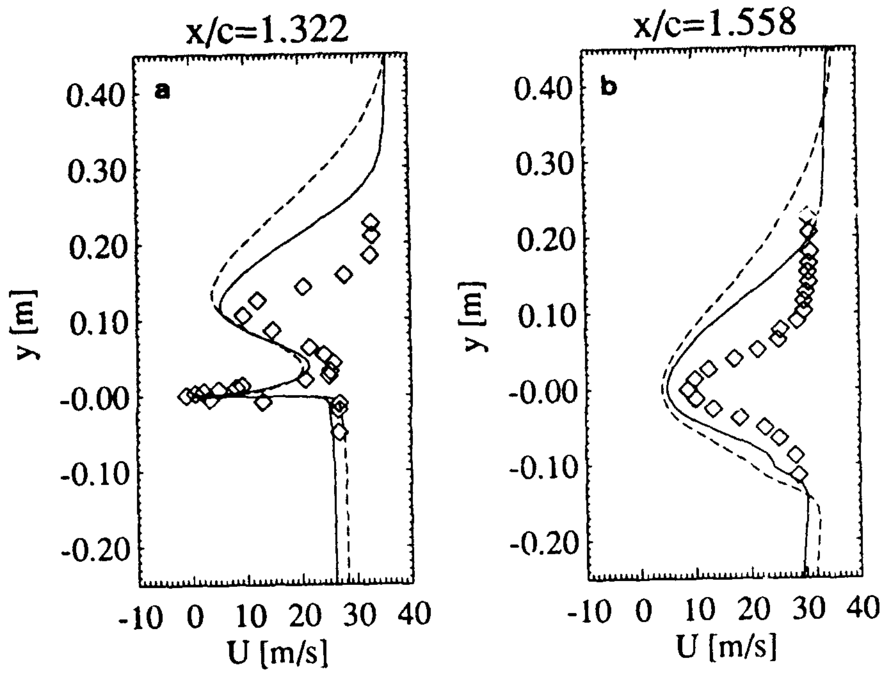

Figure 9: Mean streamwise velocity profiles at two locations downstream of the flap (TC2)
◇ Experiments [7], - - - - - (UDS) —— (CDS) present calculations

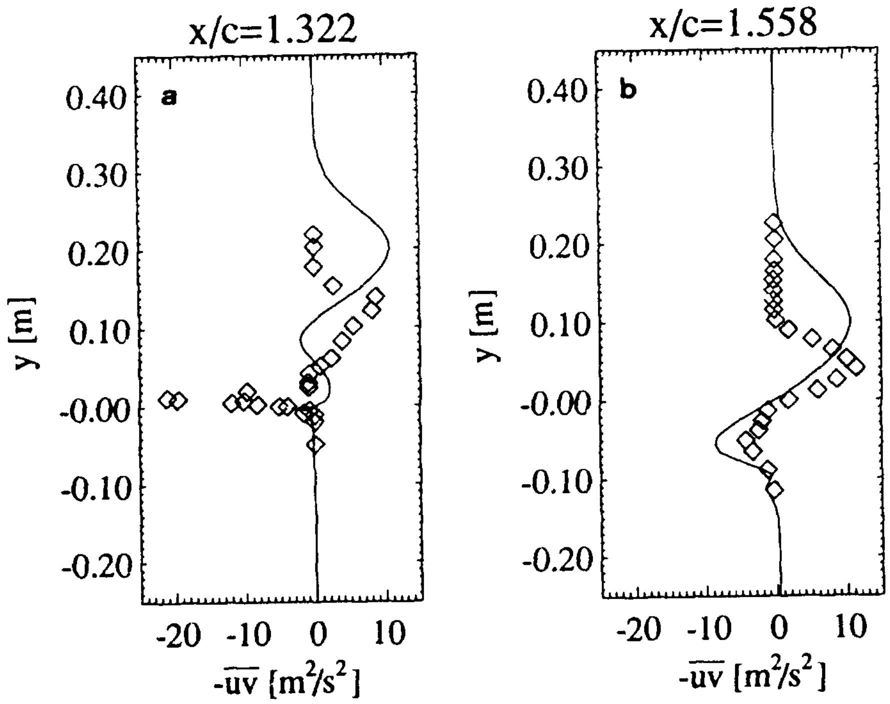

Figure 10: Reynolds shear stress profiles at two locations downstream of the flap (TC2)
◇ Experiments [7], —— present calculations

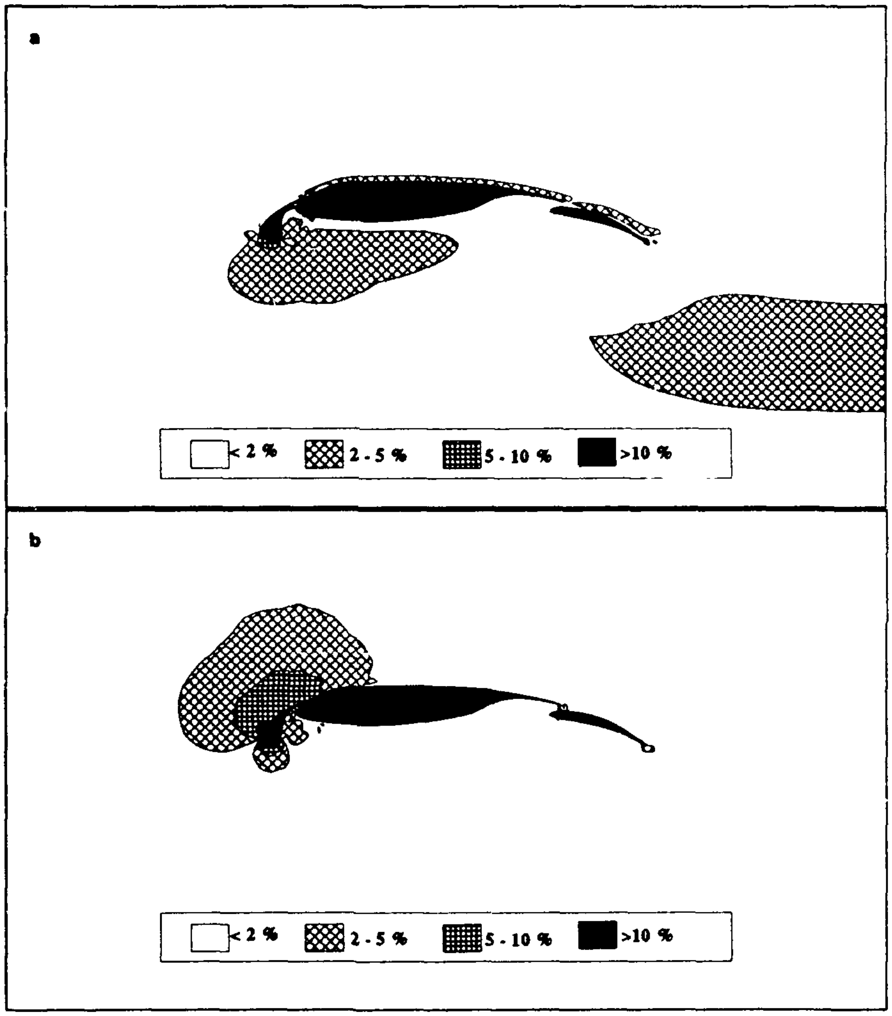

Figure 11: Numerical solution error (TC1)

a) Streamwise velocity U
b) Static pressure P

EFFICIENT SIMULATION OF INCOMPRESSIBLE VISCOUS FLOW OVER MULTI-ELEMENT AIRFOILS

Stuart E. Rogers
N. Lyn Wiltberger
Dochan Kwak
NASA Ames Research Center
Mail Stop 258-1
Moffett Field, CA 94035-1000
USA

1. SUMMARY

The incompressible, viscous, turbulent flow over single and multi-element airfoils is numerically simulated in an efficient manner by solving the incompressible Navier-Stokes equations. The solution algorithm employs the method of pseudocompressibility and utilizes an upwind-differencing scheme for the convective fluxes, and an implicit line-relaxation scheme. The motivation for this work includes interest in studying high-lift take-off and landing configurations of various aircraft. In particular, accurate computation of lift and drag at various angles of attack up to stall is desired. Two different turbulence models are tested in computing the flow over an NACA 4412 airfoil; an accurate prediction of stall is obtained. The approach used for multi-element airfoils involves the use of multiple zones of structured grids fitted to each element. Two different approaches are compared; a patched system of grids, and an overlaid Chimera system of grids. Computational results are presented for two-element, three-element, and four-element airfoil configurations. Excellent agreement with experimental surface pressure coefficients is seen. The code converges in less than 200 iterations, requiring on the order of one minute of CPU time on a CRAY YMP per element in the airfoil configuration.

2. INTRODUCTION

An increased understanding of high-lift systems will play an important role in designing the next generation of transport aircraft. Current designs for such aircraft typically involve multiple elements, such as leading edge slats and multiple-slotted flaps. The current trend is toward a more efficient, yet simpler design which will lead to reduced manufacturing and maintenance costs. At the same time, increases in lift coefficients for a given angle of attack and increases in maximum lift coefficient will lead to a larger payload capability. Improved designs will also allow for reduced noise in areas surrounding airports. Understanding of high-lift flow physics harbors the potential to improve airport capacity through a reduction of an airplane's wake vortices, allowing closer spacing between subsequent airplanes taking off and landing.

Increased knowledge of the flow physics involved with high-lift systems is therefore of greater interest than ever before as the need to improve over current designs becomes acute. Study of these configurations will require both computational and experimental efforts. Computational fluid dynamics (CFD) is playing a large role in this work. Multi-element configurations present a number of challenging problems to the numerical investigators. These include problems involving turbulent boundary layer separation, confluent boundary layers and wakes, Reynolds number effects, three-dimensional effects, compressibility effects, transition, and complex geometries. Although the problems are inherently three-dimensional, there is still much to be learned about the flow physics by studying two-dimensional models.

The computational tools available range from the more efficient and simpler inviscid/viscous coupled methods, to a Reynolds-averaged Navier-Stokes (RANS) analysis. An example of the former method is given by Kusunose et al.[1] They use a full potential method coupled with an integral boundary-layer method. These methods have been found to be successful in accurately computing the pressure distribution for multi-element airfoils, including cases up to maximum lift, some of which involve separation. The coupled method has been proven to be useful as an effective engineering design tool. This method is limited by its inability to compute beyond maximum lift conditions, and may have problems with certain features of some airfoil systems such as flap wells, thick trailing edges, or unsteady effects.

Navier-Stokes calculations for high-lift systems have been investigated by a number of authors.[2-4] Schuster and Birckelbaw[2] computed the flow over a two-element airfoil using a structured, compressible, RANS solver. The grid system used was a pointwise patched system with three zones, with C-grids around both the main element and flap, and another outer C-grid surrounding those. Good results were obtained for low Reynolds number turbulent flow. The next two authors, Barth,[3] and Mavriplis[4] both used an unstructured grid approach to handle the difficulty of discretizing multi-element geometries. They were each able to produce accurate pressure coefficient information on the airfoil surfaces. The accuracy of the unstructured grid approach, however, is limited because of the very large aspect ratio of the triangular cells required to resolve high Reynolds number boundary layer flows. Also, this approach is not well developed for three-dimensional problems. Large computational resources are required, especially CPU memory, to make these methods work for viscous flows. Unstructured methods are currently generating a lot of interest in the research community; improvements to these limitations are to be expected in the near future. Until such a time, the current authors believe that a structured grid approach is the most suitable for solving viscous multi-element problems in two and three dimensions.

The current work uses an incompressible RANS flow solver to compute the flow over multi-element airfoils. Two different grid approaches are used; the first approach employs the patched grids utilized in Ref. 2, and the second uses an overlaid grid approach known as the Chimera scheme.[5] The current work examines several airfoil flow problems in two dimensions in an effort to characterize current capability to numerically study such problems. Grid topology, computational efficiency, and resulting accuracy are issues to be examined in the current work. An incompressible flow solver is being utilized because the flow conditions for take-off and landing will generally be less than a Mach number of 0.2. In the actual flow, compressibility effects will generally be confined to a small localized region, such as near the area of a leading-edge slat. Since the incompressible Navier-Stokes system has one less equation than its compressible counterpart, less computing resources are required.

3. ALGORITHM

The current computations are performed using the INS2D computer code which solving the incompressible Navier-Stokes equations for steady-state flows[6] and unsteady computations.[7] This algorithm has also been applied to problems in three dimensions using the INS3D-UP code.[8] The code is based on the method of artificial compressibility as developed by Chorin[9] in which a pseudo-time derivative of pressure is added to the continuity equation. Thus the convective part of the equations form a hyperbolic system, which can be iterated in pseudo-time until a steady-state solution is found. For unsteady problems, subiterations in pseudo-time are performed for each physical time step. Since the convective terms of the resulting equations are hyperbolic, upwind differencing can be applied to these terms. The current code uses flux-differencing splitting modeled after the scheme of Roe.[10] The upwind differencing leads to a more diagonally dominant system than does central differencing and does not require the additional use of artificial dissipation. The system of equations is solved using a Gauss-Seidel type line-relaxation scheme. The line-relaxation scheme is very useful for computing multi-zonal grids because it makes it possible to iteratively pass ΔQ (which is the change in the dependent variables for one time step) information between the zonal boundaries as the line-relaxation sweeping takes place. The result is a semi-implicit passing of boundary conditions between zones, which further enhances the code stability.[11] The resulting code is very robust and stable. It is capable of producing steady-state solutions to fine-mesh problems in 100 to 200 iterations. More detail about the computer code can be found in Refs. 6-8.

Most of the present calculations used the turbulence model developed by Baldwin and Barth,[12,13] where the specific formulation found in Ref. 12 was used. This is a one-equation turbulence model that avoids the need for an algebraic length scale and is derived from a simplified form of the standard $k-\epsilon$ model equations. In the current application, the equation is solved using a line-relaxation procedure similar to that used for the mean-flow equations. This model has been found to be very robust and easy to implement for multiple-body configurations. The next section includes computations of flow over a single airfoil. One of the studies for this problem includes a comparison of the Baldwin-Barth turbulence model with the Baldwin-Lomax[14] algebraic turbulence model.

4. COMPUTED RESULTS

This section describes results of the current computations for various different airfoil configurations with one, two, three, and four elements.

4.1. NACA 4412 Airfoil

Calculations were performed for the flow over an NACA 4412 airfoil at a Reynolds number of 1.52 million. A C-grid with dimensions of 241x63 was used, with wall spacings on the order of $10,^{-5}$ which corresponds to y^+ values on the order of one. The grid was computed using a hyperbolic grid generator.[15] A close view of this grid is shown in fig. 1.1. In order to compute flow quantities for the points on the computational boundary in the "wake cut" line of the c-mesh, two lines of dummy points are added such that these dummy points coincide with points on the other side of the wake line. The first line of these dummy points is updated by injecting values from the coincident interior points on which they lie. Using this overlap produces smooth solutions to the equations across this computational boundary. This procedure also adds dummy points inside the airfoil. These points are merely blanked out and never used in the solution procedure. All of the C-grids in this work use this overlap.

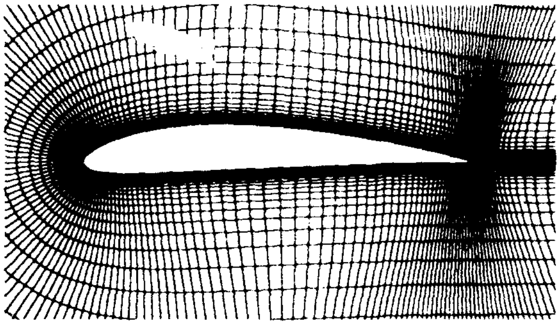

Fig. 1.1. 241x63 grid used for flow over an NACA 4412 airfoil.

This flow was computed using two different turbulence models, the Baldwin-Barth model[12] and the Baldwin-Lomax model.[14] Figure 1.2 shows a comparison between these computations and the experimental results of Coles and Wadcock[16] at an angle of attack of 13.87 degrees, which is very nearly maximum lift conditions. In the experiment the flow separated at approximately 85 percent of chord. Trip-strips were employed in the experiment on the suction and pressure surfaces at chord locations of x/c of 0.023 and 0.1, respectively. The computations thus specify these as the transition points. For the Baldwin-Barth model this is implemented by setting the the production terms to zero upstream of these locations; for the Baldwin-Lomax model the eddy viscosity is set to zero upstream of the transition location. The agreement is fairly good, with the biggest discrepancy occurring at the trailing edge where the predicted pressure is too high.

However, the Baldwin-Barth model does give a flattening of the pressure over the aft 15 percent of chord, indicating flow separation, where the Baldwin-Lomax solution does not show this tendency. This figure also shows that the computations with the transition predict a leading-edge laminar separation bubble. The experiment reports that there was no laminar separation bubble at this angle of attack, so an additional computation was run using the Baldwin-Barth model with the production terms turned on everywhere, thus the boundary layer was fully turbulent. The pressure coefficient for this is also shown in fig. 1.2. There is a slight improvement in the trailing edge area for this solution. The Baldwin-Lomax model showed no difference in the pressure or velocity solution when it was run without specifying transition, except that it removed the laminar separation bubble.

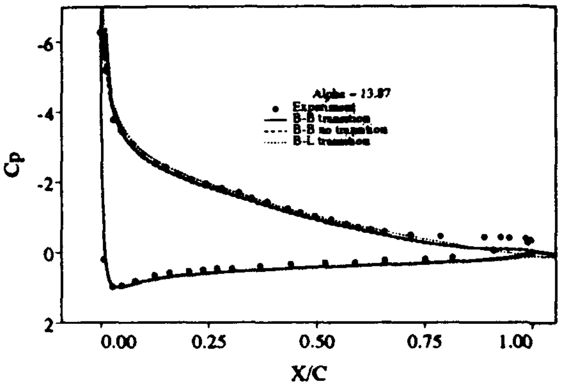

Fig. 1.2. Pressure coefficient on surface of an NACA 4412 airfoil at Reynolds number of 1.52 million comparing calculations with Baldwin-Barth and Baldwin-Lomax turbulence models and experimental data.

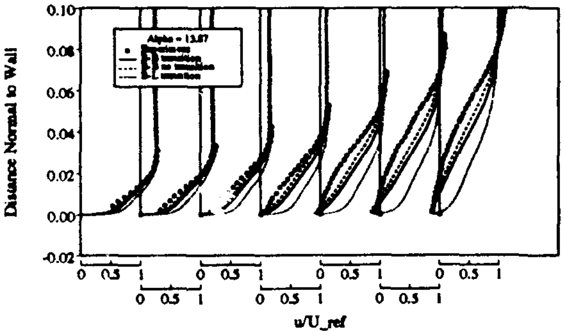

Fig. 1.3. Velocity profiles on upper surface of an NACA 4412 airfoil at streamwise stations of $x/c = 0.62$, 0.675, 0.731, 0.786, 0.842, 0.897, and 0.953.

Velocity profiles from the suction surface boundary layer are plotted in fig. 1.3 at streamwise stations of $x/c = 0.62$, 0.675, 0.731, 0.786, 0.842, 0.897, and 0.953. The profiles are shown using the streamwise component of velocity in boundary-layer coordinates, that is, the velocity component tangential to the local airfoil surface. This figure shows in greater detail the problems of the Baldwin-Lomax solutions in this region: the boundary layer profile is too full and the solution shows only a tiny region of separation. The Baldwin-Barth solution is in closer agreement with the experimental results, but also suffers from too small of a separation region. The case without transition shows the best agreement with the experimental profiles.

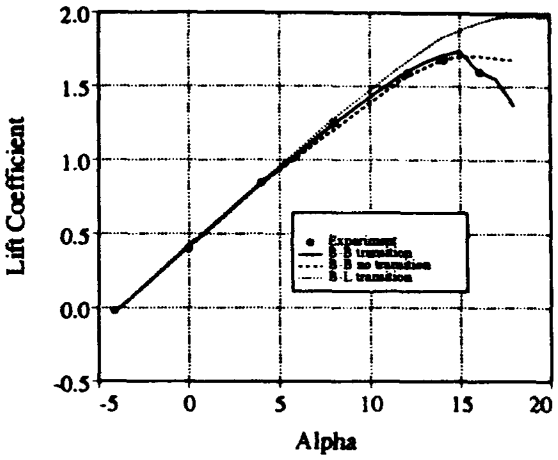

Fig. 1.4. Lift coefficient versus angle of attack for flow over an NACA 4412 airfoil.

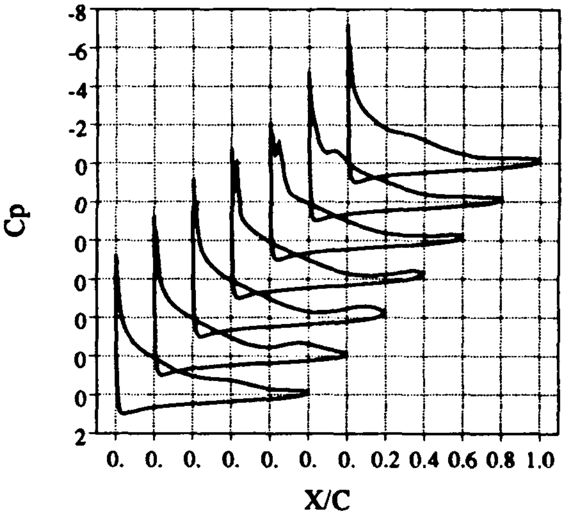

Fig. 1.5. Pressure coefficient on the surface of the NACA airfoil at 16 degrees angle of attack for seven different times during the unsteady periodic motion.

Computations were run for a range of angles of attack from zero lift to maximum lift. The lift coefficient versus angle of attack is plotted in Fig. 1.4. This shows that the Baldwin-Barth solution with transition gives very good agreement in the lift, including the prediction of stall. For all cases, as the angle of maximum lift was approached the flow tended toward unsteadyness. That is, the steady-state computations did not converge completely, which, for the artificial compressibility formulation means that the results do not satisfy the continuity equation. In these cases the code was then run in a time-accurate, unsteady mode. For the Baldwin-Barth model with transition, at an angle of attack of 14 degrees, the unsteadiness dies out when the computations are run in a time-accurate mode. At 16 degrees, an unsteady periodic behavior ensues; as shown in the figure, the mean lift drops sharply below the values from smaller angles of attack. Examination of the flow shows that the leading-edge laminar separation bubble is periodically shedding and traveling through the boundary layer on the top surface of the airfoil, and past the trailing edge. Figure 1.5 shows the pressure coefficient on the surface of the airfoil at seven different times through the period of this flow. The forming of the leading-edge vortex is evident, and it can be seen that it travels downstream and past the trailing edge.

For the Baldwin-Barth model without transition at an angle of attack of 16 degrees, all oscillations damp out and it converges to a steady-state solution. At 18 degrees, the lift continues to oscillate periodically, yet there is only a slight drop in the lift, and there is a complete absence of a leading-edge separation bubble. The Balwin-Lomax computations do not have any type of periodic unsteady behavior with or without transition. The results from this model show that a drop in lift does not occur until an angle of attack of 20 degrees.

In short, the Baldwin-Barth model shows promise for use in predicting high-lift flows, and although some deficiencies are shown here, it is significantly better than the Baldwin-Lomax model. In addition, the Baldwin-Barth model is much easier to use than the Baldwin-Lomax model, in that is does not require a length scale; it is straightforward to implement for a multi-element airfoil computation. All of the results in the later sections of this paper use the Baldwin-Barth model.

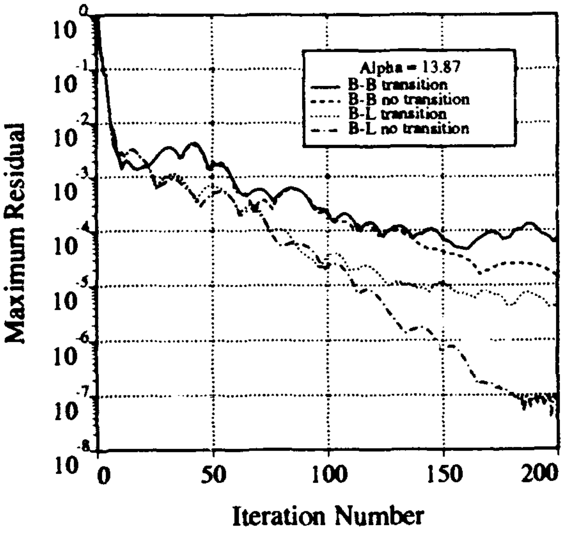

Fig. 1.6. Convergence history showing Maximum residual versus iteration number for flow over an NACA 4412 airfoil at 13.87 degrees angle of attack.

The convergence history is shown in Fig. 1.6 for the angle of attack of 13.87 degrees for both turbulence models with and without transition. In general, fast convergence is seen, with converged solutions obtained in 100 to 200 iterations. Specifying the transition tends to produce an unsteady component into the flow field which somewhat delays the convergence. It can also be seen that the Baldwin-Lomax computations converge much faster than the Baldwin-Barth model. The computing time on a Cray YMP required for this 241 x 63 mesh is 100 seconds for 200 iterations when using the Baldwin-Barth model, 90 seconds for 200 iterations with the Baldwin-Lomax model. When running the unsteady cases, the algorithm requires subiterations at each physical time step to drive the divergence of velocity toward zero. When running the unsteady 16 degree angle of attack case with a non-dimensional time step of 0.05, 40 physical time steps resulted in one period of the flow. This took about 10 minutes of computing time. Due to the difficult nature of solving the unsteady incompressible Navier-Stokes equations, it proably would not be computationally cheaper to use an incompressible formulation over a compressible Navier-Stokes code to study post-stall, unsteady airfoil flows.

4.2. Two-Element Airfoil

The geometry is made up of an NACA 4412 airfoil with an NACA 4415 flap deployed at 21.8 degrees, with the entire configuration at 8.2 degrees angle of attack. This geometry was the subject of a wind tunnel experiment by Adair and Horne.[17] The chord Reynolds number was 1.8 million, and the Mach number in the experiment was 0.09. The blockage in the wind-tunnel was severe enough that the wind-tunnel walls needed to be included in the calculations in order to get good agreement with the experimental pressure coefficients.

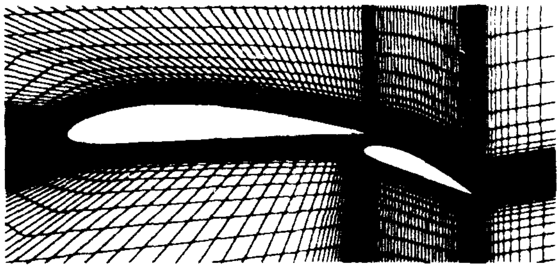

Fig. 2.1. Three-zone patched grid used to compute flow over an NACA 4412 airfoil with an NACA 4415 flap.

The airfoils were discretized using two different grid approaches. The first follows the work of Schuster and Birckelbaw[2] and uses 3 zones which are patched together using coincident points. This grid is shown in Fig. 2.1. Each of the elements is surrounded by a C-grid, and these two grids are surrounded by another C-grid which extends out to the wind-tunnel walls. The dimension of these grids are 374x44, 241x33, and 352x32, respectively, for a total of 35,000 points.

The second type of grid uses a Chimera[5] approach, in which C-grids were generated about each of the elements. To include the effects of the wind-tunnel walls these grids were inset into a third zone composed of an h-grid. A partial view of these three grids is shown at the top of Fig. 2.2, with a close-up of the main-element grid in the vicinity of the flap shown in the bottom half of this figure. These grids had dimensions of 261x49, 203x35, and 121x61, for a total of 27,500 points. To implement the Chimera approach, these grids are given to the PEGSUS[5] code. This code first punches holes into grids where they overlap a body (as shown in the bottom of Fig. 2.2). It then computes the interpolation stencils used to update the flow quantities at the fringe points of these holes, and to update the flow quantities at the outer boundaries of grids which lie inside another grid (like the outer boundaries of the c-grids seen in the top of Fig. 2.2). For both the Chimera and the patched grid approaches, the spacing next to the surfaces was set to 2×10^{-5}, which correspond to y^{+} values at the wall on the order of one.

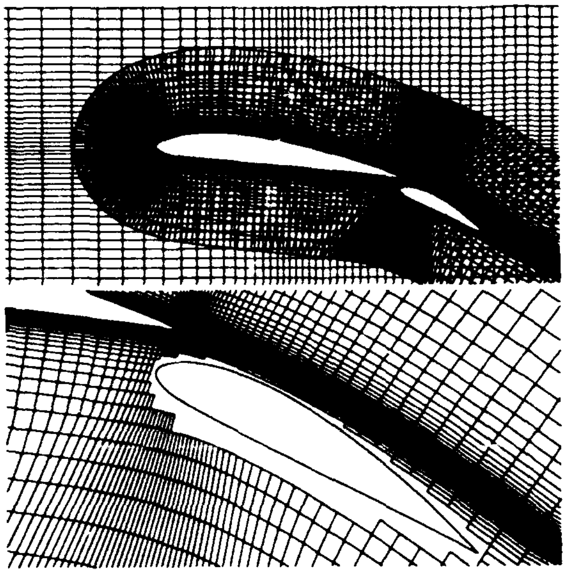

Fig. 2.2. Overlaid Chimera grid used to compute flow over an NACA 4412 airfoil with an NACA 4415 flap.

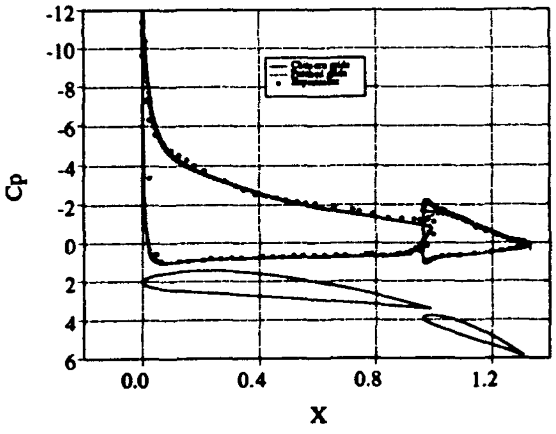

Fig. 2.3. Pressure coefficient on surface of two-element airfoil comparing both patched grid and overlaid grid schemes to experimental results.

The computational results compare well with the experimental results of Adair and Horne.[17] A plot of the pressure coefficient on the surface of the elements is shown in Fig. 2.3. Results from both of the grid approaches is shown. The biggest difference between the computation and experiment is seen in the suction peak at the leading edge of the flap. The difference might be explained by a difference in the geometry between the computations and the experiment. There was an ambiguity in the way in which the flap position is defined.

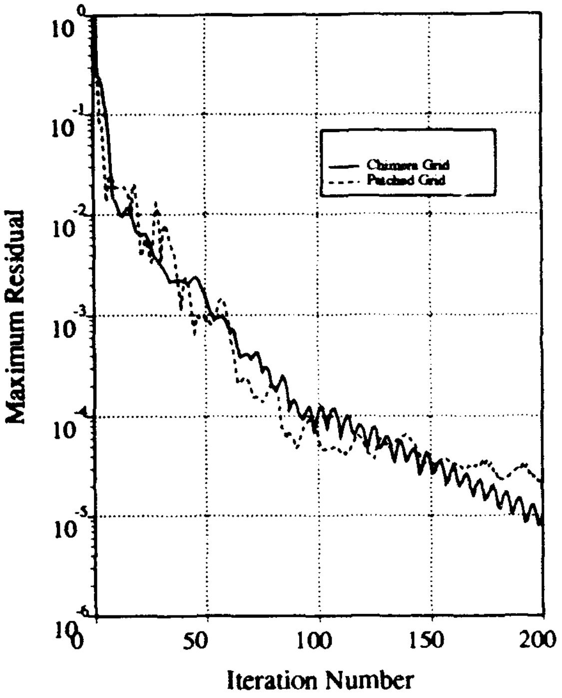

Fig. 2.4. Convergence history for flow over two-element airfoil for patched grid and overlaid grid schemes.

Figure 2.4 shows the convergence history for these computations. They both converge very well, resulting in a steady-state solution in about 100 iterations. Each of these grid cases takes about 100 seconds of CPU time on a Cray YMP for 100 iterations. The code runs at about a rate of 80 MFLOPS, and requires 36 $\times 10^{-6}$ CPU seconds per grid point per iteration. Since the Chimera approach uses about 20% fewer grid points, it takes a little less computing time. The major difference between these approaches is the amount of time and effort it takes to generate the grids. The patched grid case takes on the order of several hours of work; it involves generating inner boundaries which define the surface with the proper point distribution to ensure that the grids can be patched together. Then hyperbolic grids are marched halfway across the gap from each of the elements. The resulting outer boundaries of these are merged into a common interface where they match. The inner grids are recalculated to match this interface. Finally, the outer C-grid is marched outward using a hyperbolic grid generator. The process is tedious and is not easily repeatable for a different case (new flap placement, or flap angle), or for a different geometry. On the other hand, the overlaid grids can be generated in only a matter of minutes; one need only generate two independent hyperbolic grids about each of the elements, and then feed these into the PEGSUS code[5] as described above. Once this has been set up for one case it is very easy to reproduce it for another case or another geometry. It is for these reasons that the overlaid grid approach was adopted for the rest of the cases and geometries in this work.

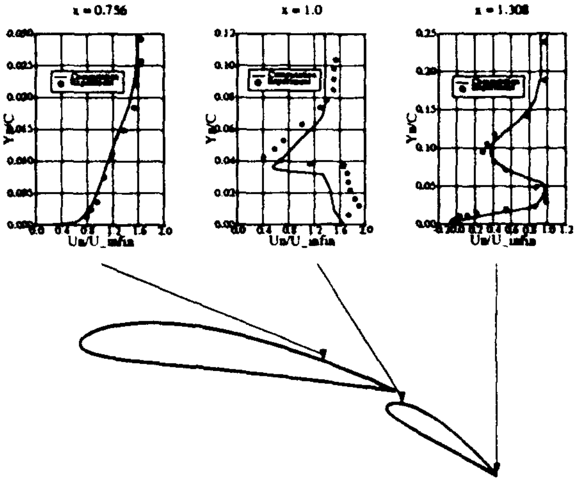

Fig. 2.5. Velocity profiles from overlaid grid calculations compared to experimental data.

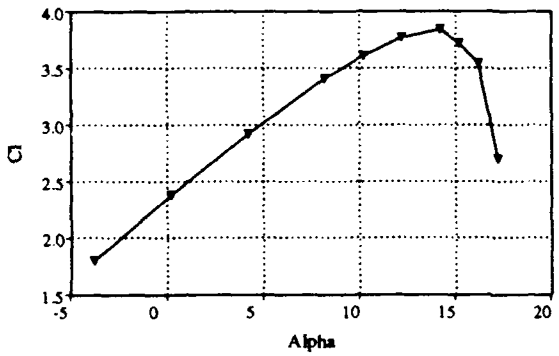

Fig. 2.6. Coefficient of lift versus angle of attack as computed by the overlaid grid approach for the two-element airfoil.

Figure 2.5 shows velocity profiles from the Chimera calculations at three locations on the top surface of the main element and flap. These are plotted with experimental measurements of the profiles by Adair and Horne.[17] These plots show fairly good agreement with the experimental results. The biggest discrepancy is the difference in the gap velocity off the surface of the flap's leading edge. This is related to the difference seen in the pressure coefficient plot in Fig. 2.3. The velocity profile from the trailing edge of the flap shows that there is a separation occurring over the top surface of the flap. This profile shows that the computational separation bubble is not as thick as that seen in the experiment, but that the computations do an excellent job of capturing the wake from the main element in this region.

Further calculations were carried out using free-stream outer boundaries (neglecting wind-tunnel walls). These calculations use the overlaid grids with two zones, where the main element grid extends beyond ten chord lengths from the airfoil. These were run at various angles of attack to show the capability to compute maximum lift conditions as well as post-stall conditions. The curve of lift coefficient versus angle of attack is shown in Fig. 2.6. The lift drops off sharply at alpha = 15 degrees, and the calculations indicate that the flow becomes unsteady beyond that angle of attack. The skin friction along the surfaces of the airfoil elements is shown in Fig. 2.7. It can be seen that the flow separates at the trailing edge of the flap even at zero angle of attack, and that this separation reduces in size with increasing angle of attack. The main element has trailing edge separation occurring at angles of attack of 12 degrees and greater. It becomes massively separated at an angle of attack of 16 degrees. At this angle of attack the flap shows evidence of a vortex passing over the top because of the large dip in the skin friction on the surface of the flap.

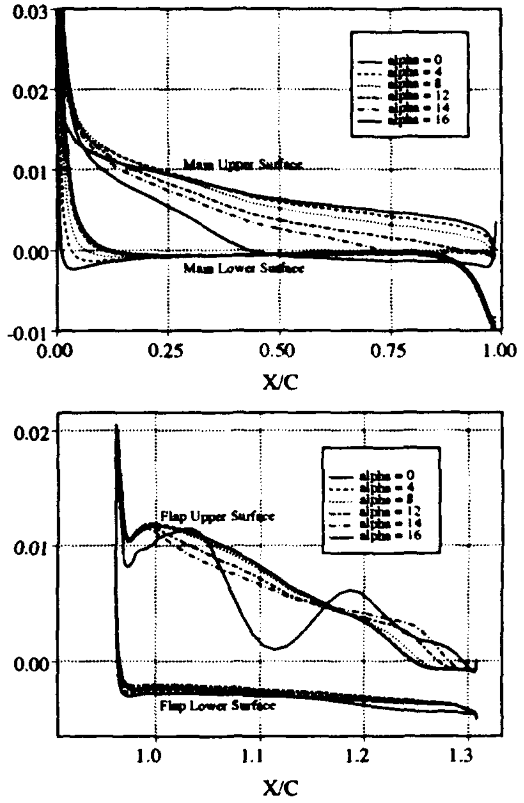

Fig. 2.7. Skin friction on the surface of the main element and flap for various angles of attack.

4.3. Three-Element Airfoil

The three element computational configuration was taken from an experimental geometry of a supercritical airfoil which has been tested by Valarezo et al.[18] This airfoil consisted of a leading edge slat deployed at -30 degrees, a main element, and a trailing edge flap deployed at 30 degrees. The experimental Mach number was 0.2 and the chord Reynolds number was 9 million. The Chimera approach was used to discretize the geometry and produce a computational grid. A C-grid was placed around each element, with the main-element grid extending out to the far field. The grids for the slat-, main-, and flap-element had dimensions of 221x41, 401x75, and 221x47, respectively, for a total just under 51,000 points. The top of Fig. 3.1 shows every other grid point in the first and third element grids, with the resulting holes caused by the main element. The second half of this figure shows the main element grid. The wake cut boundary of this grid has been aligned just above the top surface of the flap element in an attempt to put as many points as possible in the wake and boundary-layer region found there.

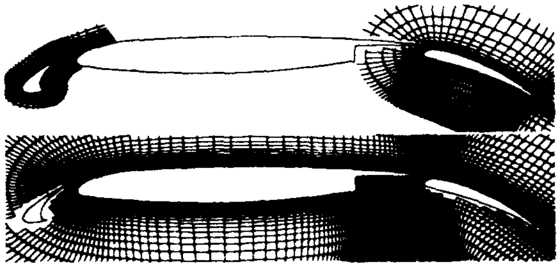

Fig. 3.1. Grid and geometry for the three-element airfoil, showing every other grid point around the slat and flap.

Fig. 3.2. Velocity magnitude contours at 20.4 degrees angle of attack.

Figure 3.2 shows velocity magnitude contours for the three element configuration run at 20.4 degrees angle of attack. The wake of the slat is clearly seen across the top of the succeeding elements. The experimental results of Valarezo et al.[18] and the computational results of this study are compared in Fig. 3.3. These figures show pressure coefficients on the surfaces of each element at three different angles of attack, 8.1, 20.4, and 23.4 degrees. Very good agreement is seen except on the suction side of the slat. Also, there is a discrepancy on the upper surface of the flap trailing edge. The experimental results show a strong adverse pressure gradient followed by a flattening in the pressure coefficient curve, which is generally evidence of flow separation. The computational results do not show this. This is probably due to the general trend of the turbulence model to underpredict the amount of separation. The experiment allowed free transition on the elements, and the computations assumed a turbulent boundary layer everywhere. Further work in this area could include use of a transition model for this calculation.

Convergence histories of these computations are shown in Figure 3.4. These computations converge well, with steady state solutions being obtained after 200 iterations, which corresponds to about 4 minutes of CPU time on a Cray YMP.

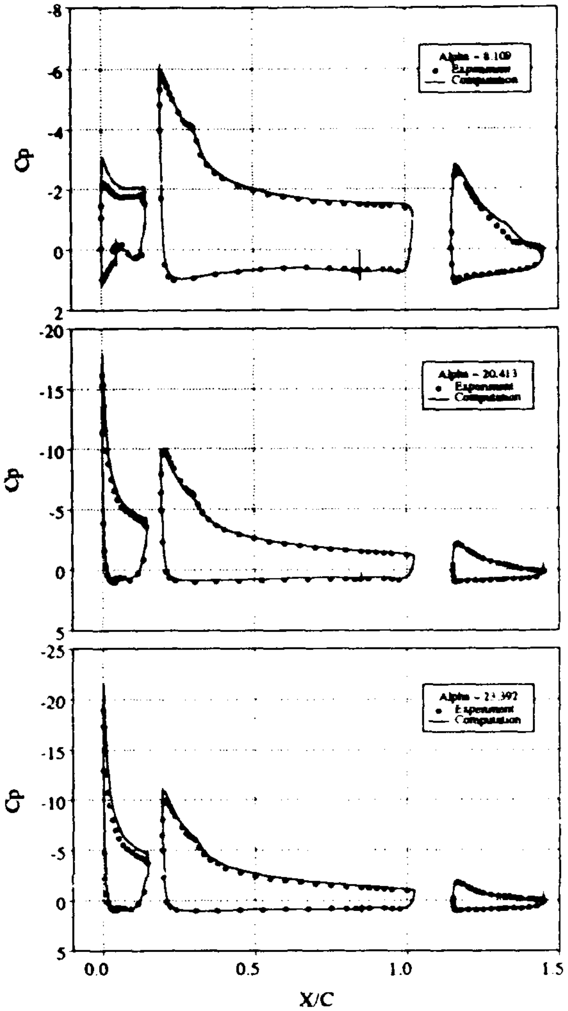

Fig. 3.3. Pressure coefficient comparing computation and experiment for angles of attack of 8.1, 20.4, and 23.4 degrees.

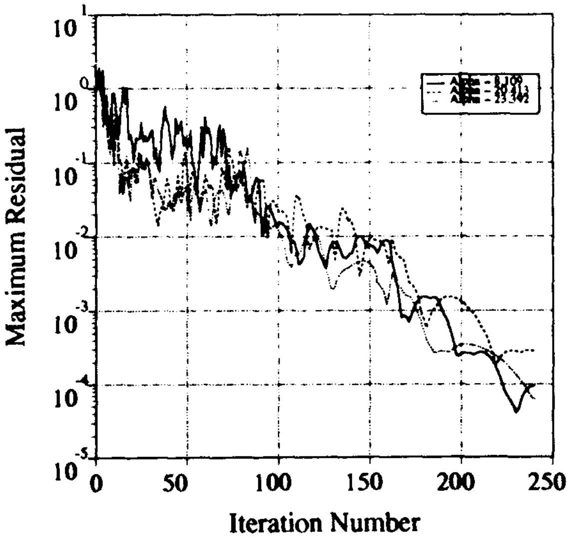

Fig. 3.4. Convergence for the three-element airfoil.

4.4. Four-Element Airfoil

The geometry is made up of a NASA 9.3 percent blunt-based, supercritical airfoil with a leading edge slat deployed at -47.2 degrees and two trailing edge flaps at 30 degree and 49.7 degrees respectively. This configuration matches the geometry used in the experimental work done by Omar et al.[19] The Mach number in the experiment was 0.201 and the chord Reynolds number was 2.83 million.

Fig. 4.1. Velocity magnitude contours at 14.25 degrees angle of attack.

The geometry was discretized using the Chimera approach. C-grids were generated around each of the elements, with the main element grid being marched out to the outer boundary. These grids were overlaid and the PEGSUS[5] code was used to create an overlaid grid. Approximately 55,000 points were used in the resulting composite grid in order to resolve the flow physics adequately in the boundary layers and wakes. The grid spacing next to the surfaces of the airfoils was 10^{-5} which ensures y^+ values of one near the wall.

The computational results of this study were compared with the the experimental results of Omar et al.[19]. Figure 4.1 shows velocity magnitude contours around the four element configuration at 14.25 degrees angle of attack. In this figure the wake from the leading edge slat is apparent over the main element. Subsequent wakes from the main element and flaps can also be observed. Plots of the pressure coefficient on the surfaces of the elements at angles of attack of 0.0, 8.13, and 14.25 degrees are shown in Fig. 4.2. Again, excellent agreement is seen except there is once more evidence that the computation of the flow over the flap underpredicts the amount of separation at the lower angles of attack.

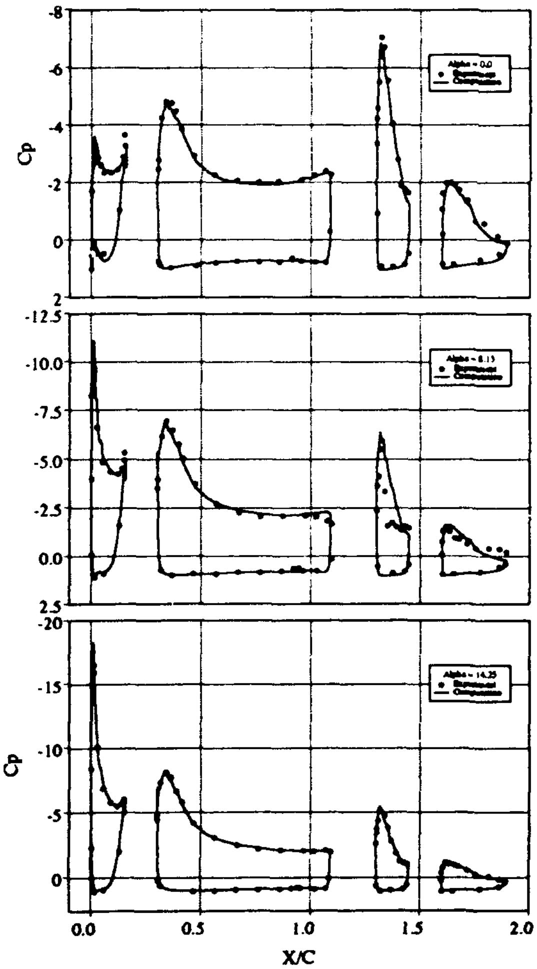

Fig. 4.2. Pressure coefficient comparing computation and experiment for angles of attack of 0.0, 8.13, and 14.25 degrees.

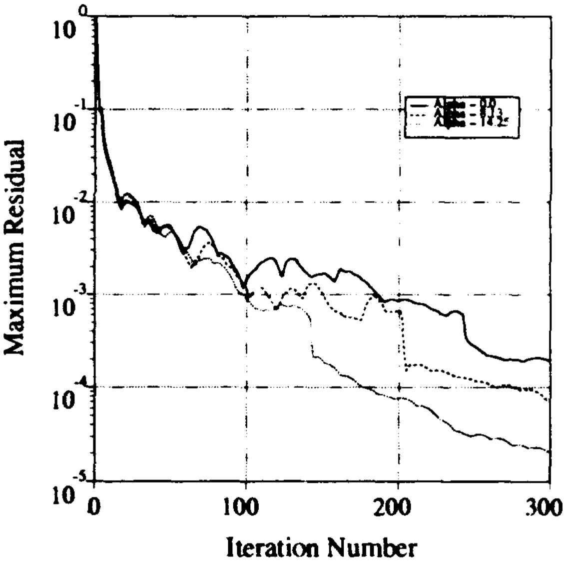

Fig. 4.3. Convergence for the four-element airfoil.

The convergence histories for the four element configuration at three different angles of attack are shown in Fig. 4.3. The computations converge well and a steady state solution is produced after about 200 iterations, which corresponds to approximately four minutes of CPU time on the Cray YMP.

5. CONCLUSIONS

An incompressible flow solver has been used to compute flow over several airfoil geometries for the purpose of developing a tool to study takeoff and landing configurations. The code is robust and produces numerical simulations in a matter of minutes. The flow over an

NACA 4412 airfoil was investigated, and the Baldwin-Barth and Baldwin-Lomax turbulence models were compared. The Baldwin-Barth model gave significantly better results, and was much easier to use, particularly for multi-element flows. The use of the Chimera overlaid grid approach was found to be much easier than using a patched grid scheme for solving multiple element airfoil flows. Both approaches are capable of producing accurate solutions. Accurate pressure prediction was shown for geometries with two, three, and four airfoil elements. The common discrepancy between these calculations and experimental results involves separated flow. The results for the NACA 4412 airfoil indicate that deficiencies with the turbulence model are the most likely cause of these inaccuracies. Work in progress with different turbulence models shows promise in remedying this. Investigation of other turbulence models and their implementation for a multi-element airfoil calculation will be the focus of future work. In addition, future work will include the extension of the current work to three dimensions.

6. REFERENCES

1. Kusunose, K., Wigton, L, and Meredith, P., "A Rapidly Converging Viscous/Inviscid Coupling Code for Multi-Element Airfoil Configurations," AIAA Paper 91-0177, January, 1991.
2. Schuster, D. M. and Birckelbaw, L. D., "Numerical Computations of Viscous Flowfields about Multiple Component Airfoils," AIAA Paper 85-0167, January, 1985.
3. Barth, T. J., "Numerical Aspects of Computing Viscous High Reynolds Number Flows on Unstructured Meshes," AIAA Paper 91-0721, January, 1991.
4. Mavriplis, D., "Turbulent Flow Calculations Using Unstructured and Adaptive Meshes," ICASE Report 90-61, September, 1990.
5. Benek, J. A., Buning, P. G., and Steger, J. L., "A 3-D Chimera Grid Embedding Technique," AIAA Paper 85-1523-CP, July 1985.
6. Rogers, S. E. and Kwak, D., "An Upwind Differencing Scheme for the Steady-state Incompressible Navier-Stokes Equations," Journal of Applied Numerical Mathematics, *8*, 1991, pp 43–64.
7. Rogers, S. E. and Kwak, D., "An Upwind Differencing Scheme for the Time Accurate Incompressible Navier-Stokes Equations," AIAA Paper 88-2583, June 1988 See also AIAA J., *28*, 2, February 1990, pp 253 262.
8. Rogers, S. E., Kwak, D., and Kiris, C., "Numerical Solution of the Incompressible Navier-Stokes Equations for Steady-State and Time-Dependent Problems," AIAA Paper 89 0463, January, 1989 See also AIAA J., *29*, 4, April 1991, pp 603-610
9. Chorin, A. J., "A Numerical Method for Solving Incompressible Viscous Flow Problems," J. Comput Phys., *2*, 1967, pp. 12-26.
10. Roe, P. L., "Approximate Riemann Solvers, Parameter Vectors, and Difference Schemes," J. Comput. Phys., *43*, 1981, pp 357–372.
11. Rogers, S. E., "On The Use of Implicit Line-Relaxation and Multi-Zonal Compuations," AIAA Technical Note 91-1611-CP, AIAA CFD Conference, Honolulu, HI, June 24-27, 1991.
12. Baldwin, B. and Barth, T., "A One-Equation Turbulence Transport Model for High Reynolds Number Wall-Bounded Flows," NASA TM 102847, Aug. 1990.
13. Baldwin, B. and Barth, T., "A One-Equation Turbulence Transport Model for High Reynolds Number Wall-Bounded Flows," AIAA Paper 91-0610, January, 1991.
14. Baldwin, B. and Lomax, H., "Thin Layer Approximation and Algebraic Model for Separated Turbulent Flows," AIAA Paper 78-257, January, 1978.
15. Cordova, J. Q. and Barth, T. J., "Grid Generation for General 2-D Regions Using Hyperbolic Equations," AIAA Paper 88-0520, January, 1988.
16. Coles, D. and Wadcock, A. J., "Flying-Hot- Wire Study of Flow Past an NACA 4412 Airfoil at Maximum Lift," AIAA J., *17*, 4, 1979, pp 321–329.
17. Adair, D. and Horne, W. C., "Turbulent Separated Flow Over and Downstream of a Two-Element Airfoil," Experiments in Fluids, *7*, 1989, pp 531-541.
18. Valarezo, W. O., Dominik, C. J., McGhee, R. J., Goodman. W. L., and Paschal, K. B., "Multi-Element Airfoil Optimization for Maximum Lift at High Reynolds Numbers," AIAA Paper 91-3332, September, 1991.
19. Omar E., Zierten, T., Hahn, M., Szpiro, E., and Mahal, A., "Two-Dimensional Wind-Tunnel Tests of a NASA Supercritical Airfoil with Various High-Lift Systems," NACA CR-2215, September, 1973.

NAVIER-STOKES CALCULATIONS ON MULTI-ELEMENT AIRFOILS USING A CHIMERA-BASED SOLVER

by

Donald W. Jasper, Shreekant Agrawal and **Brian A. Robinson**
McDonnell Aircraft Company
McDonnell Douglas Corporation
P.O. Box 516, St. Louis
Missouri, USA 63166

ABSTRACT

A study of Navier-Stokes calculations of flows about multi-element airfoils using a chimera grid approach is presented. The chimera approach utilizes structured, overlapped grids which allow great flexibility of grid arrangement and simplifies grid generation. Calculations are made for two-, three-, and four-element airfoils, and modeling of the effect of gap distance between elements is demonstrated for a two-element case. Solutions are obtained using the thin-layer form of the Reynolds averaged Navier-Stokes equations with turbulence closure provided by the Baldwin-Lomax algebraic model or the Baldwin-Barth one equation model. The Baldwin-Barth turbulence model is shown to provide better agreement with experimental data and to dramatically improve convergence rates for some cases. Recently developed, improved farfield boundary conditions are incorporated into the solver for greater efficiency. Computed results show good comparison with experimental data which include aerodynamic forces, surface pressures, and boundary layer velocity profiles.

Symbols

C_l	Section Lift Coefficient, $l/q_\infty c$
l	Section Lift
q	Dynamic Pressure, $1/2\rho u^2$
u,U	Velocity
C_d	Section Drag Coefficient, $d/q_\infty c$
d	Section Drag
C_f	Skin Friction Coefficient, τ_w/q_∞
c	Airfoil Chord
τ	Shear Stress
M	Mach Number, u/a
a	Speed of Sound
C_p	Pressure Coefficient, $(p-p_\infty)/q_\infty$
p	Static Pressure
y^+	Non-dimensional Distance from Wall, $y\sqrt{\tau w/(\rho w \mu w)}$
Re	Reynolds Number, $\rho_\infty U_\infty c/\mu_\infty$
μ	Viscosity

Subscripts:

∞	Freestream Quantity
e	Quantity at Edge of Boundary Layer
w	Quantity at Wall

INTRODUCTION

Efficient high-lift systems are critical in achieving optimum aerodynamic performance of future generation military and commercial aircraft. Well designed high-lift systems lead directly to greater operational flexibility through increased payloads, extended ranges, and decreased take-off and landing distances. Traditional high-lift design has relied on extensive wind tunnel and flight testing which is expensive and difficult due to the extremely complex flow interactions encountered. The complexity of the flow interactions requires such extreme fidelity in geometric representation and matching of test to actual operating conditions that the applicability of standard scale model aerodynamic testing is limited. In order to achieve optimum designs, new tools for rapid and efficient analysis of high-lift configurations are required. Computational Fluid Dynamics (CFD) offers great promise as a tool which provides valuable insight into the flow phenomena associated with high-lift system performance, however to provide early design guidance rapid and efficient CFD techniques must be developed and validated.

Traditionally (and for the foreseeable future) high-lift systems incorporate multi-element geometries in which a number of highly loaded aerodynamic elements interact in close proximity to each other. Figure 1 shows an example cross section of a typical configuration incorporating four elements: a leading edge slat, the main airfoil element, a flap vane, and a trailing edge flap. Such configurations generate very complex flowfields containing regions of separated flow, vortical flow, and confluent boundary layers. Laminar, turbulent, transitional, and re-laminarizing boundary layers may exist. Although high lift systems are typically deployed at low freestream Mach numbers, they may still exhibit compressibility effects due to the large pressure gradients generated. Such complex flows are extremely difficult to analyze computationally and require solution of the Navier-Stokes equations to resolve all flowfield details. It should be noted that many of the flowfield phenomena (e.g. separation, transition, turbulence, etc.) are areas of intense research in the computational community and are not yet fully amenable to computational analysis.

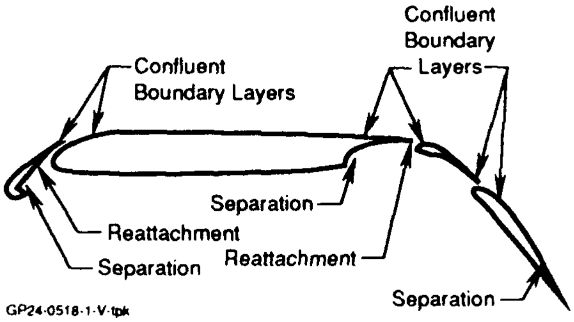

Figure 1. Typical High-Lift Configuration

One of the difficulties encountered in computational analysis of high-lift systems using the Navier-Stokes equations is the generation of suitable high quality grids about each element to capture all relevant flow phenomena. Three basic approaches to generating grids and solutions about complex configurations have been widely reported in the literature: zonal patched (or blocked) grids, unstructured grids, and overlapped (chimera) grids (Figure 2). The zonal approach (e.g. Reference 1) has been widely demonstrated on a number of geometries, and has shown excellent accuracy in the calculation of many complex viscous flows. Such an approach utilizes structured grids generated in separate zones or blocks which transfer information across common boundaries. Its major drawback in application to analysis of high-lift systems is the necessity of matching boundaries at zonal interfaces. For typical high-lift geometries the boundary matching places a large demand on grid generation capabilities and can lead to degradation in grid quality (and consequently solution accuracy) at boundaries in close proximity to the high-lift system components. The unstructured grid approach (e.g., Reference 2) readily generates grids about high-lift configurations, but can suffer in accuracy from highly stretched triangular cells generated in the boundary layer region. Unstructured grid solvers are the most recent approach to the analysis of complex geometries and show great promise, but they have not yet demonstrated the same wide applicability to complex viscous flows as structured flow solvers. The chimera grid scheme (e.g., Reference 3) utilizes overlapping, structured grids which are not required to match at boundaries. Structured grids about each element can be generated independently with no compromise in grid quality, and the experience gained in the application of structured grids to complex viscous flows can be utilized.

The intent of the present study is to develop and evaluate a technique for the rapid and efficient analysis of multi-element high-lift systems. The chimera approach was chosen because it allows for simplified generation of high quality grids and the use of proven structured grid solvers. Using the chimera approach, regions where more grid resolution is required may be assigned additional overlapping grids without modification of existing grids. Changes in high-lift configuration can be rapidly analyzed since independently gridded elements can be added or subtracted at will, and movable surfaces can be easily modelled by translation or rotation of existing grids (e.g. Reference 4). The CFL3D Euler/Navier-Stokes solver (Reference 5) modified to treat overlapping grids was selected due to its wide application to complex viscous flows and the generally excellent results obtained with its use. Initially a Baldwin-Lomax algebraic turbulence model was used for its simplicity and ease of application. However a Baldwin-Barth one-equation model (Reference 6) was incorporated to address deficiencies noted with the simpler Baldwin-Lomax model. Transition was not treated (i.e. flows were considered fully turbulent at all points). The chosen approach is capable of treating three-dimensional geometries without modification.

METHOD

The chimera scheme is a domain decomposition scheme first proposed by Benek and Steger (Reference 3). Its application can be illustrated by considering a general

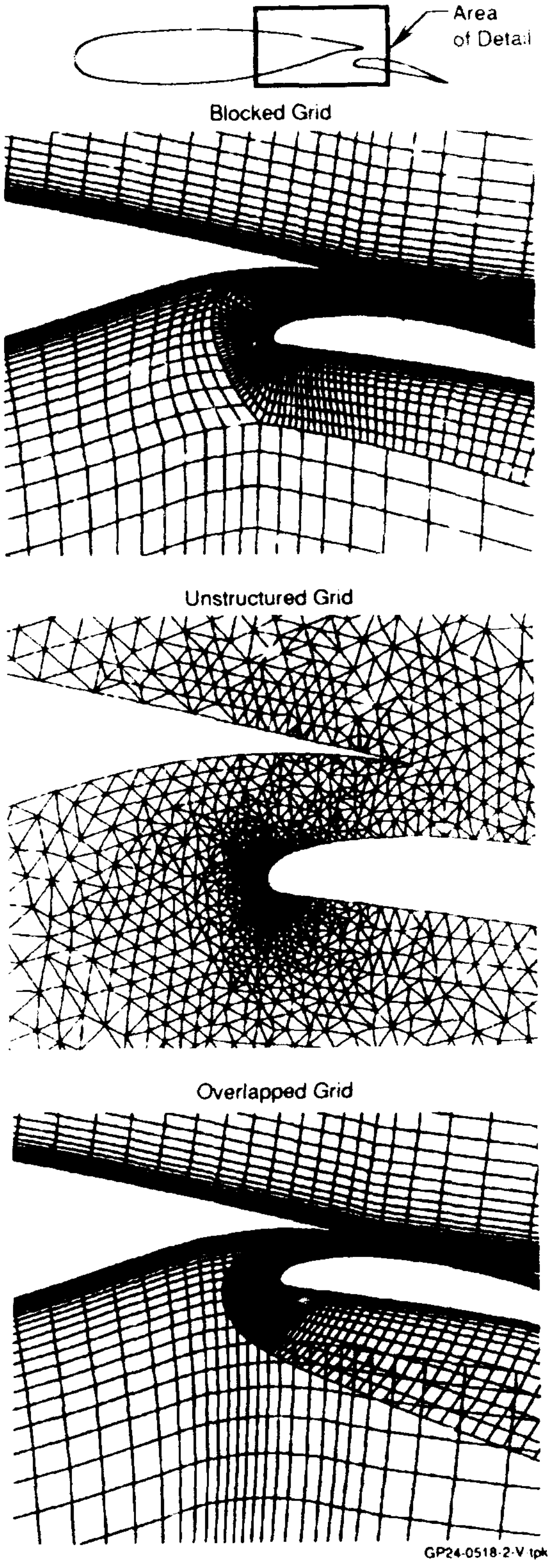

Figure 2. Unstructured, Blocked, and Overlapped Grids About Two-Element Airfoil

airfoil/flap configuration as depicted in Figure 3. Independent grids are generated about the airfoil and flap elements. The flap grid is embedded within the airfoil grid and its outer boundary is updated by interpolation from the airfoil grid. To keep the airfoil grid from calculating a solution inside the solid surface of the flap airfoil grid points which fall within the flap surface are designated hole points and removed from the solution. An artificial boundary is established in the airfoil grid surrounding the hole points and is updated by interpolation from the overlapped region of the flap grid. In this way a two-way communication is established between the airfoil and flap grids, and the complete flowfield excluding regions within solid surfaces can be calculated. The interpolation process is outlined in Figure 4 which details a portion of the overlap region between the airfoil and flap grids. At each boundary two points are interpolated. Since the flow solver difference stencil at any point uses information from at most two neighboring points in any direction, the solution is completely isolated from points within the hole.

The chimera solution takes part in two steps. In the first step a pre-processor code is executed which determines the location of hole points, determines outer boundary and hole boundary points which must be interpolated, and calculates the interpolation factors needed to update boundary points. The pre-processor code for CFL3D is called MAGGIE (Reference 7). Boundary points are updated using a bilinear interpolation scheme which utilizes the four surrounding points of the interpolating grid. It should be noted that this interpolation scheme is not conservative, and that interpolation errors are proportional to the ratio of the area of the cell being interpolated to the area of the cell providing the interpolation data (Reference 8).

The second step in the chimera solution is the flow solver, CFL3D. In this study CFL3D is used to solve the thin layer approximation of the three-dimensional, time dependent, conservation law form of the Reynolds averaged, compressible Navier-Stokes equations. The code solves the discretized flow equations implicitly using an upwind-biased spatial differencing scheme with either flux difference splitting or flux vector splitting for the convective and pressure terms, and central differencing for the shear stress and heat transfer terms. The Roe-averaged flux difference splitting scheme was employed in this study. The Baldwin-Lomax algebraic model or the Baldwin-Barth one equation model was used to calculate turbulent viscosity. In application to multi-element flows, the Baldwin-Lomax model was applied independently on each element grid with no attempt to match turbulent viscosity across chimera boundaries. It was found necessary to limit the search for the location of maximum vorticity which defines the length scale of the Baldwin-Lomax turbulence model to the first peak in vorticity and not the absolute maximum of vorticity. Turbulent viscosity for the Baldwin-Barth model was interpolated at chimera boundaries in the same manner as the flowfield variables.

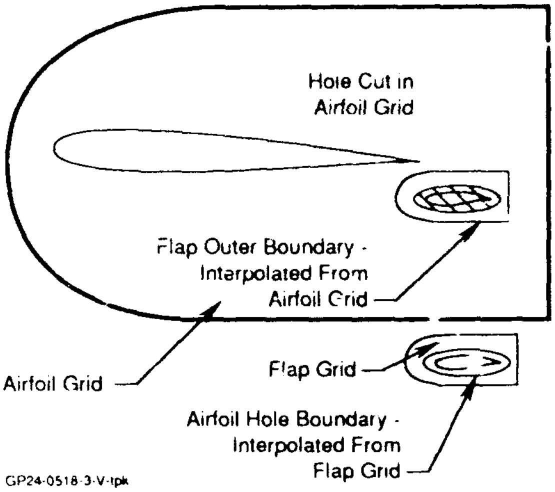

Figure 3. Definition of Chimera Interpolation Boundaries

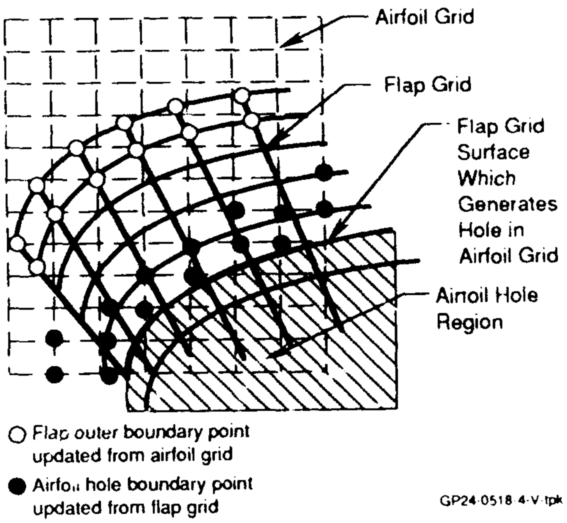

Figure 4. Detail of Airfoil/Flap Grid Overlap Region Illustrating Two-Point Overlap Interpolation

Many improvements to the MAGGIE grid pre-processor code were required to increase the speed of generating suitable chimera boundaries about complex configurations. Biedron (Reference 9) improved the search routine for selection of the points used for interpolation. New algorithms were implemented for determining which grids would be searched for interpolation factors in complex overlapping grid regions. A new algorithm for determining hole points was incorporated. This new hole search algorithm greatly improves the hole determination procedure (especially in three dimensions) and will be described in detail.

The original hole search algorithm implemented in MAGGIE is based on defining boundaries which create a surface enclosing the hole points. The outward normal direction for each boundary is prescribed to define an 'outside' of the boundary. Initially all candidate points are assumed to be hole points, and each point is tested against the boundary to determine if it lies on the 'outside' of the boundary and is therefore outside of the hole creation surface. A point is determined to be outside the boundary if the dot product of the vector from the closest point on the boundary to the candidate point with the outward surface normal vector at the hole boundary point is positive (Figure 5). This algorithm requires some user experience in defining hole creation surfaces and the division of the surfaces into boundaries (e.g. Reference 10). The new algorithm also requires the definition of a hole creation surface enclosing the hole points, however there is no need to specify outward normals or to divide the surface into boundaries. To determine if a point is within the hole creation surface, the number of times a ray from the point to infinity intersects the hole creation surface is determined (Figure 6). An odd number of intersections indicates the point is within the hole creation surface, and an even number of intersections indicates the point is outside of the hole. In practice the new hole point algorithm has proven to be much more robust than the original.

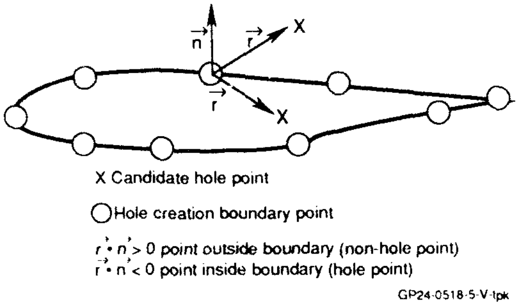

Figure 5. Original Hole Determination Algorithm

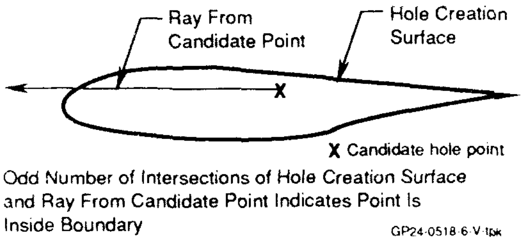

Figure 6. New Hole Determination Algorithm

In order to increase computational efficiency, improved farfield boundary conditions based on the method of asymptotic expansions (Reference 11) have been incorporated into the flow solver. These boundary conditions are derived from the Euler equations about a constant pressure rectilinear flow. They have been demonstrated to produce more accurate results when compared to those obtained using standard farfield boundary conditions on a given grid. Conversely, similar accuracy can be obtained on a smaller grid, reducing the number of points in the farfield grid and thereby reducing computation time. To apply the improved boundary condition, the farfield boundary must be defined by analytic curves, and is currently limited to parabolic curves for inflow boundaries and linear curves for outflow boundaries.

RESULTS

The CFL3D chimera code was applied to three multi-element airfoils for which test data is available. Each test was conducted to investigate physical phenomena associated with multi-element airfoils or the detailed performance of a specific multi-element airfoil configuration. Due to the nature of such testing, special attention to test technique and long established guidelines for two-dimensional airfoil testing were observed. Since the testing is aimed at acquiring airfoil data, there is no error associated with Reynolds number scaling or geometric fidelity which would be present in scale model testing of a development flight vehicle.

Two-Element Airfoil:

The first test case analyzed was a modified NLR 7301 supercritical airfoil with a slotted trailing edge flap. The airfoil was modified such that no flow separation was observed at low speed (Reference 12). Test data is available at a Mach number of 0.185 and Reynolds number of 2.51 million based on airfoil chord. No boundary layer transition device was used. Data were collected at several angles of attack for two flap gap distances (1.3% and 2.6% of airfoil chord) with a 20° flap deflection. A small laminar separation bubble near the leading edge of the airfoil was observed experimentally. Transition from laminar to turbulent boundary layer was generally seen to occur just aft of the separation bubble on the airfoil upper surface at about 2.5% airfoil chord, at about 70% chord on the airfoil lower surface, and 50% flap chord on the flap upper surface. The flap lower surface exhibited laminar flow at all times. The main element and flap boundary layers were found to be confluent for the 1.3% flap gap. The experiment also showed the flow in the flap cove region of the airfoil lower surface to be near separation at the entrance and to be experiencing re-laminarization of the boundary layer near the flap leading edge.

Representative computational grids used for this case are shown in Figure 7. Main element and flap grids are of C topology, with the main element grid extending to the farfield. Two grid densities were evaluated. The coarse grid had dimensions of 205x45 on the airfoil and 179x33 on the flap, while the corresponding fine grid dimensions were 424x91 and 199x41. Initial point spacing off the solid surfaces was adjusted to yield a y^+ of approximately one for both the fine and coarse grids. Coarse grid solutions were made using only the Baldwin-Lomax turbulence model. Convergence of the solution showed a large dependence on the turbulence model employed (Figure 8). The Baldwin-Barth model required approximately 2000 iterations to achieve force convergence, while the Baldwin-Lomax model required in excess of 8000 iterations. It required approximately 40 minutes of Cray YMP CPU time to run 2000 iterations on the fine grid using the Baldwin-Barth turbulence model, while the Baldwin-Lomax model required approximately 20% less cpu time per iteration.

Experimental pressure distributions are available at 6.0°, 10.1°, and 13.1° angles of attack, and comparison of the predicted and experimental pressure distributions are in excellent agreement for both the coarse and fine grids at both flap gap distances (Figures 9 and 10). The fine grid solutions did show a slight improvement in the prediction

sensitive to cove shape [18] case resulted in 31 blocks. A total of 90,000

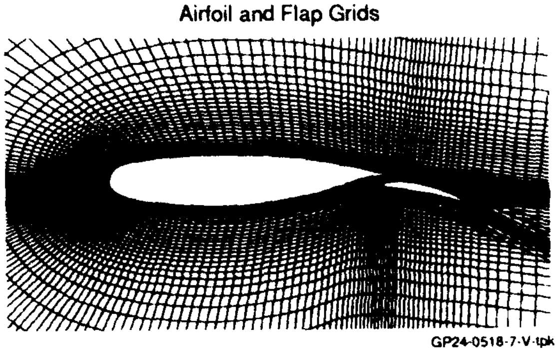

Figure 7. Computational Grids for NLR 7301 Airfoil With 20° Flap

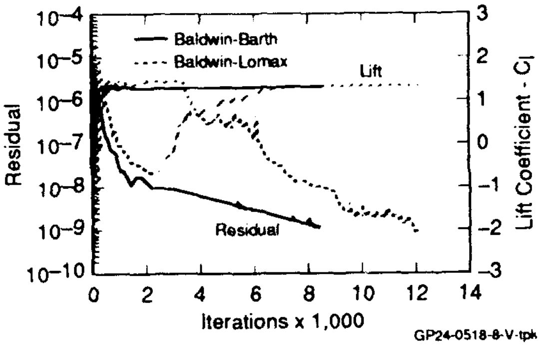

Figure 8. Convergence History for NLR 7301 Airfoil, 2.6% Gap
M_∞ = 0.185, α=6°, Re = 2.51 x 10^6, Fine Grid

of the suction peak pressure for the 1.3% flap gap geometry. Comparison of experimental and calculated lift coefficients also show good agreement (Figure 11). Coarse grid results tend to overpredict the lift for both flap gap distances, while the fine grid greatly improves the agreement for the 2.6% flap gap and gives a somewhat smaller improvement for the 1.3% gap. The 1.3% flap gap exhibited confluent boundary layers on the flap upper surface as shown by the flap boundary layer not recovering to the potential velocity before merging with the airfoil wake (Figure 12). The relatively worse agreement of predicted and experimental lift for the 1.3% gap may be attributed to a greater sensitivity of this case to the boundary layer development, which was not modelled correctly due to the laminar flow on the flap upper surface and re-laminarization of the boundary layer in the flap cove region. Coarse grid solutions would not converge at angles of attack beyond 13.1°. Fine grid results were obtained at 15.1° angle of attack with the 2.6% gap case exhibiting an oscillatory convergence. At 17.1° angle of attack the 1.3% gap case also exhibited oscillatory convergence. Computations fail to predict the abrupt stall observed experimentally at 15.1° angle of attack. The oscillatory convergence and failure to predict the abrupt stall is attributed to the inadequacy of the Baldwin-Lomax turbulence model in calculating the onset of separation and the effects of massive separation.

To investigate the effect of turbulence model on the solution, find grid calculations were made for the 2.6% flap gap case utilizing the Baldwin-Barth turbulence model. Pressure distributions (not shown) are virtually identical with those obtained using the Baldwin-Lomax model. Improved behavior near stall is obtained using the Baldwin-Barth model, with the maximum lift occurring at 14.1° angle of attack, but with a more gradual onset of stall than indicated in the experiment (Figure 13). No oscillatory behavior was noted in convergence using the Baldwin-Barth model. The Baldwin-Barth model also shows a significant improvement in prediction of turbulent boundary layer velocity profiles on the airfoil and flap upper surfaces (Figure 14), with a much improved prediction of boundary layer thickness.

Comparison of predicted and experimental skin friction distributions show reasonable agreement for both the Baldwin-Lomax and Baldwin-Barth models on the airfoil upper surface (Figure 15). Experimental skin friction coefficients are available only for turbulent flow regions, and therefore are not available for the major portion of the lower surface. Comparison of experimental and predicted drag coefficients, however, are not in good agreement for

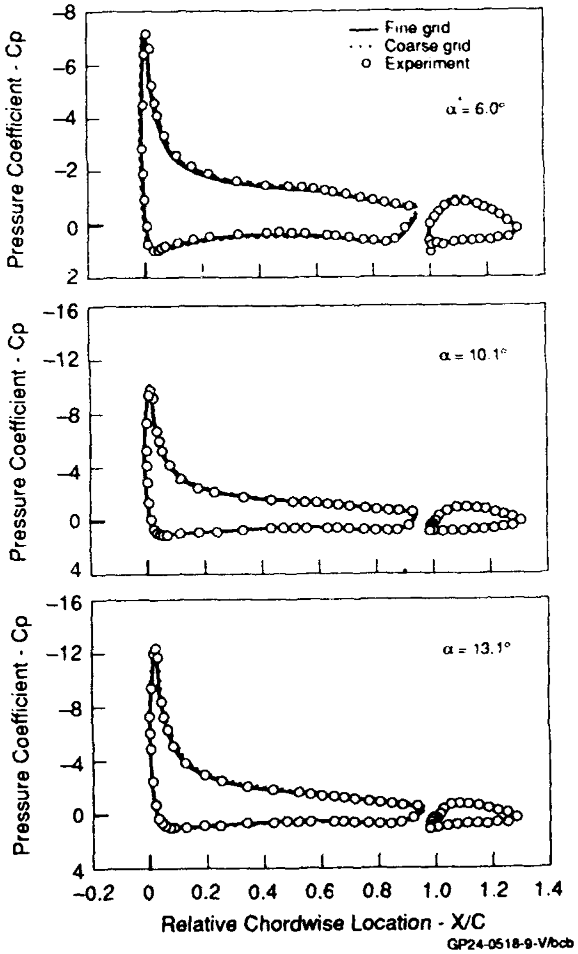

Figure 9. Computed and Expermental Pressure Distributions for the NLR 7301 Airfoil
2.6% Gap, M_∞ = 0.15, Re = 0.62 x10^6

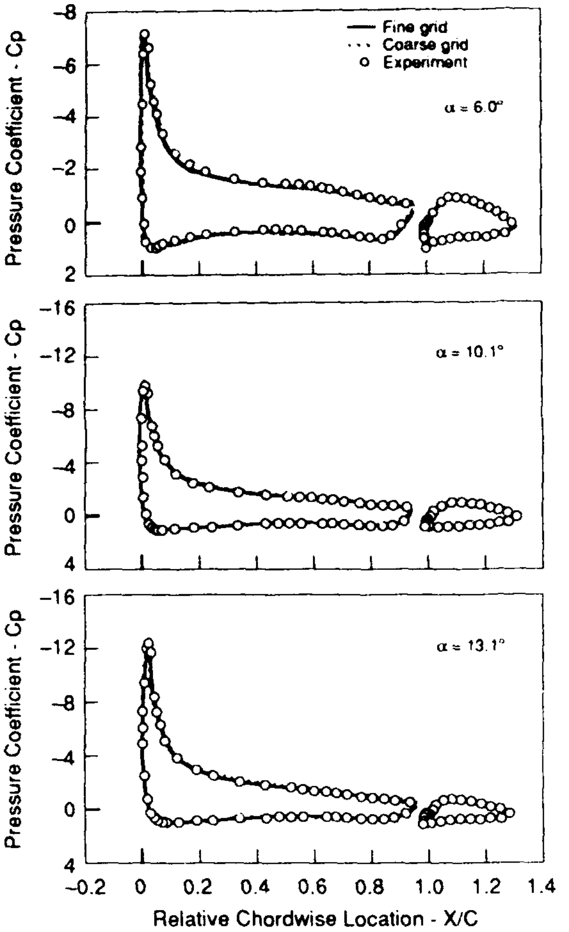

GP24-0518-10-V/bcb

Figure 10. Computed and Expermental Pressure Distributions for the NLR 7301 Airfoil

1.3% Gap, $M_\infty = 0.185$, $Re = 2.51 \times 10^6$

either the Baldwin-Lomax or Baldwin-Barth models, with the computational results two to three times higher than the experimental values. The higher predicted drag may be due in part to the extensive laminar flow which exists in the experiment but not modelled in the computations.

The improved analytic boundary conditions were also applied to the NLR airfoil. A grid with a parabolic outer boundary which extended only one chord length upstream of the airfoil leading edge and 1.7 chord lengths downstream of the airfoil trailing edge was generated about the main element. A larger reference grid was also generated which incorporated the smaller grid as a subset, but extended the outer boundary to 7 chord lengths upstream of the leading edge and 10 chord lengths downstream of the trailing edge. Pressure distributions and force coefficients generated on the smaller grid using the improved boundary conditions are in good agreement with those generated on the larger grid using the standard boundary condition, while the standard boundary condition used on the smaller grid shows considerable degradation in the solution (Figure 16). The smaller grid reduced the number of points in the main element grid by approximately 20%, with a corresponding reduction in CPU time.

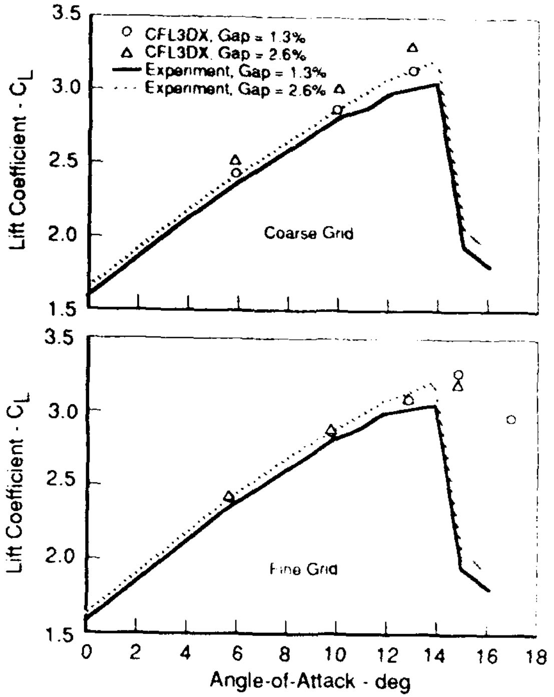

GP24-0518-11-V/pk

Figure 11. Lift Curve for NLR 7301 Airfoil With 20° Slotted Flap

$M_\infty = 0.185$, $Re = 2.51 \times 10^6$

Three-Element Airfoil:
The second test case was a GAW(1) airfoil with a slotted flap and add-on leading edge slat (Reference 13). The airfoil was tested with and without the slat present for a variety of flap and slat deflections. The test was conducted at low speed for a Reynolds number of 0.62 million. Transition was observed to occur at 5% airfoil chord on the main element upper surface, and between 50% and 65% chord on the lower surface. Transition was fixed at 10% slat chord for runs in which the slat was employed.

Computations were made with the flap deflected 40° with and without the slat. When employed, the slat was deflected 42°. Grids were again of C topology about each element with the main element outer boundary extending to the farfield and the slat and flap grids embedded (Figure 17). Addition of the slat to the basic airfoil and flap configuration required no modification or additional grid generation effort to the main element or flap grids. The grid sizes were 303x63 on the main element, 217x29 on the flap, and 193x29 on the slat. Additional cases with a refined slat grid with dimensions of 193x57 were also performed. Results were generated using the Baldwin-Lomax turbulence model as the Baldwin-Barth model failed to converge for the slatted cases.

Without the slat computed and experimental pressures are in good agreement (Figure 18), although the main element pressure peak is generally overpredicted. Some discrepancies also occur at the minimum pressure location of the trailing edge flap. In addition, a spike in pressure is generated in the computations by the sharp corners introduced by the way in which the blunt trailing edge of

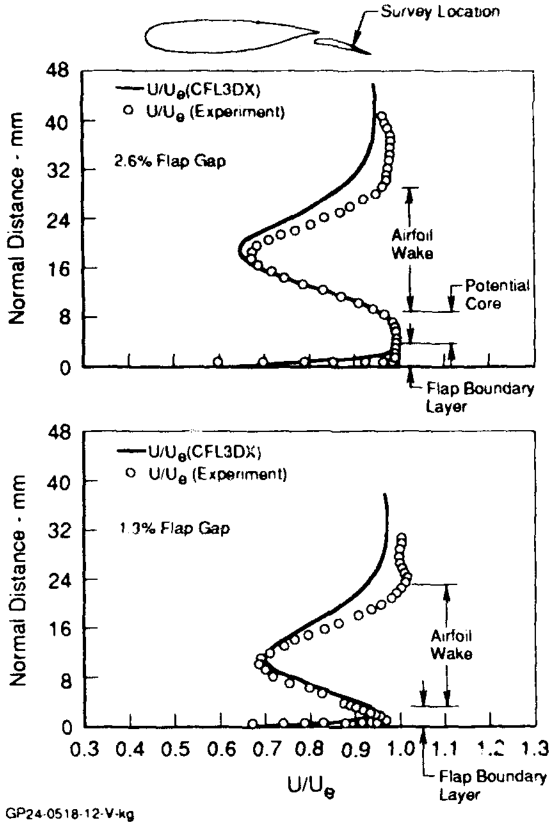

Figure 12. Upper Surface Boundary Layer Velocity Profiles at 69% Flap Chord
NLR 7301 Airfoil, $M_\infty = 0.185$,

Alpha = 6°, Re = 2.51×10^6, Fine Grid

the true flap geometry was modelled (Figure 19). Computations for the cases in which the leading edge slat was present are not in as good agreement (Figure 20). In general the computations tend to overpredict the pressure peak and overall loading of the slat and underpredict the loading of the main airfoil and flap. This behavior is clearly evident from the pressure distributions at 5.3° and 9.5° angle of attack, while at 14.07° the computational result appears to be more highly loaded on the main element than the experiment. This can be attributed to a separation on the main element which occurred in the experiment but not in the computations.

Several attempts were made to improve the calculated results for the slatted cases. The grid about the slat was refined and different hole cutting schemes were attempted to ensure that the separation which occurs under the slat surface was contained entirely within the slat grid and not near the hole boundary of the main element grid. In addition, the slat geometry was modified such that the separation underneath the slat was completely eliminated. Neither of these had any significant effect on the computed results.

Four-Element Airfoil:
To further validate the solver, the four-element airfoil of Reference 14 was analyzed. This airfoil consists of a leading edge slat, a main airfoil element, a flap vane, and a trailing edge flap. The airfoil was tested at a Mach number

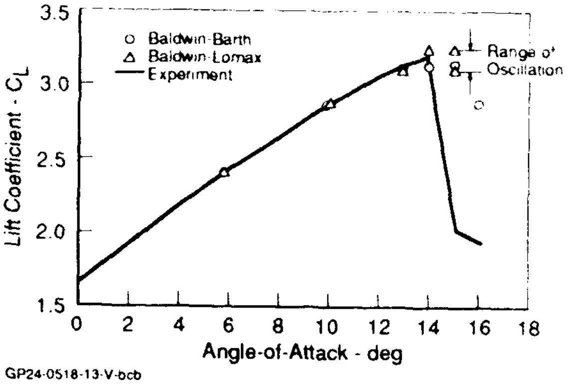

Figure 13. NLR 7301 Airfoil 2.6% Flap Gap M_∞ = 0.185, Fine Grid
Lift Coefficient vs Angle-of-Attack

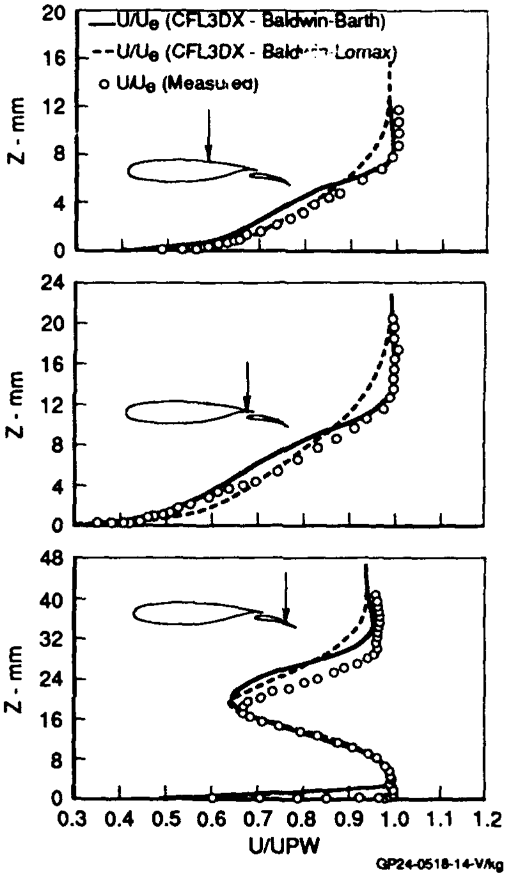

Figure 14. Computed Boundary Layer Velocity Profiles Using Baldwin-Barth and Baldwin-Lomax Turbulence Models on NLR 7301 Airfoil, 2.6% Gap, $M_\infty = 0.185$, $\alpha = 6°$, Re = 2.51×10^6

hole strategy considerably improved the agreement between the experimental and computed pressure distributions (Figure 23). The reason for the difference appears to be the different levels of turbulent viscosity which the flap grid perceives in the two different hole schemes. This is confirmed by the fact that the Baldwin-Barth turbulence model, which interpolates turbulent viscosity at chimera boundaries, did not show the same

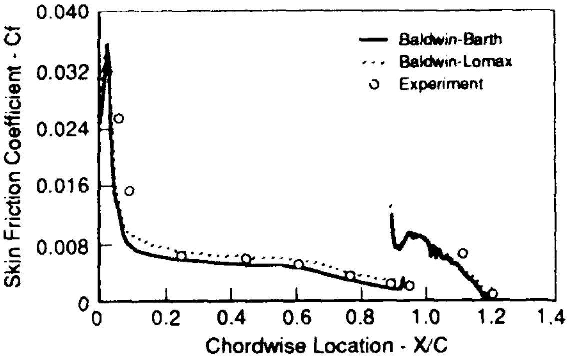

GP24-0518-15-V/jls

Figure 15. Upper Surface Skin Friction Coefficient Distribution
NLR 7301 Airfoil, 2.6% Flap Gap, $M_\infty = 0.185$, $Re = 2.51 \times 10^6$

of 0.2 and Reynolds number of 2.85 million. Computational results for this airfoil have also been reported by Rogers et al (Reference 15) using a chimera approach with an incompressible Navier-Stokes solver employing a Baldwin-Barth turbulence model.

For the present analysis C type grids were generated about each element with the main airfoil grid extending to the farfield (Figure 21). In the vane/flap region, the grids of the main airfoil, vane, and flap all overlapped. The grid interactions in this region are complex, and the solution exhibited a dependency on the way the holes were defined about the various elements when using the Baldwin-Lomax turbulence model. Two different holes were cut in the vane and flap grids near the trailing edge of the main airfoil (Figure 22) and solutions were obtained at 8.13° angle of attack. The first hole was cut around the airfoil trailing edge such that the vane and flap grids extended above the main airfoil wake, while the second hole removed all vane and flap points above the airfoil wake line. The second level of differences. Due to its better agreement with experimental data, the second hole strategy was used for all subsequent calculations.

Comparisons of experimental and computed pressure distributions are generally good (Figure 24). At 8.13° angle of attack there is a large discrepancy between experimental and predicted pressures on the vane element, apparently due to a separation on the vane upper surface which was not predicted computationally. At 0.0° angle of attack this separation has apparently not yet developed, and at 14.25° angle of attack the separation region has been reduced significantly and the computations are again in good agreement with experiment. The likely culprit for missing the separation on the vane is the turbulence model. Results at 8.13° angle of attack using the Baldwin-Barth turbulence model show virtually no difference with those presented for the Baldwin-Lomax model. The pressure results presented here (using the Baldwin-Lomax turbulence model) are consistent with those of Rogers, et al (Reference 15), who employed a Baldwin-Barth model.

CONCLUSIONS

A technique for the rapid analysis of multi-element high-lift systems utilizing the chimera approach has been evaluated. Navier-Stokes solutions have been obtained for two-, three-, and four-element airfoils using the technique, and varying agreement with experimental data has been demonstrated as a function of airfoil geometry. Accuracy of multi-element airfoil analyses depends to a large extent on the complexity of the flow to be modelled. For the two-element case without confluent boundary layer flow, excellent prediction of lift is obtained up to stall, with maximum lift observed at the same angle of attack as the experiment and the predicted value of maximum lift within 2% of the experimental value. Good prediction of turbulent boundary layer velocity profiles and skin friction is also obtained, although drag is not well predicted. Less accurate results are obtained for the case exhibiting confluent

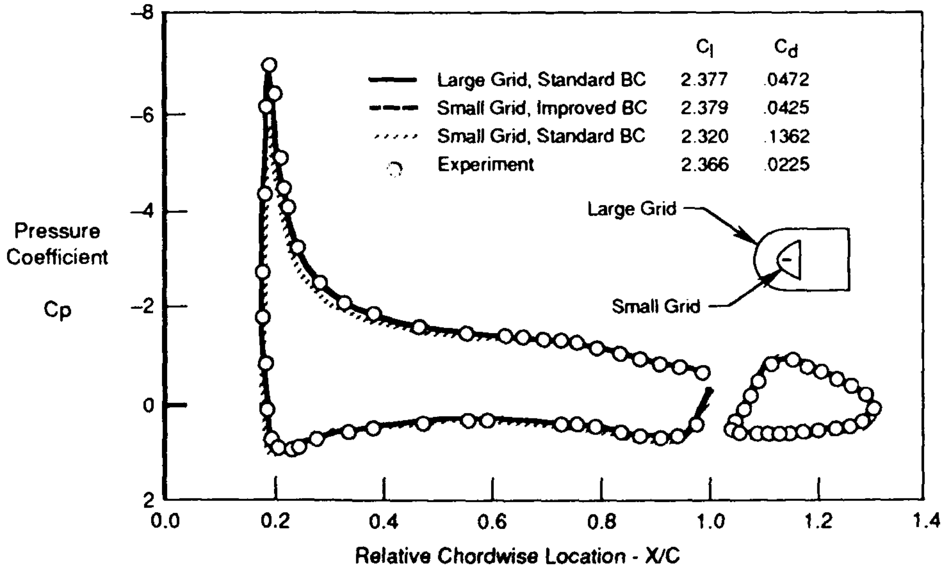

GP24-0518-16-V/jls

Figure 16. Application of Improved Boundary Conditions
NLR 7301 Airfoil, 1.3% Flap Gap, $M_\infty = 0.185$, Alpha = 6.0

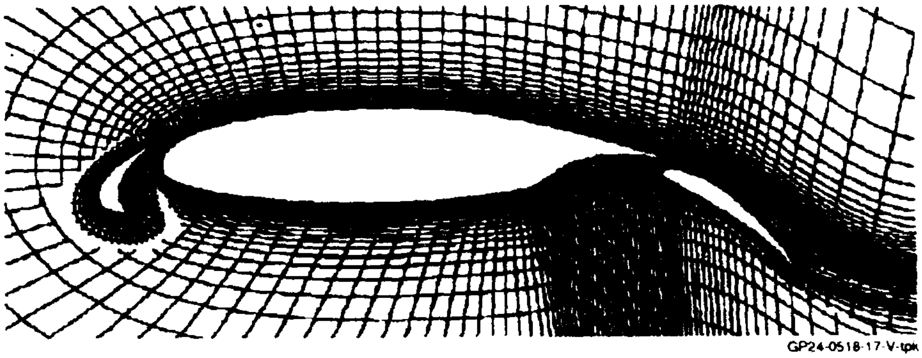

Figure 17. Grids About Three-Element Airfoil

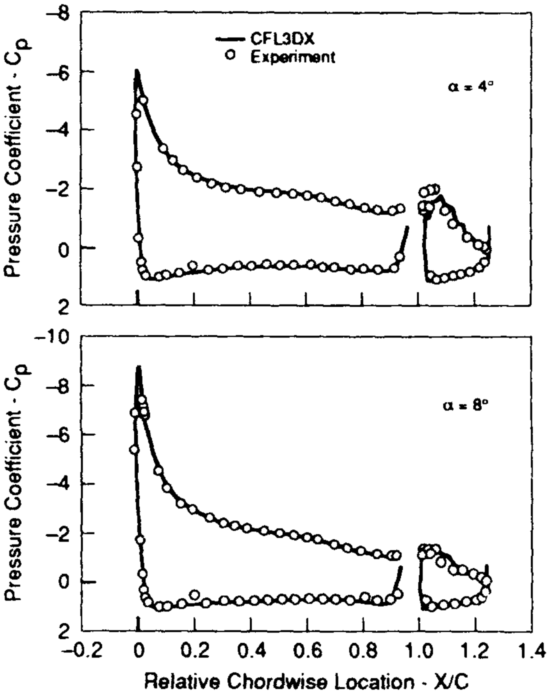

GP24-0518-18-V-bcb

Figure 18. Computed and Experimental Pressure Distributions for the GAW Airfoil With Slotted Flap

$M_\infty = 0.15,\ Re = 0.62 \times 10^6$

boundary layer flow, and consequently modelling of flap gap effect is not accurate. Calculation of gap effects may require modelling of transitional and re-laminarizing boundary layers. Pressure comparisons for the three-element airfoil are not good, probably because of the separation which occurs on the undersurface of the leading edge slat. Experimental and predicted pressure distributions are in better agreement for the four-element airfoil which exhibits no separation on the slat. Better prediction of separation, stall, and post-stall results depends on better modelling of turbulence.

The Baldwin-Barth turbulence model has been shown to be superior to the Baldwin-Lomax turbulence model. The Baldwin-Barth model allows turbulent viscosity to be matched at chimera boundaries, which reduces the dependence of the solution on the way hole boundaries are defined about the various elements. In addition, the

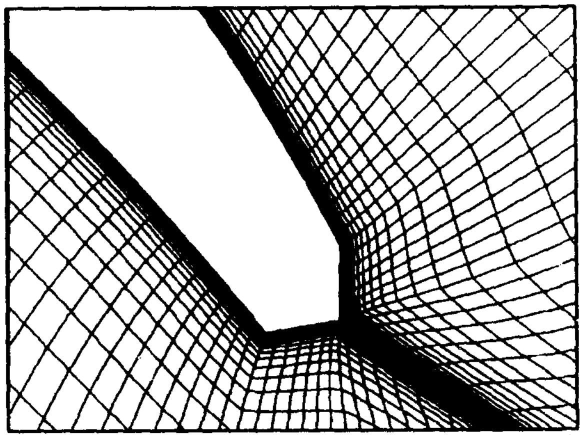

Figure 19. Trailing Edge Closure of GAW Airfoil Flap

Baldwin-Barth model better predicts the detailed boundary layer parameters and gives a more positive indication of stall, with none of the oscillatory convergence exhibited by the Baldwin-Lomax model. The Baldwin-Barth model has also demonstrated a positive effect on convergence rate which can be significant for certain cases.

The chimera approach has shown itself to be a versatile tool which can greatly simplify the grid generation effort and improve the grid quality for the Navier-Stokes analysis of multi-element airfoils. Accurate and efficient solutions can be obtained about complex configurations, limited by the applicability of the flow models employed.

REFERENCES

1. Raj, P., Olling, C.R., Sikora, J.S., Keen, J.M., Singer, S.W., and Brennen, J.E., "Three Dimensional Euler/Navier-Stokes Aerodynamic Method (TEAM)," Volume I: Computational Method and Verification, WRDC-TR-87-3074, June 1989.

2. Mavriplis, D., "Turbulent Flow Calculations Using Unstructured and Adaptive Meshes," ICASE Report No. 90-61, September 1990.

3. Benek, J.A., Steger, J.L., and Dougherty, F.C., "A Flexible Grid Embedding Technique with Applications to the Euler Equations," AIAA-83-1944, July 1983.

4. Dougherty, F.C., and Kuan, J.H., "Transonic Store Separation Using a Three-Dimensional Chimera Grid Scheme," AIAA-89-0637, January 1989.

5. Thomas, J.L., Taylor, S.L., and Anderson, W.K., "Navier-Stokes Computations of Vortical Flows Over Low Aspect Ratio Wings," AIAA-87-0207, January 1987.

6. Baldwin, B.S., Barth, T.J., "A One-Equation Turbulence Transport Model for High Reynolds Number Wall-Bounded Flows," NASA TM 102847, August 1990.

7. Baysal, O., Fouladi, K., and Lessard, V.R., "Multigrid and Upwind Viscous Flow Solver on Three-Dimensional Overlapped and Embedded Grids," AIAA Journal, Vol. 29, No. 6, 1991.

8. Takeshi, S., and Jameson, A., "Multi-Body Flow Field Calculations with Overlapping-Mesh Method," AIAA-89-2179, 1989.

9. Biedron, B., A. S & M Inc., Private Communications.

10. Suhs, N.E., and Tramel, R.W., "Pegsus 4.0 User's Manual," AEDC-TR-91-8, November 1991.

11. Verhoff, A., Stookesberry, D.C., and Agrawal, S., "Far Field Computational Boundary Conditions for Transonic Flows," Fourth International Symposium on Computational Fluid Dynamics, September 1991.

12. Van Den Berg, B., "Boundary Layer Measurements on a Two-Dimensional Wing with Flap," NLR-TR-79009-U, January 1979.

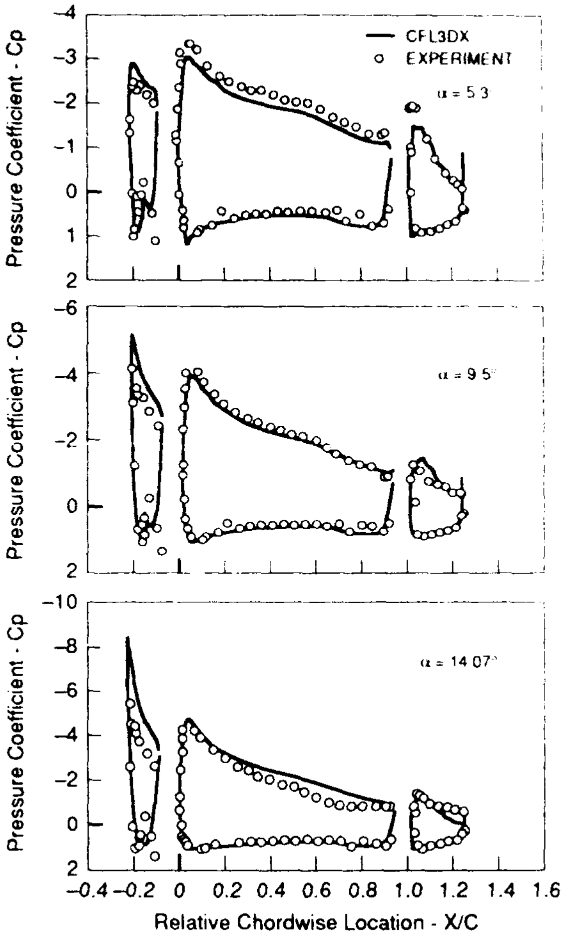

GP24-0518-20-V/bcb

Figure 20. Computed and Experimental Pressure Distributions for the GAW Airfoil With Slotted Flap and Slat
$M_\infty = 0.15$, $Re = 0.62 \times 10^6$

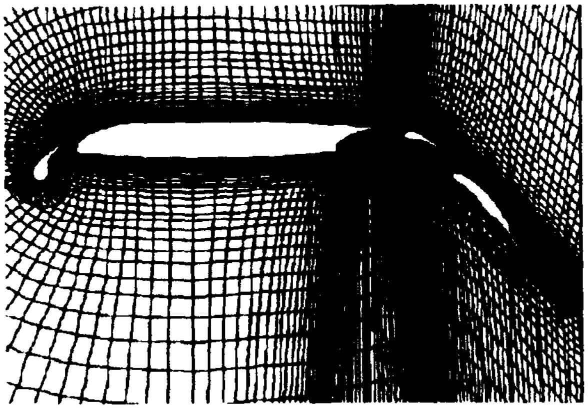

GP24-0518-21-V-tpk

Figure 21. Four Element Airfoil Grids

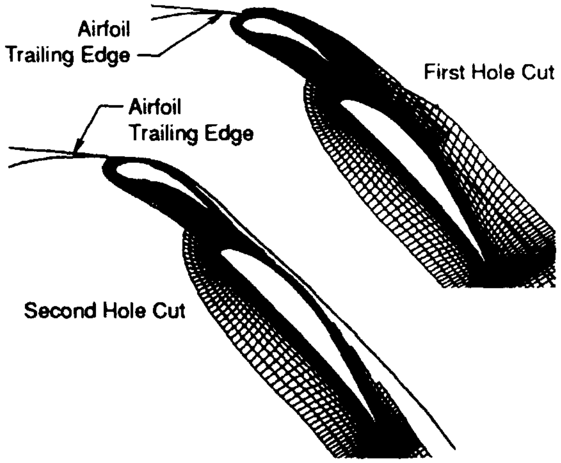

GP24-0518-22-V-tpk

Figure 22. Illustration of Two Hole Cutting Techniques for Four-Element Airfoil

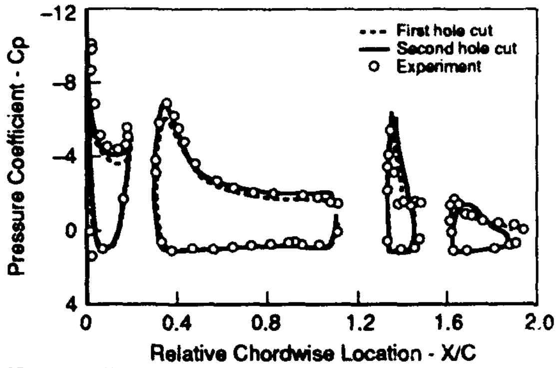

GP24-0518-23-V-tpk

Figure 23. Effect of Different Hole Boundaries on Four-Element Airfoil Pressure Distribution
$M_\infty = 0.2$, Alpha = 8.13°

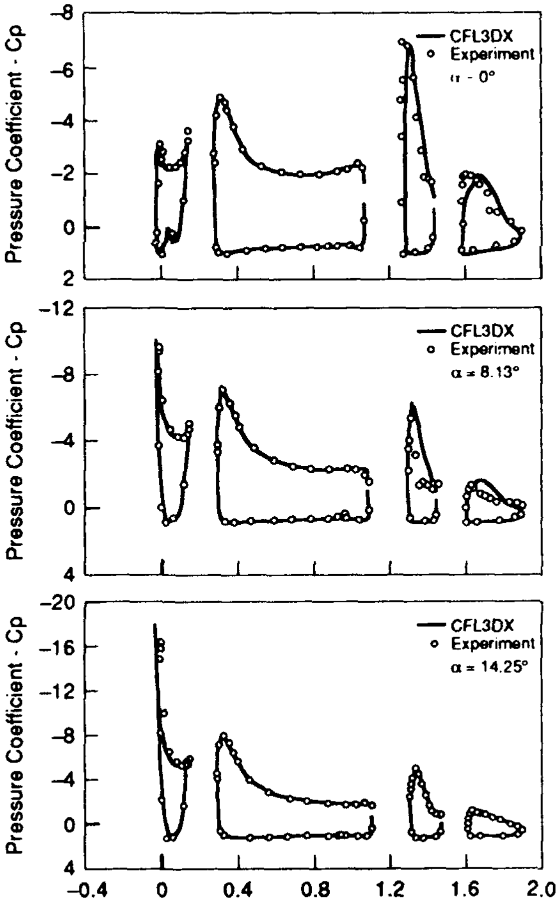

GP24-0518-24-V/jls

Figure 24. Measured and Predicted Pressures for Four Element Airfoil
$M_\infty = 0.2$, Re = 2.85×10^6

13. Braden, J.A., Whipkey, R.R., Jones, G.S., and Lilley, D.E., "Experimental Study of the Separating Confluent Boundary Layer," NASA CR 3655, June 1983.

14. Omar, E., et al, "Two-Dimensional Wind Tunnel Tests of a NASA Supercritical Airfoil with Various High Lift Systems - Volume II Test Data," NASA CR 2215, April 1977.

15. Rogers, S.E., Wiltberger, N.L., Kwak, D., "Efficient Simulation of Incompressible Viscous Flow Over Multi-Element Airfoils," Fifth Symposium on Numerical and Physical Aspects of Aerodynamic Flows, January 1992.

ACKNOWLEDGEMENTS

This work was supported under funding of the McDonnell Aircraft Independent Research and Development program. Computer resources were provided by the Numerical Aerodynamic Simulation Program at NASA Ames Research Center and by CRAY Research, Inc.

Numerical Solution of the Navier-Stokes Equations for High-Lift Configurations on Structured Composite Grids

T. E. Nelson D. W. Zingg G. W. Johnston

University of Toronto Institute for Aerospace Studies
4925 Dufferin Street, Downsview, Ontario
Canada, M3H 5T6

Summary

A numerical method is presented for the solution of the compressible Reynolds-averaged, thin-layer Navier-Stokes equations on structured composite grids as applied to high-lift configurations. The method is an adaptation of an implicit approximate factorization algorithm for block structured composite grids. Interfaces between blocks are treated by overlapping the grids and taking one layer of points from neighboring blocks. Turbulence is treated using the Baldwin-Barth one-equation turbulence model.

High-lift applications presented for comparison with wind tunnel data include: a NACA 4412 airfoil with NACA 4415 flap, a GA(W)-1 airfoil with a 29% chord flap at 30 degree flap angle and two gap settings, and a GA(W)-1 airfoil with 15% chord slat and 29% chord flap. Good agreement with experimental data is obtained for cases with fully attached flow or small regions of separated flow. For cases with extensive regions of flow separation, the thickness and extent of the separated regions are underpredicted.

Nomenclature

a	speed of sound
A, B, M	flux Jacobians
c	chord length
C_D	drag coefficient
C_L	lift coefficient
C_M	pitching moment coefficient
C_p	pressure coefficient
E, F, S	flux vectors
G	gap
h	time step
J	Jacobian
$\mathcal{M}$	Mach number
O	overlap
Pr	Prandtl number
p	pressure
Q	solution vector
$\Re$	Reynolds number
T	eigenvector matrix
u, v	Cartesian velocities
U, V	contravariant velocities
x, y	Cartesian coordinates
α	angle of attack
β	relaxation constant
γ	ratio of specific heats
δ	deflection angle
δ_ξ, δ_η	spatial central difference operators
Λ	eigenvalue matrix
ξ, η	curvilinear coordinates
ρ	density
τ	nondimensional time

Subscripts

f	flap
m	main airfoil
s	slat

Superscript

n	time step

1 Introduction

The flow around two-dimensional high-lift configurations is complex, often containing multiple separated regions, confluent boundary layers and compressibility effects, even at low onset flow speeds. The performance of high-lift devices, especially close to stall, can be difficult to predict and requires the solution of at least the Reynolds-averaged Navier-Stokes equations with a turbulence model. This is an expensive computational task which is made even more time consuming by the necessity of generating a field grid.

Considerable progress has been made in solving the Navier-Stokes equations for high-lift configurations. Recent papers on the topic include methods for the incompressible Navier-Stokes equations [1] and for the compressible Navier-Stokes equations [2], [3],[4],[5]. Investigators have employed structured, patched grids [1], [2],[3], overlapping Chimera grids [1], [5] and unstructured grids [4]. Turbulence models used include the Baldwin-Lomax model [1], [2], [3], [4],[5] and the Baldwin-Barth model [1], [5].

However, many difficulties still remain. Turbulence models which are simple enough for practical computations can be inaccurate for complex flows. Unsteady flow may occur on high-lift configurations especially near stall or post-stall. Such cases require time accurate computations. This paper applies a well-established numerical method for the Navier-Stokes equations to several high-lift configurations. Extensive comparisons with experimental data are made including turbulence data, thereby contributing to the evaluation of the Baldwin-Barth turbulence model [6].

2 Grid Generation

A computational grid is needed in the flow field surrounding the high-lift system of airfoils in order to solve the Navier-Stokes equations. Generating an appropriate grid around a practical multi-element geometry can be a difficult task. Problems encountered include blunt trailing edges, various gaps and overlaps between elements, detachable slats, and cove regions with sharp corners.

A single structured body-conforming grid cannot usually be generated around practical configurations so either unstructured grids or structured composite grids are required. By first dividing the domain into topologically rectangular blocks, a structured grid may be generated within each block. This approach is taken here and is known as multi-block. It has been used by a number of researchers for practical problems in two and three dimensions [7].

An automated procedure has been used to divide the domain into topologically rectangular blocks and generate grids [8]. The grid generation is accomplished in three steps. First the domain is divided into blocks by tracing streamlines and equipotential lines determined from the solution of the potential flow problem, computed using a panel method. Curves specifying block boundaries, block connections and boundary conditions required by the grid generator and solver are all determined automatically. The result is an H-type topology about the configuration. An example of the block decomposition and the connections that result is shown in Figure 1 for the case of an airfoil and flap. Fewer blocks could be specified by allowing multiple connections or multiple boundary conditions on block sides. However, to maintain simplicity for the flow solver, blocks with only one connection or boundary condition on each side have been permitted.

Grids of types other than H may be generated by specifying the block boundaries manually. For example, a stacked C-type grid could be generated by interactively defining the block boundaries with a CAD program. The advantage of the automated approach is the ease with which new geometries may be gridded. For instance, a matrix of gaps and overlaps for a flap optimization study may be quickly gridded with approximately the same number of points and resolution. In contrast, specifying the block boundaries interactively is a lengthy process for each geometry and would be onerous for optimization studies. The disadvantage of the automated procedure is that the H-type topology requires more points to resolve the flow than C or O type grids. This increases memory requirements and computing time for the solver.

The second step in the grid generation procedure is to distribute points on block sides and produce an interior grid. Points may be distributed by a variety of methods, but usually hyperbolic tangent distributions are used so the spacing at each end of a block side may be specified. Also, if desired, points may be clustered part way along a block side. Within each block, a starting grid is generated using a simple algebraic technique, transfinite interpolation.

Finally, the composite grid is smoothed using an elliptic grid generation method [9]. Block boundaries are usually held fixed, with fixed points on each side. However, they may also be allowed to move freely as part of the solution of the elliptic system. Or, alternatively, the boundary points may be allowed to move constrained to the original boundary curves.

The final grid is smooth, with point and slope continuity of grid lines at block boundaries. Also, grid lines are usually orthogonal at block edges. The exception is at special points, where slope continuity cannot be maintained. An example of a complete grid for the GA(W)-1 airfoil and flap in a wind tunnel is shown in Figure 2.

3 Numerical Technique for Solving the Navier-Stokes Equations

3.1 Solution Method

The solution method used here for the thin-layer Navier-Stokes equations is an adaptation of the diagonal form of the Beam and Warming implicit approximate factorization algorithm in generalized coordinates, as used in the program ARC2D [10]. The method is summarized here to enable discussion of interface conditions.

The thin-layer Navier-Stokes equations in generalized curvilinear coordinates are

$$\partial_\tau \widehat{Q} + \partial_\xi \widehat{E} + \partial_\eta \widehat{F} = \Re^{-1} \partial_\eta \widehat{S} \tag{1}$$

where

$$\widehat{Q} = J^{-1} \begin{bmatrix} \rho \\ \rho u \\ \rho v \\ e \end{bmatrix}, \tag{2}$$

$$\widehat{E} = J^{-1} \begin{bmatrix} \rho U \\ \rho u U + \xi_x p \\ \rho v U + \xi_y p \\ U(e+p) - \xi_t p \end{bmatrix}, \tag{3}$$

$$\widehat{F} = J^{-1} \begin{bmatrix} \rho V \\ \rho u V + \eta_x p \\ \rho v V + \eta_y p \\ V(e+p) - \eta_t p \end{bmatrix} \tag{4}$$

$$\widehat{S} = J^{-1} \begin{bmatrix} 0 \\ \eta_x m_1 + \eta_y m_2 \\ \eta_x m_2 + \eta_y m_3 \\ \eta_x (u m_1 + v m_2 + m_4) \\ + \ \eta_y (u m_2 + v m_3 + m_5) \end{bmatrix} \tag{5}$$

and

$$\begin{aligned} m_1 &= \mu(4\eta_x u_\eta - 2\eta_y v_\eta)/3 \\ m_2 &= \mu(\eta_y u_\eta + \eta_x v_\eta) \\ m_3 &= \mu(-2\eta_x u_\eta + 4\eta_y v_\eta)/3 \\ m_4 &= \mu Pr^{-1}(\gamma-1)^{-1}\eta_x \partial_\eta (a^2) \\ m_5 &= \mu Pr^{-1}(\gamma-1)^{-1}\eta_y \partial_\eta (a^2) \end{aligned} \tag{6}$$

With implicit Euler time marching, approximate factorization and centered spatial differences, the delta form of the algorithm is

$$[I + h\delta_\xi \widehat{A}^n][I + h\delta_\eta \widehat{B}^n - h\Re^{-1}\delta_\eta J^{-1} \widehat{M}^n]\Delta\widehat{Q}^n = \widehat{R}^n \tag{7}$$

where the right-hand side is

$$\widehat{R}^n = -h[\delta_\xi \widehat{E}^n + \delta_\eta \widehat{F}^n - \Re^{-1}\delta_\eta \widehat{S}^n] \tag{8}$$

The matrices $\widehat{A}$, $\widehat{B}$ and $\widehat{M}$ are the flux Jacobians, defined by

$$\widehat{A} = \frac{\partial \widehat{E}}{\partial \widehat{Q}}, \quad \widehat{B} = \frac{\partial \widehat{F}}{\partial \widehat{Q}}, \quad \widehat{M} = \frac{\partial \widehat{S}}{\partial \widehat{Q}} \tag{9}$$

and $\Delta\widehat{Q}^n = \widehat{Q}^{n+1} - \widehat{Q}^n$.

The diagonal form of the algorithm is

$$T_\xi \left[I + h\delta_\xi \Lambda_\xi\right] \widehat{N} \left[I + h\delta_\eta \Lambda_\eta\right] T_\eta^{-1} \Delta\widehat{Q}^n = \widehat{R}^n \tag{10}$$

where

$$\Lambda_\xi = T_\xi^{-1} \widehat{A} T_\xi \tag{11}$$

$$\Lambda_\eta = T_\eta^{-1} \widehat{B} T_\eta \tag{12}$$

and

$$\widehat{N} = T_\xi^{-1} T_\eta \tag{13}$$

The matrices Λ_ξ and Λ_η are diagonal matrices whose elements are the eigenvalues of the flux Jacobians. The viscous flux Jacobian $\widehat{M}$ cannot be diagonalized with the flux Jacobian $\widehat{B}$ so it has been dropped from the left hand side of equation (10). However, a term approximating the viscous eigenvalues is added to the diagonal, as described by Pulliam [10]. With combined second and fourth order implicit nonlinear dissipation, the diagonal algorithm requires the solution of scalar pentadiagonal systems of equations rather than block pentadiagonal systems, which are required for equation (7).

3.2 Application of Boundary Conditions

For implicit centered difference codes with explicit boundary conditions all variables must be specified at each boundary. As a result, the number of numerical boundary conditions required may exceed the number of physical boundary conditions. In a multi-block scheme, if each block is to be solved independently then additional conditions must also be specified at grid interfaces.

The boundary conditions used here closely follow the work of Pulliam [10]. The exception is a viscous outflow boundary for internal flows, specifically the case of an airfoil in a wind tunnel; then the static pressure is specified. If both the upstream and downstream pressures are known from the experiment then they may be specified directly. Otherwise the downstream pressure is adjusted such that the inflow pressure is p_∞. Thus for internal flow at a subsonic viscous outflow boundary ρ, ρu, and ρv are extrapolated from the interior and

$$p^n_{\text{outflow}} = p^{n-1}_{\text{outflow}} + \beta \Delta p^{n-1} \tag{14}$$

where β is a relaxation constant and

$$\Delta p = p_{\infty} - p_{\mathrm{inflow}} \tag{15}$$

and p_{inflow} is defined to be the average of the upper and lower wall pressures just downstream of the inlet.

3.3 Interface Conditions at Block Boundaries

In a structured data base, the solution is stored in a series of $n \times m \times 4$ arrays with the boundary between neighboring blocks stored in both blocks. The solution technique, however, requires additional information from the neighboring blocks if a solution is to be obtained for the interface points. This introduces the concept of halo points. If a block is surrounded by an extra layer of points, then prior to the next solution step, the halo points may be filled with data from the adjacent block. These data may then be used as required.

Halo points can be used in several ways. The usual approach is to determine how far away the algorithm needs data and then to copy the appropriate number of rows or columns of points. Normally, artificial dissipation is the constraining quantity and for the form of dissipation used here, three extra rows would be required. Alternatively, just one row of halo points can be used. Rather than computing the dissipation in one step, intermediate quantities can be computed and stored in workspace arrays and data passed to halo points of the workspace arrays. The advantage of the first approach is that only one copy between blocks is required at the beginning of each step. In the second approach, which is used here, less memory is needed for halo point data but additional copies are required. Care must be taken when copying data between blocks because the storage location and sign of the data may change depending on the orientation of the blocks and the data type.

Once the dissipation terms and the right hand side have been determined for each block, an implicit time step may be taken and equation (10) may be solved in two steps. If the product matrix $\hat{N}$ is split into its factors $T_{\xi}^{-1}T_{\eta}$ then equation (10) may be rewritten as shown

$$T_{\xi}\left[I + h\delta_{\xi}\Lambda_{\xi}\right]T_{\xi}^{-1}\Delta\hat{Q}^{n}_{*} = \hat{R}^{n} \tag{16}$$

$$T_{\eta}\left[I + h\delta_{\eta}\Lambda_{\eta}\right]T_{\eta}^{-1}\Delta\hat{Q}^{n} = \Delta\hat{Q}^{n}_{*} \tag{17}$$

After the ξ sweep is completed, two values of $\hat{Q}^{n}_{*}$ are obtained for the block boundaries. An intermediate update is then applied so that

$$\Delta\hat{Q}^{n}_{*I} = \frac{1}{2}\left(\Delta\hat{Q}^{n}_{*1} + \Delta\hat{Q}^{n}_{*2}\right) \tag{18}$$

the new values of $\Delta\hat{Q}^{n}_{*I}$ are then loaded into both adjacent blocks for use in the next sweep. After the η sweep is completed, the values on the boundaries are averaged again,

$$\Delta\hat{Q}^{n}_{I} = \frac{1}{2}\left(\Delta\hat{Q}^{n}_{1} + \Delta\hat{Q}^{n}_{2}\right) \tag{19}$$

and this average value is used to update the solution on both blocks. Although this simple interface condition is not nonreflecting, the resulting multi-block procedure is as robust as the original algorithm and, most importantly, converges to exactly the same solution obtained on a single block grid. At the interface, disturbances are partially reflected but these are most noticeable at start-up when the boundary conditions are ramped in. Over several hundred iterations they appear to be no worse than the reflections due to the explicit boundary conditions and the rate of convergence is not adversely effected.

It is very important that the metrics and dissipation be treated in the same manner across a block interface. Otherwise, the program may fail to converge completely or may diverge. Also, if the intermediate update is not applied then the stability of the scheme is severely degraded.

3.4 Turbulence Model

The choice of turbulence model can have a significant impact on computing times and accuracy. Usually, simple algebraic models such as the Baldwin-Lomax model have been employed [11]. These models have been used successfully for single element airfoil computations including shock/boundary-layer interactions, small separations [12] and computations near maximum lift [13].

For high-lift computations with multiple elements, simple algebraic eddy viscosity models are inadequate. Confluent boundary layers, large separated regions and separated wakes cannot be treated properly. One would expect that improved results could be obtained with one-equation or two-equation eddy viscosity models. There are indications, however, that even these models may be unable to predict the interaction of a wake and a boundary layer [14] or large separations [15] and that algebraic Reynolds stress models or even more elaborate turbulence models are required. In particular, Squire found that the strong interaction of the near wake of a slat with a main airfoil boundary layer may result in 'negative eddy viscosity' [14]. This phenomenon cannot be modelled by an eddy viscosity model. Such effects are quite local, and should not dominate the flow. As a result, one-equation or two-equation models may be adequate in many situations.

The turbulence model used in this paper is that of Baldwin and Barth [6]. It is a one-equation model that is fairly easy to implement and has recently been applied to high-lift problems by Rogers et al. [1] for the incompressible Navier-Stokes equations and by Rentze et al. [5] for the compressible Navier-Stokes equations on Chimera overset grids.

Prior to implementing the model in the multiblock code, it was tested for a single element airfoil at high lift and compared to the Baldwin-Lomax turbulence model. The test case selected, which was previously examined by Anderson et al. using the Baldwin-Lomax turbulence model [13], is a NACA 0012 airfoil at $\Re = 3.0 \times 10^6$ and $\mathcal{M} = 0.3$. The computed and experimental lift coefficients are shown in Figure 3. As may be seen from the plot, the prediction of $C_{L_{max}}$ is lower for the Baldwin-Barth model than for the Baldwin-Lomax model, which is very close to the experimental results. At angles of attack higher than 16 degrees the solution became unsteady for both turbulence models and steady post-stall solutions could not be obtained.

4 Results

4.1 NACA 4412 Airfoil with NACA 4415 Flap

The first multi-element case considered is the airfoil and flap experiment of Adair and Horne [16]. The experiment consisted of surface pressure measurements and flow field measurements of velocity and turbulence quantities using both hot-wire and laser anemometry. The airfoil section was a NACA 4412 with a NACA 4415 flap. The model was positioned at $\alpha = 8.2°$, $\delta_f = 21.8°$, $G_f = 3.5\%c$, $O_f = 2.8\%c$ and tested at $\Re = 1.8 \times 10^6$, $\mathcal{M} = 0.09$. Transition was fixed at $x/c = 0.025$ and $x/c = 0.010$ downstream from the pressure minimum on the main airfoil upper and lower surfaces respectively. On the upper surface of the flap, transition was fixed at $x/c = 0.008$ downstream of the minimum pressure; on the lower surface transition was free. The data presented were not corrected for wind tunnel wall effects, so the wind tunnel was included in the computations. Inviscid boundary conditions were applied at the wind tunnel walls to avoid computing the wind tunnel wall boundary layer. The wind tunnel test section extended two chords upstream of the leading edge and three chords downstream, so the computational boundaries were placed at the same locations. Approximately 70,000 points were used for the grid and the off-wall spacing was set to $2 \times 10^{-5}c$ to ensure that $y^+ < 1$ for the first point off the surface.

In initial computations, transition was fixed at the locations specified in the experiment. A laminar separation bubble was predicted on the main airfoil. Unfortunately, the bubble was not stable and was occasionally shed downstream, resulting in an unsteady solution. In order to obtain steady results, the transition point was moved forward to the leading edge.

The computation was performed for the NACA 4412 and NACA 4415 airfoils with both sharp and blunt trailing edges. For sharp trailing edge airfoils, the computation converged very well. With blunt trailing edges, some unsteadiness occurred in the wake region which prevented complete convergence. A comparison of the convergence history for the two cases is shown in Figure 4. Differences between the two solutions were small and the results presented below are for the blunt base airfoils.

A comparison of the pressure distribution with experiment is shown in Figure 5. The pressure distribution on the flap agrees quite well with experiment and the flow separates at 87% flap chord, close to the experimentally observed value of 93%. The computed suction peak on the main airfoil is higher than in the experiment and results in additional lift. Wind tunnel wall pressures are shown in the same figure and the agreement is fairly good except near the upstream and the downstream boundaries. The discrepancy near the boundaries indicates that the location of the boundaries may have affected the computational results.

Comparisons of velocity profiles at five stations are shown in Figure 6. As may be seen in the figure, the boundary layer is predicted quite well on the main airfoil at stations 1 and 2. The flow velocity through the slot, station 4, is underpredicted but the wake of the main airfoil is predicted fairly well. At the flap trailing edge, station 12, the computed flow has a separated boundary layer profile but the region of reversed flow is thinner than seen in the experiment. Similar results for profiles and pressure distribution were obtained by Rogers et al. [1] using an incompressible Navier-Stokes solution method with the Baldwin-Barth turbulence model.

4.2 GA(W)-1 Airfoil with 29% chord Fowler Flap

The next case considered is a GA(W)-1 airfoil with a 29% chord Fowler flap. The experimental data are from Braden, Whipkey, Jones and Lilley, who investigated the flow field for 25 combinations of flap settings, slat settings and angles of attack [17]. Included in the experiment were laser velocimeter measurements of velocity profiles, turbulence intensities and Reynolds shear stresses. Also included were surface pressure measurements, and skin friction and boundary-layer parameters derived from the profiles. All the data from the wind tunnel report were uncorrected, so wind tunnel walls were again included in the computations. The tunnel height was 3.33 chords, the upstream boundary was placed at 4 chords ahead of the leading edge and the downstream boundary was placed 5 chords downstream of the leading edge. The off-wall spacing for the grids was again set to $2 \times 10^{-5}c$ to ensure that $y^+ < 1$ for the first point off the surface. Approximately 60,000 points were used for each grid and typically 20 to 30 points were included across boundary layer regions.

Experimental test conditions were $\Re = 0.62 \times 10^6$ and 20 psf which correspond to $M = 0.116$. Transition was free but was noted to occur naturally at less than 5% chord on the upper surface of the main airfoil and between 50 and 65% chord on the lower surface of the main airfoil. For the computations, the upper surfaces of the main airfoil and flap were assumed to be fully turbulent and transition was set on the lower surfaces at 55% chord on the main airfoil and just ahead of the trailing edge on the flap.

Computations were performed on four airfoil and flap configurations. The cases selected were all $\delta_f = 30°$ with overlap $O_f = 0.0\%c$. Angles of attack of $\alpha = 4°$ and $\alpha = 8°$ were computed with two gaps, $G_f = 2.5\%c$ and $G_f = 4.0\%c$. The designations are shown in Table 1. The case with $G_f = 2.5\%c$ and $\alpha = 8°$, designated B4.5, was not included in the experiment but was computed here to examine the effect of the flap gap. For the narrow gap, cases B4 and B4.5, the flow over the flap is fully attached. However, with the wide gap, cases B1 and B2, there is a large separated flow region on the flap.

Table 1: Summary of GA(W)-1 airfoil and flap configurations.

Case	α	δ_f	G_f	O_f
B1	3.98	30	4.0	0.0
B2	7.94	30	4.0	0.0
B4	4.13	30	2.5	0.0
B4.5	8.00	30	2.5	0.0

The computed pressure distribution for case B4 agrees well with experiment, as may be seen in Figure 7. Boundary layer and Reynolds shear stress profiles for the upper surface of the main airfoil are shown in Figure 8. The velocity profiles show good agreement, although the Reynolds stress is overpredicted in the outer boundary layer.

On the flap, similar results are obtained for the confluent boundary layer velocity profiles, as shown in Figure 9. The wake of the main airfoil is captured well as is the development of the flap boundary layer. Near the trailing edge a very small separated region is predicted at station 70 but the experimental profile appears to be attached. Agreement for the Reynolds stress profiles is only fair. In the wake of the main airfoil the magnitude of the Reynolds stress is initially overpredicted but further downstream is significantly underpredicted. This agrees with results presented by Rentze et al., who showed that the Baldwin-Barth turbulence model underpredicted the eddy viscosity in the wake of a slat as it developed across the upper surface of the main airfoil [5]. This result will be discussed further in the next section.

In all four airfoil and flap computations the separation in the cove region of the main airfoil is significantly underpredicted. An example is shown in Figure 10 for case B2 which is typical of all four cases. At $x/c = 0.66$, which corresponds to the entrance of the cove, the computed boundary layer profile is attached whereas the experimental profile is separated. Further downstream at $x/c = 0.71$ and $x/c = 0.76$ the computed value of the maximum reversed flow velocity is correct but the bubble is only one-third as thick as in the experiment. After the flow reattaches, the profiles are predicted well as seen at $x/c = 0.92$. This station corresponds to the entrance of the slot and demonstrates that underpredicting the separation in the cove does not dramatically affect the slot flow and hence the flap loading. This agrees with experiments which have demonstrated that high-lift performance is fairly insensitive to cove shape [18].

For the wide gap cases, there is a large separation on the flap. For case B1, $\alpha = 4°$, the flap separation is underpredicted, as shown in Figure 11. Because the flap separation is underpredicted, the flap carries more load than it should which in turn increases the loading of the main airfoil. Profiles of the velocity in the confluent boundary layer over the flap are shown in Figure 12. The main airfoil wake is initially captured well but becomes progressively worse. The flap separation may be seen clearly at station $(x/c)_f = 0.27$. Although the computed profile is separated, the extent of reversed flow is much too small. This result is similar to that seen for the cove separation on the main airfoil. However, high-lift performance is sensitive to flap separation whereas the cove separation is not as significant.

A comparison of the lift coefficients for the computed cases with the experimental data from Braden et al. is shown in Figure 13. The effect of gap is underpredicted because the flap separation is underpredicted. Also included in the plot are corrected experimental lift coefficients from Wentz and Seetharam, which were obtained at $\Re = 2.2 \times 10^6$ [19]. The computed lift coefficients are close to the lift curve from Wentz and Seetharam because in the higher Reynolds number experiment there is less extensive separated flow.

4.3 GA(W)-1 Airfoil with Slat and Flap

The three-element configuration considered here is a GA(W)-1 main airfoil with a 15%c slat at $\delta_s = 42°$, $G_s = 1.5\%c$, $O_s = 2.5\%c$, and a 29%c Fowler flap at $\delta_f = 40°$, $G_f = 1.5\%c$, $O_f = 1.5\%c$. The entire configuration is at $\alpha = 5.3°$ and corresponds to case F-1 of Braden et al. [17].

The flow field about a three element configuration is considerably more complicated than for a flap alone. The leading edge slat depresses the suction peak on the main airfoil which tends to delay stall. However, the slat wake interacts with the boundary layer on the upper surface of the main airfoil which promotes early boundary layer separation. The merging wakes then interact with the slot flow over the flap. The flow is further complicated by the separation in the cove region of the main airfoil and on the underside of the slat. A diagram of the three element case is shown in Figure 14.

The block decomposition for the three element case resulted in 31 blocks. A total of 90,000 points were used for the grid and the off-wall spacing grids was set to $2 \times 10^{-5}c$.

A comparison of the computed pressure distribution and experiment is shown in Figure 15. As may be seen in the figure, the pressure distribution agrees very well for the main airfoil and the flap. For the slat, however, the suction on the upper surface is overpredicted. This result is obtained because the computed separation on the lower surface of the slat is too small. As may be seen from the experimental pressure distribution, stagnation pressure was recorded at 13.5%c. In the computations, however, the reattachment point is further forward, at 10%c. Therefore, effectively, the slat has more camber which results in higher loading than seen in the experiment. The details of the computed flow may be seen in Figure 16 which clearly shows the large separation on the lower surface of the slat and the point of reattachment. The flow is attached at the upper surface trailing edge of both the main airfoil and flap, so the resulting pressure distributions for these elements agree fairly well with experiment. The separation in the cove region of the main airfoil is underpredicted as before.

Comparisons of velocity and Reynolds stress profiles for the upper surface of the main airfoil are shown in Figure 17. The effect of the merging slat wake on the boundary layer profile is clearly seen in the computations but is not well resolved in the experiment. However, it appears that the wake develops and merges more quickly in the computations than is seen in the experiment. This is consistent with the results of Rentze et al. [5] for a three-element configuration with the same turbulence model.

5 Conclusions

A method for solving the compressible thin-layer Navier-Stokes equations around high-lift configurations on structured composite grids has been presented. The method is based on the approximate factorization technique used in the program ARC2D. Interfaces between blocks are treated using a simple overlapping procedure with an intermediate update. Turbulence is modelled using the Baldwin-Barth one-equation turbulence model. Grids were generated with the aid of an automated procedure which divides the domain into blocks.

Good agreement with experiment is obtained when the flow about the configuration is attached or regions of separated flow are small. Computational difficulties encountered include laminar separation bubbles, multiple regions of separated flow and slightly unsteady flow in wake regions. Results tend to be poor for cases with large regions of separated flow in critical areas such as the flap upper surface or on the slat. Generally, the extent and thickness of reversed flow regions are underpredicted. The Baldwin-Barth turbulence model works well in most instances but tends to underpredict eddy viscosity in wake regions and overpredict eddy viscosity in the outer portion of boundary layers.

References

[1] Rogers, S. E., Wiltberger, N. L. and Kwak, D., "Efficient simulation of incompressible viscous flow over single and multi-element airfoils," AIAA Paper 92-0405, 1992.

[2] Chow, R. and Chu, K., "Navier-Stokes solution for high-lift multielement airfoil system with flap separation," AIAA Paper 91-1623-CP, June 1991.

[3] Shima, E., "Numerical analysis of multiple element high lift devices by Navier-Stokes equation using implicit TVD finite volume method," AIAA Paper 88-2574-CP, 1988.

[4] Mavriplis, D. J., "Euler and Navier-Stokes computations for airfoil geometries using unstructured grids," *CASI Journal*, vol. 36, pp. 62–71, June 1990.

[5] Rentze, K. J., Buning, P. G. and Rajagopalan, R. G., "A comparative study of turbulence models for overset grids," AIAA Paper 92-0437, January 1992.

[6] Baldwin, B. S., and Barth, T. J., "A one-equation turbulence transport model for high Reynolds number wall-bounded flows," NASA TM 102847, August 1990.

[7] Weatherill, N. P., "Mesh generation in CFD," Computational Fluid Dynamics, von Karman Institute for Fluid Dynamics Lecture Series, 1984-04.

[8] Nelson, T. E., Zingg, D. W., Johnston, G. W., "Automated grid generation for high-lift configurations," Canadian Aeronautics and Space Institute: Proceedings of the Third Canadian Symposium on Aerodynamics, November 1991.

[9] Thompson, J. F., Warsi, Z. U. A. and Mastin, C. W., *Numerical Grid Generation, Foundations and Applications*. North-Holland, 1985.

[10] Pulliam, T. H., "Efficient solution methods for the Navier-Stokes equations," Lecture Notes For The Von Karman Institute For Institute for Fluid Dynamics Lecture Series: Numerical Techniques For Viscous Flow Computation In Turbomachinery Bladings, January 1986.

[11] Baldwin, B. and Lomax, H., "Thin-layer approximation and algebraic model for separated turbulent flows," AIAA Paper 78-257, January 1978.

[12] Maksymiuk, C. M., and Pulliam, T. H., "Viscous transonic airfoil workshop results using ARC2D," AIAA Paper 87-0415, January 1987.

[13] Anderson, W. K., Thomas, J. L., and Rumsey, C. L., "Application of thin-layer Navier-Stokes equations near maximum lift," AIAA Paper 84-0049, January 1984.

[14] Squire, L. C., "Interactions between wakes and boundary-layers," *Prog. Aerospace Sci.*, vol. 26, pp. 261–288, 1989.

[15] Davidson, L. and Rizzi, A., "Navier-Stokes computation of airfoil in stall using algebraic Reynolds-stress model," AIAA Paper 92-0195, 1992.

[16] Adair, D. and Horne, W. C., "Characteristics of merging shear layers and turbulent wakes of a multi-element airfoil," NASA TM 100053, February 1988.

[17] Braden, J. A., Whipkey R. R., Jones, G. S., and Lilley, D. E., "Experimental study of the separating confluent boundary-layer," Volume I - NASA CR 3655, Volume II - NASA CR 166018, 1983.

[18] Wentz, Jr., W. H. and Ostowari, C., "Additional flow field studies of the GA(W)-1 airfoil with 30-percent chord Fowler flap including slot-gap variations and cove shape modifications," NASA CR-3687, 1983.

[19] Wentz, Jr., W. and Seetharam, H. C., "Development of a Fowler flap system for a high performance general aviation airfoil," NASA CR-2443, December 1974.

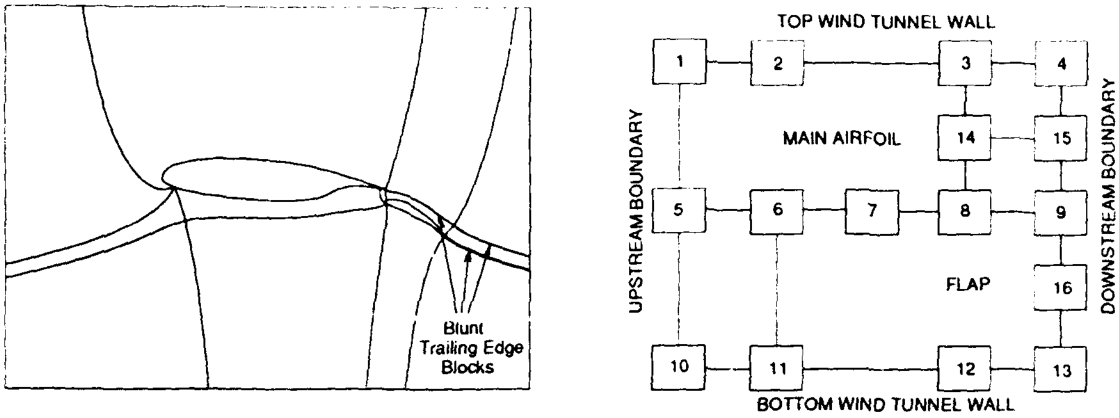

Figure 1: Automated block decomposition and the resulting block connections for the GA(W)-1 airfoil and flap in a wind tunnel.

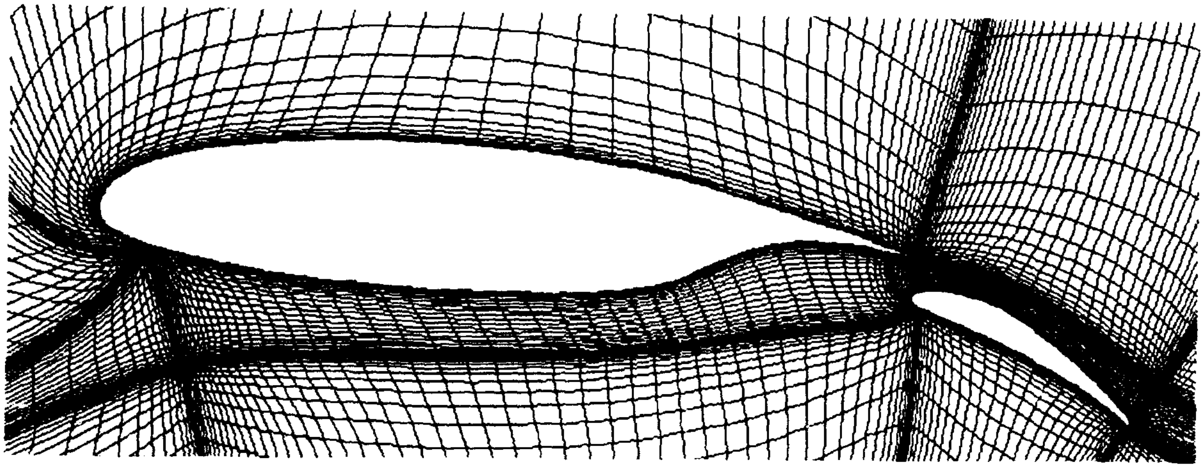

Figure 2: Near field grid for the GA(W)-1 airfoil and 29% chord Fowler flap in a wind tunnel, (plotted with every second grid line in each direction).

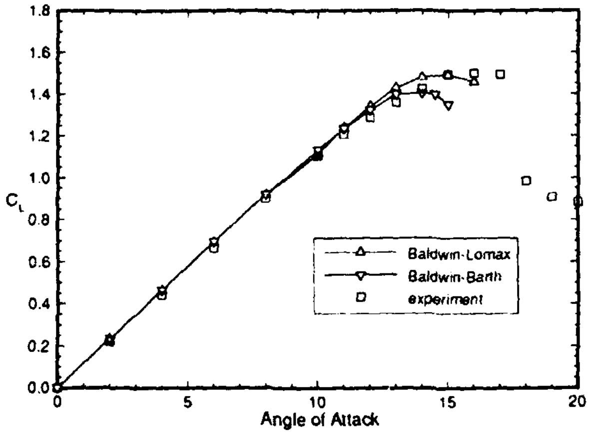

Figure 3: Computation of $C_{L_{max}}$ for NACA 0012 airfoil using the Baldwin-Barth and Baldwin-Lomax turbulence models.

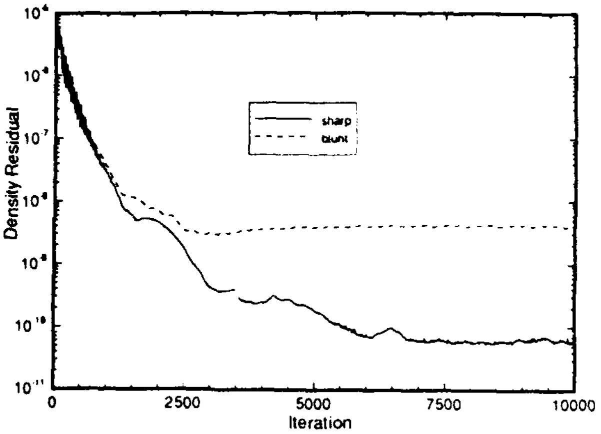

Figure 4: Convergence history for Adair and Horne test case of NACA 4412 airfoil with NACA 4415 flap. Results with sharp and blunt trailing edges.

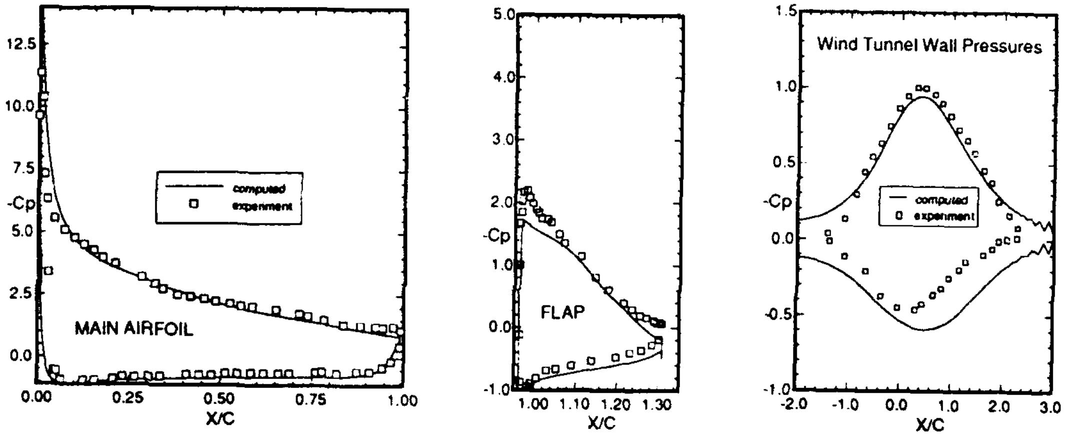

Figure 5: Surface pressures and wind tunnel wall pressures for Adair and Horne airfoil and flap test case.

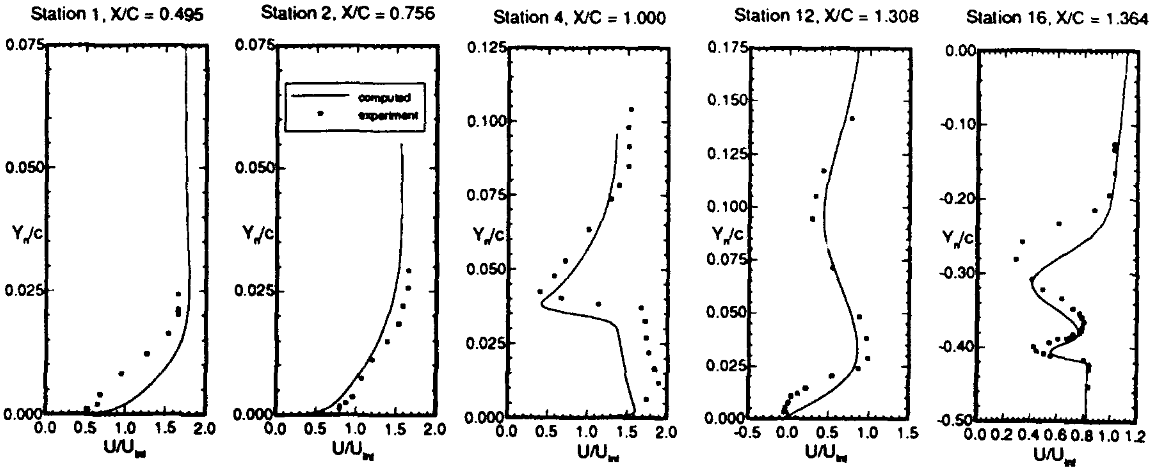

Figure 6: Comparison of velocity profiles for Adair and Horne airfoil and flap test case.

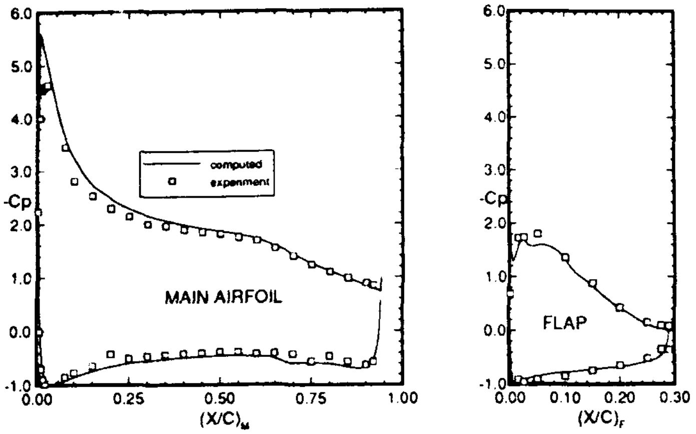

Figure 7: Comparison of experimental and computed pressure distributions for GA(W)-1 airfoil 29% chord Fowler flap case B4.

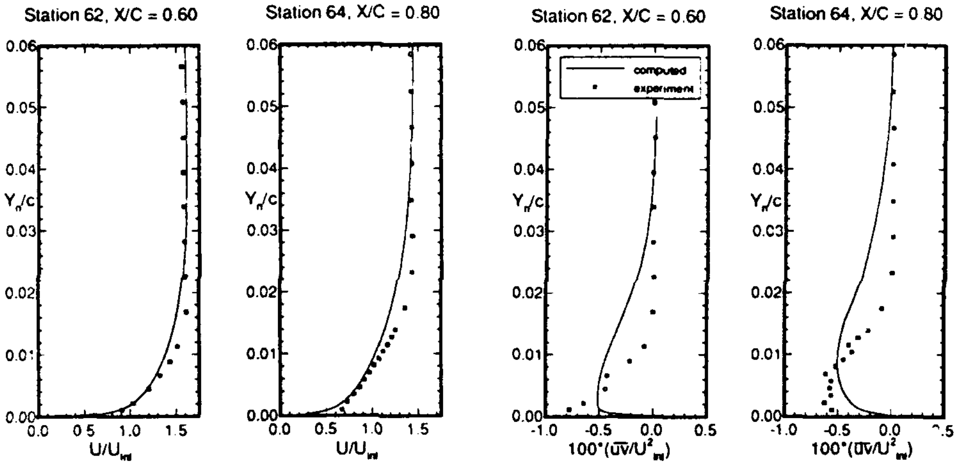

Figure 8: Boundary layer and Reynolds stress profiles on the upper surface of the main airfoil for the GA(W)-1 airfoil and flap case B4.

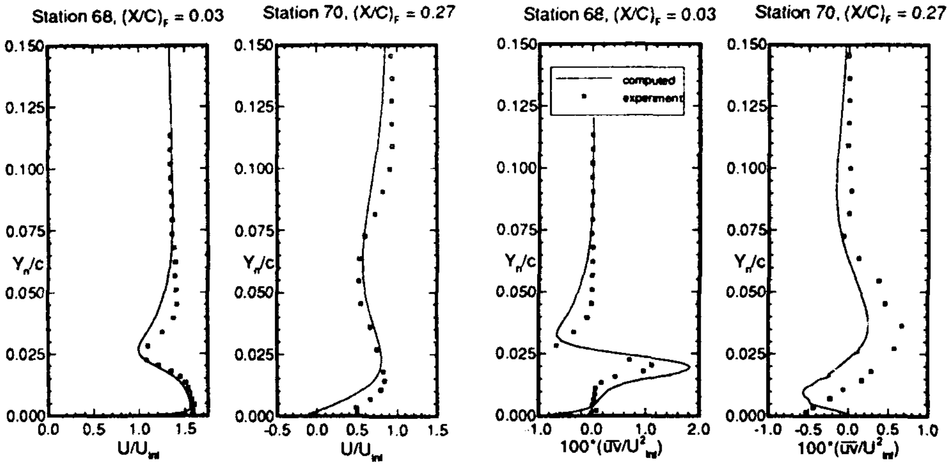

Figure 9: Boundary layer and Reynolds stress profiles on the upper surface of the flap for the GA(W)-1 airfoil and flap case B4.

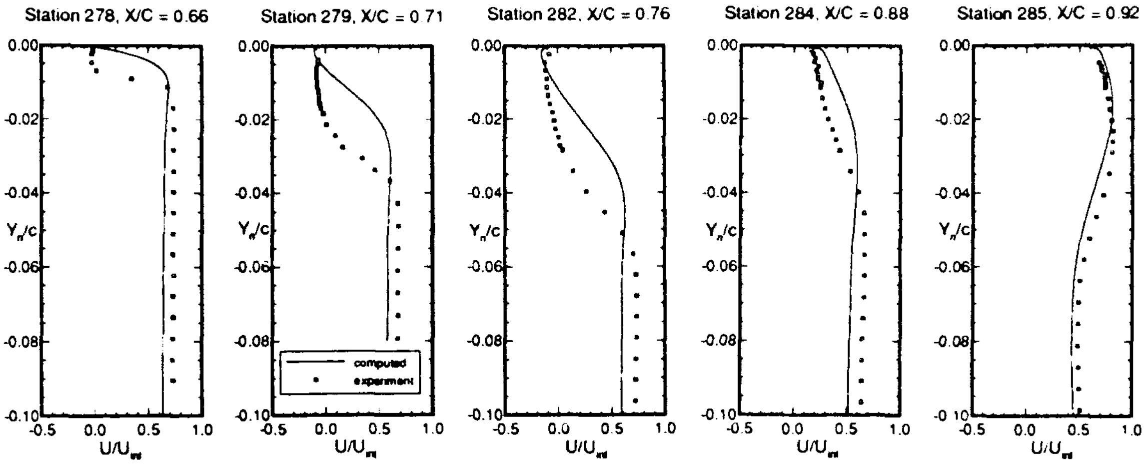

Figure 10: Boundary layer profiles in the cove region of the main airfoil for GA(W)-1 airfoil and flap case B2.

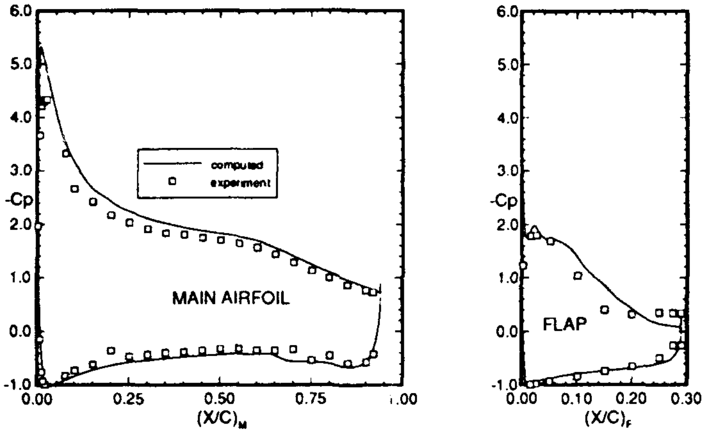

Figure 11: Comparison of experimental and computed pressure distributions for GA(W)-1 airfoil 29% chord Fowler flap case B1.

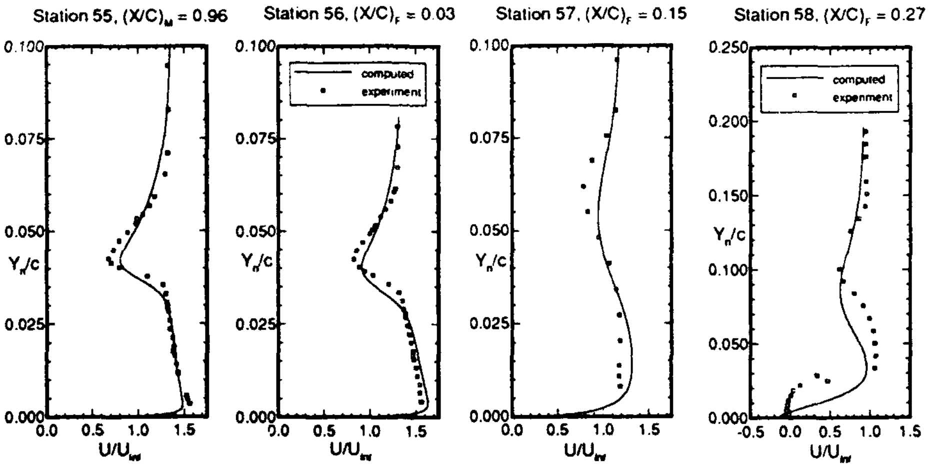

Figure 12: Boundary layer profiles on the upper surface of the flap GA(W)-1 airfoil and flap case B1.

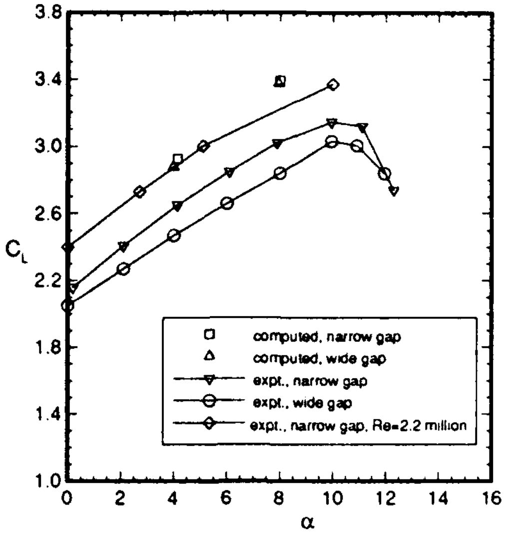

Figure 13: Lift curves for GA(W)-1 airfoil and flap test cases.

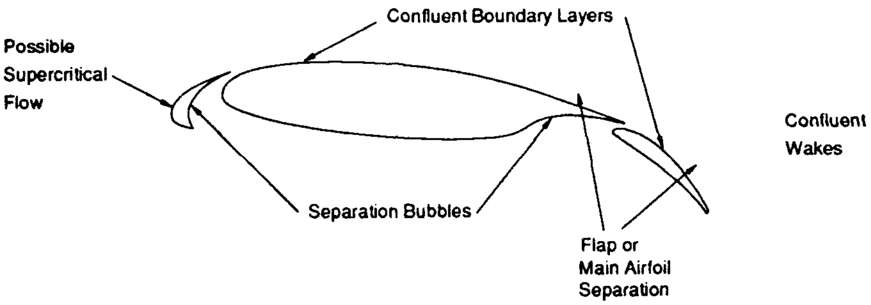

Figure 14: Flow field interactions around an airfoil with slat and flap.

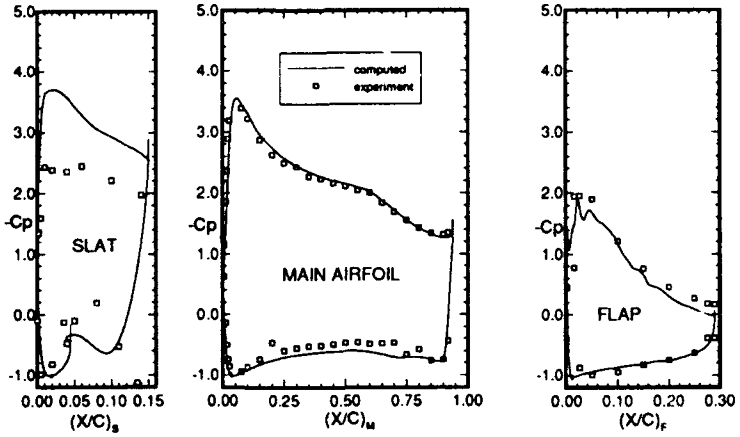

Figure 15: Comparison of experimental and computed surface pressures for GA(W)-1 airfoil with slat and flap.

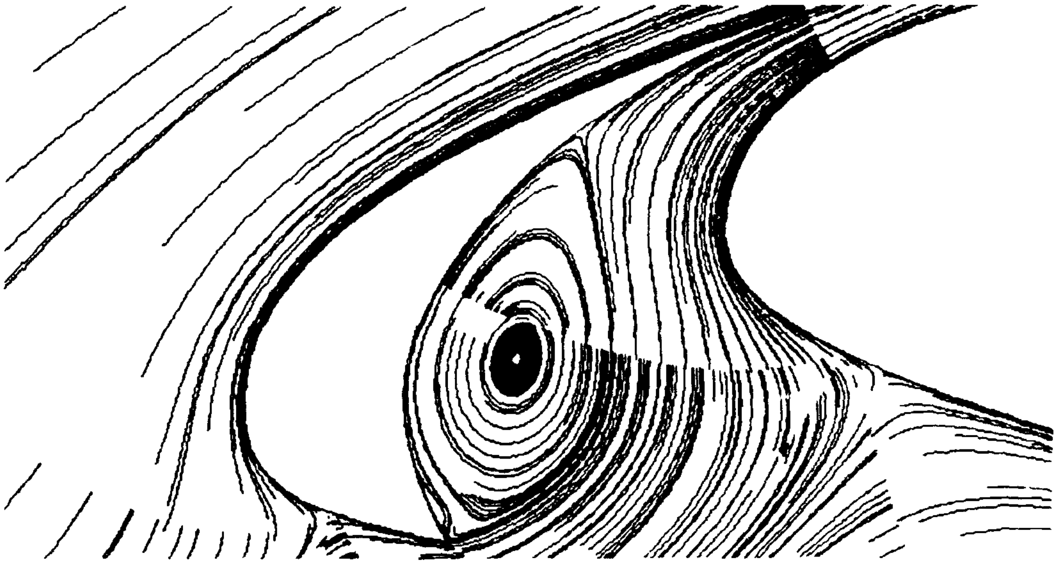

Figure 16: Streamlines on the lower surface of the slat for the GA(W)-1 airfoil with slat and flap.

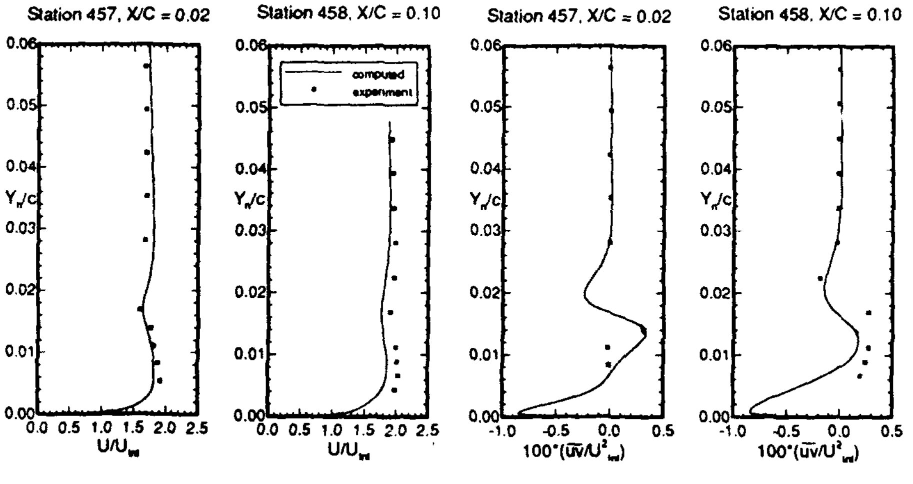

Figure 17: Velocity and Reynolds stress profiles on the main airfoil for GA(W)-1 airfoil with slat and flap.

High Reynolds Number Configuration Development of a High-Lift Airfoil

by

Walter O. Valarezo and Chet J. Dominik
Aerodynamics Research and Technology
Douglas Aircraft Company
3855 Lakewood Blvd., Long Beach, CA 90846, USA

and

Robert J. McGhee and Wesley L. Goodman
Fluid Mechanics Division
NASA Langley Research Center
Hampton, VA 23665-5225, USA

SUMMARY

An experimental program has been conducted to assess the performance of a transport multielement airfoil at flight Reynolds numbers. The studies were performed at chord Reynolds numbers as high as 16 million in the NASA Langley Low Turbulence Pressure Tunnel. Sidewall boundary-layer control to enforce flow two-dimensionality was provided via an endplate suction system. The basic airfoil was an 11.55% thick supercritical airfoil representative of the stall critical station of a new-generation transport aircraft wing. The multielement airfoil was configured as a three-element airfoil with slat and flap chord ratios of 14.48% and 30% respectively. Testing focused on the development of landing configurations with high maximum lift capability and the assessment of Reynolds and Mach number effects. Also assessed were high-lift performance effects due to devices such as drooped spoilers and trailing-edge wedges. The present experimental studies revealed significant effects on high-lift airfoil performance due to Reynolds and Mach number variations and favorable lift increments at approach angles of attack due to the use of drooped spoilers or trailing-edge wedges. However, no substantial improvements in maximum lift capability were identified. A recently developed high performance single-segment flap was also tested and results indicated considerable improvements in lift and drag performance over existing airfoils. Additionally, it was found that this new flap shape at its optimum rigging was less sensitive to Reynolds number variations than previous designs.

NOMENCLATURE

c	airfoil chord (slat and flap stowed)
C_ℓ	lift coefficient
$C_{\ell_{MAX}}$	maximum lift coefficient
C_p	pressure coefficient
M	Mach number
OH	overhang
RN	Reynolds number
α	angle of attack (degrees)
α_{STALL}	stall angle (degrees)
δ_F	flap deflection (degrees)
δ_S	slat deflection (degrees)
δ_{SP}	spoiler deflection (degrees)

1.0 INTRODUCTION

Increased performance requirements for high-lift systems in the commercial transport sector have caused renewed emphasis in multielement airfoil aerodynamics. The focus of the more recent research has been on understanding Reynolds and Mach number effects on high-lift optimization[1-5] with the ultimate aim of improving maximum lift capability as well as lift-to-drag ratios.

The majority of the reported investigations have discussed performance effects due to Reynolds and Mach number variations on generic high-lift configurations. Additionally, these studies have concentrated on reporting the results of rigging optimizations (gap/overhang) and their effect on airfoil performance. These investigations have greatly added to the existing high-lift database with relevant results at flight and near flight conditions.

This document reports on experiments conducted at high Reynolds numbers to develop performance concepts for high-lift transport aircraft applications. The concepts treated in this investigation are modifications to the trailing edge of the multielement airfoil and include deflected spoilers, trailing edge wedges, and a new single-segment flap design.

The work documented in this paper is the result of a cooperative experimental program conducted by the Douglas Aircraft Company and the NASA Langley Research Center. The experiments were conducted in the NASA Langley Low Turbulence Pressure Tunnel (LTPT) in Hampton, Virginia. The aim is to augment the existing database of Reynolds and Mach number effects on high-lift performance and new concepts.

2.0 MODEL GEOMETRIES

The model tested utilized an 11.55% thick supercritical airfoil representative of the estimated stall-critical location on an advanced design subsonic transport. The model spanned the width of the test section and had a clean (stowed) airfoil chord of 22 inches. The single-element and the multielement airfoils tested are shown in Figure 1. The slat chord ratio was 14.48% and the single-segment flap chord ratio was 30% of the stowed airfoil chord. Pressure orifices were located along the centerline of the model (146 taps for the three-element configuration) and along or near the trailing edge of each component. Surface pressures were measured via nine Electronic Sensing Pressure (ESP) modules calibrated to 15, 30, 45, and 100 psig as required by model aerodynamic loading. Accuracy for the ESP's was ± 0.1% of full scale value. Integration of pressure measurements yielded the forces presented in this publication. Four rows of streamlined support brackets for the high-lift devices (Figure 2) were required due to the very high loads (approximately 15,000 pounds) developed at some of the maximum lift conditions. The nomenclature defining the key geometric parameters of high-lift systems is shown in Figure 3.

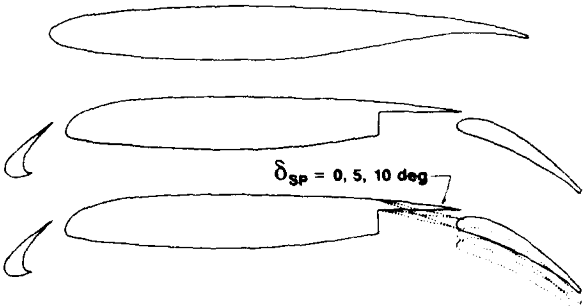

Figure 1. Airfoil Geometries Tested in the LTPT

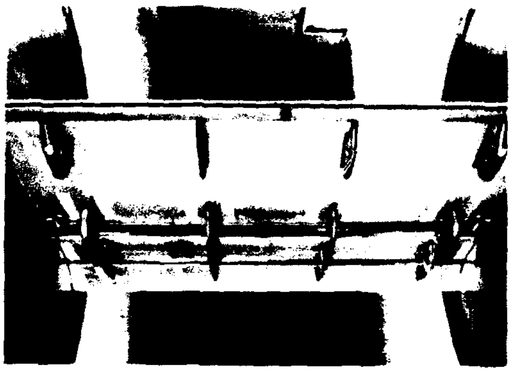

Figure 2. View of High-Lift Model Support Brackets

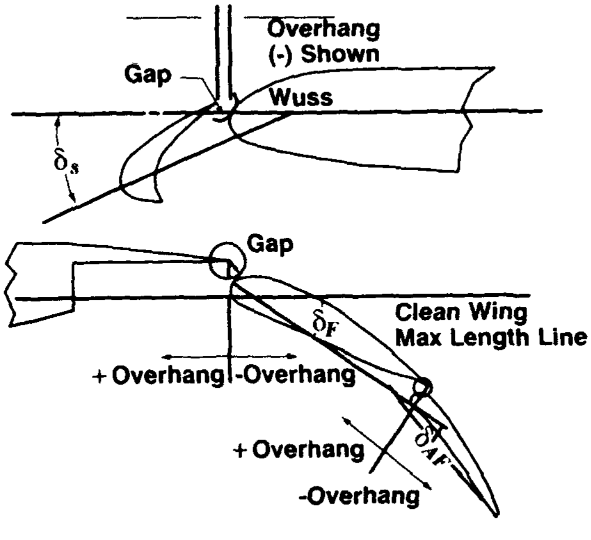

Figure 3. Nomenclature for Multielements

The model could also be configured with positively deflected spoiler surfaces with angles of 5° and 10° as shown in Figure 1. The spoiler geometry was removable and each spoiler deflection consisted of a steel model part at the appropriate deflection.

In addition to the above-mentioned configurations, trailing edge wedges which were 3% of chord in length were also tested on both the single- and three-element airfoils. A wedge angle of 30° was tested on the single-element and angles of 15°, 30°, 45°, and 60° were tested on the three-element configuration. The wedges were glued to the airfoil lower surface at the trailing edge. All wedges were sealed with Room Temperature Vulcanizer (RTV) to prevent flow through the wedge airfoil juncture. A sketch of a 30° trailing edge wedge applied to the single- and three-element airfoils is shown in Figure 4.

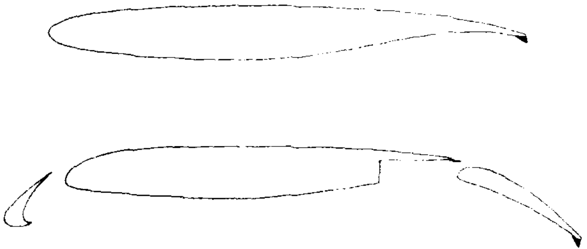

Figure 4. 30° Wedge on Single- and Three-Element Airfoils

3.0 LTPT TEST FACILITY

The Langley Low Turbulence Pressure Tunnel is a single return, closed-throat wind tunnel (Figure 5) that can be operated up to 10 atmospheres thus allowing very high Reynolds number capability[6]. The test section is 3 feet wide by 7.5 feet high by 7.5 feet long.

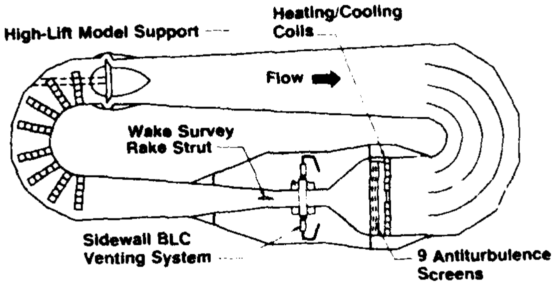

Figure 5. Schematic of Low Turbulence Pressure Tunnel

To promote two-dimensional flow over the model in view of its low aspect ratio and strong wall interference, a new side-wall boundary-layer control (BLC) system was installed in the LTPT[7]. The BLC system employed the differential pressure between the test section and the atmosphere to provide suction of the sidewall boundary-layer through porous endplates (Figures 6 and 7). The system yielded good quality two-dimensional flow over the model for the Reynolds numbers tested as indicated by the flap trailing edge spanwise pressures shown in Figure 8. The criterion used to define "two-dimensionality" was the observation (at run time) of sufficiently flat trailing edge pressures *in the spanwise* direction (±0.5% of leading edge peak). Examination of Figure 8 reveals that there are two peaks in the spanwise pressures at 15% and 85% span for the case with sidewall suction. These spikes were attributed to the presence of the outboard brackets (10.7% and 89.3% span) and were found to be relatively insensitive to sidewall suction rate. Hence, these peaks were not considered when assessing the two-dimensionality of the flow. Representative trailing edge pressures with these two spanwise stations removed are shown in Figure 8. While this procedure may appear somewhat arbitrary, it was found that removing the two pressure spikes caused by the brackets did not improve spanwise pressure distributions that were otherwise not flat (see also Figure 8.).

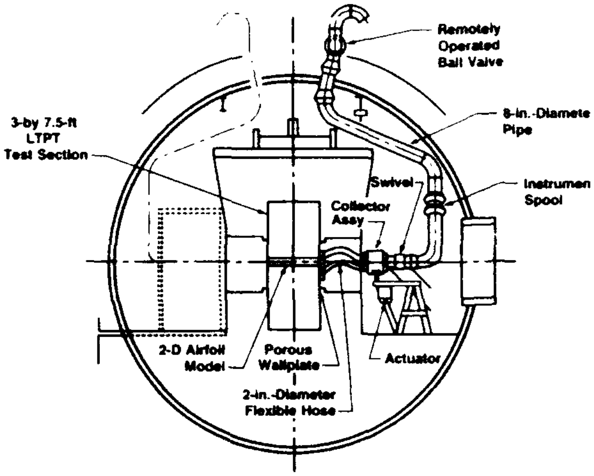

Figure 6. Boundary Layer Venting System

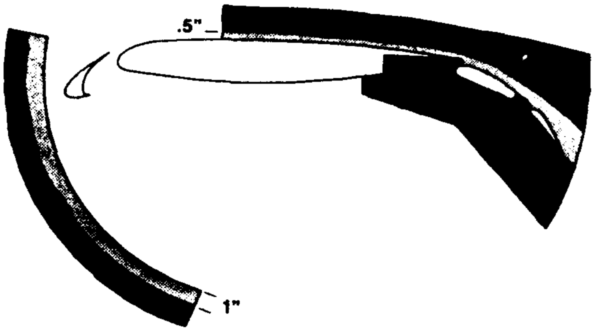

Figure 7. Porous Endplates of Boundary-Layer Control System

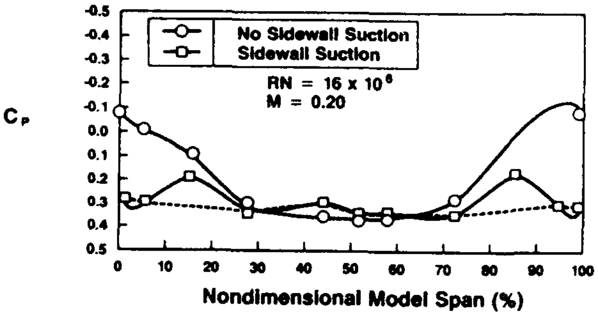

Figure 8. Comparison of Trailing Edge Spanwise Pressures With and Without Sidewall Suction. $\alpha = 16°$

4.0 RESULTS AND DISCUSSION

The following discussion reviews results obtained for drooped spoiler effects, trailing edge wedge applications, and the performance of a new generation single-segment flap design. The test results were obtained transition free at 0.20 Mach number and a chord Reynolds number of 9×10^6, unless otherwise specified. This condition is representative of full-scale at the estimated critical wing station for low-speed stall on an advanced medium range transport aircraft.

4.1 DROOPED SPOILER EFFECTS

Positively deflected spoiler surfaces (trailing edge down) have been used successfully on military aircraft to enhance lift generation. An objective of the present program was to measure the performance effects due to deflected spoiler (5°, 10°) applications on a three-element landing configuration. The flap gap and overhang were held constant to isolate the effects due to spoiler deflection.

It was found that for this airfoil application, drooping the spoiler (5° or 10°) actually decreased the maximum lift capability and stall angle (Figures 9 and 10). However, over most of the lift curve, the lift coefficient at a given angle-of-attack was considerably increased by the drooped spoiler (Figure 11). The extra lift was generated largely by the main element, as shown in Figure 11, and is a consequence of its increased aft camber. Besides generating more lift, drooping the spoiler changed the character of the stall, leading to a sharper stall.

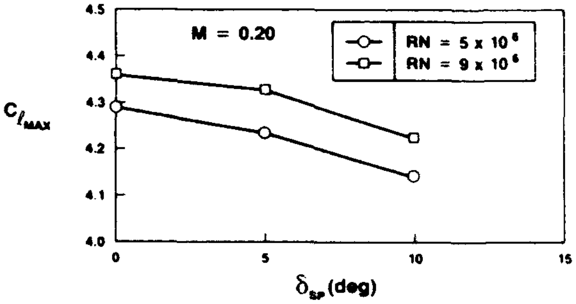

Figure 9. Effect of Spoiler Deflection on Maximum Lift of a Three-Element Airfoil. $\delta_S = 30°$ $\delta_F = 30°$

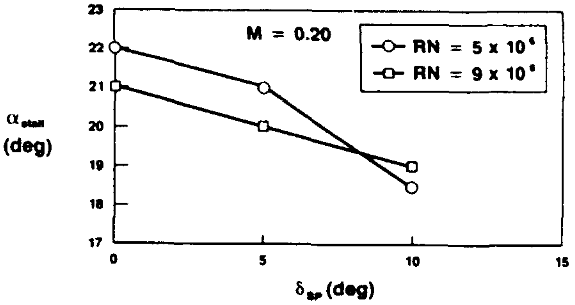

Figure 10. Effect of Spoiler Deflection on Stall Angle of a Three-Element Airfoil. $\delta_S = 30°$ $\delta_F = 30°$

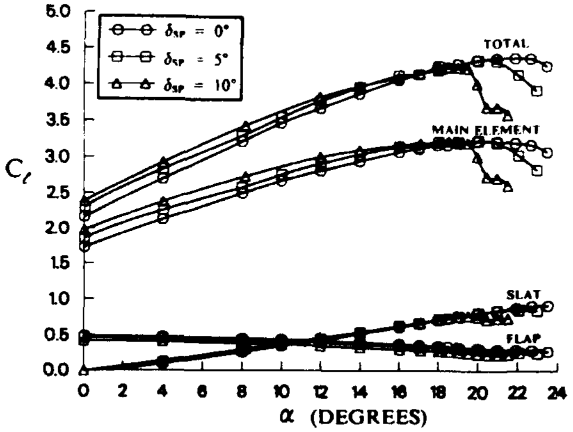

Figure 11. Effect of Spoiler Deflection on Lift of a Three-Element Airfoil, $\delta_S = 30°$ $\delta_F = 30°$

Two key observations can be made from these results. First, the increased loading on the main element leads to reduced loading on the flap (downwash) and increased loading on the slat (upwash). Second, increased loading on the slat leads to the slat stalling soon after the main element stalls. This effect is not present for the undeflected spoiler case, where the slat does not stall at all. To further illustrate these observations surface pressures at 8° angle of attack (approach) are shown in Figures 12, 13, and 14. Figure 13 clearly indicates increased circulation on the slat with increasing spoiler deflection. The authors attribute upwash from the main element as the cause for this effect. Conversely, the flap surface pressures of Figure 14 indicate reduced flap circulation with spoiler deflection. Again, the mechanism for this effect is believed to be downwash from the main element. In general, application of drooped spoilers to the present transport airfoil indicated maximum lift decrements but substantial increases in lift at a given angle-of-attack.

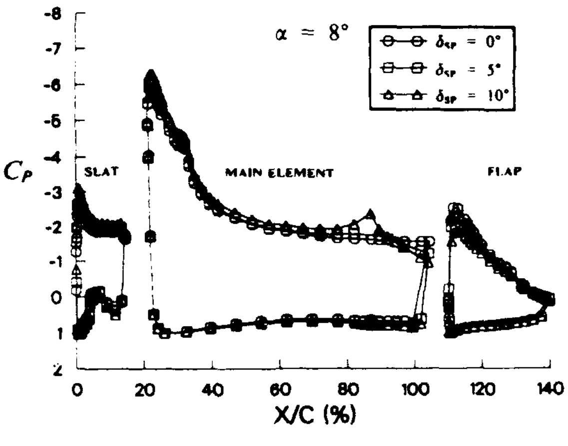

Figure 12. Effect of Spoiler Deflection on Surface Pressure Distributions of a Three-Element Airfoil, δ_S = 30° δ_F = 30°

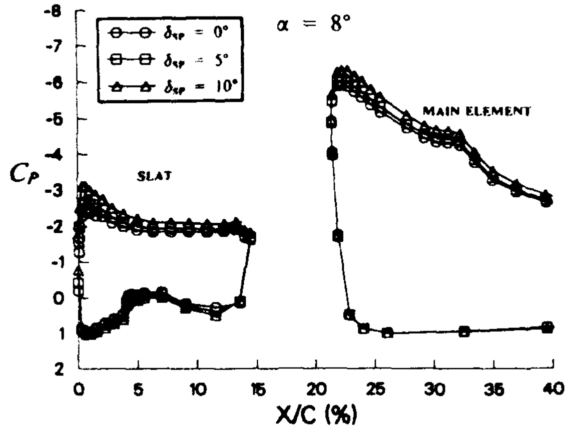

Figure 13. Effect of Spoiler Deflection on Leading-Edge Surface Pressure Distributions of a Three-Element Airfoil, δ_S = 30° δ_F = 30°

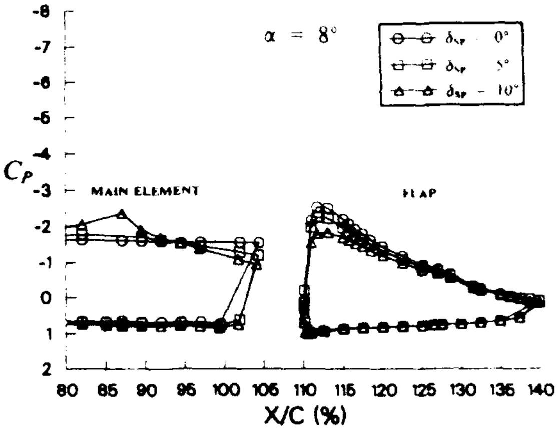

Figure 14. Effect of Spoiler Deflection on Trailing-Edge Surface Pressure Distributions of a Three-Element Airfoil, δ_S 30 δ 30

Summary results of Reynolds number effects at maximum lift for the three configurations with spoiler deflections of 0°, 5°, and 10° are shown in Figure 15. The overall trend with increasing Reynolds number is similar (increased maximum lift) to that obtained with the baseline configuration.

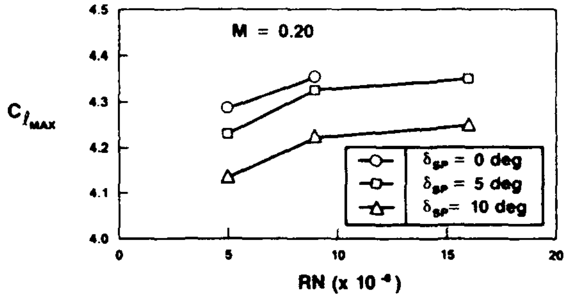

Figure 15. Effect of Reynolds Number on Maximum Lift, δ_S = 30° δ_F = 30°

4.2 TRAILING EDGE WEDGE EFFECTS

To simulate the effects of a small (3% chord) split flap on low speed performance, wedges were attached to both the single- and three-element airfoil. A wedge with an angle of 30° was tested on the single-element airfoil and 15°, 30°, 45° and 60° wedges were applied to the flap of the three-element airfoil as described in Section 2.

The intent of this study was to identify the fraction of the maximum lift increment realized on the single-element airfoil (Figure 16) that is retained when the high-lift components are deployed. It can be seen from Figure 17 that the wedge provides a lift increment throughout the lift curve that diminishes with angle of attack. The maximum lift coefficient for this three-element landing configuration is only marginally increased (+0.02) by the use of the wedge. It is worth noting that most of the increase in lift is generated by the main element and not the flap as might be expected. The mechanism for the increase in lift is the augmented loading on the much larger main element caused by upwash from the flap.

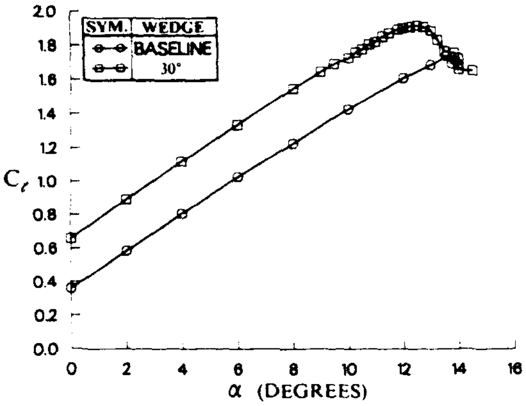

Figure 16. Effect of a 30° Wedge on the Lift of a Single-Element Airfoil

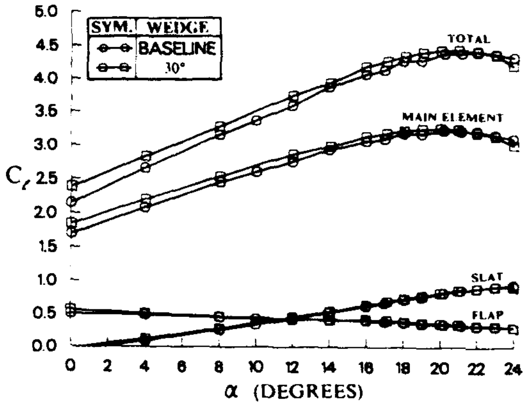

Figure 17. Effect of a 30° Wedge on the Lift of a Three-Element Airfoil, $\delta_s = 30°$ $\delta_f = 30°$

Results obtained with 15°, 30°, 45°, and 60° wedges on the three-element airfoil for a range of Reynolds numbers are shown in Figure 18. Increases in maximum lift capability (from the baseline) are more apparent for the 45° wedge application. Additionally, the maximum lift levels out at wedge angles of 45° and greater (for a Reynolds number of 9 × 10^6). The results obtained at 5 × 10^6 indicated a significant increase in maximum lift between the baseline (no wedge) and the 60° wedge application. However, at the higher Reynolds number (9 × 10^6) this increment all but disappears. Thus, testing at a Reynolds number of 5 million produces trends which do not occur at the higher Reynolds numbers.

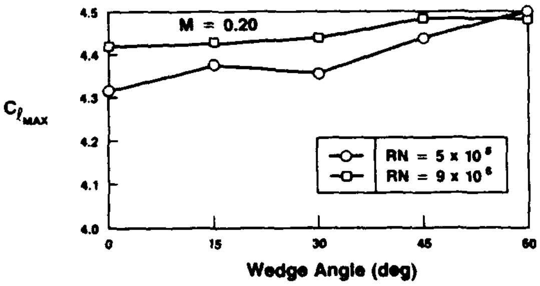

Figure 18. Effect Reynolds Number on Maximum Lift, $\delta_s = 30°$ $\delta_f = 30°$

A lift curve comparison of the baseline and the 45° wedge results is shown in Figure 19 for a Reynolds number of 9 × 10^6. As observed with the 30° wedge application, the majority of the lift increment is due to the main element of the airfoil, with an increment in maximum lift of + 0.07.

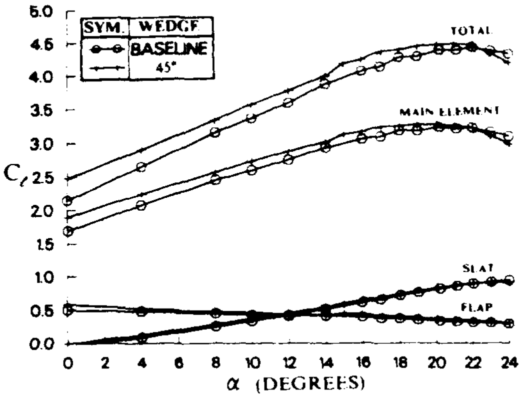

Figure 19. Effect of a 45° Wedge on the Lift of a Three-Element Airfoil, $\delta_s = 30°$ $\delta_f = 30°$

4.3 ADVANCED SINGLE-SEGMENT FLAP

An advanced flap concept developed at Douglas Aircraft was also tested and is shown in Figure 20. The new shape is significantly different than the baseline flap. The advanced flap was designed to reduce flow separation (on the flap surface) for landing flap deflections. A comparison of flap surface pressures measured at an approach condition ($\delta_f = 30°$, $\alpha = 8°$) is shown in Figure 21 and demonstrates the improvement over the baseline flap. It can also be seen that the advanced flap was able to sustain an increased suction peak while maintaining attached flow. This increased suction peak was present up to and including the maximum lift condition (Figure 22), where both flaps display attached flow. This increased suction peak increases the loading on the flap, especially at the lower angles of attack. The performance improvement due to the advanced flap is shown in Figure 23. The total lift of the three-element airfoil increases with the advanced flap. This includes a maximum lift increase of + 0.07. Notably, drag levels are reduced, especially around the approach condition ($C_\ell = 3.1$). This decrease in drag at approach is shown in Figure 24 to be 29% over the baseline flap.

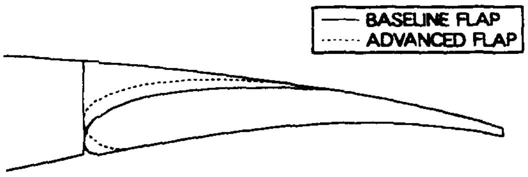

Figure 20. Advanced Flap Shape

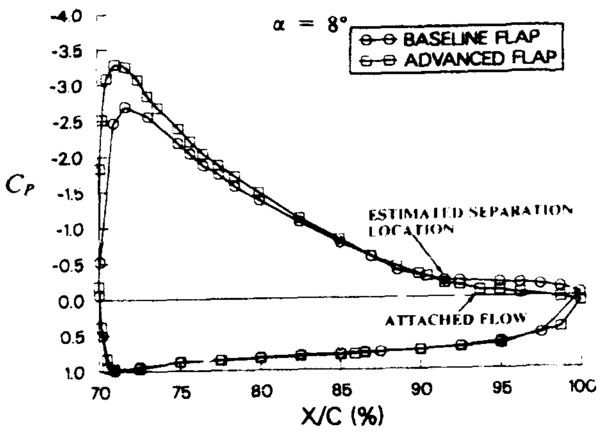

Figure 21. Flap Surface Pressures at an Approach Condition. $\delta_S = 30°$ $\delta_f = 30$

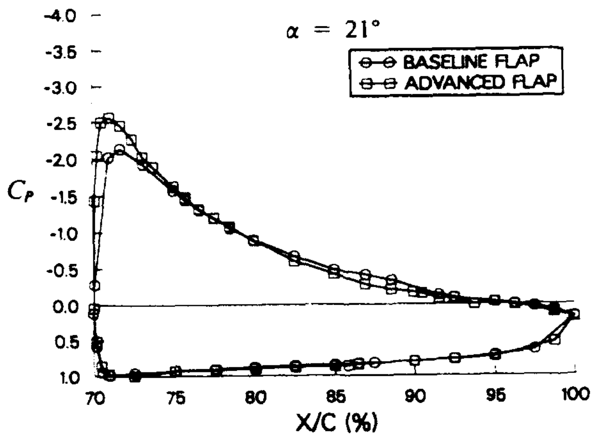

Figure 22. Flap Surface Pressures at Maximum Lift. $\delta_S = 30°$ $\delta_f = 30°$

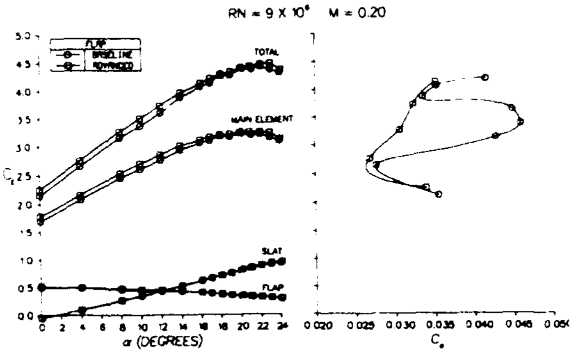

Figure 23. Comparison of the Lift and Drag for the Baseline and Advanced Flaps, $\delta_S = 30°$ $\delta_f = 30°$

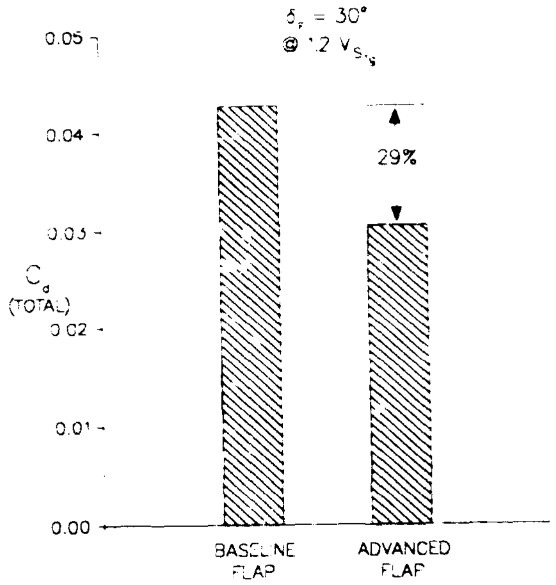

Figure 24. Total Airfoil Drag Reduction Due to Advanced Flap Shape, δ_S 30

It is interesting to note the Reynolds number trends of Figure 25 since they indicate decreased sensitivity for the advanced flap. It is expected that these results are a consequence of the absence of flow separation on the advanced flap surface.

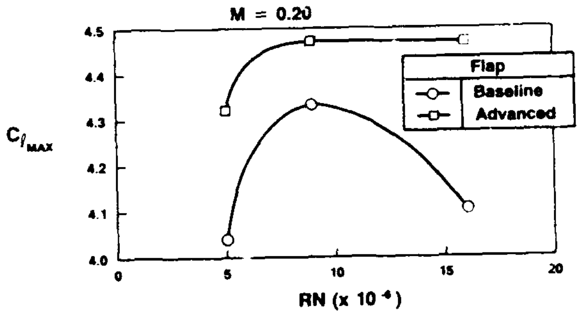

Figure 25. Effect of Reynolds Number on Maximum Lift, $\delta_S = 30°$ $\delta_f = 30°$

The new flap shape exhibits different optimization trends than that of the baseline flap[4]. Because of large-scale separation on the baseline flap, the best locations for maximum lift occurred with positive overhangs (overlapping) and large gaps (1.5 to 2.0%). The optimization for the advanced flap are shown in Figures 26 through 29. Unlike the baseline flap, the advanced flap optimizes at negative (or zero) overhangs with gaps between 1 and 1.5%. The dashed lines in Figures 26 through 29 are estimated lines of constant $C_{\ell_{MAX}}$. For the four deflections tested, the maximum lift decreases as the flap/spoiler overlap increases (more positive overhang). The flow about the advanced flap is better behaved than that for the baseline flap, thus allowing the flap to take advantage of additional Fowler motion.

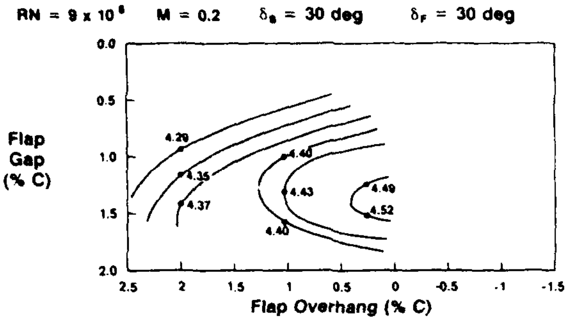

Figure 26. Maximum Lift Coefficient Contours for an Advanced Flap Shape, $\delta_f = 30°$

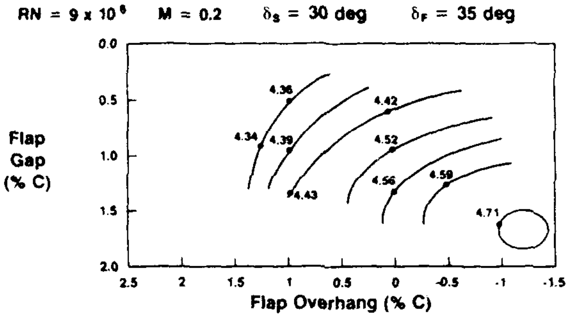

Figure 27. Maximum Lift Coefficient Contours for an Advanced Flap Shape, $\delta_f = 35°$

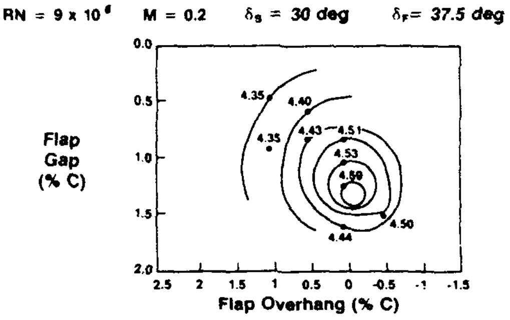

Figure 28. Maximum Lift Coefficient Contours for an Advanced Flap Shape, $\delta_f = 37.5°$

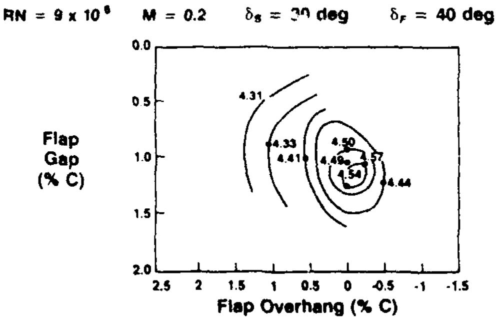

Figure 29. Maximum Lift Coefficient Contours for an Advanced Flap Shape, $\delta_f = 40°$

5.0 CONCLUSIONS

An experimental program to assess the performance of a transport multielement airfoil at flight Reynolds numbers has been conducted by Douglas Aircraft Company and the NASA Langley Research Center. The goals of this effort were to establish new high-lift technologies as well as to augment the high-Reynolds number database on multielement airfoil configurations. Several conclusions are drawn from this study:

1. The drooped spoiler (5° and 10°) decreased the maximum lift capability of the three-element airfoil landing configuration. Additionally the drooped spoiler decreased the stall angle from that of the baseline (undeflected spoiler).

2. Drooping the spoiler did increase the lift of the airfoil at pre-stall angles of attack. This additional lift was generated by the main element and is a consequence of its increased aft camber.

3. The Reynolds number effect on the drooped spoiler configuration were similar to those obtained with the undeflected spoiler. Maximum lift increased with increasing Reynolds number.

4. Trailing edge wedge applications provided a significant increase in C_ℓ and $C_{\ell_{MAX}}$ on the single-element airfoil.

5. For the 30° wedge application, the maximum lift increment measured for the single-element airfoil (0.17) was not retained for the three-element airfoil configuration (0.02). The maximum lift increment for the 45° wedge case was +0.07. Most of the lift increment was due to the main element, and not the flap.

6. Reynolds number effects on the three-element trailing edge wedge application were significant. The lower (5×10^6) Reynolds number data indicated increasing maximum lift with increasing wedge angle (up to 60°). However, the 9×10^6 Reynolds number data exhibited a much smaller increase than the 5×10^6 data. Additionally, the trends with wedge angle were not reproduced between the two Reynolds numbers.

7. A new advanced single-segment flap shape was tested. The new shape led to significantly reduced flow separation for the single-segment landing flap case. Total airfoil profile drag at approach was reduced by 29% over the baseline design.

8. The advanced flap was not as Reynolds number sensitive as the baseline flap at the higher Reynolds numbers tested.

9. The optimum rigging of the advanced flap shape was substantially different than that of the baseline design. The advanced flap optimized at smaller gaps and more negative overhangs for increased Fowler motion.

6.0 REFERENCES

1. Morgan, Harry L. Jr., Ferris, James C., and McGhee, Robert J., "A Study of High-Lift Airfoils at High Reynolds Numbers in the Langley Low-Turbulence-Pressure-Tunnel," NASA TM-89125, July 1987.

2. Wedderspoon, J.R., "The High-Lift Development of the A320 Aircraft," ICAS Proceedings 1986.

3. Fiddlers, S.P., Kirby D.A., Woodward D.S., and Peckham, D.H., "Investigations into the Effects of

Scale and Compressibility on Lift and Drag in the RAE 5m Pressurized Low-Speed Wind Tunnel," Aeronautical Journal, Paper No. 1302, March 1985.

4. Valarezo, W.O., Dominik, C.J., McGhee, R.J., Goodman, W.L., and Paschal, K.B., "Multielement Airfoil Optimization For Maximum Lift at High Reynolds Numbers," AIAA Paper 91-3332.

5. Valarezo, W.O., Dominik C.J., and McGhee, R.J., "Reynolds and Mach Number Effects on Multielement Airfoils," Fifth Symposium on Numerical and Physical Aspects of Aerodynamic Flows," California State University, Long Beach, January 1992.

6. McGhee, R.J., Beasley, W.D., and Foster, J.M., "Recent Modifications and Calibration of the Langley Low-Turbulence-Pressure-Tunnel," NASA TP-2328, 1984.

7. Paschal, K., Goodman, W., McGhee, R., Walker, B., and Wilcox, P., "Evaluation of Tunnel Sidewall Boundary-Layer-Control Systems for High-Lift Airfoil Testing," AIAA Paper 91-3243.

UNE METHODE D'INTERACTION VISQUEUX NON-VISQUEUX POUR ECOULEMENTS INCOMPRESSIBLES HYPERSUSTENTES SUR PROFILS MULTI-CORPS EN REGIME DE DECOLLEMENT PROFOND

(A VISCOUS-INVISCID SOLVER FOR HIGH-LIFT INCOMPRESSIBLE FLOWS OVER MULTI-ELEMENT AIRFOILS AT DEEP SEPARATION CONDITIONS)

J.C. Le Balleur et M. Néron

ONERA, BP 72, 92322 Châtillon Cedex (France)

Abstract.

A viscous - inviscid interaction numerical method for incompressible flows over multi-elements airfoils, which is an extension of the numerical method previously suggested for compressible attached or separated or even stalled flows over airfoils, is presented. The robust algorithms of the method are capable now to converge as well for attached flows or massively separated flows, such as induced by slope discontinuities of airfoils or slats, or such as induced by stall. The viscous - inviscid approach introduces a self-adaptative viscous grid in both normal and streamwise directions along the displacement surfaces, with everywhere a streamwise grid-resolution of the same order as the separating boundary layer thichnesses, even at slat apexes, which is believed to eliminate any aleatory effect of numerical viscosity.

The method is validated with respect to ONERA experiments, on the three-element RA16SC1 high-lift device, with the severe AMD slat-geometry. A realistic non-uniqueness of the separated flow solutions has been exhibited by the calculation method. A satisfactory agreement between theory and experiment is obtained, with the suggested 2 equation turbulence model.

Résumé.

Une méthode numérique d'interaction visqueux - non visqueux pour les écoulements incompressibles sur les profils multi-corps, qui est un prolongement de la méthode numérique suggérée précédemment pour les écoulements compressibles attachés ou décollés voire décrochés sur les profils d'ailes, est présentée. Les algorithmes robustes de la méthode sont maintenant capables de convergence tant pour les écoulements attachés que massivement décollés, tels que ceux induits par les discontinuités de pente des profils ou des becs, ou que ceux induits par le décrochage. L'approche d'interaction visqueux - non visqueux introduit un maillage visqueux auto-adaptatif à la fois en direction normale, et dans la direction de l'écoulement le long des surfaces de déplacement, avec partout une résolution de maillage dans la direction de l'écoulement du même ordre que l'épaisseur des couches limites sur le point de décoller, même aux apex des becs anguleux, ce qui élimine tout effet aléatoire de viscosité numérique.

La méthode est validée par rapport à une expérimentation ONERA, sur l'hypersustentateur triple-corps RA16SC1, avec la géométrie de bec sévère AMD. Une non-unicité réaliste des solutions d'écoulements décollés a été mise en lumière par la méthode de calcul. Un accord calcul-expérience satisfaisant est obtenu, avec le modèle de turbulence à 2 équations proposé.

1. INTRODUCTION.

La méthode numérique d'interaction visqueux-non visqueux pour les écoulements incompressibles d'hypersustentateurs présentée ici, dont l'origine remonte à la ref. [2] des mêmes auteurs, a été depuis lors développée en prolongement direct de la méthode numérique proposée par ailleurs pour les écoulements compressibles attachés ou décollés de profils d'ailes, Le Balleur [3][1][7][9], dont les progrès récents [3][1][9] ont permis de donner accès au calcul des décollements massifs et du décrochage profond.

Dans le cas de l'hypersustentation, en plus du progrès nécessaire vers le calcul des écoulements massivement décollés, qui était déjà rencontré sur les profils d'ailes au décrochage, le calcul doit aborder la plus grande complexité des écoulements visqueux, ainsi que la plus grande complexité des géométries, qui incorporent souvent des singularités, par exemple sur les becs.

La présente méthode numérique montre que la simulation numérique par interaction visqueux - non visqueux peut être rendue opérationnelle, pourvu que les progrès récemment obtenus [3][1], à la fois sur les algorithmes de couplage et sur l'extension des modèles de couche-mince, soient introduits.

La simulation par interaction visqueux - non visqueux met de plus l'accent sur les contraintes de finesse de discrétisation nécessaires, qui exigent que les pas d'espace en direction de l'écoulement dans le voisinage des décollements soient toujours maintenus du même ordre que l'épaisseur de la couche incidente qui va décoller, du moins si un calcul réaliste de ces processus de décollement est souhaité. Cette contrainte d'échelle de discrétisation, d'origine physique, introduit des échelles extrêmement petites sur les becs anguleux. Elle est évidemment toujours présente dans les calculs, dans les méthodes d'interaction visqueux - non visqueux, comme dans les méthodes de résolution "directe" d'équations de Navier-Stokes. Le défaut d'une telle résolution dicrétisée à échelle fine reviendrait à faire reposer le processus de décollement calculé sur un effet aléatoire de viscosité numérique, à moins d'introduire une modélisation locale du type " volume de controle".

S'il ne peut être fiable de faire reposer le calcul des zones voisines du décollement sur la dissipation numérique, l'introduction éventuelle d'une modélisation additionnelle dans les échelles fines ne doit pas être rejetée. Cependant, la méthodologie d'interaction visqueux - non visqueux semble maintenant offrir la possibilité d'introduire à la fois l'accès à l'échelle de résolution fine correcte au décollement, et l'accès au calcul du décollement massif, tout en conservant ces avantages habituels de très faible diffusion numérique. Dans cette optique, les raffinements locaux nécessaires du maillage sont d'un abord plus aisé si l'on maintient un calcul non-visqueux quasi-incompressible, discrétisé par méthode de singularités.

2. EQUATIONS ET MODELES.

La présente méthode de calcul, à l'exception du calcul non-visqueux incompressible, est identique à la méthode numérique proposée pour les écoulements compressibles attachés ou décollés de profils d'ailes, incluant le calcul du décrochage profond, Le Balleur [3][7][1]. On pourra se reporter à [1] pour une présentation détaillée.

2.1. Théorie de "Formulation-Déficitaire".

Les équations de Navier-Stokes sont dissociées en 2 systèmes couplés équivalents en utilisant la théorie de "Formulation-Déficitaire" de Le Balleur [4][7][9][3][1]. La théorie est utilisée ici en introduisant une troncature de couche-mince dans les équations. Cette troncature n'introduit pas de restriction majeure une fois écrite en "Référentiel de Déplacement", voir [3] ou [1].

2.2. Equations locales en "couche-mince".

Rappelons que la théorie de "Formulation-Déficitaire", proposée vers 1980 et complétée par l'introduction du "Référentiel de Déplacement" [3], permet de généraliser l'emploi d'équations de couche-mince au décollement massif. Dans ce référentiel, la direction x^2 devient sensiblement normale à la surface de déplacement (inconnue avant calcul). $x^2=0$ est alors la surface de déplacement et non-plus à la paroi, qui devient $x^2=Z_w(x^1)$. Les équations visqueuses, en théorie de "Formulation-Déficitaire" [3][1], lorsque l'on choisit de les tronquer par des approximations de couche-mince, s'écrivent, si t^{12} désigne la contrainte de cisaillement et si J, Γ^i_{jk} désignent respectivement le jacobien et les symboles de Christoffel des coordonnées curvilignes :

$$\frac{\partial}{\partial x^j} J.\begin{pmatrix} \rho u^j - \bar{\rho}\bar{u}^j \\ \rho u^1 u^j - \bar{\rho}\bar{u}^1\bar{u}^j \end{pmatrix} + \Gamma^1_{11}.\, J.\begin{pmatrix} 0 \\ \rho u^1 u^1 - \bar{\rho}\bar{u}^1\bar{u}^1 \end{pmatrix} = \frac{\partial}{\partial x^2}\begin{pmatrix} 0 \\ -Jt^{12} \end{pmatrix}$$

$$j = 1, 2 \qquad (1)$$

$$\frac{\partial}{\partial x^2}(p-\bar{p}) \equiv -\Gamma^2_{11}\left[\rho u^1 u^1 - \bar{\rho}\bar{u}^1\bar{u}^1\right] \equiv 0 + \ldots\ldots \qquad (1b)$$

$$\text{Fluide Réel} : \bar{u}^i, \bar{p}, \bar{\rho} \qquad\qquad i, j = 1, 2$$
$$\text{Pseudo-fluide-parfait} : u^i, p, \rho$$

2.3. Forme intégrale en "Référentiel de Déplacement".

Une simple intégration en x^2 de (1)(2) entre la paroi $x^2=Z_w\,(x^1)$ et l'infini fournit les équations intégrales, pleinement équivalentes. Les équations intégrales peuvent s'écrire, soit le long d'une coordonnée curviligne (x^1) sur la surface de déplacement, soit le long d'une coordonnée curviligne (s) sur la paroi. Les vitesses (visqueuse et non-visqueuse) normales à la surface de déplacement, notées $\bar{u}^2$ *et* u^2, doivent être distinguées des vitesses (visqueuse et non-visqueuse) normales à la paroi, notées $\bar{w}_n$ *et* w_n. Désignant par q le module de la vitesse non-visqueuse, et ± les cotés supérieur/inférieur en cas de nappe de sillage :

$$\frac{\partial}{\partial s}\rho.\begin{bmatrix} q\delta^1 \\ q^2\theta^{11}+q^2\delta^1 \\ q\delta - q\delta^1 \end{bmatrix}^{\pm} = \begin{bmatrix} \rho w_n - \bar{\rho}\bar{w}_n \\ \rho q^2\dfrac{Cf}{2}\cos\psi + \rho u^1 w_n - \bar{\rho}\bar{u}^1\bar{w}_n \\ \rho q E\cos\psi + \bar{\rho}\bar{w}_n \end{bmatrix}^{\pm}_{(x^1,\, Z_w)} \qquad (3)$$

$$\bar{p}(x^1, x^2) = p(x^1, x^2) + (p-\bar{p})_{2^{nd}\ order} + \ldots\ldots$$

$$\frac{\partial}{\partial s} = \cos\psi\ .\ \frac{\partial}{\partial x^1}, \qquad \sin\psi = \frac{w_n}{q}$$

avec :

$$\rho.\begin{bmatrix} q\delta^1 \\ q^2\theta^{11}+q^2\delta^1 \end{bmatrix}^{\pm}_{(x^1,\, Z_w)} = \int_{Z_w}^{\infty}\begin{bmatrix} \rho u^1 - \bar{\rho}\bar{u}^1 \\ \rho u^1 u^1 - \bar{\rho}\bar{u}^1\bar{u}^1 \end{bmatrix}^{\pm} dx^2 ,$$

$$E = \left[\frac{1}{\rho q}\,\frac{\dfrac{\partial}{\partial x^2}(t^{12})}{\dfrac{\partial}{\partial x^2}(u^1-\bar{u}^1)}\right]_{(x^2,\,\delta)}$$

En plus des équations de masse et de mouvement, le système (3), choisi ici de rang-3, inclut l'équation d'entrainement, qui est une collocation le long de la surface $x^2=\delta_{(x^1)}$ avec l'équation locale de mouvement du système (1) selon x^1. Contrairement à de nombreuses affirmations, les équations intégrales sont *moins restrictives* que celles de Prandtl, parce que $\bar{p}, p, \rho, u^j$ sont ici supposés être évolutifs selon x^2 au sein de la couche visqueuse, Le Balleur [4][8][12], cette extension ne résultant que du choix optimal de définition des épaisseurs intégrales ("Formulation-Déficitaire" par rapport aux flux).

2.4. Modèle de profils de vitesse turbulents paramétriques.

On utilise la description analytique originale des profils de vitesse moyenne turbulents suggérée précédemment, Le Balleur [7][9][8][3], modélisation construite tant pour les écoulements attachés que massivement décollés, voir [9]. Elle est ici appliquée sous sa forme la plus complète [3], avec sous-couche laminaire et terme D d'amortissement :

$$\left(\frac{\bar{u}}{q}\right)_{(a^1,\,\delta,\,x^2)} = 1 - W_{(a^1)}\,.\,F\left(\frac{x^2}{\delta}\right) \qquad \textit{loi de sillage}$$

$$+\,\frac{Cf}{|Cf|}\,.\left(1-D\right).\,\frac{1}{k}\left(\frac{Cf}{2}\right)^{1/2} Log\left(\frac{x^2}{\delta}\right) \qquad \textit{loi turbulente de paroi} \qquad (4a)$$

$$-\left(1-W\right).\,D + D\,\frac{Cf}{2}\,R_\delta\left(\frac{x^2}{\delta}\right) \qquad \textit{loi laminaire de paroi}$$

$$\text{avec :}\quad F(z) = F^{*}\left[\frac{z - z^{*}}{1 - z^{*}}\right],\quad F^{*}(z) = \left[1 - z^{1.5}\right]^{2},\quad k = 0.41$$

$$z^{*} \cong \max\left[\,0\,,\,2.406\left(a^{1} - 0.5844\right)\right]$$

$$\bar{u}_w = 1 - \frac{a^1}{A},\qquad a^1 = \left[\frac{\delta^1}{\delta}\right]_{incompressible},\qquad A = \int_0^1 F(z)\,dz$$

$$\left[\frac{Cf}{2}\right]^{1/2}\left[Log\left(R_\delta\left(\frac{Cf}{2}\right)^{1/2}\right) + 5.25k - \frac{1}{A}\right] = k\,.\,\|\bar{u}_w\| \qquad (4b)$$

Cette modélisation des profils de vitesse fournit aussi une modélisation générale de l'entrainement turbulent d'équilibre [3][7][1], compte tenu de la définition de E dans (3) :

$$E_{eq} = C_4\,.\left[1 - \bar{u}_w\right] + C_5\,.\left|\frac{Cf^1}{2}\right|^{-1/2}.\,\frac{Cf^1}{2} \qquad (4c)$$

$$C_4 = 0.062,\quad G_0 = 6.5,\quad C_5 = C_{5\,(C_4\,,\,G_0\,,\,a_0^1\,,\,Cf_0)}$$

où a_0^1, Cf_0 correspondent aux valeurs de a^1, Cf calculées pour la plaque plane en incompressible, au même R_δ et avec un paramètre de Clauser G_0.

2.5. Modèle de turbulence k-tau.

Les effets de turbulence hors-équilibre sont calculés en ajoutant le modèle à 2 équations de transport de Le Balleur [7][3], qui peut être utilisé aussi bien dans les méthodes-locales (calcul de t^{12}), et dans les méthodes-intégrales (entrainement et dissipation). Ce modèle suggéré en 1981 a pour originalité, d'une part de "forcer" le modèle de Launder-Rodi par la modélisation des profils de vitesse, ce qui le rend mieux adapté aux écoulements décollés, et d'autre part d'effectuer un calcul en termes d'écart aux valeurs données par le modèle d'équilibre (contraintes t_{eq}^{12} et entrainement E_{eq}). L'écart à l'équilibre est supposé être invariant en direction x^2, et être calculé selon x^1 par 2 équations (intégrales) de transport. Celles-ci calculent des effets d'histoire pour l'énergie cinétique turbulente moyennée en x^2 notée $\tilde{k}(x^1)$, et pour la contrainte de cisaillement de Reynolds moyennée en x^2 notée $\bar{\tau}(x^1)$:

$$\textit{Contrainte locale} :\quad t^{12} = \frac{\bar{\tau}\,(x^1)}{\bar{\tau}_{eq}\,(x^1)}\,.\left[t_{eq}^{12}\right](x^1, x^2)$$

$$t_{eq}^{12} = \lambda_1\lambda_2\lambda_3\,\rho l^2\left|\frac{\partial\bar{u}^1}{\partial x^2}\right|\frac{\partial\bar{u}^1}{\partial x^2} = \lambda_1\lambda_2\lambda_3\,\rho\,\nu_t\,\frac{\partial\bar{u}^1}{\partial x^2}$$

$$\textit{Entrainement global} :\quad E = \frac{\bar{\tau}}{\bar{\tau}_{eq}}\,E_{eq}$$

$$\bar{\delta}\frac{\partial\tilde{k}}{\partial t} + \left[\bar{\delta} - \bar{\delta}_I\right]\frac{\partial\tilde{k}}{\partial x^1} = \frac{\bar{\tau}}{\bar{\tau}_{eq}}\,\frac{q^3}{2}\,\Phi_{eq} - \bar{\varepsilon}\,\bar{\delta}$$

$$\bar{\delta}\,\frac{\partial\bar{\tau}}{\partial t} + \left[\bar{\delta} - \bar{\delta}_I\right]\frac{\partial\bar{\tau}}{\partial x^1} = 1.5\,\frac{\bar{\varepsilon}\,\bar{\delta}}{\tilde{k}}\left[\left(\frac{\tilde{k}}{\tilde{k}_{eq}}\right)^2\frac{\bar{\varepsilon}_{eq}}{\bar{\varepsilon}}\,\bar{\tau}_{eq} - \bar{\tau}\right] \qquad (4d)$$

$$\left[\frac{\bar{\varepsilon}}{\bar{\varepsilon}_{eq}}\right] = \left[\frac{\tilde{k}}{\tilde{k}_{eq}}\right]^{1.5}$$

$$\bar{\delta} = (1 - z^{*})\,\delta,\quad \bar{\delta}_I = \delta_I\left[1 - 0.45\,(1 - \bar{u}_w)\right]$$

Les coefficients et grandeurs d'équilibre qui apparaissent dans le modèle sont précisés dans Le Balleur [1][3][7].

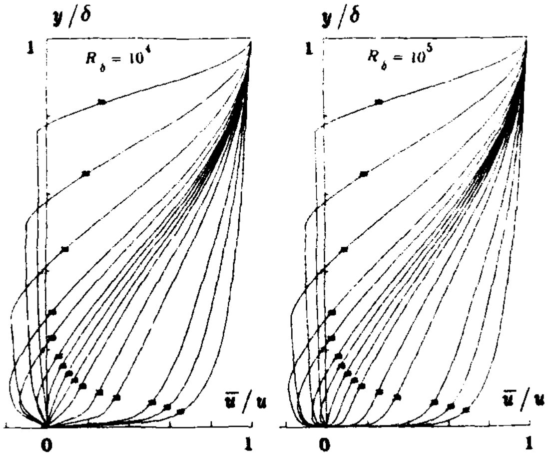

3. METHODES NUMERIQUES.

Les méthodes numériques utilisées pour la couche visqueuse et pour l'algorithme de couplage sont identiques à celles développées en fluide compressible pour les profils d'ailes, Le Balleur [3][1][7].

3.1. Méthode numérique visqueuse.

Rappelons que la méthode numérique de couche visqueuse est de nature hybride entre méthodes-intégrales et méthodes-locales.

A chaque station (x^1), les profils de vitesse paramétriques turbulents des relations (4) sont discrétisés selon x^2 entre $x^2 = Z_w$ et $x^2 = \delta$, avec un maillage en x^2/δ qui est auto-adaptatif à δ et à la forme du profil de vitesse. La discretisation auto-adaptative utilise ici 37 noeuds optimisés, dépendants de a^1, avec des schémas implicites de trapèzes pour lier les grandeurs locales et intégrales.

De station en station (x^1), le système d'équations intégrées en x^2 est discrétisé sur le maillage curviligne (x^1) de surface de déplacement, projection sur cette surface du maillage curviligne de paroi (s). Notons que l'intégration en x^2 (normale à la couche visqueuse) n'est plus ici normale à la paroi, Le Balleur [3][9] :

$$\left\{A^i_{j\,(a^1,\,q,\,\delta)}\frac{\partial\hat{f}^j}{\partial s} = b^i_1 + b^i_2\right\}^{\pm}_{(x^1,\,Z_w)}$$

$$i = 1, 5,\quad j = 1, 5, \qquad (5a)$$

$$\hat{f}^j = \begin{bmatrix}\hat{q}\\ \delta\\ a^1\\ \tilde{k}\\ \bar{\tau}\end{bmatrix},\quad b^i_1 \doteq \begin{bmatrix}\dfrac{\hat{w}_n}{q} - \dfrac{\bar{\rho}\bar{w}_n}{\rho q}\\ \dfrac{\hat{w}_n}{q} - \dfrac{\bar{\rho}\bar{w}_n}{\rho q}\\ \dfrac{\bar{\rho}\bar{w}_n}{\rho q}\\ 0\\ 0\end{bmatrix},\quad b^i_2 = \begin{bmatrix}0\\ \dfrac{Cf}{2}\cos\psi\\ E_{eq}\,\dfrac{\bar{\tau}}{\bar{\tau}_{eq}}\cos\psi\\ b^4\\ b^5\end{bmatrix}$$

$$\sin\psi = \hat{w}_n\,/\,q$$

La présente méthode reprend la discrétisation robuste en (s, x^2) développée depuis de nombreuses années, Le Balleur [7][8][3][1], *s-marching* et non-linéairement implicite en s, x^2. Elle commute différents schémas numériques en direction s, de second-ordre, ou de premier ordre si le maillage devient grossier, voir [1].

Les inconnues "non-visqueuses" du problème visqueux (5a), notées avec un signe chapeau, $(\hat{q}\ ,\ \hat{w}_n/q\ )$, doivent être couplées aux quantités correspondantes du problème non-visqueux, qui sont notées $(q,\ w_n/q)$. Pour éviter les problèmes de singularité de décollement, le problème visqueux est résolu, avant couplage, soit en mode *direct*, soit en mode *inverse*. A chaque noeud $(i, 1)$ et itération de couplage N, le système discrétisé (5a) est fermé par la relation (5b), elle-même discrétisée par des schémas centrés pour $(\partial\hat{q}/\partial s)$ et éventuellement décentrés-aval pour $(\partial q/\partial s)$:

$$\begin{cases} \varepsilon = 0 & : \text{Direct} \\ \varepsilon = 1 & : \text{Inverse} \end{cases}$$

$$\varepsilon\left[\frac{\hat{w}_n}{q} - \frac{w_n}{q}\right]^N_{i,1} + (1-\varepsilon)\left[\frac{\partial\hat{q}}{\partial s} - \frac{\partial q}{\partial s}\right]^N_{i,1} = 0 \qquad (5b)$$

La commutation d'un mode direct $(\varepsilon = 0)$ vers un mode inverse $(\varepsilon = 1)$ est asservie au paramètre de forme du profil de vitesse ($a^1 > 0.28$ par exemple), Le Balleur [7][3],

3.2. Couplage : Algorithme "Semi-inverse Massive-separation".

A chaque itération de couplage, la vitesse normale à la paroi non-visqueuse w_n^N (ou bien la discontinuité de vitesse normale non-visqueuse sur les sillages $<w_n^N>$), qui traduit l'effet de déplacement généralisé, est modifiée en chaque noeud de couplage $(i, 1)$ de manière explicite grâce à l'algorithme "Semi-inverse" de Le Balleur [6][3][10][1] :

$$\left[\frac{w_n^{N+1}}{q} - \frac{w_n^N}{q}\right]_{i,1} = \omega \cdot \left[\omega_i^1\left[\frac{\hat{w}_n}{q} - \frac{w_n^N}{q}\right]_{i,1}\right.$$

$$\left. + \omega_i^2\,\frac{1}{q}\left[\frac{d\hat{q}}{ds} - \frac{dq^N}{ds}\right]_{i,1} + \omega_i^3\,\frac{1}{q}\left[\frac{d^2\hat{q}}{ds^2} - \frac{d^2q^N}{ds^2}\right]_{i,1}\right] \qquad (6a)$$

$$0 < \omega < 2,$$

La présente méthode utilise l'extension récente "Semi-inverse Massive-separation" de l'algorithme. Ce nouvel algorithme généralise l'algorithme originel dans le cas où w_n/q cesse d'être petit, mais peut devenir de l'ordre de l'unité, Le Balleur [3][1].

Rappelons de plus que, dans la théorie numérique du couplage associée à l'algorithme "Semi-inverse", voir [1], la technique numérique *s-marching* du problème visqueux permet à chaque station $(i, 1)$ une élimination des variables internes "purement visqueuses", Le Balleur [5][6][7][3], ce qui donne β^* en chaque noeud :

$$\left[\frac{\hat{w}_n}{q} - \beta^*\,\frac{\partial\hat{q}}{\partial s} - \gamma^*\right]_{i,1} = 0\,, \qquad (7)$$

Les coefficients ω_i^1, ω_i^2, ω_i^3 ci-dessus sont, dans l'algorithme "Semi-inverse" de Le Balleur, calculés en chaque noeud (i) de couplage. Ce calcul est tel que w_n^{N+1} corresponde à la solution (linéarisée) de couplage exact sur le nombre d'onde maximal [6][7][3] α_{max} du maillage. Une surrelaxation de 2 est alors la limite de stabilité [6][7]. Pour l'algorithme "Semi-inverse Massive-separation", les coefficients s'écrivent, Le Balleur [3][1][10], en variables complexes :

$$\omega_i^{direct} = \omega_i^1 + I\ \alpha_{max}\ \omega_i^0 = \frac{1}{1 - \mu\ (\alpha_{max})}$$

$$\omega_i^{inverse} = \omega_i^2 + I\ \alpha_{max}\ \omega_i^3 = -\frac{1}{1 - \mu^{-1}\ (\alpha_{max})} \cdot \frac{\beta'}{\alpha_{max}}$$

$$\mu = \frac{\alpha\ .\ \beta^*}{\beta'}\,, \qquad (\mu \textit{ complexe}\ ,\ I^2 = -1)$$

$$\beta' = \beta\ \cos\psi - I\ \sin\psi$$

$$\beta = \left[1 - M^2\right]^{1/2}, \qquad \sin\psi = w_n^N/q$$

$$\alpha_{max} = \frac{\pi}{\Delta s\ .\ \cos\psi} = \frac{\pi}{\Delta x^1} \qquad (6b)$$

Dans ces expressions, le terme μ correspond à l'amplification complexe de l'algorithme de point fixe "direct" (μ^{-1} étant de ce fait l'amplification complexe de l'algorithme de point fixe "inverse"). On notera que la relaxation ω^2, ω^3 ci-dessus correspond à la forme originelle de l'algorithme "Semi-inverse", Le Balleur [6], c'est à dire à une relaxation optimale $\omega^{-1} = 1-\mu^{-1}$, mais que l'écriture ici en variable complexe de ω inclut également l'analyse de Wigton, Holt [11], voir [12]. On remarquera enfin que l'algorithme "Semi-inverse Massive-separation" conduit, même en subsonique, à ce que les 2 termes ω^2 et ω^3 soient actifs et non-nuls, Le Balleur [3][10].

3.3. Calcul des sillages.

Le calcul visqueux direct/inverse et le couplage en effet de déplacement sont effectués sur les sillages de la même façon que sur les couches limites, et les décollements éventuels induits par les gradients de vitesse peuvent y être calculés. Ce calcul des sillages est conduit ici dans l'hypothèse du traitement simplifié issu de la seule partie symétrique des équations, voir Le Balleur [7]. L'effet de courbure est pris en compte dans la méthode, comme dans [7], mais tous les calculs ont ici été conduits sans cet effet.

En plus de l'algorithme de couplage, on utilise pour chaque sillage l'algorithme de mise en équilibre proposé pour les profils mono-corps, Le Balleur [7], repris en détail dans [1][3].

3.4. Méthode numérique non-visqueuse.

Le calcul incompressible non-visqueux est effectué par la méthode de singularités proposée par le second auteur, déjà présentée en [2].

Dans cette méthode, le conditionnement numérique est amélioré en distribuant sur les parois des profils, dans les zones de faible épaisseur près des bords de fuite, une double répartition de singularités sources et tourbillons. L'augmentation correspondante du rang du système est utilisée pour imposer localement des conditions de régularité aux écoulements fictifs que la distribution de singularités induit à l'intérieur des profils. L'emploi d'une telle méthode de singularités mixte dans ces zones de faible épaisseur, associée à des contraintes supplémentaires appropriées permet en effet d'utiliser les singularités de façon optimale, en limitant l'erreur de discrétisation.

Un traitement numérique satisfaisant dans les zones de faible épaisseur est tout particulièrement nécessaire ici dans le cas de profils multi-corps, dont les corps principaux et les becs présentent près de leurs bords de fuite des épaisseurs généralement faibles.

Numériquement, pour les itérations de couplage, la matrice inverse du système non-visqueux discrétisé (sillages exclus) est invariante, et stockée, aussi longtemps que le maillage (adaptatif) n'est pas réactualisé.

4. RESULTATS.

Les résultats de calcul ci-dessous ont été obtenus sur un profil d'hypersustentateur construit à partir du profil supercritique RA16SC1 de l'Aérospatiale, expérimenté avec un volet et différents types de becs [13]. Dans le but d'évaluer les performances et les progrès récents du code de calcul (code VIS18b), la configuration de bec la plus sévère, dotée du bec A.M.D. , et source de décollements profonds, a été sélectionnée comme cas test. Les configurations calculées correspondent aux valeurs de -20° et -40° de l'angle de braquage du volet δ_{volet}.

4.1. Description de l'hypersustentateur triple-corps.

Contrairement à la configuration double-corps, traitée antérieurement [2] avec une version beaucoup moins avancée de la méthode de calcul, et d'une complexité aérodynamique bien moindre, la configuration triple-corps (fig.1) introduit une difficulté majeure par la géométrie du bec. Celui-ci présente en effet à l'intrados une singularité, à l'aval de laquelle se situe une cavité. La difficulté de calcul réside moins dans la singularité, et dans le décollement qu'elle déclenche dans la cavité, que dans sa géométrie particulière, les parois amont et aval y présentant en effet un angle aigu.

4.2. Conditions de calcul.

La méthode de calcul des couches visqueuses doit traiter à partir de cette singularité un décollement profond de cavité, une couche de mélange apparaissant à la singularité, avant de recoller vers l'aval. Dans un tel cas, une technique de calcul simplificatrice souvent adoptée consiste par exemple à modifier artificiellement la géométrie de la cavité, de façon à adoucir le processus de décollement.

Le recours à ce type de calcul simplificateur n'est ici pas nécessaire. La démarche retenue, permise par la méthode, grâce à sa théorie de "Formulation Déficitaire", voir [1], et au "Référentiel tangent à la surface de déplacement", a consisté à conserver la forme exacte de la cavité, et à ne modifier la géométrie qu'en émoussant l'apex de la singularité. L'émoussement est ici obtenu en introduisant un arc de cercle de très faible rayon (1,36 10^{-3}), maillé ici par 60 noeuds sur environ 150° (fig. 3,2,4). Sur cet émoussement, le processus physique de décollement (compression) peut être effectivement discrétisé. Cette discrétisation à échelle fine, dictée par l'échelle de la couche limite juste en amont, assure que le processus de décollement et de naissance d'une couche de mélange soit ici effectivement calculé et ne soit plus déterminé par les seuls effets de viscosité numérique.

Les calculs ont été obtenus en laissant la transition se développer de façon naturelle, et sans recaler les épaisseurs des couches limites. Ils sont systématiquement effectués, sauf indication contraire, avec le modèle de turbulence à deux équations de transport.

4.3. Conditions des comparaisons calcul-expérience.

Les calculs sont comparés aux résultats d'essais [13] obtenus à l'ONERA dans les souffleries S1 Ca en 1980 et F1 en 1984. Ces essais ont été effectués entre panneaux (b = 1,01 m), sur une maquette de 0,5 m de corde de référence, à une vitesse de 40 m/s, et à des nombres de Reynolds de 1,2 10^6 et 1,9 10^6. Les essais ont été effectués en transition naturelle, les efforts étant obtenus par intégration des pressions sur les profils.

La comparaison aux résultats expérimentaux doit être effectuée en tenant compte des difficultés expérimentales. En effet, sur une telle configuration multi-corps, pour préserver à l'écoulement un caractère bidimensionnel, il est nécessaire de disposer des caissons d'aspiration sur les parois latérales. Les essais ont montré que dans certaines configurations, par aspiration latérale à l'extrados du volet, il était possible de passer d'une solution décollée sur le volet à une solution non-décollée par simple variation de la pression d'aspiration.

Par ailleurs, lors de certains essais, des déformations de géométrie ont été constatées, influant notamment sur la largeur de fente corps-volet, (cas δ_{volet}=-20°), ou sur l'angle de braquage du bec, dont la valeur mesurée après essais était de 32° à l'emplanture au lieu de 30°, la valeur en cours d'essai à mi-envergure, vraisemblablement plus élevée n'étant pas connue avec certitude. Enfin, les efforts globaux obtenus par intégration des pressions induisent une incertitude au niveau du bec.

4.4. Courbe de portance. Volet braqué à 20°.

Dans cette première configuration, les angles de braquage du bec et du volet ont respectivement pour valeurs 30° et -20°. Sur la courbe de portance, les résultats de calcul, figurés par des croix, ont été obtenus jusqu'à l'incidence de 20.2°, fig. 5. Les résultats expérimentaux (F1 1984) sont représentés par des cercles. A 16°, les deux autres croix représentent les résultats obtenus avec des valeurs de l'angle de braquage du bec δ_{bec} de 32° et de 33°. L'étoile représente le résultat obtenu dans la configuration de référence avec le modèle de turbulence à 1 équation de transport.

Notons qu'au voisinage du décrochage, dans cette configuration comme dans les suivantes, le calcul est effectué par continuité, en initiant les calculs à partir de résultats obtenus à une incidence voisine.

4.5. Incidence 16°. Volet braqué à 20°.

Sur la Fig. 6, les coefficients de pression Cp(x/c) calculés sont comparés à l'expérience. Les positions des points de décollement et de recollement dans les couches visqueuses ont été indiquées sur la représentation du profil, ainsi que sur les sillages figurés dans leur position d'équilibre à convergence.

L'accord est excellent sur le volet et la quasi-totalité du corps principal. Sur le bec, ainsi que sur le corps principal à l'endroit de la pointe de Cp, la comparaison est moins bonne. Toutefois, confirmant les remarques des expérimentateurs, les calculs ont montré l'influence du paramètre de l'angle de braquage du bec, les résultats étant très différents lorsque cet angle prend, au lieu de la valeur nominale de 30°, la valeur de 32°, Fig.8, ou de 33°, Fig. 7, compatible avec les déformations de maquette.

Pour ces deux valeurs corrigées du braquage de bec, tant le niveau de Cp dans les pointes de survitesse, sur le bec et le volet, que le niveau de pression dans la zone de décollement à l'intrados du bec, sont beaucoup plus proches de l'expérience, la meilleure comparaison semblant être obtenue pour la valeur 33°, Fig.7. Remarquons qu'outre l'orientation du bec, des paramètres tels que les largeurs des fentes, non considérés ici, peuvent avoir une influence importante. En ce qui concerne la méthode de calcul, l'absence actuelle de prise en compte des couches limites confluentes peut être également responsable d'une partie de l'écart observé.

Sur les figures suivantes, la distribution de pression Cp(x/c) sur le bec a été représentée à différentes échelles, tout d'abord dans la même orientation que sur l'hypersustentateur, Fig. 9, puis afin de mieux visualiser la solution calculée au voisinage de la singularité (émoussée), après une rotation de l'image placant verticalement la bissectrice de l'angle formé par les deux parois, de part et d'autre de cette singularité, Fig. 10, 11, et 12. La position des points de décollement et de recollement a été indiquéee. Un second décollement, très limité, survient dans le sillage, à partir du bord de fuite, Fig.9 et 10. La Fig. 12 montre le détail de l'écoulement autour de la singularité émoussée. Le décollement survient sur l'arrondi, après le pic de survitesse, au maximum relatif de Cp. On observe ensuite un petit plateau de pression, toujours sur l'arrondi, qui semble se raccorder seulement plus en aval au plateau de pression associé à la cavité, Fig.12 et 11.

La figure 13 permet enfin de comparer les résultats de calcul obtenus sur le même cas de référence avec le modèle de turbulence à 1 équation de transport. Sur ce cas, les résultats sont extrêmement proches. Cette conclusion ne saurait cependant être générale. Avec le modèle à 1 équation, le niveau de Cp est très légèrement inférieur sur la partie arrière de l'extrados des trois corps, en particulier sur le bec.

Sur les figures suivantes sont présentées des vues de l'écoulement autour du bec. Les profils de vitesse, Fig.14, font apparaitre la difficulté du calcul, inaccessible aux méthodes de couche limite classique, l'orientation du vecteur vitesse par rapport à la paroi, dans la couche de mélange près de la singularité, étant voisine de 90°. Les quatre figures suivantes présentent à convergence les lignes de courant, respectivement non-visqueuses et visqueuses, Fig.15 et 16, ainsi que les isomach Fig.17 et 18. Elles font apparaitre en particulier la zone de recirculation épaisse et la position du point de recollement. L'examen de l'écoulement autour de la singularité émoussée permet de visualiser la petitesse des échelles physiques de décollement, qu'il est nécessaire de discrétiser, sous peine de remplacer le processus physique par un processus de dissipation numérique, Fig. 19.

4.6. Non-unicité des solutions. Volet braqué à 40°.

Dans la seconde configuration étudiée de l'hypersustentateur, l'angle de braquage du volet est de δ_{volet} =-40°, pour un même angle de braquage du bec δ_{bec} =30°. Dans ce cas à fort décollement, l'analyse par le calcul a mis en évidence et interprêté un phénomène de non-unicité de solution.

Le premier cas de calcul abordé, effectué à une incidence α=16°, dans les mêmes conditions que précédemment avait en effet mis en évidence une solution comportant, à l'extrados du volet, un décollement très limité près du bord de fuite Fig.20, 22, contrairement à la solution attendue, et comportant par contre un décollement intense, à facteur de forme maximal H=40.8, dans le sillage du corps principal. Il a donc été tenté de rechercher une modification des conditions d'initialisation du calcul, en agissant sur les conditions initiales ou sur le processus de convergence, mais sans modification aucune de l'ensemble du traitement numérique, afin d'explorer l'existence d'une éventuelle autre solution. Cette seconde solution, parfaitement convergée, a été trouvée effectivement, par simple diminution de la fréquence à laquelle la géométrie des sillages est remise en cause en vue de leur équilibrage (réactualisation toutes les 300 itérations, au lieu de 20). Cette modification a pour effet de figer la géométrie des sillages pendant les 300 premières itérations, pendant lesquelles s'effectue la plus grande partie de la convergence. La seconde solution A obtenue ainsi présente alors un décollement généralisé à l'extrados du volet Fig.21, 23, mais sans aucune trace du décollement précédemment observé dans le sillage du corps principal (Solution B : Fig.20, 22).

Il a ainsi été mis en évidence l'existence de *2 solutions differentes* dans une même configuration, stables toutes deux par rapport à l'algorithme de calcul, l'obtention de l'une ou de l'autre ne dépendant que de l'initialisation.

4.7. Courbe de portance à 2 branches. Volet à 40°.

Cette même observation d'un dédoublement de solution a été effectuée à d'autres incidences, puis en conduisant les calculs par continuité au sein de chacune des deux familles de solutions, chaque calcul étant initialisé à partir d'un calcul à une incidence voisine.

Dès lors que la bifurcation vers l'un ou l'autre type de solution s'est trouvée effectuée, une modification éventuelle de la fréquence de réactualisation des sillages n'a plus aucune incidence sur le type de solution, chaque calcul restant du même type que celui ayant servi à l'initialiser. Les deux branches, A et B, sont totalement disjointes sur la large plage d'angle d'incidence décrite ici, Fig.24.

L'interprétation physique du dédoublement de solution calculé paraît simple. Le braquage élevé du volet δ_{volet} =-40° impose à la partie de l'écoulement comprise entre le bec et le volet une forte déviation, inaccessible en fluide visqueux sans décollement de l'une ou l'autre couche visqueuse qui le borde. Le décollement se produit donc, soit dans le sillage du corps principal, soit sur la couche limite extrados du volet, l'écoulement ayant la double possibilité de suivre soit la direction du sillage, soit celle de l'extrados du volet. Le contrôle de la bifurcation entre ces deux familles de solutions doit pouvoir s'effectuer par modification différentielle de la pression au sein des deux couches visqueuses, c'est-à-dire par aspiration et/ou soufflage, ceci dans le calcul comme dans l'expérience.

L'examen des documents d'essais, qui mentionnent la possibilité observée d'obtenir sur l'extrados du volet une solution décollée ou non par simple modification de la pression d'aspiration sur les parois latérales, à l'extrados du volet, semble confirmer cette hypothèse. La détermination du domaine d'incidence et d'angle de braquage du volet dans lequel cette double solution survient reste ici empirique.

Sur l'une des branches, correspondant au cas du décollement dans le sillage du corps principal, il a été possible de poursuivre les calculs au delà de l'incidence de décrochage du profil triple-corps, Fig. 24. Sur l'autre branche, et pour δ_{volet}= -20°, cela n'a pas encore été possible, plusieurs difficultés se conjuguant lorsque l'on se rapproche de l'incidence de décrochage, celui-ci semblant s'effectuer de facon plus brutale que sur la branche précédente.

4.8. Incidence 16°. Volet braqué à 40°.

En sélectionnant le cas de référence expérimental, c'est-à-dire la solution présentant un décollement généralisé sur le volet, la comparaison avec les résultats expérimentaux est excellente, en particulier en ce qui concerne la zone décollée à l'extrados du volet (fig.23). Comme dans le cas à $\delta_{volet}=-20°$, la comparaison est moins bonne sur le bec et sur le corps principal, à l'endroit de la pointe de Cp. Le niveau de Cp à l'extrados du volet, en amont du décollement, est également plus faible que dans l'expérience.

Toutefois, et plus encore que dans le cas précédent, l'accord calcul-expérience s'améliore lorsque l'angle de braquage du bec prend, au lieu de la valeur nominale, la valeur $\delta_{volet}=32°$, Fig.26. La répartition de Cp(x/c) sur le bec, Fig. 25 et 27, présente le même comportement que dans le cas précédent ($\delta_{volet}=-20°$: Fig 10 et 12). La comparaison des lignes de courant et des iso-mach pour chacune des deux solutions obtenues à l'incidence $\alpha=16°$, pour $\delta_{volet}=-40°$, Fig. 28, 30 et 29, 31, (solutions déjà illustrées par les figures 20, 22, et 21, 23), montre les deux types d'écoulement possibles, avec un décollement soit dans le sillage du corps principal, soit à l'extrados du volet.

4.9. Accès au calcul du décrochage.

La méthode a montré sa capacité à traiter des cas de décollements généralisés sur une telle configuration, malgré la différence considérable d'échelle entre les épaisseurs visqueuses sur la singularité émoussée et dans le décollement principal, Fig. 32, 33, et 34d, 34g. Ces figures présentent respectivement le maillage de calcul du fluide visqueux, le champ de vecteurs et les iso-mach, à l'incidence de 19°.

La comparaison des iso-mach à diverses incidences, au cours du décrochage, fait apparaître deux étapes dans la perte de portance, déjà visibles sur la Fig. 24, la première correspondant à la remontée vers l'extrados du profil du décollement situé dans le sillage du corps principal, la seconde correspondant à sa généralisation à tout l'extrados, Fig. 34.

5. CONCLUSION.

La méthode numérique d'interaction visqueux-non visqueux présentée ici (code VIS18), intègre les progrès réalisés sur les profils mono-corps dans le cas de décollements massifs.

Elle a pu être mise en oeuvre avec succès sur un hyper-sustentateur triple-corps, dans le cas d'un bec présentant une singularité fortement prononcée, l'intrados du bec formant une cavité. Les calculs ont pu être conduits sur la géométrie réelle, simplement émoussée au niveau du point singulier par un arrondi de très faible rayon. Malgré la difficulté de discrétisation à très petite échelle imposée par cette singularité, la méthode a permis le calcul de deux configurations multi-corps dans une large gamme d'incidences.

Elle s'est avérée capable de traiter des cas d'écoulements profondément décollés autour d'un profil multi-corps, au-delà de l'incidence de décrochage.

Elle a permis de mettre en évidence, sur le cas du profil RA16SC1 avec braquage du volet a -40°, une non-unicité réaliste de la solution, les 2 solutions obtenues étant parfaitement convergées. Cette double solution, persistante sur toute la gamme d'incidence, correspond à une bifurcation entre 2 types de décollements massifs, situés tantôt dans le sillage du corps principal, tantôt sur le volet.

Remerciements. *Les auteurs adressent ici leurs remerciements à D. Blaise, P. Girodroux-Lavigne, H. Gassot, pour leur concours précieux dans les traitements graphiques, ainsi qu'à S. Henry, qui a travaillé sur ce code lors de son passage à l'ONERA.*

REFERENCES.

[1] LE BALLEUR J.C. - Viscous-inviscid calculation of high-lift separated compressible flows over airfoils and wings. Proceedings AGARD Symp. on High-lift devices aerodynamics, Banff, Canada, 5-8 October 1992, AGARD-CP-415, Paper 26, to appear.

[2] LE BALLEUR J.C., NERON M. - Calculs d'écoulements visqueux décollés sur profils d'ailes par une approche de couplage. Proceedings AGARD-CP-291, Paper 11, 1981. (ONERA TP 1980-122).

[3] LE BALLEUR J.C. - New possibilities of Viscous-Inviscid numerical techniques for solving viscous flow equations, with Massive separation. Proceedings Fourth Symp. Numerical and Physical Aspects of Aerodynamic Flows, Selected papers, chap. 4, p. 71-96, editor T. Cebeci, SPRINGER-VERLAG 1990. (or ONERA TP 1989-24 Reprint)

[4] LE BALLEUR J.C. - Computation of flows including strong viscous interactions with coupling methods. - AGARD-CP-291, General Introduction, Lecture 1, Colorado-Springs (1981), or ONERA TP 1980-121.

[5] LE BALLEUR J.C. - Viscous-inviscid flow matching : Analysis of the problem including separation and shock waves. - La Recherche Aerospatiale 1977-6, p.349-358 (Nov.1977). French, or English transl. ESA-TT-476.

[6] LE BALLEUR J.C. - Viscous-inviscid flow matching : Numerical method and applications to two-dimensional transonic and supersonic flows. - La Recherche Aerospatiale 1978-2, p. 67-76 (March 1978). French, or English transl. ESA-TT-496.

[7] LE BALLEUR J.C. - Strong matching method for computing transonic viscous flows including wakes and separations. Lifting airfoils. - La Recherche Aerospatiale 1981-3, p. 21-45, English and French editions, (March *1981*).

[8] LE BALLEUR J.C. - Numerical viscid-inviscid interaction in steady and unsteady flows. - Proceed. 2nd Symp. Numerical and Physical Aspects of Aerodynamic flows, Long-Beach, (1983), chapt.13, p. 259-284 T. Cebeci ed.,Springer-verlag, 1984, (or ONERA-TP 1983-8).

[9] LE BALLEUR J.C. - Viscous-Inviscid interaction solvers and computation of highly separated flows. - "Studies of Vortex Dominated Flows", chap. 3, p. 159-192, Proceed. ICASE symp. NASA Langley Field, USA, (july 9-10, 1985), Hussaini and Salas ed., Springer-Verlag 1987, (or ONERA TP 1986-4).

[10] LE BALLEUR J.C - New possibilities of numerical viscous-inviscid coupling, for viscous flows with massive separation, and for inviscid Zonal-methods. Proceedings GAMNI/SMAI-IMA conference on Computational aeronautical dynamics, May 17-19, 1989, Antibes, France, SPRINGER-VERLAG to appear. (or ONERA TP 1989-150 Reprint)

[11] WIGTON L.B., HOLT M. - Viscous-inviscid interaction in transonic flow - 5th CFD, AIAA Paper 81-1003, Palo-Alto (June 1981).

[12] LE BALLEUR J.C. - Viscid-Inviscid coupling calculations for two- and three-dimensional flows. Lecture series 1982-04 on Computational Fluid Dynamics, Von Karman Institute, Belgium, (March 1982).

[13] PORCHERON B. - Rapport interne ONERA N^o 28 / 1736 AY. Décembre 1985.

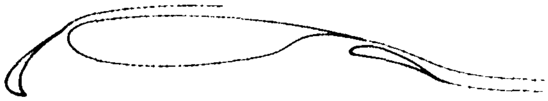

Fig. 1. Géométrie. (RA16SC1, δ_{bec} =30° , δ_{volet} = -20°).

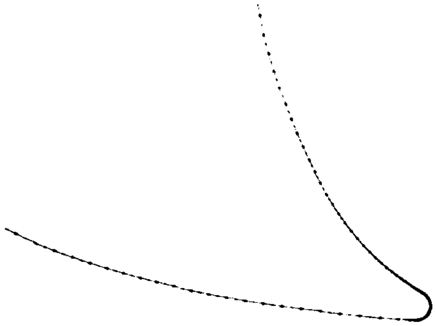

Fig. 2. Détail de la pointe du bec (singularité émoussée).

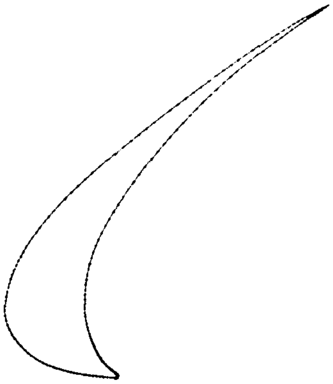

Fig. 3. Géométrie du bec AMD. Profil RA16SC1.

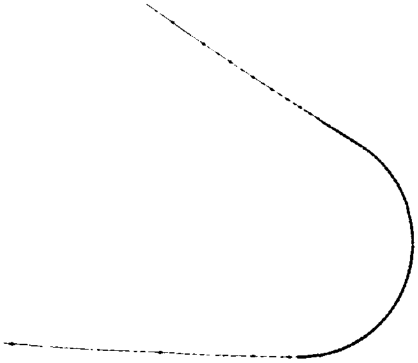

Fig. 4. Détail de l'arrondi à la pointe du bec

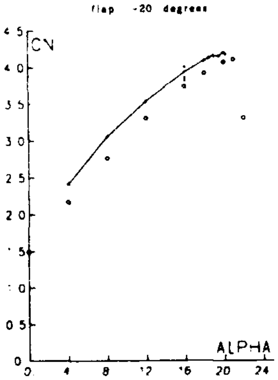

Fig. 5. Courbe de portance
(RA16SC1, M=0,123 , Re=1,8 10^6, δ_{volet} =-20°).

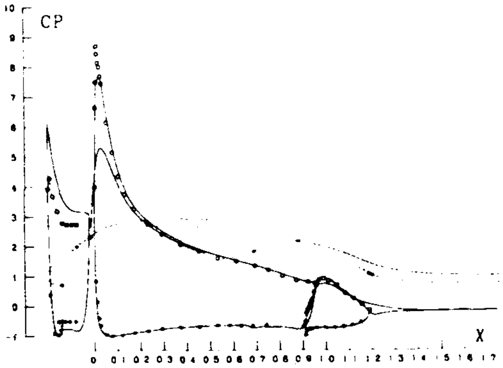

Fig. 6. Distribution de pression
(M=0,123 , Re=1,8 10^6, α=16°, δ_{bec} =30° , δ_{volet} =-20°).

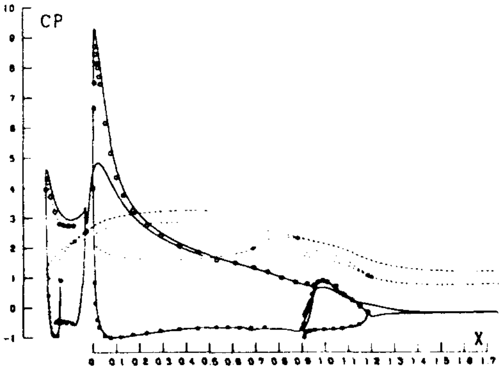

Fig. 7. Distribution de pression à la paroi
(M=0,123 , Re=1,8 10^6, α=16°, δ_{bec} =33° , δ_{volet} =-20°).

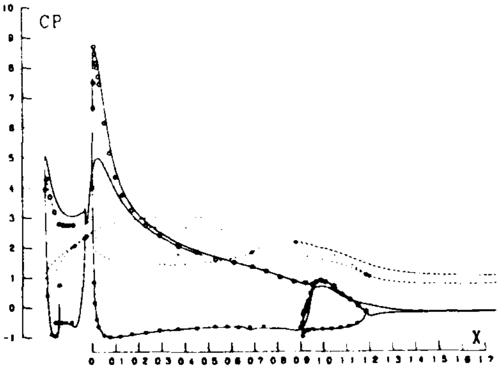

Fig. 8. Distribution de pression à la paroi
(M=0,123 , Re=1,8 10^6, α=16°, δ_{bec} =32° , δ_{volet} =-20°).

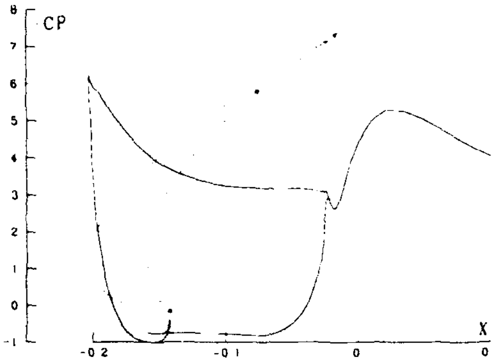

Fig. 9. Distribution de pression. Bec (orientation d'origine)
($M=0,123$, $Re=1,8\ 10^6$, $\alpha=16°$, $\delta_{bec}=30°$, $\delta_{volet}=-20°$).

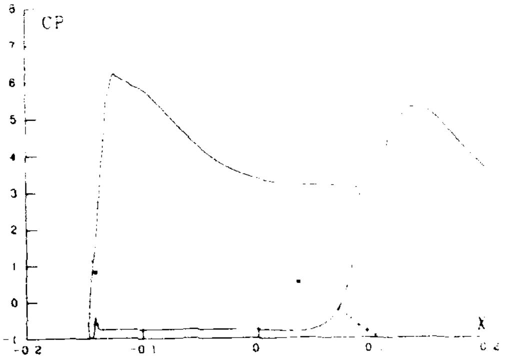

Fig. 10. Distribution de pression
Bec (orientation après rotation)
($M=0,123$, $Re=1,8\ 10^6$, $\alpha=16°$, $\delta_{bec}=30°$, $\delta_{volet}=-20°$)

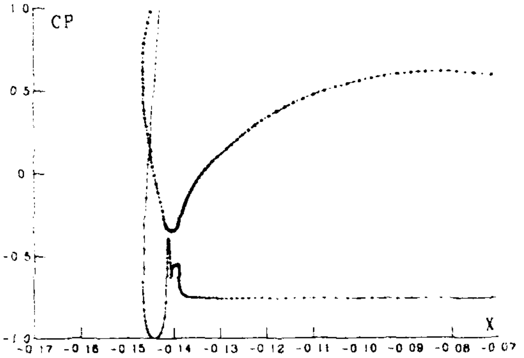

Fig. 11. Distribution de pression.
Bec (orientation après rotation)
($M=0,123$, $Re=1,8\ 10^6$, $\alpha=16°$, $\delta_{bec}=30°$, $\delta_{volet}=-20°$).

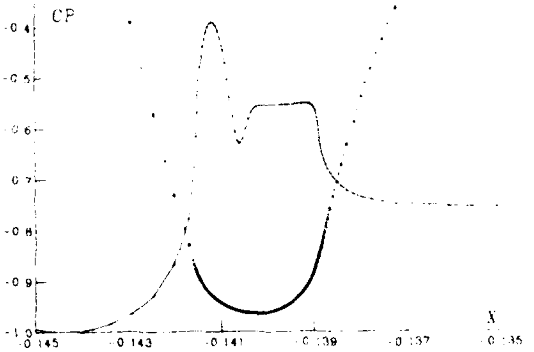

Fig. 12. Distribution de pression sur la singularité émoussée
Bec ($M=0,123$, $Re=1,8\ 10^6$, $\alpha=16°$, $\delta_{bec}=30°$, $\delta_{volet}=-20°$).

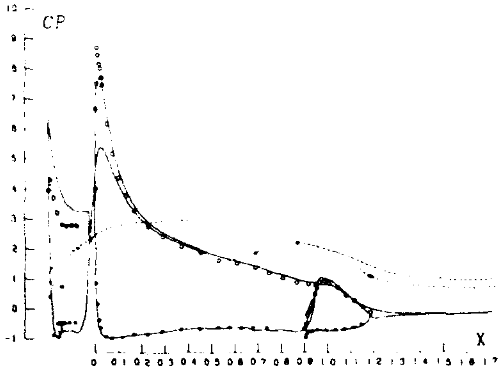

Fig. 13. Distribution de pression
($M=0,123$, $Re=1,8\ 10^6$, $\alpha=16°$, $\delta_{bec}=30°$, $\delta_{volet}=-20°$
Modèle à 1 équation de transport.

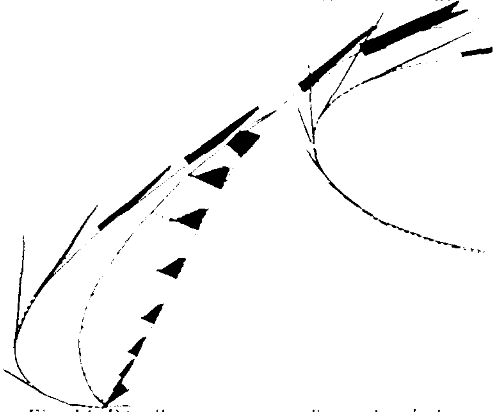

Fig. 14. Décollement massif à l'intrados du bec
Profils de vitesse
($M=0,123$, $Re=1,8\ 10^6$, $\alpha=16°$, $\delta_{bec}=30°$, $\delta_{volet}=-20°$).

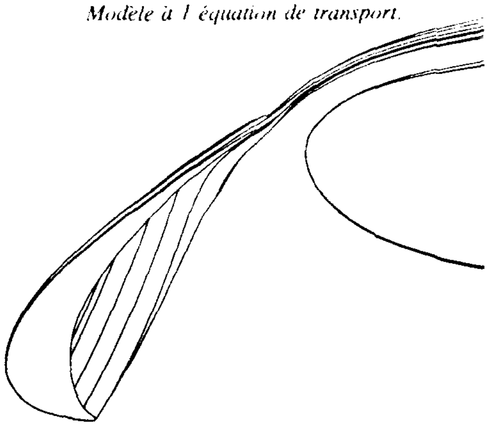

Fig. 15. Décollement massif à l'intrados du bec
Lignes de courant non visqueuses
($M=0,123$, $Re=1,8\ 10^6$, $\alpha=16°$, $\delta_{bec}=30°$, $\delta_{volet}=-20°$).

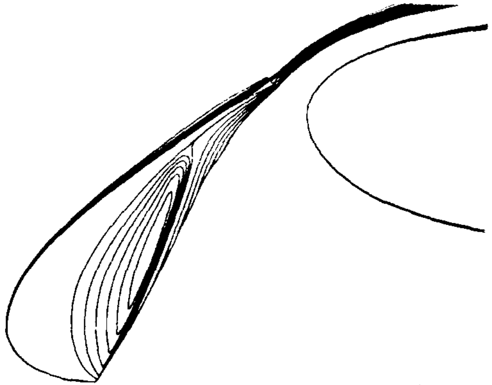

Fig. 16. Décollement massif à l'intrados du bec
Lignes de courant
($M=0,123$, $Re=1,8\ 10^6$, $\alpha=16°$, $\delta_{bec}=30°$, $\delta_{volet}=-20°$).

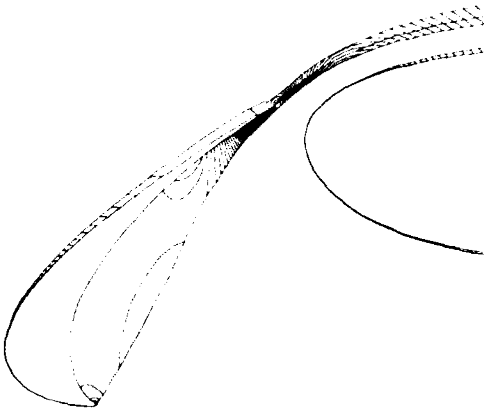

Fig. 17. Decollement massif à l'intrados du bec
Lignes iso-mach non visqueuses
($M=0.123$, $Re=1.8\ 10^6$, $\alpha=16°$, $\delta_{bec}=30°$, $\delta_{volet}=-20°$).

Fig. 18. Decollement massif à l'intrados du bec
Lignes iso-mach
($M=0.123$, $Re=1.8\ 10^6$, $\alpha=16°$, $\delta_{bec}=30°$, $\delta_{volet}=-20°$)

Fig. 19. Détail du décollement sur la singularité émoussée
Lignes iso-mach
($M=0.123$, $Re=1.8\ 10^6$, $\alpha=16°$, $\delta_{bec}=30°$, $\delta_{volet}=-20°$).

Fig. 20. Non-unicité. Profils de vitesse : Solution B
($M=0.123$, $Re=1.8\ 10^6$, $\alpha=16°$, $\delta_{bec}=30°$, $\delta_{volet}=-40°$).

Fig. 21. Non-unicité. Profils de vitesse : Solution A
($M=0.123$, $Re=1.8\ 10^6$, $\alpha=16°$, $\delta_{bec}=30°$, $\delta_{volet}=-40°$).

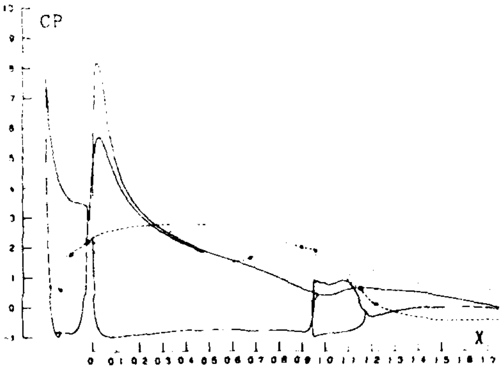

Fig. 22. Non-unicité. Distribution de pression : Solution B.
($M=0.123$, $Re=1.8\ 10^6$, $\alpha=16°$, $\delta_{bec}=30°$, $\delta_{volet}=-40°$).

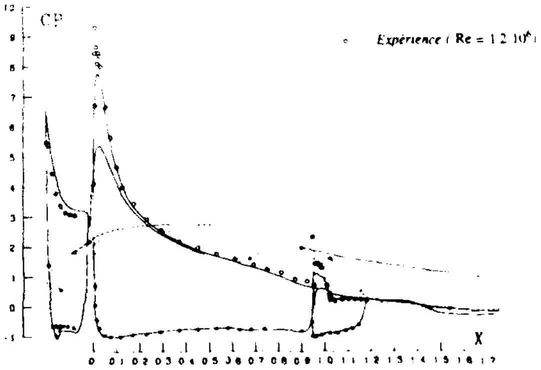

Fig. 23. Non-unicité. Distribution de pression : Solution A
($M=0.123$, $Re=1.8\ 10^6$, $\alpha=16°$, $\delta_{bec}=30°$, $\delta_{volet}=-40°$).

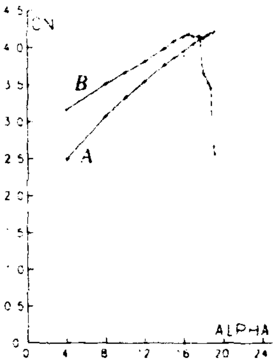

Fig. 24. Courbe de portance
(RA16SC1, M=0,123 , Re=1,8 10^6*, δ*$_{volet}$ *= -40°).*

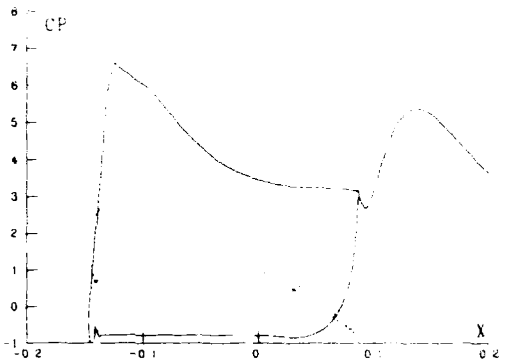

Fig. 25. Bec. Distribution de pression sur la singularité émoussée. Solution A (orientation après rotation, détail)
(M=0,123 , Re=1,8 10^6*, α=16°, δ*$_{bec}$ *=30° , δ*$_{volet}$ *= -40°)*

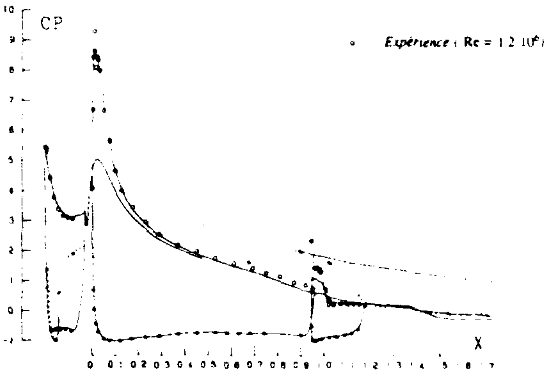

Fig. 26. Distribution de pression : Solution A
(M=0,123 , Re=1,8 10^6*, α=16°, δ*$_{bec}$ *=32° δ*$_{volet}$ *= -40°)*

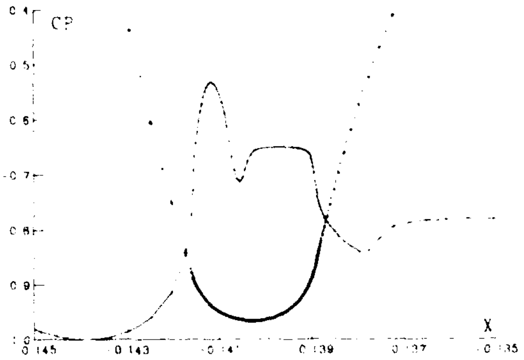

Fig. 27. Bec. Distribution de pression sur la singularité émoussée. Solution A (orientation après rotation, détail)

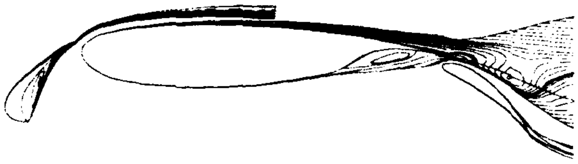

Fig. 28. Non-unicité. Lignes de courant : Solution B
(M=0,123 , Re=1,8 10^6*, α=16°, δ*$_{bec}$ *=30° , δ*$_{volet}$ *= -40°).*

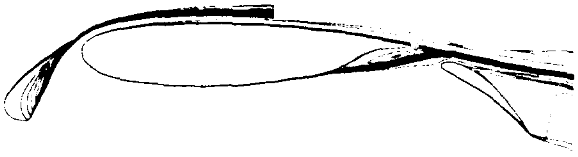

Fig. 29. Non-unicité. Lignes de courant : Solution A
(M=0,123 , Re=1,8 10^6*, α=16°, δ*$_{bec}$ *=30° , δ*$_{volet}$ *= -40°).*

Fig. 30. Non-unicité. Lignes iso-mach : Solution B
(M=0,123 , Re=1,8 10^6*, α=16°, δ*$_{bec}$ *=30° , δ*$_{volet}$ *= -40°).*

Fig. 31. Non-unicité. Lignes iso-mach : Solution A
(M=0,123 , Re=1,8 10^6*, α=16°, δ*$_{bec}$ *=30° , δ*$_{volet}$ *= -40°).*

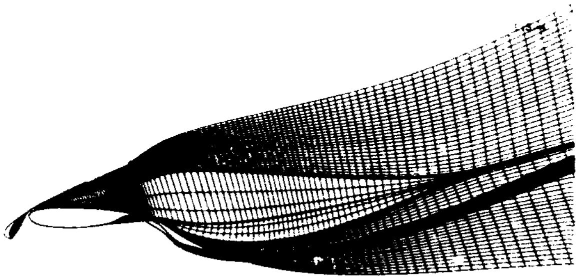

Fig. 32. Maillage visqueux auto-adaptatif : Solution B
($M=0,123$, $Re=1,8\ 10^6$, $\alpha=19°$, $\delta_{bec}=30°$, $\delta_{volet}=-40°$)

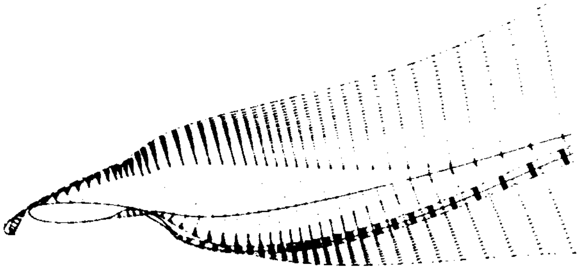

Fig. 33. Profils de vitesse : Solution B
($M=0,123$, $Re=1,8\ 10^6$, $\alpha=19°$, $\delta_{bec}=30°$, $\delta_{volet}=-40°$).

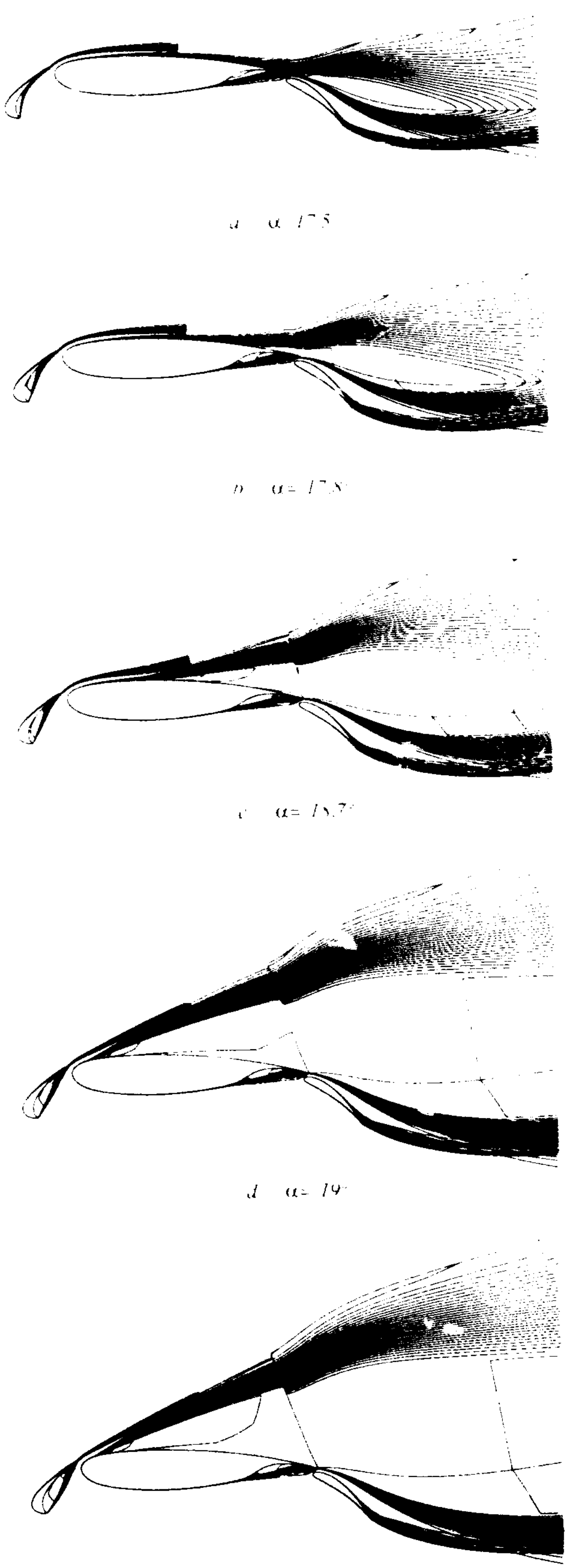

a : α= 17,5°

b : α= 17,8°

c : α= 18,7°

d : α= 19°

e : α= 19,1°

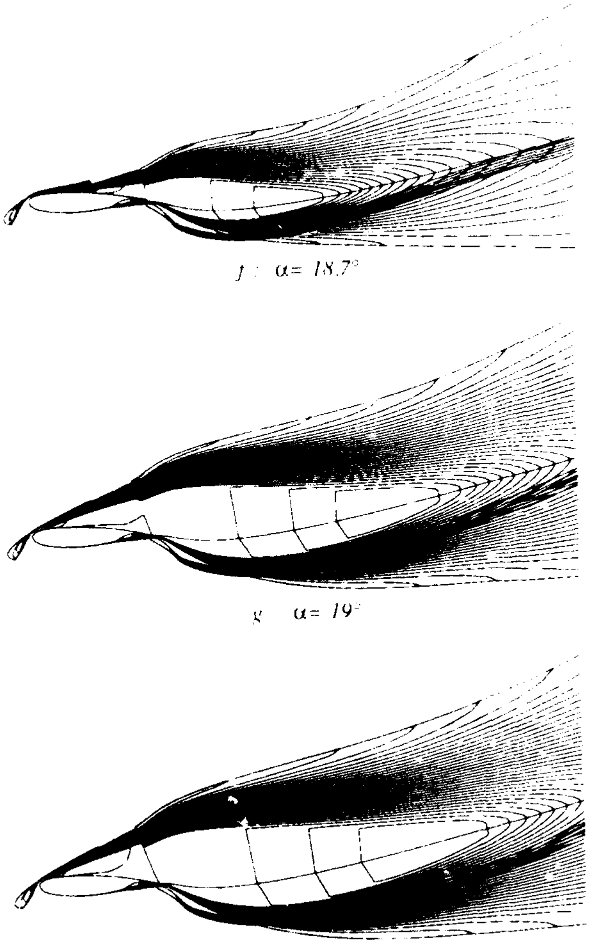

f : α= 18,7°

g : α= 19°

h : α= 19,1°

Fig. 34. Décrochage. Lignes iso-mach : Solution B
($M=0,123$, $Re=1,8\ 10^6$, $\delta_{bec}=30°$, $\delta_{volet}=-40°$)

HIGH-LIFT SYSTEM ANALYSIS METHOD USING UNSTRUCTURED MESHES

K. de Cock
National Aerospace Laboratory NLR
P.O. Box 90502
1059 CM Amsterdam, The Netherlands

SUMMARY

A 2D High-Lift configuration analysis method is described. The flow model used is based on the Euler equations, discretized on unstructured meshes. The generation of the unstructured meshes is based on the principle of successive grid adaptation with respect to the geometry. This approach makes later extension towards fully integrated grid adaptation with respect to the solution straightforward. The main characteristics of the Euler solver are upwind flux-difference splitting of the convective part of the Euler equations (second-order accurate discretisation in space) and four stage Runge Kutta local time stepping. Results obtained with this analysis method are shown for the NACA0012 airfoil and three element airfoils. Conclusions are drawn.

1. INTRODUCTION

The complexity of High-Lift system flow phenomena requires appropriate analysis methods, able to simulate a number of relevant flow mechanisms. The current High-Lift flow simulation models vary from models based on panel methods to models based on the Reynolds averaged Navier Stokes equations. A consequence of the complexity of the geometries under interest is a strong pressure on the turn-around-time of the High-Lift system analysis part in High-Lift system design methods. This turn-around-time requirement partly explains the success of panel methods in CFD. For field methods, a computational grid covering a 2D or 3D domain is always required. In order to attain sufficient accuracy while limiting the number of grid points, the grid should contain most of the grid points near to the boundaries of interest. Given the geometrical complexity of High-Lift devices, grid generation is often a hard task, resulting in a large amount of calendar time needed for grid generation. One valid approach of generating grids is the structured approach, as long as it is sufficiently automated. Examples of High-Lift results obtained with block structured meshes can be found in Refs. [1] and [2]. Another approach consists of the use of unstructured meshes (see for instance Ref. [3]). It is clear that CFD methods on unstructured meshes use more computer resources than their structured counterparts (interconnections between the grid nodes need to be stored for instance). The continuously increasing computer power is one of the reasons why the use of unstructured meshes in CFD is booming now. It is also clear that full automation is more readily achieved with unstructured meshes (Ref. [4]) since the grid generation is based on autonomous algorithms and not on partial differential equations that include interactively tuned source terms.
The current paper shows flow solutions based on the Euler equations and obtained on automatically generated unstructured meshes. It is shown that the grid generation is not dependent on the geometrical complexity of the High-Lift system.
Following cases are treated:

case1
NACA0012 single airfoil, Mach number at infinity equal to 0.85 and angle of attack equal to 1 degree.

case2
NLR422 three element airfoil, Mach number at infinity equal to 0.20 and angle of attack equal to 10 degrees.

case3
M1 three element airfoil, similar to case2 but extensively measured in the NLR HST tunnel. Mach number at infinity equal to 0.22 and

angle of attack ranging from -2.5 to 25 degrees.

2. GRID GENERATION

2.1 Context

Various algorithms for unstructured grid generation exist. The two most frequently used algorithms are

a) the Delaunay triangulation algorithm: basically this algorithm tells how to connect a given set of points into a valid triangular grid.

b) the advancing front algorithm: given the initial front (the surface grid on the geometry under interest for instance) the algorithm prescribes a method to advance the initial front towards the outer boundaries such that an unstructured grid results.

Both algorithms have been successfully used in the past and are the subject of constant further development and improvement. There are however some drawbacks of both algorithms.

Both algorithms a) and b) do not form a natural basis for grid adaptation with respect to the flow solution while a fully integrated approach of grid generation and grid adaptation is believed to be advantageous.

Algorithm a) needs an interactively made so called back ground grid to ensure certain properties of the grid like coarsening of the grid towards outer boundaries. This introduces user interaction, diminishing the automation level of grid generation based on the Delaunay triangulation algorithm.

Algorithm b) needs a suitable initial front. In case the surface grid is chosen as initial front, the construction of the surface grid becomes critical for the resulting grid quality in the neighbourhood of the surface. A mere triangulation of the CAD/CAM surface description is often not suitable enough for aerodynamic purposes. So the generation of the initial front can limit the automation level of grid generation based on the advancing front algorithm.

A third algorithm, hereafter called successive grid refinement, does not have the previously cited drawbacks. It will be shown that grid generation is considered as adaptation of an unstructured grid with respect to measurable properties of the geometries under interest. Hence adaption with respect to measurable properties of the solution is straightforward. Further the successive refinement algorithm automatically produces coarsening of the grid towards the outer boundaries of the grid and a surface grid suitable for aerodynamic purposes.

2.2 Grid generation by successive refinement.

The following assumptions are made:

A1: Let M be a given geometry around which the flow is to be calculated.

A2: Let the geometry M consist of $K_1,...,K_i,...,K_n$, a set of n non-intersecting contours.

A3: Let each contour K_i consist of m_i segments $S_1,...,S_j,...,S_{mi}$. (This allows to treat C_0 type contours, see Fig. 1).

A4: Let Sa_j be the analytical representation of a segment S_j. The analytical representation Sa_j of the segment S_j can be used to generate p_j points $P_1,...,P_k,...,P_{pj}$ on segment S_j.

A5: Let Ss_j be the spline representation of a segment S_j based on the points $P_1,...,P_k,...,P_{pj}$.

A6: Let Sp_j either be the polygonal representation of a segment S_j based on the points $P_1,...,P_k,...,P_{pj}$ or the convex hull of the spline representation Ss_j of a segment S_j.

A7: Let all polygonal representations Sp_j further be chosen such that the contours $K_1,...,K_i,...,K_n$ are closed. (Remark that the task of closing all contours is not trivial. All current flow simulation systems based on field methods, structured or unstructured, need contours which are closed.)

A8: Let G be an unstructured grid covering the geometry M. Two equivalent representations of grid G are used:

G_a: node table
node connection table per node

G_b: node table
node connection table per triangle

A9: The grid G is considered as given. It can either be a default grid consisting of 7 nodes (start from scratch) or a previously generated grid (restart).

A10: Let Sg_j be the momentary polygonal representation of a segment S_j based on the points of the grid G that would lie on the polygonal representation Sp_j of segment S_j, in case the grid generation would be stopped at that moment.

A11: Let F be a given flow solution on grid G. In the case at hand F is the solution of the Euler equations.

In order to ensure with a given flow solver a successful and reliable simulation of the flow around the given geometry M, some requirements of the grid can be identified a priori:

Rg1: The far field boundary of the grid G should lie sufficiently far from the geometry M. (usually 30 - 100 chords away from the geometry M). This distance is an input of the grid generator.

Rg2: The grid G should have most resolution in the neighbourhood of the geometry M. Coarsening of the grid G towards the outer boundary is still inevitable, even with nowadays powerful computers.

Rg3: Each node of the grid G should lie in the centre of the finite volume surrounding it. This grid smoothness requirement, if met, will favour the accuracy and convergence rate of the Euler solver.

The requirements for the polygonal representation Sg_j of the segments S_j based on the points of grid G can also be identified a priori. Important examples are:

Rs1: Each Sg_j should not be empty.

Rs2: Each Sg_j should at least consist of three points.

Rs3: The grid spacing along the geometry M should be sufficiently small in order to have enough resolution on the geometry M. If A is the total arc length of the geometry M and ΔA is the arc length between two points of any Sgj then:

$$\left(\frac{\Delta A}{A}\right)_{\text{maximum}} < \left(\frac{\Delta A}{A}\right)_{\text{prescribed}} \qquad (1)$$

should hold.

Rs4: The grid curvature along the geometry M should be sufficiently small in order to accurately represent gradients of the flow in the solver. If a, b and c are three subsequent points of any Sg_j and alpha is the angle between the vectors ab and bc then

$$\frac{\vec{ab}}{\|\vec{ab}\|} \cdot \frac{\vec{bc}}{\|\vec{bc}\|} > \cos(\alpha_{\text{prescribed}}) \qquad (2)$$

should be valid.

Rs5: All the segments Sg_j together should form closed and non-intersecting contours with the same topology as the segments Sp_j

The basics of the current grid generator can now be summarized:

- So called "grid generation" is adaptation of the given grid G with respect to the properties of the polygonal representations Sg_j of the segments S_j of geometry M.

The polygonal representions Sg_j of the segments S_j of geometry M are used to determine the refinement flags of the grid nodes.

- So called "grid adaptation" is adaptation of the given grid G with respect to the properties of the given flow solution F.
  The flow solution F is used to determine the refinement flags of the grid nodes.

Hence grid generation is the result of the recursion of following algorithms:

algo1: assignment of an "in-contour" flag (Ref. [6]).

Given a node i of the grid G, detect whether node i lies inside or outside the closed contours $K_1,\ldots,K_i,\ldots,K_n$. This algorithm is known as the Shimrat's Algorithm Ref. [7]. It requires O(K*Q) operations, K being the total number of line segments of the polygonal representations Sp_j forming together the contours $K_1,\ldots,K_i,\ldots,K_n$ and Q being the number of nodes for which the "in-contour" test is used. It can be shown that the required order of operations O(K*L) can be reduced to O((K+L) log(K+L)) (see algo2).

algo2: construction of Sgj.

Assume that a connection of representation G_a of the grid G intersects the polygonal representation Spj of a segment S_j of one of the contours K_i of geometry M.
If the grid generation would be stopped at this point, the intersection point would be one data point of Sg_j, the polygonal representation of the segment S_j based on the grid points. So by collecting in an array all intersection points, Sgj can be constructed (only grid points that have a negative "in-contour" flag can become member of Sg_j).
In essence algorithms algo1 and algo2 are equivalent to the so called geometric intersection problem which has extensively been studied for linear programming, hidden line elimination algorithms, wire layout etc. It has been proven that the problem of finding the intersecting pairs of N line segments does not require O(N*N) but O(N log(N)) operations Ref. [5]. In the particular case at hand, all the intersecting pairs consisting of a connection of representation G_a of the grid G and a line piece of the polygonal representation Sp_j of any segment S_j of the geometry M, should be found. If the grid G consists of K connections between nodes and the polygonal representations Spj of the segments Sj of the geometry M consist together of L line pieces then N = K + L. As a consequence the construction of Sg_j can be implemented in a efficient way.

algo3: control of the grid generator based on Sg_j.

Test if all Sg_j meet requirement Rs1.
If the answer is negative, then all nodes of the grid are flagged.
If the answer is positive, then ...

Test if all Sg_j meet requirement Rs2.
If the answer is negative for a particular Sg_j, then all nodes having intersecting interconnections with the corresponding Sp_j are flagged.
If the answer is positive, then ...

Test if all Sg_j meet requirement Rs3.
If the answer is negative for a particular Sg_j, then flag all nodes that have intersecting interconnections with the corresponding Sp_j causing the problem.
If the answer is positive, then ...

Test if all Sg_j meet requirement Rs4.
If the answer is negative for a particular Sg_j, then flag all nodes that have intersecting interconnections with the corresponding Sp_j causing the problem.
If the answer is positive, then ...

Test if all Sg_j together meet requirement Rs5.
If the answer is negative, then

flag the nodes that cause the problem.
If the answer is positive, then ...

Stop the refinement of flagged nodes and jump to algorithm algo6.

This algorithm consists of a logical if-then structure and requires only testing of properties of Sg_j. The number operations required is negligible.

algo4: a refinement algorithm for flagged nodes of grid G.

If i and j are two flagged nodes of grid G a new node is inserted between i and j. Further the interconnection table of representation Ga of grid G is updated. This algorithm has only local influence and requires O(M) operations, if M is the number of flagged nodes.

algo5: a smoother.

Move all internal nodes i towards the centre of gravity formed by node i and its neighbours. Algorithm algo5 helps to meet requirement Rg3.

Recursion of algorithms algo1, algo2, algo3, algo4 and algo5 until a jump is made to algo 6 results in a grid which is automatically refined towards the contours, without any user defined tuning. Hence requirement Rg2 finally will also be met. The final grid is obtained by applying algorithms algo6 and algo7 the grid:

algo6: a boundary reconstruction algorithm.

Move grid nodes linked to the polygonal representation Sg_j on to the spline representation Ss_j of the segment S_j and give them the corresponding solver boundary code. So the user has to determine in the geometry description file for each segment S_j whether it concerns a part of a solid wall, a symmetry wall, etc. This algorithm algo6 requires O(S) operations, S being the number of nodes on the boundaries.

algo7: a node killing algorithm.

Remove all nodes flagged by the "in-contour" indicator algo1. This algorithm only has local influence. It requires O(R) operations, R being the number of flagged nodes.

It is obvious that the grid generation as described is not sensitive to the complexity of the geometry M to be treated. Generation of a grid around a complex High-Lift device is as easy as generating a grid around a single airfoil.

For what concerns the extension towards 3D applications, two algorithms need special attention namely the "in-surface" indicator, algo1, and the construction of Sgj, algo2.
For the "in-surface" indicator, algo1, the intersection of K elementary triangular planes of the 3D poly surface representation Spj with L connections of representation G_a of the grid G should be found. This can be done within the same order of operations as for the 2D analogy of algo1.
For the construction of Sg_j, algo2, the same holds true.

2.3 Grid generator D2GRID.

Characteristic memory requirements of the current two dimensional grid generator D2GRID are:

reals per node: 5
integers per node: 18+2*KB

KB being the maximum number of neighbours of a node i occurring in grid G. Typically KB equals 10.

Some run time characteristics of the current two dimensional grid generator D2GRID are:

- The lowest grid level of the multi grid V cycle is generated in one grid generator run.
- Uniform refinement is used to obtain the subsequent finer grids of the multi grid V cycle. As a consequence the subsequent grids of the multi grid V cycle are nested, such that no additional interpolation data is needed.
- For the NLR422 grid of Fig. 5 the grid generation took about 2000 CPU seconds on the NLR Cyber 962.

Conclusions:

- The memory requirements do not form the bottle neck for the current grid generator.
- For three dimensional applications an efficient implementation of the *geometric intersection problem* is important.
- The vectorisation level of the algorithm is low due to the very deep IF-THEN structures.

3. EULER SOLVER

3.1 Solver algorithm.

The current flow simulation system is based on the unsteady Euler *equations (3)*:

$$\frac{\partial}{\partial t}\begin{bmatrix}\rho\\ \rho u\\ \rho v\\ \rho\left[\frac{p}{(\gamma-1)\rho}+\frac{u^2+v^2}{2}\right]\end{bmatrix} = -\frac{\partial}{\partial x}\begin{bmatrix}\rho u\\ \rho uu+p\\ \rho uv\\ \rho u\left[\frac{\gamma p}{(\gamma-1)\rho}+\frac{u^2+v^2}{2}\right]\end{bmatrix} - \frac{\partial}{\partial y}\begin{bmatrix}\rho v\\ \rho vu\\ \rho vv+p\\ \rho v\left[\frac{\gamma p}{(\gamma-1)\rho}+\frac{u^2+v^2}{2}\right]\end{bmatrix} \quad (3)$$

In equation (3) ρ is the density, p is the static pressure, u and v are the cartesian x and y components of the velocity vector in the two dimensional space and γ is the specific heats ratio. Density, cartesian velocity vector components and static pressure form the vector of primitive variables ξ, *a vector* in the four dimensional solution space. Equation (3) is to be supplemented with the perfect slip boundary condition on solid walls

$$u n_x + v n_y = 0 \quad (4)$$

and the far field boundary condition

$$M_\infty\ ,\ \alpha_\infty\ ,\ \rho_\infty\ ,\ p_\infty \quad (5)$$

In equation (4) nx and ny are the cartesian components of the unit normal to the solid wall boundary. Equations (3), (4) and (5) should be solved for the vector of primitive variables ξ. In a shorter notation equation (3) reads as:

$$\frac{\partial \zeta}{\partial t} = -\frac{\partial F}{\partial x} - \frac{\partial G}{\partial y} \quad (6)$$

In the grid generation phase the flow domain is divided into finite volumes, on an average having an hexagonal shape. An example is given *in Fig. 2*. In each grid point i the vector of primitive variables ξ is unknown. In Fig. 3 the grid around the slat of Fig. 1 is shown. The grid points are (approximately) lying in the centres of their surrounding control volumes, hence the *present method* can be characterised as a vertex centred finite volume method. Expressing that equation (6) should hold within each finite volume Ω of the grid yields:

$$\frac{d\zeta}{dt}\Big|_i \Omega_i = -\int_{\Omega_i}\left(\frac{\partial F}{\partial x} + \frac{\partial G}{\partial y}\right) d\Omega \quad (7)$$

To obtain the left hand side of equation (7) two assumptions are made:

- the shape of the finite volumes does not change in time.
- the unknowns are constant within the finite volume.

The latter assumption is due to our interest in the steady solution. Generally, a second order accurate discretisation of the right hand side of equation (7) is obtained by assuming a linear spatial variation of the primitive variables vector ξ within the finite volume. This is practically achieved by representing each component ξ_k of the vector of primitive variables by a plane in the x, y, ξ_k space. This plane is completely determined by the component ξ_k of the vector of primitive variables ξ in the centre of the finite volume and the k th component of the unique spatial gradient vector of the primitive variables vector ξ in the finite volume. So the primitive variables vector is defined within the finite volume by equation (8):

$$\xi(x,y) = \xi(x_i, y_i) + \frac{\partial \xi}{\partial x}\Big|_i (x - x_i) + \frac{\partial \xi}{\partial y}\Big|_i (y - y_i) \qquad (8)$$

The spatial gradient vector of the primitive variables vector ξ is unique since the limiting in the present scheme is applied during the approximation of the spatial gradient vector of the primitive variables vector ξ. An example for one component of the spatial gradient vector is given in equation (9):

$$\frac{\partial \xi}{\partial x}\Big|_i = \frac{1}{\Omega_i} \int_{S_i} \xi_{\text{lim. extr.}} \, n_x \, ds \qquad (9)$$

Equation (9) is the result of the Gauss theorem applied to the finite volume around node i. S_i is the surface of the volume Ω_i, nx and ny are the cartesian components of the unity outward normal on the surface S and $\xi_{\text{lim.extr.}}$ is the limited extrapolation of the primitive variables vector ξ towards the surface S_i. If the neighbours of node i are called j, equation (9) can be made discrete:

$$\frac{\partial \xi}{\partial x}\Big|_i = \frac{\sum_j \left(\xi_i + \frac{1}{2} \, \text{LIM}\,(\xi_j - \xi_i, \xi_i - \xi_k) \right) n_x \, \Delta S}{\sum_j \left(x_i + \frac{1}{2} \, (x_j - x_i) \right) n_x \, \Delta S} \qquad (10)$$

LIM in equation (10) stands for a limiter, in the present work the Van Albada limiter was used (Ref. [8]).

The underlying idea of this approach is that discontinuities (such as shocks for instance) are located on the interfaces between the finite volumes of the grid, and are not allowed to cross the finite volumes (the Gauss theorem is not applicable in case discontinuities cross the finite volume).
Applying the Gauss theorem to the right hand side of equation (7) it transforms to

$$\frac{d\zeta}{dt}\Big|_i \Omega_i = - \int_{S_i} (F n_x + G n_y) \, dS \qquad (11)$$

This equation is shortened as

$$\frac{d\zeta}{dt}\Big|_i \Omega_i = - \int_{S_i} N \, dS \qquad (12)$$

with N the normal flux at the interface S of the finite volume. Equation (12) can be integrated in time by a standard four stage Runge Kutta local time stepping method (see for instance Ref. [9]). Convergence acceleration can be done by a Full Multi Grid acceleration technique based on defect correction. We will further concentrate on the approximation of the integral in the right hand side of equation (12). For each part of the cell surface S the normal flux N should be calculated. Consider the cell interface S_{ij} between nodes i and j. Let Ni be the normal flux based on the primitive variables vector $\xi_{i\,\text{extr.}}$, the primitive variables vector ξ extrapolated from i towards the cell interface S_{ij} with equation (8):

$$N_i = N(\xi_{i\,\text{extr.}}) \qquad (13)$$

A similar definition holds for N_j. Within an upwind flux difference scheme the normal flux N_{ij} at the cell interface S_{ij} is defined as:

$$N_{ij} = \frac{N_i+N_j}{2} - \frac{1}{2} R \, |\Lambda| \, L \, (\xi_{j\,\mathrm{extr.}} - \xi_{i\,\mathrm{extr.}}) \qquad (14)$$

In equation (14) $|\Lambda|$ is the eigenvalue matrix of the discrete Jacobian of the normal flux with respect to the primitive variables vector ξ. R and L are the right and left eigenvector matrices of the same Jacobian. The discrete Jacobian of the current solver is based on the polynomial character of the components of the normal flux with respect to the primitive variables Ref. [10].
Equation (13) clearly shows that the present scheme goes back to Van Leer 's MUSCL scheme [11] such that this scheme can be expected as being monotone and second order accurate in space.

3.2 Solver D2EUL

Some memory requirements of the current two dimensional multi grid Euler solver are

reals per node: 47 + 4*KB
integers per node: 3 + 3*KB

KB being the maximum number of neighbours of a node i occurring in grid G. Typically KB is equal to 10. For the case of a structured grid 2D Euler solver with the same characteristics (same scheme, same vector computer, same compromises between speed and memory):

reals per node: 47 + 3*KB
integers per node: 3

In this case KB is equal to 4.
For a 3D multi grid Euler solver the following would be found:

reals per node: 64 + 6*KB
integers per node: 3 + 4*KB

Typically KB is now equal to 25. For the case of a structured 3D Euler solver with the same characteristics:

reals per node: 64 + 4*KB
integers per node: 3

In the latter case KB is equal to 6.

Some run time characteristics of the current two dimensional multi grid Euler solver are

- More than 4 orders of magnitude reduction in maximum residual after 1000 multi grid V cycles for a three level 45512 nodes grid around a three element airfoil.
- 74 μ-sec per multi grid V cycle and per node of the top level grid of the multi grid cycle.
- Vector operation ratio on the NLR NEC SX3-12 99.5%
- Vector length 127.6
- 573 MFLOPS (FLoating point OPerations per Second)

Conclusions can be drawn from these figures:

- The use of 2D unstructured grids requires 47 percent more storage of reals and 1000 percent more storage of integers. The use of 3D unstructured grids requires 143 percent more storage of reals and 3333 percent more storage of integers.
- KB should be as low as possible. The grid generator can be extended with a post processing algorithm that reduces KB towards the natural average of 6 in two dimensions and 12 in three dimensions. The percentages would respectively be 20, 600, 54 and 1600 percent. The lowest possible KB occurs in case the control volumes are chosen triangular.
- The largest increase of memory use is due to the storage of interconnections since the interconnections are no longer known a priori. This increase should be payed off by the advantages of using unstructured grids, mainly by the automation of the grid generation.

4. APPLICATIONS

4.1 Case1.

The computational grid has 10433 nodes. The Mach number is 0.85 and the angle of attack is 1 degree. The Mach number distribution on the surface is shown in Fig. 4. It can be seen that the scheme is monotone in the neighbourhood of the shocks and that it captures the shocks with one interior node. The present solution is compared with Ref. [13]. The Mach number distribution is very sensitive to the total pressure losses due to the dissipative character of the scheme. Once generated (at the nose of the profile) the total pressure losses are convected downstream, causing a uniform difference between the two Mach number distributions.

4.2 Case2.

Two grids around this airfoil are used. A coarse grid with 11673 nodes and one global refinement of this coarse grid with 45512 nodes. The Mach number at infinity is 0.20 and the angle of attack is 10 degrees. A global view of the fine grid is shown in Fig. 5. A detail of the coarse grid around the slat has been shown in Fig. 3. A summary of the convergence history is given in Figs. 6 and 7. Figure 6 shows the maximum residual of the mass equation occurring in the whole flow field. It can be seen that the slope of the curve deteriorates going from the coarse to the fine grid, for both the single grid and the multi grid method. Far more iterations are needed to converge in the single grid method case. Figure 7 shows the lift coefficient history. The lift coefficient is slightly higher for the fine grid, indicating that in principle another refinement of the grid is needed. For the fine grid the Mach number distribution around the whole configuration is shown in Fig. 8. Several dips in the iso Mach number lines near to the surface can be seen. These are due to the total pressure losses to which the Mach number is sensitive. The total pressure losses are caused by the dissipative character of the scheme used (mainly the limiting of the scheme, reducing the scheme locally to a first order accurate scheme). The pressure coefficient distributions around the slat, wing and flap are shown in Figs. 9, 10 and 11. In these figures a comparison is made between the current solutions on the coarse and fine grid and the solution of a potential method, in which the slat and wing cove shape are changed (by an iterative method) such that the pressure coefficient at the bubble edges is constant Ref. [12]. It is observed that the solution on the fine grid matches better the potential solution than the solution on the coarse mesh. The streamline following the bubble edge of the slat cove in the potential calculation is plotted in Fig. 12, together with the iso total pressure loss lines, found on the coarse grid. Fig. 13 shows the wing cove. It can be seen that for the slat cove the bubble edge found with the potential method does not coincide with the edge of the bubble found with the Euler method. For the wing cove the agreement is much better. Fig. 14 and 15 are the corresponding figures in case of the fine grid. It can be observed that the level of the total pressure losses diminishes on the finer grid, except in the coves where the peak value increases and the shape of the isolines changes.

4.3 Case3.

The grid used is very similar to the coarse grid around NLR422 and contains 15351 nodes. The Mach number at infinity is 0.22 and the angle of attack ranges from -2.5 to 25 degrees. Fig. 16 shows the cl - alpha curve for M = 0.22, Fig. 17 the cd - alpha curve and Fig. 18 the cm - alpha curve. Due to the effect of the dissipative character of the scheme the calculated curves fit relatively well to the measured curves. Figs. 19 and 20 give the numerical and experimental values of the pressure defect at the slat and flap cove rakes for 9 degrees incidence. Due to the perfect slip boundary condition of the Euler equations the pressure defect decreases toward the solid wall. The peak level of the pressure defect however corresponds reasonable with the experiments.

CONCLUSIONS

It is shown that the described flow simulation system is capable to successfully handle complex 2D geometries such as encountered in High-Lift systems. The main characteristic of the unstructured grid flow simulation system is the automation of the grid generation procedure. This paper illustrates the application of unstructured grid generation to solve the Euler equations for complex geometries in two dimensions. For a typical three element test case with 16000 nodes the total grid generation plus solver turn-around-time of the current flow simulation system is approximately 2 hours. The computational results are compared with experimental results and show qualitative agreement, due to the dissipative behaviour of the solution of the discrete Euler equations. A future critical issue is to account for the dissipative effects in a proper way. It requires an extension of the mathematical model to Reynolds averaged Navier Stokes equations.

ACKNOWLEDGEMENTS

The author wishes to thank Dr. B. Oskam for the fruitful discussions and the ideas about the applications of the analysis method, Ir. P. Termes for the comparison between calculations and GARTEUR AD (AG08) results and the members of the GARTEUR AD (AG08) for their permission to publish results obtained within the action groups.

REFERENCES

1. Haase, W., Brandsma, F., Helsholz, E., Leschziner, M., Schwamborn (Eds.), 'EUROVAL - A European Initiative on Validation of CFD codes', notes on numerical fluid dynamics volume XX, to be published by Vieweg.

2. De Cock, K., 'Effect of wing sweep on the solution of the continuous and discretized euler equations for a High-Lift configuration',NLR CR 91176, 1991.

3. Mavriplis, D.J., Martinelli, L., 'Multi grid solution of compressible turbulent flow on unstructured meshes using a two-equation model', ICASE Report No. 91-11, 1991.

4. Nakahashi, K., Egami, K., 'An automatic euler solver using the unstructured upwind method.', Computers and Fluids, Vol. 19, nr. 34, pp. 273-286, 1991.

5. Shamos, M.I. and Hoey, D., 'Geometric intersection problems', in 17th Annual Symposium on Foundations of Computer Science, IEEE, 1976.

6. Milgram, M.S., 'Does a point lie inside a polygon', J. Compt. Phys. 84, 1989.

7. Shimrat, M., Commun. ACM, pp.434, 606 ,1962

8. Van Albada, G.D., Van Leer, B., Roberts, W.W., 'A comparative Study of Computational Methods in Cosmic Gas dynamics', Astron. Astrophys. 108, 76-84, 1982.

9. Batina, J.T., 'Accuracy of an Unstructured-Grid Upwind-Euler Algorithm for the ONERA M6 Wing', J. Aircraft, Vol. 28, NO. 6, 1991.

10. Dick, E., 'Multigrid formulation of polynomial flux-difference splitting for steady Euler equations', J. Comput. Phys., 1, 161-174, 1991.

11. Van Leer, B., 'Towards the ultimate conservation difference scheme V, a second order sequel to Godunov 's method', J. Comput. Phys., 32, 101-136, 1979.

12. Oskam, B., Laan, D.J., Volkers D.F., 'Recent advances in computational methods to solve the high-lift multi-component airfoil problem', AGARD Conference Proceedings, No.365, 1984.

13. 'Test Cases for Inviscid Flow Field Methods', AGARD Advisory Report, No.211, 1985.

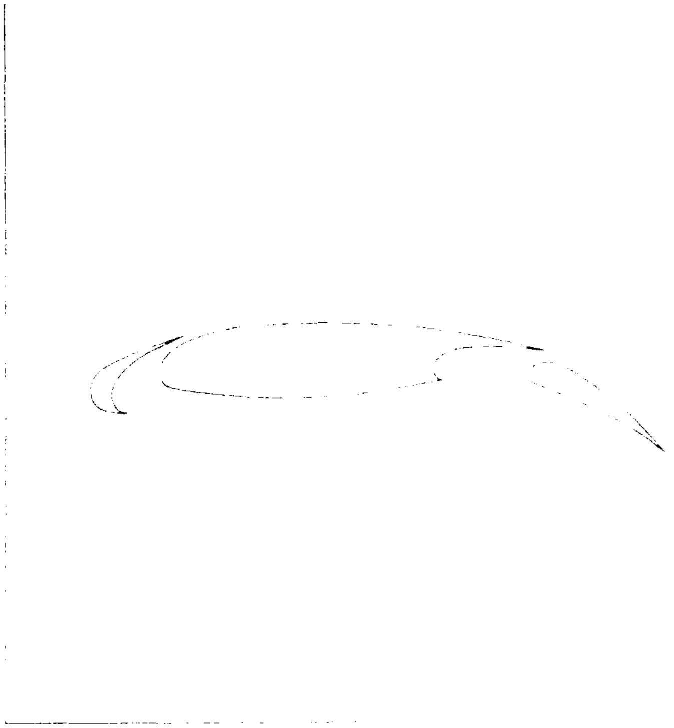

Fig. 1 Three element airfoil NLR422 (case 2)

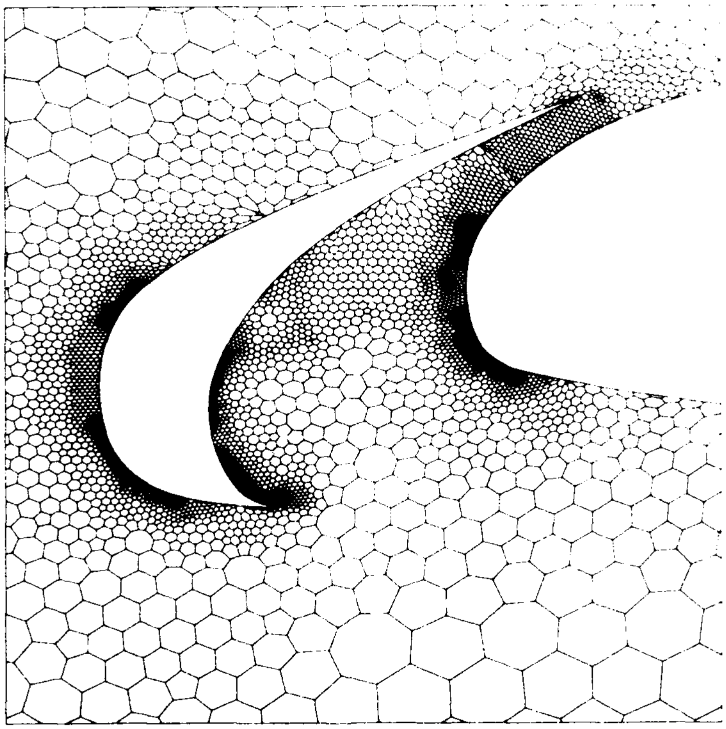

Fig. 2 Finite volumes around the slat of the NLR422 three element airfoil (case 2)

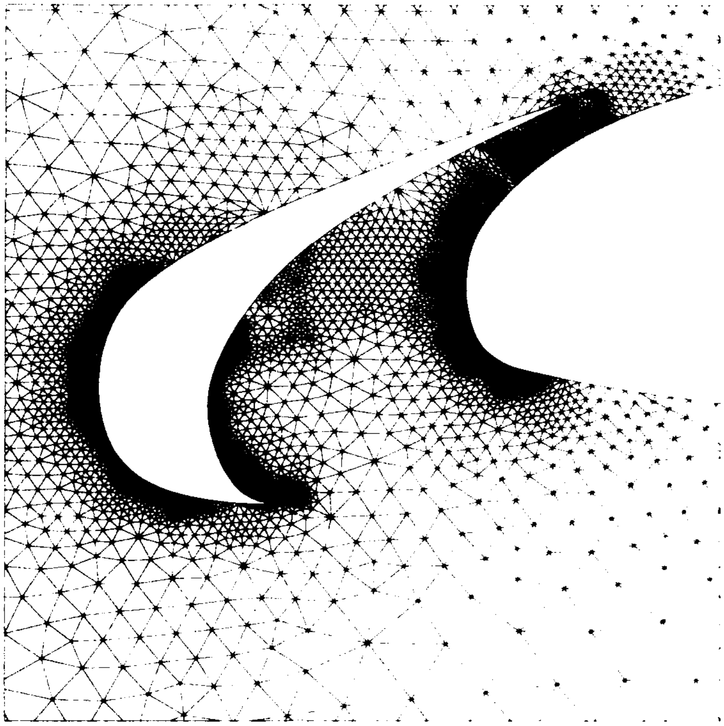

Fig. 3 Grid around the slat of the NLR422 three element airfoil (case 2)

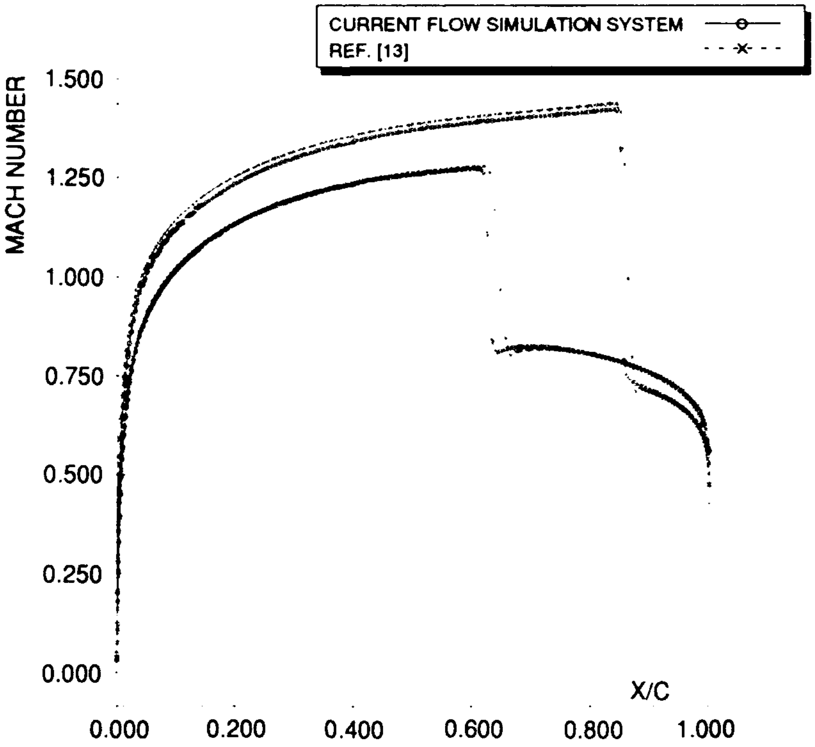

Fig. 4 Mach number distribution around the NACA0012 single airfoil (case 1)

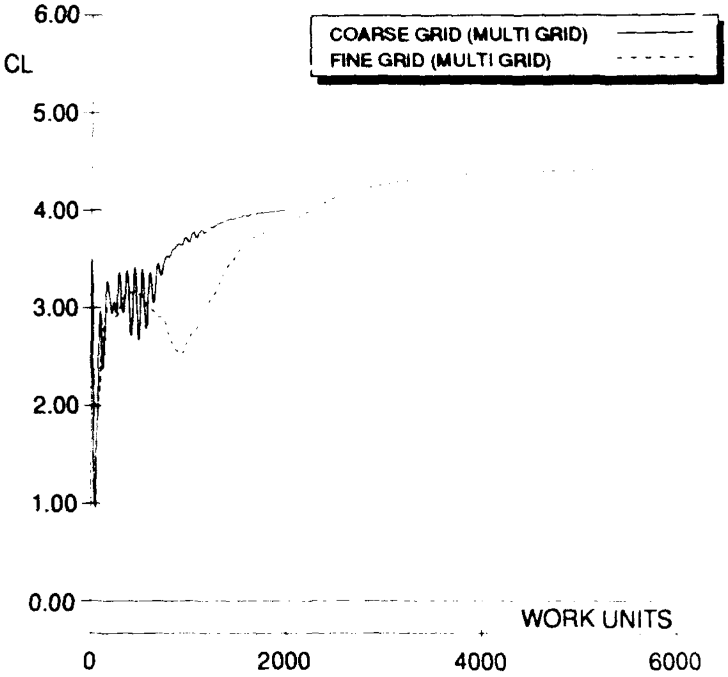

Fig. 7 Lift coefficient history (case 2)

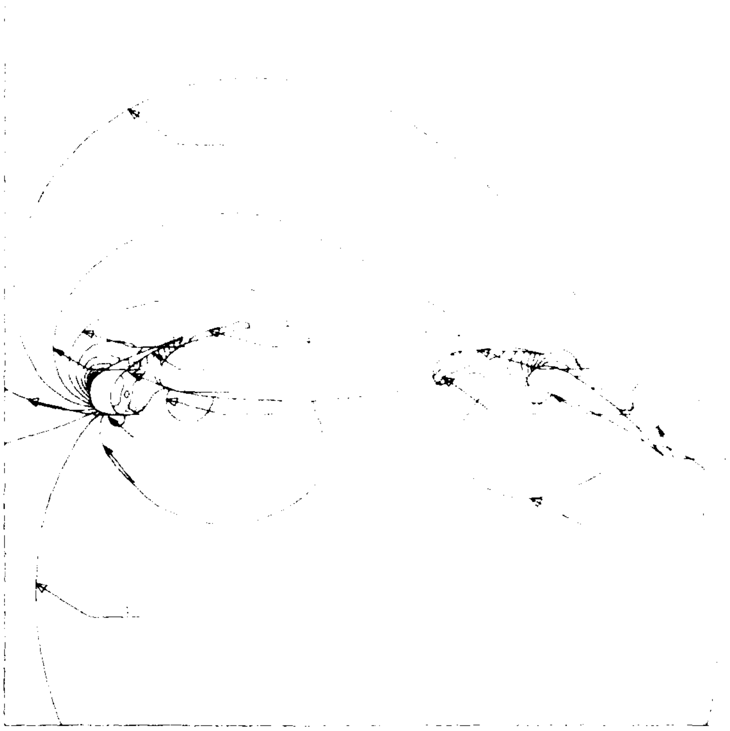

Fig. 8 Mach number distribution around the NLR422 three element airfoil (case 2)

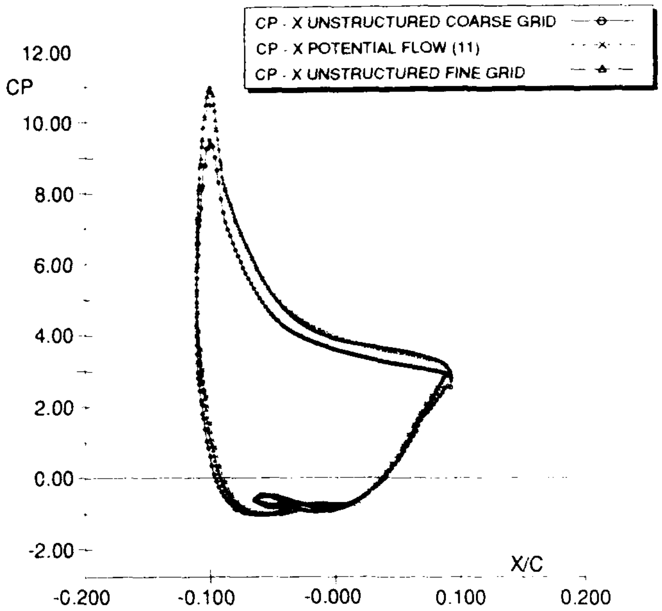

Fig. 9 Pressure coefficient distribution on the slat of the NLR422 three element airfoil (case 2)

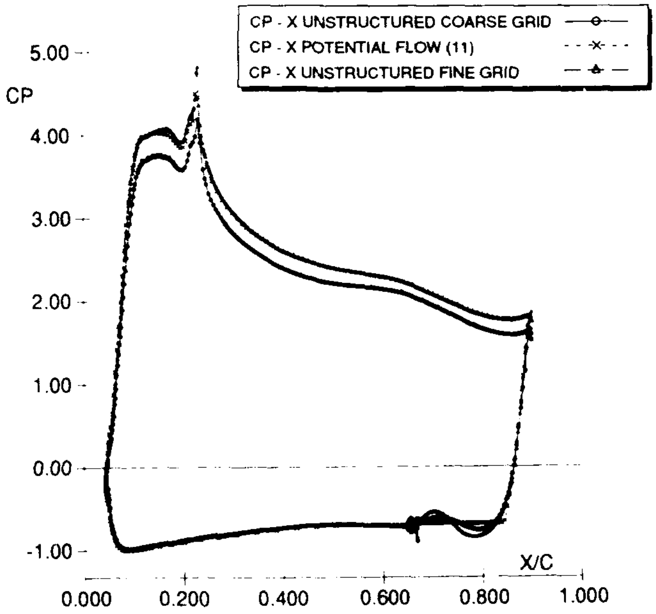

Fig. 10 Pressure coefficient distribution on the wing of the NLR422 three element airfoil (case 2)

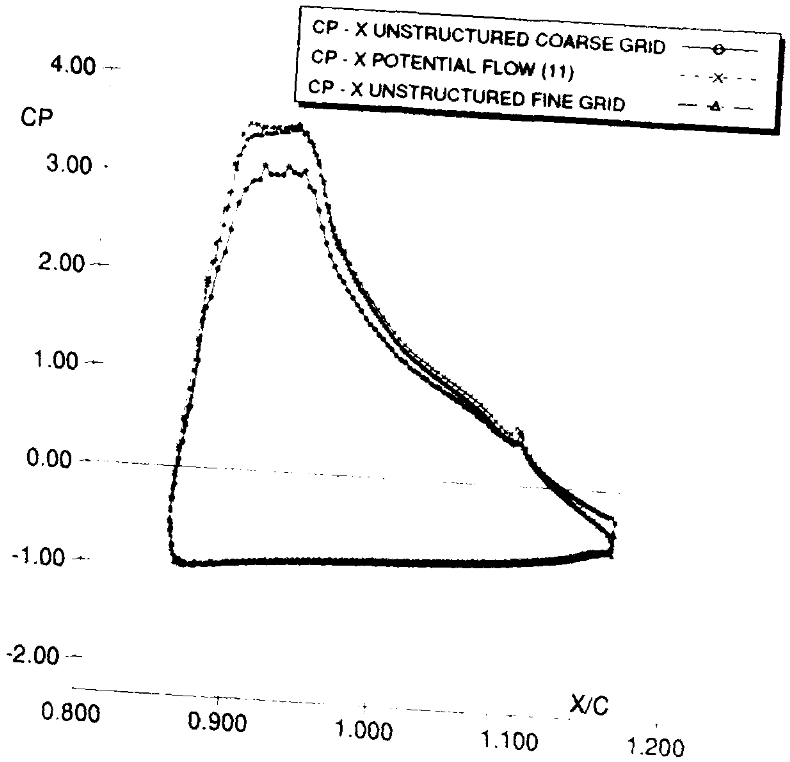

Fig. 11 Pressure coefficient distribution on the flap of the NLR422 three element airfoil (case 2)

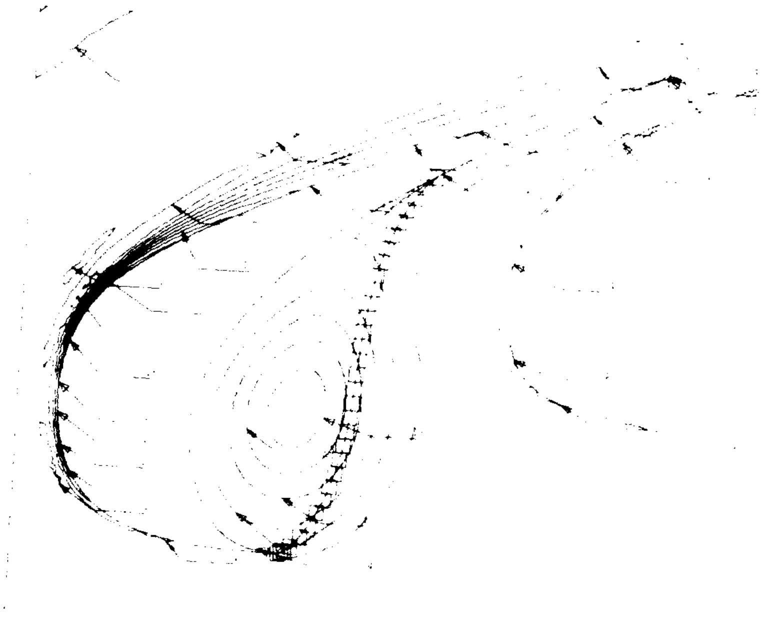

Fig. 12 Iso total pressure loss lines around the slat cove of the NLR422 three element airfoil: coarse grid (case 2)

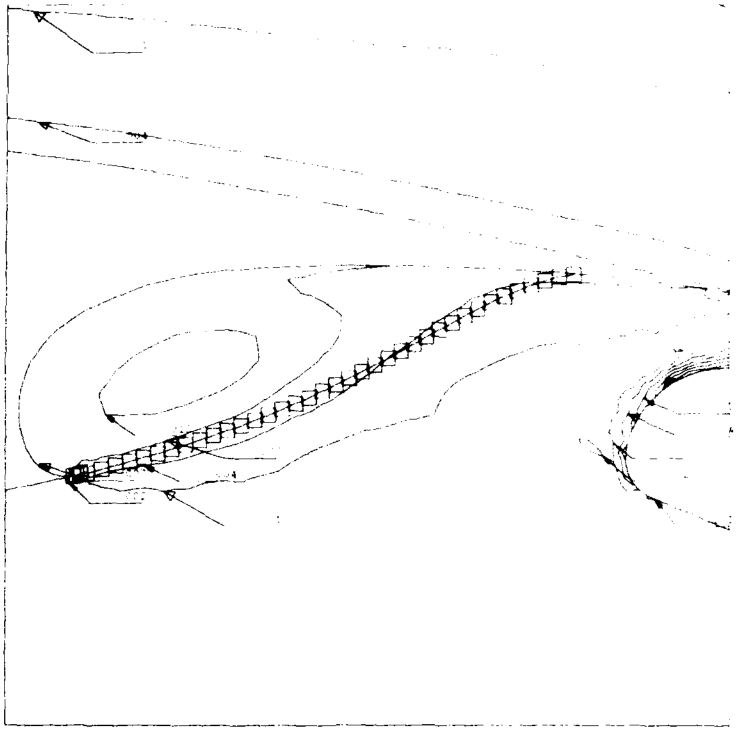

Fig. 13 Iso total pressure loss lines around the wing cove of the NLR422 three element airfoil: coarse grid (case 2)

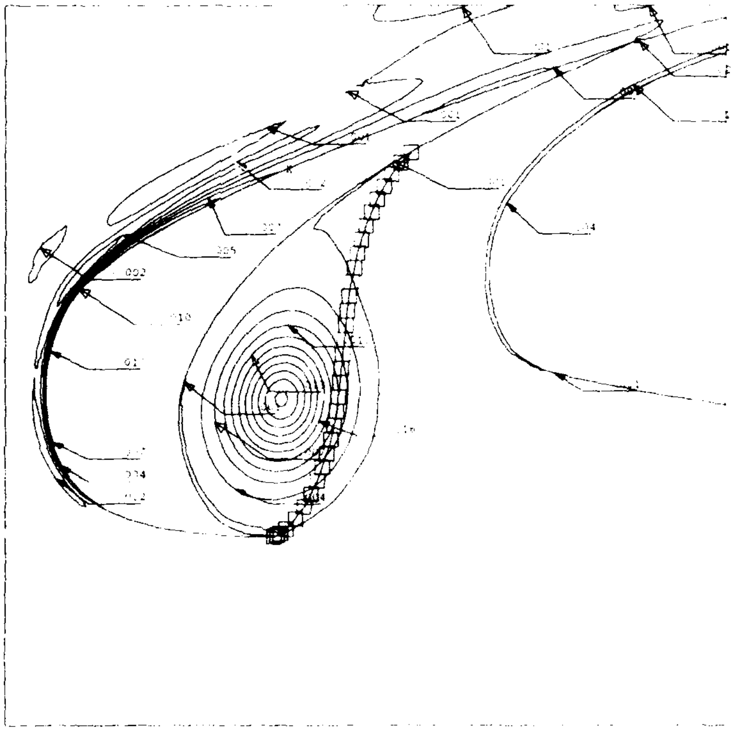

Fig. 14 Iso total pressure loss lines around the slat cove of the NLR422 three element airfoil: fine grid (case 2)

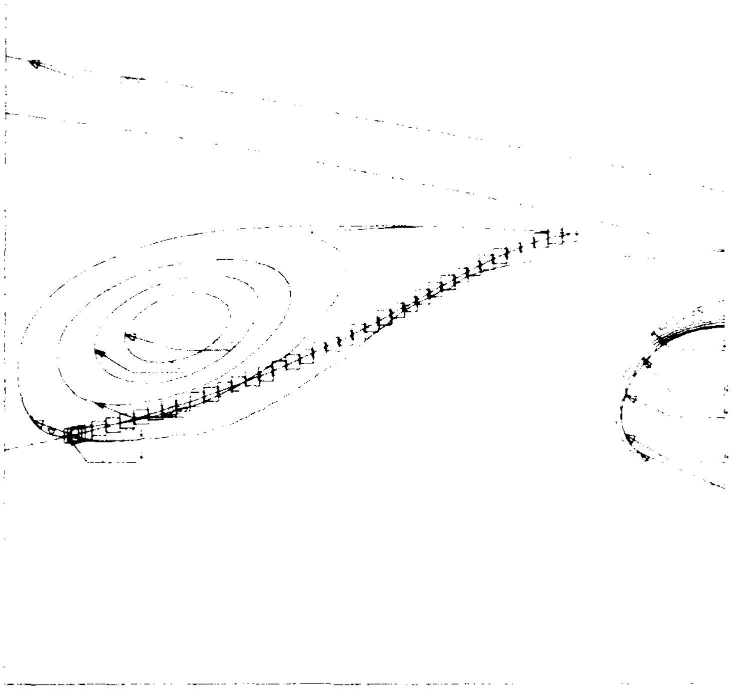

Fig. 15 Iso total pressure loss lines around the wing cove of the NLR422 three element airfoil: fine grid (case 2)

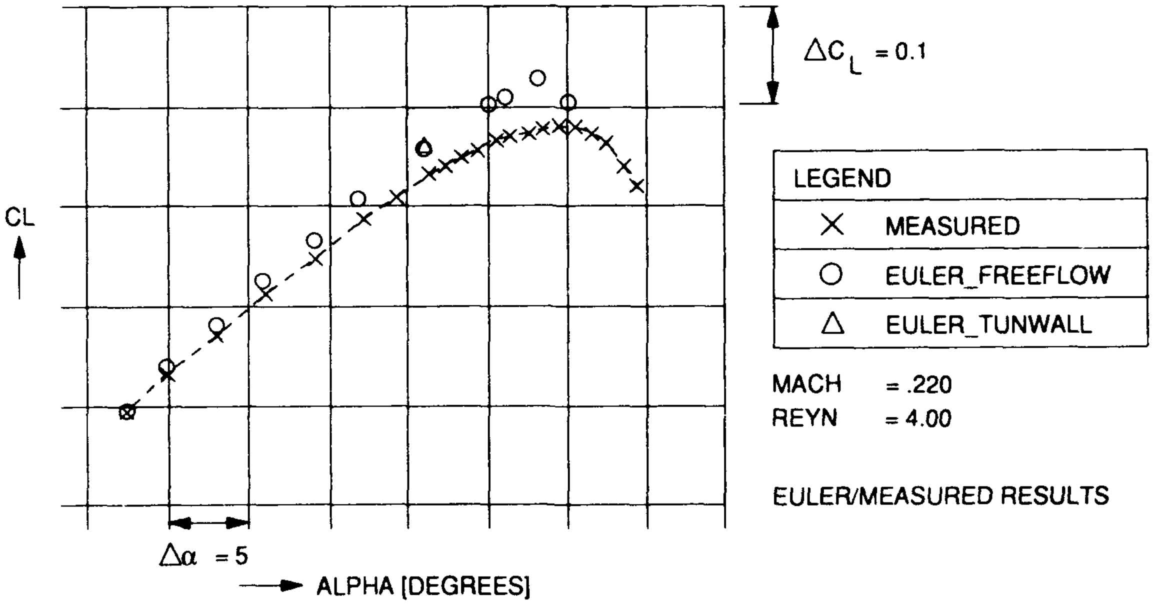

Fig. 16 cl - α diagram for the M1 three element airfoil (case 3)

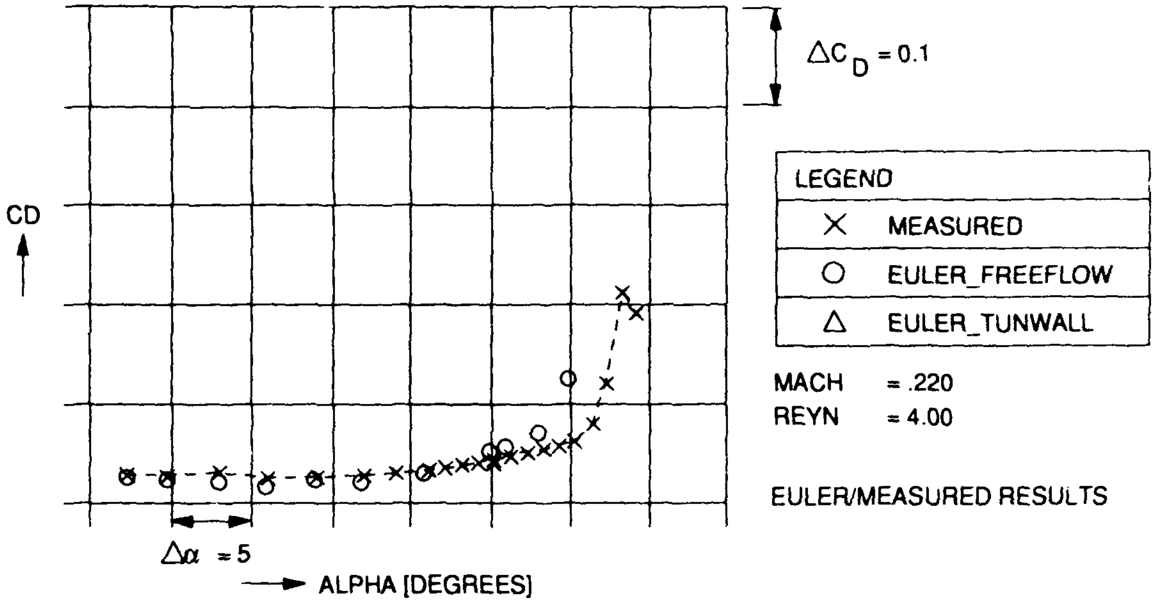

Fig. 17 cd - α diagram for the M1 three element airfoil (case 3)

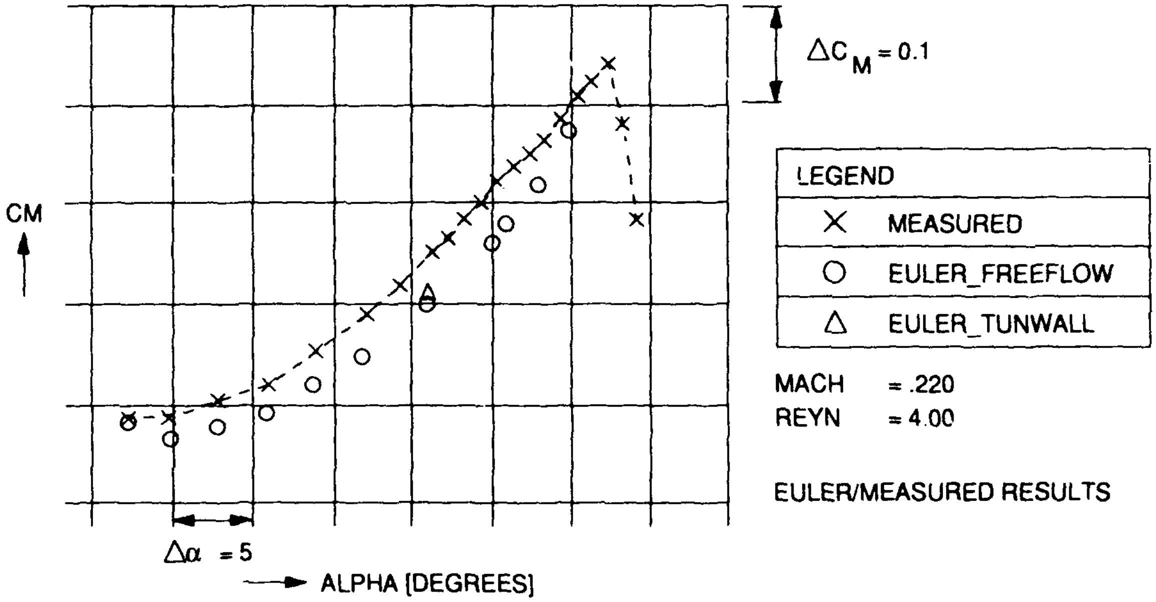

Fig. 18 cm - α diagram for the M1 three element airfoil (case 3)

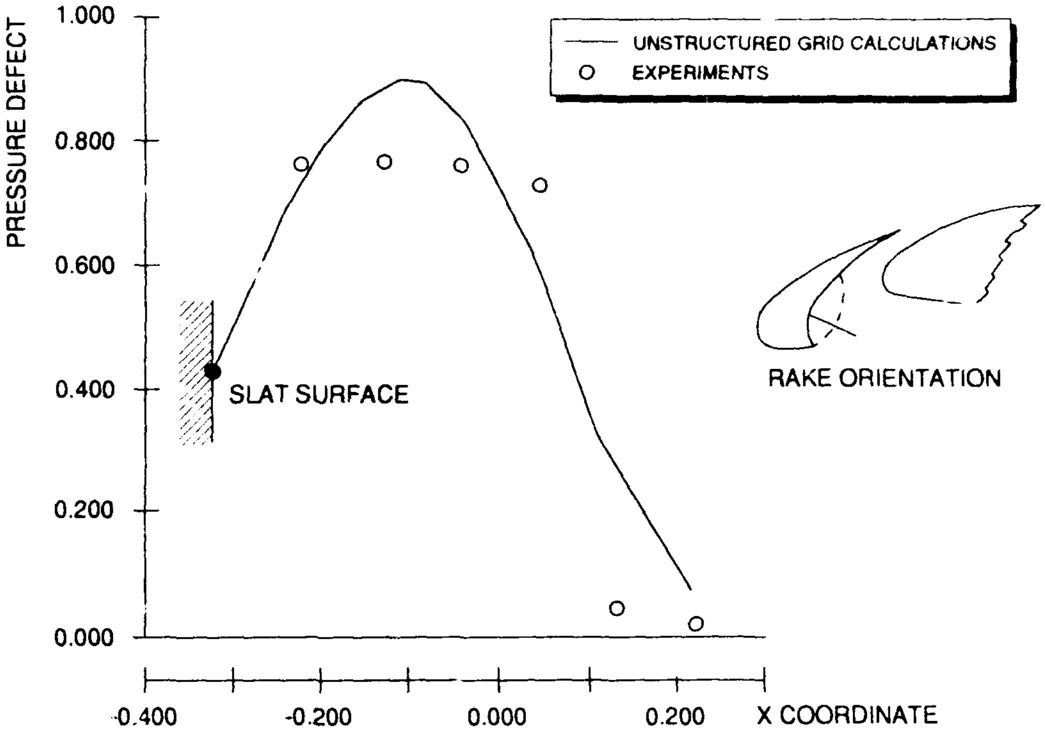

Fig. 19 Pressure defect at the slat cove rake holes of the M1 three element airfoil

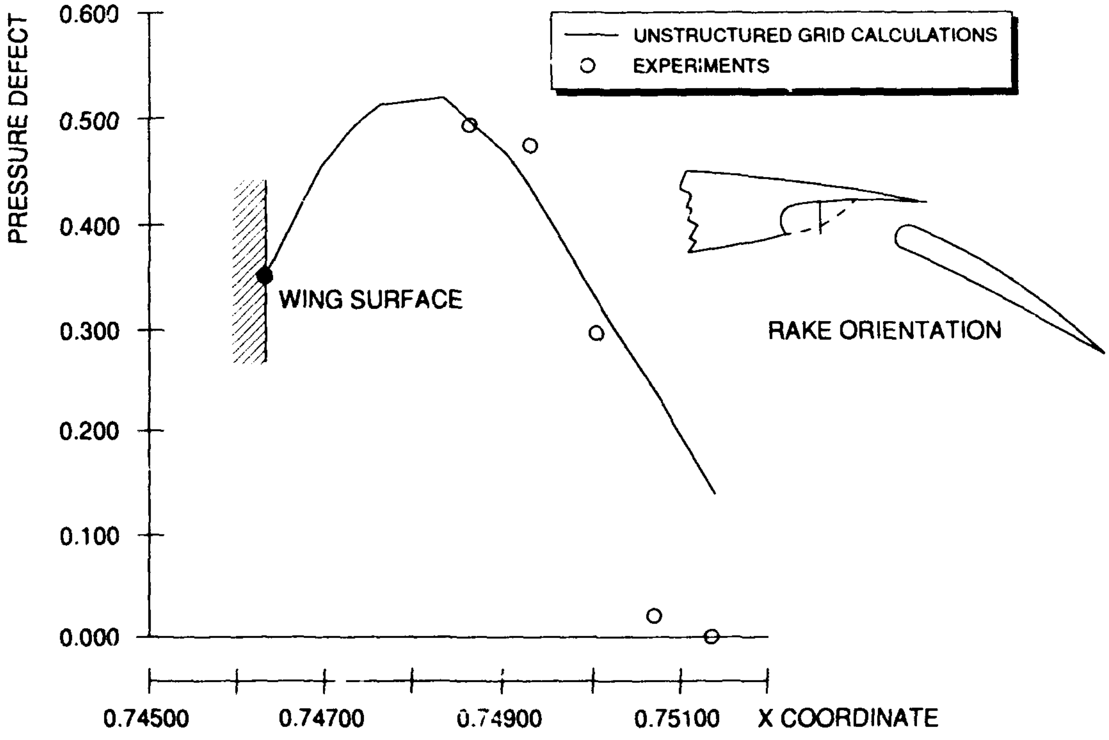

Fig. 20 Pressure defect at the flap cove rake holes of the M1 three element airfoil

PREDICTION OF THE HIGH-LIFT PERFORMANCE OF MULTI-ELEMENT AEROFOILS USING AN UNSTRUCTURED NAVIER-STOKES SOLVER

Leslie J. Johnston and Luca Stolcis*

Department of Mechanical Engineering, UMIST
PO Box 88, Manchester M60 1QD, England

SUMMARY

A detailed description is presented of a computational method to predict the aerodynamic performance of mechanical high-lift systems. The Reynolds-averaged Navier-Stokes equations applicable to compressible, two-dimensional mean flow are solved using a cell-centred, finite-volume spatial discretisation and an explicit multi-stage scheme to time march to steady-state solutions. The governing mean-flow equations are solved in conjunction with a two-equation, high-Reynolds number k-ϵ turbulence model, this level of turbulence model sophistication being considered as the minimum required to enable an adequate resolution of the complex flow physics. The geometric complexity associated with practical multi-element aerofoil configurations is addressed by adopting unstructured computational grids. Results for the RAE 2822 transonic single-aerofoil section are presented, comparing two near-wall treatments for the turbulence-transport equations. Thereafter, a detailed evaluation is presented of the predictive capability of the method, in its current form, by comparison with experimental data for the low-speed, high-lift NLR 7301 aerofoil/trailing-edge flap configuration. Results are also presented for the SKF 1.1 aerofoil/manoeuvre flap configuration over a range of transonic flow conditions, from fully-subcritical flow to supercritical flow with shock-induced separation. The level of agreement between predictions and experiment is encouraging for the cases considered. However, it is concluded that improved modelling of the complex flow physics is required, with the lack of response of the current k-ϵ turbulence model to streamline curvature being a significant limitation on quantitative accuracy around maximum lift conditions. Similarly, procedures to automatically adapt the computational grid to the flow solution would improve predictions over the extended range of conditions associated with the practical operation of a mechanical high-lift system.

INTRODUCTION

High-Lift Aerodynamics

As discussed by Lowrey[1], a transport aircraft wing must provide the lift force necessary for safe, efficient cruise flight with the required payload over a specified range. Since the cruise is usually the longest segement of a typical flight, involving the largest amount of fuel burnt, this condition tends to dominate the wing design process. The main objective of the wing design at the cruise condition is to achieve the required lift coefficient whilst minimising the drag. This can be achieved by avoiding separated flow and using modern supercritical aerofoil sections, which delay the onset of transonic drag rise. However, the cruise wing design must be adapted in order to meet the lifting requirements at low speed associated with take off and landing. In particular, high lift is required at take off to reduce the take-off speed and shorten the take-off run. But this high lift must be generated with a minimum penalty in drag, so that a safe climb rate can be maintained in the event of an engine failure. During landing, increased drag can be tolerated since this results in the availability of a large variation of glide slope with engine power setting. For this reason, lift coefficients at landing conditions tend to be much higher than those at take off. These low-speed, high-lift requirements are generally met through the use of mechanical high-lift systems, comprising slotted leading-edge slats and trailing-edge flaps.

The additional lift associated with mechanical high-lift systems is obtained due to the increased effective camber and chordwise extent of the multi-element wing. Also, a wing with deployed high-lift devices will, in general, be able to operate at higher incidence angles since the required upper surface pressure rise to the trailing edge is split over a number of wing elements. A fresh boundary layer develops on each element, which is better able to negotiate the pressure rise, so that trailing-edge flow separation is less likely to occur. Similarly, as shown by Smith[2], the circulation around the upstream wing element runs counter to that of the downstream element in the gap region, reducing drastically the leading-edge suction peak on the downstream element and so alleviating the tendency for leading-edge separation at high incidence angles.

Even for two-dimensional flows, deployment of high-lift devices results in a multi-element aerofoil configuration around which the flow development is significantly more complex than that of a single aerofoil; see the discussion of Butter[3], for example. The flow is dominated by viscous effects, in which the wakes from upstream aerofoil elements can interact with the upper surface boundary layers of downstream elements. This wake/boundary layer mixing leads to thick viscous layers which can be highly-curved due to the large effective camber of the aerofoil system. For this reason, there can exist significant pressure gradients *across* the viscous layers, in addition to the more usual streamwise pressure gradients. These latter pressure gradients may be severe enough to result in off-the-surface reverse flow in wake regions and, as discussed by Johnston and Horton[4], may be the mechanism precipitating the final stall of the configuration.

Closed recirculation zones develop in slat and flap cove regions, due to the geometric discontinuities that result from the need to be able to retract the high-lift devices to form a clean aerofoil section for cruise. The presence of gaps between aerofoil elements results in a flow that is highly-sensitive to Reynolds number, so that configuration optimisation at Reynolds numbers below flight conditions, as is sometimes the case in wind-tunnel testing, can result in misleading trends. Finally, the interaction of the circulations around the various aerofoil elements results in a large suction peak on the most forward element. This can lead to compressibility effects even

---

* Current address: CRS4, Via Nazario Sauro 10,
09123 Cagliari, Italy

though the freestream Mach number is around 0.2, with laminar shock wave/boundary layer interaction on a leading-edge slat at high incidence angles. Thus, shock-induced flow separation may be a further stall mechanism.

In order to manoeuvre effectively at transonic speeds, the wing of a combat aircraft must be able to generate high lift without incurring an excessive drag penalty or the onset of buffet. The use of a supercritical wing section enables such a performance specification to be met. However, the resulting wing section may not be well-optimised at other design conditions, with the cruise performance, in particular, being degraded due to larger than acceptable drag levels. Mechanical high-lift systems, such as trailing-edge flaps and/or leading-edge slats, can be used to enhance manoeuvring capability without compromising cruise performance. Flight tests involving F-4 and F-14 aircraft equipped with leading-edge slats, for example, have demonstrated significantly-improved climbing and turning performance, even without complete optimisation of the slat geometry.

Numerical Analysis of High-Lift Systems

The high-lift performance of multi-element aerofoil sections tends to be dominated by viscous effects, this being particularly true for the maximum attainable lift. The significant influence of viscous effects is aggravated if the clean aerofoil section is of supercritical design. Consequently, prediction methods based on the solution of inviscid flow equations are of little use for the optimisation of high-lift systems. The viscous flow development is governed by the Reynolds-averaged Navier-Stokes equations, which must be solved in conjunction with a suitable turbulence model since the set of mean-flow equations is not closed. This represents a computationally-intensive task, and so the early numerical methods employed separate inviscid flow and boundary-layer flow solvers coupled in an iterative fashion. Surface-singularity methods were generally adopted to compute the inviscid flowfield for low-speed high-lift systems, these being able to deal with multi-element configurations in a straightforward manner. Integral boundary-layer methods were the most popular approach for computing the development of the viscous layers. Representative methods in this class are those of Stevens et al[5,6], Seebohm and Newman[7], Oskam[8,9], Butter and Williams[10]. Note, however, that not all of these methods incorporate techniques to treat the mixing of wakes and boundary layers, and recirculation bubbles in cove regions are dealt with in a rather ad-hoc manner. Progress in the USA beyond these early methods, up to the late 1980s, is reviewed by Brune and McMasters[11], with King and Williams[12] presenting a corresponding review of UK work.

The development of numerical analysis methods to aid the design of efficient transonic manoeuvre devices attracted the attention of the research community in the mid 1970s. This work began with inviscid flow methods, starting with use of the small-disturbance approach by Caughey[13]. Subsequently, Grossman and Melnik[14] and Arlinger[15] developed methods which solved the full potential equation, using conformal mapping techniques to transform the flow domain external to an aerofoil/slat configuration into the annular region between two concentric circles. However, such conformal mapping methods are not easily extended to configurations consisting of more than two aerofoil elements. Rosch and Klevenhusen[16] overcame this limitation by first computing the *incompressible* flowfield using a surface singularity method. The streamlines and equipotential lines of this flow were then used as an orthogonal grid on which the full potential equation was solved, results being presented for aerofoil/slat and aerofoil/slat/flap configurations.

The computational grids obtained by the conformal mapping approach, or that of Rosch and Klevenhusen, are not necessarily optimal from the point of view of the flow solver. Also, the validity of the full potential equation is essentially restricted to flows with weak shock waves. More recently, Mavriplis[17] and Stolcis and Johnston[18] have developed inviscid flow methods based on solution of the Euler equations. In both cases, *unstructured* computational grids were used to overcome the problems associated with grid generation for closely-coupled, multi-element aerofoil configurations.

Initial attempts to produce viscous transonic flow methods involved the coupling of boundary-layer methods to the inviscid flow solver; see Grossman and Volpe[19], Leicher[20], Rosch and Klevenhusen[16]. As is also the case for low-speed, high-lift methods, the viscous/inviscid coupled approach tends to run into solution convergence problems when anything other than limited regions of flow separation are present. Also, as discussed by Johnston and Horton[4], the complex viscous layers developing over multi-element aerofoil sections are not really amenable to analysis by simple boundary-layer methods.

There are a rather restricted number of experimental data-sets available with which to validate computational methods for high-lift systems. Brune and Sikavi[21] and Nakayama et al[22] present results for realistic high-lift configurations which include measurements of both mean-flow and turbulence quantities. However, both of these data-sets are for Reynolds numbers well below full-scale conditions, leading to uncertainties regarding extrapolation of conclusions to flight Reynolds numbers. This problem is being addressed by Yip et al[23] who report in-flight measurements for the trailing-edge flap system of a Boeing 737-100 aircraft.

Modern Viscous-Flow Methods

Mechanical high-lift systems present two distinct problems which can hinder the development of efficient and accurate numerical analysis methods. Firstly, the geometric complexity associated with closely-coupled multi-element aerofoils, including sharp cut-outs in cove regions, makes it difficult to generate the computational grids required by flowfield methods. Secondly, as has already been described above, the flowfield itself is highly complex, involving interacting viscous layers, closed recirculation regions, separation from smooth surfaces etc. It is this very flow complexity, particularly at the high incidence angles associated with maximum lift conditions, that causes numerical problems with the inviscid/viscous coupled method approach. It is now generally acknowledged that such flowfields are only likely to be adequately predicted by solving the Reynolds-averaged Navier-Stokes equations, and accepting the high computational expense involved with this approach.

The motivation for the present work is the desire to be able to compute the viscous flow development around completely-representative multi-element aerofoil geometries. In addition, the resulting computational method should be capable of application at both low speed high-lift and transonic manoeuvre conditions. The complex physics associated with multi-element aerofoil flows leads naturally to the use of the Reynolds-averaged Navier-Stokes equations. These are solved in terms of mass-weighted average variables for compressible flow applications. An explicit turbulence model is required to close the set of governing mean-flow equations, and a two-equation model is adopted, as being the *lowest-order* model consistent with an ability to compute interacting viscous layers. It can be noted here that Shima[24], Mavriplis[25] and Chow and Chu[26] have used the *algebraic* turbulence model of Baldwin and Lomax[27] to compute multi-element flowfields, but this model requires rather ad-hoc modifications to deal with interacting wakes and boundary layers.

The geometric complexity of multi-element aerofoil configurations is dealt with in the present method through the use of unstructured computational grids, the method being based on the original inviscid flow solver of Stolcis and Johnston[28,29]. The use of unstructured computational grids and a two-equation turbulence model is also the approach taken by Mavriplis and Martinelli[30]. Although such a turbulence model is deemed to be the lowest-order model consistent with the complex flow physics (the recent one-equation model of Baldwin and Barth[31] may be an alternative, however), this does not guarantee that the model is adequate in a quantitative sense, a point that will be returned to below.

The present paper starts by presenting the governing mean-flow equations, and the turbulence-transport equations associated with the high-Reynolds number version of the k-ϵ two-equation turbulence model. Two alternative modelling approaches to bridging the viscosity-dominated near-wall region are then discussed. Details of the numerical discretisation scheme and solution procedure are given next. Results for the RAE 2822 transonic single-aerofoil section are presented, comparing the two near-wall treatments for the modelled turbulence-transport equations. A detailed evaluation of the method is presented for the low-speed, high-lift NLR 7301 aerofoil/trailing-edge flap configuration. The applicability of the method to transonic flows is illustrated for the SKF 1.1 aerofoil/manoeuvre flap configuration over a range of conditions, from fully-subcritical flow to supercritical flow with shock-induced separation. The paper closes with a discussion of the adequacy of turbulence modelling at the two-equation level for the complex viscous flowfields of multi-element aerofoil, high-lift systems.

GOVERNING FLOW EQUATIONS

The computational method is based on a solution of the Reynolds-averaged Navier-Stokes equations for the mean-flow development, written in terms of mass-weighted average variables for application to compressible turbulent flows. The time-averaging procedure used to obtain the set of mean-flow equations introduces new unknowns, the Reynolds stresses, and these are modelled using a scalar eddy-viscosity coefficient. Local values of this coefficient are determined by the solution of two additional modelled transport equations, for the turbulent kinetic energy and its isotropic rate of dissipation. All equations in this and subsequent sections are written in terms of non-dimensional variables, using the scalings given in equation (16).

The governing flow equations are written in integral form, to facilitate the finite-volume spatial discretisation adopted in the calculation method. Further, the time-dependent equations are to be solved, by marching in time to a steady-state solution. The resulting equations can be written as follows

$$\frac{\partial}{\partial t}\int_{\Omega} \underline{W}\, d\Omega + \int_{\Omega_s} \underline{H}.\underline{n}\, d\Omega_s + \int_{\Omega} \underline{S}^v\, d\Omega = 0 \qquad (1)$$

Ω is any two-dimensional flow domain, Ω_s is the boundary to the domain and $\underline{n}$ is the unit outward normal to this boundary. $\underline{W}$ is the vector of dependent variables

$$\underline{W} = \begin{bmatrix} \rho \\ \rho U \\ \rho V \\ \rho E \\ \rho k \\ \rho\epsilon \end{bmatrix} \qquad (2)$$

ρ, E, k and ϵ are the density, total energy per unit mass, turbulent kinetic energy per unit mass and dissipation rate of k respectively; U and V are the cartesian mean-velocity components. $\underline{H}$ is a matrix containing the flux vectors, which can be written as

$$\underline{H} = (\underline{F}^i + \underline{F}^v)\underline{i} + (\underline{G}^i + \underline{G}^v)\underline{j} \qquad (3)$$

where $\underline{i}$ and $\underline{j}$ are unit vectors in the X- and Y-directions of the cartesian coordinate system. $\underline{F}^i$ and $\underline{G}^i$ are the convective flux vectors

$$\underline{F}^i = \begin{bmatrix} \rho U \\ \rho U^2 + P \\ \rho UV \\ \rho UH \\ \rho Uk \\ \rho U\epsilon \end{bmatrix}, \quad \underline{G}^i = \begin{bmatrix} \rho V \\ \rho UV \\ \rho V^2 + P \\ \rho VH \\ \rho Vk \\ \rho V\epsilon \end{bmatrix} \qquad (4)$$

P is the static pressure and H the total enthalpy per unit mass. The various quantities are related to each other by the definitions of total energy per unit volume and total enthalpy per unit volume for a perfect gas

$$\rho E = P/(\gamma - 1) + \tfrac{1}{2}\rho(U^2 + V^2) + \rho k \qquad (5)$$

$$\rho H = \rho E + P \qquad (6)$$

γ being the ratio of specific heats, taken as 1.4 for air. $\underline{F}^v$ and $\underline{G}^v$ are the viscous diffusive flux vectors

$$\underline{F}^v = \begin{bmatrix} 0 \\ \sigma_{xx} \\ \sigma_{xy} \\ U\sigma_{xx} + V\sigma_{xy} + q_x \\ \beta_{kx} \\ \beta_{\epsilon x} \end{bmatrix},$$

$$\underline{G}^v = \begin{bmatrix} 0 \\ \sigma_{xy} \\ \sigma_{yy} \\ U\sigma_{xy} + V\sigma_{yy} + q_y \\ \beta_{ky} \\ \beta_{\epsilon y} \end{bmatrix} \qquad (7)$$

σ_{xx}, σ_{yy} and σ_{xy} are components of the stress tensor, whilst q_x and q_y are components of the heat-flux vector. β_{kx}, β_{ky}, $\beta_{\epsilon x}$ and $\beta_{\epsilon y}$ represent viscous diffusion in the transport equations for k and ϵ, the form adopted for these terms is given in the Turbulence Modelling section below. Finally, vector $\underline{S}^v$ contains the source terms in the k and ϵ equations

$$\underline{S}^v = \begin{bmatrix} 0 \\ 0 \\ 0 \\ 0 \\ S_k \\ S_\epsilon \end{bmatrix} \qquad (8)$$

where, again, the particular forms of S_k and S_ϵ are discussed in the next section.

Reynolds stresses and turbulent heat fluxes in the mean-flow equations are modelled by introducing an isotropic eddy-viscosity coefficient μ_t and a turbulent Prandtl number Pr_t. Thus, the viscous stress terms in equation (7) become

$$\sigma_{xx} = -(\mu + \mu_t)\, s_{xx} + \frac{2}{3}\rho k\,,$$

$$\sigma_{yy} = -(\mu + \mu_t)\, s_{yy} + \frac{2}{3}\rho k\,,$$

$$\sigma_{xy} = -(\mu + \mu_t)\, s_{xy} \qquad (9)$$

where the components of the mean-strain tensor are

$$s_{xx} = 2\frac{\partial U}{\partial X} - \frac{2}{3}\left(\frac{\partial U}{\partial X} + \frac{\partial V}{\partial Y}\right),$$

$$s_{yy} = 2\frac{\partial V}{\partial Y} - \frac{2}{3}\left(\frac{\partial U}{\partial X} + \frac{\partial V}{\partial Y}\right),$$

$$s_{xy} = \left(\frac{\partial U}{\partial Y} + \frac{\partial V}{\partial X}\right) \qquad (10)$$

Similarly, the components of the heat-flux vector in equation (7) become

$$q_x = -\gamma\left(\frac{\mu}{Pr} + \frac{\mu_t}{Pr_t}\right)\frac{\partial T}{\partial X}\,,$$

$$q_y = -\gamma\left(\frac{\mu}{Pr} + \frac{\mu_t}{Pr_t}\right)\frac{\partial T}{\partial Y} \qquad (11)$$

Pr and Pr_t, the laminar and turbulent Prandtl numbers, are assumed to take constant values of 0.72 and 0.9 respectively. The static temperature T in equation (11) can be evaluated using the perfect gas relation, written in the form

$$P = (\gamma - 1)\,\rho\,T \tag{12}$$

the pressure P being determined from the dependent variables in $\underline{W}$, using the definition of the total energy, equation (5). Sutherland's law

$$\mu = \frac{\gamma^{1/2}\,M}{R}\,[(\gamma-1)T]^{3/2}\left[\frac{T_\infty^* + 110.4}{(\gamma - 1)T\,T_\infty^* + 110.4}\right] \tag{13}$$

is used to evaluate the laminar viscosity μ, where M and R are the freestream Mach number and Reynolds number respectively. T_∞^* is the freestream static temperature, in kelvin.

The surface boundary conditions applied to the mean-flow equations are the no-slip conditions

$$U_w = V_w = 0 \tag{14}$$

together with the assumption of an adiabatic wall, which leads to

$$\left(\frac{\partial T}{\partial y_n}\right)_w = \left(\frac{\partial P}{\partial y_n}\right)_w = 0 \tag{15}$$

Subscript w indicates conditions at the wall and y_n is the surface normal distance.

Non-reflecting farfield boundary conditions are applied at the outer boundary to the computational domain. These are constructed using the Riemann invariants for a one-dimensional flow normal to the outer boundary; see Jameson and Baker[32] for details. The downstream outflow boundary in the wake region is treated in exactly the same way. For subsonic outflow, this amounts to an extrapolation from the interior of the entropy and the mean-velocity component tangential to the downstream boundary. The normal mean-velocity component and the speed of sound are given by the Riemann invariants, and the pressure is determined using the definition of the speed of sound. These outer-boundary conditions are modified to take into account the effect of the circulation around the lifting aerofoil system, following the approach of Thomas and Salas[33].

The following scalings have been adopted to put the governing flow equations, and all subsequent equations, into a non-dimensional form

$$X^* = X\,c^*\ ,\ Y^* = Y\,c^*\ ,\ \rho^* = \rho\,\rho_\infty^*\ ,\ P^* = P\,P_\infty^*\ ,$$

$$U^* = U\,\surd(P_\infty^*/\rho_\infty^*)\ ,\ V^* = V\,\surd(P_\infty^*/\rho_\infty^*)\ ,$$

$$E^* = E\,P_\infty^*/\rho_\infty^*\ ,\ H^* = H\,P_\infty^*/\rho_\infty^*\ ,\ k^* = k\,P_\infty^*/\rho_\infty^*\ ,$$

$$T^* = T\,P_\infty^*/(\rho_\infty^* C_v^*)\ ,\ t^* = t\,c^*/\surd(P_\infty^*/\rho_\infty^*)\ ,$$

$$\mu^* = \mu\,c^*\surd(P_\infty^*\rho_\infty^*)\ ,\ \mu_t^* = \mu_t\,c^*\surd(P_\infty^*\rho_\infty^*)\ ,$$

$$\epsilon^* = \epsilon\,(P_\infty^*/\rho_\infty^*)^{3/2}\ /\ c^* \tag{16}$$

Superscript * indicates a dimensional quantity and subscript ∞ denotes freestream conditions. C_v^* is the specific heat at constant volume, and the reference length scale c^* is usually taken as the chord of the clean aerofoil section.

TURBULENCE MODELLING

Modelling of the Reynolds stresses using a scalar turbulent viscosity coefficient results in a set of equations for the mean-flow development which have a form essentially identical to the Navier-Stokes equations for laminar flow. The two-equation k-ε turbulence model of Launder and Spalding[34] is used to determine the local values of the turbulent viscosity coefficient μ_t. This level of sophistication of turbulence model is considered to be the lowest-level appropriate to an adequate modelling of the complex flow physics of high-lift systems. The turbulent viscosity coefficient is obtained from the following relation

$$\mu_t = c_\mu\,\rho\,\frac{k^2}{\epsilon} \tag{17}$$

where c_μ is a model constant, whose value is given in equation (21). The two modelled transport equations, for the turbulent kinetic energy k and the dissipation rate ε, have been given in outline in the Governing Flow Equations section above. The turbulent diffusive transport terms in $\underline{F}^V$ and $\underline{G}^V$, equation (7), are modelled by assuming a simple scalar gradient diffusion process

$$\beta_{kx} = -\left(\mu + \frac{\mu_t}{\sigma_k}\right)\frac{\partial k}{\partial X}\ ,\ \beta_{ky} = -\left(\mu + \frac{\mu_t}{\sigma_k}\right)\frac{\partial k}{\partial Y}\ ,$$

$$\beta_{\epsilon x} = -\left(\mu + \frac{\mu_t}{\sigma_\epsilon}\right)\frac{\partial \epsilon}{\partial X}\ ,\ \beta_{\epsilon y} = -\left(\mu + \frac{\mu_t}{\sigma_\epsilon}\right)\frac{\partial \epsilon}{\partial Y} \tag{18}$$

σ_k and σ_ϵ are two further model constants. The modelled source terms S_k and S_ϵ in equation (8) involve the production P_k and the dissipation rate ε of the turbulent kinetic energy

$$S_k = -P_k + \rho\,\epsilon\ ,$$

$$S_\epsilon = -c_{\epsilon 1}\,P_k\,\frac{\epsilon}{k} + c_{\epsilon 2}\,\rho\,\frac{\epsilon^2}{k} \tag{19}$$

$c_{\epsilon 1}$ and $c_{\epsilon 2}$ are another two model constants. The term P_k representing production of turbulent kinetic energy is modelled using the turbulent viscosity coefficient μ_t

$$P_k = \left(\mu_t\,s_{xx} - \frac{2}{3}\rho\,k\right)\frac{\partial U}{\partial X}$$

$$+ \left(\mu_t\,s_{yy} - \frac{2}{3}\rho\,k\right)\frac{\partial V}{\partial Y} + \mu_t\,s_{xy}\,s_{xy} \tag{20}$$

s_{xx}, s_{yy} and s_{xy} are the components of the mean-strain tensor, and are defined in equation (10). This basic high-Reynolds number version of the k-ε turbulence model contains five constants, which take the following values

$$c_\mu = 0.09\ ,\quad \sigma_k = 1.0\ ,\quad \sigma_\epsilon = 1.3\ ,$$

$$c_{\epsilon 1} = 1.44\ ,\quad c_{\epsilon 2} = 1.92 \tag{21}$$

The k-ε turbulence model as presented above is applicable only to the fully-turbulent and outer regions of the viscous layers. Both the k and ε equations require additional near-wall damping terms if the model is to be used right down to the wall. A number of so-called low-Reynolds number models have been devised to enable use of the k and ε equations across this region; see the review of Patel et al[35]. The continuing proliferation of such low-Reynolds number k-ε models indicates the lack of a general consensus as to the most appropriate form of the near-wall damping terms. These models also turn out to require very refined computational grids near the wall, which can have serious consequences for the numerical solution algorithm. The modelled turbulence-transport equations become very stiff in this near-wall region, leading to a degradation of the convergence and stability properties of the solution algorithm; see Mavriplis and Martinelli[30] for a discussion of these points.

Two alternative approaches are generally taken to alleviate these problems in the viscosity-dominated near-wall region. The first is to 'patch' the high-Reynolds number k-ϵ model to near-wall boundary conditions, but in the fully-turbulent region of the flow rather than at the wall itself. No attempt is made to solve the turbulence-transport equations very close to the wall when using this so-called wall function approach. The second, and perhaps, more satisfactory approach is to use a simplified turbulence model to bridge the region between the fully-turbulent part of the flow, modelled using the high-Reynolds number k-ϵ model, and the wall. Both approaches have been investigated in the present work.

Wall Function Approach

Experiments indicate that for turbulent boundary layers the mean-velocity component parallel to a wall U_T obeys the semi-logarithmic law-of-the-wall

$$\frac{U_T}{U_\tau} = \frac{1}{\kappa} \log_e(y^+E) \tag{22}$$

in the fully-turbulent, near-wall region. The actual lateral extent of this region is a function of both Reynolds number and the pressure distribution along the wall. In equation (22), y^+ is defined as

$$y^+ = \rho_w \left| U_\tau \right| y_n / \mu_w \tag{23}$$

where y_n is the surface normal distance, and subscript w denotes conditions at the wall. U_τ is the wall friction velocity and is defined in terms of the wall shear stress τ_w

$$\tau_w = \rho_w U_\tau^2 \tag{24}$$

The law-of-the-wall involves two constants

$$\kappa = 0.41 \ , \quad E = 9 \tag{25}$$

κ is the von Karman constant, and the above value of E is that appropriate to smooth walls.

In the wall function approach the turbulence-transport equations are solved only in the fully-turbulent and outer regions of wall-bounded viscous layers. This is achieved by arranging that the centres of the first near-wall computational cells are in the range $30 < y+ < 300$. The k and ϵ equations are not solved in these near-wall cells, but have their values prescribed on the basis of local equilibrium of the turbulence. A balance between production and dissipation is assumed in the turbulent kinetic energy transport equation. The shear stress and mean-velocity gradient in the production term are then given by the wall shear stress and the law-of-the-wall respectively. Finally, by modelling the dissipation rate ϵ by an algebraic length scale proportional to y_n, the near-wall values of k and ϵ become

$$k = \frac{U_\tau^2}{\sqrt{c_\mu}} \ , \quad \epsilon = \frac{U_\tau^3}{\kappa y_n} \tag{26}$$

The mean-flow equations *are* solved in the near-wall computational cells, with no-slip conditions applied at the wall, equations (14) and (15). However, the wall shear stress is obtained from the friction velocity U_τ using equation (24), where the law-of-the-wall, equation (22), provides an implicit relation for U_τ itself.

One-Equation Near-Wall Model

The wall function approach to the near-wall boundary conditions for the k and ϵ equations is straightforward to implement in a numerical solution procedure. However, there are uncertainties associated with this approach in separated flow regions, mainly concerning the universality of the law-of-the-wall, equation (22), under such conditions. For this reason, it is preferable to take an alternative approach which allows resolution of the viscous layers right down to the wall. In the present work, a one-equation turbulence model is used in this viscosity-dominated, near-wall region. The particular model adopted is the near-wall part of that used by Mitcheltree et al[36] and Johnston[37], which is itself a compressible flow version of the original model of Wolfshtein[38].

The high-Reynolds number forms of the k and ϵ equations are solved as usual in the fully-turbulent and outer parts of the wall-bounded viscous layers. In addition, the k equation is also solved in the near-wall region for which $y+ < 50$, with the correct wall boundary condition

$$k_w = 0 \tag{27}$$

The wall shear stress τ_w, needed to evaluate U_τ using equation (24), is obtained from the limiting form of the momentum equation at the wall

$$\tau_w = \mu_w \left(\frac{\partial U_T}{\partial y_n} \right)_w \tag{28}$$

For $y+ < 50$, the turbulent viscosity relation, equation (17), is replaced by

$$\mu_t = c_\mu \rho k^{1/2} L_\mu \tag{29}$$

and the rate of dissipation of k is modelled using a dissipation length scale L_ϵ

$$\rho \epsilon = \rho k^{3/2} / L_\epsilon \tag{30}$$

The two length scales L_μ and L_ϵ are given by algebraic relations, varying linearly with distance from the wall, but modified by damping functions in the molecular-viscosity dominated region immediately adjacent to the wall

$$L_\mu = c_1 y_n [1 - \exp(- R_k/A_\mu)] \ ,$$

$$L_\epsilon = c_1 y_n [1 - \exp(- R_k/2c_1)] \tag{31}$$

where R_k is a Reynolds number characteristic of the turbulence

$$R_k = \rho k^{1/2} y_n / \mu \tag{32}$$

The one-equation model, near-wall formulation is completed by specification of the two additional constants

$$A_\mu = 76 \ , \quad c_1 = \kappa / c_\mu{}^{3/4} \tag{33}$$

Note that the use of R_k rather than $y+$ in the near-wall damping functions, equation (31), leads to a well-behaved model in separated-flow regions, since the turbulent kinetic energy always remains positive.

SPATIAL DISCRETISATION

The present numerical scheme employs an unstructured computational grid approach, in order to deal with the geometric complexity associated with multi-element aerofoil sections. The computational domain Ω is divided into a finite number of non-overlapping cells, the resulting grid being unstructured but boundary-conforming. The dependent variables, equation (2), within a cell are represented by their average values at the cell centre, such quantities being denoted by suffix k for cell k. The governing flow equations are now applied to each computational cell in turn, and equation (1) for a typical cell k becomes

$$\frac{\partial \underline{W}_k}{\partial t} = - \frac{1}{h_k} \int_{\Omega_c} [(\underline{F}^i + \underline{F}^v) dY - (\underline{G}^i + \underline{G}^v) dX] - \underline{S}^v{}_k \tag{34}$$

where Ω_c refers to a contour integration around the boundary of the cell, taken in the anticlockwise sense. The cell has an area of h_k which is fixed in time.

The time-dependent integral form of equation (34) suggests the use of a finite-volume formulation for the spatial discretisation, and then marching the resulting semi-discrete equations in time to reach the steady-state solution. Performing the spatial discretisation of equation (34) before the time discretisation leads to a large set of ordinary differential equations with respect to time

$$\frac{d\underline{W}_k}{dt} = -(\underline{Q}_k + \underline{V}_k) \qquad (35)$$

$\underline{Q}_k$ and $\underline{V}_k$ are discrete approximations of the convective and viscous flux integrals respectively, the latter also containing the source terms $\underline{S}^V{}_k$. The contour integration of the convective flux vectors, equation (4), is approximated by

$$\underline{Q}_k = \frac{1}{h_k} \sum_{n=1}^{\text{kedges}} (\underline{F}^i{}_n \, \Delta Y_n - \underline{G}^i{}_n \, \Delta X_n) \qquad (36)$$

where the summation is over the edges forming cell k. Fig 1 shows the notation adopted for a typical edge i, formed by the two vertices a and b, which is common to computational cells k and p. The cartesian lengths of edge i are given by

$$\Delta X_i = X_b - X_a \, , \quad \Delta Y_i = Y_b - Y_a \qquad (37)$$

The convective flux vectors on edge i can be evaluated using either the flux vectors or the dependent variables at the two appropriate cell centres. The latter approach is taken in the present method, thus

$$\underline{F}^i{}_i(\underline{W}) = \underline{F}^i(\underline{W}_i) \, , \quad \underline{G}^i{}_i(\underline{W}) = \underline{G}^i(\underline{W}_i) \qquad (38)$$

The simplest approach to evaluating the dependent variables on the cell edge is to average the two cell-centre values, for example

$$\underline{W}_i = (\underline{W}_k + \underline{W}_p) / 2 \qquad (39)$$

Equations (38) and (39) amount to a second-order, centre difference formulation on a regular cartesian grid. This approach is found to be satisfactory for the four mean-flow equations. For numerical stability of the solution algorithm, an alternative first-order upwind scheme is used for the k and ϵ equations

$$\underline{W}_i = [\, \max(0, A_i \underline{W}_k) + \min(0, A_i \underline{W}_p) \,] \qquad (40)$$

where

$$A_i = U_i \, \Delta Y_i - V_i \, \Delta X_i \qquad (41)$$

A similar procedure is used to approximate the contour integration of the viscous flux vectors, equation (7),

$$\underline{V}_k = \frac{1}{h_k} \sum_{n=1}^{\text{kedges}} (\underline{F}^V{}_n \, \Delta Y_n - \underline{G}^V{}_n \, \Delta X_n) + \underline{S}^V{}_k \qquad (42)$$

However, in this case both the mean-flow and turbulence-transport equations are treated using the second-order, centred formulation of equation (39).

The viscous diffusive flux vectors, equation (7), in $\underline{F}^V$ and $\underline{G}^V$ require evaluation of first derivatives of flow variables on the cell edges. The most obvious approach is to evaluate these derivatives at the two cell centres k and p, then average to give a value for edge i, see Fig 1. This approach may result in a de-coupling of the solution at adjacent cells, and does not contribute to the damping of errors. In the present method, the first derivatives on edge i are determined directly, by carrying out a contour integration around an auxiliary cell formed by the two vertices (a,b) and the two cell centres (k,p); see Fig 2. Dependent variables at the two vertices are evaluated by a simple interpolation of the surrounding cell-centre values. Thus, for example, the first derivatives of U on edge i are given by

$$\left(\frac{\partial U}{\partial X} \right)_i = \frac{1}{h_i} \int_{\Omega_i} U \, dY \, , \quad \left(\frac{\partial U}{\partial Y} \right)_i = -\frac{1}{h_i} \int_{\Omega_i} U \, dX \qquad (43)$$

where h_i and Ω_i are the area and contour of the auxiliary cell respectively. Finally, the source terms S_k and S_ϵ in the k and ϵ equations involve first derivatives of flow variables at the cell centres. These are evaluated using integration formulae similar to equation (43), but based on the *main* computational cells, Fig 1.

NUMERICAL DISSIPATION

The centred formulation, equations (38) and (39), for the convective flux terms in the mean-flow equations is non-dissipative. This means that any errors, such as discretisation or round-off errors, are not damped and oscillations may be present in the steady-state solution. In order to eliminate these oscillations, artificial dissipative terms are added to the right-hand side of equation (35) which, for the mean-flow equations only, becomes

$$\frac{d\underline{W}_k}{dt} = -(\underline{Q}_k + \underline{V}_k - \underline{D}_k) \qquad (44)$$

The approach of Jameson et al[39] is adopted to construct the dissipation function $\underline{D}_k$. For structured computational grids, this consists of a blend of second and fourth differences of the flow variables $\underline{W}$. Fourth differences are added throughout the flow domain where the solution is smooth, but are 'switched-off' in the region of shock waves. A term involving second differences is then 'switched-on' to damp oscillations near shock waves. This switching is achieved by means of a shock-wave sensor, based on the local second differences of pressure.

Construction of the artificial dissipative terms for unstructured grids basically follows the above procedure. However, the resulting form of the adaptive coefficients is somewhat different; see Jameson et al[40]. Within the finite-volume approach, the dissipation function for unstructured grids is calculated by a summation of the fluxes across the edges

$$\underline{D}_k = \sum_{i=1}^{\text{kedges}} \underline{d}_i^{(2)} + \sum_{i=1}^{\text{kedges}} \underline{d}_i^{(4)} \qquad (45)$$

Also, for unstructured grids the second and fourth differences of conserved variables are replaced by

$$\underline{d}_i^{(2)} = \alpha_i \, \epsilon_i^{(2)} \, (\underline{W}_p - \underline{W}_k)_i \, ,$$

$$\underline{d}_i^{(4)} = -\alpha_i \, \epsilon_i^{(4)} \, (\nabla^2 \underline{W}_p - \nabla^2 \underline{W}_k)_i \qquad (46)$$

where i denotes the edge delimiting cells k and p, Fig 1. ∇^2 is defined as

$$\nabla^2 \underline{W}_k = \sum_{i=1}^{\text{kedges}} (\underline{W}_i - \underline{W}_k) \qquad (47)$$

Note that in equation (47), $\underline{W}_i{}'$ and $\underline{W}_k$ are cell-edge and cell-centre values respectively.

The most straightforward way to construct the adaptive coefficients $\epsilon^{(2)}$ and $\epsilon^{(4)}$ in equation (46) is by a summation of first differences of pressure, this being the unstructured-grid analogue of the second difference of pressure used in structured-grid schemes. As discussed by Stolcis and Johnston[18], this leads to a formulation that is too dissipative. Therefore, the shock-wave sensor v_i in $\epsilon^{(2)}$ is constructed on a local edge basis, using only flow variables from the two adjacent cells k and p

$$v_i = \frac{\left| P_p - P_k \right|_i}{\left| P_p + P_k \right|_i} \qquad (48)$$

The adaptive coefficients then become

$$\epsilon_i^{(2)} = k^{(2)} v_i \ , \quad \epsilon_i^{(4)} = \max[0 \ , \ k^{(4)} - \epsilon_i^{(2)}] \qquad (49)$$

The scaling factor α_i in the dissipation function, equation (46), is based on the maximum eigenvalues of the convective Jacobian matrices $\partial\underline{E}/\partial\underline{W}$ and $\partial\underline{G}/\partial\underline{W}$ along the appropriate cell edge

$$\alpha_i = \left| U_i \Delta Y_i - V_i \Delta X_i \right| + c_i \sqrt{(\Delta X_i^2 + \Delta Y_i^2)} \qquad (50)$$

c_i is the local speed of sound; see equation (59). $k^{(2)}$ and $k^{(4)}$ are two empirically-chosen constants, which typically have values in the range $1/256 < k^{(4)} < 1/32$ and $1/2 < k^{(2)} < 1$.

The above formulation for the numerical dissipative terms has been developed for the Euler equations governing inviscid compressible flow. If used in this form with the Reynolds-averaged Navier-Stokes equations, this numerical dissipation may swamp the real physical dissipation in the viscous layers. The result can be modification of the boundary-layer development, the delay or suppression of flow separation and the weakening of shock waves. In many cases, the physical dissipation present in the diffusive flux terms $\underline{F}^V$ and $\underline{G}^V$ may be sufficient to prevent the build-up of oscillations, but experience indicates that some numerical dissipaion is required. Stolcis and Johnston[29] proposed the following simple scaling of $\underline{D}_k$ for the computation of turbulent flowfields

$$\underline{D}_k' = \underline{D}_k \ [\ 1 - \exp(-\ \alpha\ \mu/\mu_t)\ ] \qquad (51)$$

where α is an adjustable constant which generally is set to a value of 50. Such a scaling, based on the magnitude of the turbulent viscosity coefficient μ_t, has the advantage of also operating in wake regions remote from the aerofoil surfaces.

TIME-MARCHING SCHEME

The spatial discretisation described above reduces the governing mean-flow and turbulence-transport equations to a large system of semi-discrete ordinary differential equations, which may be written as

$$\frac{d\underline{W}_k}{dt} = \underline{R}_k \qquad (52)$$

The right-hand side of this system represents the residual error (deviation from the steady-state) in each cell k

$$\underline{R}_k = -\ (\underline{Q}_k + \underline{V}_k - \underline{D}_k) \qquad (53)$$

The integration in time of equation (52), to a steady-state solution, is performed using an explicit multi-stage scheme. Since time accuracy is not important for a steady-state solution, such schemes are selected only for their properties of stability region and damping. The following 4-stage scheme is adopted for the present work (neglecting, for clarity, the subscript k denoting a particular cell)

$$\begin{aligned} \underline{W}^{(0)} &= \underline{W}^n \ , \\ \underline{W}^{(m)} &= \underline{W}^{(0)} + \alpha_m \, \Delta t \, \underline{R}^{(m-1)} \quad \text{for } m=1 \text{ to } 4 \ , \\ \underline{W}^{n+1} &= \underline{W}^{(4)} \end{aligned} \qquad (54)$$

n is the current time level, n+1 is the new time level and following coefficients are used

$$\alpha_1 = 1/4 \ , \ \alpha_2 = 1/3 \ , \ \alpha_3 = 1/2 \ , \ \alpha_4 = 1 \qquad (55)$$

In order to minimise the computation time, the residual in equation (53) is reformulated as

$$\underline{R}^{(m)} = -\ (\ \underline{Q}^{(m)} + \underline{V}^{(0)} - \underline{D}^{(0)}\ ) \qquad (56)$$

where the expensive evaluation of the dissipation function $\underline{D}$ is carried out only at the first intermediate stage (0), and then frozen for the subsequent stages. This is known to modify the stability region of the scheme, but the steady-state accuracy and convergence characteristics appear to be preserved. Similarly, the viscous flux and source terms comprising $\underline{V}$ are also only evaluated at stage (0) and then frozen for subsequent stages.

The local time step for a given computational cell is determined as a combination of convective and diffusive time steps

$$\Delta t^*_k = \frac{\sigma \, \Delta t_k^i \, \Delta t_k^v}{\Delta t_k^i + \Delta t_k^v} \qquad (57)$$

σ being an adjustable constant, taking a value in the range 0.15 to 0.25. The inviscid time step involves the maximum eigenvalues of the convective Jacobian matrices, equation (50), for the edges forming the cell

$$\Delta t_k^i = \frac{h_k}{\displaystyle\sum_{i=1}^{\text{kedges}} \left| U_i \Delta Y_i - V_i \Delta X_i \right| + c_i \sqrt{(\Delta X_i^2 + \Delta Y_i^2)}} \qquad (58)$$

where c_i is the local speed of sound on edge i

$$c_i^2 = \gamma \ P_i \ / \ \rho_i \qquad (59)$$

The corresponding viscous time step is constructed as follows

$$\Delta t_k^v = \frac{h_k^2}{\displaystyle\sum_{i=1}^{\text{kedges}} (\gamma/\rho_i)\ (\Delta X_i^2 + \Delta Y_i^2) \left[\frac{\mu}{Pr} + \frac{\mu_t}{Pr_t} \right]_i} \qquad (60)$$

The time step given by equation (57) is then multiplied by the CFL number for use with the multi-stage scheme

$$\Delta t_k = \text{CFL} \ \Delta t^*_k \qquad (61)$$

The major disadvantage of explicit schemes such as the present one is that the magnitude of the maximum allowable time step is restricted because of the limited stability region. This restriction can be alleviated, to some extent, by marching the solution in each computational cell at the maximum allowable local time step. The transient solution is then not time-accurate, but this is of no concern since only the final steady-state solution is of interest.

CONVERGENCE ACCELERATION

Convergence to the steady-state solution can be further accelerated using the residual smoothing technique, in which the residual $\underline{R}_k$, equation (52), is replaced by an average of the residuals of the neighbouring cells

$$\bar{\underline{R}}_k = \underline{R}_k + \epsilon \nabla^2 \bar{\underline{R}}_k \qquad (62)$$

where ϵ is a smoothing coefficient and ∇^2 is defined in equation (47). Note that the smoothing is carried out implicitly, to gain the maximum benefit in accelerated convergence. Since the resulting matrix of residuals is diagonally-dominant, for the values of ϵ of interest, this implicit system can be solved by performing several *Jacobi* iterations

$$\underline{R}_k^{(m)} = \frac{\underline{R}_k^{(o)} + \epsilon \sum_{i=1}^{kedges} R_i^{(m-1)}}{1 + \epsilon\, kedges} \qquad (63)$$

where (o) refers to the unsmoothed residual, and the number of iterations required to establish the smoothed residual is small (a common value is 2). This smoothing technique allows the CFL number to be increased to 2 or 3 times the unsmoothed value.

GRID GENERATION

Unstructured computational grids cannot be represented in the same way as structured grids within a solution algorithm, since there is not a grid-point matrix in which the neighbouring elements are also neighbours in physical space. A connectivity matrix is required for unstructured grids, containing all the necessary relationships between cells, cell-edges and vertices. This information is accessed in an indirect way by the flow solver, so the choice of an optimal data-storage scheme is important.

In the present cell-centred, finite-volume formulation, this connectivity matrix is written in terms of cell edges rather than the cells themselves. This allows a very simple one-dimensional form to be adopted for the solution algorithm. The various algorithmic operations, such as the computation of fluxes, numerical dissipation, time step etc, can be written in terms of a single evaluation for each edge of the grid. These quantities are then accumulated, with the appropriate sign, for the two cells associated with each edge. A flow solver structured in this way also becomes independent of the actual shapes of the cells, enabling the mixing of triangular and quadrilateral cells, for example. It was initially supposed that there may have been an advantage to using quadrilateral cells in boundary-layer regions, particularly when using simple algebraic turbulence models; see Weatherill et al[41]. This has not been the case with the present work, involving the k-ϵ turbulence model, and the results presented below were all generated using only triangular cells.

The unstructured computational grids for multi-element aerofoil sections are generated by a three-stage procedure. Firstly, structured quadrilateral grids are generated around each aerofoil component in isolation, using simple algebraic techniques. The vertices of these various isolated grids are then overlaid and reconnected using a suitable algorithm, to produce a single grid consisting of triangular cells. In the present work, the Delaunay algorithm of Weatherill[42] is used to produce the required connectivity information, since this results in an optimal triangular grid, in terms of cell-shape regularity. It is also found beneficial to apply a simple Laplacian smoothing to the grid after the Delaunay algorithm. This approach to grid generation ensures high quality grids in the vicinity of the aerofoil surfaces, which is necessary for the adequate resolution of the viscous layers. Grid resolution and quality can be further enhanced by refinement of the initial grid, whereby specified cells are sub-divided into three smaller triangular cells. In general, this technique is required to improve resolution of wake regions, which are usually not well-aligned with the original structured grids.

RESULTS

All the results presented in this section were computed using a fixed set of flow algorithm parameters. The two numerical dissipation coefficients $k^{(2)}$ and $k^{(4)}$, equation (49), were set to 0.65 and 0.0045 respectively. The time-marching scheme employed local time steps and implicit residual smoothing, with a CFL number of 4.0. The solution was considered to be converged when the average density residual was reduced by four orders of magnitude. A comprehensive validation and evaluation of the numerical method is given by Stolcis[43]. Typical results for single- and multi-element aerofoils, at both low-speed and transonic flow conditions, are presented below.

RAE 2822 Aerofoil

The RAE 2822 aerofoil has a maximum thickness/chord ratio of 12.1% and a sharp trailing edge. Cook et al[44] present an extensive experimental study of this aerofoil in the 8ft x 6ft transonic wind tunnel at RAE Farnborough. The data-set includes surface pressure, skin friction and integral thickness distributions as well as mean-velocity profiles, at a range of flow conditions. As such, it is one of the more nearly complete aerofoil data-sets and has been used extensively to validate numerical methods. The aerofoil model has an aspect ratio of 3, and so the wind tunnel sidewalls should have little influence on the flow development. Similarly, the tunnel height/aerofoil chord ratio of 4 is large enough for linearised theory to be used to determine wind tunnel corrections for the upper and lower walls. Experience indicates that computations should use the manufactured rather than the design geometry, in order to capture correctly features of the surface pressure distribution in the leading-edge region.

Fig 3 shows results for Case 9, which is a fully-attached transonic flow condition, at a Mach number of 0.73, a Reynolds number of 6.5×10^6 and a corrected incidence angle of 2.79°. Transition is fixed at 3% chord on the upper and lower surfaces, in accordance with experiment. Two computations are shown in Fig 3, for the high-Reynolds number k-ϵ turbulence model with wall functions and with a one-equation near-wall formulation. Computational grids for the two cases were generated by direct triangulation of C-type structured grids, the two grids being essentially identical away from the immediate vicinity of the aerofoil surface. The grid for the wall function computation consisted of 23497 cells, 15522 edges and 8000 vertices, with 160 cells adjacent to the surface. The one-equation near-wall computation employed a more refined grid consisting of 25074 cells, 37849 edges and 12800 vertices, again with 160 cells adjacent to the surface.

Despite the different computational grids and turbulence models in the near-wall region, Fig 3 indicates good agreement between the two results and experiment. The minor discrepancies around the upper-surface shock-wave can probably be attributed to inadequate grid density in this region. Computed lift and drag coefficients are 0.827 and 0.0220 for the wall function approach, 0.848 and 0.0225 for the one-equation near-wall model, compared with 0.803 and 0.0168 for the experiment. Part of the over-prediction of drag coefficient is almost certainly due to the surface pressure integration with an insufficiently fine grid. Stolcis and Johnston[45] present results for Case 10, involving shock-induced separation, which show a similar level of agreement for the two near-wall formulations. For this reason, all subsequent computations presented are based on the wall function approach.

NLR 7301 Wing/Flap

Fig 4 shows the geometry for the low speed high-lift NLR 7301 aerofoil/trailing-edge flap configuration of van den Berg[46]. The flap angle is 20° and computations are presented for the larger flap gap of 2.6% of the reference chord. The experiments were carried out in the NLR 3m x 2m low-speed wind tunnel, at a freestream Mach number of 0.185 and Reynolds number of 2.51×10^6. The experiment was transition-free, but transition was fixed for the computations based on flow visualisation observations. The grid shown in

Fig 4 was generated by first producing O-type grids around the isolated aerofoil components, using the Delaunay algorithm to re-connect the vertices and then enriching the grid in the wake region of the main aerofoil. The resulting grid consisted of 12299 cells, 18567 edges and 6267 vertices, with 120 and 100 surface cells on the main aerofoil and flap respectively.

Computed surface pressure distributions for incidence angles of 6.0° and 13.1° are shown in Fig 5, and are in excellent agreement with experiment. Upper surface mean-velocity profiles on the main aerofoil and flap are well-predicted for the 6° incidence angle case, Fig 6. At the higher incidence angle of 13.1°, the displacement of the main aerofoil wake away from the flap surface is under-predicted in the flap trailing-edge region. This can be partially attributed to inadequate grid resolution in the outer wake region. However, it is likely that some of this discrepancy is due to a lack of response of the k-ϵ turbulence model to the significant flow curvature present at this high-lift condition.

The computed lift, drag and pitching moment coefficients are compared with experiment in Fig 7. The drag is consistently over-predicted by about 100%, despite the apparently good surface pressure distribution predictions of Fig 5. The limited number of surface cells in the computational grid will result in a rather inaccurate integration for the drag, however. Fig 7(a) and (c) show good agreement between predictions and experiment for the lift and pitching moment coefficient, up to the experimentally-observed stall. The computations fail completely to predict the stall, so that the lift continues to increase with incidence angle. Davidson[47] has observed a similar reluctance of computations to predict the stall of a high-lift, single-aerofoil section when using the k-ϵ turbulence model. This inability of the k-ϵ model to predict smooth-surface flow separation is, again, associated with a lack of response to flow curvature. Recent computations by Stolcis[48], employing an algebraic Reynolds-stress formulation with the k-ϵ model (a model that *does* respond to flow curvature), do predict the correct stalling behaviour for the NLR 7301 aerofoil/flap configuration.

SKF 1.1 Wing/Manoeuvre Flap

The SKF 1.1 aerofoil/manoeuvre flap configuration of Stanewsky and Thibert[49] was chosen to evaluate the present computational method for transonic flow conditions. The data-set consists of surface pressure distributions and integrated loads only, but covers a wide range of transonic conditions in a systematic manner, from fully-subcritical flow to supercritical flow with shock-induced separation. Fig 8 shows the aerofoil with a 25% chord manoeuvre flap deployed at a deflection angle of 10°, this being referred to as Configuration 5 in the data report[49]. The aerofoil/flap combination was tested in the DFVLR 1 x 1 Meter Transonic Tunnel, the model having tunnel height/chord and width/chord ratios of 5. Such a width/chord ratio should have minimised the influence of the wind tunnel sidewalls on the aerofoil/flap surface pressure distributions.

The geometric angle of incidence α has been corrected for top-and-bottom wall interference effects following the procedure recommended in the data report. For the large lift coefficients achieved in the experiment (in excess of 1.0), this amounts to a substantial correction, of the order of -3°. The integrated lift coefficient C_L and pitching moment coefficient about the quarter-chord point $C_M(1/4)$ have similarly been corrected for wall-induced streamline curvature effects. The drag coefficient C_D was measured by the wake-traverse technique and so requires no correction. All the experiments were carried out at a freestream Reynolds number of about 2.2×10^6, with free transition on both aerofoil elements.

Fig 8 shows the aerofoil/manoeuvre flap geometry, together with the inner region of the grid used in the computations. The geometry is fully-represented, with the main aerofoil element having a cut-out in the cove region into which the flap can retract to form the clean SKF aerofoil section. Both aerofoil elements also have blunt trailing edges. Transition was fixed on both aerofoil elements for the computations, at 3% and 25% chord respectively on the upper and lower surfaces of the main element, and at the leading edge on the flap. Although the experiments involved free transition, disturbances from surface pressure tappings were likely to have promoted transition in the leading-edge regions, at least on the upper surfaces.

The computational grids were constructed by first generating a structured grid of C-type topology around the basic SKF section, with outer and downstream boundaries at 15 and 11 chords respectively away from the aerofoil surface. A second C-type grid was then generated around the flap element, but with only the inner region being retained. A local grid was constructed in the flap cove region of the main aerofoil element. Finally, the vertices of these three sub-grids were reconnected to form triangular computational cells, using the Delaunay algorithm. The resulting grid consisted of 9712 cells, 14742 edges and 5031 vertices, with 140 and 100 cells on the main aerofoil and flap surfaces respectively.

Stolcis and Johnston[50] carried out a wide-ranging evaluation of the present computational method for this particular data-set. Results are presented here for a range of increasingly severe flow conditions, at various freestream Mach numbers but with a fixed incidence angle. Fig 9 compares measured surface pressure distributions with predictions, two sets of computations being shown. The first set are for the nominal experimental freestream Mach numbers, and agree reasonably well with measurements. The second set of computations include a constant increment $\Delta M = -0.02$ on the nominal freestream Mach numbers. Such an increment is consistent with solid and wake blockage effects in the experiment at these high-lift conditions. Inclusion of the Mach number increment leads to an overall improvement in the predicted surface pressure distributions, although the magnitude of the presumed ΔM appears to be too large in some cases.

Predicted variations of lift, drag and pitching moment coefficients with Mach number are compared with experiment in Fig 10. The drag levels below transonic drag rise conditions are significantly over-predicted, and this is attributed mainly to an over-prediction of the pressure drag contribution of the flap. Suction levels in the leading-edge region of the flap are critically dependent upon the shape and size of the recirculation zone in the flap cove. It is well known that the k-ϵ turbulence model tends to predict premature re-attachment for such zones, and this is consistent with the present under-prediction of suction levels around the flap leading edge. Inadequate grid resolution in this region may also be a contributory factor, however.

An overview of the predicted flowfield for a typical transonic flow condition is given by the iso-Mach number contours in Fig 11(a), which are smooth despite the unstructured nature of the computational grid. Mean-velocity vectors in the flap cove region, Fig 11(b), show clearly the closed recirculation zone formed due to separation from the sharp edge on the lower surface of the cut-out. Note that the flow re-attaches on the inner surface of the flap cove upstream of the upper surface trailing edge.

CONCLUSIONS

A computational method to predict the compressible viscous flow development around multi-element, high-lift aerofoils has been described. Solution of the Reynolds-averaged Navier-Stokes equations in conjunction with the two-equation k-ϵ turbulence model gives a basic capability for dealing with the complex flow physics of such high-lift systems. Similarly, the use of unstructured computational grids allows the method to be used in an essentially routine fashion for fully-representative, closely-coupled configurations. The method has been evaluated for low-speed, high-lift configurations and for single- and multi-element aerofoils at transonic flow conditions. The results achieved to date are encouraging, but indicate limitations in quantitative accuracy due to turbulence-modelling deficiencies at the k-ϵ level. In particular, the lack of response of the model to flow curvature is a serious problem for predictions near maximum-lift conditions and the subsequent stall. Work is underway to implement a differential stress model into the method, solving modelled transport equations for the Reynolds-stress components themselves, to overcome these limitations. Also, the grid generation procedure needs to be more automatic, and preferably adaptive to the flow within the time-stepping scheme.

ACKNOWLEDGEMENTS

The second author (LS) would like to acknowledge the support of the Commission of the European Communities, Directorate General for Science, Research and Development, Science Plan (grant SC1/900369). He was also in receipt of a fees-only studentship from the Science and Engineering Research Council.

REFERENCES

1. Lowrey, R.O., 'Evolution of Transport Wings From C-130, C-141, C-5 to C-XX', AIAA Paper 80-3038, Evolution of Aircraft Wing Design Symposium, U.S. Air Force Museum, Dayton , Ohio, USA, March 18-19, 1980

2. Smith, A.M.O., 'High-Lift Aerodynamics', AIAA Paper 74-0939, 1974

3. Butter, D.J., 'Recent Progress on the Development and Understanding of High Lift Systems', AGARD CP 365, May 1984

4. Johnston, L.J. and Horton, H.P., 'An Experimental Study of Turbulent Wake/Boundary Layer Mixing Flows', ICAS Paper 86-2.3.4, Proceedings of 15th ICAS Congress, September 7-12, 1986, London, England, pp.360/369

5. Stevens, W.A., Goradia, S.H. and Braden, J.A., 'Mathematical Model For Two-Dimensional Multi-Component Airfoils in Viscous Flow', NASA CR 1843, 1971

6. Goradia, S.H. and Colwell, G.T., 'Analysis of High-Lift Wing Systems', Aeronautical Quarterly, Vol.26, 1975, pp.88/108

7. Seebohm, T. and Newman, B.G., 'A Numerical Method For Calculating Viscous Flow Round Multiple-Section Aerofoils', Aeronautical Quarterly, Vol.26, 1975, pp.176/188

8. Oskam, B., 'A Calculation Method for the Viscous Flow Around Multicomponent Airfoils', NLR TR 79097 U

9. Oskam, B., 'Computational Aspects and Results of Low Speed Viscous Flow About Multicomponent Airfoils', AGARD CP 291, 1980

10. Butter, D.J. and Williams, B.R., 'The Development and Application of a Method for Calculating the Viscous Flow About High-Lift Aerofoils', AGARD CP 291, Paper 25, 1980

11. Brune, G.W. and McMasters, J.H., 'Computational Aerodynamics Applied to High-Lift Systems', Applied Computational Aerodynamics, Progress in Astronautics and Aeronautics, Vol.125, AIAA, New York, 1990, pp.389/433

12. King, D.A. and Williams, B.R., 'Developments in Computational Methods for High-Lift Aerodynamics', Aeronautical Journal, Vol.92, No.917, August/September 1988, pp.265/288

13. Caughey, D.A., 'An Inviscid Analysis of Transonic, Slatted Airfoils', AIAA Paper 74-541, 1974

14. Grossman, B. and Melnik, R.E., 'The Numerical Computation of the Transonic Flow Over Two-Element Airfoil Systems', Lecture Notes in Physics, Vol.59, 1976, pub. Springer Verlag, pp.220/227

15. Arlinger, B.G., 'Analysis of Two-Element High Lift Systems in Transonic Flow', ICAS Paper 76-13, Proceedings of 10th ICAS Congress, 3-8 October, 1976, Ottawa, Canada, pp.125/133

16. Rosch, H. and Klevenhusen, K.D., 'Flow Computation Around Multi-Element Airfoils in Viscous Transonic Flow', ICAS Paper 80-11.3, Proceedings of 12th ICAS Congress, 12-17 October, 1980, Munich, pp.470/479

17. Mavriplis, D.J., 'Multigrid Solution of the Two-Dimensional Euler Equations on Unstructured Triangular Meshes', AIAA J., Vol.26, No.7, July 1988, pp.824/831

18. Stolcis, L. and Johnston, L.J., 'Solution of the Euler Equations on Unstructured Grids for Two-Dimensional Compressible Flow', Aeronautical Journal, Vol.94, No.936, June/July 1990, pp.181/195

19. Grossman, B. and Volpe, G., 'The Viscous Transonic Flow Over Two-Element Airfoil Systems', AIAA Paper 77-688, 1977

20. Leicher, S., 'Viscous Flow Simulation of High Lift Devices at Subsonic and Transonic Speeds', AGARD CP.291, 1980, 6-1 to 6-15

21. Brune, G.W. and Sikavi, D.A., 'Experimental Investigation of the Confluent Boundary Layer of a Multielement Low Speed Airfoil', AIAA Paper 83-0566, January 1983

22. Nakayama, A., Kreplin, H.-P. and Morgan, H.L., 'Experimental Investigation of Flowfield About a Multielement Airfoil', AIAA J., Vol.28, No.1, January 1990, pp.14/21

23. Yip, L.P., Vijgen, P.M.H.W. and Hardin, J.D., 'In-Flight Surface-Flow Measurements on a Subsonic Transport High-Lift Flap System', ICAS Paper 92-3.7.3, Proceedings of 18th ICAS Congress, Beijing, P.R. China, 20-25 September 1992, pp.1392/1406

24. Shima, E., 'Numerical Analysis of Multiple Element High-Lift Devices by Navier Stokes Equation Using Implicit TVD Finite-Volume Method', AIAA Paper 88-2574-CP, June 1988

25. Mavriplis, D.J., 'Algebraic Turbulence Modeling for Unstructured and Adaptive Meshes', AIAA J., Vol.29, No.12, December 1991, pp.2086/2093

26. Chow, R. and Chu, K., 'Navier-Stokes Solution of High-Lift Multielement Airfoil System With Flap Separation', AIAA Paper 91-1623, 1991

27. Baldwin, B.S. and Lomax, H., 'Thin Layer Approximation and Algebraic Model for Separated Turbulent Flows', AIAA Paper 78-257, January 1978

28. Stolcis, L. and Johnston, L.J., 'Compressible Flow Calculations Using a Two-Equation Turbulence Model and Unstructured Grids', Proceedings of 7th International Conference on Numerical Methods in Laminar and Turbulent Flow, 15-19 July 1991, Stanford, California, USA, Pt.2, pp.922/932

29. Stolcis, L. and Johnston, L.J., 'Computation of the Viscous Flow Around Multi-Element Aerofoils Using Unstructured Grids', Notes on Numerical Fluid Mechanics, Vol.35, Eds. J.B. Vos, A. Rizzi and I.L. Ryhming, Pub. Vieweg, Braunschweig/Wiesbaden, 1992, pp.311/320

30. Mavriplis, D.J. and Martinelli, L., 'Multigrid Solution of Compressible Turbulent Flow on Unstructured Meshes Using a Two-Equation Model', AIAA Paper 91-0237, January 1991

31. Baldwin, B.S. and Barth, T.J., 'A One-Equation Turbulence Transport Model for High Reynolds Number Wall-Bounded Flows', AIAA Paper 91-0610, January 1991

32. Jameson, A. and Baker, T.J., 'Solution of the Euler Equations for Complex Configurations', AIAA Paper 83-1929, 1983

33. Thomas, J.L. and Salas, M.D., 'Far-Field Boundary Conditions for Transonic Lifting Solutions to the Euler Equations', AIAA Paper 85-0020, 1985

34. Launder, B.E. and Spalding, D.B., 'The Numerical Computation of Turbulent Flow', Computer Methods in Applied Mechanics and Engineering, Vol.3, March 1974, pp.269/289

35. Patel, V.C., Rodi, W. and Scheuerer, G., 'Turbulence Models for Near-Wall and Low Reynolds Number Flows: A Review', AIAA J., Vol.23, No.9, September 1985, pp.1308/1319

36. Mitcheltree R., Salas M. and Hassan H., 'A One Equation Turbulence Model For Transonic Airfoil Flows', AIAA Paper 89-0557, 1989

37. Johnston, L.J., 'Solution of the Reynolds-Averaged Navier-Stokes Equations for Transonic Aerofoil Flows', Aeronautical Journal, Vol.95, No.948, October 1991, pp.253/273

38. Wolfshtein, M., 'The Velocity and Temperature Distribution in One-Dimensional Flow With Turbulence Augmentation and Pressure Gradient', Int. J. Heat and Mass Transfer, Vol.12, 1969, pp.301/318

39. Jameson, A., Schmidt, W. and Turkel, E., 'Numerical Solution of the Euler Equations by Finite Volume Methods Using Runge-Kutta Time Stepping Schemes', AIAA Paper 81-1259, June 1981

40. Jameson, A., Baker, T.J. and Weatherill, N.P., 'Calculation of Inviscid Transonic Flow Over a Complete Aircraft', AIAA Paper 86-0103, January 1986

41. Weatherill, N.P., Johnston, L.J., Peace, A.J. and Shaw, J.A., 'A Method for the Solution of the Reynolds-Averaged Navier-Stokes Equations on Triangular Grids', Notes on Numerical Fluid Mechanics, Vol.20,Pub. Vieweg, Braunschweig, 1988, pp.418/425

42. Weatherill, N.P., 'A Method for Generating Irregular Computational Grids in Multiply Connected Planar Domains', Int. J. Numerical Methods in Fluids, Vol.8, 1988, pp.181/197

43. Stolcis, L., 'Computation of the Turbulent Flow Development Around Single- and Multi-Element Aerofoils', PhD Thesis, University of Manchester, Faculty of Technology (UMIST), 1992

44. Cook, P.H., McDonald, M.A. and Firmin, M.C.P., 'Aerofoil RAE 2822 - Pressure Distributions, and Boundary Layer and Wake Measurements', AGARD AR 138, May 1979, A6-1 to A6-77

45. Stolcis, L. and Johnston, L.J., 'Near-Wall Turbulence Models and Numerical Solution of the Reynolds-Averaged Navier-Stokes Equations Using Unstructured Grids', 13th Int. Conference on Numerical Methods in Fluid Dynamics, Rome, Italy, 6-10 July, 1992

46. van den Berg, B., 'Boundary Layer Measurements on a Two-Dimensional Wing With Flap', NLR TR 79009 U, 1979

47. Davidson, L., 'Calculation of the Flow Around a High-Lift Airfoil Using an Explicit Code and an Algebraic Reynolds Stress Model', Numerical Methods in Laminar and Turbulent Flow, Vol.VII, Part 2, 1991, Pub. Pineridge Press, Swansea, pp.852/862

48. Stolcis, L., 'Computation of the Turbulent Flow Over a High-Lift System Using an Algebraic Reynolds Stress Model', 8th Int. Conference on Numerical Methods in Laminar and Turbulent Flow, Swansea, U.K., 18-23 July, 1993

49. Stanewsky, E. and Thibert, J.J., 'Airfoil SKF 1.1 With Maneuver Flap', AGARD AR 138, May 1979, A5-1 to A5-29

50. Stolcis, L. and Johnston, L.J., 'Application of an Unstructured Navier-Stokes Solver to Multi-Element Airfoils Operating at Transonic Maneuver Conditions', AIAA Paper 92-2638, June 1992

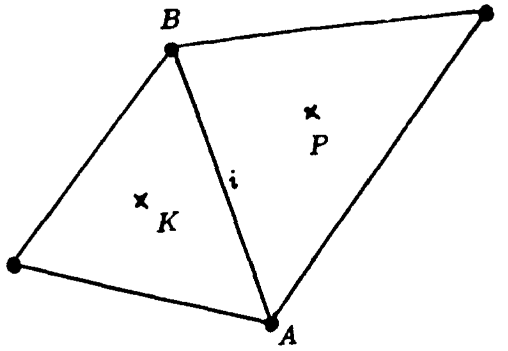

Fig. 1 Notation for computational cells and cell edges
X = cell centres; ● = cell vertices

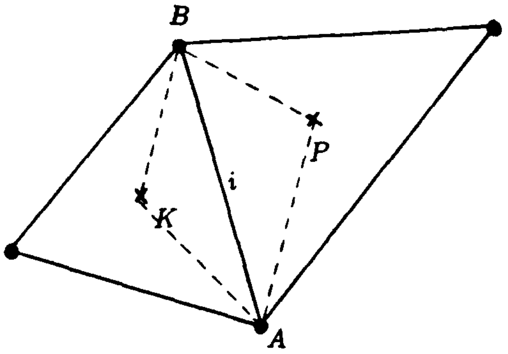

Fig. 2 Auxiliary cell (- - - - - -)
for viscous flux computation

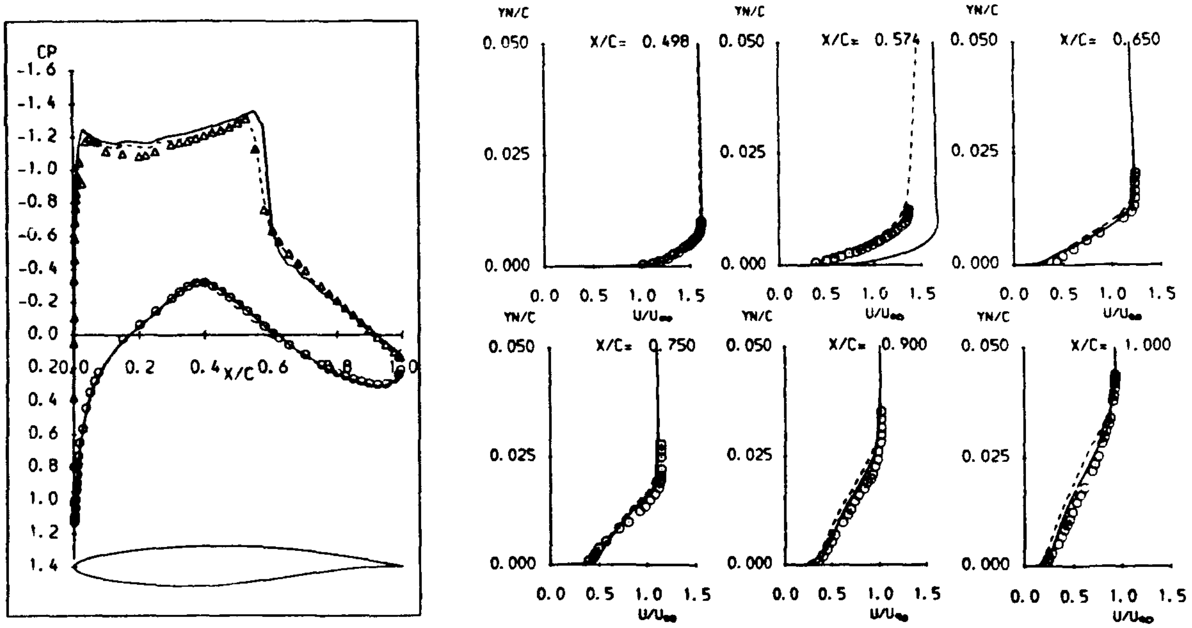

(a) Surface pressure distribution

(b) Upper surface mean-velocity profiles

Fig. 3 RAE 2822 aerofoil - Case 9 - Effect of near-wall modelling
o,Δ experiment; ——— one-equation model
- - - - - - - wall functions

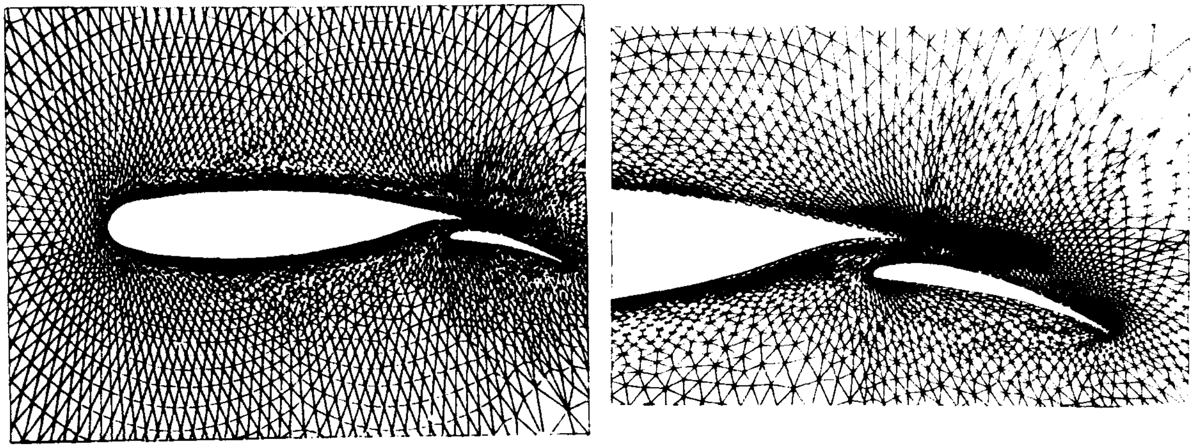

Fig. 4 Computational grid for NLR 7301 wing/trailing-edge flap configuration

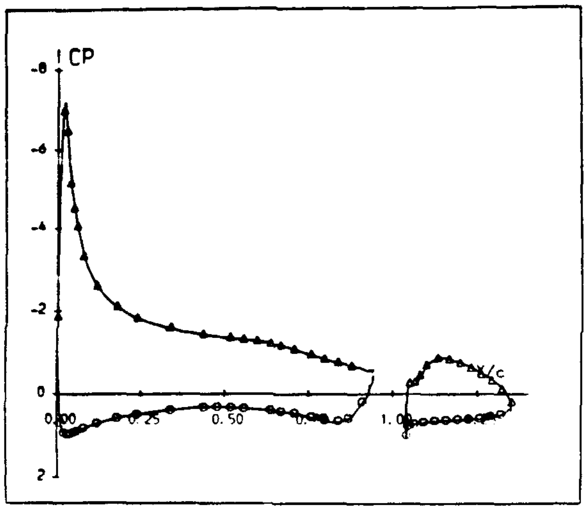

(a) α = 6.0°

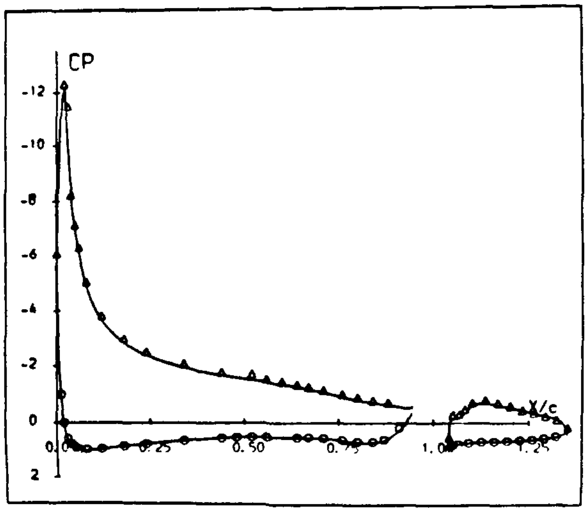

(b) α = 13.1°

Fig. 5 Surface pressure distributions for NLR 7301 wing/flap
o,Δ experiment; ——— computation

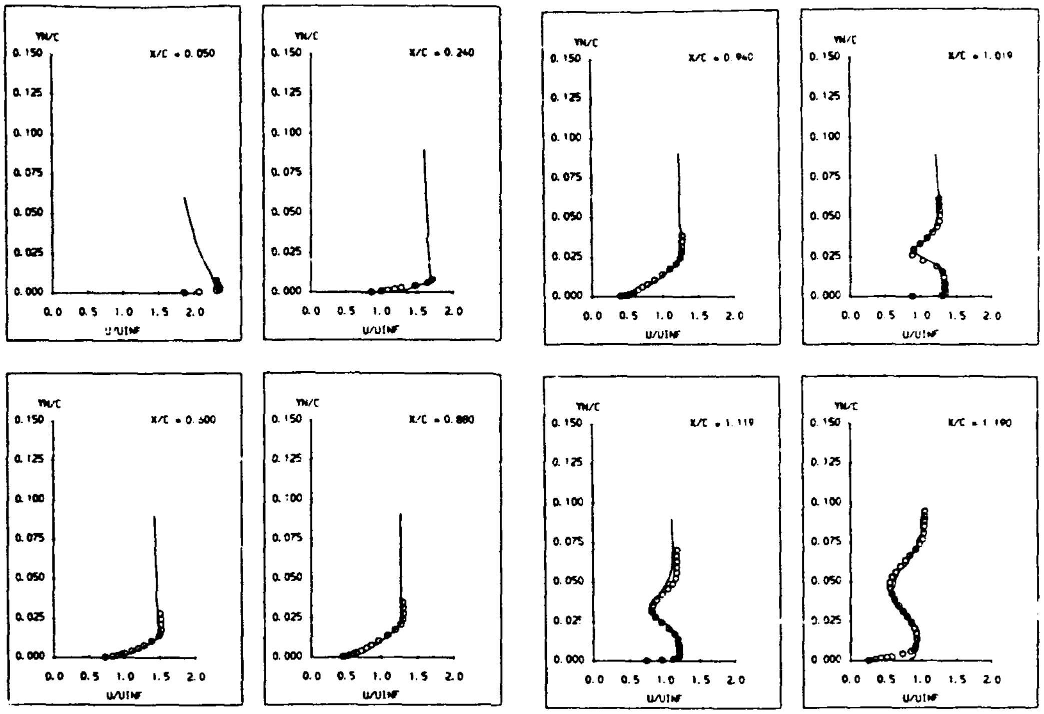

(a) α = 6.0°

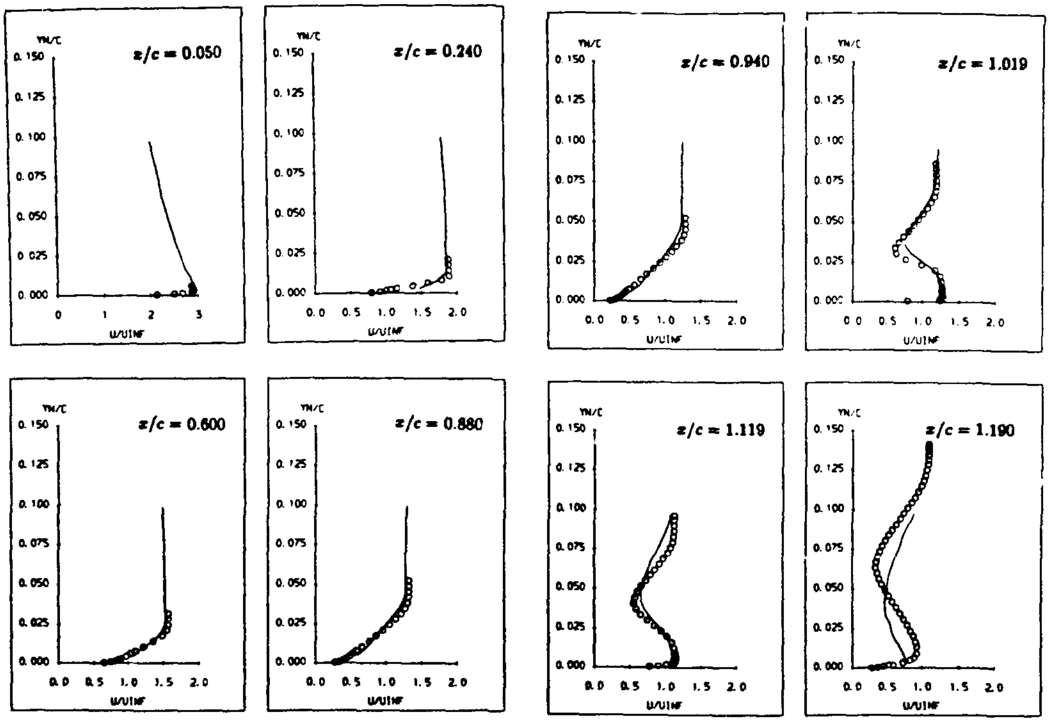

(b) α = 13.1°

Fig. 6 Upper surface mean-velocity profiles for NLR 7301 wing/flap
o experiment; ——— computation

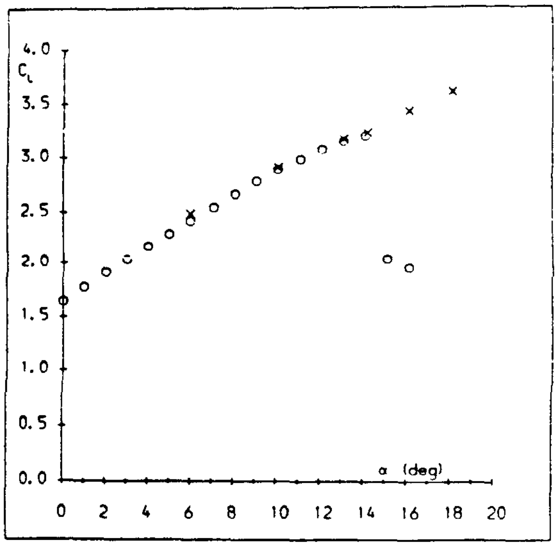

(a) Lift vs incidence

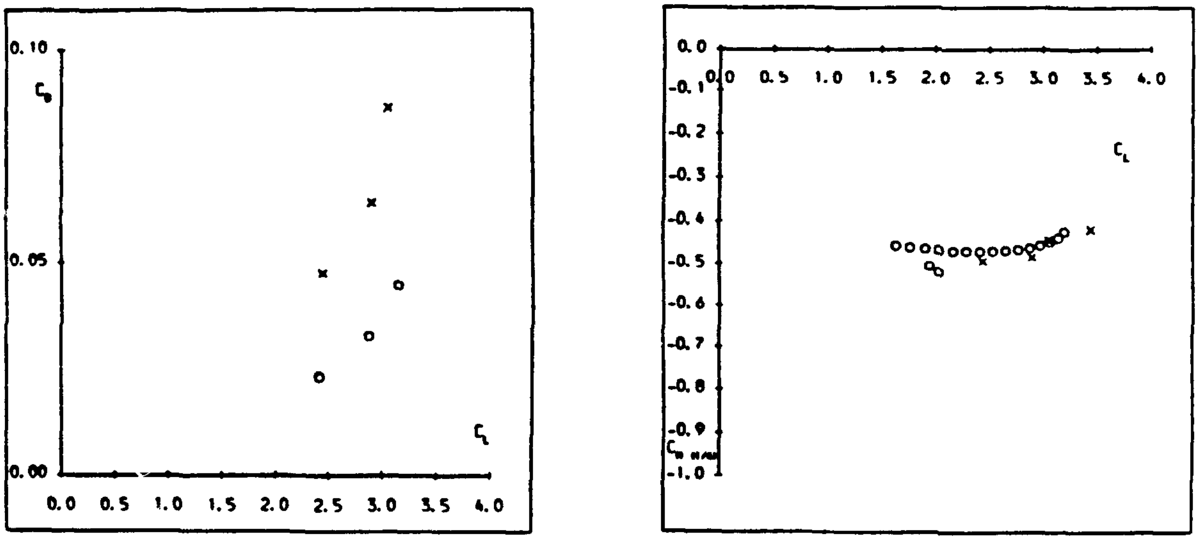

(b) Drag vs lift

(c) Pitching moment vs lift

Fig. 7 Integrated loads for NLR 7301 wing/flap
o experiment; X computation

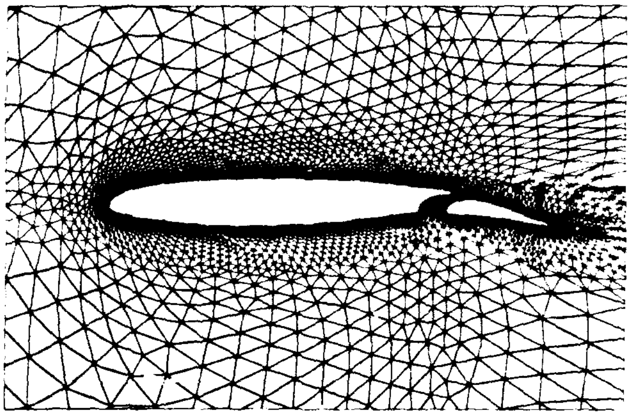

Fig. 8 Geometry and inner region of computational grid for SKF 1.1 aerofoil/flap configuration

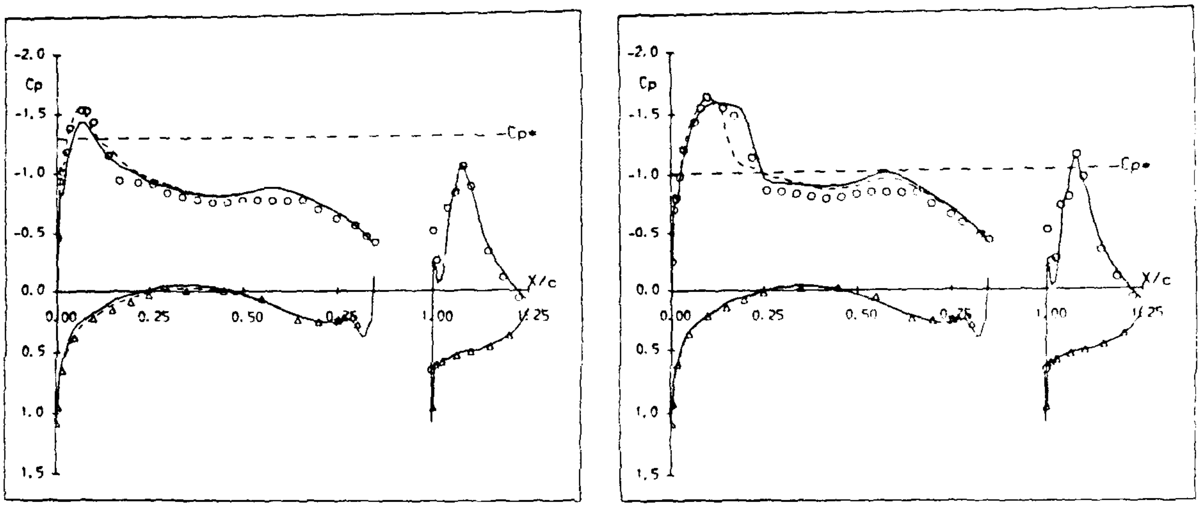

(a) M_∞ = 0.600, α = 0.18°, run 223

(b) M_∞ = 0.650, α = 0.02°, run 229

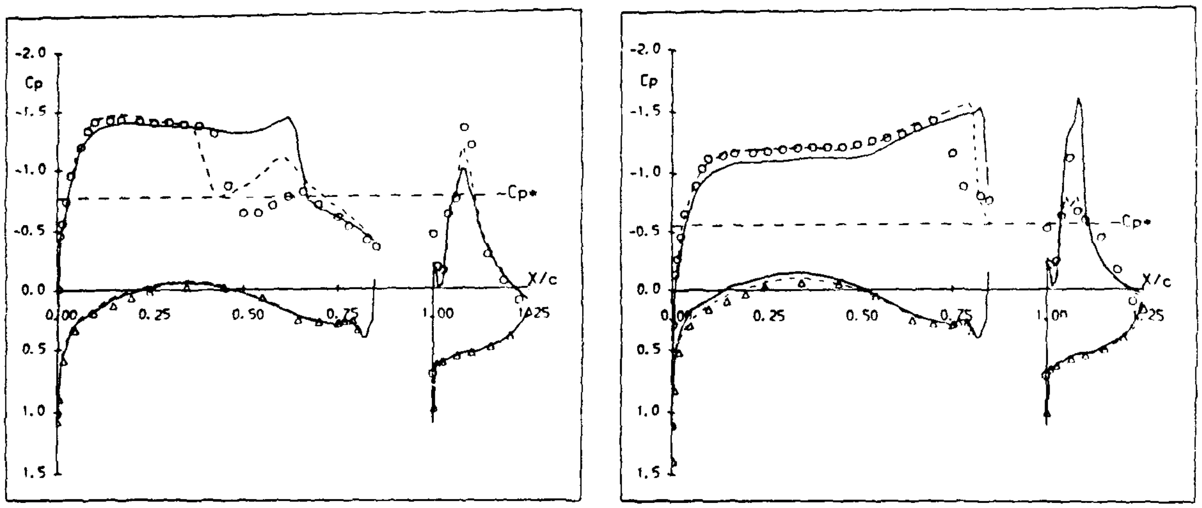

(c) M_∞ = 0.701, α = -0.15°, run 235

(d) M_∞ = 0.760, α = -0.26°, run 241

Fig. 9 Surface pressure distributions for SKF 1.1 wing/flap
Mach number sweep at α ≃ 0°
o,Δ experiment; ——— computation at nominal M_∞
------ computation including ΔM_∞

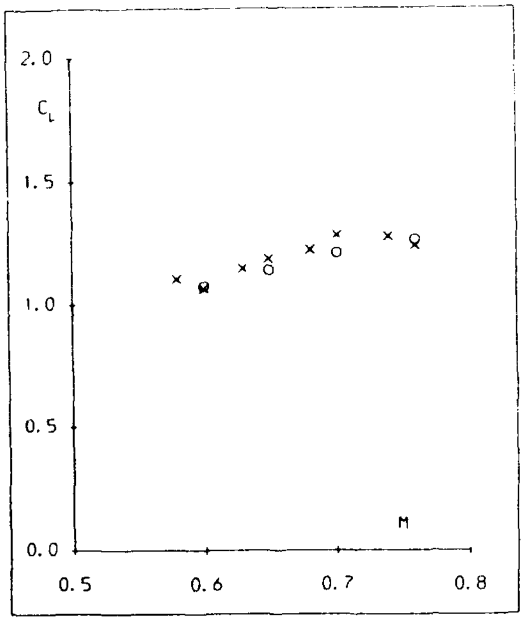

(a) Lift vs Mach number

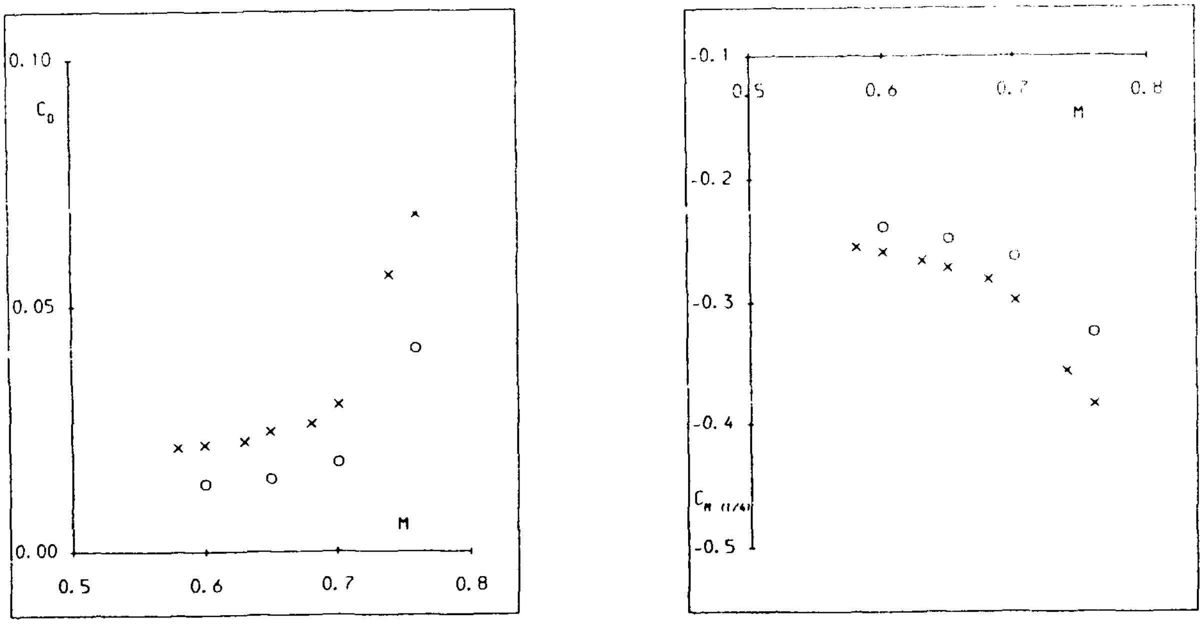

(b) Drag vs Mach number

(c) Pitching moment vs Mach number

Fig. 10 Integrated loads for SKF 1.1 wing/flap
Mach number sweep at α ≃ 0°
o experiment; X computation

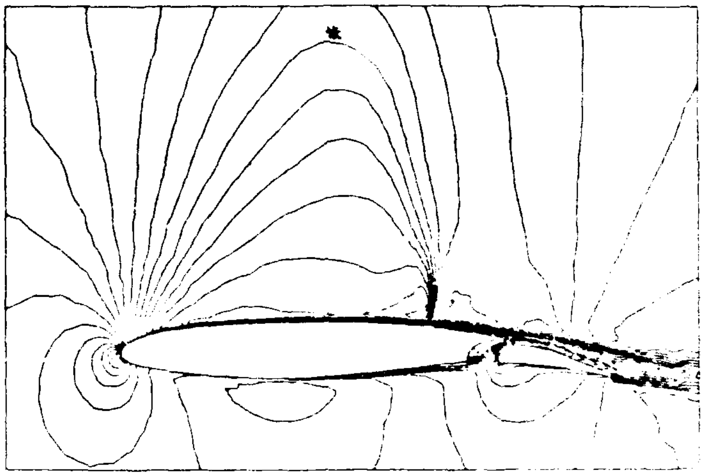

(a) Mach number contours (* indicates sonic line)

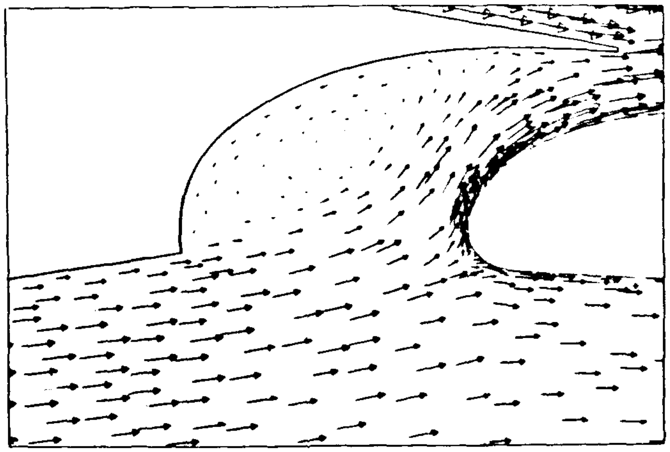

(b) Velocity vectors in flap cove region

Fig. 11 Typical computed flowfield solution for SKF 1.1 wing/flap
$M_\infty = 0.701$, $\alpha = -0.15°$, run 235

NUMERICAL CALCULATIONS OF HIGH LIFT FLOWS USING STRUCTURED AND UNSTRUCTURED METHODS

R. Bailey, J.M.A. Longo
R. Radespiel, A. Ronzheimer
A. Demler, N. Kroll
C.-C. Rossow
Institute for Design Aerodynamics
DLR-Braunschweig, Am Flughafen
D-3300 Braunschweig, Germany

SUMMARY

At the DLR Institute for Design Aerodynamics current research in the area of high lift aerodynamics is directed towards the development of a computational analysis capability for high lift systems. The Navier-Stokes equations are solved with a multigrid method based on central spatial differencing and Runge-Kutta time stepping. Two particular problems are addressed in this paper. The first concerns the calculation of maximum lift for a single airfoil and a clean wing configuration. The accuracy of the basic structured flow solver is investigated by comparing the results with experimental data for two test problems and several flow conditions. Emphasis is placed on the sensitivity of the computed solution associated with turbulence modelling. The second aspect dealt with in the present paper concerns the extension of the numerical method to multi-element airfoils. Both, the block-structured and the unstrucutred grid approach are investigated in order to explore their specific merits and limitations. Detailed comparisons of the structured and unstructured approach are presented for low Reynolds' number laminar viscous flows around a single airfoil, and for the inviscid flow around a multi-element airfoil.

LIST OF SYMBOLS

c_n	normal force coefficient
c_l, c_L	lift coefficient
c_d, c_D	drag coefficient
c_p	surface pressure distribution
E	specific total energy
$\bar{F}$	tensor of flux density
$\vec{n}$	unit vector of outward normal
M	Mach number
u,v,w	Cartesian velocity components
Re	Reynolds number
V	control volume
∂V	boundary of control volume V
α	angle of attack
η	spanwise section
ρ	density

1. INTRODUCTION

In the development of new aircraft the design of high lift systems for low speed take-off and landing capabilities is perhaps one of the most complicated aerodynamic problems. The flow around high lift configurations is characterized by many different inviscid and viscous flow regions (see e.g. [1], [2]). In particular, the existence of significant regions of separated flow and of strong wake/boundary layer interference distinguishes the high lift airfoil problem from the aerodynamic issues being faced at cruise conditions. The successful design of future efficient high lift devices will largely rely on a better understanding of the basic physics. To achieve this, both improved experimental and theoretical prediction techniques are required.

At the DLR Institute for Design Aerodynamics a numerical procedure for analyzing high lift configurations is currently being under development. The method is based on the solution of the mass averaged Navier-Stokes equations using a central spatial discretization and Runge-Kutta time stepping scheme. Rapid convergence is achieved by the use of various acceleration techniques, in particular a multigrid algorithm. The basic solver has been applied to a variety of flow problems including finite span wings and wing-body combinations [3-5].

In the present paper two particular aspects of the code development for high lift configurations are addressed. Firstly, the capability of the Navier-Stokes solver to predict the maximum lift of a single airfoil and a wing is investigated. For this analysis a structured grid approach has been used. Comparisons of theoretical results obtained with different turbulence models and experimental data are presented. Secondly, the extension of the basic flow solver to treat multi-element airfoils is discussed. Although substantial progress has been made in the development of effective algorithms for solving the Navier-Stokes equations, very often the use of these methods for practical applications is limited due to deficiencies in grid generation. Today the generation of an appropriate grid around complex aerodynamic geometries such as high lift configurations continues to be a major obstacle. For the treatment of multi-element airfoils mainly two approaches have been used in the literature, namely the block structured grid concept (see e.g. [6]) and the unstructured mesh approach (see e.g. [7]). At DLR currently both approaches are being investigated in order to explore and assess their merits and limits. First results of these investigations are shown here. The studies presented in this paper appear to be necessary steps towards the developoment of an accurate and efficient computational procedure for high lift configurations.

2. DESCRIPTION OF NUMERICAL METHODS

The governing equations are the mass-averaged Navier-Stokes equations representing conservation of mass, momentum and energy. Expressed in integral form they can be written as

$$\frac{\partial}{\partial t}\iiint_V \vec{W}\,dV + \iint_{\partial V} \bar{F}\cdot\vec{n}\,dS = 0, \qquad (1)$$

where

$$\vec{W} = [\rho,\ \rho u,\ \rho v,\ \rho w,\ \rho E]^T \qquad (2)$$

is the vector of conserved variables. The quantities ρ, u, v, w and E denote the density, the Cartesian velocity components and the specific total energy. V represents an arbitrary control volume with boundary ∂V and outer normal $\vec{n}$. The definition of the flux density tensor $\bar{F}$ is given in [3]. The equation of state for perfect gas is used to calculate pressure and temperature. The laminar viscosity is assumed to follow an empirical power law. In the case of turbulent flows the laminar viscosity, μ, is replaced by $\mu+\mu_t$, and the heat conductivity μ/Pr is replaced by $\mu/Pr + \mu_t/Pr_t$, where the eddy viscosity μ_t, and the turbulent Prandtl number, Pr_t are provided by a turbulence model. In the present work the turbulence models of Baldwin-Lomax [8] and Johnson-King [9] are used. The Baldwin-Lomax model is an algebraic model which relates the eddy viscosity to the local maximum of vorticity. This equilibrium model is widely used for computing attached and mildly separated flows. In order to allow a more accurate determination of the turbulent stresses in separated boundary layer flows, Johnson and King developed an non-equilibrium turbulence model in which both, convection and diffusion of turbulence are taken into account.

2.1 Structured Method

The basic flow solver (DLR-code CEVCATS) [3,10,11] is a finite volume method based on structured grids. The numerical approximation of Eq (1) follows the method of lines, which decouples the discretization in space and time. The physical domain around the aerodynamic body is divided into hexahedral cells by the generation of a body-fitted grid. The discrete values of the flow quantities are located at the vertices of the computational mesh cells. The cells surrounding a vertex form a super cell. The rate of change of mass, momentum and energy associated with a cell vertex is obtained by summing up the fluxes through the outer boundary of the super cell. The flux through a boundary segment is obtained by averaging the quantities at its corner points. It can be shown [12] that this cell vertex discretization scheme is first-order accurate if the distribution of the segment-normal vector is smooth over the segment, and if the cell faces do not degenerate to triangles. On smoothly varying meshes the discretization is second-order accurate. The viscous fluxes contain first derivatives of the flow variables. They are computed using a local transformation from Cartesian coordinates to the curvilinear coordinates. Details are given in [3]. In the present code the thin layer approximation is employed in which the viscous fluxes take into account gradients in the direction normal to the body and in spanwise direction only.

Since the spatial discretization is based on central differencing, dissipative terms have to be added explicitly in order to prevent odd-even point decoupling and oscillations near shock waves. The artificial dissipation model used in the structured code is based on the work of Jameson et al. [13]. A blend of fourth and second differences of the conserved variables is used to provide third order background dissipation in smooth flow regions and first order dissipation at shock waves. In order to avoid excessively large dissipation for cells with high aspect ratios present in the boundary layer, a variable scaling factor of the dissipative terms is employed. According to [14] this scaling factor is a function of the spectral radii of the Jacobian matrices associated with the three directions of the body fitted coordinate system, and accounts for varying cell aspect ratio.
The spatial discretization results in a system of ordinary differential equations in time which is advanced in time by an explicit multistage scheme. For computational efficiency, the physical viscous terms are computed on the first stage only and they are frozen for the remaining stages. Since current interest is focused on steady flow fields, various techniques are used to accelerate the convergence to steady state. With local time stepping the maximum allowable time step is used for each cell to advance the solution in time. Implicit smoothing of the residuals is employed to extend the stability region of the basic explicit multistage scheme. Using variable smoothing coefficients as a function of the cell aspect ratio and the time step can considerably improve the damping properties of the scheme for high aspect ratio cells [3]. Finally, a multigrid method according to [15] is implemented. A sequence of successively coarser meshes is used to efficiently damp out errors throughout the frequency spectrum simultaneously. Due to the less restrictive time step limitations and the smaller number of points on the coarse meshes, the solution can be advanced much more rapidly [3].

The code CEVCATS allows multiblock decomposition of the computational domain [11] which is important to treat complex aircraft geometries such as high lift systems. Considerable effort has been made to develop efficient multigrid strategies for multiblock computations [16].

2.2 Unstructured Method

In order to explore the capabilities and limits of the unstructured grid approach, the basic solution method described above has been extended to allow computations on unstructured meshes. Following the work of Mavripilis [17,18] a two-dimensional Euler/Navier-Stokes code has been developed [19,20] which uses control volumes formed by triangular elements (see Fig 1b). The numerical scheme for the solution of the full mass-averaged Navier-Stokes equations uses a spatial discretization employing a Galerkin finite element formulation. Details are given in [20]. The process is equivalent to a finite volume approximation for regular triangular meshes. As in the structured algorithm artificially constructed dissipative terms have to be added to provide background dissipation and to allow shock resolution. In the case of unstructured meshes the artificial dissipative operator is constructed as a blend of an undivided Laplacian and a biharmonic operator [17]. For Navier-Stokes calculations the dissipation model is modified according to Mavripilis [18] in order to take into account the high aspect-ratio cells present in the boundary layer and wake regions. For advancing the solution with respect to time, an explicit five stage Runge-Kutta scheme is used. As in the structured scheme convergence acceleration is achieved through local time stepping, implicit residual smoothing, and a multigrid method. In order to improve the accuracy and efficiency of the numerical procedure, a local grid adaptation procedure has been implemented. Important flow features are well defined and the overall efficiency of the unstructured scheme is not adversely effected by the adaptation procedure. The adaptation technique has been originally developed for application to Euler solutions [19] and has to be extended to be applied efficiently to viscous flows. A detailed description of the current implementation of the 2-D unstructured Navier-Stokes solver is given in [20].

3. COMPUTATION OF MAXIMUM LIFT

The structured Navier-Stokes solver described here has been applied to a wide variety of two- and three-dimensional flows. This paper addresses the capability of the Navier-Stokes solver to predict maximum lift. Since so far no turbulence model has been implemented in the unstructured solver, this investigation is restricted to the structured algorithm.

3.1 NACA 0012 Airfoil

As a first test case the two-dimensional flow around the NACA 0012 airfoil has been calculated for two Reynolds numbers Re = $3\cdot10^6$ and Re = $9\cdot10^6$ and for Mach numbers between $M_\infty = 0.3$, and $M_\infty = 0.7$ [21]. For these flow conditions experimental results of Harris [22] exist. For the computation a C-type grid with 385x65 grid points has been used. Fig 2 shows the grid structure in the vicinity of the airfoil. Two slightly different grids have been generated for the two Reynolds numbers. While the distribution of the grid points along the surface remains constant in both cases, the first spacing is $1.5\cdot10^{-5}\cdot c$ and $1\cdot10^{-5}\cdot c$ for Re = $3\cdot10^6$ and Re = $9\cdot10^6$, respectively, where c denotes the chord length of the airfoil. As in the experiment the transition from laminar to turbulent has been fixed to 5% of chord length in all calculations. For turbulent flow computations the Johnson-King turbulence model has been used.

Fig 3 shows the computed drag polars for $M_\infty = 0.3$ and $M_\infty = 0.55$ at Re = $3\cdot10^6$ (see Fig 3a) as well as for $M_\infty = 0.55$ and $M_\infty = 0.7$ at Re = $9\cdot10^6$ (see Fig 3b). The experimental results of Harris are also displayed. It has to be mentioned that in order to allow a comparison with experimental data the normal force coefficient has been plotted instead of the more usual lift coefficient. The normal force coefficient c_n is defined as

$$c_n = c_l \cos\alpha + c_d \sin\alpha , \qquad (2)$$

where α, c_l, c_d denote the angle of attack, the lift coefficient, and the drag coefficient, respectively. At lower angles of attack good agreement of computations and measurements is obtained for all Reynolds number and Mach number combinations. In the vicinity of the normal force maximum the theoretical results obtained with the Johnson-King model show discrepancies towards higher drag coefficients as compared to the experimental data. It can be said that considerable differences between computations and measurements become apparent when substantial flow separation occurs. The best agreement between theory and experiment is obtained for $M_\infty = 0.3$ for the low Reynolds number. This may be due to the fact that for these conditions only small domains of flow separation exist. The same trend can be seen in Fig 4 where the normal force coefficient is plotted versus the angle of attack. In this figure also experimental data with wind tunnel corrections [22] are displayed. Fig 5 shows the convergence history for some selected calculations. For low angle of attack around 80 multigrid cycles are required to achieve a residual reduction of 4-5 orders of magnitude. Note that with respect to the lift coefficient sufficiently converged solutions are obtained within 40 multigrid cycles. In the vicinity of maximum lift the efficiency of the Navier-Stokes solver somewhat decreases.

3.2 Wing-Body Combination

The second test case used in this analysis is the DLR-F4 wing-body combination consisting of a transonic wing of high aspect ratio and a fuselage of Airbus type. The DLR-F4 wing-body configuration was used within GARTEUR for experimental studies of 3-D transonic flow fields. An extensive data base of surface pressure distributions and total forces is available for a range of transonic Mach numbers and angles of attack. Fig 6 shows the geometry of the configuration [23]. The computational grid generated by transfinite interpolation is of C-H topology, that is C-type in streamwise direction and H-type in spanwise direction. The grid contains a total of 259 points in the streamwise direction, 59 points in the direction normal to the wing surface and 59 points in spanwise direction. The clustering of the grid lines in direction normal to the surface is sufficient to produce the non-dimensional wall coordinate y^+ to be less than unity in the cells adjacent to the solid surface.

This configuration has been analyzed extensively using the 3-D structured Navier-Stokes solver, and detailed results are given in [5]. Comparisons of computed and measured total lift coefficients versus angles of attack for three Mach numbers, $M_\infty = 0.6$, $M_\infty = 0.75$, and $M_\infty = 0.8$ are presented in Fig 7. The Reynolds number based on the mean chord is Re = $3\cdot10^6$. Calculations have been performed with three different turbulence models, the original Baldwin-Lomax model, a modified Baldwin-Lomax model according to Kays [24], and the Johnson-King model. In the computation transition was fixed on the upper wing surface at 15% of the local chord and on the lower surface at 25% chord. On the upper surface of the wing at the wing tip and the wing body junction as well as for the whole fuselage the flow was considered fully turbulent.

The agreement is quite satisfactory even beyond the onset of buffet. Up to buffet onset no difference can be found between ferences between the predicted results for this case and those for T1 are larger than those between T1 and T2. The pressure coefficient distributions shown in Fig 13 exhibit only small differences when compared to the structured grid results. This is true for each of the meshes used by the unstructured technique. Case T2 exhibits a jumb in the pressure distribution at the trailing edge of the airfoil. The reason for this is again the unbalanced dissipation stencil on the line of symmetry for this mesh. This analysis shows that generally the accuracy of the unstructured algorithm is comparable with that obtained using the structured grid approach, provided an unstructured grid without distorted cells is used.

4.2 Inviscid Flow around Two-Element Airfoil

As a second test case in order to investigate the capabilities of both structured and unstrucutred methods for the application to high lift configurations, the inviscid flow around a Karman-Trefftz airfoil associated with a flap has been chosen. The main airfoil is at zero incidence, and the flap is deflected by 30°. The Mach number is 0.15. Fig 14 shows a global view of the computational meshes used for the structured and unstructured scheme, respectively. The mesh used for the structured method consists of 3 computational blocks, a C-type block around each component, and a global C-block containing the component blocks, as can be seen in Fig 14. On the surface of the main airfoil 144 cells are located, and 112 cells on the flap. In the unstructured mesh, the main airfoil surface is represented by 128 points and the flap by 100 points. Fig 15 gives a view of the computed lines of constant Mach number for the structured and unstructured scheme, respectively. Both solutions are qualitatively as well as quantitatively in good agreement. Note that in the display of the structured results the block boundaries are also indicated by bold lines. The lines of constant Mach number pass smoothly over the boundaries. In Fig 16 a close-up view of the passage between main airfoil and flap is given. Note that on the structured mesh a grid discontinuity is located on the lower surface of the main airfoil in the trailing edge region. Fig 17 shows the corresponding flow field computed with both schemes. The solutions agree quite well in this region, too. In Fig 18 the computed pressure distributions of both approaches are compared. On the main airfoil the results of structured and unstructured method almost coincide. Only on the lower surface close to the trailing edge, the structured solution shows a discontinuity in the slope of the pressure distribution due to the mesh singularity located there. This disturbance has however no effect on the global solution. On the upper surface of the flap the unstructured scheme yields lower pressures than the structured approach. This is in better agreement with the analytical solution, as shown in [19]. The reason for this slight deficiency of the structured solution may be found in the high aspect ratio cells in this region, which are known to degrade the accuracy of the method for inviscid flows. This is also indicated by the slope of the iso-Mach lines in Fig 17, since the Mach lines of the structured solution do not intersect the upper surface of the flap as perpendicularly as in the unstructured solution. The convergence behavior of both schemes is given in Figs 19a and b. For both schemes computations have been carried out with and without multigrid acceleration. In case of the structured method Full Multigrid was used to establish a reasonable starting solution on the finest mesh, and a 4-level W-cycle has been used on the finest mesh. In the unstructured computations, a 4-level V-cycle was used. In the unstructured approach the point distribution on the coaser meshes is independent from the distribution on the finer meshes, whereas in the structured scheme each point on a coarser mesh is represented on the finer mesh. This may limit the possible number of grid levels, but careful grid generation can circumvent these limitations. The convergence properties of both schemes are very similar. For single mesh computation, about 1500 time-steps were necessary to decrease the residuals to 10^{-5}. With multigrid, for the structured method 100 cycles on the coarse mesh and 150 cycles on the finest mesh were needed, whereas in the unstructured scheme about 250 cycles on the finest mesh were used, starting directly on the finest mesh.

5. CONCLUSION

Two particular aspects of the development of a computational procedure for high lift aerodynamics have been presented. Navier-Stokes calculations on structured meshes have been carried out to predict maximum lift in the case of a single airfoil and a wing without high lift devices. Using the Johnson-King turbulence model good agreement between theoretical results and experimental data has been achieved for very high angles of attack. Rapid convergence to steady state has been obtained due to the multigrid method, making this solution method attractive for engineering applications.

The scope of the applications underlined the flexibility of the method, and comparison with experimental data demonstrated the capability of the basic CEVCATS code for maximum lift flows. The second aspect of the investigations was a direct comparison of a structured and an unstructured algorithm. Calculations of the laminar flow around the NACA 0012 airfoil showed very good agreement of the results obtained from both strategies. However, computations on different triangular meshes where always the same structured mesh was used as basis for the triangulation, showed a dependency of the solution on the mesh quality. For structured meshes the influence of the mesh quality on the solution is a well known fact. In case of unstructured schemes criteria for the necessary mesh quality are not that well established, and the computations carried out in this study indicate that mesh quality is a critical issue also for unstructured schemes. As a more complex test case the inviscid flow around a Karman-Trefftz airfoil with deflected flap was chosen. Again the solutions of both schemes agreed well with each other. For the structured scheme, a slight deficiency occurred at the mesh singularity located on the airfoil surface, the effect was however only local. More sophisticated mesh generation techniques will remedy this problem. Convergence properties of both schemes were also comparable, and the time-lag between different blocks in the structured approach caused no disadvantages with respect to the unstructured method.

The results from the investigations carried out in this study indicate that for both, structured and unstructured schemes, mesh quality is the key issue for accurate solutions. Assuming a sufficiently sophisticated mesh generation system, the block-structured approach appears as feasible as the unstructured approach for the application to complex configurations. With this argument and taking into account the uncertainties of unstructured methods with regard to three-dimensional viscous flows, at the present time high lift activities at DLR are geared towards more effective and more flexible grid generation methods for block structured flow codes.

6. REFERENCES

[1] Butler, D.J.: Recent Progress on Development and Understanding of High Lift Systems. AGARD-CP-365, pp. 1.1.-1.26, 1984.

[2] Dillner, B., May, F.W., McMasters, J.H.: Aerodynamic Issues in the Design of High-Lift Systems for Transport Aircraft. AGARD-CP-365, pp. 9.1-9.22, 1984.

[3] Radespiel, R., Rossow, C.-C., Swanson, R.C.: Efficient Cell-Vertex Multigrid Scheme for the Three-Dimensional Navier-Stokes Equations. AIAA Journal, Vol. 28, No. 8, pp. 1464-1472, 1990.

[4] Longo, J.M.A., Radespiel, R.: Vortical Flow Simulation by the Solution of the Navier-Stokes Equations. 8th Symposium on Turbulent Shear Flows, Technical University of Munich, 1991.

[5] Longo, J.M.A.: Viscous Transonic Flow Simulation around a Transport Aircraft Configuration. DGLR-Jahrestagung, Bremen, 1992.

[6] Sanetrik, M.D., Swanson, R.C.: A Multigrid Solution Procedure for Multi-element Airfoils. 5th Conference on Domain Decomposition Methods for Partial Differential Equations. Norfolk, VA, 1991.

[7] Mavripilis, D.J., Jameson, A., Martinelli, L.: Multigrid Solution of the Navier-Stokes Equations on Triangular Meshes. AIAA-89-0120, 1989.

[8] Baldwin, B.S., Lomax, H.: Thin Layer Approximation and Algebraic Model for Separated Turbulent Flows. AIAA-78-257, 1978.

[9] Johnson, D.A., King, L.S.: A Mathematically Simple Turbulent Closure Model for Attached and Separated Turbulent Boundary Layers. AIAA Journal, Vol. 23, pp. 1684-1692, 1985.

[10] Rossow, C.-C., Kroll, N., Radespiel, R., Scherr, S.: Investigation of the Accuracy of Finite Volume Methods for 2- and 3-Dimensional Flows. AGARD-CPP-437, P17.1-11, 1988.

[11] Atkins, H.: A Multi-Block Multigrid Method for the Solution of the Euler and Navier-Stokes Equations. AIAA-91-0101, 1991.

[12] Rossow, C.-C.: Berechnung von Strömungsfeldern durch Lösung der Euler-Gleichungen mit einer erweiterten Finite-Volumen Diskretisierungsmethode. DLR-FB 89-38, 1989.

[13] Jameson, A., Schmidt, W., Turkel, E.: Numerical Solutions of the Euler Equations by Finite Volume Methods Using Runge-Kutta Time-Stepping Schemes. AIAA-81-1259, 1981.

[14] Martinelli, L., Jameson, A.: Validation of a Multigrid Method for the Reynolds-Averaged Navier Stokes Equations. AIAA-88-0414, 1988.

[15] Jameson, A.: A Vertex Based Multigrid Algorithm for Three-Dimensional Compressible Flow Calculations. In: "Numerical Methods for Compressible Flows - Finite Difference, Element and Volume Techniques". Ed. by T.E. Tezduar, T.J.R. Hughes, 1986.

[16] Rossow, C.-C.: Efficient Computation of Inviscid Flow Fields around Complex Configurations Using a Multi-Block Multigrid Method. Fifth Copper Mountain Conference on Multigrid Methods, Colorado, USA, 1991.

[17] Mavripilis, D.; Jameson, A.: Multigrid Solution of the Two-Dimensional Euler Equations on Unstructured Triangular Meshes. AIAA-87-0353, 1987.

[18] Mavripilis, D.J., Jameson, A., Martinelli, L.: Multigrid Solution of the Navier-Stokes Equations on Triangular Meshes. AIAA-89-0120, 1989.

[19] Dimier, A., Ronzheimer, A.: Solution of the Euler Equations on Unstructured and Adaptive Meshes. DLR-IB 129-90/40, 1990.

[20] Bailey, R.H.: A Multigrid Algorithm for the Solution of the Navier-Stokes Equations on Unstructured Meshes for Laminar Flows. DLR-IB 129-92/19, 1992.

[21] Arnst, G.: Berechnung von Profilumströmungen und Vergleich mit Messungen. Studienarbeit Nr. 89-2, TU Braunschweig, 1989.

[22] Harris, C.D.: Two-Dimensional Aerodynamic Characteristics of the NACA 0012 Airfoil in the Langley 8-Foot Transonic Pressure Tunnel. NASA-TM-81927, 1981.

[23] Redeker, G., Müller, R., Ashill, P.R., Elsenaar, A., Schmidt. V.: Experiments on the DFVLR-F4 Wing-body Configuration in Several European Wind-Tunnels. AGARD-FDP, P.2, Symposium Naples, 1987.

[24] Kays, W.M.: Heat Transfer to the Transpired Boundary Layer. Journal of Fluid Mechanics, Vol. 30, pp. 741-773, 1967.

[25] Ronzheimer, A.: Lösung der zweidimensionalen Euler-Gleichungen durch eine Finite Volumen Diskretisierung auf unstrukturiertem Netz. DFVLR FB-88-34, 1988.

[26] Baker, T.J.: A Three-Dimensional Mesh Generation by Triangulation of Arbitrary Point Sets. AIAA-87-1124, 1987.

7. Figures

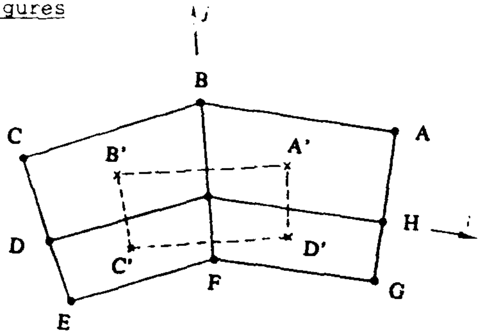

Fig. 1a Control volume in structured code.

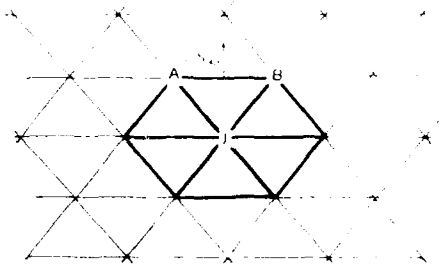

Fig. 1b Control volume in unstructured code.

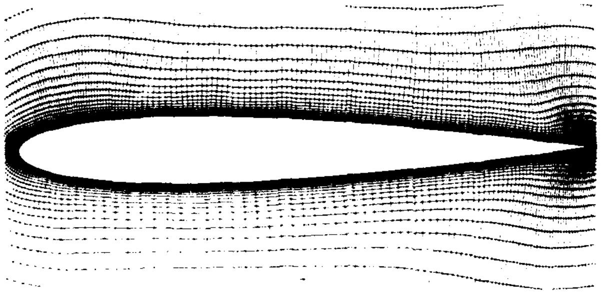

Fig. 2 Structured grid around NACA 0012 airfoil, grid 384 x 64

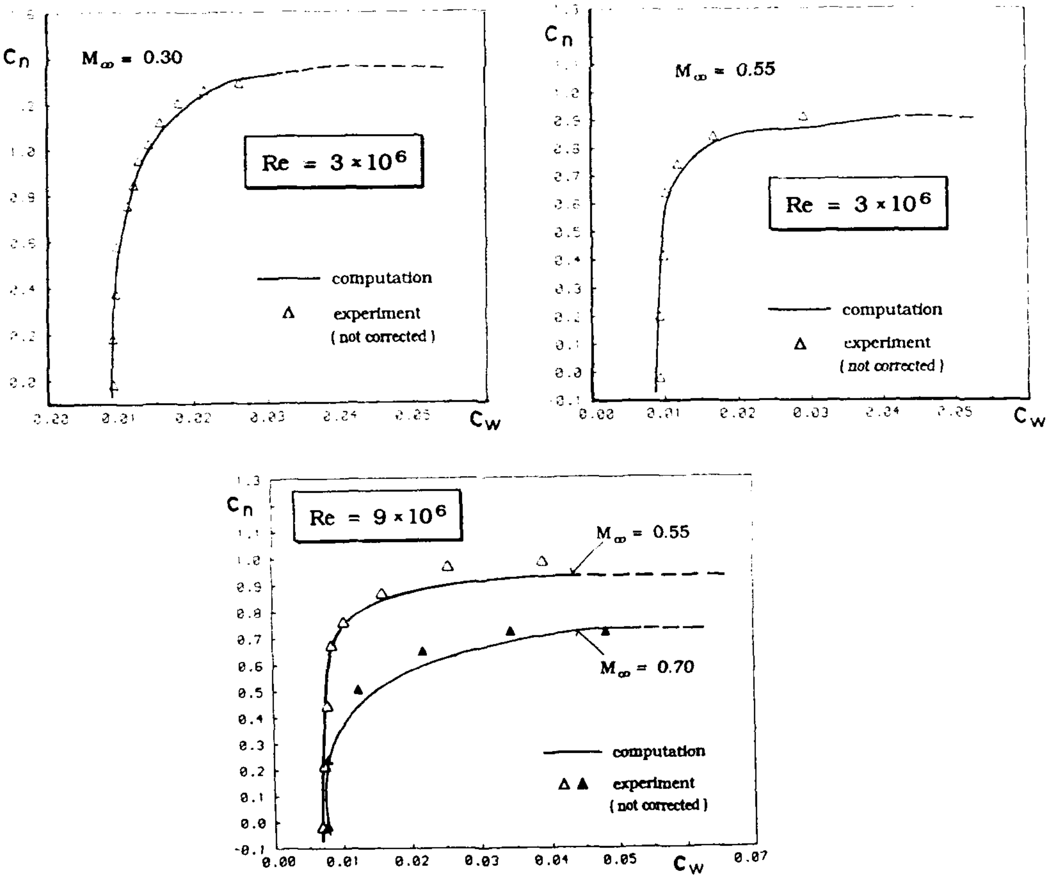

Fig. 3 Drag polar for NACA 0012 airfoil.

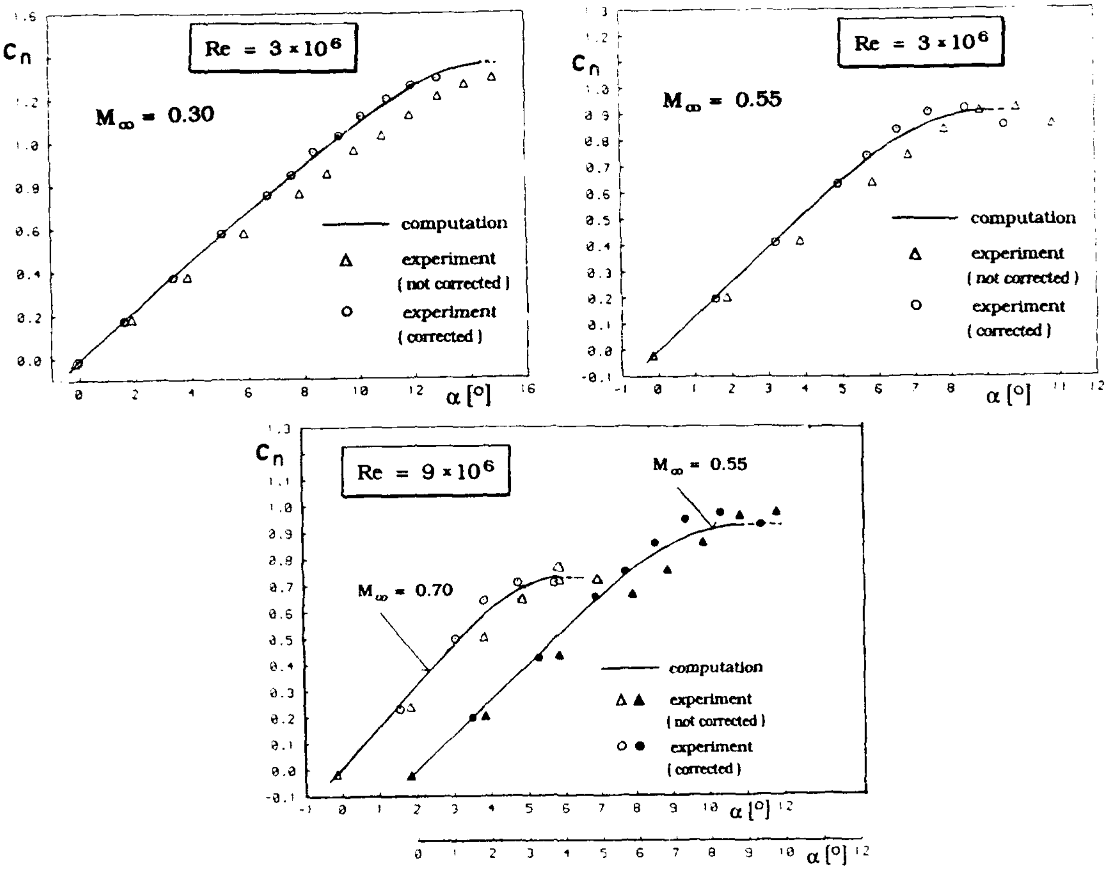

Fig. 4 Normal force coefficient versus angle of attack for NACA 0012 airfoil.

Fig. 5 Convergence history for NACA 0012 airfoil.

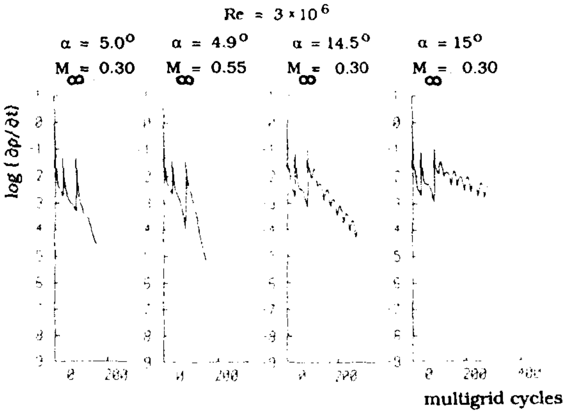

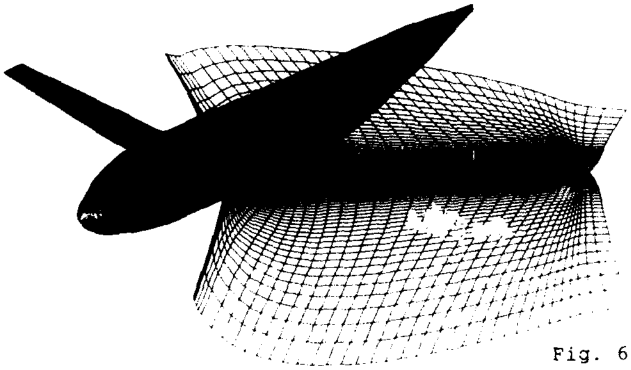

Fig. 6 DLR-F4 wing-body configuration.

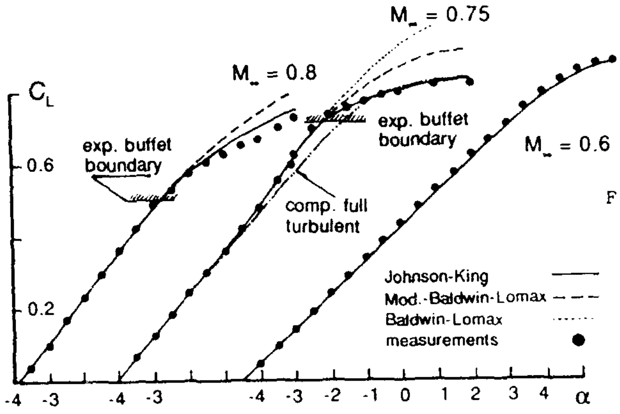

Fig. 7 Total lift coefficient versus angle of attack for DLR-F4 wing-body configuration.

Fig. 8 Drag polar for DLR-F4 wing-body configuration.

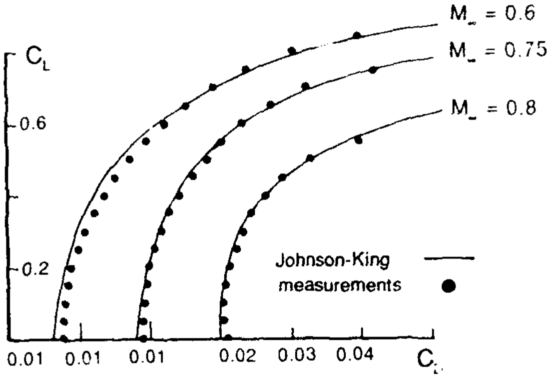

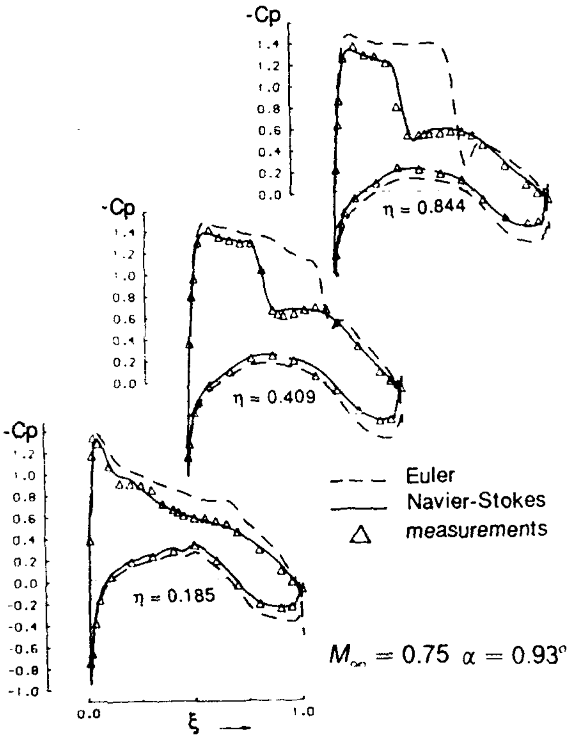

Fig. 9 C_p-distribution at three different spanwise sections. DLR-F4 wing-body configuration.

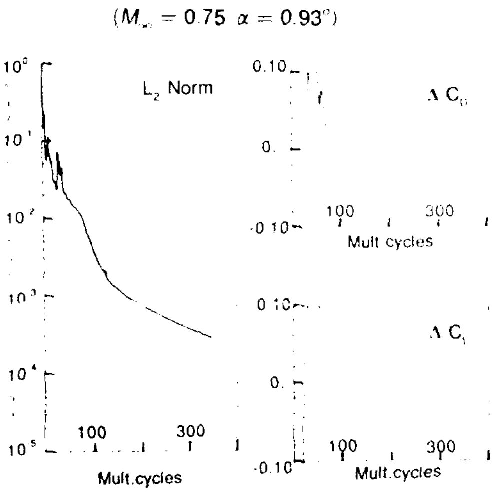

Fig. 10 Convergence history for DLR-F4 wing-body configuration.

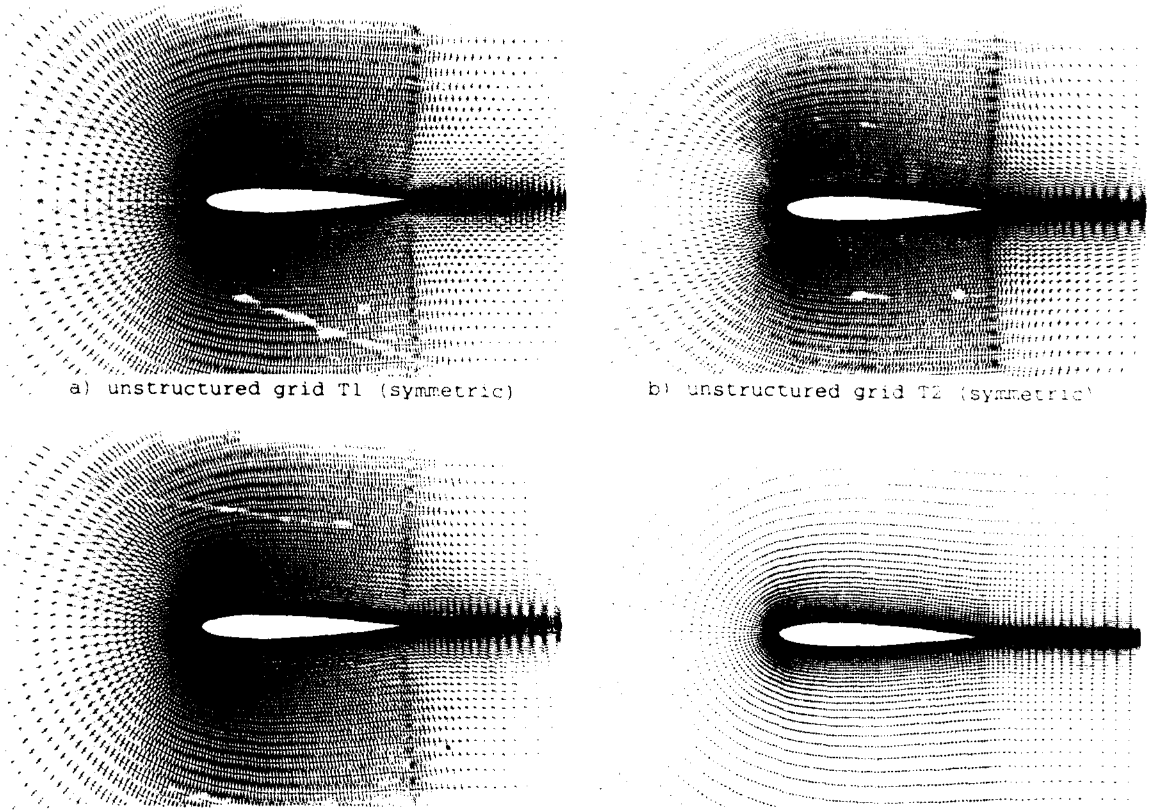

a) unstructured grid T1 (symmetric)

b) unstructured grid T2 (symmetric)

c) unstructured grid T3 (unsymmetric)

d) structured grid, 192 x 64 points

Fig. 11 Unstructured and structured grids around NACA 0012 airfoil.

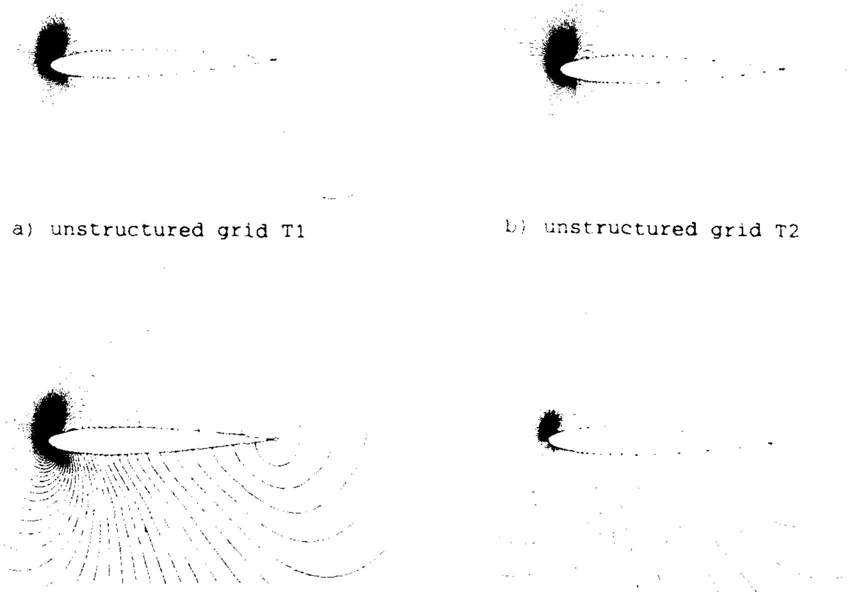

a) unstructured grid T1

b) unstructured grid T2

c) unstructured grid T3

d) structured grid

Fig. 12 Comparison of isobar contours for NACA 002 airfoil, Re = 500, $M_\infty = 0.8$, $\alpha = 10°$.

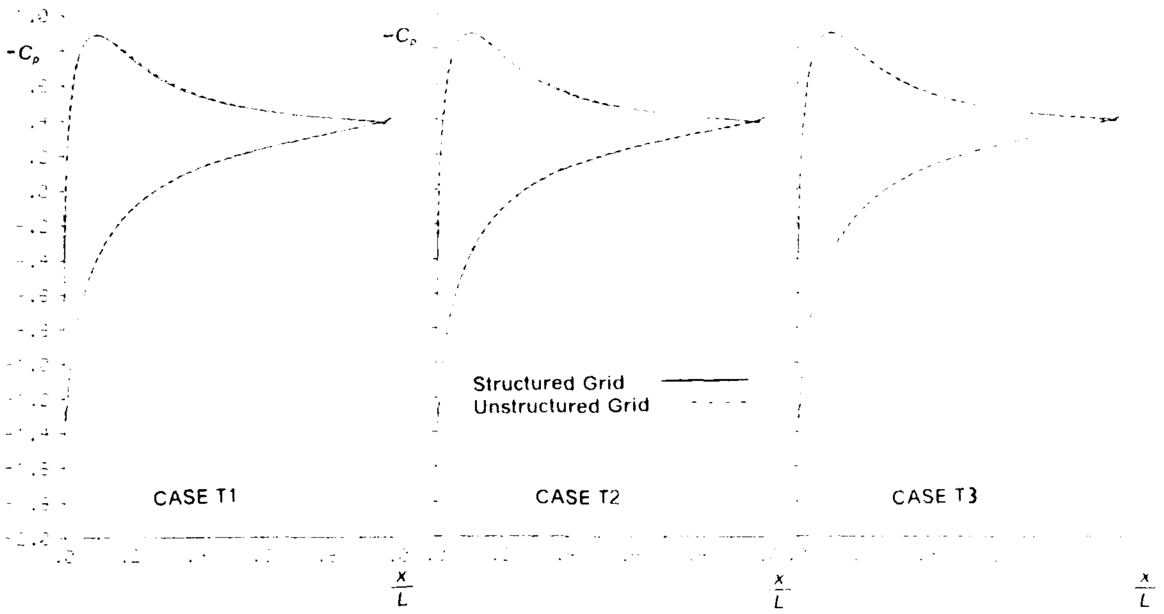

Fig. 13 Comparison of predicted surface pressure coefficients for NACA 0012 airfoil, Re = 500, M_∞ = 0.8, α = 10°.

	C_l	C_{d_p}
Grid T1	0.44822	0.14431
Grid T2	0.44881	0.14658
Grid T3	0.45057	0.14665
Structured Grid	0.44691	0.14312

Table 1 Comparison of predicted total lift and pressure drag coefficients for various grids, NACA 0012 airfoil, Re = 500, M_∞ = 0.8, α = 10°.

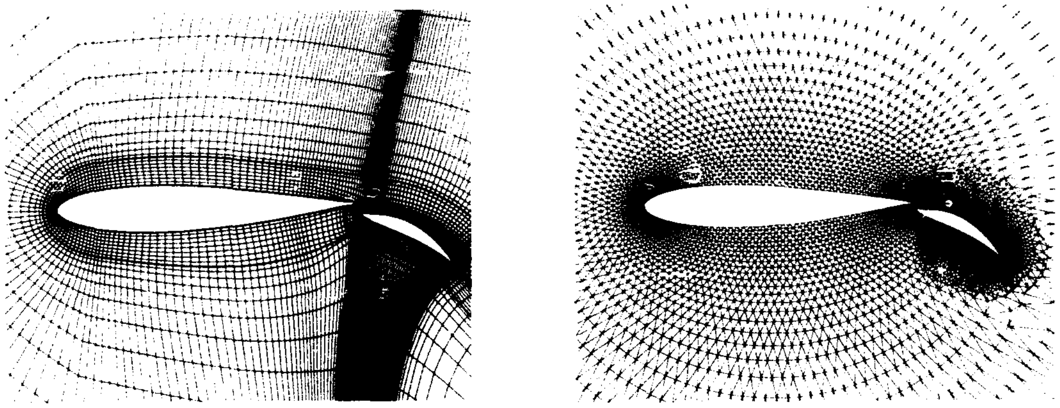

a) structured grid

b) unstructured grid

Fig. 14 Structured and unstructured grid around Karman-Trefftz airfoil with flap.

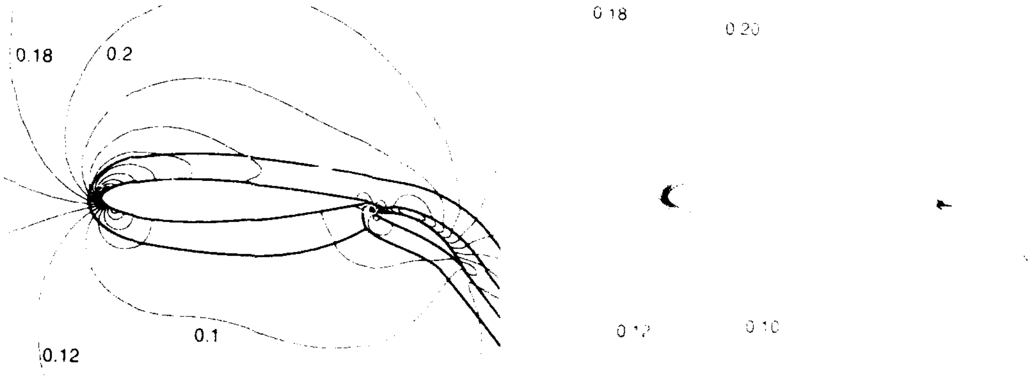

a) structured grid b) unstructured grid

Fig. 15 Iso-Mach contours for Karman-Trefftz airfoil. $M_\infty = 0.15$, $\alpha = 0°$, $\Delta M = 0.02$.

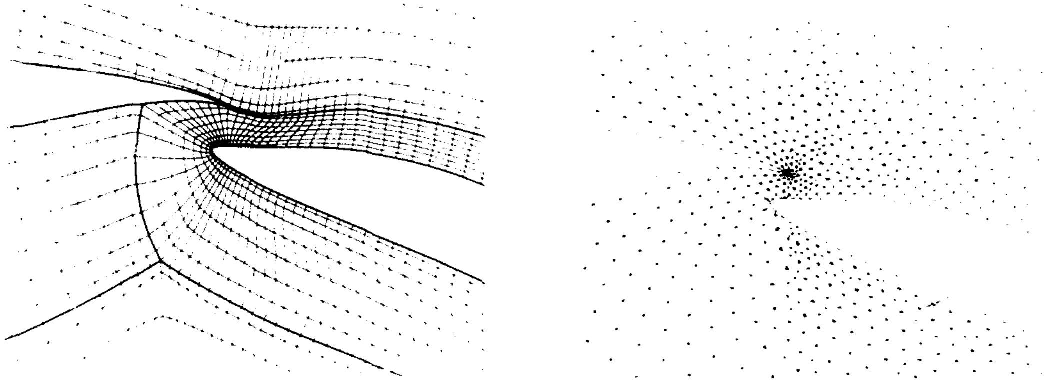

a) structured grid b) unstructured grid

Fig. 16 Enlarged view of structured and unstructured grid around Karman-Trefftz airfoil at flap region.

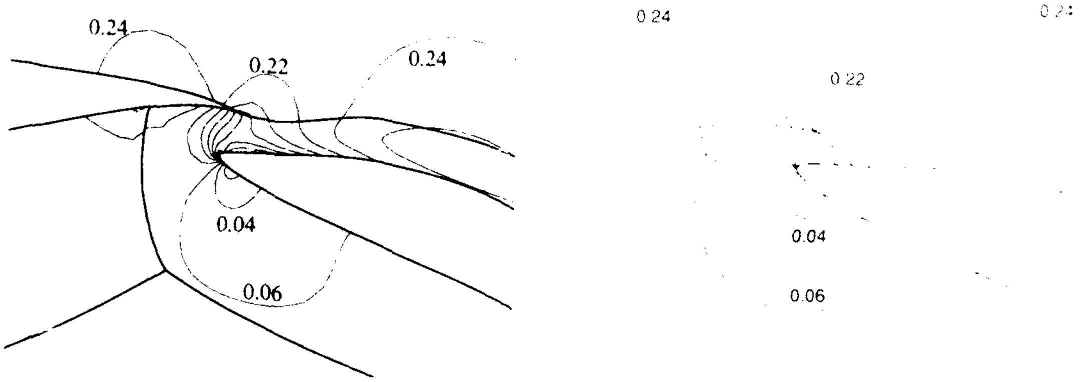

a) structured grid b) unstructured grid

Fig. 17 Iso-Mach lines for Karman-Trefftz airfoil at flap region, $M_\infty = 0.15$, $\alpha = 0°$, $\Delta M = 0.02$.

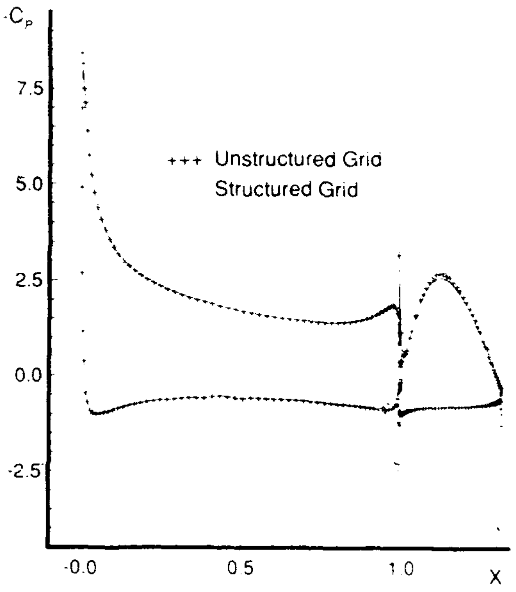

Fig. 18 Comparison of surface pressure distribution for Karman-Trefftz airfoil with flap, M_∞ 0.15, α [illegible]

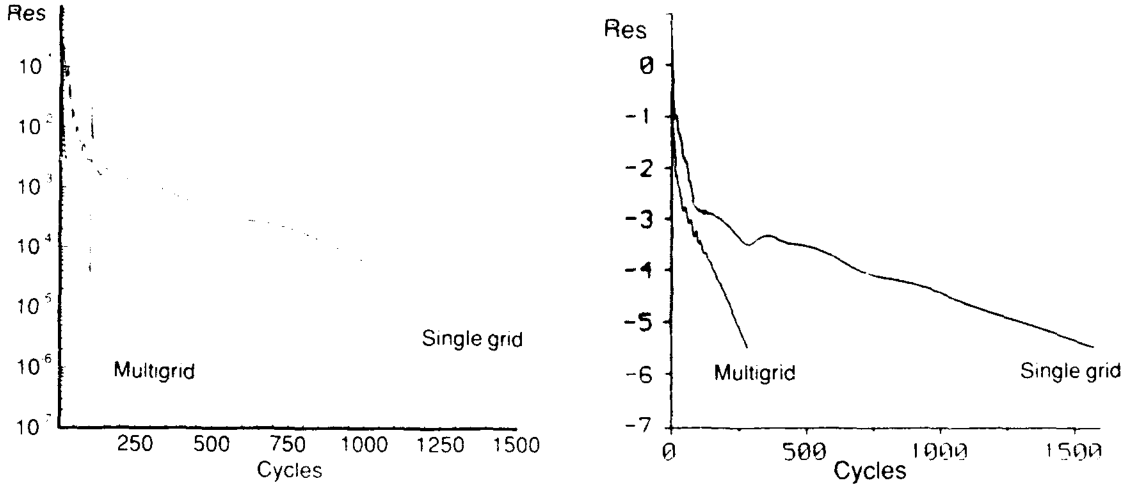

a) structured method

b) unstructured method

Fig. 19 Convergence histories for Karman-Trefftz airfoil with and without multigrid acceleration.

NAVIER-STOKES SIMULATION OF FLOW FIELD AROUND A BLOWN-FLAP HIGH-LIFT SYSTEM

by

R. Chow*, **K. Chu** and **G. Carpenter****
Corporate Research Center
Grumman Corporation
Mail Stop A08-35
Bethpage, NY 11714-3580
United States

SUMMARY

Solution of the Reynolds averaged Navier-Stokes equations is obtained to simulate the flow field around a 13% thickness super-critical airfoil slat/blown-flap high-lift system. A stacked-C mesh topology is used in conjunction with the slat and the flap trailing edge streamlines and adapted to accurately locate the strong viscous flow regions. A previously modified PARC2D implicit ADI solver is employed whereby the multiply connected boundary value problem can be treated with a single computation zone. A modelled injection boundary condition was demonstrated to connect transient flap wake vortices downstream of the computational domain. The converged surface pressures and the values of the lift coefficient are compared with the wind tunnel data at M_∞ = 0.17, Re = 3.4 M for momentum injection coefficients of $\overline{C_\mu}$ = 0.01 and $\overline{C_\mu}$ = 0.04, respectively.

1. INTRODUCTION

The development of analytic and numerical techniques is important for the design and analysis of a high-lift system. An accurate and dependable method to compute the lift can complement the laborious and expensive experimental test process to achieve a desirable configuration. Interactive methods employing an inviscid solution, coupled with a confluent boundary layer analysis, have been used for some time to compute the high-lift flow field. A long list of references using this approach can be found, for example, in the recent review article of Brune and McMasters (Ref 1). These methods, with often elaborate modelling of the boundary layer interactions, are based on the assumption that the upstream influence of the flow field is transmitted through the inviscid process. When viscous effects are small and when flow separation is limited to confined regions (i.e., shallow separation bubbles), these calculations show reasonable results that are primarily corrections of boundary layer and wake effects applied to an inviscid pressure field. These codes are fast and easy to run, and, when used conservatively and judiciously, they can function reasonably well in the traditional "evolutional" high-lift design procedure to complement an experimental intensive process. In most of these cases, the data of the base line design are well in hand and the new designs never deviate far from the original optimal ones, where, as had been pointed out by Dillner et al. (Ref 2), strong boundary layer confluency conditions rarely exist. A two-dimensional, inviscid-boundary-layer, interactive multi-element airfoil method has also been used in the high-lift wing modification study for an existing aircraft (Ref 3). More recently, interactive codes were used successfully to validate the high-lift flight test data of a civilian transport aircraft (Ref 4). In the absence of large flow separation, the study demonstrated that at near-design conditions, the interactive codes can be fine-tuned to study laminar to turbulent transition, incipient flow separation, and other boundary layer related effects at the flight Reynolds number. This knowledge is valuable for correlation and interpretation of the high-lift wind tunnel data used in the design. When the best possible high-lift configuration for a new wing is sought, wind tunnel matrix tests for the gap-overlap optimization between the high-lift elements are often pursued. While this approach is reliable in obtaining information on the best $C_{L_{MAX}}$ gain, without understanding the flow physics and their implications to the data, the process is not cost effective in that an isolated set of test results for a particular wing can not readily be made useful for another design. In general, the flow fields under these test conditions are very complicated. In most cases, they are dominated by viscous effects resulting from boundary layer confluency that can not be modelled accurately by the inviscid-boundary-layer interaction method; flow separation is a common feature and can even occur in the linear range of a lift curve.

The conditions under which a Navier-Stokes solution method is needed can be demonstrated in the following example of a pair of wind tunnel tests of a three-element airfoil high-lift system (Ref 5). The configuration shown in Fig. 1a consists of a 13% thickness supercritical airfoil with a 20% chord slat having -25 deg of extension, and a 30% chord single-slotted flap with main element/flap gap and overlap sizes, both at 2% chord. Shown in Fig. 1a are curves of C_L vs α and in Fig. 1b and Fig. 1c are pressure data collected at flap angles of δ_f = 20 deg and δ_f = 40 deg, respectively, at a nominal test Mach number of 0.17 and a chord Reynolds number of 3.4 million. Turbulent flow conditions were established over the entire high-lift system. In the linear range, C_L for the δ_f = 40 deg case is seen to be higher than for δ_f = 20 deg. The sudden changes of slope of the lift curve at δ_f = 40 deg also suggest that different flow interactions are involved as the angle of attack increases. In each case (Fig. 1b and 1c), the smooth portions of the curves on the main foil indicate the range where pressure is determined primarily by inviscid processes. The apparent change of slopes and the inflection points at the rear portion of the wing box show the extent of the upstream influence due to the presence of the flap. For δ_f = 20 deg (Fig. 1b), the flow remains attached until the point just before the stall where flap separation occurs. The slope of the separation pressure curve at α = 18.36 deg also suggests that the separated region is represented by a thick viscous layer with sizable flow entrainment. The pressure patterns in this case are not unlike those on the elements of a typical multi-flap high-lift system of a civilian transport aircraft where the flap angles between the elements remain in the 15-25 deg range. The inviscid-boundary layer interactive methods such as the MCARF code (Ref 6, 7) or the Moses code (Ref 8, 9) can treat these cases adequately, with perhaps some inaccuracies near the $C_{L_{MAX}}$.

In an effort to reduce the complexity of the system, the single slotted flap configuration is preferred in the modern design approach. The flap angle is increased in an attempt to gain lift, which usually leads to a more complex flow

---

* Senior Staff Scientist   ** Staff Scientist

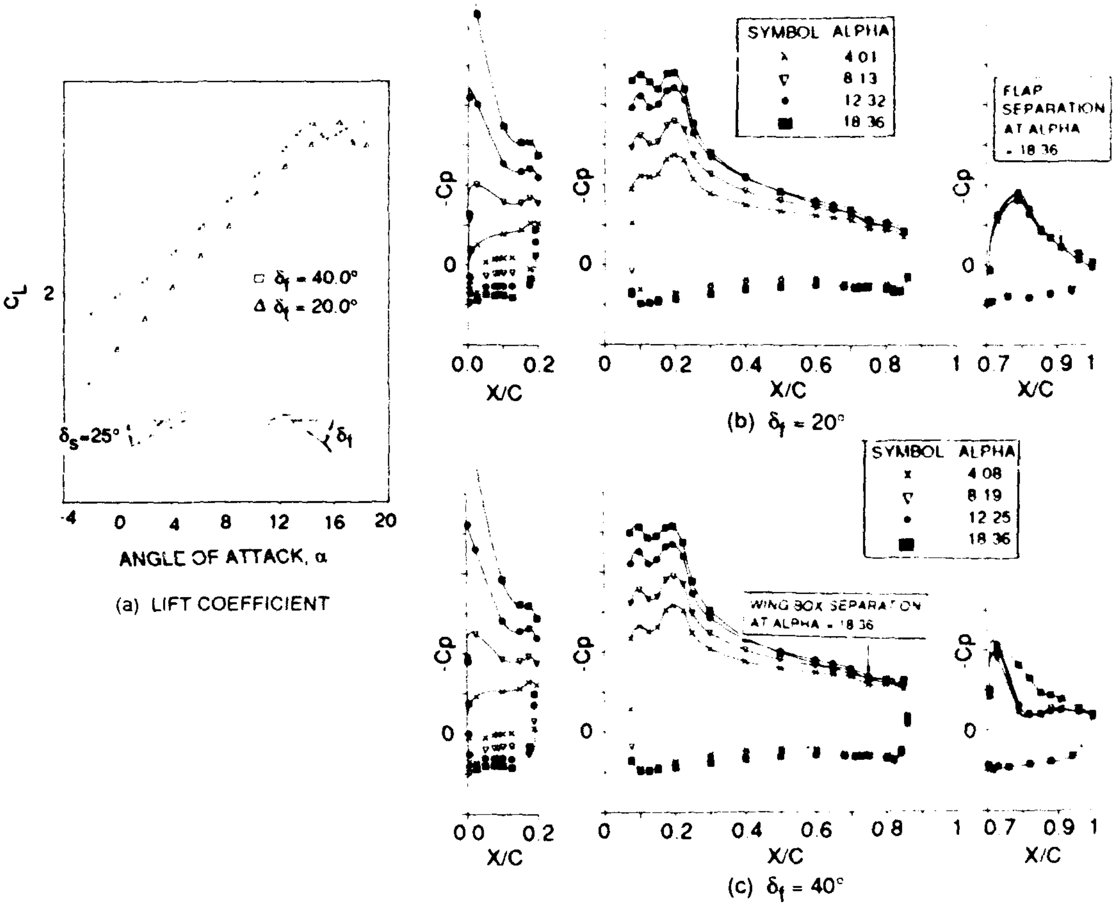

Fig. 1 Wind Tunnel Lift Coefficient Data & Surface Pressure Data for High-Lift System at Flap Extensions δ_f=20° & δ_f=40°, M=0.17, Re=3.4M

field. Fig. 1c, at a flap angle of δ_f = 40 deg, shows the pressure distribution from one such attempt. The flow field is dominated by massive flap separation even at very low angles of attack. The relatively small surface pressure gradient in the flap separated region suggests a general flow structure consisting of a mostly inviscid separated core region sandwiched between the flap boundary layer and a complex wake structure formed by the flow emanating from the main-foil cove region and the top surface main-foil boundary layer. As the angle of attack approaches $C_{L_{MAX}}$, this inviscid separated core structure begins to break up, forming a thick viscous separated region as indicated by the flap pressure slope change. The upstream influence of the wake flow field becomes so strong that the flow begins to separate on the main foil just before the stall point (see Fig. 1c). The variation of the lift coefficient in a range beyond the first C_L peak as seen in Fig. 1a suggests transitions of flow structures are occurring. The challenge of an analysis method is to accurately predict *a priori* these complicated flow fields so that meaningful trend studies can be made in the gap-overlap optimization investigations.

In Ref 9, we computed a solution in the linear range of the δ_f = 40 deg case, where massive flap separation was a dominating feature. A novel "stacked-C" mesh system was used to map the multi-element geometry into a single computation domain. The PARC2D code (Ref 10), modified exclusively for this application, was used as the flow solver. The trailing edges' streamlines and the flap separation line were adapted during iterations. This effectively reduced the mesh dependence of the solution.

Shown in Table 1 are the results of computations of C_L and C_D compared with experiment (Ref 5) for 2% and 5% chord flap gaps. It is seen that very good agreement was obtained at these angles of attack. More recently, converged solutions at higher angles of attack, approaching the $C_{L_{MAX}}$, were obtained. The results indicated, however, that a turbulence model more realistic than the algebraic one used in the PARC2D method is required in this high-angle-of-attack range to compute C_L accurately and the vortex breakup of the separated region.

In this paper, our methodology is employed to investigate solution of the Navier-Stokes equations for the flow field around a blown-flap high-lift system. It has been known (Ref 11) that lift augmentation can be achieved by properly placing a concentrated momentum jet in front of the trailing edge flap. The chordwise blowing utilizes the Coanda effect to attach a thin, high momentum sheet of fluid to the curved flap surface. The injected jet energizes the boundary layer and keeps the flow attached through large flap deflection angles; it increases wing circulation and entrains more of the freestream air, resulting in a significant increase in lift generated by the wing. The blown-flap experiment and the input data used in the present computational simulation are described briefly in the next section.

Table 1 Lift Coefficient & Drag Coefficient Comparison for Three-Element High Lift System, $M_\infty = 0.17$, Re = 3.4M

FLAP GAP SIZE	α	C_L (PRESENT)	C_L (EXP)	C_D (PRESENT)	C_D (EXP)
.02C	6.099	2.600	2.610	0.110	0.109
	8.189	2.865	2.890	0.115	0.116
.03C	6.07	2.355	2.480	0.112	0.123
	8.12	2.625	2.740	0.125	0.128
	10.15	2.900	3.010	0.135	0.136

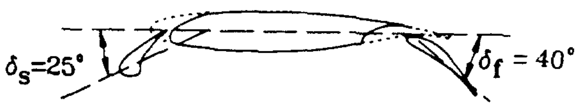

2. TWO-DIMENSIONAL BLOWN FLAP CONFIGURATION & SURFACE PRESSURE DATA

For the present Navier-Stokes numerical simulation, we have chosen a 2-D, three-element, blown-flap high-lift airfoil system as shown in Fig. 2. The wind tunnel test model used for surface pressure and force balance measurement is a two-dimensional wing panel with a two-foot chord, three-foot span, whose clean section is a 13% thickness supercritical airfoil. The high-lift experiment was part of a research program designed to explore the STOL capability of a carrier-based military aircraft (Ref 5). Extensive surface pressure and force measurements were made for various combinations of slat/conventional flap and slat/blown flap settings. For the present powered lift study, we utilize the configuration having a 20% chord slat with a -25 deg extension and a 23% chord blown flap with 43-deg extension. The wing box contains a plenum from which high pressure air was allowed to expand through a full span adjustable slot formed by the wing box upper skin and the flap upper surface. The blowing slot height can be varied by adjusting the flap position. The case we analyzed had a slot height gap of 0.006 in. Assuming an isentropic expansion to the freestream pressure p_∞, the momentum coefficient, C_μ, is given by:

$$C_\mu = \frac{\dot{m}V_j}{qc}, \tag{1}$$

where $\dot{m}$, the mass flow per unit span at the momentum slot, is given by

$$\dot{m} = \rho_j V_j h,$$

$$\text{and } \rho_j = \rho_o \left[p_\infty / P_o\right]^{1/2}, V_j = \left\{\left[\frac{2\gamma R T_o}{\gamma - 1}\right]\left[1 - \frac{p_\infty}{P_o}\right]^{\frac{\gamma-1}{\gamma}}\right\}^{1/2}.$$

ρ_O, P_O, and T_O are the plenum density, pressure, and temperature, respectively; q is the freestream dynamic pressure; and h and c are the momentum slot height and the chord length, respectively. The plenum conditions were calibrated with a given momentum slot height and maintained within certain tolerance during the measurement. The C_μ provided by the experiment was used to model the boundary condition for the present blown-flap

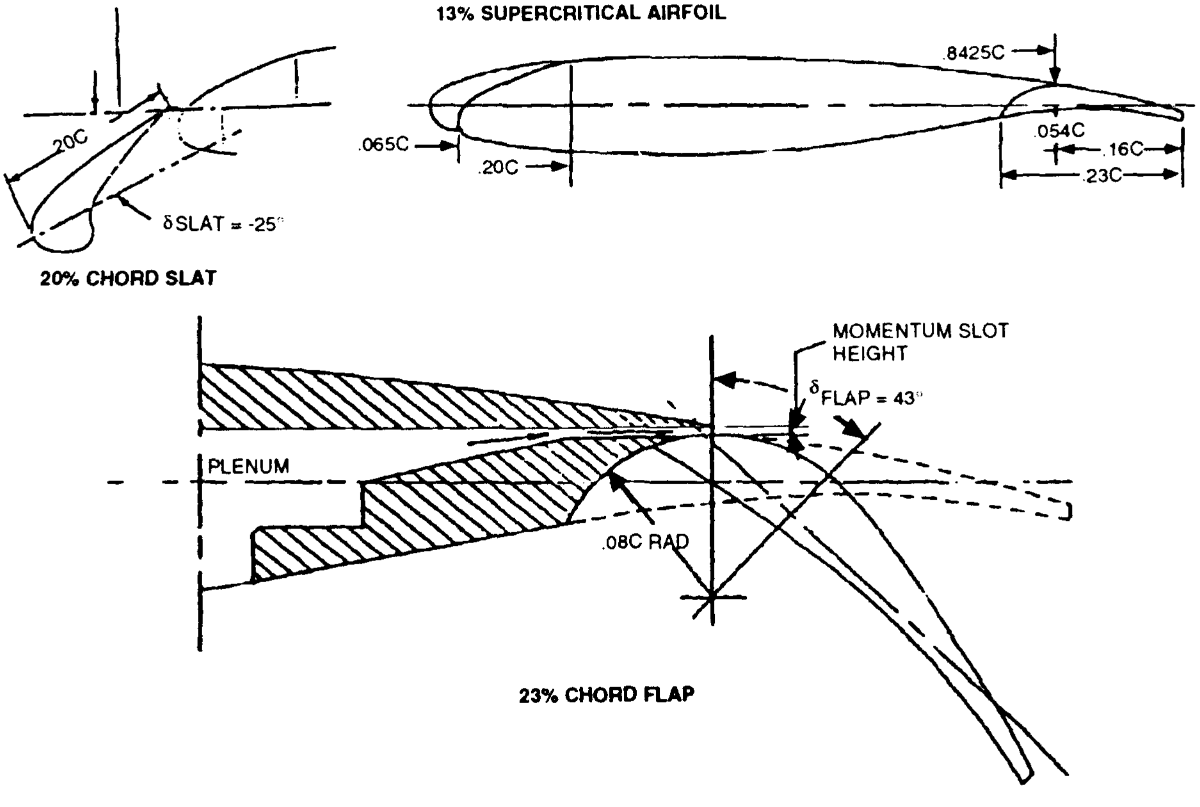

Fig. 2 Three-Element Blown Flap High-Lift System

computation. The wind tunnel conditions were the same as those used in Ref 9 to obtain the results of Table 1 with Mach number $M_\infty = 0.17$ and Reynolds number Re = 1.7M/ft. Turbulent flow was assumed. Details of the wind tunnel test setup can be found in Ref 5. Shown in Fig. 3 are examples of the surface pressures from the blown-flap experiment at an angle of attack $\alpha = 10.3$ deg and momentum coefficient values of $C_\mu = 0$ and $C_\mu = 0.012$, respectively.

3. COMPUTATION METHOD

Here, the solution procedure used in Ref. 9 for solving the Navier-Stokes equations for a standard 2-D multi-element airfoil system is extended to compute the flow over a blown-flap configuration as described above. In this computation scheme, a structured, stacked C-mesh is used whereby the physical trailing edge streamlines from the respective high-lift elements are employed to control automatically the mesh condensation for the solution accuracy required. In case flap separation occurs, the flap separation streamline can also be used to specially treat the separation zone (Ref 9). This step was not necessary in the present application. Shown in Figs. 4a and 4b are the stacked C-mesh system in the physical plane, with the boundary mesh distributions, and in the computation plane, respectively. The lines b_1d_1 and b_2d_2 in Fig. 4a are the adjacent coordinate lines corresponding to the slot trailing edge streamline. Similarly, the lines e_3c_3 and f_3d_3 are the wake cuts corresponding to the flap trailing edge streamline. Since the flap and the wing box are snugly fitted except for the momentum slot gap (see Fig. 2), they are treated as a single element. The point b_3 corresponds to the momentum slot injection location of the experiment.

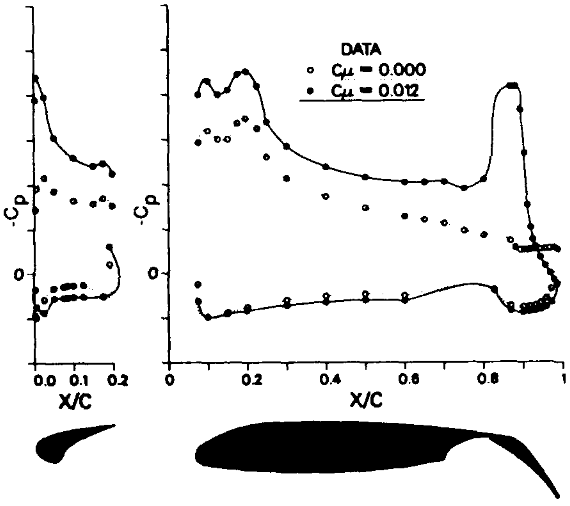

Fig. 3 Experimental Pressure Distribution for 13% Supercritical Airfoil Blown Flap System, $M_\infty = 0.17$, $\alpha = 10.3$ deg, Re = 3.4M

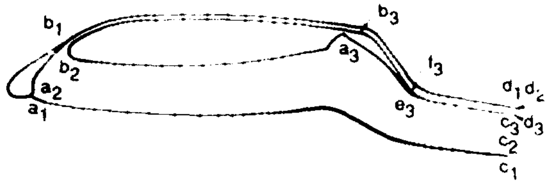

(a) SURFACE MESH DISTRIBUTION WITH SLAT & FLAP TRAILING EDGE STREAMLINES

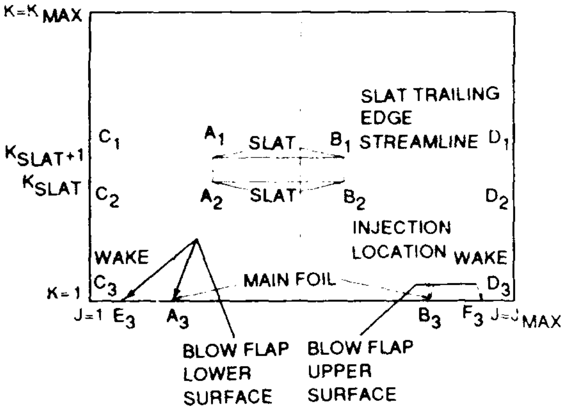

(b) COMPUTATION PLANE

Fig. 4 2-D Blown Flap System

The numerical solution for the Navier-Stokes equations is obtained using a single computation zone as shown in Fig. 4b. The flow solver is our modification of the implicit finite difference code PARC2D (Ref 9) The use of this code allows the boundary condition on the slat $A_1B_1B_2A_2$ to be prescribed directly. This unique feature allows multi-element high-lift airfoil systems to be treated conveniently with a single zone, thus avoiding the residual error control problems one usually has to monitor carefully in a multi-zone algorithm. This issue is particularly important in getting an accurate lift solution for the multi-element system. Our version of the PARC2D code for application to the high-life airfoil has the general efficiency of the NASA/Ames ARC2D code (Ref 12) as applied to a single-element airfoil calculation. However, due to the complexity of the flow field in a high-lift system, considerably more CPU time is required for a converged solution for C_L . The code uses an algebraic turbulence model loosely based on the Thomas formulation (Ref 13) of the Baldwin and Lomax model (Ref 14). Turbulent flow over the entire high-lift system was assumed in all the calculations made in the present work.

The experimental values of C_μ for the angle-of-attack survey chosen for our simulation had fluctuations of up to ± 20% from an average value of $C_\mu = 0.0107$. However, the experimental values of lift were not overly sensitive to these variations. We chose a nominal value of $\overline{C_\mu} = 0.01$ for the numerical computations (barred quantity denotes the values used in the computations). The actual experimental condition near the momentum slot exit could not be simulated easily without a controlled study of the internal flow through the gap and its interaction with the flow beyond the exit. We anticipated a fair amount of friction loss through the gap. Furthermore, the velocity distribution was expected to be different from that given by a constant value of V_j (Eq (1)) across the momentum slot gap. Without any additional knowledge, we chose the $\overline{C_\mu}$ value as the controlling magnitude to model the boundary condition in the flap. The dynamic injection pressure $\bar{\rho}_j\bar{V}_j^2$ can be computed from Eq (1) with a given $\overline{C_\mu}$. A distribution function $f(s)=\rho_j(s)\left[V_j(s)\right]^2/\bar{\rho}_j\bar{V}_j^2 \le 1$ (Fig. 5) was used for establishing the boundary condition along the

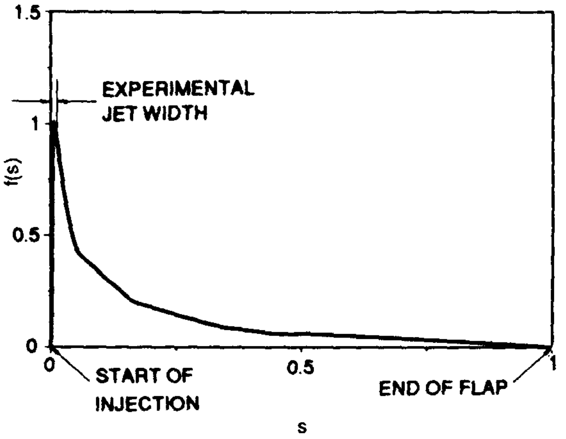

Fig. 5 Numerical Momentum Injection Distribution, $f(s)=\rho_j(s)\,[V_j(s)]^2/\bar{\rho}_j\bar{V}_j^2$

top flap surface, where s is the dimensionless running surface length measured from the experimental injection point to the flap trailing edge. The injection velocity $V_j(s)$ was assumed to be tangential to the flap surface, from which the surface velocity boundary conditions were determined. One could think of this procedure as modelling the complex local interaction by a thin shear layer across which the static pressure changes are assumed to be negligible. The function f(s) was determined through numerical experiment such that the local value was the minimum required to convect the flap vortices downstream. The effectiveness of the blowing is determined here by its elimination of the separation region on the flap. The method minimizes the details of the blowing simulation as well as provides a mechanism for convecting transient vortices downstream of the high-lift system. The validity of this approach is determined by the agreement of the calculated pressure distribution with the experimental measurements.

4. STACKED C-MESH GENERATION

The "stacked-C" computational mesh is generated interactively on a Silicon Graphics Iris-4D workstation using GRIDGEN (Ref 15), a three-dimensional, elliptic grid generation code developed by the U.S. Air Force. The process of developing the mesh begins with extracting from the database describing the slat-foil-flap geometry the input into GRIDGEN-2D, a member of the GRIDGEN family of codes used to develop two-dimensional surface grids. The grid strategy used for the high-lift multi-element airfoil is shown in Fig. 6, where the stacked C's are designated as the inner and the outer C-meshes. These divisions are usually referred to as blocks or zones for three-dimensional grids or as subfaces in GRIDGEN terminology. The combined C-mesh topology has a total of 48,521 grid points, with the normal grid index K ranging from 1 to 121 and the longitudinal index J varying from 1 to 401. One of the major challenges in developing the grid for this problem is specifying the point distributions along the subface boundaries such that grid orthogonality is met at the boundaries and grid skewness is globally minimized.

The inner subface is composed of 20,050 grid points with K=1,50 and J=1,401. The boundary for this subface with K=1 starts in the far field at J=1 and follows the anticipated flap trailing edge streamline forward, where at J=27 it attaches to the underside trailing edge of the flap. The boundary continues along the flap and around the subface geometry, specifying the airfoil and the upper surface of the flap, and exits at the upper trailing edge with J=375. The boundary then proceeds along the same anticipated streamline paths as for the initial segment (J=1,27) to the far field but is displaced from the initial segment by the local grid stepsize. The outer boundary (K=50) for the inner subface proceeds from the far field along a path mimicking the shape of the lower wing-flap edge and provides a normal approach to the slat's lower leading edge at point a_2 shown in Fig. 7. The boundary then continues from J=117 along the bottom surface of the slat and exits at the trailing edge of the slat at point b_2 with J=241. The remainder of the boundary follows the anticipated slat trailing edge streamline passing over the top of the main foil and flap and out to the far field.

The outer subface shown in Fig. 6 is defined for K=51,121 and J=1,401, resulting in 28,471 grid points. The inner boundary (K=51) of this subface follows the same path shape as for K=50, but is displaced outward by the local grid stepsize, until it attaches to the slat at point a_1, where it then proceeds around the slat's upper leading edge. The boundary exits the upper slat trailing edge at J=241 and once again follows the slat trailing edge streamline path to the far field but is displaced by the local grid stepsize from K=50. The far field boundary for K=121 represents the C topology, extending four cord lengths forward and nine lengths behind the multielement airfoil.

The distribution of grid points along the individual boundary curves is critical for insuring grid quality based on orthogonality and skewness measures. GRIDGEN-2D provides features for easily controlling point clustering as illustrated in Fig. 7, where the point distributions in the J-direction along the lower section of the slat are set essentially uniform, due to the small flow gradients in the cove region as compared to nonlinear distributions along the leading edge. Here there is significant clustering near the anticipated stagnation point required to capture the pressure suction peak, followed by a thinning of points along the upper edge due to the fact that the same number of points must span the upper and lower edges of the slat. The distributions cluster again towards the trailing edge of the slat in order to blend with distributions selected in the slot region. Another area which required considerable clustering in the J-direction is shown in Fig. 6 in the region of the momentum injection slot (J=321,332).

The height of the inner subface over the top of the airfoil or the position of K=50 above the wing is 0.013 cord lengths while the first step size in the Navier-Stokes boundary layer is 0.0000063 cord lengths. This step size was

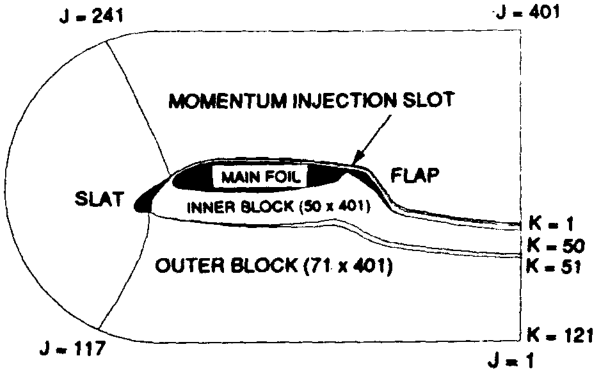

Fig. 6 Stacked C-Mesh Topology

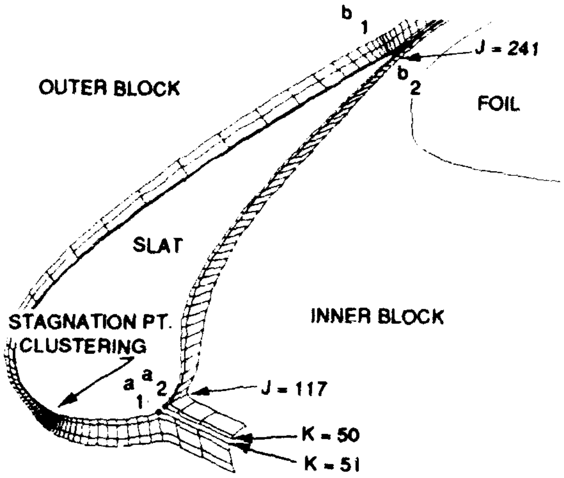

Fig. 7 Slat Geometry Specifies Block Boundaries

maintained along the upper edges and was increased to 0.00002 on average along the lower edges. With the edge clustering specified for both the inner and outer subfaces, the two-dimensional grids were generated first using the algebraic or trans-finite interpolation algorithm. Next a Laplace solver was used to eliminate grid crossings caused by the complex geometries, but it resulted in a grid where the K curves are pulled away from the surface geometry, resulting in poor orthogonality conditions. Grid quality was restored with the use of an elliptic solver using Thomas-Middlecoff control functions, with the resulting grid meshes for the inner and outer subfaces shown in Fig. 8. Details of the grid for exploded regions around the slat and flap regions are given in Fig. 9 and Fig. 10, respectively.

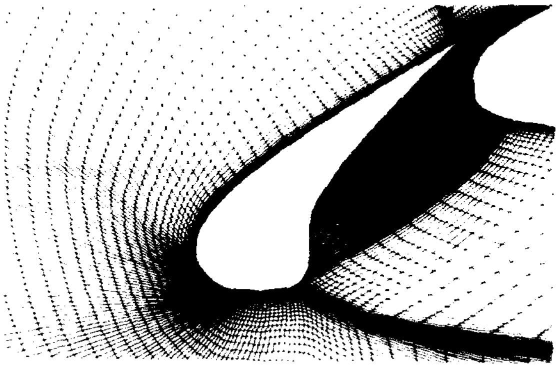

Fig. 9 Navier-Stokes Grid in Slat & Cove Region

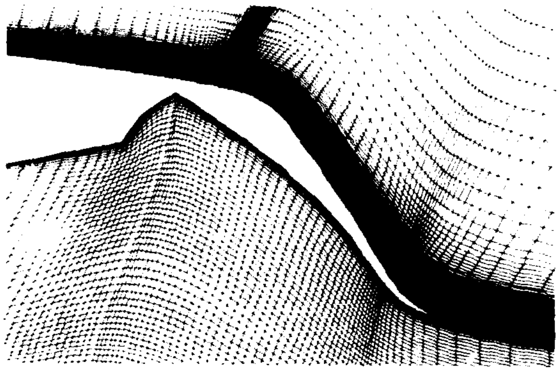

Fig. 10 Navier-Stokes Grid in Flap Region

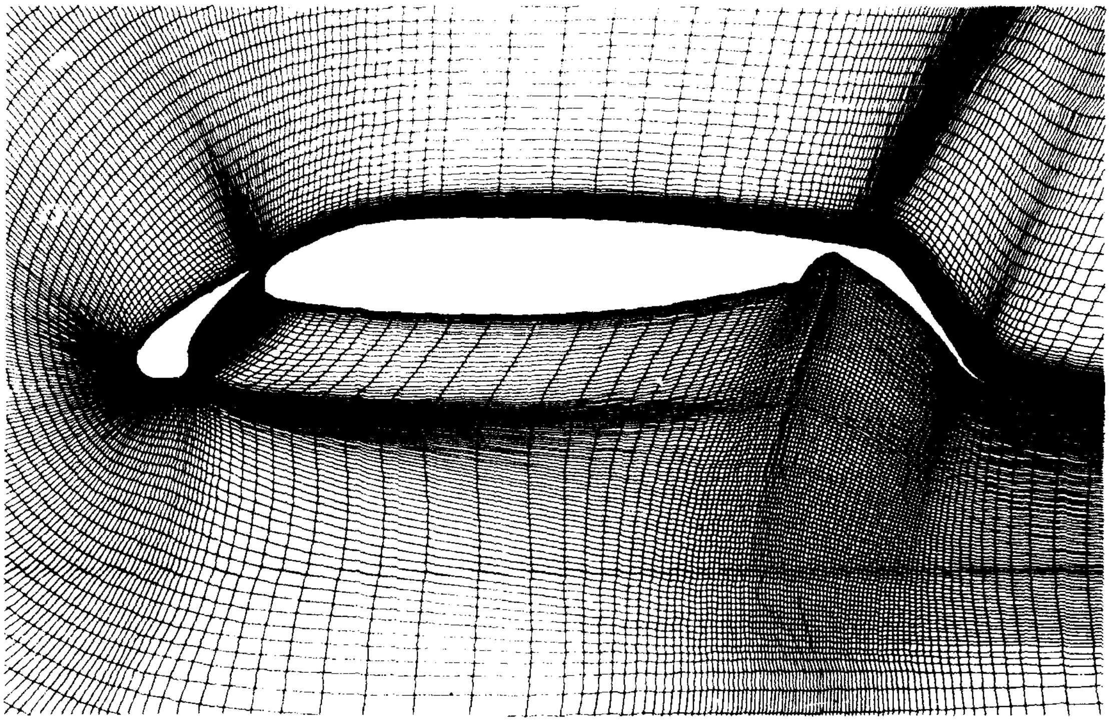

Fig. 8 Navier-Stokes Grid Around Multi-Element Airfoil

5. RESULTS & DISCUSSION

The experimental pressure distributions in Fig. 3 show that, without boundary layer control, the fluid cannot negotiate the large camber change at the flap and has separated. Thus the flap has lost its effectiveness in contributing to the lift. Data also indicated that the separation had also occurred at much lower angles of attack (not shown). It is seen that very little energy ($C_\mu = 0.012$) is required to achieve a dramatic change in the whole pressure field by shedding the vortices in the separated wake through using momentum injection. The local expansion has created a negative pressure peak and allows the flow to recompress gradually towards the trailing edge with a back-end surface pressure distribution similar to that of a typical rear-loaded airfoil. The injection also lowers the overall pressure levels on the top surfaces, including that of the slat, making the lift gain particularly effective.

For our calculation, we used a mesh with 401 cells in the streamwise direction and 121 cells in the normal direction. The Mach number, M_∞, was equal to 0.17 and the Reynolds number, Re, was 31.4×10^6. Turbulent flow condition was assumed over the entire high-lift system. The momentum coefficient, C_μ, unless otherwise mentioned was 0.01. The computation started with the standard procedure using a freestream initial condition with the surface boundary condition blended in gradually at the early cycles of the iteration. After about 5000 cycles, the flow established was largely separated even with the injection boundary condition already imposed. The time-sequenced results of the streamlines and the surface pressure solutions at an angle of attack, α, of 6.153 deg are shown in Fig. 11. We observe that, in Fig. 11a, the flow was largely separated at the mainfoil-flap juncture with the streamlines showing a slight hint of the effect of the injection. The shedding process continued as shown in Fig. 11b and 11c, and, finally in Fig. 11d, the vortical flow of the wake completely disappeared from the the flap surface. The surface pressure solution at this stage agreed very well with the experimental data except for a confined local overshoot of the result, reflecting the effect of the model of the injection boundary condition. The size of the separated cove region decreased as the flap separation was reduced. In Fig. 11a, we observe that the back-end separation had a blocking effect on the flow in the slat channel. This is a good example of the dominating nature of the back pressure for a separated high-lift flow condition. For completeness, the pressure isobars of the converged solution for this case are shown in Fig. 12, and the velocity vector field for the boundary layers on the top surfaces is shown in Fig. 13. Using the same procedure, four additional cases with angle of attack α = 2.051 deg, 10.300 deg, 14.370 deg, and 16.390 deg were computed. The computed lift coefficient, together with the force balance data and the value C_L obtained from integrating the experimental surface pressures, are shown in Fig. 14. As we mentioned, there were C_μ value fluctuations during the angle of attack survey, resulting in some scatterings of the integrated values of C_L, whereas computations were made with a $\overline{C_\mu}$ value of 0.01. The discrepancies between the force balance C_L's and those of the integrated pressure data values are somewhat puzzling and unresolved in Ref 5. One conjecture as to the cause of the differences might be an incorrect tunnel wall interference correction on the values of C_L from the force balance for the blown-flap experiments. The values of C_L from the numerical results compare well with the integrated pressure data in the linear range of the lift curve. There is some deterioration in the agreement at higher angles of attack near the $C_{L_{MAX}}$.

An additional calculation was made for a higher momentum coefficient $\overline{C_\mu} = 0.04$. The angle of attack, α, was equal to 6.195 deg. Again, the surface pressure results compare well with the data, as shown in Fig. 15. The isobars for this case are shown in Fig. 16. The streamlines are shown in Fig. 17. The converged numerical solution for C_L value was 4.22 as compared with the value from the integrated pressure data of 4.17.

6. CONCLUDING REMARKS

In the present paper, we have shown successful examples of a computation of a 2-D blown flap using the Navier-Stokes equations compared to experiment. This method can be employed to estimate the lift gain of the present type of a powered high-lift device. Since the boundary layers remain through a vortex shedding process, the simple algebraic shear-layer turbulence model used in the present calculations appears to be adequate for predicting the surface pressures. The present flow solver is very slow. It is highly desirable to develop a fast multi-grid algorithm for this type of application so that the methodology can be used as an effective engineering tool. Further sensitivity studies are required of the model of the injection boundary condition using a more carefully controlled experiment near the injection slot, which was not sufficiently provided by the present collected data.

7. ACKNOWLEDGMENT

We gratefully acknowledge the Engineering Flight Sciences Directorate of the Grumman Aircraft Systems Division for providing the wind tunnel data for the present investigation.

8. REFERENCES

1. Burne, G.W. and McMasters, J.H., "Computational Aerodynamics Applied to High-Lift Systems," Progress in Astronautics and Aeronautics, Vol. 125, Applied Computational Aerodynamics, P.A. Henne, ed., 1990, pp 389-433.

2. Dillner, B., May, F.W., and McMasters, J.H., "Aerodynamic Issues in the Design of High-Lift Systems for Transport Aircraft," AGARD CP-365, Paper 9, May 1984.

3. Waggoner, E.G., "Development of High-Lift Wing Modifications for an Advanced Capability EA-6B Aircraft," Progress in Astronautics and Aeronautics, Vol. 125, Applied Computational Aerodynamics, P.A. Henne, ed., 1990, pp 435-457.

4. Vijgen, P.M.H.W., Hardin, J.D., and Yip, L.P., "Flow Prediction over a Transport Multi-Element High-Lift System and Comparison with Flight Measurements," Aerodynamic Flows, California State University, Long Beach, January 13-15, 1992.

5 Laia, J.R., "Analysis and Test Report of 2-D Wind Tunnel Test of a 13% Super-critical Airfoil Section Fitted with Various Blown and Mechanical Flap High Lift System," Grumman Aerospace Corporation Report #XA128-900-2, July 1983.

6. Stevens, W.A., Goradia, S.H., and Braden, J.A., "Mathematical Model for Two-Dimensional Multi-Component Airfoils in Viscous Flows," NASA CR-1843, 1971.

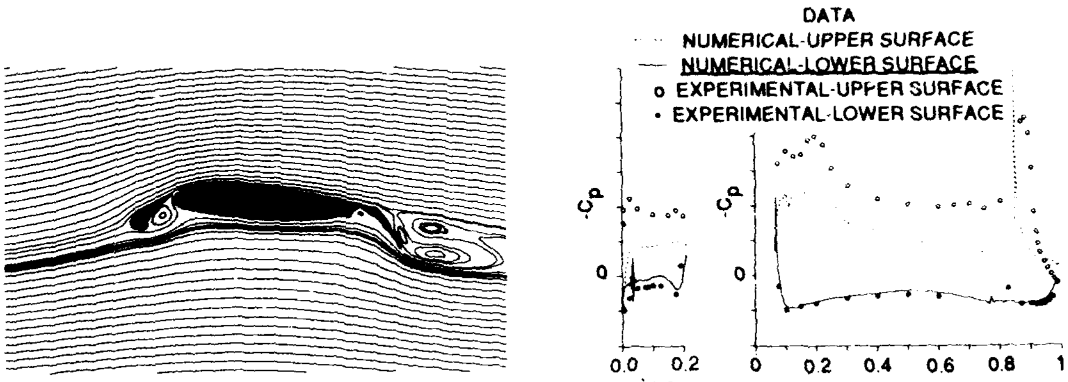

(a) 5 K CYCLES

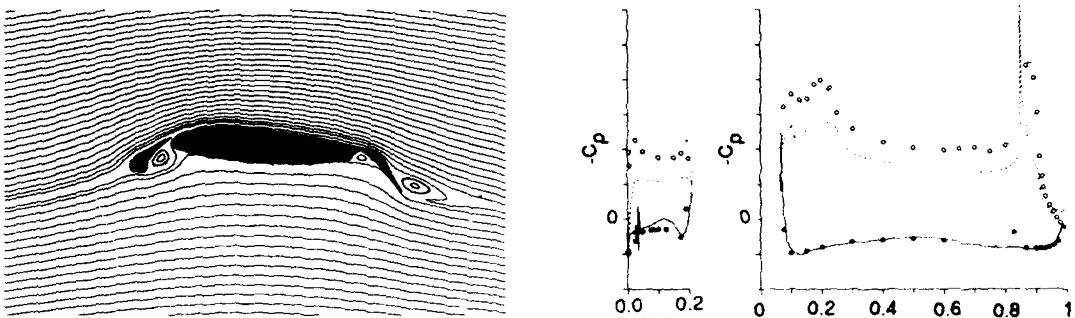

(b) 10 K CYCLES

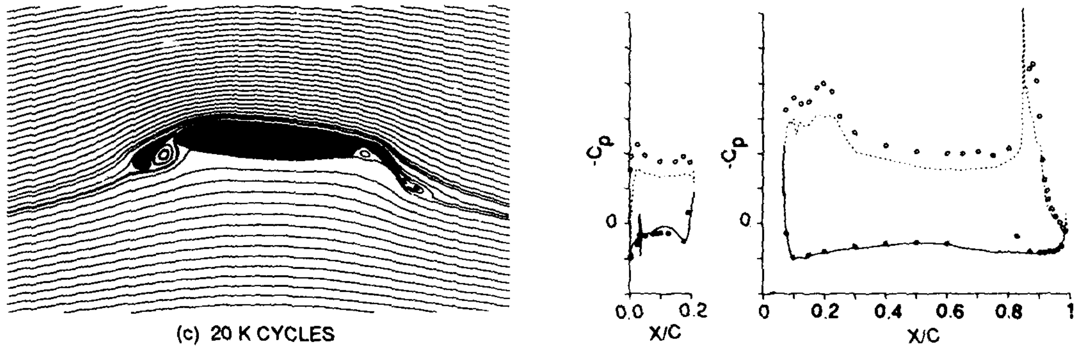

(c) 20 K CYCLES

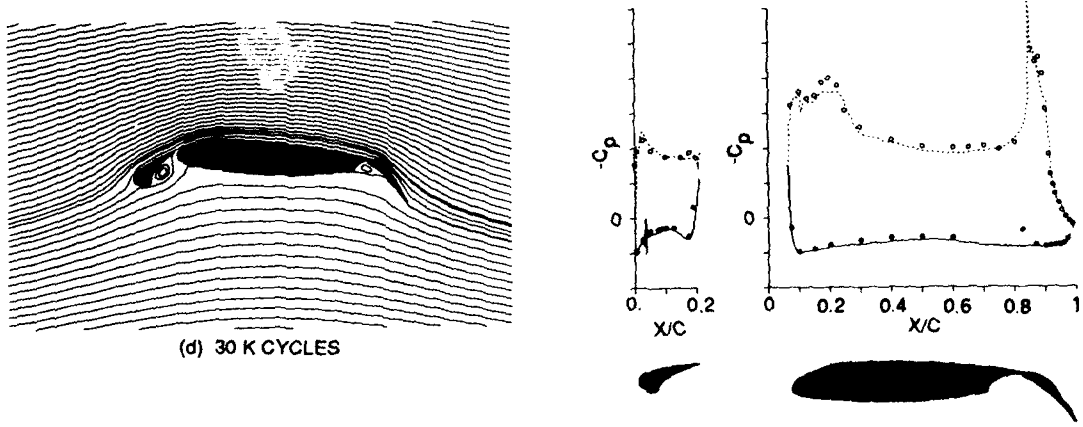

(d) 30 K CYCLES

Fig. 11 Time Sequenced Streamline Solution & Surface Pressure Solution
(M_∞=0.17, Re=3.4M, α=6.153°, $\overline{C}\mu$= 0.01)

7. Brune, G.W. and Manke, J.W., "An Improved Version of the NASA-Lockheed Multielement Airfoil Analysis Computer Program," NASA CR-145323, 1978.

8. Drela, M., "Newton Solution of Coupled Viscid/Inviscid Multi-Element Airfoil Flows," AIAA Paper 90-1470, June 1990.

9. Chow, R. and Chu, K., "Navier-Stokes Solution for High-Lift Multielement Airfoil System with Flap Separation," AIAA Pater 91-1623, June 1991.

10. Cooper, G.K., "The PARC Code Theory and Usage," Arnold Engineering Development Center Report AEDC-TR-98-24, October 1987.

11. Carr, J.E., "An Aerodynamic Comparison of Blown and Mechanical High Lift Airfoils," Proceedings of the Circulation-Control Workshop, NASA CP-2432, February 1986.

12. Pulliam, T.H., "Euler and Thin Layer Navier-Stokes Codes: ARC2D, ARC3D," Notes for Computational Fluid Dynamics User's Workshop, The University of Tennessee Space Institute, Tullahoma, TN, (UTSI Publication E02-4005-023-84), March 1984, pp 15.1-15.85.

13. Thomas, P.D., "Numerical Method for Predicting Flow Characteristics and Performance of Nonaxisymmetric Nozzles --Theory," NASA CR-3147, 1979.

14. Baldwin, B.S. and Lomax, H., "Thin Layer Approximation and Algebraic Model for Separated Turbulent Flows," AIAA Paper 78-257, January 1978.

15. Steinbrenner, J.P., Chawner, J.R., and Fouts, C.L., "The GRIDGEN 3D, Multiple Block Grid Generation System," WRDC-TR-90-3022, Vols. I & II, Wright Patterson Air Force Base, 1990.

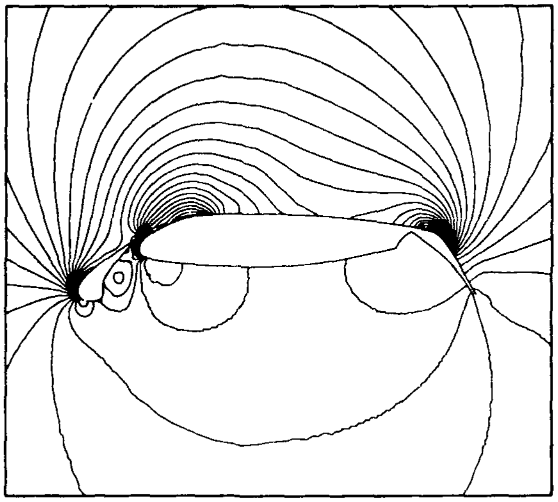

Fig. 12 Isobar Solution at M_∞=0.17, Re=3.4M, α=6.153°, $\bar{C}\mu$= 0.01

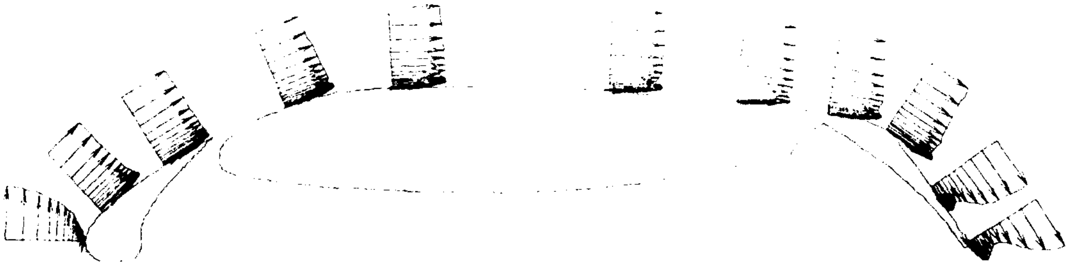

Fig. 13 Velocity Vector Field Solution on Top Surface (M_∞=0.17, Re=3.4M, α=6.153°, $\bar{C}\mu$=0.01)

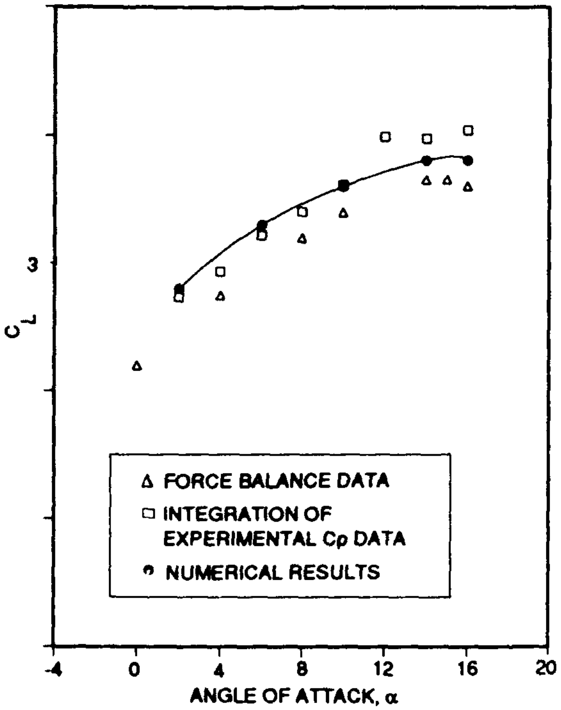

Fig. 14 Lift Coefficient Results as Compared with Tunnel Balance Data & Surface Pressure Data Integrated Values (M_∞=0.17, Re=3.4M, $\bar{C}\mu$=0.01)

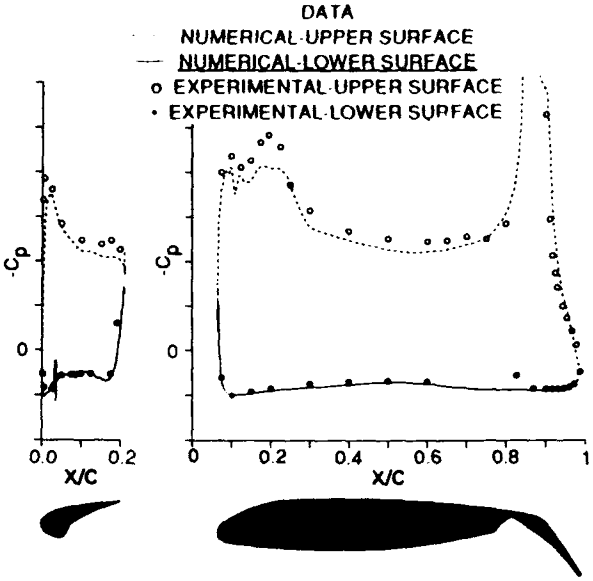

Fig. 15 Comparison of Surface Pressure Solution with Experimantal Data (M_∞ = 0.17, Re = 3.4M, α = 6.195°, $\overline{C\mu}$ = 0.04)

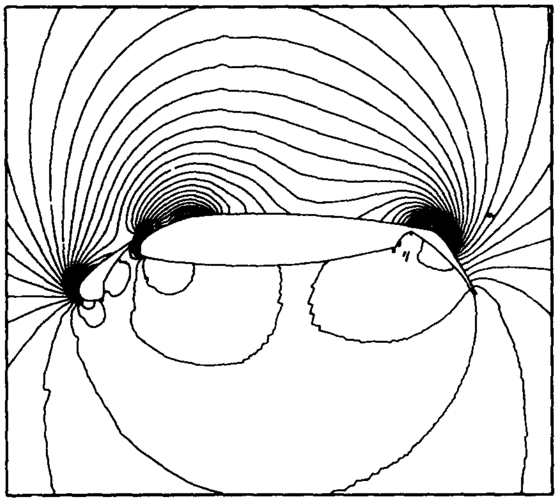

Fig. 16 Isobar Solution at M_∞=0.17, Re=3.4M, α=6.195°, $\overline{C\mu}$= 0.04

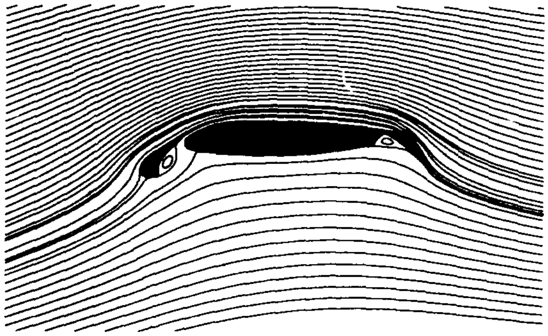

Fig. 17 Streamline Solution at M_∞=0.17, Re=3.4M, α=6.195°, $\overline{C\mu}$= 0.04

THE GARTEUR HIGH LIFT RESEARCH PROGRAMME

J.J. THIBERT
French GARTEUR Aeroresponsable
OFFICE NATIONAL D'ETUDES ET DE RECHERCHES AEROSPATIALES
ONERA - BP 72 - 92322 CHATILLON CEDEX FRANCE

SUMMARY

An extensive European wind tunnel research programme on high lift systems has been carried out in the past few years within the framework of a GARTEUR Action Group. To provide a relevant and realistic case, permission was given by British Aerospace to use a section from the A310 wing from which a 2D airfoil could be derived. A Deutsche Airbus 3D half model of the A310 aircraft has been used for the 3D test and an airfoil representative of the 59 % span section has been used for the 2D test. The wind tunnel test programme carried out in the major European low speed wind tunnels (ONERA F1 in France, NLR HST and LST in Netherlands, RAE 5 m in UK) was complemented by a full scale flight test supported by Airbus Industrie. A wide range of Reynolds numbers and Mach numbers has been covered by the test and a very comprehensive, well integrated and accurate body of data has been generated by this research programme. After presenting GARTEUR the paper deals with the Reynolds number and the Mach number effects as well as the correlations between 2D and 3D data and between wind tunnel and flight test results.

LIST OF SYMBOLS

AL	angle of attack
C	chord of retracted high lift system
C_D	total drag coefficient
C_{DW}	wake drag coefficient
C_f	skin friction coefficient
CFLTW	skin friction coefficient (Ludwing-Tillman)
C_L	total lift coefficient,
C_N	integrated normal force coefficient in wing-axis-system
C_{m25}	total moment coefficient, reference point 0.25
C_p	static presure coefficient
CW	chord of main wing
D1W	displacement thickness of B.L. and wake, based on wall pressure coefficient
KPI	pressure coefficient
M,Ma	freestream Mach number
M_L	local Mach number
Re,R	Reynolds number
Re_{59}	Reynolds number, based on retracted chord of the 59 % wing station
Re_c	Reynolds number, based on aerodynamic mean chord of half model. Reynolds number, based on retracted chord of 2D model
$\bar{R}$	attachment line Reynolds number
U, V	velocity components of 3D-B.L profile in streamline coordinate (U = streamwise component, V = crossflow component)
V	local total velocity of 3D-B.L. and wake profile
V_∞	total freestream velocity
X,Z	coordinate of the airfoil
Z	height of wake or B.L. probe
α	angle of attack
β	angle between x-axis and local total velocity of 3D-BL profile ; sideslip
δ_1	displacement thickness
η	wing station
ϕ	sweep angle

SUBSCRIPTS

c	based on retracted chord
C_{Nmax}	at maximum normal force coefficient
C_{Lmax}	at maximum lift coefficient
LE	leading edge
max	maximum
min	minimum
2D	2D flow
3D	3D flow
59	59 % wing station

1 INTRODUCTION

1.1. Garteur presentation

GARTEUR (Group for **A**eronautical **R**esearch and **T**echnology in **EUR**ope) was formed in 1973 by representatives of the Governmental departments responsable for aeronautical research in France, Germany and the United Kingdom. The Netherlands joined in 1977 and Sweden in 1991.

The GARTEUR community at the present time comprises more than 250 individuals from various research establishments, industrial companies and government authorities who actively participate in the organization.

According to its MoU, the mission of GARTEUR is to mobilize, for the mutual benefit of the GARTEUR member countries, their scientific and technical skills, human resources and facilities in the field of aeronautical research and technology for the following purposes :

- Strengthening collaboration between European countries with major research capabilities and government funded programmes.
- Continuously stimulating advances in the aeronautical sciences and pursuing topics of application-oriented research in order to maintain and strengthen the competitiveness of the European aerospace industry.
- Concentrating existing resources in an efficient manner and seeking to avoid duplication of work.
- Performing joint research work in fields suitable for collaboration and within research groups specifically established for this purpose.
- Identifying technology gaps and facility needs and recommending effective ways for the member countries to jointly overcome such shortcomings.
- Exchanging scientific and technical information.

GARTEUR is organized around three main elements (see fig. 1) :

- The GARTEUR Council, the governing body, assisted by the Executive Committee and the GARTEUR Secretary.
- The Groups of Responsables, the scientific management body and think-tank of GARTEUR.
- The Action Groups which constitute the technical expert body for programme formulation and the execution of the GARTEUR research work.

GARTEUR is an independent organization ; it has, however, no staff of its own or a common fund at its disposal. The necessary resources (staff, facilities, costs in kind) for the joint research activites are made available by the Governments of the member countries out of their national programmes, or by the participating organizations on the basis of balanced contributions.

Parallel to the formation of GARTEUR, on the industry side various collaboration arrangements between companies have been developed. When GARTEUR was formally established under the MoU in 1981, the airframe industries of the four GARTEUR countries replaced an earlier body with the Industry Group for Collaboration on Aeronautical Research and Technology in Europe (CARTE).

Representatives from Swedish industry joined CARTE in 1991.

CARTE is the formal communication link with GARTEUR and interfaces with the Executive Commitee (XC) on both policy and research matters. Relations with CARTE have also been established at other GARTEUR levels. Initially Points of Contact from industry were assigned to all Groups of Responsables, and in due course some of the industrial senior specialists themselves became Responsables. At Action Group level all CARTE companies are actively participating, and in some areas are supplemented by participants from the materials supply industry and other aerospace related companies.

GARTEUR has operated about 46 Action Groups since 1981, 25 of which have successfully finished their activities.

1.2. The High Lift Action Group programme

High levels of performance for transport aircraft high lift systems are mandatory since they play a crucial role for the payload/range of the aircraft and its noise characteristics. This has been recognized for a long time and the development of mechanical high lift systems during the past has provided practical systems which give good $C_{L_{max}}$ and L/D for today's aircraft. However the potential for further improving the performance of mechanical high lift devices is substantial but intensive efforts are required both in theoretical and experimental aerodynamics. Concerning the experimental aspect, the lack of high quality experimental data for 2D and 3D high lift configurations is one of the reasons that preclude the development of reliable and efficient theoretical methods for the design and the analysis of such complex configurations.

This is why GARTEUR decided in 1984 to set up an Action Group with the task of proposing and coordinating a major multinational research programme. Each of the four member countries FRANCE, GERMANY, THE NETHERLANDS and the UNITED KINGDOM, provided representatives both from their national research organizations as well as from their aircraft industries to contribute to this group. The Action Group therefore proposed a test programme with the following objectives :

- To study in 2D flow the Reynolds number and the Mach number effects on a selected high lift configuration.
- To study the same configuration in 3D flow.

- To study the effect of wing sweep on the transition location as a function of the Reynolds number.

- To correlate wind tunnel and flight test measurements.

To provide a relevant and realistic case, permission was given by British Aerospace to use a section from the A310 wing from which a 2D airfoil could be derived. In the period between 1985-1989, the Action Group carried out an extensive wind tunnel measurement programme on a 3D half model of the A310 aircraft and on the local sweep normalized 59 % span section in 2D flow. This wind tunnel programme was complemented by a full scale flight test programme supported by Airbus-Industrie (fig.2). This action Group AD (AG08) consists of members from ONERA, NLR, DRA, DLR, Aerospatiale, Fokker, BAe, Deutsche Airbus and Airbus-Industrie (fig.2).

2. MODELS AND TEST PROGRAMME

2.1. Models and instrumentation

The series of models used for high lift investigations of the GARTEUR AD (AG08) are :

2D model M1

2D model M3

half model M139

as shown in fig. 3. The A310 flight tests completed these tests.

The half model M139 consists of the left part of the complete MBB model M139, a 1 : 9.5 scale A310. The high lift system of the half model (Fig. 44) consists of :

- a Kruger flap in the wing root fairing

- a slat (divided in three parts) at the leading edge
- a double slotted flap (vane-flap) at the trailing edge of the inner wing and,

- a single slotted flap (Fowler flap) at the trailing edge of the outer wing.

The model is also equipped with an all speed aileron (ASA) in the engine region and a low speed aileron (LSA) on the outer wing. The 59 % wing station is located on slat 2 between slat tracks 6 and 7 and nearly in the middle of the Fowler flap.

The 2D model coordinates and settings are obtained from the A310 wing coordinates of the 59 % station using local sweep normalization process. The ordinates of the undeployed 2D section are given then by

$$(Z/C)_{2D}=(Z/C)_{3D}/\cos\phi_L(x/c)\ ,\ \delta_{2D}=\delta_{3D}/\cos\phi_L$$

where ϕ_L is the sweep of the undeployed constant x/c lines.

The programme proposed to investigate the following high lift configuration :

conf.1 Take-off configuration
conf.2 Landing configuration

The main emphasis of the research programme in the 2D and 3D tests is directed to the take-off configuration which has a well ordered flow and the landing configuration which has a separated flow on the flap. For the comparison with the corresponding 2D flow data 3D tests were performed with the half model without nacelle.

However to provide correspondence with flight tests which became a firm part later in the research programme, tests with a through-flow nacelle mounted under the wing of the half model were added for the take-off and landing configurations in the RAE-5M and ONERA F1 wind tunnels.

2.1.1. 2D Models M1 and M3

The model M1 was constructed and manufactured by DLR-Braunschweig and the instrumentation was partly carried out by DLR and completed by ONERA. The model M3 was manufactured and instrumented by NLR. The main dimensions of the model are :

	Model M1	Model M3	
		HST	LST
span (mm)	2000	2000	2250
chord (retracted) (mm)	900	400	400
aspect ratio	2.22	5	5.25

The chordwise instrumentation of models M1 and M3 is listed in fig.3 and briefly discussed below :

- *pressure taps*

  Both models have the following number of pressure taps : slat 35 taps, wing 60 taps, flap 35 taps. The diameter of the pressure holes was 0.3 mm.

- *Unsteady pressure transducers (Kulites)*

  Unsteady pressure was measured at 12 locations on the model M1 : 8 on the slat upper surface, two on the upper side of the wing nose and one on the wing shroud, one on the flap upper surface.

- *Skin friction device*

  Model M1 was equipped with 4 hot film gauges of 6 mm diameter and depth to measure skin friction : one at the slat t.e., one at the wing t.e. and two at the flap upper surface. Preston tubes with an outer diameter of 0.5 mm were mounted on the model surface to measure skin friction on model M3.

- *Boundary layer cove rakes*

  In the slat and wing cove small rakes were installed on the models M1 and M3 to measure total pressure in the separated flow region.

- *Internal boundary layer traversing mechanism*

  An internal traversing mechanism could be installed on the model M3 to measure the viscous flow at the slat [illegible] (station 1) and at the wing leading edge (station 2 x/c = 0.131).

- *Transition observation*

  Model M1 was equipped with a plastic strip of polyurethane resin on the upper surface of slat, wing and flap, to measure the laminar / turbulent transition location by infrared image technique.

2.1.2. Half Model M139

The half model M139 consists of the left wing of the existing MBB A310 - complete model M139 and of a new half fuselage manufactured by Deutsche Airbus/DLR. The main dimensions of the half model are

semi-wing reference area	1.2135 m²
semi span	2310 mm
aspect ratio	8.8
leading edge sweep	30.2°
sweep of 25%-chord	28.0°
trailing edge sweep	20.5°
aerodynamic mean chord c	614 mm
chord of 59 % wing station c_{59}	427 mm
fuselage diameter / length	594 / 4830 mm

The instrumentation of model is listed in fig. 3 and briefly discussed below :

- *pressure taps*

  In the high lift configuration 602 pressure holes with a diameter of 0.5 mm are fitted in 13 wing sections. 40 holes are located on the fuselage. The relevant 59 % wing station contains the following number of pressure taps : slat 16 taps, wing 30 taps, flap 15 taps.

- *hot film gauges*

  Three hot film gauges were glued at the slat hook : one at the 59 % wing station, one inboard and one outboard of the 59 % wing station.

- *razor blades*

  One razor-blade of 0.64 mm thickness on the flap at x/c = 0.895 and one of 0.44 mm thickness on the wing shroud at x/c = 0.7 were installed on the model at 59 % wing station to measure some skin friction values in the RAE-5M wind tunnel tests.

- *internal boundary layer traverse device*

  To measure the wing boundary layer at x/c = 0.5 of the 59 % wing station an internal boundary layer traverse device could be installed by mounting a special shroud on the main wing, the viscous shroud in Fig. 5. The internal boundary layer device, designed and built by ONERA was motorized allowing a survey height of 11 mm for the two three-hole probes that were 11 mm apart in order to obtain a total survey height of 22 mm.

2.2 Wind tunnel test programs

2.2.1. 2D Test Programs

NLR LST and HST Wind Tunnels

Extensive 2D tests with model M3 were first performed in the NLR LST and HST wind tunnels.

The model was installed vertically in the 2D test section of NLR LST wind tunnel between the two turntables in the ceiling and the floor, fig. 6. In order to determine wake drag of the wing section, a quadruple wake-rake was mounted horizontally in the tunnel with its tubes approximately one chord distance downstream of the trailing edge. An external boundary layer survey device was separately mounted on the tunnel floor.

In the NLR-HST wind tunnel the model M3 was mounted in the test section with the special 2D set-up, fig. 7. The wake was measured with a rake at a distance of 0.76 retracted chord downstream of the trailing edge. An external boundary layer traverse device, constructed on a special wind tunnel strut, was installed to measure with a dual probe the total and static pressure at the boundary layer stations.

The measurements in the NLR LST and HST wind tunnels consisted of pressure measurements, boundary layer and wake surveys and flow visualization within a Reynolds and Mach number range of $Re = 1.9 - 7.10^6$ and $M = 0.13 - 0.30$. In addition to the airfoil pressure distribution for a complete α-sweep up to stall, detailed flow investigations were carried out. These included :

- unsteady pressure measurements with Kulites at the slat nose and the main wing nose, and at the trailing edges of all three components,

- measurements of the extent of the separation bubbles in the slat and main wing coves with fixed rakes,

- skin friction measurements at the trailing edges of slat and main wing coves with Preston tubes,

- total wake surveys behind the airfoil for drag determination.

Flow visualization was carried out for the take-off and landing configurations to obtain information about flow separation and boundary layer transition, using oil flow and sublimation techniques. Boundary layer and wake surveys were carried out at 8 stations for the take-off configuration at $\alpha = 12°$ and 20°, and at 9 stations for the landing configuration at $\alpha = 12°$ and 21°, at $M = 0.22$ and $Re = 1.9.10^6$ (LST), $M = 0.22$ and $Re = 4.0.10^6$ (HST). In the HST, some extra surveys were performed at $Re = 1.9.10^6$ and $6.0.10^6$ for comparison with measurements in the LST and ONERA F1 wind tunnels respectively.

ONERA F1 Wind Tunnel

2D tests with the large 2D model M1 were carried out in the ONERA F1 wind tunnel. The model was mounted in the 2D test section, fig. 8. The external survey device was installed to measure the boundary layer profiles at the same station as on model M3 and the near wake (station 8) at $x/c = 1.06$ perpendicular to the flap chord. The far wake was measured with the same external survey device at a distance of 1.0 retracted chord perpendicular to the flap chord. The far wake was measured with the same external survey device at a distance of 1.0 retracted chord perpendicular to the wing reference chord, downstream of the trailing edge.

The measurements in the ONERA F1 wind tunnel included :

- pressure measurements as follows :

  - static pressure measurements on the element surfaces
  - unsteady pressure measurements with Kulites at the slat nose and the wing nose and at the trailing edge of all three elements
  - total pressure measurements in the slat and wing cove,

- boundary layer and wake surveys,

- skin friction measurements, and

- transition detection by thermography

for the take-off and landing configurations within a Reynolds and Mach number range of $Re = 6 - 16.4.10^6$ and $M = 0.13 - 0.30$. The boundary layer measurements were carried out at the corresponding stations for two angles of attack of $\alpha_1 = 12°$ and $\alpha_2 = 21°$, at $M = 0.22$ and three Reynolds numbers $Re = 6$, 9 and 13.10^6.

2.2.2. 3D Test Programs

Extensive 3D tests were performed on the half model M139 in the RAE-5M wind tunnel and in the ONERA F1 wind tunnel.

The half model was mounted above a peniche of 81 mm height (to separate it from the tunnel boundary layer) on a six component underfloor balance in both wind tunnels, fig. 9. To measure the wake drag at the 59 % wing station an external motorized wake survey device was installed in the ONERA F1 wind tunnel, fig. 10.

RAE-5M Wind Tunnel

The measurements in the RAE-5M wind tunnel included balance measurements, pressure measurements over the entire wing and fuselage, within a Reynolds and Mach number range of $Re_c = 3.40 - 9.2.10^6$ and $M = 0.18 - 0.34$ for the take-off and landing configuration with and without nacelle, investigations of the flow over the wing upper surface with particular emphasis on the 59 % semi-span region were carried out using oil flow visualization techniques to obtain information about flow separation , especially separation bubbles in nose regions, and china-clay visualization for transition detection. Results were obtained for the take-off and landing configurations without nacelle at $M = 0.25$ and two Reynolds numbers ($Re_c = 3.35$ and $7.33.10^6$), for two angles of attack : α_1 corresponds to $0.7\ C_{Lmax}$ and α_2 to near C_{Lmax}. Some skin friction measurements using the razor-blade-technique were also made for the same model and test conditions. Hot film measurements were performed to detect the attachment line transition on the take-off configuration with and without nacelle.

ONERA F1 Wind Tunnel

The 3D tests in the ONERA F1 wind tunnel, which were complementary to the RAE tests, were carried out over a Reynolds number range of $Re_c = 3.5 - 11.10^6$ at a Mach number of $M = 0.25$ for the take-off and landing configuration with and without nacelle. Balance measurements, pressure measurements on the entire wing and fuselage, and boundary layer and wake survey at the 59 % wing station were performed. For the attachment line investigation hot film measurements were carried out on slat and wing in the take-off and landing configurations as an aid to the interpretation of the flight tests.

In both wind tunnels an additional test was carried out at $M = 0.2$ and $Re_c = 2.58.10^6$ at atmospheric pressure to provide a direct comparison with measurements made in the DNW wind tunnel on the complete model M139.

2.3. A310 Flight Test

To provide a greater understanding of the differences between wind tunnel and flight, tests with the A310-300 prototype MSN 378 were carried out with the support of Airbus Industrie.

2.3.1. Flight Test Instrumentation

The installation and operation of the instrumentation of the starboard wing of the aircraft was under the responsability of a flight test group. The general arrangements is given in fig. 11. At the 59 % wing station the entire wing section is instrumented and at the 64,5 % station only the slat :

- **pressure holes**

  Three pressure belts were fixed around the wing box including airbrake, the flap and the slat 2, containing 25 holes on the slat, 30 holes on the wing and 15 holes on the flap. The location of the pressure holes was the same as on the half model M139 but with additional holes in the nose region of the slat.

- **hot film gauges**

Adjacent to the 59 % and at the 64,5 % station two rows of 7 hot film gauges were glued on the slat belt for the attachment line transition investigation.

- **unsteady pressure transducers (Endevco)**

For the measurement of the unsteady pressure 5 Endevco pressure transducers were flush-mounted with the slat belt surface : 4 in the slat nose region and one near the slat t.e.. Also one Endevco transducer was installed at the wing t.e.

- **boundary layer rakes**

To measure the total pressure in the boundary layer one rake was installed at the slat t.e. and one at mid-chord of 59 % station on the wing. The slat rake with a height of 30 mm comprised 14 tubes, the wing rake with a height of 160 mmn 21 tubes.

The scanivalves and the electronic equipment needed for the slat instrumentation were installed on a special bracket which was attached to the slat structure in the shroud area underneath the slat. In order to avoid causing early transition on the slat attachment line the belt on slat 2 was extended to cover its full length, as shown in the photographs of fig. 12. ONERA had built a mockup of the slat, wing and flap nose in order to achieve best fit of the belt segments. The belt surfaces were very smooth and the edges were faired by means of a filler.

2.3.2. Flight Test Program

Three test flights were successfully performed in the following sequence :

Flight n° 289 Landing configuration
Flight n° 290 Landing configuration
Flight n° 291 Take-off configuration

From the flight measurements data points with sufficiently stabilized flight parameters were selected for further evaluation :

37 data points for the take-off configuration
36 data points for the landing configuration

The Mach number and the Reynolds number envelopes which have been covered by the different test are shown in fig. 13. The Mach numbers and Reynolds numbers of 2D and 3D tests are correlated by simple sweep theory in order to compare 2D and 3D data under equivalent freestream conditions. As shown on the figure 2D test were performed at Reynolds numbers as high as those in flight and Reynolds numbers of between 1/3 and 1/2 of those in flight were achieved in the 3D test.

3. DATA ANALYSIS

The programme has generated a very comprehensive, well integrated and accurate body of data which are still under analysis. In this section some results will be presented with emphasis on Reynolds number and Mach number effects on C_{Lmax}, 2D/3D correlations, wind tunnel/flight test comparisons and Attachment Line Transition results.

3.1. Reynolds number effect in 2D flow

The evolution of the maximum lift coefficient C_{Lmax} over the measured Reynolds number range from $1.9.10^{6}$ up to $16.7.10^{6}$ and a constant Mach number of M = 0.22 is shown in fig. 14 for the take-off and the landing configurations. Favourable Reynolds effect occurs up to $6.7.10^{6}$ for both configurations. Further increasing Reynolds number has no effect on C_{Lmax} for the landing configuration while it causes a small decrease of the C_{Lmax} for the take-off configuration. In that case the forward displacement of the transition location mainly on the flap but also on the slat leads to an increase in the viscous effets which is not compensated by the effect of Reynolds number. Thus the overall circulation decreases for Reynolds numbers above 6.10^{6} as shown in fig. 15 where the Maximum Mach number on the slat is plotted versus the Reynolds number.

For the landing configuration transition on the flap is less sensitive to Reynolds number since a velocity peak occurs at the leading edge and the overall circulation is almost constant for Reynolds numbers above 6.10^{6}.

For low Reynolds numbers laminar separation bubbles are present on the three elements which increase the viscous layers and decrease the overall circulation.

A good correlation is observed between the C_{L} values obtained in the HST and F1 wind tunnels at 6.10^{6} which is confirmed by the pressure distribution plotted in fig. 16.

Detailed boundary layer surveys have been performed at 8 stations on the different elements as well as in the near wake, as shown in fig. 17 for the take-off configuration. Reynolds number effect on the wing boundary layer are presented in fig. 18 for the take-off and the landing configurations near C_{Lmax}. As shown on the figure a Reynolds number effect occurs for Reynolds numbers lower than 6.10^{6}. For this angle of attack merging between the slat wake and the wing boundary layer occurs downstream of station 3 (x/c = 0.5).

No significant Reynolds number effects have been found on the dimensions of the separated flow areas in the slat and wing coves as well as on the extent of the separation on the flap for the landing configuration. For both configurations the stall is dominated by a wing trailing edge separation.

3.2. Mach number effect in 2D flow

The Mach number effects were investigated at a Reynolds number of 4.10^6 in the NLR HST wind tunnel and at a Reynolds number of 9.10^6 in the F1 wind tunnel.

The Mach number dependence of the maximum lift coefficient C_{lmax} over the measured range $0.13 < M < 0.3$ is shown in fig.19 for $Re = 9.10^6$. A large decrease of the C_{lmax} occurs for Mach numbers above 0.22 for both the take-off and landing configurations. Pressure measurements show that the strongest effect of Mach number occurs on the main element on which a trailing edge separation appears at an angle of attack several degrees lower than αC_{lmax}.

The maximum local Mach number at the slat leading edge is plotted in fig. 20 for both configurations and the two Reynolds numbers. It increases up to values around $M = 1.3 - 1.4$ which indicates that shock boundary layer interactions are likely to occur on the slat which influence the slat boundary layer and its wake. Thus, the stall of the wing is certainly influenced by transonic flow phenomena which occur on the slat at high angle of attack.

These have been clearly observed through the signal analysis of the Kulites which were located in the slat leading edge region.

3.3. Reynolds number effect in 3D flow

Reynolds number effect has been investigated for $M = 0.25$ on the A310 half model 139 within a large Reynolds number range ($3.4.10^6 \leq Re_{3D} \leq 9.2.10^6$) in the RAE 5m wind tunnel and up to $Re_{3D} = 10.8.10^6$ in the ONERA F1 wind tunnel.

Correlation between the results from the two wind tunnels have been found to be very good. However small differences have been observed near C_{Lmax}. The data obtained on the half model 139 are also in good agreement with those obtained in the DNW wind tunnel on the complete model as shown in fig. 21.

The evolution of C_{Lmax} with Reynolds number for the take-off and landing configurations in both wind tunnels is summarized in fig. 22. For the take-off configuration with and without the nacelle as well as for the landing configuration with the nacelle the increase of C_{Lmax} is about $\Delta C_{Lmax} = 0.04$ over the whole Reynolds number range. For the landing configuration without the nacelle the effect is smaller with a tendency for the C_{Lmax} values to decrease for Reynolds numbers above 7.10^6. The effect of the nacelle on the C_{Lmax} is only significant for the landing configuration.

Considering the 59 % span section which corresponds to the airfoil tested in 2D the evolution of the normal force CN versus Reynolds number near C_{Lmax} is presented in fig. 23. These evolutions correlate with those obtained in 2D, with an increase of the CN up to $Re_{3D} = 7.10^6$ (equivalent $Re_{2D} \sim 6.10^6$) and no significant effect for higher Reynolds numbers. For that span section the nacelle generates large 3D effects as shown on the boundary layer profiles, measured at mid chord (fig. 24). Wake surveys have been carried out with a five-hole probe at $x/c \sim 1.05$ in the ONERA F1 wind tunnel. An example of the effect of the Reynolds number on the wake profiles is shown in fig. 25. Increasing Reynolds number induces a decrease of the wake size at high angle of attack and less mixing between the flap and the wing wakes.

3.4. Mach number effect in 3D flow

Mach number effect has been investigated in the RAE 5m tunnel for a Reynolds number of $7.4;10^6$ (equivalent 2D $Re = 4.10^6$). As in 2D, increasing the Mach number induces a decrease of C_{Lmax} (fig.26) for the complete model as well as a decrease of the maximum normal force coefficient of the 59 % span section (fig.27). The compressibility effects are greater for the take-off configuration. The maximum Mach number on the slat at the 59 % span section is lower in 3D than in 2D.

3.5. Comparison between wing section data and 2D flow data

Simple sweep theory has been applied to the 3D test data in order to compare the data with the 2D values. Fig. 28 shows that this simple correlation works quite well for the maximum normal force. However Reynolds number effects for the landing configuration are different due to a different flow behaviour on the flap in 2D with separation and in 3D without reparation.

For the pressure distribution the same technique using local sweep angle provides a good correlation as shown in fig. 29. Some differences appear on the main wing near $x/c = 20$ % due to different shapes for the 2D and the 3D models in the slat trailing edge junction region and on the flap. A good 2D-3D correlation is also obtained for the section wake drag up to CNmax (fig.30).

3.6. Comparison between Flight and wind tunnel data

The total lift in flight is plotted versus angle of attack for both configurations, and compared with wind tunnel data in fig. 31. The lift coefficients at flight Reynolds numbers are in good agreement with the wind tunnel data for a large range of angle of attack. Near maximum lift the lift coefficient of the aircraft is a little bit lower than that of the 3D model.

For the 59 % span section good agreement is also observed (fig. 32) in spite of the difference in Reynolds number which confirms the small influence of this parameter for this configuration. The differences near maximum lift which occur for the landing configuration is due to the flap which carries more lift in the wind tunnel than in flight, probably due to small differences in the slot geometry.

3.7. Attachment line boundary layer investigations

The state of the boundary layer along the slat attachment line was investigated in wind tunnel and in flight near the 59 % span section. This has been achieved in wind tunnel using one hot film glued in the slat near the hook for three spanwise stations (54 %, 59 % and 66 %) while for the flight test the whole slate was equipped with two raws of 7 hot films located at η = 59 % and η = 65 %.

Some typical hot film signals are shown in fig.33 for the take-off configuration with increasing Reynolds number at an angle of attack near maximum lift. These measurements in the RAE 5m tunnel indicate that the Attachment line on the slat seems to be fully turbulent at $Re_c = 7.3.10^6$ which leads to a $\bar{R}$ value in good agreement with the usual value of ~ 300. A laminar separation bubble was observed for the same conditions which implies relaminarization of the boundary layer on the upper surface.

In flight a laminar boundary layer on the slat attachment line at the 59 % station was observed for higher Reynolds numbers indicating that less disturbances cross the 59 % station in flight that in wind tunnel. These differences can be explained by the fact that the belt on the aircraft slat gives a very smooth surface while the roughness is higher for the wind tunnel model. Furthermore, the relative size of the brackets is greater in the wind tunnel. Sweep effect on attachment line transition has also been demonstrated in flight as shown in fig. 34 where the reduction of the aircraft sideslip angle by 11°.4 leads to a laminar attachment line and a decrease of the boundary layer thickness at the slat trailing edge.

4. CONCLUSION

The success of this GARTEUR high lift research programme was made possible by the excellent cooperation between the partners from industry and research establisments. Form the extensive wind tunnel tests performed on 2D and 3D A310 high lift models in the NLR, DRA and ONERA wind tunnels as well as from the flight test conducted by Airbus Industrie the following main conclusions can be drawn :

2D test

- moderate Reynolds number effect from $Re_c = 4.10^6$ up to 16.10^6,
- much more important Mach number effect,
- the C_{Lmax} is due to the stall of the main element which is induced by the slat wake-wing boundary layer interaction,
- at high angles of attack, a shock-laminar boundary layer interaction is observed on the slat and induces the thickening of the slat wake,
- the take-off configuration presents an unfavourable Reynolds number effect on the C_{Lmax} from $Re_c = 7.10^6$.

3D test

- moderate Reynolds number effect,
- important Mach number effect,
- important effect of the nacelle on the C_{Lmax} and on the boundary layer profiles at the η = 0.59 station (X/C = 0.5),
- the local sweep normalization process used for 2D-3D correlations leads to a broad agreement between the pressure distributions at any specified C_L, for the take-off configuration.
- at moderate angles of attack, the take-off configuration presents satisfactory agreement between 2D and 3D wake drag estimates,
- attachment line transition occurs on the slat from $Re_c = 7.10^6$.

Flight test

C_L, α correlations good between F.T. and W.T. data :

- for the complete aircraft at moderate C
- for the η = 59 % section

Pressure distribution correlation between half model and flight :

- quite good for take-off configuration
- some differences on wing upper surface and flap upper surface for landing configuration.

Hot Film signal analysis on slat :

- both laminar and turbulent attachment line have been observed at moderate angles of attack,
- b.l. relaminarization has been observed
- at high angles of attack a laminar attachment line is detected in flight at higher values of R than in the wind tunnel tests.

All of this substantial set of measurements has provided what is certainly the most comprehensive, well integrated, and accurate body of data dealing with muti-element aerofoils and wings operating at high lift that is available anywhere in the world. The programme of data acquisition has in itself already provided valuable detailed comparisons between three major European wind tunnels ; these have in turn led to improvements in thenderstanding and the application of test and correction techniques. Furthermore the all-too-rare availability of corresponding measurements made in flight are immensely valuable even when assessed purely on the balance sheet of advances in measurement accuracy. However, more importantly, GARTEUR member nations now have a better understanding of the flow about high-lift systems, which will facilitate the development of improved designs, together with a comprehensive data base available for the development and validation of new computational techniques. It has consequently been possible to set up a successor to the Action Group tasked with taking the first steps along the road to real improvements in the aerodynamic design of high-lift systems.

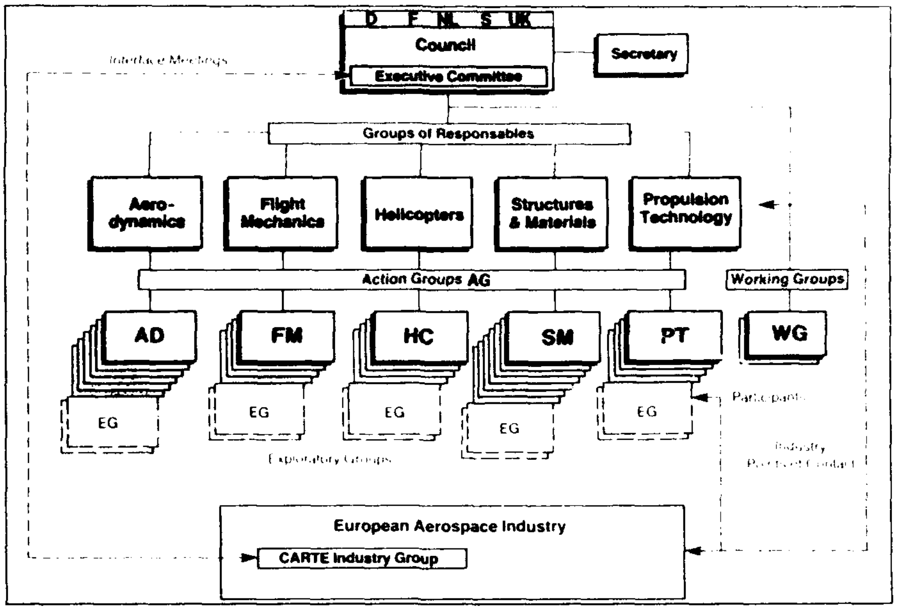

Fig.1 GARTEUR organization

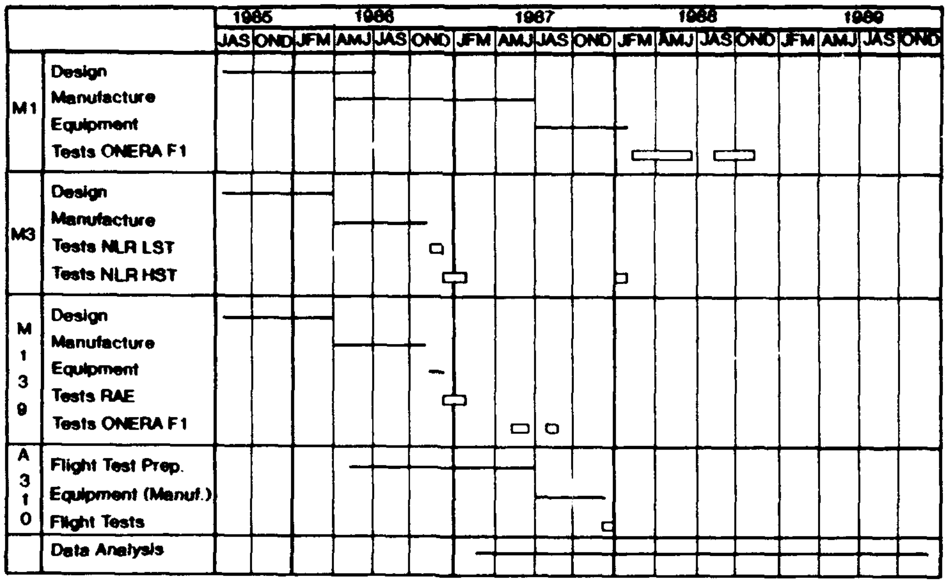

ESTABLISHMENT	PERSON
ONERA	Mr J.J. Thibert (chairman)
NLR	Dr. B. Van Den Berg (vice chairman)
DRA	Dr. S.P. Fiddes (partly)
	Mr. P.B. Earnshaw
DLR	Dr. J. Steinheuer (partly)
	Dr. G. Redeker
AS	Mrs. C. Bonnet
FOKKER	Mr. P.J. Laan
	Mr. J.N. Boer
BAe	Mr. B. Schofield (partly)
	Mr. R.W. Head (partly)
DORNIER	Mr. A.D. Welte
Deutsche Airbus	Mr. G. Dargel
	Mr. J. Scheerer (partly)
	Mr. H. Schnieder
AI	Dr. D. Schmitt
	Mr. J.P. Robert (partly)

Fig.2 GARTEUR High Lift Action Group schedule and members

MODEL		EQUIPMENT	MANUFACTURE	TEST
M 3	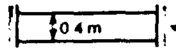 2 D - MODEL	• 130 PRESSURE TAPS • 13 KULITES • 6 RAZOR BLADES • 1 INTERNAL B L. DEVICE • 6 TUBES FOR FLOW VISUALIZATION • PLASTIC STRIP FOR TRANSITION MEASUREM. • 2 B.L. RAKES IN COVES • 4 SKIN FRICTION GAUGES	M 3 MODEL NLR	NLR - LST AND NLR - HST WITH EXTERNAL SURVEY DEVICE
M 1	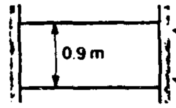		M 1 MODEL DLR	ONERA F 1 WITH EXTERNAL SURVEY DEVICE
M 2	HALF MODEL M 139 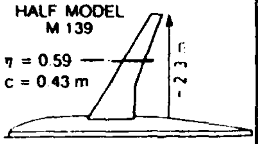 MBB - MODEL 139	• 602 PRESSURE TAPS (61 FOR $\eta = 0.59$) • HOT FILMS • RAZOR BLADES • 1 INTERNAL B L DEVICE IN THE VISCOUS SHROUD	MBB / DLR FUSELAGE + WING VISCOUS SHROUD	RAE 5 M AND ONERA F1 WITH EXTERNAL SURVEY DEVICE
AIRCRAFT	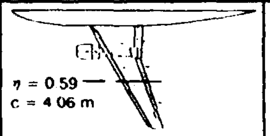 A310	• 2 ROWS OF 7 HOT FILMS • PLASTIC BELT WITH 70 PRESSURE HOLES • 2 B L RAKES • 6 ENDEVCOS	MBB - MOD LEADER (MBB, ONERA, AS)	AI

Fig.3 Models, instrumentation and wind tunnels

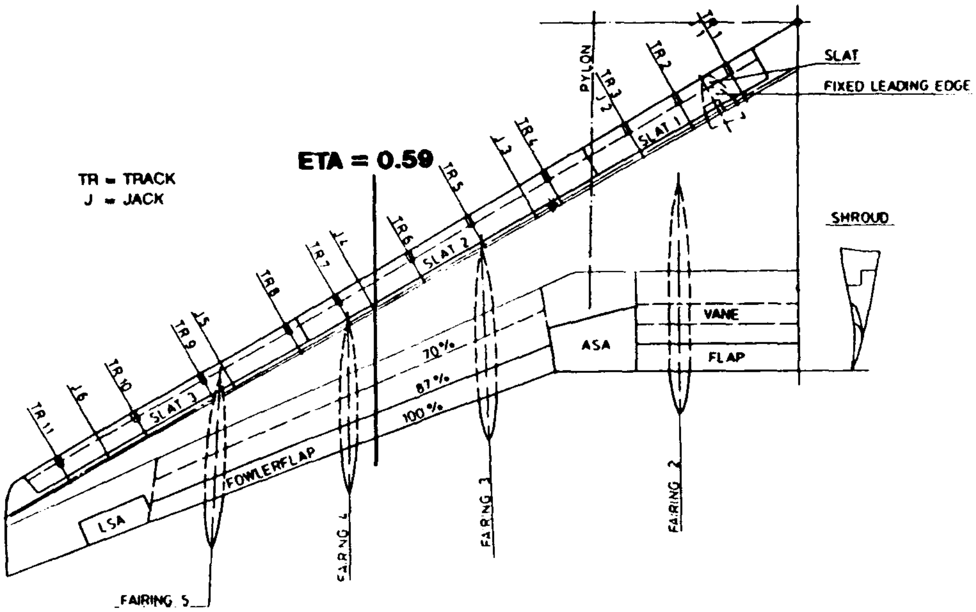

Fig.4 High lift system of half model 139

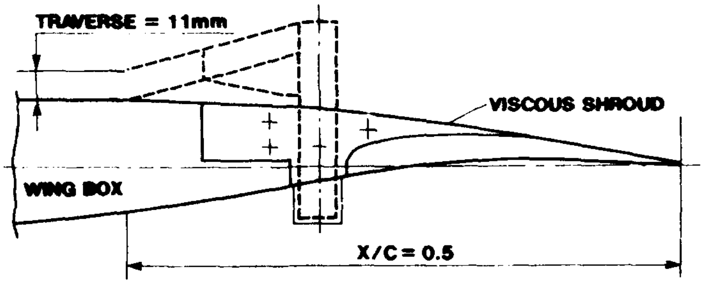

Fig.5 Viscous shroud for the half model 139

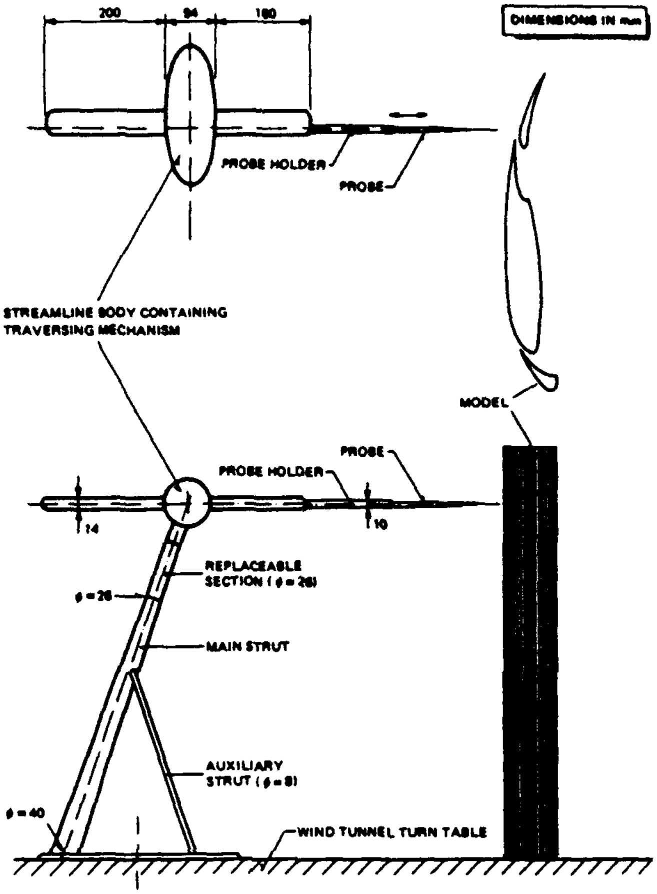

Fig.6 Sketch of the NLR LST M3 model installation and external probe traversing system

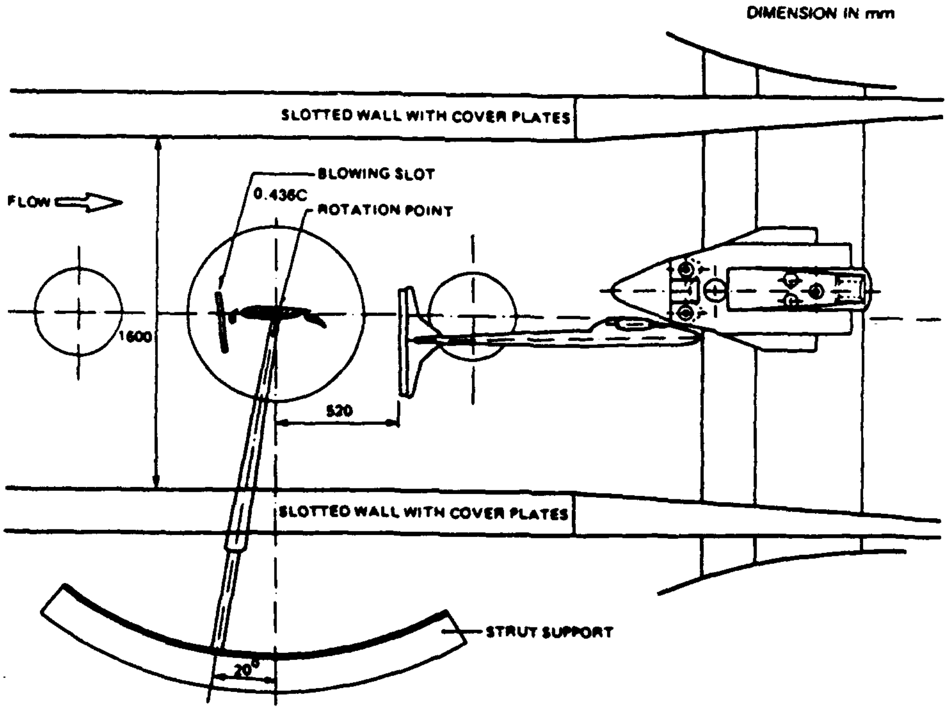

Fig.7 Test set up with model M3 in NLR HST wind tunnel

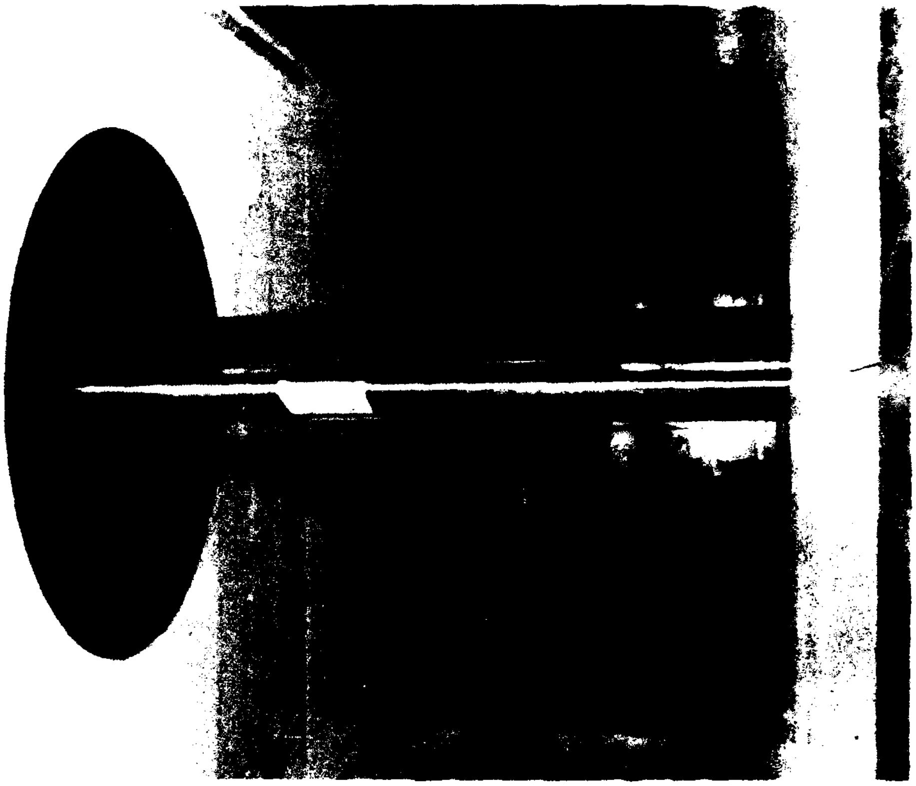

Fig.8 Model M1 in ONERA F1 wind tunnel with external Boundary Layer device survey system

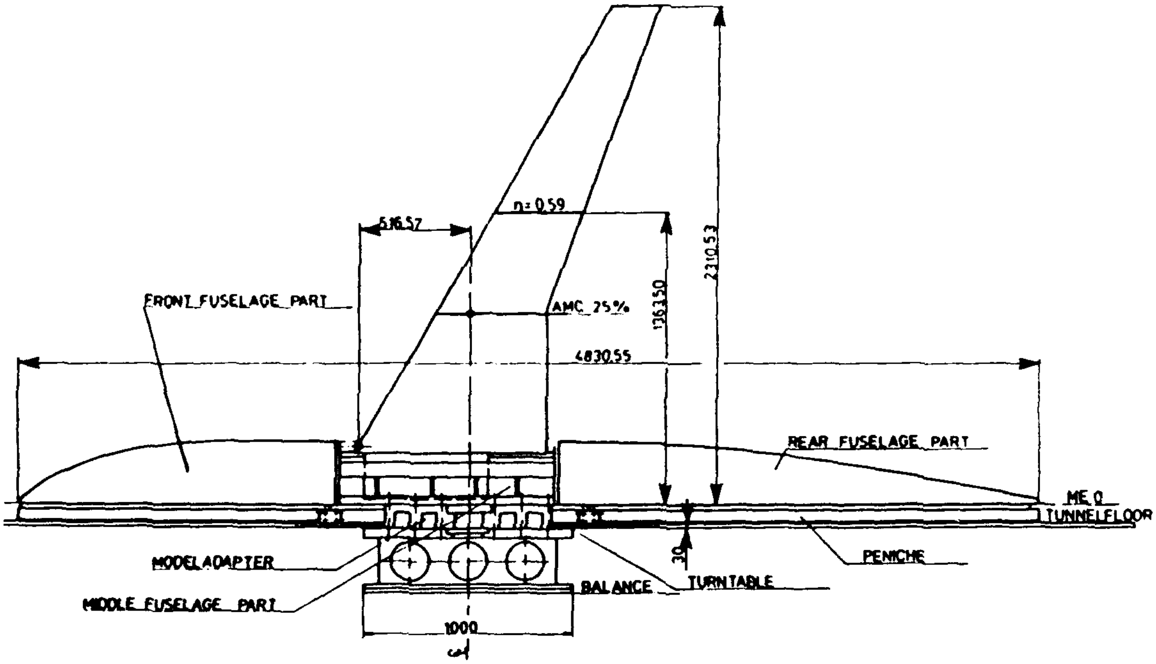

Fig.9 Half model M139 arrangement in the RAE 5m tunnel

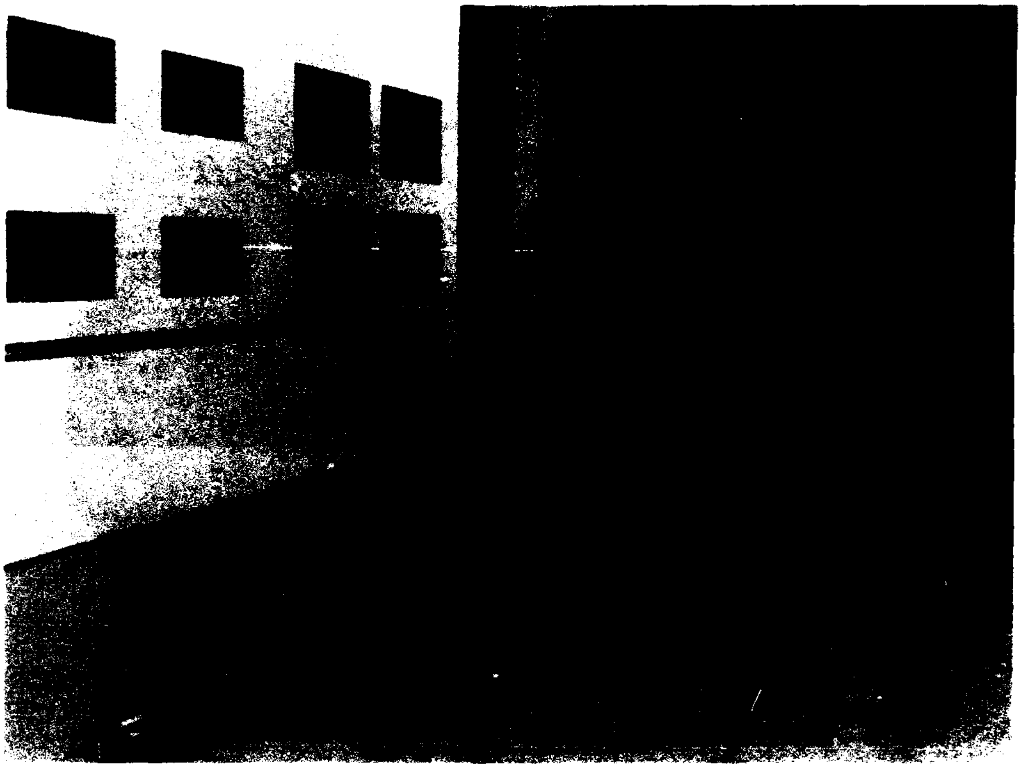

Fig.10 Half model M139 in the ONERA F1 wind tunnel with the wake survey device

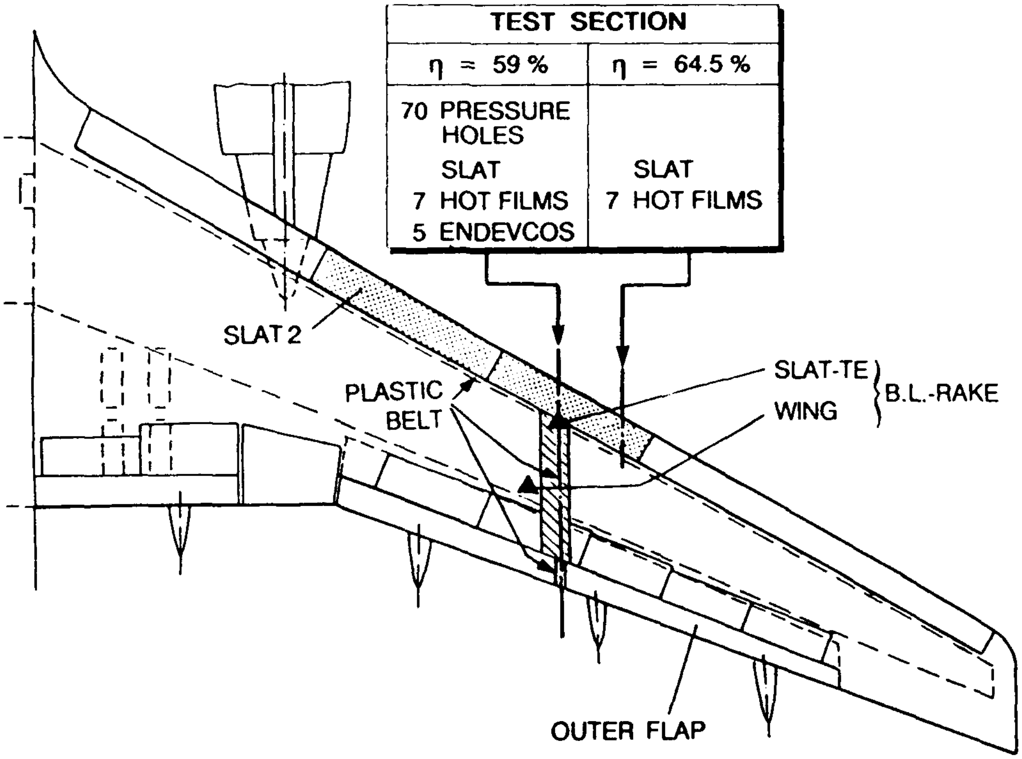

Fig.11 General arrangement of flight test instrumentation

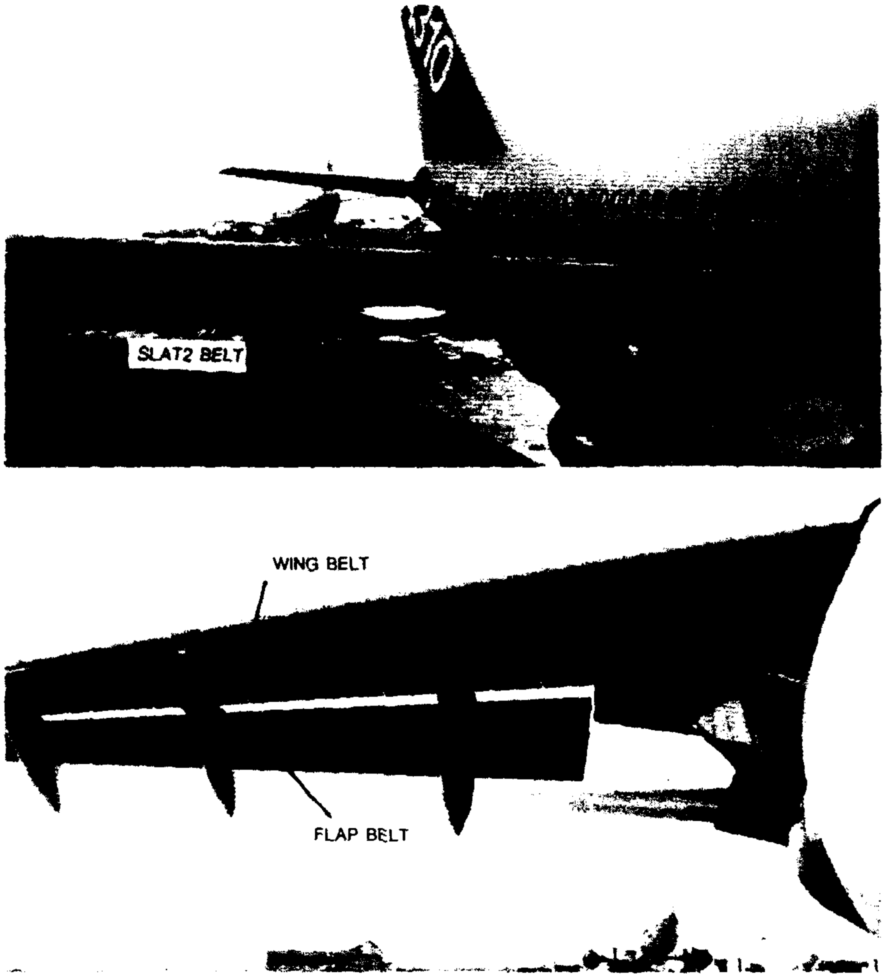

Fig.12 Belts on A310 wing for flight test

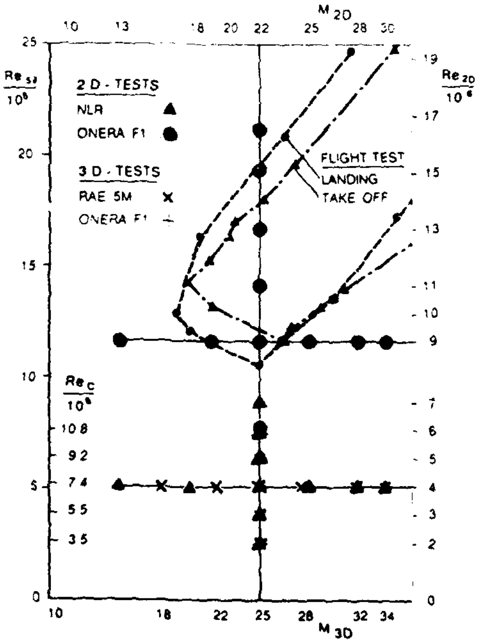

Fig.13 Test envelope

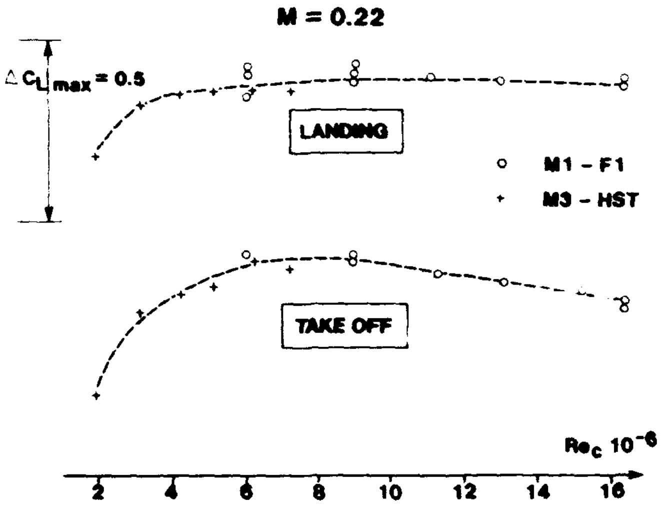

Fig.14 Reynolds number effect on $C_{L_{max}}$ in 2D flow

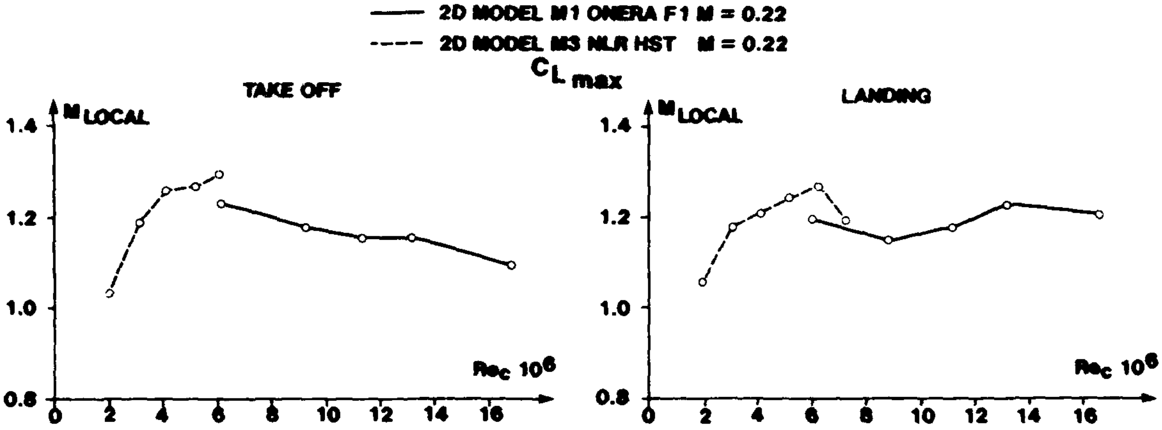

Fig.15 Reynolds number effect on maximum slat Mach number near $C_{L_{max}}$ in 2D flow

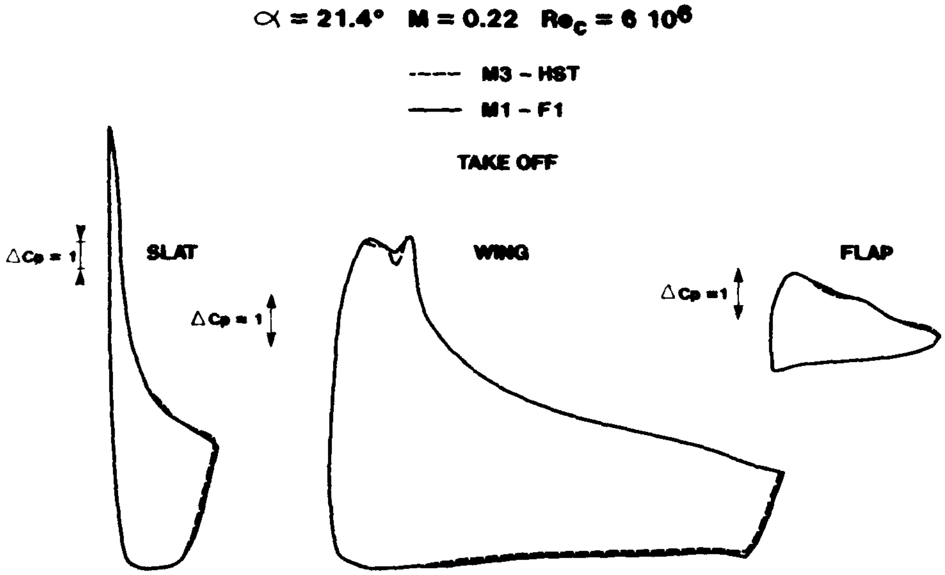

Fig.16 Comparison of HST and F1 wind tunnels data

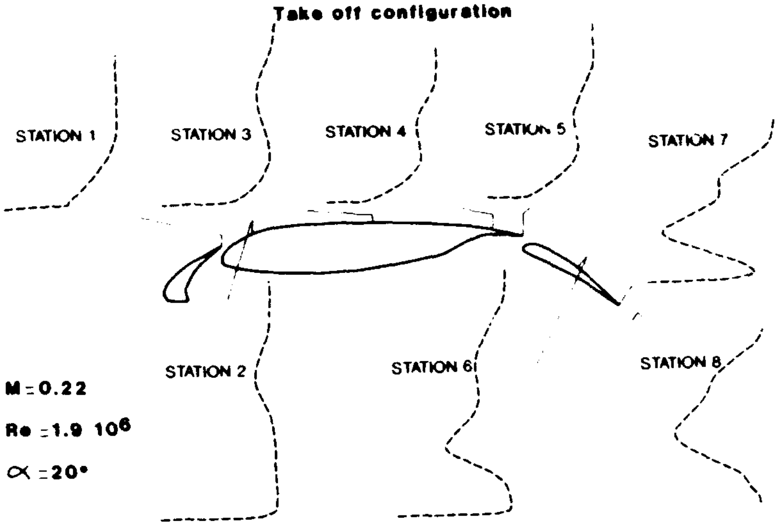

Fig.17 Example of boundary layer surveys - NLR data

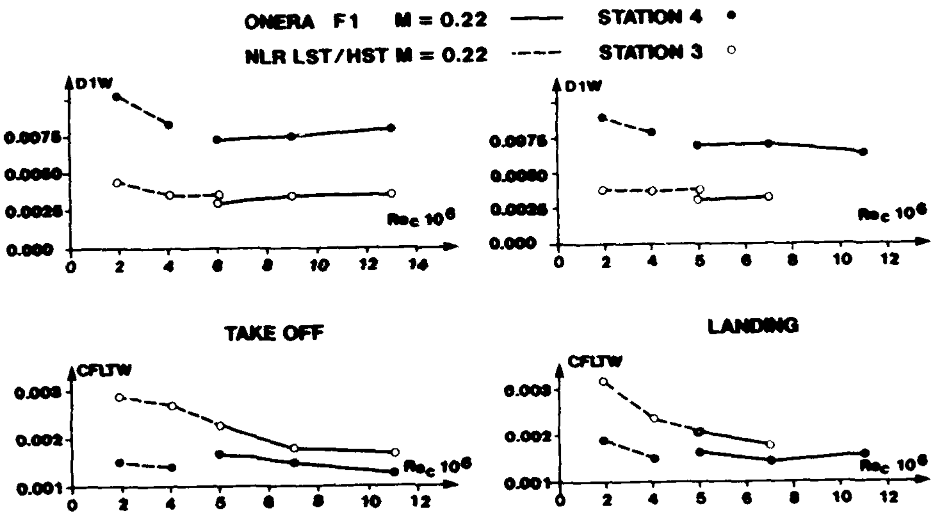

Fig.18 Reynolds number effect on boundary layer data near C_{Lmax} in 2D flow

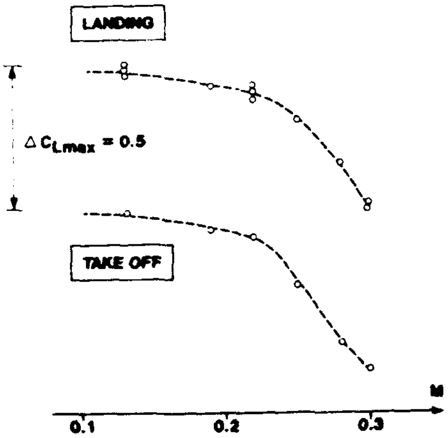

Fig.19 Mach number effect on C_{Lmax} in 2D flow

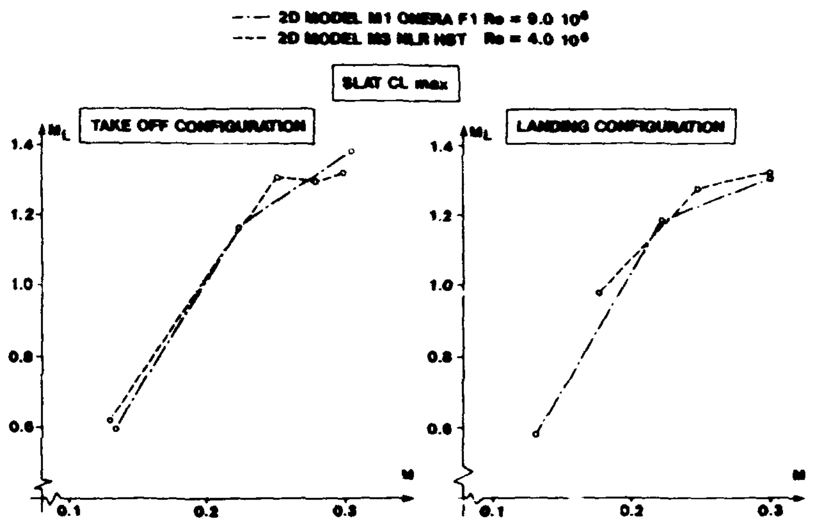

Fig.20 Mach number effect on maximum slat Mach number near $C_{L_{max}}$ in 2D flow

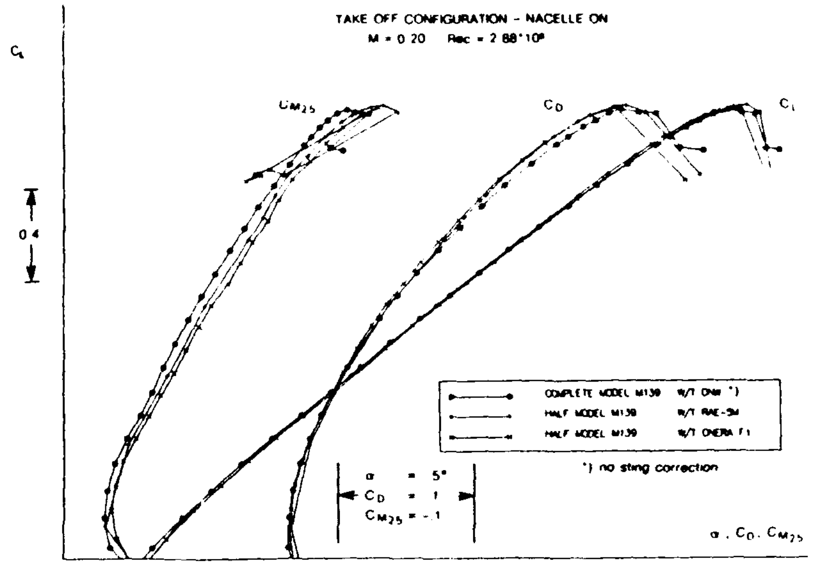

Fig.21 3D wind tunnels data comparison

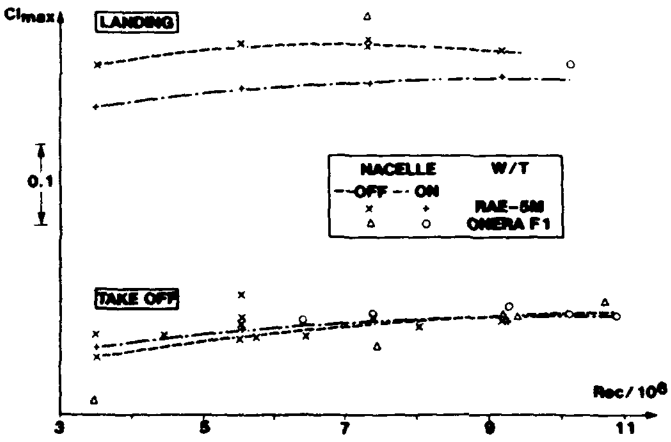

Fig.22 Reynolds number effect on maximum lift in 3D

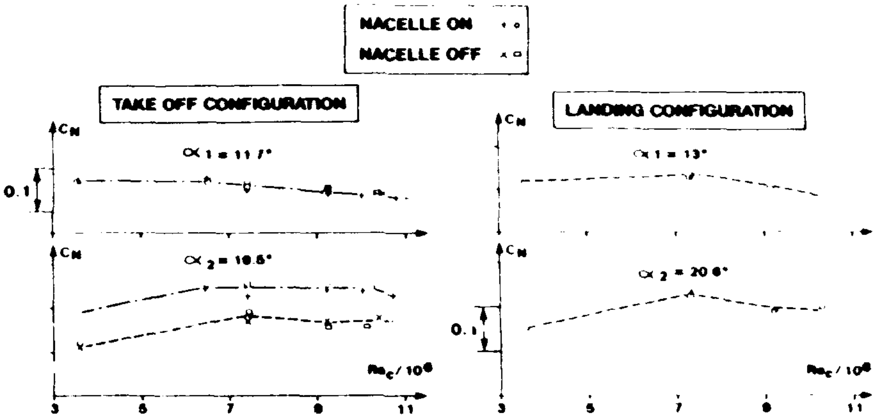

Fig.23 Reynolds number effect on section normal forces

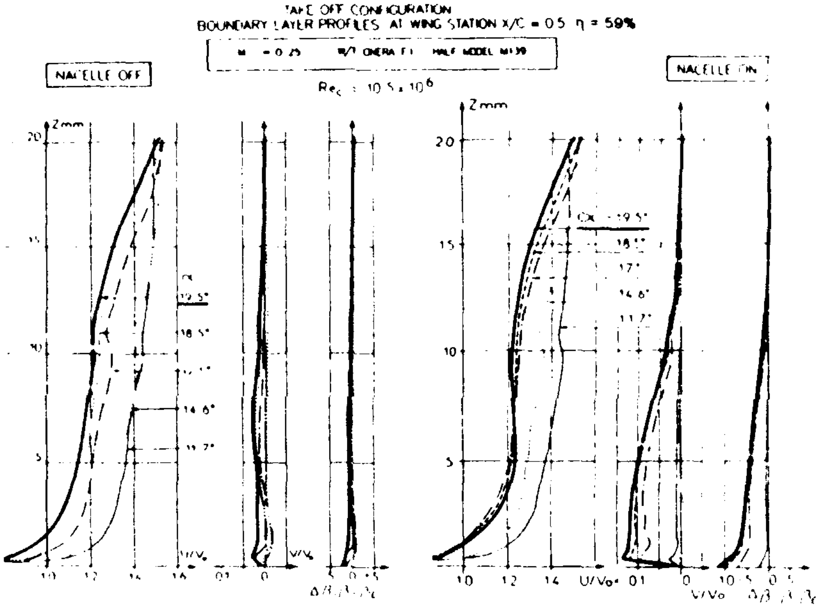

Fig.24 3D boundary layer profiles at η = 59 %

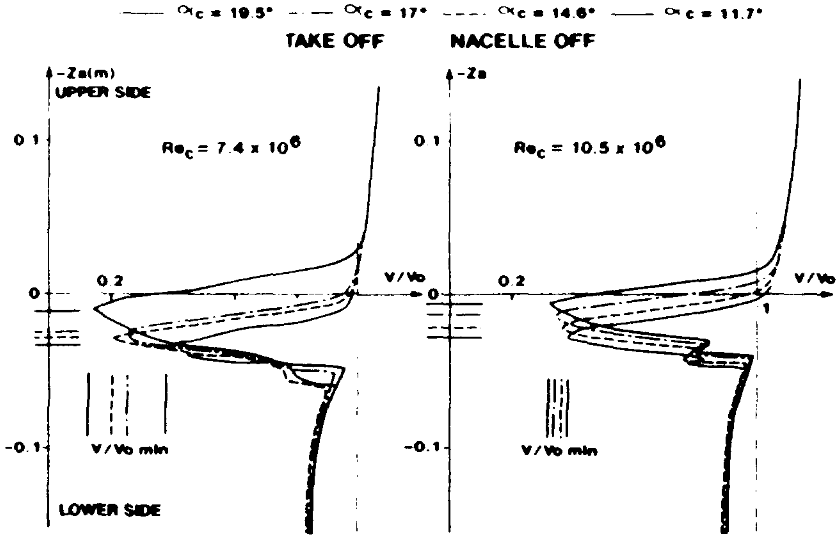

Fig.25 Near wake profiles at η = 59 %

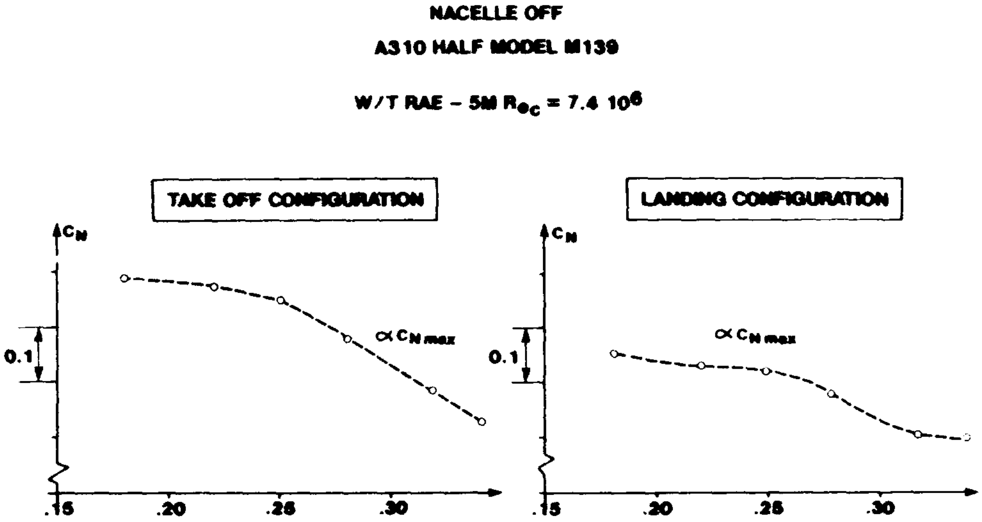

Fig.26 Mach number effect on maximum lift in 3D

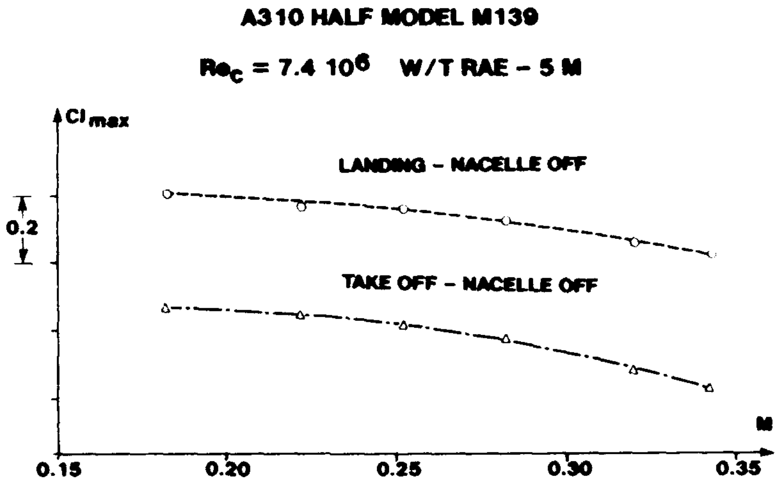

Fig.27 Mach number effect on maximum slat Mach number at η = 59 % near C_{Lmax}

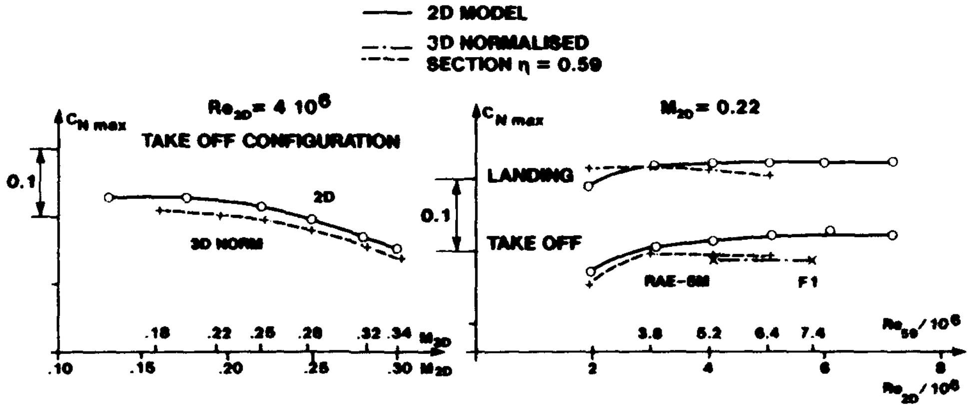

Fig.28 Normalized section η = 0.59 in 2D Flow and wing flow - Comparison of the Reynolds number and of the Mach number effects on C_{Nmax}

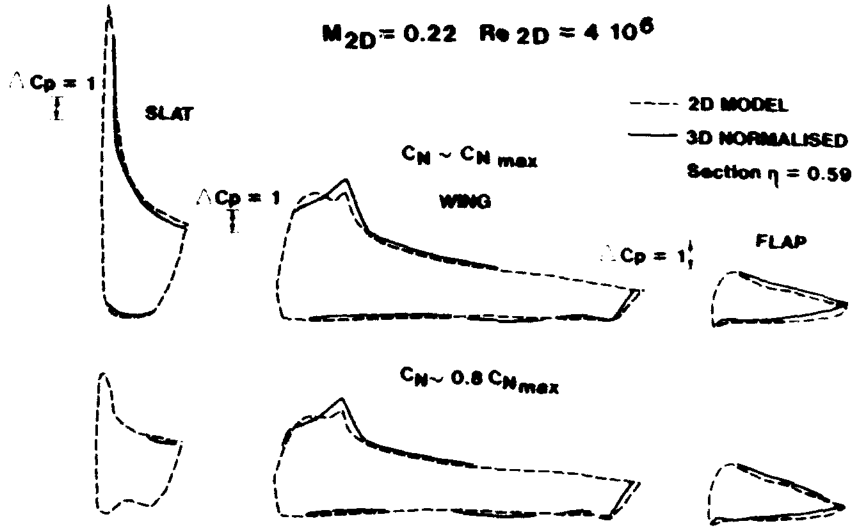

Fig.29   Normalised section $\eta = 0.59$ in 2D flow and wing flow - Comparison of the pressure distributions near $C_{N\,max}$

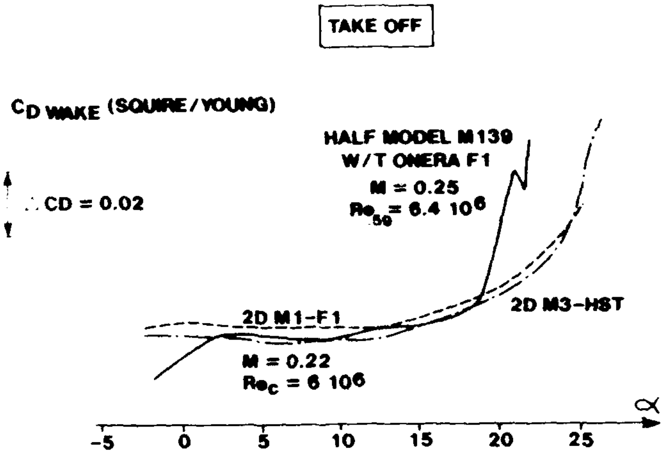

Fig.30   Normalised section $\eta = 0.59$ in 2D flow and wing flow comparison of the drag

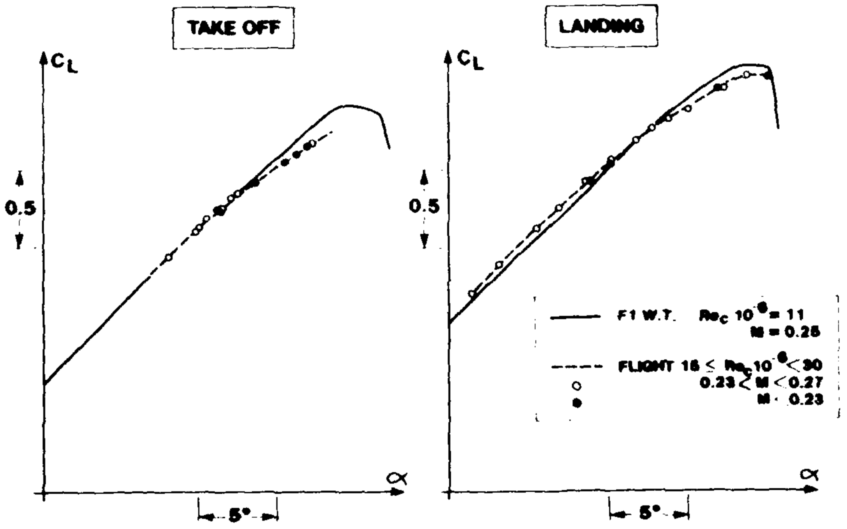

Fig.31   Wind tunnel / Flight test comparison for the total lift

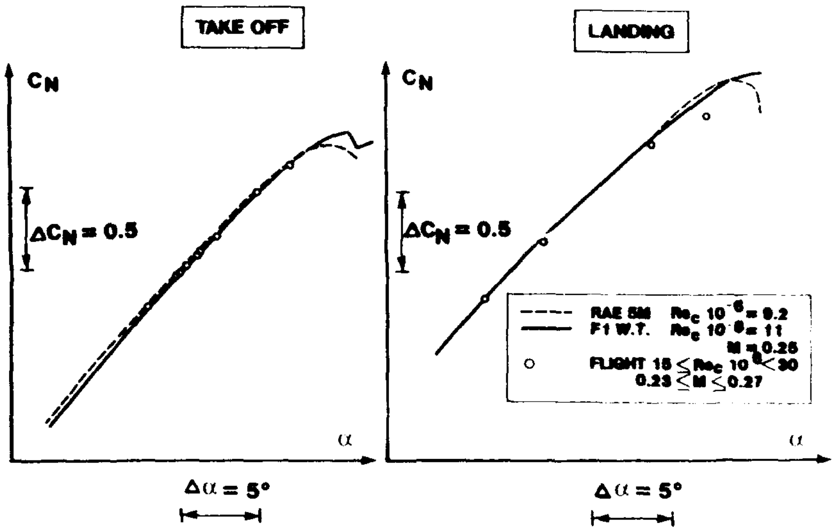

Fig.32 Wind tunnel / Flight test comparison for the η = 0.59 normal forces

α = 19.4° M = 0.25

TAKE OFF CONFIGURATION – NACELLE OFF

W/T RAE 5M HALF MODEL M139

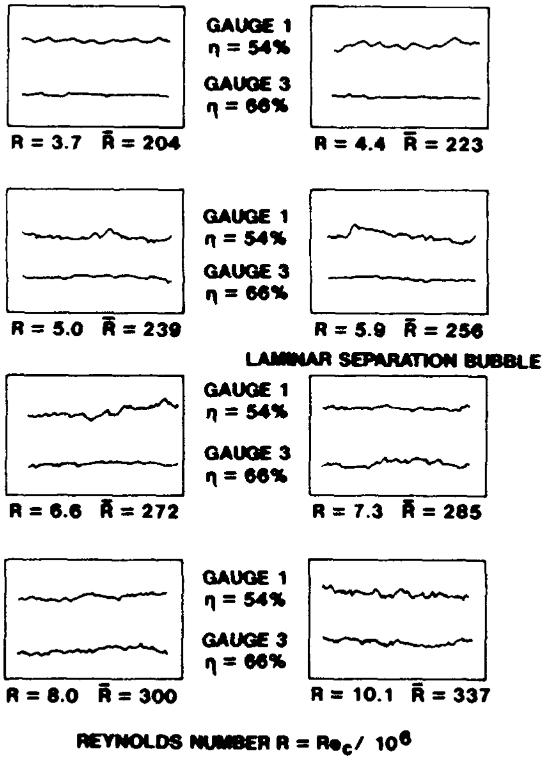

Fig.33 Slat hot film signals. RAE 5m tunnel. 3D model

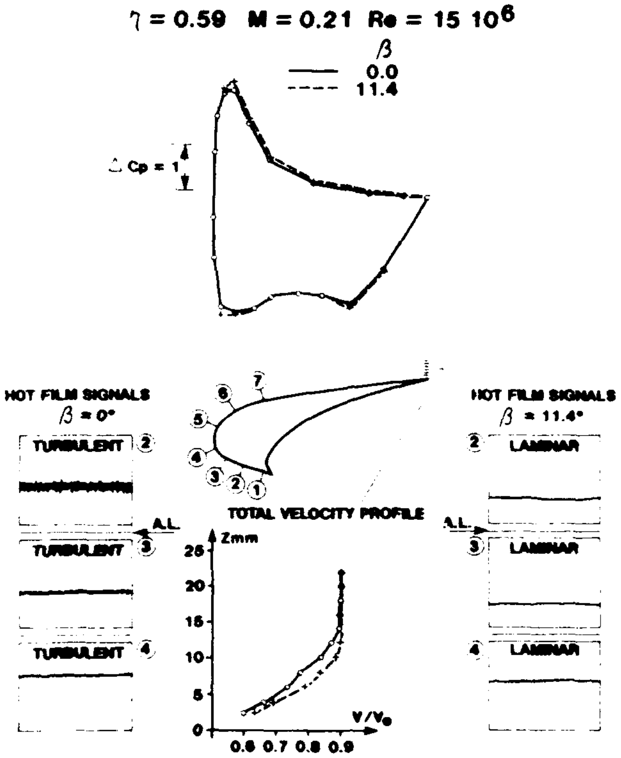

Fig.34 Flight test. Sideslip effect on attachment line boundary layer and slat trailing edge boundary layer

AN EXPERIMENTAL INVESTIGATION OF THE OPTIMUM SLAT SETTING ON A COMBAT AIRCRAFT MODEL

by

I. R. M. Moir

Defence Research Agency
Farnborough, Hampshire, GU14 6TD, United Kingdom

SUMMARY

Tests have been carried out, on a combat aircraft model with high-lift devices, in the DRA Farnborough 5 metre pressurised low-speed wind tunnel. The deflection angle and position of a leading-edge slat were varied and optimum settings established. The separate effects of Reynolds number and Mach number on overall lift coefficient and on the optimum slat setting were investigated. The results show that optimum performance is achieved at a very high slat deflection angle and the performance is strongly influenced by compressibility effects.

LIST OF SYMBOLS

c	chord
C_L	lift coefficient
C_{Lmax}	maximum lift coefficient
C_p	*pressure coefficient*
C_p^*	pressure coefficient corresponding to local Mach unity
M_0	free-stream Mach number
$\hat{M}_{local}$	peak local Mach number
Re	Reynolds number
V	free-stream velocity
x_s	slat overlap
z_s	slat gap
θ_s	slat deflection angle
α	angle of incidence
Λ	wing leading-edge sweep

1 INTRODUCTION

The flow around multi-element high-lift aerofoil sections is now relatively well understood. Extensive experimental studies, such as those in Refs 1 and 2, together with theoretical work involving CFD modelling as in Ref 3, have identified the important features of such flows, at least in two-dimensions. The conclusions have been applied with some success^3, in conjunction with concepts related to infinite swept-wing flows, to describe the flow over wings of high aspect ratio and moderate sweep, such as civil transport aircraft configurations, where root and tip effects are comparatively small in the context of the overall flow.

Extensive research has also been carried out into the mechanisms which govern the optimum relative positions of the components of a high-lift wing (*eg* slat, wing, flap), but rather less on the effects of Mach number and Reynolds number on this optimum. The location of such an optimum is obviously important, and is the result of two competing effects arising from the relative movement of the wing elements. Firstly, as the two elements are moved together, load is increasingly shared between the two surfaces, and the pressure distribution on both elements is *modified*. This increases the load on the upstream element and decreases the load on the downstream element, reducing the likelihood of flow separation on the latter.

In addition to the possibility of flow separation from the upstream element due to increasing load, the wake from this element can merge with the boundary-layer on the downstream element, thickening it and increasing the likelihood of flow separation.

It is apparent, therefore, that the high-lift device may be positioned in order to achieve a balance between the adverse and beneficial effects, leading to the concept of an optimum setting.

In addition to their application to civil transport aircraft, high-lift devices are also used on some combat aircraft, not only for improved take-off and landing performance, but also for enhanced manoeuvrability. However, combat aircraft wings are usually of higher sweep than 'civil' wings and have lower aspect ratio as well as thinner aerofoil sections, this latter characteristic leading to potential practical problems of accommodating mounting brackets for high-lift devices. These features of the wing geometry result in highly three-dimensional flows which are a severe test of the two-dimensional concepts used to describe the flow over civil wings.

In general, increased sweep shifts the spanwise loading outboard, and also tends to shift the chordwise loading forward. The pressure gradients are made more adverse near the tip as a result. Together, these effects would tend to encourage the stall to occur first near the tip, with a leading-edge type stall, which is also more likely with the thinner aerofoil sections used on combat aircraft.

It would appear then that this markedly three-dimensional flow around combat-aircraft wings means that earlier work on low-sweep, high-aspect-ratio wings may not give a good guide to the optimum positioning of high-lift devices, and probably of leading-edge slats in particular.

Thus a need was perceived for fundamental research into the general area of high-lift devices for combat aircraft wings, and with this in mind a model with a low aspect-ratio, high sweep and high taper-ratio wing was manufactured at DRA Farnborough, U.K. In the present tests, the deflection angle of the slat and its position relative to the wing were varied in order to establish the deflection and location, necessary to optimise C_{Lmax}. The freestream Mach number and Reynolds number were also varied independently in order to examine how these parameters affected the overall C_{Lmax} and optimum slat position and deflection.

2 DESCRIPTION OF MODEL

The model, designated DRA Model 495[4], is representative of a low-level strike-fighter. It was designed for general research into high-lift devices on low aspect-ratio swept wings. The general layout of the model is shown in Fig 1, in which the principal dimensions are indicated; these are also given in Table 1. The high mounted wing has an 8% thick supercritical section, and has provision for an 18% chord leading-edge slat and a 33% chord trailing-edge flap, or a plain undeflected trailing-edge. As originally designed, the slat deflection angle could be set at 25° and 35°, but for reasons discussed later, it was subsequently found necessary to make modifications to increase the available deflection to 45°. The slat position relative to the wing can be adjusted also, over the range shown in Fig 2. This range was also increased during the present tests. The slat brackets were of a special profiled design (illustrated in Fig 3) which is used to minimise the wake shed from the brackets. Such wakes are known to be entrained through the slat gap at moderate to high α's and can induce premature flow separation on the wing.

The flap also is adjustable in overlap and gap, as well as having a number of deflection angles available.

The model has a fixed fin and an adjustable tailplane, but the latter was not fitted for the present tests.

The port wing, slat and flap have provision for measurement of surface pressures by means of spanwise tubes which have tappings drilled in them at several spanwise stations, the unwanted holes being blanked off with adhesive tape, so that pressures may be measured at one discrete station. The starboard wing has tubes and tappings at one station only, near the tip. The pressures are scanned by on-board Scanivalves, and converted to electrical signals by pressure transducers.

For the present tests, the model was mounted on an underfloor six-component mechanical balance by way of a single main strut plus a jacking strut at the tail to provide pitch variation, as shown in Fig 4. The mounting allowed a range of angle of incidence of -8° to +40°, the angle being measured by on-board accelerometers.

3 TEST CONFIGURATION AND CONDITIONS

The model was tested with both the plain wing trailing-edge and with the single-slotted flap set at 20° deflection, this being the highest angle at which attached flow could be expected. The overlap and gap were set at 0% and 3% respectively, relative to the shroud trailing-edge. The model was tested with the slat set at 25°, 35° and 45° with the plain trailing-edge, and 35° and 45° only with the slotted flap.

The tests were conducted in the DRA Farnborough 5 metre pressurised low-speed wind-tunnel[5] and encompassed the range of Reynolds number and Mach number listed in Table 2; this was close to the widest range allowed by the operating envelope of the tunnel, as shown in Fig 5, and by the design stress limit of the model. Force measurements were made at small increments of angle of incidence to beyond the stall, while surface pressures were monitored at 57.8% span on the port wing and 82.6% span on the starboard wing, as shown in Fig 1. These pressures were recorded at $\alpha = 16°$, 20° and 24° and at 3.2°, 1.2° and 0.2° below the stall.

For the slat optimisation process, the slat was set at each of a number of positions in turn, and measurements of forces and pressures were made over the range of α and M_0 and Re.

4 RESULTS AND DISCUSSION

Figs 6a and 6b show an example of the variation of lift coefficient C_L with angle of incidence over the range of Reynolds number and for the range of Mach number covered in the tests, respectively.

The Figures show that a fairly high C_{Lmax} is achieved, albeit at a high angle of incidence, as would be expected for this low aspect-ratio configuration.

Fig 6a shows that C_{Lmax} is Reynolds number dependent and Fig 6b shows that it is very strongly Mach number dependent.

The foregoing suggests headings under which the results may be discussed, *ie*:

(i) Geometry effects
(ii) Reynolds number effects
(iii) Mach number effects

and these three aspects will be considered in turn.

4.1 Geometry Effects

As mentioned in the Introduction, the low aspect-ratio and high sweep of the present configuration should typically result in a high loading towards the tip. Fig 7a shows the pressure distributions at the two tapping stations, just below C_{Lmax}, and these do show much higher suction peaks at the outboard station. Comparison with results from a typical civil transport model in Fig 7b, at similar spanwise locations, also just below C_{Lmax}, shows that the latter has a much smaller variation on the slat between the tip region and the station near mid semi-span. In both Figures the pressure coefficient corresponding to local sonic velocity is indicated. In the case of the fighter configuration the slat suction peak exceeds this value in the tip region, and the implications of this local supersonic flow will be discussed in a later section.

4.1.1 Effect of Slat Deflection and Position

The original design of the model assumed that the optimum slat deflection angle and position would be similar to that established on high aspect ratio, lower sweep 'civil' wings. This resulted in the initial deflection angle of 25°, although just prior to the first tests, modifications were made to enable the slat to be set at an alternative deflection of 35°. The first tests commenced with the lower deflection angle (in conjunction with the plain trailing-edge), but, as suggested by Fig 8a which shows the variation of C_{Lmax}

with slat position, it was quickly discovered that the C_{Lmax} was still increasing when the limit of the available slat adjustment range was reached. The rapid increase in C_{Lmax}, seen in the Figure, as the slat was moved away from the wing thus reducing the load carried by the slat, indicated that it was very heavily loaded, and this probably resulted in an early flow separation, originating on the slat. This result prompted the abandonment of the 25° slat in favour of the 35° deflection which hopefully would be sufficiently less highly loaded and would enable a peak C_{Lmax} to be achieved much closer to the wing.

An example of the variation of C_{Lmax} with slat position for the 35° slat is also shown in Fig 8a. It may be seen that C_{Lmax} was now nearly 0.2 higher than for the lower slat deflection, but the position corresponding to peak C_{Lmax} was still obviously further ahead of the wing. At this stage, further modifications were made to the model, to increase the range of adjustment of the slat, enabling it to be moved further forward of the wing and also, since it was obvious that the slat was still very highly loaded at 35° provision was made for an additional increase in slat deflection to 45°.

Due to insufficient tunnel time, a full range of slat positions using the extended range for the 35° slat, in conjunction with the plain trailing-edge, was not completed, but tests on the 45° slat covered a sufficient range of positions to enable the position giving the highest value of C_{Lmax} to be located as shown in Fig 8b. It may be seen however that this maximum value is now lower than that for the 35° slat, suggesting that the optimum deflection is lower than 45°, although the corresponding optimum slat position is at a fairly small underlap relative to the wing leading-edge at the higher deflection.

A feature of the 45° slat deflection is the large drop in C_{Lmax} (about 0.4 relative to the optimum value) as 3% underlap and 1.5% gap is approached. This corresponds to a reduction in stall incidence of about 6° for this case and is presumably associated with a more rapid change to the pressure distribution, and hence the proportion of the overall load carried by the wing as the slat is moved away from it than was the case for the 35° deflection. The configuration with a slotted flap shows a much smaller loss in C_{Lmax} at this setting as will be seen in the next section.

4.1.2 Effect of Slat Position

In order to explore fully the optimisation of the 35° and 45° slats in conjunction with the single-slotted flap, additional modifications were made to the model to increase the range of slat adjustment in both x_s and z_s, as the earlier measurements showed that optimum C_{Lmax} tended to occur at more negative values of x_s and lower values of z_s than could be achieved on the model originally.

Fig 9 shows typical examples of the variation of C_{Lmax} with slat position at the two slat deflection angles for the slotted flap configuration. As with the plain trailing-edge configuration the 35° slat achieves the higher C_{Lmax}, but at the expense of an underlap greater than 4% - this amount of underlap may not be possible on a real aircraft for structural reasons. Similarly, it may not be possible to incorporate practical slat brackets to provide a 45° deflection in a thin fighter wing. Even the 35° slat may pose problems in this respect. Furthermore, it is also noticeable in Fig 9 that the slat at 45° deflection is rather more sensitive to position than it is at 35° and the lower slat deflection could be used at an off-optimum position without incurring much penalty in C_{Lmax}.

In order to determine the precise positions of the slat which correspond to optimum C_{Lmax}, values of overlap and gap for a range of values of C_{Lmax} were read off the earlier plots of C_{Lmax} against slat position and plotted in the form of constant C_{Lmax} 'contours', as illustrated in Fig 10, which is derived from Fig 9. Plots of this type enabled the optimum slat location to be determined within about ±0.2% of overlap and gap. These data enabled the variation of the optimum positions over the range of M_0 and Re to be examined - this aspect is discussed in the following sections.

4.2 Reynolds Number Effects

4.2.1 Overall Effects

The overall effect of Re on the C_{Lmax} for a fixed slat position is illustrated in Fig 11, which also shows results for a typical civil transport model at a similar M_0. It may be seen that the two configurations show a similar degree of sensitivity to Reynolds number.

4.2.2 Effect on Slat Optimum

As suggested earlier, the optimum position of the slat may vary with flow conditions. In Fig 12, the variation of x_s and z_s is plotted against Re for the two slat deflection angles at $M_0 = 0.22$. The Figure shows some apparent movement of the optima with Reynolds number, although the actual changes in x_s and z_s are of the same order as the accuracy with which the optimum positions were determined. It is reasonable to suppose that the effect of increasing Reynolds number would be to generate thinner boundary-layers, which in turn would affect the degree of wake/boundary-layer interaction. This would suggest that the optimum slat position should move closer to the wing as Reynolds number was increased. However, the results do not give clear support for this hypothesis.

Although the 35° slat appears to show the larger movement of optimum position with Re, the sensitivity of C_{Lmax} to slat position has been shown to be rather less than that for the 45° deflection, so the actual variation of optimum C_{Lmax} with Re has to be considered in order to assess the relative loss of C_{Lmax} associated with fixing the slat position for the full range of Re, and this is shown in Fig 13. The Figure shows the increment in C_{Lmax} for the slat fixed in its optimum position for the lowest Reynolds number, compared with the corresponding increment when the slat is moved to the position giving the highest attainable C_{Lmax} as Re is increased. The increment in C_{Lmax} for $\theta_s = 35°$ relative to $\theta_s = 45°$ is also included.

It may be seen that the potential loss in C_{Lmax} for a 'fixed' 35° slat is about 0.03, compared with a 're-optimised' slat. Also, the 'fixed' slat has a lower C_{Lmax} than the 45° slat at the higher Reynolds numbers. The 45° shows very little loss in C_{Lmax} when fixed at the same position through the Re range, although its C_{Lmax} is lower than that for the 're-optimised' 35° slat through the whole range.

4.3 Mach Number Effects

4.3.1 Overall Effects

The overall effect of the variation of M_0 on C_{Lmax} is shown in Fig 14 which also shows results for the civil transport model; these latter are at a rather lower Re. The plot for the combat aircraft configuration is characterised by a large reduction in C_{Lmax} between $M_0 = 0.22$ and 0.28, while the transport aircraft configuration appears to exhibit a more gradual drop off in C_{Lmax}. This compressibility effect is presumably associated with high local subsonic and supersonic flows, as suggested by Fig 7a. This is further illustrated in Figs 15a and 15b which show the variation with M_0 of peak local C_p just below C_{Lmax} on the slat and wing leading-edges for the fighter and transport configurations, at similar stations near the tip and near mid semi-span. It is seen that for $M_0 = 0.16$ (0.15 for the transport aircraft) the flow is wholly subsonic for both configurations. At $M_0 = 0.22$ the flow attains supersonic velocity on the slat near the wing tip for the combat aircraft, while the wing leading-edge is just sonic, and the inboard station is entirely subsonic, as are both stations for the transport aircraft ($M_0 = 0.21$) on slat and wing. At $M_0 = 0.28$ there is supersonic flow on the slat and wing leading-edge at both the tip and inboard station of the combat aircraft; in contrast the transport aircraft ($M_0 = 0.27$) just achieves supersonic flow at both stations, and that for the slat only.

It is interesting to note that although the 35° slat, being more highly loaded had a much higher peak suction than the 45° slat at the lower Mach numbers, at $M_0 = 0.28$ the peak suctions for the two deflections have very similar values, at least on the outboard wing. This suggests that there is an effective limit imposed on C_{pmin}, presumably by compressibility effects. This feature is illustrated in Fig 16 which shows the overall C_{pmin} plotted against M_0 for both slat deflection angles at two slat positions for each. Also shown on this plot is the variation of a maximum C_p as derived by Mayer[6]. Mayer's empirical criterion states that

$$-C_pM^2 < 1$$

compared to the theoretical limit of 1.4.

The Mayer expression gives $C_p = -12.75$ at $M_0 = 0.28$ which is very close to the apparent limiting value at this M_0 from the present tests, as seen in Fig 16, although Mayer's result was obtained from tests on a simple aerofoil at rather higher Mach numbers. This effective limit on C_{pmin} has implications for other aspects of the results, as will be seen later.

It has been shown that supersonic local velocities exist on the slat and wing leading-edges at the higher freestream Mach numbers. Using the expression given in the Annex, the combat aircraft configuration can be seen to generate local Mach numbers of up to about 1.5.

Comparison with the results for the lower sweep, high aspect-ratio case also shown in Fig 16 shows that for this latter the peak local suctions are appreciably lower, with correspondingly lower M_{local}, and that in this case the C_{pmin} is not high enough to assess whether it too conforms to the Mayer criterion. On the other hand, the large loss of C_{Lmax} experienced by the fighter configuration at the highest M_0 appears to coincide with C_{pmin} reaching the limiting value suggested by this criterion. It is postulated that the Mayer criterion may describe a 'primary' inviscid effect in which local velocity is limited by compressibility, while the more general case of loss of C_{Lmax} with increasing M_0 is a 'secondary' effect in which the boundary-layer is thickened by compressibility and results in earlier flow separation.

It would appear then that the sudden loss of C_{Lmax} between the two highest freestream Mach numbers for the combat aircraft is associated both with the spread of local supersonic flow inboard on the slat *and* wing which could give rise to compressibility-induced boundary-layer thickening resulting in an earlier stall, and also with a direct limit imposed on the maximum value of C_{pmin}, as suggested by the Mayer criterion.

4.3.2 Effect on Optimum Slat Deflection

Fig 17 shows the variation of C_{Lmax} with slat deflection angle over the range of M_0, for the plain trailing-edge configuration.

The C_{Lmax} data for the 25° and 35° are the highest achieved values, while those for the 45° slat are the optimum values. Compared with the 35° slat C_{Lmax} is *lower* at 45° deflection for $M_0 = 0.16$ and 0.22, even with the 35° slat in a non-optimum position. At $M_0 = 0.28$ the 45° develops the slightly higher C_{Lmax} - this is possibly because the 35° slat, being more highly loaded, suffers more from compressibility limitation at this higher M_0.

4.3.3 Effect on Slat Optimum

In Fig 18, the optimum values of x_s and z_s are plotted against M_0 for the 35° and 45° slat deflections, at one value of Re. As with the variation with Reynolds number, the movements are fairly small compared with the accuracy of the optimum position data.

It is to be expected that any effects due to compressibility depend on the relative loading of the slat and the wing. Hence the movement of the 35° slat optimum away from the wing initially and then back towards it as M_0 is increased may be due to the appearance of supersonic flow first on the slat and then on the wing. The 45° slat may behave differently as supersonic flow appears on the slat and wing roughly simultaneously. This will be discussed in more depth in the following section.

Fig 19 shows the overall effect of fixing the slat position for the full range of M_0, compared with re-optimising the slat at each M_0. The relative effects for the two slat deflections are shown. It is seen that the potential loss in C_{Lmax} for the 35° is about 0.05 at the highest M_0, while the 45° shows an appreciably smaller loss of about 0.01, and even the 're-optimised' 35° slat has a lower C_{Lmax} than the re-optimised 45° slat.

4.3.4 Variation of Local Mach Number

In section 4.3.1 it was shown that the high levels of peak suction on the slat and wing leading-edges were associated with local supersonic velocities, and in the discussion on slat optimisation in section 4.3.3 it was suggested that the optimum slat position could be influenced by the variation of M_{local} on these components.

Figs 20a to 20f shows the variation of the peak M_{local} on the wing and slat for both slat deflections at $M_0 = 0.16$, 0.22 and 0.28, at the outboard pressure plotting station. Also shown on the plots are the optimum slat locations as discussed in section 4.1.2. It will be seen that several of these plots have a rather 'confused' appearance, while others show a well ordered variation of peak M_{local} with slat position. The most likely explanation for this feature is that due to the sharpness of the suction peaks near C_{Lmax}, it is quite possible that there would not have been a pressure tapping coincident with the maximum suction, and the apparent value of C_{pmin} may well be in error by a significant amount. For example, if at $M_0 = 0.22$ the true C_{pmin} is -15, but the maximum recorded value is -14, the resulting error in peak M_{local} is about 0.05. It will be seen that adjustment of some of the points in the peak M_{local} plots by increments of this order could result in a much more ordered appearance.

Bearing this point in mind, the plots in Fig 20 do show some interesting features which reflect the overall variation of C_{Lmax}. Firstly, it is seen that peak M_{local} increases as expected with M_0, from totally subsonic values at $M_0 = 0.16$, to a mix of subsonic and supersonic at $M_0 = 0.22$, to almost totally supersonic values at $M_0 = 0.28$, as seen in section 4.3.1. At the highest M_0 (Figs 20e&f) the maximum peak M_{local} approaches 1.5 which corresponds to a value of C_{pmin} which comes close to satisfying Mayer's criterion as discussed in section 4.3.1. As M_0 is increased it is also obvious that the total variation of peak M_{local} over the range of slat movement also increases. This is consistent with the expression for M_{local} given in the Annex which shows that the calculated value becomes more sensitive to C_p as M_0 is increased. This effect is probably partially responsible for the less well-ordered examples of the variation of peak M_{local} with slat position. It is possible that it also has some influence on the location of the optimum slat position, at the highest M_0 at least, as will be discussed shortly.

It may also be seen that the variation of peak M_{local} for the two slat deflections differs significantly, at $M_0 = 0.28$ in particular. At this M_0 the 35° slat (Fig 20e) shows quite a small range of peak M_{local} but fairly large on the wing, while the 45° slat has a very large range of peak M_{local} and the wing has a very small range. It will be noted that in both cases the maximum value of peak local Mach number is generally close to 1.5, which, as has been seen, approximately satisfies Mayer's criterion, and this appears to impose a limit on the amount of load the slat or wing can carry. The 35° slat, being already highly loaded, quickly reaches the 'Mayer limit' as it is moved towards the wing, while the less highly loaded 45° slat is able to increase its peak M_{local} a large amount before the this limit is reached. In the latter case the wing has a peak M_{local} near 1.5 over the whole slat adjustment range, and so is near the limit suggested by Mayer, whatever the slat position. The effect is further demonstrated as M_0 is reduced (Fig 20d), where we see a much more 'balanced' variation of peak M_{local} on the slat and wing, and at these lower freestream Mach numbers the 'Mayer limit' is no longer being reached on either component.

This concept of a limiting value of C_{pmin}, and hence M_{local} adds a further parameter to the variation of the optimum slat position with M_0. As the highest freestream Mach number is approached the peak M_{local} on the slat and wing tend to have very similar values at the optimum slat setting, and this value is close to the limit suggested by Mayer. This effect is most noticeable for the 35° slat which has large differences in peak M_{local} between slat and wing at the lower M_0's. At $M_0 = 0.28$ the load on this slat therefore appears to be limited to a greater degree than for the 45° deflection. This is consistent with the earlier results for the variation of C_{Lmax} with slat deflection and M_0.

Referring to the discussion of the movement of the slat optimum with M_0 in section 4.3.3, the increase of M_0 from 0.22 to 0.28 results in a much larger shift of the optimum position towards the wing than for the increase from 0.16 to 0.22. This, as shown in Fig 20f is where the peak values of M_{local} on the wing start to reach the 'Mayer limit', and the optimum is determined solely by the maximum load on the slat, which itself is imposed by a balance of the limiting value of C_{pmin} and the slat wake/wing boundary-layer interaction.

It will be noted that the foregoing only considers data from the pressure plotting station near the wing tip. The results from the mid semi-span station have not been fully analysed, but due to the higher peak suctions in the tip region, the limiting values suggested by Mayer are not reached further inboard.

5 SYNOPSIS

Fig 21 shows the overall variation of C_{Lmax} with M_0 and Re for one slat deflection and position for the fighter configuration, with the corresponding plot for the transport aircraft. This summarises the relative effects of Reynolds number and Mach number as well as the fundamental differences between the two configurations. It must be borne in mind that any differences in absolute values of C_{Lmax} between the two configurations can be attributed at least in part to differences in flap size, type and deflection. The rate of change of C_{Lmax} with Reynolds number is remarkably similar for the two configurations, and the only significant difference would seem to be the sensitivity to M_0.

The increments in C_{Lmax} associated with slat re-optimisation (*ie* up to 0.05), discussed in sections 4.2.2 and 4.3.3, are seen to be significant in terms of total C_{Lmax}.

6 CONCLUSIONS

Tests have been carried out in the DRA Farnborough UK 5 metre wind tunnel on a model which represents a fighter configuration with a low aspect-ratio, high mounted swept wing with a supercritical section profile. The model had two basic configurations, one with a plain, undeflected wing trailing-edge, and the other with a single-slotted flap. Both configurations had a leading-edge slat with three available deflection angles, 25°,35° and 45°, although only the two higher deflections were tested with the slotted flap.

The purpose of the tests was:

(a) to examine the overall characteristics of the configuration and how these were influenced by scale and compressibility effects.

(b) to determine the optimum deflection angle and location of the slat, and

(c) to investigate how these optima varied with Mach number and Reynolds number.

To achieve these aims, overall forces and moments were measured, and surface pressures were recorded at two spanwise locations.

The main conclusions obtained from the results are:

(1) The configuration develops a high C_{Lmax} but the lift-curve slope is low as would be expected for the low aspect-ratio, resulting in a very high angle of incidence at C_{Lmax}.

(2) The slat deflection angle for optimum C_{Lmax} is between 10° and 20° higher than the typical value for a transport aircraft.

(3) The 25° and 35° slat deflections result in optimum positions which are at large values of underlap. The optimum for the 35° slat in particular is about 2% wing chord further forward than that for the 45° deflection. For an actual aircraft design, the slat brackets necessary to achieve either this large underlap or the large deflection angles involved might be difficult to incorporate in a relatively thin fighter wing. However, since the 35° slat achieves similar values of C_{Lmax} to the 45° deflection even when at a non-optimum position, it could be used at a similar value of underlap to that at the 45° optimum with only a small penalty in C_{Lmax}.

(4) C_{Lmax} shows a similar sensitivity to Reynolds number as for a typical transport aircraft. Mach number effects were quite large, particularly for values of M_0 above 0.22. This appeared to be associated with the appearance of local supersonic flow over the leading-edge, as established from the measurement of surface pressures. The values of peak C_{pmin} measured at the highest M_0 were close to those predicted by the empirical relationship of Mayer.

(5) The positions of the slat optima show small movements with Mach number and Reynolds number. The increase in C_{Lmax} for the 35° slat if it is re-optimised as M_0 and Re are varied is fairly large, with much smaller corresponding gains for the 45° slat.

(6) Consideration of the variation of the peak local Mach number on the slat and wing leading-edges near the tip shows that at freestream Mach numbers approaching 0.28, the optimum slat position coincides with an apparent limiting value of peak M_{local}. This limit appears to be close to the value predicted by Mayer's empirical relationship.

Table 1

Model Data

Quantity	Symbol	Value
Span	2s	2.700 m
Area	S	2.1465 m^2
Aspect ratio	AR	3.4
Centre-line chord	C_0	1.200 m
Tip chord	C_T	0.390 m
Mean chord	$\bar{c}$	0.795 m
	$\bar{\bar{c}}$	0.864 m
Taper ratio	λ	0.325
Leading-edge sweep	Λ	40°
Slat chord	C_s/C	18%
Flap chord	C_f/C	33%
Thickness/chord ratio	t/c	8%

Table 2

Test Conditions and Slat Positions

M	R × 10^{-6}
0.11	5.87
0.16	5.87
0.16	8.81
0.22	5.87
0.22	8.81
0.22	11.23
0.28	5.87
0.28	8.81
0.28	11.23

R is based on $\bar{\bar{c}} = 0.864$ m

$\theta_s = 35°$

x_s%	z_s%
-2	1.5
-3	-1
-3	0
-3	0.75
-3	1.5
-4	-1
-4	-0.5
-4	0
-4	0.75
-4	1.5
-5	-1
-5	0
-5	0.75
-5	1.5

$\theta_s = 45°$

x_s%	z_s%
-1	-1
-1	0
-1	0.75
-1	1.5
-2	-1
-2	-0.5
-2	0
-2	0.75
-2	1.5
-3	-1
-3	-0.5
-3	0
-3	0.75
-3	1.5

REFERENCES

1 Smith, A.M.O., "Aerodynamics of High-Lift Aerofoil Systems", *in* "Fluid Dynamics of Aircraft Stalling", AGARD CP 102, April 1972

2 Foster, D.N., Irwin, H.P.A.H. and Williams, B.R., "The Two-Dimensional Flow Around a Slotted Flap", RAE Technical Report 70164 (1970)

3 Hardy, B.C., "An Investigation of a Proposal to Extend the Use of MAVIS to Three-Dimensional Wings", RAE Technical Memorandum Aero 1840 (1980)

4 Moir, I.R.M., "A Description of a Typical Strike-Fighter Model for the RAE 5 metre Wind-Tunnel (model 495) and its Associated Half Model (model 2113)", RAE Technical Report 81022 (1981)

5 Spence, A., Woodward, D.S., Caiger, M.T., Sadler, A.J., Jeffery, R.W., "The RAE 5 metre Pressurised Low-Speed Wind Tunnel", ICAS Paper B3-05, June 1978

6 Smith, A.M.O., "Remarks on Fluid Mechanics of the Stall", *in* "Aircraft Stalling and Buffeting", AGARD Lecture Series No.74, March 1975

Annex

EFFECT OF WING SWEEP ON CRITICAL PRESSURE COEFFICIENT

A useful indicator of likely compressibility effects is the local Mach number based upon the component of velocity normal to a given sweep line. To obtain a value for the local Mach number, it is necessary to make the assumption that the flow at the spanwise station where the pressure is measured locally approximates to that on an infinite sheared wing, *ie* the spanwise component of velocity is constant and equal to $V \sin \Lambda$. With this assumption the local Mach number normal to the sweep line is given by

$$M_{local}^2 = \frac{2}{\gamma - 1}\left[\frac{1 + \left((\gamma - 1)/2\right)M_0^2 \cos^2\Lambda}{\left(1 + C_p(\gamma/2)M_0^2\right)^{(\gamma-1)/\gamma}} - 1\right] . \qquad \text{(A-1)}$$

Putting $M_{local} = 1$ we obtain

$$C_p^* = \frac{2}{\gamma M_0^2}\left[\left\{\frac{2}{\gamma+1} + \left(\frac{\gamma-1}{\gamma+1}\right) M^2 \cos^2\Lambda\right\}^{\gamma/(\gamma-1)} - 1\right] . \qquad \text{...... (A-2)}$$

Expanding this for small M_0 ;

$$= \left(\left(\frac{2}{\gamma+1}\right)^{\gamma/(\gamma-1)} - 1\right)\frac{2}{\gamma M_0^2}$$

$$+ \left(\frac{2}{\gamma+1}\right)^{\gamma/(\gamma-1)} \cos^2\Lambda + 0\left(M_0^2 \cos^4\Lambda\right) . \qquad \text{(A-3)}$$

Taking $\gamma = 1.4$, this gives:

$$C_p^* = -\frac{0.6739}{M_0^2} + 0.5283 \cos^2\Lambda + 0\left(M_0^2 \cos^4\Lambda\right) . \qquad \text{...... (A-4)}$$

Thus, for low values of M_0 (a maximum of 0.28 here) it is the first term that is dominant and rapidly varying and C_p^* is only made more negative by a relatively small amount by increasing sweep as indicated by the typical values for the two major terms in (A-4).

M_0	$0.6739/M_0^2$	Λ°	$0.5283 \cos^2\Lambda$
0.11	55.694	10	0.5224
0.16	26.324	20	0.4665
0.22	13.924	30	0.3962
0.28	8.596	40	0.3100
		50	0.2183

Hence the maximum error due to ignoring the term in Λ is about 6%.

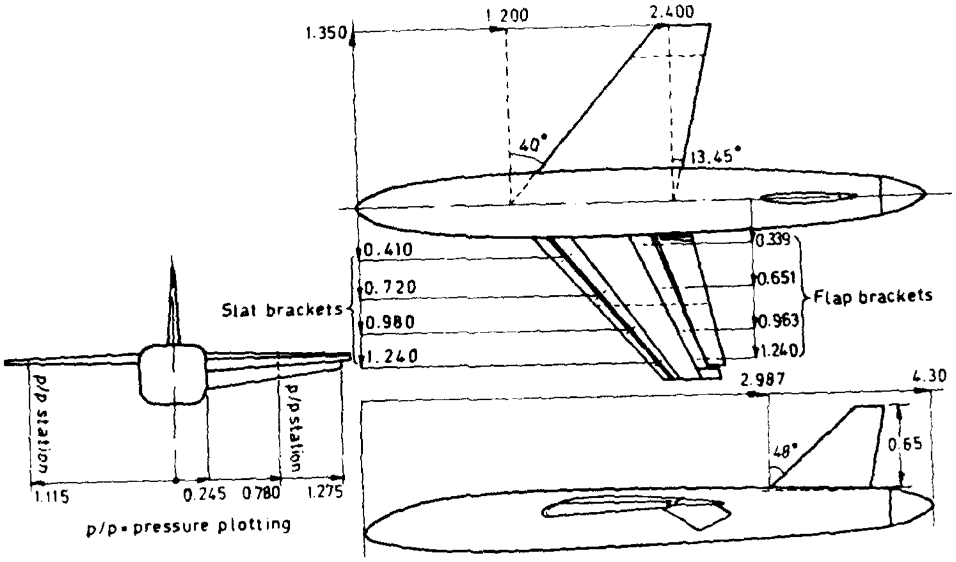

Fig 1 Combat aircraft model (M495)

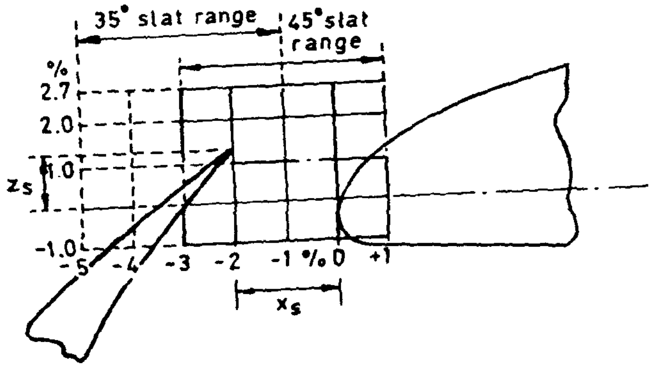

Fig 2 Slat adjustment ranges

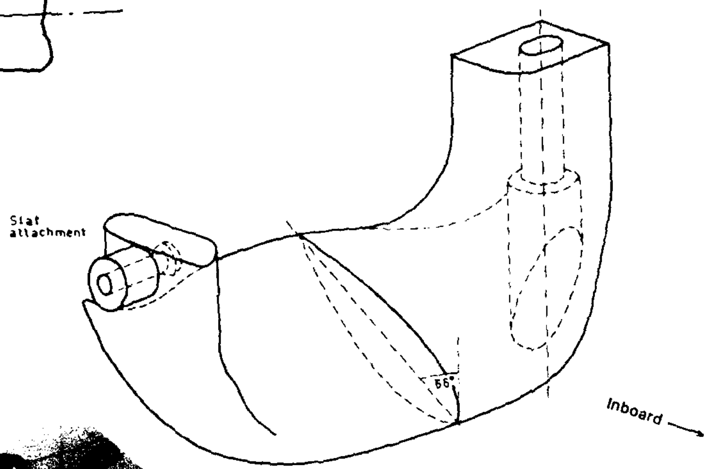

Fig 3 Profiled slat bracket

Fig 4 Model 495 in DRA 5 metre wind tunnel

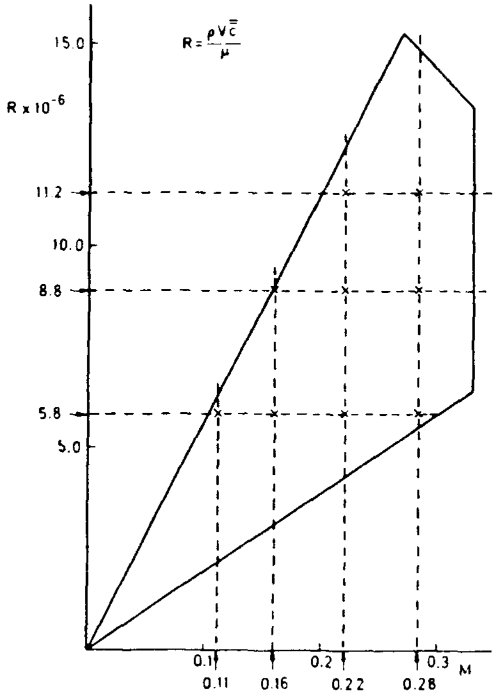

Fig 5 Tunnel envelope and M495 test conditions

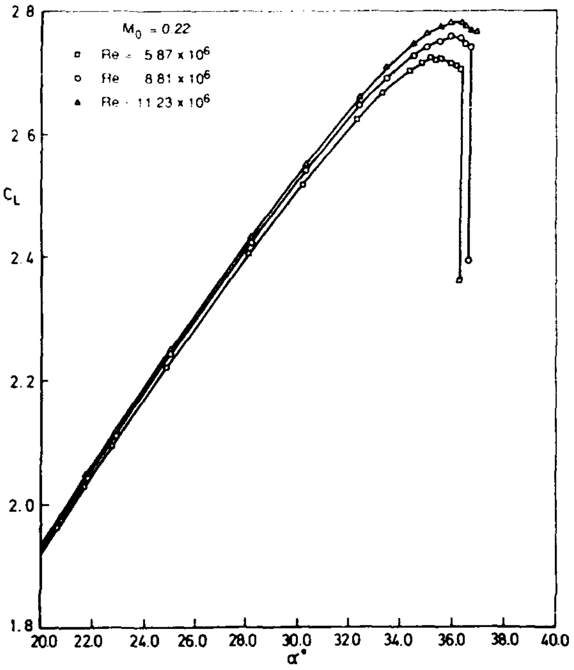

Fig 6a Variation of lift coefficient with angle of incidence and Reynolds number

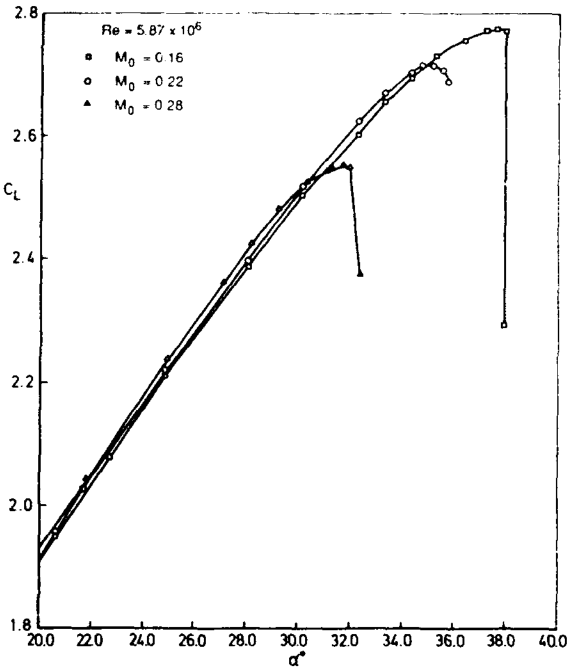

Fig 6b Variation of lift coefficient with angle of incidence and Mach number

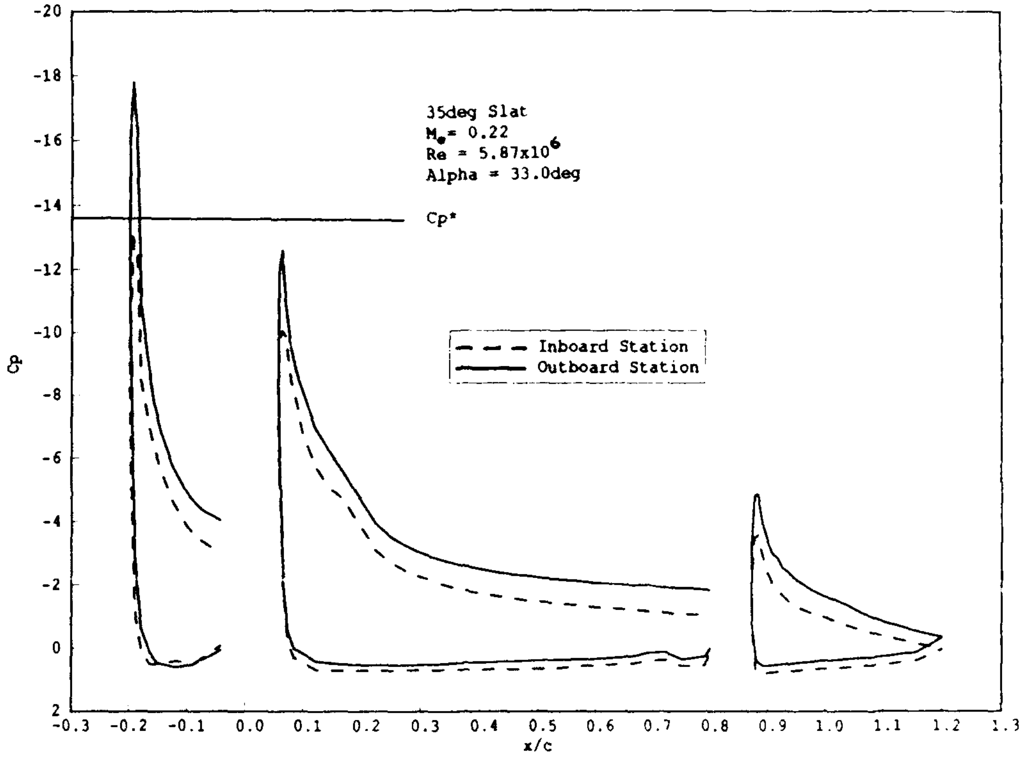

Fig 7a Comparison of chordwise variation of pressure coefficient for inboard and outboard stations of combat aircraft configuration

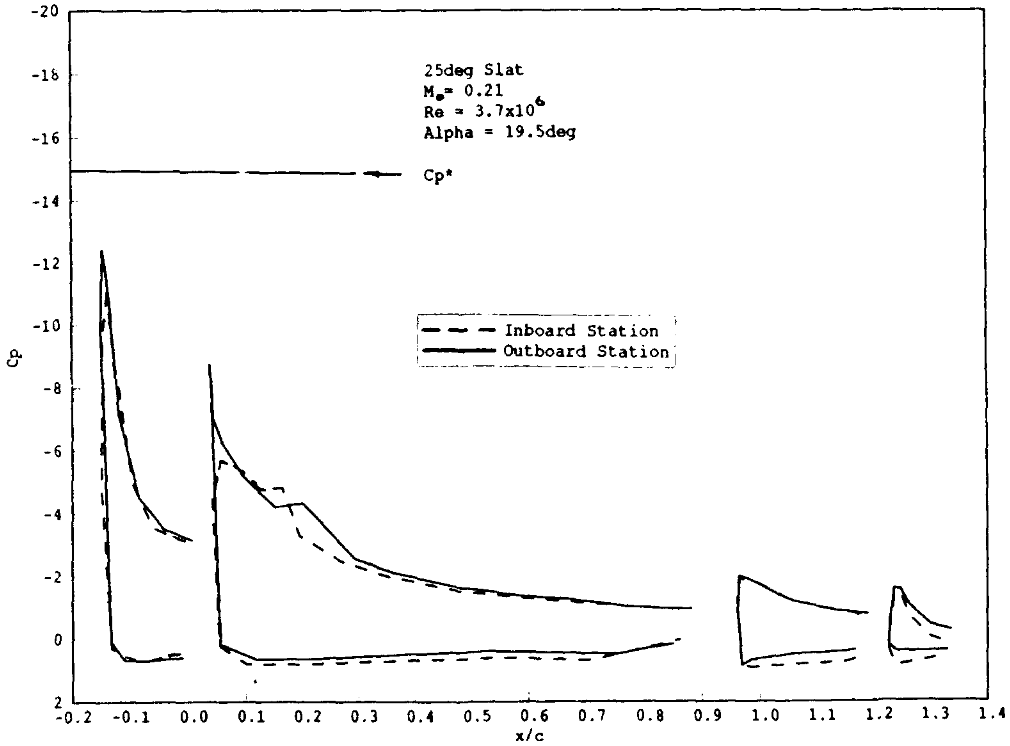

Fig 7b Comparison of chordwise variation of pressure coefficient for inboard and outboard stations of transport aircraft configuration

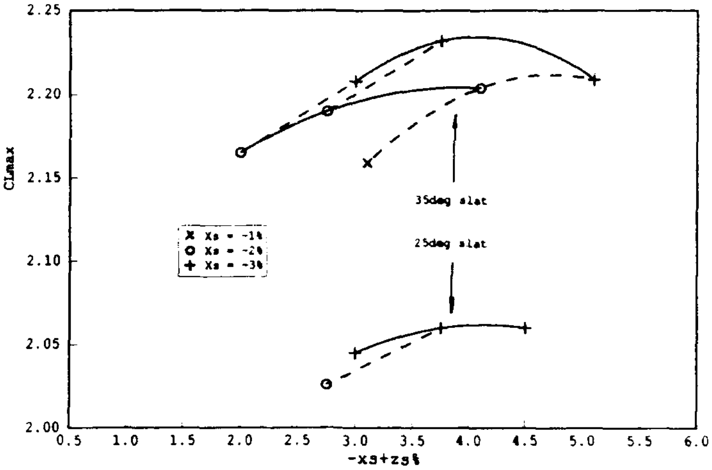

Fig 8a Variation of C_{Lmax} with slat position, for slat angles 25° and 35°, M_o=0.22, Re=5.87 x 10^6, plain trailing edge configuration

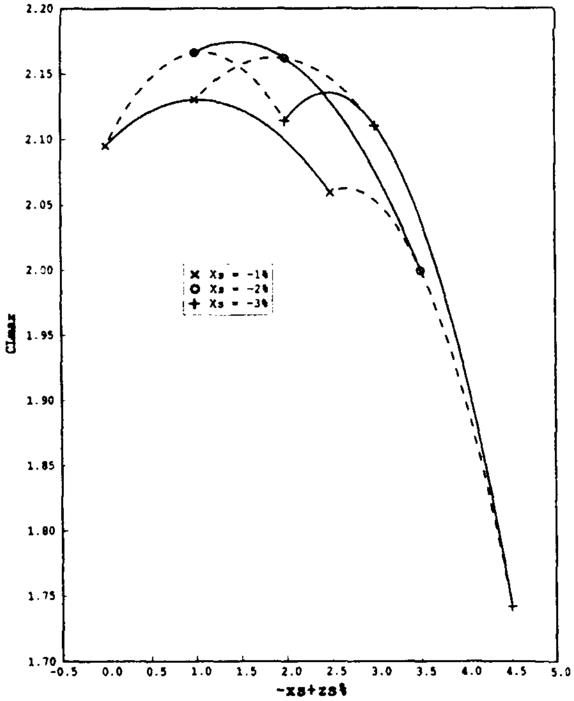

Fig 8b Variation of C_{Lmax} with slat position, for slat angles 25° and 35°, M_o=0.22, Re=5.87 x 10^6, plain trailing edge configuration

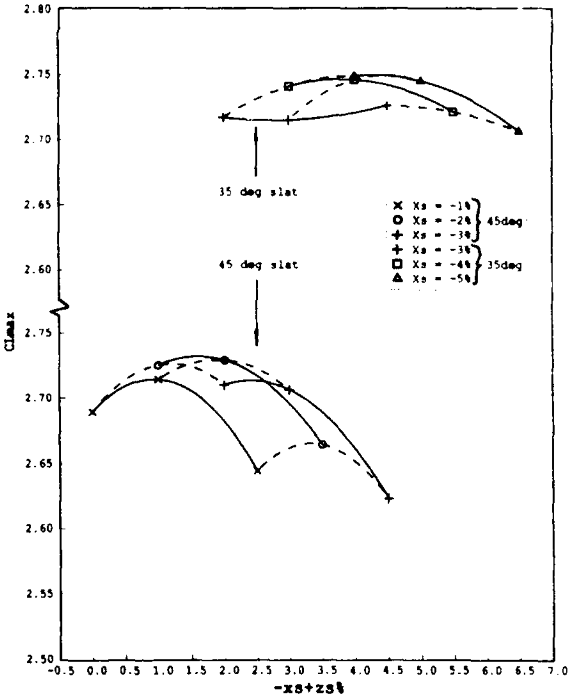

Fig 9 Variation of C_{Lmax} with slat position, 45°slat, M_o=0.22, Re=5.87 x 10^6, slotted flap configuration

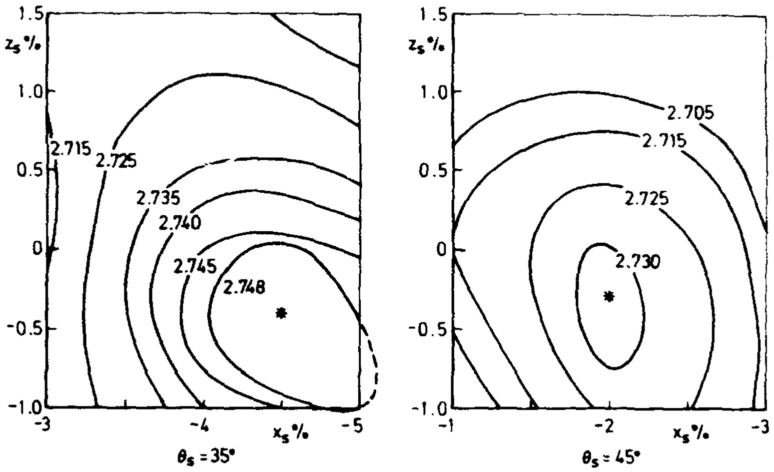

Fig 10 Variation of C_{Lmax} with slat position, M_o=0.22, Re=5.87 x 10^6

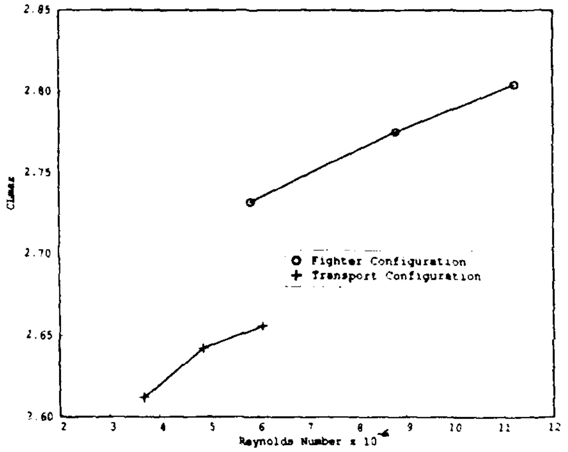

Fig 11 Comparison of variation of C_{Lmax} with Reynolds number for combat aircraft and transport aircraft

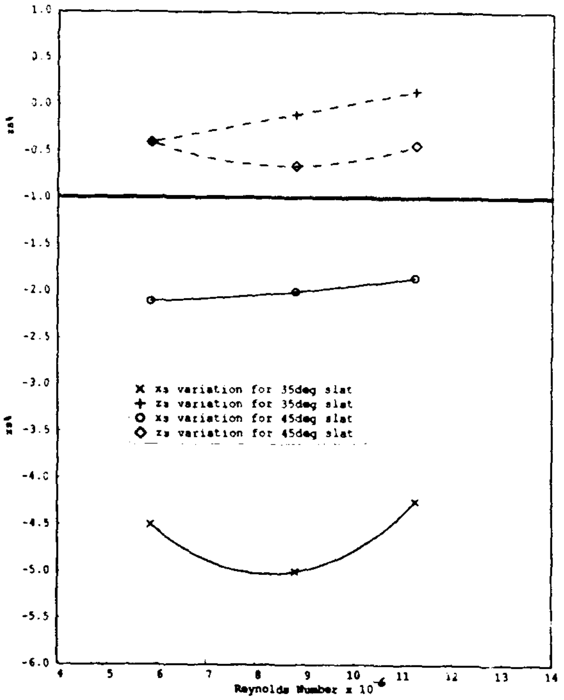

Fig 12 Variation of optimum slat position with Reynolds number

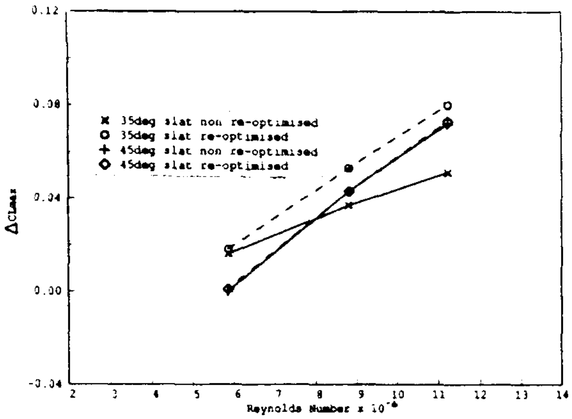

Fig 13 Gain in C_{Lmax} obtained by re-optimising slat position at each Reynolds number

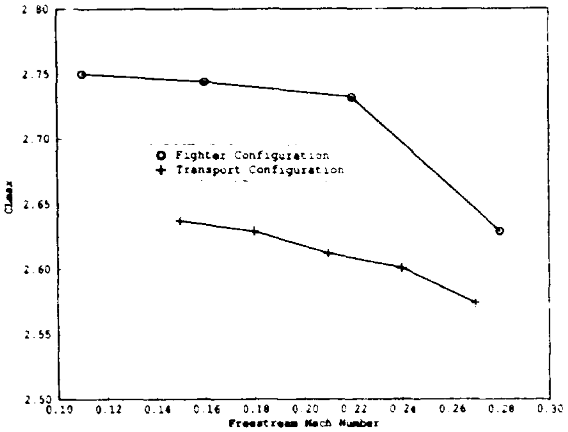

Fig 14 Comparison of variation of C_{Lmax} with Mach number for combat aircraft and transport aircraft

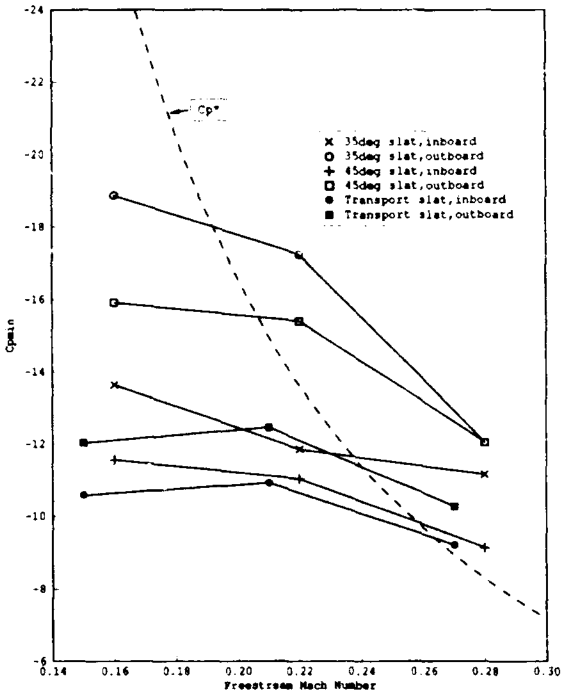

Fig 15a Variation of C_{Pmin} on slat with freestream Mach number

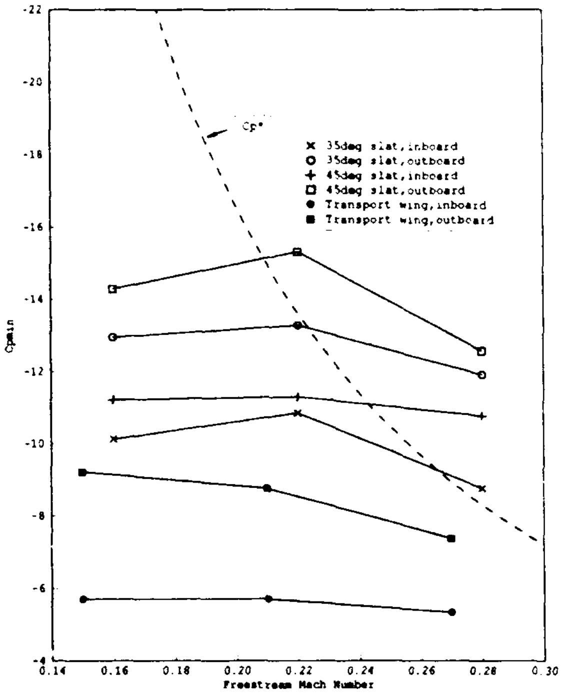

Fig 15b Variation of C_{Pmin} on wing with freestream Mach number

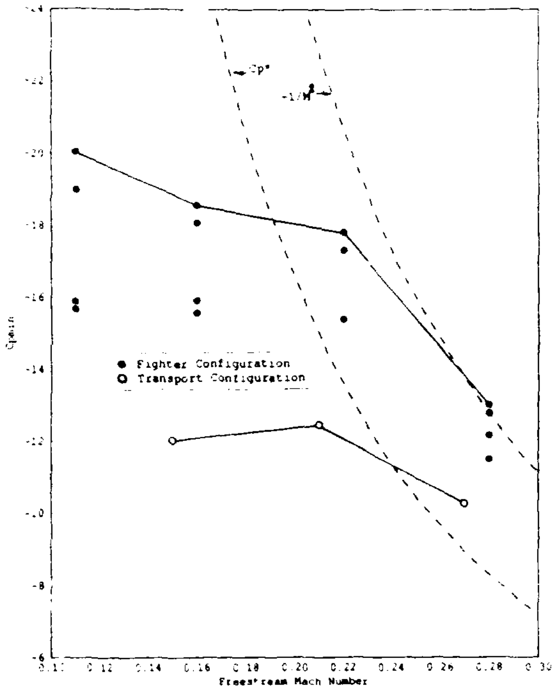

Fig 16 Variation of peak suction with freestream Mach number, indicating 'Mayer Limit'

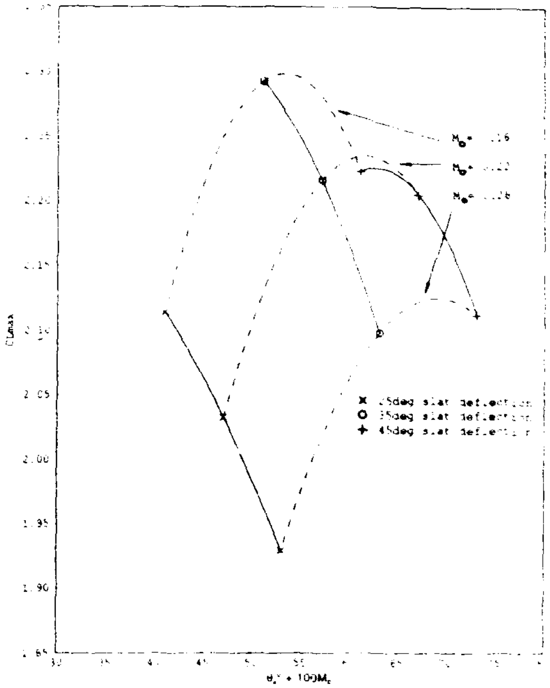

Fig 17 Variation of C_{Lmax} with slat deflection and Mach number. Plain trailing edge configuration

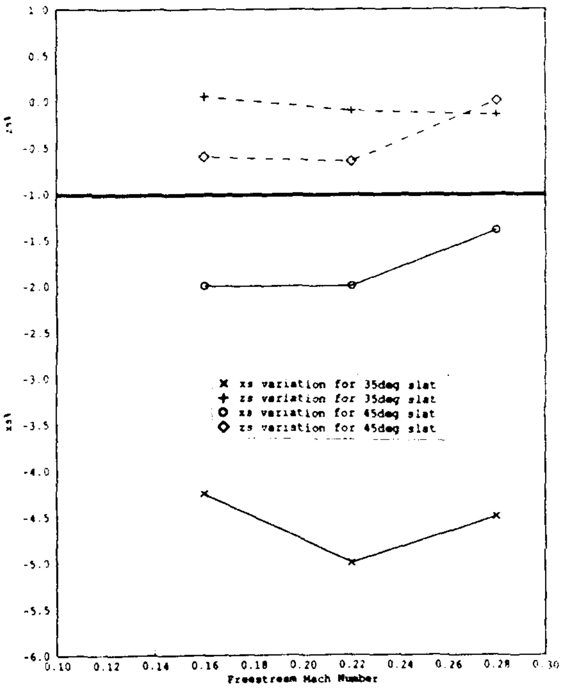

Fig 18 Variation of optimum slat position with Mach number

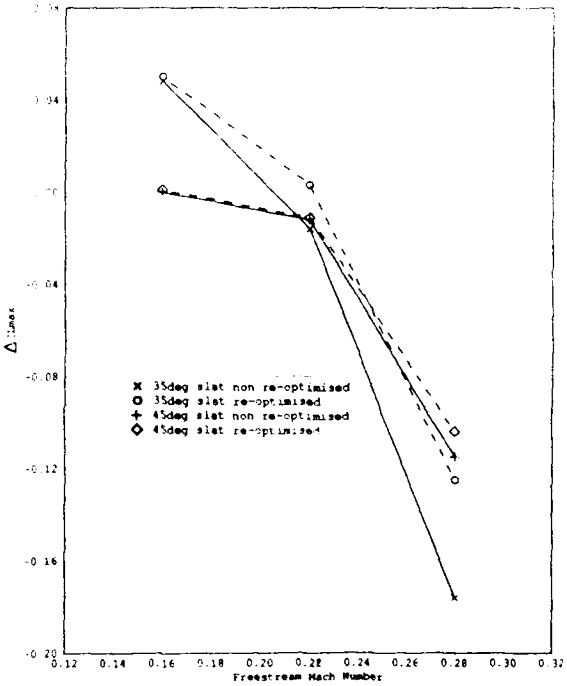

Fig 19 Gain in C_{Lmax} obtained by re-optimising slat position at each Mach number

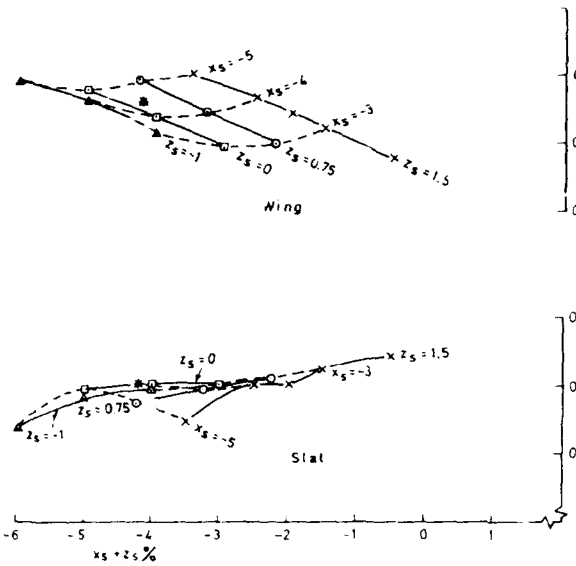

Fig 20a Variation of peak local Mach number with slat position, $\theta_s=35°$, $M_o=0.16$, $Re=11.23 \times 10^6$

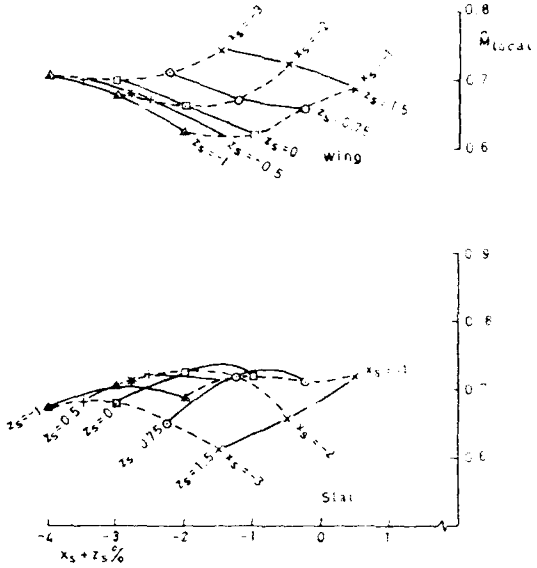

Fig 20b Variation of peak local Mach number with slat position, $\theta_s=45°$, $M_o=0.16$, $Re=11.23 \times 10^6$

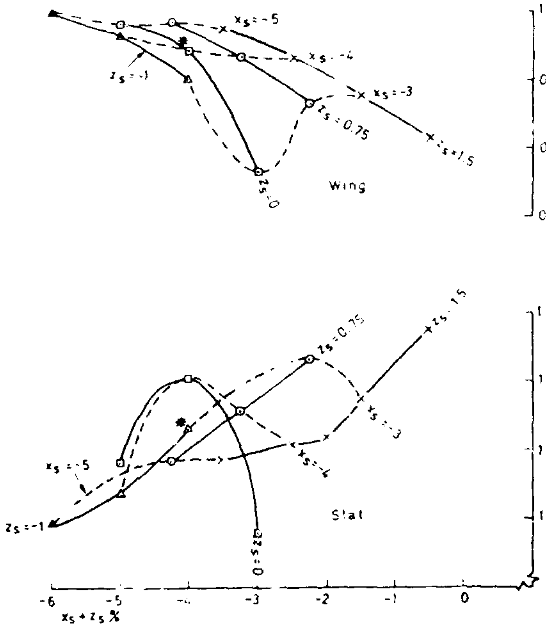

Fig 20c Variation of peak local Mach number with slat position, $\theta_s=35°$, $M_o=0.22$, $Re=11.23 \times 10^6$

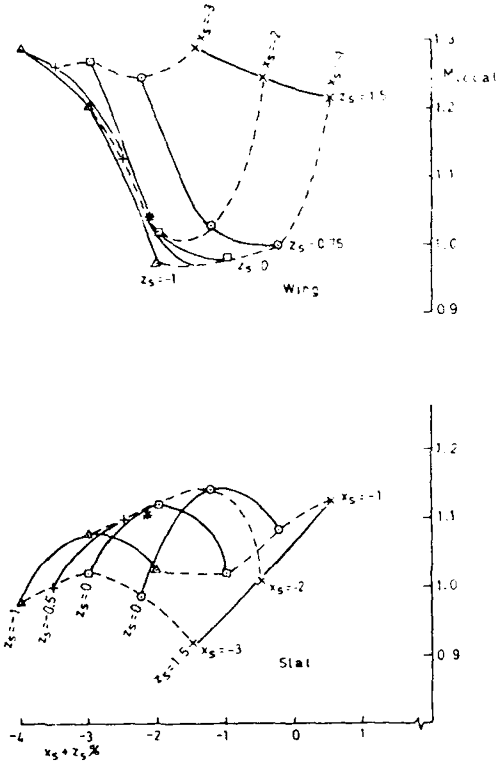

Fig 20d Variation of peak local Mach number with slat position, $\theta_s=45°$, $M_o=0.22$, $Re=11.23 \times 10^6$

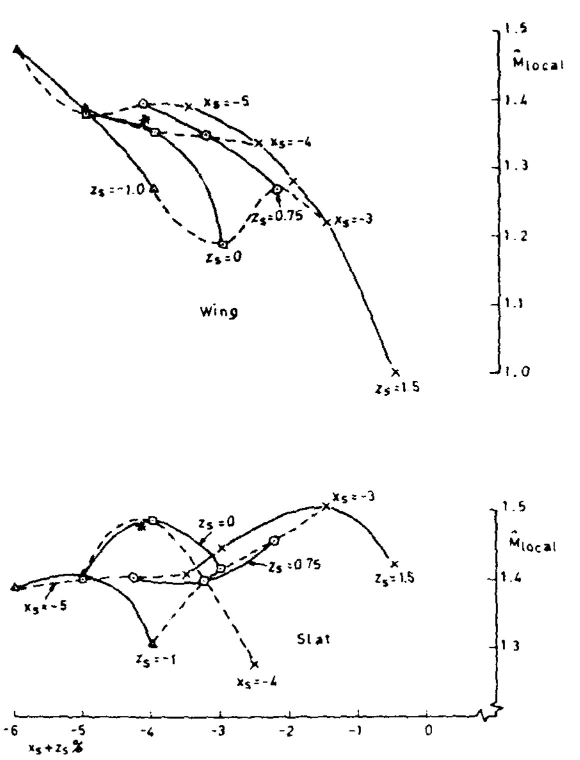

Fig 20e Variation of peak local Mach number with at position, $\theta_s=35°$, $M_o=0.28$, $Re=11.23 \times 10^6$

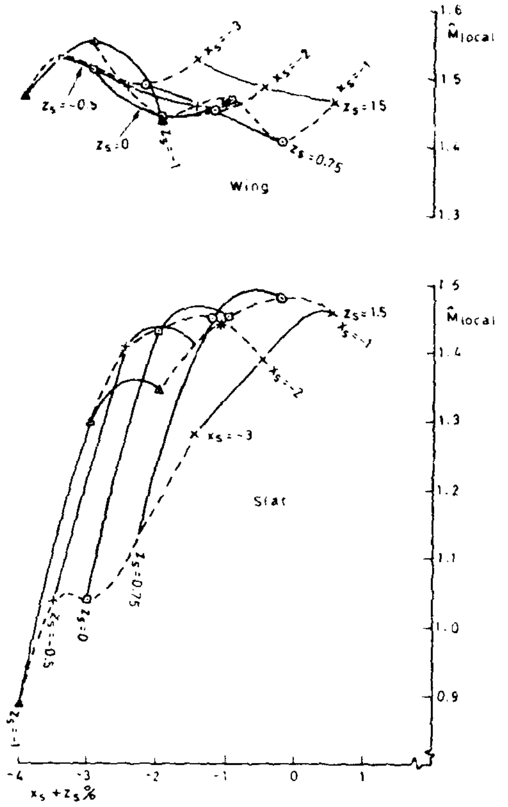

Fig 20f Variation of peak local Mach number with slat position, $\theta_s=45°$, $M_o=0.28$, $Re=11.23 \times 10^6$

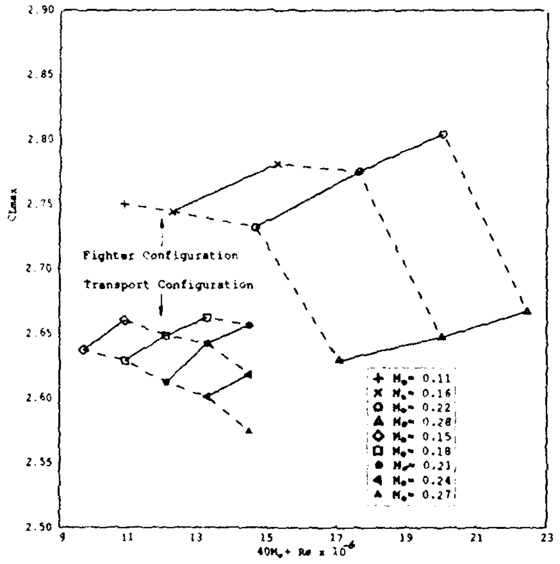

Fig 21 Comparison of variation of C_{Lmax} with M_o & Re for combat and transport aircraft configurations

AN EXPERIMENTAL INVESTIGATION OF ATTACHMENT-LINE TRANSITION ON THE SLAT OF A COMBAT AIRCRAFT MODEL

by

B. C. Hardy

Defence Research Agency
Farnborough Hampshire GU14 6TD
England

SUMMARY

An experimental investigation into scale effect at low speed and high lift has been carried out in the DRA 5 m, pressurised wind tunnel on a subsonic strike-fighter model equipped with slotted high-lift devices. The attachment-line boundary layer on the leading-edge slat was found to be turbulent on the outboard part of the wing near maximum lift for a range of unit Reynolds number. An adverse Reynolds number effect on maximum lift was measured which correlated quite well with the onset of attachment-line transition. The conditions for onset of transition were not consistent with the assumption of gross contamination by the fuselage boundary layer, the attachment-line boundary layer remaining laminar on the inboard slat to more than double the expected free-stream Reynolds number. It is suggested that this result is due to spanwise variation in attachment-line position, which results in suppression of the disturbances emanating from the root region of the high-lift wing. It is concluded that attachment-line transition is a potentially significant factor in wind-tunnel testing of high-lift wings equipped with leading-edge slats.

SYMBOLS

c	wing chord given by $c_{sw} \cos\phi$
c_{sw}	streamwise wing chord
C_{Lmax}	maximum lift coefficient
d	trip wire diameter
K	acceleration parameter
Q_∞	free-stream velocity
q	hot-film power dissipation
R	unit Reynolds number
$\bar{R}$	attachment-line Reynolds number
s	surface distance - Fig 1
U_∞	velocity normal to leading edge - Fig 1
u	velocity normal to attachment line
U_1	attachment-line velocity gradient
V_∞	spanwise component of velocity - Fig 1
x	distance normal to leading edge
α	model incidence
ε	additional spanwise velocity
η	non-dimensional spanwise distance
υ	kinematic viscosity
ϕ	sweep angle
ψ	attachment-line boundary-layer length scale

1 INTRODUCTION

The introduction into service of facilities such as the DRA Farnborough 5 m Low-Speed, Pressurised Wind Tunnel has allowed the effects of Reynolds number and Mach number on aerodynamic performance to be evaluated separately. At the 5 m tunnel, particular attention has been paid to investigating the effects of Reynolds number on the performance of high-lift wings. The impetus for this research comes from the fact that, despite the ability to achieve high Reynolds number through pressurisation, models of large transport aircraft can still only be tested to about ¼ full-scale. There is therefore a need to understand the mechanisms that cause both the Reynolds number effects that occur within the tunnel operating range, and those which might cause similar effects at higher values of Reynolds number – up to full-scale. This paper presents the results of an investigation into one of these mechanisms, and its effects, conducted in the 5 m wind tunnel on a swept-wing strike-fighter model, Model 495 [1]. The model was equipped with a leading-edge slat and single-slotted trailing-edge flap, and the objective of the tests was to investigate the effects of Reynolds number on the slat attachment-line boundary layer, and to evaluate the corresponding overall effects on the high-lift performance.

The position of transition on an aircraft wing can have a significant effect on performance, the laminar-flow wing being an extreme example. The type and location of transition is scale dependent and consequently the correct simulation of full-scale aerodynamics in a wind tunnel requires that these dependencies are understood and accounted for. Broadly speaking there are three distinct types of transition that may be significant in relation to swept wings at high lift:-

(1) Transition following the development of instabilities of the Tollmien-Schlichting type, either in an attached or separated shear layer (*eg* a laminar bubble).

(2) Transition following instability of the cross-flow velocity profile.

(3) Transition following the development of instabilities in a swept, attachment-line boundary layer.

It is the third of these, attachment-line transition, that is the focus of the present investigation. In low-speed, high-lift testing it is usually assumed that the predominant scale effect will be a favourable one, related to a general thinning of the viscous shear layers as the Reynolds number is increased. This assumption implies that the variation of transition position is small over the Reynolds number range of interest. This is generally borne out by two-dimensional calculations and experiments on high-lift configurations, where the characteristically sharp suction peak close to the leading edge of each component tends to 'anchor' transition of the Tollmien-Schlichting type close to the start of the pressure rise. However, this is not necessarily the case for three-dimensional wings, and some time ago Woodward[2] carried out boundary-layer calculations for swept, high-lift wings which indicated that attachment-line transition could supplant Tollmien-Schlichting instability as the primary transition mechanism as Reynolds number was increased. The movement of transition from close to the suction peak to the attachment line with increase in Reynolds number was predicted to result in a significant adverse scale effect on maximum lift due to the increased boundary-layer thickness implied by the forward movement of transition.

These results had important implications for wind-tunnel testing because the transition Reynolds numbers involved were found to be much lower than those relevant to high-speed flow, actually falling within the range covered by modern pressurised wind tunnels. As a consequence of these predictions, a detailed experimental investigation was carried out in the DRA 5 m tunnel using an existing model, Model 495. *In summary, this investigation* showed that attachment-line transition occurred on the slat and that there was an adverse scale effect on maximum lift. Transition on the outer wing developed broadly as predicted by the existing criterion and correlated with the adverse scale effect. On the inner wing, however, transition was delayed to much higher Reynolds numbers, suggesting that contamination of the attachment line by the fuselage-side boundary layer did not occur as expected from previous high-speed experiments. The hot-film instrumentation indicated sudden switching between laminar and turbulent states with change in model incidence, which was difficult to explain, but development of transition with increase in Reynolds number at fixed incidence was found to be monotonic, as expected, and engenders confidence that the unexpected variations with incidence were not spurious.

2 ATTACHMENT-LINE TRANSITION

The flow in the vicinity of the attachment line on a swept wing is illustrated in Fig 1, which is taken from Ref 3. The component of the free-stream velocity along the attachment line gives rise to the attachment-line boundary layer. On an infinite swept wing, the properties of this layer are invariant with distance along the attachment line. However, disturbances can propagate spanwise and, depending on the conditions, instability and transition can occur. Furthermore, because the boundary layers over the wing originate at the attachment-line, transition to turbulence there can result in turbulent flow over the whole wing.

The attachment-line boundary layer is characterised by a Reynolds number, $\bar{R}$, which is a function of the spanwise velocity at the edge of the layer, V, the corresponding kinematic viscosity, υ, and a characteristic length scale, ψ, so that $\bar{R} = V\psi/\upsilon$. A convenient form for ψ, representative of the boundary-layer thickness, is given by

$$\psi = [\upsilon/(du/ds)_{s=0}]^{1/2} \qquad (1)$$

where $(du/ds)_{s=0}$ is the velocity gradient normal to the attachment line at the edge of the boundary layer. For an infinite swept wing the velocity at the edge of the attachment-line boundary layer is given by $V = V_\infty = Q_\infty \sin\phi$, (where Q_∞ is the free-stream velocity and ϕ is the sweep angle) and the Reynolds number, $\bar{R}$, can be written

$$\bar{R} = V\psi/\upsilon = (Rsw/U_1)^{1/2} \sin\phi \ . \qquad (2)$$

Here, Rsw is the free-stream Reynolds number based on a streamwise length, c_{sw}, and U_1 is the non-dimensional attachment-line velocity gradient given by

$$U_1 = (d(u/U_\infty)/d(s/c))_{s=0} \ , \qquad (3)$$

where $U_\infty = Q_\infty \cos\phi$ and $c = c_{sw} \cos\phi$. Equation (2) is a convenient form for $\bar{R}$ and, although derived on the assumption of infinite swept-wing flow, it seems reasonable to use it for three-dimensional wings of moderate aspect ratio, except probably in the root and tip regions.

Transition becomes more likely as $\bar{R}$ is increased and Equation (2) shows that this can occur through an increase in the free-stream Reynolds number or wing sweep angle or through a reduction in the velocity gradient, U_1. The latter implies a reduction in the rate at which fluid is carried away from the attachment line and hence a thickening of the boundary layer there. The value of U_1 depends on the chordwise velocity distribution near the attachment line which is largely determined by the local surface shape. Fig 2 shows schematically the importance of this fact in distinguishing between the high-speed or cruise condition and the low-speed, high-lift condition. For the high-speed case the figure shows the attachment line near the aerofoil nose where the high curvature results in U_1 values of around 100, whereas for the low-speed case the attachment line is shown lying further aft on the lower surface where the curvature is much lower and U_1 values of around 5 (for the main wing) to 20 (for the slat) are more typical. The significance of these values is that, according to the existing criterion for infinite swept wings, they imply transition at the attachment line for some typical high-lift models in wind tunnels such as the DRA 5 m.

3 OTHER INVESTIGATIONS

The mechanism of attachment-line transition was first recognised as such during attempts by aircraft manufacturers (notably Northrop and Handley-Page) to construct laminar-flow swept wings in the early part of the 1960s. Much less laminar flow than expected was found in flight and tunnel tests and it was discovered that disturbances generated in the wing-body junction triggered attachment-line transition and hence ensured that whole wing was covered in a turbulent boundary layer. Subsequently, more detailed investigations[5-8] were made in an attempt to clarify the conditions necessary for the onset of attachment-line transition. This work ended in the early 1970s and little further was done until Poll[3,4] published the results of an extensive series of experiments on attachment-line transition and cross-flow instability in 1978.

These experiments were carried out using a swept-cylinder model which was mounted so as to eliminate the large disturbances to the boundary layer which normally arise from the root or wing-body junction. Poll was thus able to investigate the effects of artificially tripping the boundary layer. Whilst largely confirming the earlier results of Cumpsty and Head[7] and Gaster[8], which suggested that attachment-line transition following gross contamination could be characterised by a single value of $\bar{R}$ for all sweep angles and tunnel speeds, Poll was able to discover detailed results for the variation of the critical $\bar{R}$ to produce turbulence at a particular position on the attachment line with varying trip size and location. This work was extended by Paisley and Poll[9] using a tapered, swept cylinder so that the three-dimensional effects of spanwise taper were included in the experiment. This showed that the earlier 'infinite swept wing' results could be applied to the the tapered cylinder, although there was some change in the critical trip sizes.

More recently, an experimental investigation[10] into attachment-line transition on a model representative of a transport aircraft has been carried out in the DRA 5 m tunnel. The development of attachment-line transition on the unslatted leading edge of this model was clearly seen and significant differences from previous, infinite-swept results were found, but no adverse scale effect on maximum lift was observed. Relaminarisation in the favourable pressure gradient between the attachment line and the peak suction location was suggested as the probable cause of the latter result. This suggestion was based on evaluation of the acceleration parameter, K, which, in terms of velocity and distance along a streamline, is given by $\upsilon(du/ds)/u^2$. Strong favourable pressure gradients combined with low velocities lead to high value of K and a tendency to relaminarise. According to the existing criteria[4,11,12] the values of K found in Ref 10 indicated that relaminarisation was likely. It was conjectured that the expected adverse effects would be postponed by relaminarisation to higher, but less than full-scale Reynolds numbers, and it was pointed out that this could make extrapolation to full scale uncertain in some cases. Garner[13] discusses the results of similar tests also carried out in the 5 m tunnel, but on larger models, which showed very large adverse scale effects on maximum lift. On a simple wing a 7% loss was observed and evidence was found that relaminarisation occurred over the whole span at lower Reynolds numbers but only outboard at higher values. Using a specially designed leading edge, relaminarisation was eliminated and a 15% adverse scale effect on maximum lift was found. Garner observed that such large effects represent undesirable risks in scaling wind-tunnel data to flight Reynolds number.

4 MODEL AND INSTRUMENTATION

Although it was anticipated that investigation of the slat attachment-line flow would present some problems because of the proximity of the sharp slat heel (Figs 2 and 3), it was considered that the predominance of slats on modern aircraft made this a configuration of considerable interest. The choice of model was dictated by the requirement that attachment-line transition should occur within the operating envelope of the 5 m tunnel. Two-dimensional calculations coupled with simple sweep theory indicated that, on the basis of the existing criterion, Model 495 would satisfy this requirement. A full description of this model has been given by Moir[1]. It is a large, complete model representative of a subsonic strike-fighter aircraft, built to approximately one third scale. The wing planform is shown in Fig 3. A useful feature of the model for the present tests was the special slat-bracket design which, by aligning the bracket camber surface with the local flow direction at high lift, greatly reduced the flow disturbances which usually arise from the separated flows found on conventional slat brackets. For the tests reported here, the high-lift devices were deployed in a typical take-off condition with the single-slotted flap at 20 degrees deflection, and the 18% chord slat at 35 degrees deflection, measured normal to the slat quarter-chord line. The slat was positioned close to the optimum location relative to the wing for maximum lift at this angle.

The wings were equipped for pressure measurement at the three spanwise locations shown in Fig 3. The distribution of the pressure taps around the slat profile is also shown in this figure. The pressures were measured using rotary scanning switches in conjunction with Druck pressure transducers, and overall forces were measured by the under-floor, six component mechanical balance. The primary instrumentation consisted of three hot-film gauges located as indicated in Fig 3. These gauges (Dantec 55R47 glue-on probes) were positioned as close as possible to the heel of the slat and so indicated the state of the lower surface boundary layer. This had the dual advantage of eliminating any disturbance to the upper surface boundary layer and ensuring that the gauge signals reflected the state of the attachment-line boundary layer, at least at high lift. The latter follows from the low pressure gradients between the attachment line and the gauge location. The gauges were glued into shallow recesses to minimise interference effects, but were in any case very thin (0.05 mm). Because only a qualitative indication of the boundary layer state was sought, the hot-film gauges were operated in a constant-current mode when observing velocity fluctuations, though a useful additional indication of boundary layer state was provided by the mean values of heat dissipation in the gauges. This quantity was determined by measuring the heating currents required to maintain the gauges at the same mean temperatures for all measurement conditions.

Measurements were made for the single model configuration described above, at a free-stream Mach number of 0.22 and for nine values of Reynolds number between 5.5 and 14.5 million per metre. At each Reynolds number the signals from the hot-film gauges, the pressure transducers and the mechanical balance were recorded for model incidences from zero up to the stall.

5 ANALYSIS OF RESULTS

Analysis of the measurements presented two main problems, determination of the state of the slat attachment-line boundary layer from the hot-film results and estimation of the corresponding values of U_1, and hence $\bar{R}$, from the pressure distributions. As noted above, both mean and fluctuating signals were recorded from the hot-film gauges and these allowed the results to be classified with some confidence as laminar, transitional or turbulent with subsidiary distinctions between laminar-transitional and turbulent-transitional usually possible. The characteristics of the unsteady signals varied greatly with incidence, as illustrated by the examples shown in Fig 4. These results were obtained at a unit Reynolds number of 10.5 million and at moderate incidences of around 20 degrees, where the slat attachment line was close to the leading edge. Over the 1 degree change in incidence covered by Fig 4, the following interpretation was put on the traces;

Incidence	Station 1	Station 2	Station 3
21.5 degrees	turbulent/ transitional	turbulent/ transitional	laminar
22 degrees	laminar/ transitional	laminar/ transitional	laminar
22.5 degrees	turbulent	turbulent	turbulent

Typical variations of the mean signal with incidence are shown in Fig 5 for two unit Reynolds numbers. A histogram style of presentation is used as this better reflects the very sudden changes with incidence which were a feature of the results. The points which correspond to the instantaneous signals shown in Fig 4 are indicated. It should be emphasised that although the hot-film signals changed character rapidly with variation in incidence, the changes were precisely repeatable.

In order to evaluate the attachment-line velocity gradient, U_1, and Reynolds number, $\bar{R}$, using equations (2) and (3), the flow in the vicinity of the attachment line was initially assumed to behave like that on an infinite swept wing with the same sweep angle as the attachment line at the point of interest. This assumption gave a discontinuous variation in velocity normal to the attachment line, from which it was difficult to estimate U_1 accurately. In view of the highly three-dimensional nature of the flow on this wing it was considered reasonable to allow for some divergence from the infinite-swept assumption by defining a small additional spanwise flow component, so that $V = Q_\infty (1 + \varepsilon) \sin \phi$. The value of ε varied with the assumed attachment-line position but exhibited a minimum for a particular location and this was taken to be the appropriate value. This modification resulted in a smooth velocity distributions normal to the attachment line and allowed values of U_1 to be extracted from the measured pressures in a systematic way.

6 RESULTS

6.1 Attachment-line velocity gradient

Values of the attachment-line velocity gradient, U_1, were estimated from the measured pressure distributions, as described as above. This was a somewhat imprecise procedure because of the relative sparsity of chordwise pressure holes but data was recorded for several Reynolds numbers, so that average values of U_1 could be estimated with some confidence. In the case of an infinite swept wing, U_1 depends only on the chordwise position of the attachment line. Therefore, to remove the primary effects of spanwise variation in lift coefficient and hence attachment-line location, the estimated U_1 values are plotted against chordwise position in Fig 6. The range covered by the results is indicated by a shaded region – part of the variation within this band is due to uncertainty in the estimated values and part is due to the fact that the flow differs significantly from that on an infinite swept wing. The total variation is, in any case, only equivalent to an uncertainty in $\bar{R}$ of around ±6% at the higher incidences which are of most interest. Values are not plotted for the region close to the maximum because of much increased scatter. To the left of the maximum, the attachment line lies on the geometric upper surface of the slat, while to the right it lies on the lower surface. The results of a two-dimensional inviscid calculation are also shown in Fig 6, and fall within the measured band, except for the highest incidences where the attachment line is close to the slat heel. There is some uncertainty in both results in this region – the calculations were made with a smooth fairing in the cove region and the experimental results rely on a rather one-sided distribution of data, with the attachment line close to the last pressure hole. However, on balance, it is felt that more weight should be given to the experimental results because of the consistent trend shown over a wide range of experimental conditions.

6.2 Attachment-line Reynolds number

The estimated U_1 values for each hot-film station were used to determine the corresponding values of $\bar{R}$ from equation (2). The results are presented in Fig 7 in the form of the free-stream unit Reynolds number needed to give an $\bar{R}$ of 300. This is the minimum value of $\bar{R}$, according to Poll[3], for which complete turbulence may be present at some distance from a large disturbance on an infinite swept wing. Such a disturbance is termed gross contamination and is usually regarded as arising from the turbulent boundary layer at the wing-body junction. Fig 7 shows that, for incidences near the stall, the critical Reynolds numbers are within the operating envelope of the 5 *m* tunnel for all three spanwise stations. For incidences higher than 25 degrees, transition should occur first at the inboard station and progress outboard with increase in Reynolds number, due to the spanwise variation in chord. At slightly lower incidence however, the effects of spanwise variation in attachment-line location are large enough to overpower the chord variation and reverse this trend. It is clear from Fig 7 that, on the basis of Poll's criterion for large disturbances, attachment-line transition would be expected to occur at high incidence in the present experiment at all three spanwise stations and with an increasing tendency to turbulence inboard.

6.3 Hot film gauge results

The varying state of the slat lower surface boundary layer inferred from the hot-film gauge signals is summarised in Figs 8-10. In a few instances the distinction between fully turbulent and fully laminar states and the adjacent transitional states was not clear-cut, but the difference between laminar (light lines) and turbulent (heavy lines) states was marked. Turbulent flow occurs at low incidences because the attachment line lies on the upper surface and there is an adverse pressure gradient ahead of the gauge positions which gives rise to T-S instability and transition of the chordwise flow. The incidence at which this gradient changes sign is indicated in the figures. The rapid changes in boundary-layer state with incidence are apparent, though there is a clear tendency to increasing turbulence at higher incidence. The trend with increasing Reynolds number at fixed incidence is more nearly monotonic, *ie* laminar, transitional and finally fully turbulent, as expected. The $\bar{R}$ contours in Figs 8-10 show that attachment-line transition did not develop in the way expected from Poll's criterion. There was little sign of turbulence up to $\bar{R}$ values of 450 on the inboard station and up to around 350 on the mid-span station. Only on the outboard station does it appear that $\bar{R} = 300$ was a reasonable transition criterion. However, it must be remembered that the flow is three-dimensional and discussing the boundary-layer states in terms of the corresponding $\bar{R}$ values is only strictly justified for infinite-swept conditions – where $\bar{R}$ is constant across the span. On this wing the flow is strongly three-dimensional, and thus $\bar{R}$ varies significantly across the span; it would be reasonable to expect this to affect the development of disturbances within the attachment-line boundary layer. Nevertheless, the delay in development of transition on the inboard wing to such high values of $\bar{R}$ and the progression from outboard to inboard are striking differences from the expected behaviour which cannot be explained by such considerations.

6.4 Variation of maximum lift with Reynolds number

The measured variation of maximum lift coefficient (C_{Lmax}) with free-stream unit Reynolds number is shown in Fig 11. Two or three values were obtained for most Reynolds numbers and these are plotted in the figure to indicate the repeatability of the measurements. The data has been fully corrected for lift constraint and blockage effects. At low Reynolds number conventional scale effect is apparent, with the maximum lift increasing with Reynolds number. However, a maximum occurs at around 9 million and the lift subsequently falls as Reynolds number is increased further. This adverse scale effect is not large – the maximum lift only falls by around 1% – but it is potentially significant. If measurements had only been made for a range of Reynolds numbers at the left-hand part of Fig 11 (by varying tunnel speed in an atmospheric tunnel), then only the favourable trend with increasing Reynolds number would have been identified. Extrapolation of those results to full scale could lead to a significantly optimistic estimate of maximum lift. Because of the way in which attachment-line transition developed on the slat, with rapid switching between laminar and turbulent states, it is difficult to link it categorically to the adverse scale effect. However, it is possible to identify Reynolds numbers beyond which the flow at the mid and outboard stations is predominantly turbulent at the highest incidences. These Reynolds numbers are marked on Fig 11 and indicate that the adverse scale effect on maximum lift is consistent with development of attachment-line transition, bearing in mind that the maximum sectional lift coefficient (which might be expected to coincide with the position of onset of flow separation) occurs at around 78% semi-span.

7 DISCUSSION

In discussing the results of this investigation it is necessary to consider whether phenomena other than attachment-line transition could have affected the measurements. Therefore, values of the cross-flow Reynolds number and acceleration parameter have been evaluated from the measured pressure distributions. Comparison with published critical values for these parameters[4,11,12] indicates that neither cross-flow instability nor relaminarisation is likely to have had any effect on the hot-film gauge measurements at the high incidences which are of most interest. This was as expected, because the measurements were made in the lower surface boundary layer so that, at high lift, the pressure gradients between the attachment line and hot-film gauges were small. However, the possibility of relaminarisation in the upper surface boundary layer cannot be ruled out and this could delay the adverse scale effect of attachment-line transition on maximum lift to higher Reynolds numbers. On the basis of the measured transition values of $\bar{R}$ and accepted critical values of the acceleration parameter, it is considered that relaminarisation is unlikely to have greatly effected the present measurements. This conclusion is supported, of course, by the fact that the adverse scale effect observed was broadly consistent with the onset of attachment-line transition.

It is with some confidence therefore, that attachment-line transition has been identified as the dominant mechanism on the slat at high lift. In addition to the evidence for this already discussed, useful corroboration was provided by the pressure distributions, which were consistent with the existence of a laminar separation bubble on the outboard wing at low Reynolds number but not at higher values. However, transition did not develop as expected according to the accepted criterion for infinite-swept wings and possible reasons for this must be considered. Firstly, the absence of transition on the inboard wing for values of $\bar{R}$ in excess of 450 shows that gross contamination from the fuselage-side boundary layer did not occur. This represents an important difference between the present high-lift configuration and the accepted picture for cruise configurations (Ref 3 for example), which suggests that such contamination will always be present. A possible explanation for this difference is that the reduced slat lift near the wing root results in an attachment line position close to the nose so that low values of $\bar{R}$ occur and disturbances from the root are suppressed. Ref 6 shows that very rapid decay of turbulence in a region of low $\bar{R}$ is certainly possible. For cruise configurations the attachment line is likely to lie close to the section nose over most of the span so that large reductions in $\bar{R}$ over the inner wing are unlikely.

Secondly, although transition on the inner wing is delayed, as described above, transition on the outer wing occurs more or less in line with the $\bar{R} = 300$ criterion. According to Poll[3], for low levels of free-stream turbulence or other disturbance, the attachment-line boundary layer should remain laminar up to $\bar{R}$ values in excess of 700. Free-stream turbulence obviously cannot explain the present results, but surface irregularities and the slat support brackets, which intrude slightly into the slat heel, are possible sources of disturbance on the model. Poll's results[3,4] provide detailed data on the permissible size of two-dimensional roughness elements for infinite-swept cylinders, and Paisley and Poll[9] found that substantially smaller values were appropriate in the case of a tapered cylinder. The spanwise gradient of $\bar{R}$ in the present case was found to be close to the value quoted in Ref 9 and, using these results, it is estimated that a 0.06 mm diameter wire would be required to trip transition at the outboard station for $\bar{R} = 300$. The model surface was smoother than this but it is conceivable that disturbances of sufficient magnitude could have originated from the pressure holes, tubing installation or slat brackets. Such disturbances also provide the only obvious explanation for the sudden, but highly repeatable, changes in boundary-layer state which were observed. A quantitative argument cannot be made for this suggestion but the estimated trip sizes deduced from Poll's results and illustrated in Fig 12, are interesting. According to Ref 9, lower values than these would be appropriate for the present model, particularly at higher incidence. The figure shows that the trip sizes vary non-monotonically with incidence and it seems possible that this could result in the type of behaviour observed, if sufficiently large sources of disturbance were present.

The conclusion that attachment-line transition was responsible for the observed adverse Reynolds number effect on maximum lift has important implications for wind-tunnel testing. The most significant of these is the additional uncertainty in extrapolating measurements to full-scale, as mentioned previously in discussing the results of Fig 11. If the U_1 values of around 20 found in this experiment are typical, the attachment-line flow on the inboard region of the slat of all but the smallest transport aircraft is certain to be turbulent, because the resulting $\bar{R}$ values are high enough for natural transition to occur. Thus, artificially tripping transition at the attachment line in wind-tunnel tests might produce more representative results in cases where the test Reynolds number is sufficiently high for this to be possible. However, this technique would only result in a fully representative flow in cases where the boundary layer did not relaminarise downstream of the attachment line, as this process is most unlikely to occur at full scale.

8 CONCLUSIONS

The attachment-line boundary layer on the slat of a high-lift strike-fighter model, Model M495, has been found to be turbulent on the outboard part of the wing near maximum lift for a range of unit Reynolds number. An adverse scale effect on maximum lift has been measured which is consistent with the onset of attachment-line transition. However, it was found that the conditions for onset of transition were not consistent with the assumption of gross contamination by the fuselage boundary layer, the attachment-line boundary layer remaining laminar on the inboard slat to more than double the expected free-stream Reynolds number. This is in agreement with other results[10] for a simpler, unslatted high-lift wing, but contrasts with results previously obtained for the flow past non-lifting and cruise configurations, where it has been demonstrated that the fuselage side boundary layer invariably acts as a source of gross contamination. Suppression of disturbances in a region of low $\bar{R}$ near the root of the high-lift wing is suggested as the reason for this result. Transition on the outer wing was found to occur at lower Reynolds numbers, more or less in accordance with the accepted, $\bar{R} = 300$, criterion. It is concluded that attachment-line transition is a potentially significant factor in wind-tunnel testing of high-lift wings equipped with leading-edge slats. It is suggested that artificial fixing of transition on the attachment line may sometimes improve the accuracy with which full-scale flows can be represented, but that the utility of this technique will depend on an improved understanding of the effects of relaminarisation.

The present investigation has been of an exploratory nature and there is considerable scope for further work. For example, an improved understanding is necessary of the flow in the vicinity of the attachment line when it lies close to the sharp slat heel. Similarly, more detailed measurements of the attachment-line region close to the wing root might help to explain the observed absence of gross contamination. It is also important to understand the effects of free-stream Mach number and of slat position and deflection angle, all of which strongly influence the performance of a slatted wing. The first of these might be particularly interesting because supersonic flows and shock-wave boundary-layer interactions can occur on slats and so it is conceivable that attachment-line transition could alter the nature of this interaction from a laminar to a turbulent type, perhaps resulting in a favourable Reynolds number effect, in contrast to the adverse effect found at the lower Mach number of the present tests.

REFERENCES

1 Moir, I.R.M., "A description of a typical strike-fighter model for the RAE 5 metre wind tunnel (Model 495) and its associated half-model (Model 2113)". RAE Technical Report 81022 (1981)

2 Woodward, Dr D.S., "Unpublished RAE work".

3 Poll, D.I.A., "Transition in the infinite swept attachment-line boundary layer". The Aeronautical Quarterly, Vol XXX, November 1979, pp 607-629

4 Poll, D.I.A., "Some aspects of the flow near a swept attachment line with particular reference to boundary-layer transition". College of Aeronautics Report 7805 (1978)

5 Pfenninger, W., "Laminar flow control - Laminarization". Special course on concepts for drag reduction. AGARD Report 654 (1977)

6 Gregory, N.; Love, E.M., "Laminar flow on a swept leading edge". NPL Aero Memo 26 (1965)

7 Cumpsty, N.A.; Head, M.R., "The calculation of the three-dimensional turbulent boundary layer. Part III Comparison of attachment-line calculations with experiment". The Aeronautical Quarterly, Vol XX, May 1969, pp 99-113

8 Gaster, M., "On the flow along a swept leading edge". The Aeronautical Quarterly, Vol XVIII, May 1967, pp 165-184

9 Poll, D.I.A.; Paisley, D.J., "On the effect of wing taper and sweep direction on leading-edge transition". College of Aeronautics Report 8435 (1984)

10 Hardy, B.C., "Experimental investigation of attachment-line transition in low-speed, high-lift wind-tunnel testing". AGARD CP 438 (1988)

11 Beasley, J.A., "Calculation of the laminar boundary layer and prediction of transition on a sheared wing". RAE Technical Report 73156 (1974)

12 Launder, B.E.; Jones, W.P., "On the prediction of laminarisation". ARC CP 1036 (1969)

13 Garner, P.L.; Meredith, P.T.; Stoner, R.C., "Areas for future CFD development as illustrated by transport aircraft applications". AIAA Paper 91-1527 (1991)

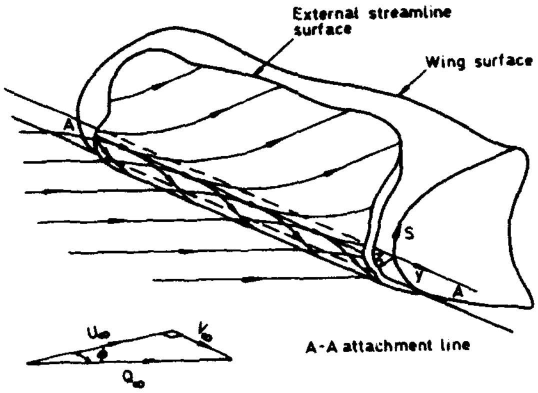

Fig 1 Flow in the vicinity of the attachment line on a swept wing (from Ref. 4).

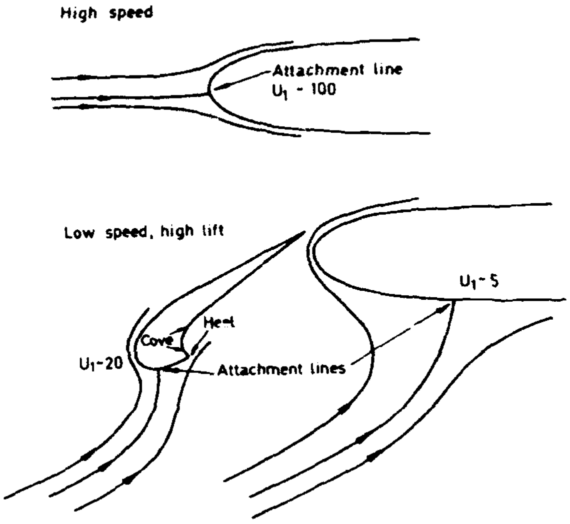

Fig 2 Attachment - Line locations for cruise and high - lift configurations.

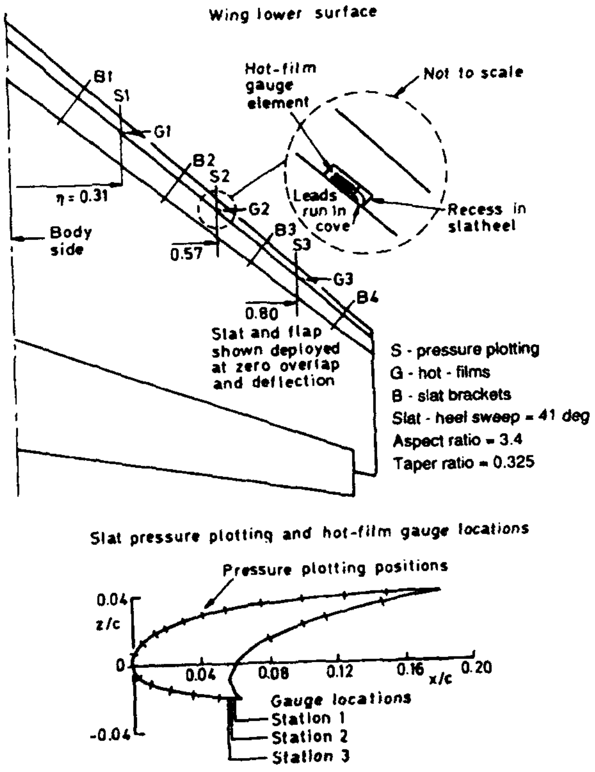

Fig 3 Model 495 Geometric details.

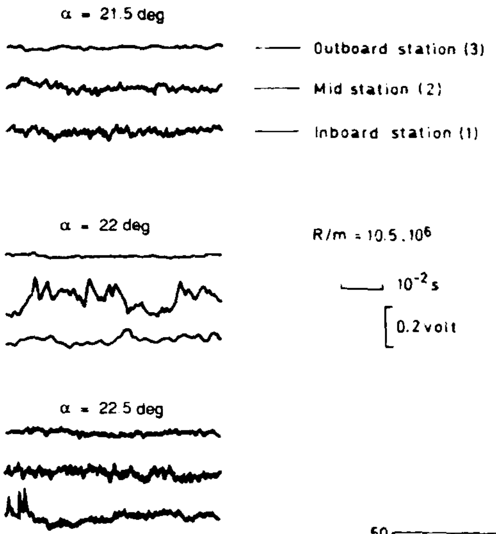

Fig 4 Typical hot - film gauge unsteady signals.

Fig 5 Typical variation with incidence of hot - film mean power dissipation.

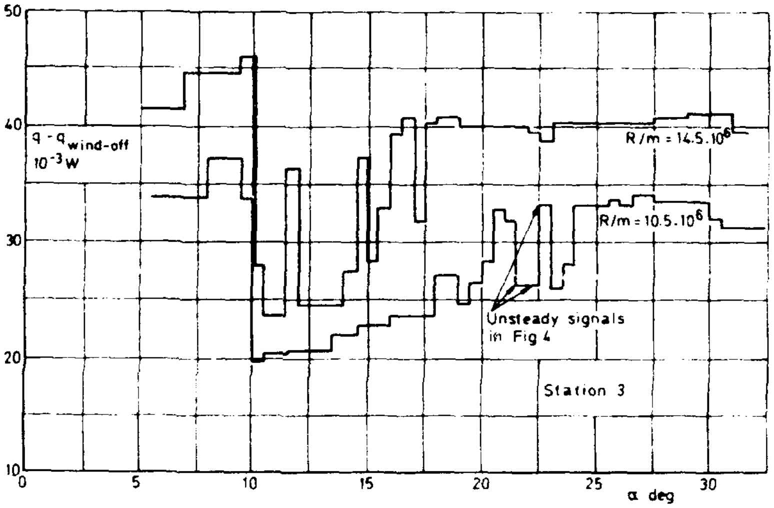

Fig 5 Typical variation with incidence of hot - film mean power dissipation.

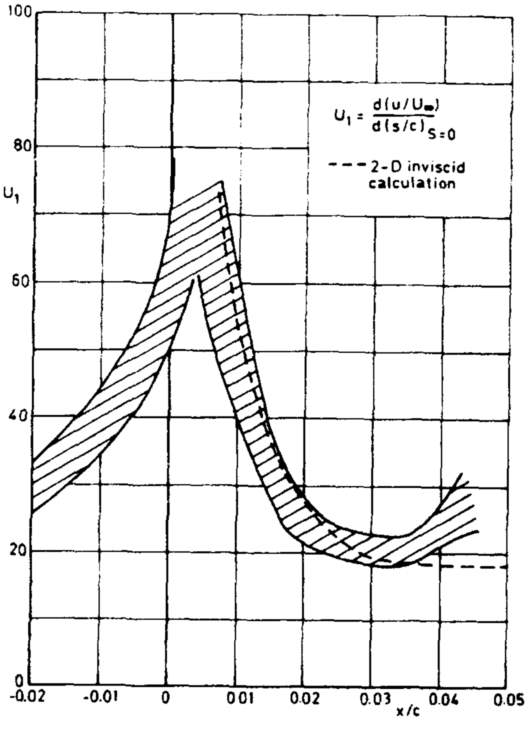

Fig 6 Range of calculated attachment line velocity gradients for all stations for several Reynolds numbers.

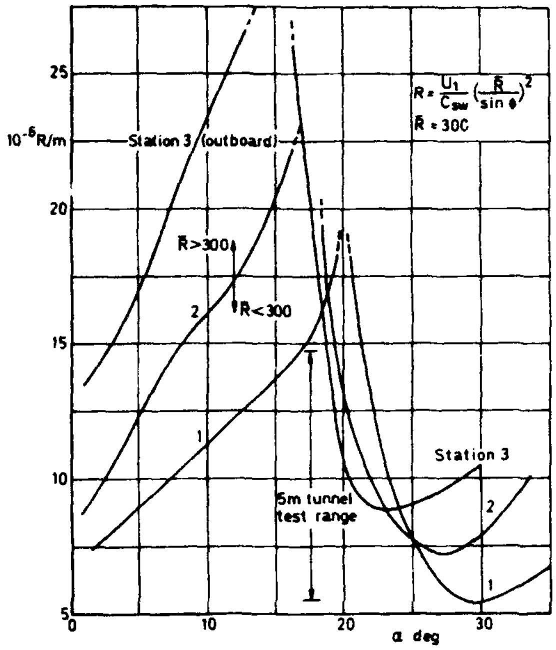

Fig 7 Variation with incidence of the unit Reynolds number required to give $\bar{R}$ = 300.

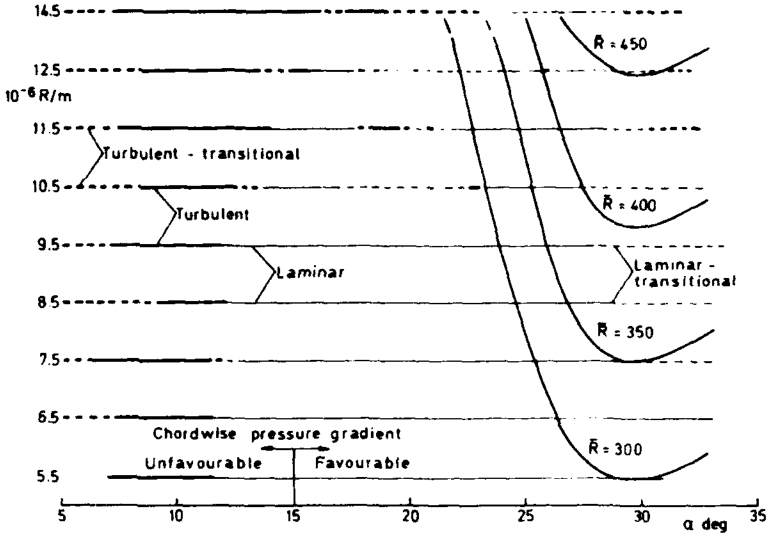

Fig 8 Variation of Boundary - Layer type with incidence and Reynolds number at inboard station 1.

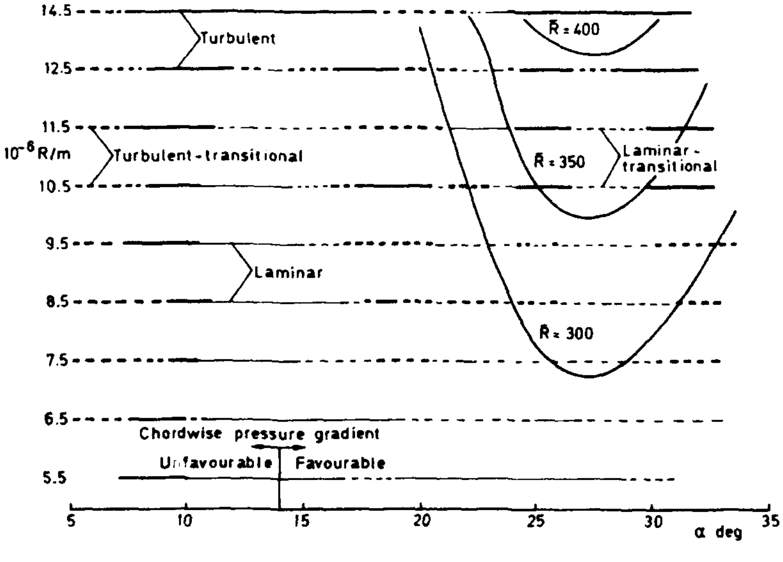

Fig 9 Variation of Boundary - Layer type with incidence and Reynolds number at mid station 2.

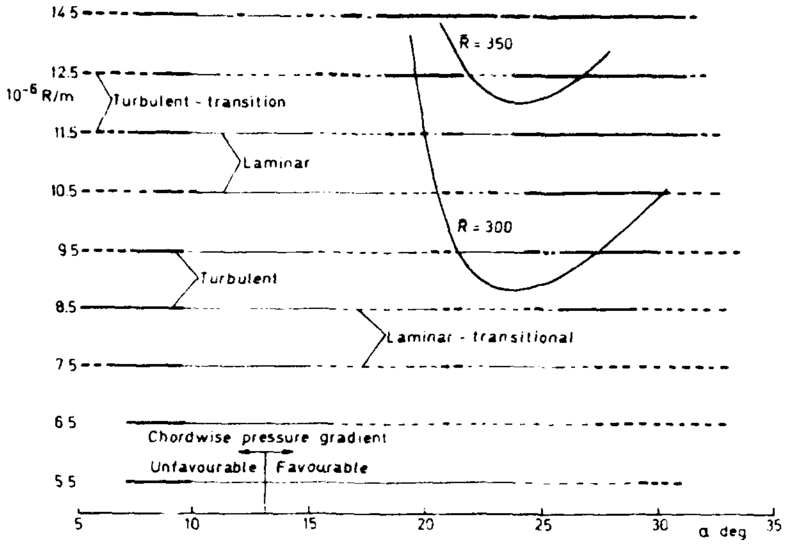

Fig 10 Variation of Boundary - Layer type with incidence and Reynolds number at outboard station 3.

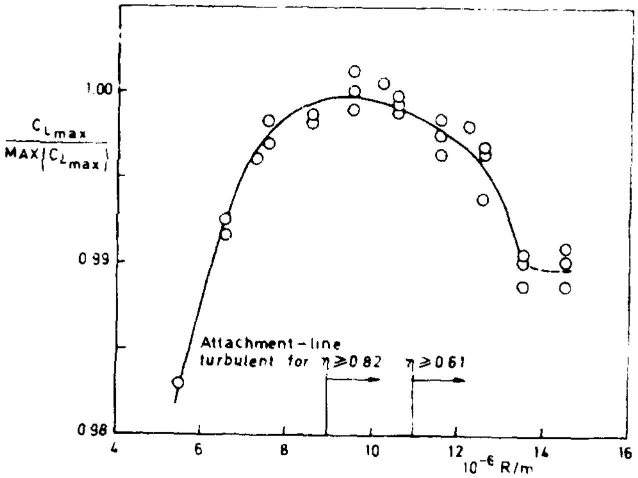

Fig 11 Variation of maximum lift with Reynolds number.

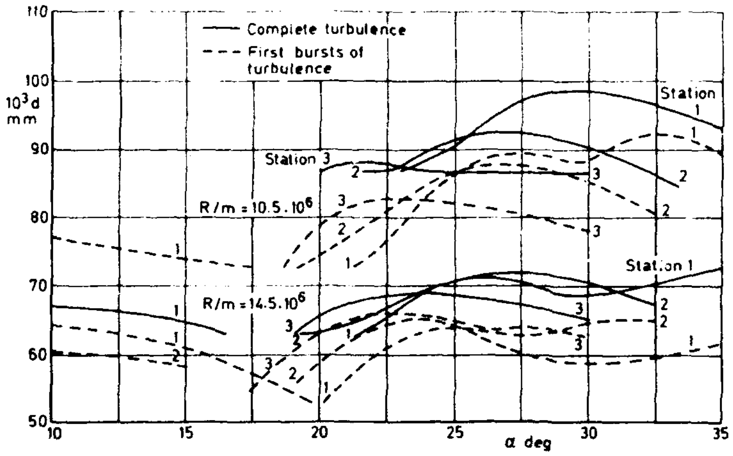

Fig 12 Variation of trip diameter with incidence for large trip - detector spacing.

VISCOUS PHENOMENA AFFECTING HIGH-LIFT SYSTEMS AND SUGGESTIONS FOR FUTURE CFD DEVELOPMENT

by

P.T. Meredith, Senior Specialist Engineer
Boeing Commercial Airplane Group
P.O. Box 3707, Mail Stop OF-AR
Seattle, WA 98124-2207
United States

SUMMARY

This paper describes a number of viscous phenomena which affect the aerodynamic performance of high-lift systems typical of commercial jet transports. The nature of these phenomena suggest a course of action regarding the continuing development of computational fluid dynamics (CFD): in addition to the ongoing work of grid generation and algorithm development, increased attention to fundamental fluid mechanics is called for.

LIST OF SYMBOLS

C_L	lift coefficient
C_{Lmax}	maximum lift coefficient
C_P	pressure coefficient
dU/dx	local velocity gradient
K	$=(\nu/U^2)(dU/dx)$, relaminarization parameter
Rbar	$=(U_\infty \sin(\Lambda)/\nu)\sqrt{(\nu/(dU/dx))}$, attachment line Reynolds number
R_c	Reynolds number referenced to chord
U	velocity at outer edge of boundary layer
U_∞	freestream velocity
x/c	non-dimensional chord location
α	angle of attack
δ^*	boundary layer displacement thickness
η	semi-span location
Λ	sweep angle or attachment line sweep angle
$\Lambda_{c/4}$	quarter chord sweep angle
ν	kinematic viscosity

INTRODUCTION

High-lift systems are used on commercial jet transports to provide adequate low speed performance in terms of take-off and landing field lengths, approach speed, and community noise. The importance of the high-lift system is illustrated by the following trade factors derived for a generic large twin engine transport.

1) A 0.10 increase in lift coefficient at constant angle of attack is equivalent to reducing the approach attitude by about one degree. For a given aft body-to-ground clearance angle, the landing gear may be shortened resulting in a weight savings of 1400 lb.

2) A 1.5% increase in maximum lift coefficient is equivalent to a 6600 lb increase in payload at a fixed approach speed.

3) A 1% increase in take-off L/D is equivalent to a 2800 lb increase in payload or a 150 nm increase in range.

While necessary, high-lift systems increase airplane weight, cost, and complexity significantly. Therefore, the goal of the high-lift system designer is to design a high-lift system which minimizes these penalties while providing the required airplane take-off and landing performance.

VISCOUS PHENOMENA AFFECTING HIGH-LIFT SYSTEM PERFORMANCE

Fig. 1 shows some of the viscous flow features affecting a typical multi-element lifting system:

attachment line transition from laminar to turbulent
relaminarization of turbulent boundary layers
transition of boundary layers from laminar to turbulent
shock/boundary layer interactions
viscous wake interactions
confluent wakes and boundary layers
separated flows

All of these features play an important role in high-lift aerodynamics and all are affected by Reynolds number. Of the above flow features, transition and development of surface boundary layers have received the most attention, though much work remains to be done in these fields. This is appropriate given that the maximum lift of a single element of a multi-element high-lift system, as well as the maximum lift of the system, are strongly dependant on boundary layer state and development, as discussed by Smith [1]. However, understanding and modeling of surface boundary layers, while necessary, is not sufficient to enable the calculation of maximum lift, the optimization of pressure distributions, and the optimization of geometric positioning of high-lift systems in general.

While it is commonly thought that increasing Reynolds number yields increasing lift, at least three of the phenomena listed above can result in decreasing lift with increasing Reynolds number, sometimes termed an adverse Reynolds number effect, as discussed by Garner, et al [2]. The three phenomena addressed in the remainder of this paper are:

viscous wake interactions
relaminarization
attachment line transition

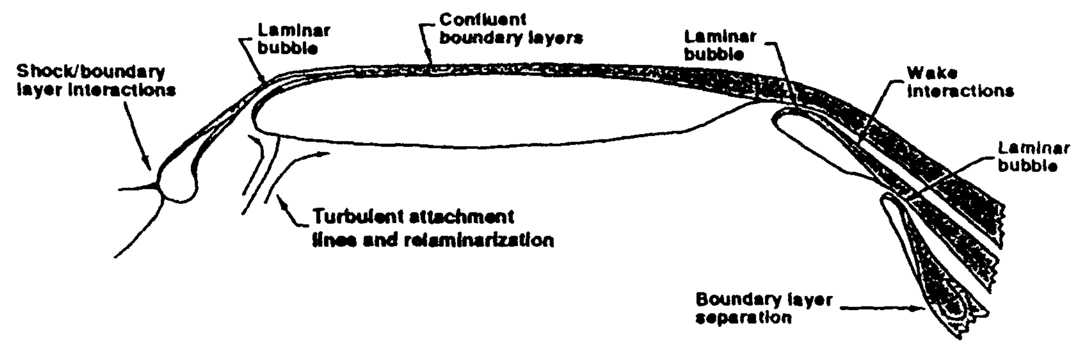

Fig. 1 Viscous flow features affecting high-lift systems

<u>Viscous Wake Interactions</u>

To illustrate the interaction of a viscous wake with a lifting surface, the interaction between a wing wake and trailing edge flap will be considered. There are two major interactions between a wing wake and a flap. First, the wing wake may become confluent with the flap boundary layer. Second, and the subject of the remainder of this section, the proximity of the wing wake to the flap upper surface results in a damping, or supression, of the flap upper surface pressure distribution, even when the viscous layers are not confluent.

The wing wake above the flap has a displacement effect on the flow field which tends to suppress the flap pressure distribution. Generally, the bigger the wing wake, the more suppressed the flap pressure distribution becomes. This is illustrated in Fig. 2 which shows a lift curve for a landing configuration having double slotted trailing edge flaps and the corresponding flap pressure distributions at two angles of attack. The flap loading is greatly reduced at high angle of attack relative to the loading at low angle of attack. Contrary to conventional wisdom, the pressure distributions and surface flow visualization (not shown) demonstrate that the decrease in flap loading is not associated with flap separation. In fact, the reduction in flap loading results from the growth of the wing wake displacement thickness with increasing angle of attack.

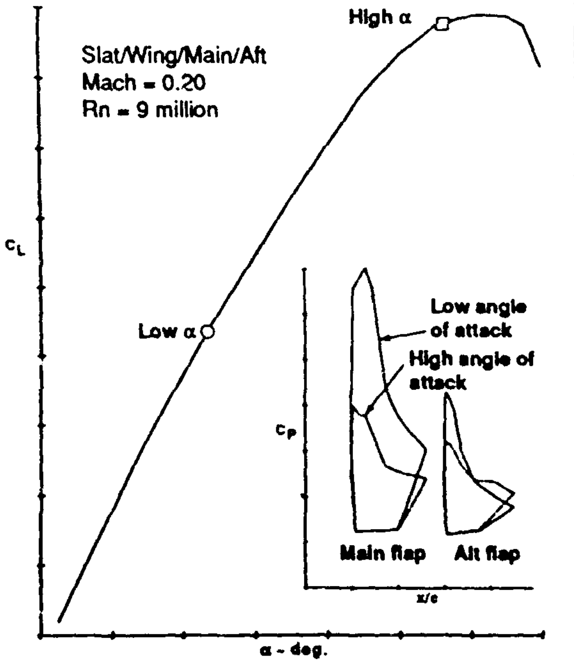

Fig. 2 Wing wake/flap interaction

Another way to change the thickness of the wing wake is to change the Reynolds number. Assume a flap is designed and *optimized* at low Reynolds number. The flap design and orientation will reflect the presence of the wing wake existing at low Reynolds number. As Reynolds number is increased, the wing wake thins and the flap load increases. This may cause or increase separation on the flap, decreasing lift in the process. The adverse effect is more likely to happen for flaps designed to maximize lift at a fixed angle of attack rather than for flaps designed to maximize $C_{L\max}$ of the system.

This phenomenon is illustrated by Figs. 3 and 4. Fig. 3 shows lift curves at two Reynolds numbers for a 2D four-element (slat, wing, vane/main flap) configuration obtained during a wind tunnel test at the NASA Langley Low Turbulence Pressure Tunnel (LTPT). The higher Reynolds number results in a large loss of lift at low to moderate angles of attack. Also shown are calculated lift levels using a 2D analysis code by Kusunose, <u>et al</u> [3] which employs a full potential solver coupled with a viscous model patterned after that used in the Euler code of Drela [4]. While the lift levels are high relative to the wind tunnel data, the trend with Reynolds number is correctly predicted. The mechanism involved is illustrated in Fig. 4 which shows the calculated wing wake displacement thickness and flap pressure distributions at the two Reynolds numbers at moderate angle of attack. At the lower Reynolds number, the wing wake becomes very thick over the main flap. As Reynolds number is increased, the wing wake thins and the main flap loading increases until the boundary layer separates, resulting in the high Reynolds number case in Fig. 4, where the wing wake is thin, the main flap is largely separated, and lift is greatly reduced. At high angles of attack, the thick wing wake surpresses the flap loading which alleviates flap separation at the higher Reynolds number such that no adverse Reynolds number effect is evident at $C_{L_{max}}$.

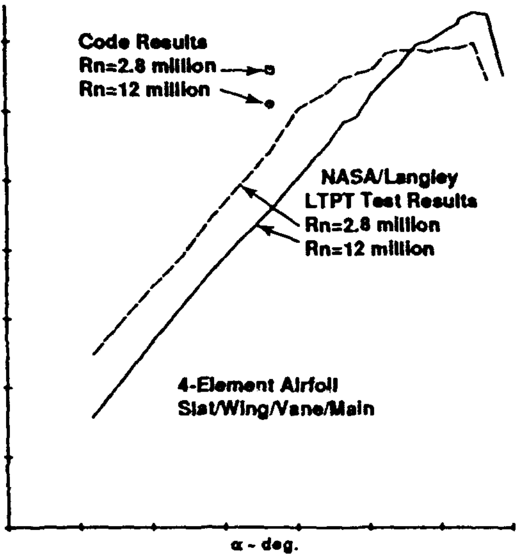

Fig. 3 Adverse Reynolds number of effect on lift

A final example of the wing wake/flap interaction is provided in Fig. 5 which shows the influence of the wake modeling on the flap pressure distributions as calculated by the previously mentioned multi-element full potential solver coupled to an integral boundary layer and wake model. The wake model contains several empirically determined parameters, one of which, termed Fw, influences the response of the wake to adverse pressure gradients. As Fw is increased from 0.20 to 0.45, the wing wake grows more rapidly in the presence of the adverse pressure gradient imposed by the flap. The thicker wake in turn suppresses the loading on the flap. Available wind tunnel data suggest the lower value of Fw but the integral wake model may be too simple to be generally valid.

In the course of the above work, the literature was reviewed to identify experimental results which would aid in improving the viscous modeling. It was found that the available wind tunnel data are limited and tests in which the viscous wakes were measured, in terms of total pressure and velocity profiles, and turbulence quantities, more limited still. The CFD developer is thus forced to adjust the viscous modeling to match surface pressure data rather than the viscous features the code is attempting to capture. To remedy this situation, much experimental work must be done to obtain the type of data necessary for continued development of CFD for high-lift applications.

Relaminarization

As discussed by Smith [1], it is very beneficial, in terms of developing maximum lift, for an airfoil or element of a high-lift system to have a laminar boundary layer up to the point of pressure recovery, the idea being to begin the recovery with as thin a turbulent boundary layer as possible. Therefore, all phenomena which affect the state of the upper surface boundary layer can be expected to play a role in the

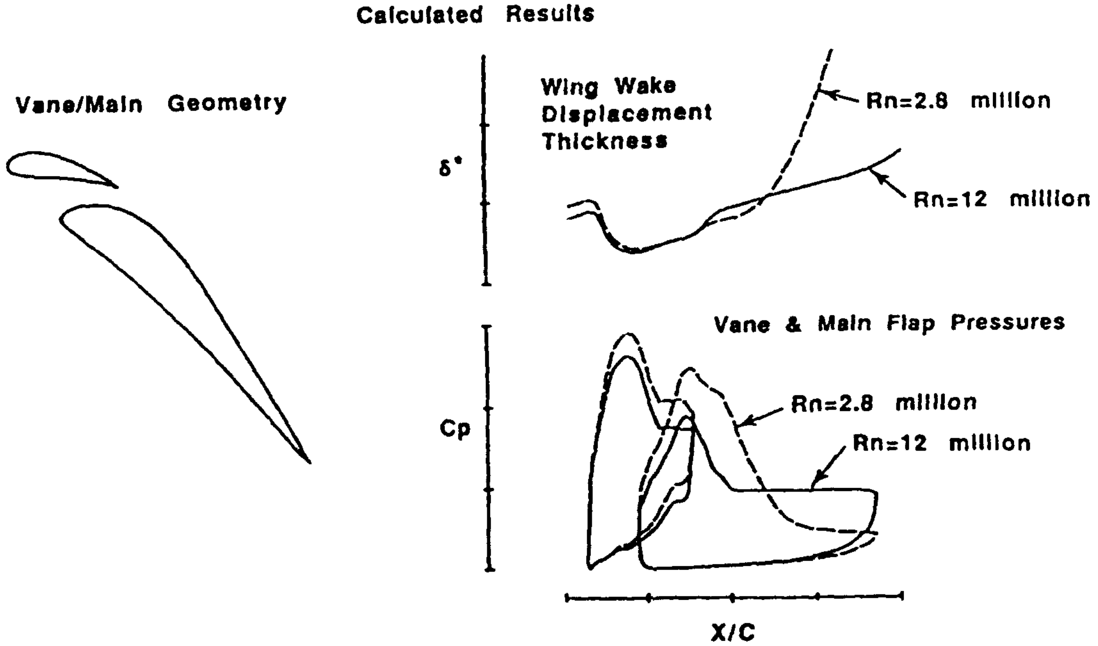

Fig. 4 Wing wake/flap interaction at low and high Reynolds number

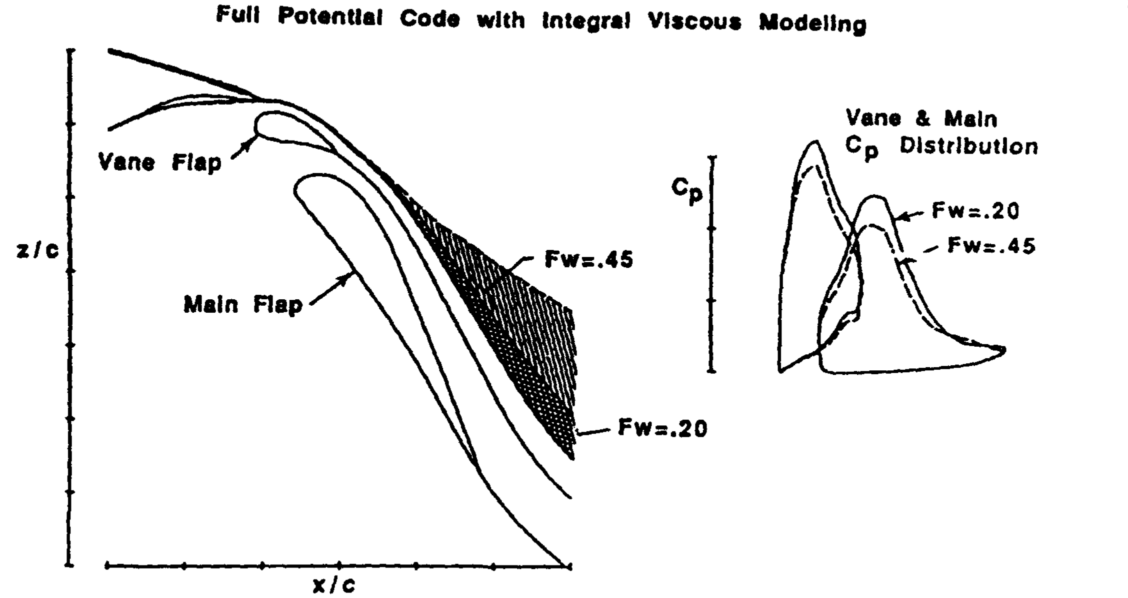

Fig. 5 Effect of wing wake modeling on wake growth and flap pressure distribution

maximum lift developed. The influence of boundary layer state on $C_{L_{max}}$ is shown schematically in Fig. 6. Referring to Fig. 6, $C_{L_{max}}$ rises with increasing Reynolds number until the initial upper surface boundary layer begins transitioning from laminar to turbulent causing a loss in $C_{L_{max}}$ with further increases in Reynolds number. After the transition process is completed, $C_{L_{max}}$ once again rises with increasing Reynolds number. Two phenomena which can cause such behavior are relaminarization and attachment line transition. While the primary subject of this section is relaminarization, attachment line transition, the subject of the next section, will be touched on in the following discussion.

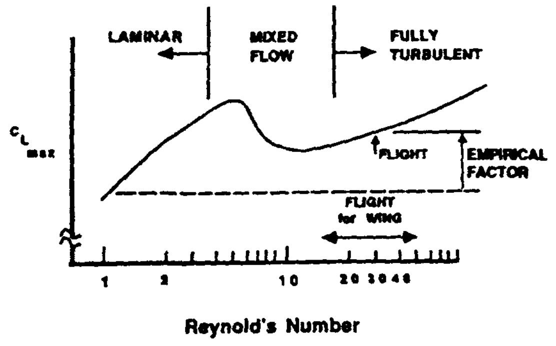

Fig. 6 Typical effect of boundary layer state on $C_{L_{max}}$

Fig. 7 shows the potential flow surface streamlines for a swept wing. The attachment line, a line of spanwise flow on the lower surface well behind the wing leading edge, is clearly shown. For a 3D swept wing, the upper surface boundary layer state is usually determined by the state of the attachment line boundary layer. However, under the right conditions, the turbulent boundary layer downstream of the attachment line may become laminar, a process termed relaminarization. In subsonic flow, relaminarization may occur under the influence of favorable pressure gradients at sufficiently low freestream Reynolds numbers.

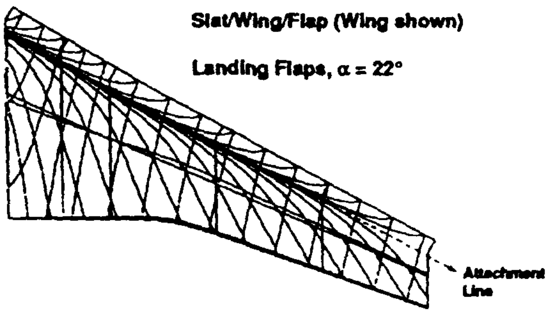

Fig. 7 Typical potential flow surface streamlines

Fig. 8 shows the trend of $C_{L_{max}}$ with Reynolds number for a simple, swept wing tested jointly by Boeing and Japan Aircraft Development Corporation (JADC) in the RAE Farnborough 5m pressure tunnel. It is seen that $C_{L_{max}}$ increases with increasing Reynolds number, reaches a maximum, and then declines, dropping 7% from the peak value at the highest Reynolds number achievable. Decreasing $C_{L_{max}}$ with increasing Reynolds number has been observed before, as discussed by Woodward, et al [5] but the magnitude of the observed loss was surprising.

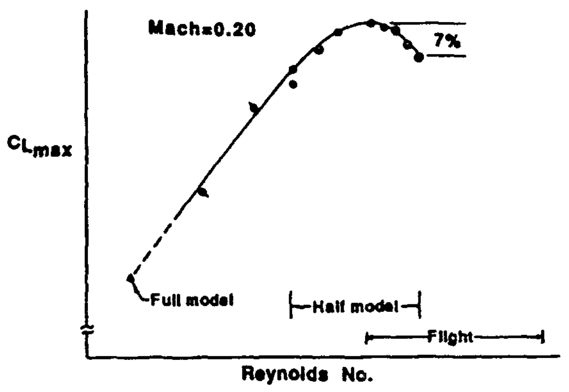

Fig. 8 Variation of $C_{L_{max}}$ with Reynolds number for a single swept wing

An investigation of the phenomenon proved interesting. Surface oil flow visualization showed a laminar separation bubble on the upper surface over the entire span at low Reynolds number. The laminar bubble began to disappear on the inboard section of the wing as Reynolds number was increased. At the highest Reynolds number, the laminar bubble was evident on only the outboard third of the wing.

One mechanism considered was the transition of the attachment line from laminar to turbulent with increasing Reynolds number. This mechanism was ruled out for three reasons. First, the observation of laminar bubbles outboard but not inboard would imply a turbulent attachment line inboard and a laminar attachment line outboard, an unlikely situation. Second, a wire trip was placed on the inboard lower suface, normal to the attachment line, to cause attachment line transition but no differences in flow characteristics were observed. Finally, calculation of the attachment line Reynolds number Rbar, after Poll [6], gave Rbar>240 at the lowest Reynolds number suggesting that the attachment line was turbulent for all Reynolds numbers tested.

The most likely mechanism is now thought to be relaminarization. At low Reynolds number, the turbulent boundary layer flowing away from the attachment line becomes laminar due to the action of the extremely favorable pressure gradient around the leading edge. As Reynolds number increases, the spanwise extent of the relaminarization decreases. The change from a mostly laminar initial upper surface boundary layer to a mostly turbulent one accounts for the observed loss in $C_{L_{max}}$.

There have been several parameters proposed as indicators of when relaminarization is likely. One parameter, K, after Launder and Jones [7], correlates reasonably well with the experiment under discussion. A value of K>3E-06 is sometimes propsed as a relaminarization criteria. Fig. 9 shows the calculated spanwise distribution of K as a function of Reynolds number. It is seen that relaminarization, as defined by K>3E-06, is likely at Reynolds numbers less than about 12 million. Also, due to the spanwise distribution of pressure gradients, relaminarization should first cease inboard with increasing Reynolds number, a result in agreement with the experimental data.

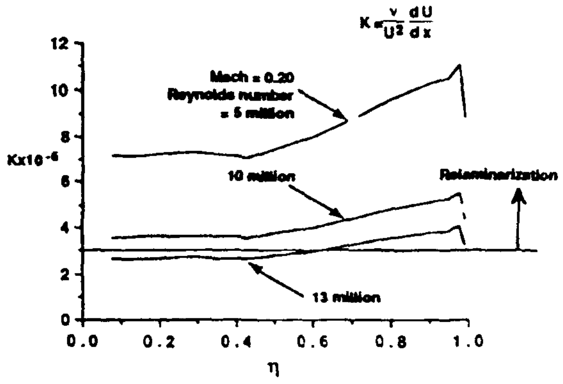

Fig. 9 Spanwise variation of the relaminarization parameter K for a simple swept wing

Additional data confirming relaminarization were acquired during a subsequent test and are briefly discussed in the next section.

Much work remains to be done to understand and be able to model relaminarization. For instance, the relaminarization parameter K does not reflect boundary layer characteristics nor the chordwise extent of the favorable pressure gradient. Also, cross flow instabilities, a function of wing sweep, can be expected to influence the propensity for relaminarization. Finally, the rapidity with which the boundary layer retransitions to turbulent flow certainly has an impact on maximum lift.

Attachment Line Transition

As previously mentioned, the state of the attachment line usually determines the boundary layer state on the upper surface. The attachment line on many high-lift devices is far behind the leading edge in a region of low curvature and subsequently small velocity gradients which favors development of a turbulent attachment line. In the absence of sufficiently large pressure gradients and at high enough freestream Reynolds numbers, relaminarization as discussed above is unlikely to occur. Therefore, in the absence of relaminarization, a turbulent attachment line results in a turbulent boundary layer over the entire upper surface.

After the experiment discussed above, a new leading edge shape was designed for the model as shown in Fig. 10. The primary desire was to avoid relaminarization, or at least confine it to lower Reynolds numbers, so that the trend of

C_{Lmax} with Reynolds number could be established with a fully turbulent upper surface boundary layer. To this end, the curvature around the leading edge was reduced in order to lessen the favorable pressure gradients promoting relaminarization. However, the resulting shape had increased curvature in the vicinity of the attachment line, increasing the likelihood of a laminar attachment line.

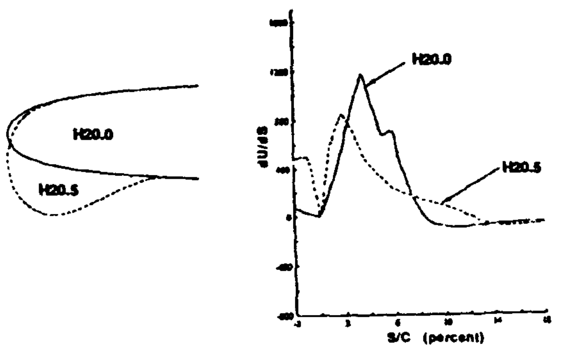

Fig. 10 Leading edge shape modification to reduce velocity gradients

The model was again tested by Boeing/JADC at the RAE 5m pressure tunnel. Some results are given in Fig. 11 which shows C_{Lmax} as a function of Reynolds number for both the initial design (H20) and the new design (H20.5). H20.5 exhibited characteristics similar to H20 in that C_{Lmax} first increases with Reynolds number, reaches a maximum, and then decreases. However, relative to H20 characteristics, the Reynolds number for peak C_{Lmax} for H20.5 was much lower and the decrease in peak C_{Lmax} was much greater, 15% as opposed to 7%, although the drop in CLmax for H20 was limited by the maximum Reynolds number attainable. Also, H20.5 showed a resumption of increasing C_{Lmax} with Reynolds number at the higher Reynolds numbers tested. While the adverse Reynolds number effect on H20 is due to cessation of relaminarization, for H20.5 it is believed to be due to attachment line transition.

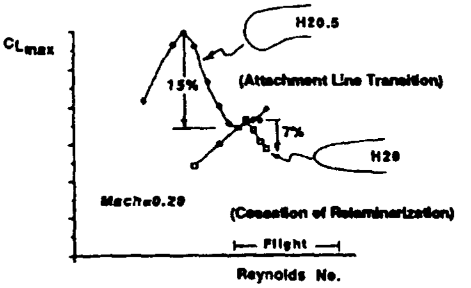

Fig. 11 Effect of leading edge shape modification on C_{Lmax} variation with Reynolds number

Fig. 12 shows the calculated spanwise distribution of the relaminarization parameter K for both H20 and H20.5 at low and high Reynolds numbers. H20.5 has greatly reduced values of K relative to H20 with K generally less than 3E-06, indicating that relaminarization is much less likely for H20.5 than for H20.

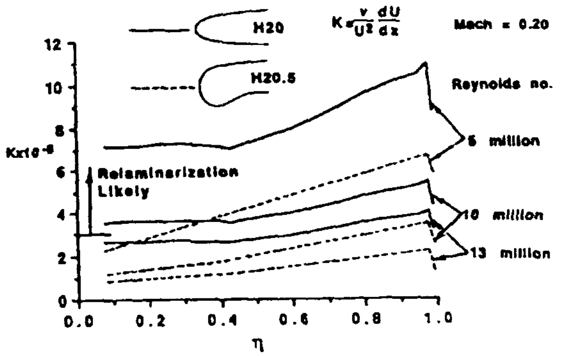

Fig. 12 Effect of leading edge shape modification on the relaminarization parameter K

Fig. 13 shows the attachment line Reynolds number Rbar for both H20 and H20.5, calculated at about 20% span, as a function of freestream Reynolds number. H20.5 exhibits a 175 unit reduction in Rbar relative to H20 at all freestream Reynolds numbers. Using an Rbar of 240 as an indicator of a turbulent attachment line, it is seen that H20 should have a turbulent attachment line over the range of Reynolds numbers being considered while H20.5 should have a laminar attachment line at low Reynolds number and a turbulent attachment line at high Reynolds number. These calculations are in reasonably good agreement with the experimental data.

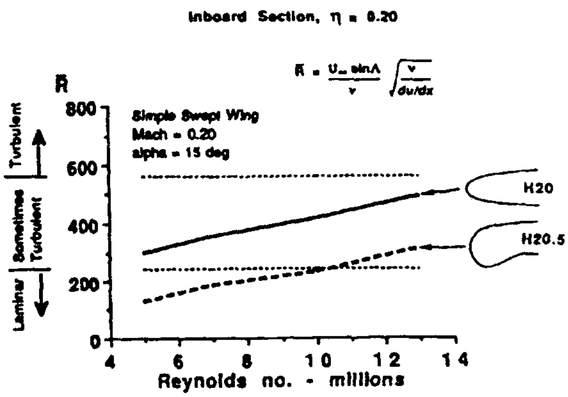

Fig. 13 Effect of leading edge shape modification on the attachment line Reynolds number Rbar

A final bit of evidence was provided by arrays of surface mounted hot film sensors installed at three spanwise stations around the leading edges of both H20 and H20.5. The hot film data, detailed discussion of which is beyond the scope of this paper, support the above conclusions. The hot film signals for H20.5 showed a laminar attachment line at low Reynolds number and a turbulent attachment line, with no relaminarization of the upper surface boundary layer, at high Reynolds number. The hot film signals for H20 confirmed that the attachment line was turbulent over the range of Reynolds numbers tested and that the adverse Reynolds number effect was due to cessation of relaminarization. Also, the data showed that C_{Lmax} is affected not only by the presence or absence of relaminarization but by the chordwise extent of the relaminarized flow which, like most viscous phenomena, is strongly a function of Reynolds number.

In summary, relaminarization and attachment line transition have a very large effect on high-lift system performance and greatly reduce the confidence with which wind tunnel data are scaled to flight Reynolds numbers. While unlikely to replace the wind tunnel, the development of CFD tools which model these phenomena will enable the design of more efficient high-lift systems and mitigate the risk of being surprised during flight test.

CONCLUSIONS and RECOMMENDATIONS

The performance of high-lift systems depends greatly on a variety of viscous flow phenomena which are strongly a function of Reynolds number. Three of the many phenomena have been addressed in this paper:

viscous wake interactions
relaminarization
attachment line transition

These phenomena are of more than academic interest as each can lead to adverse Reynolds number effects where lift at constant angle of attack (C_L) and/or maximum lift (C_{Lmax}) decrease with increasing Reynolds number.

Based on the material presented in this paper, and the research on which it is based, the following conclusions are drawn:

1) Adverse Reynolds number effects on C_L and C_{Lmax} are not uncommon.

2) Adverse Reynolds number effects on C_L and C_{Lmax} can be large.

3) Designing and testing at less than flight Reynolds number is not in general conservative and may result in expensive airplane modifications during flight testing and/or an airplane with poorer than expected performance throughout its economic life. This becomes more likely if increased performance is demanded from a high-lift system of fixed size as the system becomes more point designed.

4) Current CFD tools do not model the physics with enough accuracy and/or in enough detail to reliably predict Reynolds number effects on C_L and C_{Lmax} of highly loaded high-lift systems.

5) The existing experimental database, in terms of the number of revelant experiments and the type of data obtained, is inadequate for the purpose of improving the ability of high-lift CFD tools to predict Reynolds number effects.

To advance the state of the art in high-lift aerodynamics, the following recommendations are made:

1) Continued development of CFD tools is called for as the likelihood of developing wind tunnels for jet transport configuration development testing at flight Reynolds numbers is remote.

2) The further development of CFD requires that the greatest weaknesses of current CFD tools recieve the greatest attention. This means that increased work in fundamental fluid mechanics, rather than in grid generation or algorithm development, is warranted. Such research should be directed towards the understanding and modeling of:

   turbulence
   boundary layer and wake development
   viscous wake interactions
   transition
   relaminarization
   separated flows
   confluent flows

3) To accomplish the above recommendations, additional experimental data must be obtained. The type of data needed will require experimental researchers to focus less on testing airplane configurations and components and more on experiments designed to answer specific questions in fluid mechanics.

High-lift aerodynamics remains one of the most interesting, challenging, and rewarding of engineering disciplines. It is hoped that researchers will embrace the recommendations in this paper; advances in the understanding and modeling of the viscous phenomena discussed will benefit not only CFD for high-lift aerodynamics but CFD and fluid mechanics in general.

ACKNOWLEDGEMENTS

The author wishes to express his gratitude to his collegues in the Advanced Technology & Design group of the Boeing Commercial Airplane Group. The author also thanks the engineers and staffs of the NASA/Langley Low Turbulence Pressure Tunnel and RAE/Farnborough 5m Pressure Tunnel for their assistance in acquiring the high Reynolds number data discussed in this paper. Finally, the author wishes to thank Mr. Amano, Mr. Nakamura, and others of the Japan Aircraft Development Corporation and its member companies (Fuji Heavy Industries, Kawasaki Heavy Industries, Mitsubishi Heavy Industries) for their assistance and participation in the RAE testing discussed in this paper.

REFERENCES

1. Smith, A.M.O., "High-Lift Aerodynamics", Wright Brothers Lecture, AIAA-74-939, 1974.
2. Garner, P.L., Meredith, P.T., Stoner, R.C., "Areas for Future CFD Development as Illustrated by Transport Aircraft Applications", AIAA-91-1527, 1991.
3. Kusunose, K., Wigton, L., Meredith, P.T., "A Rapidly Converging Viscous/Inviscid Coupling Code for Multi-Element Airfoil Configurations", AIAA-91-0177, 1991.
4. Giles, M., Drela, M., Thompkins Jr., W.T., "Newton Solution of Direct and Inverse Transonic Euler Equations", AIAA Paper 85-1530, 1985.
5. Woodward, D.S., Hardy, B.C., Ashill, P.R., "Some Types of Scale Effect in Low-Speed, High-Lift Flows", ICAS Paper 4.9.3, Jerusalem, 1988.
6. Poll, D.I.A., "Transition in the Infinite Swept Attachment Line Boundary Layer", Aeronautical Quarterly Vol XXX pt. 4, pp. 607-629, 1979.
7. Launder, B.E., and Jones, W.P., "On the Prediction of Laminarisation", ARC CP 1036, 1969.

* * * * *

A STUDY OF THE USE OF HALF-MODELS IN HIGH-LIFT WIND-TUNNEL TESTING

by

P. B. Earnshaw, A. R. Green, B. C. Hardy and A. H. Jelly

Defence Research Agency
Farnborough Hampshire GU14 6TD, United Kingdom

SUMMARY

An experimental investigation into the use of half-model testing techniques specifically aimed at high-lift testing has been carried out in the 5 Metre Pressurised Wind Tunnel at the DRA, Farnborough. The aim of the programme was to provide an assessment of the extent to which the measured characteristics of a high-lift model might be compromised by, in particular, the existence of a boundary layer on the reflection plane and how any penalties might be minimised.

The results suggest that, provided care is taken with experimental technique, good agreement is possible on stall incidence as well as the absolute values of lift, drag and pitching moment.

1 INTRODUCTION

The use of half-models in wind-tunnel testing can offer several advantages. Among these are the engineering advantages of design simplification, speed of manufacture and reduction of model cost together with the operational advantages in test of the removal of support interference and the increase of model Reynolds number. However, these benefits are only offered at the expense of possible interaction between the flow over the model and the boundary layer over the reflection plane. Because of this, many wind tunnel engineers take the view that, while useful results may be achieved for lift and pitching moment, this is not necessarily true in the case of drag. An alternative view, also widely held, is that the half-model technique offers a means of establishing incremental changes to forces and moments resulting from modifications to model build but cannot provide the absolute values of these forces.

Despite these reservations, the undoubted convenience of half-models provides a strong incentive to their use - for example in attempting to define optimum slat and flap settings in the development of high lift devices. However, in this particular application where the interest centres on maximum lift and the nature of the stall, or on drag at high lift, it seems much more probable that a strong interaction between the model and the wall boundary-layer flow would be evident in the test results on the half-model.

At the 5 m wind tunnel at DRA, Farnborough, this type of test is carried out fairly frequently; it was important therefore to explore more carefully what limitations there might be on using these test techniques and to what extent the speculations discussed above were accurate, in particular as far as the assessment of high-lift characteristics was concerned.

A preliminary exploratory test programme comparing the results from a half-model test and the corresponding results from a complete model was carried out by BAe. The results suggested that there were indeed in some circumstances clear discrepancies between the two. The more comprehensive programme reported here was therefore instituted in an attempt to clarify the issue.

2 APPROACHES TO HALF-MODEL TESTING

Many different arrangements of half-model support schemes have been adopted in different wind tunnels, all offering particular advantages and disadvantages. However, in those cases where a particular effort has been made to minimise the influence of the boundary layer growth on the reflection plane, they appear to divide into two approaches:

(a) to reduce the boundary-layer thickness on the reflection plane,

(b) to reduce the influence of the latter on the aerodynamics of the model.

A very convenient and economical method of achieving (a) is to mount the model above a short reflection plane so that the distance over which a boundary layer can grow is restricted. However, at the 5 m wind tunnel, it was felt that an essential consideration should be the need to maintain as far as possible the same uniformity of the flow and known calibration over the half-model as that over a complete model. Only when this was the case could there be reasonable hope that the behaviour up to the stall would then be common between the two. This view led to a rejection of a short supported reflection plane or of an endplate where the outer wing would be able to 'see' the edges of the reflection plane. On the other hand, if a larger reflection plane were to be used, the design should be such that the stream velocities on each side of the plane should be broadly similar; if this were not the case, the oncoming stream would respond as if to an additional contraction which would require a significant streamwise distance before the flow were uniform again. To ensure that this was the case, the plane would have to be be mounted reasonably far from the test section floor and the model size would inevitably be reduced.

Initially, the technique favoured followed the approach (b) above in attempting to reduce the interaction of the floor boundary layer with the aerodynamics of the model. Thus, the model was supported with minimum clearance directly above an earthed plinth, or *peniche*, having the same outline as the fuselage. However, results from the early stages of the test programme suggested that, whether or not a plinth had been installed, it would be desirable to reduce the effective boundary-layer thickness.

Being a pressurised wind tunnel, space around the test section at the 5 m tunnel is at a premium and it would be very inconvenient to install large-diameter suction pipework. However, high-pressure pipework presents less of a problem and it has been possible to introduce a boundary-layer re-energisation system using a nozzle extending across the great proportion of the width of the test section at a point around a metre upstream of the nose of the model in use.

A calibration of blowing pressure and nozzle width was carried out against tunnel pressure and Mach number using boundary-layer rakes attached to the test section floor at three positions across the width and slightly upstream of the model nose. The choice of what was considered to be an acceptable total head distribution was of course largely arbitrary. However, plainly one of the main questions to be answered was whether, and under what circumstances, there might be any sensitivity of the model behaviour to the boundary-layer characteristics at the reflection plane.

The boundary layer profile shown in Fig 1 is typical of what was taken to be the most suitable at one particular tunnel operating condition. Evidently, the total boundary layer thickness changes throughout the tunnel working envelope but, given that an appropriate criterion for blowing pressure is applied, the character of the re-energised layer does not change substantially. In fact comparative tests at much higher energisation levels show no detectable changes in stall incidence and only small changes in forces at very much higher levels of blowing.

3 DESCRIPTION OF MODELS

In making assessments of the comparative effects of different test techniques on high-lift stall characteristics, it has to be recognised that great care must be taken to avoid even minor changes in model build. These inevitably create a risk of introducing significant flow changes in the neighbourhood of stall which in turn serve to confuse the comparisons; differences between models, support systems and possibly even tunnels offer still greater risk.

In order to minimise this complication, an existing 1:13 scale model of the A300B Airbus aircraft which had already been extensively tested at the 5 m tunnel was used. This model has been used as a general workhorse for technique development since 1978 and in particular has provided the basis for a lengthy programme of research into support interference. It happened also that BAe Hatfield had been interested in using this same model in a calibration exercise in their own tunnels and had manufactured a suitable half fuselage so that it could be tested in half-model form in a smaller tunnel. They agreed to its use by DRA for its own research programme.

Measurements for a very wide array of different configurations of the complete model were already available, in most cases using a conventional three-strut support system from an underfloor balance although, as part of the support interference programme, it had also been tested using a sting support with an internal strain-gauge balance. Apart from check tests therefore, there was no need to carry out any further testing on the complete model.

In half-model build, the model was mounted from the same underfloor balance in three positions :

(a) as close as possible to the earthed test section floor. The model support therefore passed through a hole in the latter. No attempt was made to provide a labyrinth seal but clearance was made as small as was conveniently possible in order to reduce airflow between inside and outside the test section,

(b) as close as possible to an earthed plinth, or *peniche*, of 75 mm thickness and having the same outline as that of the fuselage centre-section. The plinth was attached to the turntable which carried the balance and model and consequently rotated with the latter as incidence was changed (see Fig 2),

(c) as close as possible to a deeper plinth of 100 mm thickness in order to assess the influence of plinth height.

Given the typical size of model used in the 5 m tunnel and the overhang of the extremes of a corresponding fuselage and making due allowance for movement of the live balance platform before equilibrium was achieved, a convenient clearance between the live part of the model and the tunnel floor in the absence of a plinth was around 5 mm. The semi-span of the half-model used in this instance, obviously rather smaller than would normally be the case in a tunnel of this size, was 1.750 m.

The half-model is shown mounted in the test section in Fig 3a and since, at a later stage in the programme, it became clear that an effectively reduced floor clearance was necessary, details of the improved sealing are indicated in Fig 3b.

It must be recognised that, because of its fairly small size relative to the tunnel, the use of this half-model adjacent to an unrepresentatively thick boundary layer may well have exaggerated differences with the complete model or at the very least made such differences easier to identify.

When used with a plinth, the latter was earthed and attached firmly to the turntable. Again, apart from the height needed to accommodate the plinth, an additional clearance similar to that when used in the absence of a plinth had to be introduced between it and the live fuselage.

Since the maximum thickness of the floor boundary layer at the lower end of the tunnel operational envelope was about 100 mm reducing to around 70 mm at the high end, the plinth height that was thought to be the most appropriate was 75 mm. This height therefore was used most extensively in the comparative programme. Nevertheless, it was always evident that, at incidence, the floor boundary layer would be swept up over the fuselage regardless of plinth height. Consequently, in an effort to assess the influence of plinth height, some tests were carried out using a second plinth, 100 mm in height.

4 DISCUSSION OF RESULTS

The manner in which different configurations react to changes in half-model test procedure is complicated and may well explain why, following success in a particular instance, some laboratories adopt a procedure which has proved unsuccessful for others. Furthermore, when in particular the interest centres on stall development, especially where some effort has been spent on optimisation of the high-lift characteristics of the wing and consequently all parts of the wing are working hard, it can be more than usually difficult to reproduce the forces and moments identically following a model rebuild; even in consecutive test runs, movements of sealing materials or tape edges can manifest themselves through significant changes to the stall development but still be quite difficult to locate physically. Nevertheless, in the present test programme, it was felt that that the controlling mechanisms could be identified fairly clearly despite occasional lapses when the lack of reproducibility was evident.

In the course of these present tests, a large number of different configurations for both landing and take-off have been examined at various Reynolds numbers with and without the presence of a plinth, and with and without the use of boundary-layer re-energisation (BLRE). However, for the purposes of this paper, the data has been limited to that necessary to illustrate the various phenomena that have been identified as affecting the results. Fortunately, it has been possible to choose a single configuration to demonstrate all of the major effects: the A300B4 in take-off configuration (16°:8°/3°).

Fig 4a&b compare the lift curves for the complete model, the half-model without plinth, with 75 mm plinth and with 100 mm plinth; there was no application of BLRE in this instance. If, for the moment, we choose to regard the results for the complete model as being correct, various distinct features are apparent:

(a) the simple half-model had a lift-curve which was too low and stalled early by a little less than 2°,

(b) the half-model mounted on a 75 mm plinth had a lift-curve slope which was only marginally too high and began to stall very slightly early,

(c) the half-model mounted on a 100 mm plinth had a lift-curve slope still higher and stalled at around the same incidence as the simple half-model.

This behaviour seems at first sight to be erratic whilst also providing us with a strong predisposition to use - in this tunnel at least - a 75 mm plinth. In fact, the various interacting mechanisms are quite clear and will be discussed in the following sections.

4.1 Stall

If guidance is sought from the pitching moment behaviour, shown in Fig 5, for the same configurations discussed above, it is immediately clear that all the half-models stalled dramatically nose-down whereas the complete model stalled less severely and nose-up. The implication is that there was a very abrupt loss of lift inboard on the half-model whereas on the complete model, either the outboard wing or possibly the inboard flap stalled first. In fact, examination of the rolling moment data made it clear that it was an outboard stall in this instance.

However similar the full-model and half-model lift curves might appear in the case of the 75 mm plinth, the stall development was plainly totally unrepresentative.

At a slightly higher Reynolds number, when the reflection plane boundary layer was somewhat thinner, a magnified view of lift near stall shows (Fig 6) that now the simple half-model stalled at close to the same incidence as the 75 mm plinth case. Interestingly, the change in pitching moment through stall on both, Fig 7, had now altered completely from nose-down to nose-up. At both Reynolds numbers, the 100 mm plinth retained an inboard stall.

The impact of BLRE is shown at the lower Reynolds number of 5 x 10^6 on lift in Fig 8 and on the corresponding pitching moment in Fig 9. In this case, the stall on both the 75 mm plinth and the simple half-model was delayed but now the stall on the latter was higher than both the 75 mm plinth and the complete model.

Consider first the stall behaviour of the three half-model configurations. The introduction of a plinth, earthed or not, produced a fuselage which was effectively wider and which therefore increased the effective incidence of the inboard wing. Provided therefore that the outboard wing did not stall first, the highest plinth case should have stalled inboard first of the three. This, therefore, accounts for the fact that, at both Reynolds numbers and regardless of BLRE, the 100 mm plinth case stalled inboard and early.

Without BLRE, the simple half-model may suffer from an early inboard stall triggered by the thick reflection-plane boundary layer. With BLRE, it has already been pointed out that stall on the half-model was delayed by around a half degree. Now corrections to incidence are usually calculated at the 5 m tunnel as a suitably weighted mean of an upwash which varies across the span. In the case of the half-model, which was in fact quite small for this tunnel, the wall-induced upwash varied by no more than 0.05° across the span and can therefore be regarded as effectively constant. However, the complete model had incidence corrections both for larger wall corrections which varied significantly along the span and as a result of the presence of strut guards.

The wall-induced upwash corrections have been applied to the data as a weighted mean incidence correction which in the case of the complete A300 model corresponded to the upwash angle calculated at about 0.4 span; the contribution of wall-induced upwash *relative* to the corrected incidence is zero therefore at 40% span. On the other hand, the procedure used at the 5 m wind tunnel for applying strut and guard corrections is such that these are applied together using semi-empirical techniques; it happens to be convenient to apply the corrections to lift, drag and pitching moment rather than to incidence. While the procedure works well at incidences below stall, it does not result in a significant correction to stall incidence. The distribution of upwash due to the strut guards has been extracted from this data and is plotted together with the wall-induced corrections in Fig 10. It is evident that the outboard 20% of the wing on the complete model was at an incidence some 0.5° higher than the corrected incidence used in the plots. Plausibly therefore, given that both complete and half-models were disposed to stall outboard, the complete model would be expected to stall some 0.5° lower than the half-model.

The same simple argument ought also to apply to the 75 mm plinth case. Unfortunately, while it does do so at the higher Reynolds number, shown in Fig 6, it plainly does not do so with BLRE in Figs 8 and 9. In fact, the slight improvement of stall incidence following the introduction of BLRE to the plinth-mounted model results from a movement of separation from inboard to the neighbourhood of the pylon rather than to the outboard wing. While it is quite possible that the introduction of a plinth could so modify the lift distribution and upwash field that the mid-wing near the pylon was triggered into an early separation that did not occur at the higher Reynolds number, it may seem more reasonable to recall the difficulties mentioned at the beginning of this section of repeating stall behaviour on a wing that has been carefully optimised.

4.2 Lift-Curve Slope

A deficit in lift-curve slope can be seen on the simple half-model in Fig 4a. Initially, this had been thought to be due to the thick reflection-plane boundary layer operating on the fuselage and inboard wing particularly in view of the much closer agreement when using a 75 mm plinth but calculations made using a panel method (SPARV) showed that this latter improvement of lift-curve slope above that of the simple half-model would be expected from the change in geometry resulting from the introduction of a plinth. Furthermore the operation of BLRE, as shown already in Fig 8, provided little improvement in slope.

In fact, significant improvement in agreement between half- and complete-model lift-curve slopes (Fig 11) resulted from the installation of a baffle plate which reduced the gap between the model support and the reflection plane from around 10 mm to nearer 2 mm, together with additional sealing around the outline of the fuselage in an effort to reduce the flow of air from one side of the fuselage to the other (see Fig 3b); this was achieved without otherwise changing the model geometry. The implication therefore is that errors in the measured lift resulted more from deficiencies in the design of the support system rather than from an inability to reproduce the correct aerodynamics of the wing. Evidently, there still remained a significant lift deficit which would probably require a fundamental redesign of the model support and sealing system to reduce to an acceptable level on a model of this size. However, as suggested above, there seems to be no indication that the aerodynamics of the wing and high-lift system are compromised by lift losses at the fuselage and support system.

4.3 Pitching Moment

The influence of BLRE and plinth installation on pitching-moment behaviour in the neighbourhood of stall has already been discussed. In addition to this particular aspect however, it is evident that all three half-models had close to the same pitching moment at zero lift (Fig 5), that the slope of the pitching-moment curve measured on the simple half-model agreed quite well with that for the complete model but that the aerodynamic centre moved perceptibly forward as the plinth height increased.

The effect on pitching moment of the modifications to fuselage/reflection plane sealing discussed earlier in relation to the lift-curve slope are shown in Fig 12. In fact, the modifications were carried out in two stages, the results for both of which are shown.

The first stage applied sealing simply along the parallel section of the fuselage while the second extended these to the edge of the turntable; since the fuselage overhung the turntable at both ends, an extension around the complete fuselage was not easy to contrive.

It is clear in Fig 12 that, while very good agreement was achieved between full- and half-models by using short seals, 'improvements' to the seals by extending them towards the front and rear led to a deterioration in agreement. Evidently, although 'spillage' of lift carried at the ends of the fuselage through inefficient sealing did not lead to a detectable change in overall lift, it did make a significant contribution to pitching moment. Since a substantial length of upswept fuselage remained unsealed at the rear, it is likely that completion - and possibly improvement also - of the seals would lead to better agreement. However, given the quite respectable agreement that has already been established, it seems fair to speculate whether an error of this magnitude could result also from inadequacies of the strut and guard corrections given that a pitch strut was used to support the rear fuselage for the complete-model mounting.

4.4 Drag

It is convenient to illustrate differences in drag between different configurations by reference to the reduced drag, C_{DR}, where: $C_{DR} = C_D - C_L^2/\pi A$ and where A is the aspect ratio of the full-model in all cases.

Fig 13 shows that pre-stall, the simple half-model with BLRE had a reduced drag some 50 drag counts (0.0050) too high whereas, on a 75 mm plinth, C_{DR} was as much as 150 counts too low. This latter change was largely generated by changes to induced drag since the inviscid panel method calculations referred to earlier in fact tend to overestimate this change; the calculated drag changes due to the introduction of an earthed plinth are included in this same Figure at three incidences.

The use of improved sealing shown in Fig 14 slightly improves the similarity of the simple half-model to the full model but although the comparison is now quite close, the differences are still clear. However, it is worth pointing out that the reduced drag includes an input from the measured lift which is itself in error. If this discrepancy is removed by referring the reduced drag on the half-model to the lift at the same incidence on the complete model, Fig 14 shows that now agreement has been brought to within 15 drag counts. In effect this is equivalent to establishing that the total drag agreed to within 15 drag counts. At this level of agreement, it has to be pointed out that an error in tunnel upwash on the complete model, or of sidewash on the half-model, or indeed a combination of the two, of 0.04° would give rise to this level of discrepancy at a C_L of 2.

5 CONCLUSIONS

A substantial programme of comparative tests of a complete strut-mounted A300 model and a half-model of the same aircraft using the port wing of the complete model has been carried out in the 5 m Low-Speed Pressurised Wind Tunnel at DRA Farnborough. Since the complete model was sized for the tunnel, the half-model was evidently somewhat small and consequently interactions with the boundary layer on the reflection plane were exaggerated; this made their identification more clearcut than perhaps would normally be the case.

On the basis of this programme, various conclusions may be drawn:

(1) Unless efforts are made to reduce the effective boundary-layer thickness on the reflection plane, the use of a simple half-model mounted close to the reflection plane may possibly - although not necessarily - yield wholly unsatisfactory predictions of the stall behaviour.

(2) Where the results are indeed unsatisfactory, the technique cannot be used even for the assessment of incremental changes of model configuration at least as far as stall and post-stall behaviour is concerned.

(3) In some instances, the use of an earthed plinth (or *peniche*) to lift the half-model high in the boundary layer on the reflection plane may improve reproduction of stall incidence. However, this technique introduces consequential errors in lift-curve slope, drag and pitching moment. Furthermore, although the inboard wing may have reduced sensitivity to the boundary layer on the reflection plane, it is now adjacent to a fuselage which is effectively wider; it therefore suffers from an increased upwash around this wider fuselage and consequently a tendency to early stall due to this alternative mechanism.

(4) When the effective thickness of the boundary layer on the reflection plane has been reduced sufficiently, good reproduction of stall incidence may be achieved. Differences between the two are likely to favour the half-model given that the full model is open to disturbance from its support system.

(5) Some care must be be taken to ensure that flow from one side of the model to the other, or through the gap around the support frame, should be restricted. The immediate effect of inadequate sealing is shown as a significant loss of lift-curve slope. This particular problem has proved to be the most intractable with the present half-model design where the discrepancy between full and half-models amounted to around 1.5% on lift. However, there seemed to be no indication that this leakage interfered with the aerodynamics of the wing or of its high-lift system but was more restricted to the flow about the fuselage. With a model sized more appropriately for the tunnel and designed from the start as a half-model, it might be reasonable to expect that this discrepancy could be reduced.

(6) Just as in the case of lift, pitching moment also responds to changes in sealing around the fuselage but again giving no indication that the aerodynamics of the wing and its high-lift system are compromised in any way. In the present instance, the total absence of sealing at the extremes of the fuselage appeared to give significant changes to the pitching moment coefficient with a maximum error of around 0.01.

(7) Perhaps most surprisingly, drag appears to be the most satisfactory in that disagreement between complete and half-models over a large part of the incidence range was not worse than 15 drag counts. An improvement in this level of agreement may not be possible without greater confidence in the knowledge of the mean values of upwash and sidewash velocities existing in the empty test section; a total discrepancy of 0.04° in incidence between complete and half-models would be sufficient to generate this difference in drag at a lift coefficient of 2.

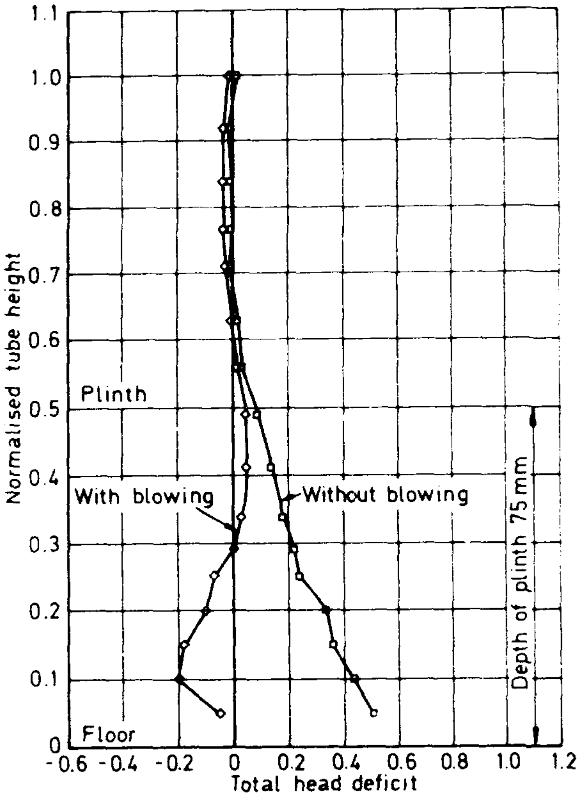

Fig 1 Comparison of velocity profiles with and without blowing

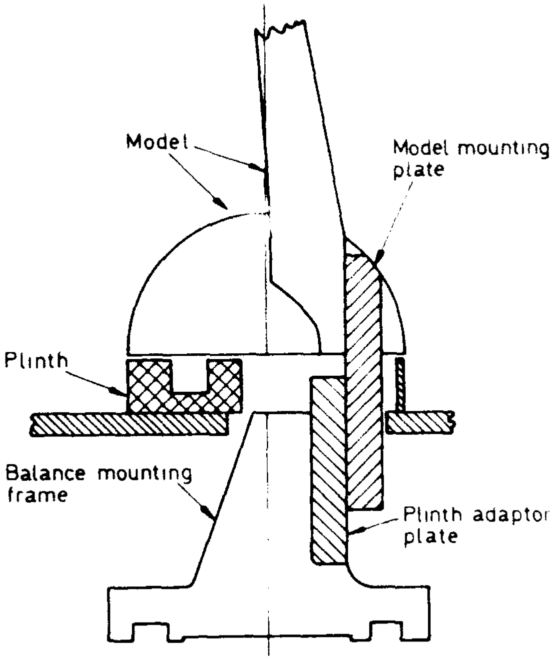

Fig 2 Half-model mounting geometry

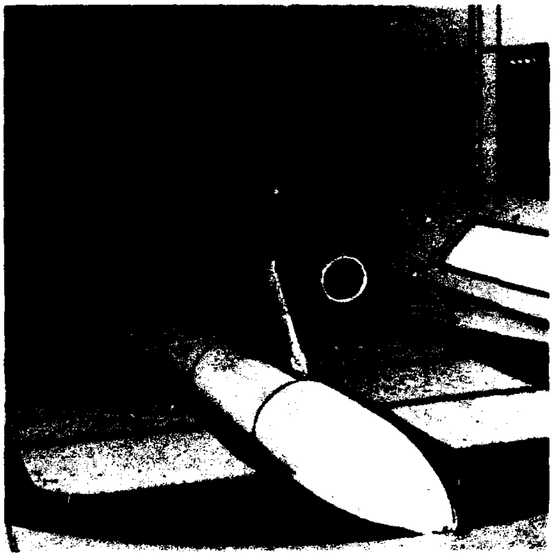

Fig 3a Half-model mounted without plinth in test section

Fig 3b Detail of improved sealing around fuselage

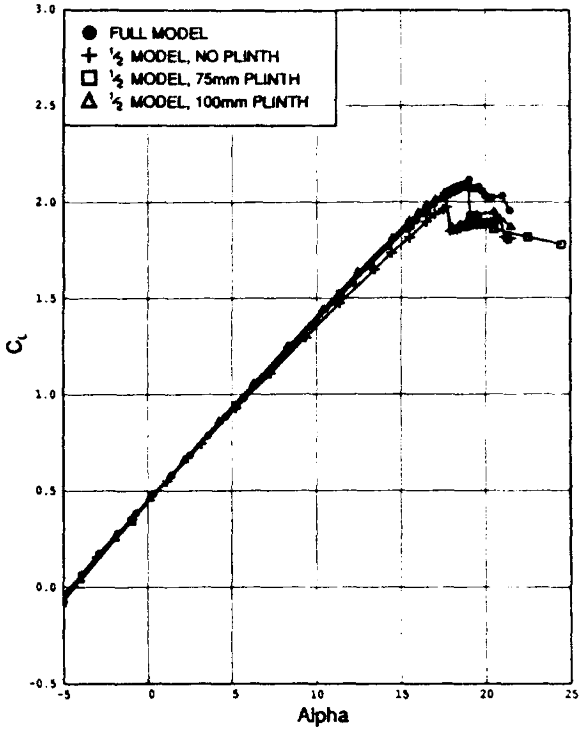

Fig 4a Effect of plinth height on C_L
M = 0.20, Re = 5.0 x 10^6

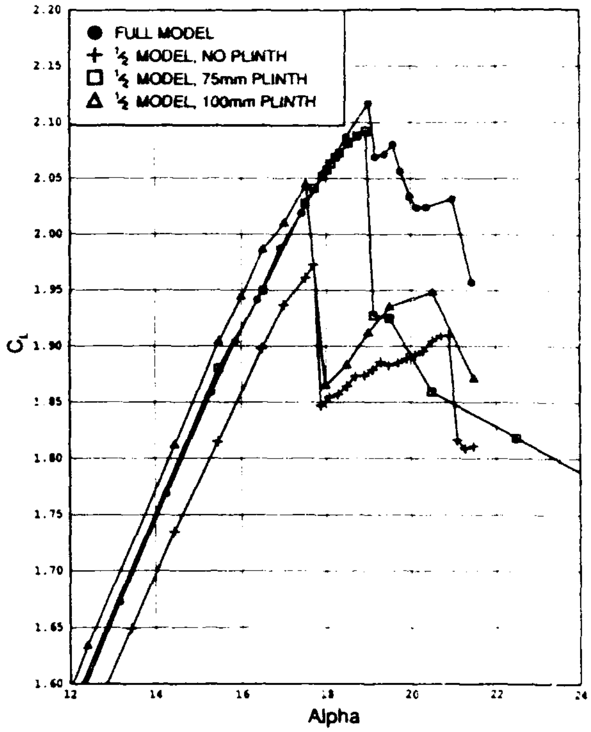

Fig 4b Effect of plinth height on C_L
M = 0.20, Re = 5.0 x 10^6

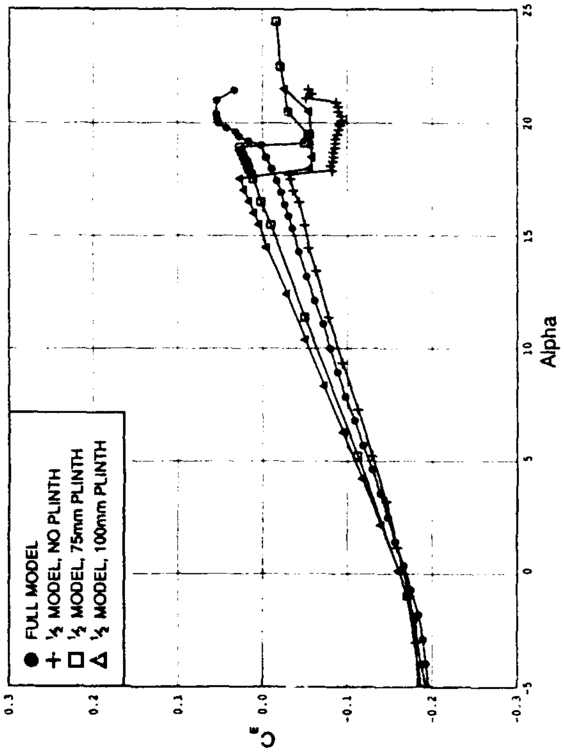

Fig 5 Effect of plinth height on C_m
M = 0.20, Re = 5.0 x 10^6

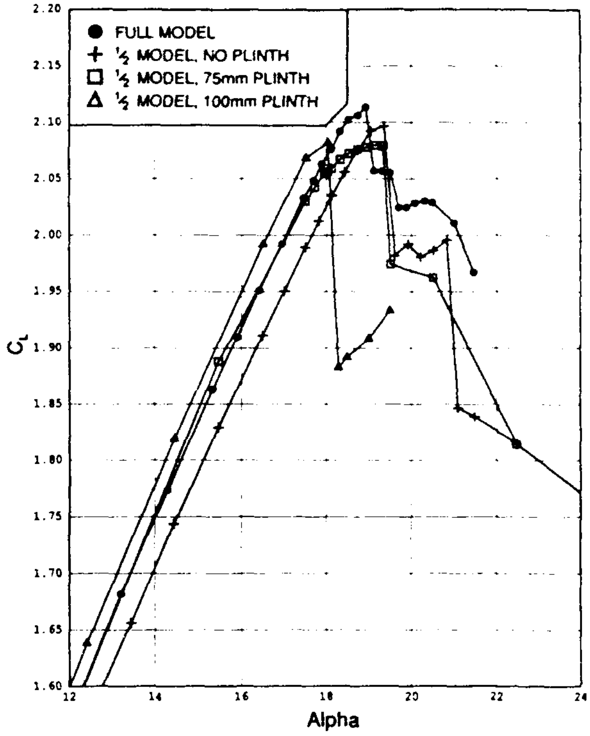

Fig 6 Effect of plinth height on C_L
M = 0.20, Re = 6.45 x 10^6

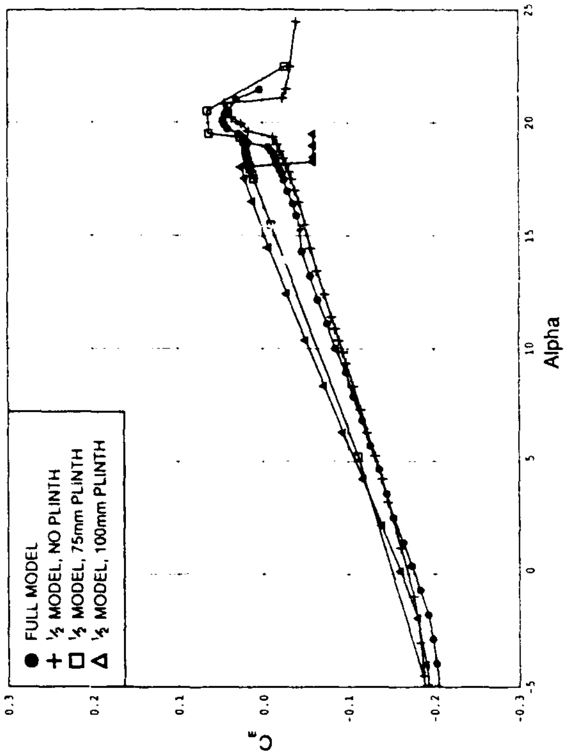

Fig 7 Effect of plinth height on C_m
M = 0.20, Re = 6.45 x 10^6

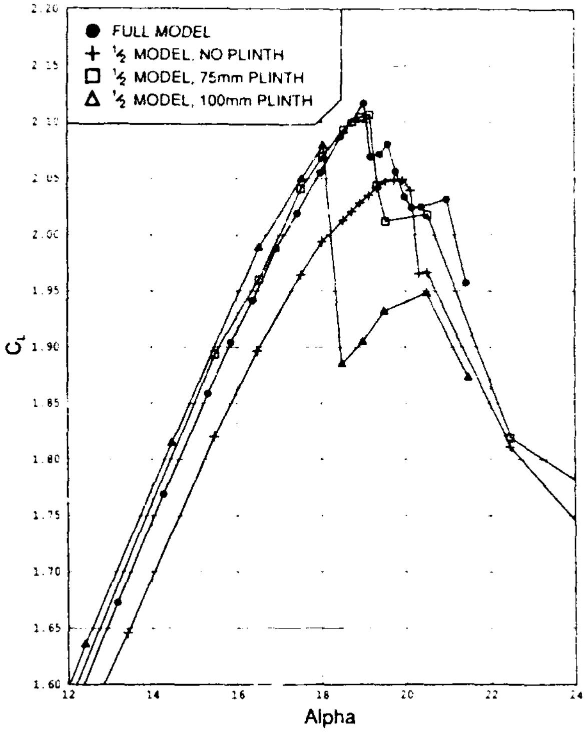

Fig 8 Effect of plinth height on C_L
M = 0.20, Re = 5.0 x 10^6

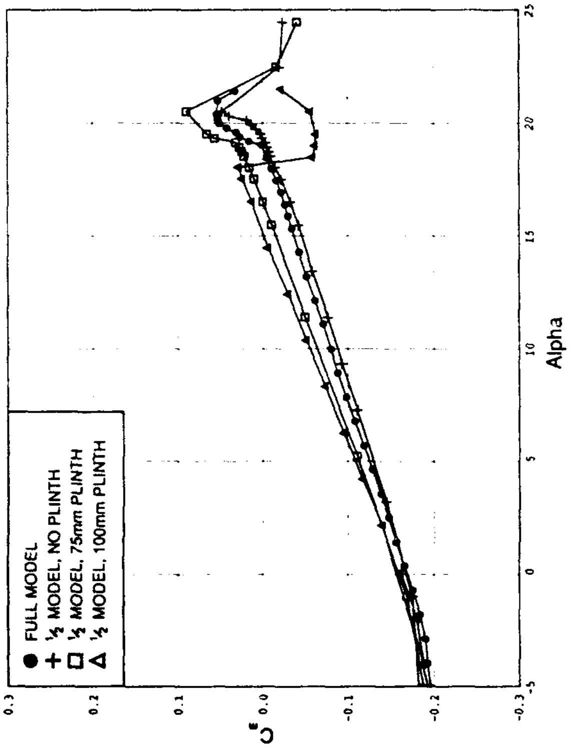

Fig 9 Effect of plinth height on C_m
M = 0.20, Re = 5.0 x 10^6

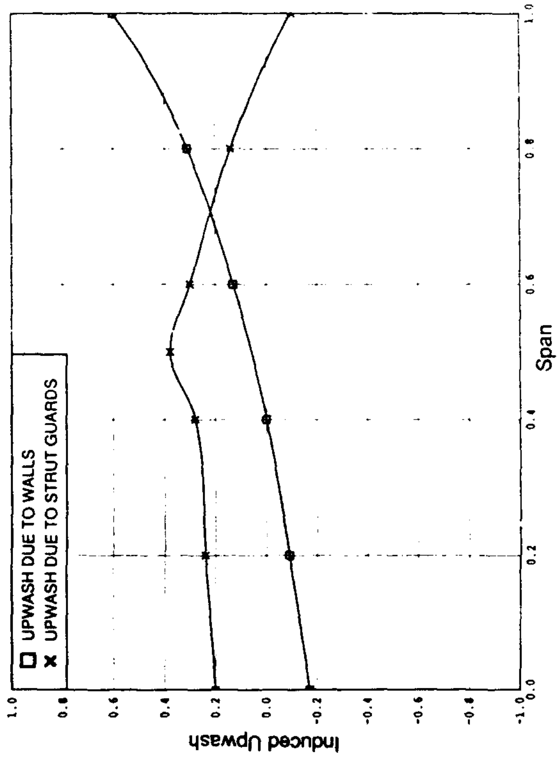

Fig 10 *Comparison of upwash due to test section walls with that due to strut guards*

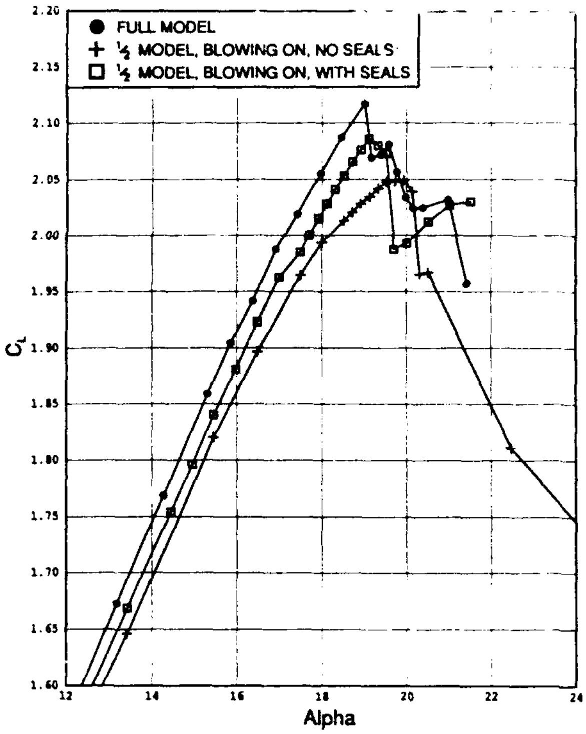

Fig 11 Effect of internal and external seals on C_L
$M = 0.20$, $Re = 5.0 \times 10^6$

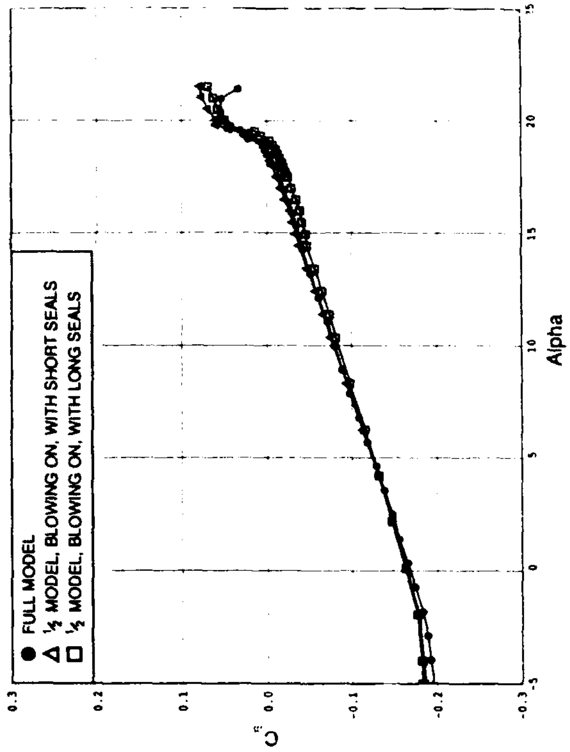

Fig 12 Effect of internal and external seals on C_m
$M = 0.20$, $Re = 5.0 \times 10^6$

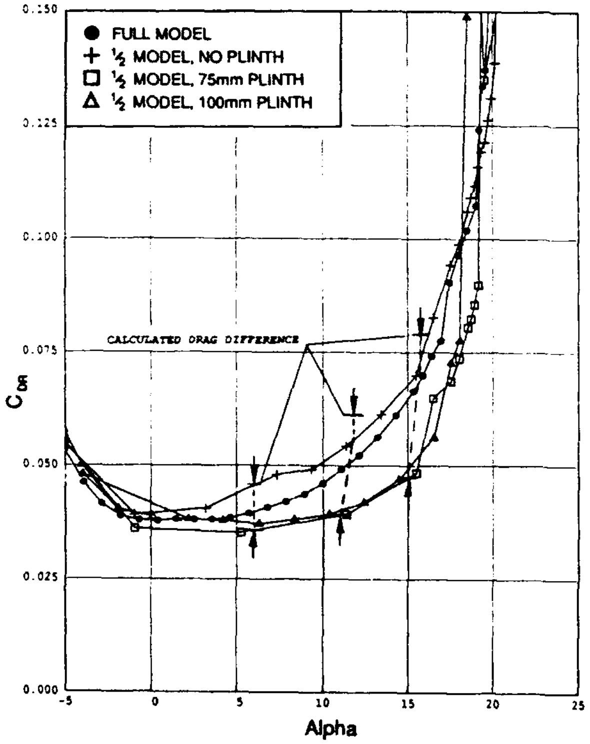

Fig 13 Effect of plinth height on CD_R
$M = 0.20$, $Re = 5.0 \times 10^6$

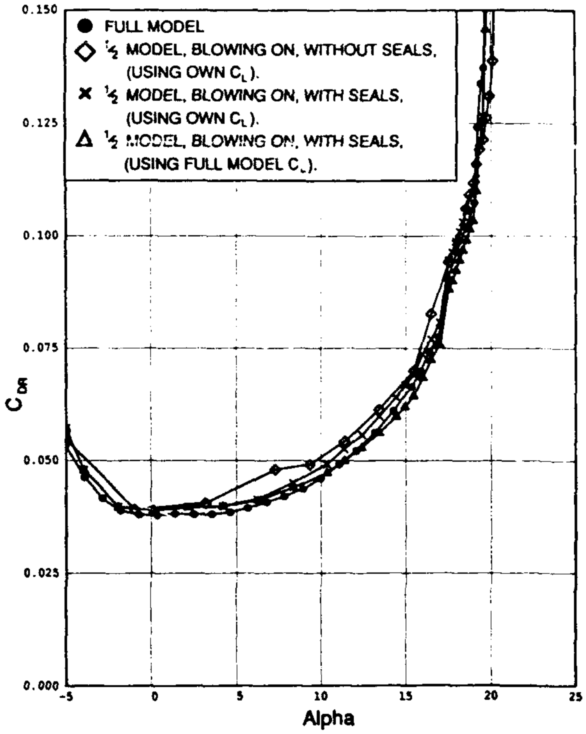

Fig 14 Comparison of full and half-model drag data

IN-FLIGHT PRESSURE DISTRIBUTIONS AND SKIN-FRICTION MEASUREMENTS ON A SUBSONIC TRANSPORT HIGH-LIFT WING SECTION

Long P. Yip
NASA Langley Research Center
Hampton, Virginia, USA 23681-0001

Paul M.H.W. Vijgen
High Technology Corporation
Hampton, Virginia, USA 23681-0001

Jay D. Hardin
Lockheed Engineering and Sciences Company
Hampton, Virginia, USA 23681-0001

C. P. van Dam
University of California, Davis
Davis, California, USA 95616-5224

SUMMARY

Flight experiments are being conducted as part of a multi-phased subsonic transport high-lift research program for correlation with wind-tunnel and computational results. The NASA Langley Transport Systems Research Vehicle (B737-100 aircraft) is used to obtain in-flight flow characteristics at full-scale Reynolds numbers to contribute to the understanding of 3-D high-lift, multi-element flows including attachment-line transition and relaminarization, confluent boundary-layer development, and flow separation characteristics.

Flight test results of pressure distributions and skin-friction measurements were obtained for a full-chord wing section including the slat, main-wing, and triple-slotted, Fowler flap elements. Test conditions included a range of flap deflections, chord Reynolds numbers (10 to 21 million), and Mach numbers (0.16 to 0.40). Pressure distributions were obtained at 144 chordwise locations of a wing section (53-percent wing span) using thin pressure belts over the slat, main-wing, and flap elements. Flow characteristics observed in the chordwise pressure distributions included leading-edge regions of high-subsonic flows, leading-edge attachment-line locations, slat and main-wing cove-flow separation and re-attachment, and trailing-edge flap separation. In addition to the pressure distributions, limited skin-friction measurements were made using Preston-tube probes. Preston-tube measurements on the slat upper surface suggested relaminarization of the turbulent flow introduced by the pressure belt on the slat leading-edge surface when the slat attachment line was laminar.

Computational analysis of the in-flight pressure measurements using two-dimensional, viscous multi-element methods modified with simple-sweep theory showed reasonable agreement. However, overprediction of the pressures on the flap elements suggests a need for better detailed measurements and improved modeling of confluent boundary layers as well as inclusion of three-dimensional viscous effects in the analysis.

LIST OF SYMBOLS

b	wing span, ft
C_f	skin-friction coefficient, τ/q_∞
C_f^*	Preston-tube-measured C_f using eq. (3)
C_L	aircraft lift coefficient, lift/$q_\infty S$
C_n	normal-force coefficient from integrated pressures
C_p	pressure coefficient, $(p-p_\infty)/q_\infty$
c	chord length, ft
$\bar{c}$	mean aerodynamic chord, 11.20 ft
d	Preston-tube diameter, in
h	pressure altitude, ft
K	relaminarization parameter, eq. (2)
M	Mach number
p	local static pressure, psf
p_∞	freestream static pressure, psf
p_t	local total pressure, psf
q_∞	freestream dynamic pressure, $\rho_\infty V^2/2$, psf
$R_{\bar{c}}$	Reynolds number based on $\bar{c}$, $V\bar{c}/\nu$
$\bar{R}$	attachment-line Reynolds number, eq. (1)
R_θ	momentum-thickness Reynolds number
S	reference wing area, 980 ft^2
s	surface streamwise coordinate, ft
V	true airspeed, ft/sec
V_i	indicated airspeed, knots
x/c	non-dimensional chordwise coordinate
y	spanwise coordinate, ft
z/c	non-dimensional thickness coordinate
α	aircraft angle of attack, deg
$\alpha_{2\text{-}D}$	wing-section angle of attack, deg
Δp	differential Preston-tube pressure, p_t - p, psf
δ_f	flap deflection, deg
Λ_{LE}	leading-edge sweep angle, deg
η	non-dimensional spanwise location, y/(b/2)
ν	kinematic viscosity, ft^2/sec
ρ_∞	freestream density, slugs/ft^3
θ	momentum thickness, ft
τ	surface shear stress, psf

Abbreviations

ESP	electronic scanning pressure
KIAS	knots indicated airspeed
LE	leading edge
TSRV	Transport Systems Research Vehicle
2-D	two-dimensional
3-D	three-dimensional

1. INTRODUCTION

High-lift system aerodynamics can significantly impact the overall design of transport aircraft in terms of sizing, performance, system complexity, and certification for safety and community-noise acceptance aspects.[1] However, the design of subsonic high-lift systems remains a technical challenge mostly due to the limited understanding of the complex flow physics associated with high-lift flows. Multi-element, high-lift flows are very sensitive to Reynolds- and Mach-number effects; and therefore, the aerodynamic performance of high-lift systems is generally difficult to extrapolate from wind-tunnel or to predict in computational fluid dynamics (CFD) studies. In order to improve the design methodology for high-lift systems, additional experimental data with sufficient flow details on transport-type swept wings are needed at flight Reynolds and Mach numbers to better understand high-lift flows. Thus far, only a very limited number of flight investigations have been conducted with sufficiently detailed flow measurements on a high-lift system for correlation with ground-based investigations and to guide 3-D CFD modeling. One such investigation was reported by Greff[2] on an Airbus A310-300 aircraft.

As part of a multi-phased research program at NASA Langley, flight tests are being conducted on the Transport Systems Research Vehicle (TSRV), a B737-100 aircraft, to obtain detailed full-scale flow measurements on a multi-element high-lift system at various flight conditions. In Phase I of the program, experiments were focused on flow visualization, pressure distributions, and flow-separation measurements on the triple-slotted Fowler flap system of the research aircraft. Phase I activities have been completed, and the flight test results were reported by Vijgen et al.[3] In Phase II, more detailed flow measurements have been planned including the main wing and leading-edge slat components. Initial Phase-II flight experiments have recently been completed on a wing section at one spanwise station to measure pressure distributions on the full chord, and these results were reported by Yip et al.[4]. Additional Phase II flight experiments are planned to provide additional full-chord pressure measurements at several spanwise stations and detailed measurements of leading-edge transition and relaminarization. In Phase III, extensive off-surface instrumentation for detailed turbulent boundary-layer and wake flow-field characteristics are planned. This paper summarizes the test results to date of the high-lift flight research program on the TSRV as well as planned further flight experiments.

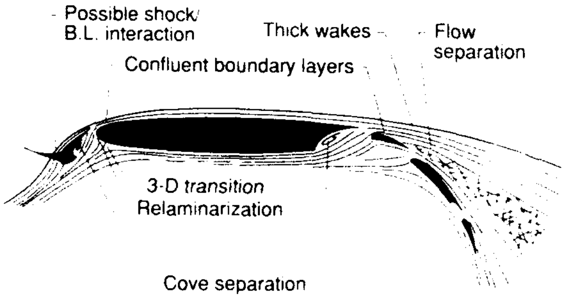

Figure 1. Multi-element flow characteristics.

2. BACKGROUND FOR HIGH-LIFT FLOWS

2.1 Multi-Element Flow Issues

The flow field around a multi element transport wing with sweep is characterized by several aerodynamic phenomena which are highly interrelated, complex in nature, and generally not fully understood (see Fig. 1). Accurate prediction of surface-pressure distributions, merging boundary-layers, and separated-flow regions over multi-element high-lift airfoils is an essential requirement in the design of advanced high-lift systems for efficient subsonic transport aircraft.[1] The availability of detailed measurements of pressure distributions and boundary-layer flow parameters at flight Reynolds and Mach numbers is critical to the evaluation of computational methods and to the modeling of turbulence for closure of the governing flow equations.[5,6] Detailed measurements and analyses of the multi-element flow field have generally been limited to two-dimensional studies. Previous detailed flow measurements in wind-tunnel investigations have included Reynolds-stress components, however, at sub-scale Reynolds numbers and only in two dimensions.[7,8,9,10] These results have been applied towards the development and validation of 2-D multi-element numerical codes.

Two-dimensional multi-element flow issues include the following:

(1) compressibility effects including shock/boundary-layer interaction on the slat;
(2) laminar separation-induced transition along the upper surfaces;
(3) confluent turbulent boundary layer(s) - the merging and interacting of wakes from upstream elements with the boundary layers of downstream elements;
(4) cove separation and reattachment; and,
(5) massive flow separation on the wing/flap upper surfaces.

Availability of detailed flow data in three dimensions at full-scale (flight) Reynolds numbers has been much more limited. To contribute to the understanding and correlation of high-lift research between wind tunnel, CFD, and flight, additional experiments are needed at full-scale Reynolds number and for 3-D swept wings. Further understanding of scale effects in both 2-D and 3-D is required to accurately extrapolate to 3-D, full-scale, flight conditions.[11,12,13]

Three-dimensional multi-element flow issues include the following:

(1) leading-edge attachment-line transition;
(2) relaminarization of turbulent flow in the leading-edge region;
(3) crossflow instability transition downstream of the attachment line;
(4) sweep effects on confluent boundary-layer development, turbulent boundary-layer separation, and separated cove flows; and,
(5) highly three-dimensional, local flow modifications; e.g., vortex generators; flap side-edge-separated flows and tip effects; and flow interactions with slat brackets and flap-track fairings, engine pylons, and landing-gear struts.

The three-dimensional multi-element issues of leading edge attachment-line transition and the potential for relaminarization are discussed in more detail in the following section.

2.2 Attachment-Line Transition and Relaminarization Issues

In three-dimensional, swept-wing flows, the flow along the attachment line (a locus of points near the leading edge dividing upper- and lower surface flows) can be laminar, transitional, or turbulent, depending on the pressure distribution, the leading-edge sweep angle, and the Reynolds number.[14,15,16] If attachment-line transition occurs, the resulting changes in the development of boundary layer flows can significantly influence the downstream turbulent flow field (i.e., confluent boundary layers and onset of separation). Relaminarization of the flow downstream of a turbulent attachment line can occur if the streamwise flow acceleration is sufficiently strong.[17,18,19] If the flow ahead of a steep adverse pressure gradient along the upper surface of the elements is laminar, an additional Reynolds-number effect can occur due to the presence of a laminar-separation bubble and its effect on subsequent turbulent-flow behavior.

The issues of leading-edge transition and relaminarization, illustrated in figure 2 for a single-element, swept wing, become very important in the extrapolation of sub-scale, three-dimensional, wind-tunnel results to flight. Typically, wind-tunnel data used to extrapolate maximum lift in flight are obtained at Reynolds-numbers conditions where wing stall is dominated by conventional scale effects (see Woodward et al.[20]). Conventional scale effects refer to the increase of maximum lift with Reynolds number due to the thinning of the turbulent boundary-layer in the wing trailing edge region and the subsequent aft movement of the trailing-edge flow separation point. At higher flight Reynolds numbers, attachment-line transition can occur causing turbulent flow to start from the attachment line. By shifting forward the starting point of the turbulent boundary layer, the trailing-edge separation location can also shift forward due to the increased growth of the turbulent boundary layer. Because of the increased extent of trailing-edge separation, a significant reduction in lift can occur. However, because of steep favorable pressure gradients associated with high-lift flows, relaminarization is possible for some sections of the wing and would thereby alleviate some of the lift loss expected as a result of the attachment-line transition. In a high-Reynolds-number wind-tunnel investigation of a swept-wing configuration without slats, maximum-lift losses of the order of 15 percent have been measured when transition occurred along the attachment line and relaminarization did not occur.[12]

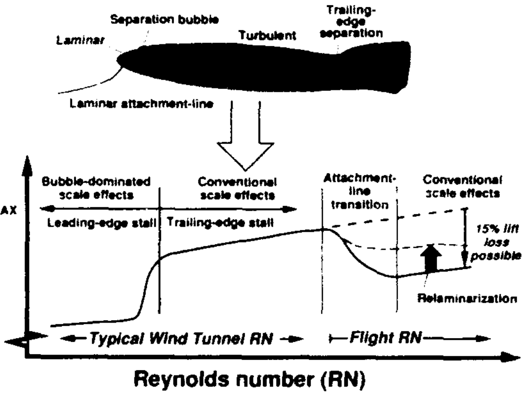

Figure 2. Effect of attachment-line transition and relaminarization on maximum lift.

An important parameter when examining the transition characteristics of the attachment-line boundary layer along the leading edge of a swept lifting surface is the attachment-line Reynolds number, $\bar{R}$, as defined by the following equation:

$$\bar{R} = \frac{W_\infty \kappa}{\nu} \qquad (1)$$

where $W_\infty = V \sin \Lambda$

and $\kappa = (\nu/U')^{0.5}$

The characteristic velocity, W_∞, is the spanwise component of the freestream velocity, and κ is the characteristic length where U' represents the inviscid velocity gradient at the attachment line in the direction normal to the attachment line.[14,15,16] For a laminar attachment-line boundary layer along an infinite swept cylinder, the momentum thickness can be shown to be $\theta = 0.404\ \kappa$, and consequently, $R_\theta = 0.404\ \bar{R}$.[21] Previous studies have shown that for $\bar{R} < 245$, the attachment-line boundary layer will tend to remain laminar, and turbulent contamination introduced in the boundary layer by significant surface roughness and intersecting turbulent shear layers will decay. For $\bar{R} > 245$, the turbulence will self-sustain, causing the attachment-line flow as well as the flow downstream of the attachment line to become turbulent. For incompressible conditions, in the absence of roughness and intersecting turbulent shear layers, attachment-line instability followed by transition will occur only if $\bar{R} > 580$.[22]

An important parameter when examining relaminarization of turbulent boundary-layer flows is the inverse Reynolds number, K, which is defined as follows:

$$K = \left(\frac{U\zeta}{\nu}\right)^{-1} \qquad (2)$$

where the characteristic velocity is represented by the local inviscid velocity, U, and the characteristic length, ζ, is defined by $\zeta = U/U_s'$ with U_s' representing the velocity gradient along the inviscid streamline.[17,23,24] For K larger than 1×10^{-6}, reversion from turbulent to laminar flow is possible, for $K > 3\times10^{-6}$ relaminarization is likely, and for $K > 5\times10^{-6}$ complete relaminarization occurs for 2-D flows (only very limited detailed data[18,19] are available to date for 3-D flows on swept wings).

Attachment-line transition, relaminarization, and crossflow instability along the elements of the B737-100 high-lift geometry were examined by Vijgen et al.[3] using predicted pressure distributions. Results of the study indicate that the attachment line along the slat and fore flap are likely to be laminar, while the attachment line along the fixed leading edge (main element) is likely to be turbulent for the 40°-flap setting at $\alpha = 0°$. In this paper, $\bar{R}$ and K are obtained from the measured pressure distributions. The attachment line along the slat in the flight experiment reported by Greff[2] on the Airbus A310-300 aircraft was measured to be laminar under certain high-lift flight conditions.

3. DESCRIPTION OF FLIGHT EXPERIMENT

3.1 Test Aircraft

The NASA Langley TSRV was the prototype aircraft used in the development of the Boeing B737-100 and has been significantly modified for flight systems research.[25] In its unmodified state, the Boeing 737-100 is a twin-jet, short-haul, subsonic transport designed to carry approximately 100 passengers with a cruise speed of Mach 0.78. In order to obtain short-field takeoff and landing performance, the aircraft incorporates a slat and triple-slotted flap high-lift system. Basic aerodynamic characteristics of the Boeing 737-100 configuration from wind-tunnel investigations have been documented in reports by Capone[26] and Paulson[27].

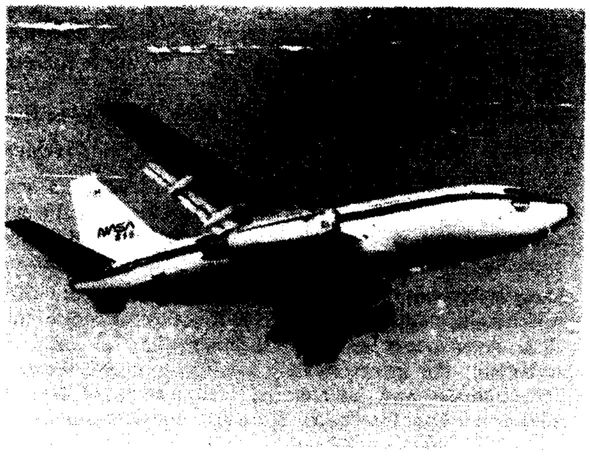

Figure 3. NASA TSRV (737-100 aircraft) in flight with 40°-flap setting and landing gear up.

Figure 3 shows the TSRV in flight with the triple-slotted flap system deployed at a 40°-flap setting (landing configuration). Figure 4 shows a planform view of the B737-100 configuration and illustrates the overall geometric characteristics. The aircraft wing is characterized by a span of 93 ft, an aspect ratio of 8.82, and a sweep angle of 25° at the quarter-chord line and 27.58° at the leading edge outboard of the underslung, low-bypass ratio engine nacelle.

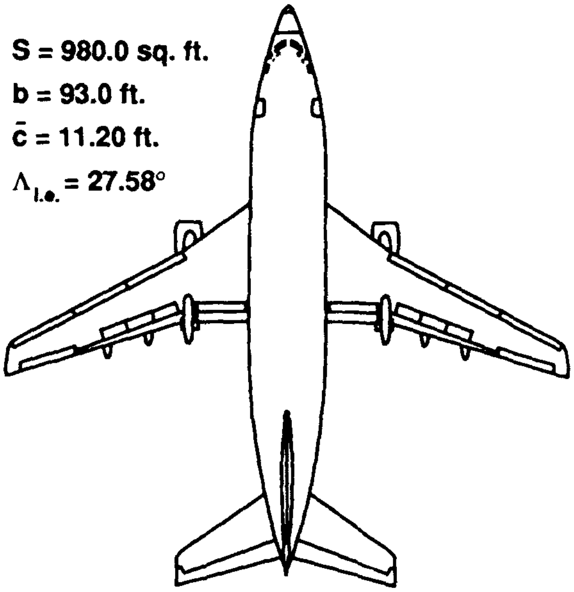

Figure 4. Planform view of the B737-100 aircraft.

Inboard leading-edge Krueger flaps and outboard leading-edge slats are extended in conjunction with the deflection of the triple-slotted trailing-edge flap system. As shown in figure 5, the outboard high-lift wing section studied in this paper consists of 5 elements: the leading-edge slat, the main wing with fixed leading edge, the fore flap, the mid flap, and the aft flap. At flap settings of 30° and 40°, the two most outboard slat segments are fully extended and deflected an additional increment from the 15° and 25° setting (see Fig. 5), effectively creating a spanwise break in the wing-planform's leading edge between the inboard slat and outboard slats (see Fig. 6). For the 15°- and 25°-flap settings, only a very small slot exists between the slat and main-wing elements (see Fig. 5).

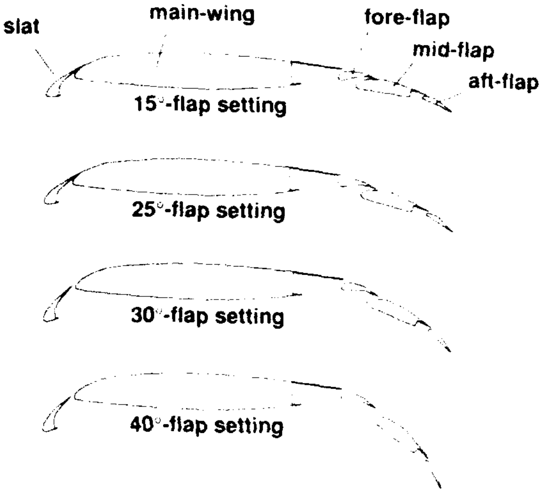

Figure 5. Wing sections at various flap settings.

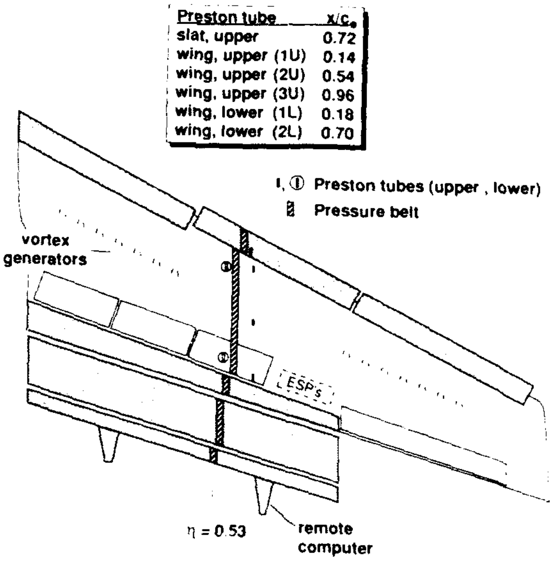

Figure 6. Instrumentation layout.

3.2 Instrumentation, Data Acquisition, and Data Reduction

Instrumentation for the full-chord, wing-section measurements is illustrated in figure 6. Surface static pressure distributions, Preston-tube skin-friction measurements, and flow-visualization results were obtained on one outboard wing section of the research aircraft. The chordwise pressure distributions were measured at a nominal spanwise station of $\eta = 0.53$ on the upper and lower surfaces of the slat, main-wing, and flap elements using thin belts of plastic tubing (0.062 in. outside diameter / 0.028 in. inside diameter) which were wrapped around each element. The belts were attached to the surface with thin (0.005 in.) adhesive tape. To minimize belt edge effects, five extra (non-functioning) tubes were added to each side, and the sides of each belt were smoothed with a silicon-rubber compound. The technique of using external pressure belts has been commonly used in previous studies and was shown to provide good results when compared to flush surface orifices.[28] The possible effect of belts on the pressure distributions in the leading-edge regions of the present high-lift system will be determined in future flights with flush orifices (see section 6). With the installation of the pressure belts, the minimum flap deflection was limited to 15°, while the standard maximum flap deflection of 40° was unchanged.

(a) $\delta_f = 40°$

Figure 7. Pressure belt and Preston-tube installation.

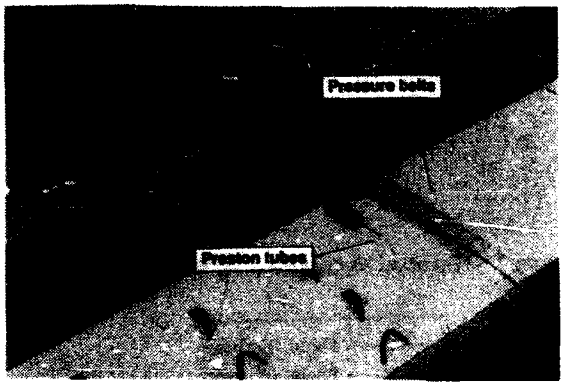

(b) close-up view, $\delta_f = 15°$

Figure 7. Concluded.

A total of 160 pressure tubes (144 for pressure distributions, 12 for static and total measurements of the Preston tubes, and 4 spare tubes) were connected to five electronically scanning pressure (ESP) modules which were located in the wing cove region (see Fig. 6). The ESP modules were maintained at a constant temperature to minimize zero shift of the measurement, and two differential-pressure transducer ranges (2.5 and 5.0 psi) allowed high resolution of the pressure data. A plenum chamber was housed in the wing cove region to provide the reference pressure for the ESP transducers; the reference pressure was monitored with an absolute pressure gauge and was related to the static pressure measured by the aircraft pitot-static probe. A small data-acquisition unit using single-board computer technology was located in the outboard flap track fairing of the wing (see Fig. 5) to access and address the ESP transducers. The digital output data were transmitted to a small, portable on-board computer for real-time display and stored on an optical disk for post-flight playback and data analysis. Pressures were recorded at a rate of 10 samples per second while aircraft flight parameters were recorded at a rate of 20 samples per second. The pneumatic lag for the longest tube length was measured in ground tests and determined to be approximately 0.5 seconds and was taken into account in the reduction of data.

In order to provide corrections of the static pressure due to probe position error for each flap setting, an airspeed calibration flight was conducted prior to the research flights using a tracking-radar method[29]. These corrections along with temperature measurements were used to compute freestream static and dynamic pressures as well as Mach and Reynolds numbers. Also, angle-of-attack corrections were obtained by calibrating the aircraft angle-of-attack vane against pitch attitude obtained from the aircraft inertia navigation system in steady-state flight conditions. Lift coefficients were determined from steady-state, 1-g flight maneuvers using aircraft weight calculated from aircraft fuel consumption measured by fuel-flow sensors. Thrust corrections obtained from standard engine performance decks were applied to the lift data to account for the thrust contribution to lift.

Flow visualization was obtained by applying nylon yarn tufts to the upper surfaces of the outboard flap and the main-wing elements (see Fig. 7) to indicate local regions of flow separation. The tuft patterns were recorded with still and video photography to allow for post-flight analysis and correlation. In addition, audio recording of pilots and flight test engineers on the video cassettes were used to discern quality of flight data samples.

Preston tubes were installed on the upper and lower surfaces of the main-wing element, and one Preston tube was installed on the slat upper surface (see Figs. 6 and 7) These probes contain a static orifice in addition to the pitot pressure orifice to measure total and static pressures within the boundary layer.[30] The Preston-tube probes were installed just outboard of the pressure belt and staggered spanwise to minimize interference effects of the probes on each other. Preston-tube measurements near the trailing edge of the flap elements were obtained during the Phase I flights at the same spanwise location and were reported in detail in reference 3. The local skin friction coefficient, C_f, was determined based on the measured pressure differential at the tube using the Law-of-the-Wall calibration for equilibrium turbulent flow. For the modified Preston tube used here, the wall shear stress was determined as follows:[30]

$$\tau = \frac{\Delta p}{\left\{ A_1 \left[\log_{10}\left(\frac{\Delta p d^2}{\rho \nu^2} \right) \right] - A_2 \right\}} \tag{3}$$

where Δp represents the differential pressure measured by the Preston tube, d represents the outside diameter of the Preston tube, and A_1 and A_2 are calibration constants where $A_1 = 38.85$, and $A_2 = 107.3$. The outside diameters of the Preston tube were d = 0.083 in. for the wing locations and d = 0.042 in. for the slat location. The above calibration expression is based on the assumption that the static and total ports of the probe are located within the region of the turbulent boundary layer that is governed by the Law-of-the-Wall. Since the boundary-layer state as well as its thickness are dependent on the flap setting and the various flight parameters, it was uncertain that all Preston tubes would operate within the appropriate calibration range at all test conditions. Because of this uncertainty, C_f computations from the Preston-tube measurements using eq. (1) are listed in this paper as C_f^* to indicate that these measurements do not necessarily reflect actual skin-friction values if the Preston-tube readings were obtained outside the valid calibration range, e.g., if the flow was laminar.

3.3 Flight-Test Conditions

The flight experiments covered a range of Reynolds and Mach numbers as the aircraft was flown to pressure altitudes up to 20,000 feet. The chord Reynolds number, $R_{\bar{c}}$, ranged from 10 to 21 million, and the freestream Mach number varied from 0.16 to 0.40. Flap deflections of 15°, 25°, 30°, and 40° were investigated at pressure altitudes of 5,000 ft, 10,000 ft, 15,000 ft, and 20,000 ft. Test conditions and test points obtained in flight are shown in figure 8 as well as lines of constant Reynolds and Mach numbers for standard atmospheric conditions. As indicated by figure 8, flight at increasing altitudes provides conditions of increasing Mach number and decreasing Reynolds number for a given indicated airspeed, V_i, which corresponds approximately to a constant lift coefficient for a given aircraft weight.

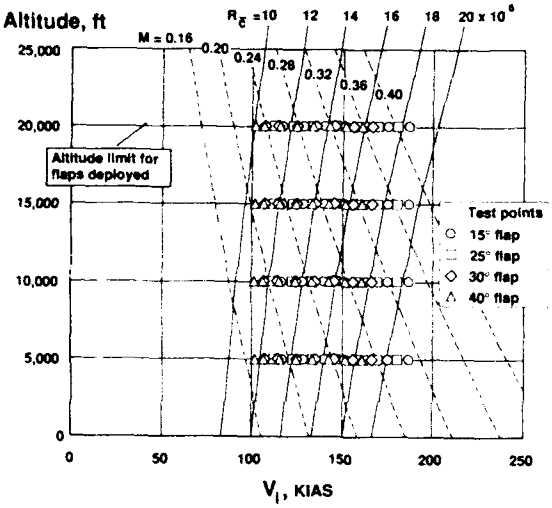

Figure 8. Flight test conditions.

The flight-test points were obtained for each of the flap settings at approximately 1-g, steady-state conditions in level flight with the aircraft initially flown at a high nominal airspeed and then slowed to the stick-shaker speed. Data were sampled for approximately 30 seconds at each constant-airspeed test point. In addition, data were recorded during the deceleration of the aircraft between selected test points. The aircraft was decelerated at a nominal rate of 1 knot per 5 seconds while constant altitude was maintained. Pertinent test points were repeated to ensure data repeatability. All data were obtained with the landing gear retracted. The research flight deck[4] on the TSRV allowed auto-throttle and auto-pilot operations of the aircraft for airspeed- and altitude-hold modes of testing. Use of the auto-pilot operations increased the productivity of the flight test and enhanced the quality of the flight data sampled.

4. FLIGHT-TEST RESULTS

In the analysis of flight data, it should be noted that test points were obtained at 1-g, level flight conditions where increasing angle of attack corresponds to slower airspeeds, and therefore, both the Reynolds number and the Mach number change with each test point (see Fig. 8).

4.1 Trimmed-Lift Data

Trimmed-lift coefficients from representative flight data at h = 10,000 ft are shown in figure 9 for the TSRV configuration with flap defections of 15°, 25°, 30°, and 40°. For the angle-of-attack range tested, the lift curves remained nearly linear with no significant slope changes except for a slight decrease in the lift-curve slope for the 15°-flap case at high angles of attack.

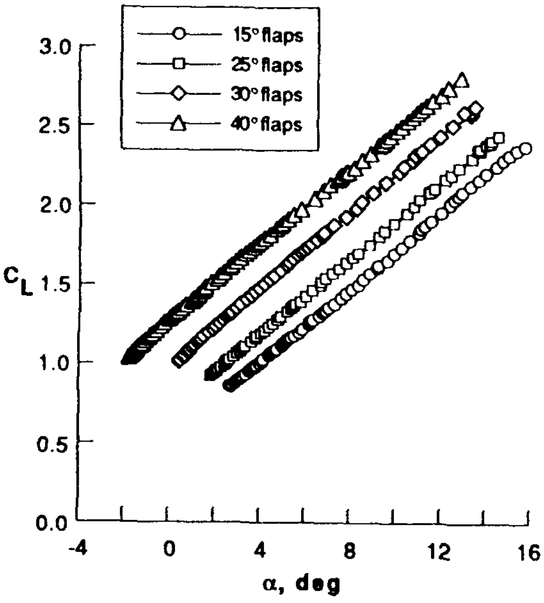

Figure 9. Trimmed lift data from flight. h = 10,000 ft.

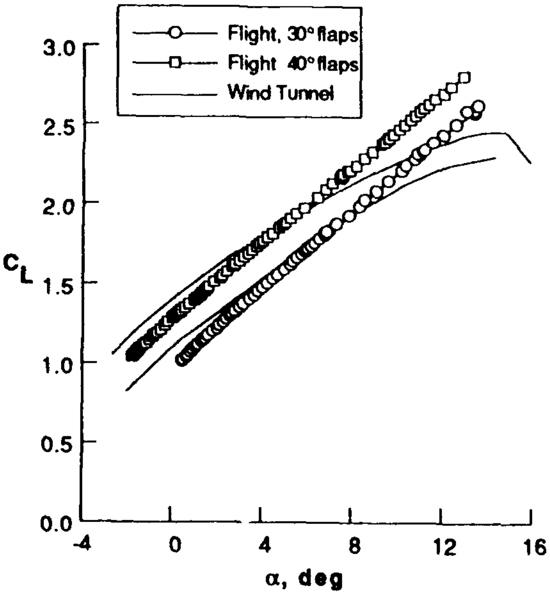

Figure 10. Comparison of flight and wind-tunnel lift data.

In figure 10, the flight lift data are compared with available wind-tunnel lift data[27] for the 30°- and 40°-flap settings. The wind-tunnel investigation used a 1/8-scale model of the TSRV with flow-through nacelles. The wind-tunnel data were obtained at test conditions of M = 0.14 and $R_{\bar{c}}$ = 1.4 million, significantly less than the flight Reynolds numbers which ranged from about $R_{\bar{c}}$ = 11 million at the high-angle-of-attack (low-speed) conditions to about 18 million at low-angle-of-attack (high-speed) conditions. Wind-tunnel force and moment data were re-computed for 18-percent $\bar{c}$, the nominal center-of-gravity location in flight, and trimmed-lift coefficients were estimated based on stabilizer requirements for trimmed flight. The comparison shows significant differences between flight and wind-tunnel data due to viscous (Reynolds-number) effects. Flight data produced a steeper and more linear lift-curve slope than the wind-tunnel data. At high angles of attack, the wind-tunnel lift-curve slope decreases with increasing angles of attack, indicating stronger viscous effects. The underprediction in the wind-tunnel data is likely due to premature flow separation at the much lower wind-tunnel Reynolds-number conditions. In the mid-angle-of-attack range, there was agreement in the lift and incremental lift values between flight and wind-tunnel data. However, at low angles of attack, the flight data were overpredicted by the wind-tunnel data. This overprediction may be a result of an inverse Reynolds-number effect on multi-element airfoils where lift decreases with increasing Reynolds number (discussed by Morgan et al.[31] and Woodward et al.[20]).

4.2 Pressure Distributions and Skin-Friction Measurements

Pressure distributions measured for all elements on the TSRV, high-lift wing section are presented in figure 11 for the 15°-, 25°-, 30°-, and 40°-flap settings from flight data for a range of angles of attack at a test altitude of h = 10,000 ft. In general, pressure distributions at other altitudes showed similar results. Several points are noted here based on the overall flight-measured pressure distributions: (1) Changing angle of attack affected primarily slat and main-wing pressure loading, and had little effect on the flap pressures. The small variance of flap loading with angle of attack is explained by the fixed deflection geometry of the upstream element which largely determines the in-flow angle for the flap element. (2) Because of sweep effects, maximum C_p values were less than the 2-D value for the stagnation point. Also, flow reattachment in the main-wing cove is indicated by C_p values close to the leading-edge attachment-line pressure. (3) Pressures at the trailing-edge of each element, except for the aft flap, do not recover completely due to the influence of the downstream element. The accelerating flow region between the elements also causes the trailing-edge pressure distributions to reflect the higher flow velocities. For example, note the decreasing main-wing element upper-surface pressures near the trailing edge with increasing flap deflection. The higher velocities near the trailing edge also relieve the pressure rise on the leading edge of the downstream element, thus alleviating potential separation problems that could cause loss in lift. These multi-element flow phenomena are attributed to the "circulation effect" and "dumping effect" as described by Smith[32].

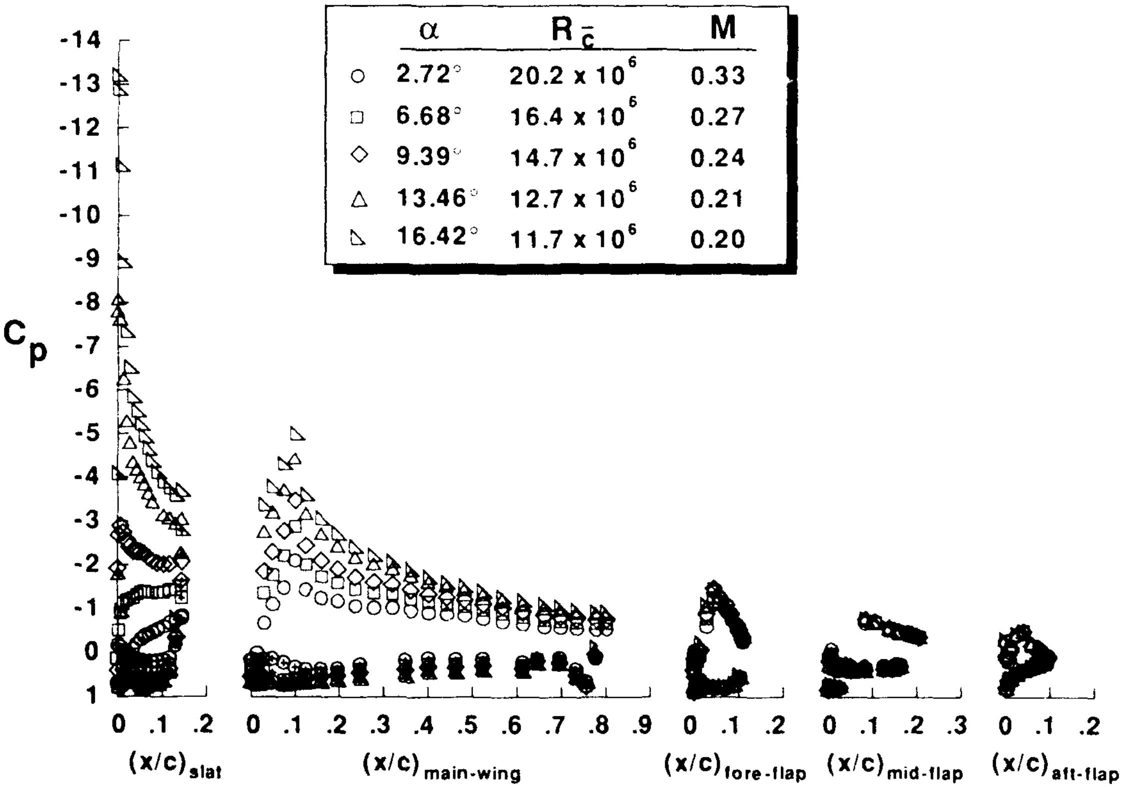

(a) δ_f = 15°

Figure 11. Wing-section pressure distributions.

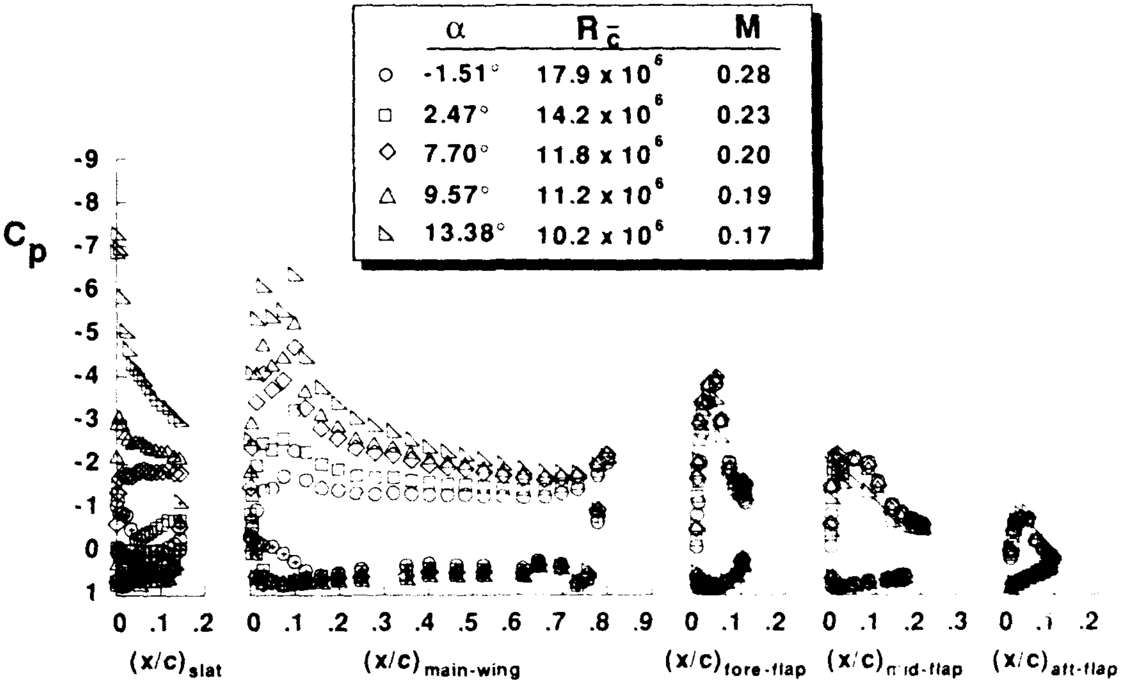

(b) δ_f = 40°
Figure 11. Concluded.

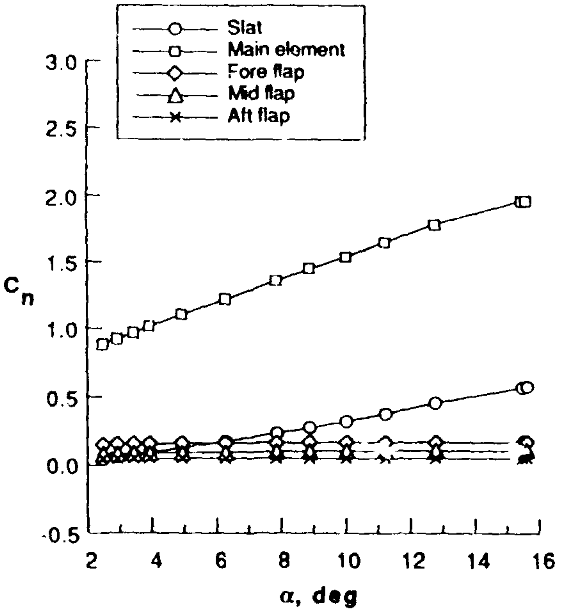

(a) δ_f = 15°
Figure 12. Wing-section normal-force coefficients.

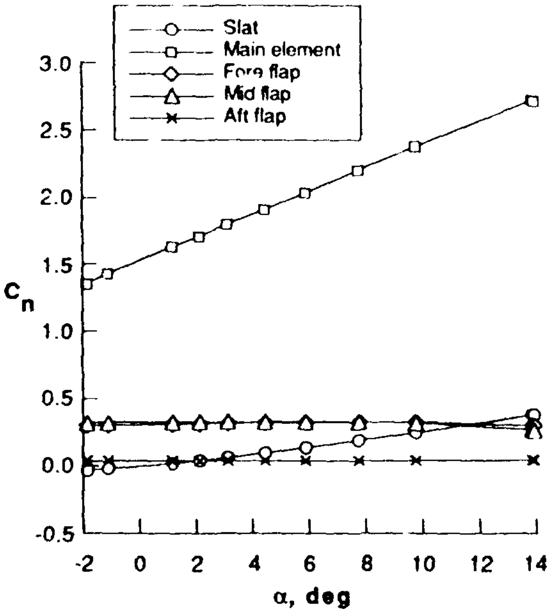

(b) δ_f = 40°
Figure 12. Concluded.

Pressure distributions for each of the elements were integrated along the wing chord in the flap-retracted cruise position (δ_f = 0°) to provide section normal-force coefficients as shown in figure 12. The results clearly indicate that the wing and slat loadings increased with angle of attack while the flap loadings remained relatively constant.

Flow characteristics of the individual high-lift, wing-section elements are examined in more detail in the following sections.

4.2.1 *Slat-element flow characteristics*

The slat pressure distributions are presented in more detail in figure 13 for the 15°- and 40°-flap settings and at several angles of attack. A comparison of the slat pressure distributions for the 15°- and 40°-flap setting shows similar results for a given angle of attack (e.g., note the pressure distributions at α ≈ 2.5°, 9.5°, and 13.5°). Both flap settings show favorable upper-surface pressure gradients at low angles of attack, nearly flat pressure distributions at mid angles of attack, and an upper-surface suction peak near the leading edge with a subsequent adverse gradient downstream at high angles of attack. For the 15°-flap setting, the upper-surface suction peak reached a minimum value of C_p = -13.18 at the highest available angle of attack, α = 16.42°. This C_p value corresponds to a local Mach number of 0.83. Even though the freestream Mach number was only 0.20, these high local velocities produce Mach effects which can adversely affect performance of high-lift systems.

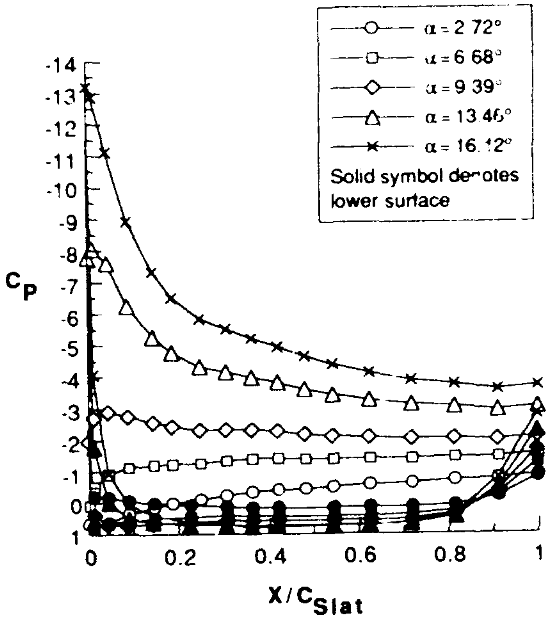

(a) δ_f = 15°

Figure 13. Slat pressure distributions.

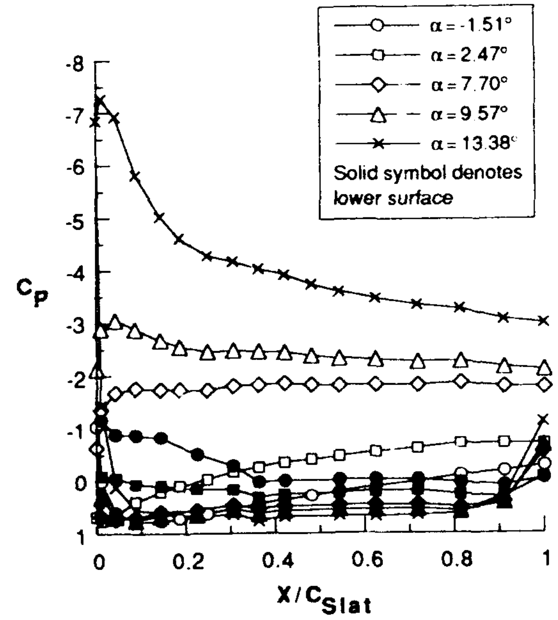

(b) δ_f = 40°

Figure 13. Concluded.

For both flap settings, the approximate position of the attachment line, as indicated by the maximum C_p value, is located on the upper surface of the slat for angles of attack less than about 4°. Consequently, for the 40°-flap setting and α = -1.51°, the slat is shown to produce negative lift (see Fig. 12b). At this negative angle-of-attack condition, the lower surface flow appears to be separated as evidenced by the nearly constant C_p value in the range of 0.05 < x/c < 0.15. On the lower surface, slat pressure ports aft of x/c = 0.30 were actually located in the slat cove (see Fig. 3). The nearly constant pressure level in the slat cove region for both flap settings at high angles of attack is indicative of the separated flow region in the cove. Near the lower-surface trailing edge, the pressure distributions indicate increasing flow velocities as a result of the slot flow between the slat and the main-wing elements. In this region, the narrow gap for the 15°-flap setting caused a larger acceleration compared to the 40°-flap setting.

In figure 14, the Preston-tube measurements on the slat are plotted as a function of aircraft angle of attack for two altitudes, h = 10,000 ft and 20,000 ft, and two flap settings, δ_f = 15° and 40°. The data show a significant increase in the measured values of C_f^* for the mid-angle-of-attack range (2.5° < α < 9.0°) for both flap settings except in the lower altitude, higher Reynolds number data of the 15°-flap setting. This increase in C_f^* can be traced to a sudden increase in the Preston-tube total-pressure reading as opposed to the static-pressure reading which varied smoothly throughout this angle-of-attack range. The flow behavior may be related to the attachment-line boundary-layer state and the phenomenon of relaminarization as discussed next.

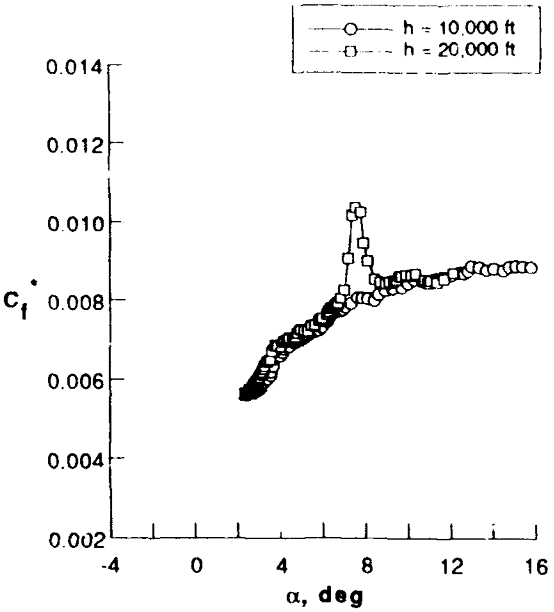

(a) δ_f = 15°

Figure 14. Slat Preston-tube measurements.

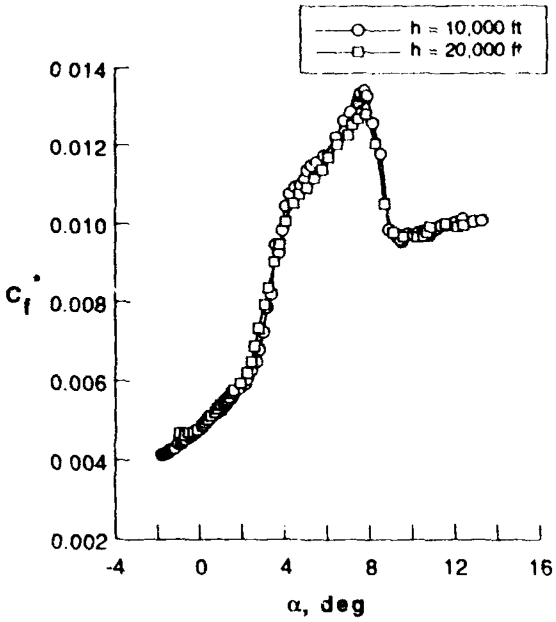

(b) $\delta_f = 40°$

Figure 14. Concluded.

Using the measured pressure distributions (Fig. 13), $\bar{R}$ is calculated and plotted in figure 15. The results show that the slat attachment line is expected to be laminar for most test conditions at a 40°-flap setting based on the criterion of $\bar{R} < 245$ for laminar attachment lines. However, it should be noted that the Preston tube was located just outboard of the pressure belts (see Fig. 5), and these belts will cause the attachment line to become turbulent. Although the turbulence introduced into the attachment-line boundary layer by the belts will decay for $\bar{R} < 245$, a comparison with Gaster's experimental results[14] depicting the decay of turbulence behind trip wires on the attachment line appears to indicate that the slat Preston tube was located in the turbulent-flow region outboard of the belt. Since the Preston-tube calibration assumes that the probe is located within a turbulent boundary layer, this introduction of turbulence from the belt wake explains the approximately normal readings by the probe at low and high angles of attack in spite of the low values of $\bar{R}$ (< 245). But attachment-line analysis using $\bar{R}$ calculations does not explain the increase in C_f^* at intermediate angles of attack. To help explain this result, the possibility of relaminarization is analyzed for the slat upper-surface region. Relaminarization produces a significant reduction in boundary-layer thickness, and this causes the Preston probe to be only partially submersed in the boundary layer as compared to being fully submersed in the turbulent case. The end result is an increase in the total-pressure reading of the Preston tube, and therefore, an accompanying increase in the value of C_f^*.

In figure 15, the maximum value for K along the upper-surface inviscid streamline, as calculated from the measured pressure distributions (assuming locally infinite swept wing conditions), is also plotted. The results, examined first for the 40°-flap setting, indicate that relaminarization, based on $K = 3 \times 10^{-6}$, would occur for angles of attack greater than approximately 2.5°; a value that is in markedly good agreement with the onset angle of attack at which the sudden increase in C_f^* was measured (see Fig. 14). Thus, the increase in C_f^* in the intermediate angle-of-attack range appears to indicate a laminar boundary-layer state at the Preston tube. The drop in C_f^* at $\alpha \approx 9°$ indicates that the boundary-layer state has become turbulent again. At this angle of attack, the change in boundary-layer state is explained by the development of a suction peak on the slat upper surface near its leading edge (see pressures in Fig. 14).

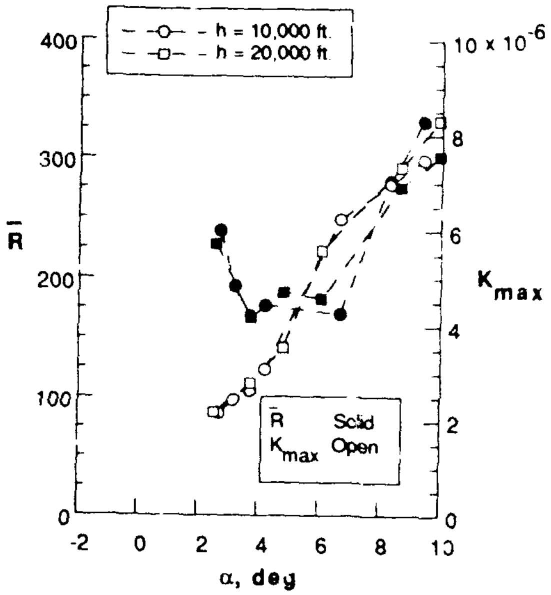

(a) $\delta_f = 15°$

Figure 15. Attachment-line Reynolds number and relaminarization characteristics for the slat upper surface.

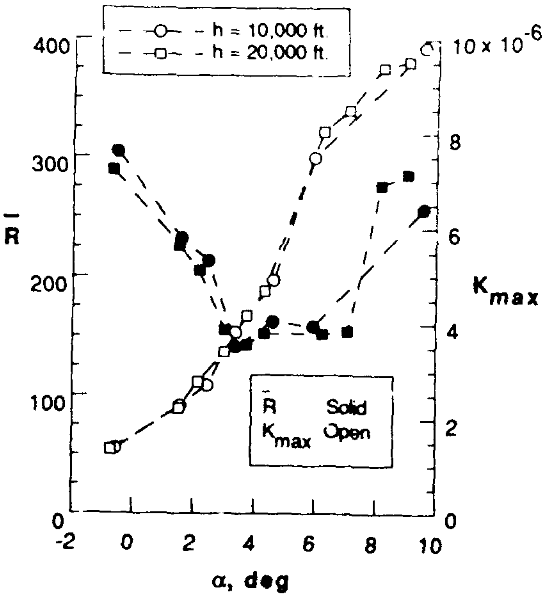

(b) $\delta_f = 40°$

Figure 15. Concluded.

Based on these results for the 40°-flap case, the use of the relaminarization parameter, K_{max}, appears to be sufficient to predict the occurrence of relaminarization in highly accelerated flows. However for the 15°-flap setting, the results in figures 14 and 15 show that K_{max}, a parameter based on a local Reynolds number, is not adequate to fully capture the flow physics of the relaminarization process for 3-D flows. For the 15°-flap setting, the increase in C_f^* first occurred at approximately $\alpha \approx 7°$ and h = 20,000 ft and did not occur at all at h = 10,000 ft. The results of figure 15 show that in this case K_{max} values must be larger than approximately 6×10^{-6} for relaminarization to occur. Also, in this case, the demise of laminar flow at the Preston tube can be correlated with the development of the leading-edge suction peak. More detailed measurements using flush-mounted static pressure orifices and hot-film sensors are planned to further study the transition phenomena on the slat (see section 6).

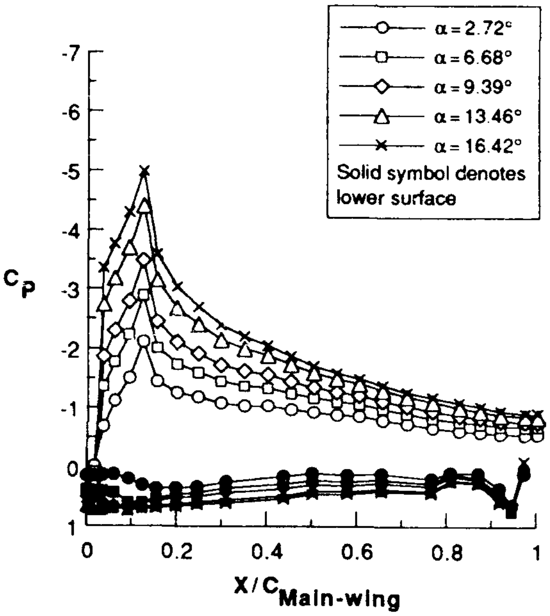

(a) $\delta_f = 15°$

Figure 16. Main-wing pressure distributions.

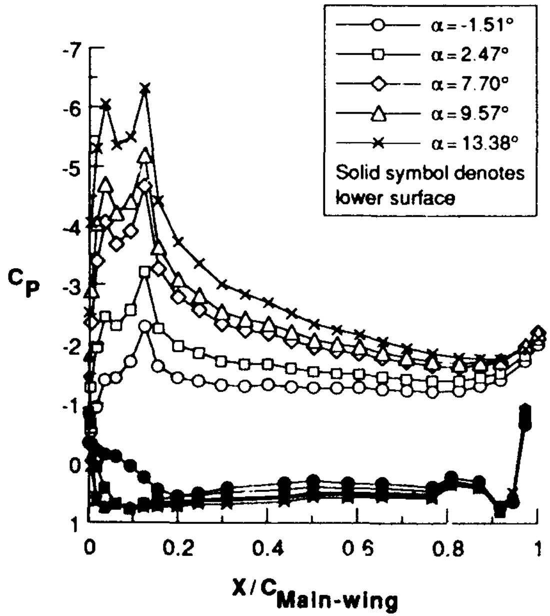

(b) $\delta_f = 40°$

Figure 16. Concluded.

4.2.2 *Main-wing element flow characteristics*

The main-wing pressure distributions are presented in more detail in figure 16 for the 15°- and 40°-flap settings at several angles of attack. In both cases, there is a large suction peak at the x/c = 0.12 location of the upper surface. A local flow acceleration was registered by the pressure belt measurement at this location which corresponds to a pressure port located just behind a notch (i.e., a forward facing step) in the leading-edge surface. The notch in the airfoil contour is a result of the slat element retracting into the main-wing leading edge for cruise flight conditions. Large flow accelerations along the leading-edge upper surface make this region conducive to relaminarization as studied in the paper by Vijgen et al.[3] However, no instrumentation was available during these initial Phase-II experiments to measure the boundary-layer state ahead of the pressure maximum point. For the 40°-flap case, the suction peak occurred at about x/c = 0.036 which is ahead of the notch in the surface and creates a double-peaked pressure distribution for most of the angles of attack shown.

On the lower surface, the 6 most-aft pressure ports are located on the spoiler lower surface in the wing cove region. Note that the lower-surface flow apparently re-attaches onto the spoiler lower surface as indicated by the high C_p value which is similar to the attachment-line value near the leading edge. The influence of the slat lower-surface, separated-flow region on the main-wing element is evidenced by the reduction in pressures in the lower-surface nose region ($x/c_{main} \leq 0.20$). For the 15°-flap setting, the slat and main-wing elements form, in effect, a single element at lower angles of attack. The slot between the slat and the main-wing element is very narrow (see Fig. 5), causing the slat leading edge to function as the stagnation region for both the slat and the main-wing elements in low- and mid-range angles of attack.

Preston-tube skin-friction measurements for the main-wing element are presented in figure 17 for the 15°- and 40°-flap cases as a function of angle of attack. Three upper-surface and two lower-surface Preston tubes were attached to the main-wing element (see Figs. 6 and 7). The data indicated high values of C_f^* for probe no. 1U in the 15°-flap case and for probes 1U, 2U, and 3U in the 40°-flap case. These high readings are indicative of the high flow velocities and thin boundary layers at those locations. Probe no. 1U is located just behind the notch in the leading-edge upper surface (see Fig. 7b). Also, in both cases, the lower-surface probe near the leading edge, probe no. 1L, experienced low C_f^* values at low angles of attack. This result is indicative of the lower-surface slat separation bubble at low angles of attack engulfing the main-wing leading-edge region on the lower surface. At 40°-flap setting, the slat is deflected an additional amount (see Figs. 5 and 7). For the 40°-flap case, the C_f^* values for the mid-chord location, probe no. 2U, and for the aft-chord location, probe no. 3U, exhibited higher values than those for the 15°-flap case. This result correlates with the widening of the slat gap, which allows higher velocity flows over this region.

4.2.3 *Flap-element flow characteristics*

A detailed study of the flap pressure distributions was presented in the paper by Vijgen et al.[3]; therefore, only a limited discussion will be presented herein. The fore-flap, mid-flap, and aft-flap pressure distributions are shown in detail in figures 18, 19, and 20, respectively, for the 15°- and 40°-flap settings and several angles of attack.

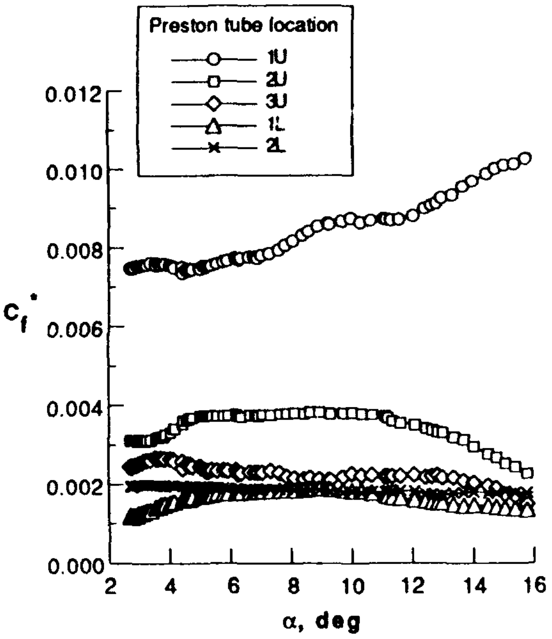

(a) δ_f = 15°
Figure 17. Main-wing Preston-tube measurements.

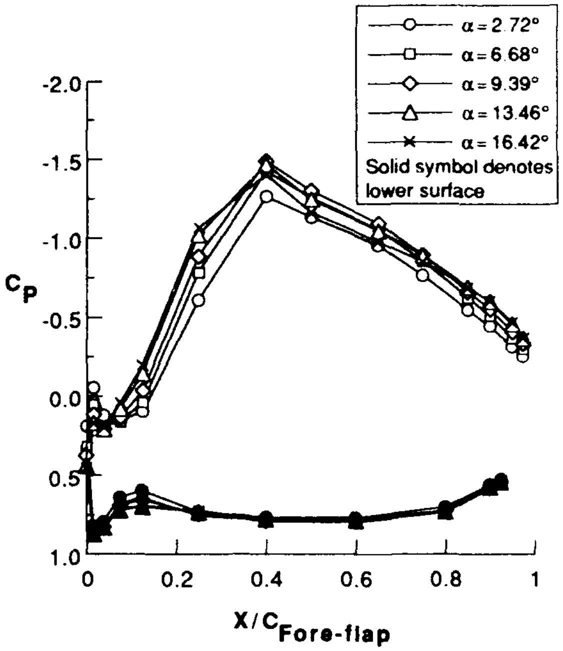

(a) δ_f = 15°
Figure 18. Fore-flap pressure distributions.

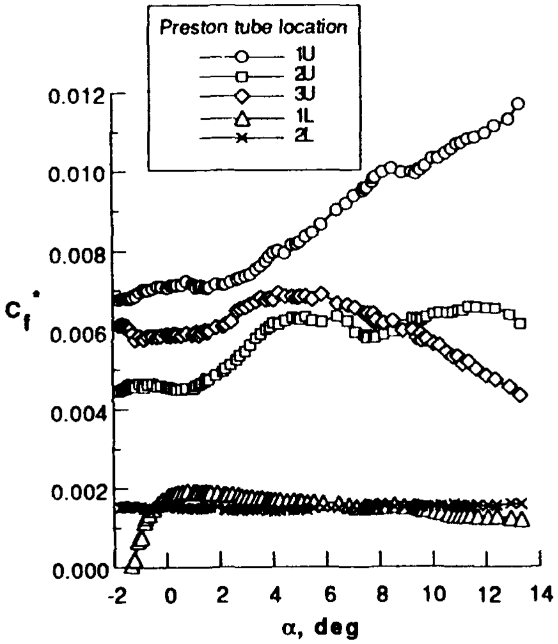

(b) δ_f = 40°
Figure 17. Concluded.

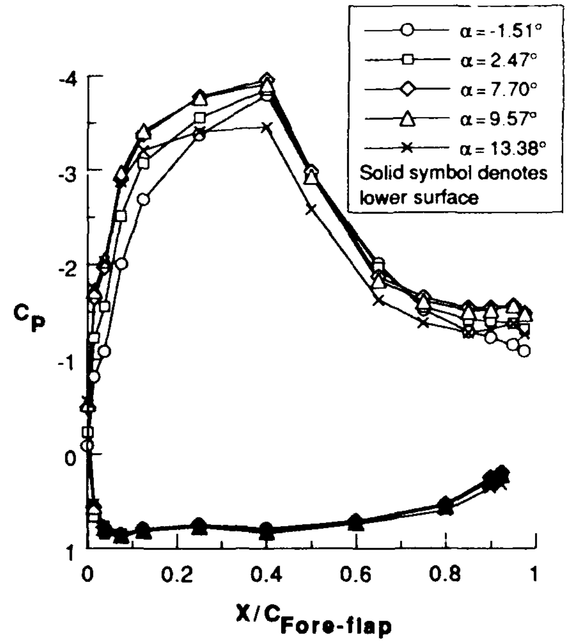

(b) δ_f = 40°
Figure 18. Concluded.

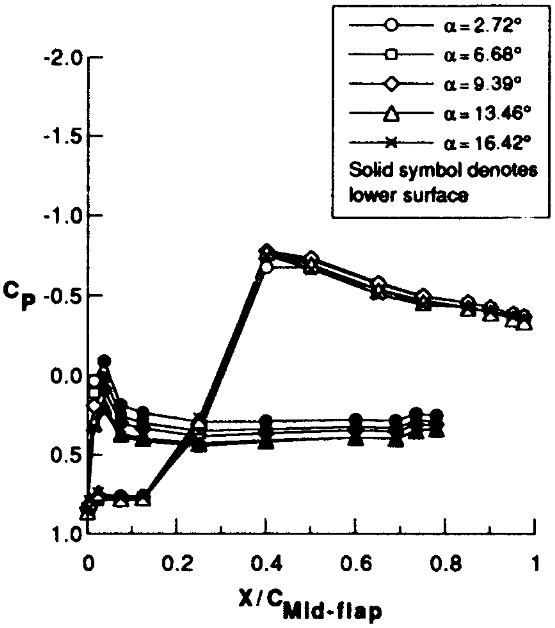

(a) δf = 15°
Figure 19. Mid-flap pressure distributions.

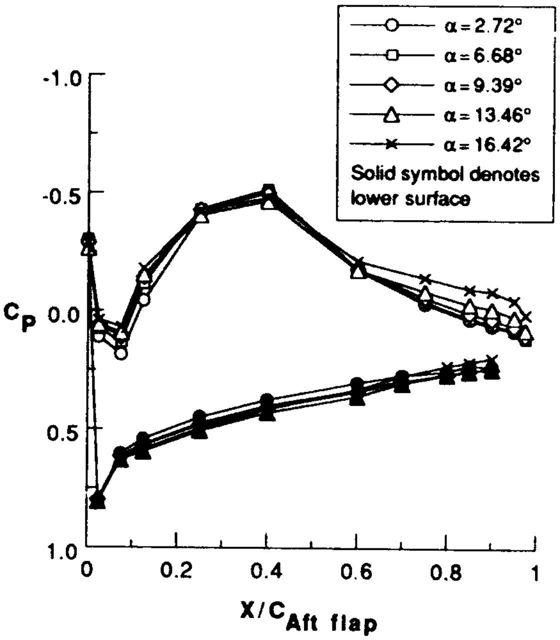

(a) δf = 15°
Figure 20. Aft-flap pressure distributions.

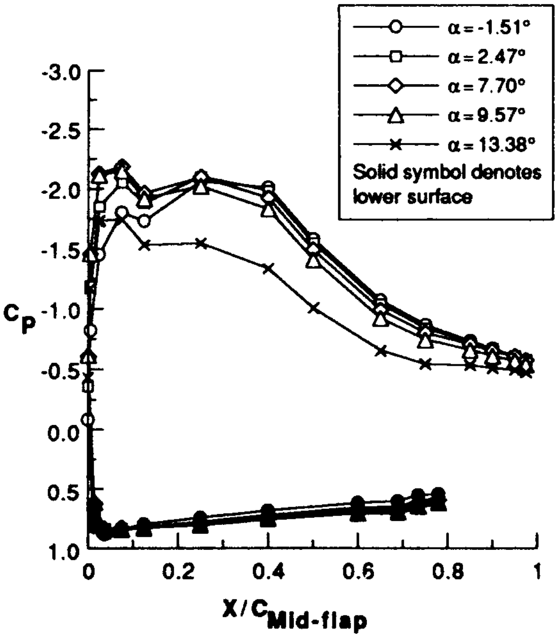

(b) δf = 40°
Figure 19. Concluded.

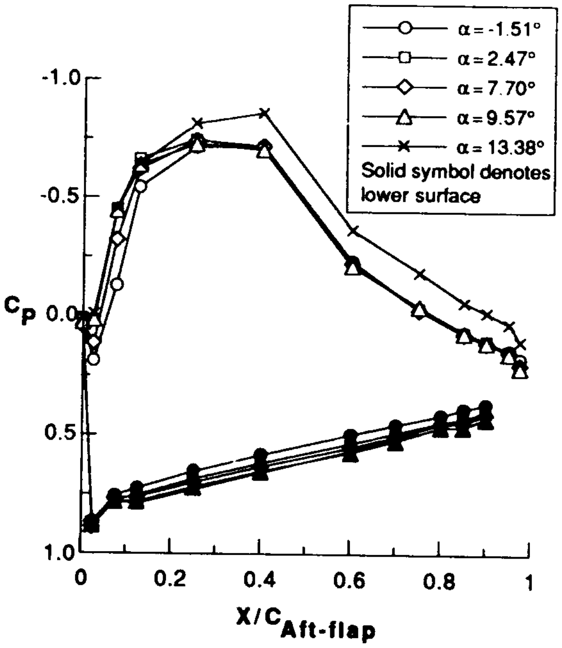

(b) δf = 40°
Figure 20. Concluded.

For the 15°-flap setting, increasing the angle of attack increased the upper-surface loading slightly while the lower-surface pressures remained nearly unchanged. These increases in loading for the fore-flap element are small compared to the increases for the slat and main-wing elements because the in-flow angle is predominantly fixed by the geometry of the flap system. No separation is indicated in the pressure distributions for the 15°-flap setting even at the highest angle of attack shown (α = 16.42°), although the decreasing trailing-edge pressures of the aft flap are indicative of a thickening boundary layer at higher angles of attack.

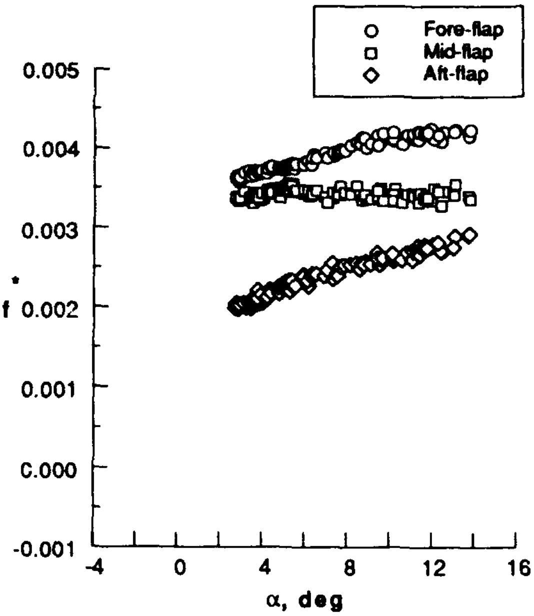

(a) δ_f = 15°

Figure 21. Flap trailing-edge Preston-tube measurements (from ref. 3). h = 10,000 ft.

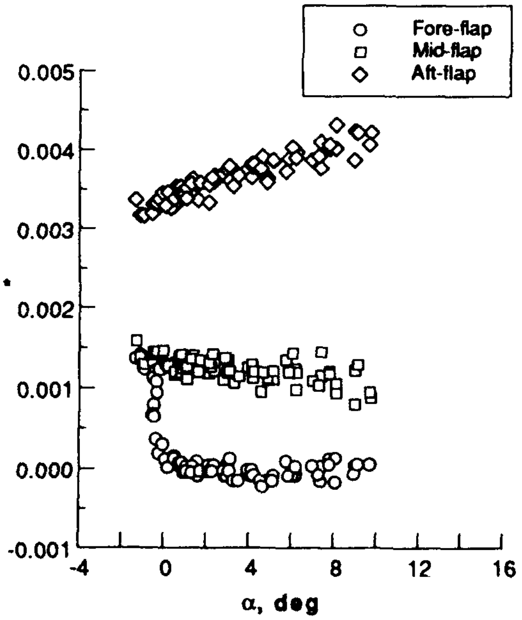

(b) δ_f = 40°

Figure 21. Concluded.

For the 40°-flap setting, the upper surface loading also increased slightly with increasing angle of attack except at the highest angle of attack shown (α = 13.38°). Flow separation near the trailing edge of the fore flap is indicated for all angles of attack shown except the lowest angle of attack (α = -1.51°). The flow separation is indicated by the nearly constant pressure level near the trailing edge upper surface of the fore flap starting at x/c = 0.80. At the highest angle of attack (α = 13.38°), a pronounced effect of the separation is also observed on the mid-flap element.

Measurements of modified Preston-tubes located at the trailing-edge of each flap element are presented in figure 21 to further examine the occurrence of flow separation (see ref. 3 for Preston-tube locations on the flap). Preston-tube measurements are presented as a function of angle of attack for the 15°- and 40°-flap settings. Negative values of C_f^* indicate flow separation at the Preston-tube location. For the 15°-flap setting, no separation is indicated for the angle of attack conditions measured. The higher readings for the fore flap correspond to the higher velocities associated with the fore-flap flow. For the 40°-flap setting, the C_f^* values indicate separated flow on the fore flap for angles of attack greater than approximately 0°.

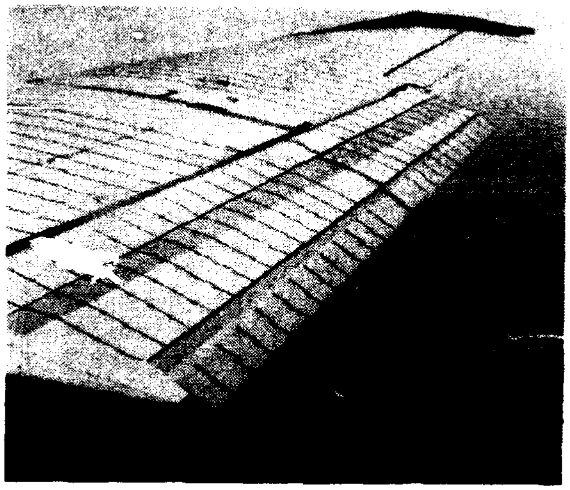

(a) δ_f = 15°, $\alpha \approx$ 9°

Figure 22. In-flight tuft flow visualization.

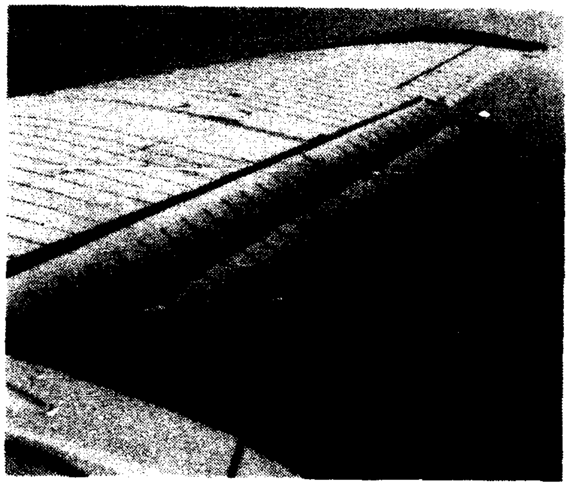

(b) δ_f = 40°, α = 7°

Figure 22. Concluded.

Typical flow-visualization results are shown in figure 22 for the 15°- and 40°-flap settings. For the 15°-flap setting, the tuft photo (Fig. 22a) is shown with the aircraft at $\alpha \approx 9°$. Even at this relatively high-angle-of-attack condition, the flow on the flap surfaces appeared streamwise with no indication of separation along the span between the flap-track fairings. For the 40°-flap setting, the tuft photo is shown with the aircraft near the stick shaker speed ($V_i \approx 105$ KIAS, $\alpha \approx 7°$) For this condition, the flow patterns showed generally attached flow on the flap system, although, in the wake of the flap track fairings, localized unsteady and separated flow regions are evident. In the region of the pressure belt locations, the flow remained attached on the main wing and the flaps except for flow separation near the trailing edge of the fore-flap element. The tuft patterns of figure 22b indicate that flow separation occurred over approximately the last 20 percent of the fore-flap chord. The tuft patterns correlate well with the previously discussed observations based on the pressure distributions and Preston-tube results. Figure 22b also indicates that the flow near the trailing edge of the aft flap is on the verge of separation at this condition although the pressure distributions does not show incipient separation. Finally, the tuft patterns near the flap/aileron edge show three-dimensional tip effects in the trailing-edge region of each flap element due to the flap-edge vortical flow field.

5. COMPUTATIONAL ANALYSIS OF PRESSURE MEASUREMENTS

A limited computational analysis of the experimental pressure distributions at the span station of $\eta = 0.53$ is presented using two currently available 2-D computational methods. The current lack of fully 3-D viscous multi-element analysis methods makes the use of 2-D methods in conjunction with simple-sweep theory necessary for the analysis of 3-D high-lift systems.[33] The sectional geometries used in the computational analyses, shown in figure 5, have been smoothly faired in the cove areas of the main-wing and mid-flap elements to facilitate the flow calculations. In the present analysis, simple-sweep theory[34] is used to account for the (inviscid) sweep effects on the pressure distributions.

One of the major challenges in applying 2-D sectional analysis methods to 3-D wing geometries is the determination of the correct local angle of attack for input to the 2-D methods. For single-element wings at low angles of attack, where viscous effects are not dominant, this may be accomplished in a relatively straightforward manner by matching the predicted and experimental section normal-force coefficients. In the case of multi-element high-lift systems, however, the use of the sectional normal-force coefficient is not feasible due to the strong viscous interactions and the presence of confluent boundary layers and flow separation. In the results presented here, the local angle of attack was determined by matching the predicted and experimental upper-surface slat pressure distributions.

5.1 Description of Multi-Element Analysis Codes

The MCARF (Multi-Component Airfoil) computer code[35,36] is a widely-used aerodynamic analysis code for 2-D multi-element airfoils. It is a potential-flow panel method and employs integral boundary-layer methods to predict the viscous flow over multi-element airfoils. The potential flow solution is obtained by solving Laplace's equation through a distribution of constant-strength source and vortex singularities distributed over the surface of each element. Compressibility effects are accounted for through the Karman-Tsien compressibility correction. An improved version of the Goradia integral, confluent boundary-layer model is employed, allowing MCARF to predict the presence of separation bubbles as well as the onset of confluent boundary-layer separation. The basic assumptions of the confluent boundary-layer model are that the static pressure normal to the element surface remains constant, and that near the trailing edge of each element the confluent boundary layer has degenerated to an ordinary turbulent boundary layer. The potential- and viscous-flow solutions are coupled through the boundary-layer displacement thickness and solved iteratively. This inviscid/viscous coupling precludes the analysis of flow regions with separation.

The MSES multi-element airfoil code[37,38] is a recently developed extension of the single-element ISES compressible flow airfoil code[39,40]. The streamline-based Euler equations and a two-equation integral boundary-layer formulation are solved simultaneously using a full Newton iteration method. The initial streamline grid is generated through the solution of a panel method at the specified angle of attack and is modified after each Newton iteration as part of the solution. Displacement bodies based on the boundary-layer and wake displacement thicknesses are used to displace the element surface geometries and are incorporated into the solution after each iteration. This strong inviscid/viscous coupling procedure enables MSES to predict the effects of laminar separation bubbles and other regions of limited flow separation on the pressure distribution. MSES is formulated to account for the effects of both asymmetric wake shapes and confluent boundary layers, although a confluent boundary-layer model is not included in the MSES version used here.[38]

5.2 Comparison with Flight Data

Results of the MCARF and MSES codes, modified as described previously, are compared to the flight-measured pressure distributions in figure 23. The comparison shows that the predicted pressure distributions are in reasonable agreement with flight-measured pressures for flap settings of 15° and 40° at the angles of attack shown. For the 15°-flap setting, where no separation was predicted or measured, the magnitudes of the flap element upper-surface pressures are slightly overpredicted. However, separated flows in the lower slat-cove and along the main-wing lower-surface leading edge are not well predicted, and the suction peak near the forward-facing step on the main-wing upper surface is not predicted in the MCARF computations. For the 40°-flap setting, where flow separation was measured on the fore flap, the pressures over the fore flap are substantially overpredicted. Although the flow separation near the trailing edge is not modeled in MCARF calculations, the location of separation onset is predicted and is in agreement with the experimental separation location on the fore flap.[3] In addition, pressures are overpredicted for the leading-edge upper surfaces for all the elements aft of the slat. This overprediction of the pressures suggests that modeling of the confluent boundary layers in MCARF as well as the present approximation of three-dimensional sweep effects is not adequate for the complex high-lift geometry studied.

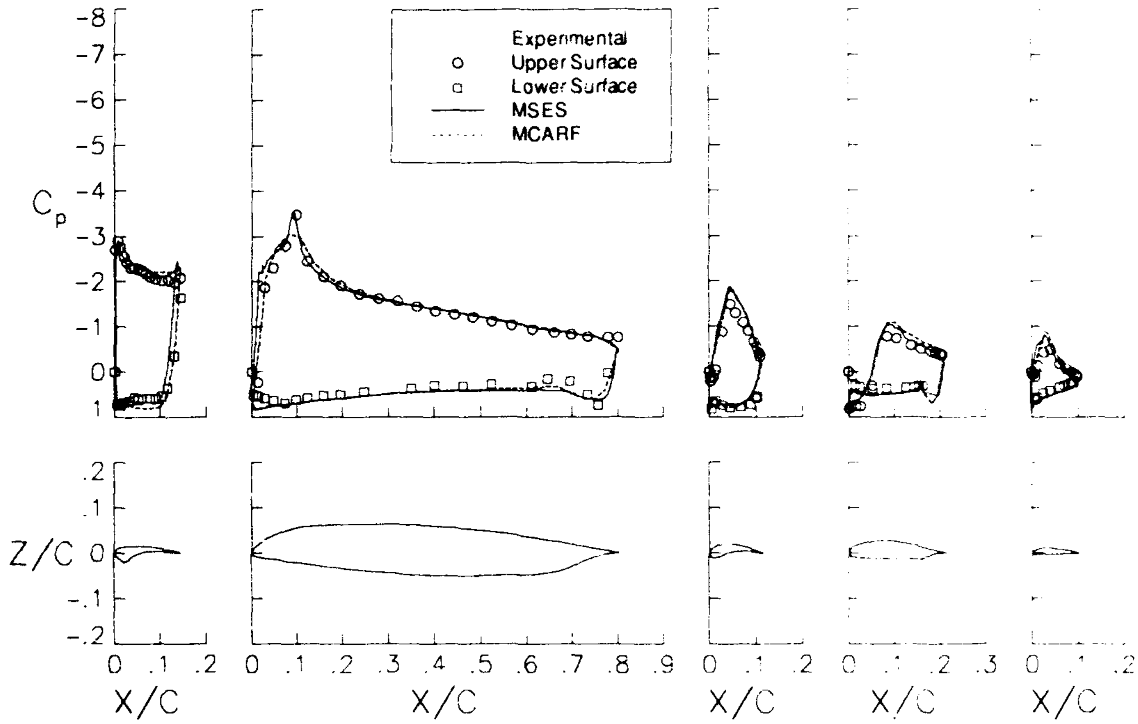

(a) δ_f = 15°, α = 9.39°, $R_{\bar{c}}$ = 14.7 million, M = 0.24
Figure 23. Comparison of predicted pressure distributions with flight measurements.

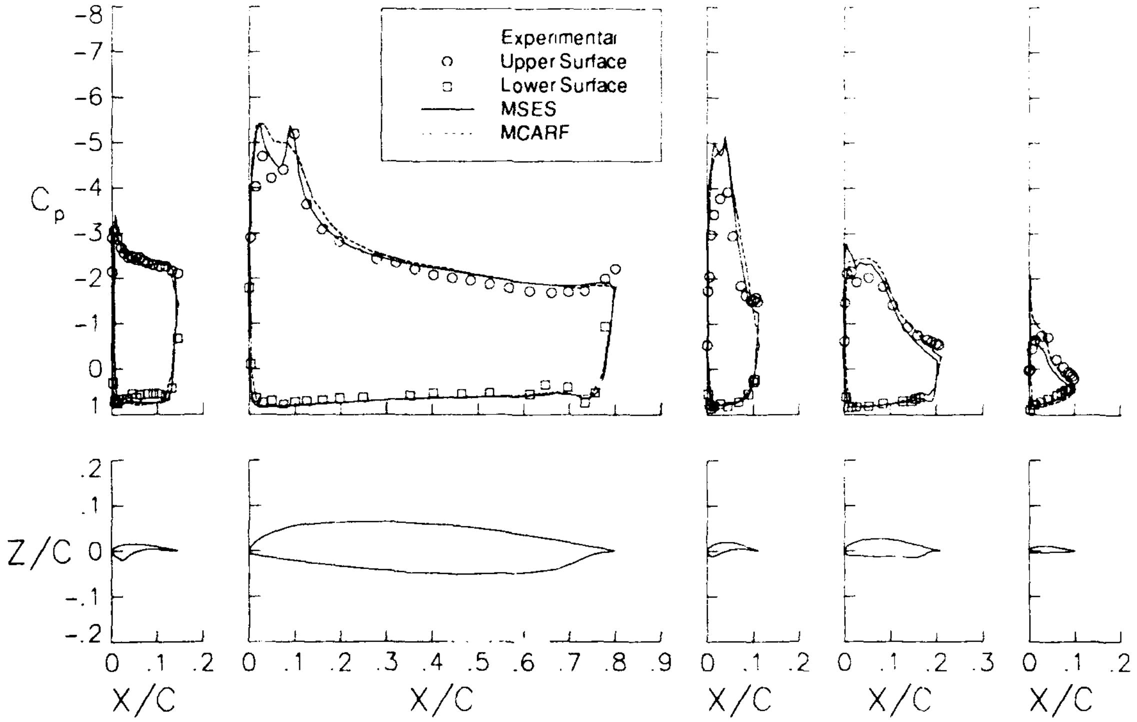

(b) δ_f = 40°, α = 9.57°, $R_{\bar{c}}$ = 11.2 million, M = 0.19
Figure 23. Concluded.

The computational grid of the MSES code are presented in figure 24 for the 40°-flap setting. Figure 24a is the final solution grid used by MSES to solve the Euler-flow equations and shows the complex streamline patterns as well as several dominant features of the solution. Most notable are the separated flow regions formed on the slat lower surface and near the trailing edge of the fore-flap. Figure 24b is a magnified view of the solution grid in the region of the flap system and reveals small regions of separation near the trailing edges of the mid and aft-flaps as well as in the cove of the mid-flap. The flow over the fore-flap appears to be separated over approximately the last twenty percent of the surface at this condition. The agreement of the measured and predicted separation near the fore-flap trailing edge indicates that the direct inviscid/viscous coupling procedure used in MSES allows reasonable modeling of the flow separation observed in flight. The near-constant pressure near the trailing edge is predicted by the MSES code (see Fig. 23b).

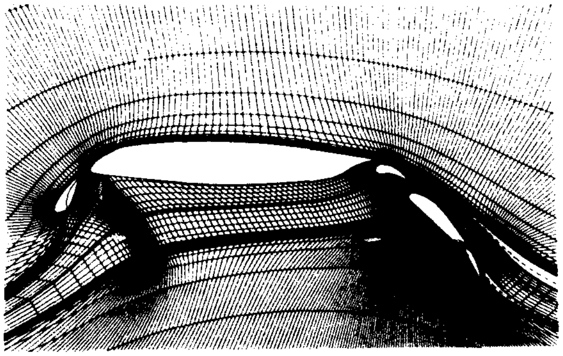

(a) 5-element high-lift system

Figure 24. MSES computational grid solution. $\delta_f = 40°$, $\alpha = 9.57°$, $R_{\bar{c}} = 11.2$ million, $M = 0.19$.

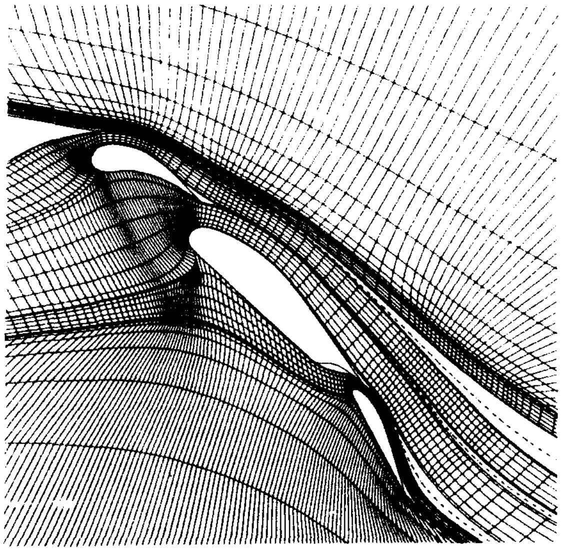

(b) flap flow characteristics

Figure 24. Concluded.

6. FLIGHT EXPERIMENT PLANS

Future flight experiments on the TSRV high-lift configuration are planned to provide measurements that address in detail several of the critical multi-element flow issues. Figure 25 illustrates the instrumentation for Phase-IIB flight experiments planned in 1993. Slat, wing spoiler, and flap spare parts have been obtained for use in these flights, allowing instrumentation to be embedded in the surfaces. A number of multi-channel ESP transducers will be used to obtain almost instantaneous pressure readings at approximately 1200 pressure ports distributed over several spanwise wing stations. The pressures will be measured using flush-mounted orifices installed on the slat, wing spoiler, and flap surfaces. Since the main-wing element is used as a "wet wing" for fuel storage, pressure belts are still needed to provide main-wing pressure distributions. Hot-film sensors will be installed along the slat, main-wing, and fore-flap leading-edge surfaces to detect transition, attachment-line, and separation characteristics. Boundary-layer rakes will be installed to determine the effect of slat wake on the main-wing flow in this phase of the research program.

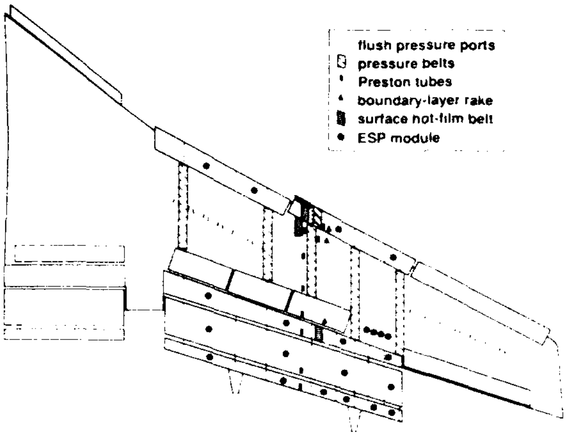

Figure 25. Phase IIB instrumentation plans.

Because of the large number of sensors, a comprehensive data-acquisition system for flight is being developed to handle in real-time the large volume of pressure and hot-film anemometer data for analysis purposes. A multi-channel anemometer data acquisition system with digital storage capability is planned in order to expedite the analysis of the high-frequency boundary-layer measurements. In addition to instrumentation for flow measurements, flow visualization is planned to provide further understanding of the flow physics on the high-lift system. Also, structural-deformation measurements will be required to complete the correlation of flight data with ground-based wind-tunnel and CFD results. Future in-flight flow measurements from this research program should provide currently unavailable flow details at full-scale flight Reynolds numbers for correlation of ground-based wind-tunnel results and a challenging validation test case for CFD analysis, particularly in the modeling of 3-D transitional and confluent boundary-layer and separation phenomena.

7. CONCLUDING REMARKS

Flight experiments are being conducted as part of a multi-phased subsonic transport high-lift research program for correlation with ground-based wind-tunnel and computational results. The NASA Langley Transport Systems Research Vehicle (B737-100 aircraft) is used to obtain in-flight flow characteristics at full-scale Reynolds numbers to contribute to the understanding of 2-D and 3-D high-lift flows including attachment-line transition and relaminarization, confluent boundary-layer development, and flow separation characteristics. This paper summarizes the test results to date of the high-lift flight research program on the TSRV as well as planned further flight experiments.

Flight tests were performed over a range of chord Reynolds numbers from approximately 10 to 20 million and freestream Mach numbers from approximately 0.16 to 0.40 for angles of attack of up to near-stall conditions. Flight test results showed that aircraft lift coefficients obtained from steady-state, trimmed conditions in level flight differed from available wind-tunnel trimmed-lift coefficients (30°- and 40°-flap settings only) due to viscous (Reynolds-number) effects. The flight-test data exhibited more linear lift curves and steeper lift-curve slopes than the wind-tunnel results for the 30°- and 40°-flap settings. Flight test results of pressure distributions, Preston-tube skin-friction measurements, and surface flow visualization over a full-chord wing section on a triple-slotted flap high-lift system were presented for the 15°- and 40°- flap settings. Measurements of the pressure distributions showed that increasing the angle of attack primarily increased slat and main-wing pressure loading, but had only a small effect on the flap-element loading. For the 40°-flap deflection, the upper surface pressures indicated flow separation near the trailing edge at all but the lowest angles of attack. Tuft-flow visualization and Preston-tube results corroborated this separation on the fore-flap trailing edge. Pressure distributions for the slat and main-wing elements showed lower-surface-separation regions, re-attachment locations, and aft movements of the attachment-line location with angle of attack. Pressure distributions on the slat upper surface reached high suction values which corresponded to locally high, but subsonic Mach numbers.

Preston-tube measurements on the slat outboard of the thin pressure belt indicated a likely laminar boundary-layer state at the Preston tube for certain conditions of angle of attack and altitude. The apparent laminar-flow readings of the Preston-tube probes could be explained by relaminarization of the belt-tripped flow under the influence of large favorable streamwise pressure gradients near the leading edge. Further flight experiments using hot-film instrumentation are planned to study the transition and relaminarization process in more detail.

A limited analysis of the experimental pressure distributions using two 2-D, viscous, multi-element computational codes with integral boundary-layer methods showed that the predicted pressure distributions were in reasonable agreement with flight-measured pressures for attached flow conditions. For the 40°-flap setting, where trailing-edge flow separation was measured over the fore flap, the pressures over the flap elements were overpredicted. This overprediction of the flap pressures suggests that current 2-D modeling of the confluent boundary-layer and three-dimensional (sweep) effects are not adequate for the present, complex high-lift geometry studied. More detailed in-flight boundary-layer measurements and the application of advanced (three-dimensional) viscous analysis methods for complex geometries will be required to further address the effects of confluent boundary-layer development on three-dimensional high-lift systems.

ACKNOWLEDGEMENTS

The work of the second author was supported under NASA Langley Contract NAS1-19299. The work of the third author was supported under NASA Langley Contract NAS1-19000. The work of the fourth author was supported in part under NASA Langley Cooperative Agreement NCC1-163.

References

[1] Dillner, B., May, F.W., and McMasters, J.H., "Aerodynamic Issues in the Design of High-Lift Systems for Transport Aircraft," *Proceedings of the Symposium on Improvement of Aerodynamic Performance Through Boundary-Layer Control and High-Lift Systems*, AGARD CP 365, May 1984.

[2] Greff, E., "In-Flight Measurement of Static Pressures and Boundary Layer State with Integrated Sensors," *Journal of Aircraft*, Vol.28, May 1991, pp. 289-299.

[3] Vijgen, P.M.H.W., Hardin, J.D., and Yip, L.P., "Flow Prediction over a Transport Multi-Element High-Lift System and Comparison with Flight Measurements," *Fifth Symposium on Numerical and Physical Aspects of Aerodynamic Flows*, T. Cebeci (ed.), California State University, Long Beach, CA, January 1992.

[4] Yip, L.P., Vijgen, P.M.H.W., Hardin, J.D., and van Dam, C.P., "Subsonic High-Lift Flight Research on the NASA Transport Systems Research Vehicle (TSRV)," AIAA Paper 92-4103-CP, August 1992.

[5] Brune, G. W., and McMasters, J. H., "Computational Aerodynamics Applied to High-Lift Systems," *Progress in Aeronautics and Astronautics: Applied Computational Aerodynamics*, P.A. Henne (ed.), Vol. 125, AIAA, New York, 1990, pp. 389 - 433.

[6] Bengelink, R.L., "The Integration of CFD and Experiment: An Industry Viewpoint (Invited Paper)," AIAA Paper 88-2043, May 1988.

[7] Olson, L.E., and Orloff, K. L., "On the Structure of Turbulent Wakes and Merging Shear Layers of Multi-Element Airfoils," AIAA Paper 81-1238, June 1981.

[8] Brune, G. W., and Sikavi, D. A., "Experimental Investigation of the Confluent Boundary Layer of a Multi-Element Low-Speed Airfoil," AIAA Paper 83-0566, January 1982.

[9] Braden, J.A., Whipkey, R.R., Jones, G.S., Lilley, D.E., "Experimental Study of the Separating Confluent Boundary-Layer," NASA CR-3655, June 1983.

[10] Nakayama, A., Kreplin, H.P., and Morgan, H.L., "Experimental Investigation of Flowfield About a Multielement Airfoil," *AIAA Journal*, Vol. 28, No. 1, pp. 14-21, January 1990.

[11] Kirkpatrick, D., and Woodward, D., "Priorities for High-Lift Testing in the 1990's," AIAA Paper 90-1413, June 1990.

[12] Garner, P.L., Meredith, P.T., and Stoner, R.C., "Areas for Future CFD Development as Illustrated by Transport Aircraft Applications," AIAA Paper 91-1527-CP, June 1991.

[13] Valarezo, W.O., Dominik, C.J., McGhee, R.H., Goodman, W.L., Paschal, K.B., "Multi-Element Airfoil Optimization for Maximum High-Lift Reynolds Number," AIAA Paper 91-3332, September 1991.

[14] Pfenninger, W., "Laminar Flow Control Laminarization, USAF and NAVY Sponsored Northrop LFC Research Between 1949 and 1967," *Special Course on Concepts for Drag Reduction*, AGARD Report No. 654, March 1977, pp. 3-1 to 3-75.

[15] Gaster, M., "On the Flow Along Swept Leading Edges," *The Aeronautical Quarterly*, Vol. 18, May 1967, pp. 165 - 184.

[16] Poll, D. I. A., "Transition in the Infinite-Swept Attachment-Line Boundary-Layer," *The Aeronautical Quarterly*, Vol. 30, Part 4, November 1979, pp. 607 - 629.

[17] Launder, B. E., and Jones, W. P., "On the Prediction of Relaminarization," ARC CP 1036, 1969.

[18] Hardy, B. C., "Experimental Investigation of Attachment-Line Transition in Low-Speed High-Lift Wind-Tunnel Testing," *Proceedings of the Symposium on Fluid Dynamics of Three-Dimensional Turbulent Shear Flows and Transition*, AGARD CP 438, 1988, pp. 2-1 to 2-17.

[19] Arnal, D., and Juillen, J. C., "Leading-Edge Contamination and Relaminarization on a Swept Wing at Incidence," *Fourth Symposium on Numerical and Physical Aspects of Aerodynamic Flows*, T. Cebeci (ed.), Cal. State University, Long Beach, CA, January 1989.

[20] Woodward, D.S., Hardy, B.C., and Ashill, P.R., "Some Types of Scale Effect in Low-Speed High-Lift Flows," ICAS Paper 4.9.3, 1988.

[21] Crabtree, L.F., Küchemann, D., and Sowerby, L., "Three-Dimensional Boundary Layers," *Laminar Boundary Layers*, L. Rosenhead (ed.), Oxford Press, 1963, pp. 409-491.

[22] Hall, P., Malik, M . R., and Poll, D.I.A., "On the Stability of an Infinite Swept Attachment Line Boundary Layer," *Proc. R. Soc. Lond.*, A395, pp. 229-245, 1984.

[23] Narasimha, R. and Sreenivasan, K.R., "Relaminarization of Fluid Flows," *Advances in Applied Mechanics* Vol. 19, 1979, pp. 221-309.

[24] Beasley, J.A., "Calculation of the Laminar Boundary Layer and Prediction of Transition on a Sheared Wing," ARC R&M 3787, 1976.

[25] White, J.J., "Advanced Transport Operating Systems Program," SAE Paper 901969, October 1990.

[26] Capone, F J., "Longitudinal Aerodynamic Characteristics of a Twin-Turbofan Subsonic Transport with Nacelles Mounted Under the Wings," NASA TN D-5971, October 1970.

[27] Paulson, J.W., "Wind-Tunnel Results of the Aerodynamic Characteristics of a 1/8-Scale Model of a Twin-Engine Short-Haul Transport," NASA TM X-74011, April 1977.

[28] Montoya, L.C., and Lux, D.P., "Comparison of Wing Pressure Distribution from Flight Tests of Flush and External Orifices for Mach Numbers from 0.50 to 0.97," NASA TM X-56032, April 1975.

[29] Gracey, W., "Measurement of Aircraft Speed and Altitude," NASA RP 1046, May 1980.

[30] Bertelrud, A. "Total Head/Static Measurement of Skin Friction and Surface Pressure," *AIAA Journal*, Vol. 15, No. 3, March 1977, pp. 436-438.

[31] Morgan, H.L., Ferris, J.C., and McGhee, R.J., "A Study of High-Lift Airfoils at High Reynolds Numbers in the Langley Low-Turbulence Pressure Tunnel," NASA TM 89125, July 1987.

[32] Smith, A.M.O., "High-Lift Aerodynamics," *Journal of Aircraft*, Vol. 12, No. 6, June 1975, pp. 501-530.

[33] Brune, G. W., and McMasters, J. H., "Computational Aerodynamics Applied to High-Lift Systems," *Progress in Aeronautics and Astronautics: Applied Computational Aerodynamics*, P.A. Henne (ed.), Vol. 125, AIAA, New York, 1990, pp. 389 - 433.

[34] Lock, R.C., "Equivalence Law Relating Three- and Two-Dimensional Pressure Distribution," ARC R&M 3346, May 1962.

[35] Stevens, W.A., Goradia, S. H., and Braden, J. A., "Mathematical Model for Two-Dimensional Multi-Component Airfoils in Viscous Flows," NASA CR-1843, 1971.

[36] Brune, G.W., Manke, J.W., "An Improved Version of the NASA-Lockheed Multielement Airfoil Analysis Computer Program," NASA CR-145323, 1978.

[37] Drela, M., "Newton Solution of Coupled Viscous/Inviscid Multi-Element Airfoil Flows," AIAA Paper 90-1470, June 1990.

[38] Drela, M., "A User's Guide to MSES V1.2," MIT Computational Fluid Dynamics Laboratory, July 1991.

[39] Giles, M.B. and Drela, M., "Two-Dimensional Transonic Aerodynamic Design Method," *AIAA Journal*, Vol. 25, No. 9, September 1987, pp.1199-1206.

[40] Drela, M. and Giles, M.B. "Viscous-Inviscid Analysis of Transonic and Low Reynolds Number Airfoils," *AIAA Journal*, Vol. 25, No. 10, October 1987, pp. 1347-1355.

HIGH LIFT AND THE FORWARD SWEPT WING

by
Dr. Lawrence A. Walchli
Wright Laboratory
Wright-Patterson AFB OH 45433-6553
United States

ABSTRACT

A broad overview of the X-29 Forward Swept Wing (FSW) Technology Demonstrator Program traces the aircraft's history from design through flight test. Brief descriptions of the aircraft and its flight control system provide insight for evaluating this unique vehicle. Wind tunnel design data substantiate theory and highlight potential solutions to a more "missionized" aircraft. Flight test results validate the X-29's wind tunnel data base and provide for piloted simulation of possible improvements for the specific X-29 technologies.

INTRODUCTION

The X-29 integrates several different technologies into one airframe as depicted in Figure 1. The aeroelastically tailored composite wing covers cause the forward swept wing to twist as it deflects, successfully delaying wing divergence. The thin supercritical airfoil, coupled with the discrete variable camber produced by the double-hinged full span flaperons, provide optimum wing performance at all flight conditions. The aircraft was designed for 35 percent static instability (time to double amplitude of about 0.15 seconds) by use of a close-coupled, variable incidence canard. Without it the wing-body combination is near-neutrally stable. The canard, which has an area about 20 percent of the wing area, produces lift and its downwash delays flow separation at the wing root. The three-surface pitch control--the canard, flaperon, and strake flap--is used by the digital fly-by-wire flight control system to control an otherwise unflyable unstable vehicle. The success of the X-29 really rests with the integration of these technologies into a single synergistic configuration built for drag reduction in turning flight.

Two X-29 aircraft were designed and built. The first entered flight testing in December 1984 and concluded in December 1988, completing 242 flights and over 200 flight hours. The primary objective of Ship #1 testing was to validate, evaluate, and quantify the benefits of the technologies on board, both individually and collectively.

The first two years of Ship #1 testing were primarily dedicated to altitude and Mach number 1g envelope expansion. Performance testing followed the envelope expansion and was completed in December 1987. Drag reduction during maneuvering exceeded design goals by about 15 percent subsonically. Finally, Ship #1 testing provided evaluations of handling qualities, military utility and agility metrics below 20 degrees angle of attack (AOA).

Ship #2, which was modified to allow high AOA testing, began flying in May 1989. Its spin chute was designed to assist the pilot in regaining control in the event of a departure from controlled flight. Control surface tutorial lights mounted in the cockpit assist in this task. The flight control system software was significantly modified in order to best utilize the various surfaces in controlling the aircraft in a post-stall environment. One g envelope expansion was completed to 66 degrees AOA and ten degrees sideslip. Accelerated entry high AOA expansion allowed all-axis maneuvering to 45 degrees. The inherent high-lift capability of the forward swept wing allowed the X-29 to roll at 70 degrees per second under approximately 2g conditions at 30 degrees AOA. The military utility of this vehicle is in a class by itself.

AIRCRAFT AND FLIGHT CONTROL SYSTEM DESCRIPTION

Two essentially identical X-29s were designed and built by Grumman Aerospace Corporation, Bethpage, New York. To reduce overall program costs, the Air Force supplied several major components of the aircraft to Grumman. These included the F-5A forebody and nosegear; F-16 main gear, actuators, airframe-mounted accessory drive and emergency power unit; F-18 F404 engine; SR-71 HDP5301 flight control computers; and F-14 accelerometers and rate gyros. Use of these time-proven components also increased the reliability of the flight vehicle.

The X-29 flight control system (FCS) is a triplex digital fly-by-wire system with triplex analog backup (as shown in Figure 2). The fail-op/fail-safe system used MIL-F-8785C and MIL-F-9490D specifications as design guides. Flying quality design goals were Level I for the primary digital mode and Level II for the analog back-up mode.

Normal aircraft operation is accomplished through the normal digital (ND) mode with its associated functional options such as automatic camber control (ACC), manual camber control (MCC), speed stability, precision approach control (PAC), and direct electrical link (DEL). ND also contains options in its gain tables for power approach (PA), up-and-away (UA), and degraded operation.

The normal digital mode has a pitch rate control law with gravity vector compensation, driving a discrete ACC system. This mode is gain-scheduled as a function of Mach number and altitude and incorporates a sophisticated redundancy management system allowing fail-op/fail-safe flight. MCC is a pilot-selected, fixed flaperon sub-mode of ND used for landing. The PAC function is a pilot-selected auto throttle system. The DEL function is a ground contact control law set which is active when any landing gear weight-on-wheel relay is open. This function fades out the longitudinal forward loop integrator, allowing direct pilot control of the canards during taxi, take-off, or landing roll-out. Gain tables for degraded operation are activated by a failure of the Attitude Heading Reference System or any two of the three angle-of-attack sensors. This function cannot be pilot-selected, nor can it be exited in flight. Degraded normal digital operation is the last option available during sensor failures prior to automatic down-moding to analog reversion.

The analog reversion (AR) mode is the back-up flight control system, designed to bring the aircraft safely back to base. The AR mode provides a highly reliable, dissimilar control mode to protect against generic digital control failures. It incorporates UA and PA functions similar to those of the ND mode. AR contains no longitudinal trim capability or pitch loop gain compensation with dynamic pressure while the aircraft is on the ground. In all other aspects, it performs like the ND control system.

The Ship #2 flight control laws were modified to permit all-axis maneuvering to 40 degrees AOA, and pitch-only maneuvering to as high as 70 degrees AOA. Below 10 degrees, the control laws are identical to those last flown on Ship #1. Between 10 and 20 degrees, the high AOA modifications are faded in until above 20 degrees they are fully functional.

The high AOA changes are fairly simple. A spin prevention logic is active above 40 degrees or below minus 25 degrees AOA with increasing yaw rate. The logic increases the authority of both the rudder pedals and lateral stick and disconnects all other lateral/directional feedbacks. Besides the spin prevention logic, an aileron-to-rudder interconnect provides for better roll coordination at high AOA. Also assisting in roll coordination is a rate-of-sideslip feedback to the rudder. Since substantial wing rock was predicted for the X-29 above 30 degrees angle of attack, a high gain roll rate-to-aileron feedback loop has been added to compensate for the unstable rolling moment coefficient due to roll rate. For a more detailed description of the control system, see Reference 1.

EVOLUTION OF THE X-29 CONFIGURATION

The X-29 Forward Swept Wing Technology Demonstrator Program was established to flight test an advanced air vehicle which incorporated forward sweep on the wing. Forward sweep was a well-known concept with fairly well-defined benefits, but because of the absence of certain enabling technologies, the concept had never been proven on a high performance fighter. The emergence of composites, and specifically their compatibility with aeroelastic tailoring, allowed a lightweight, efficient solution for delaying wing structural divergence.

An aircraft wing is swept, either forward or aft, to postpone the drag rise associated with transonic flight. It can easily be shown (Reference 2) that for an equal shock wave location, shock wave sweep, wing taper ratio, aspect ratio, and area, a forward swept wing has a lower leading edge sweep than an equivalent aft swept wing. The result is a lower profile drag and a lower root bending moment. Conversely, if the two wings are designed to have the same bending moments, the forward swept wing's aspect ratio increases, producing a further reduction of the induced drag. These points are illustrated in Reference 2 and reproduced here for convenience as Figures 3 and 4.

In addition to the transonic efficiency provided by an FSW, it proves to be a good performer in the near- and post-stall region of flight. Unlike an aft swept wing where flow separation starts at the wing tips and may cause control degradation, flow separation on an FSW originates near the wing root and proceeds outboard with the wing tips and ailerons maintaining flow attachment longest. The addition of canards on the X-29 enhances the lifting performance of the FSW by providing a downwash on the largest surface area region of the wing, delaying separation in that zone. Upper surface pressures showed that separation actually originated just outboard of the canard tip butt line and proceeded both inboard and outboard from there. Wing separation is delayed in the shadow of the canard until the lightly-loaded canard itself begins to separate.

The close-coupled, variable-incidence canard on the X-29 provides additional benefits. Its large area (20 percent of the wing) contributes significant pitching moment and direct lift with small deflections. This contributes trim lift without significant trim drag and enhances the maneuverability of the X-29. The canards and FSW were specifically optimized to produce minimum induced and profile drag over the X-29 low AOA flight envelope.

The addition of close-coupled canards on the near-neutrally stable wing-body combination of the X-29 makes the aircraft up to 35 percent statically unstable. Figure 5 from Reference 3 shows significant relaxed static stability (RSS) at all subsonic Mach numbers, with stability returning at about Mach 1.3. By using the RSS to keep the canard from overloading and helping to produce positive lift to trim, high levels of trimmed lift are maintained through the maximum lift coefficient for the configuration. By employing RSS, the variable incidence canard can unload at very high angles of attack, providing the pitching moment necessary to recover to level flight.

The final consideration in the evolution of the X-29 configuration was the concept of optimizing the wing profile for maximizing efficiency over all regions of the flight envelope. This, of course, requires variable camber. The simplest, most cost-effective method of producing variable camber on a thin supercritical airfoil is with leading and/or trailing edge devices. Various wind tunnel tests were conducted to ascertain the most appropriate configuration. The next section of this paper will provide details of this overall effort. Here I will discuss only the concept that was actually adopted for the X-29.

The discrete variable camber system on the X-29 consists of double-hinged full span flaperons. The flight control system has a manual camber control (MCC) mode wherein the flaperons can be set at a discrete setting by the pilot. The MCC mode was utilized to obtain aircraft performance at a fixed flight condition over a range of wing camber. The automatic camber control (ACC) mode was used to optimize the wing's performance over all flight conditions. In the ACC mode, the flight control computers used real time air data to adjust the flaperon settings according to a prescribed schedule. Figure 6 shows schematically how the ACC scheduling was derived from MCC results. Wind tunnel-derived drag polars were plotted for specific flaperon settings. The dashed line, faired tangentially across the polars, then defined an optimum variable camber polar. The appropriate flaperon positions were then scheduled with angle of attack to achieve this polar.

HIGH LIFT DEVICE INVESTIGATION

Early in the design process for the X-29, an effort was undertaken to investigate various high lift schemes which might be beneficial to a supercritical forward swept wing and canard configuration. Reference 4 provides the details of this wind tunnel study. A moderately cambered canard was tested. Two wing leading edge devices were examined as well as two trailing edge devices. These particular devices were generally accepted as producing the best high lift performance on aft swept wings.

The remotely driven canards were fitted with detachable leading and trailing edge flap pieces in order to increase the camber of the baseline low camber airfoil. The canard was movable 20 degrees trailing edge down and 40 degrees trailing edge up. Leading edge flap extensions were provided for 0, 5, and 10 degrees down; trailing edge extensions were 0, 10, and 20 degrees down. The test data indicated that canard lift effectiveness was independent of wing leading and trailing edge devices over the -4 to 22 degree angle-of-attack range and -4 to 16 degree sideslip angles tested. Canard camber always provided a positive lift increment, but in conjunction with a Krueger flap on the wing it reduced pitching moment effectiveness at low angles of attack. The results clearly showed benefits from canard variable camber, but when the added complexity of incorporating movable leading and trailing edge surfaces was considered, the final X-29 configuration used a single low camber, all-movable canard.

The wing extensions examined in the wind tunnel study were a Krueger flap, a leading edge slat, a single slotted extensible flap, and a double slotted extensible flap. These devices are shown in Figures 7 and 8. The Krueger flap had a 50 degree angle of incidence, while the slat was designed for 15 and 29 degrees. The single slotted flap was adjustable in increments of 20, 30, and 40 degrees down. The double slotted flap had a fixed 20 degree deflection on the first flap and incremental settings of 20, 30, and 40 degrees relative to the first flap.

Figure 9 provides the lift coefficient results for a plain flap, a configuration quite similar to the actual aircraft hardware. Integral to both curves are the effects of canard and wing stall. The 25 degree flap deflection significantly increases lift. It also accentuates the separated flow effects on the canard-wing combination.

Figures 10 and 11 give the lift performance for the single and double slotted flap in combination with the two leading edge devices. In all cases, the improvements were significant. The best combination in this test was the Krueger flap plus the double slotted trailing edge flap resulting in an improved lift coefficient of about 70 percent. However, it is clearly evident from the data that the leading edge devices lead to total separation and loss of lift in the 15 to 20 degree angle-of-attack range. Only the trailing edge flaps acting alone are suitable for the high angle-of-attack regime in up-and-away flight. The leading edge devices excel in the power approach mode of flight.

AIRCRAFT PERFORMANCE

The lift and drag characteristics of the X-29 were determined by performing push-over, pull-up (POPU) and wind-up turn (WUT) maneuvers at constant power settings. POPU maneuvers were used to obtain data for load factors under 2 g's and the WUT maneuvers for 2 g's and above. Data was obtained for angles of attack up to 20 degrees and for symmetric load factors up to 6.4 g's as corrected to 15,000 pounds gross aircraft weight. Both the automatic camber control and manual camber control options of the normal digital mode of the flight control system were investigated.

Drag polars were acquired for 0.4 to 1.3 Mach numbers. The polars were compared to wind tunnel predictions which also used the ACC control surface schedules. In general, subsonic and transonic flight test results showed lower drag coefficients than predicted. Supersonically the test data either matched predictions closely or showed higher drag coefficients. The highest lift coefficient reached in flight on Ship #1 was 1.63 at 0.4 Mach number. This was a result of the conservative angle of attack (15 degrees) and load factor (6.4 g) limitations imposed on the aircraft. These restrictions were later relaxed, but a repeat of the performance measurements was not accomplished.

Shown in Figure 12 is the comparison between a wind-tunnel-predicted drag polar and the actual flight-derived polar at 0.9 Mach and 30,000 feet pressure altitude. The wind tunnel data clearly over-predicted drag. Note the break in the curve which corresponds to an angle of attack of about seven degrees. It happened that the scheduled canard position reversed direction and the flaperon position schedule reached a limit simultaneously. This would suggest that at angles of attack below seven degrees, the ACC schedule was not correctly optimized for lift and drag.

The manual camber control mode of the flight control system was also utilized during performance testing. Figure 13 shows both MCC and ACC flight data at 0.90 Mach number and 30,000 feet. As is evident, the ACC scheduling did an excellent job of optimizing the discrete camber polars. The MCC uses fixed flaperon settings to achieve discrete values of wing camber.

To complete this low angle of attack performance analysis, let's look at the opposition. Figures 14 through 16 provide aeroperformance comparisons between the X-29 and a current high performance fighter. No attempt has been made to normalize the data or optimize either aircraft. It is simply an aircraft-to-aircraft snapshot. The induced drag polars presented show a consistent trend. The polar shape of the X-29 has been greatly improved. Although the X-29 was specifically optimized for a 0.95 lift coefficient at 0.9 Mach number and 30,000 feet, the improvement exists through its entire performance range.

While these comparisons show a significant advantage to the X-29, the X-29's lift-to-induced drag performance is far superior to its lift-to-total drag performance. This is explainable by the fact that the X-29 was put together from many pieces and parts. This resulted in a rather large profile drag for the aircraft. However, at 0.95 lift coefficient, 0.9 Mach number and 30,000 feet altitude, the X-29 excels in spite of its high profile drag. In the fighter-class arena, performance of the X-29 is impressive.

MANNED SIMULATOR PREDICTIONS

One of the fundamental characteristics of a forward swept wing is its ability to achieve relatively high angles of incidence before the wing totally separates. Once the aircraft has entered post-stall flight, its lifting performance is highly dependent on the interactions of the wing's wake region and disturbances from other portions of the aircraft. In the case of an aft-swept wing with high lift devices such as those on the F-18, fuselage, LEX and leading edge flap influences are swept generally outboard, adding additional turbulence to the wing's wake (Figure 17, reproduced from Reference 5). The forward swept wing of the X-29, without additional high lift devices, is able to avoid additional interactive turbulence since its wing tips are always in clear air. Without these additional influences, the turbulent detached flow is able to reattach itself, in a reverse direction, over a rather large four foot section of the wing at 30 degrees AOA. This is shown in Figure 18, reproduced from Reference 6. This suggests additional lift, making the X-29 a natural high lift, high angle-of-attack aircraft.

Continuing this theme of increased capability of a forward swept wing configuration, what can be done to further improve the X-29's performance? Although the X-29 Ship #2 was not specifically instrumented to directly determine the lift-drag performance at high AOA (the propulsive thrust measurement system had been removed from the engine), the aircraft flight-validated math model was sufficiently mature to provide accurate manned simulation predictions.

Figures 19-22 show the results of a canard optimization study for the very high AOA regime. With flaperon and strake deflections defined and fixed, a unique trimmed canard schedule exists at the prescribed flight conditions. These schedules are shown in Figure 19. Also shown are two ACC canard schedules which bracket the usable center of gravity range for the aircraft. The ACC schedules were established early on in the program and were intended to be the most efficient at producing lift and pitching moment while at the same time providing a margin of safety suitable for a highly unstable aircraft. Only for the plus 30 degree strake deflection did the canard achieve positive deflection (trailing edge down). This was its most highly loaded schedule.

With all three control surfaces lifting, the lift curve should show a large improvement over all other combinations presented. However, Figure 20 shows that this only holds true above 23 degrees AOA. Based on the lift curves of the various combinations, a more efficient scheduling of the control surfaces would result from using the original ACC below about 23 degrees AOA and then transitioning to a higher canard loading.

Such a solution would, of course, increase overall drag on the aircraft. Figure 21 confirms that canard loading has increased since additional drag begins to occur above 20 degrees AOA. But Figure 22 shows clearly that this solution results in a net improvement in the drag polar above 23 degrees AOA, allowing for improved turning performance. $C_{L_{MAX}}$ improves almost ten percent over the baseline ACC.

The ACC curve for an aircraft center of gravity of 453.9 inches exhibits the benefit of relaxed static stability. For the case presented, both the lift curve shape and magnitude improve when moving the c.g. aft. Although an improved control surface schedule and a more aft center of gravity produce lift benefits, care must be taken to avoid canard saturation and subsequent loss of pitch authority needed to recover the aircraft to low angle of attack.

CONCLUDING REMARKS

The X-29 with its forward swept wing has been shown to be an inherently high lift aircraft. A wind tunnel study of canard and wing high lift devices was reported. Flight tests of the unique X-29 design have been performed at high and low angles of attack using both test aircraft. The drag reduction design goals of the X-29 were demonstrated below 20 degrees using Ship #1, while the high angle of attack capability of the forward swept wing design was explored using Ship #2. A flight validated math model was used in the X-29 manned simulator to show that improvements in overall aircraft performance were possible through a simple rescheduling of the flight control surfaces. This forward swept wing canarded configuration has proven aerodynamically superior to all current high performance fighters.

REFERENCES

1. Pellicano, et al, "X-29 High Angle-of-Attack Flight Test Procedures, Results, and Lessons Learned," Society of Flight Test Engineers 21st Symposium, August 1990.

2. Frei, D., and Moore, M., "The X-29 - A Unique and Innovative Aerodynamic Concept," SAE Aerospace Technology Conference and Exposition, October 1985.

3. Walchli, L., "X-29: Longitudinal Instability At High Angle of Attack," AGARD Guidance and Control Panel Workshop On Stability In Aerospace Systems, 23-26 June 1992.

4. Frei, D., "Forward Sweep Wing Technology Integration and Evaluation Study - Task 18 and 19 - High Lift Systems Investigation," AFWAL TR-81-3024, January 1981.

5. Fisher, et al, "In-Flight Flow Visualization Characteristics of the NASA F-18 High Alpha Research Vehicle at High Angles of Attack," NASA TM 4193, May 1990.

6. Tate, B., "Surface Flow Visualization - Interim Report," unpublished, circa Fall 1990.

FIGURE 1. X-29 TECHNOLOGIES

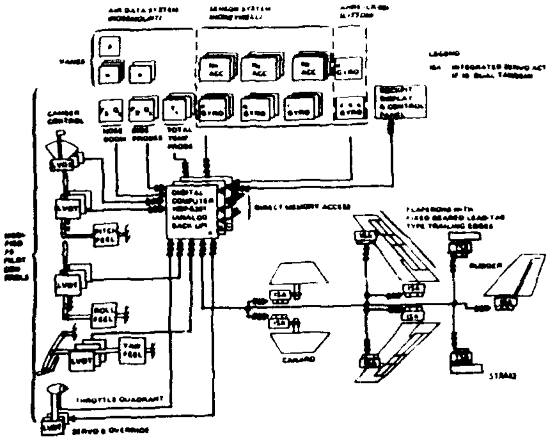

FIGURE 2. X-29 FLIGHT CONTROL SYSTEM

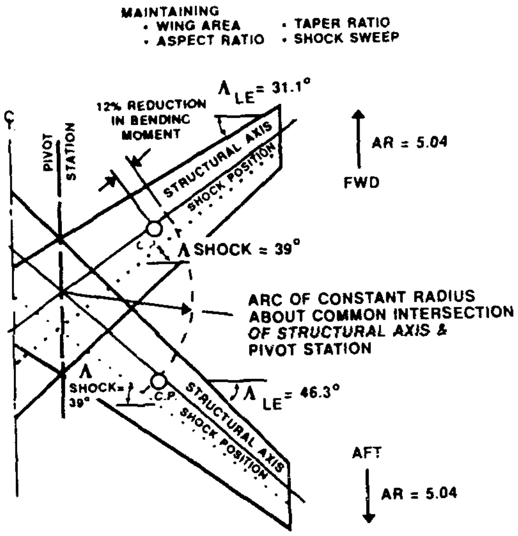

FIGURE 3. FORWARD VERSUS AFT SWEEP - REDUCED BENDING MOMENT

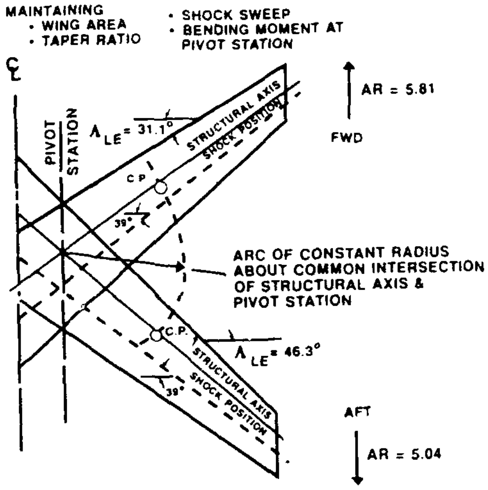

FIGURE 4. FORWARD VERSUS AFT SWEEP - HIGHER ASPECT RATIO

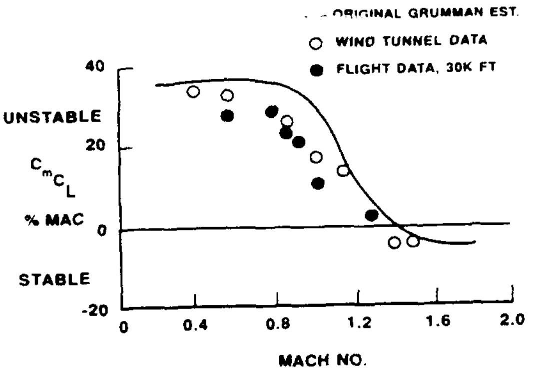

FIGURE 5. X-29 VARIATION OF LONGITUDINAL STATIC STABILITY WITH MACH NO.

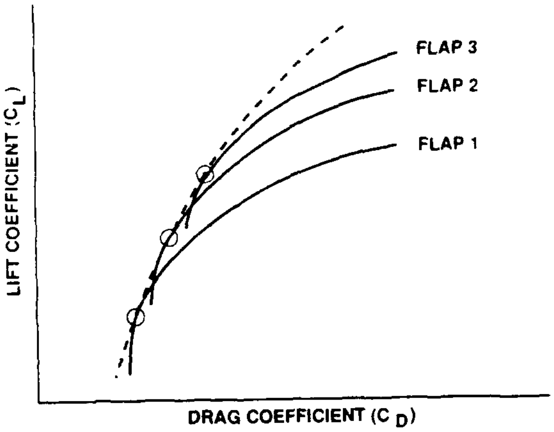

FIGURE 6. X-29 ACC SCHEDULE DERIVATION

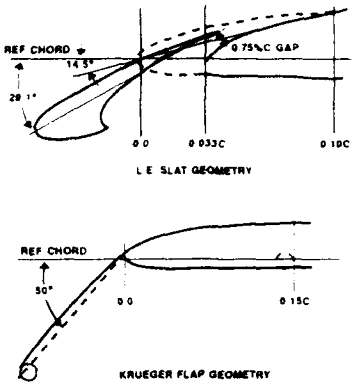

FIGURE 7. FSW HIGH LIFT LEADING EDGE DEVICES

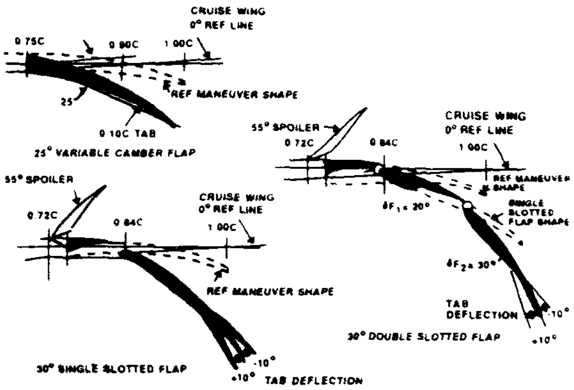

FIGURE 8. FSW HIGH LIFT TRAILING EDGE DEVICES

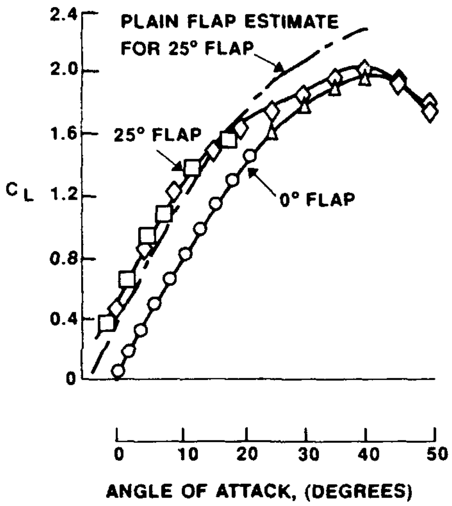

FIGURE 9. LIFT CURVE FOR PLAIN FLAP

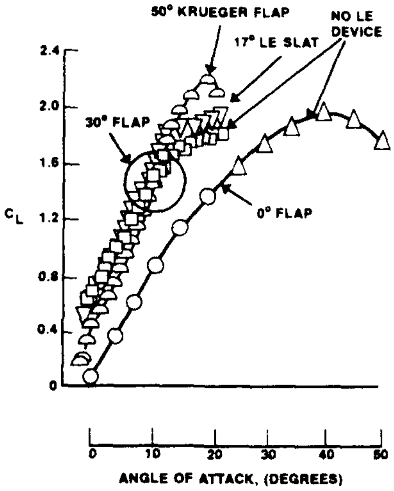

FIGURE 10. LIFT CURVE FOR SINGLE SLOTTED FLAP

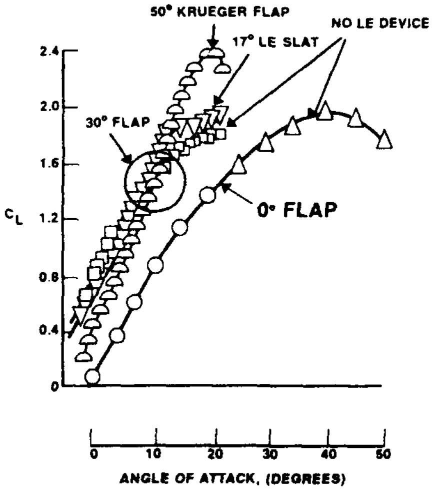

FIGURE 11. LIFT CURVE FOR DOUBLE SLOTTED FLAP

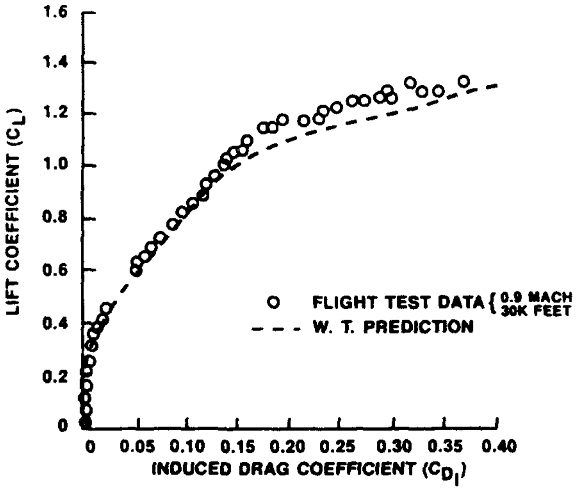

FIGURE 12. X-29 AIRCRAFT PERFORMANCE

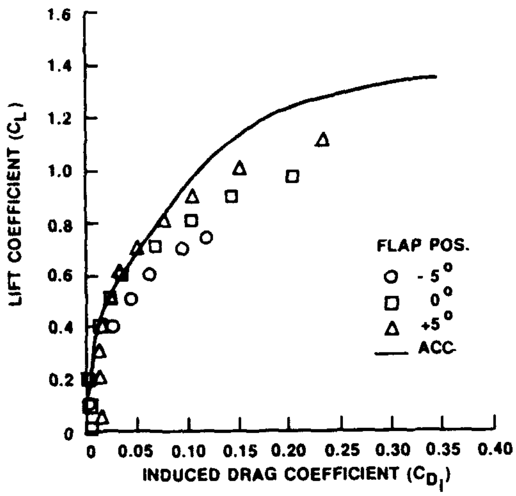

FIGURE 13. X-29 ACC/MCC COMPARISON

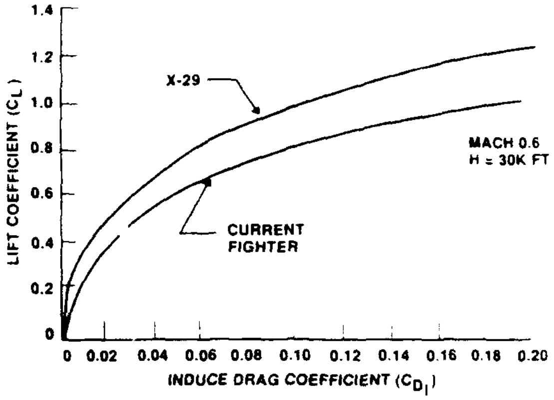

FIGURE 14. DRAG POLAR COMPARISONS - MACH 0.6

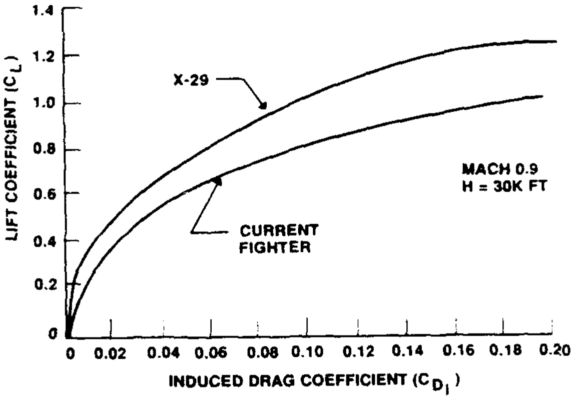

FIGURE 15. DRAG POLAR COMPARISONS - MACH 0.9

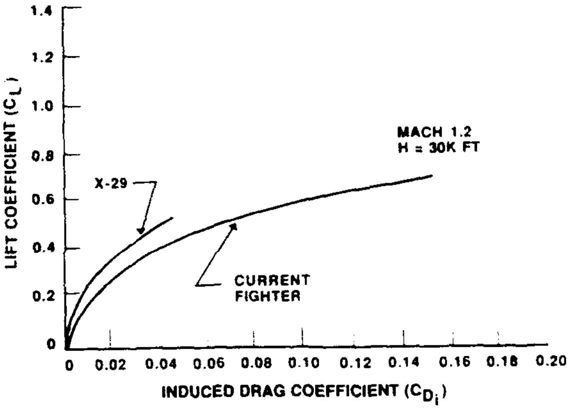

FIGURE 16. DRAG POLAR COMPARISON - MACH 1.2

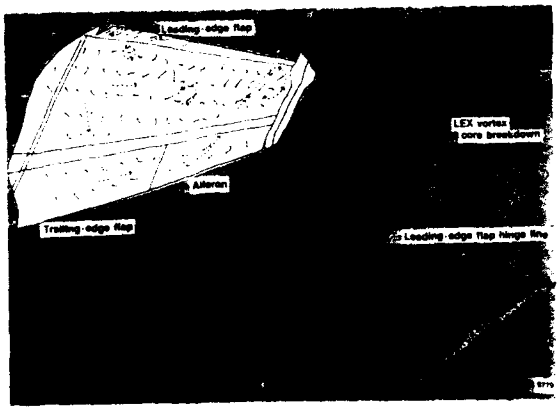

VIEW FROM CHASE AIRCRAFT, 30°

FIGURE 17. F-18 FLOW VISUALIZATION

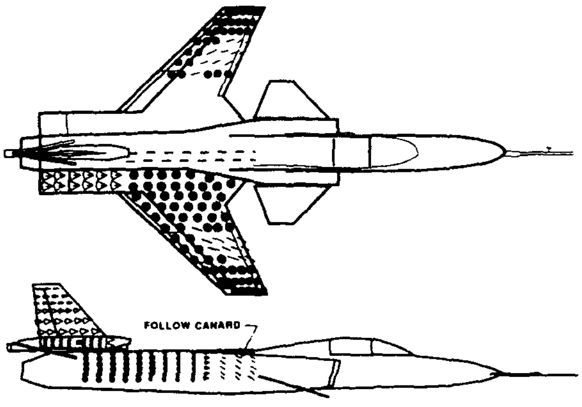

FIGURE 18. X-29 FLOW VISUALIZATION
30 DEGREES AOA

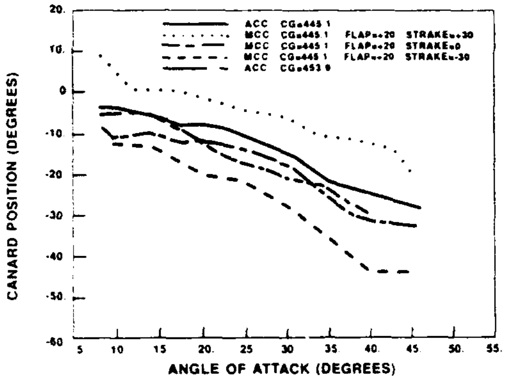

FIGURE 19. CANARD OPTIMIZATION STUDY - CANARD SCHEDULE

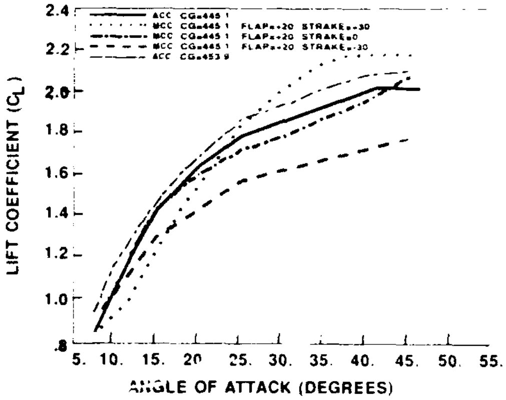

FIGURE 20. CANARD OPTIMIZATION STUDY - LIFT CURVE

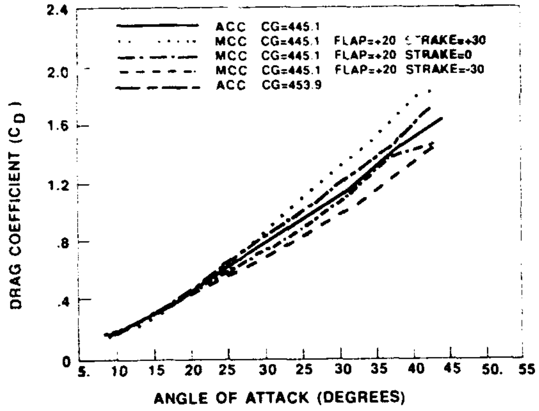

FIGURE 21. CANARD OPTIMIZATION STUDY - DRAG CURVE

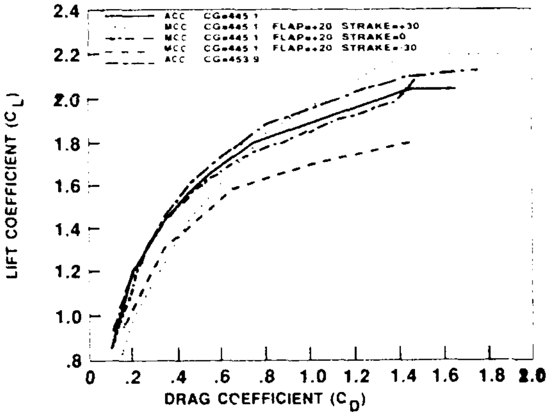

FIGURE 22. CANARD OPTIMIZATION STUDY - DRAG POLAR

A FAST COMPUTING METHOD FOR THE FLOW OVER HIGH-LIFT WINGS

K.Jacob
German Aerospace Research Establishment (DLR)
Institute of Theoretical Fluid Mechanics
Bunsenstr. 10, 3400 Goettingen, Germany

SUMMARY

A quasi-3-dimensional method for analysing the viscous steady subsonic flow over wings with flaps for high lift is briefly presented. The total iterative procedure combines a 3-dimensional inviscid lifting surface theory with a 2-dimensional surface-singularity method for analysing multi-element airfoils in a curved basic flow field. This method also includes boundary layer calculations and a model for rear separation. Also, small compressibility effects are accounted for by simple corrections, and ground effects are included by means of the reflected image technique.

First attempts to validate the method by a few theory-experiment comparisons are reported. The results are encouraging but more experimental data are needed for a thorough validation. The computing time requirements of the method are modest.

LIST OF SYMBOLS

$B_{\nu n}$, $C_{\nu n}$	influence coefficients in eq. 2
c	chord of airfoil
c_L,c_D,c_M	lift-, drag-, and pitching moment coefficients of the total wing
c_l,c_d,c_m	lift-, drag-, and pitching moment coefficients of an airfoil section
c_p	pressure coefficient $(p-p_\infty)/(V^2_\infty\rho/2)$
f	damping factor in eq. 6
h_D	ground distance in fig. 12
L	reference length for a wing; usually chord of center section with flaps retracted
M	number of wing sections in the Truckenbrodt method
M_∞ or Ma_∞	free-stream Mach number
p	static pressure
Re_∞	Reynolds number, based on V_∞ and L
r	straight distance between two points
s	wing semi-span
s_j	co-ordinate along S_j
S_j	surface of airfoil element No. j
S	starting point of rear separation region at upper surface
T	starting point of rear separation at lower surface, close to trailing edge
U	point on upper boundary of rear separation region, see fig. 4
V, V_∞	local flow velocity and free stream velocity
$v_t(s_j)$	vortex distribution on airfoil surface ≡ tangential component of flow velocity
$v_n(s_j)$	source distribution on airfoil surface ≡ normal component of flow velocity
w	velocity, induced by a vortex system
X, Y, Z	Cartesian coordinate system of the wing, fig. 2
α	angle of attack of an airfoil section
α^*, α^{**}	effective basic flow angles at trailing edge and quarter chord point
α_g	wing incidence
γ, μ	dimensionless quantities related to local lift and pitching moment according to eqs. 2a
δ_f	flap deflection angle
ϕ_B	potential function of basic flow field
η	non-dimensional spanwise distance Y/s
Λ	aspect ratio

Subscripts and superscripts:

B	basic flow
2-d	two-dimensional
ef	effective
ν, n	at section No. ν resp. n
*	trailing edge
**	quarter chord point

1. INTRODUCTION

Safety and economy at take-off and landing of an aircraft are dependant on the quality of the high lift system of the wing. This consists of various extended flaps, by which the lift coefficient c_L can be increased considerably, thus enabling the wing to maintain sufficient lift $L \sim c_L V_\infty^2$ at low speed V_∞.

For the design of good high lift systems engineers need very extensive testing or a good and fairly fast computing method for the flow around multi-component wings. The most important features of such a flow are the complexity of the geometry and the importance of viscosity effects, including flow separation.

A good review of existing methods has been given recently in ref. 1. The development of "coupled separated flow methods" for multi-element airfoils started in the 70th (refs. 2,3,4). Some progress with those methods has been achieved since (e.g. refs. 5,6,7,8) and recently several authors dealt with applying Navier-Stokes methods to multi-element airfoils (e.g. refs. 9,10). But none of these methods is perfect and all are limited to 2-dimensional flow.

Can 2-dimensional methods, even if further improved, be a real help for the design of a 3-dimensional wing? With this important question in mind, a quasi-3-dimensional method has been designed, combining 2-d viscous flow calculations for the wing sections with a 3-d lifting surface method for taking account of the essential effects of the trailing vortices. First the method was worked out and tested for clean wings only (ref. 11) and recently it has been extended to wings with flaps by H.N.V. Dutt and the author (ref. 12). In the present paper this method will be explained briefly and some results will be shown and discussed.

2. QUASI-3-DIMENSIONAL COMPUTING METHOD

2.1 Over-all concept

In order to develop an economical computing method to support the aerodynamic design of high-lift systems for civil aircrafts, one has to consider the flow around multi-component wings of moderate to high aspect ratio, operating at low speed and high lift coefficient. For such a flow it is crucial to take account of viscosity effects, including partial separation. At take-off and landing also ground effects may be important causing sometimes lift decrease when the wing approaches the ground. Eventhough the most accurate solution for such complicated 3-d flow might be obtained with Navier-Stokes methods, for reasons of economy and feasibility these methods are not considered here. Instead, we use a combination of available, approved, economical 2-d and 3-d methods, try to include the essential flow features, but also accept some simplifications and restrictions.

At a wing of high aspect ratio and low sweep the flow around a wing section is approximately 2-dimensional. But, contrary to the rectangular infinite wing, the effective basic flow field at each section of a general finite wing is not identical with the oncoming parallel flow. It is somewhat changed, because the different vortex systems of the finite wing and the infinite wing induce different velocities. The difference of these velocities has to be added to the oncoming flow to give the effective basic flow for a 2-dimensional calculation at a section. Generally, this basic flow is curved and the average angle of attack is smaller than the wing incidence.

If the effective basic flow field is known, the spanwise lift, pitching moment and drag distributions can be computed by applying a 2-d viscous flow method for multi-element airfoils to each section. On the other hand, with a known lift and moment distribution, the induced velocities and thus the effective basic flow at each section can be computed approximately by a reverse application of a 3-d lifting surface method. Therefore, both methods are applied by turns, starting with a first approximation for the spanwise lift and moment distribution and computing the converged lift distribution by iteration. The total procedure is roughly sketched in figure 1 and the main components are treated briefly in the next chapters.

2.2 3-dimensional lifting surface method

The method used at present for the 3-d calculations is the well known lifting surface method of Multhopp and Truckenbrodt (ref. 13) with Hummel's extension for including the ground effect by reflected image technique (ref. 14).

This method uses horseshoe vortices in the wing projection plane (figure 2) with a continuous 2-parameter vortex distribution in the chordwise direction and a spanwise discretisation with M wing sections at

$$\eta_\nu = Y_\nu / s = \cos(\pi\nu / (M+1)), \nu = 1,2,\ldots,M. \quad (1)$$

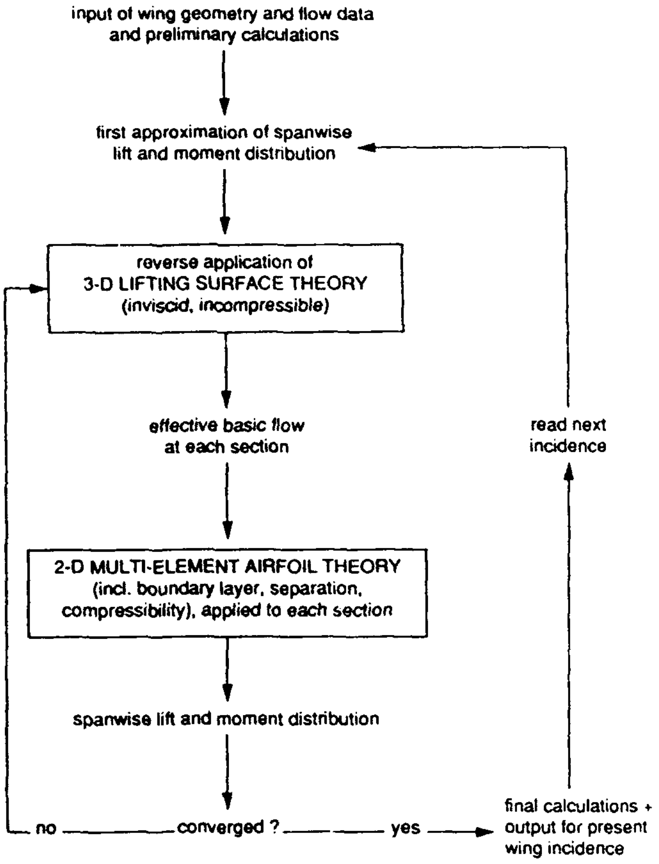

Fig. 1 Sketch of total procedure

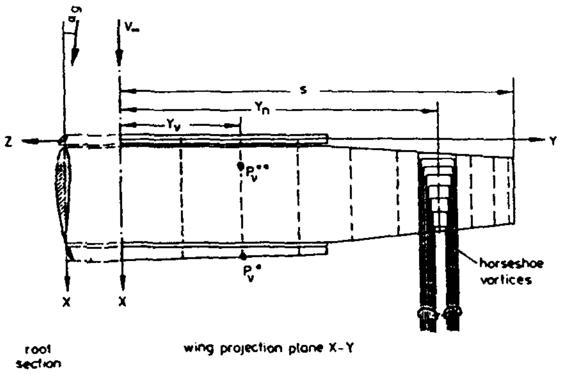

Fig. 2 A multi-component wing geometry, vortices and some notations

The law of Biot-Savart leads to linear equations for the induced velocities w^*_ν at the trailing edge and w^{**}_ν at the quarter chord points of these sections:

$$w^*_\nu/V_\infty = \sum_{n=1}^{M} (B^*_{\nu n}\,\gamma_n + C^*_{\nu n}\,\mu_n)$$

and (2)

$$w^{**}_\nu/V_\infty = \sum_{n=1}^{M} (B^{**}_{\nu n}\,\gamma_n + C^{**}_{\nu n}\,\mu_n), \quad \nu = 1,2,\dots,M.$$

Here the γ and μ are closely related to the local lift and moment coefficients c_l and c_m, namely

$$\gamma_n = c_{ln}\,LV_{ef\,n}\;/\;(4s\;V_\infty)$$

and (2a)

$$\mu_n = c_{mn}\,LV_{ef\,n}\;/\;(4s\;V_\infty)$$

and the coefficients $B^*_{\nu n}$ thru $C^{**}_{\nu n}$ are determined by the geometry of the wing projection and the number of sections M. In case of ground effect they also depend on ground distance and incidence.

The normal application of the method consists of determining the velocities to be induced, from the "equivalent thin airfoil" geometry at each section, and then computing the values of γ and μ by solving the system of linear equations (2). For more details see ref. 11.

In our total procedure (fig. 1) the lifting surface method is used in the normal way only once in the beginning, to get a first approximation to γ and μ. Within the iteration loop it is used only in a reverse way, i.e. finding the induced velocities w^*_ν and w^{**}_ν from known approximations to γ and μ by simple matrix-vector multiplication.

Then, the effective basic flow velocities at quarter chord and trailing edge of wing section No. ν are obtained by vector addition:

$$V^{**}_\nu = V_\infty + w^{**}_\nu - w^{**}_{2-d\;\nu}$$

and (3)

$$V^{*}_\nu = V_\infty + w^{*}_\nu - w^{*}_{2-d\;\nu}$$

with $w_{2\text{-}d\;\nu}$ meaning the veloctiy vector induced by the vortex lines of the infinite rectangular wing (2-d) with the section No. ν and constant $\gamma = \gamma_\nu$ and $\mu = \mu_\nu$. The formulas for evaluating the basic flow velocities are given in detail in ref. 11.

Generally, the resulting basic flow velocities will have somewhat different directions at quarter chord and trailing edge. So the basic flow field for the subsequent 2-d calculation is no longer parallel but curved. At present this flow is approximated by a circular flow, produced by a remote vortex of proper strength and position (see figure 3).

2.3 2-dimensional multi-element airfoil method

For analysing the approximately 2-dimensional, viscous flow around the multi-element airfoils at the wing sections, the author's method (ref. 2) is used, with the extensions for multiple separation (ref. 6), ground effect (ref. 15) and curved basic flow (ref. 16). Given below is a very brief presentation of the essentials of the method only.

The flow field around a multi-element airfoil is divided into different regions (see figure 4). The outer inviscid flow is treated by a surface-singularity technique, using a vortex distribution $v_t(s)$ on the surface S of each element. In addition, source distributions $v_n(s)$ are used to simulate displacement effects of boundary layers, wakes and separated flow regions, via the "transpiration method". For the boundary layers Rotta's integral method (ref. 17) is applied, and small compressibility effects are accounted for by a simple correction applied to the surface pressure distribution of the incompressible flow (see ref. 11, page 23).

For the inviscid incompressible flow with a basic flow potential ϕ_B the kinematic flow condition leads to the following system of coupled linear integral equations

$$\frac{v_t(s_k)}{2} - \sum_{j=1}^{N} \frac{\partial}{\partial n} \int_{S_j} \frac{v_t(s_j)}{2\pi} \ln r(s_k,s_j)\, ds_j = R(s_k)$$

with (4)

$$R(s_k) = \frac{\partial \phi_B}{\partial t}(s_k) + \sum_{j=1}^{N} \frac{\partial}{\partial t} \int_{S_j} \frac{v_n(s_j)}{2\pi} \ln r(s_k,s_j)\, ds_j$$

with k=1,2,...,N for an airfoil system with N elements. Here, t and n indicate the directions tangential resp. normal to the airfoil surface. Accounting for ground effect via reflected image technique leads to extending eqs. 4 by additional terms (see ref. 12, page 9).

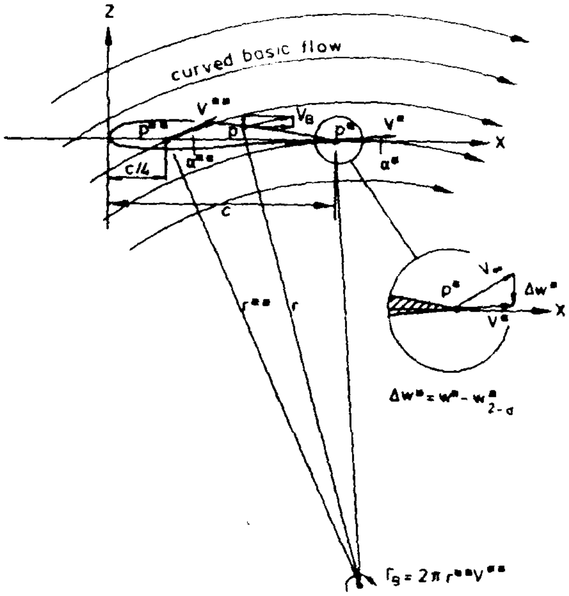

Fig. 3 Airfoil section in a curved basic flow field, induced by a distant single vortex

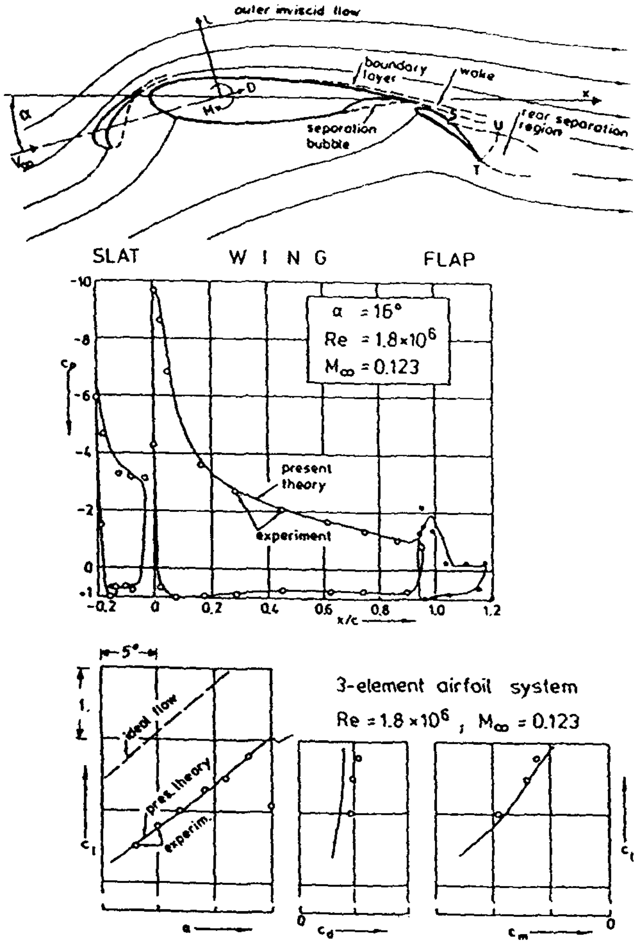

Fig. 4 2-dimensional 3-element landing configuration with different flow regions. Pressure distribution and lift-, drag- and moment coefficients from theory and experiment.

From eqs. (4), after some transformation and discretisation, v_t can be computed numerically, if the basic flow (ϕ_B) and the source distributions v_n are given and if one condition is added for each airfoil element to fix its circulation (Kutta condition or specified circulation Γ).
Solving eqs. (4) for different right hand sides and different additional conditions, a set of "fundamental flow solutions" can be obtained. Then, by superposition, a flow can be constructed, which contains a simulated separated flow region. This is demonstrated in figure 5 for the simplest case of parallel basic flow and sources on the rearmost element only. (For curved basic flow a solution with the ϕ_B of that flow has to replace solutions (a_1, a_2)).

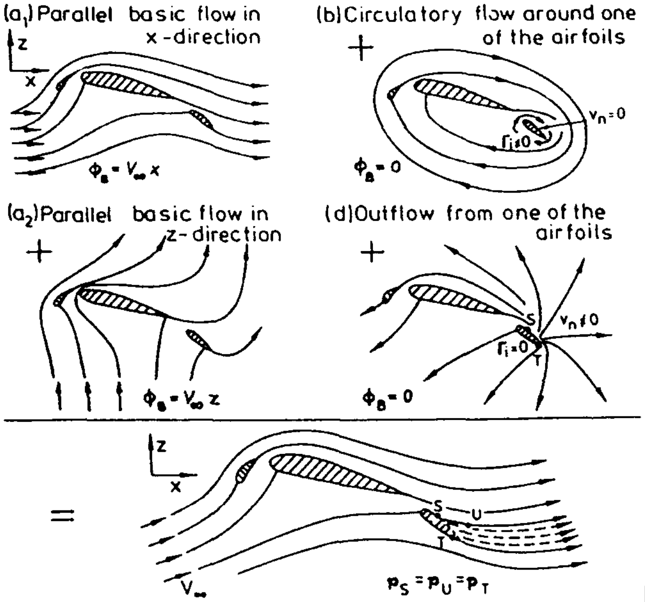

Fig. 5 Four fundamental flow solutions and flow with model for rear separation.

For the separated flow region an isobaric model is adopted, obtained approximately by demanding equal pressure at the points S, T, and U. This can be achieved by finding proper weight factors for the fundamental solutions (b) and (d).

So far a potential flow with a rear separation model can be found for any position of the starting point S. But to be physically realistic S must just be the boundary layer separation point of this flow. To find the right position of S the potential flow calculations and subsequent boundary layer calculations are executed for various positions of S, starting near the trailing edge and moving S upstream until the resulting separation point coincides with S.
For extending the method to multiple separation and for refining the wake model by adding singularities in the wake see ref. 6 and 21.

Apart from the relative simple wake model, our present method contains some more simplifications: closed separation bubbles at the lower surfaces of the slat and the main element are simply replaced by estimated contour fairings. Small compressibility effects are postulated, and possible confluence of boundary layers and wakes is not yet accounted for. Nevertheless, as can be seen from fig. 4, the method gives good results with respect to lift and pitching moment, as long as rear separation is limited to the flap, i.e. below maximum lift . However, drag prediction is not yet satisfactory.

2.4 Some details of the total procedure

Input and preliminary calculations (see fig. 1):
The wing geometry shall be given by streamwise wing sections at a sufficient number of spanwise stations, e.g. 8 "input stations" on the half wing in figure 6. Their number and distribution shall be such that the data of intermediate sections can be found by simple interpolations. For the M "Truckenbrodt stations", defined by eq. (1), the geometric data are then to be prepared, including the influence matrices B* thru C**. Also the aerodynamic characteristics $c_l(\alpha)$ etc. of all sections are now computed for given Reynolds and Mach number, assuming parallel basic flow. Finally, normal application of the lifting surface method gives a first approximation to γ and μ.

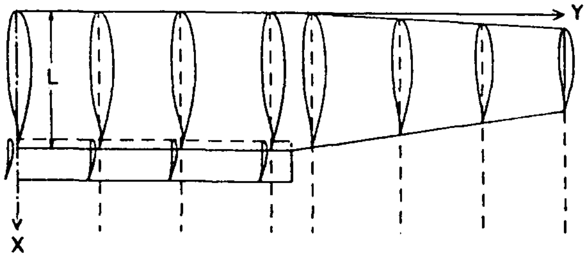

Semi span = 4L , Aspect ratio = 7.878

Airfoil: inboard - GA(W)-1 + 30% Fowler flap
outboard - GA(W)-1 clean

Fig. 6 Geometry of part span Fowler flap configuration (for flap deflection $\delta_f = 10°$).

Iterations:
For reasons of economy the inner iteration loop in fig. 1 is used in two different versions. First the 2-d calculations are replaced by simply interpolating the lift coefficients etc. from the pre-calculated aerodynamic characteristics, neglecting the curved basic

flow effect. Here the effective parallel basic flow is taken to be defined by

$$V_{ef} = V^{**} \quad and \quad \alpha_{ef} = (\alpha^{**} + 2\alpha^{*})/3 \qquad (5)$$

An improved approximation for the lift distribution can thus be obtained quickly with about 20 fast iterations. Then, starting from this approximation and applying now the full 2-d calculations with curved basic flow, the final lift distribution etc. can be obtained with only a few of these comparatively expensive iterations.

In both phases of the iteration process it turned out to be important to apply smoothing and damping to the intermediate results and to take care for a smooth transition to zero at the wing tip. Especially the damping factor for the "curved basic flow iteration" can have a considerable effect on the convergence history, as demonstrated in figure 7. Here the damping factor f is defined by

$$\gamma^{i} \leftarrow \gamma^{i-1} + f \cdot (\gamma^{i} - \gamma^{i-1}) \qquad (6)$$

with γ^i being the result of the i-th iteration. Figure 7 shows best convergence with f = 0.30, but divergence with too high f.

Final calculations and output:
Finally the coefficients c_L, c_D, c_M for the total lift, drag and moment of the wing are found by integration of the spanwise distributions, taking account of the different local directions of lift and drag, for example

$$c_L = \Lambda \int_{-1}^{+1} [\, \gamma(\eta) \cos(\alpha_g - \alpha_{ef}) - \delta(\eta) \sin(\alpha_g - \alpha_{ef}) \,] \, (V_{ef} \,/\, V_\infty) \, d\eta \qquad (7)$$

with $\delta = c_d L V_{ef} / (4s V_\infty)$ being related to the drag.

Now, all results of the last iteration are available for output, including the chordwise pressure distributions at the wing sections.

At the end it may be mentioned, that the inviscid lifting surface method gives good first approximations to γ and μ only for low wing incidence α_g. The computing time per case can be reduced considerably if the computation is done for a whole series of α_g-values, starting with a moderate α_g, increasing α_g stepwise and using always the converged γ and μ of the previous α_g as first approximation for the next one. Thus all the preliminary calculations have to be carried out only once and there are always reasonable first approximations.

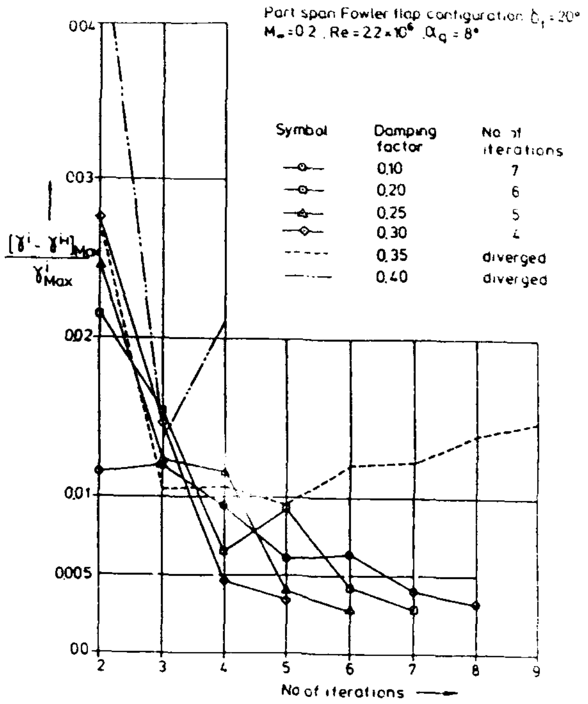

Fig. 7 Effect of damping factor on convergence history

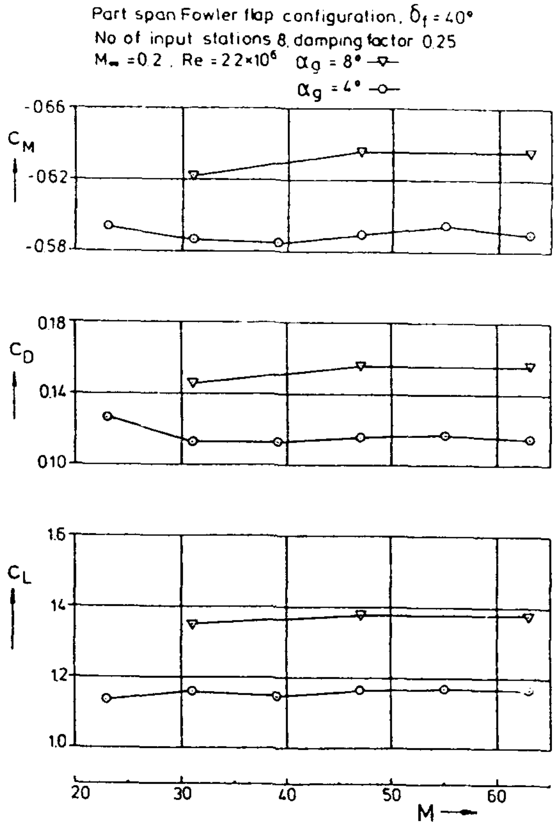

Fig. 8 Effect of number of "Truckenbrodt-stations" M on converged values of c_L, c_D, c_M.

3. SOME RESULTS

Before trying to validate the method by comparing computed and experimental results, some computational studies were carried out to see how convergence and final results are affected by the choice of various parameters.

For the wing configuration of fig. 6 the effect of damping factor f on convergence history has been shown in fig. 7. The effect of the chosen number of "Truckenbrodt-stations" M on the final force coefficients of the wing is demonstrated in figure 8. From these and other examples we found that f ≈ 0.25 and M > 40 can be recommended.

Next, figure 9 shows that the final results can be somewhat affected by the choice of the input stations. With stations No. 4 and 5 being positioned nearer to the geometric discontinuity (flap tip at η = 0.50), the γ-distribution drops more sharply and the total lift coefficient c_L is slightly reduced. Recommendations for favourable positions of the input stations can be given only after comparing with experimental distributions, carefully measured especially in the vicinity of geometric discontinuities.- The preliminary tests with the wing of fig. 6 are concluded by comparing our results for a low flap deflection and a low incidence with the results of an inviscid vortex lattice method (ref. 18). Figure 10 contains the γ-curves and the values of the total lift coefficient c_L. As expected, our viscous method gives somewhat reduced lift.

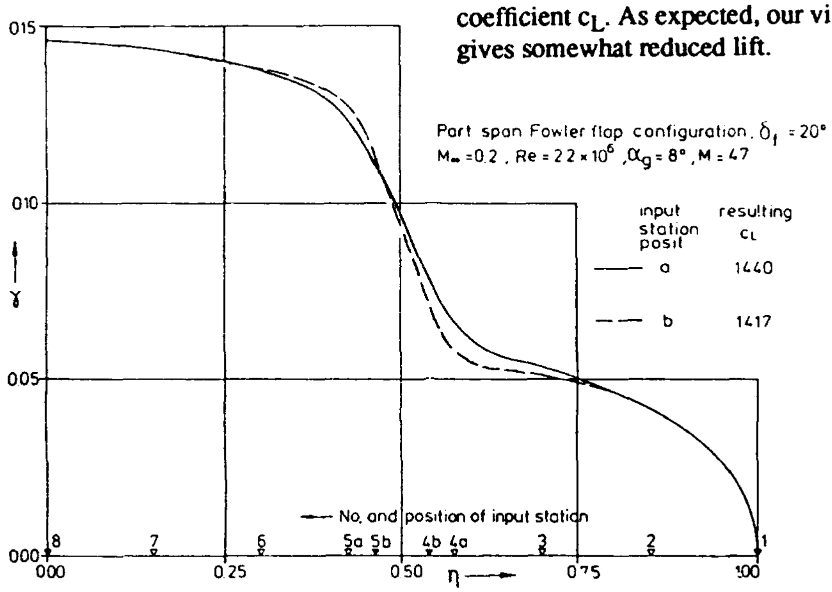

Fig. 9 Variation of spanwise γ-distribution with altered positions of the input stations.

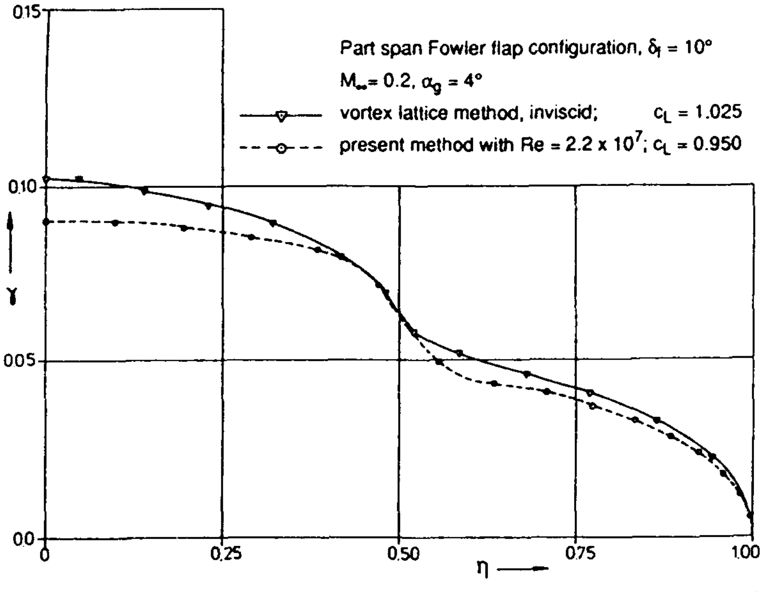

Fig. 10 Comparison of spanwise γ-distributions, computed by inviscid vortex lattice method and present viscous method.

The first comparisons of theoretical results with experiments were carried out for the simplest case, a clean rectangular wing of aspect ratio 3.1, shown in figure 11. For this wing detailed measurements are available in ref. 19, including high angles of attack with partial flow separation. The measured pressure distributions compare fairly well with the results of the "advanced method", which contains the calculations with curved basic flow. The curved flow effect is most important at wing regions with a strong spanwise lift gradient.

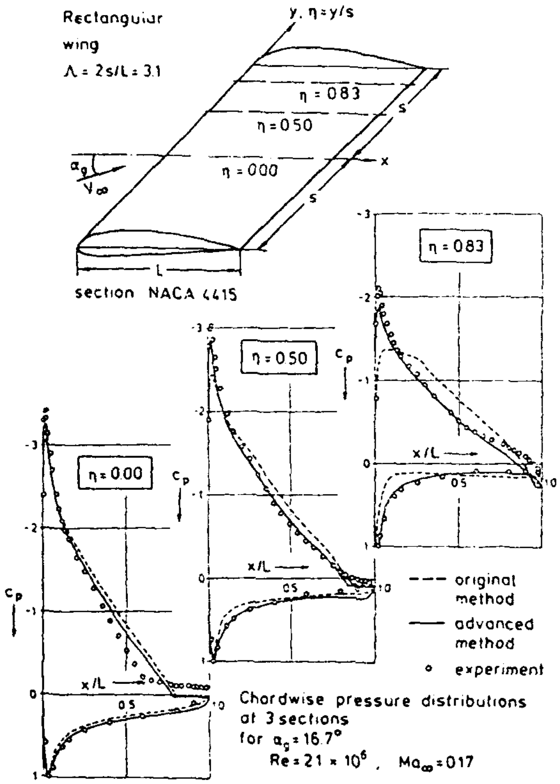

Fig. 11 Pressure distributions at different stations of a rectangular wing with aspect ratio Λ = 3.1.

In figure 12 the lift characteristics are shown for the airfoil section ($\Lambda = \infty$) and for the wing ($\Lambda = 3.1$) with and without ground effect ($h_D/L = 0.33$ resp. ∞). In all cases theory and experiment compare well, including maximum lift. Finally, in figure 13 the ground effect was investigated in more detail. Besides fair prediction of all aerodynamic characteristics, it may be noteworthy that the maximum lift is lowest at the medium ground distance $h_D / L = 0.99$. This "hight instability of lift" is indicated by theory and experiment as well.

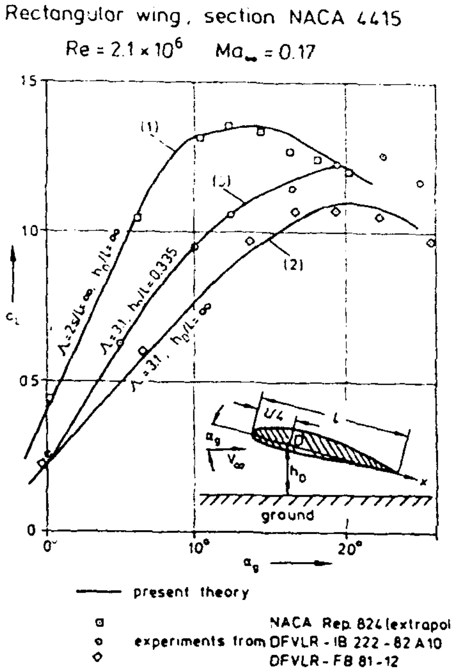

Fig. 12 Lift characteristic from theory and experiment for airfoil section (1) and for the rectangular wing without and with ground effect (2), (3).

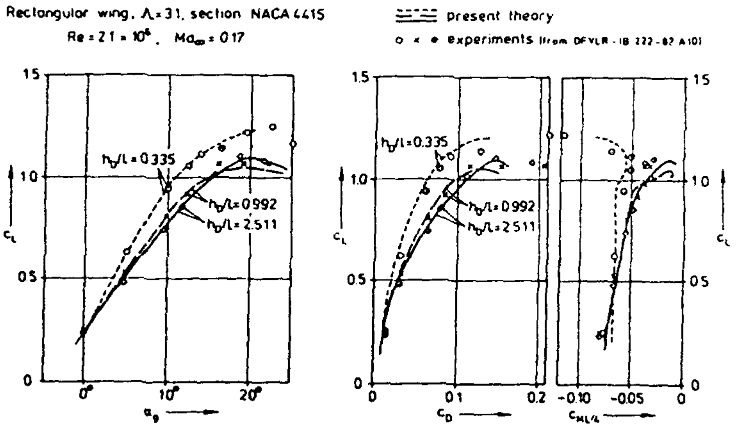

Fig. 13 Total lift, drag and pitching moment coefficients of the rectangular wing for three different ground distances h_D / L.

Next, a rectangular wing of aspect ratio 6 equipped with full span leading and trailing edge flaps is shown in figure 14. For this configuration measured pressure distributions at section A-A are available in ref. 20 and compared with our theoretical results for a low and a high wing incidence α_g. At $\alpha_g = 6°$ the results for 2-d flow are also shown, and the effect of the finiteness of the wing can well be seen.
The results of experiment and present method compare fairly well, except for the region below the slat and the main element nose at $\alpha_g = 6°$. There is probably a large separation bubble which was not modelled properly. At the high $\alpha_g = 18°$ there is very good agreement in this region, probably due to disappearance of the bubble. Also the separation on the flap (level and extension of constant pressure) is well predicted. The pressure differences on the rear part of the main element upper side might partly be due to geometrical differences.

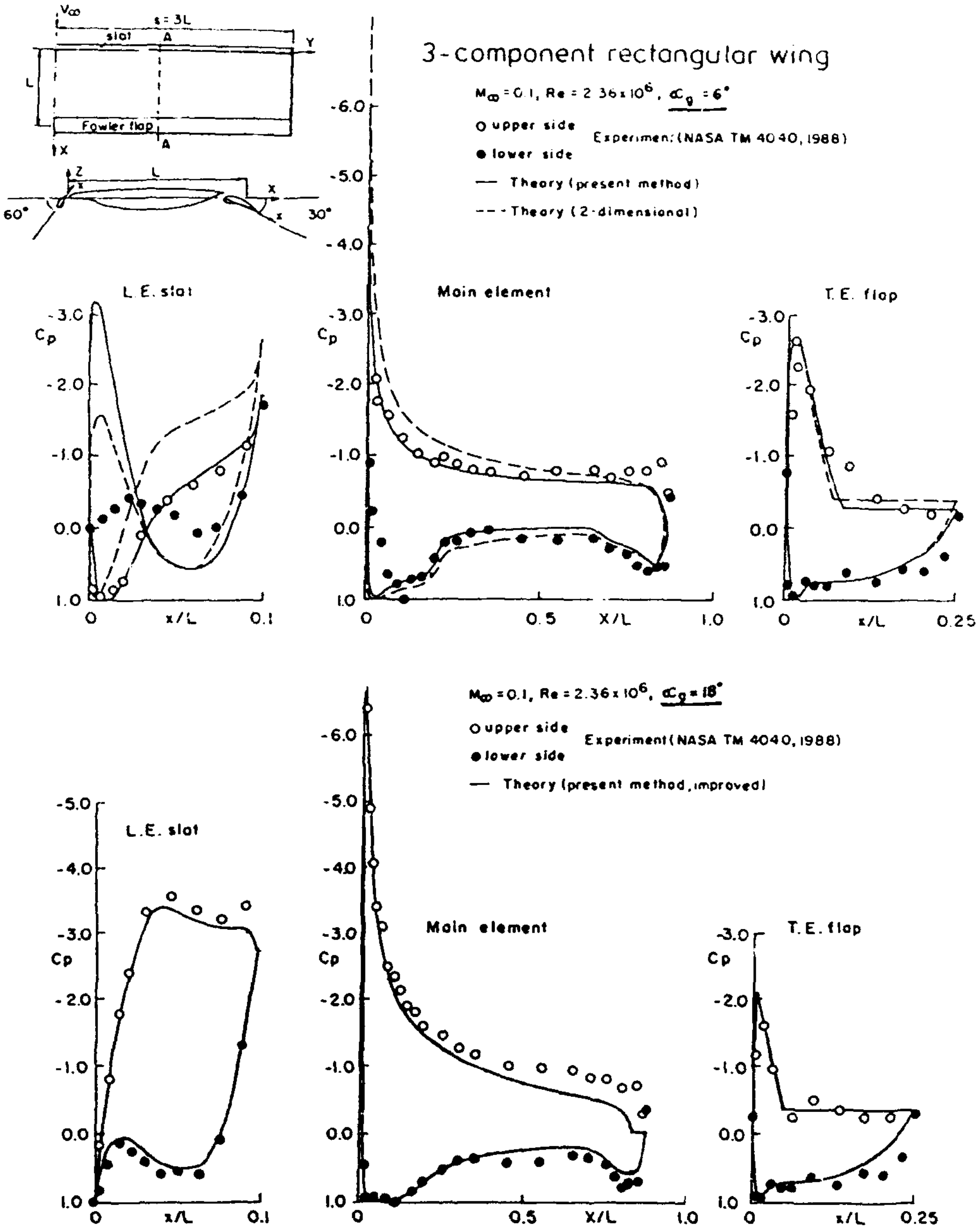

Fig. 14 Geometry of a 3-component rectangular wing and pressure distributions at section A-A for a low and a high wing incidence α_g.

Next, a swept wing with 28° sweep and a constant 3-element section, is shown in figure 15, and the computed wing lift coefficients c_L are compared with measurements. Here we found that the agreement can be improved, if the trailing vortices in the lifting surface theory are turned upward by $\alpha_g/2$. (This has been done approximately by just rotating the induced velocity vectors w* and w** counterclockwise by $\alpha_g/2$.)

The computations do not yet include an infinite swept wing correction for the pressure distributions. Nevertheless, for wing incidences up to about 25° the lift of this 3-component swept wing is fairly well predicted. For comparison the computed lift for the unswept wing is also shown.

For more general and more realistic wings with taper and part span flaps no proper measurements were available to the author. So only computed results are shown in figure 16 for an almost realistic wing landing configuration with full span slat and 75% span Fowler flap. The converged results were obtained with 7 iterations and they look reasonable. The spanwise lift distribution drops near the flap tip and the pressure distributions show some separation on the flap and on the outer wing near the flap tip (station No. 3). Given on the figure are also the total wing force coefficients and the computing time requirement.

On an IBM 3090 computer about 4 minutes CPU-time were needed for this case, and in the previous example (fig. 15) an average of about 2.5 minutes was needed per wing incidence.

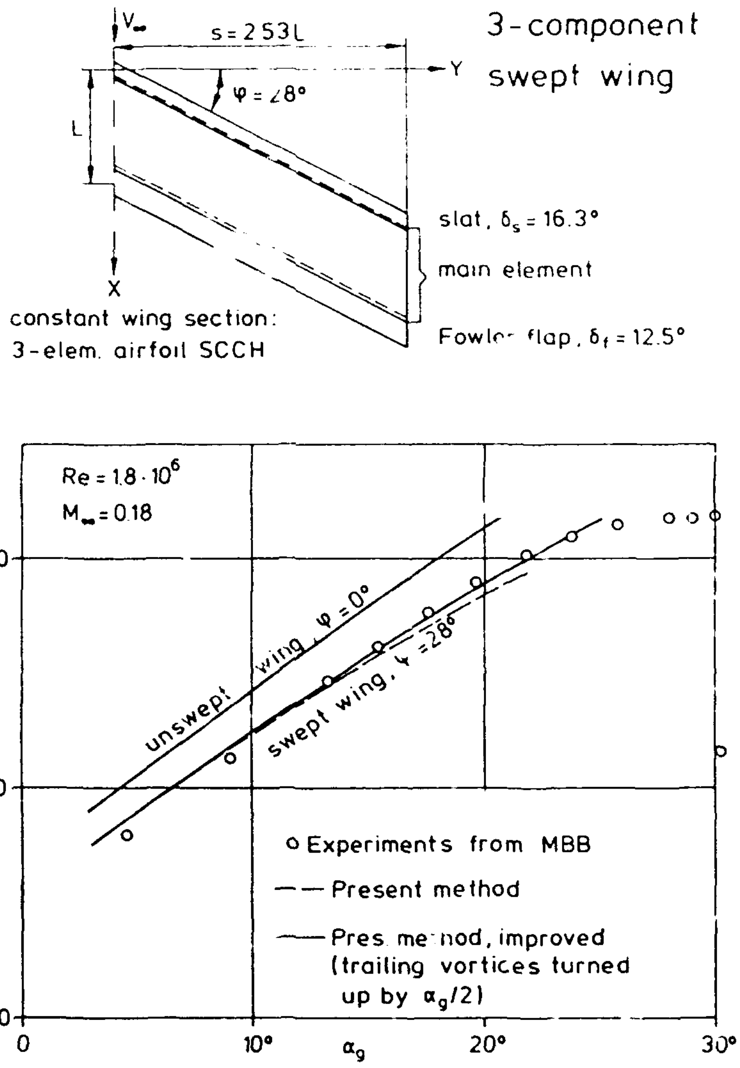

Fig. 15 Geometry of a 3-component swept wing and total lift coefficients from theory and experiment.

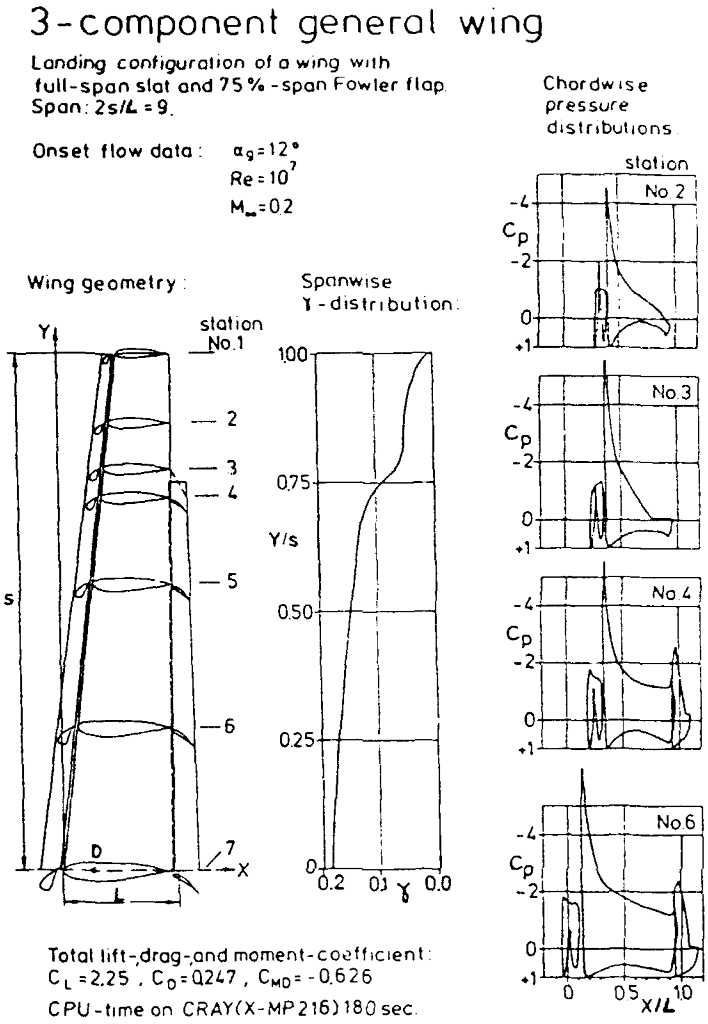

Fig.16 Geometry of a 3-component general wing and some results obtained with the present method.

4. CONCLUSIONS

A relatively fast and simple method for approximately predicting the subsonic steady viscous flow around wings of moderate to high aspect ratio has been presented. The total iterative procedure combines a 3-d inviscid lifting surface method with 2-d viscous flow calculations for the wing sections (airfoils in curved basic flow fields). Essential high-lift flow features, e.g. complex geometry and viscosity effects including separation and also ground effects are taken into account.

After successful tests for clean wings at high angles of attack, the method has been extended and applied to various multi-component wings. The computations converged, the computing time requirements are modest and the results look reasonable. Very few proper experiments for multi-component wings were available to the author for theory-experiment comparison. The few presented results are encouraging but not sufficient for thorough validation of the method. Further validation is required.

Certainly the method is restricted to wings of moderate to high aspect ratio and low to moderate sweep. For such wings the proposed way of coupling fast 2-d and 3-d methods seems to by very useful. Present limitations with respect to wing incidence and Mach number originate mainly in the 2-d method, presently applied. To extend the scope of the total method and increase the accuracy, it may be helpful to use a more advanced 2-d multi-element airfoil method, containing e.g.

- refined models for the open wakes (e.g. ref. 21) and for the closed bubbles,
- allowance for possible wake-boundary layer confluence,

- more accurate treatment of compressibility near suction peaks.

Moreover, the total method might be improved, for example, by using,

- infinite swept wing corrections for the local pressure distributions,
- a more sophisticated model for the curved basic flow,
- more careful treatment of the wing regions in the vicinity of geometric discontinuities.

Despite of the mentioned restrictions the author is hoping, that the presented method -or it's next improved version-will become a helpful tool to engineers for the design of high-lift wing configurations.

REFERENCES

1. Brune, G.W., McMasters, J.H.: Computational Aerodynamics Applied to High-Lift Systems. Applied Computational Aerodynamics, Vol. 125 of Progress in Astronautics and Aeronautics, AIAA, ISBN 0-930403-69-X, 1990
2. Jacob, K., Steinbach, D.: A Method for Prediction of Lift for Multi-Element Airfoil Systems with Separation. AGARD CP-143, April 1974
3. Henderson, M.L.: A Solution to the 2-d Separated Wake Modeling Problem and its Use to Predict $c_{L\max}$ of Arbitrary Airfoil Sections. AIAA Paper 78-156, Jan. 1978
4. Olsen, L.E.: Optimization of Multi-Element Airfoils for Maximum Lift. NASA CP-2045, Vol. 1, March 1978
5. LeBalleur, J.C., Neron M.: Calcul d'coulements visqueux decolles sur profil d'ailes par une approche de couplage. AGARD CP-291, Aug. 1980
6. Jacob, K.: Berechnung von Profilsystemen bei Unterschallströmung mit mehrfacher Ablösung. DFVLR-FB 81-24, 1981
7. Dargel, G., Jakob, H.: Berechnung von Klappenprofilströmungen mit Ablösung auf der Basis gekoppelter Potential und Grenzschichtlösungen. Strömungen mit Ablösung. DGLR-Ber. 88-05, S. 267-278, 1988
8. King, D.A., Williams, B.R.: Developments in Computational Methods for High-Lift Aerodynamics. Aeronautical Journal, Vol. 92, No. 917, Aug./Sept. 1988
9. Shima, E.: Numerical Analysis of Multiple Element High Lift Devices by Navier-Stokes Equation Using Implicit TVD Finite Volume Method. AIAA Paper 88-2574-CP, June 1988
10. Fritz, W.: Numerical Simulation of 2-d Turbulent Flow Fields with Strong Separation. Internat. Concil of Aeronautical Sciences, Paper 88-4, 6.4, 1988
11. Jacob, K.: Advanced Method for Computing the Flow around Wings with Rear Separation and Ground Effect. DFVLR-FB 86-17, 1986
12. Dutt, H.N.V., Jacob, K.: Viscous Subsonic Flow Computation for Wings with Flaps for High-Lift. DFVLR-IB 221-89 A 16, 1989
13. Truckenbrodt, E.: Tragflächentheorie bei inkompressibler Strömung. Jahrbuch 1953 der Wissenschaftl. Gesellschaft für Luftfahrt.
14. Hummel, D.: Nichtlineare Tragflügeltheorie in Bodennähe. Zeitschrift für Flugwissenschaften 21, Heft 12, 1973
15. Steinbach, D.: Berechnung der Strömung mit Ablösung für Profile und Profilsysteme in Bodennähe oder in geschlossenen Kanälen. Zeitschrift für Flugwissenschaften und Weltraumforschung 2, Heft 5, 1978
16. Chen, Y.Q., Jacob, K.: Computation of Flow around Wings with Rear Separation, Including the Curved Basic Flow Concept. DFVLR-IB 221-84 A 08, 1984
17. Rotta, J.C.: FORTRAN-Rechenprogramm für Grenzschichten bei kompressiblen ebenen und achsensymmetrischen Strömungen. DLR-FB 71-51, 1971
18. Rajeswari, B., Dutt, H.N.V.: Non-Planar Vortex Lattice Method for Analysis of Complex Multiple Lifting Surfaces. NAL India, TM AE 8606, Aug. 1986
19. Bippes, H., Turk, M., Jacob, K.: Experimentelle Untersuchungen zur abgelösten Strömung an einem Rechteckflügel. DFVLR-FB 81-12, 1981
20. Applin, Z.T., Gentry, G.L.: Pressure Distributions from Subsonic Tests of an Advanced Laminar Flow Control Wing with Leading and Trailing Edge Flaps. NASA TM 4040, parts I and II, July 1988
21. Jacob, K.: Improved Wake Modeling for Flow Around Multi-Element Airfoils. DLR-IB 221-92 A 06 ,1992

ACKNOWLEDGEMENTS

I want to express my thanks to:
my institute for supporting this work, my colleagues at DLR Dr. Steinbach and Dr. Bippes and our former guest scientists Mrs. Chen from BUAA Beijing and Dr. Dutt from NAL Bangalore for much help and good cooperation, and Mrs. Alberti for carefully preparing the manuscript.

CALCULATION OF MULTIELEMENT AIRFOILS AND WINGS AT HIGH LIFT

Tuncer Cebeci*
Aerospace Engineering Department
California State University, Long Beach
Long Beach, California 90840, USA

SUMMARY

A calculation method based on an interactive boundary-layer approach to multielement airfoils and wings is described. For two-dimensional flows, the method is applied to three types of airfoil configurations with and without flap wells in order to demonstrate its applicability and accuracy to general high-lift configurations. This method, extensively tested for single airfoils as a function of shape, angle of attack, and Reynolds number, is shown here to apply equally well to multielement airfoils. The calculation method is also applied to a wing and wing/flap configuration in order to demonstrate its promise for addressing three-dimensional flows. Preliminary results indicate that with further development, the method, as for multielement airfoils, will also become a practical, accurate and efficient tool for multielement wings.

1. INTRODUCTION

In recent years, there has been a renewed interest to design more efficient and easier to build high-lift systems. Primary objectives are lower cost and lower drag, which lead to lower noise. Extensive measurements have been reported for this goal by Nakayama[1], Alemdaroglu, summarized by Nakayama[2], and Valarezo et al.[3-4] The data of Nakayama are for a three-element airfoil with a leading-edge slat and for a single-segment flap; these data were obtained at NASA Langley's Low Turbulence Pressure Tunnel (LTPT). Those of Alemdaroglu are essentially for the same but smaller model and were obtained at the low-speed wind tunnel of California State University, Long Beach. The data of Valarezo et al. were also obtained at NASA Langley's LTPT and correspond to measurements at high Reynolds numbers. These data add to the previously obtained data on multielement airfoils by van den Berg[5], van den Berg and Oskam[6], Oskam et al.[7], Omar et al.[8,9] and Olson and Orloff[10] and allow the development and validation of computer programs to analyze high-lift systems.

Several airfoil-analysis and design algorithms have been developed in the past decade and have been based on one of two approaches, either as numerical solutions of the Reynolds-averaged Navier-Stokes equations or as interaction between inviscid and boundary-layer equations.[11] The former approach involves the numerical solution of elliptic equations so that information travels in all directions through pressure, velocity and viscous and turbulent stress gradients. As a result, the solution method requires simultaneous calculation of the pressure, velocity components, and stress tensor throughout the flowfield and this, in turn, implies a trade-off between accuracy and cost. This limitation is a function of computers and programming methods and these are likely to improve with time so that solutions of the Navier-Stokes equations, with proper consideration of momentum conservation in two directions together with longitudinal diffusion, are likely to be a major component of design methods of the future. The combination of the largest main-frame computers and structured and unstructured and multigrid techniques has already been shown to be very powerful as, for example, by Mavriplis[12], Rogers et al.[13], Barth.[14] and as we shall see, in the papers to be presented in this meeting.

Regardless of which approach is used to solve the conservation equations, one must calculate the onset of transition in the development of the design algorithm so that the effects of wind tunnel and flight Reynolds numbers can be properly identified. As we shall see later, the components of the multielement airfoils at wind tunnel Reynolds numbers can have relatively lower Reynolds numbers than that of the main airfoil. At chord Reynolds numbers less than 500,000, the components can have large separation bubbles, with the onset of transition occurring inside the separation bubble. As a result, their behavior can be significantly different than the main airfoil at higher Reynolds numbers. For this reason, an accurate calculation procedure not only requires the solution of the conservation equations by either approach, but also requires the prediction of transition, modelling the transitional turbulent flow, which is different than the flow at high Reynolds numbers.

The approach to be described in this paper is based on the solutions of inviscid and boundary-layer equations with the onset of transition computed with the e^n-method based on linear stability theory; this method has been tested extensively for single-element airfoils, as described for example by Cebeci et al.[15,16], and by Cebeci.[17] These studies have shown that the flows around a number of airfoil geometries, with angles of attack up to and beyond that of stall, and including regions of extensive separated flow, can be represented accurately and with low cost for both high and low Reynolds numbers.

The present paper is concerned with the extension of this method to multielement airfoils and wings with and without flap wells. The following section, Section 2, describes the calculation method for two-dimensional flows to obtain the results of Section 4. The calculation method for three-dimensional flows is described in Section 3 with results presented in Section 5. The paper ends with a summary of the main conclusions and a statement of the further steps to be taken toward the provision of a general method for calculating

---

*Professor and Chairman

multielement airfoils and wings at high lift.

2. CALCULATION METHOD: TWO-DIMENSIONAL FLOWS

The calculation method for two-dimensional flows uses the panel method of Hess and Smith[18] and a solution of the boundary-layer equations in which the turbulence model is given by the algebraic eddy viscosity (ε_m) formulation of Cebeci and Smith.[19] With b denoting $1 + \varepsilon_m/\nu$, the continuity and momentum equations can be written as

$$\frac{\partial u}{\partial x} + \frac{\partial v}{\partial y} = 0 \tag{1}$$

$$u \frac{\partial u}{\partial x} + v \frac{\partial u}{\partial y} = u_e \frac{du_e}{dx} + \nu \frac{\partial}{\partial y}\left(b \frac{\partial u}{\partial y}\right) \tag{2}$$

In the absence of mass transfer, the boundary conditions on the airfoil are:

$$u = v = 0, \qquad y = 0 \tag{3a}$$

$$u \to u_e(x), \qquad y \to \infty \tag{3b}$$

and in the wake, where a dividing line at $y = 0$ is required to separate the upper and lower parts of the inviscid flow, and in the absence of the normal pressure gradient, they are:

$$y \to \pm\infty, \quad u \to u_e(x); \quad y = 0, \quad v = 0 \tag{4}$$

2.1 Interaction Law

To perform the calculations for flows with separation, an inverse procedure is used and the external velocity is computed as part of the solution. According to the formulation discussed in Ref. 15, the edge boundary condition is written as

$$u_e(x) = u_e^0(x) + \delta u_e(x) \tag{5a}$$

where $\delta u_e(x)$ is computed from the Hilbert integral

$$\delta u_e(x) = \frac{1}{\pi} \int_{x_a}^{x_b} \frac{d}{d\sigma}(u_e \delta^*) \frac{d\sigma}{x - \sigma} \tag{5b}$$

This inverse boundary-layer formulation is appropriate to airfoils and to those parts of airfoils without surface discontinuities such as flap wells. Where flap wells occur, a different formulation of the inverse procedure is required, and that used here is described below.

The calculation of the flow in the flap-well region is similar to that over a backward-facing step. A large portion of the flow separates immediately after the sudden change of the geometry, and the size of the reversed-flow region depends mainly on the step height, on the gap, and the overhang. The flow reattaches and gradually recovers downstream in the flap-well region or in the wake. The calculation of flows of this kind is difficult, and potential theory is not adequate because of the singularity that occurs at the geometry discontinuity and the strong viscous effects in the separated flowfield. Thus, an initial distribution of displacement thickness is assumed, and the relaxation formula

$$(\delta^*)^{\nu+1} = (\delta^*)^{\nu} \left[1 + \omega \left(\frac{u_{ev}}{u_{ei}} - 1\right)\right] \tag{6}$$

is used in the inverse method to replace the Hilbert integral formulation of the external boundary condition. The new edge boundary conditions are given by Eq. (3b) and Eq. (6), where u_{ev} and u_{ei} correspond to the external velocities computed by the boundary layer and inviscid methods, respectively, and ω is a relaxation parameter. At the end of the flap-well region, the solution procedure reverts to the Hilbert-integral approach.

2.2 Turbulence Model

The turbulence model used to represent the flow on the airfoil is expressed in terms of the Cebeci and Smith eddy-viscosity formulation,

$$\varepsilon_m = \begin{cases} (\varepsilon_m)_i = \{0.4y[1 - \exp(\frac{-y}{A})]\}^2 \left|\frac{\partial u}{\partial y}\right| \gamma_{tr} & 0 \le y \le y_c \quad (7a) \\ (\varepsilon_m)_o = \alpha \left| \int_0^\infty (u_e - u)dy \right| \gamma_{tr}\gamma & y_c \le y \le \delta \quad (7b) \end{cases}$$

where α is a constant assumed to be 0.0168 and

$$A = 26\nu u_\tau^{-1}, \qquad u_\tau = \left(\frac{\tau}{\rho}\right)_{max}^{1/2}, \qquad \gamma = \frac{1}{1 + 5.5(y/\delta)^6} \tag{8a}$$

The condition used to define y_c is the continuity of the eddy viscosity so that Eq. (7a) is applied from the wall outward (inner region) until its value is equal to that given for the outer region by Eq. (7b). The expression γ_{tr} represents the transition region and is given by

$$\gamma_{tr} = 1 - \exp\left[G(x - x_{tr}) \int_{x_{tr}}^{x} \frac{dx}{u_e}\right] \tag{8b}$$

Here x_{tr} is the location of the beginning of transition and G is defined by

$$G = \frac{3}{C^2} \frac{u_e^3}{\nu^2} R_{x_{tr}}^{-1.34} \tag{8c}$$

where C is 60 for attached flows and the transition Reynolds number $R_{x_{tr}} = (u_e x/\nu)_{tr}$.

In the flap-well region, the above formulas are modified so that

$$\varepsilon_m = \varepsilon_m^{(I)} + (\varepsilon_m^{(F)} - \varepsilon_m^{(I)})(1 - e^{-(x-x_o)/\lambda L}) \tag{9}$$

Here $\varepsilon_m^{(I)}$ denotes the eddy viscosity corresponding to the velocity profile above the separated region, and $\varepsilon_m^{(F)}$ includes the total region from the wall. The expressions for $\varepsilon_m^{(I)}$ and $\varepsilon_m^{(F)}$ are given by:

$$\varepsilon_m^{(I)} = \begin{cases} \{0.4(y - y_o)[1 - e^{-(y-y_o)/A}]\}^2 \left|\frac{\partial u}{\partial y}\right| \gamma_{tr} & \begin{array}{l} y > y_o \\ 0 \leq y < y_c \end{array} \\ \alpha\, u_e \left| \int_{y_o}^{\infty} (1 - \frac{u}{u_e}) dy \right| \gamma \gamma_{tr} & \begin{array}{l} y > y_o \\ y_c \leq y \leq \delta \end{array} \\ 0 & y < y_o \end{cases} \qquad (10a)$$

$$\varepsilon_m^{(F)} = \begin{cases} \{0.4y\,[1 - e^{-y/A}]\}^2 \left|\frac{\partial u}{\partial y}\right| \gamma_{tr} & \\ & \text{for } y > 0 \\ \alpha\, u_e \left| \int_0^{\infty} (1 - \frac{u}{u_e}) dy \right| \gamma \gamma_{tr} & \end{cases} \qquad (10b)$$

where y_o is the location of $u = 0$, λ is a relaxation parameter (usually around 10), L is a characteristic length, and x_o is the beginning of the flap-well.

The corresponding expressions in the wake are:

$$\varepsilon_m = (\varepsilon_m)_w + [(\varepsilon_m)_{t.e.} - (\varepsilon_m)_w] \exp\left[\frac{(x - x_o)}{20\delta}\right] \qquad (11)$$

where $(\varepsilon_m)_{t.e.}$ is the eddy viscosity at the trailing edge computed from Eqs. (4.7) and (4.10) and $(\varepsilon_m)_w$ is the eddy viscosity in the far wake given by the larger of

$$(\varepsilon_m)_w^{\ell} = 0.064 \int_{-\infty}^{y_{min}} (u_e - u) dy \qquad (12a)$$

and

$$(\varepsilon_m)_w^{u} = 0.064 \int_{y_{min}}^{\infty} (u_e - u) dy \qquad (12b)$$

with y_{min} denoting the location where the velocity is a minimum.

2.3 Transition Method

For two-dimensional high Reynolds number flows, the onset of transition can conveniently be calculated from the formula given by Michel[20]

$$R_\theta = 1.174\,(1 + \frac{22,400}{R_x})\, R_x^{0.46} \qquad (13)$$

where $R_\theta = u_e\theta/\nu$ and $R_x = u_e x/\nu$. For low Reynolds number flows, Eq. (13) is not appropriate and it is necessary to use the e^n-method. This method, first suggested by Smith and Gamberoni[21] and Van Ingen[22], is based on the linear stability theory and can also be used for high Reynolds number flows as well as three-dimensional flows, as we shall discuss later in the paper. According to this method, for two-dimensional flows the solutions of the Orr-Sommerfeld equation,

$$\phi^{iv} - 2\alpha^2\phi'' + \alpha^4\phi - iR(\alpha\bar{u} - \omega)(\phi'' - \alpha^2\phi) + iR\alpha\bar{u}''\phi = 0 \qquad (14)$$

are obtained for given velocity profiles $\bar{u}$ and $\bar{u}''$ and for a set of specified dimensional frequencies ω^*. Amplification rates α_i are then computed as a function of x, and for each frequency the value of n is obtained from the integral

$$n = -\int_{x_o}^{x} \alpha_i dx \qquad (15)$$

Transition is obtained from the resulting curves corresponding to the maximum amplification factor by assuming a value of n, commonly taken to be between 8 and 10.

2.4 *Solution Procedure*

A brief description of the solution procedure used in this method is as follows. The panel method provides an external velocity distribution based on a body shape in which the flap-well region is assumed to be absent and identifies the stagnation point. The interactive boundary-layer approach leads to solutions on the upper surface from the stagnation point through the regions of laminar, transitional and turbulent flow to the trailing edge. Similarly, it provides results for the lower surface up to the beginning of the flap-well. A displacement thickness distribution, $\delta^*(x)$, is assumed in the flap well and, with the continuation method described in Ref. 24 and with the initial velocity profile similar to that of a backward-facing step, calculations proceed to the trailing edge. With the upper and lower surface velocity profiles computed at the trailing edge, the calculations are *extended into the wake. As a consequence of the above, a blowing velocity is available on the airfoil and in the wake. In the flap-well region, the blowing velocity* v_n *is defined by*

$$v_n = \frac{d}{dx}(u_e\delta_m^*) \qquad (16)$$

where $\delta_m^* = \delta^* - \delta_t$. Here δ_t corresponds to the body shape assumed to exist over the flap-well. Elsewhere, the blowing velocity is given by

$$v_n = \frac{d}{dx}(u_e\delta^*) \qquad (17)$$

With the blowing velocity distribution known, a new distribution of external velocity $u_{ei}(x)$ is obtained from the panel method. As before, the boundary-layer solutions on the upper and lower surfaces of the airfoil are obtained with the Hilbert integral. In the flap-well, with u_{ev} *known from the previous flap-well calculation, a new* δ^*-distribution is available from Eq. (6), which is used to obtain solutions up to the trailing edge. This sequence of calculations is repeated for the whole flowfield until convergence is achieved. Additional details are provided in Ref. 23.

3. CALCULATION METHOD: THREE-DIMENSIONAL WINGS

The extension of the method of the previous section to three-dimensional flows has the ingredients shown in Fig. 1. The purpose of the interface program placed between the inviscid and three-dimensional inverse boundary-layer methods is to process the geometry and inviscid velocity data for

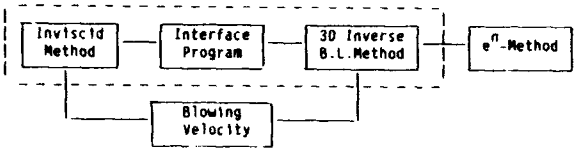

Fig. 1. The interactive boundary-layer method.

input to the boundary-layer program. The basic input to this program is the definition of the wing configuration which is used by a geometry subroutine to construct a nonorthogonal coordinate system and compute the associated geometrical parameters, which consist of geodesic curvatures and metric coefficients needed in the boundary-layer calculations. Some of the generated data are used later in a velocity subroutine to determine the inviscid velocity components at the boundary-layer grid points and to transform the inviscid velocity components on the surface, calculated in a Cartesian coordinate system, into the boundary-layer coordinate system. This operation consists of dot products of velocity vectors as well as chordwise and spanwise interpolation. Further velocity and geometry data processing is done in a subroutine which separates the generated information into upper and lower surfaces of the wing for boundary-layer calculations.

3.1 *Inviscid Method*

The inviscid flow is computed by the Hess surface-source panel method, which is applicable to a complete airplane configuration. In this method a general body is represented by means of a set of quadrilateral panels as shown in Fig. 2. A three-dimensional configuration in general consists of lifting sections, such as a wing or pylon, for which there is a well-defined trailing edge and nonlifting sections such as fuselage. Under the Hess formulation, all panels are assigned an independent source distribution, while those on a lifting section are assumed to carry a bound vorticity distribution. The variation of this bound vorticity in the streamwise direction is assumed, while its variation in the spanwise direction is adjusted to satisfy the Kutta condition at the trailing edge. The complete solution for a prescribed flow condition is, therefore, obtained by simultaneously satisfying a condition of zero normal velocity at a control point on each panel of the body together with a Kutta condition at each trailing-edge panel.

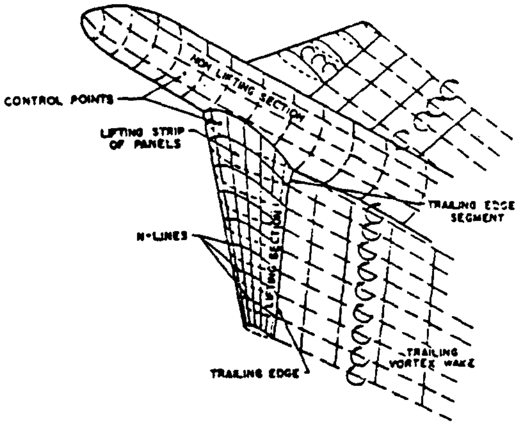

Fig. 2. Wing/body configuration.

The nature of the Kutta condition adopted by the many panel methods that are currently available varies greatly. While the condition adopted by Hess assumed equal upper and lower surface pressures at the trailing edge, other methods make use of other derived conditions which do not guarantee a pressure match at the trailing edge. Since we are also interested in the computation of inviscid flows with viscous effects, and since the behavior of the boundary-layer at the trailing edge can have a significant effect on the overall solution, the approach adopted here is more realistic and blends in well with the previous studies on two-dimensional flows employing interaction procedures.

3.2 Inverse Boundary-Layer Method

Viscous flow calculations are performed by solving the three-dimensional boundary-layer equations in the inverse form. These equations for a nonorthogonal coordinate system with the eddy-viscosity concept are[25]

$$\frac{\partial}{\partial x}(uh_2 \sin\theta) + \frac{\partial}{\partial z}(wh_1 \sin\theta) + \frac{\partial}{\partial y}(vh_1h_2 \sin\theta) = 0 \qquad (18)$$

$$\frac{u}{h_1}\frac{\partial u}{\partial x} + \frac{w}{h_2}\frac{\partial u}{\partial z} + v\frac{\partial u}{\partial y} - K_1u^2\cot\theta + K_2w^2\operatorname{cosec}\theta + K_{12}uw$$
$$= -\frac{\operatorname{cosec}^2\theta}{\rho h_1}\frac{\partial p}{\partial x} + \frac{\cot\theta\operatorname{cosec}\theta}{\rho h_2}\frac{\partial p}{\partial z} + \nu\frac{\partial}{\partial y}\left(b\frac{\partial u}{\partial y}\right) \qquad (19)$$

$$\frac{u}{h_1}\frac{\partial w}{\partial x} + \frac{w}{h_2}\frac{\partial w}{\partial z} + v\frac{\partial w}{\partial y} - K_2w^2\cot\theta + K_1u^2\operatorname{cosec}\theta + K_{21}uw$$
$$= \frac{\cot\theta\operatorname{cosec}\theta}{\rho h_1}\frac{\partial p}{\partial x} - \frac{\operatorname{cosec}^2\theta}{\rho h_2}\frac{\partial p}{\partial z} + \nu\frac{\partial}{\partial y}\left(b\frac{\partial w}{\partial y}\right) \qquad (20)$$

where x denotes the axial direction, z the spanwise direction, and y is normal to the surface. Here h denotes the metric coefficients, K the curvature parameters, and θ the angle between the coordinate lines x = const. and z = const.

The above equations, together with those for the plane of symmetry and along the chordwise direction, are solved by Keller's two-point finite-difference method (box scheme) subject to the following boundary conditions

$$y = 0, \quad u = 0, \quad v = 0, \quad w = 0 \qquad (21a)$$

$$y = \delta, \quad u = u_e(x,z), \quad w = w_e(x,z) \qquad (21b)$$

To account for flow separation, as in two-dimensional flows, a form of the interaction law of Veldman[26] is used by modifying the two-dimensional interaction formula given by Eq. (5) to account for the interaction in the x- and z-directions in three steps. In step one, an initial displacement surface is generated by solving a quasi-three-dimensional form of Eqs. (18) to (20) with all derivatives with respect to z neglected, that is,

$$\frac{\partial}{\partial x}(uh_2 \sin\theta) + \frac{\partial}{\partial y}(vh_1h_2 \sin\theta) = 0 \quad (22)$$

$$\frac{u}{h_1}\frac{\partial u}{\partial x} + v\frac{\partial u}{\partial y} - K_1u^2\cot\theta + K_2w^2\operatorname{cosec}\theta + K_1uw = -\frac{\operatorname{cosec}^2\theta}{\rho h_1}\frac{\partial p}{\partial x} + \nu\frac{\partial}{\partial y}\left(b\frac{\partial u}{\partial y}\right) \quad (23)$$

$$\frac{u}{h_1}\frac{\partial w}{\partial x} + v\frac{\partial w}{\partial y} - K_2w^2\cot\theta + K_1u^2\operatorname{cosec}\theta + K_{21}wu = \frac{\cot\theta\operatorname{cosec}\theta}{\rho h_1}\frac{\partial p}{\partial x} + \nu\frac{\partial}{\partial y}\left(b\frac{\partial w}{\partial y}\right) \quad (24)$$

with the external velocity distribution $u_e^0(x)$ obtained from the panel method. The second step involves interaction between the inviscid flow equations and the quasi-three-dimensional flow equations. As in two-dimensional flows, the solutions of the boundary-layer equations are used to compute distributions of blowing velocity on the surface and these allow the inviscid flow solutions to be updated. In step three, after the calculation of the initial conditions in the (y,z) and (x,y) planes, the fully three-dimensional boundary-layer equations are solved with the external velocity components resulting from step two. As before, the spanwise velocity component is assumed to correspond to its inviscid value. The viscous flow solutions are obtained by marching in the spanwise direction at each advancing chordwise location. This represents the first phase in an interactive loop which involves the fully three-dimensional boundary-layer equations. In the subsequent phases, as before, the blowing velocity distribution is used to obtain improved inviscid flow solutions so that the fully three-dimensional boundary-layer equations can be solved in accordance with the iteration scheme shown in Fig. 1.

3.3 Transition Method

We again use the e^n-method and solve the Orr-Sommerfeld equation, which for three-dimensional flows is given by

$$\phi^{iv} - 2(\alpha^2 + \beta^2)\phi + (\alpha^2 + \beta^2)^2\phi - iR(\alpha\bar{u} + \beta\bar{w} - \omega)[\phi'' - (\alpha^2 + \beta^2)\phi] + iR(\alpha\bar{u}'' + \beta\bar{w}'')\phi = 0 \quad (25)$$

Here α and β denote the dimensionless wave numbers in the x- and z-directions and ω the radian frequency. Our eigenvalue procedure differs from those used by Malik[27] and Mack[28]. It is based on the saddle-point method of Cebeci and Stewartson[29], which, unlike the approaches of Malik and Mack, does not assume a relationship between the two wave numbers α and β but computes it from the requirement that $\partial\alpha/\partial\beta$ is real. According to this requirement, the wave orientation and growth direction of the disturbance are given by

$$\left(\frac{\partial\alpha}{\partial\beta}\right)_{\omega,R} = -\tan\gamma = -\frac{z}{x} \quad (26)$$

where γ is the angle the wave makes with the x-axis. With α and β connected through Eq. (26), and with the disturbance propagating along the way given by the two terms on the right-hand side of Eq. (26), the disturbances are damped if the amplification rate defined by

$$\Gamma = \alpha_i - \beta_i\left(\frac{\partial\alpha}{\partial\beta}\right)_{\omega,R} \quad (27)$$

is > 0, neutral if $\Gamma = 0$ and amplified when $\Gamma < 0$. Once α and β are computed with the constraints of Eq. (26), the amplification rate Γ is obtained from Eq. (27); additional calculations are then made for different values of $\partial\alpha/\partial\beta$ so that new values of α and β are calculated to determine the maximum value of Γ.

This method has been evaluated in terms of measurements reported for the flow around a swept wing equipped with a cambered leading edge and attached to a half fuselage and for the flow around a prolate spheroid at 10 degree incidence.[30] It has been shown that it is convenient to use, particularly because of the neutral stability curves (zarfs) which facilitate the calculation and avoid uncertainties associated with the choice of magnitude and location of the critical frequencies. In general, the calculated values of the onset of transition are in very good agreement with measured values.[30]

3.4 Solution Procedure

While the calculation of the onset of transition is important for airfoils, it is of utmost importance for three-dimensional flows. Unlike the two-dimensional flows where transition occurs in the region of flow deceleration, in three-dimensional flows it often occurs in the region where the flow accelerates. The sweep angle and Reynolds number strongly influence the location of transition and requires that its calculation becomes a part of the computational strategy.

In the present method, the stability/transition calculations are first performed for three-dimensional laminar boundary layers obtained for a prescribed pressure distribution, so that the inviscid and viscous flow equations can then be solved according to the interaction scheme shown in Fig. 1. The quasi-three-dimensional forms of the equations are solved chordwise in the inverse mode to obtain the interaction coefficients needed in the solution of the full three-dimensional boundary-layer equations. Several sweeps on the wing and in the wake are performed and new inviscid flow solutions with viscous effects are obtained. This procedure is repeated until the convergence of the solutions; the transition calculations are then repeated to obtain new transition locations on the wing for the next phase of the interactive boundary-layer calculations. The whole process is repeated until the flowfield and transition locations converge.

4. RESULTS AND DISCUSSION: TWO-DIMENSIONAL FLOWS

We now use the interactive boundary-layer procedure of Section 2 to calculate the performance characteristics of single airfoils without (Section 4.1) and with (Section 4.2) flap wells, two-element airfoils (Section 4.3), and three-element airfoils corresponding to slat, airfoil, and flap combinations (Section 4.4). For single airfoils, we also consider flows at low Reynolds numbers since these flows become important on the components of high-lift systems at wind tunnel Reynolds numbers.

4.1 Single Airfoil Without Flap Well

In calculating airfoil flows at high Reynolds numbers with the interactive method of Section 2, the onset of transition is obtained from Eq. (13) with the transition region represented by the γ_{tr}-term in Eq. (8b), except where the boundary layer separates upstream of this location, in which case transition is assumed at the separation location. Studies indicate that, while the turbulence model of Section 2.2 is adequate for almost all airfoil flows at low and moderate angles of attack, it is necessary to make improvements to this model at high angles of attack corresponding to near stall and post-stall conditions. One approach discussed and developed by Johnson and King[31] and Johnson and Coakley[32] is to adopt a nonequilibrium eddy-viscosity formulation ϵ_m in which the CS model serves as an equilibrium eddy viscosity $(\epsilon_m)_{eq}$ distribution. An ordinary differential equation (ODE), derived from the turbulence kinetic energy equation, is used to describe the streamwise development of the maximum Reynolds shear stress $-(\rho \overline{u'v'}_m)$, or $-\overline{u'v'}_m$ for short, in conjunction with an assumed eddy-viscosity distribution which has $\sqrt{-\overline{u'v'}_m}$ as its velocity scale. In the outer part of the boundary layer, the eddy viscosity is treated as a free parameter that is adjusted to satisfy the ODE for the maximum Reynolds shear stress. In essence, this model treats the parameter α in Eq. (7b) as a variable and determines it as described above.

Another approach to improve the predictions of the CS model in flows with adverse pressure gradient and separation[33], is to relate the parameter α to a parameter F by

$$\alpha = \frac{0.0168}{F^{2.5}} \tag{27a}$$

Here F denotes the ratio of the product of the turbulence energy by normal stresses to that by shear stress evaluated at the location where shear stress is maximum, that is

$$F = \left[\frac{(\overline{u'^2} - \overline{v'^2})\partial u/\partial x}{-\overline{u'v'}\ \partial u/\partial y}\right]_{(-\overline{u'v'})_{max}} \tag{27b}$$

Before Eq. (27a) can be used in Eq. (7b), an additional relationship between $(\overline{u'^2} - \overline{v'^2})$ and $(-\overline{u'v'})$ at $(-\overline{u'v'})_{max}$ is needed. This is done by assuming that the ratio in Eq. (27b)

$$\beta = \left[\frac{\overline{u'^2} - \overline{v'^2}}{-\overline{u'v'}}\right]_{(-\overline{u'v'})_{max}} \tag{27c}$$

is a function of $R_T = \tau_w/(-\overline{u'v'})_{max}$ which, according to the data of Nakayama[34] is represented by

$$\beta = \frac{6}{1 + 2R_T(2 - R_T)} \tag{27d}$$

for $R_T < 1.0$. For $R_T \geq 1.0$, β is taken as

$$\beta = \frac{2R_T}{1 + R_T} \tag{27e}$$

Introducing the above relationships into the definition of F and using Eq. (27a), the following expression for α is obtained

$$\alpha = \frac{0.0168}{[1 - \beta(\partial u/\partial x)/(\partial u/\partial y)]^{2.5}} \tag{28}$$

where β is given by Eqs. (27d) and (27e).

Figure 3 shows a comparison between calculated and measured lift coefficients for the NACA 0012 airfoil at two chord Reynolds numbers. As can be seen, in accord with the measurements[35], the calculation method is able to compute c_ℓ for all angles of attack and satisfactorily account for the effects of Reynolds number. Figure 4 shows similar comparisons for the NACA 23012 airfoil at two chord Reynolds numbers, indicating again good agreement with measurements. Additional comparisons and discussion are provided in Ref. 33.

The calculation of airfoils at low Reynolds numbers requires changes to the turbulence model of Section 2.2 and to the procedure used to obtain the onset of transition location. According to the γ_{tr} model used

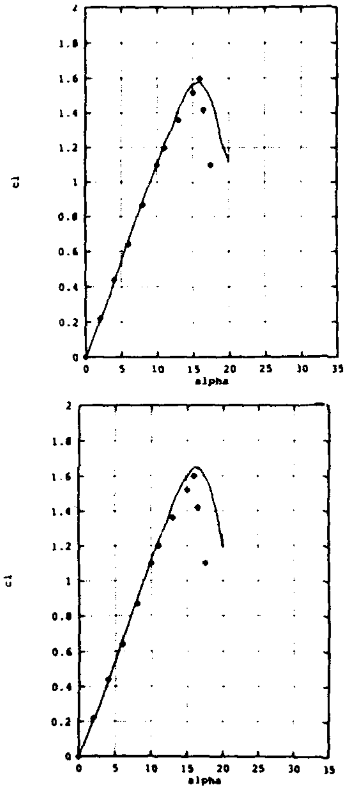

(a)

(b)

Fig. 3. Effect of Reynolds number on the lift coefficient of the NACA 0012 airfoil: (a) $R_c = 6 \times 10^6$, and (b) $R_c = 8.8 \times 10^6$.

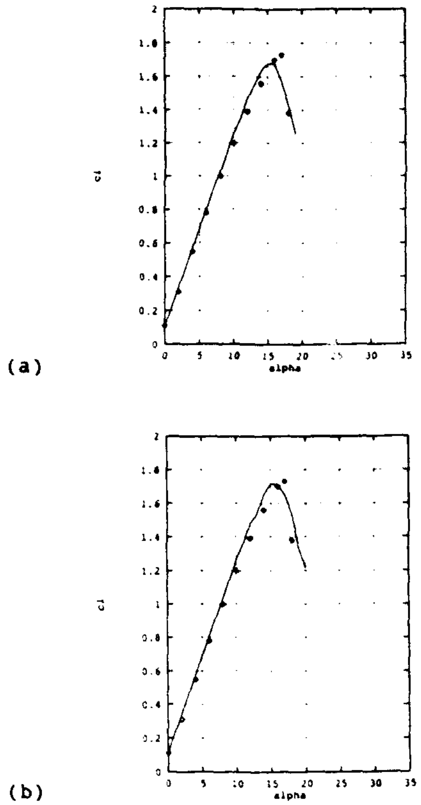

Fig. 4. Effect of Reynolds number on the lift coefficient of the NACA 23012 airfoil: (a) $R_c = 3 \times 10^6$, and (b) $R_c = 8.8 \times 10^6$.

in the CS model and given by Eqs. (8b) and (8c), the extent of the transition region $R_{\Delta x}$ is related to the transition Reynolds number $R_{x_{tr}}$ by

$$R_{\Delta x} = CR_{x_{tr}}^{2/3} \tag{29}$$

which shows that $R_{\Delta x}$ increases with decreasing $R_{x_{tr}}$. This expression was obtained from data based on attached flows and is not applicable to flows with separation. Experiments show that the extent of a separation bubble and the location of transition depend upon the Reynolds number. At high Reynolds numbers, transition usually corresponds to the location of separation and the length of the bubble is relatively short. At low Reynolds numbers, transition can occur inside the bubble and can strongly influence the nature of flow. To take account of the corresponding effects, a correlation formula was devised by Cebeci[17] to represent C in Eq. (8c) in terms of $R_{x_{tr}}$, and based on experimental data which show separation-induced transition at low Reynolds numbers. This correlation formula is shown in Fig. 5 together with the experimental data obtained for several airfoils. The data, which encompasses a typical low Reynolds number range from $R_c = 2.4 \times 10^5$ to $R_c = 2 \times 10^6$, falls conveniently on a straight line on a semi-log scale and can be represented by the equation

$$C^2 = 213 \, [\log R_{x_{tr}} - 4.7323] \tag{30}$$

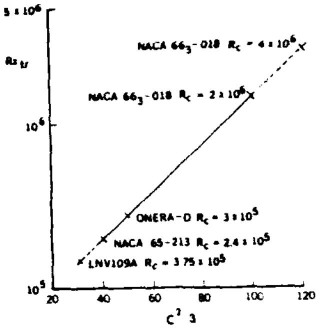

Fig. 5. Variation of $C^2/3$ with transition Reynolds number $R_{x_{tr}}$.

Care should be taken in the use of this equation outside the range of experiments, particularly at high Reynolds numbers where the separation bubble is likely to be small and a limiting value of C = 60 applies.

The application of Eq. (30) requires the location of the onset of transition and this is obtained with the e^n-method discussed in Section 2.3. The manner in which it is obtained is described in Ref. 17.

In the studies reported in Ref. 17, the accuracy of the interactive method was evaluated for a number of airfoils and overall good agreement with experiment was observed. We now consider the Eppler airfoil and present a sample of results for a chord Reynolds number of 300,000 for a wide range of angles of attack and compare the predictions with the experimental data of McGhee et al.[35] obtained in the Langley Low-Turbulence Pressure Tunnel (LTPT). The tests were conducted over a Mach number range from 0.03 to 0.13 and a chord Reynolds number range from 60 x 10^3 to 460 x 10^3. Lift and pitching-moment data were obtained from airfoil surface pressure measurements and drag data from wake surveys. Oil flow visualization was used to determine laminar-separation and turbulent-reattachment locations.

Figure 6a shows a comparison between the calculated and measured distributions of pressure coefficients for angles of attack of 0 and 8 deg. The calculated lift and drag coefficients shown in Fig. 6b indicate remarkably good agreement with experiment for all angles of attack up to stall. There the computed lift coefficients begin to deviate from data, indicating higher values than those measured; the discrepancy increases with an increase in Reynolds number, and the solutions do not follow the poststall behavior. We believe the reason for this discrepancy lies in the turbulence model. Whereas the results presented in Figures 3 and 4 made use of the CS model with the parameter α computed from Eq. (28), those in Fig. 6 were made with $\alpha = 0.0168$.

The calculated values of the chordwise location of laminar separation (LS), turbulent reattachment (TR), and the onset of transition are given in Table 1 for several angles of attack. The experimental results of this table are subject to some uncertainty because of difficulties associated

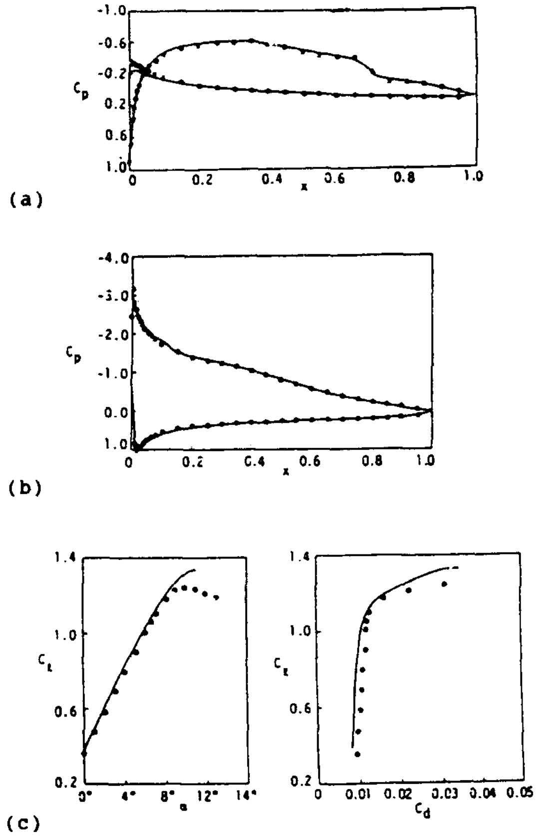

Fig. 6. Comparison of calculated (solid lines) and measured (symbols) pressure-coefficient distributions at: (a) α = 0 deg, (b) α = 8 deg, and (c) lift and drag coefficients for $R_c = 3 \times 10^5$.

Table 1. Experimental and calculated laminar separation (LS), and turbulent reattachment (TR), and transition locations on the upper surface of the Eppler airfoil.

α	Experiment		$(\frac{x}{c})$	Calculated	
deg	LS	TR	tr	LS	TR
0	0.48	0.69	0.63	0.51	0.72
2	0.45	0.62	0.58	0.46	0.67
4	0.40	0.58	0.52	0.43	0.60
5	0.39	0.55	0.49	0.415	0.57
6	0.38	0.50	0.43	0.42	0.50
6.5	0.38	0.44	0.40	0.41	0.46

with the surface visualization technique. With this proviso, comparison between measured and calculated values must be considered outstanding. It should be noted that when there is a separation bubble, the transition location obtained from the e^n method occurs within the bubble in all cases and in accord with experimental observation, leads to reattachment some distance downstream.

4.3 Single Airfoil with Flap Well

Figure 7 shows the geometry of the LB 572 single airfoil with flap well tested in the low-speed wind tunnel of the California State University, Long Beach (CSULB). The pressure distributions of Fig. 8 allow comparison between calculation and the experimental data for the Reynolds number of 0.5×10^6 and transition locations at

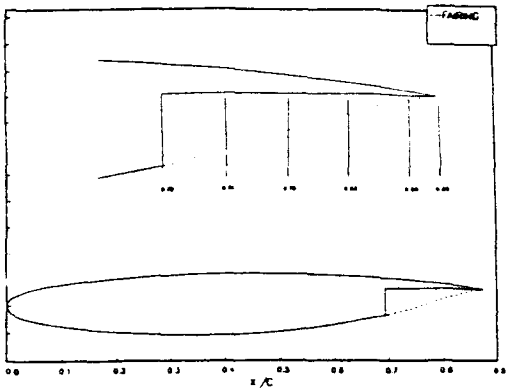

Fig. 7. LB 572 single airfoil with flap-well cut.

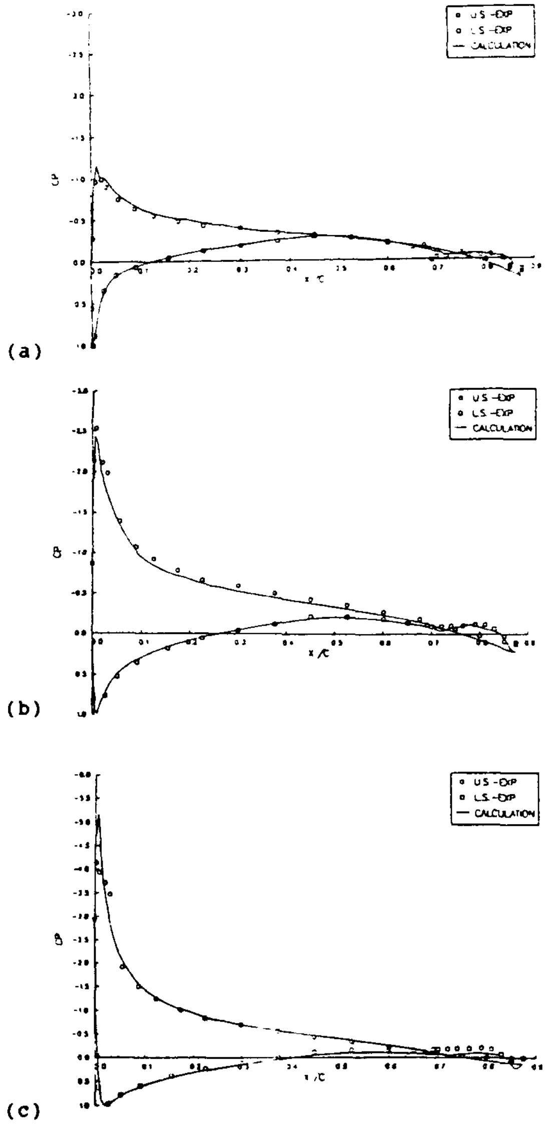

Fig. 8. LB 572 airfoil pressure distribution for $R_c = 0.5 \times 10^6$ at (a) α = 5.0, (b) α = 8.0, (c) α = 12.0.

25% of the chord on both surfaces. In general, the results are in good agreement for angles of attack up to 12°. The upper surface peak, registered by the calculations close to the leading edge, is in part due to the better spatial resolution of the calculation method. Close to the trailing edge, there is some disagreement between the upper surface pressure distributions that may stem from approximations made about the flap well region and the way the Kutta condition was specified in the panel method. However, the pressure coefficient curves well represent the flow behavior in the flap-well region: the constant pressure values indicate a recirculation area followed by a rapid increase of pressure close to the trailing edge which signifies reattachment of the separated flow.

Velocity profiles corresponding to angle of attack of 5° and the location of the displacement thickness are presented in Fig. 9 together with the recirculation streamlines in the flap well region. Figure 9a compares the velocity profiles of the present calculation with experimental data of Alemdaroglu[2] at six locations in the flap-well cut. The initial profiles at the step are in good agreement, but comparison of the downstream profiles shows that computation predicts a less retarded flow than is indicated by measurement. The possible explanation is that the eddy-viscosity formulation used models for a stronger mixing than is appropriate for the separated flow after a step. Further downstream, close to the trailing edge, the computed profiles have larger negative velocities near the wall than measured profiles, which may mean that a too weak mixing model was applied to the reattaching flow. Figure 10 shows that the skin-friction distribution vanishes in the plane of the step and becomes negative, corresponding to the reverse flow up to x/c of around 0.87. The location of reattachment in the flap well region was observed to move upstream from the trailing edge with increasing angle of attack.

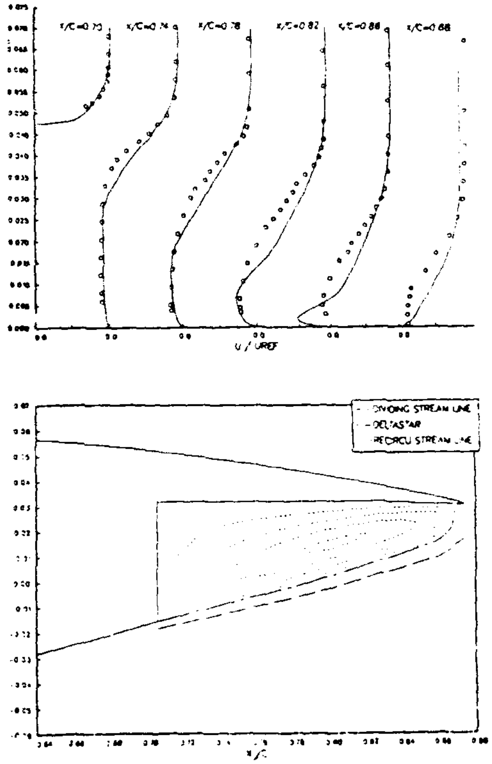

Fig. 9. LB 572 airfoil for $R_c = 0.5 \times 10^6$ at $\alpha = 5.0$. (a) Velocity profiles in the flap-well region, (b) Recirculation streamlines and the location of the displacement thickness.

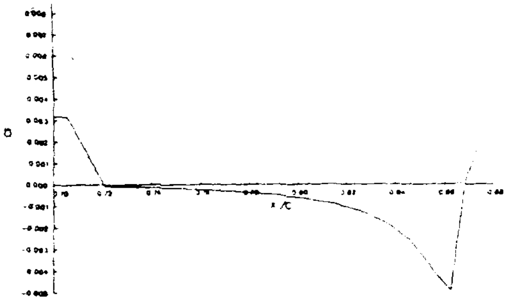

Fig. 10. Calculated local skin-friction coefficient in the flap-well region for $\alpha = 5°$.

4.3 Two-Element Airfoils

In a previous study, a similar interactive approach was used to compute the performance characteristics of three two-element airfoils.[36] The inviscid flow solutions were obtained by the conformal-mapping method of Halsey[37], rather than the panel method used here, and the viscous-flow calculations were performed without accounting for the wake effects, either behind the main airfoil or the flap. The calculation method provided results which agreed with experimental information within the accuracy of the measurements up to an angle of attack that was sufficiently small so that there was either no separation or very small separation on the airfoil, and the gaps between the elements were comparatively large. In this way, the difficulties in computing the wake of each airfoil and accounting for the merging of the shear layers between the airfoil and the flap, and extending the range of the computational method to higher angles of attack, were postponed to a later time.

In the studies reported here, we first performed calculations with the present method, which did not include the wake effect and compared the results with those obtained with the earlier code[36] with its different inviscid flow method. After ensuring that the results of both codes were essentially the same, the wake effects were introduced into the present method and calculations were repeated for the three two-element airfoils to investigate the role of the wake effect on the solutions.

The first two-element airfoil corresponded to that investigated by Van den Berg[5] and discussed in subsequent papers by Van den Berg and Oskam[6] and Oskam, et al.[7] It comprised a supercritical main airfoil (NLR 730) with a flap of 32% of the main chord at a deflection angle of 20 degrees, close to the highest value that could be used without onset of flow separation. This configuration was studied at a Reynolds number of 2.51 x 10^6 for a range of angles of attack up to 13.1° with consideration of the wake of the main element only.

Figure 11 allows a comparison between the calculated and experimental results of the NLR 7301 airfoil. Figures 11a and b show the surface pressure distributions at $\alpha = 6°$ and 13.1°, respectively, and Fig. 11c shows the effect of wake on the computed lift coefficients. The calculated and experimental values of local skin-friction coefficient c_f and dimensionless momentum thickness θ/c for the two angles of attack, Figures 11d and 11e, show that the boundary layer on the upper surface is approaching separation but has not reached it. Consistent with the studies on single airfoils, the wake effect is relatively small due to the absence of flow separation but has improved the agreement with experiment.

The second case involves a NASA supercritical airfoil, 24 in. in length, with a 7 in. flap at a deflection angle of 20 degrees. The experiments were carried out in the 36 x 96 in. wind tunnel of the Boeing Research Laboratories at a Mach number of 0.2 and have been documented by Omar et al.[8,9] Figures 12a and 12b show the surface-pressure distributions for angles of attack of 0° and 8.93°, respectively. As can be seen, the inclusion of the wake in the calculations makes a slight improvement on the main airfoil but not on the flap where the results obtained without the wake effect are better. The results in Fig. 12c show that the calculated lift coefficients with the wake are in better agreement with data than those without the wake effect.

4.4 Three-Element Airfoils

With the positive results of Figs. 8 to 12 for an airfoil with a flap-well and for two two-element airfoils, it is appropriate to consider the application of the interactive boundary-layer method to a three-element airfoil with a flap well. The chosen configuration is shown on Fig. 13 and corresponds to the high-lift model tested in the NASA Langley wind tunnel at a Reynolds number of 5 x 10^6. The slat deflection angle was -30 degrees and the flap deflection angles 15 and 30 degrees with angles of attack of 4 to 20 degrees. The measurements were made by a combination of hot-wire and laser-velocimetry techniques, the latter was primarily used in regions of separated flow.

Calculations were initially made on smooth bodies without explicitly considering the flow in the flap-well region. Also, because the potential flow theory predicts flow singularities at the discontinuity of the airfoil geometry, the sharp corner of the slat and the flap-well cut out of the main airfoil were smoothed to prevent solutions from breaking. Figure 13 shows the modified geometry of this airfoil with the flap-well fairing and the rounded slat used in calculations. The so-called "experimental fairing" refers to the

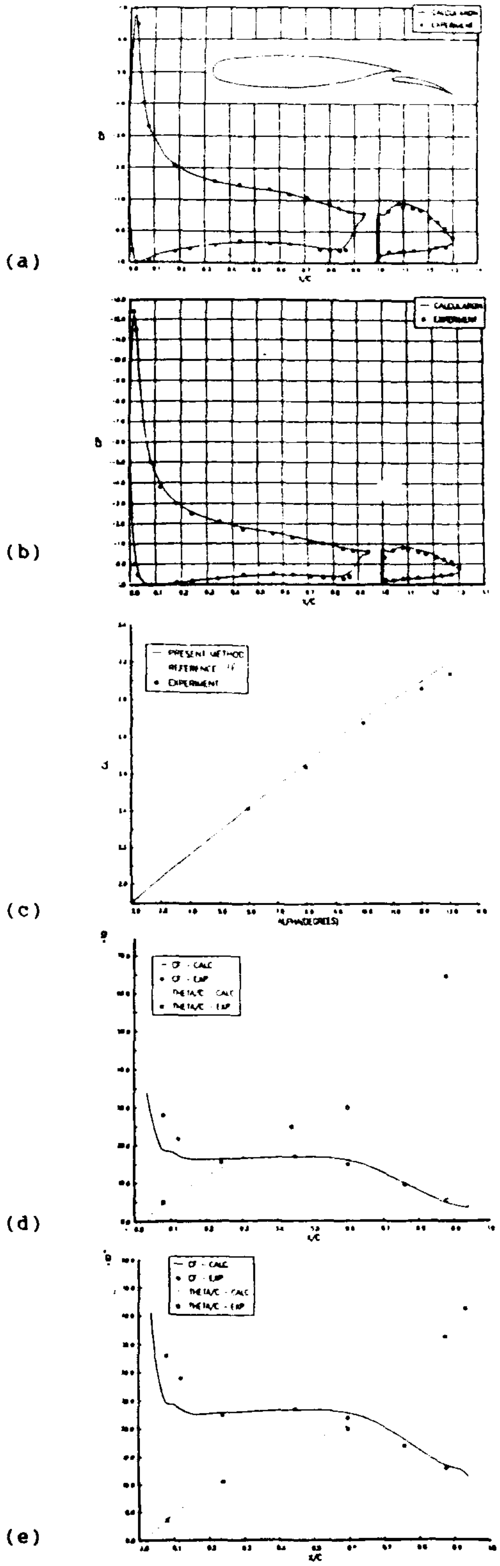

Fig. 11. NLR 7301 wing with flap. Calculated and measured: (a) Pressure distribution at $\alpha = 6°$, (b) Pressure distribution at $\alpha = 13.1°$, (c) Lift coefficients, (d) Local skin-friction coefficients, c_f, and momentum thicknesses, θ/c, on the upper wing surfaces at $\alpha = 6°$, (e) Local skin-friction coefficients, c_f, and momentum thicknesses, θ/c, on the upper wing surfaces at $\alpha = 13.1°$.

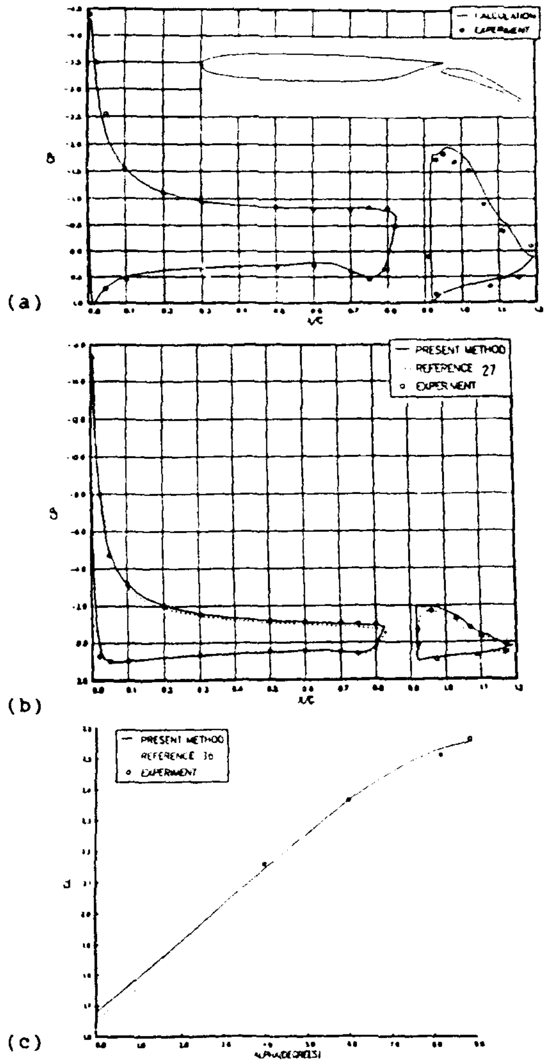

Fig. 12. NASA supercritical two-element airfoil. Calculated and measures, (a) pressure distributions at $\alpha = 0°$, (b) at $\alpha = 8.93°$, (c) lift coefficients.

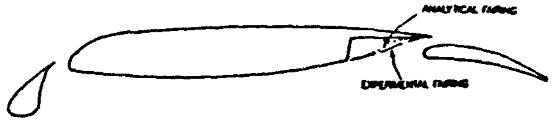

Fig. 13. The three-element airfoil with analytical and experimental fairing. $\delta_s = -30°$, $\delta_f = 15°$.

dividing streamline, which was determined from measurements, while the "analytical fairing" was drawn arbitrarily. Reference 23 presents a comparison between the measured and calculated surface pressure distributions on the slat, main airfoil, and flap at three angles of attack (4°, 12° and 16°) for the configuration with the experimental fairing, and the corresponding distributions at the same angles of attack for the configuration with analytical fairing. Overall, the calculated results agree well with experimental data.

Finally, the method of Section 4.2 was applied to include the calculation inside the flap-well. The results, shown in Fig. 14, agree well with measurements for all the cases indicated above and including angles of attack up to 20°. This confirms that it is unnecessary to make a priori assumptions about the fairing shape, and allows for further detailed investigations of the recirculation flow in the flap-well, such as the gap and overhang effects. Figure 15 shows the variation of lift coefficient with angle of attack, confirming that the present calculation method leads to values which are in close agreement with experiment.

Comparison of pressure coefficients for a flap deflection angle of 30°, Fig. 16, allows similar conclusions to be drawn to those of the previous paragraph. Also, the calculated lift coefficients shown in Fig. 17 are very close to measurements.

5. RESULTS AND DISCUSSION: THREE-DIMENSIONAL FLOWS

The calculation method described in Section 3 for three-dimensional high-lift configurations is in the evaluation stage. So far the studies are limited to wing and wing-flap geometries. The experimental data being used to evaluate the method is due to Lovell[38] who has reported lift, drag and pitching moment coefficients over an extensive range of configurations of the high-lift system on a wing of basic aspect ratio 8.35 and with a trailing-edge planform extension and a body added. In Section 5.1 we first present the results for the wing alone and in the subsequent section we present results for a wing/flap configuration.

5.1 Wing Alone

The wing tested in Ref. 38 has an airfoil section having a considerable rear loading with the maximum thickness of 10.7% occurring at 37.5% chord and the maximum camber occurring at 75% chord. It has no twist nor dihedral, has a quarter-chord sweep angle of 28° and taper ratio of 1/4. The experiments were conducted at a test Reynolds number of 1.35×10^6.

Figure 18 shows a comparison between the calculated and measured lift coefficients. As can be seen, there is some viscous effect even at very small angles of attack which becomes much more pronounced at higher angles of attack. The interactive boundary-layer method solutions, obtained either by using the strip theory approximation or by the full three-dimensional approach, improve the solutions considerably. In the former case, the calculated results agree reasonably well with data at low and moderate angles of attack, but with increasing incidence angle they begin to deviate from the measured values of lift coefficient. In the latter case, the three-dimensional flow solutions with the blowing velocity v_n obtained from

$$v_n = \frac{1}{h_1 h_2 \sin\theta} \left[\frac{\partial}{\partial x} (h_2 \sin\theta \delta_x^*) + \frac{\partial}{\partial z} (h_1 \mathrm{sub}\theta \delta_z^*)\right] \qquad (31)$$

and the displacement surface Δ

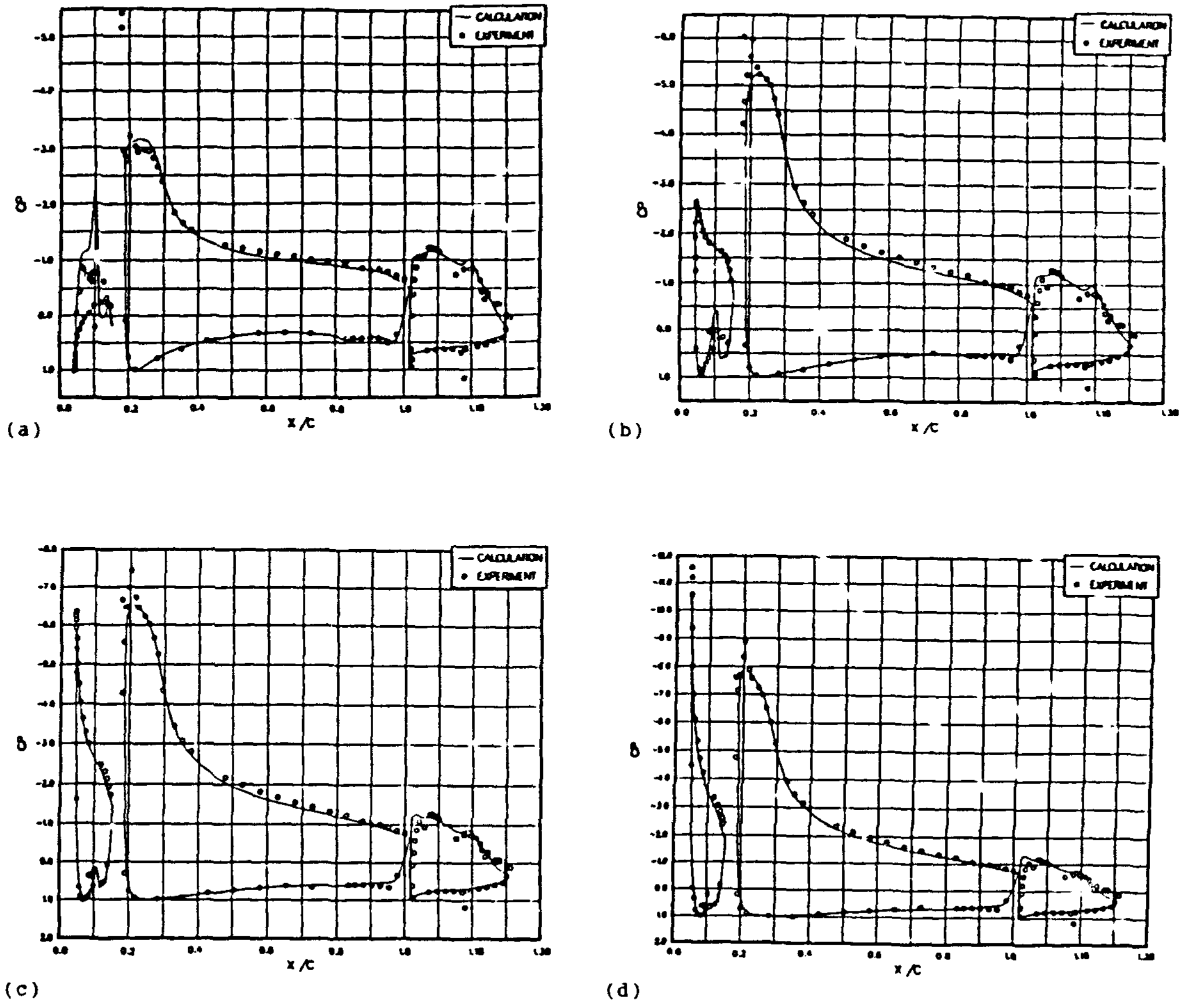

(a) (b) (c) (d)

Fig. 14. Calculated and measured pressure distributions on the three-element airfoil for δ_f = 15° and R_c = 5 x 10^6 at (a) α = 4°, (b) α = 12°, (c) α = 16°, (d) α = 20°.

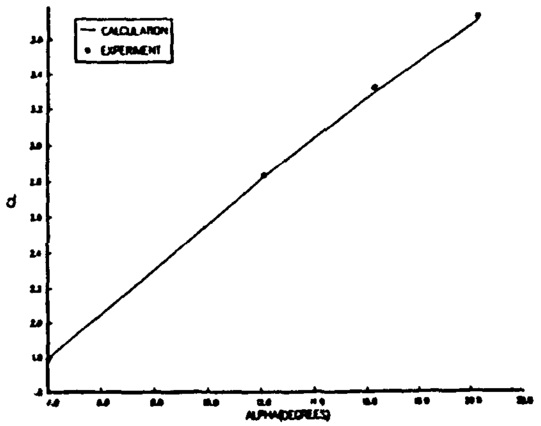

Fig. 15. Variation of the lift coefficient with angle of attack for the three-element airfoil with δ_f = 15° and R_c = 5 x 10^6.

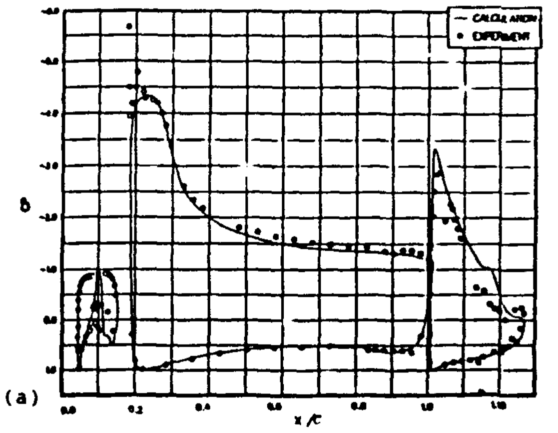

(a)

Fig. 16. Calculated and measured pressure distributions on the three-element airfoil with δ_f = 30° and R_c = 5 x 10^6, (a) α = 5°, (b) α = 15°, (c) α = 18°, (d) α = 20°.

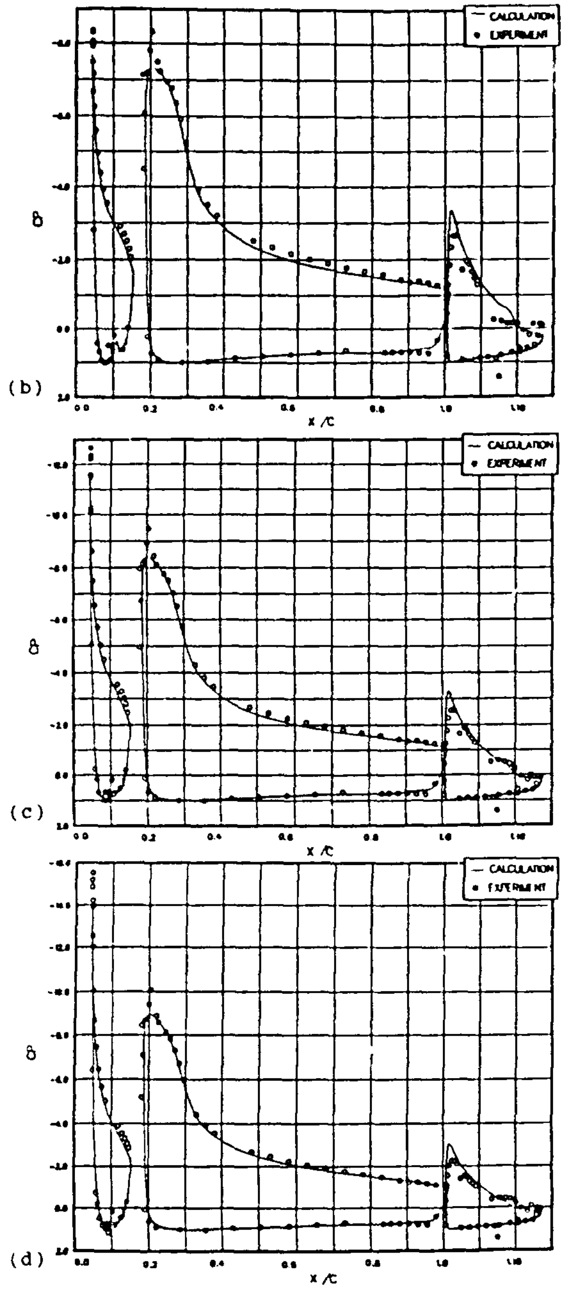

Fig. 16. Continued.

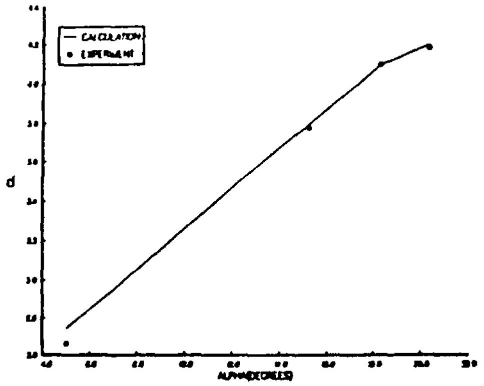

Fig. 17. Variation of the lift coefficient with angle of attack for the three-element airfoil with $\delta_f = 30°$ and $R_c = 5 \times 10^6$.

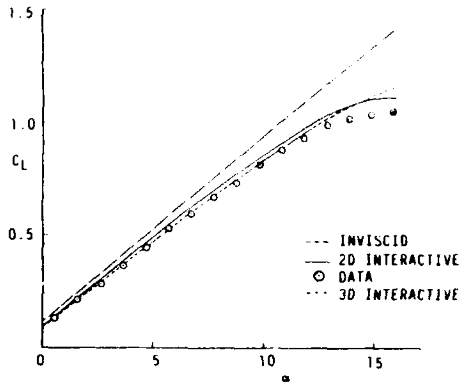

Fig. 18. Comparison of calculated and measured lift coefficients for the experimental wing data reported in Ref. 38.

$$\frac{\partial}{\partial x}\left[u_e h_2 \sin\theta(\Delta - \delta_x^*)\right] + \frac{\partial}{\partial z}\left[w_e h_1 \sin\theta(\Delta - \delta_z^*)\right] = 0 \qquad (32)$$

used to satisfy the Kutta condition in the inviscid method of section 3.1, provide very good agreement with experimental data up to the stall angle. As in airfoil flows without improvements to the turbulence model, the calculated results begin to deviate from the measured values and continue to increase past the stall angle. Work is in progress towards generalizing the improved turbulence model for three-dimensional flows.

5.2 Wing/Flap Configuration

Figure 19 shows the results for a wing/flap configuration corresponding to a flap deflection angle of 25°. The viscous flow calculations were first performed with transition specified at 5% from the leading edge of the wing and flap. After the convergence of the solutions, the stability properties of the velocity profiles were analyzed by using the 3D version of the e^n-method for the wing and the 2D version of the e^n-method for the flap. The reason for the use of the 2D version of the stability/transition method is due to the low Reynolds number flow on the

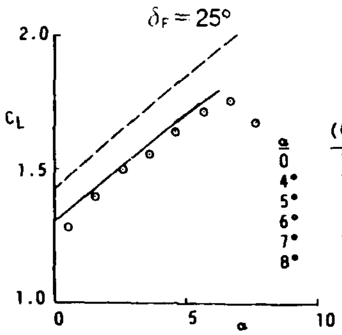

α	$(C_\ell)_{inv}$	$(C_\ell)_{vis}$
0	1.43	1.31
4°	1.77	1.63
5°	1.85	1.71
6°	1.93	1.78
7°	2.01	1.85
8°	2.09	1.93

Fig. 19. Comparison of calculated and measured lift coefficients for the wing/flap configuration.

flap. While the Reynolds number varied from 0.66×10^6 to 1.75×10^6 on the wing, it varied from 0.26×10^6 to 0.68×10^6 on the flap. A previous study[39] had shown that crossflow effects at relatively low Reynolds numbers ($R_c < 0.5 \times 10^6$) are small and transition calculations performed with either the 3D or 2D versions of the e^n-method essentially yield the same results.

The stability/transition calculations for the flap indicated the strong low Reynolds number effect with separation bubbles around 10 to 15 percent in extent and with transition occurring inside the separation bubble. These studies are still in progress, and the results shown in Fig. 19 correspond to results with transition specified at 5% chord from the leading edge and thus do not include those obtained from the stability/transition analysis. The calculated results in Fig. 19 show discrepancies even at lower angles of attack, and it is believed that with improved stability/transition calculations, the results will agree much better with data.

6. CONCLUDING REMARKS

The results and discussion of the previous sections show that the present interactive method, with its consideration of the flap-well region and the wakes, leads to pressure coefficient distributions and values of lift that are in good agreement with experiment for single and multielement configurations with angles of attack up to and beyond stall.

For multielement wing flows, the preliminary results are encouraging. Calculations show the importance of low Reynolds number effect on the components of the high-lift configuration at wind tunnel Reynolds numbers, and indicate that a calculation method, either based on the solutions of the Navier-Stokes equations or on a combination of inviscid and viscous flow solutions, must include the prediction of the onset of transition as part of the calculation procedure.

7. REFERENCES

1. Nakayama, A., "Flowfield Survey Around High-Lift Airfoil Model LB 546", McDonnell Douglas Co. Rpt MDC J4827, 1987.

2. Nakayama, A., "An Experimental Investigation of a Flow Around the Flap Well of a Multielement Airfoil", Douglas Aircraft Co. Rpt MDC K4310, 1990.

3. Valarezo, W.O., Dominik, C.J. and Wilcox, P.A., "High Reynolds Number Test Results for a Supercritical Multielement Airfoil", McDonnell Douglas Rpt MDC K5545, Dec. 1990.

4. Valarezo, W.O., Dominik, C.J. and McGhee, R.J., "Reynolds and Mach Number Effects on Multielement Airfoils", in "Proceedings of the Fifth Symposium on Numerical and Physical Aspects of Aerodynamic Flows", 13-15 January 1992, California State University, Long Beach, CA.

5. Van den Berg, B., "Boundary-Layer Measurements on a Two-Dimensional Wing with Flap", NLR TR 79009U, 1979.

6. Van den Berg, B. and Oskam, B., "Boundary-Layer Measurements on a Two-Dimensional Wing with Flap and a Comparison with Calculations", AGARD CP-271, 1979, Paper 18.

7. Oskam, B., Hahn, D.J. and Volkers, D.F., "Recent Advances in Computational Methods to Solve the High-Lift Multicomponent Airfoil Problem", NLR Rpt MP84042U, 1984.

8. Omar, E., Zierten, T. and Mahal, A., "Two-Dimensional Wind-Tunnel Tests of a NASA Supercritical Airfoil with Various High-Lift Systems. 1 - Data Analysis", NASA CR-2214, 1973.

9. Omar, E., Zierten, T., Hahn, M., Szpiro, E. and Mahal, A., "Two-Dimensional Wind-Tunnel Tests of a NASA Supercritical Airfoil with Various High-Lift Systems. 2 - Test Data", NASA CR-2215, 1977.

10. Olson, L.E. and Orloff, K.L., "On the Structure of Turbulent Wakes and Merging Shear Layers of Multielement Airfoils", AIAA paper 81-1238, June 1981.

11. Garner, P.L., Meredith, P.T. and Stoner, R.C., "Areas for Future CFD Development as Illustrated by Transport Aircraft Applications", AIAA Paper No. 91-1527, 1991.

12. Mavriplis, D.J., "Research on Unstructured Grid Techniques for CFD at ICASE", Paper presented at the CFD Conference, NASA Ames, 12-14 March 1991.

13. Rogers, E.S., Wiltberger, N.L. and Kwak, D., "Efficient Simulation of Incompressible Viscous Flow Over Single- and Multielement Airfoils", AIAA Paper No. 92-0405, 1992.

14. Barth, T.J., "CFD Algorithms on Unstructured Meshes", Paper presented at the CFD Conference, NASA Ames, 12-14 March 1991.

15. Cebeci, T., Clark, R.W., Chang,, K.C., Halsey, N.D. and Lee, K., "Airfoils with Separation and the Resulting Wakes", Journal Fluid Mechanics, Vol. 153, pp. 323-347, 1986.

16. Cebeci, T., Jau, J., Vitiello, D. and Chang, K.C., "Prediction of Post-Stall Flows on Airfoils", in "Numerical and Physical Aspects of Aerodynamic Flows, IV", (ed. T. Cebeci) Springer-Verlag, N.Y., 1989.

17. Cebeci, T., "Essential Ingredients of a Method for Low Reynolds-Number Airfoils", AIAA J., 27, 1983, pp. 1680-1688.

18. Hess, J.L. and Smith, A.M.O., "Calculation of Potential Flow About Arbitrary Bodies." Prog. in Aerospace Sci., 8, Pergamon Press, N.Y., 1966.

19. Cebeci, T. and Smith, A.M.O., "Analysis of Turbulent Boundary Layers", Academic Press, N.Y., 1974.

20. Michel, R., "Etude de la Transition sur les Profiles d'Aile," Establisement d'un Critere de Determination de Point de Transition et Calculde la Trainee de Profile Incompressible, ONERA Rpt. 1/1578A, 1951.

21. Smith, A.M.O. and Gamberoni, N., "Transition Pressure Gradient and Stability Theory", in "Proceedings of the International Congress of Applied Mechanics", Brussels, 4, 1956, p. 234.

22. Van Ingen, J.L., "A Suggested Semi-Empirical Method for the Calculation of the Boundary-Layer Region", VTH71, VTH74, Delft, Holland, 1956.

23. Cebeci, T., Jau, J., Vitiello, D., "An Interactive Boundary-Layer Approach to Multielement Airfoils at High Lift", AIAA Paper No. 92-0404, January 1992.

24. Hess, J.L., "Calculation of Potential Flow About Arbitrary Three-Dimensional Lifting Bodies", Douglas Aircraft Co. Rpt. J5679-01, 1972.

25. Bradshaw, P., Cebeci, T. and Whitelaw, J.H., "Engineering Calculation Methods for Turbulent Flows", Academic Press, London, 1981.

26. Veldman, A.E.P.,"New, Quasi-Simultaneous Method to Calculate Interacting Boundary Layers", AIAA J., 154, 1981, pp. 79-85.

27. Malik, M.R., "COSAL - A Black-Box Compressible Stability Analysis Code for Transition Prediction in Three-Dimensional Boundary Layers", NASA CR 165952, 1982.

28. Mack, L.M., "Boundary-Layer Stability Theory", AGARD Report No. 709, 1984.

29. Cebeci, T. and Stewartson, K., "Stability and Transition in Three-Dimensional Flow", AIAA J., 28, 1980, pp. 398-405.

30. Cebeci, T., Chen, H.H., Arnal, D. and Huang, T.T., "A Three-Dimensional Linear Stability Approach to Transition on Wings and Bodies of Revolution at Incidence. AIAA J., December 1991, pp. 2077-2085.

31. Johnson, D.A. and King, L.S., "A Mathematically Simple Turbulence Closure Model for Attached and Separated Turbulent Boundary Layers", AIAA J., 23, 1985, pp. 1684-1692.

32. Johnson, D.A. and Coakley, T.J., "Improvements to a Nonequilibrium Algebraic Turbulence Model", AIAA J., 28, 1990, pp. 2000-2003.

33. Cebeci, T., "An Approach to Computational Fluid Dynamics", book in preparation.

34. Nakayama, A., "Measurements in the Boundary Layer and Wake of Two Airfoil Models", Douglas Aircraft Co. Rpt. MDC J2403, 1988.

35. McGhee, R.J., Jones, G.S. and Jouty, R., "Performance Characteristics from Wind-Tunnel Tests of a Low Reynolds-Number Airfoil," AIAA paper 88-0607, January 1988.

36. Cebeci, T., Chang, K.C., Clark, R.W. and Halsey, N.D., "Calculation of Flow Over Multielement Airfoils at High Lift", Journal of Aircraft, Vol. 14, pp. 546-551, 1987.

37. Halsey, N.D., "Potential Flow Analysis of Multielement Airfoils Using Conformal Mapping", AIAA Journal, Vol. 17, p. 1281, 1979.

38. Lovell, D.A., "A Wind-Tunnel Investigation of the Effects of Flap Span and Deflection Angle, Wing Planform and a Body on the High-Lift Performance of a 28° Swept Wing", CP No. 1372, 1977.

39. Cebeci, T., Chen, H. H. and Lee, B.P., "Calculation of Three-Dimensional Low Reynolds Number Flows", to be published in J. Aircraft, 1993.

WAKE STRUCTURE AND AERODYNAMIC BEHAVIOR OF HIGH LIFT AIRCRAFT CONFIGURATIONS DURING UNSTEADY MANEUVERS IN GROUND EFFECT

A.Baron, M.Boffadossi
Dipartimento di Ingegneria Aerospaziale del Politecnico di Milano
Via C. Golgi, 40 - 20133 Milano - Italy

SUMMARY

A non linear unsteady vortex lattice scheme is used and flight dynamics equations are solved in order to predict the structure of the wakes and the instantaneous distribution of the aerodynamic loads on high-lift aircraft configurations, during general unsteady take-off maneuvers in ground effect.

The numerical scheme here presented can treat an arbitrary number of mutually interfering lifting and moving control surfaces having arbitrary plan form and camber. Wakes can be released in the flowfield from any of the sharp edges of the lifting surfaces, depending on their plan form, aspect ratio and angle of attack, while the effects of the fuselage are ignored in the present formulation.

Turbulent diffusion of the cores of the Rankine vortex filaments is regarded as a pre-eminent factor in a correct simulation of the development of unsteady interfering wakes. A vortex core diffusion model is used capable to deal even with the severe roll-up of the mutually interfering wakes developing *close and impinging on the ground.*

Typical applications of the unsteady vortex lattice scheme are presented, aimed at illustrating the capabilities of the code.

LIST OF SYMBOLS

C	wing root chord
C_L	lift coefficient
$\mathbf{F_a}$	total aerodynamic force
$\mathbf{I}$	aircraft moment of inertia
K	constant in the turbulent diffusion model
ℓ	spanwise dimension of the elementary portion of shear layer
$\mathbf{L}$	load on undercarriage leg
$\mathbf{m}$	mass
$\mathbf{M_a}$	moment of the aerodynamic forces about barycentric axes
r_c	vortex core radius
$\mathbf{r}$	relative position vector
$\mathbf{R}$	absolute position vector
$\mathcal{R}$	rotation tensor
S	surface of the cross section of the vortex core
t	time
$\mathbf{T}$	dimensionless time $T=tU/C$
$\mathbf{T}$	engine thrust
$\mathbf{Q}$	aircraft weight
U	characteristic velocity

$\mathbf{v}$	relative velocity (aircraft fixed frame of reference)
$\mathbf{V}$	absolute velocity
x,y,z	coordinates in the aircraft fixed barycentric frame of ref.
x_k,y_k,z_k	coordinates in the surface fixed frame of reference
X,Y,Z	coordinates in the absolute frame of reference
α	angle of attack
$\vec{\gamma}$	linear vortex density vector
Γ	circulation
ω_y	angular velocity component along y

suffixes

G	center of gravity
h	hinge axis
k	generic K-th lifting surface
m	main undercarriage
n	nose undercarriage
o	initial value; undeflected position
P	generic point P
y	y component

1. INTRODUCTION

The antithetical requirements for high speed cruise and short take-off and landing capabilities of modern aircrafts has promoted the development of more and more efficient high-lift systems (Dilliner et al., 1984).

While the ability in numerically predicting the performances of multi-component airfoils at high angle of attack, even in viscous and compressible flows, has been enormously improved in recent years, limited advances have been obtained in the numerical simulation of the complex vortical flows developing past and interfering with the lifting surfaces of complete aircraft configurations .

However, a detailed knowledge of the geometry of the three-dimensional wakes is essential for both an effective optimization procedure of the high-lift devices and the preliminary choice of the aircraft configuration.

As a matter of fact, high-lift devices are not merely required to produce maximum lift: other constraints have to be accounted for, such as their drag. Whilst there are substantial opportunities in reducing the profile drag of leading and trailing edge devices, by improving their sectional design and optimization major performance improvements, particularly at high angles of attack, will only come from an improved capability of predicting the complex vortical flow past three-dimensional wing geometries.
High-lift devices indeed necessarily influence the induced drag which strongly depends on wing and flap planforms, camber and twist, and their trim drag penalty is a function of the relative position of wing, flaps, and control surfaces. Both induced and trim drag can only be evaluated provided the complex interaction between three-dimensional wakes and lifting surfaces is correctly predicted (Butter, 1984).

Furthermore, high-lift devices are used on most aircrafts during take-off and landing maneuvers, namely during flight phases which are critical because of unsteadiness and ground proximity. Both unsteadiness and ground effect can produce strongly non linear aerodynamic effects and interferences, which can significantly affect the controllability and the operative safety of the aircraft.

Finally, knowledge of the time evolution of the wakes produced by high-lift configurations is also essential for attempting to reduce the hazardous persistence of the vortices in the proximity of high air traffic density airports.

2. GROUND EFFECT

When an airplane flies close to the ground, at a height comparable with its wing chord, it experiences an increase in lift and remarkable changes in drag and pitching moment. This phenomenon is called ground effect.
Ground effect is particularly significant for V/STOL and military low aspect-ratio aircrafts, mainly because of the strength and the complex shape of the unsteady wakes they produce.

Starting from the first basic theory developed by Wieselsberger in 1922, extensive research, both theoretical and experimental, has been devoted to understanding and predicting ground effect.

Wieselsberger's steady formulation ignored the effect of the bound vortex in the image however, introducing an image of the real wing below the ground plane and using the basic concepts of the lifting-line theory of Prandtl, he was able to calculate a correction to the induced drag and angle of attack of wings out of ground effect.
Since then, almost all investigators adopted the virtual image concept to obtain a theoretical or numerical simulation of the ground effect.

Unsteadiness was first introduced in a two-dimensional ground effect model by Chen and Schweikhard in 1985, who considered a straight imposed wake and found that unsteady effects can be such to completely modify the steady state predictions.

The findings of Chen and Schweikhard started extensive experimental work on finite wings of various plan forms in both steady and unsteady ground effects (Chang and Muirhead, 1985 and 1987).

Finally, in 1985, Katz proposed a comprehensive numerical model for the prediction of the unsteady ground effect, which also included a freely deforming wake. He adopted a vortex-lattice scheme and investigated the behavior of finite span lifting surfaces close to ground, so evidencing again that the increases in aerodynamic loads due to unsteadiness can be approximately twice those produced in steady state conditions.

The same free-wake approach has been adopted in the present work and, using the virtual image technique, a design tool has been derived capable to to predict the instantaneous load distribution and geometry of the wakes on multiple lifting surfaces, during general unsteady maneuvers in ground effect.

3. THE COMPUTATIONAL METHOD

The numerical simulation of unsteady airplane maneuvers obviously requires time dependent schemes, which allow to reproduce the actual time dependent boundary conditions representing the instantaneous velocity, flight attitude and location of the aircraft with respect to the ground. The motion of the aircraft can be either assigned or computed through flight dynamics models and appropriate control laws (see next paragraph).

The Navier-Stokes equations constitute a complete mathematical model for general three-dimensional unsteady flows of viscous fluids and can therefore model all of the complex phenomena mentioned above.
However, their solution requires, even for an incompressible fluid, storage capabilities and computing times which are still unacceptable. Although computer performances are dramatically increasing, recourse to simpler mathematical models, such as those based on the irrotational flow hypotheses, is still justified, if not unavoidable.

In the present work, results concerning the take-off maneuver of high-lift aircraft configurations are presented, obtained using an unsteady vortex lattice scheme. Details of the mathematical and numerical approach are given in Baron et al. 1989, 1990, 1991 and 1992, where various applications of the vortex-lattice scheme to fixed and rotary wings are also reported. Only the main features and limitations of the method are here summarized.

Wakes and flowfield are computed simultaneously, starting from an initial state of rest. Wings are impulsively started and wakes are generated with a Lagrangian process during which, at each time step, the vorticity present on their edges is convected in the field (Belotzerkowskii, 1977; Kandil et al., 1977; Hoeijmakers, 1983; Konstandinopoulos et al., 1985; Mook, 1988; Katz and Maskew, 1988; Baron et al., 1990).
At each time step, a new row of vortex panels is added to the wakes, which are convected in the field in such a way that the free vortex sheets are force-free.
A Lagrangian generation of the wakes does not require a first guess of their configuration, which can be critical when complex high-lift configurations have to be considered.

Wings, flaps and tail planes of arbitrary plan form and camber are simulated as surfaces of negligible thickness and separation can be imposed on any of their sharp edges.
Lifting surfaces and wakes are discretized into a finite number of surface panels. Each panel is made up of straight vortex segments lying on the edges of the panel, forming a closed loop with constant circulation (Mook, 1988).
The unknown values of the circulations on the lifting surface panels are determined, at each time step, by imposing the zero normal velocity condition on the solid surfaces, including the surfaces of the virtual image of the aircraft below the ground plane.

Pressure distributions are computed by means of the unsteady Bernoulli equation. Lift and moment coefficients are obtained by integration of pressure.

In order to compute the velocity induced by vortex segments, the Biot-Savart law is used, together with a viscous core diffusion model, physically consistent with the turbulent diffusion mechanism of continuous shear layers (Baron et al., 1990).
Rankine vortices are assumed to be "equivalent" to the elementary portions of the

physically continuous shear layers they replace in the numerical scheme. Therefore, their core radii spread in such a way that their cross sectional area S and circulation $\Gamma=\gamma\ell$ are equal, at each time, to *spreading and circulation* of an elementary portion of continuous shear layer containing the same vorticity. This model also implies that the enstrophy of the vortex lattice is equal to the enstrophy of the continuous turbulent shear layer and introduces a correct amount of energy dissipation in the wakes.

This implies a rate of change of the radius r_c of the Rankine vortex cores given by:

$$\frac{dr_c}{dt}=\frac{K\,\Gamma}{2\pi r_c} \tag{3.1}$$

where Γ is the circulation of the vortex filament considered and the experimental diffusion constant K, for both forced and unforced turbulent shear layers, assumes a universal value equal to 0.095 (Liepmann and Laufer 1947; Brown and Roshko, 1974; Oster and Wygnanski, 1982; Lesieur, 1987).

Forms analogous to (3.1) are also proposed by Squire (1965), Govindaraju and Saffman (1971) and Leonard (1980) for the turbulent diffusion of single line vortices, however they involve empirical constants the value of which cannot be defined in a general form. The present approach brings to a diffusion model consistent with the behavior of continuous turbulent shear layers and, in addition, information of experimental nature is introduced in a fully general way.

Moreover, most commonly used vortex core diffusion models turn out to be strongly dependent on the number of vortex filaments used to discretize the continuous distribution of vorticity in the flowfield (Rusak et al., 1985). The present approach, on the contrary, is virtually independent on discretization, the turbulent diffusion being explicitly related to the circulation of each vortex filament and, therefore, to the number of vortices.

This brings to a kind of "self adaptation" of the model and explains why, in a variety of applications, the vortex core turbulent diffusion model proved to be capable to cope, without *any form of tuning*, with the crucial aspects related to the roll-up process of unsteady interfering wakes as well as to the interaction of vortex filaments with both the solid lifting surfaces and ground.

A final comment can be done on the computing efficiency of unsteady vortex lattice schemes.

The simulation of unsteady vortical flows is intrinsically expensive from a numerical point of view, as the circulations of the transversal vortical filaments, which are virtually absent at steady state, must also be accounted for. In addition, a Lagrangian generation of the wakes requires longer computing times before a sufficiently representative portion of the shed wakes is produced.

However, a significant computing time saving can be obtained if only the mutual induction of the wake elements and the lifting surfaces is considered, while self-induction of the vortex filaments is neglected, for the farther portion of the shed wakes.

Self-induction effect simulation is a peculiar property of *vortex lattice schemes* and proves to be essential for a correct determination of the configuration of the wakes. However, as a matter of fact, in the "far wake" it only acts in increasing the local roll-up and stretching processes of the vortical sheets, without affecting at all their induction (and the aerodynamic load distribution) on the lifting surfaces far upstream.

It turns out that, for practical purposes, in most cases, vorticity in the wake can be simply convected, starting from a downstream distance of the order of some wing spans. Being most of the computing time devoted to the evaluation of the self-inducing effects, this procedure enormously speeds up the computations, without affecting the accuracy of the numerical predictions.

4. FRAMES OF REFERENCE AND FLIGHT DYNAMICS MODEL

In order to determine the instantaneous unknown values of the circulations on the lifting surface panels, the zero normal velocity condition on the solid surfaces is imposed, at

each time step.
This implies that the coefficients of the aerodynamic influence matrix, which rely on the instantaneous location and attitude of each surface element in the absolute frame of reference, must be computed.

Moreover the instantaneous velocity of the control point of each surface panel must be prescribed. This is the result of both the linear and angular velocities of the aircraft and obviously depends on the instantaneous linear and angular accelerations. These, in turn, rely on the mass and moment of inertia of the airplane and on the distribution of the aerodynamic loads on its surfaces.
Therefore appropriate frames of reference and flight dynamics equations must be considered.

An absolute ground fixed frame of reference $O(X,Y,Z)$ and an aircraft fixed frame of reference $G(x,y,z)$, having its origin in the center of gravity G of the airplane, are defined.
An additional k-th local frame of reference is introduced $H_k(x_k,y_k,z_k)$, fixed with each k-th lifting surface. The origin of the k-th frame of reference is coincident either with the leading edge of the fixed k-th surface, or with the hinge axis of the k-th control surface.

At time t, the relative position vector $\mathbf{r}_p(t)$ of a generic point P laying on the k-th lifting surface, in the aircraft fixed frame of reference, can be expressed as a function of its position $\mathbf{r}_{po}$ in the local frame $H_k(x_k,y_k,z_k)$, as:

$$\mathbf{r}_p(t) = \mathcal{R}_k(t)\,\mathbf{r}_{po} + \mathbf{r}_{hk} \tag{4.1}$$

where $\mathcal{R}_k(t)$ is the tensor associated with the rotation of the k-th surface, with respect to its undeflected angular position. $\mathcal{R}_k(t)$ therefore expresses the instantaneous contribution to the displacement of point P associated to the deflection imposed to the k-th control surface. $\mathbf{r}_{hk}$ is the location of the hinge axis of the k-th control surface in the aircraft fixed frame of reference.

The absolute position vector $\mathbf{R}_p(t)$ of point P, can be is given by:

$$\mathbf{R}_p(t) = \mathcal{R}(t)\,\mathbf{r}_p(t) + \mathbf{R}_G(t) \tag{4.2}$$

where $\mathcal{R}(t)$ is the tensor associated with the rotation of the aircraft, with respect to its initial angular position at time $t=0$, and $\mathbf{R}_G(t)$ is the absolute position vector of the center of gravity of the airplane.

Consequently, the absolute velocity $\mathbf{V}_p(t)$ of a generic point P laying on the k-th surface can be determined according to:

$$\mathbf{V}_p(t) = \mathbf{v}_p(t) + \mathbf{W}(t) \wedge (\mathbf{R}_p(t) - \mathbf{R}_G(t)) + \mathbf{V}_G(t) \tag{4.3}$$

where $\mathbf{W}(t)$ is the instantaneous angular velocity of the aircraft, $\mathbf{V}_G(t)$ is the linear velocity of its center of gravity, and $\mathbf{v}_p(t)$ is the velocity of point P in the airplane fixed frame of reference:

$$\mathbf{v}_p(t) = \mathbf{v}_{hk}(t) + \mathbf{w}_k(t) \wedge \mathbf{r}_p(t) \tag{4.4}$$

where $\mathbf{v}_{hk}(t)$ is the relative instantaneous velocity of the k-th hinge axis, around which the angular velocity of the k-th control surface is $\mathbf{w}_k(t)$. $\mathbf{v}_{hk}(t)$ is obviously equal to zero for fixed hinge flaps and control surfaces.

If the motion of both the aircraft and the control surfaces is assigned "a priori", the instantaneous values of $\mathbf{W}(t)$, $\mathbf{V}_G(t)$, $\mathbf{v}_{hk}(t)$ and $\mathbf{w}_k(t)$ are known.
Otherwise, only the deflection laws for the control surfaces are imposed, while $\mathbf{W}(t)$ and $\mathbf{V}_G(t)$ are determined through the dynamic balance of the forces and moments produced by the integration of the instantaneous pressure coefficients. In the present formulation a simple flight dynamics model based on the following rigid body equations is adopted.

The linear momentum conservation is imposed:

$$\mathbf{m}\,\dot{\mathbf{V}}_G = \mathbf{F_a} + \mathbf{T} + \mathbf{Q} + \mathbf{L_n} + \mathbf{L_m} \qquad (4.5)$$

where **m** is the mass of the aircraft, $\dot{\mathbf{V}}_G$ is the linear acceleration of its center of gravity, $\mathbf{F_a}$ is the sum of the aerodynamic lift and drag, **T** is the engine thrust (assumed to be constant), **Q** is the airplane weight, $\mathbf{L_m}$ and $\mathbf{L_n}$ are the forces exerted by the nose and main undercarriage legs, during the take-off run.

The conservation law for the angular momentum about the center of gravity of the airplane, in its plane of symmetry, brings to:

$$I_{yy}\,\dot{\omega}_y = \mathbf{M_{ay}} + x_n\,L_n + x_m\,L_m \qquad (4.6)$$

where I_{yy} is the moment of inertia of the aircraft about the y axis, $\dot{\omega}_y$ is the component of the angular acceleration around the y axis, $\mathbf{M_a}$ is the moment of the aerodynamic forces with respect to the center of gravity and the last two terms represent the moments of the forces exerted by the undercarriage legs during the take-off run.

Equations (4.5) and (4.6) are used to determine the dynamic behavior of the aircraft during its flight. Obviously, during the take-off run $\mathbf{L_n}$, $\mathbf{L_m}$ and their moments are unknown, and both the vertical component of the linear acceleration and the angular acceleration $\dot{\omega}_y$ are equal to zero, while, when $\mathbf{L_n}$ goes to zero, the rotation phase takes place, and the airplane angular acceleration $\dot{\omega}_y$ must be computed.

5. THE SELECTED AIRCRAFT CONFIGURATIONS

The unsteady take-off maneuver in ground effect is numerically simulated and analyzed in the next paragraphs for various high-lift configurations, which reasonably approximate STOL military or civil transport aircrafts (see **Fig.1**).

The basic aircraft configuration has the following geometrical characteristics.
The wing has a taper ratio of 0.5, a root chord C equal to 5.4 meters, a span equal to 40 meters and a surface of 176 m^2. It is located 0.8 root wing chords above ground.
The tail plane has the same taper ratio, a span equal to 3 C and is located in the plane of the wing with its apex 2 root wing chords downstream the trailing edge of the wing. The hinge axis of the elevator is located at 2/3 of the local tail plane chord.

In its basic configuration (**A**), the airplane is fitted with double slotted trailing edge flaps having a span and a central cutout equal to 5.36 and 0.87 root wing chords respectively. Each flap element has a constant chord equal to 0.2 C. The flap elements are set to an angle of attack of 11.25 and 22.5 degrees respectively.

Additional double slotted flap configurations (**B** and **C**), are obtained by only modifying the flap planforms, while maintaining their surface unchanged.
Configuration **B** has flaps with constant chord increased 50% with respect to the basic configuration, and a proportionally reduced span, the central cutout being unchanged.
Configuration **C** is obtained from the basic one by introducing cutouts simulating the presence of wing-mounted engines, and consequently increasing the flap span to 6.1 C.
A further configuration **D** is defined, having a single slotted flap with constant chord spanning the whole wing, set at 22.5 degrees.

For all of these configurations, the airplane is assumed to have a mass of 34.000 Kg, a moment of inertia around the y axis equal to 400.000 Kg m^2, a center of gravity located in the plane of symmetry at 50% of the wing root chord and at 0.4 root wing chords above ground.

6. COMMENTS ON THE NUMERICAL SIMULATION OF UNSTEADY TAKE-OFF MANEUVERS IGE

The attention is focused in this paragraph on some general aspects related to the use of vortex lattice schemes in the numerical simulation of unsteady aircraft maneuvers in ground effect.

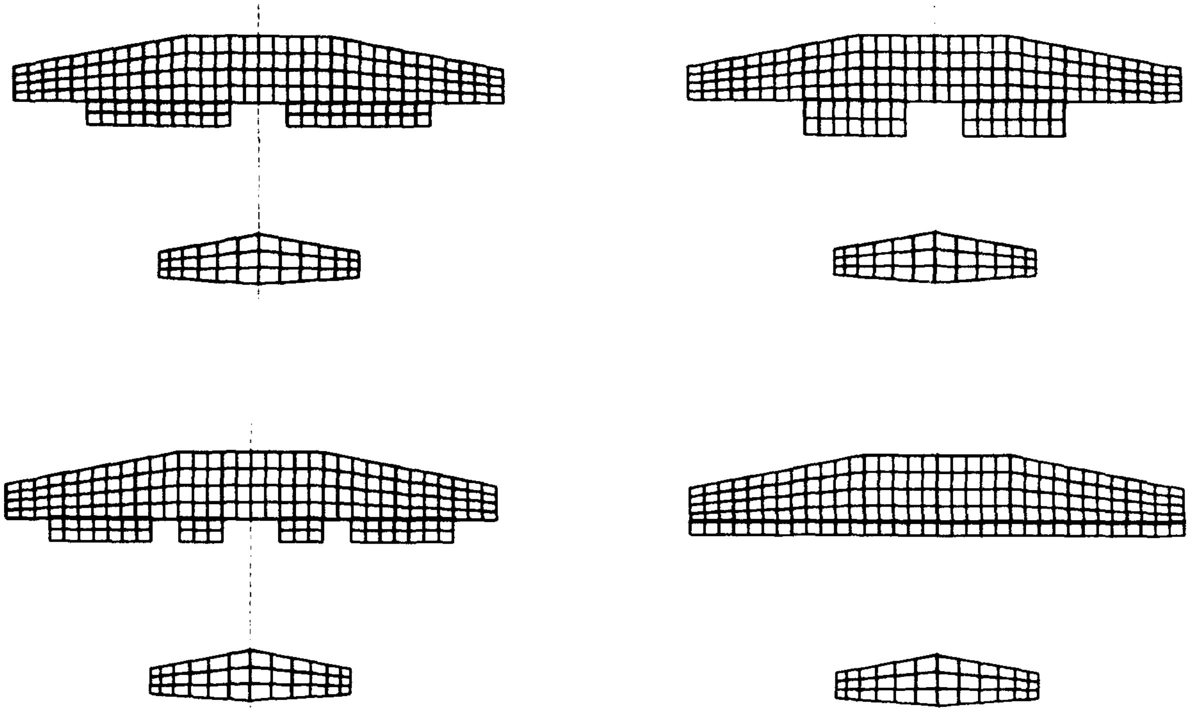

Fig.1 - The selected A, B, C and D high-lift aircraft configurations

The time dependent evolution of the wakes past the basic aircraft configuration, reported in **Fig.2**, impressively evidences the capability of unsteady vortex lattice schemes in treating evolutive vortical flows.
However, as mentioned in paragraph 3, this is only possible provided the turbulent diffusion process of the cores of the discrete vortices is adequately modeled in a general and physically consistent way.

Also the accuracy of the geometrical discretization, particularly in the spanwise direction, brings to an increasingly better definition of the configuration of the wakes and to a more accurate prediction of the load distribution on the lifting surfaces, but obviously requires rapidly growing computing times.
A preliminary analysis of the sensitivity of the scheme to panel density has shown that, for relatively low taper and high aspect-ratio plan forms, an acceptable prediction of the aerodynamic load distributions can be obtained even with the limited number of vortex panels used in these simulations. Solutions are only negligibly improved by further increasing the number of panels.

Flowfield and aerodynamic loads rely upon the instantaneous location of the shed wakes. Therefore, an appropriate integration time step must be used to accurately evaluate the displacement of the nodes of the vortex lattice. Moreover, the time discretization also affects the longitudinal dimension of the vortex panels in the wake, so influencing the uniformity of the vortex elements. Though not strictly compulsory, time discretization should be such to produce nearly uniform vortex elements on wakes and lifting surfaces. These are known to increase accuracy of the solutions and stability of the numerical scheme. The numerical results here presented have been obtained using a dimensionless integration time step T=0.25, which meets rather well the antithetical requirements of accuracy and computing time.

In order to describe how the take-off maneuver is accomplished, reference is made in the following to **Fig.3**, where the time history of the lift coefficients of wing, flap and tail plane is reported for the airplane configuration A, in ground effect (IGE).

A numerical analysis of the whole take-off maneuver (including the take-off run, the rotation phase and the final climb) can be performed by using the vortex lattice scheme, imposing appropriate deflections to the control surfaces, and integrating the flight dynamics equations 4.5 and 4.6. However, attention is focused in the present work to the simulation of the rotation phase of the aircraft, during which unsteadiness of the flight condition and time varying ground effects are believed to play a significant role.

Therefore, in order to speed-up the numerical simulation, the initial part of the actual take-off run has been replaced by an impulsive start.
Then, once the effects of the impulsive start are sufficiently damped and an approximately steady state configuration of the near wakes is attained (T=7 approx., in **Fig.3**), the elevator is progressively deflected from 0 to -20 degrees, at a rate of 30 degrees per second.

At the instant deflection begins, the tail surface lift decreases and starting vortices are shed in the field at the edges of both the stabilizer and the elevator.

Note that the relative location and attitude of the elevator panels vary progressively with respect to both the panels of the fixed portion of the tail plane and wing. This implies that the coefficients of the aerodynamic influence matrix must be computed at each time step, during the deflection phase of the elevator.

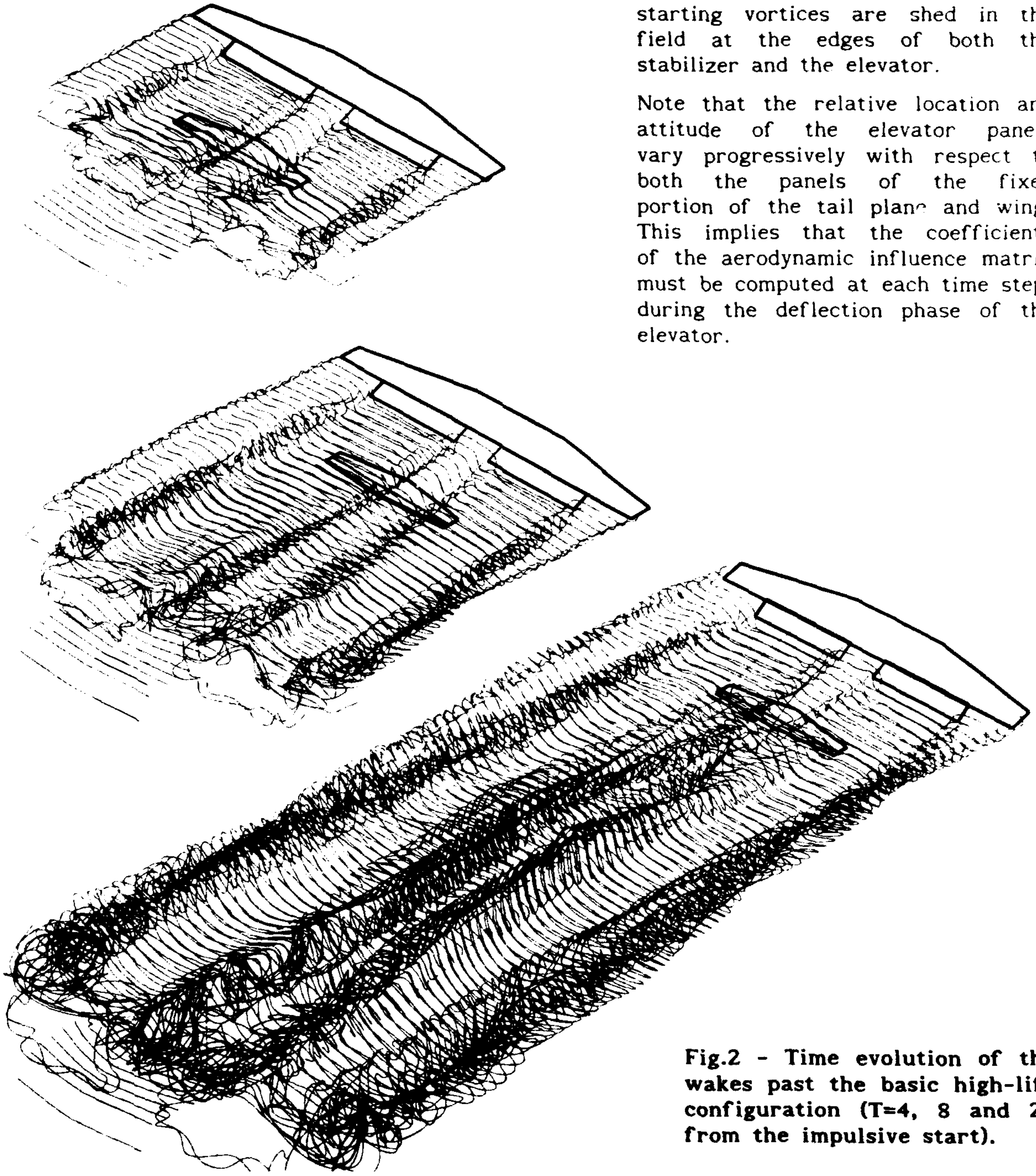

Fig.2 - Time evolution of the wakes past the basic high-lift configuration (T=4, 8 and 20 from the impulsive start).

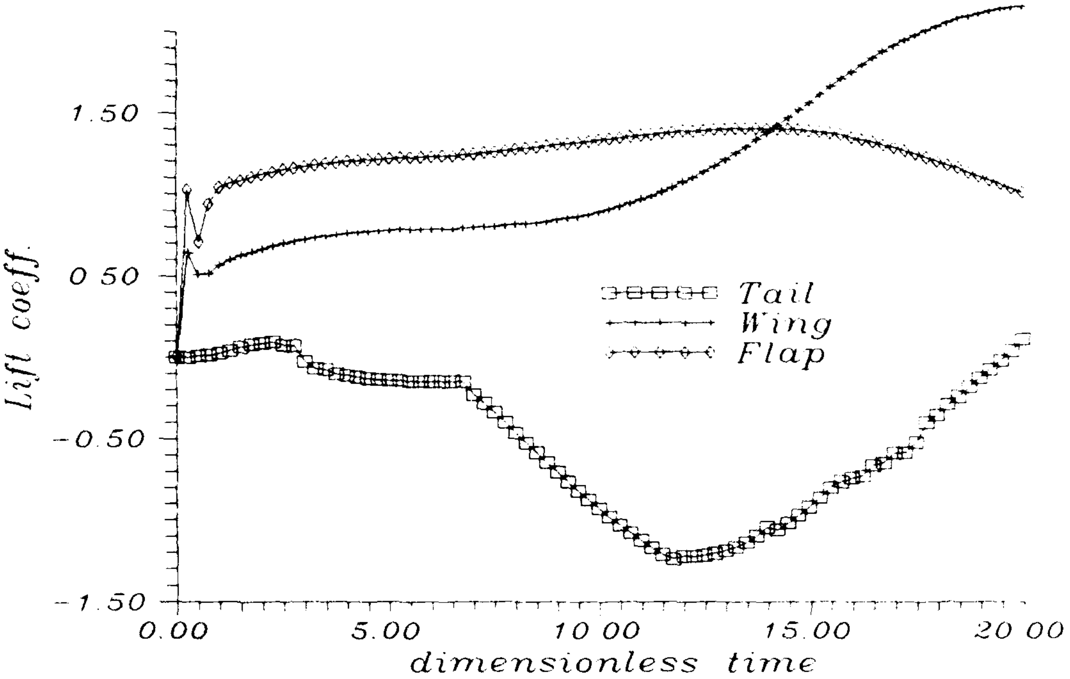

Fig.3 - Time history of the lift coefficients of wing, flap and tail plane for configuration A, during the impulsively started take-off maneuver IGE.

As a consequence of the elevator deflection (time units from 7 to 12 approx., in **Fig.3**), the aircraft is subject to a pitching moment which progressively grows until the nose wheel lifts up and it starts rotating in its plane of symmetry, according to the dynamic equilibrium laws. Initial rotation takes place around the axis of the main undercarriage wheels, which also provide the vertical force still necessary to balance the aircraft weight.
This rotation produces a progressively increasing angle of attack and causes the lift of the wing and flaps to increase while the negative lift of the tail plane reduces.
During this phase, the distance from the ground of both the lifting and the control surfaces of the aircraft varies significantly with time and the unsteady ground effect begins to play an important role.
Also the mutual induction of the lifting surfaces and their time varying interference with the shed wakes cause non linear aerodynamic effects.

During the rotation phase, which has a relatively short duration, the horizontal component of the velocity of the aircraft can be reasonably assumed to vary negligibly with time. This justifies the adoption of a simplified flight dynamics model in which the equation for the horizontal component of the momentum is eliminated and a constant horizontal acceleration is imposed to the aircraft. Although the practical consequences of this simplification are completely negligible, both in terms of computing time and complexity of the numerical scheme, it allows to perform numerical simulations which can more easily be analyzed in a comparative way. In fact, provided the same law is imposed to the deflection of the elevator, all of the rotation phases will start at the same dimensionless time, with the same value of the horizontal component of the velocity, independently on the particular examined configuration.
When the angle of attack of the airplane reaches a value of approximately 10 degrees, lift becomes larger than weight, the airplane starts climbing, and ground effect progressively reduces.

Also during the rotation, the take-off and the climbing phases the coefficients of the aerodynamic influence matrix must be computed at each time step, not only because of the control law imposed to the elevator, but also due to the fact that the lifting surfaces vary their distances and attitudes relative to their virtual images below the ground.

the configuration with analytical fairing.
Overall, the calculated results agree well
with experimental data. and the displacement surface Δ

7. THE INFLUENCE OF GROUND ON THE TAKE-OFF MANEUVER

Ground proximity affects the evolutive structure of the wakes released by the lifting surfaces. Ground confines the vertical development of the wakes and promotes a consequent spanwise spreading.

This is clearly evident in **Fig.4**, where the plan and lateral views of the wakes of configuration **A** are shown, at T=18, for both the OGE and the IGE maneuvers.
Although the outboard displacement of the tip vortices of wing and flaps does not completely alter the global structure of the wakes, it significantly enhances their interaction with the tail plane.

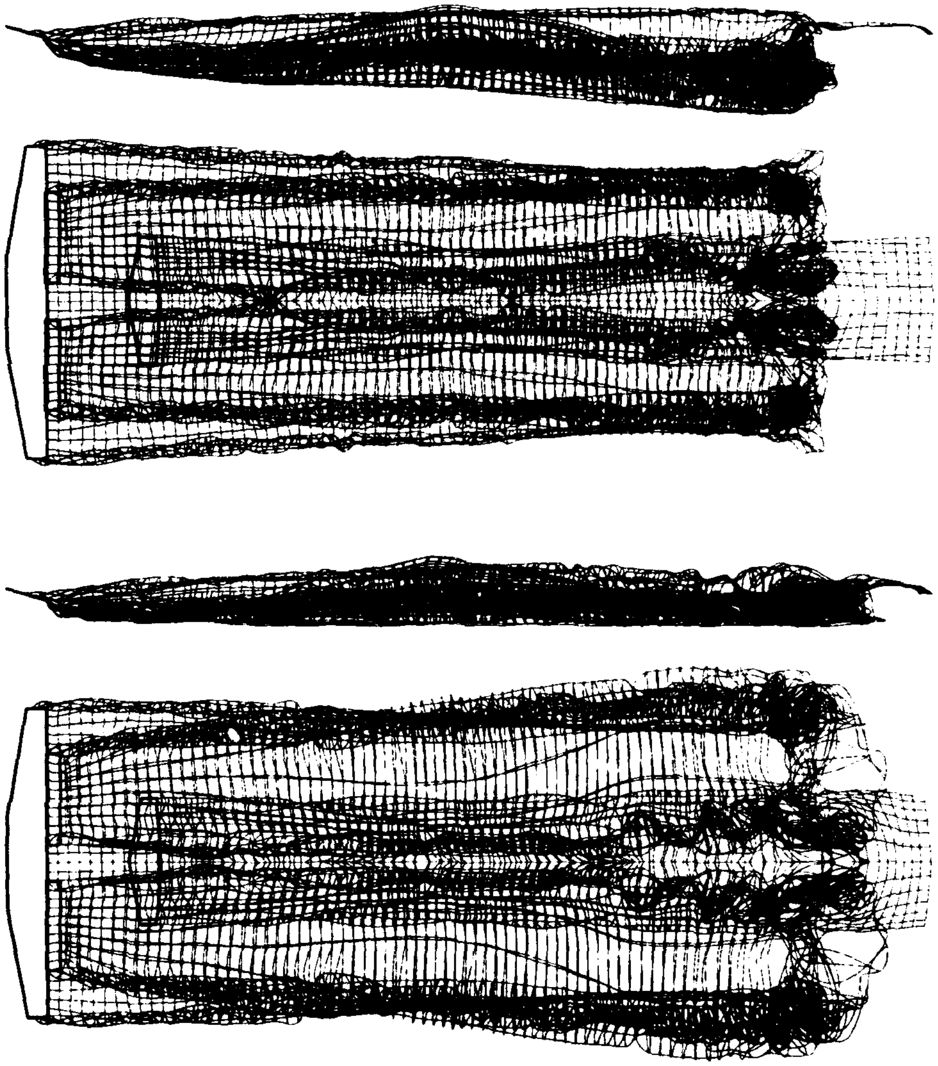

Fig.4 - Plan and lateral views of the wakes of configuration A, OGE (top) and IGE.

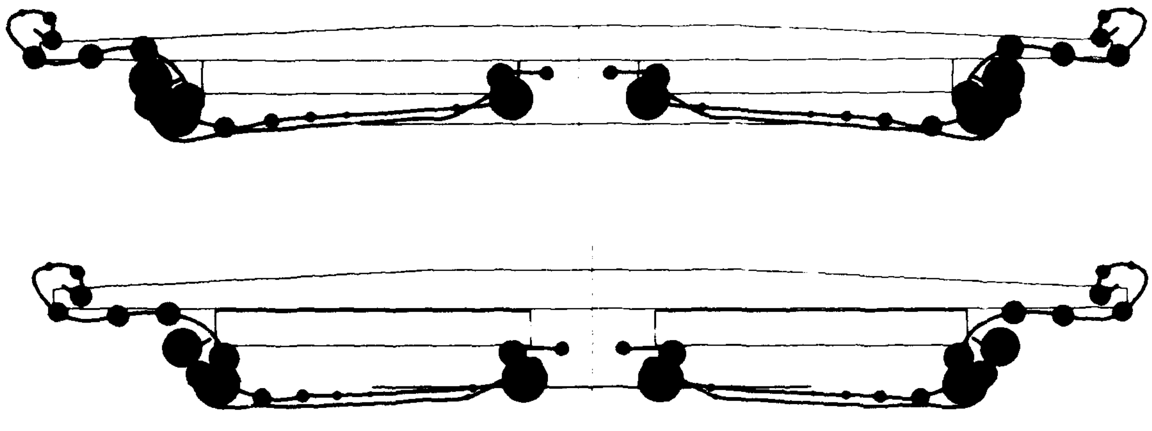

Fig.5 - Cross section of the wakes released by the wing and flaps of configuration A, IGE and OGE.

This is also confirmed by **Fig.5**, where the cross sections of the IGE and OGE wakes of configuration **A**, are shown for comparison, in a plane normal to the ground, 1 root wing chord downstream the wing trailing edge. Solid circles are used to represent the cross section of the longitudinal vortical filaments, which have radii proportional to their circulation.

Not only stronger vortices are produced in ground effect (IGE), but also their location relative to the tail plane is modified in both spanwise and vertical directions (also see **Fig.4**).

As a consequence, unsteady ground effects can be responsible for significant modifications in the efficiency of the tail plane and can remarkably affect the take-off maneuver.

In **Fig.6** the time evolution of the DCL developed by the tail plane, with respect to the IGE maneuver of **Fig.3**, is reported (DCL is defined as CL(OGE)-CL(IGE)).

In addition to a stronger sensitivity to the starting wake released by the wing upstream (T≃2), the tail plane in ground effect is always shown to produce a reduced negative lift.

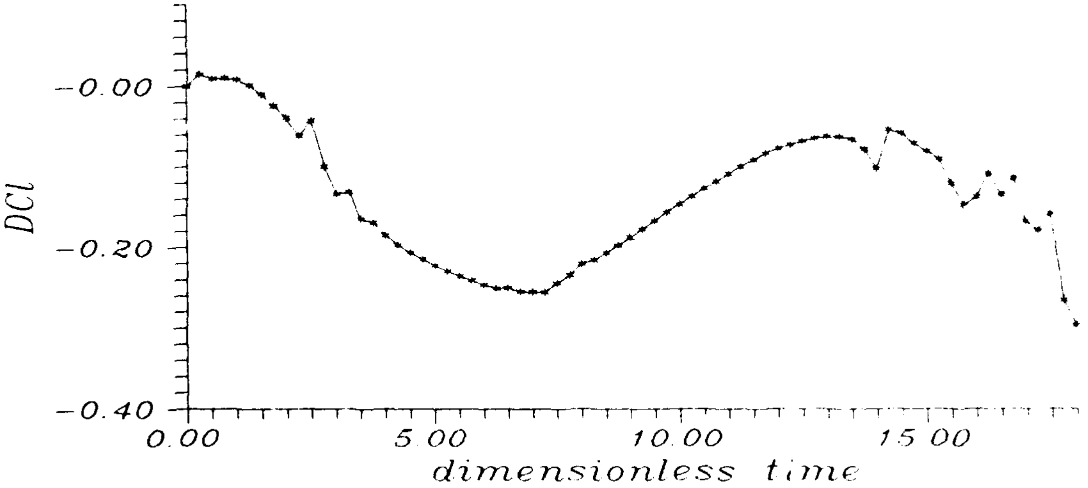

Fig.6 - Time history of the lift coefficient produced by the tail plane OGE, with respect to the IGE condition.

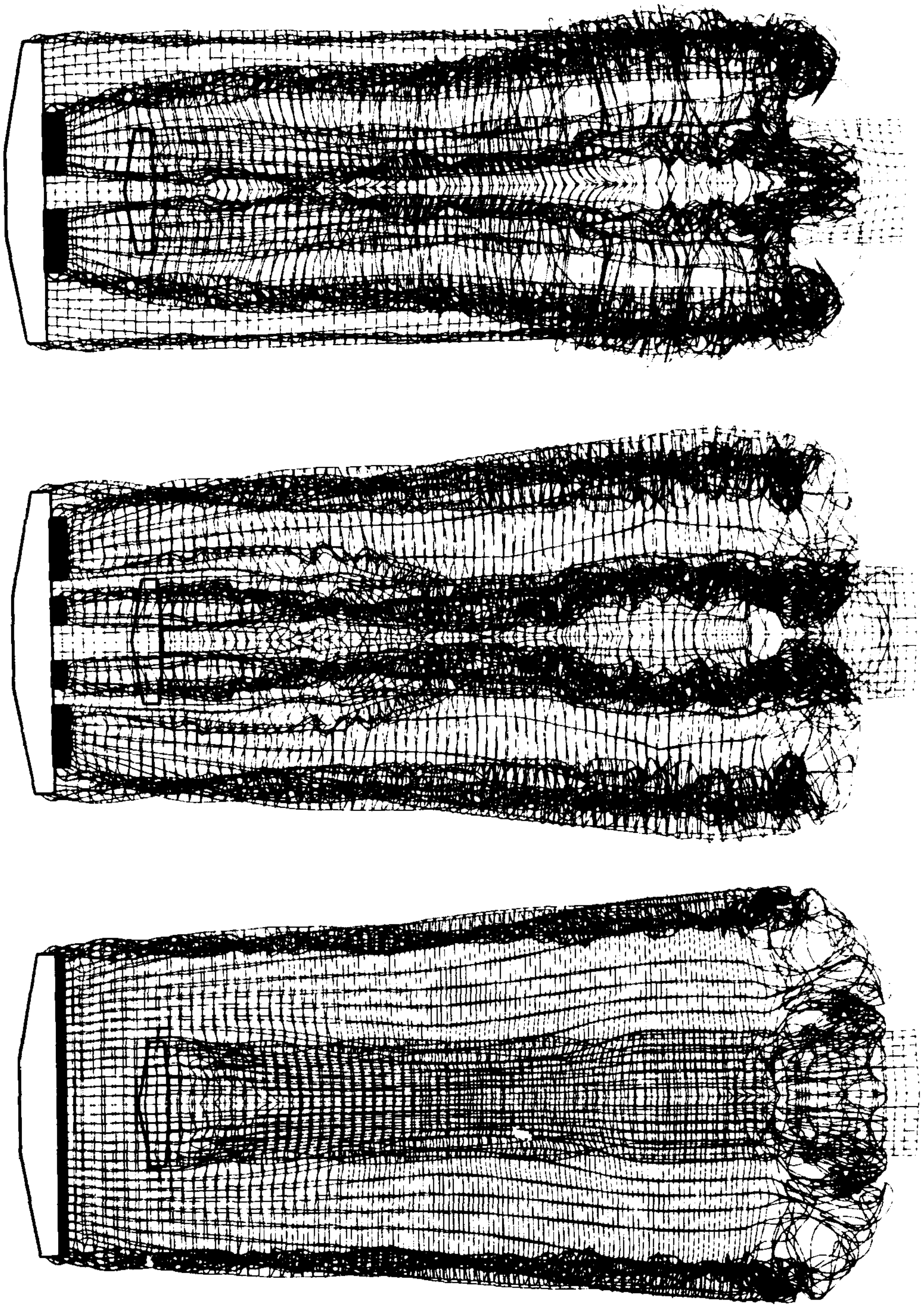

Fig.7 .- Plan view of the wakes of the aircraft configurations B (top), C and D (bottom), in the final stage (T=20) of the take-off maneuver IGE.

Une troisième originalité de la méthode, introduite plus récemment, est de généraliser l'emploi de ce mailleur algébrique à des géométries plus complexes (quelconques) par adjonction d'une technique de superposition de transformations

Massive-separation" pour le couplage, la méthode bidimensionnelle stationnaire (codes VIS05 et VIS07, Viscous-Inviscid-Solver-07) a donné accès au calcul du décrochage et du post-décrochage. Les Fig. 6-12-13 reproduisent ici les résultats [1]

8. THE INFLUENCE OF VARIOUS HIGH-LIFT CONFIGURATIONS

The influence of various flap configurations on the take-off maneuver in ground effect are examined.

In **Fig.7** plan views are shown of the wakes produced, during the take-off maneuver, by the aircraft configurations **B**, **C** and **D** defined in paragraph 5.
Although all of the considered configurations approximately produce the same amount of lift, streamwise vorticity in their wakes is distributed in completely different patterns, as evidenced in **Fig.8**, where the solid circles used to represent the cross section of the longitudinal vortices, have radii proportional to the strength of each vortex filament.

Various are the consequences of the different vorticity distribution in the wakes.
Structural loads, for instance, and induced drag depend on the spanwise distribution of lift which, in turn, relies on vorticity distribution. Highly concentrated unsteady vortices can induce vibratory loads on the tail surfaces, can be ingested by tail-mounted engines or induce fatigue loads on the propellers of canard configurations.

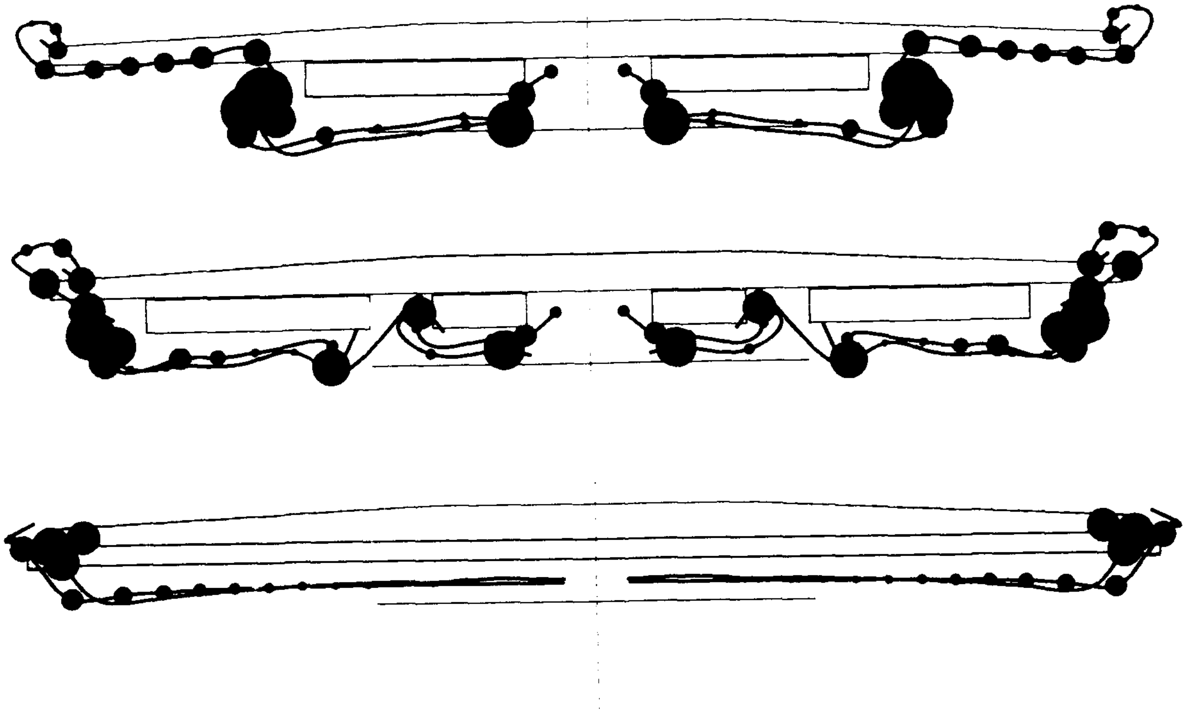

Fig.8 - Cross section of the wakes past various high-lift aircraft configurations IGE, in a plane 1 root wing chord downstream the wing trailing edge (T=18).

As an example, the effect of the structure of the wakes is shown in **Fig.9** on the spanwise lift distribution on the tail plane of the examined configurations.

9. CONCLUSIONS

High-lift devices are mainly used during unsteady maneuvers in ground effect. Their design and optimization, together with the controllability and operative safety of aircrafts, relies on the capability of predicting the complex structure of the three-dimensional unsteady vortical flows which develop close and interfere with the control surfaces and ground.

A numerical approach to the simulation of unsteady maneuvers in ground effect, based on a non linear vortex lattice scheme and a simple flight dynamics model, has been presented and applied to various reasonably realistic high-lift aircraft configuration. Further developments of the scheme will allow to account also for the fuselage effects, which have been neglected in the present formulation.

For design purposes, the developed vortex lattice scheme seems to constitute a reasonable compromise between the antithetical needs of complete mathematical models of complex flows and required computing times.
All of the main physical features of the examined flows seem in fact to be retained in the numerical simulations, despite of the quite crude vortex lattice model used to discretize the continuous distribution of vorticity in the flowfield. this is partly ascribable to the use of a fully general model for the diffusion of the Rankine vortex filaments.

In addition to the significant role played by ground proximity, the numerical simulations also evidence how the choice of appropriate high-lift configurations can completely modify the structure and the inducing effect of the vortical wakes shed in the flowfield.

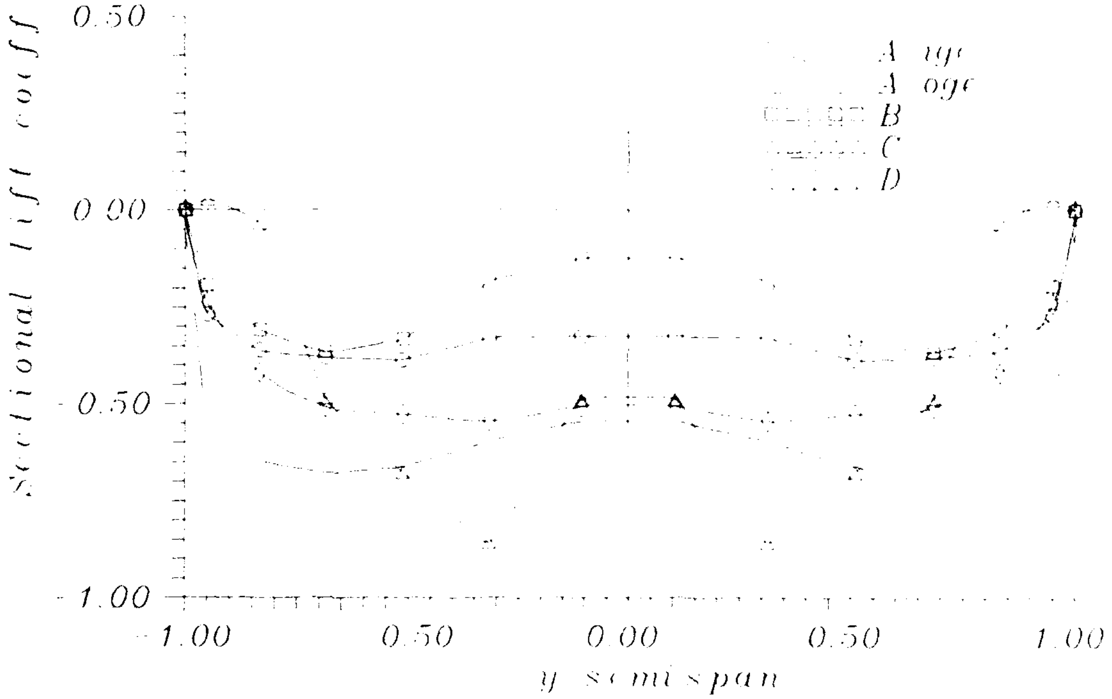

Fig.9 - **Spanwise lift distribution on the tail plane of various high-lift aircraft configurations (A, B, C and D), during a take-off maneuver IGE (T= 18).**

REFERENCES

BARON A., BOFFADOSSI M. (1989), "Simulazione numerica di scie vorticose non stazionarie tridimensionali", Proceedings of the X° Convegno Nazionale di Aeronautica e Astronautica, Pisa.

BARON A., BOFFADOSSI M., DE PONTE S. (1990), "Numerical simulation of vortex flows past impulsively started wings", AGARD-CP-494.

BARON A., BOFFADOSSI M. (1991) ,"Numerical Simulation of Unsteady Rotor Wakes", Proceedings of the XVII-th European Rotorcraft Forum, Berlin, Paper N°91-69.

BARON A., BOFFADOSSI M. (1992), "Unsteady Free Wake Analysis of Closely Interfering

BARON A., BOFFADOSSI M. (1992), "Unsteady Free Wake Analysis of Closely Interfering Helicopter Rotors", XVIII-th European Rotorcraft Forum, Avignon, Paper N° 108

BELOTZERKOWSKII S.M. (1977), "A study of unsteady aerodynamics of lifting surfaces using the computer", Annual Review of Fluid Mechanics, Vol.9, pp. 469-494.

BROWN G.L., ROSHKO A. (1974), "On density effects and large structure in turbulent mixing layers", Journal of Fluid Mechanics, Vol.64, pp. 775-816.

BUTTER D.J. (1984), "Recent progress on development and understanding of high lift system", AGARD-CP-365

CHANG R.C., MUIRHEAD V.U. (1985), "Investigation of Dynamic Ground Effect", NASA-CP-2462

CHANG R.C., MUIRHEAD V.U. (1987), "Effect of Sink Rate on Ground Effect of Low-Aspect-Ratio Wings", Journal of Aircraft, Vol.24, pp.176-180

CHEN Y.S., SCHWEIKHARD W.G. (1985), "Dynamic Ground Effects on a Two-Dimensional Flat Plate", Journal of Aircraft, Vol.22, pp.638-640.

DILLINER B., MAY F.W., MCMASTER J,K. (1984), "Aerodynamic issue in the design of high lift systems for transport aircraft", AGARD-CP-365

GOVINDARAJU S.P., SAFFMAN P.G. (1971), "Flow in a turbulent trailing vortex", The Physics of Fluids, Vol.14, No.10, pp. 2074-2080.

HOEIJMAKERS H.W.M. (1983), "Computational vortex flow aerodynamics", AGARD-CP-342

KANDIL O.A., ATTA E.H., NAYFEH A.H. (1977), "A three dimensional steady and unsteady asymmetric flow past wings of arbitrary plan forms", AGARD-CP-227.

KATZ J. (1985), "Calculation of the Aerodynamic Forces on Automotive Lifting Surfaces", Journal of Fluid Engineering, Vol.107, pp.438-443

KATZ J., MASKEW B. (1988), "Unsteady low speed aerodynamics model for complete aircraft configurations", Journal of Aircraft, Vol.25, No.4, pp 302-310.

KONSTANDINOPOULOS P., MOOK D.T., NAYFEH A.H., WATSON L. (1985), "A vortex lattice method for general, unsteady aerodynamics", J. of Aircraft, Vol.22, No.1, pp 43-49.

LEONARD A. (1980), "Vortex method for flow simulation", Journal of Computational Physics, Vol.37, pp. 289-335.

LESIEUR M. (1987), "Turbulence in fluids, stochastic and numerical modelling", Martinus Nijhoff Publishers, Dordrecht.

LIEPMANN H.W., LAUFER J. (1947), "Investigation of free turbulent mixing", NACA-TN-1257.

MOOK D.T. (1988), "Unsteady aerodynamics", VKI L.S. 1988-07 on "Unsteady Aerodynamics"
OSTER D., WYGNANSKI I. (1982), "The forced mixing layer between parallel streams", Journal of Fluid Mechanics, Vol.23, pp. 91-130.

RUSAK Z., SEGINER A., WASSERSTROM E. (1985), "Convergence characteristic of a vortex-lattice method for nonlinear configuration aerodynamics", Journal of Aircraft, Vol.22, No.9, pp. 743-749.

SQUIRE H.B. (1965), "The growth of a vortex in turbulent flow", The Aeronautical Quarterly, Vol.16, pp. 302-306.

WIESELSBERGER C. (1922), "Wing Resistance Near the Ground", NACA-TM-77

CALCUL PAR INTERACTION VISQUEUX NON-VISQUEUX DES ECOULEMENTS COMPRESSIBLES FORTEMENT DECOLLES AUX GRANDES PORTANCES SUR PROFILS D'AILES ET VOILURES

(VISCOUS-INVISCID CALCULATION OF HIGH-LIFT SEPARATED COMPRESSIBLE FLOWS OVER AIRFOILS AND WINGS)

J.C. Le Balleur

ONERA, BP 72, 92322 Chatillon Cedex (France)

Abstract.

The viscous-inviscid interaction transonic numerical method previously defined by the author for computing attached or separated flows over airfoils, including the deeply stalled flows, is extended into a new three-dimensional method for strongly separated flows over wings at high-lift and compressible speeds.

The numerical non-linearly implicit boundary layer technique (direct/inverse), the turbulent models, the grid generation and grid-adaption, the coupling and wake-equilibration algorithms, the inviscid full-potential schemes, are extended in three-dimension, with approximation on the viscous equations (2.75D-local). New theoretical results are given on the singularities and characteristic cones of the fully three-dimensional boundary layer in inverse mode. A new "Massive-separation 2.75D" extension of the "Semi-inverse" algorithm of Le Balleur for coupling is given and detailed, together with its stability-theory.

Results are shown for 2D-stall, and for 3D separated flows over rectangular or swept wings, with satisfactory agreement between theory and experiment. A self-adaptation technique of the grid to the viscous effects is displayed. The results demonstrate that the viscous-inviscid interaction methods give a full access to the calculation of three-dimensional separation.

Résumé.

La méthode numérique d'interaction visqueux-non visqueux transsonique définie précédemment par l'auteur pour le calcul des écoulements attachés ou décollés sur les profils d'ailes, incluant le calcul du décrochage profond, est ici étendue en une nouvelle méthode tridimensionnelle pour les écoulements fortement décollés sur des ailes, aux grandes portances et en fluide compressible.

La technique numérique non-linéairement implicite de couche limite (directe/inverse), les modèles turbulents, le générateur de maillage et son auto-adaptation, les algorithmes de couplage et de mise en équilibre du sillage, le schéma non-visqueux potentiel-complet, sont étendus au tridimensionnel, avec une approximation sur les équations visqueuses (2.75D-local). Des résultats théoriques nouveaux sont donnés sur les singularités et cônes caractéristiques de la couche limite pleinement tridimensionnelle en mode inverse. Une extension nouvelle "Massive-separation 2.75D" de l'algorithme de couplage "Semi-inverse" de Le Balleur est donnée et détaillée, en même temps que sa théorie de stabilité.

Des résultats sont montrés pour le décrochage 2D, et pour des écoulements 3D-décollés sur aile rectangulaire ou aile en flèche, avec un accord calcul-expérience satisfaisant. Une technique d'auto-adaptation du maillage aux effets visqueux est présentée. Les résultats démontrent que les méthodes d'interaction visqueux-non visqueux donnent un plein accès au calcul du décollement tridimensionnel.

1. INTRODUCTION.

La simulation numérique par "interaction visqueux-non visqueux" offre la possibilité de développer des méthodes à plus faible dissipation numérique, et à plus faible coût, que les techniques de "résolution directe" d'équations de Navier-Stokes. L'investissement dans cette méthodologie, malgré ce double avantage, semble toutefois avoir été desservi par l'idée ancienne et maintenant inexacte que son domaine de développement serait toujours plus limité, notamment vis à vis du décollement étendu, et surtout du décollement tridimensionnel.

Par les progrès des algorithmes de couplage, l'accès au calcul des décollements avait pu être ouvert, en 2D ou 2.5D. Ces progrès sur le couplage avaient été d'abord obtenus par introduction de l'algorithme "Semi-inverse" de Le Balleur [6][1] en 1978, algorithme général subsonique/supersonique doté d'un controle de stabilité autonome, puis par l'algorithme "Semi-inverse" simplifié de Carter [10] de 1979, équivalent à une intégrale première de la partie subsonique du précédent, puis par l'algorithme "Quasi-simultaneous" de Veldman [11] de 1981, algorithme subsonique de type Gauss-Seidel, puis enfin par l'algorithme instationnaire-consistant "Semi-implicite", Le Balleur, Girodroux [12][13], de 1984.

Plus récemment, l'algorithme "Semi-inverse" originel de 1978 a conduit à 2 nouveaux algorithmes qui le généralisent, Le Balleur [1]. Le premier est l'algorithme "Semi-inverse Massive-separation", algorithme stationnaire ayant ouvert l'accès aux calculs de décollement massif et de décrochage.

Cet algorithme est ici repris et étendu aux calculs 3D-approchés ("2.75D"). Le second est l'algorithme "Semi-inverse Pseudo-unsteady", obtenu en modifiant le préconditionnement non-visqueux de l'algorithme originel par introduction du caractère pseudo-instationnaire des solveurs Euler, ce qui a donné accès à des méthodes robustes et rapides pour l'interaction choc - couche limite [1].

L'accès au *calcul du décollement* tridimensionnel, plus complexe à obtenir, a souvent été décrit à tort comme hors de portée de la méthodologie d'interaction visqueux-non visqueux. Bien que, de par sa complexité, la théorie 3D du couplage n'ait pu être directement dégagée, les études exploratoires, par exemple de Wigton, Yoshihara, Wai [29][30][31], Carter, Edwards, Davis, Hafez [26][27], Cebeci et al. [28], Steger, van Dalsem [32], ont d'abord mis en évidence des possibilités de calcul de petits décollements 3D.

Présentement, la méthode transsonique 2D (ou 2.5D) suggérée antérieurement pour les écoulements de profils d'ailes décollés ou en décrochage, Le Balleur [7][1], est ici étendue au calcul tridimensionnel sur des voilures décollées, en introduisant des équations visqueuses approchées ("2.75D"-local) mais avec un calcul non-visqueux complet d'équation du potentiel. Les méthodes originales mises au point dans la méthode bidimensionnelle, Le Balleur [1], notamment la technique numérique de couche limite directe/inverse, ainsi que sa modélisation, l'algorithme de couplage "Semi-inverse" et sa théorie de stabilité, le générateur algébrique de maillage et son auto-adaptation aux effets visqueux, l'algorithme d'équilibrage du sillage, le solveur potentiel-complet, sont ici généralisés en 3D. Les premiers résultats présentés démontrent l'accès de la méthode au calcul du décollement tridimensionnel, avec large décollement. Notons qu'une extension instationnaire menée parallèlement sur la même méthodologie visqueuse, Le Balleur, Girodroux [21], avec un choix opposé d'*équations visqueuses* 3D-complètes et de calcul non-visqueux approché (petites perturbations), démontre aussi l'accès au calcul du décollement tridimensionnel.

2. EQUATIONS.

Les équations de Navier-Stokes sont dissociées en 2 systèmes couplés équivalents en utilisant la théorie de "Formulation-Déficitaire" de Le Balleur [4][7][14][1], proposée vers 1980, et complétée vers 1989 par l'introduction du "Référentiel de Déplacement" [1] qui permet de généraliser l'emploi d'équations de couche-mince au décollement massif. La théorie est valable aussi bien pour les équations complètes de Navier-Stokes que pour des équations de "couche-mince".

2.1. Théorie de "Formulation-Déficitaire".

On note avec un signe "barre" l'écoulement visqueux turbulent réel, assujetti aux équations de Navier-Stokes moyennées. On note sans ce signe un écoulement fictif superposé "pseudo-fluide-parfait", assujetti aux équations d'Euler, défini partout dans l'espace, même à l'intérieur des régions visqueuses. On considère des coordonnées cartésiennes X^i et curvilignes $x^j(X^i)$, les composantes cartésiennes $\bar{U}^i$ et contravariantes $\bar{u}^j$ de la vitesse, le jacobien $J = \det(\partial X^i/\partial x^j)$, les symboles de Christoffel Γ^i_{jk}, le tenseur métrique g^{ij} ou g_{ij}, les composantes cartésiennes T^{ij} et contravariantes t^{ij} du tenseur des contraintes, la densité $\bar{\rho}$, l'enthalpie totale $\bar{h}_T$, la pression totale $\bar{p}_T$, ainsi que les variables correspondantes dans le "pseudo-fluide-parfait".

2.1.1. Théorie complète : Navier-Stokes.

La théorie de "Formulation-Déficitaire" de Le Balleur propose une résolution indirecte des équations de Navier en traitant d'une part la différence entre équations d'Euler et de Navier-Stokes, et d'autre part les équations d'Euler, par des schémas numériques différents. Le système numérique obtenu, de rang double, vise l'obtention d'une technique à très faible dissipation numérique, aussi bien pour des équations de Navier complètes, que pour des équations de couche-mince. Notons que la théorie de "Formulation-Déficitaire" ne décompose pas le vecteur vitesse en introduisant des vitesses-déficitaires $(u^i - \bar{u}^i)$, mais décompose au contraire les équations de Navier sous forme additive par rapport aux flux. La théorie introduit un double jeu de variables primitives, pour le champ-réel et pour le champ-fictif Euler, avec couplage fort (couplage exact) des champs Navier et Euler :

$$\frac{\partial}{\partial x^j} J . \begin{bmatrix} \rho u^j - \bar{\rho}\bar{u}^j \\ \rho u^i u^j - \bar{\rho}\bar{u}^i\bar{u}^j + t^{ij} \end{bmatrix} + \Gamma^i_{jk} J . \begin{bmatrix} 0 \\ \rho u^j u^k - \bar{\rho}\bar{u}^j\bar{u}^k + t^{jk} \end{bmatrix} + J\ g^{ij} \frac{\partial}{\partial x^j} \begin{bmatrix} 0 \\ p - \bar{p} \end{bmatrix} = 0 \quad (1)$$

Fluide Reel : $\bar{u}^i, \bar{p}, \bar{\rho}, \bar{h}_T$

Pseudo-fluide-parfait : u^i, p, ρ, h_T $\qquad i, j, k = 1, 2, 3$

$$g_{ij} = \frac{\partial X^k}{\partial x^i}\frac{\partial X^l}{\partial x^j} G_{kl}, \qquad J = \det\left[\frac{\partial X^i}{\partial x^j}\right] = \left[\det(g_{ij})\right]^{1/2},$$

$$\Gamma^i_{kj} = \frac{1}{2} g^{im} \left[\frac{\partial g_{km}}{\partial x^j} + \frac{\partial g_{jm}}{\partial x^k} - \frac{\partial g_{jk}}{\partial x^m}\right], \qquad g^{im} g_{mj} = G^i_j$$

$$\bar{u}^j = \frac{\partial x^j}{\partial X^i} \bar{U}^i, \qquad t^{kl} = \frac{\partial x^k}{\partial X^i}\frac{\partial x^l}{\partial X^j} T^{ij}, \qquad \bar{q}^2 = g_{ij}\ \bar{u}^i\ \bar{u}^j$$

$$\frac{\partial X^i}{\partial x^k}\ \frac{\partial x^k}{\partial X^j} = G^i_j, \qquad G^i_j = G_{kl} = G^{mn} = Kronecker.$$

La théorie écrit le couplage exact par raccordement continu des 2 champs ("matching") lorsque l'on s'éloigne vers l'extérieur des couches visqueuses, ce qui évite toute dépendance de la solution à un choix arbitraire d'épaisseur visqueuse δ, et ce qui s'est avéré aussi, Le Balleur [5][8], éliminer toute anomalie de couche visqueuse "supercritique" au sens de Crocco-Lees :

$$0 = \lim_{x^3 \to \pm\infty} \begin{bmatrix} u^i - \bar{u}^i \\ p - \bar{p} \\ \rho - \bar{\rho} \\ h_T - \bar{h}_T \end{bmatrix}, \qquad i = 1, 2, 3$$

Ce couplage apporte les conditions aux limites qui assurent la détermination du champ fictif "pseudo-fluide-parfait", avec unicité dans le cas non-visqueux potentiel, et avec la nécessité de conditions supplémentaires dans le cas non-visqueux Euler, voir Le Balleur [3][23][19][20].

2.1.2. Théorie "NS-couche-mince".

De même que dans une résolution "directe Navier-Stokes couche-mince" habituelle, la direction x^3 peut ici être particularisée, et les termes de contraintes tronqués :

$$\frac{\partial}{\partial x^j} J.\begin{bmatrix} \rho u^j - \bar{\rho}\bar{u}^j \\ \rho u^i u^j - \bar{\rho}\bar{u}^i \bar{u}^j \end{bmatrix} + \Gamma^i_{lk} J.\begin{bmatrix} 0 \\ \rho u^l u^k - \bar{\rho}\bar{u}^l \bar{u}^k \end{bmatrix} + J\, g^{ij} \frac{\partial}{\partial x^j}\begin{bmatrix} 0 \\ p - \bar{p} \end{bmatrix} = \frac{\partial}{\partial x^3}\begin{bmatrix} 0 \\ -J t^{i3} \end{bmatrix} \quad (2a)$$

$$i, j, k = 1, 2, 3$$

Les équations "Navier-Stokes couche-mince" sont dépendantes du choix du maillage, cette incertitude (majeure) étant acceptée dans les méthodes de résolution directes "Navier-Stokes".

2.1.3. "NS-couche-mince" en "Référentiel de Déplacement".

La théorie de "Formulation-Déficitaire" élimine cette dépendance abusive en déterminant aérodynamiquement la direction x^3 par la sélection d'un "Référentiel de Déplacement", Le Balleur [14][1], voir Fig. 1.

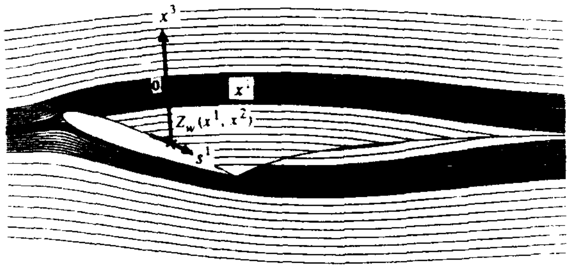

Fig. 1. "Référentiel de Déplacement" (décollement massif).

En théorie de "Formulation-Déficitaire", l'obtention des équations de couche-mince par développement asymptotique nécessite en effet que non seulement la vitesse normale visqueuse $\bar{u}^3$ soit petite, mais aussi que la vitesse normale non-visqueuse fictive superposée u^3 soit elle-même petite, ce qui est réalisé par choix du "Référentiel de Déplacement". Dans ce référentiel, qui étend la validité des équations de couche-mince au calcul des décollements-massifs, la direction x^3 devient sensiblement normale à la surface de déplacement (inconnue avant calcul), $x^3 = 0$ étant alors la surface de déplacement et non-plus à la paroi. De plus il est possible sans restriction majeure, dans ce référentiel, de tronquer encore les équations de couche-mince au niveau de l'équation de mouvement en x^3. Par développement en δ (jauge d'épaisseur de couche visqueuse), il vient au premier ordre :

$$\frac{\partial}{\partial x^j} J.\begin{bmatrix} \rho u^j - \bar{\rho}\bar{u}^j \\ \rho u^i u^j - \bar{\rho}\bar{u}^i \bar{u}^j \end{bmatrix} + \Gamma^i_{lk}. J.\begin{bmatrix} 0 \\ \rho u^l u^k - \bar{\rho}\bar{u}^l \bar{u}^k \end{bmatrix} = \frac{\partial}{\partial x^3}\begin{bmatrix} 0 \\ -J t^{i3} \end{bmatrix} \quad (2b)$$

$$i = 1, 2 \quad j = 1, 2, 3 \quad k, l = 1, 2$$

$$\frac{\partial}{\partial x^3}(p - \bar{p}) \cong - g_{3i}\, \Gamma^i_{lk}\left[\rho u^l u^k - \bar{\rho}\bar{u}^l \bar{u}^k\right] \cong 0 + \ldots\ldots \quad (2c)$$

2.1.4. Forme intégrale "Référentiel δ^*" (NS-couche-mince).

Une simple intégration en x^3 de (2b) entre la paroi $x^3 = Z_w(x^1, x^2)$ et l'infini fournit les équations intégrales, pleinement équivalentes. Notant q le module de la vitesse non-visqueuse, et ± les cotés supérieur/inférieur en cas de nappe de sillage :

$$\frac{\partial}{\partial x^j} J\rho.\begin{bmatrix} q\delta^j \\ q^2\theta^{ij} + q u^i \delta^j \\ u^j \delta - q\delta^j \end{bmatrix}^{\pm} + \frac{\partial Z_w}{\partial x^j} J.\begin{bmatrix} \rho u^j - \bar{\rho}\bar{u}^j \\ \rho u^i u^j - \bar{\rho}\bar{u}^i \bar{u}^j \\ \bar{\rho}\bar{u}^j \end{bmatrix}^{\pm}_{x^3 = Z_w}$$

$$+ \Gamma^i_{jk} J\rho.\begin{bmatrix} 0 \\ q^2\theta^{jk} + q u^j \delta^k \\ 0 \end{bmatrix}^{\pm} = J.\begin{bmatrix} \rho u^3 - \bar{\rho}\bar{u}^3 \\ \rho q^2 \dfrac{Cf^i}{2} + \rho u^i u^3 - \bar{\rho}\bar{u}^i \bar{u}^3 \\ \rho q E + \bar{\rho}\bar{u}^3 \end{bmatrix}^{\pm}_{(x^1, x^2, Z_w)}$$

$$i, j, k = 1, 2 \quad (3a)$$

$$\bar{p}(x^1, x^2, x^3) = p(x^1, x^2, x^3) + (p - \bar{p})_{2^{nd}\ order} + \ldots$$

$$\bar{h}_T(x^1, x^2, x^3) = h_T(x^1, x^2, x^3)$$

avec :

$$J\,\rho.\begin{bmatrix} q\delta^j \\ q^2\theta^{ij} + q u^i \delta^j \end{bmatrix}^{\pm}_{(x^1, x^2, Z_w)} = \int_{Z_w}^{\infty} J.\begin{bmatrix} \rho u^j - \bar{\rho}\bar{u}^j \\ \rho u^i u^j - \bar{\rho}\bar{u}^i \bar{u}^j \end{bmatrix}^{\pm} dx^3 ,$$

$$E = \left[\frac{1}{\rho q} \; \frac{\dfrac{\partial}{\partial x^3}(t^{i3})}{\dfrac{\partial}{\partial x^3}(u^i - \bar{u}^i)}\right]_{(x^1, x^2, \delta)}$$

Les équations intégrales 3D peuvent s'écrire, soit le long de coordonnées curvilignes (x^1, x^2) tracées sur la surface de déplacement, soit le long de coordonnées curvilignes (s^1, s^2) tracées sur la paroi et dont la projection orthogonale sur la surface de déplacement coincide avec (x^1, x^2). Les vitesses (visqueuse et non-visqueuse) normales à la surface de déplacement, notées $\bar{u}^3$ *et* u^3, doivent être distinguées des vitesses (visqueuse et non-visqueuse) normales à la paroi, notées $\bar{w}_n$ *et* w_n. Notant ψ l'angle (Ox^3, *normale a la paroi*) :

$$\frac{1}{\cos\psi^j}\,\frac{\partial}{\partial s^j} J\rho.\begin{bmatrix} q\delta^j \\ q^2\theta^{ij} + q u^i \delta^j \\ u^j \delta - q\delta^j \end{bmatrix}^{\pm} + \Gamma^i_{jk} J\rho.\begin{bmatrix} 0 \\ q^2\theta^{jk} + q u^j \delta^k \\ 0 \end{bmatrix}^{\pm}$$

$$= \frac{J}{\cos\psi}\begin{bmatrix} \rho w_n - \bar{\rho}\bar{w}_n \\ \rho q^2 \dfrac{Cf^i}{2}\cos\psi + \rho u^i w_n - \bar{\rho}\bar{u}^i \bar{w}_n \\ \rho q E \cos\psi + \bar{\rho}\bar{w}_n \end{bmatrix}^{\pm}_{(x^1, x^2, Z_w)} \quad (3b)$$

$$i, j, k = 1, 2$$

$$\frac{\partial}{\partial s^1} = \cos\psi^1 . \frac{\partial}{\partial x^1}, \qquad \frac{\partial}{\partial s^2} = \cos\psi^2 . \frac{\partial}{\partial x^2}$$

En plus des équations de masse et de mouvement, le système (3) écrit ici, choisi de rang-4, inclut l'équation d'entrainement, qui est une collocation le long de la surface $x^3 = \delta_{(x^1, x^2)}$ avec les équations locales de mouvement du système (2) selon x^1 ou x^2. Contrairement à de nombreuses affirmations, les équations intégrales sont *moins restrictives* que celles de Prandtl, parce que $\bar{p}, \bar{h}_T, p, \rho, u^i, h_T, p_T$ sont ici supposés être évolutifs selon x^3 au sein de la couche visqueuse, Le Balleur [4][9][22], cette extension ne résultant que du choix optimal de définition des épaisseurs intégrales ("Formulation-Déficitaire" par rapport aux flux). Notons que seules les équations intégrales de mouvement (et donc d'entrainement) sont ici approchées en couche-mince. L'équation de continuité de (3a)(3b) est une intégrale *exacte*, valable aussi pour les équations de Navier-Stokes complètes, Le Balleur [4][9][22]. Elle détermine l'exact *effet de déplacement généralisé*, traduit par la vitesse normale non-visqueuse à la paroi w_n, ou bien par un saut de vitesse normale non-visqueuse $\langle w_n \rangle$ sur les nappes de sillage. Pour simplifier, on se limitera dans la suite au cas :

$$\cos\psi^2 = 1, \qquad \cos\psi^1 = \cos\psi = \left\{1 - \left(\frac{w_n}{q}\right)^2\right\}^{\frac{1}{2}}$$

ce qui correspondrait en 3D aux cas où l'écart entre surface de déplacement et paroi dépendrait peu de x^2 ou s^2.

Enfin, l'intégration en x^3 de la relation (2c) fournit $(p - \bar{p})_{2^{nd}\ order}$ en (x^1, x^2, Z_w) ainsi que des sauts de pression non-visqueux correctifs sur les nappes de sillages (*effet de courbure généralisé*). Celui-ci, en cas d'approximation de couche-mince, peut être, soit *négligé* au *premier* ordre, soit modélisé comme un terme d'ordre supérieur. Dans cette seconde hypothèse, on peut en particulier adopter la modélisation de "Courbure-induite" suggérée vers 1980, Le Balleur [4][7][14][1], moins restrictive que la théorie de couche limite, et en meilleur accord avec les théories asymptotiques de bord de fuite données par Melnik [2][17][18].

2.2. Choix d'une "métrique de surface locale".

Les équations curvilignes ci-dessus sont générales et s'appliquent dans tout système de coordonnées curviligne ou orthogonal. L'expérience a cependant montré qu'il est avantageux, contrairement aux usages habituels en couche limite, de sélectionner une "métrique de surface locale" simple sur la paroi (s^1, s^2) (ou le long de la surface de déplacement x^1, x^2), pour les calculs de couche visqueuse.

Utilisant la trace à la paroi du maillage non-visqueux i, j, k, les coordonnées de surface locales sont ici définies en choisissant pour coordonnée s^1 l'abscisse curviligne le long des lignes $(j = cst, k = 1)$, et pour coordonnée s^2 l'abscisse curviligne *dans la direction orthogonale à* s^1 *tracée sur la surface*. Ce choix de métrique, avantageux pour la simplification majeure des équations ($\Gamma^i_{jk} = 0$), apporte de surcroît des avantages de précision numérique après discrétisation des équations. La contre-partie de ces avantages est évidemment que les lignes $(i = cst, k = 1)$ ne sont plus des lignes $s^1 = cst$.

2.3. Troncature visqueuse "3D-approchée" (2.75D).

Dans de nombreux calculs visqueux tridimensionnels, il reste strictement hors de portée d'utiliser des maillages de discrétisation offrant la même densité de noeuds dans les 2 directions tangentielles (s^1, s^2) aux couches visqueuses.

Pour le problème discrétisé, le grand allongement inévitable des mailles (en envergure par exemple sur un calcul de voilure), même s'il est compatible avec la tridimensionnalité du fluide non-visqueux, conduit en général, pour le problème numérique visqueux, à rendre illusoire l'accès à la tridimensionnalité complète. Les équations visqueuses 3D-complètes, une fois discrétisées sur des mailles à fort allongement, réintroduisent numériquement en effet des troncatures non-controlées, voire des distorsions d'aliasing et de dissipation numérique.

Pour ces configurations de calcul 3D-visqueux à fort allongements de mailles, c'est à dire pour tous les cas où la tridimensionnalité du maillage et de la discrétisation ne peut suivre la tridimensionnalité des équations analytiques, il parait plus avantageux de controler analytiquement les troncatures de tridimensionnalité visqueuse inévitables. La méthodologie d'interaction visqueux-non visqueux offre à nouveau un avantage, en pouvant découpler les troncatures numériques visqueuses et non-visqueuses.

On choisit ici de conserver les pleines équations 3D pour la partie non-visqueuse, et d'introduire une troncature visqueuse 3D-approchée, qualifiée de troncature visqueuse "2.75D". En chaque noeud de calcul visqueux, on introduit une direction tangentielle à la couche visqueuse λ^* dans laquelle les dérivées sont tronquées. Cette troncature n'a qu'un faible poids sur les équations discrétisées, étant donné l'aliasing qui serait de toute manière introduit par l'allongement des mailles et par une discrétisation en s^2 insuffisante à l'échelle visqueuse

$$\cos\lambda^* \cdot \frac{\partial}{\partial s^1} + \sin\lambda^* \cdot \frac{\partial}{\partial s^2} = 0 \qquad (3c)$$

Cette troncature visqueuse "2.75D" étant appliquée de manière "locale", ce qui la rend similaire dans ses effets à une troncature numérique par maillage grossier, tous les paramètres calculés, visqueux et non-visqueux, restent totalement évolutifs dans la direction λ^* et donc parfaitement tridimensionnels. Suivant le choix de λ^*, la direction locale de troncature de dérivée peut aller de la simple direction s^2 définie par le maillage $(\sin\lambda^* = 1)$, à toute autre direction locale aérodynamiquement remarquable, par exemple perpendiculaire aux lignes de courant non-visqueuses.

3. MODELES TURBULENTS 3D.

Le nombre d'équations intégrales ci-dessus donne un système fermé pour le calcul du champ local visqueux lorsque les profils de vitesse moyenne ainsi que les profils de turbulence sont supposés relever d'une modélisation à 3 paramètres (δ, a^1, a^2). Avec un modèle de turbulence à N-équations de transport, qui augmente de N le rang du système (3) ainsi que le nombre de variables-indépendantes, ce rang-3 concerne *seulement l'écoulement moyen*. Les paramètres (δ, a^1, a^2) sont fonctions de (x^1, x^2).

3.1. Profils de vitesse paramétriques.

On utilise la description analytique paramétrique originale de rang-3 des profils de vitesse moyenne turbulents suggérée précédemment, Le Balleur [7][14][9][1], d'abord en 2D puis en 3D. La modélisation a été construite pour inclure tant les écoulements attachés que massivement décollés, voir [14]. Elle est ici appliquée sous sa forme la plus complète [1], avec sous-couche laminaire et terme D d'amortissement, Fig. 2 :

$$\left(\frac{\bar{u}^i}{q}\right)_{(a^1, a^2, \delta, x^3)} = \frac{u^i}{q} - W^i_{(a^1, a^2)} \cdot F\left(\frac{x^3}{\delta}\right) \qquad \textit{loi de sillage}$$

$$+ \; T^i_{(a^1, a^2)} \cdot \left(1 - D\right) \cdot \frac{1}{k} \left(\frac{Cf}{2}\right)^{1/2} Log\left(\frac{x^3}{\delta}\right) \qquad \textit{loi turbulente de paroi}$$

$$-\left(\frac{u^i}{q} - W^i\right) \cdot D + T^i \, D \, \frac{Cf}{2} \, R_\delta\left(\frac{x^3}{\delta}\right) \qquad \textit{loi laminaire de paroi}$$

$$i = 1, 2 \qquad (4a)$$

$$avec : \quad F(z) = F^*\left(\frac{z - z^*}{1 - z^*}\right), \qquad F^*(z) = \left(1 - z^{1.5}\right)^2,$$

$$z^* = \text{Fonction de } \left(\frac{\delta^i}{\delta}\right)_{incompressible}, \qquad k = 0.41 \quad .$$

Les paramètres de forme indépendants a^i choisis peuvent par exemple être ceux du repère orthogonal tangent aux lignes de courant non-visqueuses.

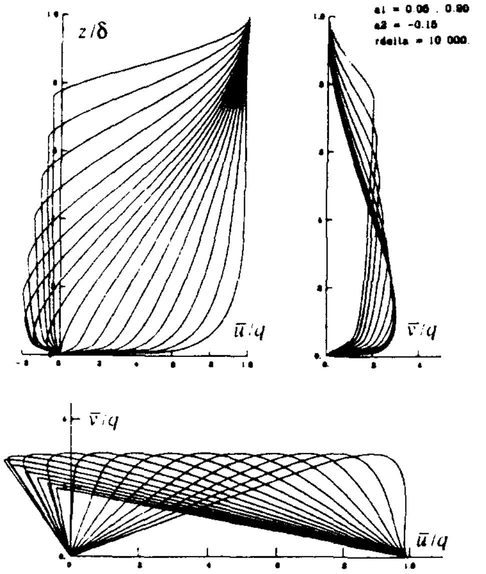

Fig. 2. Profils de vitesse paramétriques 3D-turbulents, discrétisés à chaque station (a^1 = .05-.90, a^2 = −.15, $R_\delta = 10^4$)

Les expressions de T^i, W^i, Cf^i, D, z^* sont détaillées dans [1][14]. Le modèle reprend l'idée de forme composite additive (loi de paroi - loi de sillage) proposée par Coles [16] pour les écoulements attachés, mais la forme a été ici généralisée aux écoulements décollés, et les fonctions de sillage F^*, F sont différentes. La simple loi de sillage de Coles serait totalement irréaliste en écoulement massivement décollé. La modélisation $z^*(\delta^i/\delta)$ est déduite de l'analyse des singularités de couche limite au décollement, Le Balleur [5], de l'analyse des cônes caractéristiques des systèmes d'équations et de la récupération de "l'influence amont" en écoulement décollé [14][5][8], ainsi qu'enfin de la capacité à décrire le cas-limite des couches de mélanges 2D isobares, Le Balleur [14].

Le vecteur unitaire T^i est sensiblement parallèle au frottement Cf^i, et Cf est déduit d'une modélisation de loi de paroi "universelle" projetée sur T^i (le profil n'est pas une courbe plane dans la région de paroi), voir [1].

$$\tilde{u}^i_w = \frac{u^i}{q} - \frac{a^i}{A}, \qquad a^i = \left[\frac{\delta^i}{\delta}\right]_{incompressible}, \qquad A = \int_0^1 F(z)\,dz$$

$$\left[\frac{Cf}{2}\right]^{1/2}\left[Log\left(R_\delta\left[\frac{Cf}{2}\right]^{1/2}\right) + 5.25k - \frac{1}{A}\right] = k\,.\,\|\tilde{u}_w\| \qquad (4b)$$

La compressibilité ne modifie pas les profils de vitesse. Les profils de densité sont ici déduits de la vitesse dans l'approximation adiabatique isenthalpique $\bar{h}_T = h_T$. L'entrainement n'est pas modifié. L'effet de compressibilité retenu pour le frottement et la dissipation globale s'écrit :

$$Cf^i_{compressible} = Cf^i\left[1 + 0.5\left(\gamma - 1\right)M^2\right]^{-\frac{1}{2}}$$

Pour les régions laminaires enfin, les relations de fermeture sont déduites des solutions auto-semblables, Le Balleur [7].

3.2. Modèle de turbulence d'équilibre.

Lorsque l'hypothèse de turbulence d'équilibre est suffisante, l'entrainement exact E défini par (3a) a pu être modélisé à partir du modèle de profils de vitesse turbulents ci-dessus et d'un modèle de longueur de mélange, Le Balleur [7][9][14][1]. L'expression finale de ce modèle original d'entrainement d'équilibre E_{eq} est donnée dans [1]. Il a permis d'étendre la modélisation de l'entrainement aux écoulements 2D ou 3D décollés, même massivement, sans faire appel à l'empirisme.

On utilise ici l'ajustement le plus récent suggéré pour les constantes ainsi que pour l'effet de nombre de Reynolds [1].

$$E_{eq} = C_4\,.\left[1 - \tilde{u}^1_w\right] + C_5\,.\left[\frac{Cf^1}{2}\right]^{1/2}.\,\frac{Cf^1}{2} \qquad (4c)$$

$$C_4 = 0.062, \quad G_0 = 6.5, \quad C_5 = C_{5\,(C_4,\,G_0,\,a_0^1,\,Cf_0)}$$

La direction x^1 est ici celle des lignes de courant non-visqueuses. a^1_0, Cf_0 correspondent aux valeurs de a^1, Cf calculées pour la plaque plane en incompressible, au même R_δ et avec un paramètre de Clauser G_0. Les deux seules données du modèle sont la constante C_4, qui est proportionnelle au carré du niveau de longueur de mélange dans les couches limites d'équilibre, et la pseudo-constante G_0, paramètre de Clauser de plaque plane (qui peut être fonction de R_δ).

3.3. Modèle de turbulence 2-équations k-tau.

Les effets de turbulence hors-équilibre sont calculés en ajoutant le modèle à 2 équations de transport de Le Balleur [7][1], présentement utilisé en théorie 2D (par tranches) le long de x^1. Le modèle peut être utilisé aussi bien dans les méthodes-locales (calcul de t^{ij}), et dans les méthodes-intégrales (entrainement et dissipation).

Ce modèle suggéré en 1981 a pour première originalité de "forcer" le modèle de Launder-Rodi par la modélisation ci-dessus des profils de vitesse, ce qui notamment le rend mieux adapté aux écoulements décollés. Sa seconde originalité est d'effectuer un calcul en termes d'écart aux valeurs données par le modèle d'équilibre (contraintes t^{i3}_{eq} et entrainement E_{eq}). Cet écart à l'équilibre est supposé être invariant en direction x^3, variable en directions x^1, x^2, et être calculé à partir de 2 équations (intégrales) de transport. Celles-ci calculent des effets d'histoire pour l'énergie cinétique turbulente moyennée en x^3 notée $\tilde{k}(x^1, x^2)$, et pour la contrainte de cisaillement de Reynolds moyennée en x^3 notée $\tilde{\tau}(x^1, x^2)$:

$$\textit{Contrainte locale} \;:\; t^{13} = \frac{\tilde{\tau}\,(x^1, x^2)}{\tilde{\tau}_{eq}\,(x^1, x^2)}\,.\left[t^{13}_{eq}\right](x^1, x^2, x^3)$$

$$t^{13}_{eq} = \lambda_1\lambda_2\lambda_3\,\rho l^2\left|\frac{\partial \bar{u}^1}{\partial x^3}\right|\frac{\partial \bar{u}^1}{\partial x^3} = \lambda_1\lambda_2\lambda_3\,\rho\,\nu_t\,\frac{\partial \bar{u}^1}{\partial x^3}$$

$$\textit{Entrainement global} \;:\; E = \frac{\tilde{\tau}}{\tilde{\tau}_{eq}}\,E_{eq}$$

$$\textit{Dissipation globale} \;:\; \Phi = \frac{\tilde{\tau}}{\tilde{\tau}_{eq}}\,\Phi_{eq}$$

$$\delta\frac{\partial \tilde{k}}{\partial t} + \left[\delta - \delta_l\right]\frac{\partial \tilde{k}}{\partial x^1} = \frac{\tilde{\tau}}{\tilde{\tau}_{eq}}\,\frac{q^3}{2}\,\Phi_{eq} - \tilde{\varepsilon}\delta$$

$$\delta\,\frac{\partial \tilde{\tau}}{\partial t} + \left[\delta - \delta_l\right]\frac{\partial \tilde{\tau}}{\partial x^1} = 1.5\,\frac{\tilde{\varepsilon}\delta}{\tilde{k}}\left[\left(\frac{\tilde{k}}{\tilde{k}_{eq}}\right)^2\frac{\tilde{\varepsilon}_{eq}}{\tilde{\varepsilon}}\,\tilde{\tau}_{eq} - \tilde{\tau}\right] \qquad (4d)$$

$$\left(\frac{\tilde{\varepsilon}}{\tilde{\varepsilon}_{eq}}\right) = \left(\frac{\tilde{k}}{\tilde{k}_{eq}}\right)^{1.5}$$

avec :
$$\delta\tilde{\varepsilon}_{eq} = 0.5\, q^3 \Phi_{eq} = \int_0^{\delta} t_{eq}^{13} \frac{\partial \bar{u}^1}{\partial x^3}\, dx^3$$

$$\tilde{k}_{eq} = q^2 \left[0.045\, \lambda_1\lambda_2\lambda_3 \left(1-\bar{u}_w^1\right) \Phi_{eq}\right]^{0.5},$$

$$\tilde{\tau}_{eq} = \lambda_1\lambda_2\lambda_3\, q^2\left[\, 0.09 \left(1 - \bar{u}_w^1\right)\right]^2$$

$$\bar{u}_w^1 = 1 - \frac{a^1}{A}, \quad a^1 = \int_0^{\infty} \frac{u^1-\bar{u}^1}{q}\, \frac{dx^3}{\delta},$$

$$\tilde{\delta} = \left(1-z^*\right) \delta, \quad z^* \cong \max\left[\, 0\, ,\, 2.406\left(a^1- 0.5844\right)\right]$$

$$\delta_l = \delta \left[1 - A^*(1 -\bar{u}_w^1)\right], \quad A^* = \int_0^1 F^*(z)\, dz = 0.45$$

$$\Phi_{eq} \cong Cf^1\, \bar{u}_w^1 + 0.018 \left(1 - \bar{u}_w^1\right)^3$$

Dans ce modèle, $\tilde{\delta}$, $\bar{u}_w^1$ représentent les échelles de longueur et de vitesse effectives de la couche turbulente, telles qu'analysées par la modélisation ci-dessus des profils de vitesse moyenne, en évitant l'empirisme d'un modèle de type Baldwin-Lomax. $l(x^3/\delta)$ et ν_t sont une longueur de mélange et une viscosité turbulente, données par des modèles d'équilibre. $\lambda_1, \lambda_2, \lambda_3$ sont des coefficients caractérisant les divers effets de turbulence d'équilibre, voir Le Balleur [7]. Ils sont proches de 1 pour les couches limites habituelles. λ_1 est proche de 2 pour les sillages habituels, λ_2 et λ_3 caractérisant les effets de courbure et de turbulence extérieure du modèle, précisés dans [7].

4. METHODE NUMERIQUE VISQUEUSE.

La méthode numérique de couche visqueuse proposée est de nature hybride entre méthodes-intégrales et méthodes-locales. Les grandeurs (vitesse, densité,..), même modélisées, sont en effet discrétisées à chaque station selon la normale avec un maillage auto-adaptatif. La méthode numérique discrétise donc des profils paramétriques selon x^3, et un système d'équations intégrées en x^3 dans l'espace (x^1, x^2). Les schémas de discrétisation, variables avec la densité locale du maillage en x^1, ont la capacité d'être non-linéairement implicites en (x^1, x^3). Ces schémas sont x^1*–marching*, l'absence de la capacité multi-marching "MZM" [24][25] étant ici compensée par la possibilité de calcul en modes "*direct*" et "*inverse*".

4.1. Méthode hybride intégrale/locale.

A chaque station (x^1, x^2), numériquement, les profils de vitesse paramétriques 3D-turbulents des relations (4) sont discrétisés selon x^3, entre $x^3 = Z_w$ et $x^3 = \delta$, avec un maillage en x^3/δ qui est auto-adaptatif à δ et à la forme du profil de vitesse, caractérisée par le paramètre a^1. La discrétisation auto-adaptative utilise présentement 37 noeuds, optimisés en direction x^3 et dépendants de a^1, avec des schémas implicites de trapèzes pour lier les grandeurs locales et intégrales. La densité est déduite de la vitesse par l'approximation adiabatique isenthalpique $\bar{h}_T = h_T$.

De station en station dans l'espace (x^1, x^2), le système d'équations intégrées en x^3, valable aussi dans le cas d'une pure méthode-locale, est discrétisé sur le maillage curviligne (x^1, x^2) de surface de déplacement, projection selon x^3 du maillage curviligne de paroi (s^1, s^2). Notons que les 2 maillages liés, de paroi (s^1, s^2) et de surface de déplacement (x^1, x^2), se différencient en cas de décollement massif, et que l'intégration en x^3 (normale à la couche visqueuse) n'est alors plus normale à la paroi, Le Balleur [1][14]. Les équations en (x^1, x^2) projetées sur la paroi (s^1, s^2) s'écrivent :

$$\left\{A_{j\,(a^1,\, a^2,\, m,\, \delta)}^{1i} \frac{\partial \hat{f}^j}{\partial s^1} + A_{j\,(a^1,\, a^2,\, m,\, \delta)}^{2i} \frac{\partial \hat{f}^j}{\partial s^2} = b_1^i + b_2^i + b_3^i \right\}_{(x^1,\, x^2,\, Z_w)}^{\pm}$$

$$i = 1, 6, \quad j = 1, 8, \qquad (5a)$$

$$\hat{f}^j = \begin{bmatrix} \hat{m} \\ \hat{\alpha} \\ \hat{h}_T \\ \hat{p}_T \\ \delta \\ a^1 \\ a^2 \\ \tilde{k} \\ \tilde{\tau} \end{bmatrix}, \quad b_1^i = \begin{bmatrix} \dfrac{\hat{w}_n}{q} - \dfrac{\bar{\rho}\bar{w}_n}{\rho q} \\ \dfrac{u^k}{q}\dfrac{\hat{w}_n}{q} - \dfrac{\bar{\rho}\bar{u}^k\bar{w}_n}{\rho q^2} \\ \dfrac{\bar{\rho}\bar{w}_n}{\rho q} \\ 0 \\ 0 \end{bmatrix}, \quad b_2^i = \begin{bmatrix} 0 \\ \dfrac{Cf^k}{2}\cos\psi \\ E_{eq}\, \dfrac{\tilde{\tau}}{\tilde{\tau}_{eq}} \cos\psi \\ b^5 \\ b^6 \end{bmatrix}$$

$$\sin\psi = \hat{w}_n \,/\, q\,, \qquad k = 1, 2$$

Rappelons que la vitesse normale à la paroi visqueuse est notée $\bar{w}_n$. La vitesse normale à la paroi non-visqueuse est ici notée $\hat{w}_n$. Les termes b_3^i sont des termes éventuels de métrique non-orthogonale. La présente méthode numérique hybride intégrale/locale prend pour inconnues indépendantes les grandeurs non-visqueuses de paroi, vitesse $\hat{q}$ ou nombre de Mach réduit $\hat{m} = .5\,(\gamma-1)\,\hat{M}^2$, vitesse normale à la paroi $\hat{w}_n/q$ (déplacement), angle $\hat{\alpha}$ entre vitesse et axe-s^1 sur la surface (s^1, s^2), pression totale $\hat{p}_T$, et enthalpie totale $\hat{h}_T$, plus les inconnues indépendantes purement visqueuses, épaisseur de couche visqueuse δ, paramètres de forme $a^1 = (\delta^1/\delta)_{incompressible}$, $a^2 = (\delta^2/\delta)_{incompressible}$, et les paramètres de turbulence $\tilde{k}$, $\tilde{\tau}$.

Compte-tenu de la troncature 3D-approché, les dérivées en s^2 sont liées aux dérivées en s^1 par la relation (3c). Il vient :

$$\left\{\left[A_j^{1i} - \frac{\cos\lambda^*}{\sin\lambda^*}\, A_j^{2i}\right]_{(a^1,\, a^2,\, m,\, \delta)} \cdot \frac{\partial \hat{f}^j}{\partial s^1} = b_1^i + b_2^i + b_3^i \right\}_{(x^1,\, x^2,\, Z_w)}^{\pm}$$

$$i = 1, 6, \quad j = 1, 8, \qquad (5b)$$

La discrétisation en (s^1, s^2) de la présente méthode 3D est déduite de la discrétisation robuste en (s^1, x^3) développée depuis de nombreuses années, Le Balleur [7][9][1], s^1*–marching* et non-linéairement implicite. Les schémas numériques en direction s^1 sont de second-ordre et à 2-noeuds de type "trapèzes-amont". Les schémas de second-ordre de méthode des trapèzes en direction s^1 sont commutés vers un schéma plus robuste de premier-ordre décentré-amont en s^1, là où le maillage devient grossier (grandes valeurs de $\Delta s^1/\delta$). Pour des valeurs plus élevées de $\Delta s^1/\delta$, un sous-maillage en s^1 est ajouté (zones non-décollées). Une technique de Newton est enfin introduite pour résoudre itérativement les pleines non-linéarités induites par A_j^{1i}, A_j^{2i}, b_k^i, en utilisant une estimation approchée numérique des Jacobiens $\partial A_j^{1i}/\partial f$, $\partial A_j^{2i}/\partial f$, $\partial b_k^i/\partial f$, avec $f \sim (\delta, a^1, a^2)$, ce qui rend la discrétisation non-linéairement implicite en (s^1, x^3).

Les équations et schémas ci-dessus fournissent également une résolution numérique des sillages visqueux, avec leur pleine dissymétrie, moyennant doublement du rang du système (réunion des demi-sillages supérieur et inférieur, notés ± de part et d'autre de la surface des minima de vitesse), Le Balleur [7]. Ce calcul dissymétrique complet est ici effectué en 2D. Le traitement simplifié de la seule partie symétrique des équations de sillage [7], qui ramène le calcul de sillage à un système de même rang que la couche limite, et qui est obtenu dans les relations (5a)(5b) avec $Cf = 0$, $\bar{w}_n = 0$, $a_+^1 = a_-^1$, $f^j = .5\,(\,f_+^j + f_-^j\,)$, est ici utilisé en 3D.

Enfin, comme des itérations additionnelles sur le solveur numérique visqueux sont nécessaires pour le couplage, le problème non-linéaire visqueux complet (5a)(5b) n'est pas résolu à chaque itération de couplage, et des solutions linéarisées, avec les matrices A_j^{1i} , A_j^{2i} gelées à leurs valeurs à l'itération de couplage précédente, sont réalisées à la plupart des itérations de couplage, à titre de technique d'accélération de convergence.

4.2. Modes Direct / Inverse.

Les cinq inconnues non-visqueuses du problème numérique visqueux (5a)(5b), notées avec un signe chapeau, ($\hat{m}$, $\hat{w}_n/q$, $\hat{h}_T$, $\hat{p}_T$, $\hat{\alpha}$), doivent être couplées au quantités correspondantes du problème non-visqueux, qui sont notées (m, w_n/q, h_T, p_T, α).

Avant de réaliser ce couplage complet sur les 5 inconnues non-visqueuses, ce qui est obtenu itérativement par l'algorithme de couplage, des calculs visqueux découplés sont réalisés, dans lesquels 4 inconnues non-visqueuses seulement sont couplées. On impose alors au système (5a)(5b) l'enthalpie totale ($\hat{h}_T = h_T$), la pression totale ($\hat{p}_T = p_T$), et la direction de la vitesse ($\hat{\alpha} = \alpha$), plus une condition additionnelle à définir.

Une commutation entre différentes conditions additionnelles doit être introduite (modes direct-inverses) afin de surmonter le problème de singularité de décollement, comme c'est déjà le cas en 2D, Le Balleur [5]. En tridimensionnel, le problème de singularité s'identifie avec le calcul par marche en espace, et avec le respect des domaines de dépendance imposés par les cônes caractéristiques des systèmes hyperboliques (5a)(5c) ou (5b)(5c) (voir ci-dessous). En écoulement attaché, le système visqueux en mode "direct" peut être résolu par marche en espace, mais selon les lignes de courant non-visqueuses. La condition additionnelle est alors le nombre de Mach ($\hat{m} = m$). Le maintien d'une résolution x^1*–marching*, décollement inclus, demande qu'un mode "inverse" soit commuté avant que le cône de dépendance du mode direct n'interdise ce mode (et donc bien avant le cas limite de décollement-2D). La condition additionnelle imposée est alors la vitesse de transpiration non-visqueuse ($\hat{w}_n/q = w_n/q$). Malgré la résolution x^1*–marching*, l'influence amont d'origine visqueuse (décollement) est pleinement recouvrée à l'étape de couplage, où l'on réalise simultanément ($\hat{h}_T = h_T$, $\hat{p}_T = p_T$, $\hat{m} = m$, $\hat{w}_n/q = w_n/q$, $\hat{\alpha} = \alpha$).

Au total, à chaque noeud (i, j, 1) et itération de couplage N, le système discrétisé (5a)(5b) est fermé par 4 relations (5c), discrétisées par des schémas centrés pour ($\partial\hat{m}/\partial s^1$) et éventuellement décentrés-aval pour ($\partial m/\partial s^1$) :

$$\hat{\alpha} = \alpha\ , \quad \hat{h}_T = h_T\ ,\ \hat{p}_T = p_T\ , \qquad \begin{cases} \varepsilon = 0 & : \text{Direct} \\ \varepsilon = 1 & : \text{Inverse} \end{cases}$$

$$\varepsilon\left[\frac{\hat{w}_n}{q} - \frac{w_n}{q}\right]^N_{i,j,1} + (1-\varepsilon)\left[\frac{\partial\hat{m}}{\partial s^1} - \frac{\partial m}{\partial s^1}\right]^N_{i,j,1} = 0 \qquad (5c)$$

La commutation d'un mode direct ($\varepsilon = 0$) vers un mode inverse ($\varepsilon = 1$) est présentement connectée aux paramètres de forme du profil de vitesse. Elle est liée tantôt comme en bidimensionnel au seul paramètre en direction des lignes de courant non-visqueuses ($a^1 > 0.28$ par exemple), Le Balleur [7][1], tantôt aux 2 paramètres longitudinaux et transversaux, de façon à ce que le cône caratéristique du mode "direct" estimé d'après a^1, a^2 (voir ci-dessous) reste, à chaque station x^1 où $\varepsilon = 0$, positionné en amont de la direction de troncature λ^*.

4.3. Singularités 3D. Cônes caractéristiques (Direct/Inverse).

Les systèmes 3D-complet (5a)(5c) sont hyperboliques en espace, en mode direct et en mode inverse, et des domaines de dépendance, définis par des cônes caractéristiques dans l'espace (s^1, s^2), doivent être respectés par les méthodes de marche en espace, aussi bien en mode direct qu'en mode inverse.

Les systèmes 3D-approchés direct/inverse issus de (5b)(5c), qui peuvent s'écrire toujours sous la forme (5b), et qui n'introduisent que la dérivée en s^1, sont singuliers lorsque :

$$\det\left[A_j^{1i} - \frac{\cos\lambda^*}{\sin\lambda^*}\,A_j^{2i}\right] = 0 \qquad (5d)$$

En mode direct aussi bien qu'en mode inverse, l'examen de la relation (5d) montre que la condition de singularité du système 3D-approché (5b)(5c) est strictement identique à celle de recherche d'une direction caractéristique λ^* du système 3D-complet (5a)(5c). Cette identité entre équations aux valeurs propres pour les singularités du système 3D-approché, et pour le cône caractéristique du système 3D-complet, révèle que le système 3D-approché n'introduit aucune perte d'information au niveau des domaines de dépendance par rapport au système 3D-complet, ces domaines de dépendance étant *identiques*. Il révèle d'autre part que le franchissement des singularités du système 3D-approché (5b)(5c) en mode direct s'identifie à la naissance d'une influence-amont selon x^1 (pour la direction de troncature λ^* considérée), et par conséquent à la nécessité de commuter le calcul x^1*–marching* vers le mode inverse.

La modélisation issue des profils de vitesse (4a) peut être utilisée pour analyser les singularités et directions caractéristiques, comme effectué à l'origine en 2D et 2D-instationnaire, Le Balleur [5]. Le calcul analytique des directions caractéristiques a été effectué avec le modèle (4a) simplifié par $Cf = 0$, $D = 0$, $z^* = 0$, comme déja utilisé en 2D dans [5]. La comparaison du cône caractéristique en mode direct, qui s'écrit en repère orthogonal tangent aux lignes de courant non-visqueuses comme l'enveloppe des directions :

$$\frac{dx^2}{dx^1} = \left[\frac{-a^2}{0.4014 - a^1}\ ,\ \frac{-a^2}{0.6417 - a^1}\ ,\ \frac{-a^2}{1.599 - a^1}\ ,\ 0\right],\quad (\textit{direct})$$

et du cône en mode inverse, qui s'écrit dans le même repère :

$$\frac{dx^2}{dx^1} = \left[\frac{-a^2}{0.6417 - a^1}\ ,\ \frac{-a^2}{1.283 - a^1}\ ,\ 0\ ,\ \frac{a^2}{a^1}\right],\quad (\textit{inverse})$$

avec $0 < a^1 < \Lambda$, $\Lambda = 0.6417$, $2\Lambda = 1.283$, $1-(1-\Lambda)^{1/2} = 0.4014$, $1+(1-\Lambda)^{1/2} = 1.599$, a montré que le mode inverse réduisait l'ouverture du cône caractéristique par rapport au cône obtenu en mode direct dans les mêmes conditions (aux grands paramètres de forme a^1), et que le demi-angle maximal du cône caractéristique dans le plan (s^1, s^2) en mode inverse était borné à 90°, au lieu de 180° en mode direct, Le Balleur, Girodroux [21]. La borne 90° en mode inverse n'est atteinte de plus que pour une valeur infinie du paramètre de forme longitudinal H_i (soit $a^1 = \Lambda$). Ceci autorise, en mode inverse, la marche en espace en toutes circonstances, mais en direction des lignes de courant non-visqueuses.

De ce fait, la méthode 3D-approchée (5b) peut être aménagée pour éviter de franchir une singularité en mode inverse, ce qui équivaudrait à violer le domaine de dépendance imposé par le cône caratéristique. Pour ce faire, la direction de troncature λ^* est ici progressivement rapprochée de la perpendiculaire aux lignes de courant non-visqueuses, au fur et à mesure de l'accroissement d'ouverture du cône caratéristique en mode inverse, calculé en chaque noeud à partir de a^1, a^2 et des relations ci-dessus.

5. METHODE NUMERIQUE NON-VISQUEUSE.

La méthode numérique, nouvelle, est une extension en tridimensionnel de la méthode de traitement de l'équation du potentiel-complet, mise au point et introduite pour le décrochage 2D, Le Balleur [1].

Elle discrétise l'équation du potentiel développée en coordonnées curvilignes, sur un maillage structuré i, j, k quelconque, en transsonique :

$$\left[g^{mn} - \frac{u^m}{a}\frac{u^n}{a} \right] \cdot \left[\frac{\partial^2\Phi}{\partial x^m \partial x^n} - \frac{\partial x^l}{\partial X^a}\frac{\partial^2 X^a}{\partial x^m \partial x^n}\frac{\partial\Phi}{\partial x^l} \right] = 0$$

$$a = \left[\frac{1}{M_o^2} + \frac{\gamma-1}{2}\left(1 - q^2\right) \right]^{\frac{1}{2}}, \quad q^2 = g^{mn}\frac{\partial\Phi}{\partial x^m}\frac{\partial\Phi}{\partial x^n}$$

$$m, n, l, a = 1, 2, 3$$

La discrétisation i, j, k est effectuée avec la métrique $x^1 = i$, $x^2 = j$, $x^3 = k$. Elle utilise pour les dérivées du potentiel des schémas différences-finies centrés en subsonique, à 7 noeuds plus schémas de dérivées secondes croisées, complétés par un décentrement de type Murman-Cole aux noeuds supersoniques. L'évaluation des termes métriques est effectuée sur la même molécule de discrétisation que celle du potentiel, et avec les mêmes schémas pour les dérivées de X^m et de Φ, ce qui permet de se rapprocher des formulations volumes finis.

La résolution du système discret est faite par relaxation-ligne SLOR, avec traitement implicite des conditons limites sur la paroi, ainsi que des coupures de sillage. Le traitement du champ lointain (Dirichlet) est un comportement de type tourbillon plus source, évolutif en envergure, couplé à la circulation. La non-linéarité du potentiel est traitée par une méthode de point fixe, les composantes contravariantes u^m et la vitesse q étant déduites du potentiel au moyen de schémas centrés.

Les conditions aux limites sur la paroi et sur la nappe de sillage sont controlées par les effets visqueux de déplacement et de courbure. Le calcul sur maillage en C est effectué en prolongeant l'aile par une coupure (non-portante), numériquement traitée comme la nappe de sillage. Les conditions aux limites, discrétisées en demi-maille dans la dirextion $x^3 = k$, s'écrivent sur la paroi :

$$w_n = \left[g^{33} \right]^{-\frac{1}{2}} g^{3m}\frac{\partial\Phi}{\partial x^m}, \qquad \textit{déplacement}$$

Sur la nappe de sillage, les conditions de "saut" (notées < >) :

$$< w_n > = \left[g^{33} \right]^{-\frac{1}{2}} g^{3m} < \frac{\partial\Phi}{\partial x^m} >, \qquad \textit{déplacement}$$

$$< q > = \left[g_{11} \right]^{-\frac{1}{2}} < \frac{\partial\Phi}{\partial x^1} >, \qquad \textit{courbure}$$

utilisent l'approximation habituelle des techniques numériques "potentiel-complet" sur l'estimation du terme $<q>$.

6. ALGORITHMES DE COUPLAGE.

Les algorithmes font appel à une théorie numérique originale du couplage qui a pu être suggérée précédemment, Le Balleur [6][7][1][15], et qui est ici généralisée. Celle-ci traite le problème où des résolutions par domaines doivent être couplées par leurs conditions aux limites sur une surface commune (s^1, s^2) discrétisée en $(i, j, 1)$. La théorie est aussi applicable pour coupler 2 sous-domaines non-visqueux dans un pur calcul en fluide-parfait [1][15].

6.1. Théorie numérique du couplage. Stabilité.

La théorie numérique proposée pour le couplage de sous-domaines fournit une estimation de préconditionnement originale pour les opérateurs numériques de surface, "visqueux" et "non-visqueux", qui se trouvent introduits sur la surface-frontière $(i, j, 1)$ des champs tridimensionnels (i, j, k) à coupler. Dans le problème discret, ces opérateurs numériques de surface $(i, j, 1)$ sont ceux qui pourraient être obtenus par une élimination des noeuds intérieurs (i, j, k) sur les équations discrètes des champs visqueux et non-visqueux.

Les opérateurs de préconditionnement proposés donnent accès à une théorie de stabilité applicable à tout algorithme de couplage explicite, par exemple aux algorithmes "direct" et "inverse" de point fixe. Il donnent accès en outre au calcul des champs de coefficients de relaxation nécessaires pour stabiliser ces algorithmes.

La théorie a enfin permis la naissance d'algorithmes de couplage originaux plus élaborés, comme l'algorithme "Semi-inverse", Le Balleur [6][1][15]. L'algorithme "Semi-inverse" et ses généralisations résultent en effet d'un couplage exact (donc implicite), sur le nombre d'onde maximal, des opérateurs numériques de préconditionnement.

6.1.1. Préconditionnement : "Opérateur non-visqueux" (2.75D).

L'opérateur numérique de surface "non-visqueux" du couplage, dont l'évaluation par élimination des noeuds intérieurs est en général impraticable, est estimé ici par une stratégie de petites perturbations linéarisées analytique, avec décomposition de Fourier sur la surface $(i, j, 1)$ et filtrage numérique par la discrétisation.

La théorie, proposée précédemment en bidimensionnel puis en quasi-3D (2.5D), Le Balleur [6][3], est ici étendue en "2.75D". Elle considère des perturbations stationnaires isentropiques du champ de vitesse, en module, vitesse normale, direction, autour de la solution convergée finale $q_o(s^1, s^2)$, $w_{no}(s^1, s^2)$, $\alpha_o(s^1, s^2)$ sur la surface $(i, j, 1)$:

$$\begin{bmatrix} q' \\ w'_n \\ \alpha'_n \end{bmatrix}_{(x^1, x^2, x^3)} = \begin{bmatrix} q - q_o \\ w_n - w_{no} \\ \alpha - \alpha_o \end{bmatrix}$$

Elle suppose des équations de perturbation potentielles de type Prandtl-Glauert autour de la solution localement figée q_o, w_{no}, α_o. Les coordonnées curvilignes sont ici choisies avec x^1 en direction de la vitesse non-perturbée, la surface (x^1, x^2) étant une surface de courant (surface de déplacement), et la direction x^3 étant normale à (x^1, x^2) :

$$\left[g^{mn} - \frac{u^m}{a}\frac{u^n}{a} \right] \frac{\partial^2\phi'}{\partial x^m \partial x^n} + \frac{\partial^2\phi'}{\partial x^3 \partial x^3} = 0$$

$$m, n = 1,2$$

La théorie analyse les perturbations émanant de la surface (x^1, x^2) avec décomposition de Fourier sur la surface et filtrage par la discrétisation $(i, j, 1)$. Les perturbations, de nombres d'onde notés $(\alpha_1, \alpha_2, \alpha_3)$, ont alors un comportement tantôt exponentiel tantôt harmonique dans la direction x^3 :

$$\phi' = \phi \,.\, e^{I(\alpha_1 x^1 + \alpha_2 x^2 + \alpha_3 . x^3)}, \qquad \alpha_2 = 0 \quad (\textit{en 2.75D})$$

$$u'_1 = I\ \alpha_1.\phi', \quad u'_2 = I\ \alpha_2.\phi' = 0, \quad u'_3 = I\ \alpha_3.\phi', \qquad (I^2 = -1)$$

$$\frac{u'_3}{u'_1} = \frac{\alpha_3}{\alpha_1} = I\ \left[g^{11} - \left[\frac{u^1}{a}\right]^2 \right]^{\frac{1}{2}}$$

Sur la surface (x^1, x^2), en désignant respectivement par u, v les projections de la vitesse sur l'axe x^1 et sur sa normale :

$$q' = \left[g_{11} \frac{u^1}{q} + g_{21} \frac{u^2}{q} \right] . u'^1 = \frac{u}{q} \; u'^1$$

Finalement, pour tout nombre d'onde ($\alpha_1, \alpha_2, \alpha_3$), l'opérateur non-visqueux "2.75D" de préconditionnement de la théorie numérique du couplage s'écrit :

$$u'^3 = I \;.\; \beta \;.\; q' \;, \qquad (\beta \; complexe\,, \; I^2 = -1)$$

$$\beta = \sin\lambda \left\{ \left[\left(\frac{q}{u} \right)^2 \left[1 - M^2 \left(\frac{u}{q} \sin\lambda - \frac{v}{q} \cos\lambda \right)^2 \right] \right] \right\}^{\frac{1}{2}}, \qquad (6a)$$

$$\cos\lambda = g_{21} \left[g_{11}\, g_{22} \right]^{-\frac{1}{2}}$$

Dans le cas où la surface de déplacement ne s'écarte pas trop de la paroi, ce qui peut inclure des décollements d'étendue quelconque mais tels que w_n/q reste modéré (en pratique non-supérieur à 0.4 environ), la théorie de préconditionnement peut négliger la différence entre u'^3 et w'_n

$$u'^3 = w'_n$$

Pour tout nombre d'onde ($\alpha_1, \alpha_2, \alpha_3$), on a alors, sur la paroi :

$$\begin{bmatrix} w_n - w_{no} \\ q - q_o \end{bmatrix}_{i,j,1} = \sum_{\alpha_1, \alpha_2} \begin{bmatrix} w'_n(\alpha_1, \alpha_2) \\ q'(\alpha_1, \alpha_2) \end{bmatrix} . \; e^{\,I(\alpha_1 \; x^1 + \alpha_2 \; x^2)}$$

$$\left[w_n - w_{no} \right]_{i,j,1} = I \;.\; \beta \;.\; \left[q - q_o \right]_{i,j,1}, \qquad (6b)$$

$$(\beta \; complexe\,, \; I^2 = -1)$$

6.1.2. Préconditionnement non-visqueux "Massive-separation".

Dans le cas d'un *décollement massif, la direction* x^3 (*normale* à la vitesse non-visqueuse et donc à la surface de déplacement) n'est plus normale à la paroi. La vitesse normale de perturbation w'_n dépend alors de q', et l'opérateur non-visqueux correspondant, donné dans Le Balleur [1], devient :

$$w'_n \;=\; q' \;\; \sin\psi + u'^3 \; \cos\psi \;, \qquad \sin\psi = w_n/q$$

$$u'^3 = I \;.\; \beta \;.\; q'$$

$$w'_n = I \;.\; \left[\beta \cos\psi - I \;\; \sin\psi \right] q' \;=\; I \;.\; \beta' \;.\; q'$$

Pour tout nombre d'onde ($\alpha_1, \alpha_2, \alpha_3$), on a alors, sur la paroi :

$$\left[w_n - w_{no} \right]_{i,j,1} = I \;.\; \beta' \;.\; \left[q - q_o \right]_{i,j,1}, \qquad (6c)$$

$$(\beta' \; complexe\,, \; I^2 = -1)$$

De plus, le nombre d'onde maximal en direction x^1 ou s^1 compte tenu du filtrage opéré par le maillage de discrétisation est modifié, Le Balleur [1] :

$$\alpha_{\max} = \frac{\pi}{\Delta s^1 \;.\; \cos\psi} = \frac{\pi}{\Delta x^1} \qquad (6d)$$

6.1.3. Préconditionnement : "Opérateur visqueux" (2.75D).

Compte tenu de la formulation numérique s^1–*marching* du problème visqueux, il a été montré qu'il est possible d'y effectuer, à chaque station (i, j ,1), une élimination des variables internes "purement visqueuses", Le Balleur [5][6][7][1], ce qui réduit le problème visqueux à une seule relation connectant les variables non-visqueuses de paroi. Cette relation (parfois dite fonction d'influence visqueuse) constitue précisément l'opérateur de surface visqueux recherché de la théorie numérique du couplage. Cette élimination des variables purement visqueuses, qui peut inclure si nécessaire les schémas de discrétisation à la station (i, j) (méthodes-locales), élimine ici δ, a^1, a^2, $\bar{k}$, $\bar{\tau}$ dans le système (5a)(5b) et donne :

$$\left[\frac{\hat{w}_n}{q} - \beta^*_k \; \frac{\partial \hat{f}^k}{\partial s^1} - \gamma^* \right]_{i,j,1} = 0 \;, \qquad k = 1, 3 \qquad (7)$$

$$\hat{f}^k = \left\{ \hat{q} \;, \hat{h}_l \;, \hat{p}_l \right\}$$

La relation peut être écrite à volonté sous la sous forme différentielle ci-dessus, ou sous sa forme discrétisée. Les non-linéarités visqueuses "raides" (ou singularités) sont incluses dans les 3 coefficients β^*_k, qui dépendent fortement de i, j. Compte tenu des relations (5c) qui imposent un couplage direct sur les 2 grandeurs $\hat{h}_l$, $\hat{p}_l$, le seul coefficient local important pour la théorie numérique de couplage est β^*_1.

6.2. Algorithme "Semi-inverse Massive-separation" (2.75D).

A chaque itération de couplage, la vitesse normale à la paroi *non-visqueuse* w_n^N (*ou bien la discontinuité de vitesse* normale non-visqueuse sur les sillages $<w_n^N>$), qui traduit l'effet de déplacement généralisé, est modifiée en chaque noeud de couplage (i, j, 1) de manière explicite grace à l'algorithme "Semi-inverse" de Le Balleur [6][1][15], étendu ici en tridimensionnel-approché ("2.75D") :

$$\left[\frac{w_n^{N+1}}{q} - \frac{w_n^N}{q} \right]_{i,j,1} = \omega \left[\omega^1_{i,j} \left[\frac{\hat{w}_n}{q} - \frac{w_n^N}{q} \right]_{i,j,1} \right.$$

$$\left. + \; \omega^2_{i,j} \; \frac{1}{q} \left[\frac{\partial \hat{q}}{\partial s^1} - \frac{\partial q^N}{\partial s^1} \right]_{i,j,1} + \; \omega^3_{i,j} \; \frac{1}{q} \left[\frac{\partial^2 \hat{q}}{\partial s^1 \partial s^1} - \frac{\partial^2 q^N}{\partial s^1 \partial s^1} \right]_{i,j,1} \right]$$

$$0 < \omega < 2 \qquad (8),$$

Notons que si l'algorithme n'est pas tridimensionnel, l'approximation "2.75D" definie ici est plus complète que l'approche quasi-3D (2.5D) qui était déja précisée [3][1].

Les coefficients $\omega^1_{i,j}$, $\omega^2_{i,j}$, $\omega^3_{i,j}$, dans l'algorithme "Semi-inverse" de Le Balleur, sont calculés en chaque noeud (i,j) de couplage. Ce calcul est tel que w_n^{N+1} corresponde à la solution (linéarisée) de couplage exact sur le nombre d'onde maximal [6][7][1] $\alpha_{\max}$ du maillage. Une surrelaxation de 2 est alors la limite de stabilité [6][7]. Pour l'algorithme "Semi-inverse Massive-separation", les coefficients s'écrivent, Le Balleur [1][15], en variables complexes :

$$\omega^{direct}_{i,j} = \omega^1_{i,j} + I \;\; \alpha_{\max} \; \omega^0_{i,j} = \frac{1}{1 \; - \; \mu\,(\alpha_{\max})}$$

$$\omega^{inverse}_{i,j} = \omega^2_{i,j} + I \;\; \alpha_{\max} \; \omega^3_{i,j} = \frac{1}{1 \; - \; \mu^{-1}\,(\alpha_{\max})} \; \frac{\beta'}{\alpha_{\max}}$$

$$\mu = \frac{\alpha_1 \;.\; \beta^*_1}{\beta'}, \qquad (\mu \; complexe\,, \; I^2 = -1)$$

$$\beta' = \beta \;\; \cos\psi - I \;\; \sin\psi$$

Dans ces expressions, l'extension en "2.75D" de l'algorithme "Semi-inverse Massive-separation" suggéré en 1989 [1][15] est contenue dans le terme β donné par la relation (6a). Le terme μ correspond à l'amplification complexe de l'algorithme de point fixe "direct" (μ^{-1} étant de ce fait l'amplification complexe de l'algorithme de point fixe "inverse"). On notera que la relaxation ω^2, ω^3 ci-dessus correspond à la forme originelle de l'algorithme "Semi-inverse", Le Balleur [6], c'est à dire à une relaxation optimale $\omega^{-1} = 1-\mu^{-1}$, mais que l'écriture ici en variable complexe de ω inclut également l'analyse de Wigton, Holt [19], voir [22]. On remarquera enfin que l'algorithme "Semi-inverse Massive-separation" conduit, même en subsonique, à ce que les 2 termes ω^2 et ω^3 soient actifs et non-nuls, Le Balleur [1][15].

6.3. Algorithme "Equilibrage de nappe de sillage".

On utilise l'algorithme d'équilibrage de sillage suggéré en 1981, Le Balleur [7][1], pour les profils d'ailes. Cet algorithme, issu des techniques numériques du couplage visqueux-non visqueux, peut être utilisé tout aussi bien en calcul non-visqueux. La méthode numérique peut traiter l'équilibrage 3D, en appliquant l'algorithme 2D sur chaque surface $j = cst$.

Dans le cas visqueux, l'algorithme d'équilibrage de sillage s'ajoute à l'algorithme d'effet de déplacement, lequel assure seulement les conditions correctes de "saut" de vitesse normale non-visqueuse $<w_n/q>$ sur la nappe ("saut" qui devient nul en fluide-parfait) :

$$(w_n/q)_+ + (w_n/q)_- = (\hat{w}_n/q)_+ + (\hat{w}_r/q)_- \qquad (9a)$$

L'algorithme d'équilibrage effectue d'abord, avec les conditions correctes de saut de vitesse normale, un calcul sur une géométrie de nappe approchée $Z^N_{w\,i,j,1}$ à l'itération N. Après convergence de l'algorithme de couplage dans le cas visqueux, ce calcul donne les vitesses normales non-visqueuses relatives à cette géométrie de nappe, de part et d'autre de celle-ci $(w_n/q)^N_+$, $(w_n/q)^N$.

L'équilibrage est obtenu lorsque non seulement la relation (9a) est satisfaite, mais lorsque aussi $(\hat{w}_n/q)_+ = (w_n/q)^N_+$, et par conséquent $(\hat{w}_n/q)_- = (w_n/q)^N_-$ (avec $\hat{w}_n/q = 0$ dans le cas non-visqueux). La quantité :

$$\left(\frac{\partial \hat{Z}_w}{\partial s^1} - \frac{\partial Z^N_w}{\partial s^1}\right)_{i,j,1} = 1/2\left[(\hat{w}_n/q)_+ - (w_n/q)^N_+ - (\hat{w}_n/q)_- + (w_n/q)^N_-\right]_{i,j,1}$$

fournit l'erreur angulaire de pente de la nappe à chaque noeud de couplage. L'algorithme d'équilibrage relaxe alors cette pente en chaque noeud, la nouvelle géométrie de nappe étant déduite de la pente par intégration selon i depuis le bord de fuite :

$$\left(\frac{\partial Z_w}{\partial s^1}\right)^{N+1}_{i,j,1} = \left(\frac{\partial Z_w}{\partial s^1}\right)^N_{i,j,1} + \omega \cdot \left[\left(\frac{\partial \hat{Z}_w}{\partial s^1}\right)_{i,j,1} - \left(\frac{\partial Z_w}{\partial s^1}\right)^N_{i,j,1}\right] \qquad (9b)$$

$$0 < \omega < 1,$$

Cet algorithme d'équilibrage a des propriétés similaires à une méthode de Newton, avec convergence quadratique.

7. MAILLAGE AUTO-ADAPTATIF.

On utilise pour le champ non-visqueux une méthode de génération algébrique de maillage originale mise au point en 1981 pour les profils d'ailes, Le Balleur [7]. La méthode est ici étendue au tridimensionnel en appliquant la technique 2D plan par plan ($j = cst$), avec une frontière externe identique dans chaque plan, Fig. 3.

La méthode construit, Fig. 3-4-5, par intégration numérique selon k, un maillage algébrique en C où les lignes $i = cst$ sont des paraboles, en éliminant toutefois la technique des paraboles de transformation conforme, de facon à pouvoir répartir les noeuds à volonté et uniformément sur la frontière externe. Les lignes $k = cst$ sont obtenues par contrôle de la distribution des noeuds sur chaque ligne $i = cst$ entre la paroi et la frontière externe, Fig. 3-4-5.

La seconde originalité de la méthode est d'introduire une technique de contrôle monodimensionnelle de resserrements multiples du maillage. Ce module de génération de maillage transforme une répartition de noeuds $X(i)$ existante en une répartition nouvelle $X^*(i)$ qui introduit un nombre quelconque de resserrements locaux, réglables indépendamment en intensité, largeur et forme, par superposition (additive ou multiplicative) de fontions de resserrement élémentaires de classe C^∞ (fonctions exponentielles, Gaussiennes par exemple). La monotonie de la fonction $X^*(i)$ est assurée en traitant la transformation sur les dérivées dX^*/di, dX/di, positives, le maillage final $X^*(i)$ étant restitué par intégration numérique. Ceci introduit en outre une source de lissage favorable. Ce module de maillage peut de plus, dans la transformation $X^*(i)$, placer 4 noeuds à des abscisses fixes ou déterminées.

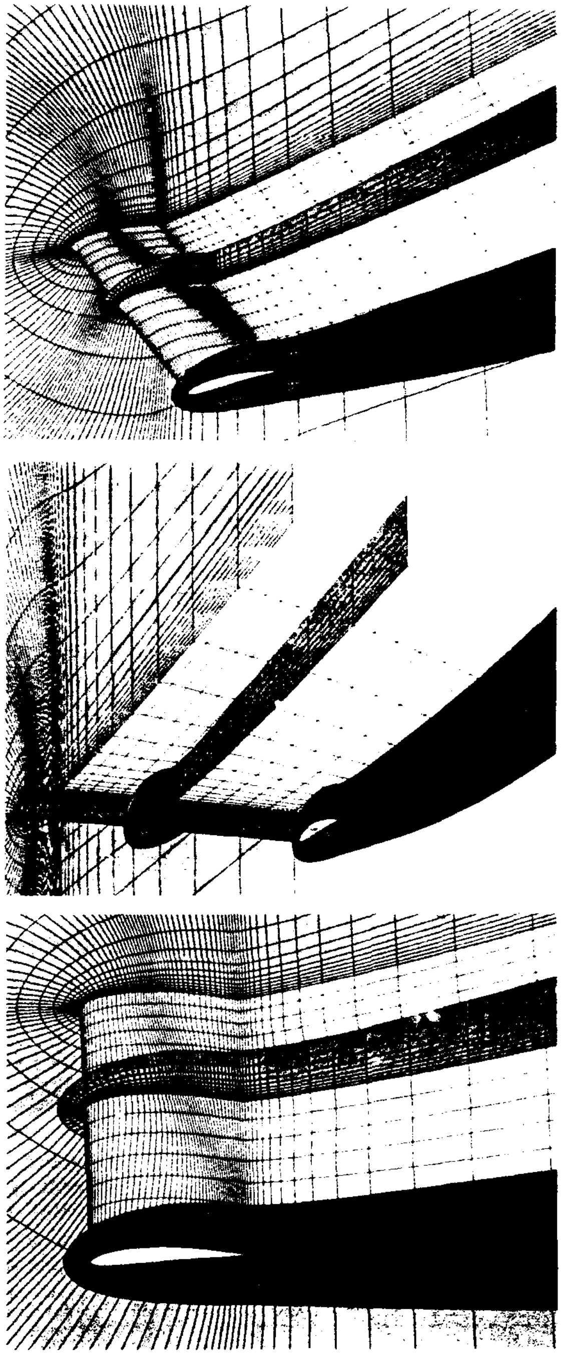

Fig. 3. Méthode de génération de maillage adaptatif 3D. (NACA4412, A = 6, M = .18, α = 17°, Re = 4.2 10⁶)

Une troisième originalité de la méthode, introduite plus récemment, est de généraliser l'emploi de ce mailleur algébrique à des géométries plus complexes (quelconques) par adjonction d'une technique de superposition de transformations analytiques. Ces transformations, par distorsion du maillage de base et avec minimisation d'aplatissement des mailles aux points singuliers, permettent ici par exemple le maillage en C avec bord de fuite émoussé (ellipse p. ex.), Fig. 5. L'originalité de la technique est de superposer des transformations de distorsion (3D) monotones à supports bornés. Des superpositions de 2 distorsions élémentaires, translation et rotation, suffisent à obtenir un large champ d'application.

L'auto-adaptation du maillage non-visqueux prend en compte la géométrie exacte de la nappe de sillage, itérativement déterminée par l'algorithme d'équilibrage. Des raffinements mobiles du maillage (selon ξ et éventuellement selon ζ), sont introduits pour adapter la maille locale Δs^1 à l'échelle δ d'interaction visqueuse dans les zones d'interaction forte telles que décollements et pieds d'ondes de choc, Fig. 3-4-5, et sont déplacés de manière itérative. A chaque itération d'auto-adaptation du maillage, une interpolation bilinéaire par cellule de la solution est effectuée.

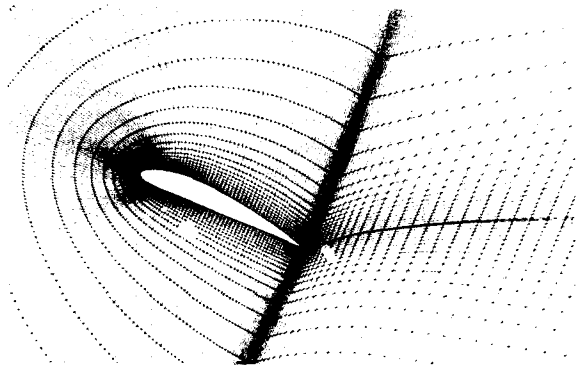

Fig. 4. Maillage auto-adaptatif : champ non-visqueux
(NACA4412, M = .18, α = 24°, Re = 4.2 10^6)

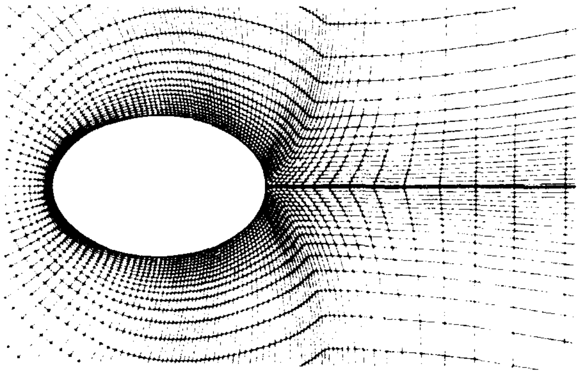

Fig. 5. Méthode de génération de maillage algébrique
(Corps émoussé, maillage en C,
raffinements auto-adaptatifs à la viscosité)

8. RESULTATS 2D.

8.1. Décrochage profond.

Grâce au double progrès du "Référentiel de Déplacement" pour les équations visqueuses, et de l'algorithme "Semi inverse Massive-separation" pour le couplage, la méthode bidimensionnelle stationnaire (codes VIS05 et VIS07, Viscous-Inviscid-Solver-07) a donné accès au calcul du décrochage et du post-décrochage. Les Fig. 6-12-13 reproduisent ici les résultats [1] obtenus sur le profil NACA4412 expérimenté par Hastings [33], avec la version la plus complète de la méthode. Dans

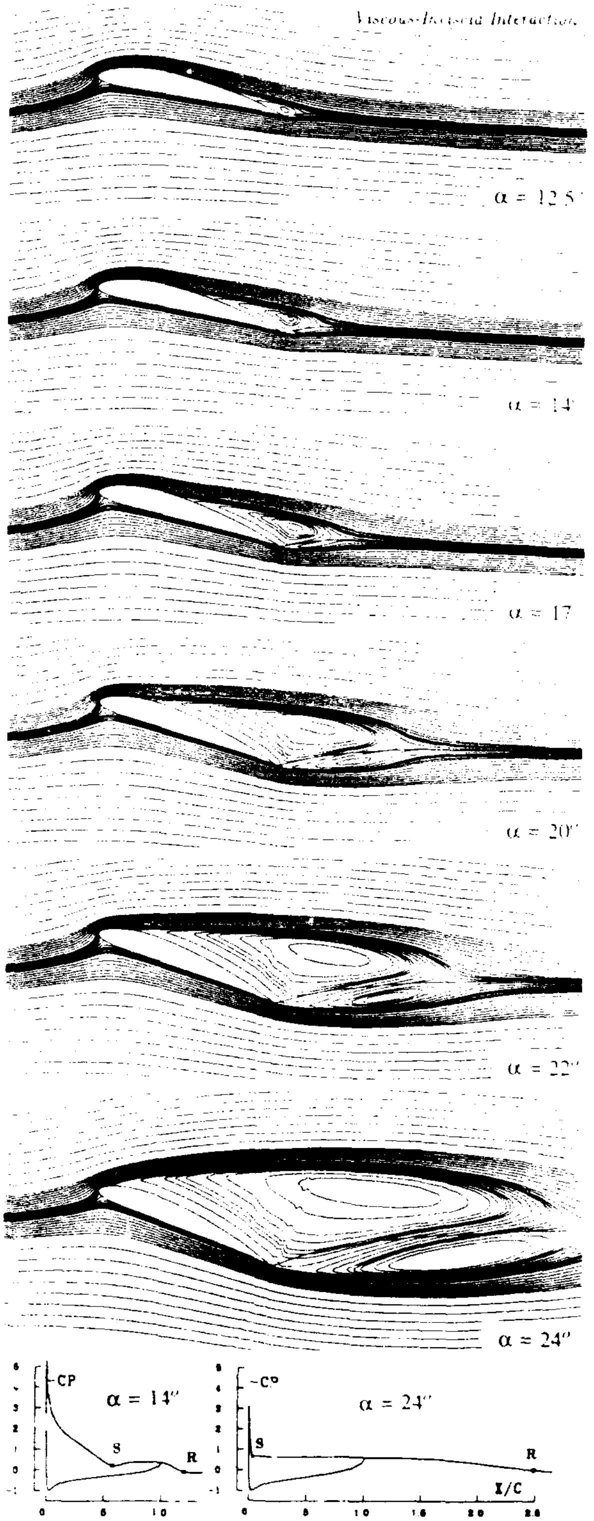

Fig. 6. Histoire de décrochage. Lignes de courant et pressions pariétales (NACA4412, M = .18, Re = 4.2 10^6,

celle-ci, le sillage est calculé avec sa pleine dissymétrie et la nappe de sillage non-visqueuse est mise en équilibre exactement (code VIS07), *sur* le lieu des *minima* de vitesse. Ce calcul du sillage avec positionnement exact donne accès à la pleine restitution des champs locaux moyens et fluctuants, lignes de courant, iso-vitesses, iso-turbulence, Fig. 6-10-11. Le calcul restitue bien, Fig. 6, le passage d'une topologie à 1 tourbillon de bord de fuite au CLmax vers une topologie d'écoulement moyen à 2 larges tourbillons contra-rotatifs en décrochage. Avec le modèle $k-\tau$ à 2 équations proposé pour les écoulements décollés, dès que la transition est correctement modélisée [1], un bon accord calcul-expérience est observé sur la courbe de portance jusqu'à son maximum, Fig. 13, ainsi que sur la distribution de pression à portance maximale, Fig. 12. Dans l'état actuel, les codes VIS05, VIS07, permettent des calculs à maillage auto-adaptatif robustes et routiniers jusqu'à des incidences 28^o ou 30^o, Fig. 10-11.

8.2. Maillage auto-adaptatif.

Dans l'évaluation de la simulation numérique par interaction visqueux-non visqueux, l'attention doit être portée non seulement sur la modélisation et les algorithmes visqueux, mais encore sur les avantages d'auto-adaptation automatique du maillage qu'elle apporte par rapport aux techniques de résolution directe d'équations de Navier-Stokes. La technique d'interaction visqueux-non visqueux inclut en effet en elle-même le problème d'auto-adaptation du maillage qui est nécessaire à grand nombre de Reynolds, et dont l'impact sur la simulation numérique à nombre de Reynolds élevé est sans doute bien supérieur au dilemne du choix entre équations complètes (toujours tronquées par le filtre des maillages) et équations de couche-mince.

Le dédoublement numérique "visqueux - non visqueux" avec recouvrement des domaines de calcul de la présente technique apporte l'avantage d'un traitement dédoublé lui-aussi de l'auto-adaptation aux effets visqueux, Fig. 4-7-8, Fig. 5-9. Il offre donc un nombre de degrés de liberté accru pour l'auto-adaptation du maillage, par rapport aux techniques de résolution directe. La Fig. 7 montre à convergence le maillage "visqueux" auto-adaptatif à l'épaisseur de couche visqueuse et au profil de vitesse dans la couche, qui est introduit ici en théorie de "Formulation-Déficitaire", et par conséquent en recouvrement du maillage "non-visqueux" auto-adaptatif de la Fig. 4, avec coincidence des noeuds sur la paroi et sur la nappe de sillage. Les maillages complets du calcul, Fig. 8 et Fig. 9, montrent la totale auto-adaptation de maillage obtenue dans la présente simulation numérique par interaction visqueux-non visqueux, tant pour la capture des sillages, bords de fuite, points de décollement, que pour celle des couches limites et couches de mélange. Ce maillage explique la faculté offerte par cette méthodologie numérique de pouvoir augmenter indéfiniment, et sans viscosité numérique majeure, le nombre de Reynolds accessible. Les calculs ont ici été effectués sur des maillages 257x32 (champ non-visqueux) plus 257x37 (champ visqueux). Un doublement du maillage visqueux dans la direction normale, en fin de convergence, n'aurait pas augmenté

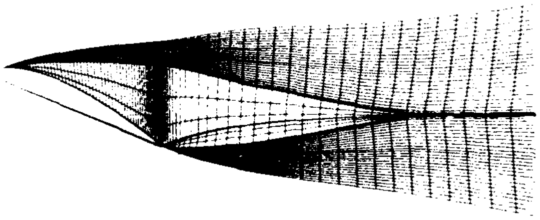

Fig. 7. Maillage auto-adaptatif : champ visqueux.
(*NACA4412*, $M = .18$, $\alpha = 24^o$, Re = 4.2 10^6)

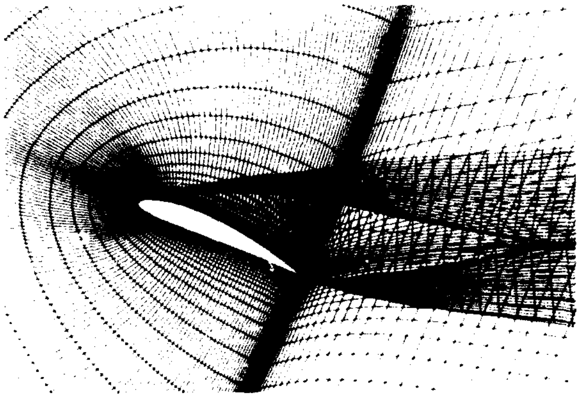

Fig. 8. Maillages auto-adaptatifs complets
d'interaction visqueux-non visqueux
(*NACA4412*, $M = .18$, $\alpha = 24^o$, Re = 4.2 10^6)

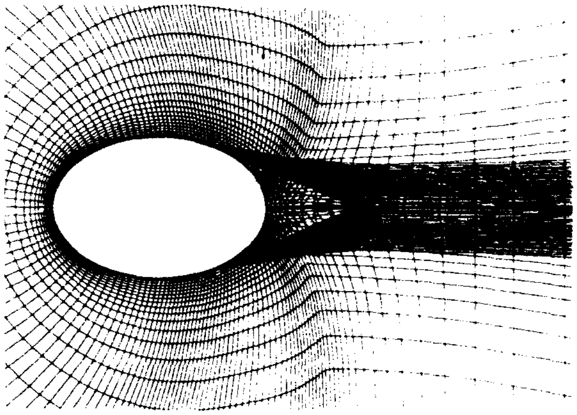

Fig. 9. Maillages auto-adaptatifs complets
d'interaction visqueux-non visqueux.
(*Ellipse*, $M = .18$, $\alpha = 0^o$, Re = 4.2 10^6)

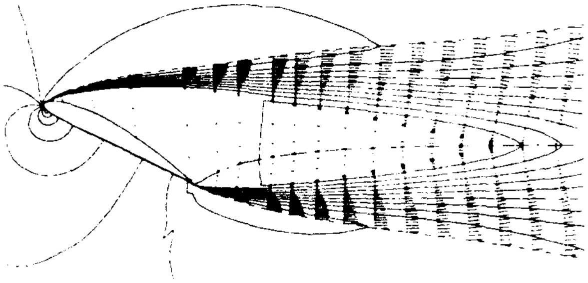

Fig. 10. Ecoulement moyen : profils de vitesse moyenne et lignes iso-vitesse. (*NACA4412*, $M = .18$, $\alpha = 28^o$, Re = 4.2 10^6)

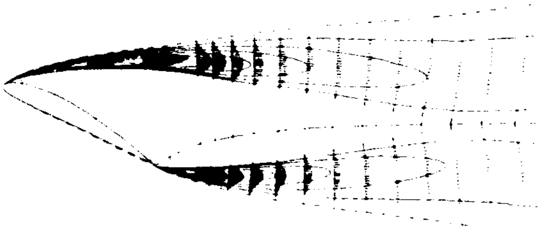

Fig. 11 Turbulence profils d'énergie cinétique et lignes iso
(*NACA4412*, $M = .18$, $\alpha = 28^o$, Re = 4.2 10^6)

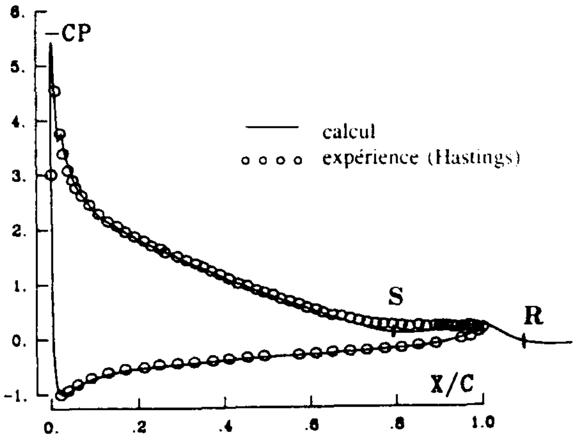

Fig. 12. Pression à la paroi à portance maximale CLmax.
(NACA4412, M = .18, α = 12.5°, Re = 4.2 10⁶,
x_{tr_s} = .014, x_{tr_i} = .113, modèle 2 éq.)

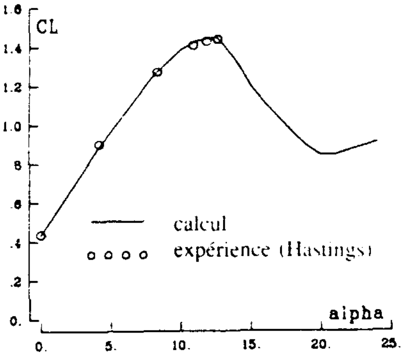

Fig. 13. Courbe de portance. Décrochage.
(NACA4412, M = .18, Re = 4.2 10⁶, modèle 2 éq.)

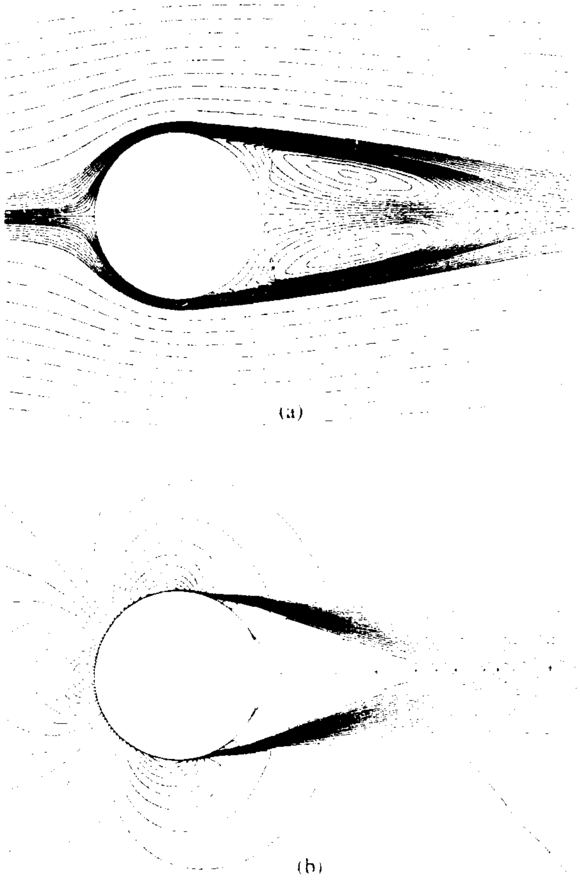

Fig. 14. Décollement massif. Lignes de courant et iso-Mach.
(Cylindre circulaire, M = .18, Re = 4.2 10⁶)

notablement le coût du calcul. Notons enfin qu'un sous-maillage unilatéral (selon i) du calcul visqueux se trouve introduit automatiquement, de plus, dans les zones de faible interaction visqueuse le nécessitant.

8.3. Cylindre circulaire.

L'accès des méthodes d'interaction visqueux-non visqueux au calcul du décollement massif est enfin illustré par la possibilité de calcul du cas-limite du cyclindre circulaire, Fig. 14, au moyen du code VIS05 - profil d'aile. La présente théorie de "Formulation-Déficitaire" et son "Référentiel de déplacement" éliminent ici les difficultés de couche-mince ou de référentiel de couche-limite discontinu au (pseudo-) bord de fuite. L'algorithme "Semi-inverse Massive separation" et la théorie numérique du couplage proposée démontrent sur ce cas-test leur application jusque dans le cas-limite sévère où le vecteur vitesse "non-visqueux" à la paroi devient orthogonal à cette paroi (et non plus tangent comme en couche limite). Un décollement turbulent à azimuth réaliste de 110° est ici prédit par le code VIS05, en calcul stationnaire.

9. RESULTATS 3D.

L'extension en tridimensionnel de la méthode numérique (code VIS11) conserve exactement, plan par plan, les mêmes caractéristiques d'auto-adaptation du maillage aux effets visqueux que celle de la Fig. 8. Le maillage moins riche utilisé ici en tridimensionnel est 131x21x20 (champ non-visqueux) plus 131x15x37 (champ visqueux), avec sous-maillage additionnel visqueux selon i dans les zones de couche limite mince attachée.

9.1. Voilure rectangulaire NACA4412.

Des calculs de validation numérique de la méthode ont d'abord été obtenus sur une aile NACA4412 rectangulaire d'allongement 6 en atmosphère illimitée, en conservant les mêmes conditions de vitesse et de nombre de Reynolds que celles de Hastings. La Fig. 15 montre les lignes de frottement calculées en turbulent aux grandes incidences sur l'extrados de la voilure, et les lignes de force du champ de vitesse sur la nappe de proche sillage. Les lignes d'accumulation de décollement et de recollement montrent l'apparition du décollement. On peut remarquer en particulier l'importante zone de décollement calculée à l'incidence 17°, le décollement de l'aile prenant ici naissance par l'emplanture (plan de

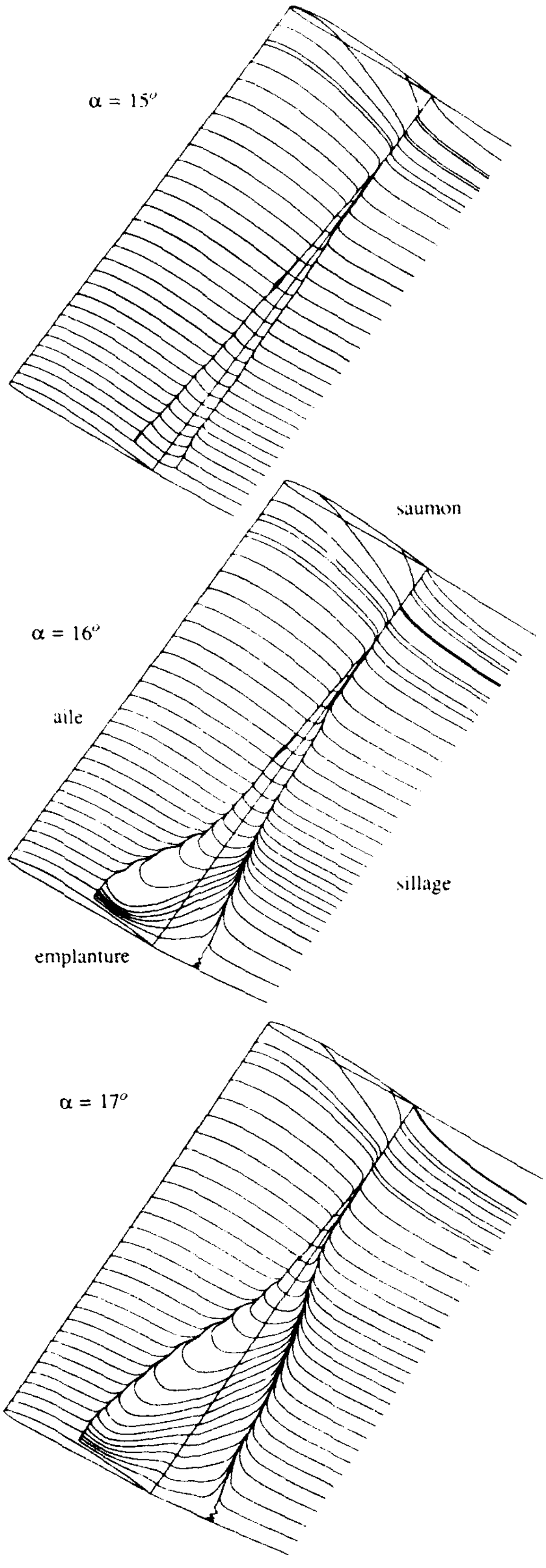

Fig. 15. Lignes de frottement. Extrados. Maillage fixe. Aile rectangulaire NACA4412, allongement = 6. (M = .18, Re = 4 10^6, turbulent)

symétrie). La Fig. 3 montre que la nappe de sillage est mise en équilibre. La Fig. 16 fournit les distributions de pression calculées en envergure à l'incidence 17°, et montre l'apparition d'un plateau de pression dans la zone décollée. Les résultats des Fig. 15-16 correspondent à des calculs sur des maillages où l'auto-adaptation est réalisée pour ce qui est du calcul visqueux et de l'équilibrage de la nappe, mais qui sont dépourvus d'auto-adaptation du maillage de surface au décollement (cas-b de la Fig. 17). Dans ces calculs sur maillage de surface orthogonal, l'approximation de troncature visqueuse est alors $\sin \lambda^* = 1$.

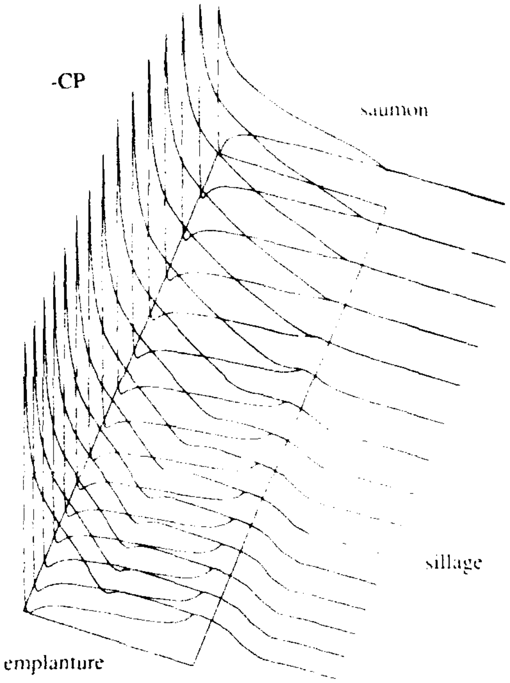

Fig. 16. Distribution de pression à la paroi. Aile rectangulaire NACA4412, allongement = 6. (M = .18, α = 17°, Re = 4 10^6, turbulent)

9.2. Calcul à maillage de surface auto-adaptatif.

La technique de maillage auto-adaptative mise au point dans la présente méthode (code VIS11) permet aussi l'auto-adaptation du maillage de surface, par rapport aux effets visqueux de décollement, cas-a de la Fig. 17. L'auto-adaptation du maillage de surface est ici asservie au passage en mode inverse du calcul visqueux, c'est à dire asservie au cône caratéristique et au domaine de dépendance local du calcul de couche limite couplée.

Dans ces calculs, l'hypothèse d'une direction λ^* de troncature visqueuse parallèle aux lignes $i = cst$, qui est acceptable lorsqu'elle est possible, et qui ne conduit pas alors à des modifications majeures des solutions par rapport au calcul avec $\sin \lambda^* = 1$, ne peut cependant être maintenue sur un maillage de surface distordu par adaptation à un grand décollement. Le calcul avec λ^* parallèle aux lignes $i = cst$ sur un maillage convergé tel que celui de la Fig. 17 cas-a ne peut en effet être

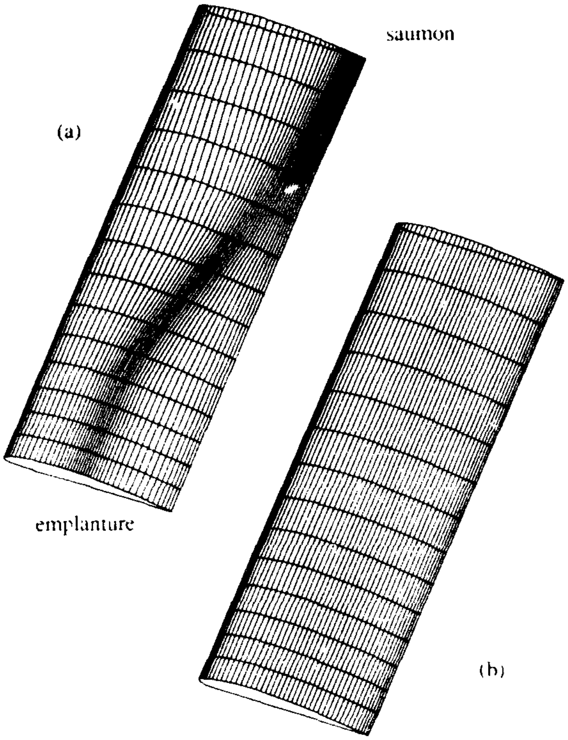

*Fig. 17. Maillage de surface auto-adaptatif aux effets visqueux.
Aile rectangulaire NACA4412, allongement = 6.
(M = .18, α = 17°, Re = 4 10^6, turbulent)*

effectué sans violer les domaines de dépendance et cônes caractéristiques de couche limite en mode inverse. Une direction λ^* calculée en chaque noeud, en fonction de l'obliquité du maillage de surface et du cône caractéristique inverse local, est donc introduite. Elle évolue entre la direction $i = cst$ et la direction orthogonale aux lignes de courant non-visqueuses. Le calcul confirme que l'impact du choix de λ^* sur les solutions reste faible, le test étant ici effectué sur le résultat sensible qu'est le frottement, et dans le cas défavorable de la plus forte incidence 17°, Fig. 18-19. On peut noter que le calcul avec maillage de surface auto-adaptatif et sin λ^* = 1, Fig. 18, reproduit sensiblement le résultat sin λ^* = 1 obtenu sans maillage de surface adaptatif de la Fig. 15, et que la solution sur maillage de surface adaptatif avec sin λ^* calculé, Fig. 19, ne conduit qu'à un léger accroissement de la zone décollée.

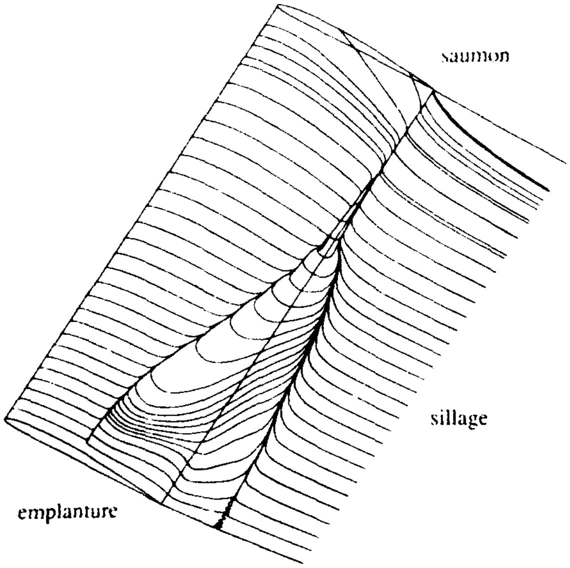

*Fig. 18. Lignes de frottement. Maillage auto-adaptatif. Sin λ^* = 1.
Aile rectangulaire NACA4412, allongement = 6.
(M = .18, α = 17°, Re = 4 10^6, turbulent)*

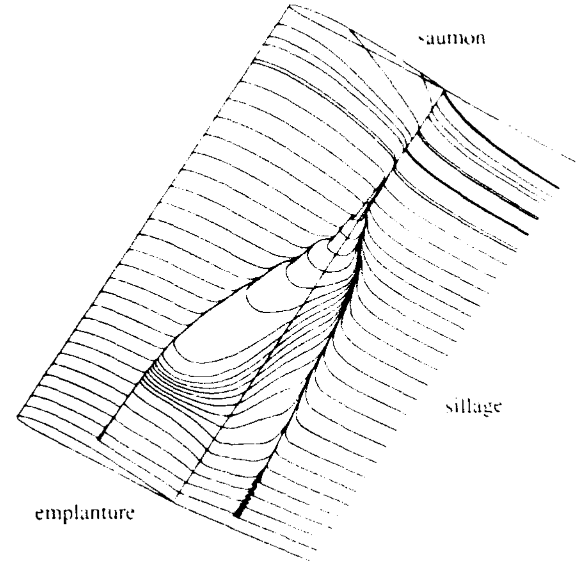

*Fig. 19. Lignes de frottement. Maillage auto-adaptatif. Sin $\lambda^* \neq 1$
Aile rectangulaire NACA4412, allongement = 6
(M = .18, α = 17°, Re = 4 10^6, turbulent)*

9.3. Voilure en flèche AS27-V41.

Une première validation quantitative de la méthode de calcul tridimensionnelle VIS11 par comparaison calcul-expérience a été obtenue sur la voilure en flèche AEROSPATIALE V41, qui a été expérimentée à grande échelle sur une maquette "avion" [34] dans les souffleries de l'ONERA, et dont les caractéristiques sont déjà plus proches de celles des voilures industrielles.

La Fig. 20 montre le maillage de surface du calcul et indique la géométrie de la voilure. Le calcul est réalisé en turbulent. La transition expérimentale est déclenchée. La Fig. 21

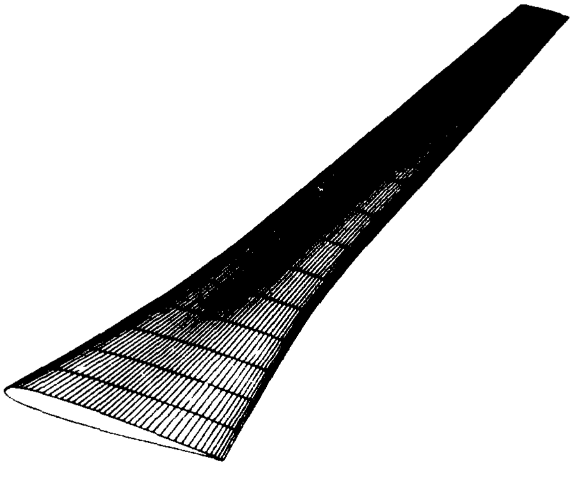

Fig. 20. Aile AS27-V41 (allongement=9.5). Maillage de surface.

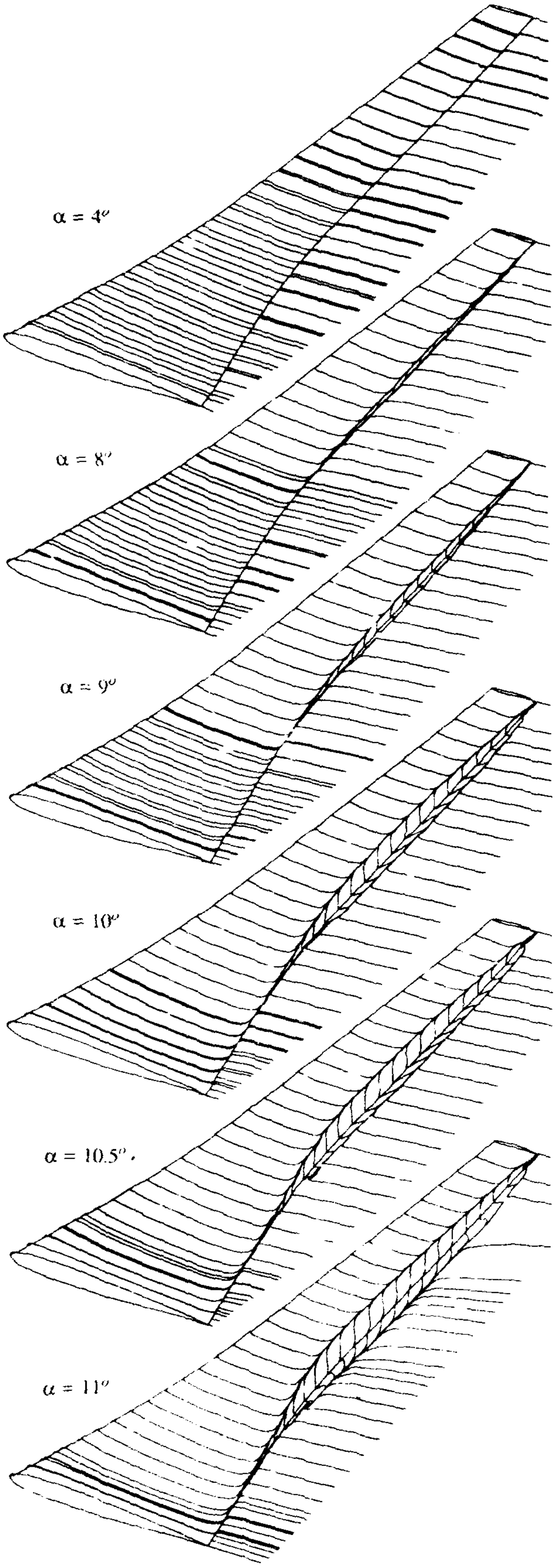

Fig. 21. Lignes de frottement. Extrados. Aile AS27-V41.
(M = .24, $R_{envergure}$ = 7.8 10^6, turbulent, modèle 2 éq.)

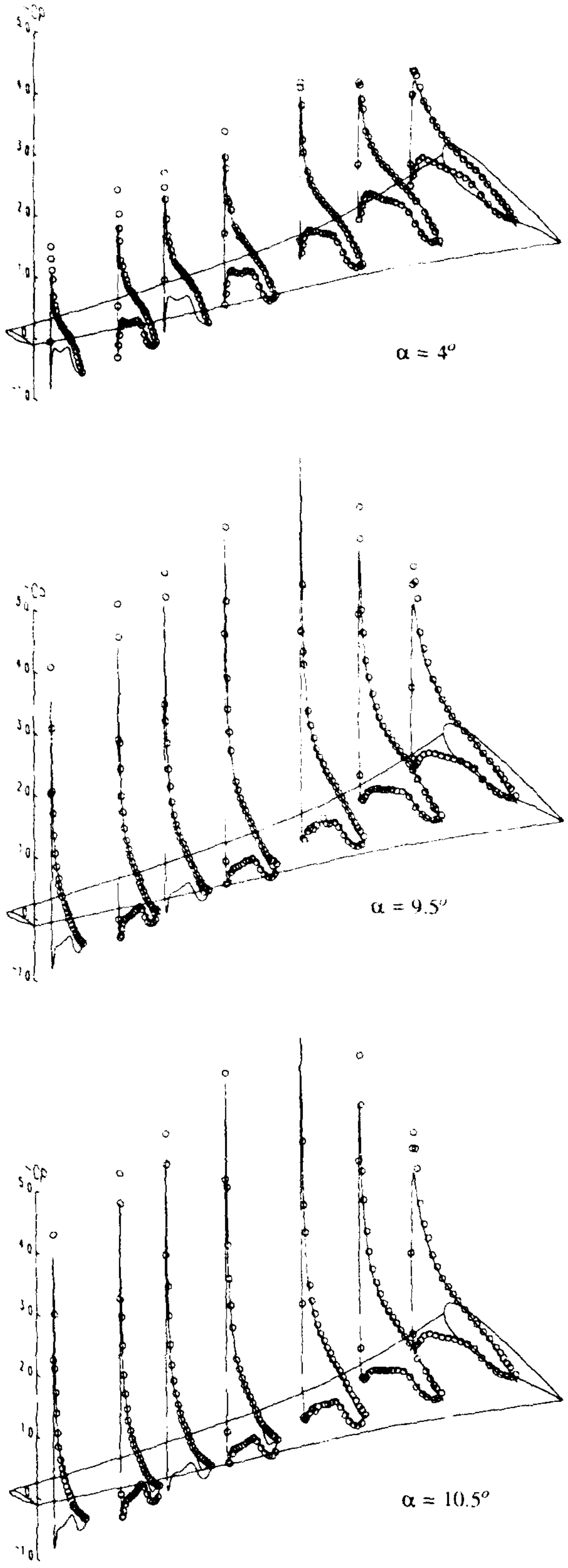

Fig. 22. Comparaison calcul-expérience.
Distribution de pression. Aile AS27-V41.
(M = .24, $R_{envergure}$ = 7.8 10^6, turbulent, modèle 2 éq.)

reproduit l'évolution en incidence des lignes de frottement calculées sur l'extrados de la voilure, ainsi que les lignes de force du champ de vitesse sur la nappe de proche sillage (mise en équilibre), aux fortes portances. Les lignes d'accumulation de décollement et de recollement qui apparaissent, Fig.21, montrent le développement en incidence du décollement calculé, jusqu'au CLmax, avec le modèle turbulent à 2 équations $k-\tau$ proposé. L'incidence 11° correspond sensiblement sur cette aile à la limite d'opérationnalité du code VIS11 (au stade préliminaire actuel). Les comparaisons calcul-expérience obtenues sur les distributions de pression à la paroi pour ces configurations décollées à forte portance, Fig.22, semblent être très satisfaisantes, de même que dans le cas non-décollé à l'incidence 4°.

10. CONCLUSIONS.

Une méthode numérique nouvelle d'interaction visqueux-non visqueux transsonique pour le calcul des écoulements décollés sur les voilures aux fortes portances (code VIS11, Viscous-Inviscid-Solver-11), a pu être définie. Une technique 3D-approchée pour les équations visqueuses (2.75D-local), adaptée à l'allongement inévitable des mailles en envergure, est proposée. Le nouveau code VIS11 offre de surcroit une première approche de calcul tridimensionnel à maillage auto-adaptatif aux échelles d'interaction visqueuse.

Des résultats nouveaux ont été dégagés sur les singularités et cônes caractéristiques de couche limite tridimensionnelle en mode inverse. Des résultats théoriques nouveaux ont aussi été obtenus sur l'algorithme de couplage "Semi-inverse" de Le Balleur ainsi que sur sa théorie de stabilité, en débouchant sur une nouvelle extension "Semi-inverse Massive-separation 2.75D" de l'algorithme, compatible avec le calcul des voilures décollées.

Des comparaisons calcul-expérience satisfaisantes sur le champ de pression ont pu être obtenues, avec le modèle turbulent 2 équations $k-\tau$ proposé, tant sur le profil NACA4412 au CLmax et au décrochage, que sur la voilure en flèche AS27-V41 de type avion civil, à grande portance et avec décollement.

Ces résultats démontrent que les méthodes d'interaction visqueux-non visqueux donnent un plein accès au calcul du décollement tridimensionnel.

Remerciements. *L'auteur adresse ici ses remerciements à la Société AEROSPATIALE, qui lui a aimablement communiqué les répartitions de pression expérimentales sur la maquette AS27-V41, ainsi qu'au Service technique officiel francais STPA du Ministère de la Défense, qui a soutenu financièrement cette expérimentation.*

Il remercie aussi D. Blaise, P. Girodroux-Lavigne, H. Gassot, pour leur concours précieux dans les traitements graphiques.

11. REFERENCES.

[1] LE BALLEUR J.C. - New possibilities of Viscous-Inviscid numerical techniques for solving viscous flow equations, with Massive separation. Proceedings Fourth Symp. Numerical and Physical Aspects of Aeorodynamic Flows, Selected papers, chap. 4, p. 71-96, editor T. Cebeci, SPRINGER-VERLAG 1990. (or ONERA TP 1989-24 Reprint)

[2] MELNIK R.E. - Turbulent interactions on airfoils at transonic speeds - Recents developments - Agard Conference on Computation of viscous-inviscid interaction, Colorado Springs (1980), AGARD-CP-291, Paper 10, (1981).

[3] LE BALLEUR J.C. - Numerical flow calculation and viscous-inviscid interaction techniques - Recent Advances in Numerical methods in Fluids, Vol. 3 : Computation methods in viscous flows, p 419-450, W. Habashi editor, Pineridge Press (1984).

[4] LE BALLEUR J.C. - Computation of flows including strong viscous interactions with coupling methods. - AGARD-CP-291, General Introduction, Lecture 1, Colorado-Springs (1981), or ONERA TP 1980-121.

[5] LE BALLEUR J.C. - Viscous-inviscid flow matching : Analysis of the problem including separation and shock waves. - La Recherche Aerospatiale 1977-6, p.349-358 (Nov.1977). French, or English transl. ESA-TT-476.

[6] LE BALLEUR J.C. - Viscous-inviscid flow matching : Numerical method and applications to two-dimensional transonic and supersonic flows. - La Recherche Aerospatiale 1978-2, p. 67-76 (March 1978). French, or English transl. ESA-TT-496.

[7] LE BALLEUR J.C - Strong matching method for computing transonic viscous flows including wakes and separations. Lifting airfoils. - La Recherche Aerospatiale 1981-3, p. 21-45, English and French editions, (March 1981).

[8] LE BALLEUR J.C, PEYRET R., VIVIAND H. - Numerical Studies in high Reyrolds number aerodynamics - Computers and Fluids, Vol. 8, n° 1, p. 1-30, (March 1980)

[9] LE BALLEUR J.C - Numerical viscid-inviscid interaction in steady and unsteady flows. - Proceed. 2nd Symp. Numerical and Physical Aspects of Aerodynamic flows, Long-Beach, (1983), chapt.13, p. 259-284 T. Cebeci ed.,Springer-verlag, 1984, (or ONERA-TP 1983-8).

[10] CARTER J.E. - A new boundary layer interaction technique for separated flows. - AIAA paper n° 79-1450, 4th Comp. Fl. Dyn. Conference, (July 1979).

[11] VELDMAN A.E.P. - New quasi-simultaneous method to calculate interacting boundary layers. - AIAA J. Vol. 19, n° 1 (1981), p.79-85.

[12] *LE BALLEUR J.C., GIRODROUX LAVIGNE P.* - *A semi-implicit and un*steady numerical method of viscous-inviscid interaction for transonic separated flows. - La Recherche Aerospatiale 1984-1, p 15-37, English and French editions, (Jan. 1984).

[13] LE BALLEUR J.C, GIRODROUX-LAVIGNE P. - A viscous-inviscid interaction method for computing unsteady transonic separation. - Proceed. 3rd Symp. Numerical and Physical Aspects of Aerodynamics Flows, Long-Beach (jan.1985), T. Cebeci ed., Springer-Verlag (1986).

[14] LE BALLEUR J.C - Viscous-Inviscid interaction solvers and computation of highly separated flows. - "Studies of Vortex Dominated Flows", chap. 3, p. 159-192, Proceed. ICASE symp. NASA Langley Field, USA, (july 9-10, 1985), Hussaini and Salas ed., Springer-Verlag 1987, (or ONERA TP 1986-4).

[15] LE BALLEUR J.C - New possibilities of numerical viscous-inviscid coupling, for viscous flows with massive separation, and for inviscid Zonal-methods. Proceedings GAMNI/SMAI-IMA conference on Computational aeronautical dynamics, May 17 19, 1989, Antibes, France, SPRINGER-VERLAG to appear. (or ONERA TP 1989-166 Reprint)

[16] COLES D.E. - Tle law of the wake in turbulent boundary layers. JFM Vol 1, part 2 (1956).

[17] MELNIK R.E., MEAD H.R., JAMESON A. - A Multi-grid method for the computation of viscous/inviscid interaction on airfoils - AIAA-Paper 83-0234 (1983).

[18] MELNIK R.E., BROOK J.W. - The computation of Viscid/Inviscid interaction on airfoils with separated flow. -
Proceed. Numerical and Physical Aspects of Aerodynamics Flows III, Long-Beach (1985), Springer-Verlag 1986, p77-101, editor Cebeci.

[19] WIGTON L.B., HOLT M. - Viscous-inviscid interaction in transonic flow - 5th CFD, AIAA Paper 81-1003, Palo-Alto (June 1981).

[20] LE BALLEUR J.C., BLAISE D. - Computation of separated internal flows and shock wave-boundary layer interactions by viscous-inviscid interaction. - La Recherche Aerospatiale 1985-4, p. 211-227, English and French editions, (July 1985).

[21] LE BALLEUR J.C.,GIRODROUX LAVIGNE P. - Calculation of fully three-dimensional separated flows with an unsteady viscous-inviscid interaction method. Fifth Symp. Numerical and Physical Aspects of Aeorodynamic Flows, California State University, Long-Beach (USA), January 13-15 1992. (ONERA TP 1992-01 Reprint)

[22] LE BALLEUR J.C. - Viscid-Inviscid coupling calculations for two- and three-dimensional flows. Lecture series 1982-04 on Computational Fluid Dynamics, Von Karman Institute, Belgium, (March 1982).

[23] LE BALLEUR J.C. - Progrès dans le calcul de l'interaction fluide parfait fluide visqueux . Proceedings AGARD-CP-351, Paper 1, Copenhague, (1983).

[24] LE BALLEUR J.C., LAZAREFF M. - A Multi-Zonal-Marching integral method for 3D boundary-layer with viscous-inviscid interaction - Proceed. 9th ICNMFD, June 1984, Saclay, France. Lecture Notes in Physics, 218, p.351-356, Springer-Verlag 1985.

[25] LAZAREFF M., LE BALLEUR J.C. - Development of the MZM numerical method for 3D boundary layer with interaction on complex configurations. Proceedings 8th GAMM conference, Notes on Numerical Fluid Mechanics, Vol. 29, VIEWEG, Braunschweig 1990. (or ONERA TP 1989-174)

[26] EDWARDS D., CARTER J. - Analysis of three-dimensional separated flow with the boundary-layer equations. - AIAA Paper 85-1499, July 1985.

[27] DAVIS R.L., CARTER J.E., HAFEZ M. - Three-dimensional viscous flow solutions with a vorticity-stream function formulation. - AIAA Journal, Vol. 27, no 7, p 892-900, July 1989.

[28] CEBECI T., CHEN L.T., CHANG K.C., PEAVEY C.C. - An interactive scheme for three-dimensional transonic flows. - Proceed. 3rd Symp. Numerical and Physical Aspects of Aerodynamics Flows, Long-Beach, USA (Jan. 1985), T. Cebeci ed., Springer-Verlag (1986).

[29] WIGTON H., YOSHIHARA H. - Viscous-inviscid interactions with a three-dimensional inverse boundary layer code. - Proceed. 2nd Symp. Numerical and Physical Aspects of Aerodynamic flows, Long-Beach, USA, January 1983.

[30] WAI J.C., BAILLIE J.C., YOSHIHARA H. - Computation of turbulent separated flows over wings - Proceed. 3rd Symp. Numerical and Physical Aspects of Aerodynamics Flows, Long-Beach, USA, Jan. 1985.

[31] YOSHIHARA H., WAI J. - Transonic turbulent separation on swept wings. A return to the direct formulation. - AIAA Paper 84-0265, Reno, USA, January 1984.

[32] STEGER J.L., van DALSEM W.R. Developments in the simulation of separated flows using finite difference methods. - Proceed. 3rd Symp. Numerical and Physical Aspects of Aerodynamics Flows, Long-Beach, USA, Jan. 1985.

[33] HASTING R.C., WILLIAMS B.R. - Studies of the flow filed near a NACA4412 aerofoil at nearly maximum lift - Aeronautical Journal, p. 29-44 (January 1987).

[34] PUJOL C., DELORT M. - Développement exploratoire aérodynamique. Synthèse de l'exploitation des mesures sur la maquette AS27 dans la soufflerie S1Ma. Rapport AEROSPATIALE 445.077 / 83, Octobre 1983.

FORTY YEARS OF HIGH-LIFT R&D - AN AIRCRAFT MANUFACTURER'S EXPERIENCE

E. Obert
Fokker Aircraft B.V.
P.O. Box 7600
1117 ZJ Schiphol
The Netherlands

SUMMARY

In the course of four decades a large amount of high-lift applied research and development has taken place at the Fokker Company. In the 'fifties and 'sixties the F-27 and the F-28 were developed. In the 'eighties these aircraft were developed further into the Fokker 50 and Fokker 100. In the seventies an extensive R&D programme was performed in preparation of a possible successor to the F-28 leading to the F-29 project study. In each case two- and three- dimensional windtunnel models were investigated in numerous configurations. In the last decade these investigations have increasingly been preceded by theoretical investigations. Where data are available comparisons have been made with flight test data. Of each development programme a detailed account is presented. Particular attention is paid to Reynolds-number effects and the interconnection between the high-speed cruise and low-speed high-lift design requirements.

LIST OF SYMBOLS

A	Wing aspect ratio
b	Wing span
c	Airfoil section chord
$\bar{c}$	Wing mean aerodynamic chord
c_d	Airfoil section drag coefficient
C_D	Aircraft drag coefficient
c_l	Airfoil section lift-coefficient
$c_{l_{max}}$	Airfoil section maximum lift coefficient
C_L	Aircraft lift coefficient
$C_{L_{max}}$	Aircraft maximum lift coefficient
$(C_{L_{max}})_{V_{min}}$	Aircraft maximum lift coefficient based on minimum speed reached in the stall manoeuvre (FAA definition)
$CL_{max,\ 1\text{-}g}$	Aircraft maximum lift coefficient based on the speed at which the "g-break" occurs
$(CL)_{1.2Vs}$	$(C_{L_{max}})_{V_{min}}/1.44$
$(\Delta c_l)_{\alpha=0}$	Increase in section lift coefficient due to flap deflection at α=0.
CL_{T-0}	Aircraft lift coefficient for the aircraft-less-tail
c_m	Airfoil section pitching moment coefficient
$(\Delta C_m)_{\alpha=0}$	Increase in airfoil section pitching moment coefficient due to flap deflection at α=0
i_h	Tailplane setting
$(L/D)_{1.2Vs}$	Lift-drag ratio at a speed 20 percent above the stalling speed
Cp	Static pressure coefficient, $\frac{P-Po}{q}$
M	Mach number
P	Local static pressure
Po	Static pressure of the undisturbed airflow
q	Dynamic pressure
Re_c	Reynolds number related to the airfoil section chord
$Re_{\bar{c}}$	Reynolds number related to the wing mean aerodynamic chord
S	Wing area
α	Airfoil section angle-of-attack
α_R	Aircraft angle-of-attack with reference to the fuselage centre line
δ_e	Elevator angle
δ_f	Flap angle
δ_s	Slat angle

I. INTRODUCTION

When the Koninklijke Nederlandse Vliegtuigenfabriek Fokker N.V. (Royal Dutch Aircraft Factory Fokker) restarted design and production of its own aircraft after the Second World War good high-lift characteristics were not among the prime goals pursued in the design activities. Fokker's first designs, the F-25 Promotor, the S-11 Instructor, S-12, S-13 and S-14 Mach-trainer were touring aircraft and military trainers where airframe-propulsion integration and flight handling required much more attention than maximum performance. For these designs split flaps were good enough.

In 1950 however, a design study was started on a two-engined transport aircraft which was envisaged as a successor to the then ubiquitous Douglas DC-3 or C-47. This was seen as a tremendous challenge. The C-47 was at that time easy to obtain at very reasonable prices and had for its days quite reasonable field performance. The new aircraft, the Fokker F-27 Friendship would be equipped with the not yet generally accepted turboprop engine (the Rolls-Royce Dart RDa6) in order to obtain lower operating costs and a significant increase in productivity through a higher cruising speed. Take-off power rose from 1200 hp for the C-47 to 1600 shp for the F-27 Mk100. The higher cruising speed demanded a higher wing loading for optimum cruise performance. Wing loading increased from 139 kg/m² (28.4 lb/sq.ft) for the C-47 to 253 kg/m² (51.7 lb/sq.ft). As the span of both aircraft was practically identical (29 m or 95 ft) the span loading MTOW /b² increased from 15.11 kg/m² (3.10 lb/sq.ft) for the C-47 to 21.06 kg/m² (4.32 lb/sq.ft).
Finally the aircraft would be certified according to the U.S. certification regulations CAR 4b which were considerably more stringent, both with respect to performance and to flight handling, than was the certification basis for the original DC-3. Nevertheless, the DC-3 field performance was to be duplicated.

Thus a set of very demanding aerodynamic design requirements was formulated for low-speed flight (high maximum lift in take-off and landing, high lift-drag ratio's at take-off and landing conditions and excellent low-speed flight characteristics both in all-engine and one-engine-out flight conditions). This special attention for low-speed flight, both with regard to aircraft performance and to flight handling has ever since the original design of the F-27 been a trade mark of Fokker designs as these have always primarily been aimed at the short- and medium haul market.

II. THE BEGINNING - DEVELOPING THE HIGH-LIFT CHARACTERISTICS OF THE FOKKER F-27 FRIENDSHIP

When one looks into the open literature for data on airfoil section high-lift characteristics available in 1950 one finds that most of the data is compiled in four publications:

a. Theory of Wing Sections (Abbott and von Doenhoff, ref. 1).
b. Summary of airfoil data, NACA TR 824 (Abbott, von Doenhoff, Stivers, ref. 2).
c. Summary of section data on trailing-edge high lift devices, NACA TR 938 (J.F. Cahill, ref. 3).
d. The Aerodynamic Characteristics of Flaps, ARC R&M 2622 (A.D. Young, ref. 4).

The data in these publications concern either tests with efficient high-lift devices on airfoil sections which were then considered obsolete such as the NACA 4- and 5-digit series and the British RAF-sections or the, at that time, modern NACA 6-series laminar flow sections but at moderate relative thickness (10 to 12%). Data from systematic tests on a large series of NACA 6-series airfoil sections equipped with a 0.20c split flap were available however. Also a very limited set of data on thick NACA 6-series sections with double-slotted flaps can be found.

All test data indicated however that within the airfoil classification system used at that time both older and later section families showed the highest maximum lift coefficients at a relative thickness of about 12% for the clean section and of about 20% with a deflected trailing-edge flap. This is illustrated in figure 1 taken from ref. 1.

Because of the desire to minimise induced drag both in take-off and in cruise a wing of very high aspect ratio was required for the F-27. An aspect ratio A=12 was felt to be achievable provided the flutter requirements could be met without significant weight penalties. This could be safeguarded by providing maximum cross-sectional area in the wing torsion box. Therefore maximum airfoil thickness was required over the greater part of the wing span.

Thus a happy coincidence occurred between the requirements concerning wing weight and stiffness and low-speed high-lift characteristics, albeit at the expense of a somewhat higher profile drag.

The F-27 wing is defined by a 21% thick root section and a 15% thick tip section. As a consequence at the outer end of the flap at 70% half-span the wing section relative thickness is still 18% . Thus on average over the wing part covered by the trailing-edge flap the relative wing thickness is 20% .

The governing airfoil sections on the F-27 wing are:

NACA 64_4 - 421 (mod	(root)
NACA 64_4 - 418 (mod)	(70% half-span)
NACA 64_4 - 415 (mod)	(tip)

The selection of these particular sections was entirely based on a analysis of available windtunnel test data from open literature. The modifications consisted of straitening-out the cusps on the rear upper surface.

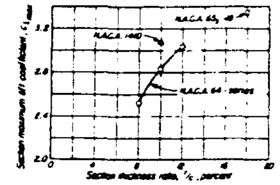

Effect of thickness ratio and type of wing section on maximum lift with double-slotted flaps.

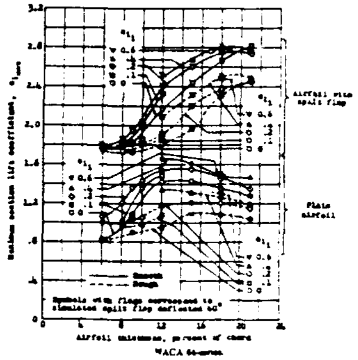

Variation of maximum section lift coefficient with airfoil thickness ratio and camber for several NACA airfoil sections

Fig. 1 Effect of airfoil section thickness on $C_{l\max}$ (from ref. 1).

Windtunnel tests for the analysis and optimization of the high-lift characteristics were performed on two models:

a. A complete model at scale 1 : 15 measured on a six-component external mechanical balance at $Re_c = 0.8 \times 10^6$ and $M = 0.12$

b. A two-dimensional airfoil section model with section chord C = 600 mm spanning the complete tunnel test section between the side walls (tunnel width = 3.00 m). The airfoil section was NACA 64_4-421 (mod). The model consisted of three parts of equal span. The outerparts were fixed to turning tables on the tunnel side walls. The centre part was fitted to the outer parts through strain-gauge balances with which normal and tangential forces and pitching moments could be measured. This arrangement was supposed to minimise the effect of lift loss near the tunnel walls due to flow separation in the corners between model surface and tunnel wall. Additionally drag was measured with a wake rake at one rake position for the majority of tests. Only a limited number of pressures were measured with a wandering static tube to obtain data for loads analysis. Most tests were performed at a Reynolds Number $Re_c = 2.3 \times 10^6$.

For the analysis of the flight handling characteristics separate outer wing and tail surface models were used to obtain detailed control surface hinge moment data.

Inially both the complete model and the two-dimensional model were equipped with a double-slotted flap with a total chord equal to 31% of the section chord, with fixed vane and a fixed point of rotation. In subsequent test series different types of flap, all with the same total flap chord were investigated on the two-dimensional model (see figure 2) together with minor variations in the shape and relative position of flap and vane on the double-slotted flaps and in the location of the fixed rotation axis. Also the effect on lift and drag was investigated of variations in the shape of the lower shroud of the flap cavity on the wing. Furthermore the effect of flap brackets was investigated.

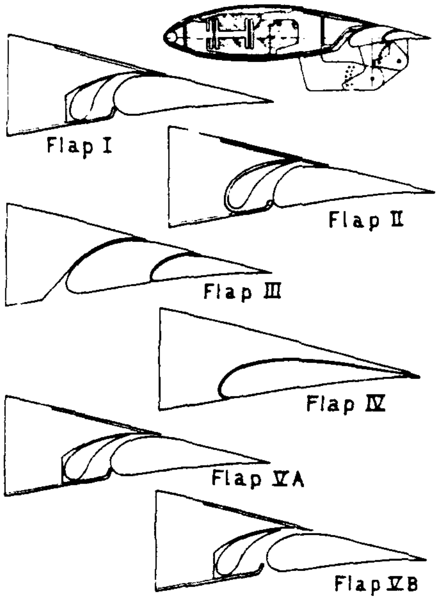

Fig. 2 Flap configurations tested on the F-27 2-D model.

Representative $C_{L_{max}}$ - values recorded for the various flap types are presented in the table below.

Flap no	Flap type	Flap setting	Re_c	$C_{L_{max}}$
I	Double-slotted, fixed vane	40 deg	2.2×10^6	2.80
II	Double-slotted fixed vane	50 deg	2.2×10^6	3.13
III	Compound flap	40/35 deg	2.2×10^6	3.76
IV	Fowler	45 deg	1.7×10^6	3.68
Va	Double-slotted, fixed vane	55 deg	2.2×10^6	3.37
Vb	Double-slotted, fixed vane	50 deg	2.2×10^6	3.27

The data obtained on the two-dimensional model led to the conclusion that the use of the compound flap would be advantageous. This flap was a double-slotted flap on which the front and rear flap were of roughly equal chord and on which the rear flap could move relative to the front flap.

This flap offered not only a very high maximum lift in the landing, but, when the rear flap was not deflected thus closing the second slot, low drag for take-off conditions could be realised. Furthermore this flap allowed the use of a fixed hinge and offered a reasonable section pitching moment, two advantages which made it superior to the Fowler flap. Figure 3 shows lift curves for the double slotted flaps with fixed vanes and for the compound flap as measured on the two-dimensional model.

The compound flap was then tested on the complete F-27 model at scale 1:15 and showed indeed a marked improvement in the maximum lift coefficient for landing. This is illustrated in figure 4.

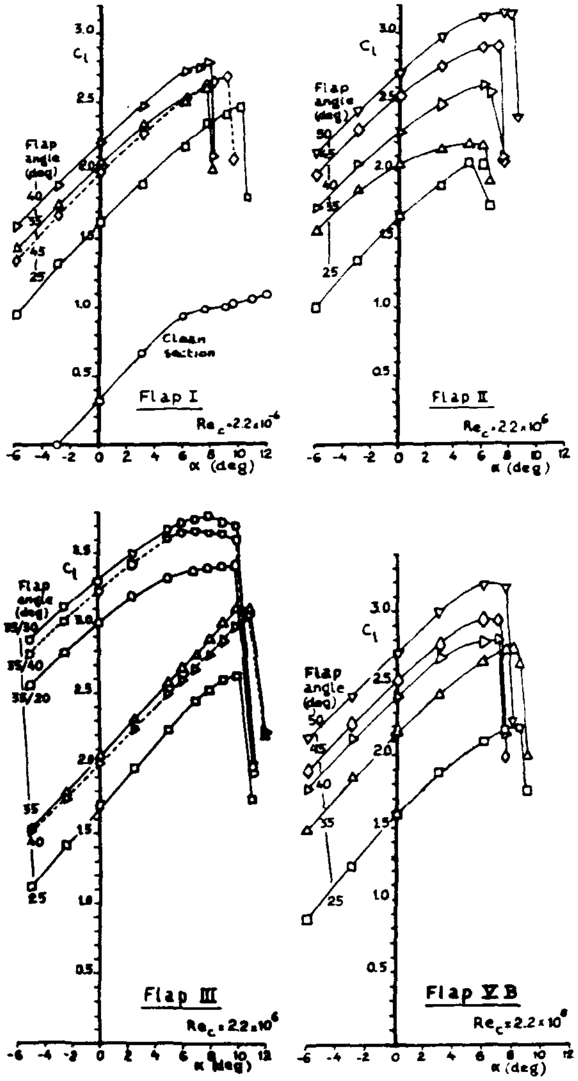

Fig. 3 Lift curves for four flaps tested on the F-27 2-D model.

When the first F-27 prototype started test flying in November 1955 it quickly showed to have less than satisfactory flight characteristics. In particular with large flap deflections and a fair degree of engine power longitudinal stability including the flare characteristics in the landing were considered unsatisfactory. This was aggrevated by shortcomings in lateral and directional control.

After only a limited number of flights it was therefore decided to fix the rear flap to the front flap in the neutral position and continue flight testing with the single-slotted flap configuration. The maximum flap angle became thus 40 degrees.

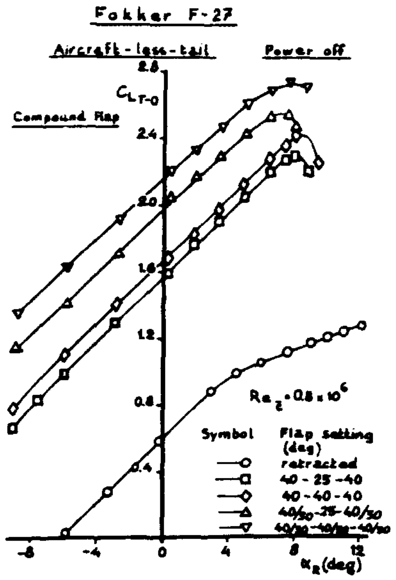

Fig. 4 The F-27, windtunnel model. scale 1:15, - Lift curves.

At one stage in the flight test programme in 1957 stabilizer effectiveness with leading-edge roughness was to be investigated at extreme negative stabilizer angles-of-attack. As the leading-edge de-icing system contained pneumatic boots, which function only when some ice accretion has occurred, a limited amount of leading-edge roughness must be tolerable.
Leading-edge roughness was simulated for this test by the application of bird-seed. At one condition with the flaps fully deflected the aircraft pitched forward at the application of power reaching zero g and plunging into a vertical dive.
Retracting the flaps and closing the engine throttles saved the situation.

As a result of this experience the inner wing flap extension mechanism was altered such that at each flap setting the deflection of the inner flaps is only two-third of the outer flap extension. Thus, the maximum deflection of the inner flaps on the F-27 is 26 deg. Also, the stabilizer leading edge was cambered upward as shown in figure 5. These two measures completely elimininated the possibility of negative tailplane stall over the complete range of flap settings, operating speeds and power settings even at push-overs up to 0.5 g.

So a design which was originally intended to be equipped with very effective double-slotted flaps (the "compound flap") was finally certified with single-slotted flaps with reduced settings on the inboard panels. This resulted in a decrease in maximum lift coefficient of 15 percent but was necessitated by the flight handling certification requirements, both for all-engine and single-engine flight.

As a part of design studies into possible further development of the F-27 flight tests were performed in 1960 on a highly modified F-27 prototype. The modifications consisted of:

a. The reactivated double-slotted compound flap as used during the very first flight. On the inboard flaps the aft flap was fixed in the neutral position.

b. A variabel-incidence tailplane mechanically coupled to the flaps such that with flaps retracted the stabilizer setting i_h = -1 deg (stabilizer nose down) and i_h = + 3.5 deg with the flaps fully down.

c. An enlarged elevator with modified balance nose and a spring tab.

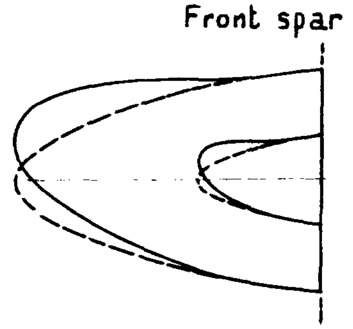

Fig. 5 F-27 horizontal tailplane. Modified leading-edge for production aircraft.

Although the improvement in $C_{L_{max}}$, compared to the standard aircraft, as predicted by the windtunnel testdata could be realized, (figure 6) the flight handling characteristics were still considered unsatisfactory and no further development work was performed on this configuration.

So, what did the development history of the F-27 teach us ? It tought us that for a medium-speed propeller aircraft design for high-lift is not so much a matter of coming up with an efficient flap system on a suitable airfoil section but much more a matter of keeping the high lift literally "under control". The combination of high-lift and high engine power leads at take-off and landing speeds to very high propeller thrust coefficients with associated strong adverse slipstream effects on the flight characteristics in pitch, roll and yaw both in all-engine and single-engine flight. Concerning the longitudinal characteristics a detailed analysis of these phenomenae is presented in ref. 5

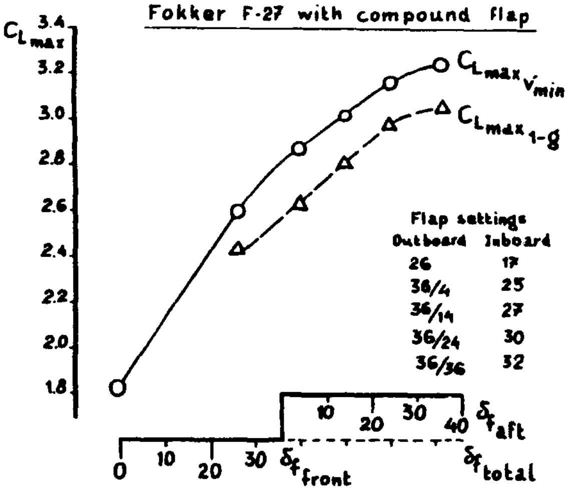

Fig. 6 Maximum lift from flight tests on the F-27 prototype equipped with the compound flap.

The basic wing sections were taken from open literature, the various flap sections were drawn with available French curves keeping practical experience by others in mind and the range of flap gaps and overlaps to be investigated in the windtunnel were again taken from open literature with an eye on acceptable flap bracket size and the associated flap extension mechanism. No theoretical design tool was used neither was one available and pressure distributions were not considered for high-lift design .
Still, apart from the measures taken because of aircraft control considerations, no modifications were required on the flap system on the actual aircraft. Also no tailoring of the stall characteristics was required. The F-27 has perfect wing stalling characteristics without any protrusions such as leading-edge stall strips or fences.
And a 1-g $C_{L_{max}}$ = 2.6 for an aircraft with single-slotted flaps and $C_{L_{max}}$ = 3.05 for an aircraft with double-slotted flaps are still respectable numbers even today.

Obtaining satisfactory characteristics on the basic F-27 over the complete flight envelope for the manually controlled elevator, ailerons and rudder took however the greater part of a two-year development and flight test programme. (1955 - 1957)

III **HIGH LIFT COMBINED WITH JET SPEEDS - THE DEVELOPMENT OF THE HIGH-LIFT CHARACTERISTICS OF THE F-28 Mk1000**

In 1961 design studies were initiated on a jet transport aircraft with a capacity of 44 passengers, soon to be increased to 65 passengers, and cruise speeds up to M = 0.75. This aircraft was meant to complement or succeed the F-27. As the aircraft was intended for the lower end of the market and as in many cases it would be the first time a possibly less experienced airline would operate jet aircraft it was felt that optimum flight handling characteristics coupled with maximum simplicity in the aircraft systems were mandatory. This feeling was strengthened by early experience with the Boeing 707, Douglas DC-8 and Caravelle where the absence of slipstream effects as a safety factor coupled with (on the first two mentioned aircraft) less-than-optimum control characteristics lead to a number of serious incidents.

Finally, the new aircraft was to have a field performance comparable to that of the F-27.

The new aircraft, the Fokker F-28 Fellowship would not be bothered by adverse slipstream effects. Instead, a new potential problem area was introduced: transonic aerodynamics.
At Fokker's early experience had been gained with transonic aerodynamics in the design and flight testing of the S-14 Mach Trainer.

In the design of this aircraft transonic tuck-under, a nose-down pitching tendency caused by flow separation due to shockwave - boundary - layer interaction and exhibited also by many present day jet aircraft when flying at transonic Mach-numbers, had been prevented by a novel design approach.
In this approach it was reasoned that the nose-down pitching tendency stemming from the changing pressure distribution on the wing once this flow separation occurred could be compensated by a changing downwash condition at the horizontal tailplane. The increased downwash which was required for this compensating aircraft nose-up pitching moment would have to be caused by properly positioned additional trailing vortices from the wing. This required that the initial flow separation with its associated local dip in the wing spanwise lift distribution occurred at a spanwise position just outboard of the tailplane tips. In order to obtain the flow separation pattern as described above the airfoil section at 40 percent halfspan was made thicker than the root and tip section.

The airfoil sections on the S-14 which had a straight wing were of the British RAE EC-XX40 series and had the following thicknesses:

root	12.1%
40% half-span	14.5%
tip	12.0%

As the S-14 had a negligible tuck-under tendency between M = 0.78 and M = 0.82 requiring less than 10 lb change in stick-force over that small speed range (see ref. 6) the principle was assumed to work.

The same approach was followed in the initial design of the F-28.
The original wing design of the F-28 had zero sweep at the 40% chord line. Again, the section at 40 percent half-span was thicker than the root section. The initial windtunnel model demonstrated however a larger than expected pitch-down tendency at transonic Mach-numbers, possibly due to the high horizontal tailplane. In subsequent design steps the wing sweep was therefore increased to 16 degrees at the quarter-chord line maintaining the concept of the spanwise thickness distribution as described above. In its final configuration the high-speed pitching characteristics were so much improved up to M_D that no Mach-trim compensator or other pitch-augmentation system was required on the certified aircraft.

The governing sections on the F-28 wing have the following relative thickness:

root	13.6%
40% halfspan	14.0%
70% halfspan	10.5%
tip	10.0%

Since the development of the S-14 insight in airfoil section characteristics had increased in two significant area's:

a. Systematic analysis of a large number of windtunnel test data had indicated that basically three types of airfoil section stall could be distinguished: (ref. 7).

   trailing-edge stall
   leading-edge stall
   thin-airfoil stall

Furthermore it was established that the type of stall was to a large extend determined by the leading-edge shape. The governing parameter was the ordinate of a point on the upper surface at 1.25% from the leading-edge (ref. 8). This is in effect the combined effect of nose camber and leading-edge radius.
This coordinate could even be correlated with the maximum lift coefficient at a given Reynolds number particularly for thinner sections with little camber.

b. Following research at NACA in the '30s and in Germany during World War Two the NACA modified 4-digit airfoil sections were shown to have superior highspeed characteristics when compared to standard NACA 4- and 5-digit series and the later laminar flow sections such as the NACA 6-series. NACA modified 4-digit sections differ from the standard 4-digit sections in their location of maximum thickness (40% to 50% chord instead of 30%) and their leading-edge parameter (= leading-edge radius ^{t}/chord).
   It turned out that at a given lift-coefficient and

> relative thickness higher drag divergence Mach numbers could be achieved when the leading-edge radius was larger than on the more conventional airfoils.

This was found to be caused by the way the initial area of supersonic flow on the section upper surface developed with increasing Mach number. Whereas on convential airfoil sections at cruise lift coefficients and subsonic Mach-numbers the upper surface pressure distribution either shows a slight rearward slope from the leading-edge onwards or shows maximum super velocities near their mid-chord point the sections with larger leading-edge radii show a sharp leading-edge suction peak. This difference causes an almost explosive development of the area with supersonic flow on the conventional airfoil once the critical Mach-number is surpassed resulting in strong shockwaves and flow separation. On the NACA modified 4-digit series the area with supersonic flow extends gradually from the leading edge, often with a degree of isentropic recompression and ending in a weak shock leading to higher drag divergence Machnumbers.

So, here was a situation were, contrary to earlier days, low- and high-speed characteristics were not correlated to airfoil sections or section families as a whole but specific characteristics of the geometry and the pressure distribution could be correlated with specific aerodynamic characteristics. These discoveries were the first step in the development of a process in which the designer obtained the possibilities to tailor airfoil sections to his own specific needs instead of picking an airfoil section from a catalogue.

In 1962 18 airfoil sections were thus defined by Fokker and tested in a small transonic tunnel at NLR at Reynolds numbers up to $2.2 \times 10.^6$. In figure 7 an overview of these sections is presented. Most sections have large leading-edge radii. Sections no 17, 18, 5 and 6 were used in defining the final F-28 wing.

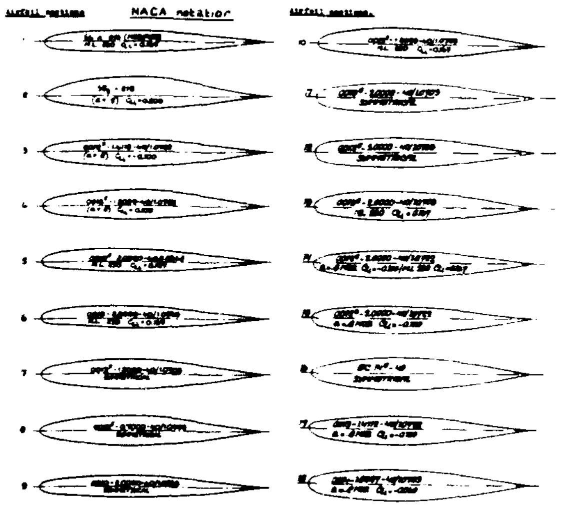

Fig. 7 Transonic airfoil sections tested in the NLR High-Speed Pilot Tunnel.

No leading-edge devices were envisaged for the F-28. For the trailing-edge flaps again requirements were formulated for very high maximum lift for take-off and landing configurations combined with high lift-drag ratio's at take-off and landing conditions at $1.2V_s$ and $1.3\ V_s$ respectively. In particular for the landing it was considered important to achieve low drag as sufficiently extra drag, if required, would be available from rear-fuselage speed brakes.

In order to determine the most suitable flap configuration for the F-28 a two-dimensional model was made based on an airfoil section which came very close to the actual wing section at 60 percent halfspan. The model spanned the height of the NLR low-Speed Tunnel (2m) and was provided with a large number of pressure tappings. The model could be provided with any of seven different flaps with a chord of 32% of the wing chord. (See figure 8). The model chord with flap retracted was 0.60 m and most tests were performed at $Re_c = 2.8 \times 10^6$. As the lift and the pitching moment would be determined via pressure integrations and the drag was obtained via wake rake measurements the model was directly fixed to the upper and lower turning tables on the windtunnel floor and ceiling. As there were at that time no provisions to remove or re-energize the boundary layer on the tunnel floor and ceiling near the model considerable flow separation occurred at high lift in the corners formed by the tunnel walls and the model surface. This prevented the realisation of true two-dimensional flow to a considerable extend at high-lift conditions resulting in considerable distortion of the upper part of the C_l - versus $-\alpha$ curves for the various configurations tested. A procedure had therefore to be defined to estimate the maximum lift coefficient for each test for the equivalent two-dimensional flow condition. This was based on assuming a near-linear curve up to the angle-of-attack for total flow break down. (See figure 9). Tuft investigations which showed that in most cases leading-edge stall occurred justified this approach.

A detailed comparison was made for the various flaps concerning maximum lift, lift-to-drag ratio's, pitching moment and sensitivity to flap gap flow disturbances due to flap bracketry and flap suspension mechanisms. This led to the choice of the double-slotted flap with movable vane (flap no 6) as the most suitable configuration for further development. Figures 10 and 11 show some testdata obtained in this analysis.

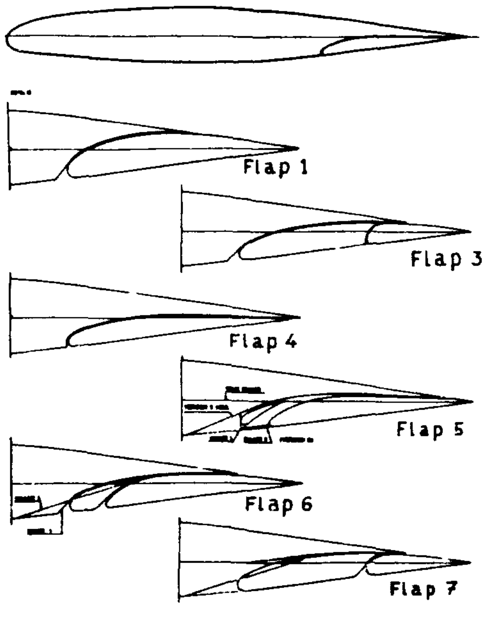

Fig. 8 Flap configurations investigated during the F-28 development.

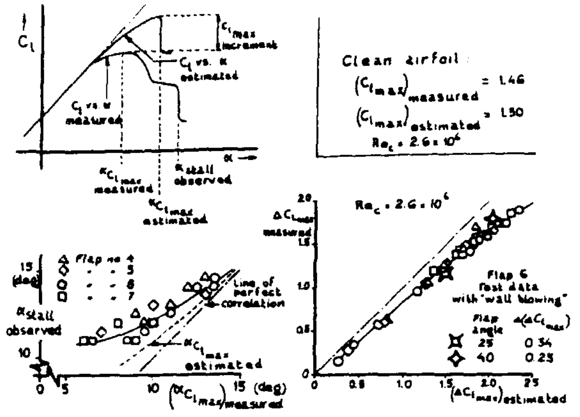

Fig. 9 Correction procedure applied to the 2-D testdata during the F-28 development.

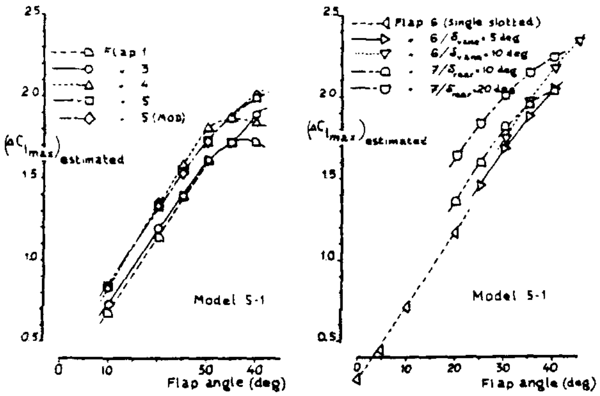

Fig. 10 F-28 - 2-D maximum lift.

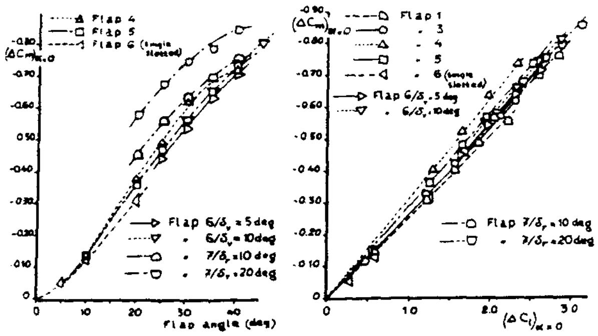

Fig. 11 F-28 - 2-D pitching moment coefficients.

As the F-28 flap was assumed to be fitted on roller tracks far more freedom was available to define optimum intermediate flap positions. This lead to a much larger test programme on the two-dimensional model for the F-28 than on the corresponding F-27 model. Automated electronic data reduction helped much however to keep the test period within acceptable limits.

Just as during the design of the F-27 no theoretical tools were used in the design of the various flaps studied for the F-28. Again French curves were used for defining their geometry. Practical considerations such as upper wing shroud trailing edge angles and thicknesses and clearances with the flaps retracted, sealing provisions and practical roller paths and flap track shapes were considered of more importance.

Much attention was also paid again to minimizing drag, in particular for the take-off flap positions. This resulted in the adoption of movable flap shroud doors (see figure 12).

Having defined the flap geometry with its associated extension path two complete models, equipped with the double-slotted flap, which spanned 70 percent of the wing span, were tested. The larger one, at scale 1:12, in the NLR low-speed tunnel (LST) and the smaller one at scale 1:20 in the NLR High-Speed Tunnel at M = 0.19 at a tunnel pressure of 4 atm. These tests were performed at Reynolds numbers of $Re_c = 1.4 \times 10^6$ in the LST and $Re_c = 1.0$, 1.4 and 2.8×10^6 in the HST.
Also a half model at scale 1:12 was investigated in the HST at Reynolds numbers up to $Re_c = 5 \times 10^6$. On this model only the flow separation pattern at the stall could be studied as a function of Reynolds number as no force balance was fitted.

In the performance calculations for the F-28 it was assumed that $C_{L_{max}} = 1.5$ for the clean aircraft and $C_{L_{max}} = 2.5$ for the aircraft in the landing configuration would be realised, according to the definition of $C_{L_{max}}$, and this value being obtained with the procedure as described in the certification requirements, of CAR 4b. Using the two-dimensional data with the classical Weissinger extended lifting-line theory and using limited available data on Reynolds-number effects on maximum lift and on the difference between 1-g $C_{L_{max}}$ and CAR 4b (minimum speed) $C_{L_{max}}$ the conclusion was that this was achievable. At that time (1961/'62) this was seen as a considerable achievement as the jet aircraft then flying (Boeing 707, DC-8, Caravelle, Convair Coronado) reached $C_{L_{max}}$-values of the order of 2, even when equipped with leading-edge devices.

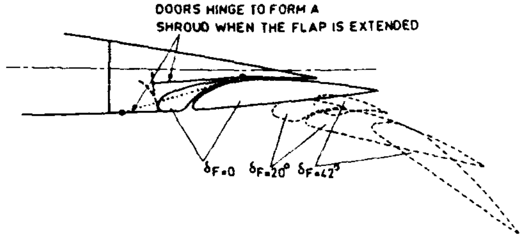

Fig. 12 F-28 - Hinged lower surface flap shroud doors for minimum drag.

When the LST- and HST-models were tested it was found that the expected $C_{L_{max}}$-values were realised, but the stalling characteristics were unacceptable both in pitch (offering too little resistance to achieving extreme angles-of-attack in post-stall conditions) and in roll.

Concerning the latter the models showed tip stall at low Re-numbers and a sudden flow separation over the complete wing on the half-model at $Re_c = 5 \times 10^6$. Clearly, some stall control device(s) was (were) required to initiate stall on the inboard wing.

On both the complete models and on the half-model a number of wing fences were tested at different/ spanwise positions alone or in combination with inboard stall strips. Longitudinal stability at the stall was clearly improved and in particular on the half-model at $RE_c = 5 \times 10^6$ wing stall started clearly on the inboard wing. All stall control devices lowered CLmax by C_{Lmax} = -0.1 to -0.15, however. (Figure 13).

So came the time that the stall was to be investigated on the prototype aircraft in 1967. After an extensive flight test programme aimed at obtaining satisfactory handling characteristics combined with a minimum loss in maximum lift a configuration was frozen with a single short leading-edge stall fence at Wing Station 3784 (mm from the fuselage centre line) combined with a stall strip just inboard of the fence the size of a match stick. The latter is there to ascertain a consistent flow separation behaviour. The stalling characteristics are such that no stick-pusher is required. Figure 14 shows the various C_{Lmax}-values measured in the windtunnel and on the full scale aircraft.
Refs. 9, 10 and 11 present more details on the aerodynamic development of the Fokker F-28 Mk1000.

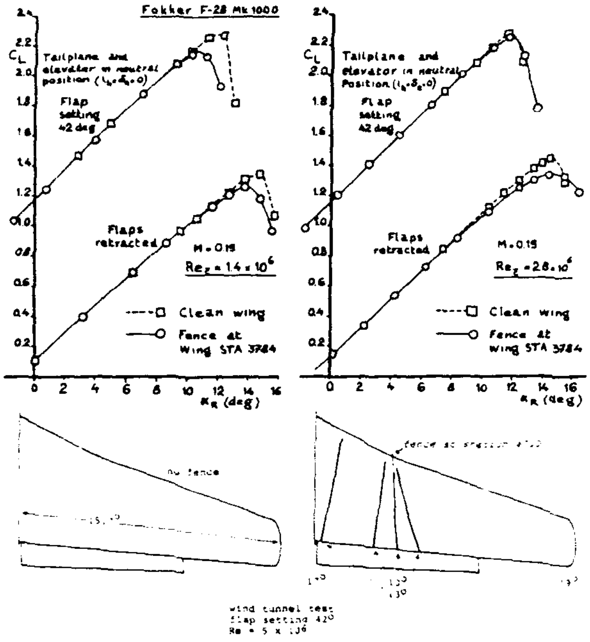

Effect of fence on progression of flow separation

Fig. 13 Effect of stall control devices on maximum lift and flow separation pattern.

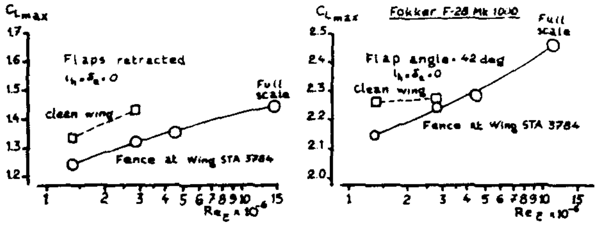

Fig. 14 F-28 MK1000 - maximum lift as a function of Reynolds number.

So, what did we learn, concerning high-lift characteristics, in the development of the Fokker F-28 Fellowship ?

We learned the following:

a. Wing geometry requirements have to be considered integrally, for both high-speed and for low-speed flight, in particular when no leading-edge devices are used.

b. Tayloring stalling characteristics both in roll and in pitch has to be considered as early as possible in the design as it is most likely to affect maximum lift and thus aircraft performance.

c. Good handling characteristics in combination with minimum lift loss can only be determined reliably in windtunnel tests at high Reynolds numbers.

d. For reliable windtunnel testdata details of the flap mechanism have to be reproduced faithfully on the model.

IV LEADING-EDGE DEVICES

As part of continuing efforts to increase the versatility of the F-27 a study was started in 1968 to analyse the potential of equipping the F-27 wing with slats.
A windtunnel test was performed on the original two-dimensional model used in the F-27 development programme. Apart from the original airfoil section two modifications were tested:

a. A modified leading-edge section with a larger leading-edge radius than on the basic section combined with some leading-edge camber.

b. A leading-edge section equipped with a slat.

The tests showed that a modified fixed leading-edge showed only limited increase in C_{Lmax} notwithstanding the increase in leading edge radius whereas the slat could improve C_{Lmax} by as much as ΔC_{Lmax} = 1.0 over the complete flap range (Figure 15).

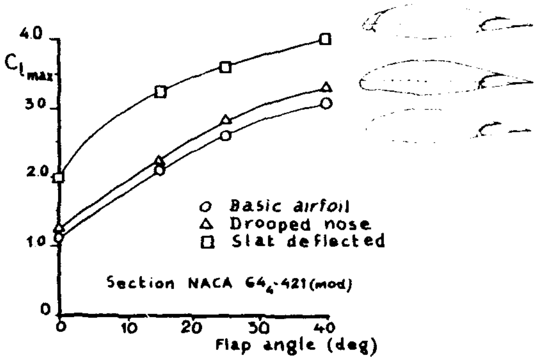

Fig. 15 Leading-edge modification and slat tested on the F-27 2-D model.

In the late '60's windtunnel tests were performed in the NLR-LST on a two-dimensional model equipped with a slat and a single- or a double-slotted flap. Two slat shapes and three main component leading edge shapes were investigated. The second single-slotted flap had, compared to the basic single slotted-flap a smaller leading-edge radius and consequently a stronger upper surface curvature.

The double-slotted flaps differed in their design method. The first flap was defined entirely on an empirical basis, keeping in mind some inhouse formulated design rules and with an eye on seemingly succesful vane shapes from open literature (figure 16). The total flap chord was 30 percent of the section chord. The other double-slotted flap was designed on a theoretical basis. The total flap chord of this latter flap was 35 percent of the section chord.
The airfoil section chord was 0.75 m leading to a maximum test Reynolds number Re = 3 x 10^6.
The various components investigated on this model, indicated here as model A, are shown in figure 17.

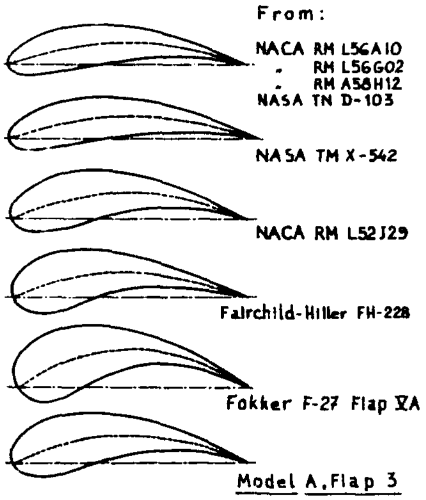

Fig. 16 Vanes shapes found from literature.

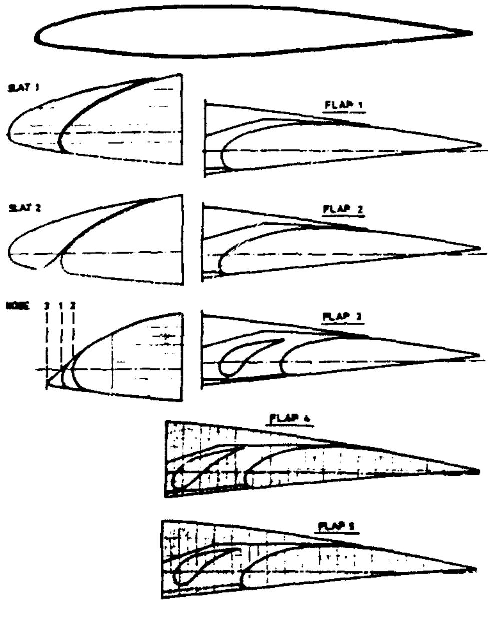

Fig. 17 High-lift devices tested on the 2-D model, Model A.

Prior to the design of the model under consideration NLR had installed a boundary layer blowing system in their low-speed tunnel which produced near-two-dimensional flow conditions in the tunnel test section, also at very high lift conditions. (Ref. 12).

This considerably improved the credibility of the test data and, incidentally had also proved the correctness of the correction procedure adopted for the F-28 test data mentioned in chapter III (Figure 18).

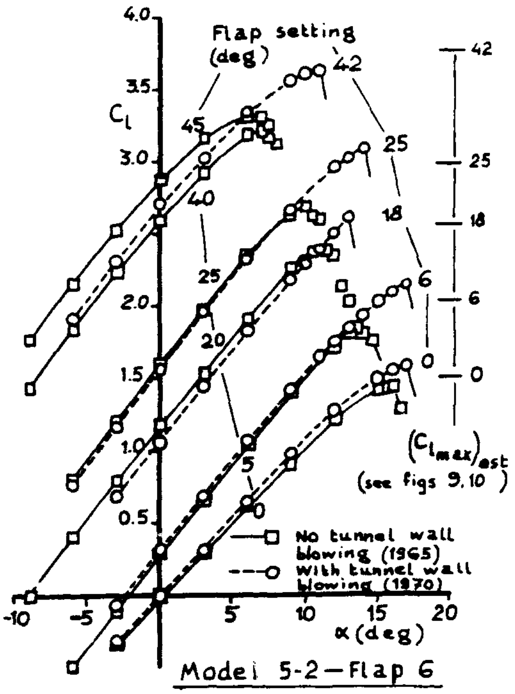

Fig. 18 Effect of tunnel wall blowing on lift curves-F-28 2-D model, Model 5-2.

The tests on the new 0.75 m chord model which consisted of the now standard integrated-pressures tests for lift and pitching moment and wake-rake measurements for drag were performed on a number of different slat-main component-vane-flap configurations at many combinations of gaps, overlaps and deflection angles.

The tests produced the following results:

a. The two single-slotted flaps produced for all practical purposes identical maximum lift notwithstanding the differences in geometry. (Figure 19a).

b. Removing the "hook" on the slat lower surface did not improve the slat's high lift characteristics. (Figure 19b).

c. Decreasing the radius on the main component's leading edge had no effect on maximum lift unless the leading edge radius became extremely small. (Figure 19c).

d. The three double-slotted flaps (as a third flap the vane of the first flap was combined with the other main flap) produced practically identical maximum lift if the difference in extended chord was taken into account. (Figure 19d).

e. The routine availability of detailed pressure distributions allowed an extensive study of various flow phenomenae such as the development of areas of controlled separated flow in slat and flap shroud cavities, the movement of stagnation points as a function of configuration parameters. An analysis of boundary layer conditions on a routine basis was of course not possible with the available test data.

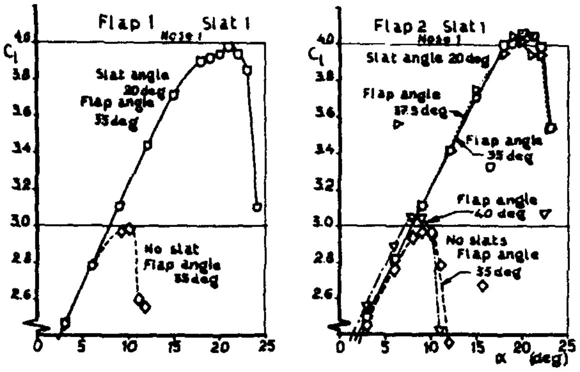

Fig. 19a Effect of single-slotted flap shape.

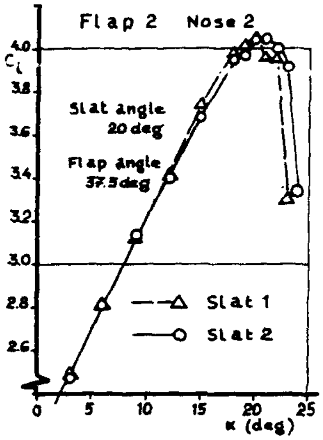

Fig. 19b Effect of slat shape.

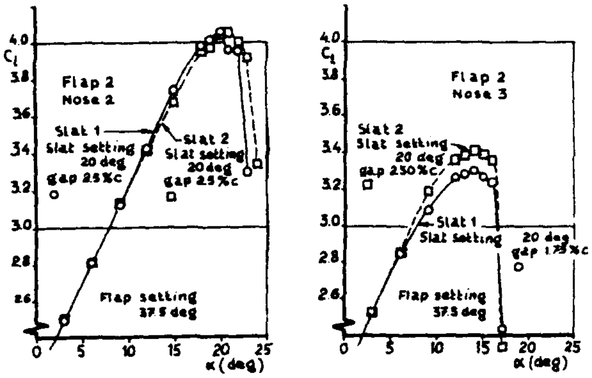

Fig. 19c Effect of fixed leading-edge shape.

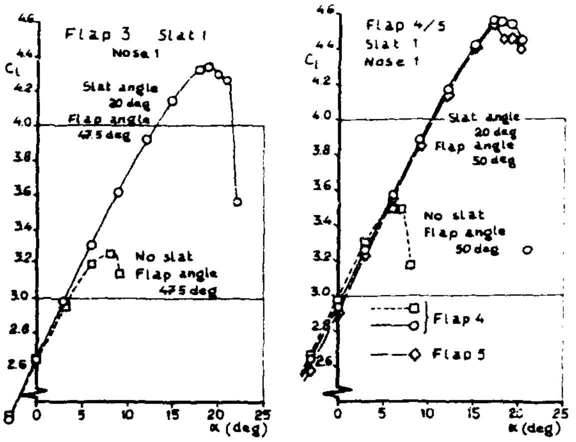

Fig. 19d Effect of double-slotted flaps.

Fig. 19 Windtunnel test data from Model A - Lift curves.

V DEVELOPMENT OF THE SLATTED VERSION OF THE F-28 FELLOWSHIP, THE F-28 MK 6000

As the Maximum Take-off Weight of the F-28 Mk 1000/2000 had increased from its initial design value of 54000 lb to 65000 lb and engine thrust had not changed, a need was seen to improve the aircraft's take-off and landing performance.
Slats seemed to offer one possibility.
Therefore, in 1970 a study was initiated to analyse the various possible ways to improve the F-28 field performance.
This resulted in the definition of 5 slat shapes, slats A to E, to be investigated on the two-dimensional F-28 model, Model 5-2. (Figure 20).
These slat shapes were again defined without any use of theory but under consideration of some design rules based on previous experience such as minimum slat trailing-edge angle for stiffness, sufficiently long lower surface to allow for stagnation point travel with increasing angle-of-attack, etc.).

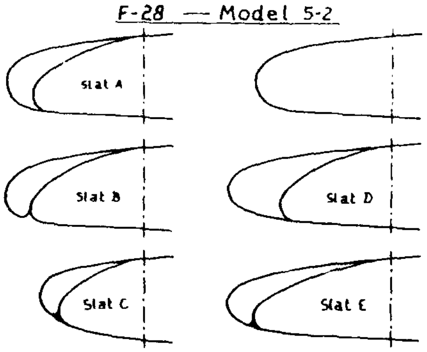

Fig. 20 Slat shapes investigated on the F-28 2-D model.

Some significant test results from this investigation are presented in figures 21 and 22.

The most important conclusions from this investigation were:

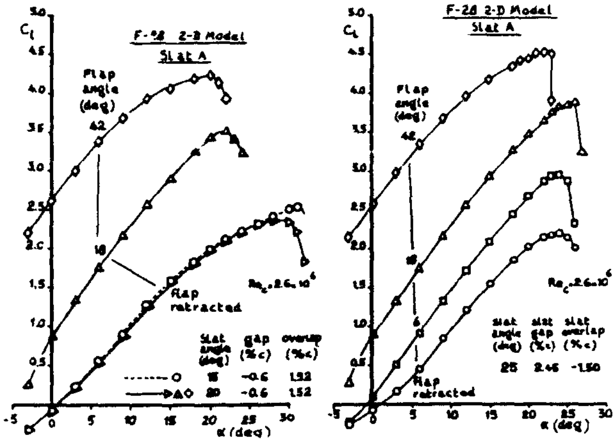

Fig. 21 F-28 2-D model - Lift curves for various slat settings.

a. Increasing the slat chord from 16% c to 19.5% c did not increase the maximum lift coefficient. (Both for slats D and E when compared with slat A).

b. For maximum lift the most attractive slat deflection seems to be 25 deg. with a fairly wide gap and underlap.

c. Decreasing the slat angle and slat gap and underlap lowered both the maximum lift and the drag.

d. At low lift coefficients their is no smooth flow through the slat gap. When this flap condition occurs the lift coefficient drops rapidly and the drag increases very rapidly at decreasing angle-of-attack.

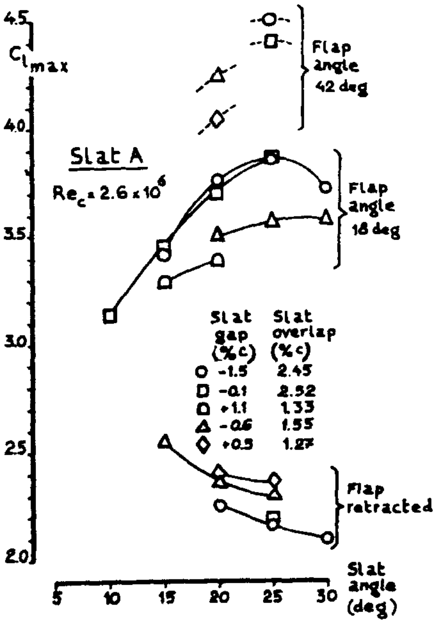

a. Effect of slat setting on $C_{L_{max}}$.

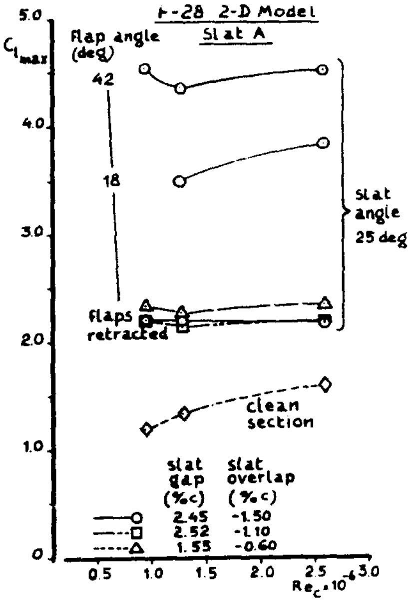

b. Effect of Reynolds number on $C_{L_{max}}$.

Fig. 22 F-28 2-D model.

The testdata from these 2-D tests were considered of sufficient interest to continue investigations on a three-dimensional model. The scale 1:12 F-28 LST-model was modified in 1971 to incorporate slats and tested subsequently. Initially 7 slat positions were investigated on this model, Model 8-5. Slat A from the 2-D tests was adopted as the slat shape to be investigated resulting in an unmodified wing shape with the slat retracted. These initial tests produced two surprises:

a. $C_{L_{max}}$ decreased when the slat angle was decreased from 25 to 15 degrees. Improvement of the wing root fairing shape improved $C_{L_{max}}$ significantly, however. (Figures 23 and 24)

b. The drag increase due to slats at take-off conditions had a dramatically high level with the slat angle at 25 deg and was significantly lower at slat angle = 15 deg. (Figure 25).

In the end 25 slat positions were investigated before it was accepted that additional measures had to be taken to arrive at acceptable aircraft lift-drag ratio's.
It was clear that the large number of slat brackets (rails on the real aircraft), simulated bleed air pipes for de-icing, etc. had a large extra drag contribution but this could not explain the large effects of slat angle.
Clearly some three-dimensional effects affected the flow picture to a considerable extend but a true explanation could not be found.

Adopting finally the slat configuration given as position no. 5 on Model 8-5 the additional measure taken to obtain the desired lift-drag ratio's consisted of a wing span increase (0.75 m span extension at each tip. This configuration was then tested in the NLR Low-Speed Tunnel as Model 8-7 at $Re_c = 1.4 \times 10^6$, in the High-Speed Tunnel as Model 6-4 at Reynolds numbers up to $Re_c = 2.8 \times 10^6$ and on the F-28 halfmodel Model 7-8 (which since the development of the F-28 Mk 1000 had been equipped with a 5-component balance) at Reynolds numbers up to $Re_c = 5 \times 10^6$.

Apart from $C_{L_{max}}$ and C_L/C_D at take-off and landing conditions the windtunnel tests on these models centered on two other design requirements:

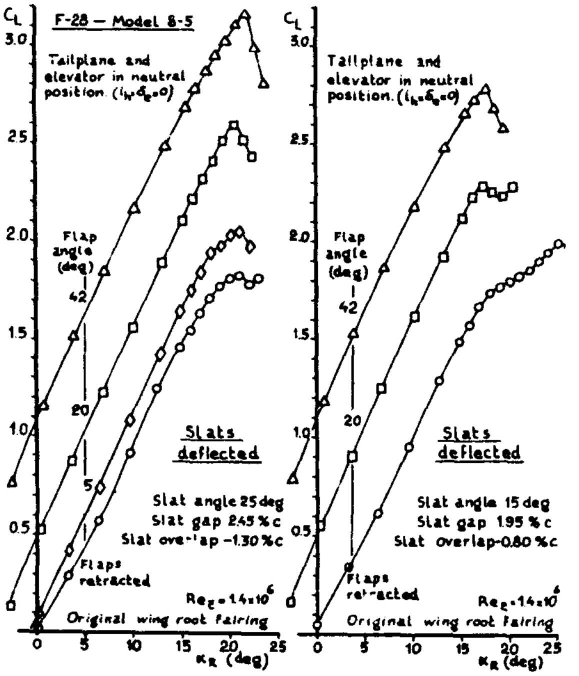

Fig. 23 F-28 Model 8-5. - Effect of slat angle on $C_{L_{max}}$.

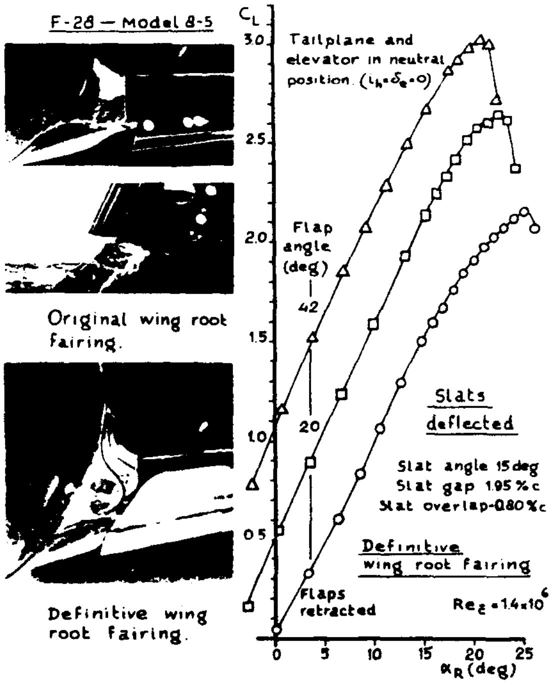

Fig. 24 Effect of wing root fairing shape on $C_{L_{max}}$.

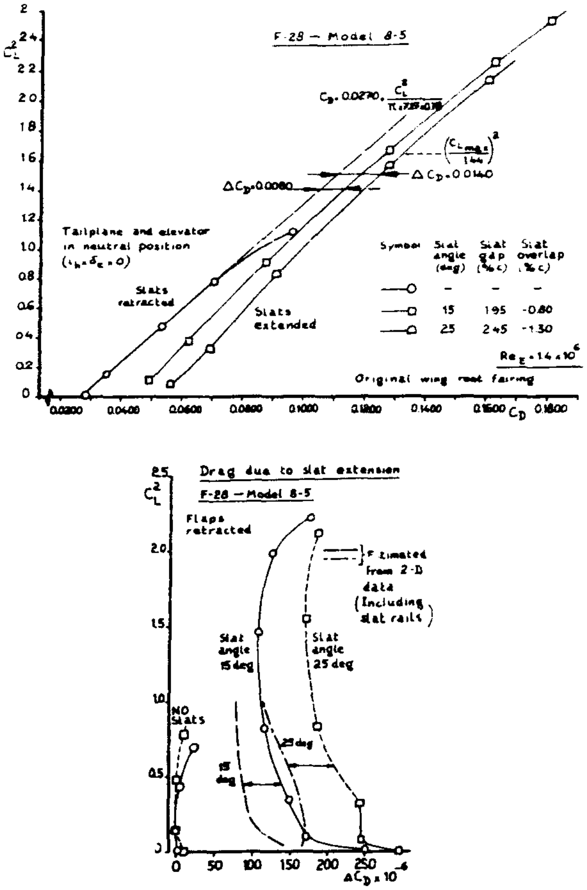

Fig. 25 Effect of slat angle on drag - F-28 Model 8-5.

a. securing satisfactory stalling characteristics, both in roll and in pitch. Concerning the latter in particular post-stall behaviour required attention.

b. Securing undisturbed engine operation at high angles-of-attack.

Stalling characteristics received a great deal of attention. Many different devices such as fences, stalling strips, stall promotors and spring loaded closing plates, the latter partially or completely closing the inner wing slat gap, were investigated at different Reynolds-numbers on the various models. Also various wing-root fairing shapes were analysed. The best compromise between a high $C_{L_{max}}$ and good stalling characteristics was thought to be obtained with the fence and stall strip as were present on the Mk 1000/2000 and a small stall promotor when the slat was extended. Also the wing-root fairing which became exposed when the slat extended had to be tailored carefully. The possibility of the need for a stick-pusher to prevent a locked-in stalled condition was recognized however.

Proper engine operation at high angle-of-attack became questionable when it was noticed that at that condition a strong vortex, springing from the inboard slat end, entered the engine intake. Intake flow analysis with the aid of total pressure rakes showed that this vortex could be suppressed significantly by installing a Kruger-flap between the fuselage and the slat.

When the full-scale development of the slatted version of the F-28 under the designation F-28 Mk 6000 was undertaken (for a description see ref. 13) the following aerodynamic configuration was adopted:

a. It was based on the F-28 Mk2000.

b. The wing span was increased by 0.75 m span extension at each tip.

c. Wing slats were adopted with a single extended position for both take-off and landing as close as possible to slat position no. 5 on Model 8-5/8-7, given minor restrictions from practical considerations.

d. A spring-loaded stall promotor on the inboard wing would be added. This decreased the slat gap with the slat in the extended position. (Figure 26)

e. A wing-root Kruger flap was added. (Figure 26)

f. The wing-root fairing at the leading edge was tailored for optimum inboard wing separation control near the stall. This affected the pitching moment in the stall in a positive way. (Figure 24).

g. A stick pusher would be developed.

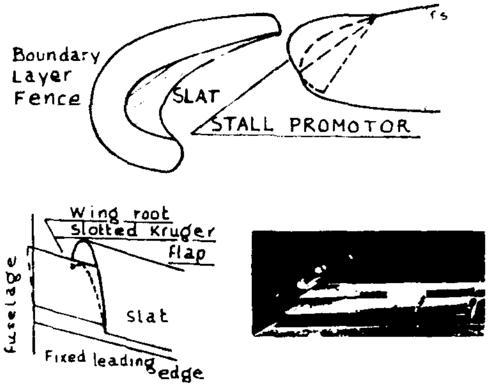

Fig. 26 F-28 MK6000 - Stall control devices.

Further windtunnel tests at higher Reynolds numbers on both a complete model (model 6-4) and on a half model (Model 7-7/7-8) showed a marked effect of Reynolds number on the drag due to high lift devices, in particular at lift coefficients of interest. (Figure 27)

When the prototype F-28 Mk 6000 was flight tested we were in for a new surprise. The maximum lift coefficient at full-scale conditions turned out to be much higher than estimated. In fact it was higher than considered to be useful.

Therefore in a very early stage of the flight test programme the slats were slightly retracted on their circular tracks from 15 deg to a slat angle of 13 degrees in an effort to decrease drag at take-off. The maximum lift turned out to be hardly influenced by this modification.

Furthermore both stall promotor and Kruger flap turned out to be unnecessary. Lateral characteristics including aileron characteristics turned out to be excellent up to extremely high angles-of-attack. Pitch stability in the stall at extreme aft centre-of-gravity position was small but positive. To prevent inadvertent large angle-of-attack excursions at the stall with very course control inputs a stick-pusher was installed.

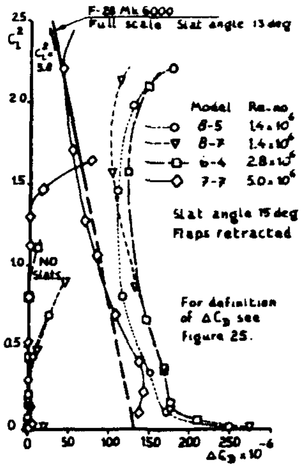

Fig. 27 Effect of Reynolds number on drag due to slats

Figures 28 to 31 show comparisons of some significant parameters as measured in the windtunnel, as estimated for the full-scale aircraft and as derived from flight tests.

From the development of the high-lift characteristics of the F-28 Mk 6000 the following lessons were drawn:

a. Again it became clear that small details on the high-lift devices had to be reproduced accurately.

b. Significant three-dimensional effects can occur in the flow about wing slats on swept wings, in particular concerning drag.

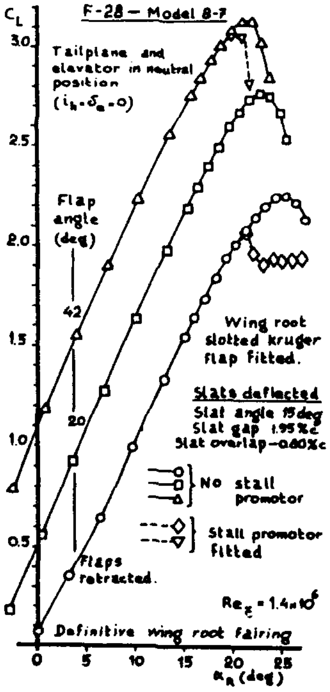

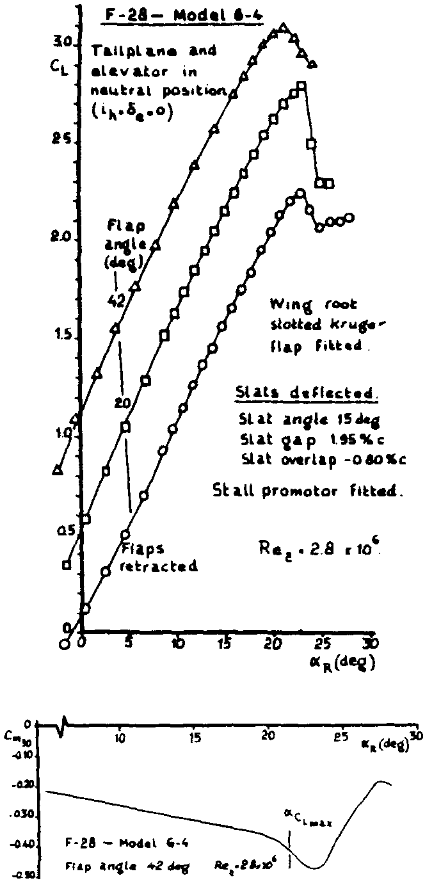

Fig. 28 F-28 MK6000 - Lift curves of the LST model, Model 8-7 and the HST model, Model 6-4.

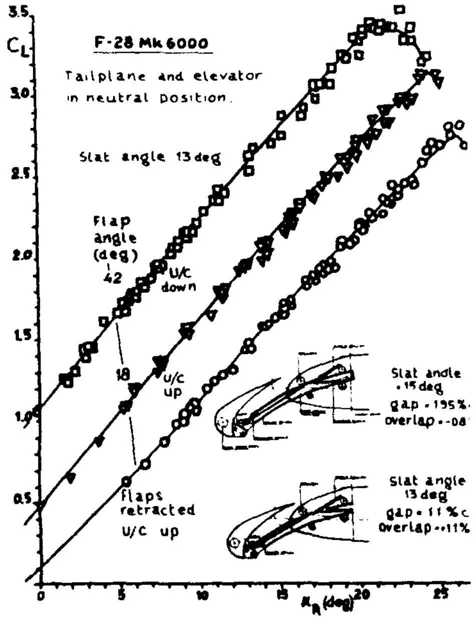

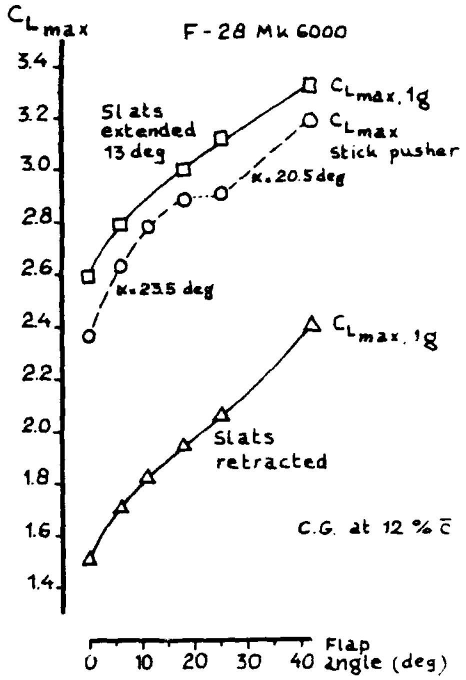

Fig. 29 F-28 MK6000 - Full scale lift curves and maximum lift.

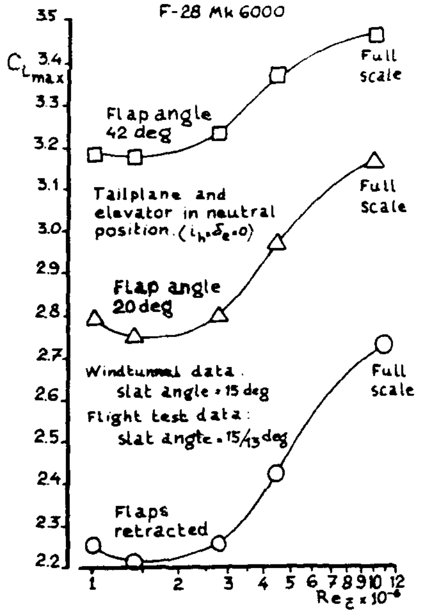

Fig. 30 Effect of Reynolds number on maximum lift.

c. Tailoring stalling characteristics of an aircraft equipped with slats in combination with a T-tail requires great care. Again windtunnel tests at high Reynolds numbers seem mandatory.

d. Significant Reynolds-number effects may still occur above Re_c = 5 x 10^6.

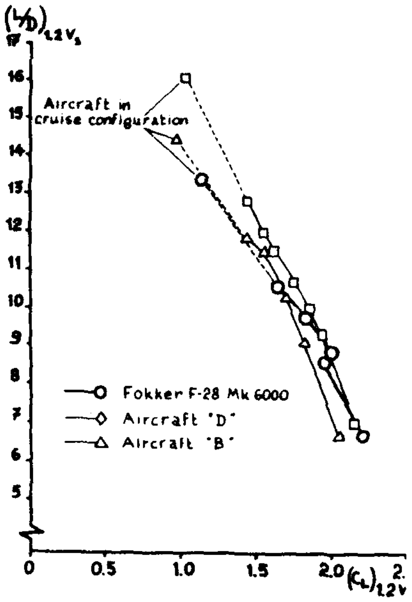

Fig. 31 Lift-drag ratio's with extended High-Lift devices.

V HIGH-LIFT CHARACTERISTICS OF ADVANCED TRANSONIC AIRFOILS

a. AIRFOIL SECTIONS

In 1968 Nieuwland and Spee at NLR published their results that proved both mathematically and experimentally that transonic flow with complete isentropic recompression existed as a stable flow condition.
To define airfoil sections for the windtunnel investigation a design method was developed at NLR based on hodograph theory. With this method a series of so-called quasi-elliptical airfoil sections were developed. Initially only symmetrical airfoil sections were developed. In later years also cambered airfoils were designed with this method although this was a cumbersome process. The first cambered airfoil was NLR 7101 with 14.1 percent relative thickness followed in 1973 by NLR 7301 with 16.5 percent relative thickness. As these sections had very thick leading edges it was decided to analyse the high-lift characteristics of section NLR 7301 with a number of high-lift devices in what became in the end an extensive test programme lasting from 1974 to 1977.
The tests were performed in the NLR 3x2m Low Speed Tunnel on a model, spanning the tunnel from floor to ceiling, having a chord = 0.570 m giving a maximum Reynolds no. = 2.6 x 10^6. Wall blowing was applied.
The slat and flap configurations investigated are shown in figure 32.
Lift, pitching moment and drag were again obtained through static pressure integration over the component surfaces and through wake rake measurements. In the latter 3 wake profiles were measured for each data point. Some maximum lift data are presented in figures 33 and 34.

Note that with the double-slotted flap with movable vane a $C_{L_{max}}$ = 5.00 was reached when a slat was fitted.

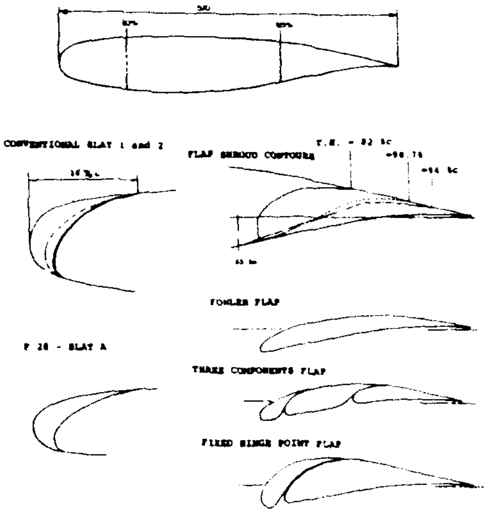

Fig. 32 High-lift devices tested on airfoil section NLR 7301.

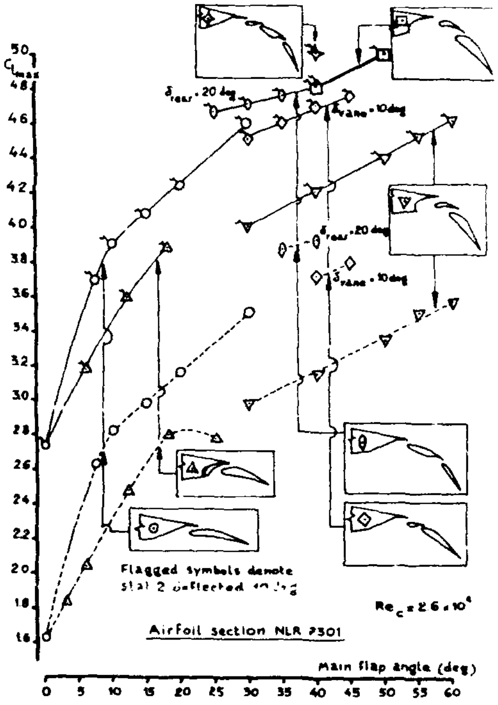

Fig. 33 Airfoil section NLR 7301. - some maximum lift data.

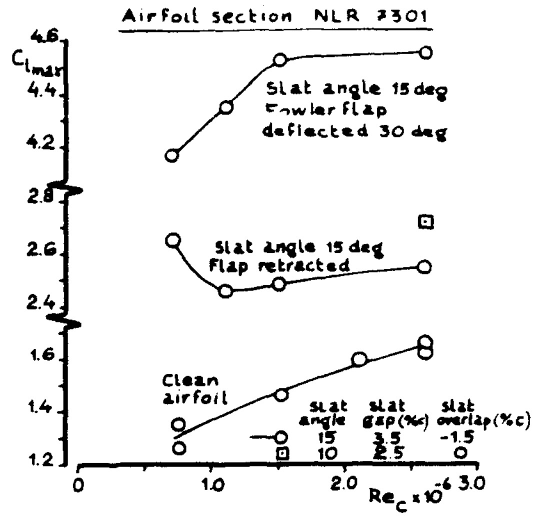

Fig. 34 Effect of Reynolds-number on maximum lift. - section NLR 7301 with slat and flap.

The results obtained in these tests clearly indicated that higher $C_{L_{max}}$-values could be obtained than on earlier sections investigated. The thick leading edges to which this was attributed presented a problem for high-speed flight however. Although the pressure distribution adopted had in theory zero wave drag at the design condition low-Reynolds-number tests showed a considerable drag creep at Mach numbers below the design Mach Number. Some tests were performed at the Lockheed CFF facility up to $Re_c = 30 \times 10^6$ which showed that at higher Re-numbers the drag creep did decrease. Today, this can also be calculated with Drela's programme ISES (ref. 14). (See figure 35).

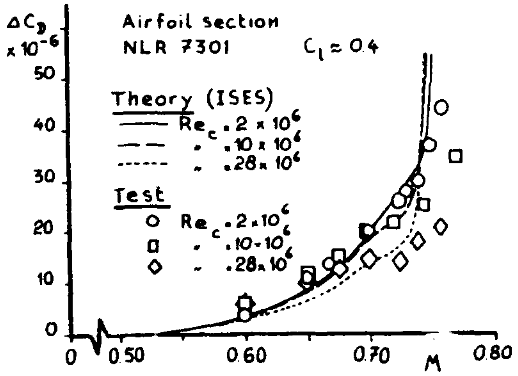

Fig. 35 NLR 7301 - Effect of Reynolds number on drag creep at high Mach numbers.

In 1977 however it was felt that a high peak Mach-number ($M_{local} \approx 1.30$) in the supersonic flow region near the nose of the section would introduce the unacceptable risk of a large transonic drag creep. Therefore new sections were designed which produced lower peak Mach-numbers near the leading-edge in the design condition. This led to lower leading-edge radii. One such section was NLR 7703. In order to investigate the effect of this thinner leading edge a modification was performed on the LST-model changing the section to a quasi NLR 7703 section indicated as NLR 7703 Mod.
Figure 36a shows the new section. The larger chord (c = 0.677 m) leads to a maximum $Re_c = 3.1 \times 10^6$.

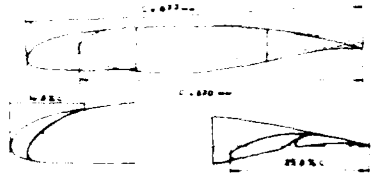

a Model NLR 7703 mod

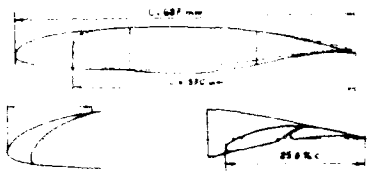

b Model F-29-16

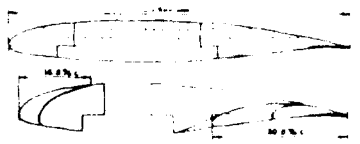

c Model F-29-12

Fig. 36 2-D models with high-lift devices tested between 1978 and 1981.

This configuration was investigated in 1978 and 1980. Because of the large spanwise variations in drag found in earlier tests the drag measurements on section NLR 7703 Mod were based on wake profiles measured at 8 spanwise stations. In figure 37 some maximum lift data are presented in comparison with data from section NLR 7301.

A second modification with an even smaller leading edge radius was also investigated with a slat in 1980. This configuration, Model F-29-16 is illustrated in figure 36b.

Finally in 1981 a two-dimensional model, F-29-12 was designed based on the same section as Model F-29-16 but with a 30 percent double-slotted flap. This model was intended for high Reynolds-number investigations at varying Mach-numbers in the NLR High-Speed Tunnel (HST). Reynolds numbers between $Re_c = 1.8 \times 10^6$ and 7.0×10^6 could be obtained.

Lift, pitching moment and drag were obtained in the same way as in the LST.
The airfoil section with its high-lift devices are shown in figure 36c. Some test data are presented in figure 38.

Apart from overall data this test produced insight in the effect of specific details in the flow such as the effect of Mach-number and Reynolds-number on the maximum local Mach-number at the leading-edge suction peak. As an example figure 39 is presented.

Throughout the period described in this chapter slat and flap shapes were determined empirically based on previous experience.

Finally, in the second half of the 1980's Fokker has participated in a GARTEUR high-lift research programme.

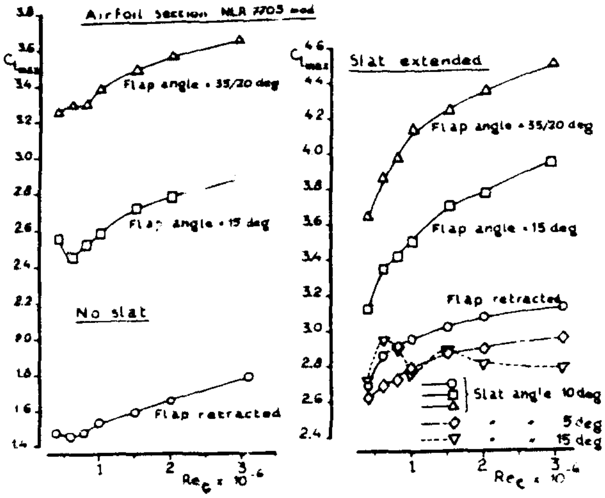

Fig. 37 Airfoil section NLR 7703 MOD with high-lift devices. - Effect of Re-no on maximum lift.

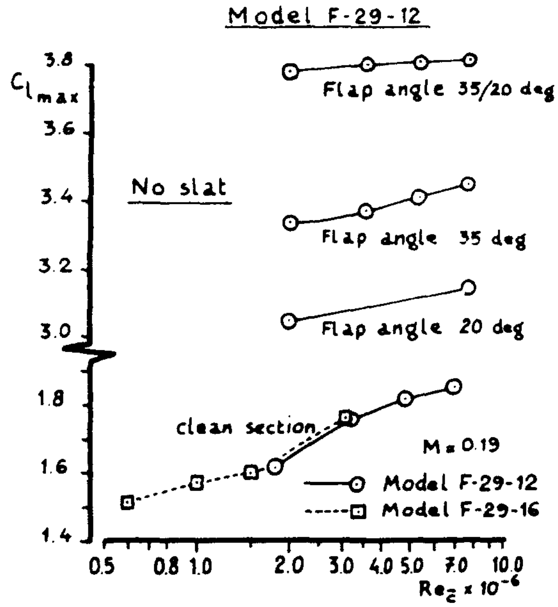

Fig. 38 Model F-29-12 - Maximum lift.

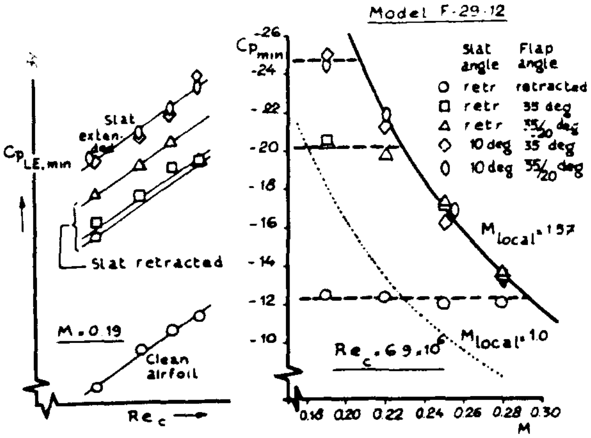

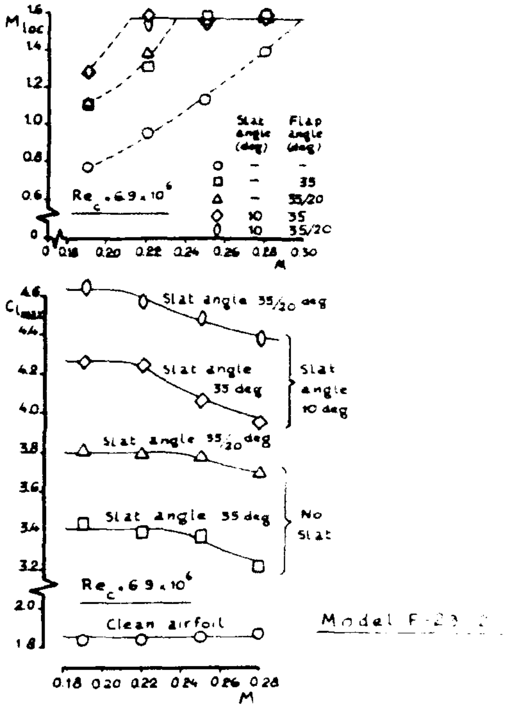

Fig. 39 Effect of Mach-number and Reynolds-number on maximum lift.

b. AIRCRAFT CONFIGURATIONS

Between 1975 and 1982 an extensive research and development programme concerning a successor to the F-28 was executed in the Netherlands. The programme started with a windtunnel investigation both on two- and on three-dimensional models to analyse the aerodynamic characteristics and the associated possible economic benefits of the newly developed advanced transonic airfoils. Nieuwland and Spee, Garabedian, Korn and Bauer and later Jameson had, together with a number of British researchers and helped by the advances in digital computer technology in the mid-seventies made it possible to design airfoils with a considerable area of supersonic flow on the upper surface.

Transonic pressure distributions were not entirely new. Aircraft such as the Douglas DC-8, DC-9, DC-10, Lockhead C-141 and L-1011, De Havilland Trident and Vickers VC-10 Boeing 737 and 747 and Fokker F-28 and even the later versions of the Boeing 707 at high weight had local areas of supersonic flow terminated with a weak shock on their wing upper surface at cruise conditions (see ref. 15). The developments just mentioned allowed however to extend the area of supersonic flow to at least 50 percent of the wing chord over most of the wing span in a controlled design process eliminating much of the earlier cut-and-try approach. This allowed either a thicker wing with higher aspect ratio or a thicker and lighter wing or a higher wing loading.

As the Fokker company concentrated historically on the short-to-medium haul market and field performance was felt to be as important as cruise performance the possibility to increase wing thickness was considered to be of greater benefit than increasing wing loading and thus design lift coefficient. Thus the initial wing designs were based on the experience obtained with airfoil sections such as NLR 7301 of 16.5 percent relative thickness as described in the first part of this paragraph. In the course of the aircraft development process which went from a highly modified F-28, the Super F-28 via the F-29 to the McDonnell Douglas-Fokker MDF-100 a gradual shift in the balance between cruise and field performance led to wing designs which became thinner with less blunt leading edges. As an illustration figure 40 presents a three-view drawing of the F-29 at a certain stage, project P-325 from January 1980. This trend in wing design history found its parallel in the development of the airfoil section models including their high-lift devices as mentioned before.

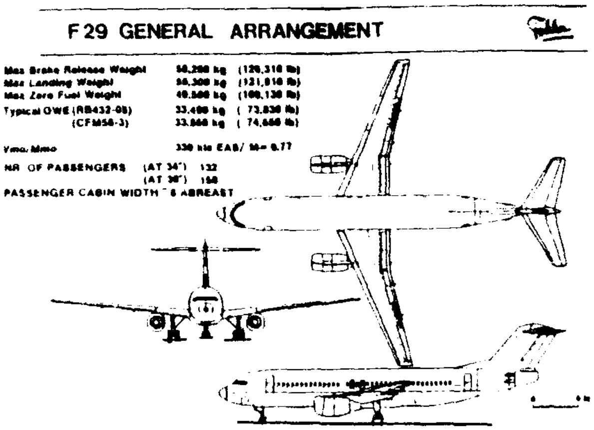

Fig. 40 Fokker F-29. - Project F325.

The following table illustrates the development history as characterised by a number of design parameters for each high-speed model wing.

Year	Complete Windtunnel model	Aspect Ratio	Wing sweep	(t/c) Kink (%)	M_{DES}	$C_{L_{DES}}$
1975	SKV-1	8.0	20 deg.	16.0%	0.75	0.45
1976	SKV-2	8.0	20 deg.	16.0%	0.75	0.45
1977	SKV-3	11.0	16 deg.		0.745	0.45
1977	SKV-4	8.0	20 deg.	16.0%	0.75	0.45
1978	SKV-5	11.0	16 deg.	15.0	0.75	0.45
1979	SKV-5 Mod-T3	11.0	16 deg.	15.0%	0.75	0.45
1979	SKV-6	11.0	21 deg.	13.4%	0.75	0.52
1980	SKV-8	11.0	21 deg.	13.4%	0.75	0.52
1980	F-29-1	10.0	21 deg.	13.5%	0.75	0.55
1981	F-29-2	10.0	21 deg.	12.9	0.75	0.55
1981	F-29-3	9.8	23.5 deg.	12.9	0.77	0.55
1981	F-29-4	10.0	21 deg.	12.5	0.77	0.55
1981	F-29-5	10.0	23 deg.	12.4	0.77	0.55
1982	F-29-19	10.8	23 deg.	12.0	0.77	0.55

Furthermore three half models were tested in the HST to analyse Re - no effects.

Model designation	Basic wing shape	Max test Re-No at M = 0.19	Max. test Re-no at M = 0.75
SKV-5½	SKV-5	4.9×10^6	10×10^6
SKV-7 (-1 to -6)	SKV-3	3.6×10^6	-
F-29-10(-1 to -6)	F-29-2	5.0×10^6	10×10^6

To investigate low-speed characteristics three complete low-speed models were produced for the NLR Low-Speed Tunnel (LST). These models, tested at $Re_c = 1.0 \times 10^6$ were:

a. SKV-LST-1, with the wing shape SKV-3
b. SKV-LST-2, basically identical to model SKV-LST-1 but with a modified inner wing resembling that of wing SKV-5.
c. SKV-LST-3 based on wing shape SKV-6.

In figure 41 the three wing planforms are presented. Figure 42 shows the overall shape of model SKV-LST-1.

All three models, tested in 1977, 1978 and 1979 could be equipped with slats and double-slotted (tabbed Fowler type) flaps, the latter spanning 75% of the wing span. Slat and flap positions could be varied. Furthermore aileron power, many different spoiler-panel configurations, engine positions both on the rear-fuselage and under the wing were analysed. Stalling characteristics, both in pitch and roll were also investigated. (All three models had a T-tail).

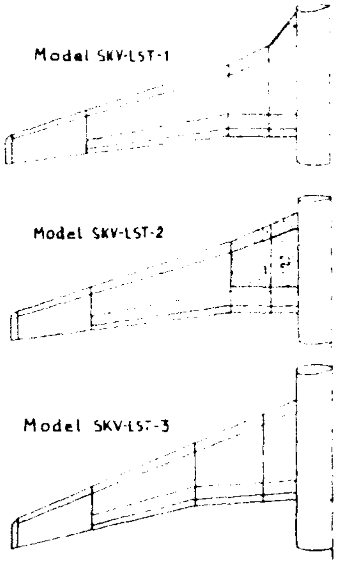

Fig. 41 Wing planforms of models SKV-LST-1, -2, -3.

The effect of Reynolds-no variation on the low speed characteristics of model SKV-LST-3 was analysed by testing the actual left-wing of this model at high Reynolds-number as a halfmodel in the HST tunnel of NLR. This model, designated SKV-7 could also be tested in combination with a blown nacelle. This allowed the analysis of engine-airframe integration effects including the measurements of static and dynamic flap pressures.

The test set-up of model SKV-7 with blown nacelle has been described in ref. 16. In this test the nacelle plus pylon and strut (through which high-pressure air was fed) was physically isolated from the wing. The wing was fitted on the 5-component balance. Engine strut and halfmodel were coupled however outside the tunnel test section so the combined structure could be set at varying angle-of attack. (Figure 43)

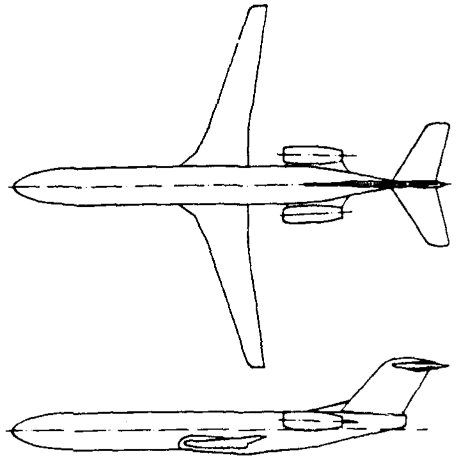

Fig. 42 Model SKV-LST-1.

MODEL SKV-7 WITH WAKE RAKE AND KULITES ON FLAP

MODEL SKV-7 WITH LOW TAIL

Fig. 43 Half model testing with blown nacelle.

Fokker has in general good experience with the use of halfmodels (figure 44 is given as an example). For accurate data an extensive matching procedure is required however (see ref. 17).

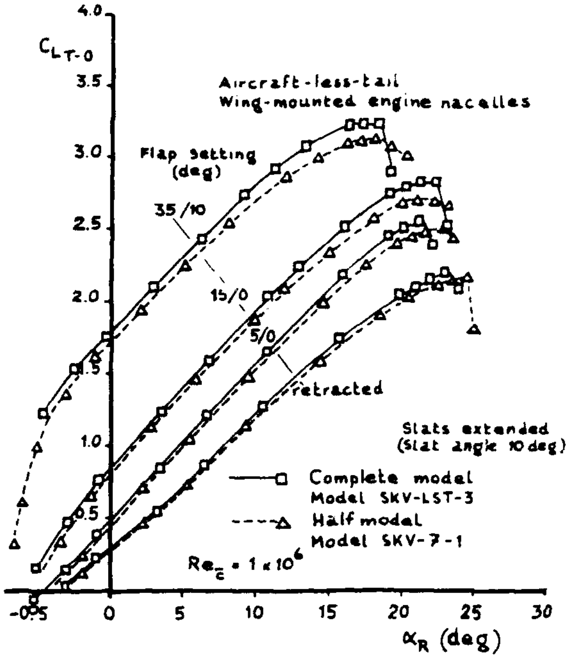

Fig. 44 Comparison of lift curves from halfmodel and complete model testing.

Finally in 1981 and 1982 the models F-29-1 (figure 45) and F-29-2 (the latter without slats) were also tested in low-speed configurations, both with a fuselage-mounted horizontal tail and with a T-tail. The low-speed wing characteristics of model F-29-2 were checked at high Reynolds-numbers on the halfmodel Model 10. In its later configuration this model was also investigated with a slat and a wing leading-edge shape closely resembling that of Model F-29-5.

In figure 46 $C_{L_{max}}$, tail-off is presented as a function of Reynolds number and flap and slat setting for a number of models.

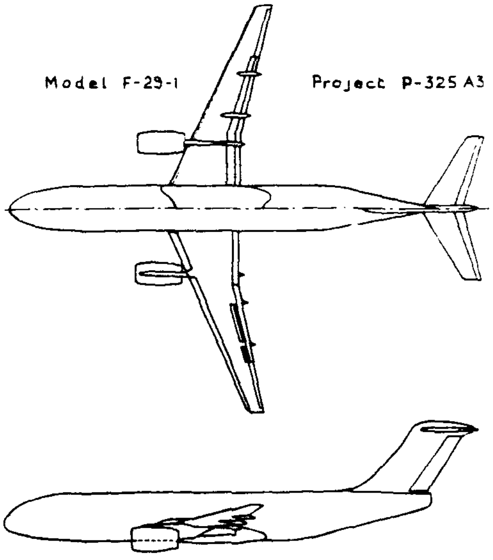

Fig. 45 F-29 - Model 29-1.

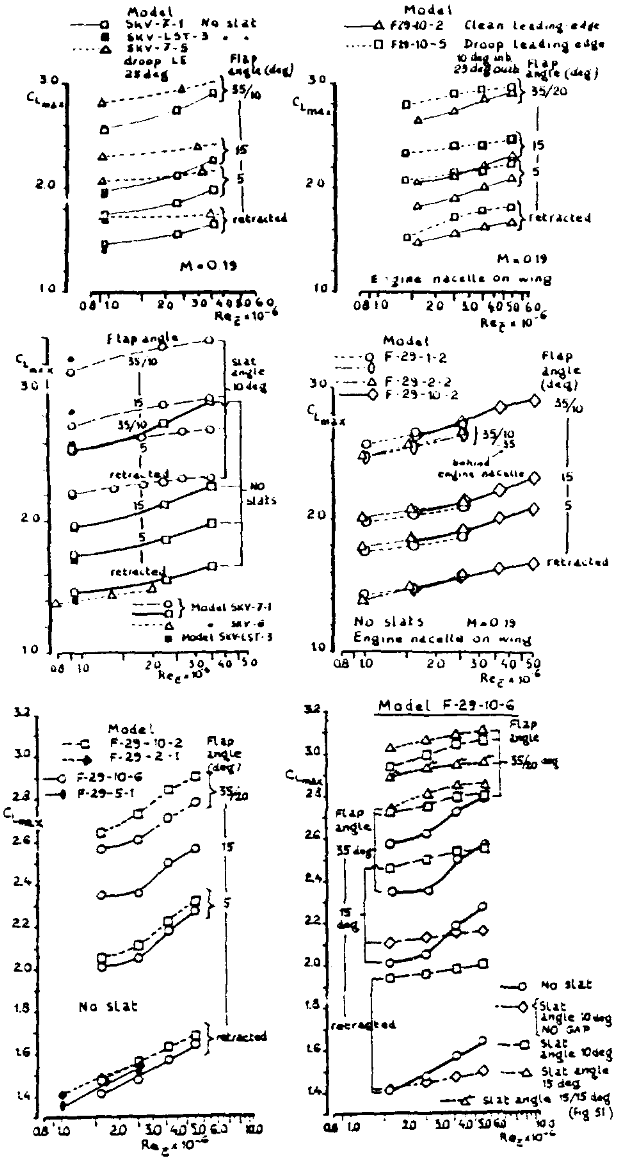

Fig. 46 Effect of Re-no on maximum lift. - Various halfmodels and complete models.

The investigations into the high-lift characteristics of advanced transonic airfoils, both for 2-D and in 3-D configurations tought us the following:

1. Modern transonic airfoil sections can combine good high-speed characteristics with high maximum-lift for take-off and landing configurations.

2. In particular for high design cruise Mach-numbers and lift coefficients a very strong interrelation exists between these design cruise parameters and the achievable high-lift characteristics. Leading-edge and trailing-edge shapes depend heavily on design cruise condition.

3. Reynolds-number does not only affect overall characteristics such as lift, drag and pitching moment but also optimization procedures such as finding the optimum slot shape for slats and flaps. This is illustrated in the following example: Slat and flap configurations for take-off and landing had been determined for Model SKV-LST-1 based on initial experience with the 2-D NLR 7301 model. These initial 2-D tests suggested that the optimum slat position would be:
slat angle 15 deg
slat gap 3.5% local wing chord
slat overlap -1.5% local wing chord
As figure 47 shows this produced an impressive C_{Lmax} = 3.64 for landing at $Re_c = 1 \times 10^6$.
After more extensive tests on the 2-D model the conclusion was reached that a better slat position would be:
slat angle 10 deg.
slat gap 2.5% local wing chord.
slat overlap 0
This slat position was investigated on model SKV-LST-2. Contrary to our expectations this latter model, which had an identical geometry as model SKV-LST-1 except for the inner wing, showed for all configurations a much lower C_{Lmax} than the previous model: for landing C_{Lmax} = 3.36 was obtained (Figure 48). Due to the sharper leading-edge C_{Lmax} is even lower (C_{Lmax} = 3.26) on model SKV-LST-3. (Figure 49).

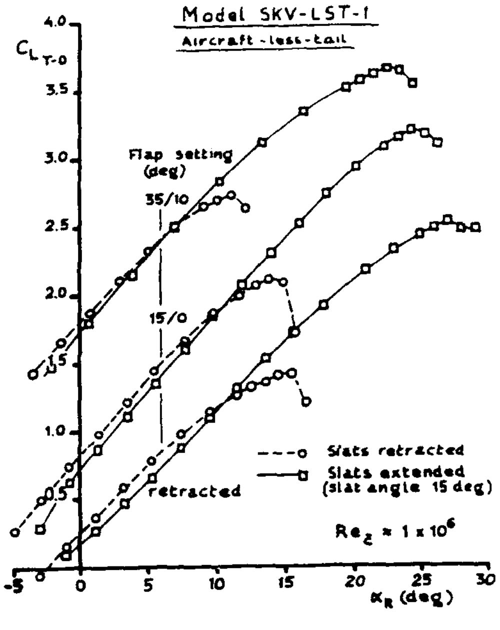

Fig. 47 Lift curves of model SKV-LST-1.

A careful analysis of the 2-D data showed that at $Re_c > 1 \times 10^6$ the smaller slat gap gave indeed higher increases in maximum lift than the large gap. At the lower Reynolds-numbers (and this is where the wing tip region, which stalled first, operated at in the windtunnel) the large gap produced higher maximum lift values (figure 50).

This means that, had the configuration of model SKV-LST-1 been investigated at higher Reynolds-numbers the increase in C_{Lmax} had been considerably lower.

Similar Reynolds-number effects were noted when a "droop leading-edge" was investigated on model F-29-10.5 (Figure 46).
These results and data from tests with deflected slats without a slat gap suggest that for sections with relatively thick leading-edges and on wings with a moderate sweep angle these high-lift devices are not very effective.

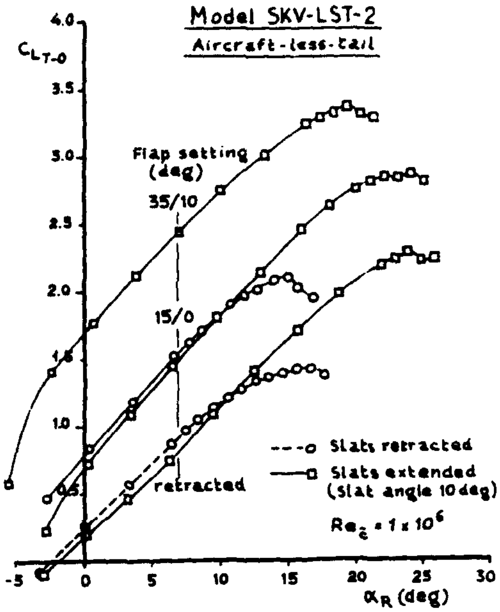

Fig. 48 Lift curves of model SKV-LST-2.

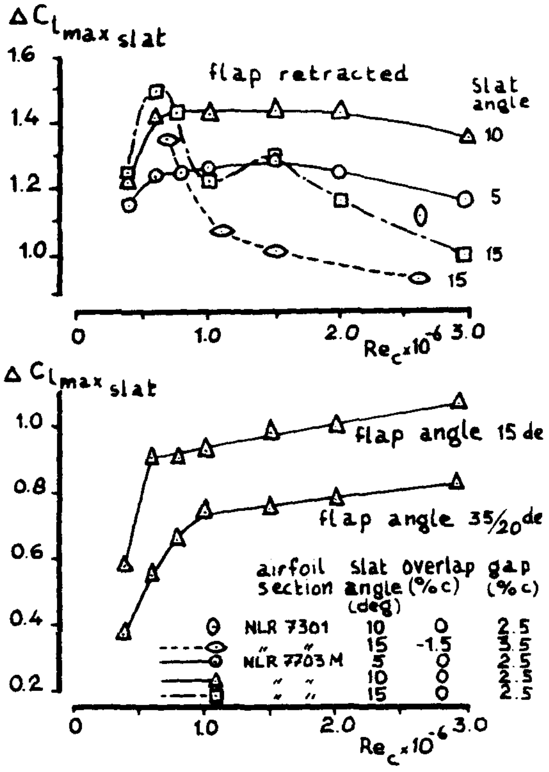

Fig. 50 Effect of Re-no on increase in maximum lift due to slat extension.

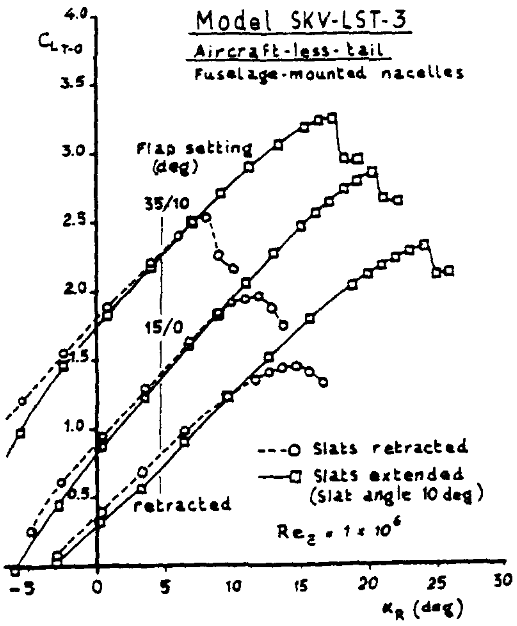

Fig. 49 Lift curves of model SKV-LST-3.

4. Engines fitted under the wing can be effectively used to control flow separation patterns at wing stall. Provided that great attention is paid to details of the pylon-slat-leading edge intersection the loss in lift can be made negligible. (Figure 51). The latter used to be a strong argument for rear-fuselage engine positions in the past.

5. A large number of, sometimes interrelated, design parameters have to be considered when choosing and optimizing highlift configurations (See, for example figure 52 which shows the engine nacelle drag to be a function of both lift coefficient and flap setting when the nacelle is mounted under the wing.

6. As in the windtunnel development of the F-28 Mk 6000 a strong interrelation was found between increases in maximum lift and in drag for various slat configurations (Figure 53).

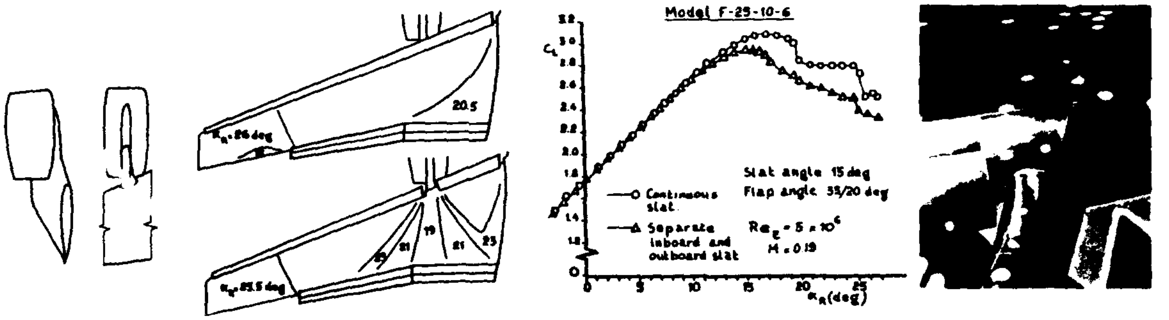

Fig. 51 Effect of slat cut-out on stall pattern and maximum lift.

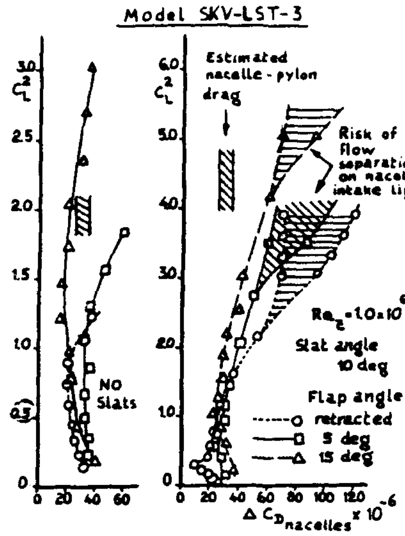

Fig. 52 Under-wing engine nacelle drag.

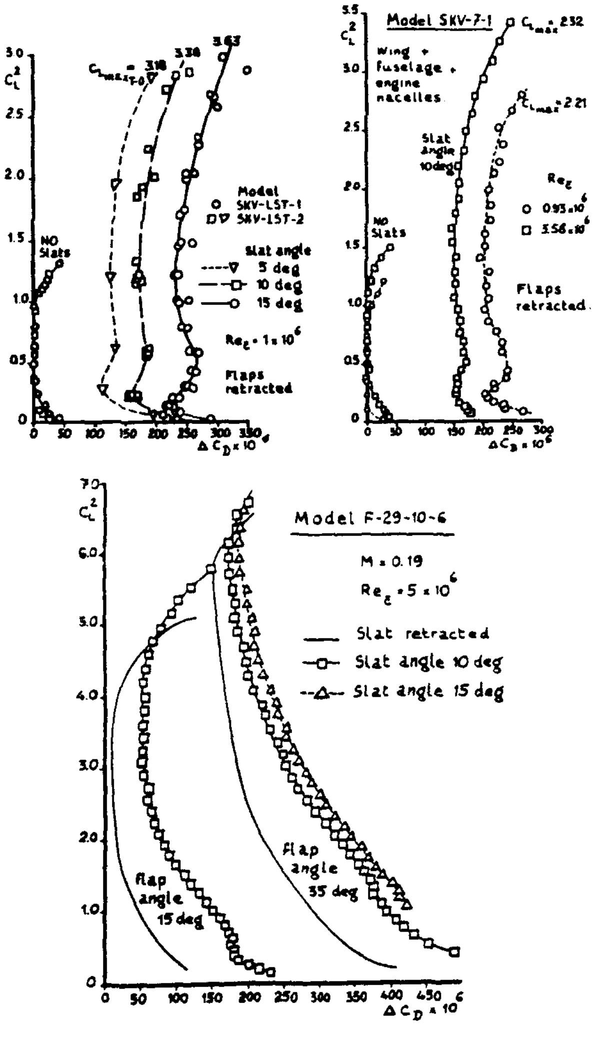

Fig. 53 Effect of slat setting on low speed drag.

VI THE HIGH-LIFT DEVELOPMENT OF THE FOKKER 50 AND FOKKER 100

a. THE FOKKER 50

The design studies on the Fokker 50 (as on the Fokker 100) started in 1982. The Fokker 50 was to be equipped with Pratt and Whitney PW 125 engines producing 2500 shp in take-off and go-around (10 percent more than the most powerful Rolls-Royce Dart engine on the F-27) and with new propellers. In order to obtain maximum insight in the stability and control characteristics of the aircraft at the highest propeller thrust coefficients a 1 : 5 scale windtunnel model with a wing span of 5.40 m was built and tested in the Dutch-German Windtunnel DNW in the 8 x 6 m test section at Reynolds numbers up to $Re_L = 3.2 \times 10^6$. The model was equipped with turbine-powered simulators driving variable-pitch propellers through a 2.7 : 1 reduction gear box.

In an aerodynamic sense wing and flap systems remained identical to those on the F-27. These tests provided detailed insight in the flow conditions at the tail at high thrust coefficients. Also tests with modified elevator, rudder and ailerons, the latter now equipped with hornbalances showed that the improvements sought could be realised. Flight tests were performed in two stages. On an old F-27 bought by Fokker for experimental purposes, the modified control surfaces were investigated. On the two Fokker 50 prototypes the overall performance and flight handling characteristics were analysed.

Overall the flight test results were in accordance with predictions. Maximum lift coefficients and stall characteristics of the F-27 were repeated or slightly improved upon, again without the use of any stall control device. The only difference in this respect (apart from different take-off flap settings) is the decrease in maximum flap deflection from 40 deg on the F-27 to 35 deg on the Fokker 50.

The flight handling characteristics in roll and yaw were improved compared to the F-27 but to obtain satisfactory longitudinal handling characteristics over the desired c.g. range a "smart" bungee was developed which applies a constant force in the longitudinal control system the height of which is dependent on engine power and flap setting.

As on the F-27 not performance but flight handling provided the biggest challenge at high lift conditions.

b. THE FOKKER 100

The aerodynamic development of the Fokker 100 was described in ref. 18.

In order to obtain an early insight in the effect of the proposed leading- and trailing edge modification to the F-28 wing which would lead to the Fokker 100 wing, the old 2-D F-28 model, Model 5 was modified again and tested in the NLR Low Speed Tunnel in Amsterdam as Model 5-3. Figure 54 shows the improvement obtained compared to the F-28 both for the clean section and for the high-lift configurations. This figure also presents some theoretical predictions. As in the mean time theoretical prediction methods (covered in the next paragraph) had improved considerably these were for the first time used in the actual design process not only for the 2-D analysis but also on the complete wing in the clean configuration. The analysis of the spanwise distribution of leading-edge suction peak with increasing angle of attack helped to predict the initial stalling characteristics (Figure 55). The agreement between predicted and actually achieved full-scale maximum lift is excellent. However, again a lengthy flight test programme was required to obtain the best fence and stalling strip location for an optimum balance between performance and flight handling characteristics, the latter including tail buffet in the stall. The certified $C_{L_{max}}$-values for all flap settings is presented in figure 56. Note the high $C_{L_{max}}$-values available for take-off notwithstanding the absence of a slat.

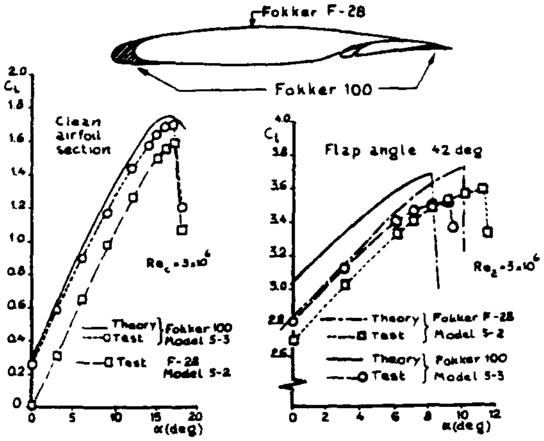

Fig. 54 Fokker 100 - Improvement in 2-D maximum lift.

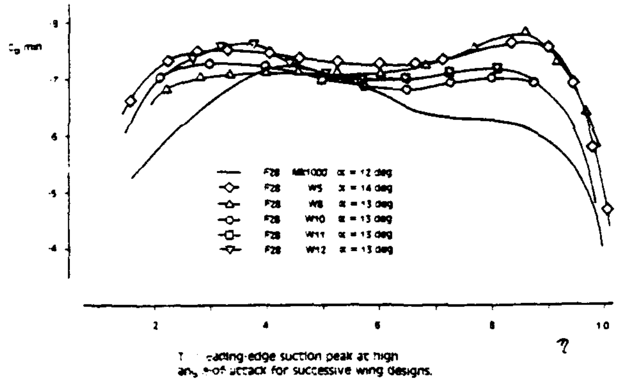

Fig. 55 Fokker 100 - Development of the spanwise distribution of the leading edge suction peak.

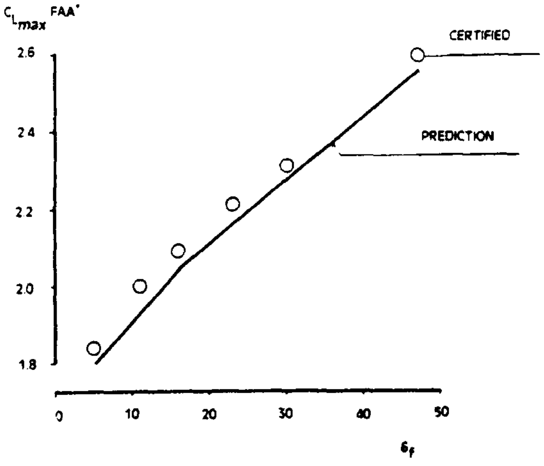

Fig. 56 Fokker 100 - Certified $C_{L_{max}}$.

VII THE PREDICTION OF HIGH-LIFT CHARACTERISTICS - THE ROLE OF THEORY

Computational fluid dynamics, (and, in the days before the digital computer, aerodynamic theory) can be divided into two working area's:

I. The mathematical description and analysis of a given situation concerning a body moving in a fluid.
II. The determination of the limits of validity of the description and analysis of this particular situation.

The first area concerns for example the attached flow about a wing section at a given angle-of-attack or the stable leading-edge vortex flow on a sharp-edged slender delta wing.

The second area concerns the boundary-layer separation on a two-dimensional airfoil at reaching $C_{L_{max}}$ or the vortex bursting on the sharp-edged slender delta.

Pressure distributions and boundary-layer conditions in attached flow have been analysed since the dawn of aviation. Analysis of controlled vortex flow started in 1940 by Jones at NACA.

The determination of boundary layer separation on two- and certainly on three-dimensional bodies on a theoretical basis led to meaningful results only in fairly recent times. This is notwithstanding the fact that for aircraft design this matter is of equal importance as the detailed analysis of an aircraft's characteristics in attached flow.

The explanation lies of course in the far greater complexity of three-dimensional boundary-layers in adverse pressure gradients than of potential flow. A fundamental theoretical principle such as the description of potential flow through sinks, sources, dipoles and vortices is still lacking in boundary layer theory notwithstanding the great effort being put in turbulence modelling.

For wings, or even airfoil sections, equipped with flaps and/or slats even the calculation of detailed pressure distributions and local boundary-layer conditions with attached flow has not yet reached the desired degree of accuracy let alone their integration into lift, drag and pitching moment.

For practical design purposes purely theoretical methods for high-lift design contain therefore still too high a degree of uncertainty. However, mixed with a proper degree of empiricism they become very useful tools, if not in producing the final answer than at least in guiding the way to the optimum design solution. But, perhaps even more important, in the case of high lift devices theory has provided insight in the interrelation between the various components of a multi-component airfoil. The break - through, in my opinion, came with the publication of A.M.O. Smith's paper:
"Aerodynamics of High-Lift Airfoil Systems".

in AGARD C.P. 102 in 1972 (ref. 19).
In this paper it was clearly shown that an airfoil with a slat and a flap consisted actually of a combination of separate close-coupled airfoils with a strong mutual interaction. Suddenly the relations between suction peaks, dumping velocities, upwash and downwash and the resulting pressure distributions and boundary layer conditions fitted into a pattern.
We understand now, for example, why slats with small leading-edge radii have to be deflected further than slats with large leading-edge radii and why small-chord

flap vanes are ineffective. It is now also clear why each slat has an optimum deflection. Too large slat angles produce too high supervelocities on the main component (figure 57).

The understanding of the physics led to an understanding of the critical areas in the pressure distribution.

As an example figure 58 illustrates that on the double-slotted flap 3 a vane position A leads to a too low vane loading and a too high flap loading. Consequently the flow on the flap stalls. Vane position B gives a much better loading division and consequently produces a higher $C_{L_{max}}$ (see figure 33).
But, as figure 58b illustrates, for practical purposes an empirical design rule as presented in 1961 (the tangent to vane and flap upper surface) leads to similar conclusions.

On single airfoils trailing-edge separation has been studied on a theoretical basis (with some empiricism such as a constant static pressure in the area of separated flow) since the 1960's. At NLR $C_{L_{max}}$ was calculated as a function of Reynolds-number in 1977 for the airfoil section NLR 7301. Both a trailing-edge separation criterion and a (very crude) leading-edge criterion were considered.

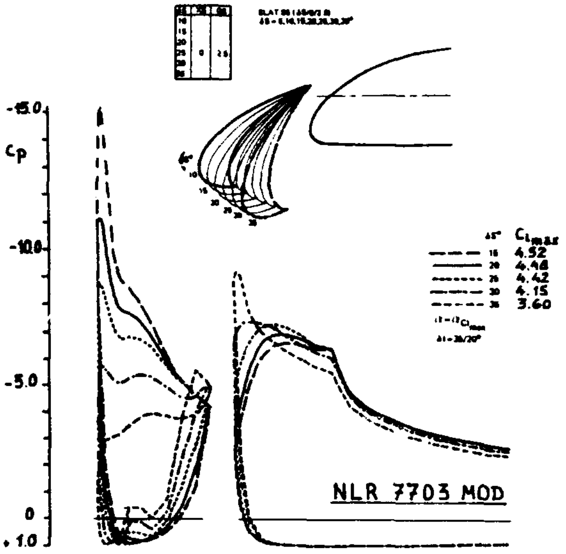

Fig. 57 Effect of slat deflection on peak supervelocities on slat and main body.

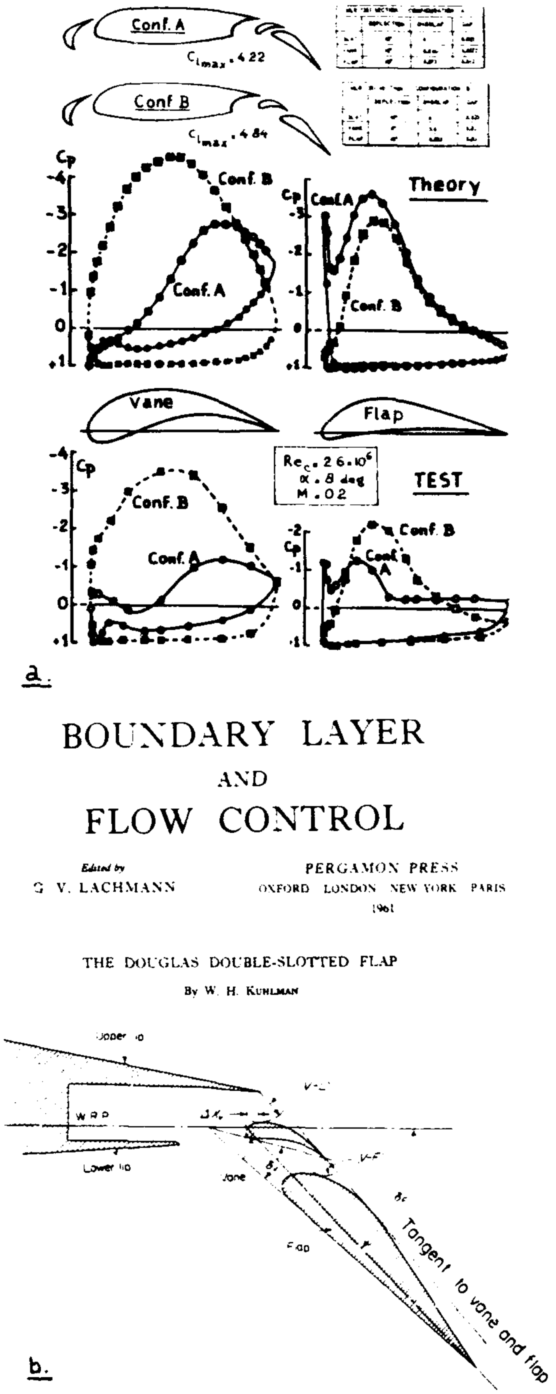

BOUNDARY LAYER
AND
FLOW CONTROL

Edited by
G. V. LACHMANN

PERGAMON PRESS
OXFORD LONDON NEW YORK PARIS
1961

THE DOUGLAS DOUBLE-SLOTTED FLAP
By W. H. KUHLMAN

Fig. 58 Interaction between the circulation on the vane and the flap on a double-slotted flap.

Since 1985 a computerprogramme, ULTRAN V is available. This programme although based on transonic small perturbation theory coupled to a boundary layer theory gives a very accurate description of the flow conditions over the rear part of the airfoil section including a separated boundary layer. This allows the determination of maximum lift due to trailing-edge separation. A transonic full-potential flow solver, the programme TRAFS allows, when corrections are applied for boundary-layer effects through the concept of displacement thickness, an accurate calculation of the leading-edge suction peak. By means of an empirical correlation between minimum static pressure as a function of Re- , an Mach-number and leading-edge curvature the occurrence of leading-edge stall can be determined. By comparing the data from computions with both the programmes ULTRAN V and TRAFS the maximum lift of single airfoils can be estimated. Some data are presented in figure 59.

In the early eighties all available 2-D test data on high-lift configurations available at Fokker's were analysed systematically. This led to the conclusion that on high-lift configurations $C_{L_{max}}$ could be determined by either of 4 types of flow separation. These are illustrated in figure 60.

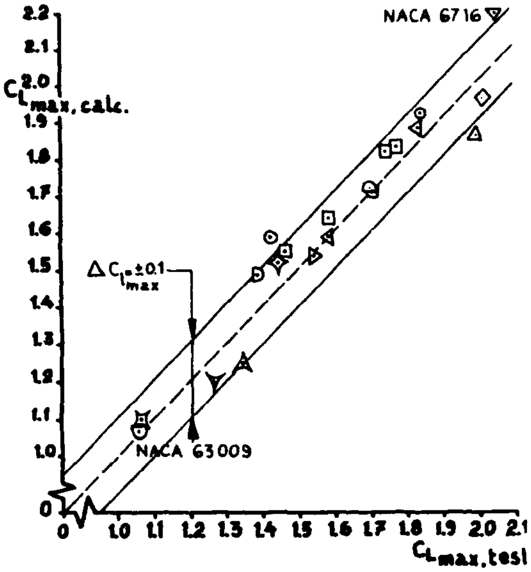

Fig. 59 Maximum lift of clean airfoils. - Theory and experiment.

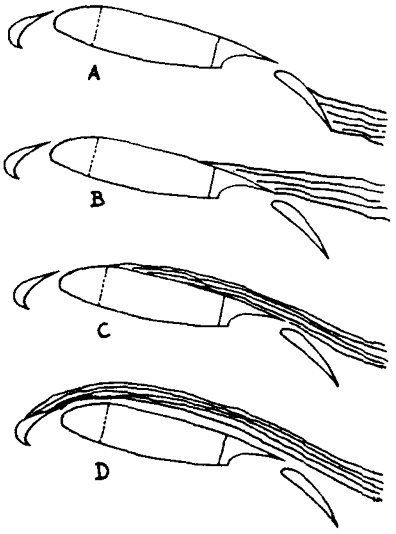

Fig. 60 Four types of flow separation determining maximum lift.

Modern theory can reasonably well cope with trailing-edge separation provided no confluent wakes and boundary layers occur.

At NLR a computer programme VISWAKE was developed (B. Oskam et al, ref. 20) which allows an accurate computation of the pressure distribution and lift, drag and pitching moment on multi-component airfoils as a function of angle-of-attack including maximum lift, provided $C_{L_{max}}$ was determined by flow separation at the trailing-edge of any component.

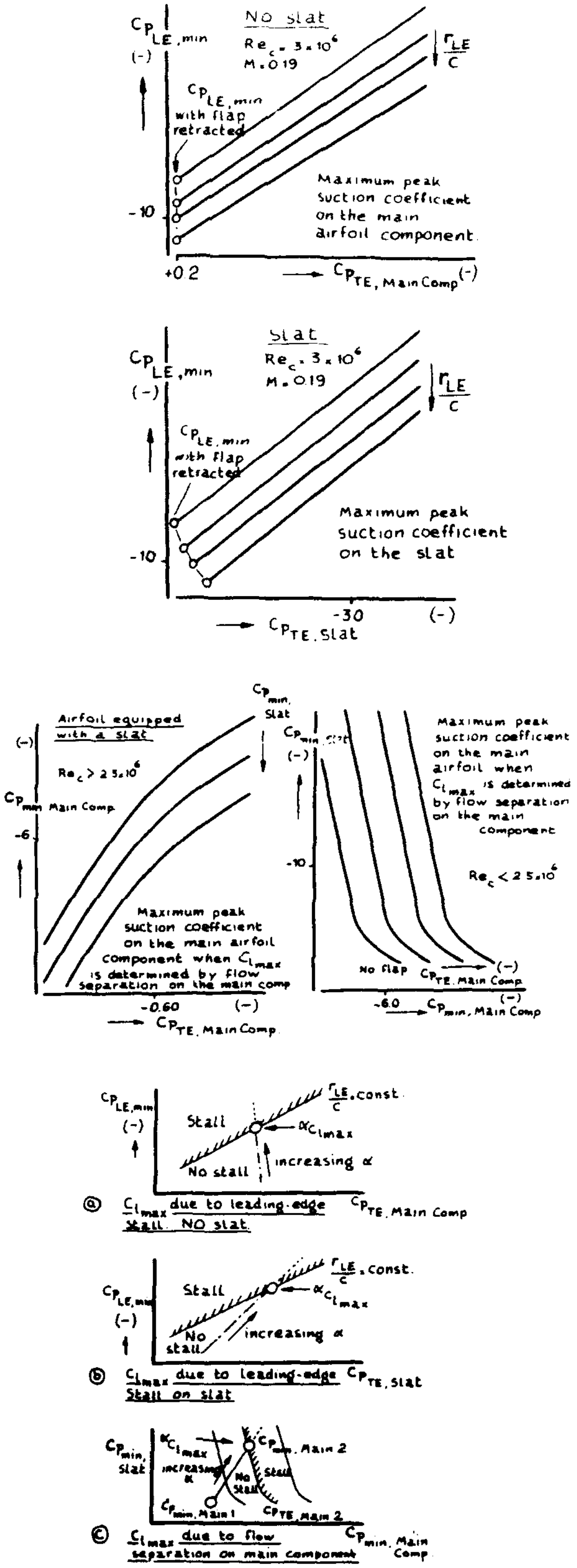

Fig. 61 Semi-empirical procedure to determine $C_{L_{max}}$ of a multi-component airfoil section.

Of particular significance in this programme is the modelling of the wake of each component including the strong interaction with the pressure field around the next airfoil component.

The large data base from windtunnel tests allowed the determination of some empirical criteria for the maximum height of the leading-edge suction peak before leading-edge stall occurs on slat or main component as a function of leading-edge curvature and dumping velocities. Accurate determination of leading-edge peak velocities at a given angle of attack is required of course.

In figure 61 the character of the empirical criteria is presented together with the development of the various significant parameters on a particular configuration as a function of angle-of-attack. The parameter which first exceeds a limit determines maximum lift.

Although the programme VISWAKE is a programme based on theory for incompressible flow it produces nevertheless very reasonable answers concerning maximum lift (See figure 62). In figures 63 and 64 some examples are presented of pressure distribution, lift, drag and pitching moment for a section with slat and double-slotted flap.

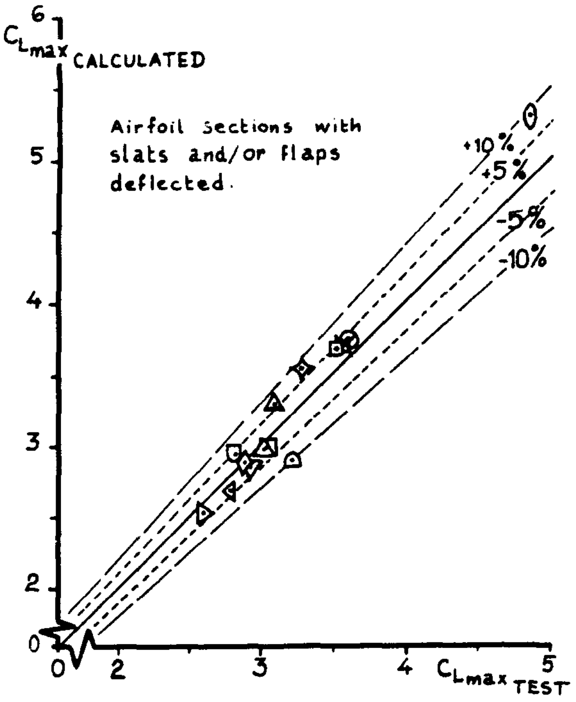

Fig. 62 Calculated $C_{L_{max}}$ for airfoil sections equipped with high-lift devices.

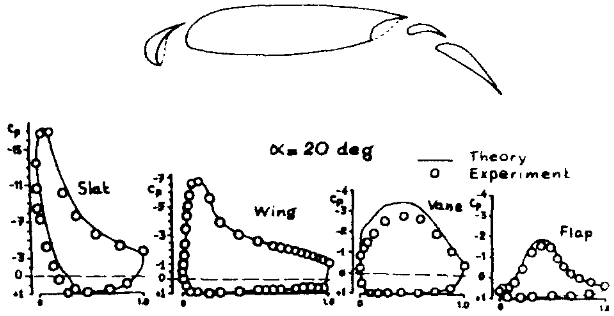

Fig. 63 Measured and calculated pressure distribution.

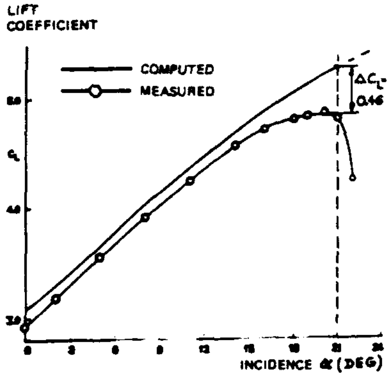

LIFT AS FUNCTION OF INCIDENCE

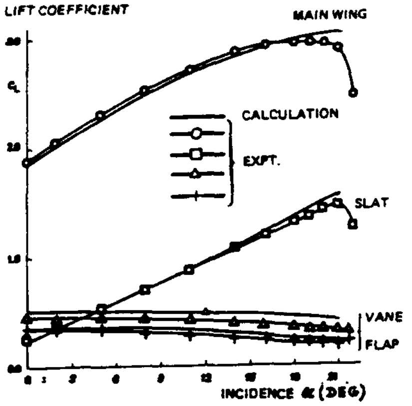

CONTRIBUTION OF VARIOUS ELEMENTS TO LIFT

Fig. 64 Lift on the various component of a multi-component airfoil.

In three-dimensional flow $C_{L_{max}}$-prediction is possible at least for high-aspect-ratio wings by combining 2-D analysis with lifting line theory or with 3-D panel methods.

Lift, drag and pitching moment below the stall for a complete aircraft configuration are computed by combining 2-D data (in particular for lift and section drag at higher flap angles this is taken from an empirical data base) with a non-planar lifting surface programme (NPLS).

An example of the panel distribution and some basic aerodynamic data are presented in figure 65 for the F-29. Estimated lift-drag ratio's for a trimmed Fokker 50 are presented in figure 66.

Some examples have been presented of the use of theory in the analysis and design of high lift configurations. A great progress has been made in the last two decades in particular in determining $C_{L_{max}}$ for such configurations.

Nevertheless, the accuracy of flow calculations is still insufficient to determine the choice of an optimum high-lift configuration for a given set of design requirements. Here the windtunnel will for the foreseable future still have the last say.

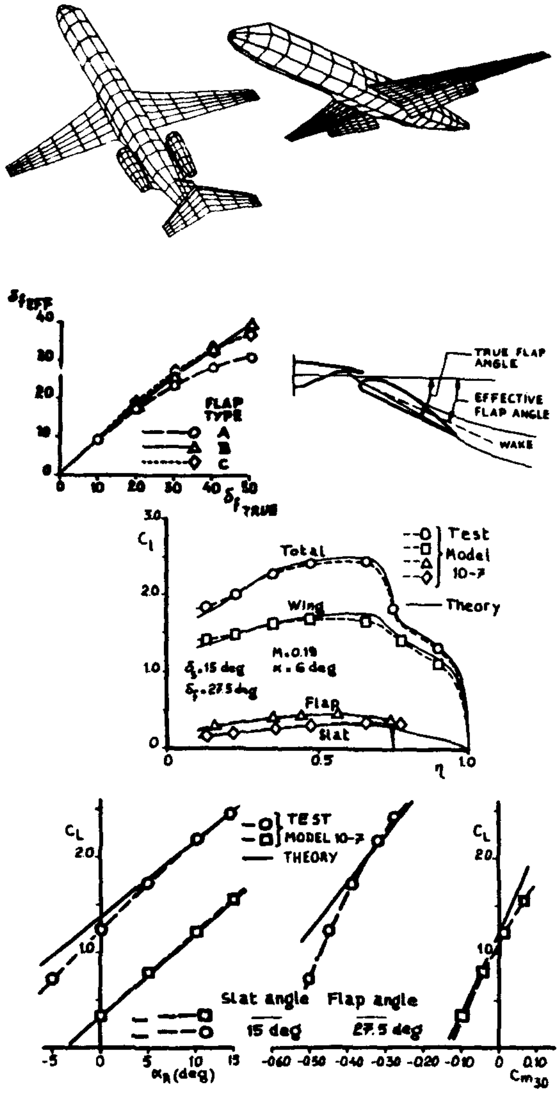

Fig. 65 Aerodynamic characteristics estimated with a Non-Planar Lifting Surface Programme (NPLS).

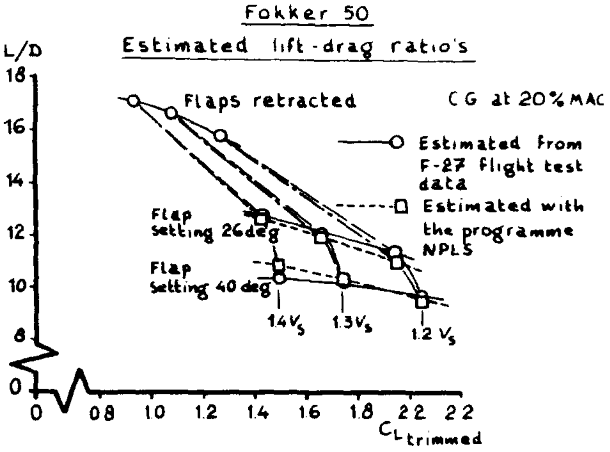

Fig. 66 Estimated lift-drag ratio's of the Fokker 50

CONCLUSIONS

Forty years of high-lift research and development at Fokker have produced a wealth of testdata combined with extensive experience in the fields of computation and windtunnel and flight testing.

These forty years have shown the following developments and tought the following lessons:

1. Due to commercial pressures, in combination with technologies in the areas of computation and windtunnel testing techniques which were continuously being developed, a steady improvement in the accuracy of the prediction of full-scale aircraft performance and flight handling characteristics has been required and, in many cases, has been achieved over the years.

2. In view of the above the need to perform windtunnel tests at the highest possible, or affordable, Reynolds-numbers can not be overemphasized, also in the early stages of a design process when the optimum configuration is still to be determined.

3. The role of computational fluid dynamics in the design process has greatly increased. However, in the design of high-lift configurations the actual component geometry is still to a large degree defined empirically.
Theory has, however, helped very much to understand flow phenomenae and has provided guidelines for the design of high-lift devices.

4. For improved understanding of details in the flow physics and for application in the design of moderately swept high-aspect ratio wings 2-D data, both from theory and from windtunnel tests provide still very useful data.

5. At present, a fair degree of empirical data has to be fed into the computational methods in order to make optimum use of theory. For this access to a large empirical data base is a prerequisite.

6. In many cases the discrepancy between theoretical and test data for a particular high-lift configuration is of the same order as the difference in aerodynamic characteristics between the different configuration options one has to choose from for a given set of design parameters. In other words: the final choice of the most suitable high-lift configuration is still made on the basis of windtunnel tests.

7. The above is true for 2-D flow. For a wing-body-nacelle combination with slotted slats and part-span flaps the meaningful use of computational fluid dynamics for design purposes is still limited. However, this should not deter, but be seen as a challenge for, the CFD-community.

AKNOWLEDGEMENT

The activities described in this paper were and are a team effort. In particular the cooperation between the code developers and windtunnel test people at the National Aerospace Laboratory, NLR and the aerodynamicists at Fokker should be mentioned. May the following names be representative for this group effort:

For NLR
H. Tijdeman
J.W. Slooff
B. Oskam
R. Houwink
A. Elsenaar
B.v.d. Berg
J.A. van Egmond
K.W. Muller

For Fokker
J.v. Hengst
B.J. Warrink
J.N. Boer
W.H.A.R. Willemse
N. Voogt
D.F. Volkers
Tj. Schuringa
P. de Boer

But above all, Prof. J.H.D. Blom should be mentioned who was at Fokker in charge of aerodynamics between (roughly) 1947 and 1975 who so much stimulated us to look into flow phenomenae and not only at overall characteristics and who tought us integrated design long before expressions such as concurrent engineering and design-build teams became fashionable.

REFERENCES

1. Abbott,I.H.and von Doenhoff,A.E, "Theory of Wing Sections"
2. Abbott,I.H, von Doenhoff,A.E.and Stivers,L.S. ,"Summary of Airfoil Data", NACA TR 824,
3. Cahill, J.F., "Summary of Section Data on Trailing-edge High-lift Devices", NACA TR 938.
4. Young, A.D., "The Aerodynamic Characteristics of Flaps", ARC RM 2622,
5. Obert, E., "Low-speed Stability and Control characteristics of Transport Aircraft with Particular Reference to Tailplane Design", in "Take-off and Landing", AGARD CP 160, April 1974, Paper 10.
6. Blom, J.H.D., "Experience in Predicting Subsonic Aircraft Characteristics from Windtunnel Analysis", in "Flight/Ground Testing Facilities Correlation" AGARD CP187, June 1975, Paper 16.
7. Mc Cullough, G.B. and Gault, D.E. "Examples of Three Representative Types of Airfoil-section Stall at low Speed", NACA TN 2502, 1951.
8. Gault, D.E., "A correlation of Low-Speed Airfoil-section stalling characteristics with Reynolds Number and Airfoil Geometry", NACA TN 3963, 1957.
9. Schuringa, Tj., "Aerodynamics of Wing Stall of the Fokker F-28", in "The Fluid Dynamics of Aircraft Stalling", AGARD CP 102, April 1972, Paper 20.
10. van Doorn, J.T.M., Han, S.O.T.H., Obert, E., "Comparison of Fokker F-28 "Fellowship" Windtunnel and Flight Data. - A summary, "in" Yearbook 1973 of the Netherlands Association of Aeronautical Engineers", 1973, paper 5.
11. Anon, "Fokker F-28 Fellowship", Aircraft Engineering, June/July 1967.
12. Vos, D.M., "Low-Speed Windtunnel Measurements on a Two-dimensional Flapped Wing Model using Tunnel Wall Boundary-Layer Control at the Wing-Wall Junctions", NLR TR 70050 V.
13. Anon, "F-28 - Development of the Mk 5000/6000", Aircraft Engineering, October/November 1973.
14. Drela, M., Giles, M, "ISES, a Two-dimensional Viscous Aerodynamic Design and Analysis Code, Paper AIAA no 87-0424, 1987.
15. Obert, E., "The Supercritical Airfoil - An Evolution or a Revolution ?" DGLR/GARTEUR 6 Symposium on Transonic Configurations, Bad Harzburg, Germany, June 1978.
16. (Nacelle blowing).
17. Boersen, S.J., Elsenaar, A., "Half-model Testing in the NLR High-Speed Tunnel HST: It's Technique and Application", NLR MP 83036U, 1983.
18. Obert, E., "The Aerodynamic Development of the Fokker 100", in "Proceedings of the 16th Congress of the International Council of the Aeronautical Sciences (ICAS). August/September 1988.
19. Smith, A.M.O., "Aerodynamics of High-Lift Airfoil Systems", in "Fluid Dynamics of Aircraft Stalling", AGARD CP-102, 1972.
20. Oskam, B., Laan D.J., Volkers, D.F. "Recent Advances in computational Methods to Solve the High-lift Multi-component Airfoil Problem", NLR MP 84042U. Also in "Improvement of Aerodynamic performance through Boundary-layer Control and High-lift Systems, AGARD CP365, 1984 Paper 3.

High-Lift Research: Application to the Design of the ATR72 Flap

P. Capbern
AEROSPATIALE Avions
316, route de Bayonne
31060 Toulouse Cedex 03
(France)

SUMMARY:

Due to slightly reduced Clmax objectives in landing configuration for the ATR72, compared to the ATR42, the high-lift system of the ATR72 is made up of a single dropped hinge flap, whereas the ATR42 was equipped with a double slotted vane type flap. Elimination of the vane has had a beneficial effect in greatly simplifying the high-lift system for the ATR72.

This simplification has been achieved while ensuring that Clmax levels are maintained or improved at same flap deflection (up to the value required for landing), and take-off L/D ratio is improved, which has a direct repercussion on operational performance, such as minimum runway lengths and maximum take-off weight. This aerodynamic performance has been achieved thanks to the systematic introduction, since 1985, of numerical methods in the design phase, in addition to the empirical and experimental methods used almost exclusively until then. The ATR72 flap is indeed the first to be essentially designed with numerical methods at AEROSPATIALE.

Beside this, more severe new regulations for turbo-prop A/C, leading to a restriction in the use of large flap deflections for the ATR42, the effect of the elimination of the vane on Clmax has been numerically investigated for this A/C. This study having shown promising results, some wind-tunnel and flight test verifications were conducted, which confirmed the reliability of the numerical tools.

The development of new design and analysis methods has been pursued; it has involved, on one hand, an extension of their field of use and the quality of the modeling, and, on the other, a reduction in the design cycle time. The objective was twofold: better optimization of high-lift systems, and, above all, an appreciable reduction in the associated design costs.

RESUME

Du fait d'objectifs de Czmax d'atterrissage un peu moins forts que pour l'ATR42, le système hypersustentateur de l'ATR72 est constitué d'un volet simple à rotation, alors que l'ATR42 était équipé d'un système à double-fente, avec un volet et un déflecteur. La suppression de ce dernier a eu l'effet bénéfique de simplifier nettement le système hypersustentateur pour l'ATR72.

De plus, cette simplification a été réalisée tout en assurant des niveaux au moins équivalents de Czmax à iso-braquage (jusqu'à la valeur requise pour l'atterrissage), et un gain de finesse au décollage, qui se répercutent directement sur les performances opérationnelles, telles les longueurs de pistes minimales et la masse maximale au décollage. Ces performances aérodynamiques ont été obtenues grâce à l'introduction systématique, à partir de 1985, des méthodes numériques en phase de conception, en complément des méthodes empiriques et expérimentales presque exclusivement utilisées jusqu'alors. Le volet ATR72 est en effet le premier qui ait été essentiellement conçu par la voie numérique à AEROSPATIALE.

D'autre part, de nouvelles règlementations plus sévères pour les avions à hélice ayant conduit à une restriction importante dans l'utilisation des grands braquages de volet pour l'ATR42, l'effet de la suppression du déflecteur de volet sur les Czmax a été étudié par calcul pour cet avion. Du fait des résultats prometteurs obtenus, des essais en soufflerie et en vol ont étés conduits, confirmant la fiabilité des outils numériques.

Le développement de nouvelles méthodes de conception et d'analyse s'est aussi poursuivi; il a porté d'une part sur l'extension de leur domaine d'utilisation et sur la qualité des modélisations, et d'autre part sur la réduction du cycle de conception. L'objectif était double : meilleure optimisation des systèmes hypersustentateurs, et surtout réduction notable des coûts d'étude associés.

1 - INTRODUCTION

1.1 General context

Generally, the choice and design of the ATR72 flap are largely based on the information obtained from the ATR42.
Let us recall that the double-slotted high-lift system of the ATR42 consists of a main flap at the front of which a vane is attached (see fig. 1), the fixed assembly of these 2 items being rotated around a materialized pivot.

However, unlike the ATR42, the design critical phase for the ATR72 is the take-off phase, the target Clmax on landing being slightly reduced.
As maximum flap deflection must therefore be changed from 45° to approximately 35°, the upstream slot (between the main body and the vane) is masked throughout almost the whole deflection range preventing full benefit from being drawn from the double-slotted system.

This fact, plus the high manufacturing costs for the vane, led to the idea of a single-slotted flap for the ATR72, the *single rotation kinematic system being conserved.*

This choice was substantiated by the fact that the ATR72 flap would be the first one to benefit from the systematic use of the computational aerodynamic methods whereas the ATR42 system was designed using methods which were mainly empirical and experimental. This should allow us to change from a double-slotted flap to a single-slotted flap without loosing the aerodynamic performances (for a given flap deflection).

Note that as the two aircraft have very similar characteristic wing planforms, with airfoils of the same family, the ATR42 is a very adequate reference for the design of the ATR72 flap.

Also, as the sweep of the wing is moderate, a mainly two-dimensional approach is justified.

1.2 Objectives

These objectives were defined with respect to the ATR42:

$Clmax_{72} \geq Clmax_{42}$ + 2% for δ_f from 15° to 35° (δ_f denoting the flap deflection)

$(L/D)_{72}$ at 1.2Vs $\geq$ $(L/D)_{42}$ at 1.2 Vs for δ_f = 15° and 25° (L/D denoting the Lift-to-Drag ratio and Vs denoting the stall speed)

1.3 Design parameters

The various parameters taken into account for the design were the following:

- relative flap chord
- length of fixed trailing edge panel
- shape of flap
- position of pivot

The latter defines the position of the flap (gap, overlap) for each deflection angle (see definitions on fig. 2).

2 - STATE OF THE ART OF COMPUTATIONAL METHODS IN 1985

2.1 Difficulties to be solved

The flows around the high-lift configurations (fig. 3) have various characteristics making them especially difficult to calculate:

- presence of areas with separation followed by reattachment on lower surface of the slats and the fixed trailing edge panel
- turbulent separation on upper surface of highly deflected flaps
- wake/boundary layer confluence phenomenon
- frequent presence of laminar bubbles in the leading edge areas
- possible presence of a supersonic area in the vicinity of the slats leading edges.
- lastly, numerical difficulties specific to the panel methods used for the analysis and caused by the thin trailing edges.

2.2 Research undertaken

The high-lift related research was conducted along 3 main lines, with a strong support from the French National Agency DRET (groupe VI).

<u>2D viscous flows</u> (1983/84)
A 2D viscous-inviscid strong-coupling method developed at ONERA [1] in order to calculate incompressible flows around multi-component airfoils was industrialized and validated at Aérospatiale [2].

<u>3D flows</u> (1985/86)
A panel method was developed, first in 2D then in 3D in order to calculate the flow around high-lift configurations, able to take into account very thin trailing edges [3].

<u>Optimization</u> (1985 to 1987)
The development of a numerical optimization method for high-lift systems was undertaken. This study has allowed a first stage in this field to be completed, leading to a code which could be used to optimize the overlap. Results were also obtained in defining some objective functions for Clmax from Inviscid Flow methods, whose low computing time is particularly well adapted to optimization [4].

3 - ATR72 FLAP DESIGN

3.1 Computational tools and methodology

The CFD codes used during the theoretical design phase were as follows:

- Inviscid Flow method FP2D for multi-element airfoils (this being the panel method mentioned in paragraph 2.2),
- Mono-element inverse transsonic method,
- Incompressible Viscous method for multi-component airfoils (this being the viscous-inviscid coupling method mentioned in paragraph 2.2),
- Optimization method, under development (usable only for overlap optimization).

At that time, none of these methods gave a reliable indication of the drag. However, the coupling method, gave a Clmax estimation. We therefore defined by the computational channel both the shape of the flap and the family of pivots meeting the Clmax targets. This allowed us to devote the wind tunnel tests to the choice of pivot offering the best lift-to-drag ratio on take-off.

3.2 Preliminary phase

The first parameter to be defined was the relative chord of the flap (which can be kept constant over the span as on the ATR42). A value of 30%, same as that on the ATR42 (including the vane), was a good trade-off between the effect on the Clmax and the structural constraints.

The choice of the fixed trailing edge panel end (84%) was also the result of a trade-off, a high value would lead to the lowering of the pivot and an increase in the size of the fairings and a low value would lead to a reduction in the extended chord.

3.3 Computational phase

3.3.1 Shape of flap

The shape was defined in landing configuration for a given deflection (δ_f = 35°), a fixed gap and overlap.

The principle can be summarized as follows (fig. 4):

- for a given initial shape and for an imposed lift level close to the Clmax level considered, an FP2D calculation is made in complete configuration mode then a calculation on the flap alone conserving its own lift coefficient.

- the pressure distribution for the complete configuration is then modified empirically on the flap in order to reduce the risk of separation.
- the previous modification is transferred to the pressure distribution of the isolated flap to make the reverse calculation which is only possible for the mono-element configuration.
- the shape obtained is modified in order to comply with the clean profile in the imposed portions.
- 2 control calculations are then made on the complete configuration: an Inviscid Flow calculation allows the pressure distribution effectively obtained to be compared with the target distribution; then, a Viscous Flow calculation allows us to directly estimate if the modified shape leads to a gain in Clmax.

If one of the two calculations is not satisfactory, the operations are repeated with a new modification to the pressure distribution. If, on the contrary, the new shape leads to an improvement, it can be used as the initial shape for a new iteration of the process and so on until being close enough to the optimal shape.

3.3.2 Preliminary kinematic optimization

This consisted in an optimization of the overlap for several flap deflection values (δ_f = 32.5°, 35°, 37.5°) for a fixed value of the gap (ranging from 1.5% to 3%). Remember that the gap cannot be optimized without taking into account the confluence of the viscous layers and therefore, to a greater extent, under Inviscid Flow assumptions.

3.3.3 Sum-up of the computational phase

This phase therefore allowed us:
- to obtain a complete definition of the shape of the flap which would have been very expensive to obtain in the wind tunnel
- to define a pivot envelope (see fig.5) guaranteeing that the Clmax targets will be obtained in order to limit the wind tunnel tests to the choice of the pivot in order to optimize the lift-to-drag ratio on take-off.

3.4 2D test results

2-D tests were made in the C.E.A.T S10 wind tunnel, assuming that the differences between the A/C in flight and the 2-D wind tunnel test are the same as those measured for the ATR42.

These tests therefore allowed us first of all to optimize the kinematics. From the various pivots defined during the theoretical phase, most met the landing Clmax target. In compliance with the planned strategy, it was possible to effectively choose the pivot on the δ_f = 15° characteristics (Cd at 1.2 Vs and Clmax, see fig.6), taking into account its vertical position which determines the size of the flap fairings.

For the selected pivot, the comparison with the ATR42 flap (fig. 7 and 8) shows:
- a gain in the Clmax in compliance with targets for $15° < \delta_f \leq 35°$
- a reduction of 25 % in the drag at 1.2 Vs for δ_f = 15°.

4 - TECHNICAL AND FINANCIAL BENEFITS

4.1 Reduction in production costs related to simplifying the flap

The main benefit is the reduction in the flap manufacturing costs by the deletion of the vane.

This metallic part (high curvatures incompatible with the use of carbon) is subjected to a chemical milling operation which first implies the installation then the cutting out of a rubber mask before the sheet metal is etched in an acid bath. These operations are made tricky by the high curvature on the vane which in addition has a shape which varies spanwise for the outer elements.

A significant reduction in manufacturing costs is therefore obtained, associated with a 7% weight saving, a rare combination worth mentioning.

4.2 Operational gains

The flight tests confirmed the Clmax gains (for a given deflection angle) obtained in the wind tunnel for the ATR72: the increase in the Clmax with respect to the "clean" configuration is greater by approximately 10 points than that which was obtained for the ATR42 (these being aerodynamic values at 1 g not taking eventual stick pusher limitations into account).

As concerns the lift-to-drag ratio at 1.13 Vs1g (or 1.2 Vsmin), for δ_f = 15°, the relative gain provided by the single-slotted flap can be estimated at 4 %.

This gain in lift-to-drag ratio affects the operational performances on take-off:
- the maximum weight of the 2nd segment (ISA at sea level) changes from 21.3 T to 22 T; note that the low value, which corresponds to an ATR72 with a double-slotted flap is lower than the MTOW (21.5T) and would therefore lead to a degraded nominal mission: - 100 NM or -2 pax.
- the length of the "balanced" runway is reduced at iso-weight by approximately 60 meters (that is 4 to 5 %) for the take-off phase.

5 - ELIMINATION OF THE ATR42 VANE

5.1 Introduction

This successful design of the ATR72 flap was recently exploited for the ATR42. A more severe regulation for turbo-prop A/C [5] having reduced the maximum flap deflection eventually used for the ATR42 (from 45° to around 27°), the good performance of the ATR72 single-slotted flap gave the idea to simplify the ATR42 flap system, by deleting the vane without any change of the kinematics, thus strongly reducing the weight of the high-lift system. This idea was justified by the fact that up to δ_f =27°, the vane remains entirely covered by the fixed trailing edge (see fig.9), with no addition of extended chord. Therefore, the effect of the elimination of the vane was numerically investigated for this A/C.

5.2 Numerical investigation

This study was achieved with the new version of the 2-D viscous-inviscid strong coupling method developed at ONERA (see §6.3), performing calculations at the flight Reynolds number, with and without the vane for a set of flap deflections, varying from 15 to 45°, and for a fixed

angle of attack ($\alpha=14°$). It is believed that such an approach allows a correct evaluation of the effect on Clmax, in the sense that the trailing edge high lift system mainly affects the lift level, without any noticeable change in α_{max}. The comparison of the calculated pressure distributions for $\delta_f=27°$ is given on fig.10 and 11. It can be observed that the direct contribution of the vane is very limited, in the sense that the suction on its upper surface is compensated by an equivalent one on the lower surface of the fixed trailing edge (see fig.10). Moreover, the lift of the flap is slightly increased by the elimination of the vane, even though the separation point moves only slighty forward. Without vane,the optimum flap deflection is 27° (see fig.12), with a rapid growth of the separated area for higher deflections. However, it must be mentionned that this optimum is probably under-estimated, due to a general tendency of the method to over-predict the separations. For high deflections the configuration with vane becomes naturally more efficient, the deflection of the flow due to the vane reducing the separation on the flap.
Beside that, it was checked that without vane, the flap gap keeps acceptable values up to δ_f around 33°.

5.3 Experimental validation

These promising results could allow a wind-tunnel test to be performed, in order to confirm them, and also to specify the optimum deflection more accurately. These tests were performed in the S10 wind-tunnel at CEAT (Toulouse), with a 2-D low-speed model representing a mid-section of the ATR42 wing, and consisted in balance measurements of global forces. These tests indicated an increase in Clmax due to the elimination of the vane, up to $\delta_f=36°$, the optimum flap deflection being 33° (see fig.12), thus globally confirming the predictions from CFD. The slight under-estimation of the optimum flap deflection has already been adressed in the previous paragraph; the failure of the code to predict the loss of lift with the vane for moderate deflections is probably due to the lack of a modelling for viscous layers confluence, for such a configuration, with a very small gap between the vane and the fixed trailing edge. The difference in level is partly due to the lower Reynolds number in wind-tunnel (2,3M to be compared with 4,7M in flight, at Vs condition).

Some flight tests were finally performed in order to validate the previous 2D results on the aircraft. Cl(α) curves are shown on fig.13, for several flap deflections, with a fair correlation with the wind-tunnel results. It can however be noticed that the increase in Clmax predicted in wind-tunnel ,estimated +0,13 after 3D transposition, is higher than in flight (+0,08). It can be explained by the difference in Reynolds number (2,3M in wind-tunnel and 4,7M in flight), in the sense that the small gap already mentionned between the vane and the fixed trailing edge, causes probably less problems in flight, where viscous layers are thinner.

This operation is a good example where a combined use of CFD and wind-tunnel can allow a reduced flight test campaign, with a very good level of confidence, and thus can lead to a reduction of A/C modification cost.

6 - CURRENT HIGH-LIFT RESEARCH

6.1 Objectives

As high-lift is not a highest priority sector at AEROSPATIALE, research in this field remains limited and concerns 3 subjects:
- reduction in design costs
- improved flow prediction
- capacity to process different types of aircraft

6.2 Reduction in design costs: shape optimization

6.2.1 Motivations

Although constantly concerned with reducing the computational times, whatever the calculation code, the research entering specifically into this category mainly concerns the optimization methodology.

We have seen (paragraph 3.3.1) that although the shape design methodology based on the inverse calculations leads to satisfactory shapes, its implementation is especially long and laborious. What is more, from the formulation point of view, it is based on an improvement process, and not on shape optimization in the strict sense of the term.

Lastly, this method specific both to Clmax optimization and to Inviscid Flow approach does not offer good development perspectives.

6.2.2 Characteristics of the OPTHYP method

All the above reasons have led to the development of a new method based on optimization in line with the research already conducted in this field (see § 2.2). In particular, we have kept the idea of a criterion based on the separation risk assessed under Inviscid Flow conditions.

The use of a viscous flow code would in fact today lead to extremely prohibitive calculation times.

The new OPTHYP method recently made operational for shape optimization (Clmax) of high-lift devices has the following characteristics:
Analysis methods: FP2D panel code
- Criterion: minimization of the separation risk (for a fixed Cl level), assessed by integrating Stratford coefficients,
- Shape generation (through the MICA2 geometry system, developed at AEROSPATIALE by the Aerodynamics Design Section),
- Constraint: compliance with the areas imposed by the clean airfoil.

The method was validated on various test cases (ATR72 single-slotted flap, upstream flap of a double-slotted system designed for a laminar airfoil, A310 slat), leading to shapes with Clmax's of same order of magnitude as those of the reference shapes.

Apart from the basic geometrical data, the implementation of this method only requires one preliminary Clmax estimation. This estimation can be obtained, if applicable, by viscous calculations on a preliminary shape but will already be known for all of the more conventional cases.

6.2.3 *Benefits*

This new approach leads to a spectacular reduction in the time required to obtain a shape when compared with the methodology based on inverse calculations: the time required is reduced from several weeks (or even several months) to only several hours!

The benefit thus obtained is especially difficult to calculate as it depends to a great extent on the case considered but will be without doubt around 100 or 200 engineer hours per high-lift device.

This gain in time can, if applicable, be used to take additional parameters into account (flap chord, length of fixed trailing edge panel or even spanwise shape optimization, etc.) leading to a better optimization of the high-lift system.

6.3 Improving flow predictions

It is within this context that an improved version of the 2D high viscous-inviscid coupling method developed by ONERA [6] was introduced and validated at AEROSPATIALE in 1987 [7]. A comparison with wind-tunnel results (see fig.14) for a single-slotted flap configuration shows a good correlation, including high flap deflections, and it can be noticed that stall seems correctly predicted for this case. This method is still undergoing development at ONERA.

For the three-dimensional aspect, support has been granted to ONERA in order to implement strong coupling between the FP3D panel code, developed by AEROSPATIALE (see § 2.2), with a 3D boundary layer method [8]. This method should allow the flows around the engine installations to be calculated but could also be used for the 3-D high-lift configurations.

As concerns the drag, the current version of the strong-coupling code could be submitted to a specific evaluation, on the basis of available tests. If the results turn out to be favorable, an optimization of the high-lift systems as regards drag could be considered.

6.4 Capacity of processing other types of aircraft

The ATR72 high-lift system was relatively simple on the one hand by its type (single-slotted flap), and on the other hand by the low 3-dimensional character (low sweep, high aspect ratio) of the wing. Nevertheless, various studies have allowed the processing capacity to be extended to other types of configurations:

- Laminar wings

Experience has been acquired both on the design of new types of high-lift devices (double-slotted flaps , leading edge Kruger flaps) and on specific problems posed by laminar wings [9]. An example of pressure distributions calculated by strong-coupling on a NLF airfoil equipped with a double-slotted flap is shown on fig.15. Current studies should allow an investigation to be made, in particular, on the leading edge stall phenomenon; their prediction by computational codes and by semi-empirical criteria will be assessed.

- GARTEUR High-Lift group

Aérospatiale took part in this high-lift research programme, centered on the Mach and Reynolds effects and on the 2D/3D transpositions.

The test case selected (A310) has, among other things, allowed experience to be acquired on the calculation of configurations with leading edge slats and on taking a swept wing into account (simple sweep theory).

Finally, note that the shape optimization code OPTHYP allows all types of flaps (single- and multiple-slotted) to be processed and also leading-edge device (conventional slats, or kruger flaps).

The capability of processing the high-lift systems of various types of aircraft is therefore today largely effective and this at moderate study costs.

7 - CONCLUSIONS

The development of the high-lift computational methods and their introduction into the design framework has allowed benefits to be obtained at 3 different levels:

- improvement in operational performances thanks to a better optimization of the high-lift system,

- improvement in the production process, mainly by simplifying the high-lift systems,

- reduction in the design costs by developing new and more efficient methodologies and by reducing the wind tunnel tests.

The capability of processing different types of configurations has been validated and can be used for new projects.

AKNOWLEDGEMENTS

The author wishes to aknowledge helpful discussions with JL Chavanne, who also kindly provided the Flight Tests data.
It is also a pleasure to mention the importance of the contribution from C.Bonnet, J.Bousquet and C.Van de Kreeke in the work presented here.

REFERENCES

[1] JC Le Balleur, M.Néron: "calculs d'écoulements visqueux décollés sur profils d'ailes par une approche de couplage" (AGARD CP291, Pap.11, 1981)

[2] P.Capbern: "Eléments de validation des techniques de mesure et des méthodes de calcul en Aérodynamique des systèmes hypersustentés" (L'Aéronautique et l'Astronautique n°122, 1987)

[3] V.Rivoire, P.Eichel: "Méthode d'analyse tridimensionnelle de systèmes hypersustentateurs" (N.T. Aérospatiale 443528/87, Juil.87)

[4] C.Bonnet: "Méthode de conception d'un système hypersustentateur bidimensionnel" (N.T. Aérospatiale 443507/87, Mars 87)

[5] G.Cattaneo: "Evolution règlementaire en matière de certification des avions civils en conditions givrantes" (AGARD CP-496, paper 4, Déc. 91)

[6] S.Henry, JC Le Balleur: "Développement des méthodes d'intéraction visqueux-non visqueux pour le calcul des profils hypersustentés" (RTS ONERA n°29/1736 AY, 1986)

[7] P.Capbern: "Industrialisation et première évaluation d'une nouvelle version de la méthode ONERA de couplage fort sur multi-profils" (N.T. Aérospatiale 443527/87, Juil.87)

[8] M. Lazareff, JC Le Balleur: "Development of the MZM numerical method for 3D boundary layers with interaction on complex configuration" (Vieweg, V29, Oct.90)

[9] P.Capbern: "Theoretical and experimental study of high-lift device for a NLF airfoil" (First European Forum on Laminar Flow Technology, Hamburg, March 92)

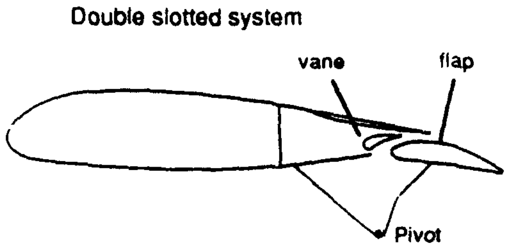

Figure 1 : ATR42 High lift device

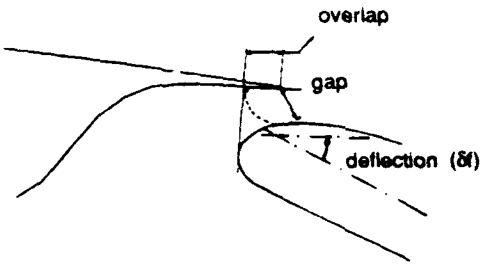

Figure 2 : Kinematics definitions

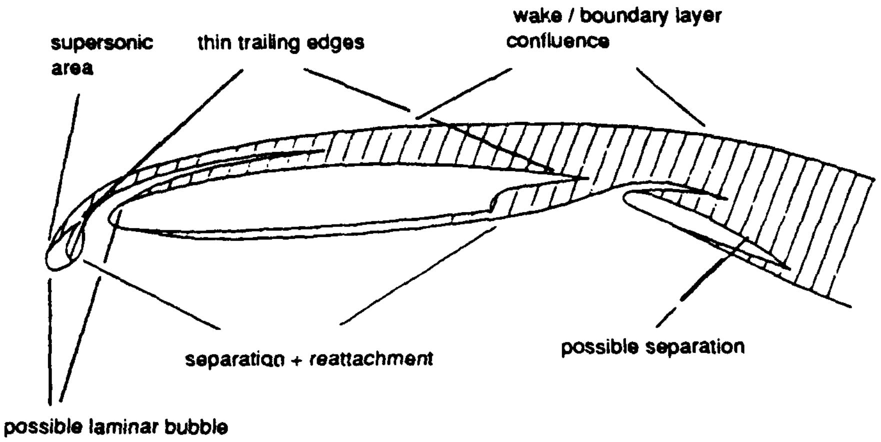

Figure 3 : Difficulties to be solved : the flow around a high lift configuration

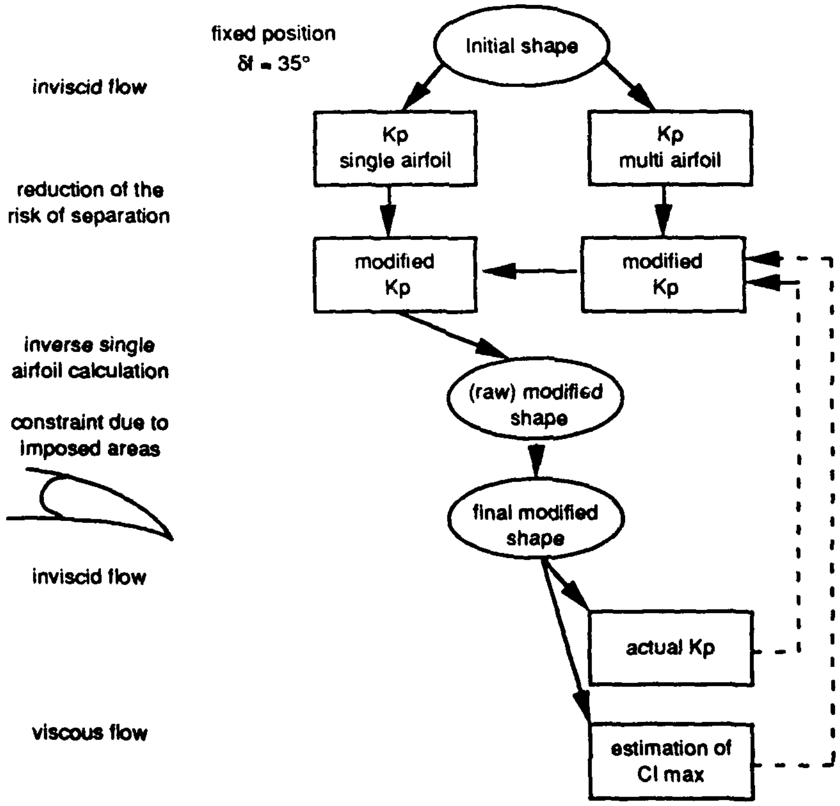

Figure 4 : The shape of the flap optimized for Cl max

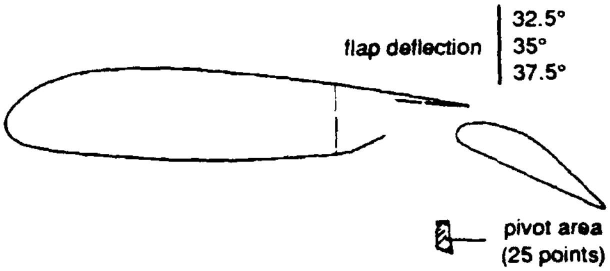

Figure 5 : Definition of a set of pivots meeting the landing Clmax

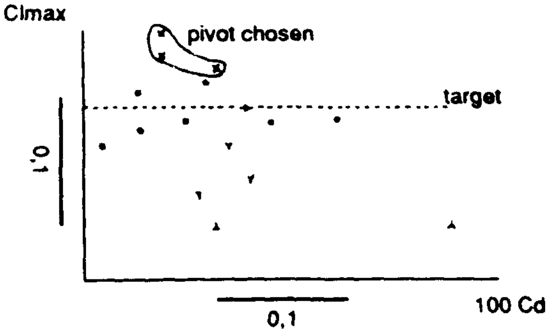

Figure 6 : Optimisation of the lift to drag ratio in take off configuration (δf = 15°)

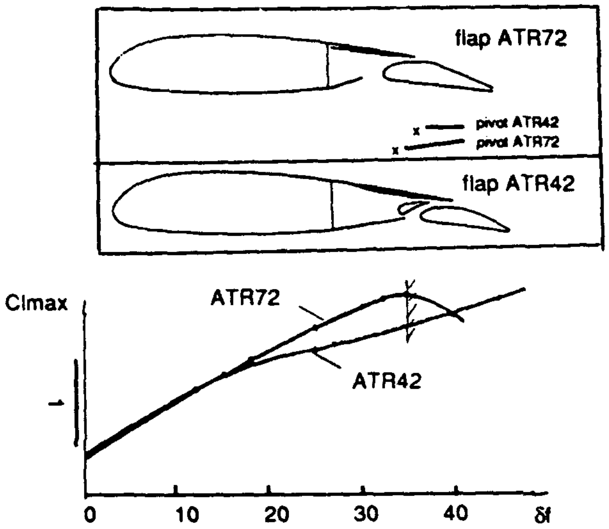

Figure 7: 2D W/T test (S10 - CEAT) comparison ATR42 / ATR72

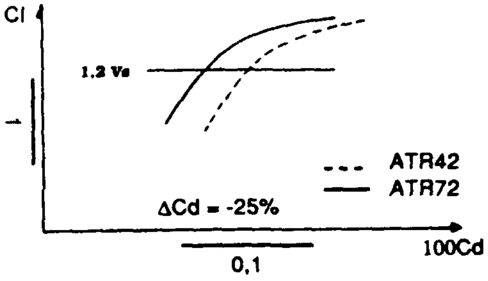

Figure 8 : Wake drag in take off configuration (δf = 15°)

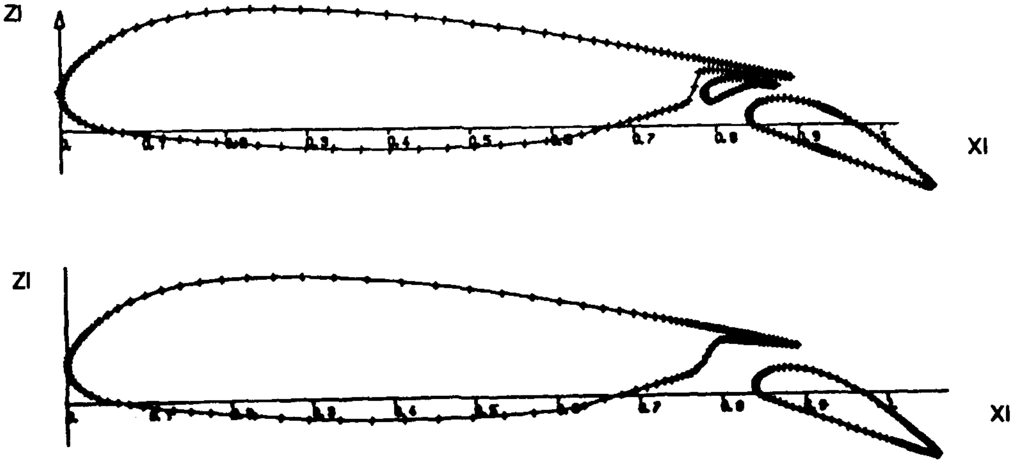

Figure 9 : Configurations with / without vane (δf = 27 °)

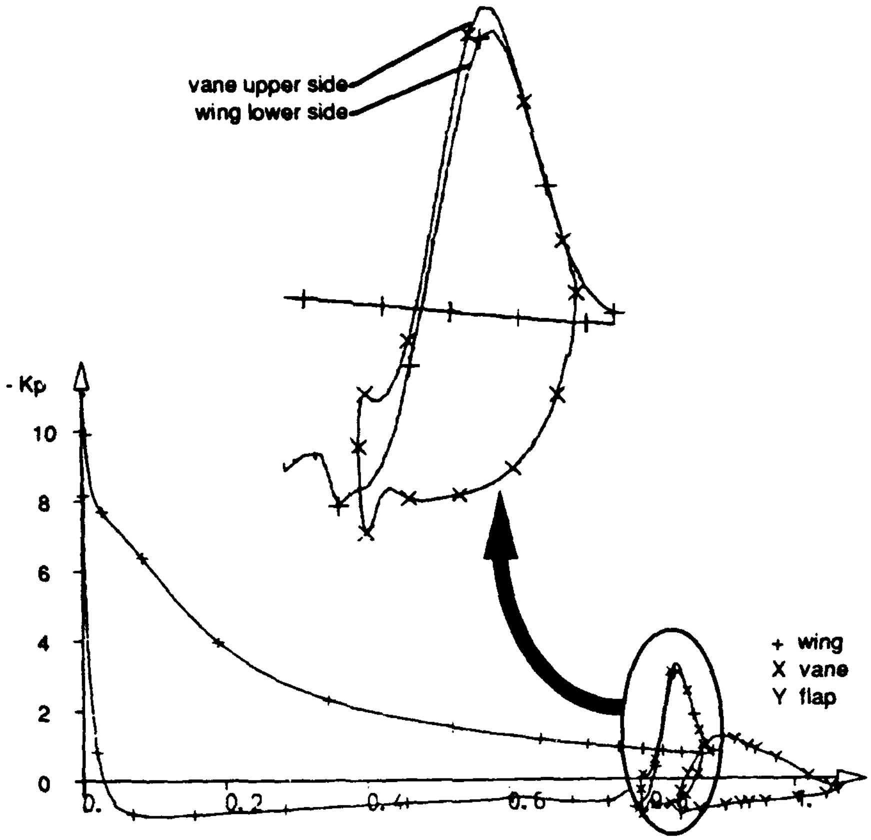

Figure 10 : Strong coupling calculation - Configuration with vane
($\delta f = 27°$, $\alpha = 14°$, Re = 4.7 10^6)

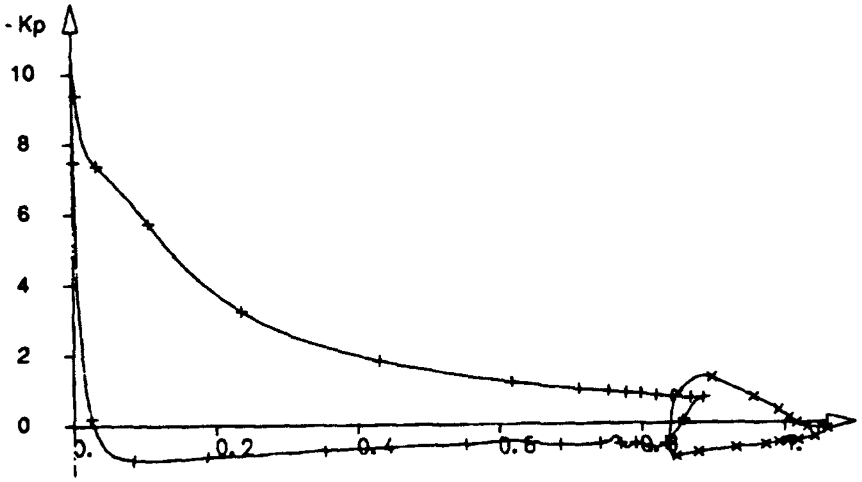

Figure 11 : Strong coupling calculation - Configuration without vane
($\delta f = 27°$, $\alpha = 14°$, Re = 4.7 10^6)

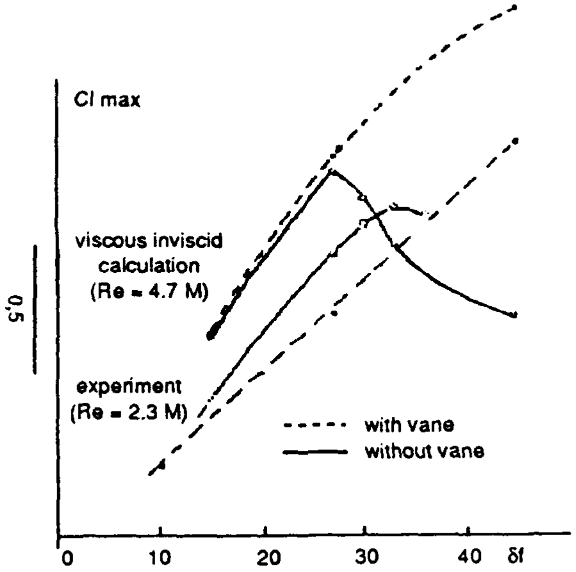

Figure 12 : Effect of the vane on Clmax

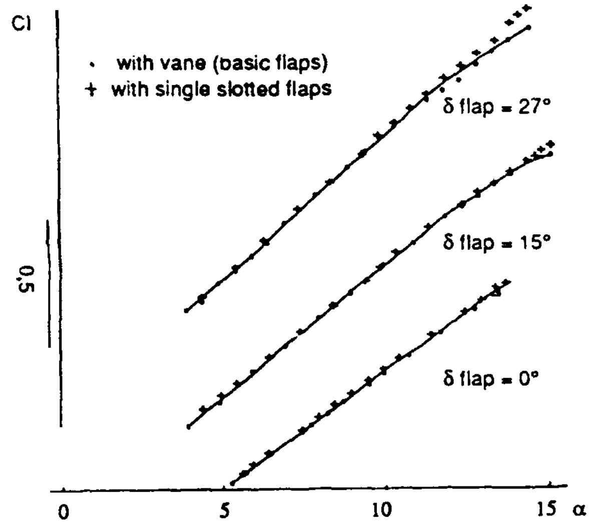

Figure 13 : ATR42 Fligh test : effect of the vane on Cl (α) curves

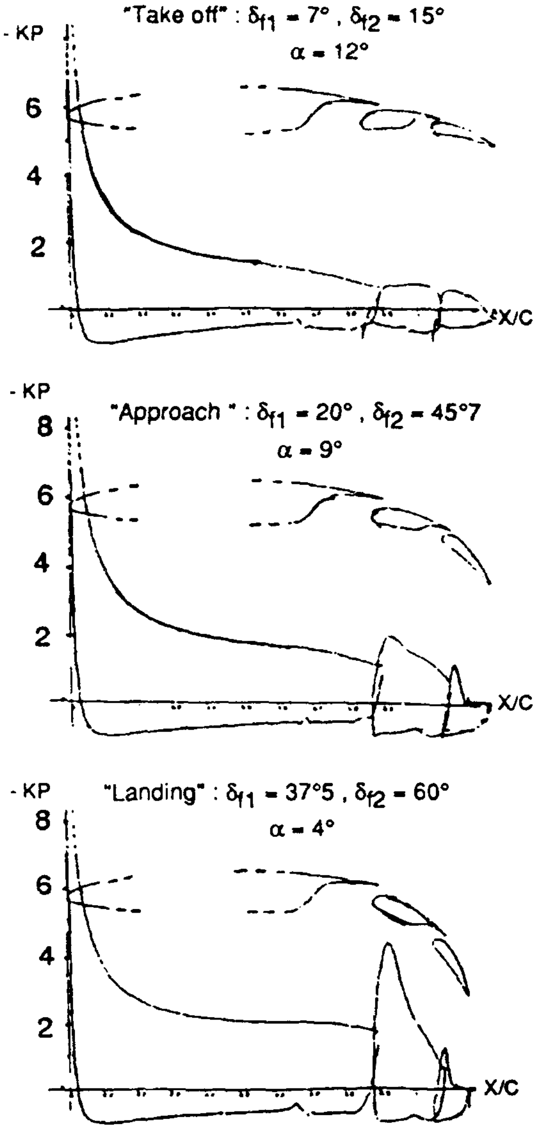

Figure 15 : High lift device for an NLF airfoil : Computation by ONERA strong coupling method (Re = 2.25 10^6)

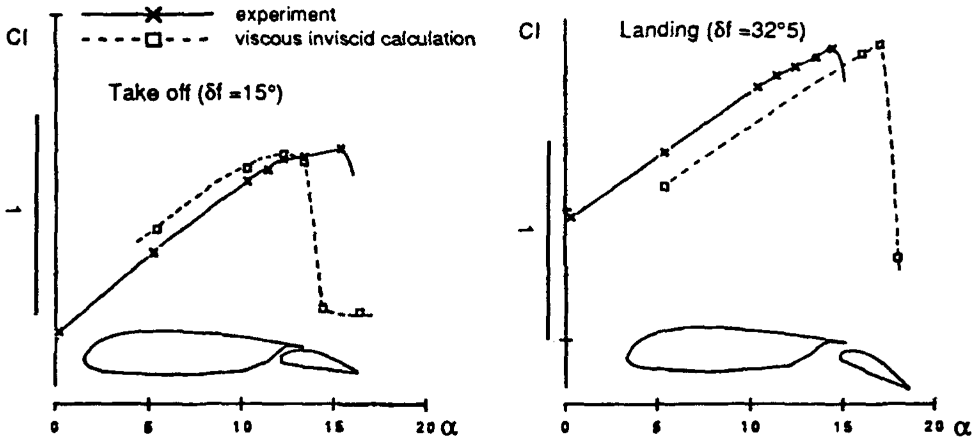

Figure 14 : Viscous inviscid coupling method (ONERA) Comparison calculation / experiment for ATR72 flap

THE AERO-MECHANICAL DESIGN OF A NOVEL FOWLER FLAP MECHANISM

J.R. Mathews
Aerodynamics Department
Aircraft Division
Short Brothers plc
Belfast BT3 9DZ, UK

SUMMARY

The flow around a 2-dimensional wing and flap is reviewed using inviscid and viscous computational fluid dynamic techniques. In particular, the effect of flap gap is explored. The results indicate that for optimum aerodynamic performance at low flap angles, flap gaps in the region of 2 to 3% are required. A novel 4-bar Fowler flap mechanism is described which is shown to give these required gaps for flap angles greater than 3 degrees. Such a mechanism can be readily optimised for minimum flap overlap at specified take-off flap settings. A comparison of a track and roller arrangement with the 4-bar mechanism indicates significant advantages for the latter.

LIST OF SYMBOLS

B	boundary layer parameter
C_d	drag coefficient (2-D)
C_l	lift coefficient (2-D)
C_L	lift coefficient (3-D)
C_m	pitching moment coefficient (2-D)
C_p	pressure coefficient
L/D	lift to drag ratio
M_{inf}	free stream Mach number
Re	Reynolds number
S	normalised transpiration velocity
s	coordinate along the surface
U	local flow velocity
U_{inf}	free stream velocity
U_{max}	maximum local flow velocity
U_{te}	local velocity on the upper surface at 97% wing chord
U^I	inviscid velocity
U^V	viscous velocity (from inverse boundary layer equation)
v_s	transpiration velocity
Δx	panel length
α	incidence
δ^*	boundary layer displacement thickness
ρ	local density
θ	boundary layer momentum thickness

INTRODUCTION

The design and optimisation of a high lift system to minimise the direct operating cost of an aircraft remains a very complicated but essential task for the designer. To produce a genuinely optimum design the dependence of the objective function upon all the design variables must be known. Seldom, however, does the designer have time to determine all the functional relationships. As a consequence the design seldom achieves the global minimum because the objective function is not correctly specified or its dependence upon all the design variables is not fully appreciated. The design of high lift systems cannot be based solely upon maximum aerodynamic performance but is constrained by weight, cost, ease of manufacture, maintainability, reliability and the mechanics of the flap movement.

High lift system design involves the application of specialised knowledge from a wide variety of fields e.g.

Aerodynamics
Structures
Systems
Reliability
Manufacturing
Finance

For the aerodynamicist, high-lift system design arguably involves one of the most complicated flows to predict accurately. Typically it may involve high speed modelling difficulties (transonic flow around a leading edge slat) along with complicated viscous flows (separating boundary layers and interacting wakes with boundary layers). This paper reviews simple 2-dimensional flow considerations (inviscid and viscous) and considers the application of a novel 4-bar mechanism (Patent pending) for flap deployment.

INVISCID FLOW AROUND A FLAPPED AEROFOIL

The incompressible, inviscid flow around a multi-element aerofoil may be examined using a simple panel method. The panel method used here follows that originally proposed by Newling (Ref. 1). This method uses a piecewise constant source and piecewise linear continuous vorticity distributions on each panel. The Kutta condition is satisfied by setting the vorticity to zero at the trailing edge. In order to close the set of equations it is assumed that opposite panels on the upper and lower surfaces have the same source density. Similarly, opposite panel nodes are assumed to have the same vorticity strength.

The stability and convergence of the method is indicated on figure 1 where the effect of increasing the number of panels is shown. The lift and drag coefficients are computed using trapezoidal integration of the predicted pressure distribution. The contribution due to the trailing edge thickness is ignored. (The NACA0012 section has a trailing edge thickness of 0.25% of the chord.) Although the trailing edge contribution to both the lift and drag integrals is ignored, the asymptotic drag value appears correct.

The accuracy of the method is indicated in figure 2 where the panel method predictions are compared with an analytic solution by Williams (Ref. 2) for a 2 element aerofoil.

Using this panel method the effect of reducing the flap gap upon the inviscid, incompressible flow around a 2 element aerofoil is shown in figure 4. (The definitions of flap overlap and gaps are shown in figure 3.) Both the wing and flap sections are based on a NACA0012 section. The flap (30% chord) is deflected to 30 degrees and set at zero overlap. (It is assumed that for optimum aerodynamic performance the flap overlap will be near zero.) Using this geometry the following inviscid generalisations may be made :

i) As the flap gap is reduced, i.e. the flap brought closer to the main aerofoil, the flap lift reduces and the wing element lift increases at such a rate that the total lift increases.

ii) Reducing the flap gap reduces the flap peak velocity, and increases both the wing peak velocity and the wing 'dumping', or trailing edge, velocity.

In general, for zero flap overlap, these trends are repeated for lower flap angles with decreasing magnitude.

Figure 5 shows the effect of flap gap for the flap set at 15 degrees and 5% overlap. (For take-off flap angles, the constraints on the flap mechanism usually result in significant flap overlaps.) For large gaps these results follow the previous trends for zero overlap. However, for gaps less than 2% the velocities in the region between the flap and the wing get very large, as indicated by the maximum velocity on the flap. This results in a rapid increase in the flap lift and reduction of wing lift with the net effect being an over all increase in lift.

VISCOUS FLOW AROUND A FLAPPED AEROFOIL

The inviscid results indicated in figures 4 and 5 suggest that in viscous flows the following may be expected to occur :

i) The reduction of the flap peak velocity will reduce the effective adverse pressure gradient on the upper surface of the flap. For the upper surface on the wing aerofoil, the effective adverse pressure gradient increases very gradually with decreasing gap, as indicated by the difference between the wing peak and dumping velocities in figure 4. For a given incidence these inviscid trends suggest that for low flap angles there will be a range of gaps for which the flow is attached on both sections, with the optimum being the smaller gap to maximise the lift. As the flap angle increases the range of gaps required to keep the flow attached will reduce until it is no longer possible for the flow to be attached on both sections.

ii) Due to the higher adverse pressure gradient on the wing one can also forecast that the stalling incidence of a wing and flap combination will be less than that of the basic wing aerofoil. As the flap is brought closer to the wing, the wing peak velocity increases rapidly resulting in a very severe adverse pressure gradient just downstream of the leading edge. This will increase the likelihood of the wing aerofoil section exhibiting a leading edge stall.

iii) For a positive flap overlap, as the flap gap is reduced, the rapid increase in the peak velocity on the flap is likely to lead to the premature separation of the boundary layer from the flap upper surface. This in turn will lead to the loss of flap lift and may cause a levelling off or a reduction in the total lift. Likewise, the high velocities and subsequent adverse pressure gradient experienced by the lower boundary layer on the wing in the cove region may also result in separation.

As a cautionary note, it is important to recognise that these inviscid trends can only be expected to apply in the real viscous flow if the effects of viscosity are confined to relatively thin boundary layers in the immediate vicinity of the surfaces and their wakes. In this case, the outer inviscid flow will dominate and the interaction between the inner viscous and outer inviscid parts will be comparatively weak. However, as the boundary layers approach separation the interaction between the outer and inner flows becomes increasingly strong till eventually the flow is dominated by viscous effects.

The inviscid panel method has been coupled with an integral boundary layer and wake code, based on the RAE lag-entrainment method. In regions of adverse pressure gradient the code uses an inverse form of the boundary layer equations. Following the work of Le Balleur (Ref. 3) and Lock and Williams (Ref. 4) the inverse boundary layer equations are integrated to calculate a velocity from a specified viscous source strength distribution, or normalised transpiration velocity (S) :

$$S = \frac{v_n}{U} \qquad (1)$$

where v_n is the transpiration velocity used in the inviscid flow to simulate the displacement effect of the boundary layer :

$$v_n = \frac{1}{\rho}\frac{d}{ds}\left(\rho U \delta^*\right) \qquad (2)$$

From an initial guess of the S distribution an iterative procedure follows, cycling between the inviscid and viscous solutions. The choice of using S as the independent variable in the inverse boundary layer equations seems natural as it directly links the inviscid and viscous solutions. In the direct part of the viscous calculation S is updated using equations (1) and (2). In the inverse region the normalised transpiration velocity is updated from the formula :

$$\Delta S = \frac{f B \theta \Delta x}{\Delta x U^{V} + \pi B \theta} \left[\frac{1}{U^{V}} \frac{dU^{V}}{ds} - \frac{1}{U^{I}} \frac{dU^{I}}{ds} \right] \qquad (3)$$

where B is a function of the boundary layer shape parameters and the local Mach number. Putting f=1 recovers Le Balleur's formula. It has been found, however, that in many cases the rate of convergence may be accelerated by increasing f.

According to equation (3) convergence will be obtained (i.e. $\Delta S=0$) when U^V/U^I = constant. Although this is a necessary condition for convergence it is not sufficient, unless $U^V/U^I = 1$. Fortunately the scheme does normally 'converge' with $U^V = U^I$, although there are occasions along the wake where 'convergence' is obtained with the constant in the range 0.85 to 1.15. Decreasing Δx decreases the rate of convergence and so the suitability of equation (3) for updating the normalised transpiration velocity S on finely panelled geometries is questionable.

The Karman-Tsien compressibility correction is used to modify the incompressible Cp's predicted by the panel method.

Figure 6 compares the predicted force and pitching moment coefficients with those obtained from experiment for a simple wing and flap (Ref. 5). The lower surface of the wing aerofoil was designed for no separation. (To compute the flow around a realistic flapped aerofoil it is necessary to replace the physical cove shape on the wing lower surface with a smooth fairing.) Both the lift and drag coefficients have been predicted to an acceptable degree of accuracy. (The predicted drag is obtained by applying the Squire and Young drag formula at the end of the wake.) The maximum lift and stalling incidence are also adequately predicted.

In figure 7 the predicted wing and flap pressure distributions are compared with those measured in the wind tunnel. These results along with other investigations have demonstrated that for similar types of configurations, the method predicts the pressure distributions and force coefficients to an acceptable engineering accuracy.

Using this viscous code, the analysis of the NACA0012 wing and 30% flap set at 15 degrees and 5% overlap for various flap gaps was repeated at a Reynolds number of 6 million and Mach number 0.15. Transition was fixed on both the flap and wing except where laminar separation was predicted ahead of the fixed position. In such cases Horton's method (Ref. 6) is used to predict the bubble length and growth in the boundary layer momentum thickness.

For gaps less than 1.3% the large velocity gradients, both favourable and adverse, on the wing lower surface in the region of the flap give rise to considerable difficulties in the integration of the boundary layer equations. The results shown in figure 8 are similar to the previous inviscid results in figure 5 except that the total lift coefficient has a maximum value for a gap of approximately 2%.

Figure 9a shows the predicted variation of L/D with gap for $\alpha=0$. Again the results show a maximum for a gap of 2%. (Further analysis of this test geometry indicated that the maximum lift coefficient is very insensitive to flap gap with the predicted value being approximately 2.9 for the range of gaps considered.) Figure 9b shows the predicted variation of drag with gap at a $C = 2.0$, which corresponds to $0.7C_{l\max}$. The results clearly indicate that minimum drag occurs for a gap of approximately 2.5%. Although the geometry is atypical, these results are in agreement with wind tunnel measurements for a GA(W)-2 aerofoil and flap (Ref. 7).

One important viscous effect not modelled by the above method is the viscous wake boundary layer interaction. When the wake from an upstream element grows into the developing boundary layer on a downstream aerofoil, the resulting interaction may lead to separation of the boundary layer. Due to this adverse interaction, the previously discussed inviscid trends with flap gap may be reversed, effectively limiting the minimum gap that can be used. One may anticipate that this wake/boundary layer interaction is dependent upon geometric parameters such as the flap gap and the extent of the flap chord aft of the wing shroud. Figure 10 is an example of this effect as predicted using Irwin's model (Ref. 8) for the wake boundary layer interaction on the NACA0012 wing and flap configuration as used in figures 5,8 and 9. There is clearly a rapid loss in lift as the flap gap is reduced below 2.5%. In addition to this loss of lift a rapid increase in drag occurs.

DEVELOPMENT OF A 4-BAR FLAP LINKAGE SYSTEM.

Conventional roller and track systems commonly used to generate a Fowler-type flap deployment possess several inherent disadvantages e.g.

Large number of parts
High weight
High cost
Vulnerability to contamination
Wear
High maintenance cost

These aerodynamic results, along with wind-tunnel investigations, consistently indicate that for aerodynamic efficiency it is desirable to deploy the flap in such a manner so as to minimise the flap overlap and provide a reasonably generous flap gap, typically in the region of 2 to 3%. A novel 4-bar linkage, as shown in figure 11, has been devised for flap deployment as an alternative to the track and roller mechanism. Two swinging links (A and B) are used to join the flap arm, which is rigidly attached to the flap, to a wing mounted beam. The proportions of the links are chosen to 'programme' the flap translation and rotation to give the slot gap and minimum overlap required for an aerodynamically efficient arrangement. An example of slot gap and overlap with flap angle is shown in figure 12. The initial chordwise extension is relatively large for small angular flap movement. The flap gap opens rapidly during the first few degrees of movement from the stowed position. (In effect the flap drops, translates backwards and then rotates.)

Figure 12 also shows the locus of the instantaneous centre of rotation with flap angle. For this particular geometric arrangement, the centre of rotation initially moves upwards to infinity, at which point the flap movement is purely translational. The centre then approaches from the bottom left and indicates that as the flap approaches its maximum angle it is rotating about a progressively decreasing radius. The 4-bar linkage is effectively equivalent to that of a hinged flap having a continuously variable pivot. As the instantaneous centre of rotation is in general some distance from the flap the effective torsional stiffness of the system will be low. This therefore necessitates, in common with tracked flapped systems, the use of a coordinated multi-point flap drive system.

Flap linkage systems have been successfully used in the past, e.g. on the Boeing B747SP and the Douglas DC-8 aircraft. The main advantages of the current 4-bar mechanism over previous linkages is its simplicity and superior aerodynamic efficiency at low flap angles due to the large gap and low overlap characteristic.

To preserve constant % flap overlap and gap along the span of a tapered wing, where both the flap leading edge and shroud are wing generators, it is necessary to scale the linkage at each support in proportion to the local wing chord. This produces a pseudo conical flap motion for which it is necessary to provide freedom for spanwise movement in some of the links. Figure 13 shows schematic cross sections through the A and B links at the inner and outer supports of a flap segment. At the inboard support the shaft that carries the A link has only rotational freedom within its bearing thus enabling it to react any spanwise loads. The remaining links have self-aligning bearings and are therefore free to accommodate the relative spanwise movement.

Figure 13 also gives an indication of the maximum flap fairing width and depth required by the mechanism. A detailed design study indicated that for a 25% flap chord and 90% shroud, the maximum flap fairing width was approximately 10% and the depth was 13% of the local wing chord. These values are comparable to the fairing dimensions for a track and roller mechanism.

A constrained optimisation method has been applied to determine the optimum positions of the joints to maximise the aerodynamic performance of the deployed flap. As a constraint, the landing position of the flap is pre-set in terms of the flap angle, overlap and gap. (Previous investigations have indicated that the optimum overlap for landing is close to zero, with several investigations indicating that a slightly negative overlap may be desirable.) The stored, or nested, position of the flap is also known.

Figure 14 shows a linkage designed by the optimisation process for a 28% flap chord, 90% shroud with the constraints that the landing flap setting was 30 degrees with zero overlap and a gap of 3.2%. Since it is known that the optimum overlap for maximum L/D for take-off is near zero the objective function for minimisation was taken as the flap overlap at a typical take-off flap setting of 10 degrees. The optimiser indicated that to achieve the desired minimum overlap at 10 degrees the kinematics of the optimised linkage result in small negative flap angles in the early stages of the flap deployment. This negative angle, constrained to be less than 4 degrees, is unlikely to cause handling difficulties for the short time that it exists. The achievement of such a low overlap and reasonable gap for a flap angle of 10 degrees is particularly encouraging and indicates the aerodynamic advantages of adopting such a simple linkage system for flap deployment.

If a higher landing flap angle is stipulated in the optimisation process with the other constraints unchanged, the resulting optimised overlap for the take-off flap setting is larger resulting in a lower L/D. This highlights the importance of balancing the landing flap requirements (essentially maximising $C_{L_{max}}$) with the take-off requirements (maximising L/D at an appropriate C_L).

COMPARISON WITH A TRACK AND ROLLER FLAP MECHANISM.

Figure 15 compares the flap overlaps and gaps for a track and roller mechanism with a representative 4-bar linkage. The superior overlap characteristics of the linkage mechanism is immediately apparent along with the much larger gaps at low flap angles. One disadvantage of the linkage relative to the track and roller is that it would not be suitable as a variable camber device (Ref. 9).

The following table summarises the results of a study comparing the overall performance of both flap mechanisms for the same flap chord and wing shroud. The track data were taken as the datum.

Aspect	Track	4-bar Linkage
Flap Weight	Datum	-19%
Direct Maintenance Costs	Datum	-40%
Take off Performance		
ISA, S/L		
: BFL	Datum	-2%
: WAT Limit	Datum	+6%
ISA+28°C, 5000 ft		
: BFL	Datum	-5%
: WAT Limit	Datum	+7%

where BFL is the Balanced Field Length and WAT is the Weight Altitude Temperature Limit. The results quoted for the WAT limit cases refer to the change in the aircraft payload + fuel weight.

CONCLUSIONS

The ability of a simple 2-dimensional panel method coupled with an inverse formulation of the lag-entrainment boundary layer equations for modelling high-lift flows has been demonstrated with adequate accuracy. Using such a tool, analysis of the flow around a simple wing and flap test geometry indicates that for optimum aerodynamic performance flap gaps typically greater than 2% are required.

A simple 4-bar flap support mechanism has been designed to position the flap with such a gap whilst also giving a low flap overlap. Relative to a flap track system, the 4-bar mechanism results in significant improvements in the overall airframe efficiency.

REFERENCES

1. J.C. Newling "An improved two dimensional multi-element program."
HSA-MAE-R-FDM-0007 , 1977

2. B.R. Williams "An exact test case for the plane potential flow about two adjacent lifting aerofoils."
RAE TR 71197 , 1971

3. J.C. Le Balleur "Calcul desecoulementsa forte interaction visqueuse au moyen de methodes de couplage."
AGARD CP291 , 1980

4. R.C. Lock and B.R. Williams "Viscous-Inviscid interactions in external aerodynamics."
Prog. Aerospace Sc. Vol.24 , 1987

5. B. van den Berg "Boundary layer measurements on a two-dimensional wing with flap."
NLR TR 790090 , 1979

6. H.P. Horton "A semi-empirical theory for the growth and bursting of laminar separation bubbles."
ARC CP 1073 , 1967

7. W.H. Wentz "Wind tunnel test of the GA(W)-2 airfoil with 20% aileron, 25% slotted flap, 30% Fowler flap and 10% slot-lip spoiler."
NASA CR-145139 , 1977

8. H.P.A.H. Irwin "A calculation method for the two dimensional turbulent flow over a slotted flap."
ARC CP 1267 , 1974

9. E. Greff "Aerodynamic design and integration of a variable camber wing for a new generation long/medium range aircraft."
16th ICAS Congress Jerusalem
Paper no. 88-2.2.4 , 1988

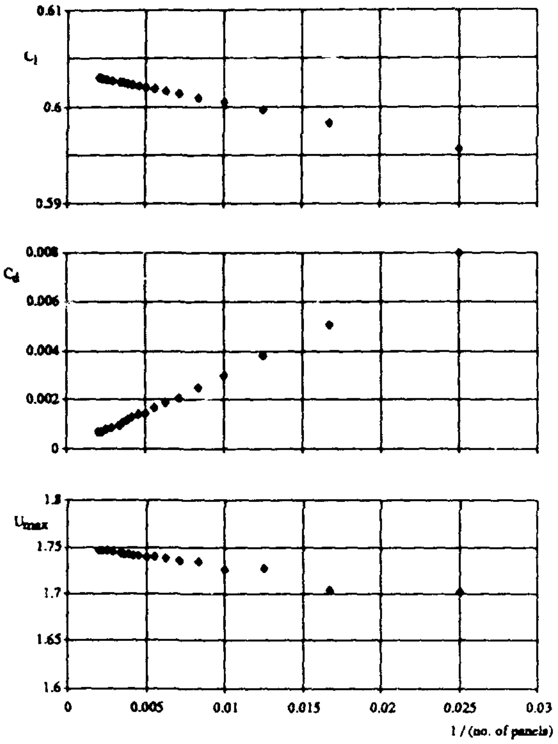

FIGURE 1 Effect of the number of panels on the predicted inviscid, incompressible solution for a NACA0012, $\alpha = 5°$.

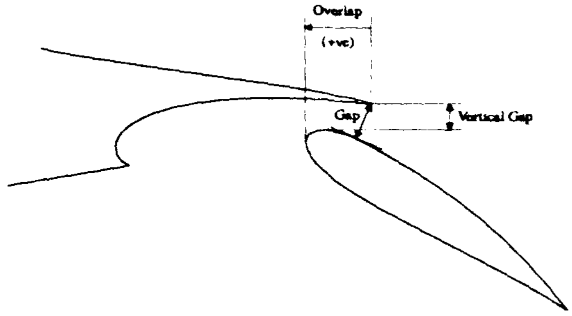

FIGURE 3 Definition of flap overlap and gaps, measured as a % of the local wing chord.

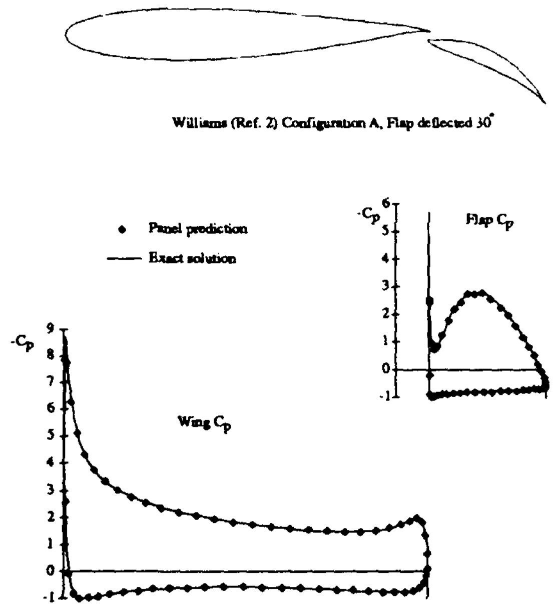

FIGURE 2 Exact and predicted pressure distributions for the Williams flapped aerofoil (Ref. 2) Configuration A, Flap deflected 30°.

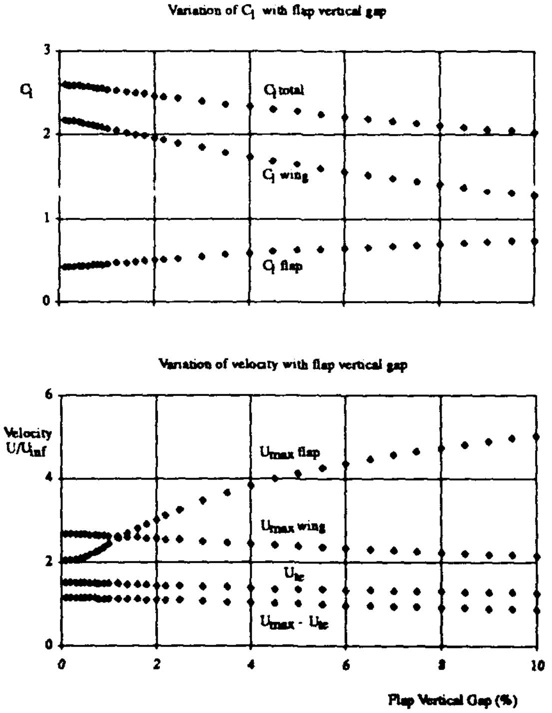

FIGURE 4 2D inviscid, incompressible trends for a NACA0012 wing and flap. Flap chord = 30%, deflected 30°. Overlap = 0, $\alpha = 0°$.

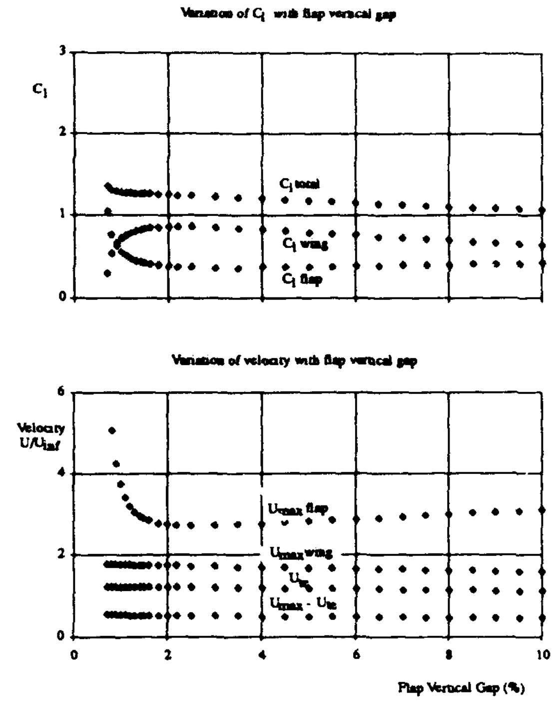

FIGURE 5 2D inviscid, incompressible trends for a NACA0012 wing and flap. Flap chord = 30%, deflected 15°. Overlap = 5%, $\alpha = 0°$.

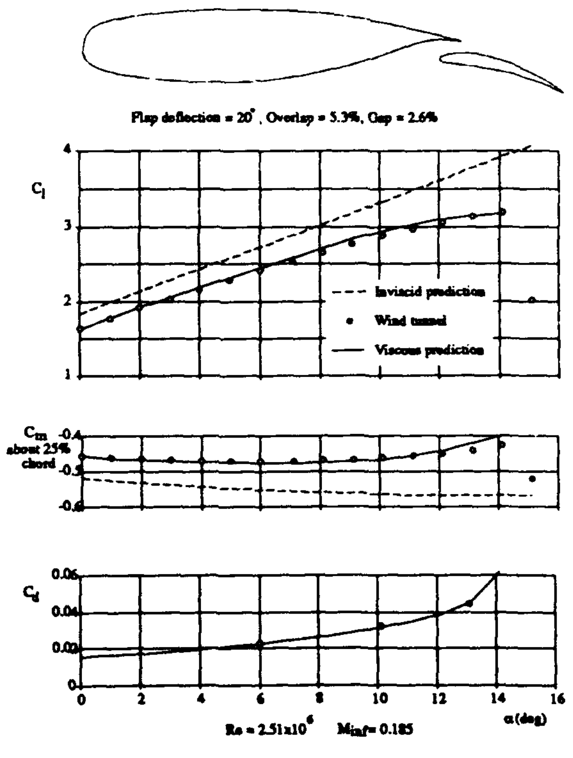

FIGURE 6 Lift, moment and drag coefficients for the NLR flapped aerofoil (Ref. 3).

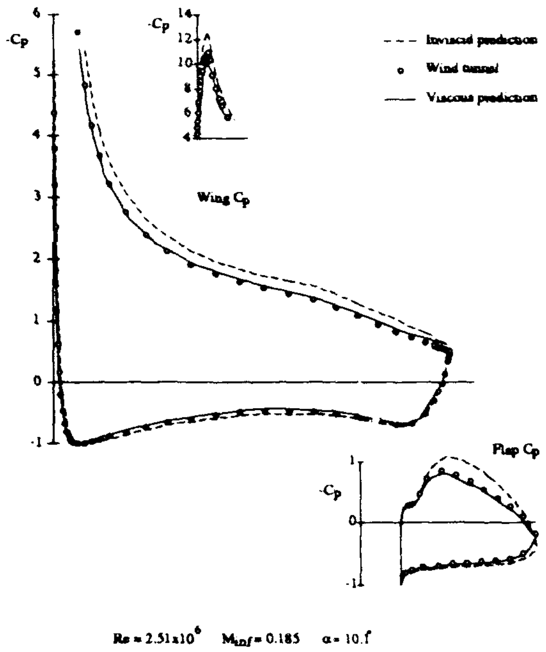

FIGURE 7 Predicted and measured pressure distributions for the NLR flapped aerofoil (Ref. 3).

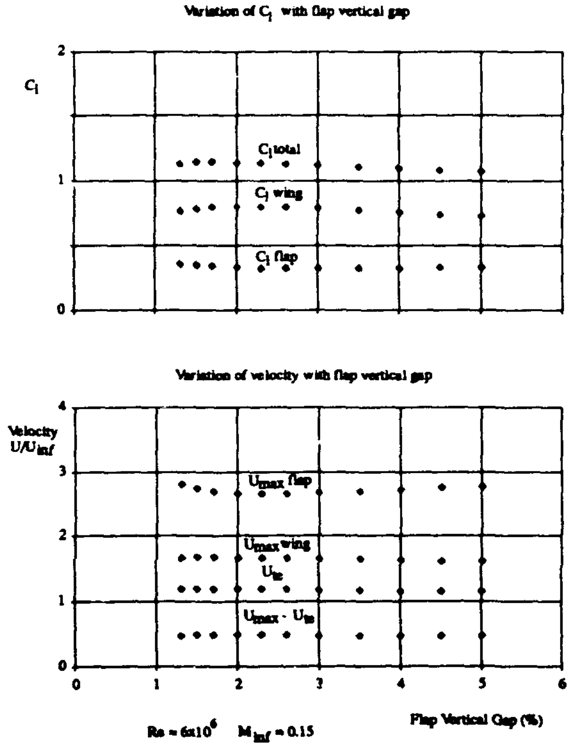

FIGURE 8 2D predicted viscous trends for a NACA0012 wing and flap. Flap chord = 30%, deflected 15°. Overlap = 5%, $\alpha = 0°$.

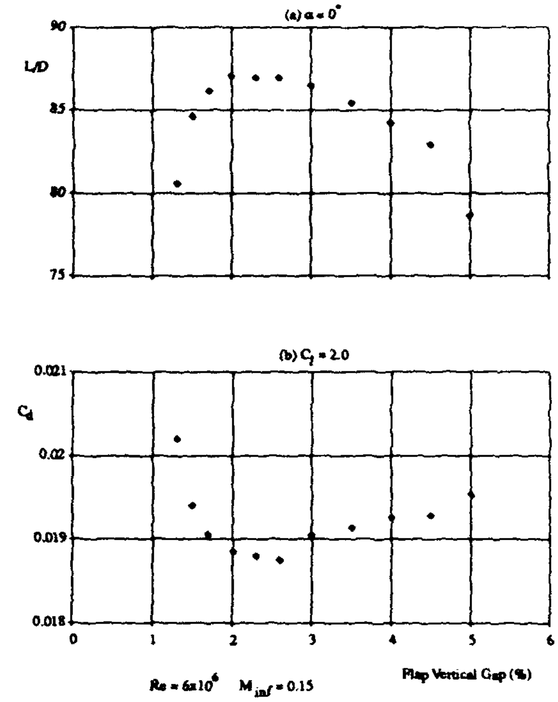

FIGURE 9 2D predicted lift and drag trends for a NACA0012 wing and flap. Flap chord = 30%, deflected 15°. Overlap = 5%.

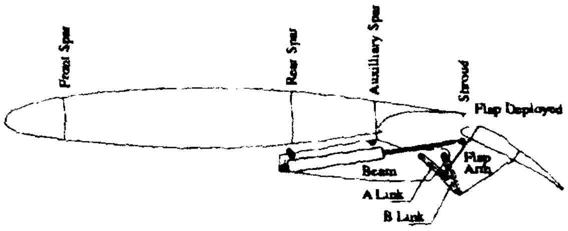

FIGURE 11 The 4-bar linkage mechanism.

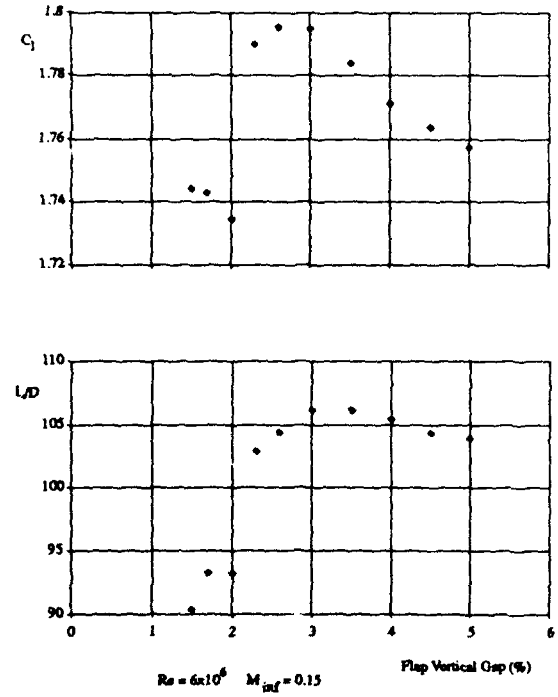

FIGURE 10 Effect of wake/boundary layer interaction on the lift and drag trends for a NACA0012 wing and flap. Flap chord = 30%, deflected 15°. Overlap = 5%, α = 5°.

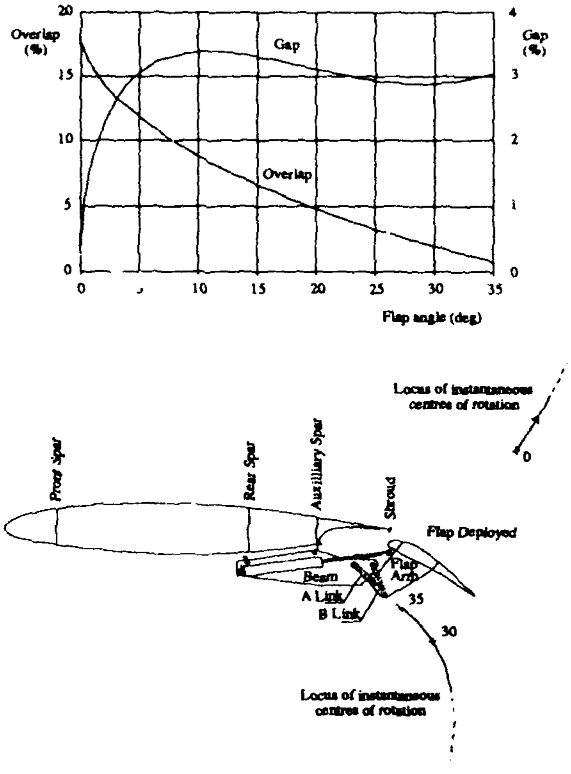

FIGURE 12 Flap overlap and gap characteristics for the 4-bar linkage mechanism.

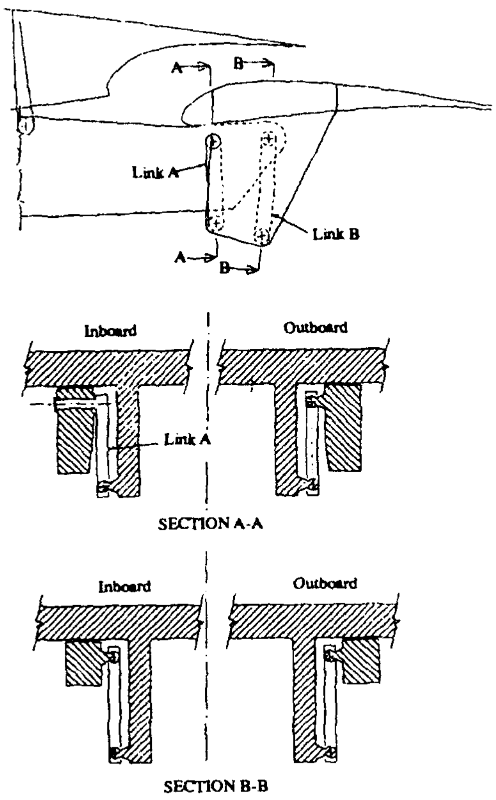

FIGURE 13 Cross-sections through the links.

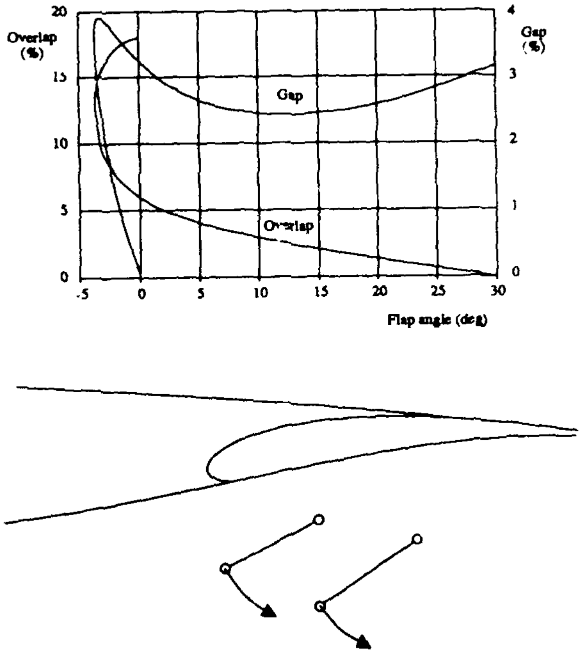

FIGURE 14 Optimised linkage for minimum overlap at a flap angle of 10°.

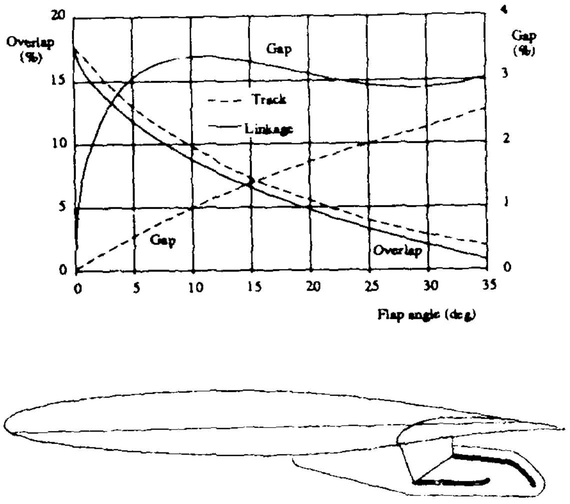

FIGURE 15 Comparison of track with linkage.

DESIGN, DEVELOPMENT AND FLIGHT EVALUATION OF THE BOEING YC-14 USB POWERED LIFT AIRCRAFT

TED C. NARK

BOEING DEFENSE & SPACE GROUP
Post Office Box 3999
Seattle, Washington 98124-2499
M/S 11-PC USA

SUMMARY

The Boeing YC-14 was designed to perform a 400nm mission carrying a 26000# payload and land in 2000 feet on a semi-prepared landing strip. The high-lift system was one that had never been flown before, a upper surface blowing (USB) concept utilizing the "Coanda" effect. The take-off and landing performance estimates developed from wind tunnel data were completely substantiates in the flight test program. The critical issue of continuing either a landing or take-off after the loss of one of the two CF6 engines was also proven in the flight test program. The design details behind the performance of the YC-14 are discussed and some of the performance features of the airplane are explained.

INTRODUCTION

The Boeing YC-14, and its competitor the Douglas YC-15, began life as elements of the Air Force AMST (Advanced Medium STOL) program which was initiated with release of an RFP in 1971. The YC-14 flew for the first time on August 9, 1976. The competition for the production contract was won by the Douglas C-15. The mission was substantially changed, particularly with respect to its STOL properties, and the airplane is being built today by McDonnell-Douglas as the C-17.

The basic design goals for the AMST mission were basically very simple and are listed in Figure 1. Fundamentally it was to be a flying truck capable of handling almost any of the fighting gear the Army had in its inventory and it had to deliver a 27,000 pound payload to a battle field 400 nautical miles away. It had to land on a 2000 ft. unprepared runway, off-load the payload and then take-off with another load and return to base. The specifications were very broadly spelled out and it gave the two companies, Boeing and Douglas, a great deal of leeway in configuring the vehicle. There was one other objective which was instrumental in configuring the airplane. That was, the cost to produce the airplane was an important issue.

CONFIGURATION

The YC-14 configuration is shown in figure 2. The fuselage was sized to handle almost all of the equipment in the Army inventory. It was configured to allow aerial delivery of both troops and equipment out of the aft cargo door and troops from a side door just aft of the main gear. The most significant feature of the YC-14 was probably the two CF6 engines placed on top of the wing.

The twin engine design was due to the results of an analysis that indicated such a design was possible using an existing modern engine (CF6) and would be both cheaper and simpler to build than a four engine configuration. In addition accident statistics confirmed that twin engine airplanes have fewer engine shutdowns and were safer to fly. In addition to the Air Force requirements, Boeing established an in-house design philosophy, three elements of which are worth nothing here. First the airplane must be easy to fly on final approach. It should fly like a conventional jet airplane to avoid adding an extra burden to the pilot training program and at the same time be safe to fly. Second the airplane must have engine out performance equal to conventional jet aircraft, that is, be able to continue a STOL take-off or landing with an average military crew with an engine out. And thirdly, as mentioned earlier, it must be a configuration with a low cost of ownership.

Low cost of ownership included both low unit fly-away cost as well as low maintenance costs. A great deal of thought went into selecting the materials and processes used in producing the YC-14. Parts and pieces were configured to lower the manufacturing costs. For example the wing structure had a main spar that was straight and continuous from tip-to-tip. The wing center section was constant chord to allow this use of constant airfoil sections. The same thing was done for the vertical tail, which was designed with a constraint chord fin. The body structure was composed of simple structural elements.

At the time of the AMST competition there were two serious powered lift concepts considered for the design. The engine blown flap (EBF) and the upper surface blown (USB) flap. As you can imagine, there were many design issues to be considered in selecting an approach, and as you might also expect there was no clear cut winner. Douglas, after what must have been serious considerations, selected the EBF concept with four JT8D engines for the YC-15. Boeing on the other hand placed its bet on the USB concept, with two CF6 engines, for the YC-14. The USB configuration allowed the engines to be placed close together over the wing minimizing both the rolling moment and yawing moment associated with an engine out. The coanda effect, the design feature behind the USB flap, was shown by both NASA Langley tests and tests at Boeing, to effectively turn the flow through as much as 70^o with less than 10% thrust loss. Another design feature following from an over-the-wing design was the lessening of the concern over foreign object damage when operating on the un-improved runways required by the design requirements. The thrust reverser was designed to deflect all the thrust-- not just the primary flow-- forward and upward. This allowed the reversers to operate effectively down to zero forward speed without any concern of re-ingesting the hot gases in the inlet, and at the same time improved the braking force associated with the landing gear.

From the laws of physics, a 2000 foot landing distance equates to an approach speed of somewhere between 80 and 90 knots. For conventional aircraft (non-powered lift)W/qS is defined as C_L, but for a powered or propulsive lift airplane a more suitable name is landing lift efficiency. Because of the thrust dependent lift vector, W/qS can be quite a bit larger than the aerodynamic C_L. In the case of the YC-14 with an engine out, W/qS is just about twice as large as a conventional jet such as the 727 (Figure 3.) With all engines operating (neglecting the effects of a failed engine) the YC-14 can approach at 65 knots and land in about 1150 ft.

The design of the USB high lift system incorporating the USB flap was instrumental in achieving a W/qS of almost 4, with an engine out.

The high lift system was made up of a number of complimentary elements (Figure 4). It had full span (8 segments) two-position variable camber Kruger leading edge flaps, full span leading edge blowing, using 8th and 14th stage engine bleed air, and double slotted center and outbound flaps. The two position double slotted flaps behind the engine were sealed with the engines operating and open behind a dead engine. Vortex generators, or turning vanes on the wing behind the engine, were used to assist in spreading the flow outboard. An USB/nozzle door on the outboard size of the nozzle exit also assisted in spreading the flow outboard .

The entire high lift system was designed to continue a STOL takeoff or landing with a critical engine imperative. The leading edge Kruger flap was designed with a tapered plan form and a spanwise change in camber from root to tip. It represented a very unique solution of a difficult design problem. The leading edge Boundary Layer Control (BLC) System (Figure 5) was designed to supply engine bleed air to the entire wing from whichever engine was functioning and to accomplish this with a pnuematic design, no electrical or mechanical switching.

The aerodynamics of the leading edge blowing system was a unique design challenge. The wind tunnel testing of BLC was accomplished with the blowing orifice as a slot, producing a continuous jet across the span. In addition the mass flow across the wing was distributed in proportion to the local wing chord to approximate an uniform blowing coefficient along the wing span. The slot blowing design was considered impractical for the full scale airplane. A design using small holes was developed. The design of the leading edge blowing nozzle and plenum system is shown in Figure 6. With a series of tests of both the slot nozzle at model scale and drilled holes nozzles at full scale it was possible to correlate the aerodynamic efficiency at model scale with the full scale performance of the airplane.

The leading edge BLC system was itself a coanda surface device. The small drilled holes created small jets of air, which after impinging on the coanda surface spread out and merged into an effective sheet of air, simulating the slot nozzle, as it was turned by the coanda surface. The spanwise mass flow was varied by changing the size of the drilled holes and the hole spacing in each plenum. The hole spacing was selected so that if a hole were to plug up the two adjacent holes would spread together to create a thinner, but still a continuous jet. The system in flight worked flawlessly, if either engine failed the system continued to function without interruption.

The unpowered outboard flaps (Fig. 4) were of conventional design and were supported by an external hinge point to avoid the mechanical complexities and maintenance issues of alternative approaches. The USB flap had to be sealed to function in the propulsive lift mode. With an engine out both the lift and drag penalties of such a configuration were too severe to be acceptable. A mechanism, triggered by a single actuator, was designed to convert the sealed USB flap with an engine operating to a double slotted flap behind the dead engine. This converted the high lift system on the dead engines wing to a double slotted flap, with leading edge blowing, from the side of the nacelle to the aileron. To accomplish this configuration change an engine out sensor was designed to identify which engine had failed.

With the decision to implement such a sensor came a whole new approach to handling the continued approach or continued take-off with an engine out. Model scale tests demonstrated that the turning of the gas jet by the coanda effect was enhanced as the jet flow was less concentrated or more evenly distributed over the coanda surface. In practice, thinning of the flow was enhanced on the YC-14 with two design features. The first was a nozzle door on the outboard side of each nacelle, and the second was the addition of turning vanes on the wing just behind the engine exhaust plane. Both features were activated when the flap handle was placed in a landing flap detent. With an engine failure the nozzle door on the dead engine was closed and the turning vanes stowed to reduce the drag on the dead engine wing.

The high lift system was designed and developed as a result of a very comprehensive scale model test program. A lot of the early developmental testing of the high lift system elements and exhaust nozzle features were accomplished with a half model in a 9'x9' non-return tunnel located in Seattle. The complete model (at the same scale, as the half model) was tested in the 20'x20' Vertol tunnel in Philadelphia, PA to obtain the influence of the propulsive lift on the control system and develop the engine out system for the take-off and landing configuration.

The test program was an invaluable asset in establishing the design and performance of the critical engine inoperative configuration. A partial list of the many design issues successfully resolved in the wind tunnel are listed in Figure 7. The last three items in the list were brought about by problems uncovered in flight test and then wind tunnel tested to provide solutions that resulted in substantial reduction in the high speed cruise drag.

STOL PERFORMANCE

The wind tunnel was the source of the W/qs/max data used in predicting the STOL performance of the YC-14. Figure 8 compares the wind tunnel W/qs/max data for flaps 60 USB 50° (nominal landing flap configuration) with the corresponding flight test data. It is plotted against the jet thrust coefficient of the live engine. It is appropriate to point out at this time that the field length performance requirements established by the Air Force were all to be met with a critical engine inoperative. The performance with all engine operations was especially outstanding. It could land at 65 knots in about 1150 ft and take-off in a ground roll of 1,100 feet.

The requirement to produce landing performance with an engine out resulted in an interesting situation for a twin engine, powered lift airplane. With an engine out on one wing, that wing has basically no powered lift except leading edge blowing. The approach speed was essentially established by the lift obtainable on the wing with the dead engine. The key to the YC-14's success was embodied in two unique design features. First the live engine could support the leading edge boundary layer control system on both sides of the airplane. Second with an engine out, the wing with a dead engine had a well designed double slotted flap from the side of body clear out to the aileron, a very effective high lift system. This presented the configuration with one more crucial design challenge, there was just too much lift on the live engine wing at the power required to maintain the glide slope on one engine. In effect the powered lift had to be "killed" as the engine power came up or the airplane would roll over on its side. Suffice to say this didn't happen. It is interesting to note that it was possible to build a twin engine high lift system with a trimmed

W/qs/max ≈4 (Figure 8) with one engine operating. Also notice how well the W/qs/max measured in the wind tunnel agrees with the flight test data. Figure 9 displays the same data only now is terms of minimum speed, V_{min}. For a STOL airplane the minimum speed can be based on a control limit or an aerodynamic lift limit (wing stall). On the YC-14 it was a wing stall that determined the minimum speed. The minimum speeds determined from flight test (data at the thrust required for approach on a 60° glide slope {T/W ≈0.21},) is at least as good at the wind tunnel data would predict for the same condition. In general the high lift performance of the YC-14 during flight test was always as good as predicted by the wind tunnel data base.

The take-off of a STOL airplane in 2000 ft. is dependent on two features, thrust, lots of it, and W/qs/max for the take-off flap configuration. Parametric studies conducted during the early design phase in the development of the YC-14 indicated that a $0.25 \leq T/W \leq 0.30$ was required to accelerate the airplane to a reasonable lift-off speed. Built into this take-off process was a W/qs/max≈3.5. To put these numbers in perspective the engine-out T/W for the YC-14 is greater than the all engine T/W for a conventional jet transport and the YC-14 W/qs/MAX with an engine out in the take off configuration is substantially greater than the W/qs/max of a conventional jet in the landing configuration.

The key to the success of the YC-14 twin engine STOL configuration was heavily dependent on the availability of the GE CF-6 engine. It represented almost a perfect match to the STOL performance in both take-off and landing as well as the cruise performance in terms of thrust and fuel burned. The flap configuration for take-off is rather unique. The USB flap behind the engine was retracted to produce the most horizontal thrust for acceleration, and the outboard double slotted flaps were at 30° to produce an acceptable W/qs/max of 3.5 with an engine out.

An important part of the YC-14 mission requirement was to continue either a STOL landing or take-off after the loss of an engine. Placing the engines over the wing to utilize the USB powered lift concept and placing the wing on top of the fuselage to minimize the influence of the ground on the lifting system had the benefit of allowing the engines to placed very close to the fuselage thereby minimizing the thrust induced rolling moment associated with a single engine operation in an approach configuration. Figure 10 shows that the increment in lift caused by the loss of an engine, which is responsible for the engine out rolling moment, has an apparent moment arm equal to the distance of the nacelle from the center line of the airplane. This implies that the engine out rolling moment can be minimized by placing the nacelle as close to the fuselage as possible, a definite advantage for an over the wing engine installation on a high wing configuration. On a take-off, after the loss of an engine, control of the moments about the directional axis is also critical. Again moving the engine as close to the fuselage as possible had a significant impact on reducing the yawing moment coefficient associated with an inoperative engine. Figure 11 illustrates that the 4 engine YC-15 with JT8D-17 engines had a somewhat smaller engine out yawing moment coefficient with a critical outboard engine inoperative to contend with than did the YC-14 with an engine inoperative. Also note the significant difference between both the YC-14 and YC-15 compared to a conventional twin engine 737. The control of the YC-14 engine out rolling moment and yawing moment were a critical issue in the developing the YC-14.

Not only were the YC-14 rolling and yawing moments high, but the speeds at which they had to be controlled were much lower than conventional jet aircraft. The net result of having to produce a large moment coefficient at low " q " (low speed) is the requirement for large or multiple control surfaces (or both) that move very rapidly and through large angles to provide aircraft agility at STOL speeds. It was decided that double-hinged or anti-balance surfaces offer an attractive compromise to overly large simply hinged surface.

A comparison of the differences in the vertical tail of a 737 and YC-14 are shown in Figure 12. A similar set of information comparing the YC-14 horizontal stabilizer with that of the 727-100 is shown in Figure 13. It is quite evident from a review of the material presented in Figure 12 and 13 that a STOL control system, as represented by the YC-14, is very different from that for a conventional jet transport represented by the 737.

In order to achieve a 2000 foot landing distance by military rules requires approach speeds on the order of 90 knots (Figure 14). But that alone is insufficient. A very effective retarding force is also required, and the airplane once on the ground must stay there and not bounce back into the air. In addition the pilot must be able to control the airplane on the glide slope to a precise and positive touchdown. This embodies designing a configuration with effective thrust reversers on the engines, a robust, rugged set of brakes, a landing gear which is tuned to a high rate of descent at touchdown (≈10FPS), precise glide path control, even in adverse weather conditions, and a lift dump system that "kills" the lift and puts the weight of the aircraft on the gear at touchdown. The YC-14 design addressed each of these issues with a very positive approach.

The thrust reverser not only had an effective reverse thrust component (≈40%), it also contributed a sizeable downward thrust component to increase the normal force on the gear and thereby increase the braking force. The braking system had a coefficient of braking friction of μ=0.42, and coupled with an anti-skid mechanism was a very effective at bringing the airplane to a stop on the ground. The landing gear was designed (Figure 15) to routinely land at a rate of sink at touchdown of 6 to 10 FPS. This coupled with a approach speed of approximately 86 knots allows the YC-14 to fly down a 6° glide slope (commercial transports routinely use 2-1/2°-3°) and make a no flare or partial flare landing at STOL weights on a very soft field without exceeding the design rate-of sink at touchdown . In actual practice, the airplane hits the ground, the gear compresses smoothly and the airplane is on the ground to stay. A switch on the landing gear then triggers a signal to the spoilers on both sides of the wing, from just outboard of the nacelle to just inbound of the aileron, to come up, directly "dumping" the aerodynamic lift on to the gear and maximizing the braking effectiveness immediately on touchdown.

To make a precision landing the airplane must be in control of the glide path in all weather conditions. This is especially difficult for an airplane with propulsive lift, which almost always fly on the "back side" of the polar (Figure 16). The YC-14 design was developed to give a military pilot the feeling on the front side the polar, --- the way he was fundamentally trained to fly. It was felt that in an emergency situation the pilot could not be expected to remember a unique set of flying qualities associated with a STOL airplane. The decision was made early in the program that there should be no reason to retrain the pilots. The STOL airplane would be made to fly like a conventional airplane. This was accomplished by developing a computer controlled, triply redundant, electrical flight control system (EFCS). Once a computer was added to the flight control system the opportunities to exploit it became unlimited. The back side polar problem was solved by incorporating a speed hold module into the EFCS. The pilot had a very simple task to master on approach. Use the stick to point the nose of the airplane where he wanted to land. Everything else was taken care of for him by the EFCS. Servos where coupled to the throttle and the USB flap. On approach a "speed hold" signal was developed and coupled to a conventional attitude hold mode. Once the target speed was set with a dial indicator, the EFCS would modulate the throttle and USB flap to maintain speed. The attitude hold mode would keep the wings level and the pilot would control the pitch plane with the control wheel, his only task. In the event of an engine failure during approach the pilot continued to control the pitch plane. The engine failure detection system coupled into the EFCS triggered a series of events which took pre-programmed measures to trim out the airplane about all three axis leaving the pilot to continue to control pitch plane dynamics to maintain flying the 6° glide slope. His only task was to continue pointing the nose of the plane at the touchdown point.

The maximum deviation from the 6° glide slope on an engine-out go-around was less than 15 feet and less than 5 feet on a continued approach. An engine out landing could be successfully accomplished from an engine failure at any altitude. In addition, the thrust reversers alone would support landing on icy runways. A similar approach was developed to handle an engine out on take-off. A summary of some of its more significant EFCS modes is shown in Figure 17. Having a computer in the control loop proved to be an invaluable tool and in my opinion it proved itself on more than one occasion.

As you can see developing a short field airplane around a high lift system is more involved than just designing the high lift system . Some of the elements involved in developing a successful short field airplane are detailed in Figure 18. The landing performance of the YC-14, which had designed into it the features described in Figure 18, is shown in Figure 19,. It represents the statistics on the STOL landing dispersion. It includes landings with all engines operating and a critical engine inoperative. It represents the data from 108 landings. The piloting task was to hit an aiming point on the runway. The measurement is the distance, in feet, between the pilot's aiming point and where the plane actually touched down. The average of all the errors was under 16 feet on the long side, and 63%- of all the landing were made within ± 74 feet of the aim point.

In summary the YC-14 met or exceeded all its STOL design requirements. The low speed properties of the airplane were adequately predicted with data from low speed wind tunnel tests. The concept of operating a safe, twin-engine, STOL airplane, was substantiated.

HIGH SPEED DESIGN

There was more to the success of the YC-14 airplane than its STOL capabilities. It could also fly at a mach number of 0.68, almost in keeping with the commercial jet fleet of airplanes. This presented the design with another challenge. The first and most important was to "camouflage" the high lift system for high speed cruise.
The upper surface contour of the USB flap was basically circular. The most cost effective design was determined to be achieved with an external hinge point. This design also was consistent with using the USB flap as a control element on approach. The six hinge points on each wing were provided with fairings which are very evident in a front or back view of the YC-14. The engine nozzle was specifically contoured to achieve a widely spread jet, a high jet turning configuration, but, not an acceptable high speed configuration. In cruise there was a scrubbing drag, it was considered a part of the nozzle thrust coefficient of 0.97 and accounted for in all the pre-flight test performance estimates. A lot of effort was expended in designing the nozzle that would both enhance the exhaust jet turning at low speeds and have minimum impact on cruise performance. The empirically defined parameters are shown in Figure 20. The problem was that nozzles with good turning almost always had unacceptable high cruise drag and good cruise nozzles characteristically did not turn the flow well at low speed. The net result is that a nozzle designed for cruise can have a 10% improvement in cruise drag and ΔM_{crit}= 0.05 over a high turning nozzle design, while a high turning nozzle can have a maximum lift improvement of ΔC_L=1.3 over a good cruise nozzle. The variable geometry nozzle went along way toward a compromise design.
Another critical area with respect to cruise drag was the flow between the nacelle, wing leading edge and fuselage. It was a particular difficult flow channel to configure for both acceptable high lift and high speed properties A moveable leading edge device was first designed, but it was a mechanical nightmare. After extensive wind tunnel testing a compromise fixed leading edge was developed and worked successfully. There were two areas of concern with the YC-14 high speed drag uncovered in flight test. The up-swept aft body and the large gear pods. Both had drag levels that were judged to be unacceptably high. The gear pods were necessary because of the requirements on the dimensions of the cargo compartment and the high wing configuration, left no volume in which to store the gear, hence an external fairing or gear pod was created. The up-swept aft-body was a by-product of the requirement of loading and unloading rolling stock through the aft cargo door.
The flight test drag level of the original configuration was 12% higher than expected. As later found out in the wind tunnel, the flow around the gear rod was interacting with the cross flow over the aft fuselage and the flow over the upswept aft body was badly separated. The solution, identified and solved in the wind tunnel, was composed of two parts. First the gear pod was redesigned to close the lines in two dimensions, like a wing shape, rather than in three dimensions like a body of revolution. Second, strakes were added to the aft fuselage to assist in keeping the aft body cross flow attached. Before the flight test program ended the strakes and gear pod improvement were tested in flight and improved the cruise drag by 5%.

The control system as mentioned before had to be very responsive and have a large authority to possess satisfactory handling qualities at STOL speeds. The YC-14 operated over a dynamic pressure range of almost twice that of a conventional jet transport (Figure 21). This leads to a situation where the control system tuned for STOL flight speeds was too powerful for cruise flight. The elevator for cruise flight was only 1/3 of the available span. The high speed rudder is only two-thirds of the available span and pressure limited to reduce the throw.

CONCLUSIONS

The YC-14 performed well, meeting or exceeding all the design goals. The pilots who flew it where all impressed by its flying qualities. The airplane in general was an operational success, but the YC-15 won the prize.

BOEING YC-14 DESIGN REQUIREMENT AT LOW COST

- 27,000 LB (12,247 KG) PAYLOAD
- 400 NAUTICAL MILE (741 KM) RADIUS
- 2,000 FT (609.6M) FIELD LENGTH CAPABILITY
- 11.7 FT (3.57M) WIDE X 11.3 FT (3.44 M) HIGH X 47 FT (14.33M) LONG BOX (REQUIRED)
- 53,000 LB (24,000 KG) OVERLOAD PAYLOAD (2.25G)
- 2600 NAUTICAL MILE FERRY RANGE
- TURBO-JET TRANSPORT CRUISE SPEEDS

FIGURE 1

USAF/Boeing Advanced Medium STOL Transport Prototype – YC-14

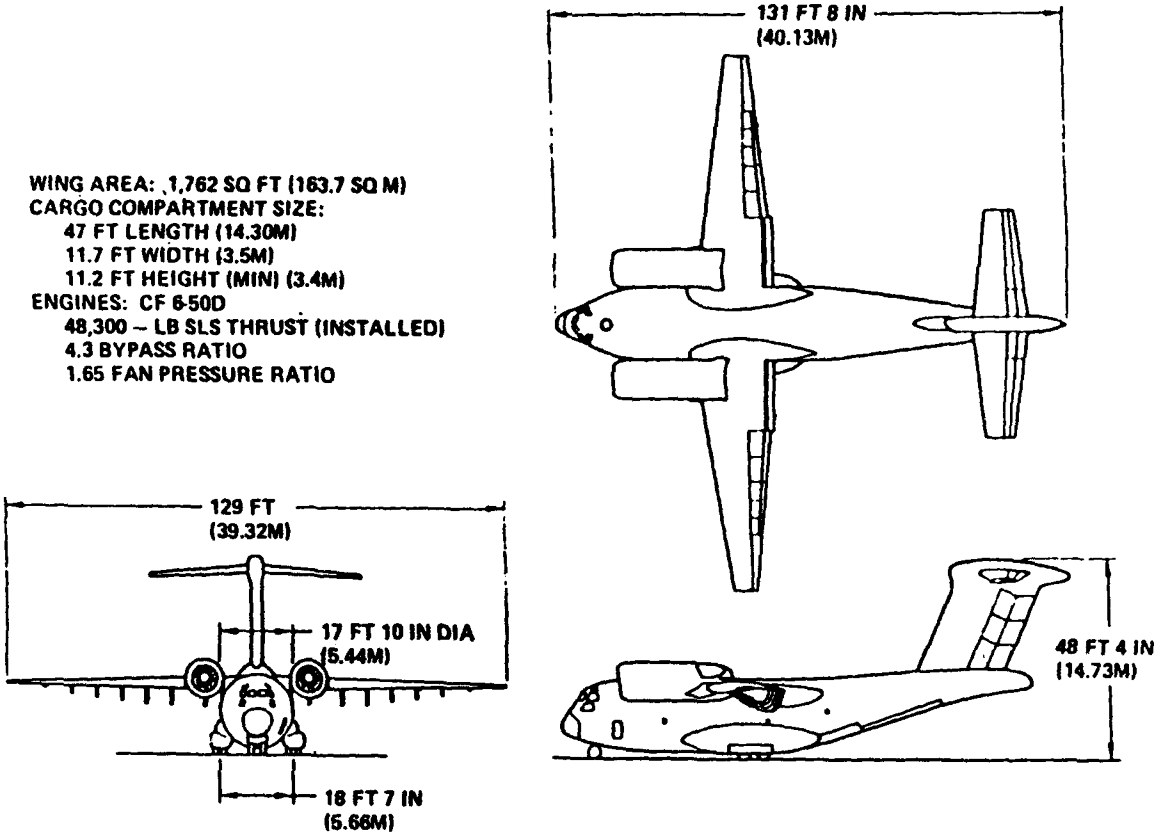

WING AREA: 1,762 SQ FT (163.7 SQ M)
CARGO COMPARTMENT SIZE:
47 FT LENGTH (14.30M)
11.7 FT WIDTH (3.5M)
11.2 FT HEIGHT (MIN) (3.4M)
ENGINES: CF 6-50D
48,300 – LB SLS THRUST (INSTALLED)
4.3 BYPASS RATIO
1.65 FAN PRESSURE RATIO

FIGURE 2

Landing Lift Efficiency

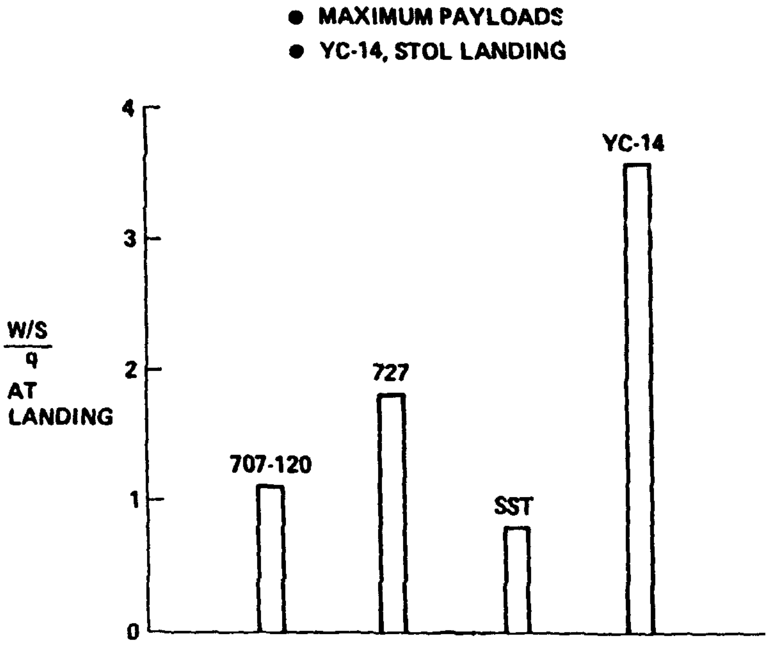

FIGURE 3

YC-14 HIGH LIFT SYSTEM
(OUTBOARD OF NACELLE/USB FLAP)

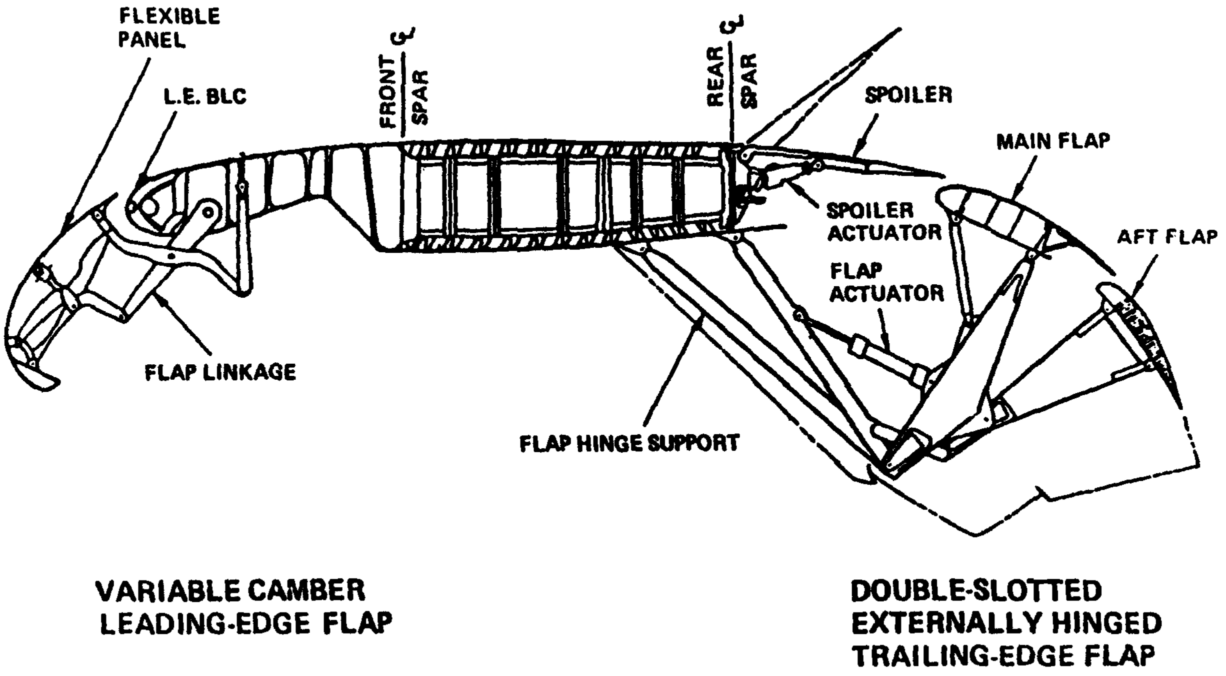

FIGURE 4

YC-14 BLC System

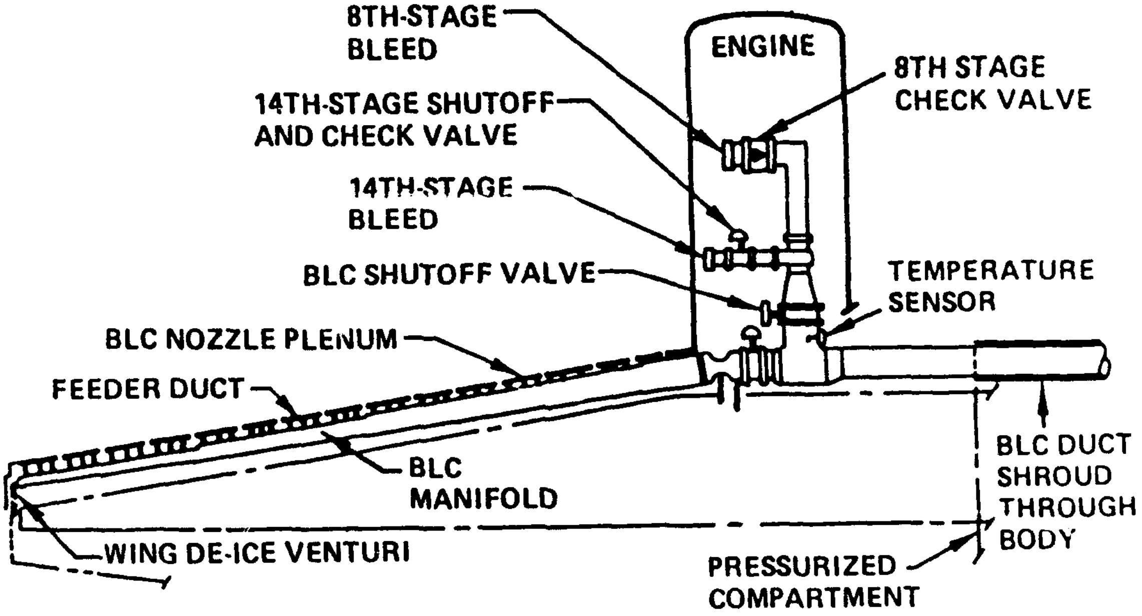

FIGURE 5

YC-14 L.E. BLC Nozzle Plenum

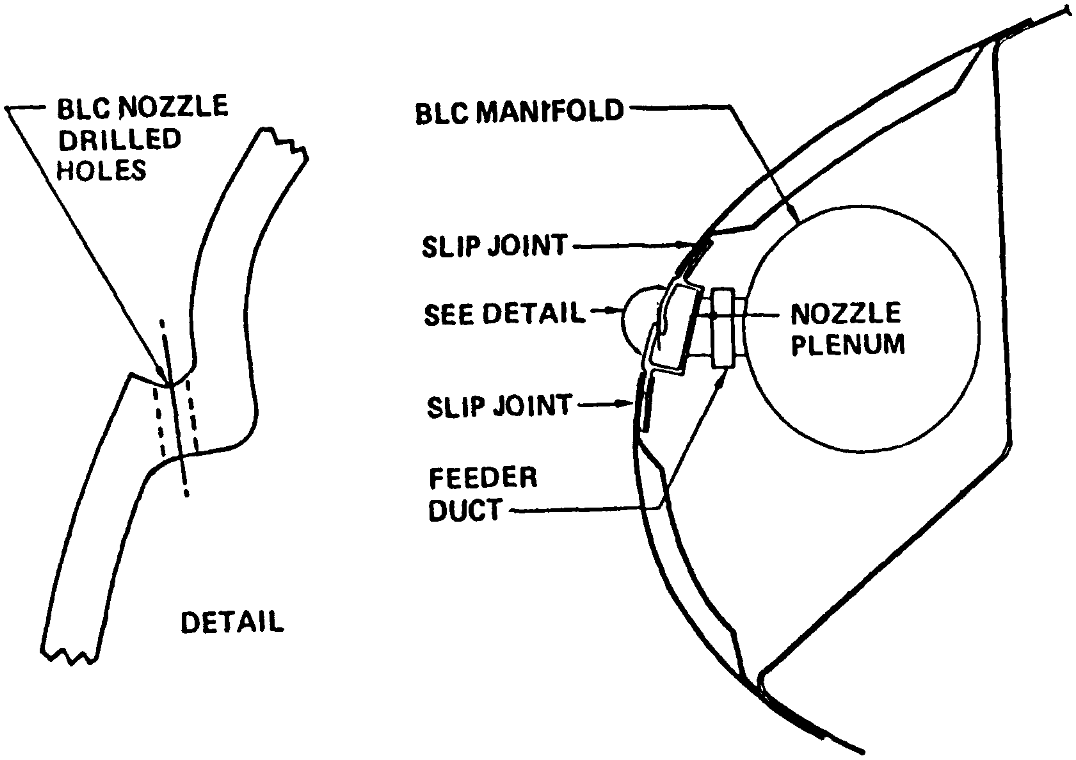

FIGURE 6

ISSUES RESOLVED IN WIND TUNNEL

- INCREMENTAL LIFT DUE TO JET EXHAUST
- INFLUENCE OF GROUND PROXIMITY ON ALL FORCE AND MOMENT COMPONENTS
- SOLUTION TO A SIDE FORCE PROBLEM ASSOCIATED WITH AN ENGINE OUT
- AIRCRAFT CONFIGURATION FOR OPTIMUM CLIMB GRADIENT WITH A CRITICAL ENGINE INOPERATIVE
- APPROACH SPEED AND APPROACH CONFIGURATION FOR LANDING WITH A CRITICAL ENGINE INOPERATIVE
- REDESIGN OF GEAR POD IN THE PRESENCE AN UPSWEPT AFT BODY
- REDESIGN OF NOZZLE DOOR ACTUATOR FAIRING
- DESIGN OF AFT BODY STRAKES

FIGURE 7

YC-14
SINGLE ENGINE OUT MAXIMUM LIFT FLIGHT TEST DATA

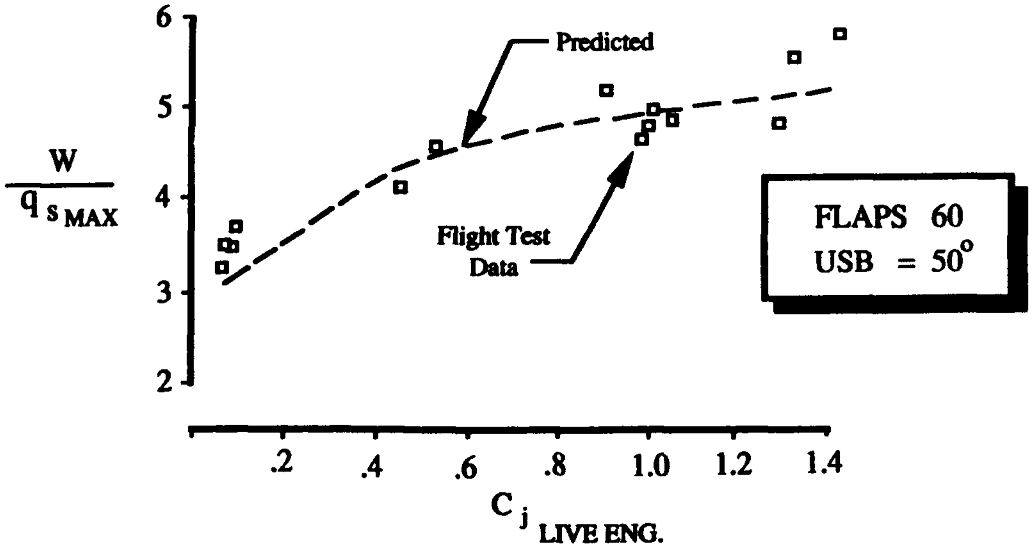

FIGURE 8

YC-14
SINGLE ENGINE OUT MINIMUM SPEEDS
FLIGHT TEST DATA

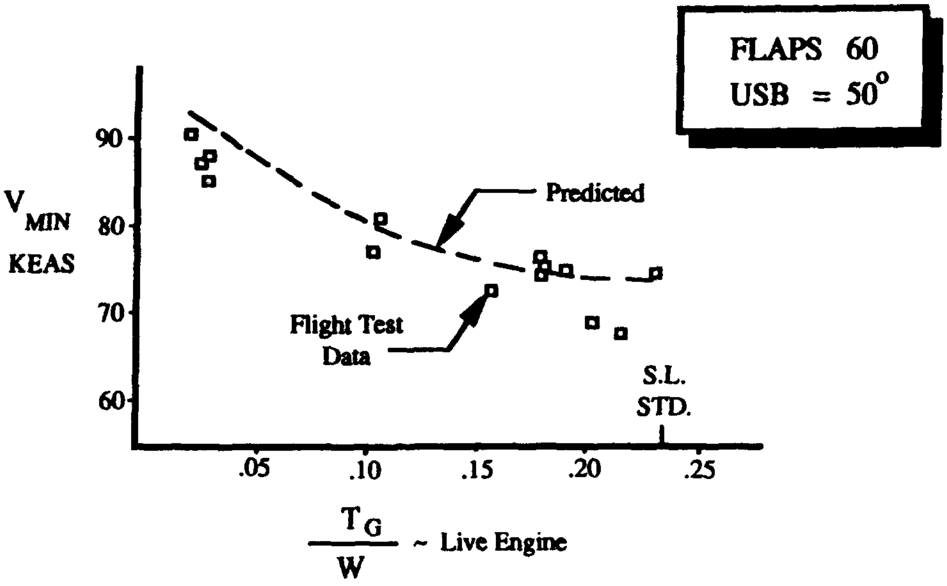

FIGURE 9

Engine-Out Rolling Moment

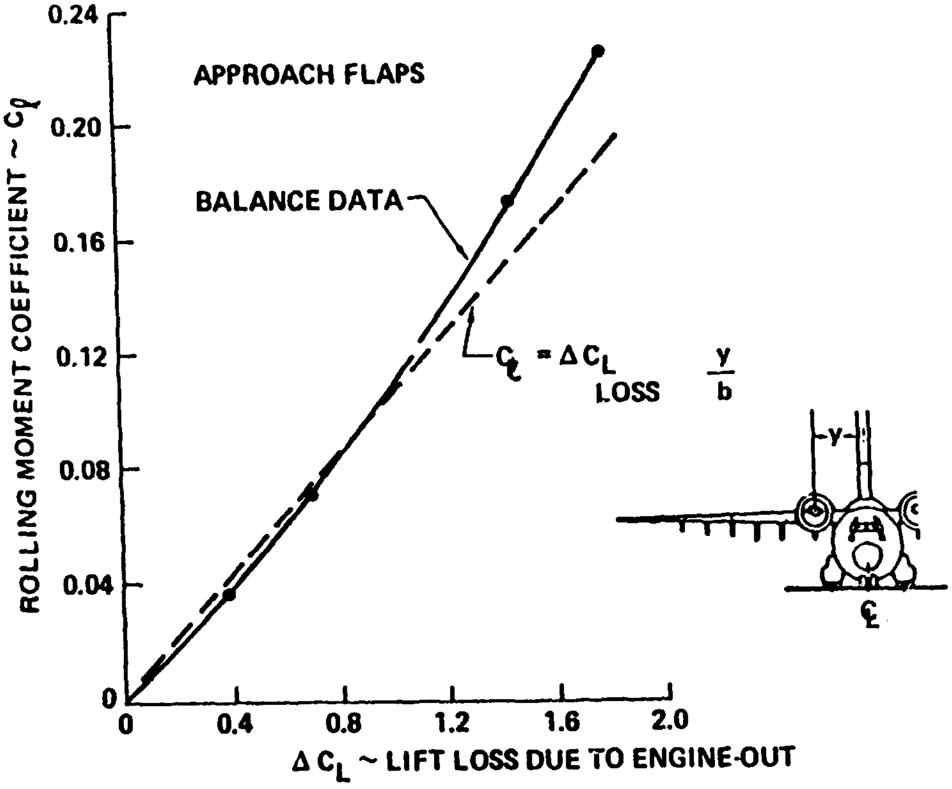

FIGURE 10

Engine Out Control

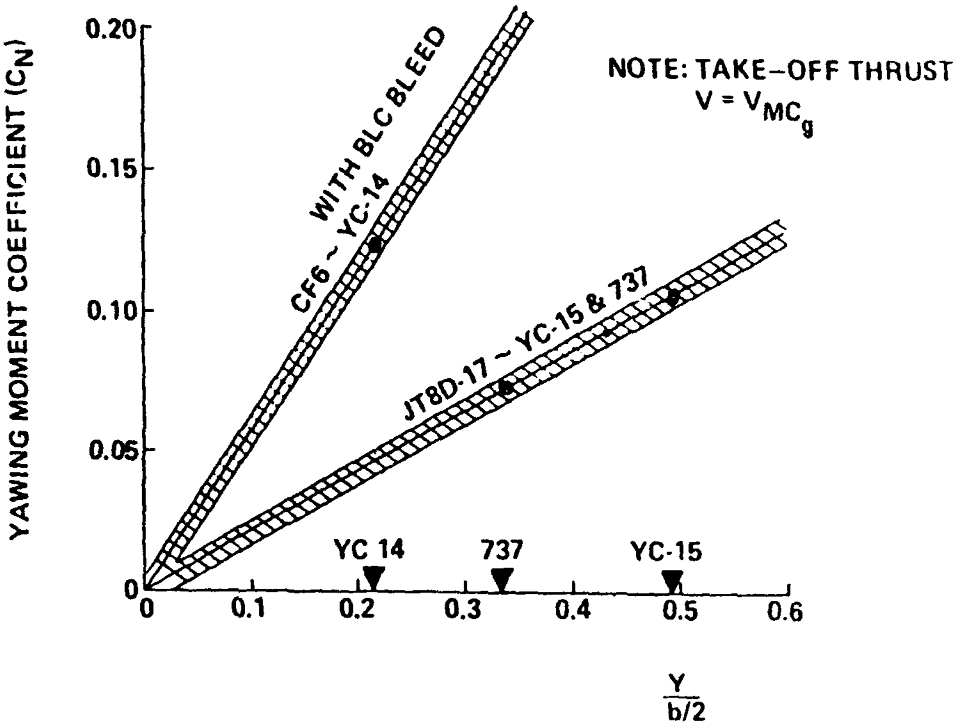

FIGURE 11

YC-14
VERTICAL STABILIZER FEATURES

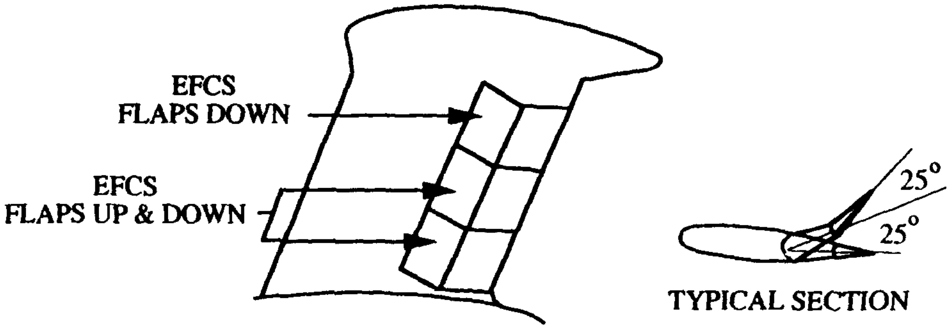

	Λ_{H}	% RUDDER CHORD	$\overline{V}$	ΔC_L @β=0 RUDDER	Rudder Throw (⊥ TO H)
YC-14	25°	43/21.5	0.13	1.0	25°/50°
737-100	22°	25	0.09	0.67	24°

FIGURE 12

YC-14
HORIZONTAL STABILIZER FEATURES

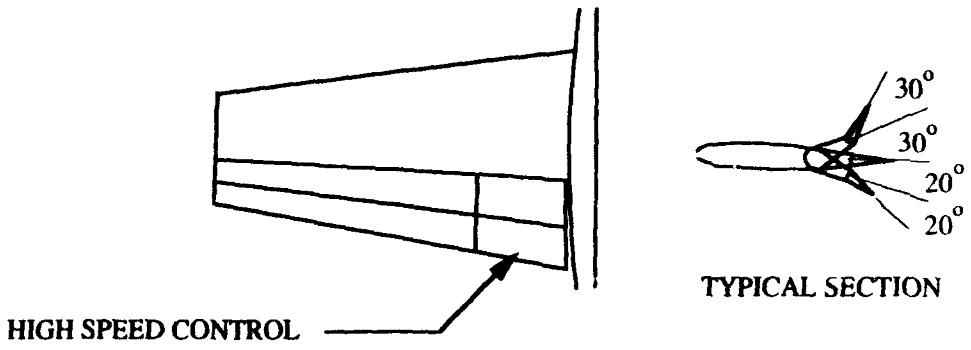

	$\Lambda_{\frac{c}{4}}$	AR	% ELEVATOR CHORD	$\overline{V}_H$	C_L MAX	ELEVATOR THROW	
						TRAILING EDGE DOWN	TRAILING EDGE UP
YC-14	3.5°	5.00	38/19	1.6	1.60	20°/40°	30°/60°
727-100	35.0°	3.25	25	0.9	1.15	17°	26°

FIGURE 13

LANDING COMPARISONS

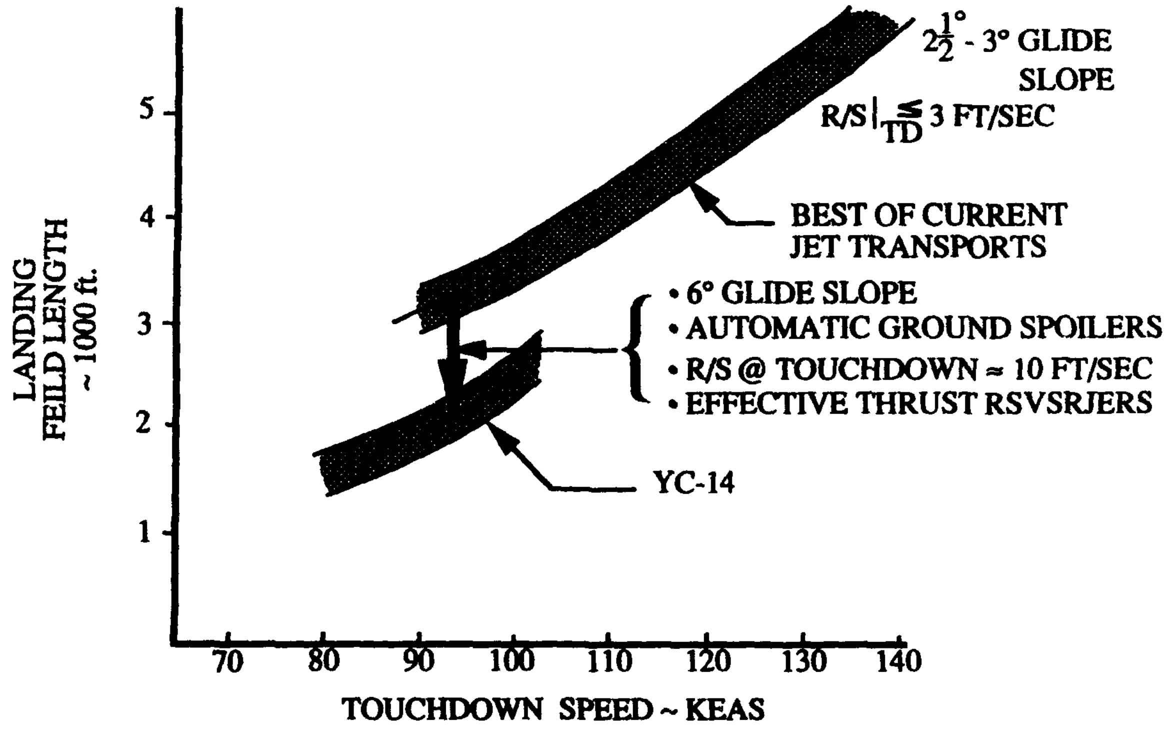

FIGURE 14

Long Stroke Landing Gear

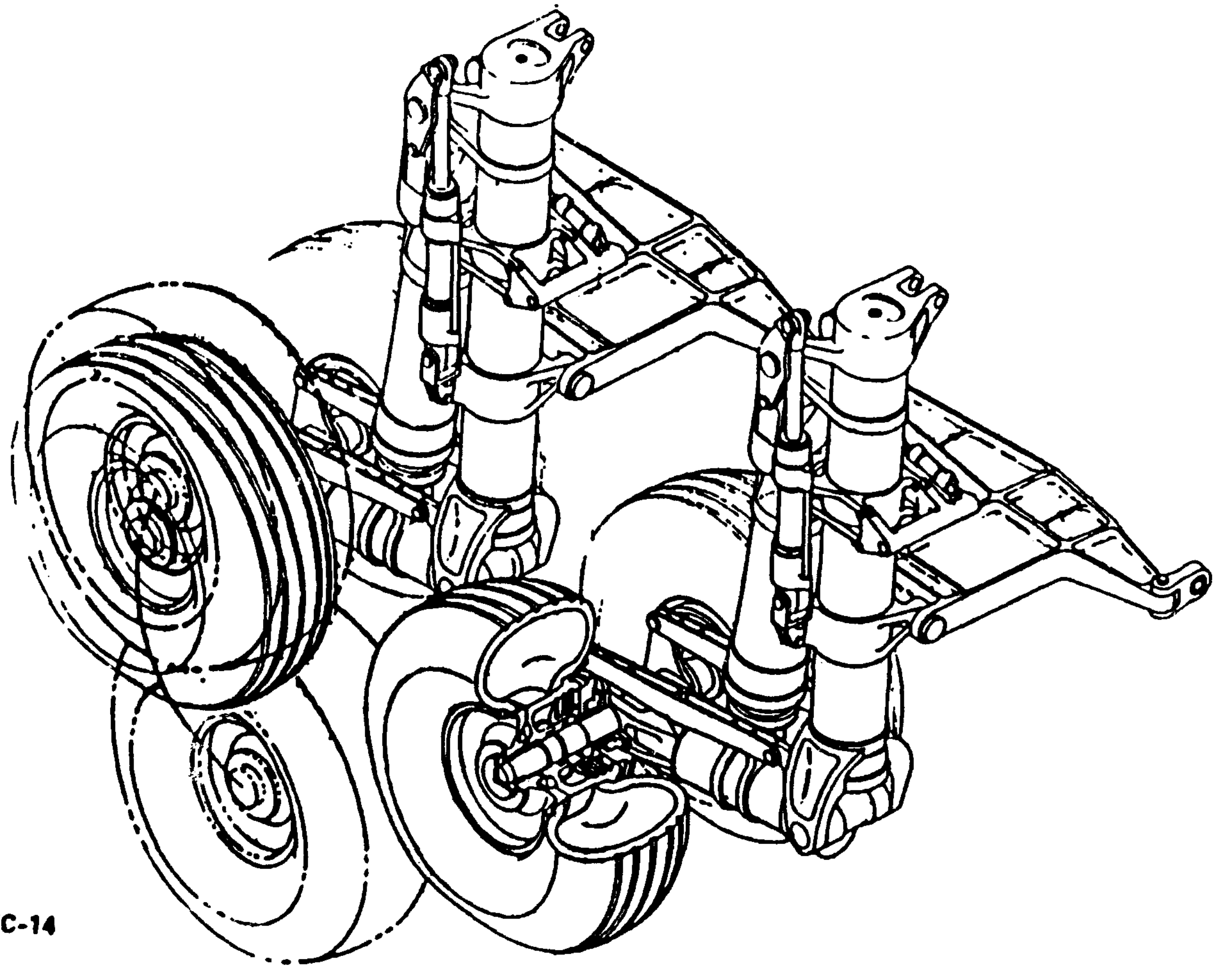

FIGURE 15

YC-14
GLIDE PATH CONTROL

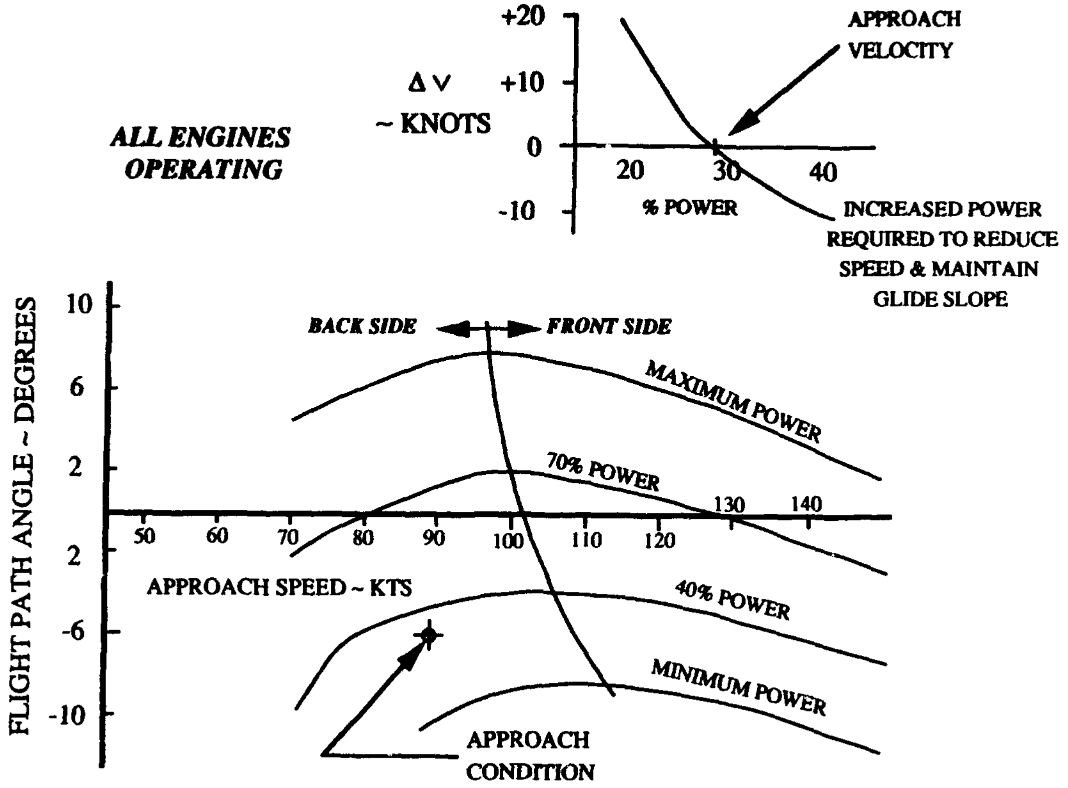

FIGURE 16

ADVANCED ELECTRICAL FLIGHT CONTROL SYSTEM

- SPEED HOLD MODE FOR APPROACH AND LANDING
- LOAD LIMITER FOR USB FLAP
- PROGRAM THE CONTROL SYSTEM WITH SPEED
- FULL-TIME ENGINE FAILURE DETECTION SYSTEM
- AFTER AN ENGINE FAILURE
    - ADVANCES THROTTLE ON LIVE ENGINE
    - MATCHES USB FLAP TO OUTBOARD FLAP ON DEAD ENGINE SIDE
    - RE-TRIMS LIFT SYSTEM ON LIVE ENGINE SIDE
    - RE-TRIMS PITCH PLANE

FIGURE 17

DESIGN FEATURES OF A SUCCESSFUL STOL CONFIGURATION

- SIMPLE TO FLY ~ NO SPECIAL PILOT TRAINING
- EFFECTIVE HIGH LIFT SYSTEM ~ VAPP 90 KNOTS
- WELL DESIGNED GEAR ~ ALLOW HIGH R/S AT TOUCHDOWN
- EFFECTIVE THRUST REVERSER
- EFFECTIVE GROUND SPOILERS
- ELECTRICAL FLIGHT CONTROL SYSTEM

FIGURE 18

YC-14
STOL LANDING DISPERSION

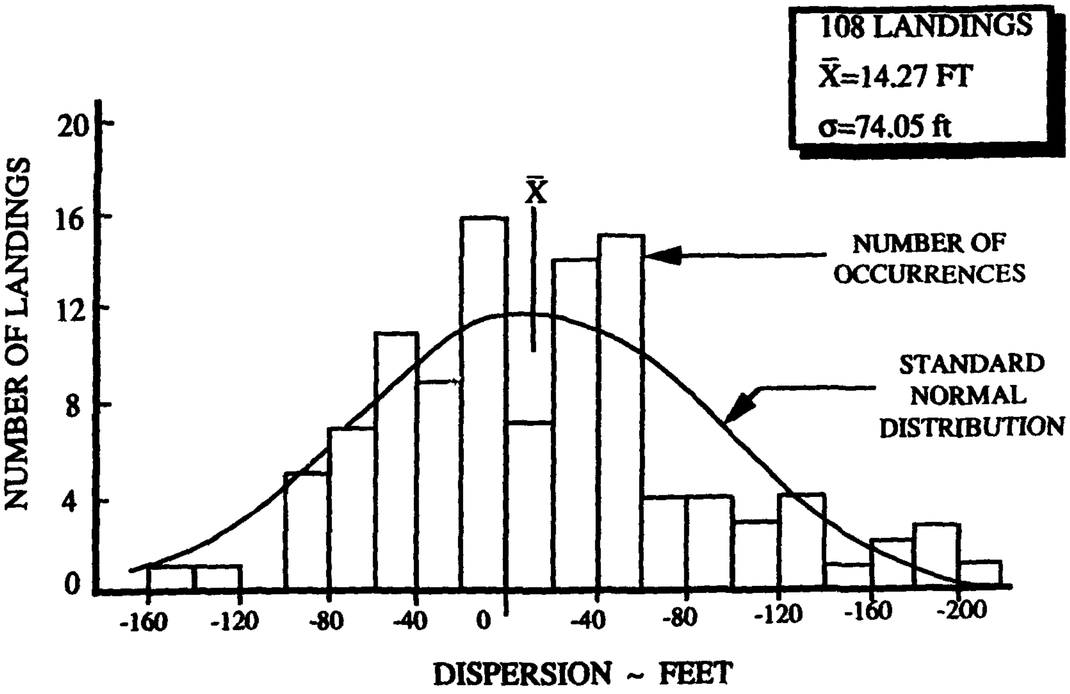

FIGURE 19

DEFINITION OF MAJOR NOZZLE PARAMETERS

β = KICKDOWN ANGLE (NAC ℄)
γ = BOATTAIL ANGLE (NAC ℄)
φ = CUTBACK ANGLE (INBD & OUTBD)
θ = FLARE ANGLE (INBD & OUTBD)
W = WIDTH
H = HEIGHT
$AR_e = \frac{\text{EFFECTIVE FLOW AREA}}{H^2}$

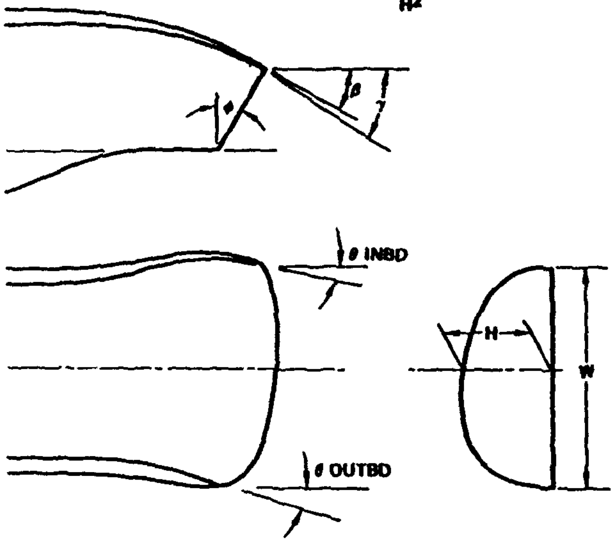

FIGURE 20

Operating Dynamic Pressure Ratios

- MAXIMUM PAYLOADS
- YC-14, STOL LANDING
- q = DYNAMIC PRESSURE

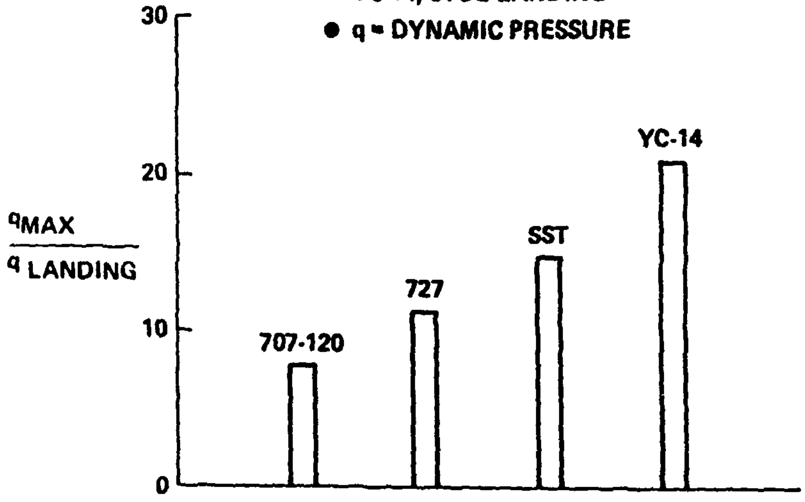

FIGURE 21

HIGH-LIFT DESIGN FOR LARGE CIVIL AIRCRAFT

A. Flaig, R. Hilbig
AERODYNAMICS DEPARTMENT
DEUTSCHE AIRBUS GMBH
HÜNEFELDSTR. 1-5, 2800 BREMEN, GERMANY

SUMMARY

A general reflection of the high-lift system design process is given in the first part of the presentation. First the objectives and constraints are reflected which drive the high-lift design for civil transport aircraft. Further information is given on the applied theoretical methods and the Deutsche Airbus wind-tunnel strategy.

An example of the high-lift system design process is given in the second part of the presentation. This deals with the conversion of a single-slotted Fowler flap to a part span double-slotted flap, a high-lift system which was developed by Deutsche Airbus for the A321.

LIST OF SYMBOLS

C_L	lift coefficient
CL_{max}	maximum lift coefficient
C_D	drag coefficient
L/D	lift to drag ratio
α	angle of attack
α_{limit}	maximum ground rotation angle
V_{LOF}	lift-off speed
V_{Smin}	minimum dynamic stall speed
V_{S1g}	steady flight (1g) stall speed
ASA	all speed aileron
TPS	turbine power simulator
FAR	Federal Aviation Requirements

1. INTRODUCTION

Within the European AIRBUS consortium, Deutsche Airbus (DA) is jointly responsible for the low speed aerodynamics of the AIRBUS types and variants, Fig. 1.

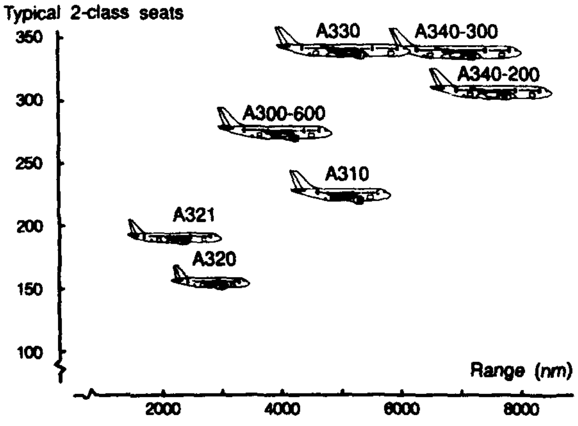

Figure 1. Airbus Product Line

The DA aerodynamics worksharing part covers the whole spectrum of high-lift system development, beginning with aero performance predictions for new projects, design and optimization of high-lift devices and preparation and analysis of wind-tunnel tests.

The primary consideration in the design of high-lift systems is the achievement of the required airfield performance, which generally implies high maximum lift capabilities for landing and even high lift to drag ratios for take-off combined with the constraint of minimum deterioration of the cruise performance.

In general the required airfield performance for civil and military transport aircraft is different due to their specific operating conditions, Fig. 2. In comparison to civil operation, military tactical operation has to consider take-off and landing on short and unpaved runways even in hostile surroundings. This requires lower approach speeds, higher decent rates and better climb-out capabilities. Therefore, military transports require significantly higher maximum lift capabilities (which may be achievable only with powered high-lift systems) and also higher thrust to weight ratios than typical for civil transport aircraft.

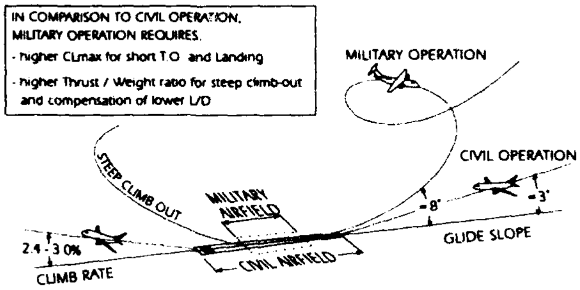

Figure 2. Airfield Performance

However, the high-lift design for civil transport aircraft is no less complicated, because safety and economic considerations play an more important role and encourage the designer to achieve the required maximum lift and climb-out capability with a high-lift system of minimum complexity ('design to cost') and maximum reliability.

A general reflection on the high-lift system design process for civil transport aircraft will be given within this paper. First, the major design objectives and constraints will be reviewed. Next, the DA wind-tunnel and model strategy will be explained. Some comments will also be given on the applied theoretical methods.

In the second part of the paper an example for the high-lift design is given. This deals with the conversion of the A320 single-slotted fowler flap system to a double-slotted flap system, which was necessary to satisfy the increased requirements for airfield performance of the A321, the stretched version of the A320.

2. GENERAL DESIGN ASPECTS

The mission of a civil aircraft is to transport a given payload over a specific range with maximum efficiency. The efficiency can be quantified as direct operating costs (DOC), which incorporate costs for fuel, airframe, crew, maintenance, taxes, etc. Minimizing the DOC is the main aim in civil transport aircraft layout. Due to the complex relations between the aircraft configuration and the DOC parameters, trade-off studies have to be done to determine the optimum combination of wing planform, weight and thrust for a specific aircraft project.

The choice of specific cruise capabilities, such as speed, range, initial altitude, climb capabilities and buffet boundaries defines the targets for the aerodynamic design. With consideration of the advanced available technology in aerodynamics and structures, the primary wing design parameters, such as loading, span, sweep, aspect ratio, twist and thickness have to be optimized.

Some of these primary wing design parameters strongly influence the efficiency of the high-lift system and have to be taken into consideration in the trade-off optimization process.

A high wing loading, for example, increases the necessary maximum lift capability to satisfy the required airfield performance. This will increase the high-lift system complexity and hence the weight and costs. Increasing the wing aspect ratio is beneficial for the high-lift efficiency, while increasing the wing-sweep is disadvantageous.

Another important parameter in aircraft sizing is the thrust to weight ratio. For civil transport aircraft the required thrust is usually determined by take-off field length considerations.

Due to the interrelations between wing planform and high-lift system efficiency, the final design is generally a compromise between optimum cruise efficiency and acceptable airfield performance. This optimum is usually found in an iterative design process.

3. OBJECTIVES AND CONSTRAINTS OF HIGH-LIFT DESIGN

The general objective in high-lift system design is to match the airfield performance requirements in terms of approach speed, take-off field length and climb rate.

Furthermore the design has to guarantee maximum flight safety which means good handling qualities, moderate approach speeds and 'normal', controllable stall characteristics.

Having selected the primary aircraft design parameters, e.g. wing loading, the required aerodynamic performances of the high-lift system can be derived from airfield performance investigations for the most critical conditions. The investigations include take-off field length and landing distance calculation, in accordance to the operating rules specified in FAR 25 for civil transport aircraft.

3.1 Airfield Performance Requirements

When discussing the airfield performance requirements, a separate view of the take-off and landing situation is appropriate, because the requirements on the aerodynamic qualities of the high-lift system are different.

3.1.1 *Take-Off*

In general the take-off performance is characterized by the field length, which is a function of the wing loading, the thrust loading and the aerodynamic efficiency of the high-lift system. The interrelations between these parameters can be highlighted when reflecting the general take-off procedure with consideration of the specific FAR requirements for civil transport aircraft.

As illustrated in Fig. 3, the take-off field length is defined as the total of ground roll distance which is required to accelerate from the resting position to the lift-off speed V_{LOF}, plus an airborne distance to overfly an obstacle height of 35ft.

According to the FAR, V_{LOF} has to be 1.1 times the minimum 'unstick' speed V_{MU}, which is defined as the minimum speed at which the aircraft can safely take-off with one engine inoperative. V_{MU} is not only a function of the aircraft maximum lift capability, because tail interferences with the ground can limit the usable angle of rotation which reduces the usable lift coefficient. Therefore, if V_{MU} is increased, the required ground

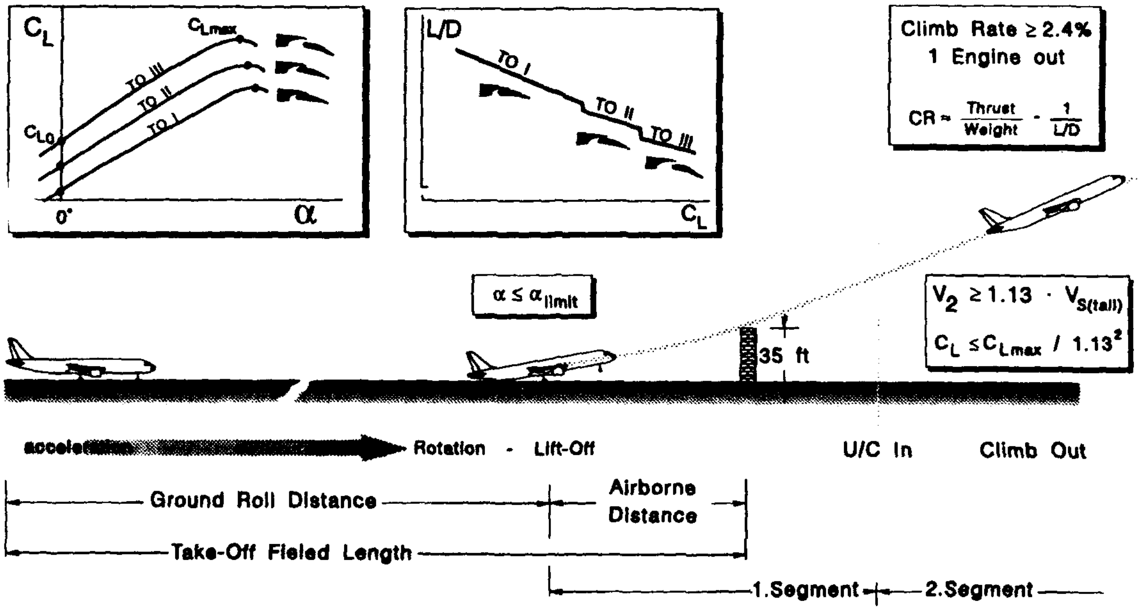

Figure 3. Take-Off Procedure

roll distance inevitably will be increased, too. Especially for aircraft versions with stretched rear fuselage this V_{MU} limitation can be of particular significance for the high-lift design. In that case the maximum usable angle of attack (not the maximum achievable lift coefficient) will be the dominant parameter which limits the usable lift of the take-off configuration.

After lift-off, the next speed of interest is the take-off climb speed V_2, which must be achieved when the aircraft reaches 35ft height above the ground. V_2 must be greater than 1.2 times the minimum dynamic stall speed V_{Smin}, and greater than 1.1 times the minimum control speed V_{MC}. V_{Smin} is usually 0.94 times the stall speed in a 1g steady flight, a flight condition which is comparable to wind tunnel conditions and therefore related to CL_{max}. Hence, V_2 must be greater than 1.13 times V_{S1g}, or in terms of lift coefficients: CL_{V2} must be below $CL_{max}/1.13^2$.

After take-off, the second segment climb begins when the undercarriage is retracted. According to the FAR, the minimum second segment climb-rate with one engine inoperative must be greater than 2.4% for aircraft with two engines (3.0% for aircraft with four engines) and the minimum speed must be V_2.

Approximately the climb rate is a function of the thrust to weight and the lift to drag (L/D) ratios as defined by the following equation:

$$CR = \left(\frac{\text{Thrust}}{\text{Weight}} - \frac{1}{L/D} \right)$$

This means, for a given thrust to weight ratio, the climb rate is directly related to the L/D.

A typical envelope of L/D versus CL is shown in the small diagram within Fig. 3. The steps in the envelope separate the different take-off configurations. The right end of each envelope segment indicates the maximum usable lift coefficient for second segment climb of the specific configuration (usually $CL_{max}/1.13^2$).

It is obvious, that a higher lift coefficient, as achievable with a higher flap setting for example, decreases the L/D and consequently climb rate, while the ground-roll distance is reduced.

Therefore the aerodynamic optimization of the take-off configuration is aimed at finding the best compromise between lift capability and L/D efficiency to satisfy the requirements for both the take-off field length and the climb rate.

3.1.2 *Landing*

The final approach of civil transport aircraft is performed on a glide slope of 3 deg. The typical approach speeds of major jet powered aircraft lie between 130kts and 150kts. Due to the evident correlation between approach speed and accident rate, the landing performance design is mainly concerned with achieving moderate approach speeds within the aforementioned range. In order to provide some future stretching potential, the design approach speed for a new project is normally more orientated towards the lower value.

The FAR requires that the approach speed has to be 1.3 times higher than the minimum dynamic stall speed Vsmin, which has been previously defined as 0.94 V_{S1g}. This 1g stall speed and the design wing loading for landing determine the maximum lift coefficient which has to be achieved by the high-lift system. Another aspect of flight safety during approach is the pilot's ground visibility, which is dependent on the pitch attitude of the fuselage and consequently angle of attack. Especially when designing a high-lift system with slat or Krueger flap, care must be taken that their effect of increasing the usable angle of attack is not compromising the ground visibility. In this case efficiency of the trailing edge flap must be improved to achieve the required approach lift coefficient at reduced angle of attack.

Furthermore, the adverse effects of landing configuration L/D on the go-around climb capability and the approach engine rating has to be considered. A lower approach L/D, for example, has to be compensated by higher engine thrust rating, which typically causes better engine response characteristics for flight path corrections or transition from approach to go-around condition. This item can be a partial problem for aircraft with single-slotted flap high-lift devices, because their typical approach L/D may be 'too good'. On the other hand, a lower L/D degrades the go-around climb rate, which must be greater than 3.2% with all engines operative. Therefore the limitation of the landing weight is the usual way to provide the required climb capability.

In principle, the required maximum lift capability for the landing configuration determines the complexity of the high-lift system, in particular the number of slots (or elements) of the trailing edge devices. The degrading effect of wing sweep on the maximum lift efficiency necessitates an increase in the complexity of the high-lift system.

The general trend of maximum lift efficiency versus system complexity is illustrated in Fig. 4.

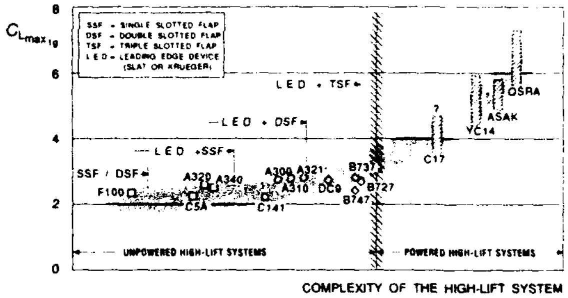

Figure 4. Lift efficiency versus high-lift system complexity

Firstly an example is given of some transport aircraft demonstrating the limits of conventional unpowered high-lift devices, and secondly of some experimental aircraft demonstrating the efficiency of powered high-lift devices. It is obvious, that the maximum lift limit for unpowered high-lift systems (on a aircraft with typical 25deg wing sweep) is in the order of 3, while powered high-lift systems with additional active boundary layer control may achieve maximum lift coefficients up to 7.

3.2 High-Lift Design Constraints

The cruise wing design determines a lot of important design parameters for the high-lift devices, such as chord and thickness distribution, aspect ratio, trailing-edge kink location, etc. Only the type of the high-lift devices, the shape, the spanwise extension and the settings can be chosen by the high-lift designer, but with consideration of some constraints, which will be discussed next.

3.2.1 *General Constraints*

Usually the chordwise extension of the high-lift devices is limited by the location of the front-spar and rear-spar respectively, which can not be changed due to considerations of wing stiffness (twist, bending) and internal fuel volume, Fig. 5.

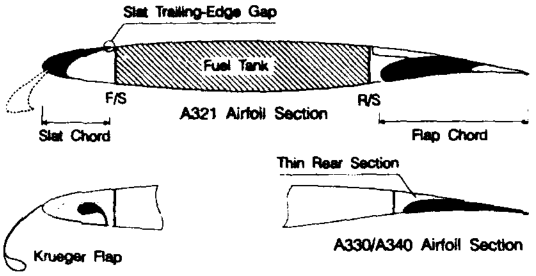

Figure 5. General Constraints on High-Lift Design

Especially the required fuel capacity for a long-range aircraft can be of particular significance in the wing sizing. Moreover, the inner wing flap chord of a typical low set wing aircraft is limited by the required storage space for the retracted main undercarriage.

After the chordwise extension of the leading edge and trailing edge devices has been fixed, the next design item is the optimization of their shapes.

The typical leading edge devices of today's transport aircraft are slats and Krueger flaps. In the case of a slat, the profile of upper and lower surface is defined by the cruise wing nose shape. Therefore only the shape of the slat inner side and the nose of the fixed-wing can be optimized.

A Krueger flap with a folded nose or flexible shape, as an example, generally offers greater design freedom to achieve an ideal upper surface shape, and thus gains a little in L/D and CL_{max}. But, trade-off studies carried out in the past for A320 and A340 have shown, that this advantage for the Krueger flap is compromised by a more complex and heavier support structure than required for a slat.

For future projects the trend of preferring slats instead of Krueger flaps may change, because the envisaged wings with laminar flow technology can not be realized with any small step and gap on the upper surface, as are usually present behind the trailing edge of a retracted slat. For this reason, Krueger flaps will offer some advantages, because they are typically retracted in a storage bay on the lower side, which is a less sensitive region of the wing.

The crucial point in the chordwise layout of the trailing-edge devices is their relative thickness, which is dictated by the rear shape of the cruise wing.

The typical state-of-the-art cruise wing airfoils, such as represented on the Airbus A340/A330, are characterized by a relative thin rear-end shape. The resulting small flap thickness causes some problems for the flap design. It is obvious, that the smaller stiffness of a relatively thin flap has to be compensated by heavier structure and possibly more spanwise support stations, which both increase weight and costs.

Moreover the realization of a multi-element flap can fail if the thickness of the single elements is insufficient for production. Also influenced by the relative flap thickness is the aerodynamic efficiency. Usually the flap efficiency is limited by the onset of flow separation on the upper surface. Therefore the main objective in flap shape design is to increase the angle of flap deflection at which flow separation occurs. This is usually done by controlling the pressure peak at the nose and the following pressure gradients by the adequate shape design. It is apparent that a thin flap offers less possibilities to modify the shape and thereby the pressure distribution in the intended manner. Unfortunately this can cause some loss in efficiency.

3.2.2 *Constraints in Kinematic Design*

We at Airbus prefer slats as leading-edge devices instead of Krueger flaps due to their modest support complexity. In a typical design, e.g. as represented on A320 and A340, the slats are supported by circular tracks, which are directly actuated by rotary drives, Fig. 6.

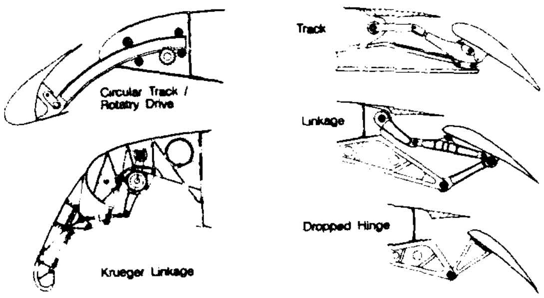

Figure 6. Support of High-Lift Devices

Usually the radius of each slat track is different in spanwise direction due to wing taper. However, with small spanwise changes of the slat setting and some variation of the track's vertical attachment to the front-spar, the radius of several tracks can be made identical, which simplifies manufacturing and saves cost.

It is apparent that both the aerodynamic efficiency of the trailing-edge devices as well as the complexity of the support system depend on the number of flap elements employed and on the type of the flap support itself.

The structure of a track type flap support system, as an example, is generally more complex than that of a dropped-hinge or a linkage support system.

But typically, the track type kinematics offer more design freedom to realize the optimum relation between flap Fowler movement and flap deflection for both take-off and landing configurations. This is the reason why track type flap support systems are inevitable for the utilization of trailing edge flaps for 'variable camber technology', which may be envisaged for cruise performance optimization of future projects such as FLA or Airbus Ultra-High-Capacity-Aircraft.

However, a good compromise between aerodynamic efficiency and total system complexity can be achieved - in our view- by a flap system with minimum elements combined with a support system of higher complexity. This was demonstrated by the advanced high-lift systems of the A320 and A340, where typical airfield performance requirements on today's short and even long-range aircraft are satisfied by a track supported single-slotted fowler flap system.

4. HIGH-LIFT SYSTEM DESIGN

The task of the high-lift system designer is to achieve the aerodynamic targets by choosing the type of the high-lift device, defining its shape and spanwise extension, and optimizing its settings.

In general, the lift characteristics of a two-dimensional wing section depend on its effective camber and on the boundary layer control. The camber is increased by deflection of a trailing edge flap, and the attachment of the boundary layer on the flap is controlled by the setting and shape of the flap.

In addition the onset of boundary layer separation on the main profile is delayed with a leading-edge flap, such as Krueger or slat, which increases the usable angle of attack and subsequently the maximum lift capability.

When applying the two-dimensional design to a definite wing, the lift efficiency is principally decreased by three-dimensional flow effects due to finite span, sweep, nacelle interaction, spanwise limitation and cut-outs of the high-lift devices.

The optimization of the three-dimensional high-lift design is mainly aimed at minimizing these effects.

4.1 Theoretical Methods

Although the application of advanced theoretical methods tends to play an even more important role in the aerodynamic design of aircraft, their use in the high-lift field is virtually limited to two-dimensional problems. Because of the complex flow around a three-dimensional wing in high-lift configurations, the necessity of wind-tunnel testing for configuration optimization and especially for stall investigation is unquestioned.

4.1.1 *Two-dimensional Methods*

Usually the optimization of the two-dimensional design of the high-lift devices is iteratively done on the basis of calculated pressure distribution. Due to the significant effect of the boundary layer flow on the high-lift efficiency, the applied theoretical methods must incorporate viscous effects.

The method used by Deutsche Airbus (1) is based on a potential flow theory, which is combined with an inverse boundary layer and wake flow iteration. This method incorporates solutions for the following typical flow problems of multi-element high-lift airfoils, Fig. 7:

- transition from laminar to turbulent boundary layer;
- determination of flow separation regions, which can be either short separation bubbles or large region separations from one or more elements;
- confluence of wake and boundary layer flow, even for multi-element configurations.

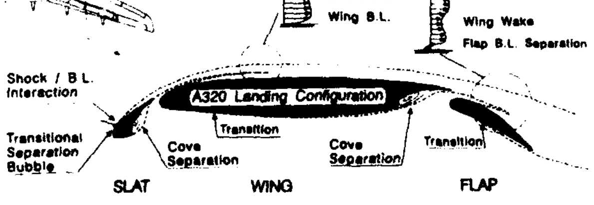

Figure 7. Flow on High-Lift Airfoil

Our experience has shown, that the evaluated trends, in terms of lift efficiency, profile drag and boundary layer stability, due to shape and setting are represented correctly. Problems occur only with the close coupled arrangement of two single elements, e.g. slat and fixed wing with small slat deflections, because the applied theory does not incorporate a satisfactory solution for the direct confluence of two boundary layers. In general this is not significant, because the shape optimization is usually done for the landing configuration with maximum deflection of all devices.

It has been found, that the optimizing of the two-dimensional shape at deliberately chosen spanwise sections of the finite wing is sufficient for the three-dimensional shape design of the high-lift devices, while the final optimization of the settings must take into account the three-dimensional flow.

4.1.2 *Three-dimensional Methods*

The available methods for the theoretical consideration of the three-dimensional flow is mainly based on panel methods, such as VSAERO, which is applied by Deutsche Airbus in the high-lift design procedure.

The general problem when applying panel methods is the expensive preparation of the panel grid, which is necessary to represent the complex geometry of a wing with extended high-lift devices. Therefore, the application is unpractical within the iterative design process, e.g. for setting optimization, but is useful to study effects on the spanwise lift distribution and the lift curve slope in the linear regime.

Although the panel method incorporates approximate solutions for the three-dimensional boundary layer consideration (which obviously improves the lift curve slope representation), they are insufficient for prediction of the stall characteristics or the total drag, because significant interactions between boundary layer and wake/vortex flow are not considered.

4.2 Wind-Tunnel Strategy

In spite of the fact that any wind-tunnel test results need some interpretation to be transferred to the real flight condition, which is undoubtely one of the most difficult items in high-lift design, the most reliable results can be generally obtained with large scale models in large and pressurized high Reynolds number tunnels. Due to the expense of such tests, the normal practice is to carry out most of the development tests in smaller tunnels at lower Reynolds numbers, and then use large tunnels for verification of the achieved optimization, or for the investigation of special items.

4.2.1 *Deutsche Airbus Low-Speed Wind Tunnel*

Deutsche Airbus is in a position to carry out most high-lift development work in its own low-speed wind tunnel at Bremen, the test section of which measures 2.1m to 2.1m, Fig. 8. This is a situation which offers Deutsche Airbus the advantage of more test flexibility in the development process.

We mostly use half-models with a span of approximately 1.3m. In general, this span is sufficient for a correct geometrical representation of the three-dimensional wing, including the high-lift devices. Typically, our half-models are equipped with through-flow nacelles, but turbine powered simulators (TPS), blown nacelles or propfan simulators can also be employed to simulate propulsion effects. The availability of state-of-the-art equipment for surface flow-visualization, wake-flow

Figure 8. Deutsche Airbus Low-Speed Tunnel

visualization, wake-frequency analysis and pressure distribution measurements offers excellent conditions for high-lift development work.

The disadvantage of the low Reynolds number, which is in the order of $1.3*10^6$, is generally compensated by verification of the evaluated modification trends at higher Reynolds numbers. This is usually done by testing some configurations with the same half-model in the ONERA F1 tunnel, which is a pressurized tunnel allowing Reynolds numbers of $6*10^6$. The practice of 'back-to-back' testing the same model in both tunnels for several different projects has led to comprehensive experience in the interpretation of half-model results obtained at low Reynolds numbers.

4.2.2 *German-Dutch Wind-Tunnel (DNW)*

Another wind-tunnel employed by DA in the high-lift design process is the DNW tunnel, which is a large atmospheric low-speed tunnel, situated in the Netherlands, with a test section of 8m by 6m, Fig. 9.

Figure 9. German-Dutch Wind-Tunnel

Usually the tests are performed at a Mach number of 0.2, achieving a Reynolds number of $2.6*10^6$. The span of typically employed complete models is in the order of 5m. This size guarantees a highly detailed representation of the aircraft geometry including undercarriage, moveable surfaces, tracks and fairings.

Generally the model is supported by a moveable sting, which is connected directly to the fuselage internal balance. The six component strain gauge balance has demonstrated high sensitivity and long time repeatability.

Therefore, with respect to the excellent flow quality in terms of low turbulence, this tunnel is primarily used for low-speed performance investigations, with special regard to second segment climb L/D. These tests include intensive jet interference investigations by means of turbine powered simulators (TPS).

Furthermore the DNW tunnel is especially suitable for ground effect investigations, even with jet simulation by TPS, due to its moveable model support and effective separation of the tunnel floor boundary layer, which additionally is combined with a moving belt ground plane.

The investigation of wing downwash, tail efficiency and lateral stability completes the standard test program which Deutsche Airbus carries out in the DNW.

4.2.3 *ONERA F1 Tunnel*

The effects of Mach and Reynolds number variation on L/D, maximum lift coefficient and stall characteristics are investigated on a second low-speed complete model in the French ONERA F1 tunnel, Fig. 10. This tunnel can be pressurized up to 4 bars. Thereby Reynolds numbers of $6*10^6$ are achievable at 0.2 Mach number with the typically employed models of 3m span.

Figure 10. ONERA F1 Tunnel

4.3 **High-Lift Design Process**

As outlined in Fig. 11, the high-lift system design process can be split in three successive phases: pre-development, development and pre-flight.

4.3.1 *Pre-Development Phase*

The aim of the pre-development phase is to demonstrate a high-lift concept which achieves the required airfield performance of a new project. This is usually done in an iterative design process.

Within the iteration cycle several alternative concepts are developed on the basis of the preliminary cruise wing design. First, the aerodynamic characteristics of the different concepts are theoretically estimated. The methods applied for this purpose were developed by DA and are based mainly on lifting-line and lifting-surface theory, which were modified to incorporate our comprehensive data base of empirical investigations.

The estimated aerodynamic qualities of the most promising high-lift concepts are then used to establish a preliminary aero-data-base for airfield performance calculations. At any stage of

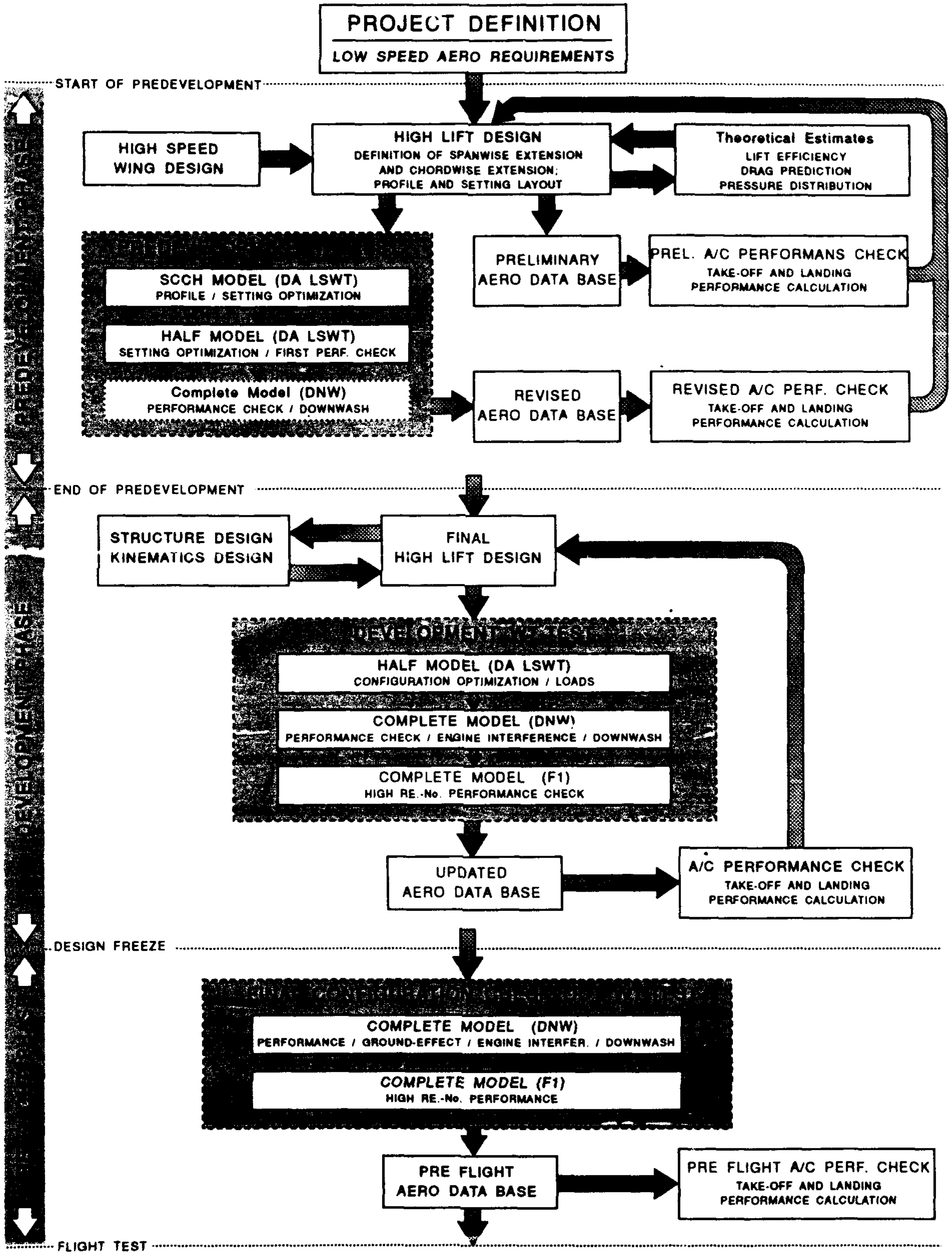

Figure 11. Scheme of High-Lift Design Process

the development phase the results of these calculations are directly compared to the required airfield performance to demonstrate the achieved design progress.

After the initial design cycle has led to a realizable high-lift concept, the next step is to design in greater detail. At this stage, more use will be made of wind-tunnel testing, usually starting with a Swept-Constant-Chord-Half-model (SCCH). This model is useful for pre-optimizing settings and preliminary check of the aerodynamic loading on the high-lift devices.

The next step is half-model testing with correct representation of the three-dimensional wing, the nacelle and the wing-fuselage juncture. The half-model is provided with variable brackets for setting optimization and is also employed for flow-visualization, preliminary performance testing, pressure distribution measurements and wake-flow analysis.

The optimized design is then tested on a large scale complete model in the DNW facility. Finally, the results of the complete model tests are used to demonstrate the achieved aerodynamic performance of the pre-developed high-lift concept.

4.3.2 *Development Phase*

Usually the final design is initiated by the official go-ahead for a new project.

The task of the high-lift designer is then to adapt the pre-developed high-lift concept to the geometry of the final cruise wing design, which has to be done in close cooperation with the structure and kinematic designer.

The further development of the high-lift system is mainly driven by improving the CL_{max} in the landing and the L/D in the take-off configurations. This is done by the iterative optimization of the settings and the geometric details, such as slat/pylon juncture, nacelle strakes etc. Within this work, the wind-tunnel testing is intensified and executed in the previously mentioned sequence of half-model and complete model testing.

The obtained aerodynamic performance in terms of lift slope, drag and CL_{max} are first scaled to flight conditions and then trimmed to agreed reference conditions. The applied method as developed by Deutsche Airbus (2) incorporates trends between wind-tunnel and flight test, which have been derived from previous projects.

4.3.3 *Pre-Flight Phase*

After design freeze the complete models are updated to the final aircraft configuration and then tested in the DNW tunnel and ONERA F1 tunnel, respectively. Both tests generally deal with final performance check-out. The DNW test is aimed more towards the take-off performance with engine interference and ground effect investigations, while the F1 test is primarily aimed at evaluating Reynolds number trends and maximum lift performance.

The combined results, obtained from two different models in two excellent wind-tunnels and then scaled to flight conditions with the experience of prior projects, represent a pre-flight data base of high confidence.

4.4 Items of Design Optimization

An essential part of the design optimization is aimed at minimizing the three-dimensional interference effects on high-lift performance, which are usually caused by the nacelle installation, wing-fuselage juncture, cutouts and spanwise limitations of the high-lift devices, Fig. 12.

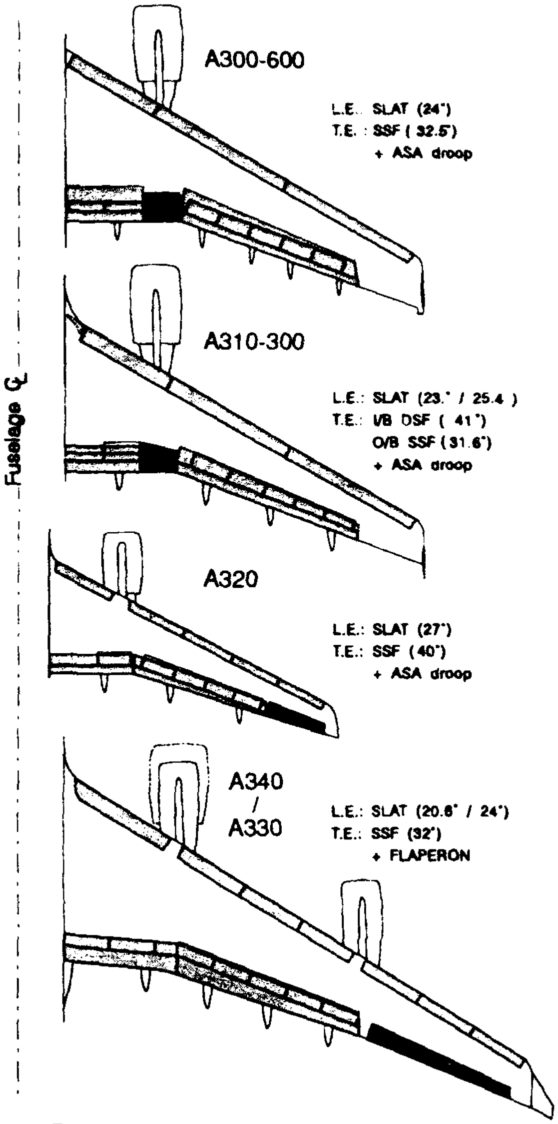

Figure 12. Arrangementd of High-Lift Devices

These interferences are dominated by the effects of wakes and vortices which influence wing stalling characteristics, induced drag, flap vibration and tail buffet. Typically such wakes and vortices are shed from the edges of the extended high-lift devices, their tracks and the nacelle-pylon-wing juncture.

Therefore, the efforts in three-dimensional design optimization firstly are concentrated on these details to minimize their detrimental effects on the aerodynamic characteristics. Secondly the beneficial effects of attached vortex flow are utilized on the wing boundary layer and thereby on the stall behavior, e.g. by application of nacelle strakes.

This consideration is of significant importance since the close coupling between high-bypass nacelles and the wing (e.g. A320 and A340) dominates the wing stall and CL_{max}. Typically, the close nacelle/wing arrangement requires a slat cutout at the pylon, which subsequently initiates premature stall further downstream, Fig. 13.

Nacelle strakes, which shed a vortex at higher angles of attack, are employed to feed energy into the boundary layer flow which delays separation and improves CL_{max}.

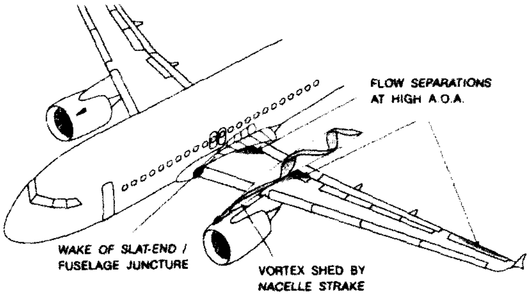

Figure 13. Wake/Vortex - Boundary Layer Interaction

The beneficial effect of vortex boundary layer interaction can also be utilized to delay flow separation at the wing root trailing edge region by adequate design of the slat-end fuselage juncture.

The optimization of the wake/vortex flow effects require flow field investigations. Usually this is done by application of the Crowder wake imaging system, a five-port-probe pressure survey system and smoke/laser vortex visualization technique, Fig. 14.

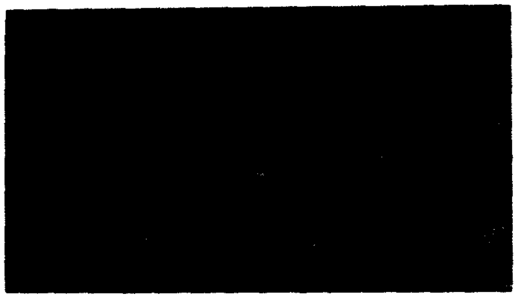

Figure 14. Wake-Flow behind A340 Wing in T.O.

It is apparent, that the nacelle/wing interference problem will be significantly increased by the introduction of very high-bypass engines ('Super-Fan') to future projects. This problem highlights the need for three-dimensional flow field investigations - especially with engine jet simulation - to demonstrate the flow-interactions and then to minimize their penalizing effects.

5. FEATURES OF THE A321 HIGH-LIFT SYSTEM

A general reflection of the high-lift design process was given in the preceding sections of this paper. One example of this process, the development of the high-lift system for the Airbus A321, will be described next.

In 1989 Airbus Industrie reacted to the increasing market demand for a 180 to 200 seat short to medium range airliner, and decided to close the gap between the existing 150 seat A320 and the 220 seat A310 by a stretched version of the A320, the A321, which will first fly in March 1993, Fig. 15.

In comparison to the baseline aircraft, the A321 fuselage is stretched by 8 frames ahead of the wing and 5 frames behind, which increases the payload capacity by 36 seats and 3 LD3 containers. This stretching causes an 13% increase of the maximum take-off and landing weight.

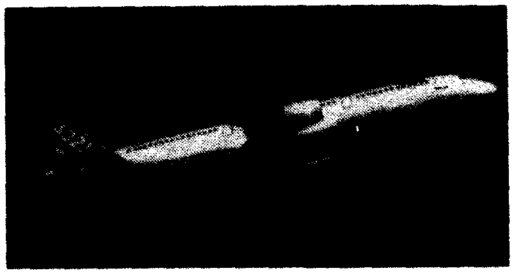

Figure 15. Airbus A321 Airliner

The major goal for the aerodynamic design of the A321 is defined by the requirement that airfield and cruise performance should be comparable with that of the A320. It is apparent that an optimized design as represented by the high-lift system and the cruise wing of the A320 needs some modifications to master a 13% weight increase with optimum efficiency.

Typically the design efforts on stretched aircraft versions are driven by demands of minimum changes to the baseline aircraft. Therefore the necessary wing structure modifications for the A321 are restricted to the rear part of the trailing edge flaps. These modifications include a spanwise varying chord extension, which increases the wing area by approximately 2.6%, and replacement of the single-slotted flap by a double-slotted flap.

5.1 Requirements of the High-Lift System

The required efficiency of the A321 high-lift system was driven by the demand of having comparable airfield performance with that of the A320.

In terms of lift, a 13% increase in weight necessitates an increase in the operational lift coefficients of the same order. Furthermore the rear fuselage insert reduces the maximum allowable ground rotation angle for take-off and landing flare by approximately 2 degrees, Fig. 16.

Summarizing the required lift capability demands 13% more lift at 2° less incidence.

Especially the reduction of the usable incidence requires a significant increase in the lift coefficient at constant incidence (C_{L0}). This can usually be achieved by increasing the effective airfoil camber, e.g. by further deflecting of the trailing-edge flap. However, this is not a practical solution for the A320's single-slotted fowler flap, because a deflection beyond the present 40° for landing will cause flow-separation on the flap and subsequently a loss in lift.

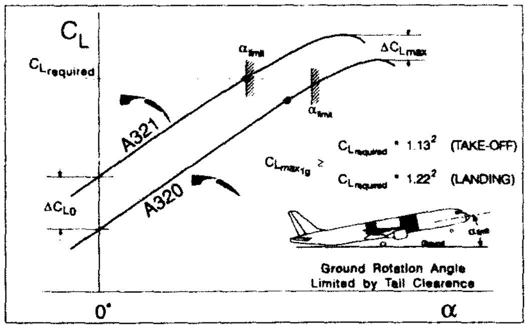

Figure 16. Lift Requirement on Stretched Version Aircraft

The alternative was to replace the single-slotted flap by a double-slotted flap, which allows higher deflections without flow separations.

With a double-slotted flap concept, the required lift efficiency in terms of CL_0 and CL_{max} may be achievable with any configuration. But, the double-slotted flap will cause more profile and induced drag at constant lift. In addition the friction drag of the fuselage inserts will further increase total drag. Thus, the compromised L/D of the A321 was a crucial point in take-off performance consideration, and the major design efforts were concentrated on take-off L/D optimization.

With consideration of the previously given approximation for the climb rate, it is apparent that the required second segment climb performance can only be satisfied if the weight and drag rise is compensated by an increased take-off power. This was offered by thrust enhanced versions of the A320 power-plants, the CFMI CFM56-5B1 and the IAE V2500-A5, which both offer approximately 16% more take-off power. The availability of these engine versions were prerequisite for the feasibility of the A321.

5.2 High-Lift System Design

The layout of the double-slotted flap system was dominated by the demand for minimum structural changes. In particular, the nose-part, the track-support and the actuation system of the A320 flap had to be preserved with only minor changes necessary to compensate for higher loadings. This restriction generally excludes the application of a vane flap type double-slotted flap system, as represented by the inboard flap of the A310. Fortunately the relatively thick rear profile of the A320 allowed an auxiliary fowler flap (tab) to be incorporated into the rear part of the main flap.

5.2.1 *Two-dimensional Layout*

After pre-development wind-tunnel testing of the principle flap/tab concept had demonstrated satisfactory lift efficiency, the final design was initiated by optimizing the two-dimensional arrangement of flap and tab.

Therefore studies were carried out to investigate the effect of the ratio of tab chord to the total flap chord and the length of the shroud on the profile drag, lift efficiency and stall sensitivity.

These studies, based on viscous pressure distribution calculations, indicated firstly, that the optimum tab chord was in the order of 40% of the total chord and secondly, that the shroud length should be as large as possible. In general, however, the effect of the shroud length is relatively small in comparison to the total tab efficiency. Therefore, including consideration of shroud stiffness, a shroud length of 10% of the total flap chord was finally chosen, Fig. 17.

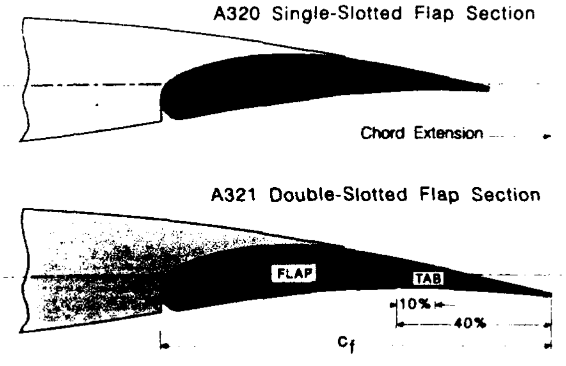

Figure 17. Comparison of A320 and A321 Flap Section

5.2.2 *Three-Dimensional Layout*

From the aerodynamic point of view the spanwise arrangement of the A320 trailing edge devices represents an optimum design, because the spanwise flap extension is not divided by any cut-out and even the intersection between inboard and outboard flap is sealed at all settings. This assures a continuous spanwise lift distribution and minor penalties due to wake and vortex flow. The spanwise lift distribution is further improved by aileron drooping.

The first design intention was to realize a continuous double-slotted flap along the full flap span. Unfortunately, this concept had to be changed due to structural constraints, because the inboard tab was partly hid by the engine's fan jet, and the outboard tab end became to small for manufacture. Therefore the tab span was finally limited on the I/B flap between the fuselage and track 2 and on the O/B flap between the kink and track 3, as illustrated in Fig. 18.

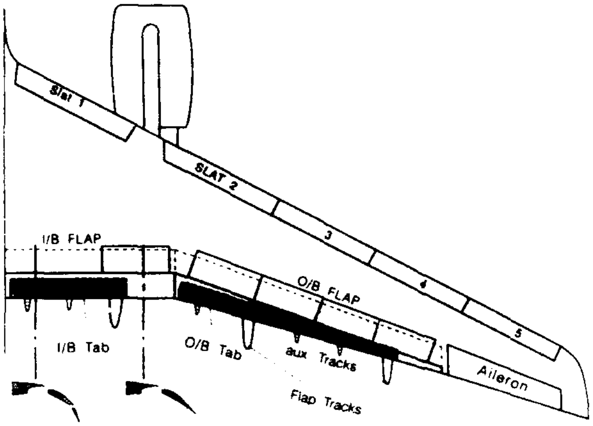

Figure 18. Wing Planform of A321

5.2.3 *Kinematic Layout*

The A321 main flap element is supported by a track guided carriage and actuated by a rotary drive system. The new tab element is supported by a four hinge linkage system, which is indirectly actuated by a drive rod, Fig. 19. This rod couples the movement of the main flap carriage with that of the tab linkage support.

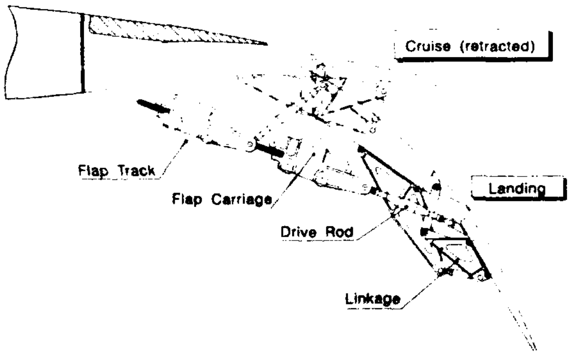

Figure 19. A321 Flap/Tab Support

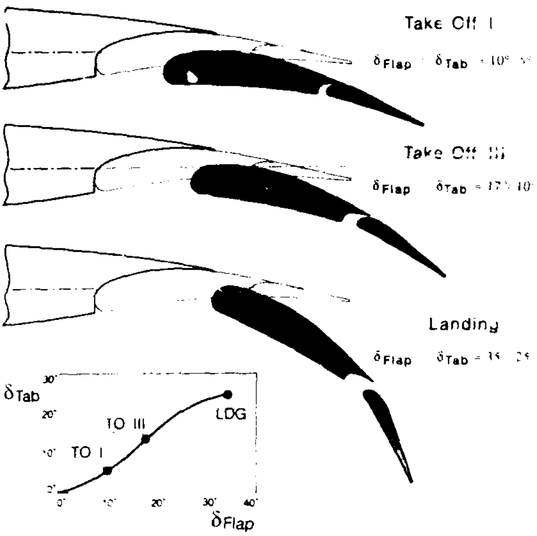

Figure 20. Flap/Tap Settings

In comparison to an alternatively investigated track support, the linkage system is simpler, lighter and smaller , and can be integrated completely into the main track fairings.

A disadvantage of the linkage system is the restricted function of the tab movement relative to the flap, because it can be defined for only two settings, usually for one intermediate take-off configuration and for the landing configuration.

The intention of the initial kinematic design was to keep the tab gap sealed in the take-off configurations for optimum L/D, and open with a large slot for landing to achieve high CL_{max}. However, our intention could not be realized due to restricted tab kinematics. Therefore, take-off setting variations were intensively investigated during wind-tunnel testing. The results suggested that a small gap of 0.5% of total flap chord provided little better L/D than a sealed gap, and further, that gaps up to 1% could be tolerated. This increased gap margin relaxed the kinematic constraints and allowed a kinematic design which satisfies the aerodynamic requirements in terms of gap, overlap and tab/flap deflection for all configurations,Fig. 20.

5.2.4 *Setting Optimization*

In general, the profile drag at constant lift increases with profile camber, or flap/tab deflection, respectively. Therefore the optimum L/D for each take-off configuration can be obtained with the minimum flap/tab deflection that achieves the required lift.

The determination of the minimum flap/tab deflections was based on the diagram shown in Fig. 21. The grid demonstrates the lift coefficients which can be obtained with different combinations of flap to tab deflections at a constant incidence of 9.7°, which represents the operational limit of the ground rotation angle. The required lift coefficients for the three take-off configurations are marked on the left axis. Additionally the function of the designed flap-to-tab gearing is given as a function of the grid. By means of this curve, the feasible flap and tab settings were determined which achieve the required lift coefficients.

Wind-tunnel investigations have demonstrated that the L/D could be further improved by modification of the spanwise lift distribution through a differential deflection of the I/B and O/B tab. This aspect was realized by the final kinematic design, which provides a maximum deflection of 20° for the I/B tab and 25° for the O/B tab, while the main flap's deflection is 35° on I/B and O/B.

5.3 Performance Status

The aerodynamic performance, achieved with the A321's high-lift system during high Reynolds number wind-tunnel tests, is given in Fig. 22 for the lift and in Fig. 23 for the L/D. Especially the increments of CL_0 and CL_{max} given relative to the A320's single-slotted flap demonstrate the superior lift capability of the part span double-slotted flap system. Additionally the lift increments for a single-slotted flap are given, the chord of which was identical to the double-slotted

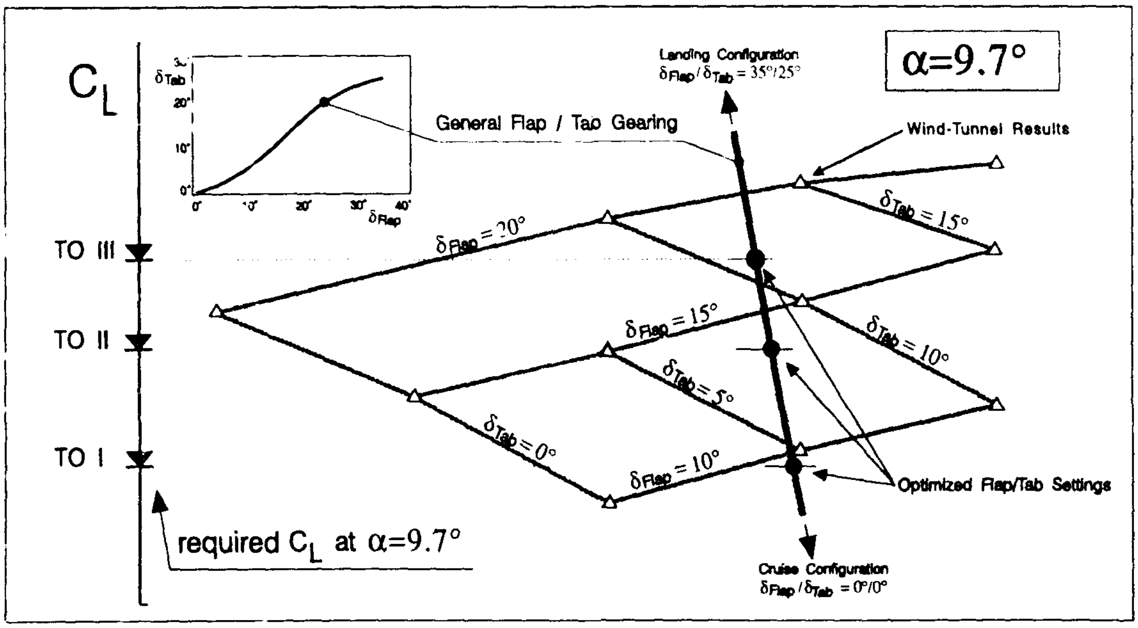

Figure 21. Flap/Tab Setting Optimization

flap with retracted tab. Its marginal performance, especially the decreasing maximum lift at deflections higher than 25° demonstrates that the required lift capability for the A321 can only be satisfied with a double-slotted flap

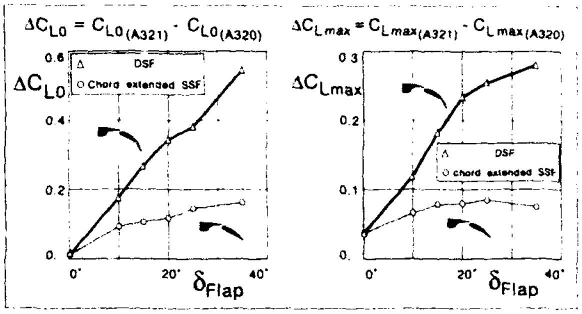

Figure 22. A321 Lift Efficiency

The envelope of L/D versus CL for all take-off configurations is illustrated in Fig. 23 for A320 and A321. In comparison to the A320 it is shown that the operational lift regime for all A321 configurations could be extended with only minor deterioration in L/D. When considering the total amount of drag increase due to fuselage extension, auxiliary tab-hinge fairings, tab-edge vortices and increased effective camber, it is evident that the L/D efficiency of the double-slotted flap alone is slightly better than that of the A320's single-slotted flap.

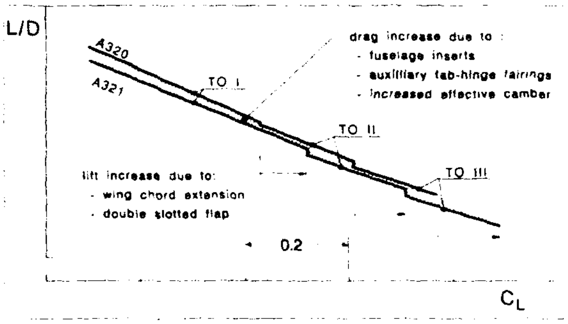

Figure 23. L/D Comparison of A320 and A321

6 CONCLUSIONS

A general reflection on the high-lift design process was given in the first part of this paper.

It was discussed, that the application of theoretical methods in the high-lift design process, at present, is sufficient only for the two-dimensional design cases such as shape optimization.

In spite of the advances in three-dimensional computational methods, their use for maximum lift and total drag prediction is still insufficient due to the unconsidered complex interactions between boundary layer flow and wake/vortex flow on a wing in high-lift configuration. Therefore the necessity of wind-tunnel testing is unquestioned for the high-lift development as well as for performance prediction.

The Deutsche Airbus wind-tunnel strategy was described, which is aimed at carrying out the majority development tests in our own low-speed tunnel and to employ the large tunnels for verification, final performance check-outs and investigation of special items.

The second part of the paper dealt with the design and optimization of the A321's trailing-edge high-lift system.

It was demonstrated that the significantly increased lift requirements for the stretched version aircraft could be satisfied by a conversion of the basic single-slotted fowler flap to a part span double-slotted flap, even with consideration of the 'minimum change' philosophy.

The forecasted growth of the world-wide civil air transport is obviously limited by the traffic - slot - capacity of the major airports, with some of them having already reached their operating limits. This situation can be eased by improving the approach and take-off procedures to increase the airport traffic density and by using smaller airports even for long range operation for traffic decentralization.

Therefore, the airfield performance of future civil transport aircraft need to be increased in terms of decent and climb capability, field length and maneuverability, thereby tending towards the airfield performance of military transport aircraft.

References

1. G. Dargel, H. Jacob, "Berechnungsverfahren für viskose Klappenprofilströmungen - Rechenprogramm HILI", ZKP, Flügel kontrollierter Strömung, Ergebnisbericht Nr. 9, LFK 8510 5
2. B. Haftmann, F.-J. Debbeler, H. Gielen, "Takeoff Drag Prediction for AIRBUS A300-600 and A310 Compared with Flight Test Results", Journal of Aircraft, 25, 12, December 1988, pp1088-1096
3. R. Hilbig, "Aktuelle Entwicklungen in der Aerodynamik" DGLR 91-155, September 1991
4. M. Karvin, A.Flaig, "Modification der AIRBUS A320 Flügelhinterkante zur Optimierung der Flugleitstungen für die gestreckte Variante A321", DGLR 90-074, October 1990, pp1275-1283
5. D. Schwetzler, "Effect of Slat 1 Inner End Modification on Wing Root Flow", Deutsche Airbus, EF12-13/91, 1991, (unpublished)

HIGH LIFT SYSTEMS FOR TRANSPORT AIRCRAFT WITH ADVANCED AIRFOILS

B.Eggleston
Director Technology and Research
R.J.D.Poole
Senior Research Aerodynamics Engineer
de Havilland Inc.
Garratt Blvd.,Downsview,
Ontario, Canada, M3K1Y5

1. SUMMARY

This paper describes an on-going program of R&D into the development of high lift systems for future propeller driven regional transport aircraft.

The work includes tests of two-dimensional airfoils and flaps, while half models are used for wing integration development. Comparisons are made between earlier commuter airfoil designs and advanced supercritical airfoils capable of NLF, using single and double-slotted flap systems in both cases. The advanced airfoils were also tested with a leading edge slat. Some effects of Reynolds' number on lift characteristics are reviewed which show airfoils without leading edge slats were more sensitive at the scale of half model used and that higher Reynolds' numbers may be required.

The advanced airfoils stalled at lower incidences than the commuter airfoils which are much thicker and better tailored to high lift performance. Advanced airfoils will likely require an additional flap segment to achieve similar lift to commuter airfoils. Leading edge slats gave large increases in maximum lift coefficients (up to 30%), which would allow substantial increases in wing loading if needed for the future.

The half model development has entailed work on improving the sealing of the fuselage to the tunnel wall to minimize leakage. The paper provides some details of such work on high lift models and also on models used for cruise drag investigations.

2. LIST OF SYMBOLS

c	wing chord
C_D	drag coefficient
$C_{D\pi}$	drag coefficient based on S_π
C_L	lift coefficient
C_{Lmax}	maximum lift coefficient
C_M	pitching moment coefficient
M	freestream Mach number
R_E	freestream Reynolds' number based on mean chord
S	reference wing area
S_π	reference frontal area
t	airfoil thickness
V_s	stall speed
α	incidence
α_{stall}	stall incidence
δ_{FF}, δ_{TF}	foreflap/trailing flap deflection.
Δ	increment

3. INTRODUCTION

The current generation of turboprop powered commuter aircraft in airline service, operate at cruise Mach numbers up to about 0.5. At such speeds there are few significant compressibility problems. Hence wing airfoils can be made quite thick and design pressure distributions can be tolerated which favour low speed, high lift performance. In contrast, the next generation of commuter aircraft will cruise substantially faster and it is possible that future propeller driven types will cruise at speeds of Mach 0.7 or more.

At higher cruise speeds, the design of the airfoils and wings will need care to avoid undue compressibility problems and also interference from propeller slipstream effects, such as swirl and increased velocities. Also, these problems must be tolerated while retaining, or even improving on high lift performance, in order to maintain similar field performance at the higher wing loadings desirable with advanced configurations. Thus, we can expect growing emphasis on improving high lift systems in the future.

The work to be reported here concerns an on-going R&D program at de Havilland Inc., which is examining the design of airfoils, high lift systems and wing design features suitable for future commuter aircraft. The testing includes two-dimensional airfoil sections with various flap systems, complemented by tests of half-models with similar high lift systems in order to study three-dimensional wing integration effects. The airfoils investigated to date included relatively thick sections (18-21% maximum t/c) suitable for earlier lower speed commuter aircraft, as shown in figure 1. More recently, a new family of advanced supercritical airfoils suitable for cruise speeds of at least Mach 0.7 were tested, figure 2.

The cruise performance of the advanced airfoils used in this work, and their design objectives, were described in several earlier reports, references 1, 2, 3 and 4. Notably, the airfoils were designed to achieve low cruise drag and high drag rise Mach numbers with fully turbulent boundary layers present. However, the design pressure distributions were also made suitable for sustaining extensive natural laminar flow (NLF) in suitably "clean" conditions. All airfoils in this family have demonstrated NLF drag "buckets" near their design conditions. Also of significance, these airfoils have relatively blunt nose shapes which were tailored to diminish suction peaks at high incidences to retain reasonable high lift performance at low speeds. This paper will describe some results of the airfoil and flap system section testing, including Reynolds' number effects. The main focus of this paper will be on issues arising from the high lift results.

During the early stages of wing development work, the use of half models is particularly effective as a means of simplifying and reducing costs of models and testing. This research program involved significant efforts in improving the half model test techniques used at the Institute for Aerospace Research (IAR) of the National Research Council, Canada (NRC), in order to obtain more reliable results from high lift testing and also at cruise conditions. This paper describes some of the ongoing developments from such activities.

4. AIRFOIL SECTION TESTS

4.1 Airfoil Geometries

The high lift airfoil testing included the 18 and 21% thick commuter designs shown in figure 1, and the advanced airfoil of 16% maximum thickness/chord ratio included in figure 2. In all cases the airfoils were tested with single and double-slotted flaps. The flaps occupied about 38% wing chord when retracted, figure 3. This gave the same amount of flap chord and fowler action as the Dash 8. The advanced airfoil was also tested with a cambered leading edge slat to extend its maximum lift capabilities, figure 4.

The airfoil section testing used the high Reynolds number, 0.38m x 1.5m two-dimensional wind tunnel at the IAR/NRC, shown in figure 5. In selected cases some testing was undertaken at Reynolds numbers appropriate to full scale operation (6 to 10 million) and also at a lower value (2 million) to obtain data matching the scale of the half model testing.

4.2 Flaps-Up Tests

Some results from the flaps-up, low-speed tests are given in figure 6. A comparison of the lift performance shows the advanced airfoil stalled 2 to 3 degrees sooner, while achieving maximum lift coefficients quite similar to the earlier generation airfoils. The minor differences found in aerodynamic characteristics are unlikely to have any significant aircraft performance or operational implications.

4.3 Flaps Extended Tests

Results for testing with flaps extended to 25 degrees are given in figure 7. Again the advanced airfoil testing demonstrated an earlier stall angle by 2 to 3 degrees which resulted in a reduction in maximum lift coefficient of about 7%. In figure 8 the maximum lift coefficients achieved are summarized as a function of flap angle. These results show that the maximum lift performance of the advanced airfoil was 5 to 10% below the 18% commuter airfoil values and the largest differences were found at lower flap angles.

In figure 9 the summary chart is expanded to include some results from tests on the advanced airfoil with double-slotted flaps at 25/35 and 35/35 degrees of deflection. These flaps increased the maximum lift coefficients available by 10 to 15%, and were able to exceed the maximum lift performance of the commuter airfoils having single-slotted flaps.

4.4 Leading Edge Slat Tests

Typical results for the effects of a leading edge slat on lift, for double-slotted flaps with 15/15 degree deflections, are shown in figure 10. The slat added about 0.9 to the maximum lift coefficient and extended the stall incidence by about 8 degrees. Notice that for negative incidences below about -5 degrees the slat spoiled the lower surface flow and abrupt lift losses occurred.

The effects of leading edge slats are also included in the summary of maximum lift coefficients shown in figure 9. The highest maximum lift coefficients exceeded 5 for cases with leading edge slats and double-slotted flaps at large flap deflection angles. Such values are about 35% higher than the commuter airfoils with single slotted flaps and, in principle, this should allow substantial increases in aircraft wing loadings to be accommodated, without changing field size requirements.

4.5 Reynolds' Number Effects on Commuter Airfoils

The 21% thick airfoil was tested at Reynolds' numbers of 2 million and 6 million. Lift effects are shown in figure 11 for a flap deflection of 35 degrees. In tests where the flap location was optimized for a Reynolds' number of 6 million (defined as position #1 in the figure) and then tested again at 2 million, the effects below stall were found to be very small. However at stall there was a minor penalty of about 3% on maximum lift, while the stall angle was reduced by about 2 degrees.

The flap was also placed at a location found to be an optimum from half-model tests made at 2 million Reynolds' number. The flap nose was located further under the wing shroud (see sketch) and the results show a significant increase in the lift below stall relative to the location #1. The maximum lift was found slightly greater, while stall occurred about 2 degrees sooner than at location #1.

The summary in figure 12 compares maximum lift from tests at 6 million Reynolds' number with values found at 2 million with the flap at the half-model optimum location. At the lower flap angles, reductions of up to 9% of maximum lift were found, versus about 3% found at 35 degree flap deflection. From such tests it appears that commuter airfoils are not unduly sensitive to Reynolds' number effects down to values appropriate to the current half model. However, testing the half models at higher Reynolds' numbers would help diminish the corrections needed for scale effects.

4.6 Reynolds' Number Effects on Advanced Airfoils

The effects of Reynolds number were also investigated for the 16% thick advanced airfoil and flaps, both with and without the leading edge slat. Typical lift results for a case without a slat, with the flap location optimized for 6 million Reynolds number, are shown in figure 13. Tests made at a reduced Reynolds' number of 2 million for the same location showed a loss in maximum lift performance of about 5%, and there was negligible change in stall incidence for this configuration. At the lower flap angles the advanced airfoil showed smaller lift losses due to Reynolds' number effects (2-5%), in contrast to the behavior found with the commuter airfoil.

Typical results for tests with a leading edge slat are shown in figure 14 for a configuration with double-slotted flaps deflected 15/15 degrees. In this case the tests at lower Reynolds' number showed negligible changes in lift below stalling angles. The maximum lift was penalized less than 2% for this case, while the stall incidence was found to be essentially unaltered.

The airfoil section testing without slats indicates that larger half models may be desirable for flap development work, in order to diminish the corrections needed for Reynolds' number effects. In the case of models having leading edge slats, the scale of the current half model appears adequate for preliminary development work.

5. HALF MODEL TESTING

5.1 High Lift Model Features

The experimental investigation used a research model in the IAR 2m x 3m low-speed wind tunnel. The model was tested with various wings during this development program. An installation using a high mounted wing with commuter airfoils is shown in figure 15, and its features were fully described in reference 2. Tests have also studied a low wing with some results reported in reference 2. A photograph of the configuration tested with the advanced airfoils is shown in figure 16.

A half model was used to maximize the Reynolds' numbers and model size for a given tunnel, while substantially reducing costs for the model and testing relative to an equivalent complete model. However, half models introduce difficulties with sealing between the fuselage and the tunnel wall. Sealing is needed to diminish leakage and the resulting lift-loss and anomalies in the drag and pitching moment measurements. Such issues will be discussed in more detail later in the paper.

The wind tunnel model in figure 16 had a wing of 1.52m semi-span and an overall aspect ratio of twelve. An advanced airfoil of 16% maximum thickness to chord ratio was used at the model centre line and one of 13% at the wing tip. Some features of the model included :

- variable span flaps extending to 60 or 80% span with plain sealed ailerons outboard
- double-slotted flaps, also operable together as a single slotted flap
- a full span, cambered leading edge slat
- slipstream simulation using an eight bladed propeller driven by an 80 hp air motor
- compressed air supply to the motor via internal wing ducts
- the ability to return the motor exhaust back through the wing and thence off-balance with low interference
- a detachable outer wing panel so that the model can be installed in the IAR 1.5m x 1.5m transonic tunnel for cruise testing.
- a removable tailplane for measurements of downwash and tailplane/elevator effectiveness.

The IAR 2m x 3m low speed wind tunnel in Ottawa was used for the half model testing. This tunnel can operate up to 0.35 Mach number. For the majority of the high lift testing a Mach number of 0.20 was used, corresponding to a Reynolds number of 1.5 million based on the mean chord of the wing. A limited amount of testing was performed at lower speeds on the commuter wing to investigate Reynolds number effects.

5.2 Development of Model to Floor Sealing

Early on in the half model high lift testing, it was realized that the fuselage drag levels were unacceptably high due to excessive leakage between the model and the tunnel floor. While it was accepted that such installations do not normally provide accurate drag measurements, there was concern that leakages could affect lift also, so it was considered desirable to make improvements.

The 2m x 3m tunnel has a plywood floor and a turntable supported on a steel beam structure. Models were provided with clearances of the order 6mm to allow for waviness in the floor and for its lifting under aerodynamic loads. Tests of the isolated fuselage demonstrated the magnitude of the problem and figure 17 shows that initially the drag was about three times greater than predictions. The gaps between the model and floor were reduced to minimums and a skirt was added made from adhesive backed aluminium foil. The underfloor gaps around the model mounting block were also reduced to minimums just avoiding fouling to reduce venting from outside. These modifications enabled the fuselage drag to be reduced to about twice predicted values. These tests were all made with a large V-shaped, floor mounted, vortex generator ahead of the model in order to thin the boundary layer about the model.

Some follow-on work has investigated cruise drag with half models in the IAR 1.5m x 1.5m Transonic Wind Tunnel. In that tunnel the installation can be made with much tighter clearances as the walls are more rigid and less wavy, and the balance stiffness is high so deflections are low. In order to improve the installation it was decided to use a non-metric filler (stand-off) plate between the model and wall, see figure 18. The gaps between the fuselage, plate and tunnel wall were small, of the order 1 to 1.5mm, and they were sealed using spring loaded teflon strips. In this case there is no flow path for leakage past the balance as it is internally sealed and the tunnel is within a plenum. Static pressure rails are mounted on the tunnel porous walls and they provide data for corrections including model buoyancy effects. For this installation the measured drag for the isolated fuselage was about 80% of estimates. Tests on wing/fuselage/nacelle configurations reported in reference 5 showed good correspondence with lift/drag polars from aircraft tests.

A new model and mounting system is now under development for the IAR 1.5m x 1.5m wind tunnel, to achieve further improvements in drag measurements. This uses complete models mounted on a slim, centre-line plate. Again, static pressure rails are used on the walls for deriving tunnel corrections. Tests of a fuselage in isolation have shown drag values similar to estimates, although the tare corrections of the mount have yet to be established, figure 17.

From the foregoing work it appears that the half model approach still requires further development in the IAR 2m x 3m wind tunnel installation before it can be used reliably for parameters other than lift.

5.3 Half Model Test Results

5.3.1 Airfoil/Flap Characteristics With Slat Off

The lift data from half model tests with commuter and advanced airfoils are shown for cases with flaps retracted, and with 25 degrees deflection, in figure 19. The data shown are for cases without a nacelle. The half model results exhibited similar features to the airfoil section data discussed previously. The stall with the advanced airfoils occurred about three to four degrees sooner and maximum lift was reduced accordingly. The reduction in stall angles observed with the advanced wing may lead to some restriction on the largest flap deflection usable for landing, arising from the stall margins needed in ground effect at touchdown attitudes during maximum effort landings. This situation may well dictate the use of leading edge devices, particularly on wings with thinner sections or less tolerant designs than those used here.

The variation of maximum lift with main flap angle obtained for cases with single and double-slotted flaps are summarized in figure 20. At larger flap deflections the advanced wing achieved maximum lift coefficients about 10% less than the commuter wing. Accordingly, more powerful flaps are required and, as shown in the figure, about 15 degrees deflection on the second flap element was needed to recover the deficiency, excepting the contribution from trim losses needed for complete configurations.

5.3.2 Airfoil/Flap Characteristics With Slat-On

Experimental lift curve data for tests with and without leading edge slats using the wing with advanced airfoils, are shown in figure 21. The model's lift characteristics again exhibited similar behavior to the airfoil section data discussed previously. A summary of the effect of slats on maximum lift coefficients is presented in figure 22. These data show increments in $C_{L_{max}} > 1$, corresponding to at least 30% over the $C_{L_{max}}$ in slat-off cases.

The slat increased stall angles by more than ten degrees out to values about 25-30 degrees. Such extreme angles will require special attention to the tailplane design relative to current propeller driven transports which are satisfactory without needing variable incidence or any leading edge devices.

Also to be noted, the undersurface stall behavior induced by the slat at negative angles of incidence found in 2-D tests, persisted into the wing behavior. Such behavior is not unexpected on an unswept, high aspect ratio wing, while with swept planforms where slats are normally used such effects may be obscured. Certification requires that civil aircraft be flown beyond V_{flap} (1.8 x V_s) and to near zero "g" conditions, so safe excursions into this region will be necessary. Although it may be feasible to demonstrate satisfactory flight in the spoiled region, the option of retracting the slats could be exercised to ease longitudinal control.

The gains in field performance from leading edge slats will not be as significant as the increases in maximum lift they conferred in these experiments. When aircraft land they normally have angles of incidence in the range zero to five degrees, as dictated by flap angle and the requirement to approach at 1.3 V_s. During the landing flare the aircraft pulls "g", there is a small speed loss of maybe 5-10%, and incidence increases to near the maximum permitted by tail strike, say to values of 8-12 degrees. Thus, the most important factor governing landing performance is the range of lift coefficient available in the range of usable incidence between zero and about 12 degrees, rather than the absolute value of $C_{L_{max}}$. As a result, unless the usable range of lift can be increased in concert with using slats, they will not augment landing performance significantly. This means that to fully exploit slats, aircraft will need more powerful flap systems.

5.4 Comparisons with Aerodynamic Predictions

The simple nature of a high aspect ratio, unswept wing enables lift to be adequately predicted using lifting line methods. Comparisons are presented in figure 23 showing predicted and experimental lift curves for the commuter wing with flaps retracted and also with 25 degrees of deflection. The method accounts for the non-linear behavior of the lift with incidence across the wing span. The agreement is generally good, although sometimes difficulty is found in predicting maximum lift reliably at large flap angles and semi-empirical fixes to the input data are used to force solutions.

The lifting line procedure also predicts the wing pitching moment contribution. The tunnel data can be used to obtain an approximation to this contribution by subtracting the isolated fuselage values from values for the complete model. This, of course, leaves the interaction effects of wing on fuselage still present in the net result. The variation of predicted pitching moments with incidence and those derived from the experiments, are presented in figure 24 for the commuter wing with flaps retracted, while figure 25 shows data for 25 degrees of flap. The agreement is reasonable with only a small residual difference in pitching moments of about $\Delta C_M = -0.04$, which did not vary strongly with incidence within the usable range of incidence.

6. CONCLUSIONS

The paper has described research on high lift developments comparing earlier commuter airfoils with advanced airfoils suitable for aircraft cruising at speeds above Mach 0.7 . This work is still on-going. Based on the results presented here the following conclusions are made:

a) The half model approach to high lift development was found satisfactory for preliminary work. It still requires further development on model mounting and in particular on fuselage/tunnel floor sealing to be reliable for drag and pitching moments as well as lift.

b) The relatively thick advanced airfoils of this study were able to achieve C_{Lmax} performance within 5 to 10% of earlier commuter airfoils when using similar flap systems. This was demonstrated using two-dimensional airfoil section tests and also with half models.

c) Leading edge slats added considerably to C_{Lmax} by extension of the stall incidence out to values of 25-30 degrees, giving gains in $C_{Lmax} > 30\%$ at all flap angles.
However, in order for aircraft to benefit from slats in terms of achieving shorter field sizes or increases in wing loading, they will need to be used in concert with more powerful flaps.

d) Reynolds' number effects on lift performance were found to be significant for tests without leading edge slats. Hence, half model testing for high lift development needs to be done at larger scale. Alternatively, more extensive testing of two-dimensional airfoils may be used in conjunction with reliable model-to-full scale wing prediction methods.

e) Predicting the high lift performance of high aspect ratio, unswept wings as used in this study can be done with relatively simple, lifting-line procedures.

ACKNOWLEDGEMENT

The research programs discussed here were jointly funded projects of de Havilland Inc. and The Program for Industry and Laboratory Participation (PILP) of the National Research Council of Canada during the years 1980 to 1987.

REFERENCES

1. Poole, R.J.D., and Teeling, P.,
"Airfoils for Light Transport Aircraft",
SAE 81076, April 1981

2. Eggleston, B.,
"R&D in the Evolution of the Dash 8",
CASI Journal, Vol. 30, September 1984

3. Eggleston, B., Poole, R.J.D., Jones, D.J.,
Khalid, M., "Thick Supercritical Airfoils with Low Drag and Natural Laminar Flow",
Journal of Aircraft, Vol. 24, June 1987

4. Khalid, M. and Jones, D.J.,
"A Summary of Transonic Natural Laminar Flow Airfoil Development at NAE"
NAE-AN-65, May 1990

5. Mokry, M., Digney, J.R., Poole, R.J.D.,
Doublet-Panel Method for Half-Model Wind-Tunnel Corrections,
Journal of Aircraft, Vol. 24, May 1987

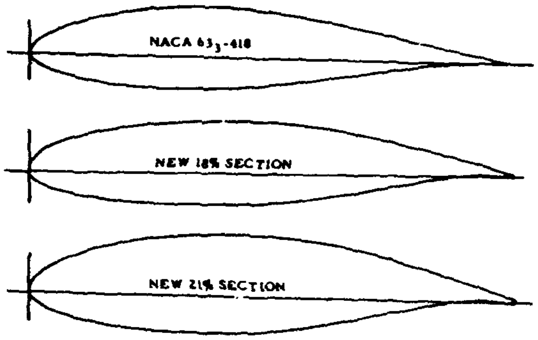

FIGURE 1. COMMUTER AIRFOILS

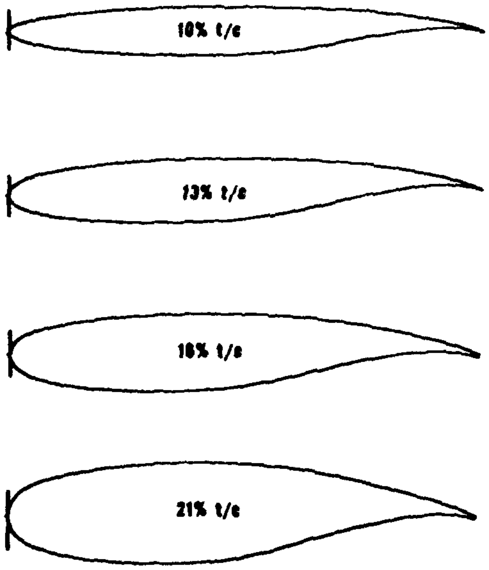

FIGURE 2. ADVANCED AIRFOIL FAMILY

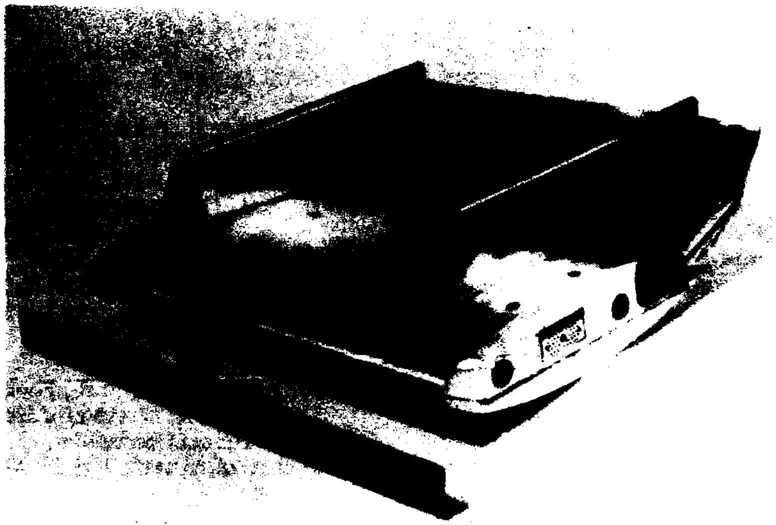

FIGURE 3. MODEL OF 21% THICK COMMUTER AIRFOIL WITH FLAPS

FIGURE 4. MODEL OF 16% THICK ADVANCED AIRFOIL WITH FLAPS AND SLAT

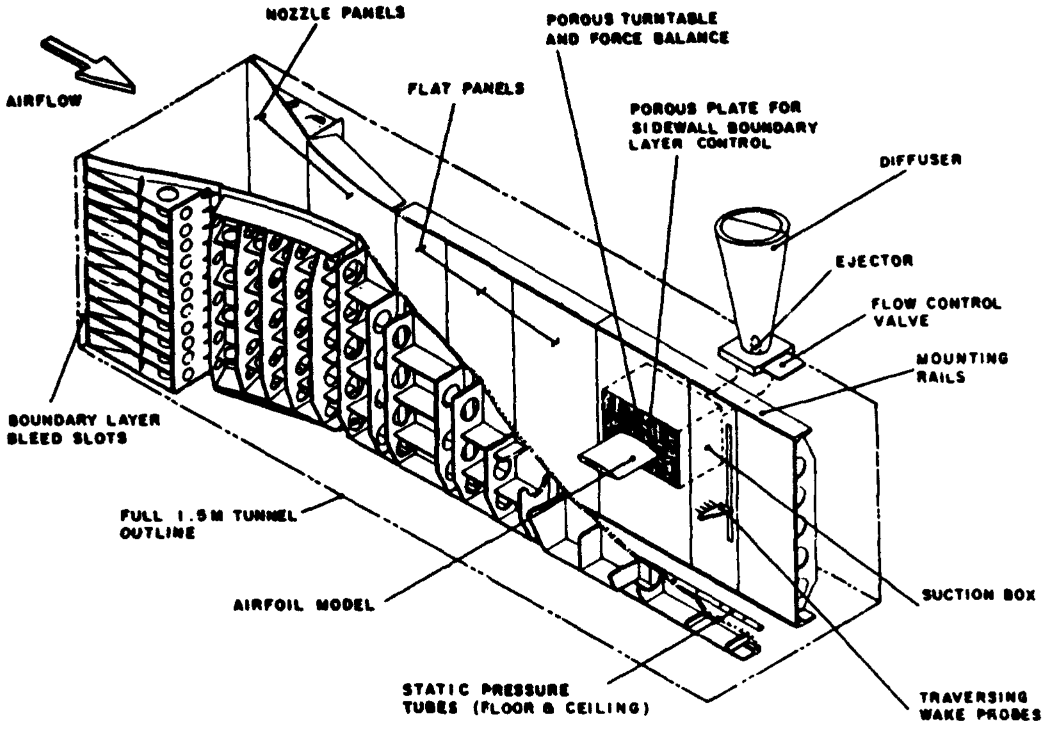

FIGURE 5. I.A.R. TWO-DIMENSIONAL WIND TUNNEL

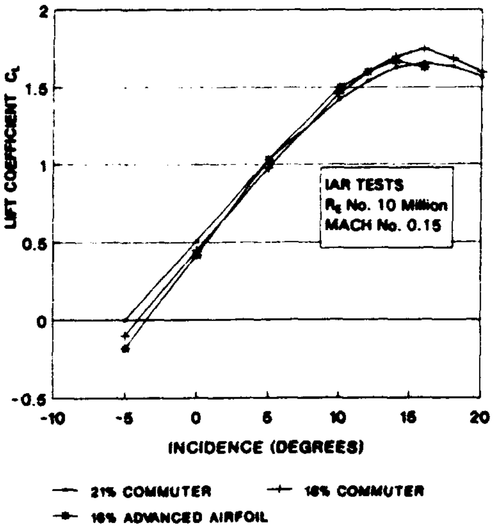

FIGURE 6. COMPARISON OF LIFT PERFORMANCE
FLAPS RETRACTED

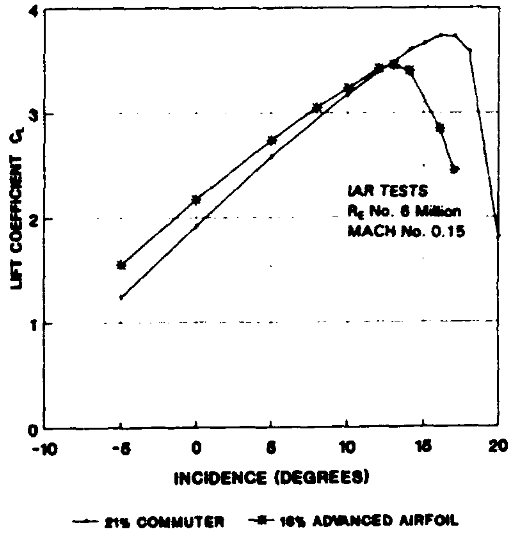

FIGURE 7. COMPARISON OF LIFT PERFORMANCE
Flaps 25 degrees

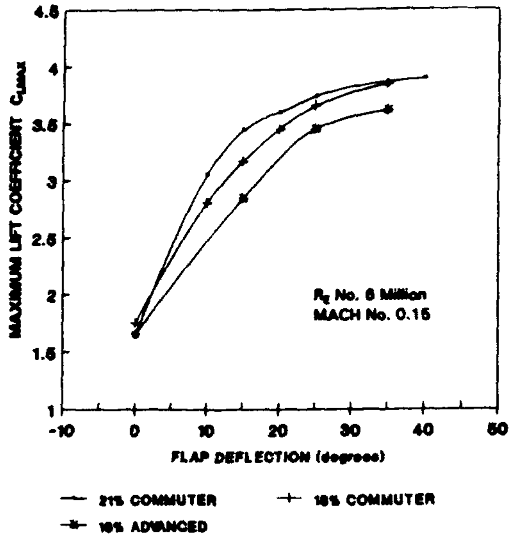

FIGURE 8. COMPARISON OF C_{LMAX} PERFORMANCE WITH FLAP ANGLE
Single Slotted

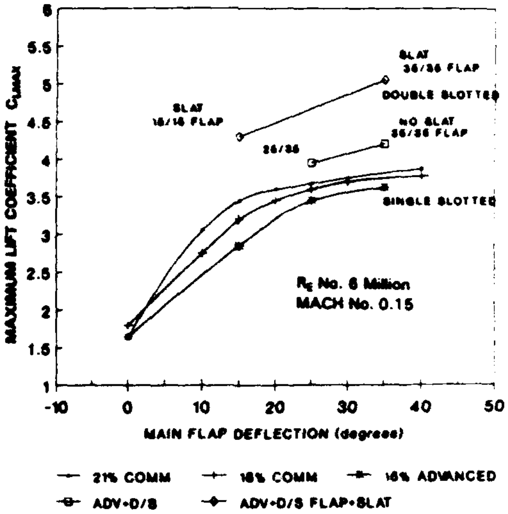

FIGURE 9. COMPARISON OF C_{LMAX} PERFORMANCE WITH FLAP ANGLE
(Various High Lift Systems)

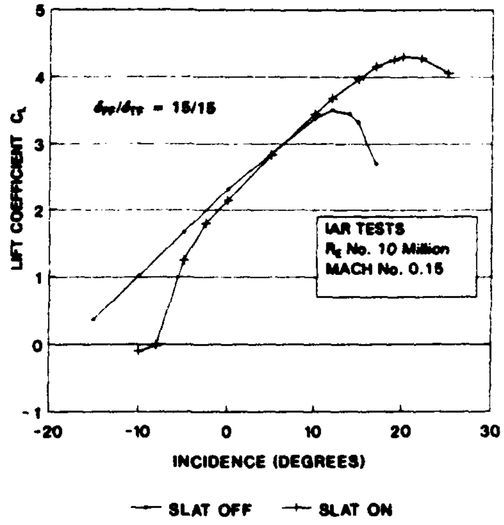

FIGURE 10. ADVANCED AIRFOIL LIFT PERFORMANCE
Effect of Slat

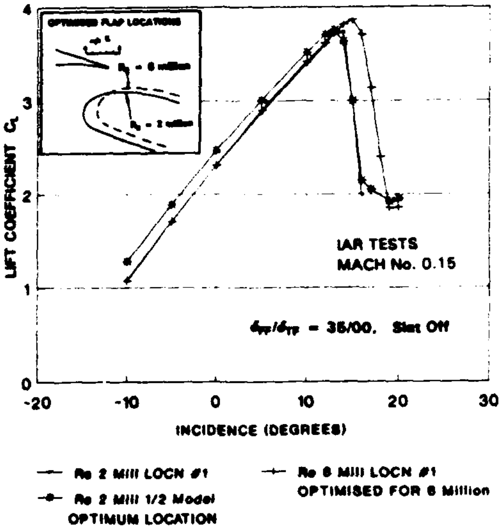

FIGURE 11. REYNOLDS NUMBER EFFECT ON COMMUTER AIRFOILS

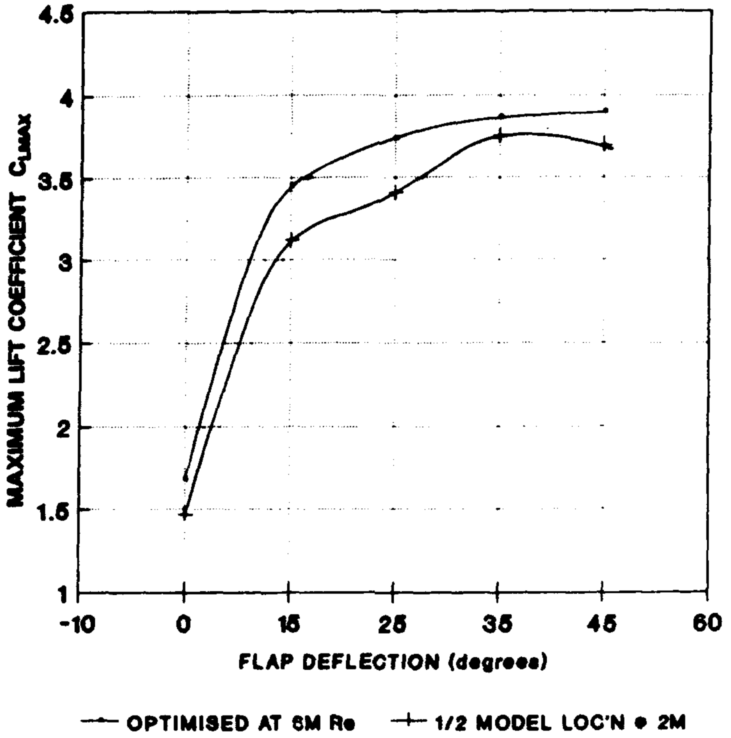

FIGURE 12. EFFECT OF REYNOLDS NUMBER AND FLAP LOCATION ON COMMUTER AIRFOIL MAXIMUM LIFT COEFFICIENT

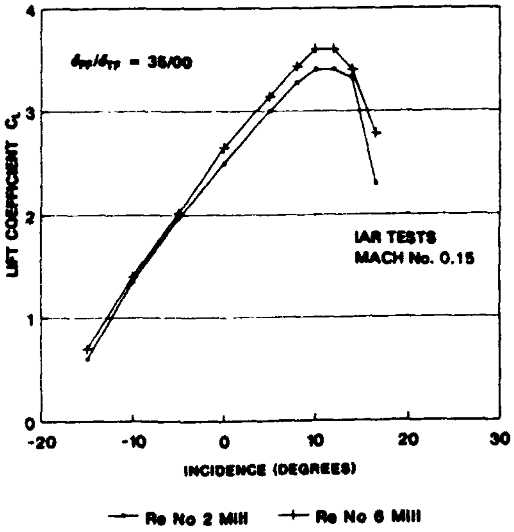

FIGURE 13. REYNOLDS NUMBER EFFECT ON ADVANCED AIRFOILS
No slot

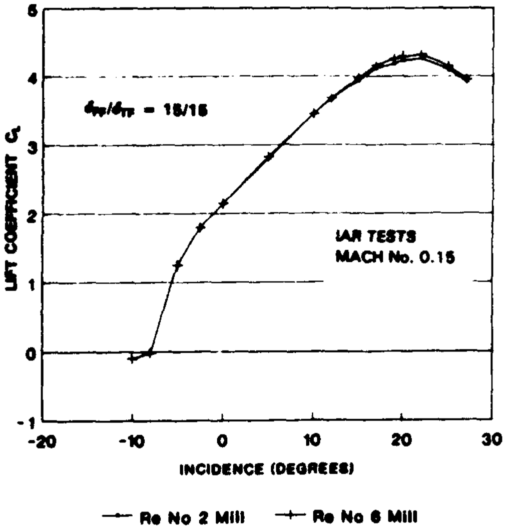

FIGURE 14. REYNOLDS NUMBER EFFECT ON ADVANCED AIRFOILS
With slot

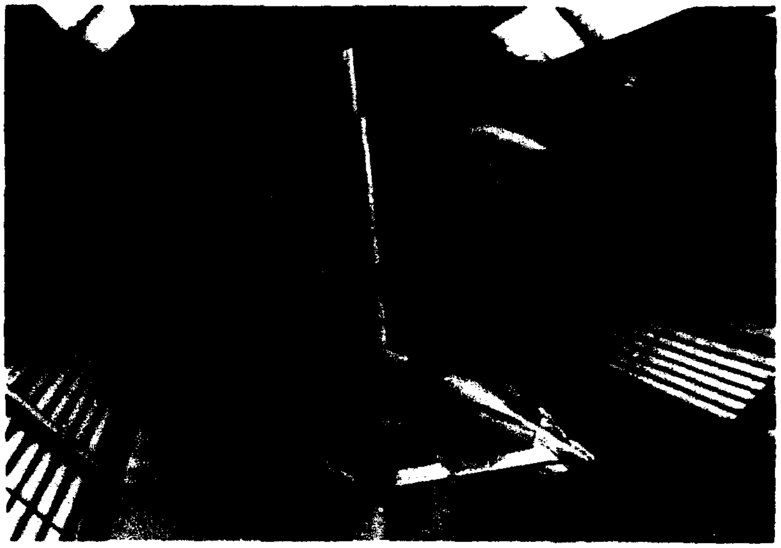

FIGURE 15. **REFLECTION PLANE MODEL**
Commuter Airfoils - Low Speed Tunnel

FIGURE 16. **REFLECTION PLANE MODEL**
Advanced Airfoils - Low Speed Tunnel

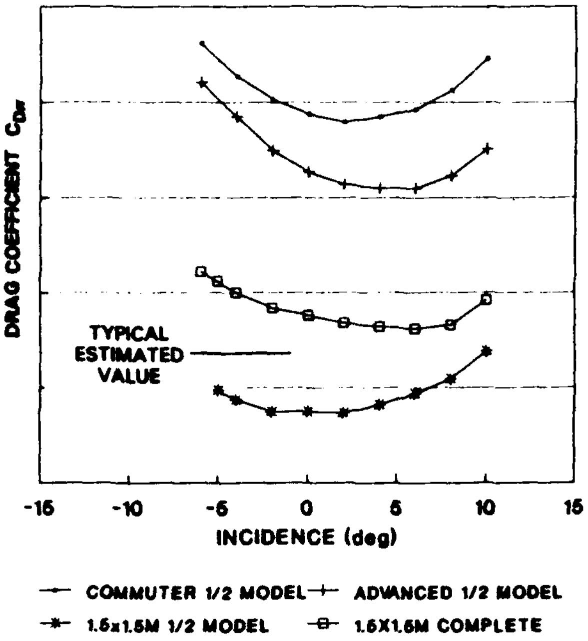

FIGURE 17. ISOLATED FUSELAGE DRAGS
Various Installations

IAR 1.5m TRANSONIC TUNNEL

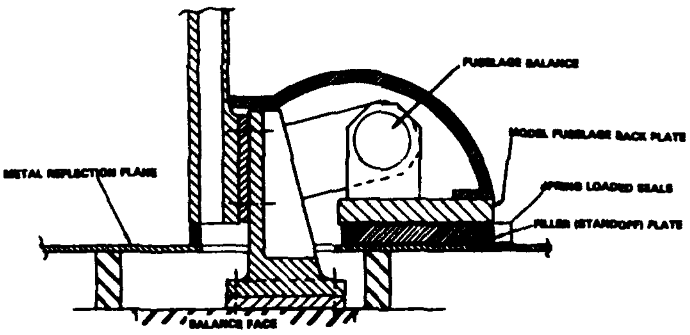

IAR 2m x 3m LOW SPEED TUNNEL

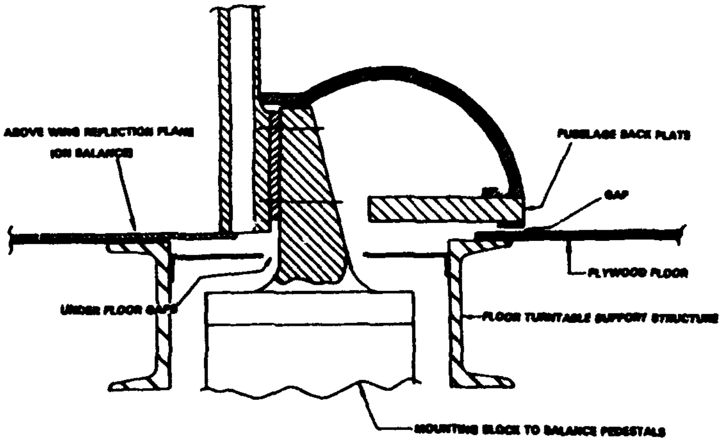

FIGURE 18.

REFLECTION PLANE MODEL - MOUNTING SYSTEMS

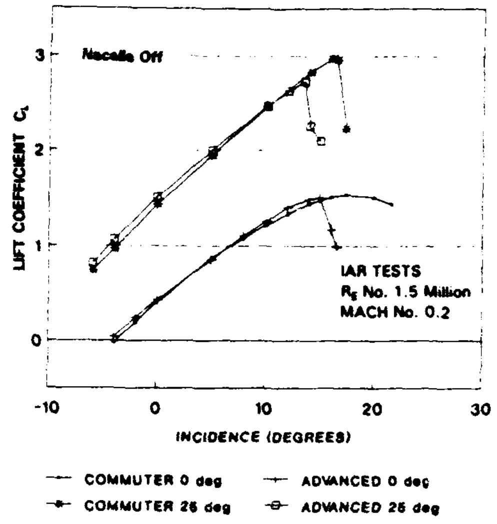

FIGURE 19. HALF MODELS - LIFT PERFORMANCE
Single Slotted Flap

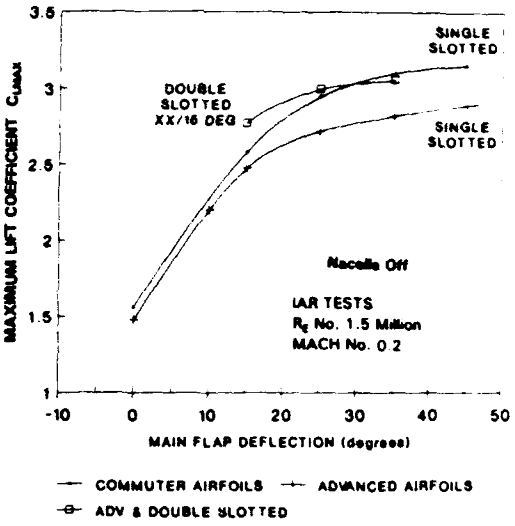

FIGURE 20. HALF MODELS - LIFT PERFORMANCE
Single and Double Slotted Flaps

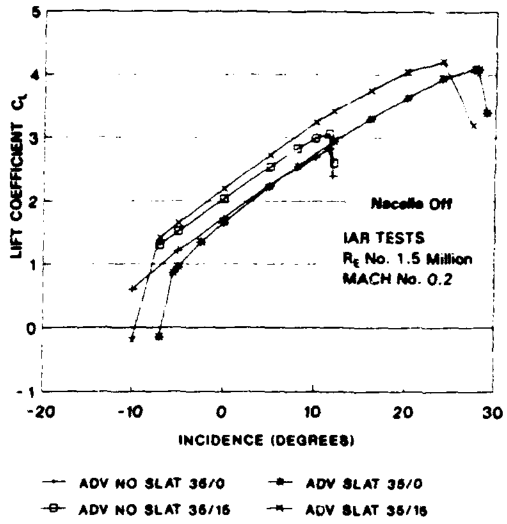

FIGURE 21. HALF MODELS - LIFT PERFORMANCE
Single and Double Slotted Flaps, Slat

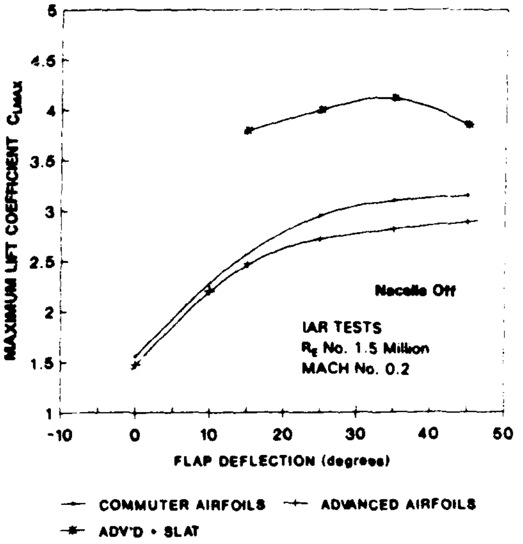

FIGURE 22. HALF MODELS - MAXIMUM LIFT PERFORMANCE
Single Slotted, Double Slotted and Slat

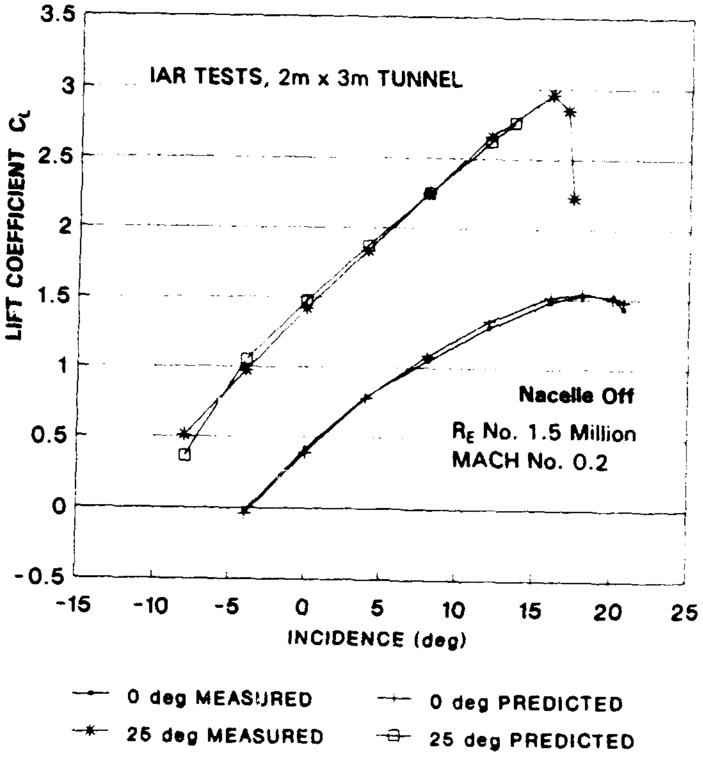

FIGURE 23. COMPARISON WITH PREDICTIONS
Commuter Airfoils - Lift

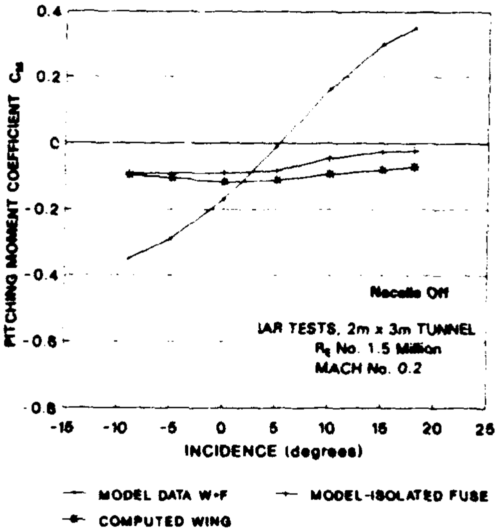

FIGURE 24. COMPARISON WITH PREDICTIONS
Commuter Airfoils - Pitching Moment, Flaps Retracted

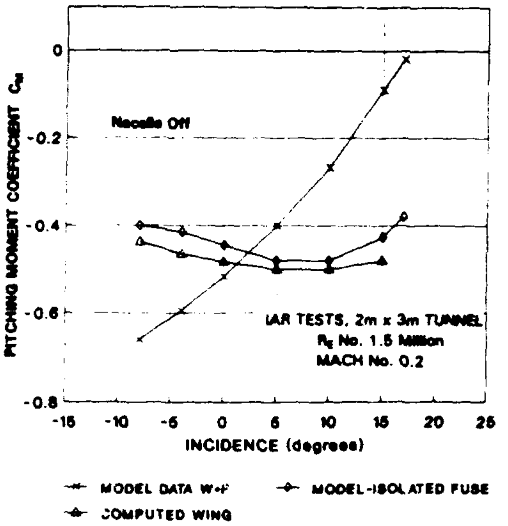

FIGURE 25. COMPARISON WITH PREDICTIONS
Commuter Airfoils - Pitching Moment, Flaps 25 degrees

CHOICE AND OPTIMIZATION OF A HIGH-LIFT SYSTEM FOR AN ADVANCED AMPHIBIOUS AIRCRAFT

M.A. Averardo
M. de Leo
V. Russo
Flight Technology - D.T.T.
ALENIA AERONAUTICA
80038 Pomigliano D'Arco - Napoli - Italy

SUMMARY

The design history of a flap system for an advanced amphibious aircraft is presented in this paper. All the most significant phases of the 2D theoretical studies and the experimental 2D and 3D investigations which have allowed to achieve the final geometry of the high-lift device will be described and, hence, the design criteria, the methods of analysis, the choices will be pointed out.

Starting from the preliminary design of several flap systems, the development of this project needed a great deal of numerical studies and Wind-Tunnel tests in order to select, step by step, the most efficient geometries and to optimize the flap configurations. So, different technical aspects involved with these activities will be discussed: the choice of the flap types to be investigated, related to the special aerodynamic requirements of an amphibious aircraft and to the needs of other design areas (structure, weight, production); the geometrical elements affecting the aerodynamic performance of a high-lift device; general problems connected with theoretical and experimental studies of multi-body systems.

Nomenclature

ALPHA	airfoil angle of attack	(deg)
c	airfoil chord	
CL	airfoil lift coefficient	
CLmax	maximum lift coefficient of airfoil	
CL'	aircraft lift coefficient	
CD	airfoil drag coefficient	
Cm	airfoil pitching-moment coefficient	
Cp	local pressure coefficient	
D	aircraft drag	
D( )	variation of	
DF	flap deflection	(deg)
Re	Reynolds number	
t	airfoil thickness (percent c)	
OV	overlap value (percent c)	
V	aircraft velocity	
X	chordwise non-dimensional co-ordinate	

1. INTRODUCTION

The studies of the flap system play a key role for the aircraft design; the operational features of every type of aircraft, indeed, are strongly affected by the low-speed performance and, so, by the aerodynamic characteristics of the wing high-lift device.

The way a flap system for an advanced amphibious aircraft was designed (as shown in this paper) represents, in general, the activities concerning the development of a new flap geometry and, in particular, the efforts made in researching an efficient high-lift system for a specific project.

A complex technical process, from the early numerical analyses of flapped airfoil configurations until recent experimental investigations of an aircraft scale model, led to the final choice of the high-lift device; different aspects are involved: general design requirements and all the factors which, from the aerodynamic viewpoint, concurred to define the flap system.

1.1. Aerodynamic requirements and design criteria

Amphibious aircraft, more than conventional aircraft, need high low-speed performance: take-off from water, scooping (relative to the fire-fighting version) and alighting in high sea-state, in fact, are very critical basic conditions which determine the operative flight range for this kind of aircraft and, hence, may make an amphibious a successful one.

Therefore, high aerodynamic efficiency in take-off and scooping and high lift values in landing and alighting are essential requirements for a flap system. In particular, very important is the flap efficiency during the take-off from water when, as pointed out by the diagram in fig.1, both aerodynamic and hydrodynamic drag affect the take-off run.

But in designing a wing high-lift device, the effectiveness from the aerodynamic point of view is only one of the elements to be taken into account: the needs relative to the structure, weight, control systems must, in fact, also be considered. Moreover, especially for amphibious aircraft, due to the adverse environmental conditions where often they operate, cost and maintenance easiness play a key role in defining the general characteristics of a flap system.

In this project, structural needs together with problems relative to the control devices to be fitted in the rear part of the wing have sensibly affected, for instance, the choice concerning the flap chord, while cost, maintenance and weight have been some of the determining factors in directing the design towards high-lift systems involving simpler technical solutions.

1.2. Design strategy

This section provides a synthesis of the activities performed for designing the high-lift device, based on a series of theoretical and experimental investigations of several flap geometries. The different phases of this study follow the logical sequence (depicted in fig.2) of typical works in aerodynamics.

After a preliminary and more general analysis, the attention was focused on two flap systems, having the same (or similar) chord length: double-slotted (vane-flap type) and single-slotted flap devices. Each of them was, at first, theoretically studied in order to attain as efficient geometries as possible; then, a 2-D Wind-Tunnel testing of the two types of flap was performed. Through the same approach (theoretical analysis and subsequent experimentation) a single-slotted high-lift system, characterized by a larger flap chord and by a new designed slot geometry of the main-body, was studied for obtaining an improvement of the airfoil high-lift characteristics.

At the end of these 2-D investigations, a great deal of information about the performance achievable by means of different types of flap system was available; on the basis of these data and also considering the factors which, beyond the aerodynamic design, concern the activities of other groups involved in this project (structures, flight mechanics, production, control systems) the high-lift device was chosen.

Finally, Wind-Tunnel tests of a 1:15 scale model of the aircraft were useful to verify, in three-dimensional flow conditions, the performance of the selected flap and to optimize its configuration.

2. GEOMETRIES

The high-lift device under study is relative to airfoils derived from NACA 6-series wing sections, modified in the regions of leading edge and trailing edge, with percent thickness varying from 18 to 15. Flapped configurations of two airfoils (percent thickness of 16 and 18) were especially investigated; for each one, as mentioned before (sec.1.2), single and double-slotted (vane-flap) systems were studied. A picture of the two types of flap is given in fig.3.

Evaluations concerning the high-lift performance achievable through such flap devices, based on previous experiences and literature data about wing sections, led to a preliminary definition of the chord length: values of 30 per cent for vane-flap and of 30 to 35 per cent for single-slotted flap systems.

2.1. Why a vane-flap

Taking into account the need of achieving lift performance as high as possible, since the preliminary phases of this study the potentialities of several double-slotted flap systems have been considered. However, due to the manufacturing and maintenance difficulties, in addition to weight and cost penalties, relative to the linkage system when a relative motion between the flap elements is required, the interest has been soon directed towards double-slotted devices whose fore element (vane) and the main(aft)-flap deflect together as a unit around a fixed pivot. Indeed, such a system, thanks to the boundary-layer control performed by the vane, allows to achieve, especially at large deflections, higher lift values than the ones obtainable through single-slotted flaps and, at the same time, does not involve the typical structural complexity of the multi-body devices.

2.2. Why a single-slotted flap

The investigation of high-lift systems which involved simple structural solutions has always been a primary interest for this project; therefore, contemporaneously with the development of the vane-flap, several single-slotted flap geometries were analysed, looking for attaining, by means of an appropriate shaping, aerodynamic characteristics (especially values of the maximum lift coefficient) close to the ones obtainable through more complicated systems as multi-body flaps. On this scenario, theoretical and experimental studies of a family of single-slotted flaps (with different chord extents) were carried out; in particular, analyses of systems with a 30% and, more recently, a 35% flap chord took place.

2.3. Problems in designing slotted-flap systems

Not only the flap geometry, but also the slot(s) contour, the lip location, the combinations of gap and overlap (fig.4) determine the performance of a single or multi-slotted high-lift device; such a system, indeed, may be considered as a whole of geometrical characteristics, each of them directly affects the aerodynamic behaviour of the airfoil and, at the same time, also affects the role played by the other ones. This makes the design of slotted flap systems a very complicated task, as confirmed, in developing this project, by the large number of theoretical studies and experimental tests were needed for achieving a successful geometry, able to provide the high-lift performance required.

In particular, very difficult is the analysis of flapped geometries (concerning, for instance, different gap/overlap values) at incidence approaching the stalling angle, because in this case, while no accurate theoretical predictions are possible, the low values of local Reynolds number in the slot(s) region(s) make also the experimental investigation a complex one.

2.4. Flap setting

The choice of the flap deflections relative to the operative flight conditions of the aircraft is a crucial phase for the design of a high-lift system. In general, the flap setting is the result of a compromise between the need of achieving lift performance in landing as high as possible and the requirements of high aerodynamic efficiency during take-off and the other low-speed flight operations.

The solution of such a problem becomes a very difficult one when considering flap devices whose rearward movement is defined by a circular path around a single pivot, because, in this case, much more complicated is to optimize the different configurations. In the case under study, deflection angles of 40 to 45 degrees for single-slotted devices and of 45 to 50 degrees for vane-flaps were taken into account as suitable maximum values, while deflections of 15 and 30 degrees were considered as potential for take-off and approach, respectively. On the basis of these values, a preliminary design of geometries was developed; the subsequent phases of the theoretical study and the experimental investigation involved a more detailed analysis of flap deflections, in order to evaluate the airfoil performance in a wide range of configurations.

3. THEORETICAL 2-D STUDIES

3.1. Choice of the numerical code

Before starting on the theoretical studies, a preliminary investigation of methods for the analysis of multi-element geometries in viscous flow was carried out. Taking into account, in particular, the need of estimating the aerodynamic performance of flapped airfoils at high incidence, in presence, hence, of large separated regions, several codes [1,2] were considered, looking for the most suitable one.

The program used is a multi-methods code [2], providing different singularity methods for the inviscid solution and different integral methods for the boundary-layer equations. Concerning the potential field, symmetric distributions of singularities (sources and vortices) on planar panels have been preferred, on the basis also of previous numerical experimentations, to other techniques as Douglas-Neumann, Hess, Green, etc. The solution of laminar and turbulent boundary layers has been achieved, respectively, through Thwaites and Green methods, with direct/inverse techniques. Other program features are the transpiration method for the viscous-inviscid interaction and the empirical criterion of Michel-Smith for the laminar-turbulent transition. The Squire-Young formula is used for calculating the drag coefficient.

3.2. Geometrical Pre-Processing

The paneling is a very important phase for the theoretical study of bodies in viscous flow field; in fact, a good geometry simulation with an accurate points spacing is an essential requirement for a correct analysis of the boundary layer, especially with regard to the laminar-turbulent transition and flow separation phenomena. Moreover, the prediction of aerodynamic characteristics for multi-bodies is strongly affected by the panels distribution in the region(s) of confluent boundary layers, where the computation becomes more complicated.

Therefore, considering the geometrical complexity of the bodies to be analysed, a preliminary study concerning, for each body, the choice of the paneling type and the number of corner points was needed, depending on the relative positions of the airfoil elements and the angle of attack. For instance, in studying flap systems at low deflections (when stronger is the interaction of the flow fields generated by each body) it was necessary to increase the number of panels for obtaining a satisfactory convergence of the iterative process and, so, more accurate results.

An example of paneling for the main-body/vane-flap system is shown in fig.5; the law for distribution of panels (cosine of curvilinear abscissa for the main-body and the aft-flap, constant curvilinear abscissa for the vane element) is pointed out in the slot -entry region. Typical values of panels number for this geometry were: 120/140, 50/60, 60/80 for the main-body, vane and aft-flap, respectively.

In general, for the comparative studies of vane-flap and single-slotted flap systems (as well as of the airfoil clean configuration), the geometries were simulated in such a way as to realize, especially (for multi-bodies) in the slot(s) region(s), similar panels distributions relatively to the number and the length of panels.

3.3. Analysis method

Since the principal aim of the theoretical study was to investigate the high-lift characteristics, primary emphasis was given to the analysis of geometries at large flap deflections and high angles of attack. First of all, it was tryed to get results at incidence close to the expected stalling angle of attack of the airfoil, in order to evaluate the aerodynamic behaviour of the different configurations at the most critical operative conditions. Then, a detailed study in a wide range of flap setting and incidence angles was performed.

Besides the values of lift, drag and pitching-moment coefficients, the pressure distributions were taken into account as very effective means of aerodynamic inspection. In fact, from the analysis of the pressure profiles over the whole airfoil, as well as over the surfaces of each body and over small regions (slots, confluence of boundary layers), it was possible to investigate in detail the different geometries.

Further data about the development of the boundary layer (as the location of the laminar-turbulent transition and flow separation regions) were also considered for a more accurate aerodynamic study.

3.3.1. About the prediction of airfoil stall

The evaluation of the maximum lift coefficient of airfoils through theoretical methods, already a very complicated matter for a single body [3], becomes a much more difficult one when considering multi-body systems in viscous flow. In many cases, indeed, in presence of large separated regions, in addition to the complex fluid dynamic mechanisms connected with the boundary layers interaction, no accurate prediction of the aerodynamic characteristics is possible. However, as the theoretical methods used allow to well simulate the behaviour of a single-body almost up to the stall, on the basis of the results relative to the airfoil clean configuration it was possible to indirectly estimate the stalling angle of geometries with the flap deflected. As consequence, the analysis of such systems was stopped at incidence far enough from the critical values of the angle of attack, but so high as to obtain, anyway, significant information on the effectiveness of the different flap configurations.

3.4. Analysis of vane-flap systems

During the first phase of the study the attention was focused on different combinations of vane and main-flap [4]. In particular, it was taken a special care of designing their relative position, as the effectiveness of the boundary-layer control strictly depends on the way the slot between the two flap elements directs the high-energy air over the upper surface of the aft body.

Some geometries characterized by different relative dimensions of the two bodies were designed, in order to investigate the sensitivity of the aerodynamic flow field and, so, the influence of such modifications on the airfoil performance. Concerning the flap devices shown in fig.6a, sensible better results were achieved through the system having the longer vane and the smaller main-flap, as denoted by the pressure distributions (fig.6b) obtained with the flap deflected 45 degrees at high incidence.

Significant variations of the high-lift characteristics also occurred when flap geometries relative to different vane positions were studied, as the elements (fig.7a) with a relative rotation of two degrees around the leading edge of the vane. The comparison of the respective pressure profiles (fig.7b) shows a more efficient boundary-layer control performed, at large deflections, through the geometry "A"; in fact, in spite of very similar contributions to the total lift value by the two flap arrangements, the different levels of the chordwise pressure distribution over all the upper surface of the main-body involve different lift performance of the airfoil (about 3%).

The study of the vane-flap relative to several gap/overlap combinations (related to different positions of the flap rotation centre) has also played a key role in defining the geometry of this flap system [5]. Among the configurations analysed, two geometries, although characterized by quite different overlap values (fig.8a), gave the same results in terms of global lift performance. They are representative of flap positions involving substantial differences about the slot-end geometry and, so, about the mechanism for the boundary-layer control. From the comparison of the relative pressure profiles (fig.8b), in particular two effects can be observed: while the converging main slot relative to the forward flap position allows to better energize the flow over the upper surface of the main body, the more extended flap involves a larger lift contribution by the vane, due to a stronger fluid acceleration in the region of confluent boundary layers. Situations like this, depending on the complex phenomena connected with multi-body systems in viscous flow, were frequently observed during the study concerning a wide grid of pivot positions. It must be said, however, that the relative behaviour of generic flap configurations may sensibly change, especially at large deflections, by increasing the angle of attack; so, more internal flap positions, even though more effective at low and medium incidence, might cause anticipation of airfoil stall, due to stronger adverse pressure gradients.

The lift curves concerning the airfoil equipped with one of the most efficient vane-flap systems are shown in fig.9a; to be noted the flap effectiveness in progressively improving the airfoil lift performance. Furthermore, considering also the pitching-moment coefficient (fig.9b), one can observe that the pressure centre (located, approximately, at the quarter chord point with flap retracted) shifts rearward (about 0.02c) by increasing up to 15 degrees the flap deflection, while it shifts forward (about 0.03c) by varying the deflection from 15 to 45 degrees.

3.5. Analysis of single-slotted flap systems

Two phases have characterized the design of the single-slotted devices: the first one concerned the project of flaps with chord varying from 30 to 32 per cent of airfoil chord and configurations similar to the vane-flap under study; the second one [6] was relative to a single-slotted system with more significant modifications of geometry and an increased (0.35c) flap chord.

3.5.1. Thirty/Thirty-two per cent flaps

Several geometries and, for each one, several configurations (relative to different gap/overlap values) were studied. The flap profiles were designed likewise the vane-flap system previously analysed; however, some little modifications of curvature were introduced. The results obtained, compared with the ones concerning equivalent configurations (with the same gap/overlap values) of the vane-flap, showed a sensible decrease of high-lift performance, especially at large flap deflections, where the effectiveness of the boundary-layer control rapidly goes down.

One of the single-slotted flaps studied and the vane-flap, both deflected 45 degrees around the same pivot, are compared in fig.10a. The relative pressure distributions (fig.10b) clearly denote the loss of effectiveness associated to the single-body flap system; the sensible lower expansion over the upper side of the airfoil points out the function of the vane element of the double-slotted device which energizes the flow and, so, delays separation.

3.5.2 Thirty-five per cent flap

The study of single-slotted devices with a larger flap chord was carried out trying to improve the lift performance estimated for similar geometries having a smaller chord length and, so, trying to approach or, if possible, to attain the theoretical results relative to the vane-flap system with a smaller chord (0.30c).

Since the basic geometrical condition was to not change either the curvature or the airfoil thickness, the flap geometries analysed resemble, for the rear part, the profiles of the vane-flap and single-slotted systems previously defined. Obviously, according to the problems (discussed on sec.2.3) concerning the design of slotted-flap devices, the project of the new geometry involved a series of studies about the geometrical elements which concur to define a high-lift system: the slot-entry profile, the lip extent and, above all, the gap and overlap values. In this case, the slot shape of the main-body was sensibly modified, due to the increment of flap chord, while the lip was moved towards the normal trailing-edge position for taking greater benefits of the extended flap configuration.

Concerning the pivot, a careful analysis was needed, in order to attain, for each deflection connected with the large backward flap movement, an efficient boundary-layer control through an appropriate (converging) slot. As an example of the sensible variations of performance by changing the pivot, pressure profiles (fig.11) concerning different overlap values indicate that more internal flap positions provide, at large deflections, better results.

a) Comparison with the vane-flap

In fig.12, showing the flap system under study and the vane-flap device, the change made in the rear part of the main-body, the variation of the airfoil curvature at high deflection, the different chord extents may be observed.

Of great interest is the relative behaviour of the two flaps at different angles of deflection (see fig.13). While these systems involve quite similar lift values at high deflections when, due to large separated regions, the boundary-layer control through the vane plays a key role, a sensible increment of performance by means of the single-slotted geometry was attained at small and medium deflections, when the airfoil chord extent (with the flap deflected), the shape of the slot, the local curvature and, in general, the elements which all together make a multi-bodies geometry become more significant. The pressure distributions (fig.14) reflect this situation.

The polar and pitching-moment curves denote similar trends for the two flaps up to 30 degrees of deflection: in fact, no significant variations of efficiency exist, while the differences in terms of pitching-moment coefficients are proportional to the lift values. On the contrary, a rather different behaviour of the single-slotted flap can be observed at large deflections (45 degrees), when the location of the pressure centre shifts forward (about 0.02*c) relatively to the vane-flap system.

b) Comparison with smaller single-slotted flaps

In the whole range of flap deflections a very large improvement of lift performance was attained through the new single-slotted flap, whose geometry is compared (fig.15a) with a 30% single-body flap. As pointed out by the pressure distributions (fig.15b), the stronger expansion over the upper surface of the main-body is responsible for the high increase of the total lift values achieved through the extended system, while the flap contributions are quite similar.

3.6. Concluding remarks

This series of theoretical studies provided a good prediction of the aerodynamic performance of airfoils equipped with single or double-slotted flaps. In fact, although the analysis of multi-element geometries is a very difficult one, the computation methods allowed to evaluate the characteristics of high-lift devices also at conditions (high incidence and large flap deflections) where more significant and, at the same time, more complex the study of such systems becomes.

Concerning, in particular, the investigation of gap and overlap, a special topic for the flap design, rather definite indications, depending on type of geometry (single or double-slotted), were obtained. According to the theoretical analysis, indeed, while more external positions of the vane-flap turned out to be better, single-slotted geometries needed, in general, a more definite converging slot (connected with larger overlap values) for achieving an effective bondary-layer control.

From the whole spectrum of the investigations performed, the vane-flap appeared as a very efficient geometry for attaining the special requirements of a flap system for amphibious aircraft; in fact, it was necessary to increase the chord of single-slotted flaps up to 35% for achieving (at large deflections) and improving (at small deflections) the performance of airfoils equipped with the vane-flap (0.30c). It was just the extended single-body flap a possible alternative to the vane-flap system, as confirmed by the subsequent experimental studies.

Nevertheless, an intensive Wind-Tunnel experimentation of all the high-lift devices studied was planned, looking for the information needed for confirming and better defining the theoretical results.

4. EXPERIMENTAL 2-D STUDIES

Somewhat definite results concerning the most powerful high-lift systems had been achieved at the end of the theoretical studies. Therefore, the experimentation was aimed at analysing especially the vane-flap device, after its estimated higher performance in comparison with equivalent (of equal chord) single-slotted systems was verified; afterwards, as potential for alternative solution, the extended (35% of airfoil chord) single-slotted flap was tested.

4.1. Investigation planning

The first phase of the experimental studies concerned the investigation of airfoils equipped with the vane-flap and families of single-slotted devices with 30-32 per cent of chord extent. Through quasi-2D tests in the Wind Tunnels of Naples University and of Turin University, the comparative studies were performed, while an experimental analysis of the vane-flap system in strictly 2-D conditions took place in the Wind Tunnel of Stuttgart University [7].

The second part of the experimentation, held in the Wind Tunnel of Naples University (1991), was devoted to the single-slotted geometry with 35% of airfoil chord.

4.2. Investigation methods

The indication from the theoretical study about the most efficient combinations of gap and overlap, for each flap geometry, was useful to pilot the experimental activities. In fact, through Wind-Tunnel tests, in many cases, the airfoil aerodynamic characteristics relatively to some particular pivot positions were analysed, trying to optimize such configurations and, thus, avoiding teting other feasible flap arrangements.

For each high-lift system and each configuration, the airfoils were experimented at different flap deflections, in order to attain a clear picture of performance for all the operative flap range.

4.3. Preliminary tests of vane-flap and single-slotted systems

The early Wind-Tunnel testing consisted in determining the most powerful configuration(s) for the vane-flap geometry; several arrangements of the vane element were experimented, as well as the pivot positions which, on the basis of the theoretical study, might have allowed the best airfoil performance.

From the tests concerning different relative positions of the two flap elements, variations of lift values (about 4%, at high deflections) quite similar to the ones given by the theoretical analysis (sec.3.4) were found.

Also the results obtained with regard to the aerodynamic behaviour of the airfoil by varying the gap/overlap combinations confirmed, for the most part, the theoretical predictions. The curves of fig.16, for instance, indicate the variation of high-lift performance associated to different overlap values; in this case, the more external flap position, although less efficient up to high incidence, allows to sensibly improve the airfoil aerodynamic characteristics close to the stall. This situation, typical of the vane-flap behaviour at large deflections, has been decisive for the conclusive definition of the flap system.

During the same campaign, some single-slotted flaps were tested, not only in order to determine other potential wing high-lift devices, but also for evaluating the loss of lift performance in comparison with the vane-flap system. Several lift curves relative to the vane-flap and to one of the most efficient single-slotted flaps experimented are shown in fig.17. This diagram is representative of the difference of lift values achievable, at large and small deflections, through single or double-slotted flaps (with the same chord), as derived, in accordance with the indication of the theoretical study, from this experimentation.

4.4. Experimentation of the vane-flap system (Part 2)

Two airfoils with a maximum percent thickness of 16 and 18, equipped with the vane-flap device, were tested in the Wind Tunnel of Stuttgart University. The aim of this campaign was to investigate the vane-flap system in strictly 2-D conditions, after its geometry had been defined as result of theoretical studies and previous experimentations.

Several tests, referring to different experimental conditions (techniques of laminar-turbulent transition, Reynolds number) were performed for both airfoils. The most interesting results are presented in fig.18. As shown by the lift curves, the behaviour of the two airfoils is similar, both at small and large flap deflections, also by varying the Reynolds number. The information obtained, with special regard to the maximum lift coefficient, were useful to predict the aircraft low-speed performance achievable, in full scale, through this flap system.

4.5. Experimentation of the extended single-slotted flap.

The last campaign of 2-D Wind-Tunnel tests concerned the experimental study of the single-slotted device with the increased (35%) flap chord.

This system has given very interesting results, confirming its greater potentiality, already known from the theoretical analysis, in comparison with the vane-flap. As clearly denote the lift curves (fig.19), the performance achieved at small and medium deflections is sensibly better than the one obtained through the double-slotted system, while with the full deflected flap it is rather difficult to analyse the behaviour of the airfoil equipped with the two high-lift devices, in spite of different values of the maximum lift coefficient. Anyway, what appears with evidence is the improvement of the airfoil lift performance obtainable through this single-slotted flap, considering the whole operative range of deflections. Furthermore, the new system, compared to the vane-flap geometry, does not involve significant penalties of drag and pitching-moment coefficients.

5. CONCLUSION OF TWO-DIMENSIONAL STUDIES

The end of the Wind-Tunnel 2-D tests has represented a milestone for the flap system design, as the following phases concern a series of correlation activities between the results of the experimental and theoretical studies and, then, the final choice of the high-lift device.

5.1. Comparative analysis of theoretical and experimental results

The design of the flap system has been based, as in general for a new geometry design, on the study of different configurations, trying to achieve, through the analysis of the relative performance, the flap profile, the slot shape, the pivot position which, all together, make an effective high-lift device. The theoretical study first and, then, the experimental investigation were aimed at performing such a comparative analysis; the geometries and the relative flap arrangements, as derived from the theoretical design, were experimented through a series of Wind-Tunnel tests in order to verify all the theoretical indications and predictions.

According to this "qualitative" method of comparison between the theoretical and experimental results, the Wind-Tunnel experimentation has confirmed for the most part, as pointed out in the previous sections, the theoretical conclusions referring to the different types of flap tested, different flap and slots profiles, different gap/overlap values and so on.

An absolute comparison, made possible by the strictly 2-D conditions of the Wind-Tunnel testing (see sec.4.4), is presented for the vane-flap system in fig.20, where some experimental results, obtained for different flap deflections, are compared with the ones derived from the theoretical analysis. First of all, the very good accordance between the theoretical and experimental lift curves concerning the airfoil clean configuration may be observed; moreover, in spite of an over-estimate of airfoil performance with the flap deflected, the quite similar values of the curves gradient in the whole range of deflections confirmed the validity of the theoretical predictions. Remarkable is also the accordance of the theoretical and experimental values of pitching-moment coefficient: not only considering the absolute data, but also because of the similarity of the curves slope, which confirmed the estimate of position of the aerodynamic centre at different flap deflections.

5.2. Choice of the flap system

The theoretical and experimental 2-D studies have given three main answers. The first one is the vane-flap, which can be considered as the main object of the whole project: that is a flap system, without special structural complications, able to satisfy the aerodynamic requirements. The second one is the gain of lift performance attainable through double-slotted devices with reference to single-slotted flaps having the same chord. The third one is the single-body flap with the increased chord: born as alternative solution to the vane-flap, this system has shown, indeed, great potentialities.

On the basis of such results, rejected the hypothesis of single-slotted flaps with small chord (up to 30%), from the aerodynamic point of view no doubt existed about the advantages connected with the extended single-slotted system in comparison with the vane-flap. In fact, the remarkable improvement of lift performance in almost the whole range of flap deflections, theoretically estimated and also confirmed by the Wind-Tunnel 2-D experimentation, clearly indicated such a high-lift device as the most efficient, also considering possible drag and pitching-moment penalties in three-dimensional conditions.

But, what made very difficult the choice of the most suitable high-lift system was the influence of other design areas which, in addition to the aerodynamic criteria, had to be considered. In fact, problems connected with the structure, weight, control systems, production and maintenance costs, etc., which had already sensibly affected, at the beginning, this project in determining feasible types of flap, also played a key role in conclusion of the two-dimensional studies, when the final decision about the flap system was taken.

So, structural and manufacturing complexities, weight, problems relative to the arrangement of several control devices, were all factors, depending on the larger flap chord and a more complex linkage system (due to the more downward pivot location) which penalized the extended single-body flap. The design of such a system, thus, was stopped at this point, without performing a 3-D testing.

As consequence, the vane-flap which, since the beginning of this study, had been considered as a very powerful system for achieving the lift performance needed and which through theoretical and experimental investigations confirmed this potentiality, was chosen as high-lift device. This was the flap which equipped the 1:15 scale model of the aircraft, during the 3-D Wind-Tunnel tests campaigns.

6. EXPERIMENTAL 3-D STUDIES

The aircraft performance achievable, in a wide field of aerodynamic conditions, through the flap system selected have been analysed on the basis of Wind-Tunnel tests [8] performed on a 1:15 powered model of the aircraft (Turin University). In fact, experimentations concerning different values of thrust coefficient, in free-air and ground-effect, both with full operating propulsive system and in one engine-out condition, were carried out for the whole flap setting, also by varying the deflection of the other movable surfaces (elevator, rudder, ailerons, spoilers).

Before these experiments, a flap testing concerning different pivot positions was performed, in the same Wind Tunnel and on the same aircraft model. The object of this preliminary investigation was to analyse, in three-dimensional conditions, the behaviour of the high-lift system by changing the gap/overlap combinations, looking for a configuration able to satisfy the aerodynamic requirements: high efficiency at small and medium deflections (take-off and approach), high values of CLmax at medium and large deflections (approach and landing).

The results confirmed, in general, the conclusions of the two-dimensional studies; in particular (fig.21), a very interesting result is the improvement of values relative to the maximum lift coefficient and the stalling angle of attack achievable, at large deflections, by means of more external flap positions, in accordance with the theoretical predictions and the indications from the two-dimensional experimental analysis (see sec.4.3, fig.16).

7. CONCLUSION

When the study of the flap system started, the best type of high-lift device, the best flap positions, the most suitable values for the angles of deflection, were all unknown elements.

Previous experiences concerning theoretical and/or experimental studies of multi-body systems and other data derived from literature of wing sections were able to provide a few partial indications about the above questions and, in general, the problems connected with the aerodynamic study of multi-element geometries. Only applications to specific projects, indeed, can provide, in general, the data needed for designing a flap system; so, only theoretical studies and experimental investigations, devoted to analyse a great number of flap configurations, have allowed to achieve the final goal of this work.

The flap system chosen is the answer to different needs: structural and manufacturing solutions in accordance with the general design criteria for this type of airplane, aimed at reducing the costs of production; high aerodynamic effectiveness in the whole range of operational low-speed conditions, in accordance with the requirements of an "advanced" aircraft.

Acknowledgements

The authors wish to express their own gratitude to colleagues of the Aerodynamics department for their suggestions and cooperation. Special thanks to Mr.M.Manco for his contribution to the lay-out of this paper, particularly with regard to the diagrams and the other pictures.

REFERENCES

1. Cebeci, T., Jau, J., Vitiello, D.: An Interactive Boundary-Layer Approach to Multi-element Airfoils at High Lift. AIAA 30th Aerospace Sciences Meeting, Reno, Nevada, 1992.

2. de Nicola, C., Coiro, D., Losito, V.: An efficient Multi-Methods Computer Code for the Prediction of the Inviscid and Viscous Flow over Multi-Component Airfoils. - AIAA, 1st National Fluid Dynamic Congress, Cincinnati, Ohio, 1988.

3. Cebeci, T., Jau, J., Vitiello, D.: Prediction of Post-Stall Flows on Airfoils. - IV Symposium on Numerical and Physical Aspects of Aerodynamic Flows, CSULB, January 1989.

4. Russo, V., Gugliotta, F., Vitiello, V.: Studio per la Definizione di un Sistema di Flap a Doppia Fessura e Confronto con Flap a Singola Fessura. - VII Congresso Nazionale AIDAA, Napoli, 1983.

5. Averardo, M., A.: Study of vane-flap configurations - Internal ALENIA Reports 5B790013 (1990), 5B790025 (1990).

6. Averardo, M., A., de Leo, M.: Study of a new single-slotted flap -Internal ALENIA Reports 5B791017 (1991), 57B91085 (1991)

7. Althaus, D., Wurz, W.: Wind-Tunnel tests on the SH316 and SH318 airfoils. (Ordered by ALENIA). Stuttgart, 1989.

8. Esposito, G., Manco, M.: Wind-Tunnel tests on 1:15 powered model of Advanced Amphibious Aircraft. Internal ALENIA Report 57B91101 (1991).

9. Abbott, I., H., von Doenhoff, A., E.: Theory of wing sections. Dover Publications Inc., New York, 1959.

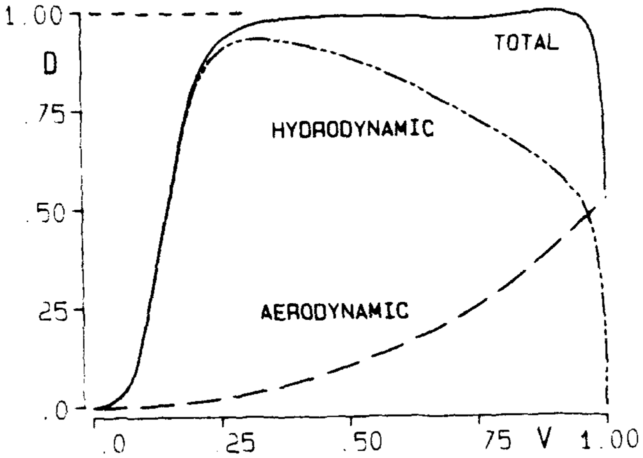

Fig.1 - Drag components of aircraft during take-off from water up to lift-off velocity.

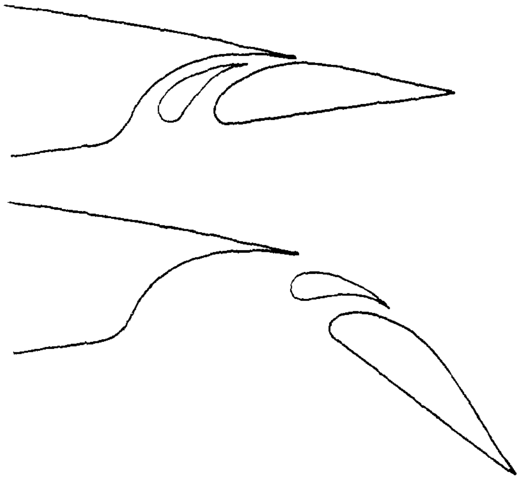

Fig.3 - Some of the flap systems studied: retracted and deflected positions.

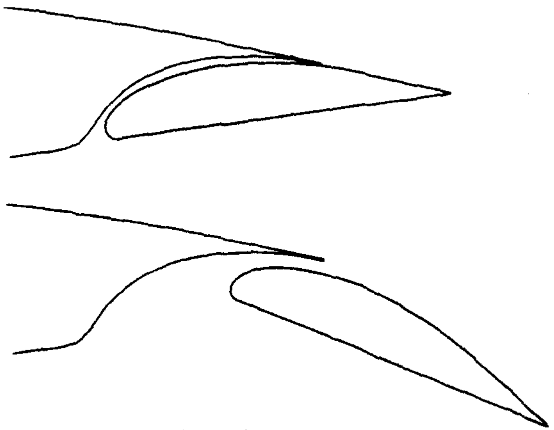

Fig.3 - (concluded)

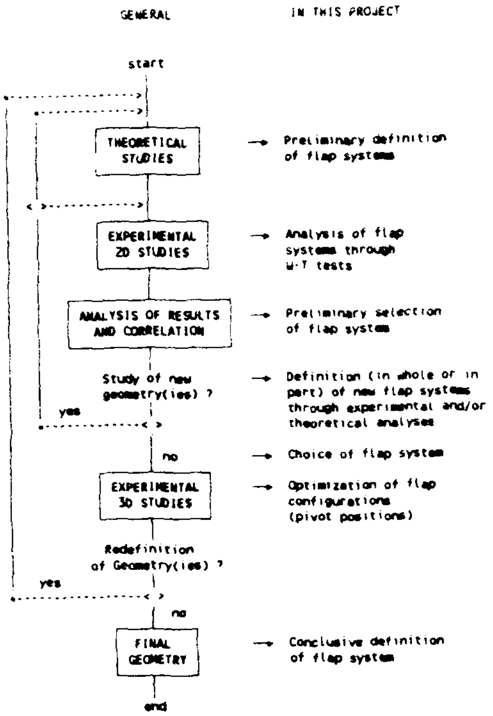

Fig.2 - Flow chart of standard activities for the aerodynamic design.

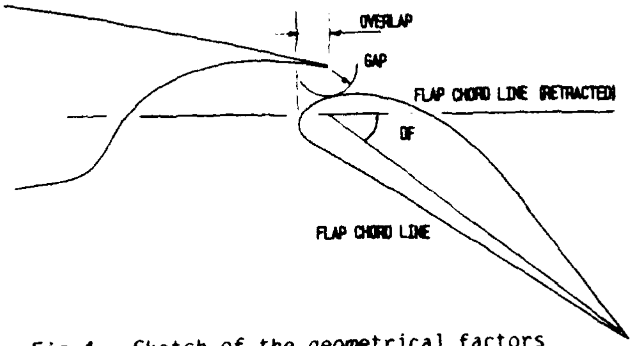

Fig.4 - Sketch of the geometrical factors (gap, overlap) affecting the flap position for a given deflection.

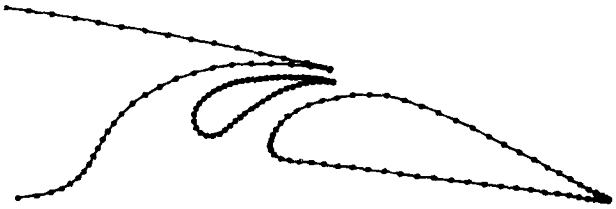

Fig.5 - Paneling of main-body/vane-flap geometry: detail of flap elements and slot-entry region.

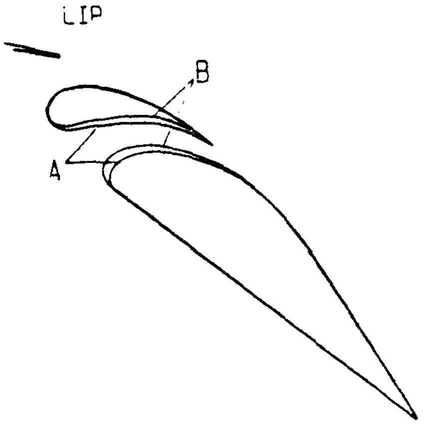

Fig.6a - Different configurations of vane and main-flap.

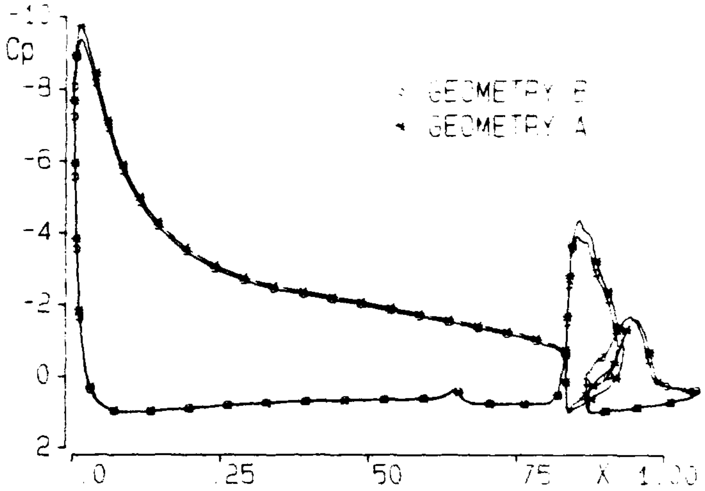

Fig.6b - Theoretical pressure distributions.

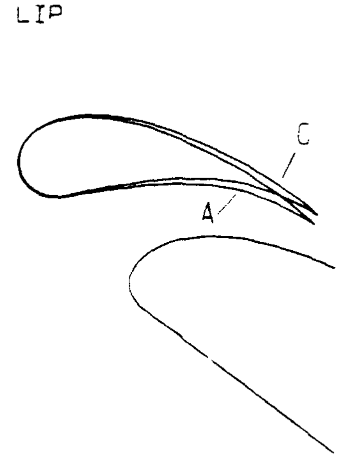

Fig.7a - Vane-flap system: different positions of the fore element.

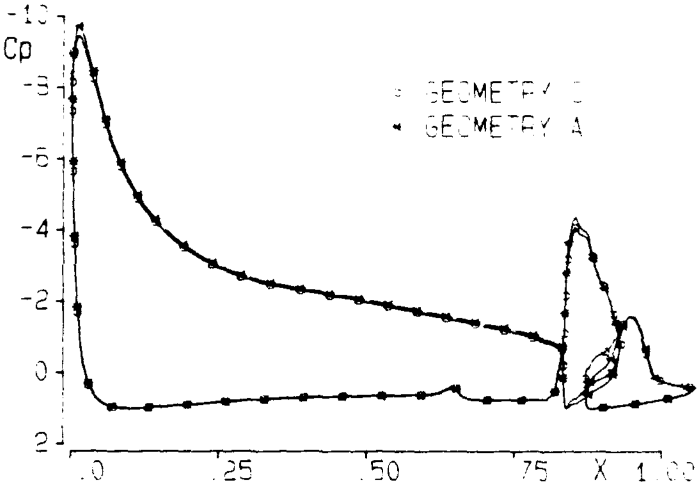

Fig.7b - Theoretical pressure distributions.

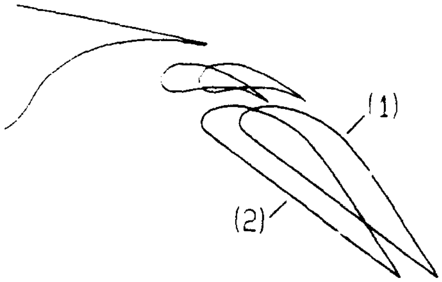

Fig.8a - Configurations of vane-flap system for different overlap values.

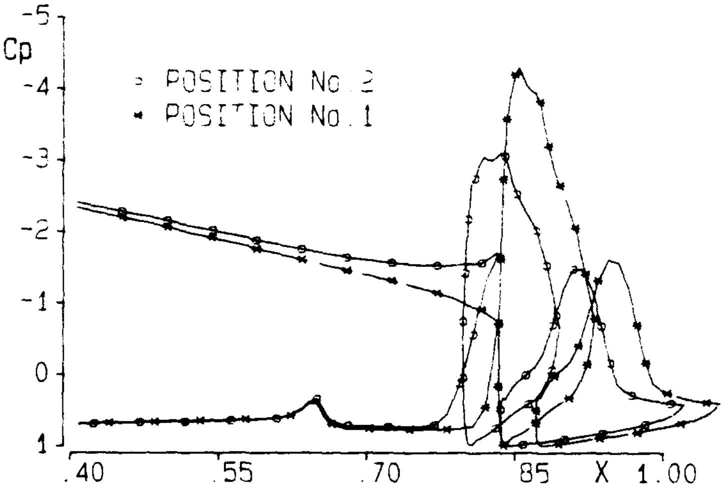

Fig.8b - Theoretical pressure distributions (detail).

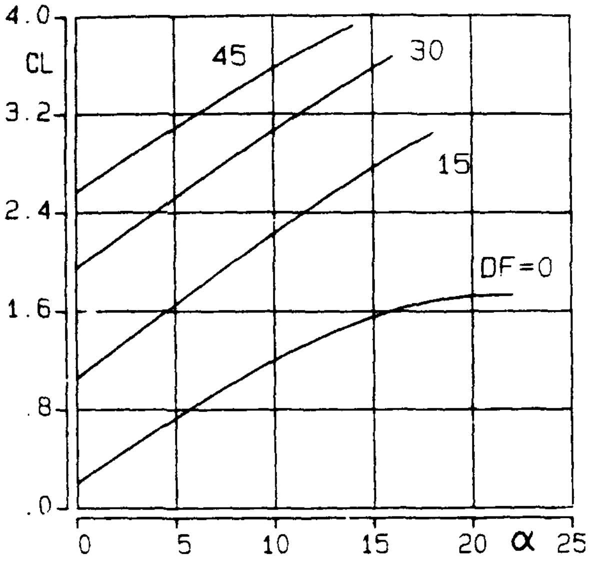

Fig.9 - Theoretical aerodynamic coefficients of the airfoil equipped with the vane-flap system (0.30c).
a) Lift curves

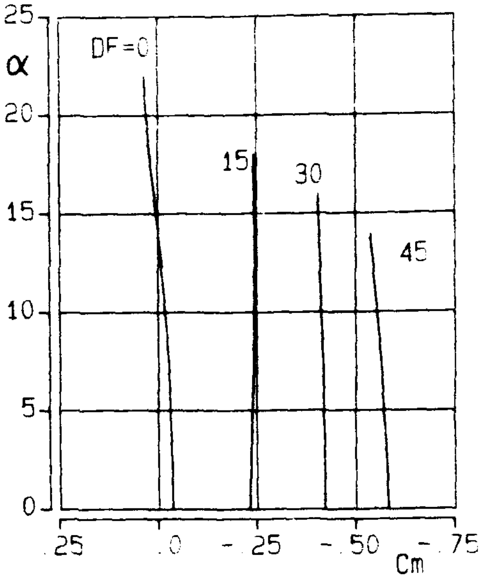

Fig.9 - (concluded) b) Pitching-moment curves

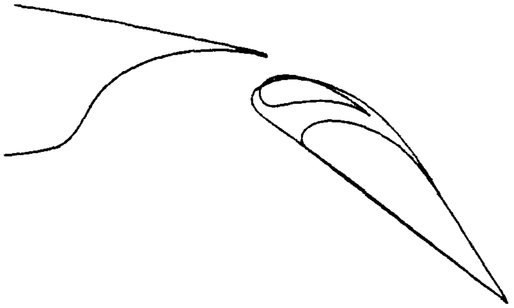

Fig.10a - Comparison of vane-flap and single-slotted systems (0.30c).

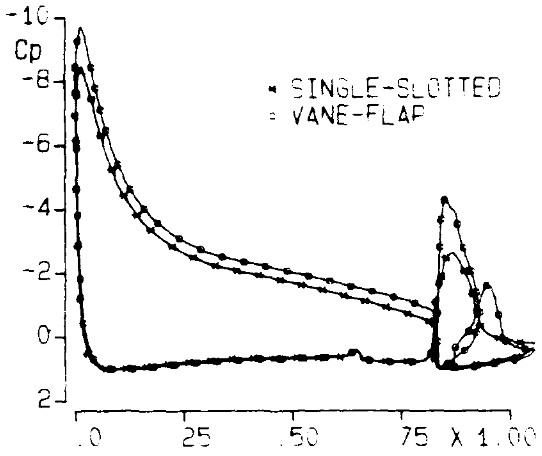

Fig.10b - Theoretical pressure distributions.

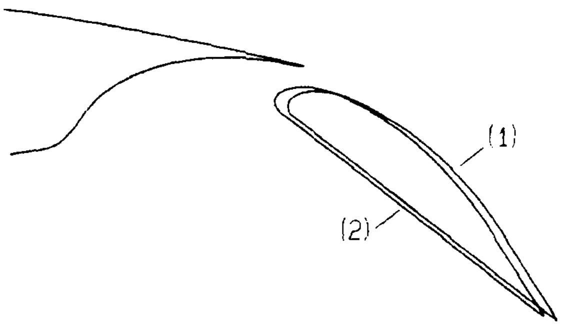

Fig.11a - Different configurations of single-slotted flap (0.35c).

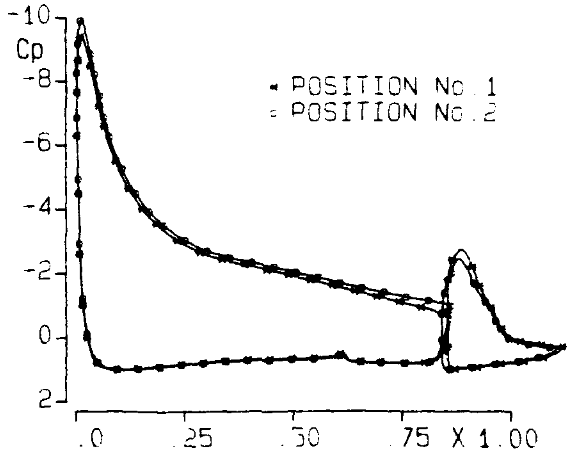

Fig.11b - Theoretical pressure distributions.

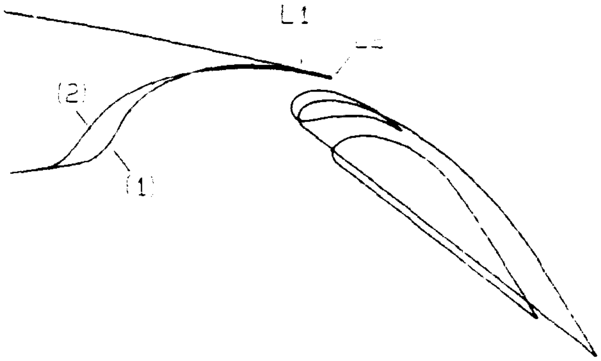

Fig.12 - Vane-flap [0.30c] (1) and single-slotted [0.35c] (2) systems; L1, L2: respective lip positions.

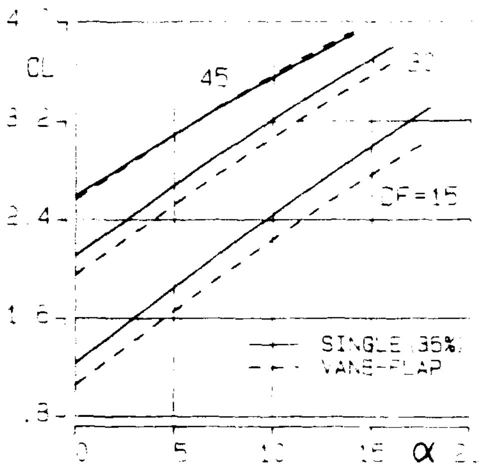

Fig.13 - Theoretical aerodynamic coefficients for vane-flap [0.30c] and single-slotted [0.35c] systems.
a) Lift curves

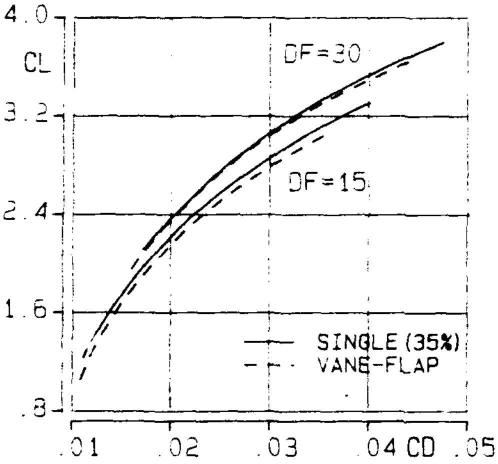

Fig.13 - (continued) b) Polar curves

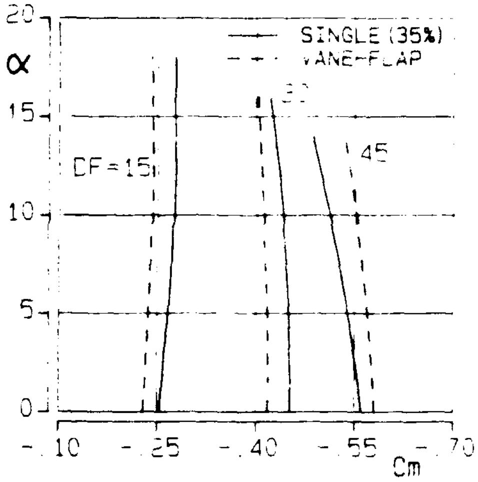

Fig.13 - (concluded) c) Pitching-moment curves

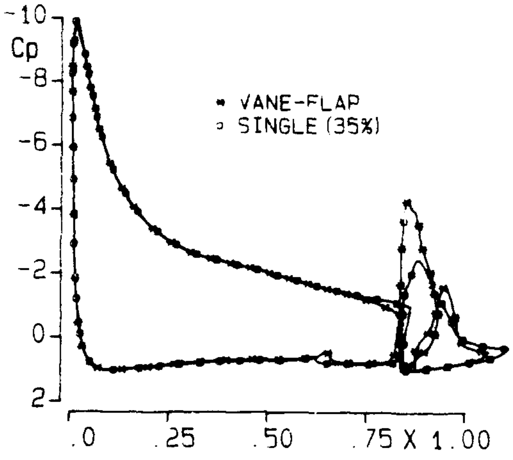

Fig.14 - Theoretical pressure distributions of vane-flap (0.30c) and single-slotted (0.35c) systems; DF=45.

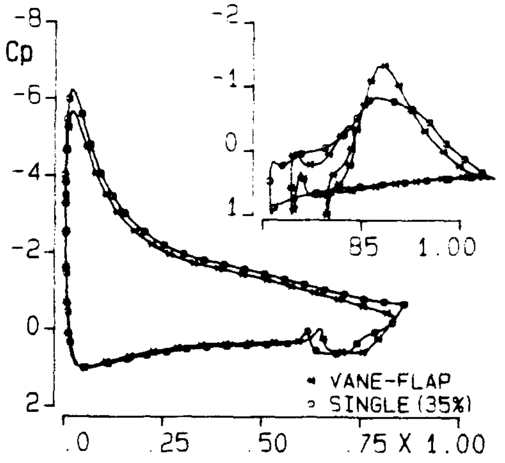

Fig.14 - (concluded) DF=15

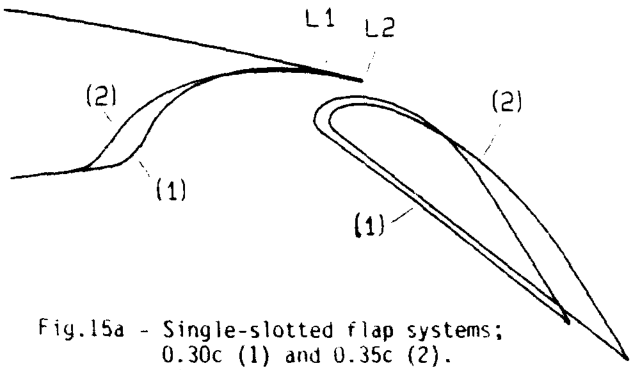

Fig.15a - Single-slotted flap systems; 0.30c (1) and 0.35c (2). L1, L2: respective lip positions.

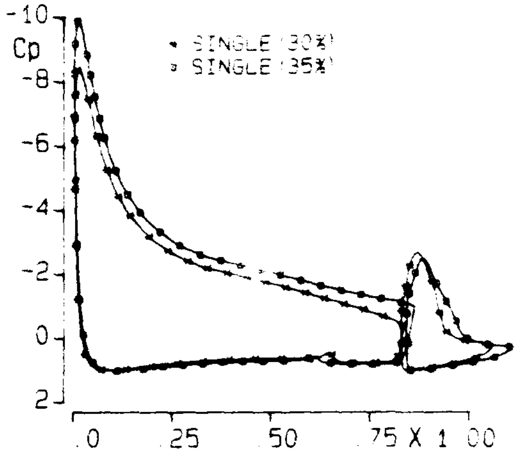

Fig.15b - Theoretical pressure distributions.

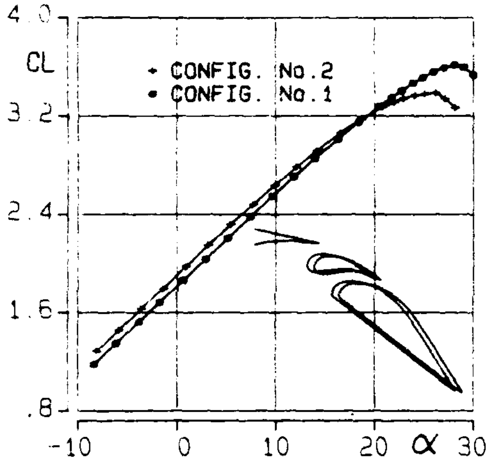

Fig.16 - Experimental lift curves concerning rearward (1) and forward (2) positions of vane-flap geometry (0.30c).

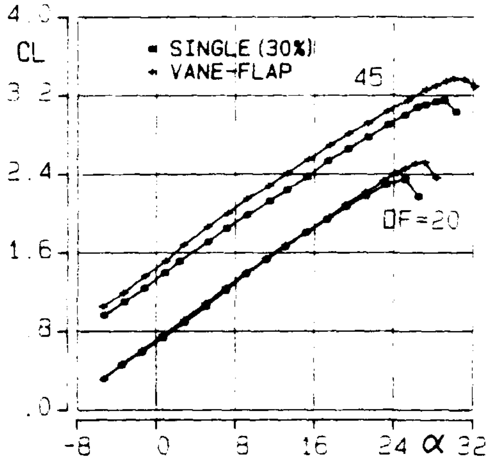

Fig.17 - Experimental lift curves for vane and single-slotted flaps (0.30c).

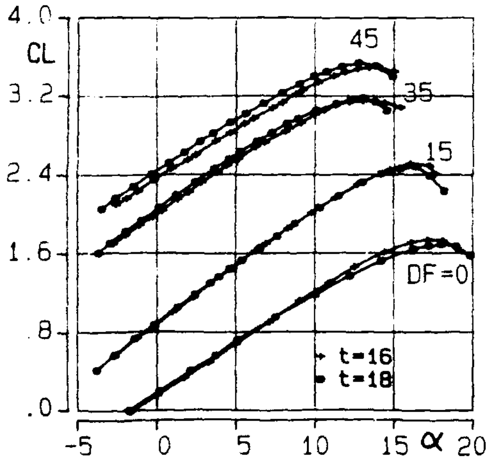

Fig.18 - Experimental lift curves for airfoils equipped with vane-flap system (0.30c); Re=5*10**6

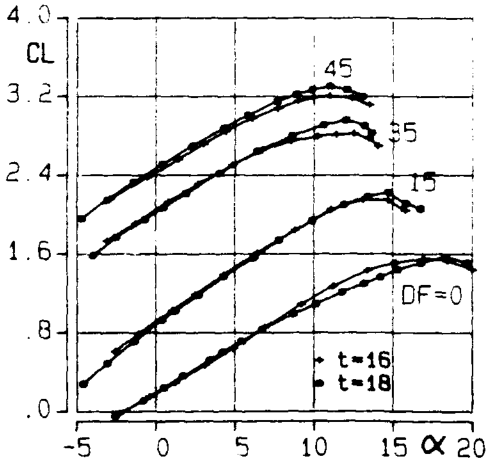

Fig.18 - (concluded) Re=1.5*10**6

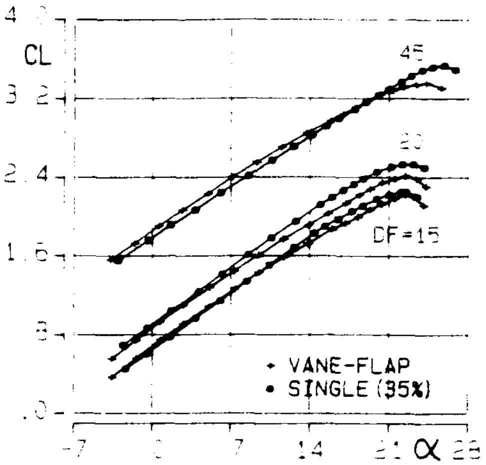

Fig.19 - Experimental lift curves for vane-aft (0.30c) and single-slotted (0.35) flaps.

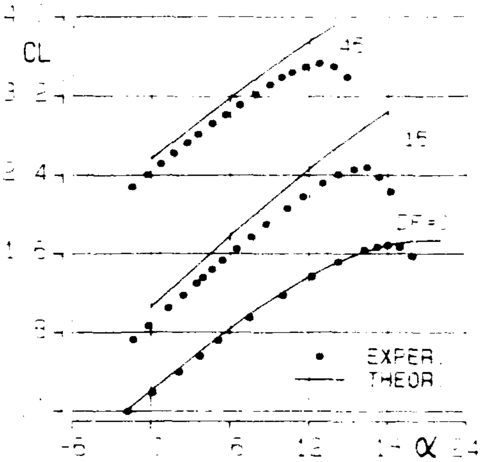

Fig.20 - Theoretical and experimental values of airfoil with vane-flap system (0.30c); a) Lift curves

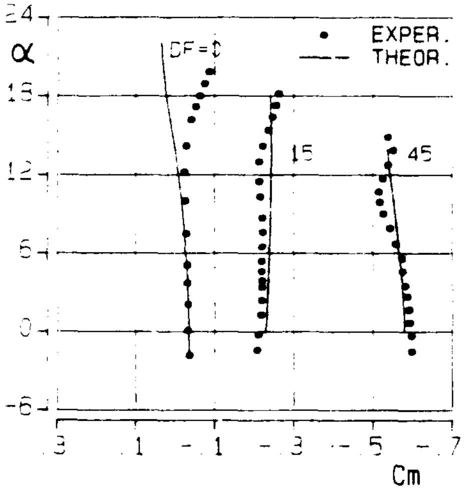

Fig.20 - (concluded) b) Pitching-moment curves

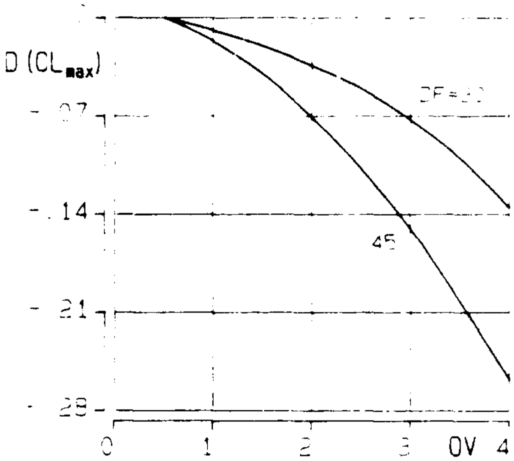

Fig.21 - Variation of aerodynamic characteristics of the aircraft versus overlap values.
a) Maximum lift coefficient

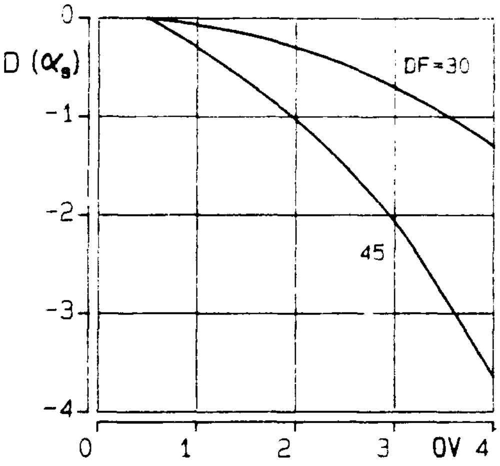

Fig.21 - (concluded) b) Stalling angle

ROUND TABLE DISCUSSION

Dr. D. Woodward, DRA, Farnborough, U.K.

We have now reached the end of the presentation of papers, and now we have come to the time when we attempt to pull together all lessons that have been learned and demonstrated during the week. It is my pleasure to chair this technical discussion session and introduce to you your technical evaluator.

Before I do that I would like to take a few minutes to give my personal impressions of what has happened here during this week. Unfortunately, I did not manage to hear all the presentations because I was away at committee meetings, but nevertheless the papers that I did hear, mainly yesterday afternoon and yesterday evening and on the first day, give me the feeling that the Symposium has achieved most of the objectives that Lou Williams and I set for it when we first put it together.

Firstly, the papers yesterday afternoon and today have showed, I believe, the many facets of the operation that influence the selection of the high-lift system. This morning Dr. Flaig showed clearly the reasons why the flap system on the A 320 had to be redesigned for the mission for A 321. Dr. Nark last night introduced to us all the other key features that have to come together in order to produce a successful STOL airplane. Dr. Mathews, yesterday afternoon, introduced the important features of the mechanical design of the flap system. Mr. Averado introduced to us this morning the special features associated with an amphibious aircraft.

The CFD papers earlier in the week demonstrated that we now have the capability to calculate the detailed flow around the high-lift system; not yet well enough to dispense with wind tunnel testing, but well enough to reveal key features of the flow which are quite difficult to measure experimentally. I was extremely surprised by the size and shape of the separation region beneath the slat cove. When we used to make calculations of pressure distributions back in the National High-Lift Program days, we couldn't calculate that separation region so we use to use engineering judgement and the french curve to draw what we thought was the sensible shape. I have to admit that having seen the measurements by Dr. Alemdaroglu and the Navier Stokes calculations, that we were a mile away from the shape that actually is there. It is much larger than I would have thought it was, and I found that particularly striking.

Thirdly, I was also pleased to see the general agreement that there seems to be now on the importance and the types of scale effect on high-lift systems and the importance of the Mach number effect. This is a message which we, from the 5 meter tunnel, have been giving out for some time now but it is nice to know that other people are getting similar results and drawing the same conclusions.

So let us now find out whether Don Whittley agrees with the things that I have said. I am sure he has much more to say, much more detailed and clear distinctions to draw than I have done. Don Whittley, who is your Technical Evaluator, began his technical life in England, (like many Canadians), at Saunders Roe on the Isle of Wight. Saunders Roe were well known manufacturers of flying boats; he tells me he used to ride on the towing carriage over a seaplane tank making measurements - an interesting experimental technique which I have not had the pleasure of experiencing myself. He came to Canada in 1947 and joined AVRO Canada. He worked on the C-102 jetliner, the CF-100 jet fighter and continued there until 1960 which coincided with the cancellation of the Arrow project. I remember that particularly well. It was about the time when I was coming towards the end of my apprenticeship at de Havilland of Hatfield in England. There were many people a year or two ahead of me who crossed the Atlantic to green fields to work for AVRO Canada on this high tech project and it all went rather sour. I can remember one chap who came back. He reacted very quickly to the cancellation and managed to put his house on the market and sell it about 3 or 4 days before everyone else had recovered from the shock. He managed to recover his money and set off again, whereas other people, I heard, found it much more difficult. So, that was a very traumatic time, I guess for AVRO Canada. He then joined de Havilland Canada and worked on powered lift for the rest of his career, working on the augmentor wing program and the ejector lift vector thrust program, which involved tests in the Ames 40 x 80 and 80 x 120 tunnel. He has previous links with AGARD, having been involved with the AGARD Advanced Aerosystems Study on AV-STOLdesignated AAS 14, and he worked on the flight research of the augmentor wing Jet-Stol airplane which also involved NASA Ames, and received for that work the McCurdy Award, which is the premier design award for the Canadian Aerospace Institute. So he is well qualified to evaluate the work that we have been doing here this week. So, now I invite you, Don Whittley, to tell us whether we made a good job of it or not.

Mr. D.C. Whittley, Canada

Mr. Chairman, Committee Members and Delegates. Contrary to what has been suggested, in fact I plan to keep my remarks quite short making just a few broad observations and thereby leaving as much time as possible for the Round Table Discussion. As we come to the close of 3 or 4 days of intensive deliberation relating to high lift, one thing I think is clearly evident, we are involved not only with high-lift, but also with high-tech. It is perhaps fair to say that there is more high-tech in high-lift than in any other aspect of aircraft design. Therefore, proportionally it demands a great deal of time and effort. What then makes it so high tech?

First we have the utter complexity of the fluid dynamics involved. At times it seems almost overwhelming, does it not? Hence, the need for highly sophisticated theoretical methods. Many of our speakers made reference to this complexity in the past few days.

Secondly, there is the demanding requirement placed on experimental facilities and flow measuring devices in order for results to be at all meaningful. Hence, the need for our high-tech facilities. What then justifies the time and effort? First, there is the crucial importance of getting this aspect of design correct the first time around because the consequences of a shortfall, relative to prediction, can be quite harmful. Then there is the knowledge that substantial benefit can result from improvements in high lift performance and/or simplification in design for the same performance. It was Dr. Meredith who gave us some trade-off figures in this respect.

Finally, there is the need to reduce the cost and time of the design process, or at least keep them within bounds. It is apparent that improvements in technology can help in all these respects.

Another broad observation concerns the close interrelation between theory and experiment associated with high-lift technology. CFD can provide an insight to the basic fluid dynamics involved and thereby help in the formulation of wind tunnel programs and in the interpretation of wind tunnel results. It seems to me in this sense that CFD becomes almost akin to flow viz. Similarly, advanced measuring techniques can detect unsuspected phenomena and in turn, lead to improvement in the CFD code. I think it was in one of the question and answer periods that someone pointed out that we are unlikely to see bigger and better wind tunnels in the foreseeable future. Therefore, we must make the best of what we have. I believe that the synergism which results from close association between theoretical and experimental work is the answer to this particular problem. Also, just yesterday, talking with Dr. Haines, he pointed out that it is not only the disciplines that need to interact: we have to ensure that those who understand the physics keep close to those who understand the mathematics. We may need to introduce some formal means, or perhaps should I say structured means to make this happen, rather than just getting together, as we have in this past week, once in a decade.

In terms of overall perspective we should be reminded that our High-lift Symposium this week has focussed largely on a particular segment of high-lift, namely, moderate to high aspect ratio transport aircraft. True, we had a brief glimpse at high-lift as it relates to combat aircraft, and in that respect we were reminded that this involves more than just takeoff and landing. Similarly, especially last night, a peek into the rather diverse world, and peculiar world perhaps, of powered lift. We might also note that we have not even discussed high-lift as it relates to the next generation SST. No doubt this and more would make good subject matter for some future conference, but the point I really wish to make is that conclusions drawn and recommendations made as a result of our meeting here in Banff would not necessarily hold true across the entire field. I myself happen to have certain rather fixed ideas about how one goes about verification of a powered-lift design.

That our High-lift Symposium here in Banff has been a great success is certainly without question. We have learned of marked progress in CFD methods since Brussels 1984, which was the last high-lift AGARD symposium, and this was apparent with respect to both viscid-inviscid interaction methods and full Navier Stokes solutions, all clearly at the cutting edge of the high-lift technology. We have learned of the increase in the use of pressured wind tunnels to isolate the effects of Reynolds number and Mach number, as our Chairman has just noted; of improvements in model testing methods, a better understanding of half-models for example; more careful correlation between tunnel and flight measurements; advanced measuring techniques to probe the basic fluid dynamics; the predominance of viscous effects and the need for a much better understanding. Apparently there have been a few surprises along the way since Brussels '84 in this last respect. We heard about high-lift technology in the workplace and the extent to which industry has adopted new methods, and we have seen that nothing is likely to replace a 3-D test of the final configuration at relatively high Reynolds number, and so on. These deliberations, it would seem, lead naturally to two key questions: firstly, how mature is transport high-lift technology as we find it today? That is to say, in terms of industrial use rather than scientific curiosity. Are we in fact now almost there, or is there still a long way to go? For example, at the Brussels meeting, I recall being much impressed by a paper in which Dillner and May described the CFD methods for high-lift design and analysis, which were already in daily use in the Boeing design office at that time.

Fairly comprehensive CFD methods were quite well established in industry in 1984. Since then, over the past 8 years, CFD methods and more careful testing have become growing and important ingredients of high-lift design procedures on a much broader front. Clearly, the adoption of such technologies to replace purely empirical methods is a transitional process and takes place in different ways in different places and to suit differing needs. I think the paper on the ATR 72 flap by P. Capbern of Aerospatiale was a good example of that, and our final paper today, by M. Averado similarly.

However, given that there are substantial performance gains yet to reap, and given that there remain lurking risks to be eliminated, and given that there are further economies to be made in terms of design, cost and time - all three most certainly true to some degree - my second question then would be: where should the emphasis and direction lie for the future with respect to both theory and experimentation?. A few of our speakers have already expressed some opinion in this regard also.

Finally, a word to the authors about my report. I have been asked by the Executive Committee to largely avoid a commentary paper by paper; that would simply make life too easy for me, but rather provide an overall assessment of the technical issues relating to high lift as a whole. In view of this, please do not feel spurned if your particular paper is not dealt with in my report in specific detail. So then, back to my two questions and then back to the Chair.

Firstly, "How mature is our transport high-lift technology as we find it today?" and secondly, "Where should the emphasis and direction lie for the future with respect to both theory and experiment?". I hope, Mr. Chairman, that some of our time can be spent this morning in response to these two questions.

Mr. L.J. Williams, NASA Washington, USA
Thank you. If anyone would have any comments or questions, we will be happy to take them.

Prof. Dr. G.E.A. Meier, DLR, Gottingen, Germany
I would like to make some comments from the point of view of a fluid dynamicist who has not too much experience in the field of technical applications, but I would like to summarize my impressions on the problems in our high-lift devices. First of all, I see a main problem in the 3-D effects which occur because we have swept wing problems, swept wings with end effects for all the details of flaps, slats, and so on. Then we have the 3-D structures of transition which have not been mentioned here, because in all our experiments we have to force transition and also in the calculation, but we get also 3-D effects from the transition to turbulence. The fourth thing I would like to mention are aeroelastic deformations which have not been tackled too much, but which I think also are a severe problem in experiments in flight tests.

Another major regime of problems is the flow separation. Here we have real deficits in knowledge about location and shape of separation bubbles and how to determine them theoretically. Then there is the influence of transition to flow separation; this influence is not quite clear, especially the Reynolds number problem which has been mentioned several times. Another point which has not come through very much is unsteady flow. I think a lot of these flow fields we have considered here in the conference are highly unsteady and cause flutter and in the transonic case also buffet. My feeling is that this is also causing a technical problem with material fatigue. Finally, the onset of stall and post stall is also something which has to be taken up.

So from this list of problems I have deduced what we have to do, a lot of work for fluid dynamicists. We have to provide, I think, more knowledge and fundamentals in unsteady compressible 3-D flows, we have to find good boundary layer models for these complicated flow fields; we have to tackle the 3-D separation and attachment problems; we have to think over advanced geometries for high-lift applications and we have also to make considerations about high Reynolds number flows. Finally, we need more knowledge about jet and swirl interactions with airfoil flaps, slats and so on. This is my list of problems, I have no solutions, but I think that it is worthwhile that fluid dynamicists accept and deal with these practical problems.

Mr. L.J. Williams, NASA Washington, USA
That was very good and appropriate. It looks like another subject for a symposium.

M. J. Bosquet, Aerospatiale
I would like to share the feeling I had during this conference taking the point of view of an aircraft manufacturer. I think the high-lift design seems to be largely dominated by experimental work. But it seems that there are two domains. The first one is represented by the wings which have very small or zero sweep angle; the other one by large sweep angle wings. For the first domain (small sweep angle), it seems that the 2-D calculations have enough accuracy to represent the flow, and in this case I got the feeling that what we call the Navier Stokes method seems to be almost ready to enter into the design team. I said almost ready because it seems that first, the problem of grid generation seems to be solved, then turbulence modelling is not completely solved, but it seems that it is sufficient to tune some coefficients and this could be good enough. The third problem is the computational time which seems not to be so high and could be sufficiently small enough for industrial applications. Then I expect that we will see in the near future Navier Stokes or large coupling methods enter into the industrial design field. In the second domain with large sweep I think that 2-D calculations are not sufficient enough because in the case of wings with large sweep angle, three dimensional boundary layer calculations are necessary. Two-D calculations are not very interesting. So in this case probably we will need for a long time very large wind tunnel facilities and a lot of work in the wind tunnels. But it seems that in this case coupling methods could be of interest.

Mr. A.B. Haines, ARA, UK

As Don Whittley said, we have come a long way since 1984, both in CFD and in the understanding of the flow over a wing with high-lift devices. But Dr. Woodward said when he was introducing this session, that there was a fair amount of data at high-lift available to study even before we decided to build a 5 metre tunnel in England and an F 1 tunnel in France. I think he posed the question whether we took the right decision. At that time, we were well aware that there were strong Reynolds number effects up to about 6 or 7 million and that there were not only Reynolds number effects, there were Mach number effects so that we needed a pressurized tunnel. We have seen plenty of examples of that in the last three days. But we have also seen examples of significant scale effects at Reynolds numbers above 6 or 7 million: scale effects which are not so understandable and are not so predictable. So, in an ideal world, we need tunnels for even higher Reynolds numbers. I think it was Mr. Meredith yesterday that we have got to fact the fact that we may not get these tunnels, and therefore, we must exploit CFD. I would like to make two points about whether that does meet the need.

First of all, I think if you are going to believe that, the CFD calculations for any particular case should be made for more than one Reynolds number. The disappointing thing to me in this conference is that when there have been CFD calculations, they have been made merely for one Reynolds number, either a model test Reynolds number or in one or two cases a full-scale Reynolds number. Now to repeat a calculation for more than one Reynolds number I am well aware means a significant amount of work because the transition mechanism as David showed the first morning may be very different full-scale and model scale. You don't just press a button and say that you will repeat the calculation putting in a different R. You have got to begin your thinking all over again and ask what is the transition mechanism, etc. I think that if the CFD people did a fair number of examples showing how results varied with Reynolds number with full understanding of the physics, we would learn quite a lot. It is a pity that at the moment, the CFD people have not shown any keenness to do this. They have not recognized that to do it for more than one Reynolds number is an important element, and that is where we are going to have to rely on CFD in the future if Mr. Meredith is right.

The second point is, "can we calculate the real situation?". Most of the CFD we have seen has been either for 2-D wings or at the best for 3-D wings where the wings are simple and the flow is reasonably quasi two-dimensional. I think that the CFD people should study one particular figure in Herr Flaig's paper this morning which drew attention to three problem areas on his aircraft. One was at the wing root, one was close to the wing-pylon-nacelle junction and one was near the tip. In none of those areas was the flow anything like two-dimensional. I have met young aerodynamicists who have said, "Ah, but if the aircraft designer was doing his job properly, there wouldn't be problem areas there. The whole wing would behave like quasi two-dimensional flow". But someone who says that completely misunderstands the aims of aircraft design. To have the whole wing stall at the same moment would be catastrophe. These areas where the flow is not 2-D are not necessarily problem areas. They are areas where by deliberate design you produce a premature stall or a late stall in order to get the correct stall development over the wing. So these are features of the flow that just must be calculated if we are going to do the job by CFD. Those are the two points I wanted to make. We are still a long way to go. We've gone from 1984 to 1992; 8 years to 2000. I think we need another conference before 2000.

Dr. D. Woodward
I just wanted to come back a little bit on the comments made by Professor Meier. He mentioned in particular unsteady flow. I think we need not to get ourselves in a position where we criticize too much what we have done here this week.

We didn't set out to cover vortex flows and vortex flaps and high-lift due to vortices because we had a conference on that only about a year ago. Then the other comment he made was that we hadn't done enough on transition. I suppose that one can't disagree - one has never done enough on transition. I think it is worth highlighting the fact that we have, during this symposium and previously, identified transition mechanisms which were regarded as somewhat academic 10 years ago -in particular the attachment line transition problem - and shown that this is a mechanism which occurs frequently at high Reynolds number and has major effects on the way the flow develops. So I think that we have gone some way in covering his comments on transition.

R. Bengelink, Boeing, Seattle, USA
I would like to make a couple of observations based on thinking about many of the presentations of this week also. Airplanes are designed by engineers. Engineering is not something we learn at school. We learn the foundational knowledge at school but engineering is something that we learn by practicing it over the years. We learn that we are to use the tools that are available to us to develop an insight into what is going on and as a result come up with an aerodynamic configuration that does the job better than has been done before. While there certainly has not, at least this week, been an adversarial relationship between those who are focussing on the CFD tools and those who are focussing on the experimental tools, there certainly continues to be an atmosphere of competitiveness. I would like to suggest that given the level of understanding that we have today with each of those tools that we have to develop more of a teamwork attitude. Today we do much better at being able to visualize the flow field than in calculating forces with CFD. From the wind tunnel side of things it is the other way around. The expensive and very difficult tests are those where we are trying to understand the flow field around the model, such as the three-dimensional features of so-called two-dimensional testing. I think that if both the computational and the experimental groups saw themselves as members of that same team, chartered to provide the tools necessary for a good engineer to be able to do his job properly and took that team approach; for example, how do we blend an ability to understand the flow field using CFD with the ability to understand what is happening to the measured forces on the model properly, we might find ourselves able to progress more rapidly. Until we get those flow models in our mind and act on themas engineers, we are not really going to make the kind of progress in developing airplanes that we should.

Prof. Ir. E. Obert, Fokker Aircraft BV, Netherlands
I would like to add a remark to what the previous speaker said. What struck me the past couple of days is that the people who are working on CFD and are very much involved in what is happening in the boundary layer often refer to turbulence models. That means they primarily consider turbulent boundary layers. We, as engineers, are interested in the question: When does the flow separate? It is assumed that separation will be more predictable due to a better representation of the flow physics by these turbulence models. That means CFD specialists talk about the question: When does the turbulent boundary layer separate? This suggests that $C_L$max is primarily determined by turbulent boundary layer separation, trailing edge separation.

I am aware that many of today's transport aircraft which have very large wing chords and consequently even in the stall operate at a fairly high Reynolds number reach $C_L$max through trailing-edge separation. However, I find it difficult to believe that leading edge stall, which we frequently see in the wind tunnel is completely irrelevant for full-scale aircraft. Having been on a number of stall tests myself on tufted F28's and F100's, my feeling is that leading edge stall is still an important physical phenomena for full-scale aircraft. I am aware that this matter is very difficult to tackle, even more difficult than answering the question, "When does trailing edge separation occur?", but I still think that we should be aware that that is an area that deserves attention.

Mr. B. Elsenaar, NLR, Netherlands
If I might continue a little bit along this line. I missed basic experimental contributions of the physics of high-lift problems. I am thinking about things like bubble bursts, about local separations, about mixing of wakes and boundary layers. We need building block experiments in that area to understand the physics. I didn't notice any paper that really addressed these topics. In addition to this I would like to mention that I think that in view of the very complicated physics essential to high-lift, I would rather see solutions of Navier Stokes equations for isolated parts of the flow field, to look into detail to the bubble developments, to separation, to the mixing of layers rather than applying Navier Stokes codes to complete multi-element airfoil configurations and to look at the final results in terms of pressure distribution. I think that the building block part was a little bit neglected in this conference.

Mr. L.J. Williams
I agree with that. We were hoping to get more papers along that line.

Mr. P. Capbern, Aerospatiale, Toulouse, France
In these three days we have seen a lot of comparisons between calculation and experiment, but there is something which appeared very clearly. Everybody tried to compare $C_L$max level from their calculations to experiment, but we have hardly seen any result of comparison for drag. I think that if $C_L$max is often the key issue for a project, there are some projects, and they are not so rare, where the lift to drag ratio in the second segment climb is more important than $C_L$max itself. So there is perhaps a message for people involved in method development that they should try to validate their methods for drag prediction. I know it is a very hard job, but we should try to do that especially with a far field condition and not only by integrating the pressure field and the skin friction field on the shape itself. I am convinced that some interesting investigations could be achieved and therefore, it was a message I would like to send to those people.

Mr. L.J. Williams
I think it is a very good message and a challenge.

D. Ashill, DRA, Bedford, UK
Barry Haines has already highlighted the importance of understanding scale effects at high Reynolds numbers, and we have had a number of presentations during the last few days on attachment line transition and re-laminarization indicating their significance.

I would like to mention another possible scale effect which is that even after the flow becomes turbulent close to the leading edge, the turbulent boundary layer will locally have quite a low Reynolds number, let us say based on momentum thickness. This is another potential source of unpredictable scale effects which I think people need to take into account, either theoretically or in interpreting their wind tunnel test data.

Prof. J.W. Slooff, NLR, Netherlands
I would like to add a little to what several of the preceeding speakers have said about the physics of the flow; that relatively little attention was paid to that, and also to Pat Ashill's remark on things that may happen at the leading edge. It would seem, given the fact that little attention was paid to the physics of high-lift systems, that if we understand everything about the various mechanisms of stall. I am not quite convinced that that is the case. For example, I am aware of at least three different types of leading edge stall mechanisms: short bubble and long bubble bursting, and a third variant which I call turbulent leading edge stall. I believe the notion of the latter was introduced at the former high-lift meeting of the Fluid Dynamics Panel. There we have a situation with a laminar separation bubble followed by reattachment, transition at or around reattachment, and a turbulent boundary layer with a very steep adverse pressure gradient right after the bubble in which the friction coefficient goes through zero locally when the angle of attack is increased. It is very difficult to discriminate between this kind of turbulent leading edge stall and a bubble bursting type stall. I have not seen anything of such nature at this symposium. Moreover, I think, now turning to CFD, that it will take quite some time before CFD codes will be able to discriminate between the various types of leading edge stall, or other types of stalls for that matter. The details of the flow mechanisms, in the leading edge area in particular, are such that, apart from the problems with local turbulence and transition modelling, we also have a resolution problem in the sense that we will need very, very small meshes in order to resolve all the phenomena. CFD for high-lift, even in two dimensions, will not be mature until we are able to discriminate between the various types of physical phenomena.

Another point that I would like to make or bring to your attention is the possibility of exploiting the third dimension as I call it. On three dimensional wings we have part-span flaps and slats, with a lot of vortices coming off all the edges. These may give rise to, e.g., higher induced drag levels than we would like. It has occurred to me that there may be a point in investigating whether flap track fairings and the like could serve the dual purpose of covering the gear and mechanisms and of promoting a more orderly type of flow at the flap edges. For example in such a way that they lead to a lower level of induced drag, in the same sense as a winglet works at the tip of a wing. One might, perhaps also get a little increase in $C_{L}max$, because you have smaller losses at the flap edges. I would like to see some research of this nature in the future. I have the feeling that there may be some benefit in there.

Mr. L.J. Williams
I think that that is a very good comment. Carrying that even further I would like to see some work that combines the high-lift system with the wake vortex problem, trying to eleviate that while getting lower induced drag.

Dr. D. Woodward
There are two comments I would like to make. One is related to what Prof. Obert was saying. It is certainly true that some full-size aircraft are assailed with a leading edge stall behavior. The British Aerospace Hawk certainly has a leading edge stall. This has been shown by doing oilflows in flight and when the airplane lands you can still see the oilflow in the bubble. The second involves another important detail of the flow on which we haven't seen any work - and this is related to the compressibility effect on high-lift systems. If you actually do the calculation in 2-D of the external flow around a high-lift airfoil, you find that the supersonic patch, which we all have identified from the surface pressure distribution, is only some 10 to 12 boundary layer thicknesses high. This is very different from the transonic shock wave boundary layer interaction and there must be a much larger interaction of the boundary layer on the shock pattern. In addition, of course, it is normally a shock interaction with a laminar boundary and not a turbulent one. This is quite an unknown flow field and since the key feature is very small, I don't know how the experimentmight be conducted.

Mr. F. Kafyeke, Bombardier Canadair, Canada
I would like to make two comments from an airplane manufacturer's point of view. First, I would like to know if the experimental research that has been shown here, the national high-lift program in the UK, or the Garteur program in Europe, will eventually find its way into data sheets which can help designers in a preliminary design phase of an airplane. Secondly, can someone talk about the effects of things like slat gaps and steps and the sealing of slats and the effect on the overall performance of the real airplane. I wonder if some research has been done in that area.

Mr. L.J. Williams
That sounds like a good question for Dr. Woodward to address.

Dr. D. Woodward
Unfortunately, I think that the answer is very simple, it is no to the first question. For the reason that despite all the work we did, it is still not enough to form what one would be happy to see as a data sheet on which people might base preliminary designs. We actually spent quite a long time trying to analyse the drag, for instance. Now, bearing in mind, of course, that most of the work that we did was on that end-plate model, we faced very great difficulty in trying to extract meaningful drag data from that model. I don't know whether you had a chance to read the written paper, but we set out originally saying that there was no problem about this, we can do a wake traverse the same as we do in 2-D flow, and this will tell us what the drag is. Unfortunately, because of the large trailing vorticity, the drag calculated this way varies downstream very rapidly as the wake gets stretched out, so we gave up that idea and then we decided to try to subtract the induced drag from the force balance measurements. Some people believed that they could do that and others were more skeptical. I don't think that we really managed to get anything other than comparative data on the drag in particular.

When it comes to maximum lift, maybe you could do something, but you need to do a lot more variations in flap and slat design than we did. We did two slat chords and a range of Krugers, but there are a lot of other questions that still were not answered by that data set and we were doing that work for 6 to 7 years. It slowed down towards the end because the funding was reduced, but it still took a long time to gather. A larger data set would require a correspondingly larger investment of time and money. I would have to pass the question on sealing to either someone from Boeing or Airbus because I do not know the answer to that. Anybody got any comments?
No one is prepared to say. I think that sealing is a great problem, but I don't have any very practical experience of it.

Prof. Dr. Ir. J.L. Van Ingen Delft University, Netherlands

I don't have a comment but a question. The question of the preceding speaker was, "will these basic things find their way into data sheets". A question to the designers might be, "do you need data sheets in the future or can we come as far as providing computer programs which are reasonably accurate to be used as a design tool". To me, my first reaction is that these data sheets are something of the past, but I am not a designer, so I think they should react to that.

Prof. Ir. E. Obert, Fokker Aircraft
Although hesitating to react, being a representative from one of the smaller companies, I am strictly speaking for myself, not for the whole design community. I think that we should distinguish between different phases. Before an aircraft, or a program, gets a full-scale development go-ahead, one needs, in the pre-feasibility/feasibility study phase, to be able to look at many different configurations to go through a large number of design loops in a fairly short time. I think the general complaint concerning many computer programs is that they are too cumbersome for day-to-day use. In particular, when you want to have accurate results, you have to incorporate many details in the representation of the configuration. Consequently, yes, I think data sheets in one way or another (data bases, data compilations) will be required in the future as well, but in the first place for the initial design phase. When you continue in that development process, you will concentrate more and more on a specific configuration that you want to optimize and then of course you will have to go to more elaborate processes like using complicated computer programs and complicated wind tunnel models.

Dr. J. McCroskey, NASA Ames Research Center, USA
Just a short comment to respond to David Woodward's question about experimental techniques for looking at these little bubbles and shock wave boundary layer interactions. Many of you will remember that maestro of flow visualization, Henri Werlé at ONERA, who, about 25 years ago, introduced the idea to study leading edge bubbles in a small water tunnel by taking the leading edge of an airfoil and terminating it with a blown flap, to be able to generate high suction on the leading edge. With this configuration, he was able to increase the size of the model by approximately a factor of 10. I have thought many times that this should be a useful technique in other types of investigations. I proposed it for dynamic stall investigations on airfoils, but it seems to me that this would be a technique of use in a compressible high subsonic wind tunnel.

Mr. A. B. Haines
Sorry to appear again, but I wanted to respond to the gentleman in the front who wanted evidence on the effects of caps and sealing of slats. There was quite a lot of work done about 1965 in the development of the Super VC 10 on that subject. Broadly speaking, of course, a great deal of work has been done by various people on steps, ridges, gaps, by testing these on the walls of wind tunnels including the 8 foot tunnel at DRA Bedford. The results on the slats was consistent with these general results provided you took account of the fact that the local Mach numbers in the cruise could be very high, in the neighborhood of where the back end of the slat fitted on the upper surface. Also, you could do quite a lot of damage to the wave drag, so it is not just a case of a serious effect on the viscous drag. You can quite modify the development of the supercritical region and so the issue is important. But you won't find the data, because no one wants to admit to having done it badly. When the slat is a good fit, the effects are trivial.

Prof. S. De Ponte, Politecnico, Italy
Everybody has discussed computation of two-dimensional flows, but I have never seen a two-dimensional separation bubble, for example. I have seen straight separation lines, straight attachment lines, but three-dimensional flow inside the bubble. I have never seen a two-dimensional separation. So I wonder why we compare calculation with measurements in which we suppose the flow is two-dimensional, but we measure three-dimensional flow in real mesurements. How can we compare these facts or how can two-dimensional calculations be reliable?

Mr. B. Elsenaar, NLR
The question of two-dimensionality has been worrying a working group of AGARD that had to select test cases for CFD validation during the last couple of days. But the problem I think is probably more severe in transonics than it is in subsonic flow. That is my personal view and I would like to explain it a little bit. One thing is that two-dimensional separation bubbles, laminar separation bubbles, can be easily visualized on a two-dimensional airfoil. That is not a problem, they are there. From the point of view of the turbulent separation that starts on the flap or on the main airfoil, it's possible to keep the flow two-dimensional in my view with side-wall blowing or side-wall suction. I watched numerous experiments (I am only familiar with the blowing technique that we apply at NLR) where the blowing was such that you could actually see the stall of the airfoil. You could visualize this by putting tufts on the flap, and on the main airfoil and you could really see the complete airfoil stall at a certain point. So, I think that two-dimensionality can be realized in an experiment. There is one critical remark that I would like to make. That is the use of fairings and brackets to attach the slat and the flap to the main airfoil. They introduce wakes and these wakes will introduce a kind of displacement in the boundary layer and in the wake downstream. To derive drag from two-dimensional airfoils by means of the wake-rake technique, therefore might be more cumbersome and more troublesome. The determination of drag for two-dimensional airfoils is, I think, both from the theoretical point and from the experimental point a rather difficult thing to do. It is still one of the basic questions that remains open for the future.

Prof Ir. E. Obert, Fokker, Netherlands
The question of why we are interested in research on two-dimensional airfoils and how good we can really realize two-dimensional flow should be coupled to the question of what you are looking for. From the point of view of the designer you are looking for maximum accuracy in the prediction of certain targets, certain goals. If on high aspect ratio wings with not too much sweep, a knowledge of two-dimensional flow, how imperfect it may be, can help you in strengthening your belief in your final prediction, then I think the designers are quite happy. If there are discrepancies between real flow and theory, we accept that, but it is better than nothing.

Mr. B. Eggleston, de Haviland, Canada
Just coming back to the comment about large flap brackets, as a user of large flap brackets, I am naturally sensitive. We have done some interesting work where in fact we tested the models flaps up with the brackets in place. Then to get a handle on the penalty due to the flap brackets, we put inserts in and repeated the test. They are significant. There is no doubt that if you want good two-dimensional flow you don't leave those large flap brackets on. Interestingly enough though, you may still want to have some of the gaps that are present in the flap system when it is retracted. There can be minor leakages through the gaps of the flap system that can attach flow right at the back. You can see significant changes in drag. How you set that arrangement up without having brackets is an interesting challenge and you might think about how you are going to do it.

Prof. R.J. Kind, Carleton University, Canada
I am a little surprised that we haven't heard more of a plea for better turbulence modelling. I think that it is fair to say that if we had a perfect turbulence model, which isn't really in sight, all we need to do is put it into the Navier Stokes equations and we can solve more or less anything. The numerical methods are coming along very well. To me it seems that one of the key areas where the fundamental people have to focus more attention is on turbulence models. Most of what we saw in this meeting was either mixing length type models, Baldwin and Lomax and so on, or K-epsilon models, that is, two-equation models. I think that many of us are aware that even the two-equation models have quite serious shortcomings; they are limited to certain categories of flow and you have to tune the constants and so on. I would put in a plea, as Dr. Elsenaar did, for more building block type of experiments whose focus is on improving the turbulence models.

Another comment on the matter of two-dimensional or three-dimensional separated flows. I too worry about the notion of a two-dimensional separation bubble. We know that, at least in a lot of cases and depending somewhat on aspect ratios, cavity flows tend to be inherently three-dimensional, even if we suck the end-walls and all the rest. Nevertheless, I think two-dimensional experiments or nominally two-dimensional experiments are the way to go in developing turbulence models, at least initially. If we can't do it in two-dimensional flows, we certainly can't do too well in three.

Dr. D. Woodward
Can I just make a comment on the separation bubble issue. With some research done at Queen Mary College, London, starting with an unswept short separation bubble which was induced on a plate by an external pressure distribution and then this plate was swept around to 30 degrees. In fact, the flow development normal to the leading edge is exactly the same in both cases.

So, at least for a short separation bubble, the addition of sweep, in fact does induce significant flow along the bubble in the reattachment region, but the actual size and the shape of the bubble is not changed; it is exactly the same normal to the leading edge. This underlines the fact that two-dimensionality may actually be an abstract concept which doesn't exist precisely, pedantically in reality, but nevertheless is a very useful engineering concept.

Mr. L.J. Williams
At the risk of giving an answer that some of us may not want to hear, I would like to ask Ted Nark if what he has seen the last few days would have changed the design of the YC 14.

Dr. T.C. Nark, Boeing, USA

I am afraid I have no information that addresses the kind of problems associated with that powered lift configuration. For example, our half-model testing was developmental in nature. We used it for investigating differences between candidate configurations, recognizing that there might be some error in the absolute value. Understanding that we had a design schedule, we did the best we could with the tools available at the time. If the task had been to design the "best" powered lift system, I would have needed better engineering tools than were then available. By using testing rather than analysis I accepted the inadequacies of testing and made use of the benefits. That was the time in the program when if you didn't get the job accomplished today, there would be no airplane tomorrow. You now have the capability of developing new tools that would have made my job easier in the past and will make the same job easier in the future.

Prof. Dr. Ir. J.L. Van Ingen, Delft University

I wanted to comment on the issue of 2-D separation bubbles. I think I have watched more low speed separation bubbles in my life than anybody else in the audience. Indeed, if you look at a separation bubble filled with smoke, even if it is nominally 2-D, you see 3-D flows. Of course, where you see it is in the low momentum parts of the bubble, and these apparently are not determining the overall shape. If you use a 2-D calculation for a separation bubble, you get more or less the right answers.

Prof. Ir. E. Obert

Dr. Woodward mentioned at the beginning of this conference that there are certain phenomenae which have misunderstood in the past or have been described in a certain erroneous way which then are passed on from generation to generation for decades, for example, the fact that a leading edge slot or a flap slot re-energizes a boundary layer. I would like to share an experience that I went through when I was collecting material for my lecture notes. That concerns the stalling characteristics of high aspect ratio swept wings. From our initial experiences and observations in the late 1940's we have come up with this picture that highly swept slender or high aspect ratio swept wings produce tip stall, if you have more or less the same airfoil section and not too much twist. This is caused by an outward flow of the boundary layer. Consequently, the tip stalls much earlier than you would expect on the basis of the equivalent two-dimensional flow situation. I found an NACA report from the 1950's (NACA RM A52A10) where tests on the following half model were reported.

NACA RM A52A10

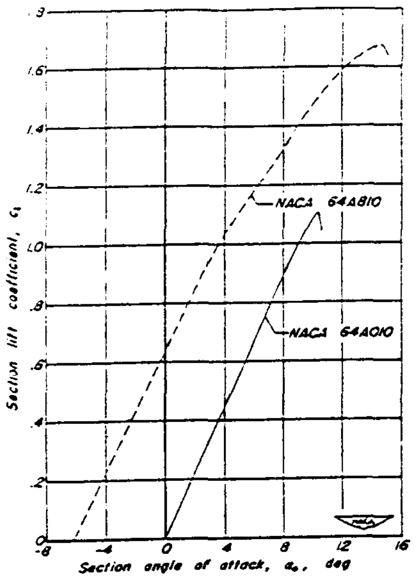

Lift characteristics of the two airfoil section models.

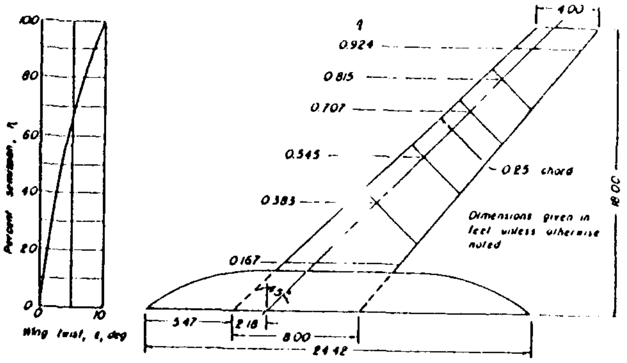

Dimensions of the semispan wing-fuselage models including the orifice station locations and the twist distribution for the cambered, twisted wing.

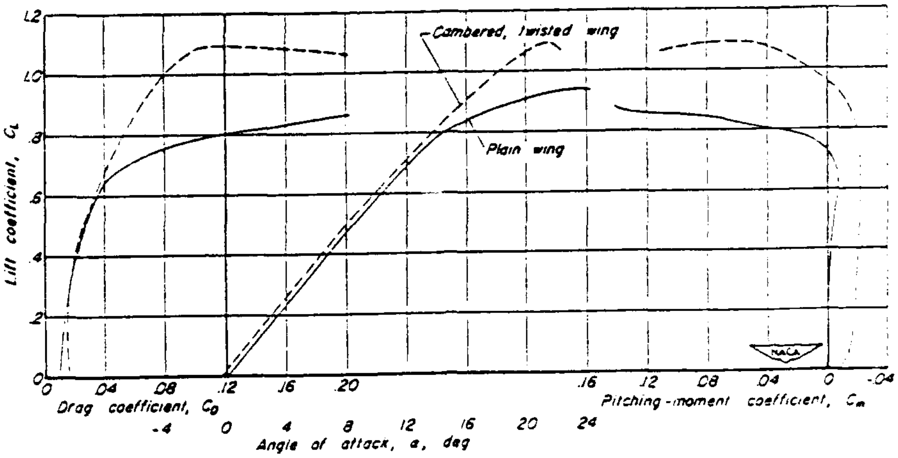

Drag, lift, and pitching-moment characteristics of the two wing models.

Relation between section and wing maximum lift coefficient. (I)

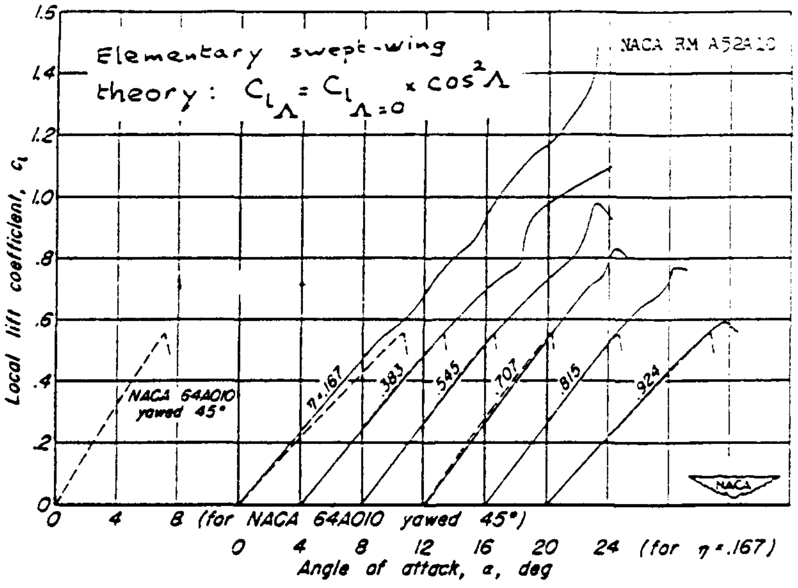

(a) Plain wing.

Figure 8.— Comparisons of local lift curves on the wing models with those derived from two-dimensional data and span loading theory.

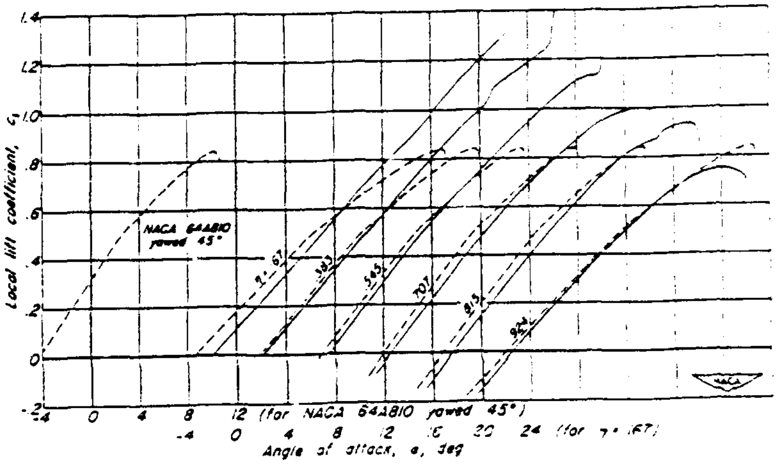

(b) Cambered, twisted wing

Relation between section and wing maximum lift coefficient. (11)

As you see, there were a number of wing sections equipped with pressure tapping. This wing was tested in two shapes, one as a flat wing with NACA 64A010 airfoil section and another one based on a highly cambered airfoil section NACA 64 A810, a design lift coefficient of 0.8 and highly twisted. If one now looks at the C_L-alpha curves for the various sections one sees that at the tip the C_L-alpha curve is very similar to the equivalent curve in sheared two-dimensional flow whereas further inboard the C_L-alpha curves continue to much higher angles-of-attack. In other words, the tip stall is not caused because the tip stalls earlier than what one would expect, but the tip stall occurs because the inboard wing keeps attached flow much longer than you would expect, apparently by some sort of boundary layer removal on the inboard wing. I think most of us still tell our younger collaborators and students the original story. That is what I wanted to share with you concerning high lift characteristics on swept wings.

Mr. L.J. Williams
Thank you for that insight. Now are there any other comments? I would just like to wrap it up with a couple of comments. Although I agree with David that we achieved the objectives that we had in mind when this Symposium was conceived two and a half years ago, we never intended that this Conference be anything more than a status report on the development of high-lift system aerodynamic technology. We never expected that it would be the final say on the matter. I think with that in mind I would like to see this be a Symposium that happens about every five years so that we could follow the developments in high-lift technology and perhaps even speed it up. One of the things that we would like to have seen in this Symposium a little more than we did are some new innovative ideas. With that in mind I would like to ask Don Whittley to give us a feeling for what Zurakowski would have said if he was with us today.

Mr. D.C. Whittley
I happen to be sharing a few past experiences with Lou Williams the other day about the very famous test pilot Janus Zurakowski. I don't know how many of you know of Janus Zurakowski. Does that name mean anything? Just a few. He was a Polish fighter pilot during the Battle of Britain and after the war he became Assistant Chief Test Pilot at Gloucester Aircraft. As such he was doing a lot of flight testing on the Gloucester Meteor, which you may remember was one of the early twin engine jet fighter aircraft. Zurakowski invented one of the only new manoeuvres since the Immelmann turn. This was actually written up in TIME magazine. His aerobatics were known as Zurabatics. The aerobatic manoeuvre he performed was known as the Zura cartwheel. He would take the Meteor aircraft and climb vertically to zero speed: once the aircraft reached zero speed he would cut one engine and the airplane would do a cartwheel, go into a spin and come down, all within the immediate vicinity of the airfield. This was performed at the Farnborough Airshow on a number of occasions. He left the U.K. and joined the team of AVRO Canada, flying CF 100's and he was the pilot to fly first the CF 105 supersonic delta-wing fighter. He was always a very ingenious kind of a guy and very interested in the technical background to the flying program. He had bright blue eyes and a deep stare and a ruddy complection. Very often he would come into my office and with a twinkle in his eye and in a very high pitched Polish broken accent he would say, "anything new or funny". This rather tickled Lou, as I had been sharing with him the idea that we hadn't really looked at very much here in Banff which is really new or funny (such as the vortex flap, for instance), but maybe one of these days we can.

Mr. L.J. Williams
Maybe the ideas are out there but people are just too embarrassed to bring them forward in this particular setting. Maybe in the bar later. At this point I would like to thank Kazik in particular for suggesting this as a venue for this Symposium. I think a lot of the success of the Symposium is due to the venue, the Hotel is perfect, the size of the conference room is perfect, the accommodations were excellent, and it was amazing that even with the outstanding scenery and the restaurants in the area, I would have to say that the fact that we have had a full attendance for the whole Symposium validated the dedication of the attendees more than anything else. At this point I would like to turn it over to our FDP Chairman.

Prof. Ir. J.W. Slooff
Thank you, Lou. Ladies and Gentlemen, this is the end of three and a half very interesting days. It is my duty to bring it, with some reluctance, to an official end. I think the days were interesting in the technical as well as the recreational sense that Lou already hinted at.

This meeting and its success would not have been possible without the hard work and help of several people. First of all, I also would like to thank our Canadian hosts for inviting us here and in particular the local, but not so very local, coordinator, Dr. Kazik Orlik-Ruckemann and his co-panel member also from Canada, Prof. Dick Kind for selecting this site, Banff, and its Park Lodge with its excellent facilities. Kazik and Dick, please convey our thanks to the Canadian National Delegates and thank you personally for bringing us here and exposing us to the beauty of the Canadian Rockies and its National Parks. We certainly will remember the ice fields, Lake Louise, the elk and the moose and the squirrels and the chipmunks.

Switching to the primary reason for our presence here, that is our meeting on High-Lift Aerodynamics, I would like to compliment the Program Committee with the success of the meeting. In particular, of course, Dr. David Woodward and Dr. Lou Williams for their initiatives and efforts. We also thank Dr. Whittley for his on-the-spot technical evaluation of the meeting, which is a very hard thing to do. We are certainly looking forward to your written report on the meeting. Thank you very much.

Thanks are also due to a number of people that have assisted us to run the meeting smoothly. At the desk we were assisted by two charming ladies Mrs. Alison Day and Mrs. Sarah Pearson. We were assisted by a team of interpreters who very often, I am sure, had the difficult job of keeping up with the pace of some of our speakers. I would like you to applaud also for Teresa Beauregard, Susan Ourion, Carol Savard and Madeleine Terrien. There is also the technician for the audio visual aids. We thank Jason Penner for serving our eyes and ears. Last but not least I would like to thank our Executive, Winston Goodrich and his secretary, Anne-Marie Rivault for their indispensable and as usual highly successful efforts to run the meeting smoothly.

Finally, I would like to draw your attention to some of the future activities of the Fluid Dynamics Panel. Our next meeting is in Winchester on "Computational and Experimental ssessments of Jets in Cross-Flow". We have a fall meeting in Brussels next year on "Wall Interference Support and Interference in Flow Measurements" and we have a number of Special Courses planned that you can also see on this vu-graph. In this rapidly changing world the mission and task of NATO with AGARD in its wake, are in the process of reorientation and are subject of discussion. I am sure that you will agree with me that AGARD has a very good reason to continue its work in the spirit of this past week. Perhaps with a little reorientation here and there, and perhaps a little redirection of emphasis or attention, but certainly not in a disruptive way. You can support AGARD by disseminating the information on this vu-graph and the message of AGARD in general. I might add that as a result of the changing world, we will, in all probability, have at our fall meeting in Brussels, the first contribution from a scientist from the former Soviet Union. That is something that, I am sure, we are all looking forward to.

This really is the end. Thank you all for your patience and for your personal contributions to the success of this Symposium. I hope that you will be able to stay a few days longer to further enjoy the Rockies. I wish you all a safe journey home.

REPORT DOCUMENTATION PAGE

1. Recipient's Reference	**2. Originator's Reference** AGARD-CP-515	**3. Further Reference** ISBN 92-835-0715-0	**4. Security Classification of Document** UNCLASSIFIED UNLIMITED

5. Originator
Advisory Group for Aerospace Research and Development
North Atlantic Treaty Organization
7 Rue Ancelle, 92200 Neuilly sur Seine, France

6. Title
HIGH-LIFT SYSTEM AERODYNAMICS

7. Presented at
the 71st Fluid Dynamics Panel Meeting and at the Symposium held in Banff, Alberta, Canada, 5th—8th October 1992.

8. Author(s)/Editor(s) Various	**9. Date** September 1993
10. Author's/Editor's Address Various	**11. Pages** 508

12. Distribution Statement
There are no restrictions on the distribution of this document. Information about the availability of this and other AGARD unclassified publications is given on the back cover.

13. Keywords/Descriptors

High lift devices
Aerodynamics
Design
Flaps — control surfaces
Leading edge slats
Wing slots
Boundary layer control
Model tests
Wind tunnel tests

14. Abstract

The AGARD Fluid Dynamics Panel (FDP) sponsored a Symposium on "High-Lift System Aerodynamics" which was held 5th—8th October 1992 in Banff, Alberta, Canada. This report includes the 32 technical papers developed for the Symposium along with an edited transcript of the Round Table Discussion held at the end which addressed issues raised during the Symposium. In addition, the Technical Evaluation Report — aimed at assessing the success of the Symposium in meeting its objectives and its relevance to the technical needs of the aerospace community — is also included in this document.

The Symposium objectives were to address:

(1) how, given the role and configuration of an aircraft, the most appropriate high-lift system can be selected,
(2) how, having selected a type of high-lift system, an efficient detailed design can be produced, and
(3) the experimental and analysis techniques which are necessary to explore and enhance the performance of a high-lift system.

Thus, although the aerodynamics of high-lift systems was the dominant theme, the very pertinent aspects of weight, simplicity, reliability, and structural and mechanical integrity were an integral part of the Symposium, and were treated in the papers presented. In this sense, this Symposium has attempted to take a broader view of the high-lift system than has been taken by similar conferences in the past.

AGARD Conference Proceedings 515
Advisory Group for Aerospace Research and
Development, NATO
HIGH-LIFT SYSTEM AERODYNAMICS
Published September 1993
508 pages

The AGARD Fluid Dynamics Panel (FDP) sponsored a Symposium on "High-Lift System Aerodynamics" which was held 5th—8th October 1992 in Banff, Alberta, Canada. This report includes the 32 technical papers developed for the Symposium along with an edited transcript of the Round Table Discussion held at the end which addressed issues raised during the Symposium. In addition, the Technical Evaluation Report — aimed at assessing the success of the Symposium in meeting its objectives and its relevance to the technical needs of the aerospace community — is also included in this document.

P.T.O.

AGARD-CP-515

High lift devices
Aerodynamics
Design
Flaps — control surfaces
Leading edge slats
Wing slots
Boundary layer control
Model tests
Wind tunnel tests

AGARD Conference Proceedings 515
Advisory Group for Aerospace Research and
Development, NATO
HIGH-LIFT SYSTEM AERODYNAMICS
Published September 1993
508 pages

The AGARD Fluid Dynamics Panel (FDP) sponsored a Symposium on "High-Lift System Aerodynamics" which was held 5th—8th October 1992 in Banff, Alberta, Canada. This report includes the 32 technical papers developed for the Symposium along with an edited transcript of the Round Table Discussion held at the end which addressed issues raised during the Symposium. In addition, the Technical Evaluation Report — aimed at assessing the success of the Symposium in meeting its objectives and its relevance to the technical needs of the aerospace community — is also included in this document.

P.T.O.

AGARD-CP-515

High lift devices
Aerodynamics
Design
Flaps — control surfaces
Leading edge slats
Wing slots
Boundary layer control
Model tests
Wind tunnel tests

AGARD Conference Proceedings 515
Advisory Group for Aerospace Research and
Development, NATO
HIGH-LIFT SYSTEM AERODYNAMICS
Published September 1993
508 pages

The AGARD Fluid Dynamics Panel (FDP) sponsored a Symposium on "High-Lift System Aerodynamics" which was held 5th—8th October 1992 in Banff, Alberta, Canada. This report includes the 32 technical papers developed for the Symposium along with an edited transcript of the Round Table Discussion held at the end which addressed issues raised during the Symposium. In addition, the Technical Evaluation Report — aimed at assessing the success of the Symposium in meeting its objectives and its relevance to the technical needs of the aerospace community — is also included in this document.

P.T.O.

AGARD-CP-515

High lift devices
Aerodynamics
Design
Flaps — control surfaces
Leading edge slats
Wing slots
Boundary layer control
Model tests
Wind tunnel tests

AGARD Conference Proceedings 515
Advisory Group for Aerospace Research and
Development, NATO
HIGH-LIFT SYSTEM AERODYNAMICS
Published September 1993
508 pages

The AGARD Fluid Dynamics Panel (FDP) sponsored a Symposium on "High-Lift System Aerodynamics" which was held 5th—8th October 1992 in Banff, Alberta, Canada. This report includes the 32 technical papers developed for the Symposium along with an edited transcript of the Round Table Discussion held at the end which addressed issues raised during the Symposium. In addition, the Technical Evaluation Report — aimed at assessing the success of the Symposium in meeting its objectives and its relevance to the technical needs of the aerospace community — is also included in this document.

P.T.O.

AGARD-CP-515

High lift devices
Aerodynamics
Design
Flaps — control surfaces
Leading edge slats
Wing slots
Boundary layer control
Model tests
Wind tunnel tests

The Symposium objectives were to address:

(1) how, given the role and configuration of an aircraft, the most appropriate high-lift system can be selected,
(2) how, having selected a type of high-lift system, an efficient detailed design can be produced, and
(3) the experimental and analysis techniques which are necessary to explore and enhance the performance of a high-lift system.

Thus, although the aerodynamics of high-lift systems was the dominant theme, the very pertinent aspects of weight, simplicity, reliability, and structural and mechanical integrity were an integral part of the Symposium, and were treated in the papers presented. In this sense, this Symposium has attempted to take a broader view of the high-lift system than has been taken by similar conferences in the past.

ISBN 92-835-0715-0

The Symposium objectives were to address:

(1) how, given the role and configuration of an aircraft, the most appropriate high-lift system can be selected,
(2) how, having selected a type of high-lift system, an efficient detailed design can be produced, and
(3) the experimental and analysis techniques which are necessary to explore and enhance the performance of a high-lift system.

Thus, although the aerodynamics of high-lift systems was the dominant theme, the very pertinent aspects of weight, simplicity, reliability, and structural and mechanical integrity were an integral part of the Symposium, and were treated in the papers presented. In this sense, this Symposium has attempted to take a broader view of the high-lift system than has been taken by similar conferences in the past.

ISBN 92-835-0715-0

The Symposium objectives were to address:

(1) how, given the role and configuration of an aircraft, the most appropriate high-lift system can be selected,
(2) how, having selected a type of high-lift system, an efficient detailed design can be produced, and
(3) the experimental and analysis techniques which are necessary to explore and enhance the performance of a high-lift system.

Thus, although the aerodynamics of high-lift systems was the dominant theme, the very pertinent aspects of weight, simplicity, reliability, and structural and mechanical integrity were an integral part of the Symposium, and were treated in the papers presented. In this sense, this Symposium has attempted to take a broader view of the high-lift system than has been taken by similar conferences in the past.

ISBN 92-835-0715-0

The Symposium objectives were to address:

(1) how, given the role and configuration of an aircraft, the most appropriate high-lift system can be selected,
(2) how having selected a type of high-lift system, an efficient detailed design can be produced, and
(3) the experimental and analysis techniques which are necessary to explore and enhance the performance of a high-lift system.

Thus, although the aerodynamics of high-lift systems was the dominant theme, the very pertinent aspects of weight, simplicity, reliability, and structural and mechanical integrity were an integral part of the Symposium, and were treated in the papers presented. In this sense, this Symposium has attempted to take a broader view of the high-lift system than has been taken by similar conferences in the past.

ISBN 92-835-0715-0

NATO OTAN
7 RUE ANCELLE · 92200 NEUILLY-SUR-SEINE
FRANCE
Télécopie (1)47.38.57.99 · Télex 610 176

DIFFUSION DES PUBLICATIONS
AGARD NON CLASSIFIEES

Aucun stock de publications n'a existé à AGARD. A partir de 1993, AGARD détiendra un stock limité des publications associées aux cycles de conférences et cours spéciaux ainsi que les AGARDographies et les rapports des groupes de travail, organisés et publiés à partir de 1993 inclus. Les demandes de renseignements doivent être adressées à AGARD par lettre ou par fax à l'adresse indiquée ci-dessus. *Veuillez ne pas téléphoner.* La diffusion initiale de toutes les publications de l'AGARD est effectuée auprès des pays membres de l'OTAN par l'intermédiaire des centres de distribution nationaux indiqués ci-dessous. Des exemplaires supplémentaires peuvent parfois être obtenus auprès de ces centres (à l'exception des Etats-Unis). Si vous souhaitez recevoir toutes les publications de l'AGARD, ou simplement celles qui concernent certains Panels, vous pouvez demander à être inclu sur la liste d'envoi de l'un de ces centres. Les publications de l'AGARD sont en vente auprès des agences indiquées ci-dessous, sous forme de photocopie ou de microfiche.

CENTRES DE DIFFUSION NATIONAUX

ALLEMAGNE
Fachinformationszentrum,
Karlsruhe
D-7514 Eggenstein-Leopoldshafen 2

BELGIQUE
Coordonnateur AGARD-VSL
Etat-Major de la Force Aérienne
Quartier Reine Elisabeth
Rue d'Evere, 1140 Bruxelles

CANADA
Directeur du Service des Renseignements Scientifiques
Ministère de la Défense Nationale
Ottawa, Ontario K1A 0K2

DANEMARK
Danish Defence Research Establishment
Ryvangs Allé 1
P.O. Box 2715
DK-2100 Copenhagen 0

ESPAGNE
INTA (AGARD Publications)
Pintor Rosales 34
28008 Madrid

ETATS-UNIS
National Aeronautics and Space Administration
Langley Research Center
M/S 180
Hampton, Virginia 23665

FRANCE
O.N.E.R.A. (Direction)
29, Avenue de la Division Leclerc
92322 Châtillon Cedex

GRECE
Hellenic Air Force
Air War College
Scientific and Technical Library
Dekelia Air Force Base
Dekelia, Athens TGA 1010

ISLANDE
Director of Aviation
c/o Flugrad
Reykjavik

ITALIE
Aeronautica Militare
Ufficio del Delegato Nazionale all'AGARD
Aeroporto Pratica di Mare
00040 Pomezia (Roma)

LUXEMBOURG
Voir Belgique

NORVEGE
Norwegian Defence Research Establishment
Attn: Biblioteket
P.O. Box 25
N-2007 Kjeller

PAYS-BAS
Netherlands Delegation to AGARD
National Aerospace Laboratory NLR
P.O. Box 90502
1006 BM Amsterdam

PORTUGAL
Força Aérea Portuguesa
Centro de Documentação e Informação
Alfragide
2700 Amadora

ROYAUME UNI
Defence Research Information Centre
Kentigern House
65 Brown Street
Glasgow G2 8EX

TURQUIE
Milli Savunma Başkanlığı (MSB)
ARGE Daire Başkanlığı (ARGE)
Ankara

Le centre de distribution national des Etats-Unis (NASA/Langley) ne détient PAS de stocks des publications de l'AGARD.
D'éventuelles demandes de photocopies doivent être formulées directement auprès du NASA Center for Aerospace Information (CASI) à l'adresse suivante:

AGENCES DE VENTE

NASA Center for
Aerospace Information (CASI)
800 Elkridge Landing Road
Linthicum Heights, MD 21090-2934
United States

ESA/Information Retrieval Service
European Space Agency
10, rue Mario Nikis
75015 Paris
France

The British Library
Document Supply Division
Boston Spa, Wetherby
West Yorkshire LS23 7BQ
Royaume Uni

Les demandes de microfiches ou de photocopies de documents AGARD (y compris les demandes faites auprès du CASI) doivent comporter la dénomination AGARD, ainsi que le numéro de série d'AGARD (par exemple AGARD-AG-315). Des informations analogues, telles que le titre et la date de publication sont souhaitables. Veuiller noter qu'il y a lieu de spécifier AGARD-R-nnn et AGARD-AR-nnn lors de la commande des rapports AGARD et des rapports consultatifs AGARD respectivement. Des références bibliographiques complètes ainsi que des résumés des publications AGARD figurent dans les journaux suivants:

Scientifique and Technical Aerospace Reports (STAR)
publié par la NASA Scientific and Technical
Information Program
NASA Headquarters (JTT)
Washington D.C. 20546
Etats-Unis

Government Reports Announcements and Index (GRA&I)
publié par le National Technical Information Service
Springfield
Virginia 22161
Etats-Unis
(accessible également en mode interactif dans la base de données bibliographiques en ligne du NTIS, et sur CD-ROM)

Imprimé par Specialised Printing Services Limited
40 Chigwell Lane, Loughton, Essex IG10 3TZ